Ecological Informatics 53 (2019) 100980

Contents lists available at ScienceDirect

Ecological Informatics

journal homepage: www.elsevier.com/locate/ecolinf

Estimation of growth regulation in natural populations by extended family of growth curve models with fractional order derivative: Case studies from the global population dynamics database

Amiya Ranjan Bhowmick[a], Tridip Sardar[b], Sabyasachi Bhattacharya[c,*]

[a] Department of Mathematics, Institute of Chemical Technology, Mumbai 400019, India
[b] Department of Mathematics, Dinabandhu Andrews College, 54, Raja S. C. Mallick Road, Baishnabghata, 24 Parganas (South), West Bengal, India
[c] Agricultural and Ecological Research Unit, Indian Statistical Institute, 203, B. T. Road, Kolkata 700108, India

ARTICLE INFO

Keywords:
Memory
Population time series
Return rate
Posterior distribution
Model selection

ABSTRACT

Estimating the trend in population time series data using growth curve models is a central idea in population ecology. Several models, mainly governed by differential or difference equations, have been applied to real data sets to identify general growth pattern and make predictions. In this article, we analyze ecological time series data by fitting mathematical models governed by fractional differential equations (FDE). The order of the FDE (α) is used to quantify the evidence of memory in the population processes. The application of FDE is exemplified by analyzing time series data on two bird species *Phalacrocorax carbo* (Great cormorant) and *Parus bicolor* (Tufted titmouse) and two mammal species *Castor canadensis* (Beaver) and *Ursus americanus* (American black bear) extracted from the global population dynamics database. Five different population growth models were fitted to these data; density-independent exponential, negative density-dependent logistic and θ-logistic model, positive density-dependent exponential Allee and strong Allee model. Both ordinary and fractional derivative representations of these models were fitted to the time series data. Markov chain Monte Carlo (MCMC) method was used to estimate the model parameters and Akaike information criterion was used to select the best model. By estimating the return rate for each of the time series, we have shown that populations governed by FDE with a small value of α (high level of memory) return to the stable equilibrium faster. This demonstrates a synergistic interplay between memory and stability in natural populations.

1. Introduction

The relationship between per capita growth rate and population size/density, termed as density dependence, is a central issue in ecological theory and a long debated one in the literature (Turchin, 2003). It is used to make predictions of natural populations and to analyze management options in many areas including conservation (Turchin, 2002), pest management (Turchin, 1994), risk assessment (Gerber et al., 2004) and many others. Several mathematical models are calibrated using counts or harvest data and try to extract information about the deterministic trend in population trajectory (Eberhardt et al., 2008). Several internal and external effects (mainly physiological and environmental, repectively) on the biological system have been considered to develop new models. Recently, many researchers are interested to investigate the influence of memory on the population dynamics. This manuscript deals with the analysis of population time series data by using mathematical models which contain a parameter quantifying the evidence of memory.

Different studies have found that memory plays important role for behavioral changes in animals, e.g. cooperation. Chimpanzees are highly suggestive to share episodic memory and baboons use their memory of recent interactions to make inferences (Cheney, 2011). Hence, it is indicative that memory based actions affect several aspects of population behavior that are directly correlated with population growth rates. Populations with higher ability to learn from previous experiences are more likely to have a better survival prospect. So far our knowledge is concerned, no studies have been done to understand the growth of natural population based on the abundance data that takes into account the effect of memory. In this paper, we assume that the observed population abundance is a function of some memory based ecological/behavioral characteristics, such as migration, predator avoidance, mate location, refuge activities etc. We present a new method to analyze ecological time series data by fitting mathematical models governed by fractional differential equations (FDE).

* Corresponding author at: Department of Mathematics, Institute of Chemical Technology, Mumbai 400019, India.
E-mail address: sabyasachi@isical.ac.in (S. Bhattacharya).

https://doi.org/10.1016/j.ecoinf.2019.100980
Received 22 August 2018; Received in revised form 27 June 2019; Accepted 4 July 2019
Available online 06 July 2019

In experiments related to learning and memory are usually considered as rats, pigeons and some primate species as the study subjects, but the psychological assessment and corresponding inferences are generally similar across species or contexts (Healy and Jones, 2002). Song learning in passerine and imprinting in precocial birds are two important examples of learning and memory [see reviews in Catchpole and Slater, 2008; Bolhuis and Honey, 1998]. For example, Godard (1991)'s experiment showed that male songbirds can even remember their neighbors from previous years. Repeating the experiment, it was confirmed that the bird Hooded warblers were able to remember the position of previous years and responds accordingly. More importantly, the long term memory effect is closely associated with the breeding cycle (Godard, 1991), which is an important correlate of growth rate of the species. There could be many factors related to memory that can potentially influence the population growth rates.

Memory is an integrated part of living organisms whatever primitive it is in nature. In biological systems memory is stored as a series of information gathered during the course of past and present events, inducing an episodic memory (Clayton and Dickinson, 1998) and it generally helps in making future decisions (Clayton et al., 2001). Studies on blood feeding mosquitoes (including *Aedes aegypti*) revealed the fact that mosquitoes did not feed randomly on host blood, but they used their prior experience about a host location and a host defensiveness to select a host to feed on (McCall and Kelly, 2002). Some examples of memory based actions on a long time scales are: (1) aquatic zooplankton exhibited memory-based phenomenological responses: small changes in the environment induce morphological defence organs such as helmet formation and the development of spines through cyclomorphosis (Black and Slobodkin, 1987). (2) Optimal foraging, group hunting, prey refuge, prey switching, anti–predator defence etc. These fundamental ecological phenomena, distributed over almost all living species, are examples of memory based actions.

In particular mate choice and foraging are two well studied components in behavioral ecology, where memory and learning ability have been explored significantly. It has been observed that many times female birds have chosen their mates during breeding season based on the memories of previous choice. Examples of such evidences are growing (Catchpole and Slater, 2008). Significance of memory and past experiences have been explicitly considered to analyze the animal movement data (Dalziel et al., 2008; Smouse et al., 2010). Optimal foraging theory has enriched the state of the art of memory based behavioral ecology in both laboratory and field studies. By incorporating learning and memory (including error making) in the optimal foraging framework the models provided a significant improvement in making accurate predictions of foraging behavior than the previous models (Stephens and Krebs, 1986). Memory based actions have been suggested as possible explanation for the paradox of enrichment, which remained a paradox in ecological literature creating several sparkling discussions (Rana et al., 2013). There are several evidences available that strengthen the correlations between population dynamics and memory based actions not only in ecology and epidemiology but in other disciplines as well e.g. earthquake study (Zheng et al., 2012).

Memory based actions affect several aspects of population behavior that are directly correlated with population growth rates. Populations with higher ability to learn from previous experiences are more likely to have a better survival prospect. To understand the growth dynamics of populations growth models are fitted to the time series data of population abundances. Several deterministic and stochastic models have been used to describe the population dynamics accurately. In addition, there are several statistical approaches available to identify the forms of growth model in time series data but, there is no single test appeared that outcompetes the others (Fox and Ridsdill-Smith, 1995). Hence, development of novel modeling approaches to describe the population dynamics has always been warranted.

If the population has a non-overlapping generation, differential equations adequately describe the growth over time (Murray, 2002). Fractional derivatives have been used as a mathematical tool to describe the memory and the hereditary properties of various materials and processes (Caputo and Mainardi, 1971). In other words, fractional dynamic systems, in application, can adequately represent some long-term memory and non-local effects that are typical for many anomalous processes (Datsko and Luchko, 2012). Recently, Bolton et al. (2014) proposed a fractional Gompertz growth model that gave important insights in analyzing the growth of tumour data. The authors used the data on the volumes of Rhabdomyosarcoma tumors in mice for calibration of the proposed model and found that the fractional order model gave better fitting than the first order Gompertz model.

In this work we extended some existing growth models to incorporate memory by fractional order derivatives. We have chosen some common growth models which have been used successfully to detect density dependence in population ecology. Our biological motivation to develop such extended family was that we assumed the observed population abundance is a function of memory. Results are compared with the prediction capability of the models with ordinary differential counterpart. Different sections of the manuscript are described as follows: (1) we first provide the details of the growth curve models considered for time series analysis; (2) development of fractional order formulation of these models to incorporate memory in the population dynamics and (3) analysis of time series data from global population dynamics database using both ODE and FDE models.

2. Materials and methods

2.1. Population growth models

Several models have been developed and tested in ecological literature to model density dependent regulation and the relationship between abundance and growth that emerges as one of the primary goals of population ecology (Clutton-Brock et al., 1997; Sibly et al., 2005). In this manuscript the choice of growth models were inspired by the work of Gregory et al. (2010) who fitted six population growth models to population time series data to assess the form of density dependence using multi-model inference technique. We added one more candidate, the θ-logistic model that has been widely used as a model for density dependent growth regulation (Sibly et al., 2005). In the following we provide details of the models considered with relevant information from the literature.

The oldest candidate in modeling of population regulation is the exponential law, starting point of the elucidation of population ecology. This model is characterized by a constant per capita growth rate and the population size grows unboundedly over time,

$$\frac{dN}{dt} = rN \tag{1}$$

where r is the intrinsic growth rate and $N(t)$ represents the population size at time t, assumed to be a continuously differentiable function of t. The simplest candidate of the (negative) density dependent population regulation is characterized by the logistic growth model, where population is bounded by the environmental carrying capacity (K) (Verhulst, 1838).

$$\frac{dN}{dt} = rN\left(1 - \frac{N}{K}\right) \tag{2}$$

The θ-logistic model (Gilpin et al., 1976; Gilpin and Ayala, 1973) defines a general class of models of density regulation as function of only a single parameter θ that regulates the density dependent mechanism. In this model framework, the population is assumed to have maximum fitness when they are small in numbers. As population size

increases, per capita growth rate decreases monotonically, due to intra-specific competition being main regulatory mechanism (unlike Allee model, see below). The θ-logistic model is given by:

$$\frac{dN}{dt} = rN\left[1 - \left(\frac{N}{K}\right)^{\theta}\right] \tag{3}$$

The Allee effect, named after ecologist W. C. Allee, corresponds to density mediated drop in population fitness when they are small in numbers (Allee, 1931; Dennis, 1989; Fowler and Baker, 1991; Stephens and Sutherland, 1999). The harmful effects of inbreeding depression, mate limitation, predator satiation etc. reduce fitness as the population size decreases. In such populations, the maximum fitness is achieved by the species at an intermediate population size, unlike logistic or theta-logistic growth models. In recent decades, due to increasing number of threatened and endangered species, the Allee effect has received much attention from conservation biologists. Related theoretical consequences and the empirical evidences have made the Allee effect an important component in both theoretical and applied ecology. In general two types of Allee effects have been observed in the natural populations across a variety of taxonomic groups, viz. component and demographic Allee effect. The component Allee effect modifies some component of individual fitness with the changes in population sizes or density. If the per capita growth rate is low at small density but remains positive, is called the weak demographic Allee effect. The strong Allee effect is characterized by a threshold density below which the per capita growth rate is negative and in such a situation if the population size falls below the threshold, the extinction is deterministic. The critical density is called the Allee threshold and has significant importance in conservation biology (Hackney and McGraw, 2001), population management (Liermann and Hilborn, 1997; Myers et al., 1995) and invasion control (Johnson et al., 2006). There are a large number of studies available in the literature on the mathematical modeling of the demographic Allee effect (see Table 3.1 Courchamp et al. (2008)).

We have considered the following two models demonstrating the Allee effect in species growth profile; exponential Allee (model (4)) and strong Allee (model (5)). In the exponential Allee growth model, which assumes a constant per capita growth rate independent of population size unless a critical lower Allee threshold (A) exists, above which growth rate may be depressed and below which growth rate is negative (Eq. (4)).

$$\frac{dN}{dt} = r(N - A) \tag{4}$$

$$\frac{dN}{dt} = rN\left(1 - \frac{N}{K}\right)\left(\frac{N}{A} - 1\right) \tag{5}$$

2.2. Extension of existing growth models

Fractional differential equations have been used in the literature to incorporate memory in the population growth model. Fractional calculus deals with differentiation and integration of arbitrary order. It was originated almost in the same time when Newtonian or Leibniz calculus appeared. It was developed through the pioneering work works of many mathematicians of 18^{th} and 19^{th} centuries. However, the research activities in applied sciences has increased significantly after the appearance of the classic book by (Oldham and Spanier, 1974). For the sake of completeness, we present a brief introduction of the fractional calculus in Appendix A. In this manuscript, the fractional counterpart of the growth curve models have been considered. The models are listed below:

$$\frac{d^{\alpha}N}{dt^{\alpha}} = rN \tag{6}$$

$$\frac{d^{\alpha}N}{dt^{\alpha}} = rN\left(1 - \frac{N}{K}\right) \tag{7}$$

$$\frac{d^{\alpha}N}{dt^{\alpha}} = rN\left[1 - \left(\frac{N}{K}\right)^{\theta}\right] \tag{8}$$

$$\frac{d^{\alpha}N}{dt^{\alpha}} = r(N - A) \tag{9}$$

$$\frac{d^{\alpha}N}{dt^{\alpha}} = rN\left(1 - \frac{N}{K}\right)\left(\frac{N}{A} - 1\right) \tag{10}$$

where $\alpha \in (0, 1]$. For each of the above equations, we have discussed the stability of different equilibria. We have also studied the existence and uniqueness of the solutions for the models (8), (9) and (10) (B). Results corresponding to the models (7) and (6) can be considered as a subcases of the models (8) and (9), respectively (corresponding to $\theta = 1$ and $A = 0$, respectively). It is to be noted that for fractional order models (6–10) unit of the growth rate constant (r) is (time$^{-\alpha}$) (Dokoumetzidis et al., 2010).

2.3. Data source

Global population dynamics database (GPDD) contains more than 5000 time series on population abundances obtained from various forms of population surveys. It has provided an opportunity for ecologists to study population dynamical patterns over a wide range of taxa (Inchausti and Halley, 2001). This is a large collection of animal and plant population data throughout the world covering in total 1896 taxonomic groups, collected from more than one thousand different locations. The GPDD version2.0 is available as a database on Microsoft Access platform that can be downloaded from http://www.sw.ic.ac.uk/cpb/cpb/gpdd.html.

We selected GPDD because it has been widely studied focusing many aspects of population dynamics, e.g., extinction risks (Brook and Bradshaw, 2006; Saha et al., 2013), population cycles (Murdoch et al., 2002), fisheries management (Saha et al., 2013) and effects of weather (Knape and de Valpine, 2012). Sibly et al. (2005) undertook an ambitious study of this problem by examining population growth rates using 1780 time series of 674 species of four taxonomic groups, namely, birds, mammals, bony fishes and insects from the GPDD (NERC Centre for Population Biology, 2010). Their analysis gave rise to several discussions and criticism addressing the shape of density dependence (Getz and Lloyd-Smith, 2006; Ross, 2006, 2009) and the strength of density regulation (Brook and Bradshaw, 2006; Sibly et al., 2007; Ziebarth et al., 2010). However, no unified conclusion has been achieved so far. Bhowmick et al. (2015) recently proposed a model of cooperation and calibrated the model by using the data from GPDD.

To apply the fractional order models to real data, we considered four population time series data on mammals and birds (two from each group). These four species was taken as test bed species only. Statistical methods, described in the manuscript, can be extrapolated for other species data as well. All the species have been selected from different taxonomic groups. The reason for choosing mammals and birds' data sets is that they have documented to have memory effect. The bird species are *Phalacrocorax carbo* (Great cormorant, GPDD ID 9330) and *Parus bicolor* (Tufted titmouse, GPDD ID 1197) and the mammal species are *Castor canadensis* (Beaver, GPDD ID 200) and *Ursus americanus* (American black bear, GPDD ID 116). These species were chosen as they are well studied and reliable source of information are available. Great cormorants are one of the most widespread of cormorant species, with a cosmopolitan distribution. Great cormorants are found throughout Europe, Asia, Africa, Australia, and in north–eastern coastal North America. The mating system is monogamous and the great cormorant pairs may return to the same nest site year after year if they had

Table 1
Estimated parameters of the ten growth curve models (1–5, 6–10) for the population *Parus bicolor (1197)*. α and θ are dimensionless quantities. Units of K, A and $N(0)$ are counts of breeding pairs, according to the source available in GPDD. Units of r are time^{-1} and $\text{time}^{-\alpha}$ for ODE and FDE models respectively.

Parameters	α	r	K	θ	A	$N(0)$
ODE						
Exponential model (1)		0.0520 (0.0160 – 0.0917)				4.0628 (2.0484 – 6.4670)
Logistic model (2)		0.2159 (0.0256 – 1.0774)	181.7146 (7.3728 – 1685.0057)		–	
θ-logistic model (3)		0.0575 (0.0168 – 0.1414)	50090.9129 (9.5693 – 143551.4790)	50.3862 (2.0983 – 205.8189)	–	
Exponential allee model (4)		0.0663 (0.0120 – 0.1502)			2.4882 (0.0941 – 6.7666)	4.9443 (2.7290 – 7.5668)
Strong allee model (5)		0.4593 (0.0313 – 1.6581)	10.9609 (1.1953 – 32.1082)		3.3749 (0.1090 – 13.0608)	3.7662 (0.9381 – 7.7814)
FDE						
Exponential model (6)	0.5945 (0.1479 – 0.9804)	0.04643 (0.01 – 0.0908)				3.0485 (0.9008 – 5.9343)
Logistic model (7)	0.5787 (0.1411 – 0.9743)	0.0467 (0.0101 – 0.0937)	4797.4381 (188.0180 – 9731.6450)			2.9867 (0.8786 – 5.7036)
θ-logistic model (8)	0.5882 (0.1299 – 0.9762)	0.04065 (0.0071 – 0.08291)	5122.40 (251.50 – 9782.7067)	494.8687 (22.8519 – 980.4699)		3.1770 (1.0306 – 6.1045)
Exponential allee model (9)	0.6091 (0.1514 – 0.9807)	0.062 (0.0050 – 0.1491)			2.5806 (0.0976 – 7.8017)	4.4074 (1.7469 – 7.995)
Strong allee model (10)	0.5925 (0.13 – 0.9775)	0.5293 (0.0145 – 1.7854)	7.9485 (1.0362 – 19.4459)		6.9732 (0.8256 – 19.0423)	4.5344 (1.6899 – 9.009)

successful breeding at that site before. Populations in the western Atlantic and Europe have increased, with some range expansion, in the last 50 years (Animal Diversity Web). Related description of the data of other species (e.g. habitat information, taxonomic details, data source, sampling protocol etc) can be obtained from NERC Centre for Population Biology (2010).

2.4. Estimation of parameters

We used the analytical solutions of the differential equations to estimate the model parameters. Exact solutions of the ODE models (1), (2), (3), (4) and (5) are given as follows

$$N(t) = N(0)e^{rt} \tag{11}$$

$$N(t) = \frac{K}{1 + \left(\frac{K}{N(0)} - 1\right)e^{-rt}} \tag{12}$$

$$N(t) = \frac{K}{\left[1 + \left(\left(\frac{K}{N(0)}\right)^{\theta} - 1\right)e^{-r\theta t}\right]^{\frac{1}{\theta}}} \tag{13}$$

$$N(t) = A + (N(0) - A)e^{rt} \tag{14}$$

$$N(t) = \frac{N(0)\left(Ke^{\frac{r(K-A)t}{K}} - A\right) + AK\left(1 - e^{\frac{r(K-A)t}{K}}\right)}{N(0)\left(e^{\frac{r(K-A)t}{K}} - 1\right) + K - Ae^{\frac{r(K-A)t}{K}}} \tag{15}$$

where, $N(0)$ is the initial population size.

There is no method available in the literature to find the exact solution of the systems (7), (8) and (10). Some analytical approximate techniques are available to solve the non-linear fractional order differential equations, (see Bhalekar and Daftardar-Gejji (2012), Daftardar-Gejji and Jafari (2006), He (1999), etc). For example, the New Iterative Method proposed in Daftardar-Gejji and Jafari (2006) was found to be very useful in many applications in different areas (Oldham and Spanier, 2006). In this manuscript, we solve fractional order Eq. (6), Eq. (7), Eq. (8), Eq. (9), and Eq. (10) using predictor-corrector method of Adams-Bashforth-Moulton studied by Diethelm and Freed (1999). Stability, convergence and accuracy of the method were studied by Diethelm et al. (2004) and Garrappa (2010).

The following parameters have been estimated from the data: (i) species growth rate 'r'; (ii) carrying capacity 'K' (except for the models (1), (4), (6) and (9)); (iii) The shape parameter 'θ' (for models (3) and (8)); (iv) Allee threshold 'A' (for models (4), (5), (9) and (10)); (v) order of the fractional derivative 'α' (for models (6), (7), (8), (9) and (10)) and (vi) initial population size $N(0)$ for all the models.

For biological feasibility all parameters were assumed to be positive and Allee threshold parameter was less than $N(0)$ (initial population size). If the starting population is below the Allee threshold, it is bound to go to extinction. The order of the fractional derivative, $\alpha \in (0, 1]$. The growth curve models (1–5) and (9–10) were fitted to the aforesaid data. Let ϵ be the error of fit which follows additive independent Gaussian distribution having an unknown variance σ^2.

$$y_t = N(t, \widehat{\theta}) + \epsilon, \quad \epsilon \sim \mathcal{N}(0, \sigma^2) \tag{16}$$

where $\widehat{\theta} \in \mathbb{R}^M$ contains all unknown parameters in each of the ten models. $N(t, \widehat{\theta})$ is the expected population size which is the given by the solution of growth models. We assumed independent Gaussian prior specification for $\widehat{\theta}$:

$$\theta_i \sim \mathcal{N}(\nu_i, \eta_i^2), \quad i = 1, 2, ..., M. \tag{17}$$

and Gamma distribution as the prior for the inverse of the error variance:

$$p(\sigma^{-2}) \sim \Gamma\left(\frac{n_0}{2}, \frac{n_0 S_0^2}{2}\right). \tag{18}$$

The prior parameter choices were obtained by least square minimization (Haario et al., 2006). The complete estimation procedure along with the MATLAB codes is available in the supporting material. The prior parameters ${S_0}^2$ and n_0 in (18) can be interpreted as the prior mean for σ^2 and the prior accuracy as imaginary observations, respectively. The likelihood function $p(y|\theta, \sigma^2)$ for R observations for growth

Table 2
Estimated parameters of the ten growth curve models (1–5, 6–10) for the population *Phalacrocorax carbo (9330)*. α and θ are dimensionless quantities. Units of K, A and $N(0)$ are counts of breeding pairs, according to the source available in GPDD. Units of r are time^{-1} and $\text{time}^{-\alpha}$ for ODE and FDE models respectively.

Parameters	α	r	K	θ	A	$N(0)$
ODE						
Exponential model (1)		0.07 (0.059 – 0.0812)				120.5447 (99.3715 – 143.2207)
Logistic model (2)		0.1443 (0.0898 – 0.1973)	715.5304 (508.1377 – 1456.1154)			85.6943 (60.3964 – 115.7219)
θ-logistic model (3)		0.0942 (0.0811 – 0.1087)	451.1438 (428.002 – 476.9457)	62.8039 (9.7443 – 113.4992)		94.1537 (78.2484 – 110.58)
Exponential allee model (4)		0.0769 (0.0621 – 0.0992)			27.039 (0.8039 – 86.057)	127.6083 (104.5703 – 154.2854)
Strong allee model (5)		0.3505 (0.1601 – 0.6118)	514.9943 (454.4874 – 656.5636)		88.9049 (16.1260 – 133.6725)	108.5726 (75.9020 – 137.7764)
FDE						
Exponential model (6)	0.4801 (0.1218 – 0.9526)	0.0571 (0.0405 – 0.0742)				78.0441 (27.5911 – 129.4571)
Logistic model (7)	0.6506 (0.2378 – 0.9865)	0.1351 (0.0781 – 0.2017)	1286.5490 (544.9771 – 2955.4162)			65.6722 (28.1819 – 101.6318)
θ-logistic model (8)	0.8133 (0.7469 – 0.8368)	0.09007 (0.08448 – 0.09337)	465.5037 (465.4912 – 465.5365)	436.8106 (436.7592 – 437.1093)		81.4272 (81.3459 – 81.8412)
Exponential allee model (9)	0.4490 (0.1162 – 0.8884)	0.0625 (0.0437 – 0.0844)			22.7124 (0.3248 – 76.2133)	86.5371 (34.3407 – 138.5)
Strong allee model (10)	0.7557 (0.3625 – 0.9923)	0.1236 (0.0168 – 0.3391)	497.7417 (445.3613 – 584.4442)		86.6796 (35.3406 – 133.6595)	122.7608 (97.1807 – 150.7289)

Table 3
Estimated parameters of the ten growth curve models (1–5, 6–10) for the population *Castor Canadensis (200)*. α and θ are dimensionless quantities. Units of K, A and $N(0)$ are counts of all individuals, according to the source available in GPDD. Units of r are time^{-1} and $\text{time}^{-\alpha}$ for ODE and FDE models respectively.

Parameters	α	r	K	θ	A	$N(0)$
ODE						
Exponential model (1)		0.0324 (0.0274 – 0.0379)				166017 (133387 – 200942)
Logistic model (2)		0.1120 (0.0743 – 0.1541)	729134 (640597 – 886731)			66976 (32932 – 110497)
θ-logistic model (3)		0.6117 (0.1036 – 2.05)	825594 (669316 – 1218112)	0.2632 (0.02418 – 0.93)		58155 (22324 – 108774)
Exponential-allee model (4)		0.0345 (0.02828 – 0.0429)			29182 (756.4629 – 96353)	175026 (140941 – 213927)
Strong allee model (5)		0.1397 (0.0946 – 0.2105)	699850 (627689 – 801937)		31795 (1382.06 – 77551)	74989 (42020 – 98382)
FDE						
Exponential model (6)	0.3273 (0.1089 – 0.7804)	0.0245 (0.01818 – 0.0318)				82455 (33508 – 160230)
Logistic model (7)	0.4874 (0.1525 – 0.9435)	0.1295 (0.0632 – 0.2356)	1451448 (721551 – 3271701)			37343 (6206.69 – 91931)
θ-Logistic model (8)	0.5271 (0.1356 – 0.9551)	0.0860 (0.0443 – 0.1642)	868752 (633907 – 1404015)	5.1085 (0.6417 – 26.9163)		46773 (13155 – 91518.69)
Exponential allee model (9)	0.3254 (0.1077 – 0.7714)	0.0264 (0.0194 – 0.0362)			24485 (560.49 – 85041)	97184 (41400.75 – 172949)
Strong allee model (10)	0.3889 (0.2030 – 0.7418)	0.0123 (0.00002 – 0.1701)	1014917 (963307 – 1057625)		42157 (10529 – 79335)	78229 (73569 – 79911)

curve models (five ODE models and five FDE models) with a Gaussian error is

$$L(y \mid \hat{\theta}, \sigma^2) = (2\pi)^{-R/2}\sigma^{-R}\exp\left\{\frac{SS(\hat{\theta})}{2\sigma^2}\right\} \tag{19}$$

where, $SS(\hat{\theta})$ is the sum of squares function defined as:

$$SS(\hat{\theta}) = \sum_{i=1}^{R}[y_{t_i} - N(t_i, \hat{\theta})]^2. \tag{20}$$

Posterior distribution of the unknown parameter vector $\hat{\theta}$ of the ten models is generated using Delayed Rejection Adaptive Metropolis algorithm (DRAM) (Haario et al., 2001, 2006). MCMC toolbox in MATLAB, written by Marko Laine (Laine, 2008), was used to estimate the unknown parameter vector $\hat{\theta}$ for the ten growth curve models (1–5, 6–10). Geweke's Z-scores (Geweke, 1991) were examined to ensure the chain convergence. Estimated parameters of the ten growth curve models (1–5, 6–10) for the four species are given in Table 1, Table 2, Table 3 and Table 4, respectively. Selection criterion of the best model/models among ten growth curve models (1–5, 6–10) for a given population time series data is discussed in Section (2.5).

Table 4
Estimated parameters of the ten growth curve models (1–5, 6–10) for the population *Ursus americanus (116)*. α and θ are dimensionless quantities. Units of K, A and $N(0)$ are counts of breeding pairs, according to the source available in GPDD. Units of r are time^{-1} and time$^{-\alpha}$ for ODE and FDE models respectively.

Parameters	α	r	K	θ	A	$N(0)$
ODE						
Exponential model (1)		0.2224 (0.1959 – 0.2708)				127.5862 (79.85 – 149.23)
Logistic model (2)		0.2438 (0.2018 – 0.3386)	19888 (1728.46 – 48311.66)			125.93 (76.866 – 149.24)
θ-logistic model (3)		1.1243 (0.217 – 3.677)	20178 (1512.8 – 48363)	0.3916 (0.0168 – 2.5571)		117.65 (64.3580 – 148.2297)
Exponential allee model (4)		0.2464 (0.2047 – 0.3302)			30.5749 (1.0393 – 91.2765)	130.8919 (86.3495 – 149.4635)
Strong allee model (5)		0.3070 (0.2143 – 0.5716)	15544.62 (1271.76 – 47518.12)		36.6762 (1.2259 – 107.79)	128.3791 (85.5499 – 149.25)
FDE						
Exponential model (6)	0.4404 (0.1323 – 0.9056)	0.1669 (0.1012 – 0.2348)				100.3941 (37.7664 – 147.3170)
Logistic model (7)	0.4802 (0.1333 – 0.9422)	0.1971 (0.1294 – 0.2781)	24985.93 (3638.26 – 48680)			99.21 (32.4914 – 147.72)
θ-logistic model (8)	0.6742 (0.1961 – 0.9938)	2.7251 (1.0303 – 3.9543)	6406.03 (1833.55 – 16098.45)	0.1634 (0.02679 – 0.4095)		95.62 (19.2758 – 147.8072)
Exponential allee model (9)	0.3647 (0.1134 – 0.8498)	0.1805 (0.1063 – 0.2598)			39.16 (0.9914 – 105.3963)	112.44 (52.53 – 148.69)
Strong allee model (10)	0.7038 (0.2129 – 0.9912)	0.4485 (0.0116 – 3.1358)	1033.85 (635.44 – 1523.93)		75.36 (17.96 – 132.0326)	120.87 (59.42 – 149.1145)

2.5. Selection of best model

Model selection is a procedure to identify a model that has the best agreement with the data (called as the 'best model') among a set of models (Johnson and Omland, 2004). It can be used to identify the hypothesis that is best fitted to the observations. Two criteria commonly used in ecology, and evolution are the Akaike Information Criterion (AIC) (Akaike, 1973) and the Schwarz Criterion (also known as Bayesian information criterion, or BIC) (Schwarz, 1978). We use AIC to identify the best model among the ten growth curve models (1–5, 6–10). We obtain the following expression for AIC (Akaike, 1973; Johnson and Omland, 2004):

$$\mathrm{AIC} = -2\ln[L(\hat{\theta}_p \mid y, \hat{\sigma}^2)] + 2\rho \tag{21}$$

where ρ is the number of unknown parameter and $L(\hat{\theta} \mid y, \hat{\sigma}^2)$ is the likelihood of the model parameters (more precisely, their maximum likelihood estimates, $\hat{\theta}_p$) given the data.

Taking natural logarithm 'ln' in both sides of (19) we get:

$$\ln[L(y \mid \hat{\theta}, \sigma^2)] = -\frac{R}{2}\ln(2\pi) - R\ln(\sigma) - \frac{1}{2\sigma^2}SS(\hat{\theta}). \tag{22}$$

In Eq. (22), the unknown quantities are $\hat{\theta}$ and σ. Using conditional conjugacy property of gamma distribution, the posterior distribution of σ^{-2} is also a gamma distribution with the probability density function:

$$p(\sigma^{-2} \mid y, \hat{\theta}) = \Gamma\left(\frac{n_0 + n}{2}, \frac{n_0 S_0^2 + SS(\hat{\theta})}{2}\right). \tag{23}$$

The conditional conjugacy property makes it possible to sample and update σ^2 within each Metropolis-Hastings simulation step for the other parameters. Thus only unknown quantity in Eq. (22) is $\hat{\theta}$. So for the ten growth curve models (1–5, 6–10), the expression of AIC is given by:

$$\mathrm{AIC} = -2\log\left(\frac{SS(\hat{\theta}_p)}{n}\right) + 2\rho. \tag{24}$$

We used the following calculations based on Akaike information Criterion (AIC) (Akaike, 1973) to determine which model/models are best supported by the data. Once each model is fitted to the data, an AIC score has been computed by (24). We then calculate the differences in these scores between each model and the best model ('the best model' has the minimum AIC score among the models).

$$\Delta_i = \mathrm{AIC}_i - \mathrm{AIC}_{\min}. \tag{25}$$

The likelihood of a model, g_i, given the data, y, is given by $\exp\left(-\frac{\Delta_i}{2}\right)$. Model likelihood values were normalized across the ten growth curve models (1–5, 6–10), so that they sum to 1 as

$$W_i = \frac{\exp\left(-\frac{\Delta_i}{2}\right)}{\sum_{j=1}^{10}\exp\left(-\frac{\Delta_j}{2}\right)}. \tag{26}$$

Here W_i's are known as Akaike weight (Johnson and Omland, 2004) that provide a relative weight of evidence for each model. Akaike weight can be interpreted as the probability that model i is the best model for the observed data, given a set of models. Model/models for which Akaike weight (W_i) is greater than 0.9 can be considered as best model/models over a given data set.

2.6. Choice of prior distribution

To check the impact of different choice of prior distribution, we have used the `modMCMC` function which is available in `R` with the package `FME` (Soetaert and Petzoldt, 2010). We have performed simulation of the posterior samples using DRAM as described in the Method section. We have mainly emphasized on two different choice of prior distribution: normal, uniform and non-informative. The `modMCMC()` function allows user defined prior functions. For the normal prior, the prior mean and variance were estimated by nonlinear least square method (using `modFit` function). The initial covariance is the inverse of the Hessian matrix of the nonlinear model fitting. For non-informative prior, in which all the parameters are equally likely and uniformly sampled from the interval $(0, \infty)$. Choice of the prior

Table 5
Central tendency (mean, median, mode), variance and skewness of the posterior distribution with respect to different choice of priors. The data of *Castor Canadensis* (200) has been used for this comparison. Kolmogorov Smirnov (K−S) test has been performed to compare the equality of distributions based on the posterior samples. For all the parameters, use of uniform prior and non-informative prior gave the same posterior distribution (p-value > 0.05).

Castor Canadensis (200)					
Prior	Posterior mean	Mode	Median	Standard deviation	Skewness
$N(0) \sim \text{uniform}(0, 10^6)$	6.6223×10^4	4.046×10^4	6.477×10^4	1.954×10^4	0.432
$r \sim \text{uniform}(0, 3)$	1.126×10^1	1.439×-1	1.117×10^{-1}	2.017×10^{-2}	0.309
$K \sim \text{uniform}(0, 10^6)$	7.283×10^5	6.757×10^5	7.174×10^5	6.347×10^4	1.897
$N(0) \sim \mathcal{N}(6.146 \times 10^4, 200^2)$	6.146×10^4	6.141×10^4	6.146×10^4	9.916×10^3	−0.0044
$r \sim \mathcal{N}(.1149, 200)$	1.153×10^{-1}	1.108×10^{-1}	1.152×10^{-1}	2.003×10^{-5}	0.1716
$K \sim \mathcal{N}(7.105 \times 10^5, 200)$	7.105×10^5	7.105×10^5	7.105×10^5	1.002×10^4	0.0423
$N(0) \in (0, \infty)$	66,969.10908	4.420×10^4	6.489×10^4	2.026×10^4	0.5143
$r \in (0, \infty)$	0.11246	1.207×10^{-1}	1.116×10^{-1}	2.074×10^{-2}	0.3117
$K \in (0, \infty)$	728,090.28433	7.287×10^5	7.165×10^5	6.460×10^4	1.699

distribution for the model parameters of the best selected models are presented in Table 5 and Table 6. Central tendency (mean, median, mode), variance and skewness of the posterior distribution are also reported. Whether the posterior distributions deviate significantly with respect to different priors, we have used the Kolmogorov-Smironov test. Note that the first 50,000 samples are considered as burn-in stage. Since, the model parameters are of different order of magnitudes, initial model variance was set to the mean of the unweighted least square residuals from the model fit. The chain for σ^2 has been initialized with the mean square error after the initial model fit. Since, the models are highly nonlinear in nature, a low weight has been given to the prior.

Three different choice of priors have been considered, namely, uniform, normal and non-informative prior. The parameter choices are given in the Table 5 and Table 6 for *Castor Canadensis* and *Phalacrocorax carbo*, respectively. Standard deviation of the posterior distribution is significantly affected by the variance of the normal prior distribution for $N(0)$ and K. For very large variance of order 10^6, the impact is negligible. The same has been observed for the posterior distribution r as well. However, posterior central tendencies are not impacted by this. Another important observation is that a small prior variance leads to small variance in the posterior samples. Since, no additional information is available on the species biology from the field information regarding the parameters, a non-informative prior would be a preferred choice. In the manuscript we have demonstrated the impact of priors on the posterior for two species only. For the other species similar analysis can be carried out for both ODE and FDE models.

2.7. Return time

The return rate is used as a measure of stability in animal populations that describes how the population responds to disturbances when deflected from the equilibrium abundance at carrying capacity. It is defined as the rates at which the population reverts back to equilibrium size when perturbed and used in conservation biology (Barker and Sibly, 2008; May et al., 1974; Sibly et al., 2003, 2007). Return rates are estimated as the slope of per capita growth rate vs. ln$N$, measured at carrying capacity K, thus,

$$\text{Return rate} = -\left[\frac{\mathrm{d}\left(\frac{1}{N}\frac{\mathrm{d}N}{dt}\right)}{\mathrm{d}(\ln N)}\right]_K = -\lambda, \text{ (say)}.$$

The return time (T_R) is the reciprocal of the return rate defined as

$$T_R = -\frac{1}{\lambda},$$

i.e. the more negative λ the faster perturbations die out. Since the models (1), (4), (6) and (9) have no stable equilibrium state therefore growth of the population that follows these models return time (T_R) can not be evaluated. For logistic growth model with both ordinary and

Table 6
Central tendency (mean, median, mode), variance and skewness of the posterior distribution with respect to different choice of priors for the species *Phalacrocorax carbo* (9330).

Phalacrocorax carbo (9330)					
Prior	Posterior mean	Mode	Median	Standard deviation	Skewness
$N(0) \sim \text{uniform}(0, 10^3)$	102.116	110.427	102.0693	7.696	0.085
$r \sim \text{uniform}(0, 3)$	0.095	0.0874	0.0948	6.567849×10^{-3}	0.2697
$K \sim \text{uniform}(0, 10^3)$	449.8895	443.7215	449.6369	1.149540×10^1	0.3218
$\theta \sim \text{uniform}(0, 10^2)$	246.915	155.4622	246.985	1.353286×10^2	0.0179
$N(0) \sim \mathcal{N}(100, 100)$	102.7346	89.6581	102.5405	7.7714	0.1583
$r \sim \mathcal{N}(0.1, 100)$	0.0945	0.1046	0.0944	0.0065	0.1225
$K \sim \mathcal{N}(450, 100)$	449.69202	454.9154	449.3475	11.3349	0.3371
$\theta \sim \mathcal{N}(432, 200)$	380.8826	394.2015	390.6417	70.2984	−0.6863
$N(0) \in (0, \infty)$	102.2140	112.7078	102.1684	7.7928	0.0517
$r \in (0, \infty)$	0.0949	0.0891	0.0947	6.537868×10^{-3}	0.2174
$K \in (0, \infty)$	450.0958	454.9384	449.9082	11.4437	0.1836
$\theta \in (0, \infty)$	245.8546	330.2614	246.4034	1.348402×10^2	0.0169

Table 7
AIC values of the ten growth curve models (1–5, 6–10) for a given population data. Bold entry in each column represents smallest AIC value.

AIC	Parus bicolor (1197)	Phalacrocorax Carbo (9330)	Castor Canadensis (200)	Ursus americanus (116)
ODE				
Exponential model (1)	259.2413	38288	$5.90 \cdot E + 11$	348801
Logistic model (2)	271.3584	21315	$3.46 \cdot E + 11$	337944
θ-logistic model (3)	256.8006	10,166	$3.50 \cdot E + 11$	391676
Exponential allee model (4)	260.4468	33096	$5.73 \cdot E + 11$	416101
Strong allee model (5)	295.6333	16446	$3.71 \cdot E + 11$	502654
FDE				
Exponential model (6)	257.9877	24812	$4.71 \cdot E + 11$	392429
Logistic model (7)	269.718	19757	$3.53 \cdot E + 11$	230,590
θ-logistic model (8)	240.674	22811	$3.34 \cdot E+11$	334291
Exponential allee model (9)	262.0354	26921	$4.88 \cdot E + 11$	244973
Strong allee model (10)	262.1953	18251	$1.56 \cdot E + 12$	1293814

fractional order derivatives i.e. the models (2) and (7) have the same expression of the T_R which is given as follows:

$$T_R = \frac{1}{r}. \tag{27}$$

This implies that as r become larger the return time becomes shorter i.e. populations that grow faster are more resistant to perturbations. The unit of r is per time (/years), so the unit of return rate if years. Similarly, for the θ-logistic and the strong Allee growth curve models, the Eq. (3), Eq. (8), Eq. (5) and Eq. (10), have the expression of T_R are (in both ODE and FDE framework):

$$T_R = \frac{1}{r\theta}, \tag{28}$$

and

$$T_R = \frac{1}{r\left(1 - \frac{A}{K}\right)}. \tag{29}$$

We have computed T_R for each of the species using the parameter estimates obtained from both ODE and FDE models.

3. Results and discussion

AIC values and AIC weights for ten designated growth curve models (1–5, 6–10) are given in Table 7 and Table 8 respectively. The θ-logistic model (3) was found to be the best among ODE models (see Table 7) for the species *Parus bicolor (1197)* and *Phalacrocorax carbo (9330)*. The logistic model (2) was found to be the best among ODE models (see Table 7) for the species *Castor Canadensis (200)* and *Ursus americanus (116)*. Using FDE models, for the species *Parus bicolor (1197)* and *Castor Canadensis (200)*, the θ-logistic model (8) is the best model. For the species *Phalacrocorax carbo (9330)*, the strong Allee model (10) was the best model and for *Castor Canadensis (200)*, the logistic model (7) was found to be the best model.

Fitting of the best ODE and FDE models for the four time series data are depicted in Fig. 1 and Fig. 2, respectively. Correlation between the posterior sample values of the memory parameter α and growth rate parameter r is depicted in Fig. 3. From Fig. 3, we can infer that species memory parameter (α) has an inverse relationship with the species growth rate (r) i.e. increase in species memory ($\alpha \to 0$) will increase species growth rate. This is biologically justified since several species utilize their past experiences to increase their reproductive fitness from previous successful mating. For example learning from the past experiences, selection of specific traits from history significantly modifies the individual mate preferences in dogs (Daniels, 1983).

Using simulated time series from the θ-logistic model Clark et al. (2010) reported that the relationship between r and θ was linear in the logarithmic scale, which described a rectangular hyperbola in linear scale. The scatter diagram of posterior distributions of r and θ for the species *Ursus americanus* (American black bear, GPDD ID 116) is in well agreement with the results obtained by them (see Fig. 4). Similar interplay was observed for the other three species using the θ-logistic model. Similar results were obtained by Eberhardt and Breiwick (2012) from the fitting results of generalized logistic model to 27 time series data from GPDD.

Gregory et al. (2010) considered both density dependent and

Table 8
Akaike weights of the ten growth curve models (1–5, 6–10) for a given population data. Bold entry in each column represents largest Akaike weight.

AIC	Parus Bicolor (1197)	Phalacrocorax Carbo (9330)	Castor Canadensis (200)	Ursus Americanus (116)
ODE				
Exponential model (1)	$9.286838E-05$	0	0	0
Logistic model (2)	$2.171066E-07$	0	0	0
θ-logistic model (3)	$3.146728E-04$	1	0	0
Exponential allee model (4)	$5.082728E-05$	0	0	0
Strong allee model (5)	$1.162641E-12$	0	0	0
FDE				
Exponential model (6)	$1.738136E-04$	0	0	0
Logistic model (7)	$4.930391E-07$	0	0	0
θ-logistic model (8)	9.993229E-01	0	0	1
Exponential allee model (9)	$2.296872E-05$	0	0	0
Strong allee model (10)	$2.120386E-05$	0	1	0

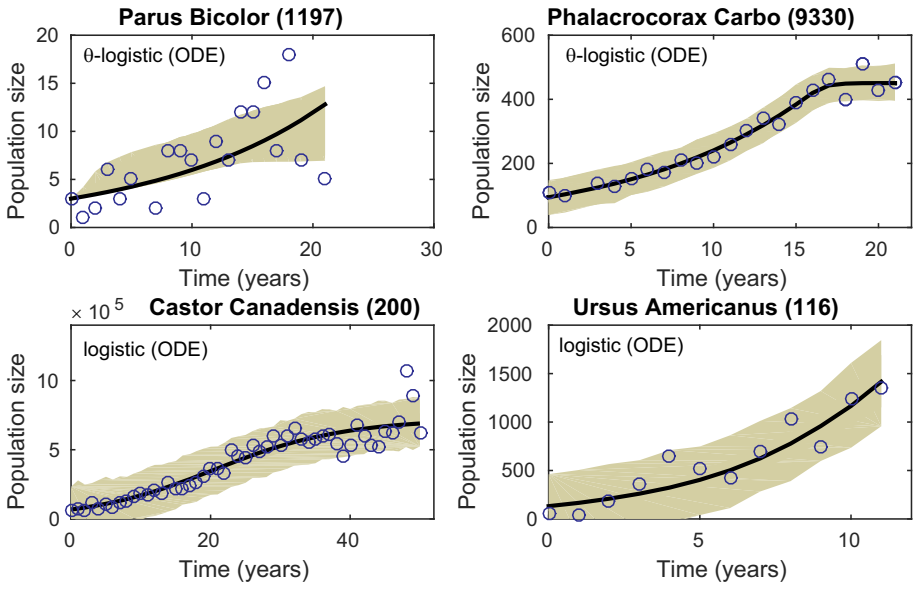

Fig. 1. Best fitted ODE models for the four population time series data among the five ODE growth curve models (1) to (5). Blue circles indicate the population counts of individuals for *Castor Canadensis* and *Ursus americanus*, where as for *Parus bicolor* and *Phalacrocorax carbo*, they represents the number of breeding pairs. The shaded areas represent the 95% confidence band, which is output ranges induced by the parameter uncertainty in the model. (For interpretation of the references to colour in this figure legend, the reader is referred to the web version of this article.)

density independent growth models, where per capita growth rate was modeled as a function of population size or density. The models were chosen in such a way so that they are nested, therefore, multimodel inference techniques were appealing. On the contrary, we have assumed the continuous counterpart of the models by replacing per capita growth rate by $\frac{1}{N}\frac{dN}{dt}$. While estimating the model parameters the explicit solutions of the differential equations as function of time were used. Hence, the models were no longer nested. So, in principle, the two approaches are different but, that will not affect the method of comparing the models using AIC. Because AIC is an estimator of relative expected Kullback-Leibler information for both nested and non nested models. Posterior distribution of parameters for the best ordinary and fractional growth models for the studied species are depicted in C (Fig. F-8, Fig. F-9, Fig. F-10 and Fig. F-11, respectively).

The initial population size $N(0)$ has been considered to be the part of the uncertainty analysis by posterior distribution except for the species *Parus bicolor*. The initial population size for this species was very small, hence, many mcmc runs gave negative population sizes during simulations. As a result, the chains for posterior distributions did not converge for other parameters. Increasing the number of simulation did not fix the problem. It should be noted that this problem appeared only for the fitting of ODE model (logistic), however, for FDE this problem did not appear. As a result, for *Parus bicolor* (1197), FDE model provides different mean and generates much wider uncertainty bound than ODE model, but for other three species, the model outputs (means and uncertainties) are almost same between FDE model and ODE model. The posterior distributions of the error terms associated with the model predictions (σ) is depicted in Fig. 5. Because of conjugate family, the posterior distribution of σ^2 also follows the inverse gamma distribution. The posterior distribution of errors are presented for the best models

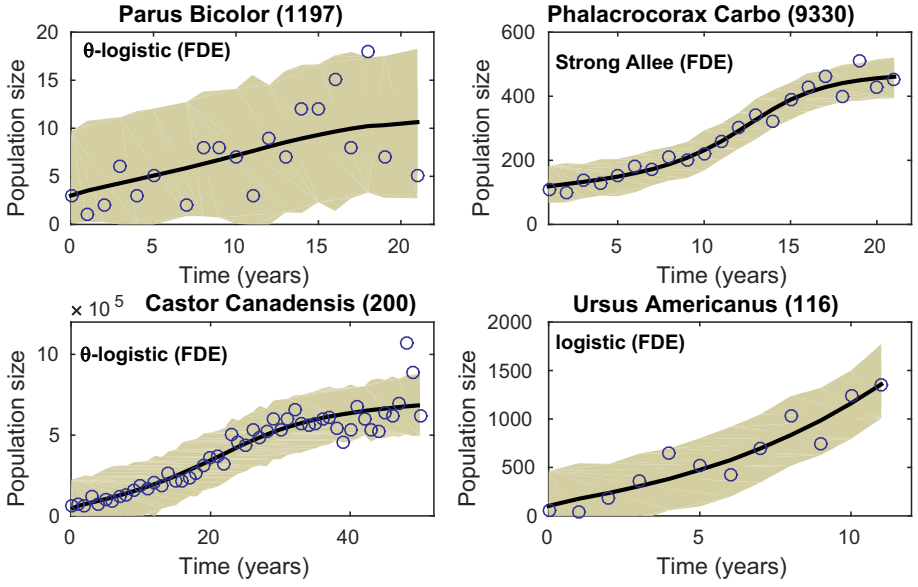

Fig. 2. Best fitted FDE models for the four population time series data among the five FDE growth curve models (6) to (10). Blue circles indicate the population counts of individuals for *Castor Canadensis* and *Ursus americanus*, where as for *Parus bicolor* and *Phalacrocorax carbo*, they represents the number of breeding pairs. The shaded areas represent the 95% confidence band, which is output ranges induced by the parameter uncertainty in the model. (For interpretation of the references to colour in this figure legend, the reader is referred to the web version of this article.)

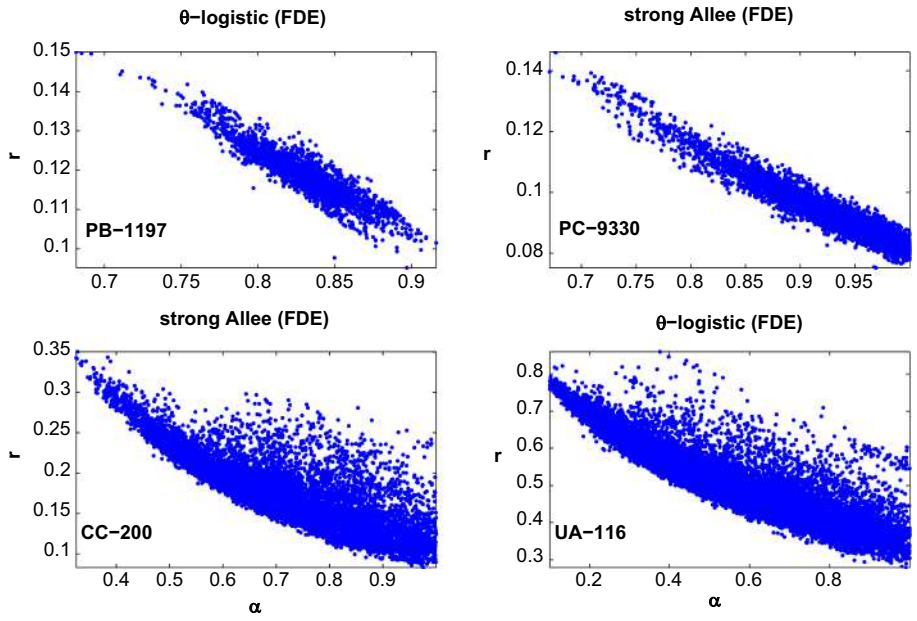

Fig. 3. Correlation between the memory parameter α and growth rate parameter r for the four best fitted models for the four species in FDE set up. *Parus bicolor* (PB-1197) *Phalacrocorax carbo* (PC-9330) *Castor Canadensis* (CC-200) and *Ursus americanus* (UA-116). Since, α is inversely proportional to the memory, it is clear that the species memory has a positive correlation with growth rate r.

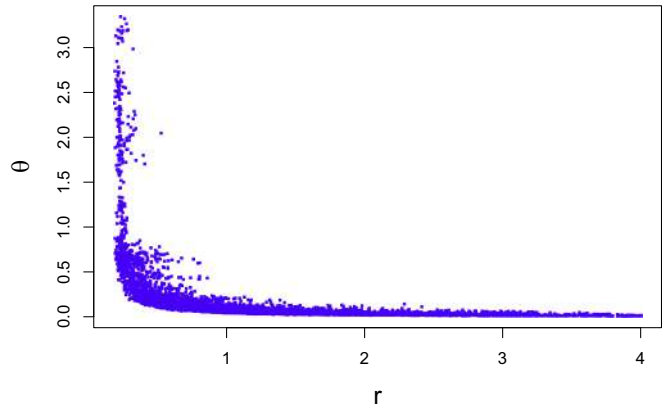

Fig. 4. Correlation between the posterior samples of the parameters r and θ of θ-logistic model for the species *Ursus americanus*.

only.

The goal of this study was to explore the interaction between memory and species survival and whether the strength of such interactions can be formulated from the time series data. More precisely, our hypothesis is that the species with stronger memory has better survival prospect. To verify this empirically, we estimated the return time (T_R) of the populations using the best fitted models. The parameter estimates corresponding to the best fitted models were used to evaluate the value of T_R. We observed that for a particular species, estimated return time was shorter using FDE than the estimated value using ODE (except for the species *Phalacrocorax carbo (9330)*)(Fig. 6). This observation is in well agreement with the fact that stronger memory are able to recover from disturbance faster than the species with shorter memory.

From the expression of the return time (T_R) it is clear that $T_R \propto \frac{1}{r}$ and from Fig. 3 it is evident that $r \propto \frac{1}{\alpha}$, hence $T_R \propto \alpha$. This mathematical relationship is in well agreement with the biological interplay between return time and memory. The species with stronger memory will be more resistant to environmental perturbations. Such information may be useful in conservation biology, since the parameter α may provide an estimate of their memory capacity ($\alpha \to 0$ implies ideal memory and $\alpha \to 1$ implies no memory). If the mode of the posterior distribution is close to 1, the species has weaker memory. We have studied the posterior distribution of α for each of the species in FDE framework (Fig. 7). For the species *Phalacrocorax carbo (9330)*, estimated return time was found to be larger in FDE than the ODE framework. For this species the posterior distribution of α is negatively skewed and the mode is close to 1 (Fig. 7). This is indicative of a lower level of memory; hence, the return time has been found to be more for this species. Thus, we expect that the estimates obtained from FDE models would be more appropriate in making predictions of species' persistence at future time than the ODE models.

In the usual growth curve analysis of population time series, the model parameters are estimated based on the sample data and the population prediction intervals are constructed accordingly. For this type of analysis the differential equations an important mathematical tool. The model parameters have specific biological meaning and its estimates determine the species demographic profile. As mentioned earlier, memory is an inherent mechanism for the growth and survival of the species. However, it is not captured in ODE based models of population growth. Incorporating the memory by means of fractional order derivative, we get more information about the species which are determined by using the posterior distribution of α. In a nutshell, model governed by FDE captures more information about the population than the models governed by ODE. Hence, FDE based models will improve the population growth simulation than the ODE models. One has to keep in mind that the inference must be drawn by comparing several models by suitable statistical criterion, like, AIC, BIC.

4. Conclusion

In this article, we have used the FDE models to incorporate memory into the abundance as a function of a single parameter α. The posterior distribution of the parameter α provided a potential insight about the species memory. Quantifying species memory may aid in better management decisions in conservation of natural populations. Since population growths are exaggerated by stochastic fluctuations, a stochastic treatment would give more insight and population level consequences. It will be our future endeavor to study the stochastic behavior of population regulation under fractional differential equation set up. In particular estimation of species persistence by simulating the

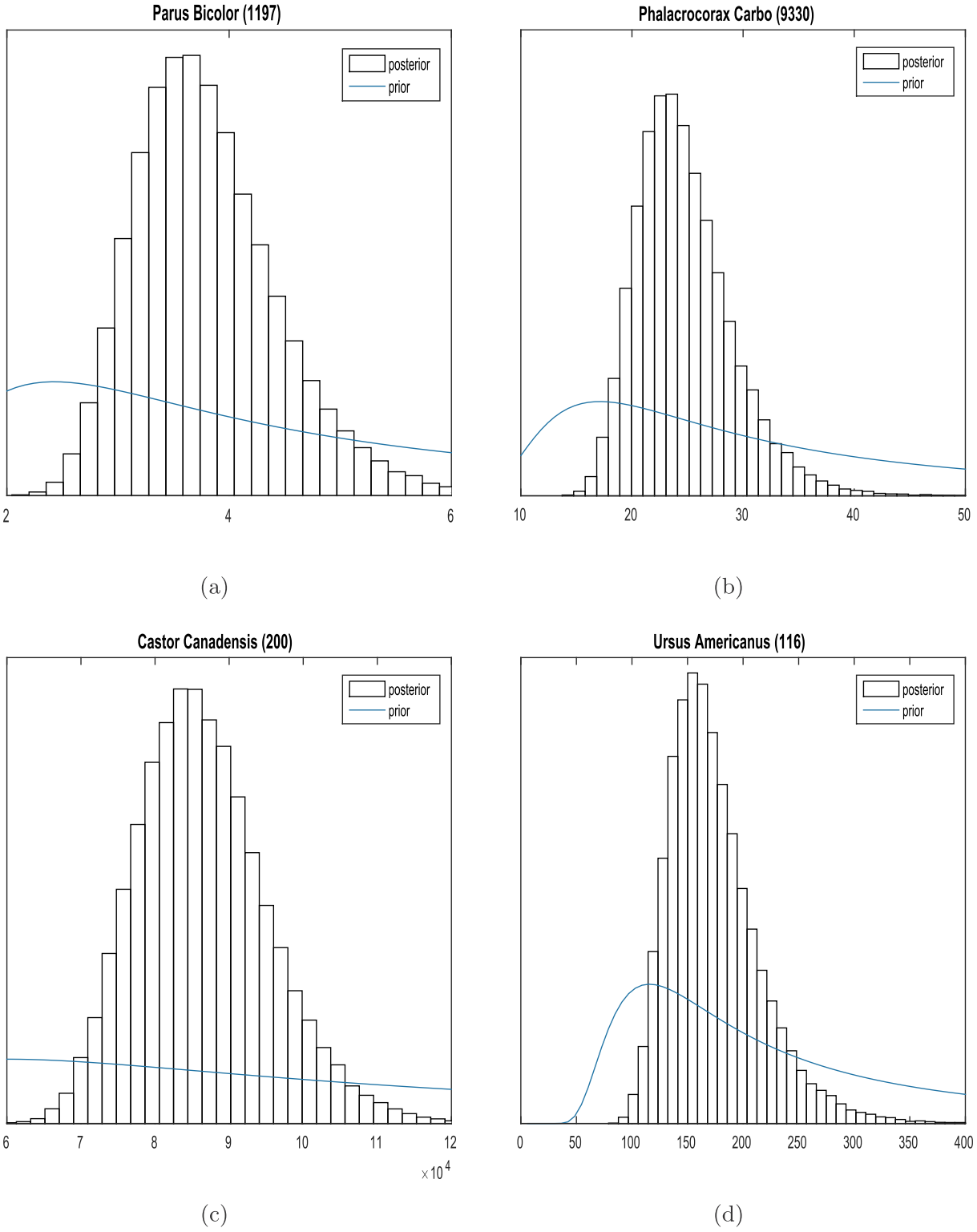

Fig. 5. The posterior distributions of the error terms associated with the model predictions (σ). The blue line indicates the prior distribution. (For interpretation of the references to colour in this figure legend, the reader is referred to the web version of this article.)

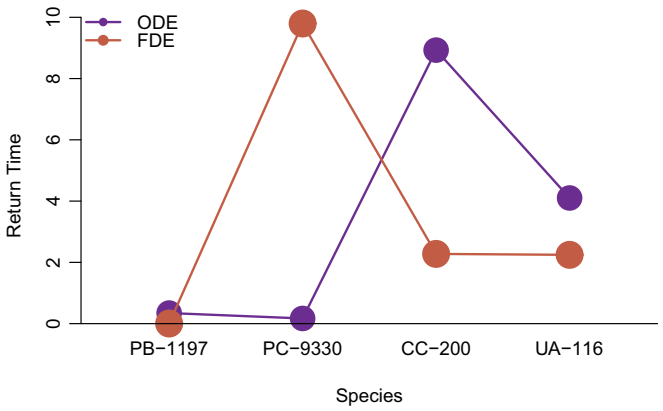

Fig. 6. Comparison of return time (T_R) of the best fitted model among ODE models with the best fitted models among FDE models given the four species data. Blue and red circles denote the values of T_R corresponding to ODE systems and FDE systems, respectively given a population growth data. PB-1197 = *Parus bicolor* (1197), PC-9330 = *Phalacrocorax carbo* (9330), CC-200 = *Castor Canadensis* (200) and UA-116 = *Ursus americanus* (116). Data for calculating T_R for the four species are taken from Table 1, Table 2, Table 3 and Table 4, respectively. (For interpretation of the references to colour in this figure legend, the reader is referred to the web version of this article.)

population dynamics using stochastic FDE models will be more precise as compared to the ODE models.

Current study gave us a tool for estimating the strength of memory. This is important from conservation point of view. The species whose posterior distribution of alpha is close to zero, their recovery rate will be faster. So, the designated four examples and their distribution of the memory already reflect the strength of memory (more or less). For example, this study suggests the potential for a long term memory for *Ursus americanus*. Such information may aid in setting up laboratory experiment to explore animal behaviour.

Acknowledgement

Authors are thankful to two anonymous reviewer and the editor for constructive suggestions that significantly improved the manuscript than its earlier version. ARB acknowledges the summer school on "Matrix Methods and Fractional Calculus, 2014" organized by Center for Mathematical and Statistical Sciences and Science and Engineering Research Board, Department of Science and Technology, Government of India. ARB thanks F. Minardi for valuable discussions on the concept of fractional calculus during the summer school. Authors thank Ankita Malu for the help in preparing the graphical abstract. The authors have no conflict of interest.

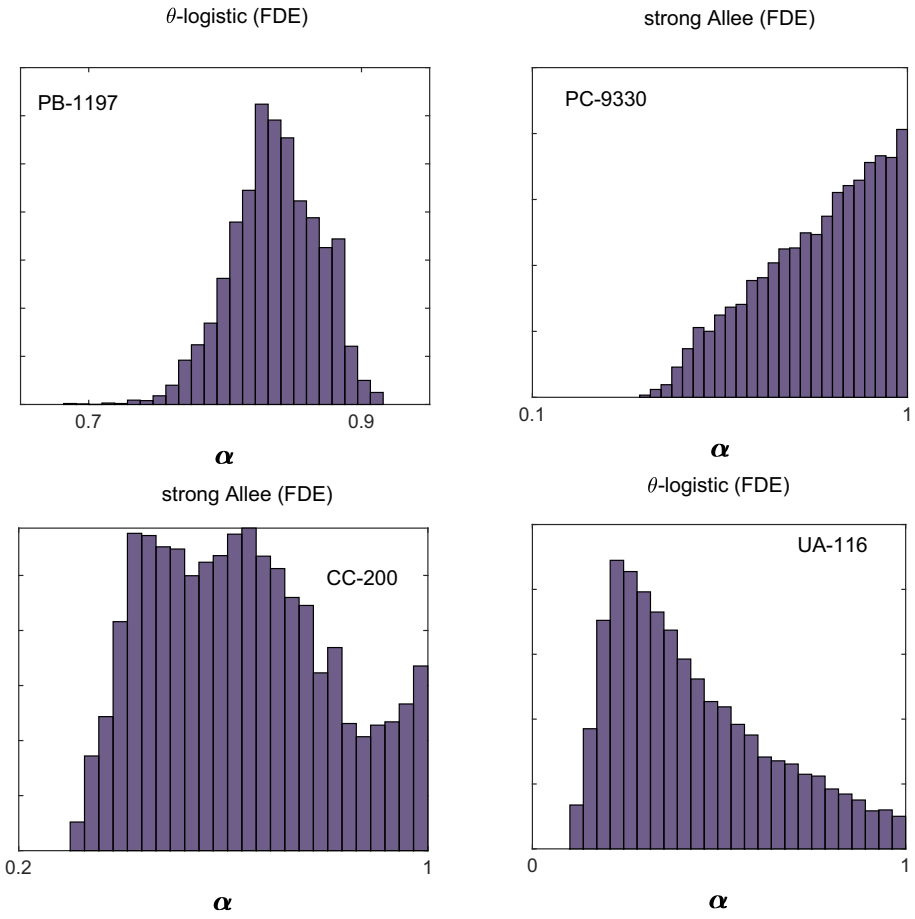

Fig. 7. Posterior distribution of the memory parameter α for the four studies species. PB-1197 = *Parus bicolor* (1197), PC-9330 = *Phalacrocorax carbo* (9330), CC-200 = *Castor Canadensis* (200) and UA-116 = *Ursus americanus* (116).

Appendix A. Some basic properties of fractional derivatives and integrals

To define the fractional integral, we consider the following n-fold repeated integral formula given by,

$$I_{a+}^{n}\phi(x) = \int_a^x \int_a^{x_{n-1}} \dots \int_a^{x_1} \phi(x_0)\mathrm{d}x_0 \dots \mathrm{d}x_{n-1}, \quad a \le x < b,\ n \in \mathbb{N} \tag{A-1}$$

where $a > -\infty$ and $b \le +\infty$. The function $\phi(x)$ is assumed to be locally integrable in the interval $[a,b)$. The Cauchy representation of the above $n-$fold repeated integral of convolution type formula is

$$I_{a+}^{n}\phi(x) = \frac{1}{(n-1)!}\int_a^x (x-\xi)^{n-1}\phi(\xi)\mathrm{d}\xi, \quad a \le x < b. \tag{A-2}$$

Using the fact that $(n-1)! = \Gamma(n)$, the definition can be extended to arbitrary order $\alpha(>0)$; the fractional integral of order α is defined by

$$I_{a+}^{\alpha}\phi(x) = \frac{1}{\Gamma(\alpha)}\int_a^x (x-\xi)^{\alpha-1}\phi(\xi)\mathrm{d}\xi, \quad a \le x < b,\ \alpha > 0. \tag{A-3}$$

For $a = 0$, the fractional integral ${I_{0+}}^{\alpha}$ is the Riemann-Liouville fractional integrals. A dual form of the formula A-3 is given by,

$$I_{b-}^{\alpha}\phi(x) = \frac{1}{\Gamma(\alpha)}\int_x^b (\xi-x)^{\alpha-1}\phi(\xi)\mathrm{d}\xi, \quad a < x \le b,\ \alpha > 0.$$

In literature, ${I_{a+}}^{\alpha}$ and ${I_{b-}}^{\alpha}$ are called progressive (right-handed) and regressive (left-handed) integral operators respectively. Taking $a = -\infty$ and $b = +\infty$ in the above definitions, we obtain the Liouville-Weyl fractional integral operators. The fractional integrals satisfy the semigroup property given by,

$$I_{a+}^{\alpha}I_{a+}^{\beta} = I_{a+}^{\alpha+\beta}, \quad I_{b-}^{\alpha}I_{b-}^{\beta} = I_{b-}^{\alpha+\beta}, \quad \alpha, \beta \ge 0,$$

where $\mathbf{I}_{a+}^{0} = \mathbf{I}_{b-}^{0} = \mathbb{I}$, the identity operator.

For $a < x < b$ and $m-1 < \alpha \le m$, the fractional order derivative operator of order α is defined as the left inverse of ${I_{a+}}^{\alpha}$,

$$D_{a+}^{\alpha}\phi(x) = D^m I_{a+}^{m-\alpha}\phi(x), D_{b-}^{\alpha}\phi(x) = (-1)^m D^m I_{b-}^{m-\alpha}\phi(x)$$

The above definition is due to Riemann and Liouville and known as Riemann-Liouville fractional derivatives. However, an alternative definition of fractional derivative has been introduced by Caputo (1967); Caputo and Mainardi (1971). The Caputo derivative (name given by Podlubny (1999)) of a function $\psi(t)$ is defined as,

$${}^{C}D^{\alpha} = \begin{cases} \dfrac{1}{\Gamma(m-\alpha)}\displaystyle\int_0^t \frac{\psi^{(m)}(\tau)}{(t-\tau)^{\alpha+1-m}}\mathrm{d}\tau, & m-1 < \alpha < m \\ \dfrac{\mathrm{d}^m}{\mathrm{d}t^m}\psi(t), & \alpha = m \end{cases} \tag{A-4}$$

This is also symbolically represented as ${}^{C}D^{\alpha} = J^{m-\alpha}D^m$, $m-1 < \alpha \le m$, where $J^{m-\alpha}$ is the Riemann-Liouville integral operator of order $m-\alpha$. The Caputo derivative involves a memory effect via convolution between an integer-order derivative and a power of time (Datsko and Luchko, 2012; Diethelm, 2010). There are also other definitions of fractional integrals are available: Reisz-Feller fractional calculus and the Grünwald-Letnikov definition. Recently Mathai (2014) generalized both left and right hand fractional integral operators for the functions of matrix arguments. The author provided an excellent connection between the statistical distributions of product and ratio of two independent positive continuous random variables to the fractional integral operators.

We list some important properties for Caputo fractional differential and integral operators in the appendix. For detail proofs and mathematical results readers are encouraged to see Matignon, 1996; Podlubny (1999); Diethelm (2010); El-Sayed and Gaafar (2001); El-Sayed (1996, 1998); Gorenflo and Mainardi (1997); El-Sayed et al. (2004).

Let $\beta, \gamma \in \mathbb{R}^+$ and $\alpha \in (0,1)$, then we have.

1. $J^{\beta}: L^1 \to L^1$, and if $f(x) \in L^1$, then $J^{\gamma}J^{\beta}f(x) = J^{\beta}J^{\gamma}f(x) = J^{\gamma+\beta}f(x)$. This property is known as the semigroup property of the fractional order integration.
2. $\lim_{\beta\to n} J^{\beta}f(x) = J^{n}f(x)$ uniformly on $[0,b]$, $n = 1,2,3,\dots$, where $J^{1}f(x) = \int_0^x f(s)ds$.
3. $\lim_{\beta\to 0} J^{\beta}f(x) = f(x)$ weakly.
4. If $f(x)$ is absolutely continuous on $[0,b]$, then $\lim_{\alpha\to 1}\frac{\mathrm{d}^{\alpha}f(x)}{\mathrm{d}t^{\alpha}} = \frac{\mathrm{d}f(x)}{\mathrm{d}t}$.
5. If $f(x) = k \ne 0$, k is a constant, then $\frac{\mathrm{d}^{\alpha}f(x)}{\mathrm{d}t^{\alpha}} = 0$.

a. Following El-Sayed et al. (2004), we have the following lemma.

Lemma 1. Let $\beta \in (0,1)$; if $f \in C[0,T]$, then $J^{\beta}f(t)|_{t=0} = 0$.

Appendix B. Stability analysis

B.1. Equilibrium and stability for the model (8)

System (8) has two positive equilibrium, $N_{eq} = 0$ and $N_{eq} = K$, respectively. Stability of the two equilibrium depends upon the solution of the following linear fractional order differential equation (see, Matignon (1996), El-Sayed et al. (2007), Matouk (2009)).

$$\frac{\mathrm{d}^{\alpha}x}{\mathrm{d}t^{\alpha}} = f'(N_{eq})x, \tag{A-5}$$

where, $f(N) = rN\left[1 - \left(\frac{N}{K}\right)^{\theta}\right]$ and $x(t) = N(t) - N_{eq}$.

Now,

$$f'(N) = r\left[1 - \left(\frac{N}{K}\right)^{\theta}\right] - r\theta\left(\frac{N}{K}\right)^{\theta}. \tag{A-6}$$

Therefore, evaluating value of $f'(N)$ in (A-6) at the two positive equilibriums, we obtain $f'(0) = r$ and $f'(K) = -r\theta$. Solving Eq. (A-5) corresponding to two equilibrium points respectively, we have:

$$x(t) = N(0)E_{\alpha}(rt^{\alpha}), \tag{A-7}$$

and

$$x(t) = [N(0) - K]E_{\alpha}(-r\theta t^{\alpha}), \tag{A-8}$$

where, $x(0) = N(0)$ corresponding to $N_{eq} = 0$, $x(0) = N(0) - K$ corresponding to $N_{eq} = K$, and $E_{\alpha}(z) = \sum_{k=0}^{\infty} \frac{z^k}{\Gamma(\alpha k + 1)}$ is the one parameter Mittag-Leffler function with parameter α (see, Podlubny (1999), Diethelm (2010)).

Following Matignon's results (see Matignon (1996)) as $|\arg(r)| = 0 < \frac{\alpha\pi}{2}$ and $|\arg(-r\theta)| = \pi > \frac{\alpha\pi}{2}$ (since, $\alpha \in (0, 1]$, $r > 0$ and $\theta > 0$), therefore the equilibrium point $N_{eq} = 0$ is unstable and $N_{eq} = K$ is locally asymptotically stable.

B.2. Existence and uniqueness of solution of the model (8).

Let, $I = [0, T]$, $T < \infty$ and $C(I)$ be class of all continuous functions defined on I, with norm

$$\|x(t)\| = \sup_t |e^{-Mt}x(t)|, M > 0 \tag{A-9}$$

which is equivalent to the sup-norm $\|x(t)\| = \sup_t |x(t)|$. When $t > \sigma \geq 0$ we write $C(I_{\sigma})$.

Definition 1. We will define $x(t)$ to be a solution of the initial value problem (8) if.

1. $(t, x(t)) \in D$, $t \in I$ where $D = I \times B$, $B = \{x \in R: |x| \leq b\}$.
2. $x(t)$ satisfies (8).

We state and prove the following theorem.

Theorem 1. The initial value problem (8) has a unique solution $x \in C(I)$, $x' \in X = \{x \in L_1[0, T], \|x\| = \|e^{-Mt}x(t)\|_{L_1}\}$.

Proof. We write the system (8) as

$$J^{1-\alpha}\frac{d}{dt}N = rN\left[1 - \left(\frac{N}{K}\right)^{\theta}\right] \tag{A-10}$$

operating J^{α} both side of (A-10) we have

$$N(t) = N(0) + J^{\alpha}r\left(N - \frac{N^{\theta+1}}{K^{\theta}}\right) \tag{A-11}$$

Now let the operator $F: C(I) \to C(I)$ be defined by

$$FN(t) = N(0) + J^{\alpha}r\left(N - \frac{N^{\theta+1}}{K^{\theta}}\right) \tag{A-12}$$

Then, for any two $N_1, N_2 \in C(I)$ such that $N_1 \geq N_2$, we have

$$\begin{aligned} e^{-Mt}(FN_1 - FN_2) &= re^{-Mt}J^{\alpha}\left[(N_1 - N_2) - \frac{1}{K^{\theta}}(N_1^{\theta+1} - N_2^{\theta+1})\right] \\ &\leq r\int_0^t \frac{(t-s)^{\alpha-1}}{\Gamma(\alpha)}e^{-M(t-s)}[N_1(s) - N_2(s)]\left[1 + \frac{1}{K^{\theta}}(N_1^{\theta}(s) + N_2^{\theta}(s))\right]e^{-Ms}ds \\ &\leq \frac{\left(1 + 2\frac{b^{\theta}}{K^{\theta}}\right)}{M^{\alpha}}r\|N_1 - N_2\|\int_0^t \frac{s^{\alpha-1}e^{-Ms}}{\Gamma(\alpha)}ds. \end{aligned}$$

Thus,

$$\|FN_1 - FN_2\| \leq \|N_1 - N_2\|\frac{\left(1 + 2\frac{b^{\theta}}{K^{\theta}}\right)r}{M^{\alpha}}.$$

If we choose M such that $M^{\alpha} > \left(1 + 2\frac{b^{\theta}}{K^{\theta}}\right)r$, we obtain $\|FN_1 - FN_2\| \leq \|N_1 - N_2\|$. Therefore, The operator F defined in (A-12) has a unique fixed point. Consequently, the integral Eq. (A-11) has a unique solution $x \in C(I)$. Also from lemma 1, $J^{\alpha}\left(N - \frac{N^{\theta+1}}{K^{\theta}}\right)\Big|_{t=0} = 0$. Again from Eq. (A-11), we have

$$N(t) = N(0) + r\left[\frac{t^{\alpha}}{\Gamma(\alpha+1)}\left\{N(0) - \frac{N^{\theta+1}(0)}{K^{\theta}}\right\} + J^{\alpha+1}\left\{N'(t) - \frac{\theta+1}{K^{\theta}}N^{\theta}(t)N'(t)\right\}\right],$$

$$\frac{dN(t)}{dt} = r\left[\frac{t^{\alpha-1}}{\Gamma(\alpha)}\left\{N(0) - \frac{N^{\theta+1}(0)}{K^{\theta}}\right\} + J^{\alpha}\left\{N'(t) - \frac{\theta+1}{K^{\theta}}N^{\theta}(t)N'(t)\right\}\right],$$

and

$$e^{-Mt}\frac{dN(t)}{dt} = re^{-Mt}\left[\frac{t^{\alpha-1}}{\Gamma(\alpha)}\left\{N(0) - \frac{N^{\theta+1}(0)}{K^{\theta}}\right\} + J^{\alpha}\left\{N'(t) - \frac{\theta+1}{K^{\theta}}N^{\theta}(t)N'(t)\right\}\right],$$

from which it can be shown that $x \in C(I)$ and $x' \in X$. Now from Eq. (A-11), we get

$$\frac{dN(t)}{dt} = r\frac{d}{dt}J^{\alpha}\left[N(t) - \frac{N^{\theta+1}(t)}{K^{\theta}}\right],$$

$$J^{1-\alpha}\frac{dN(t)}{dt} = rJ^{1-\alpha}\frac{d}{dt}J^{\alpha}\left[N(t) - \frac{N^{\theta+1}(t)}{K^{\theta}}\right],$$

$$\frac{d^{\alpha}N}{dt^{\alpha}} = r\frac{d}{dt}J\left[N(t) - \frac{N^{\theta+1}(t)}{K^{\theta}}\right],$$

$$\frac{d^{\alpha}N}{dt^{\alpha}} = rN(t)\left[1 - \left(\frac{N(t)}{K}\right)^{\theta}\right].$$

and

$$\begin{aligned} N(0) &= N(0) + J^{\alpha}\left[N(t) - \frac{N^{\theta+1}(t)}{K^{\theta}}\right]\Bigg|_{t=0}, \\ &= N(0). \end{aligned} \tag{A-13}$$

Last result holds using lemma 1. Therefore the integral Eq. (A-11) is equivalent to the initial value problem (8) and this proves the theorem. □

B.3. Equilibrium and stability for the model (9).

System (9) has only one positive equilibrium $N_{eq} = A$. Solving system (9) we have the following solution

$$N(t) = (N(0) - A)E_{\alpha}(rt^{\alpha}) + A. \tag{A-14}$$

Following Matignon's results (see Matignon (1996)) as $|\arg(r)| = 0 < \frac{\alpha\pi}{2}$ therefore $N(t)$ increases as t increases. Therefore, $N_{eq} = A$ is always unstable.

B.4. Existence and uniqueness of solution of the model (9).

System (9) is a linear fractional order differential equation. Following Theorem 3.2 in (Podlubny, 1999) the system (9) has a unique continuous solution.

B.5. Equilibrium and stability for the model (10).

The fractional order system (10) has two positive equilibrium $N_{eq} = A$ and $N_{eq} = K$, respectively. Stability of two positive equilibrium corresponding to system (10) depends upon the solution of the following linear fractional order system (see, Matignon (1996), El-Sayed et al. (2007), Matouk (2009)).

$$\frac{d^{\alpha}x}{dt^{\alpha}} = f'(N_{eq})x, \tag{A-15}$$

where, $f(N) = r\left(1 - \frac{N}{K}\right)(N - A)$ and $x(t) = N(t) - N_{eq}$. Now,

$$f'(N) = -\frac{r}{K}(N - A) + r\left(1 - \frac{N}{K}\right). \tag{A-16}$$

Therefore, evaluating value of $f'(N)$ in (A-16) at the two positive equilibriums, we obtain $f'(A) = r\left(1 - \frac{A}{K}\right)$ and $f'(K) = -r\left(1 - \frac{A}{K}\right)$. Let, $r\left(1 - \frac{A}{K}\right) = \lambda$. Then $f'(A) = \lambda$ and $f'(K) = -\lambda$. Therefore, $\lambda >$ or < 0 if and only if $\frac{A}{K} < 1$ or > 1. Solution of the system (A-15) corresponding to two positive equilibriums $N_{eq} = A$ and $N_{eq} = K$, of the system (10), respectively given as follows

$$x(t) = [N(0) - A]E_{\alpha}(\lambda t^{\alpha}). \tag{A-17}$$

and

$$x(t) = [N(0) - K]E_{\alpha}(-\lambda t^{\alpha}). \tag{A-18}$$

Therefore if $\lambda > 0$, then $|\arg(\lambda)| = 0 < \frac{\alpha\pi}{2}$ and $|\arg(-\lambda)| = \pi > \frac{\alpha\pi}{2}$, since, $\alpha \in (0, 1]$. Thus, any solution that start nearer to A will moves away

from A and the solution that starts nearer to K will decay to K. In other words, if $A < K$, A is unstable and K is locally asymptotically stable. Now if $\lambda < 0$, then $|\arg(\lambda)| = \pi > \frac{\alpha\pi}{2}$ and $|\arg(-\lambda)| = 0 < \frac{\alpha\pi}{2}$. Therefore, if $A > K$, then A is locally asymptotically stable and K is unstable.

B.6. Existence and uniqueness of solution of the model (10).

The following result hold.

Theorem 2. The initial value problem (10) has a unique solution $x \in C(I)$, $x' \in X = \{x \in L_1[0,T], \|x\| = \| e^{-Mt}x(t)\|_{L_1}\}$.

Proof. We transform the fractional order system (10) to the following integral equation

$$N(t) = N(0) + J^{\alpha} r\left(1 - \frac{N}{K}\right)(N - A). \tag{A-19}$$

We define the operator $F: C(I) \to C(I)$ defined as

$$FN(t) = N(0) + J^{\alpha} r\left[N\left(1 + \frac{A}{K}\right) - \frac{N^2}{K} - A\right]. \tag{A-20}$$

Let, N_1, $N_2 \in C(I)$ such that $N_1 \geq N_2$. Then from (A-20) we have,

$$\begin{aligned} e^{-Mt}(FN_1 - FN_2) &= re^{-Mt}J^{\alpha}\left[\left(1 + \frac{A}{K}\right)(N_1 - N_2) - \frac{1}{K}(N_1^2 - N_2^2)\right] \\ &\leq r\int_0^t \frac{(t-s)^{\alpha-1}}{\Gamma(\alpha)} e^{-M(t-s)}(N_1 - N_2)\left[1 + \frac{A}{K} + \frac{(N_1 + N_2)}{K}\right]e^{-Ms}ds \\ &\leq \frac{r\left[1 + \frac{A}{K} + \frac{2b}{K}\right]}{M^{\alpha}}\|N_1 - N_2\| \int_0^t \frac{s^{\alpha-1}e^{-Ms}}{\Gamma(\alpha)}ds. \end{aligned}$$

This implies that

$$\|FN_1 - FN_2\| \leq \|N_1 - N_2\| \frac{r\left(1 + \frac{A}{K} + \frac{2b}{K}\right)}{M^{\alpha}}.$$

If we choose M such that $M^{\alpha} > r\left(1 + \frac{A}{K} + \frac{2b}{K}\right)$, then we have

$$\|FN_1 - FN_2\| \leq \|N_1 - N_2\|.$$

Therefore, Operator given in (A-20) has a unique fixed point and consequently, the integral Eq. (A-19) has a unique solution $N \in C(I)$. Also we have from lemma 1

$$J^{\alpha}\left[N\left(1 + \frac{A}{K}\right) - \frac{N^2}{K} - A\right]\Big|_{t=0} = 0$$

Again, from (A-19) we have

$$N(t) = N(0) + r\left[\frac{t^{\alpha}}{\Gamma(\alpha+1)}\left\{N(0)\left(1 + \frac{A}{K}\right) - \frac{N^2(0)}{K} - A\right\} + J^{\alpha+1}\left\{N'\left(1 - \frac{A}{K}\right) - \frac{2NN'}{K} + A\right\}\right],$$

$$\frac{dN}{dt} = r\left[\frac{t^{\alpha-1}}{\Gamma(\alpha)}\left\{N(0)\left(1 + \frac{A}{K}\right) - \frac{N^2(0)}{K} - A\right\} + J^{\alpha}\left\{N'\left(1 - \frac{A}{K}\right) - \frac{2NN'}{K} + A\right\}\right],$$

and

$$e^{-Mt}N'(t) = re^{-Mt}\left[\frac{t^{\alpha-1}}{\Gamma(\alpha)}\left\{N(0)\left(1 + \frac{A}{K}\right) - \frac{N^2(0)}{K} - A\right\} + J^{\alpha}\left\{N'\left(1 - \frac{A}{K}\right) - \frac{2NN'}{K} + A\right\}\right].$$

From these above expression it can be easily shown that $x \in C(I)$ and $x' \in X$. Again from (A-19) we have

$$\begin{aligned} \frac{dN}{dt} &= r\frac{d}{dt}J^{\alpha}\left[N\left(1 + \frac{A}{K}\right) - \frac{N^2}{K} - A\right], \\ J^{1-\alpha}\frac{dN}{dt} &= rJ^{1-\alpha}\frac{d}{dt}J^{\alpha}\left[N\left(1 + \frac{A}{K}\right) - \frac{N^2}{K} - A\right], \\ \frac{d^{\alpha}N}{dt^{\alpha}} &= r\frac{d}{dt}J^{1-\alpha}J^{\alpha}\left[N\left(1 + \frac{A}{K}\right) - \frac{N^2}{K} - A\right], \\ \frac{d^{\alpha}N}{dt^{\alpha}} &= r\frac{d}{dt}J\left[N\left(1 + \frac{A}{K}\right) - \frac{N^2}{K} - A\right], \\ \frac{d^{\alpha}N}{dt^{\alpha}} &= r\left(1 - \frac{N}{K}\right)(N - A). \end{aligned}$$

Again, from (A-19) we have

$$\begin{aligned} N(0) &= N(0) + rJ^{\alpha}\left[N\left(1+\frac{A}{K}\right) - \frac{N^2}{K} - A\right]\Big|_{t=0}, \\ &= N(0) + 0, \\ &= N(0). \end{aligned} \tag{A-21}$$

Therefore, the integral Eq. (A-19) is equivalent to the initial value problem (10) and this proves the theorem.

Appendix C. Marginal posterior distribution of all parameters

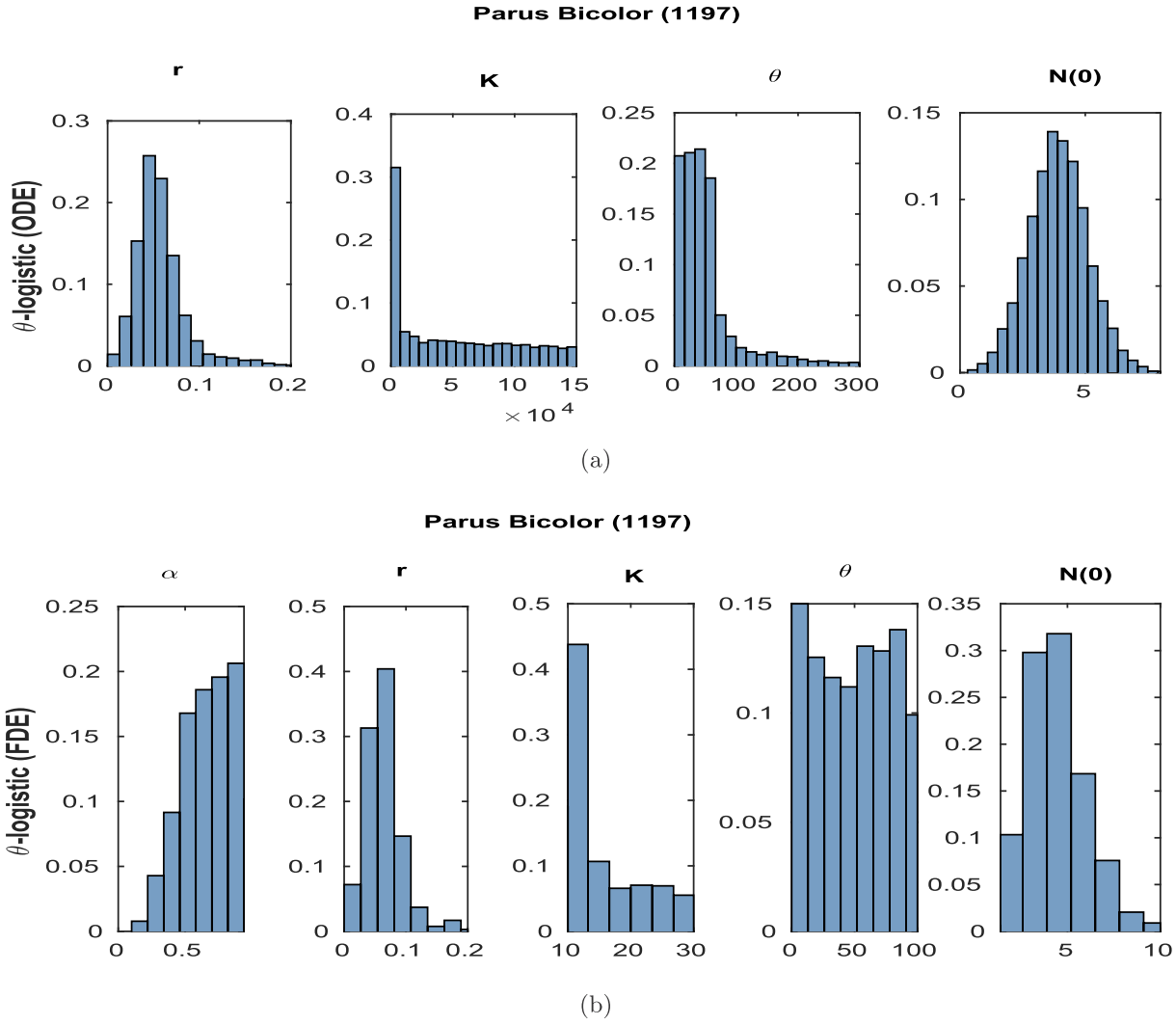

Fig. F-8. Marginal distributions of different parameters of the best fitted growth curve models (3) and (8) in ODE and FDE corresponding to growth data of the species *Parus bicolor* (1197). Fractional order θ-logistic model (8) has been selected as the best model according to AIC values.

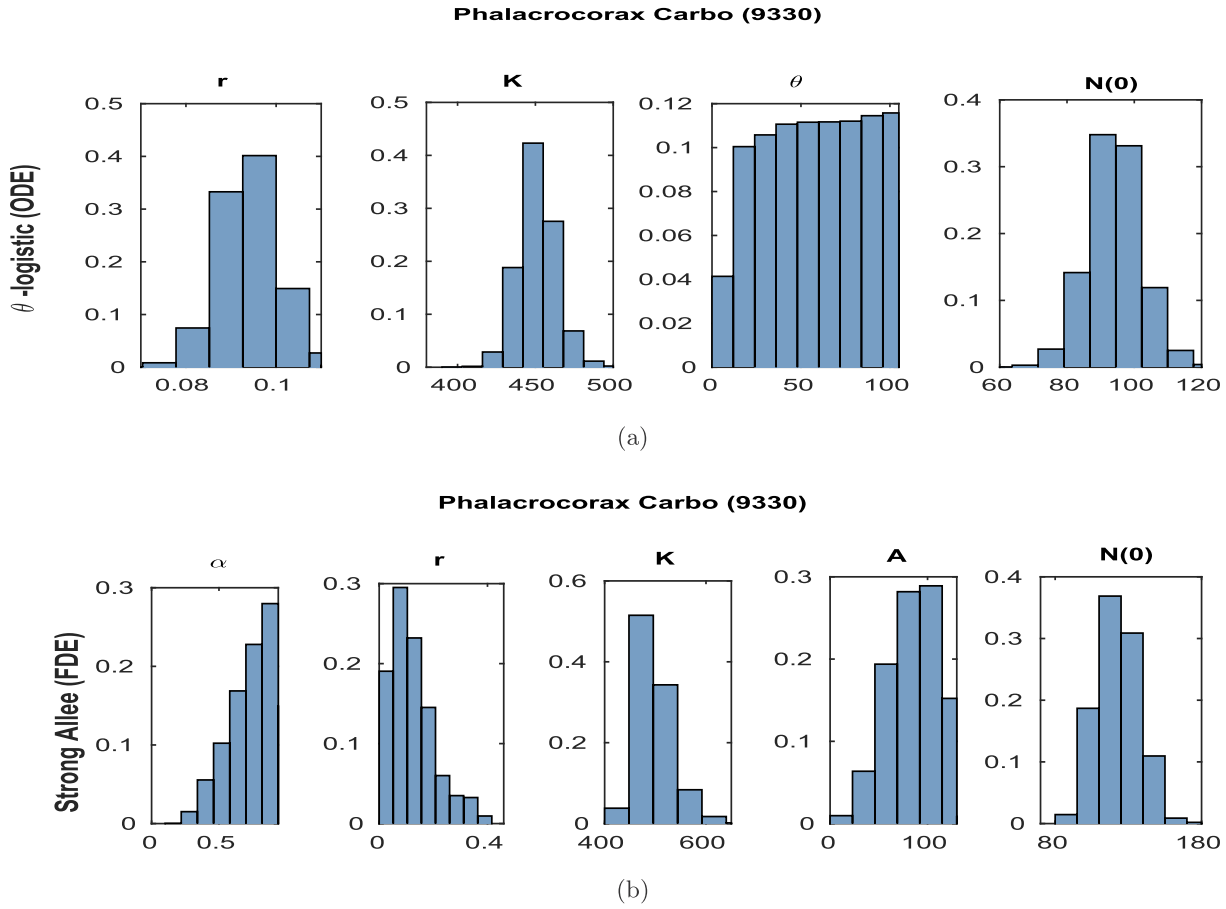

Fig. F-9. Marginal distributions of different parameters of the best fitted growth curve models (3) and (10) in ODE and FDE corresponding to growth data of the species *Phalacrocorax carbo* (9330). Fractional order strong Allee model (10) has been selected as the best model according to AIC values.

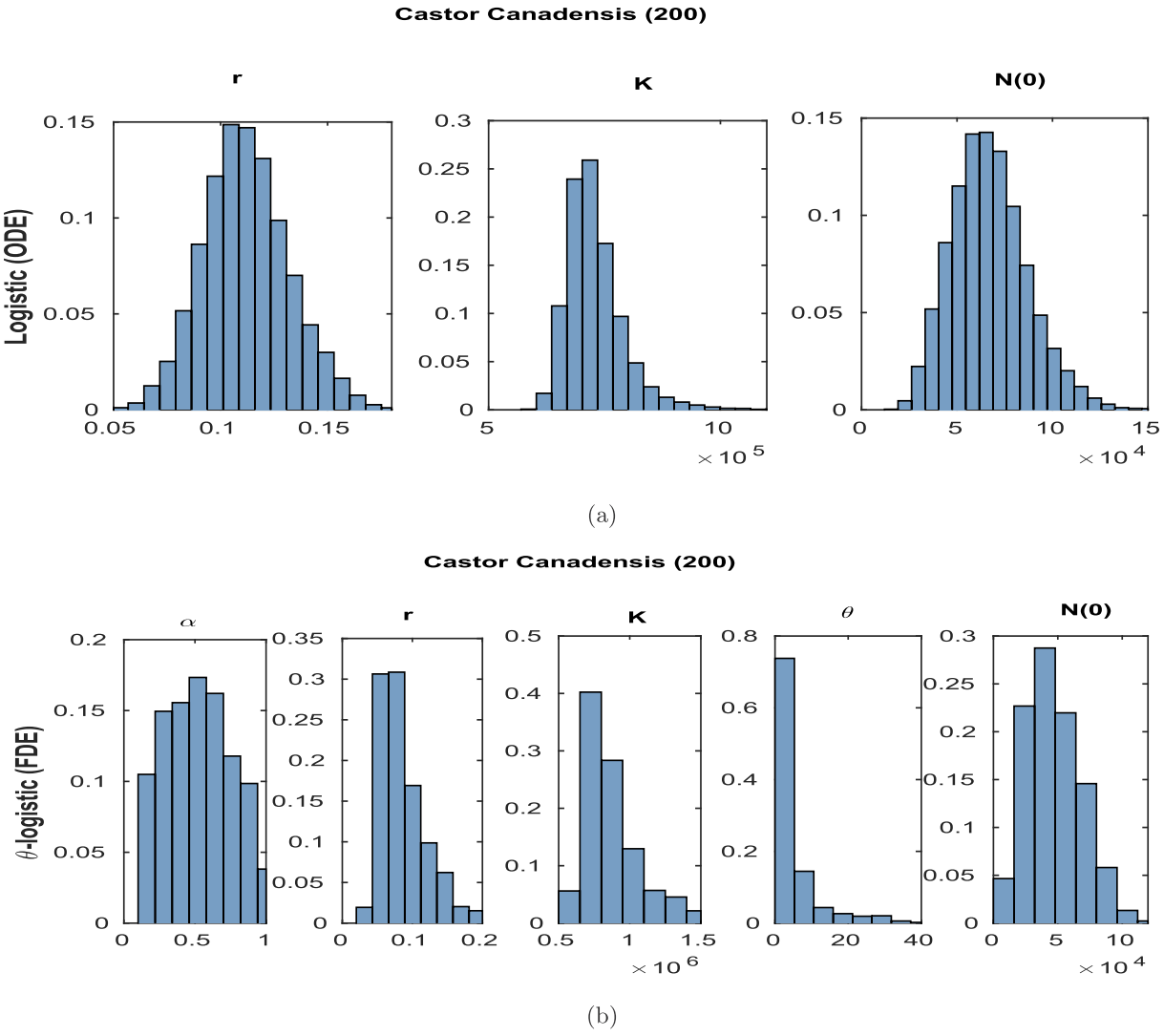

Fig. F-10. Marginal distributions of different parameters of the best fitted growth curve models (2) and (8) in ODE and FDE corresponding to growth data of the species *Castor Canadensis* (200). Fractional order θ-logistic model (8) has been selected as the best model according to AIC values.

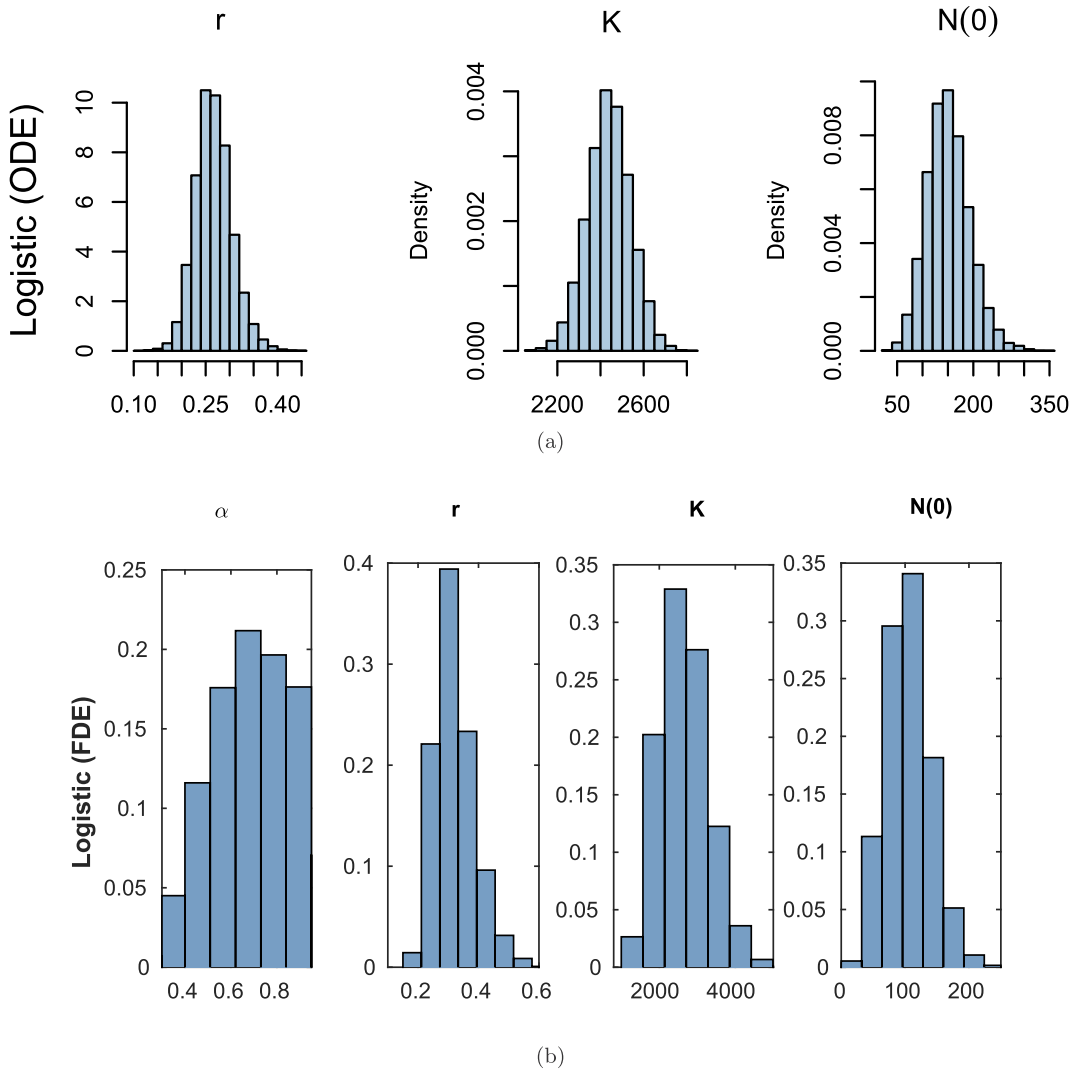

Fig. F-11. Marginal distributions of different parameters of the best fitted growth curve models (2) and (8) in ODE and FDE corresponding to growth data of the species *Ursus americanus* (116). Fractional order θ-logistic model (7) has been selected as the best model according to AIC values.

References

Akaike, H., 1973. Information theory as an extension of the maximum lilelihood principle (Ed.) In: Petrov, B.N., Csaki, F. (Eds.), Second International Symposium on Information Theory. Akademiai Kiado, pp. 267–281.

Allee, W.C., 1931. Animal aggregations. In: A Study in General Sociology. University of Chicago Press, Chicago.

Barker, D., Sibly, R.M., 2008. The effects of environmental perturbation and measurement error on estimates of the shape parameter in the theta-logistic model of population regulation. Ecol. Model. 219, 170–177.

Bhalekar, S., Daftardar-Gejji, V., 2012. Solving fractional-order logistic equation using a new iterative method. Int. J. Diff. Equa. 2012, 1–13.

Bhowmick, A.R., Saha, B., Ray, S., Chattopadhyay, J., Bhattacharya, S., 2015. Cooperation in species: interplay of population regulation andextinction through global population dynamics database. Ecol. Model. 312, 150–165.

Black, R.W., Slobodkin, L.B., 1987. What is cyclomorphosis? Freshw. Biol. 18, 373–378.

Bolhuis, J., Honey, R., 1998. Imprinting, learning, and development: from behaviour to brain and back. Trends Neurosci. 21, 306–311.

Bolton, L., Cloot, H.J.J., Schoombie, S.W., 2014. A proposed fractional-order gompertz model and its application to tumour growth data. Math. Med. B. 1–21.

Brook, B.W., Bradshaw, C.J.A., 2006. Strength of evidence for density dependence in abundance time series of 1198 species. Ecology 87 (6), 1445–1451.

Caputo, M., 1967. Linear models of dissipation whose Q is almost frequency independent: part II. Geophys. J. R. Astron. Soc. 13, 529–539.

Caputo, M., Mainardi, F., 1971. A new dissipation model based on memory mechanism. Pure Appl. Geophys. 91, 147.

Catchpole, C.K., Slater, P.J.B., 2008. Bird Song Biological Themes and Variations. Cambridge University Press, Cambridge.

Cheney, D.L., 2011. Extent and limits of cooperation in animals. In: Proceedings of the National Academy of Sciences, USA. vol. 108. pp. 10902–10909.

Clark, F., Brook, B.W., Delean, S., Akcakaya, H.R., Bradshaw, C.J.A., 2010. The theta-logistic is unreliable for modeling most census data. Methods Ecol. Evol. 1, 253–262.

Clayton, N.S., Dickinson, A., 1998. Episodic-like memory during cache recovery by scrub jays. Nature 395, 272–274.

Clayton, N.S., Griffiths, D., Emery, N.J., Dickinson, A., 2001. Elements of episodic-like memory in animals. Phil. Trans. R. Soc. B 356, 1483–1491.

Clutton-Brock, T., Illius, A., Wilson, K., Grenfell, B., MacColl, A., Albon, S., 1997. Stability and instability in ungulate populations: an empirical analysis. Am. Nat. 149, 195–219.

Courchamp, F., Berec, L., Gascoigne, J., 2008. Allee Effects in Ecology and Conservation. Oxford University Press, Oxford.

Daftardar-Gejji, V., Jafari, H., 2006. An iterative method for solving nonlinear functional equations. J. Math. Anal. Appl. 316, 753–763.

Dalziel, B.D., Morales, J.M., Fryxell, J.M., 2008. Fitting probability distributions to animal movement trajectories: using artificial neural networks to link distance, resources, and memory. Am. Nat. 172, 248–258.

Daniels, T.J., 1983. The social organization of free-ranging urban dogs. II. Estrous groups and the mating system. Appl. Anim. Ethol. 10, 365–373.

Datsko, B., Luchko, Y., 2012. Complex oscillations and limit cycles in autonomous two-component incommensurate fractional dynamical systems. Math. Balk. (N. S.) 26, 65–78.

Dennis, B., 1989. Allee effects: population growth, critical density, and the chance of extinction. Nat. Resour. Model. 3, 481–538.

Diethelm, K., 2010. The Analysis of Fractional Differential Equations. Springer, Berlin.

Diethelm, K., Freed, A.D., 1999. The FracPECE subroutine for the numerical solution of differential equations of fractional order (Eds.) In: Heinzel, S., Plesser, T. (Eds.), Forschung und Wissenschaftliches Rechnen 1998. Gessellschaft fur Wissenschaftliche

Datenverarbeitung, Gottingen, pp. 57–71.
Diethelm, K., Ford, N., Freed, A., 2004. Detailed error analysis for a fractional Adams method. Num. Algoritm. 36 (1), 31–52.
Dokoumetzidis, A., Magin, R., Macheras, P., 2010. Fractional kinetics in multi-compartmental systems. J. Pharmacokinet. Pharmacodyn. 37, 507–524.
Eberhardt, L.L., Breiwick, J.M., 2012. Models for population growth curves. ISRN Ecol. 2012, 1–7.
Eberhardt, L.L., Breiwick, J.M., Demaster, D.P., 2008. Analyzing population growth curves. Oikos 117, 1240–1246.
El-Sayed, A., 1996. Fractional differential-difference equations. J. Fract. Cal. 10, 101–106.
El-Sayed, A., 1998. Nonlinear analysis: theory, methods & applications. Nonlinear Anal. 33 (2), 181–186.
El-Sayed, A., Gaafar, F., 2001. Fractional order differential equations with memory and fractional-order relaxation-oscillation model. Pure Math. Appl. 12.
El-Sayed, A., Gaafar, F., Hashem, H., 2004. On the maximal and minimal solutions of arbitrary orders nonlinear functional integral and differential equations. Math. Sci. R. J. 8 (11), 336–348.
El-Sayed, A., El-Mesiry, A., El-Saka, H., 2007. On the fractional-order logistic equation. Appl. Math. Lett. 20, 817–823.
Fowler, C.W., Baker, J.D., 1991. A review of animal population dynamics at extremely reduced population levels. In: Reports of the International Whaling Commission. vol. 41. pp. 545–554.
Fox, D.R., Ridsdill-Smith, J., 1995. Tests for density dependence revisited. Oecologia 103 (4), 435–443.
Garrappa, R., 2010. On linear stability of predictor-corrector algorithms for fractional differential equations. Int. J. Comput. Math. 87 (10), 2281–2290.
Gerber, L.R., Buenau, K.E., Vanblaricom, G., 2004. Density dependence and risk of extinction in a small population of sea otters. Biodivers. Conserv. 13 (14), 2741–2757.
Getz, W.M., Lloyd-Smith, W.O., 2006. Comment on "on the regulation of populations of mammals, birds, fish, and insects I". Science 311, 1100.
Geweke, J., 1991. Evaluating the Accuracy of Sampling-Bases Approaches to Calculation of Posterior Moments. Federal Reserve Bank of Minneapolis: Research Department Staff Report, pp. 148.
Gilpin, M.E., Ayala, F.J., 1973. Global models of growth and competition. Proc. Natl. Acad. Sci. U. S. A. 70 (12), 3590–3593 December.
Gilpin, M., Case, T., Ayala, F., 1976. θ-selection. Math. Biosci. 32, 131–139.
Godard, R., 1991. Long-term memory of individual neighbours in a migratory songbird. Nature 350, 228–229.
Gorenflo, R., Mainardi, F., 1997. Fractional calculus: integral and differential equations of fractional order (Ed.) In: Carpinteri, A., Mainardi, F. (Eds.), Fractals and Fractional Calculus in Continuum Mechanics. Springer, Wien, pp. 223–276.
Gregory, S.D., Bradshaw, J.A., Brook, B.W., Courchamp, F., 2010. Limited evidence for the demographic Allee effect from numerous species across taxa. Ecology 91 (7), 2151–2161.
Haario, H., Saksman, E., Tamminen, J., 2001. An adaptive metropolis algorithm. Bernoulli 7, 223–242.
Haario, H., Laine, M., Mira, A., Saksman, E., 2006. Dram: efficient adaptive mcmc. Stat. Comput. 16, 339–354.
Hackney, E., McGraw, J., 2001. Experimental demonstration of an allee effect in american ginseng. Conserv. Biol. 15, 129–136.
He, J., 1999. Variational iteration method – a kind of non-linear analytical technique: some examples. Int. J. Non-Linear Mech. 34 (4), 699–708.
Healy, S.D., Jones, C.M., 2002. Animal learning and memory: an integration of cognition and ecology. Zoology 105 (4), 321–327.
Inchausti, P., Halley, J., 2001. Investigating long-term ecological variability using the global population dynamics database. Science 293 (5530), 655–657.
Johnson, J., Omland, K.S., 2004. Model selection in ecology and evolution. Trends Ecol. Evol. 19 (2), 101–108.
Johnson, D., Liebhold, A., Tobin, P., Bjornstad, O., 2006. Allee effects and pulsed invasion by the gypsy moth. Nature 444, 361–363.
Knape, J., de Valpine, P., 2012. Are patterns of density dependence in the global population dynamics database driven by uncertainty about population abundance? Ecol. Lett. 15, 17–23.
Laine, M., 2008. Adaptive MCMC Methods with Applications in Environmental and Geophysical Models. Ph.D. Thesis. Finnish Meteorological Institute.
Liermann, M., Hilborn, R., 1997. Depensation in fish stocks: a hierarchic Bayesian meta-analysis. Can. J. Fish. Aquat. Sci. 54, 1976–1984.
Mathai, A.M., 2014. Fractional integral operators involving many matrix variables. Linear Algebra Appl. 446, 196–215.
Matignon, D., 1996. Stability results for fractional differential equations with applications to control processing. In: Computational Engineering in System Application, pp. 963 Lille, France.
Matouk, A., 2009. Stability conditions, hyperchaos and control in a novel fractional order hyperchaotic system. Phys. Lett. A 373, 2166–2173.
May, R.M., Conway, G., Hassel, M.P., Southwood, T., 1974. Time delays, density-dependence and single-species oscillations. J. Anim. Ecol. 43 (3), 747–770.
McCall, P., Kelly, D., 2002. Learning and memory in disease vectors. Trends Parasitol. 18 (10), 429–433.
Murdoch, W.W., Kendall, B.E., Nisbet, R.M., Briggs, C.J., McCauley, E., Bolser, R., 2002. Single-species models for many-species food webs. Nature 417, 541–543.
Murray, J.D., 2002. Mathematical Biology. Springer, Berlin.
Myers, R., Barrowman, N., Hutchings, J., Rosenberg, A., 1995. Population dynamics of exploited fish stocks at low population levels. Science 269, 1106–1108.
NERC Centre for Population Biology, I. C, 2010. The Global Population Dynamics Database v2.0. URL. http://www.sw.ic.ac.uk/cpb/cpb/gpdd.html.
Oldham, K.B., Spanier, J., 1974. The Fractional Calculus: theory and Applications of Differentiation and Integration to Arbitray Order. Dover Publications.
Oldham, K.B., Spanier, J., 2006. Fractional Calculus in Bioengineering. Begell House Publishers.
Podlubny, I., 1999. Fractional Differential Equations. Academic Press, San Diego, California.
Rana, S., Bhattacharya, S., Pal, J., NGurkata, G.M., Chattopadhyay, J., 2013. Paradox of enrichment: a fractional differential approach with memory. Physica A 392, 3610–3621.
Ross, J.V., 2006. Comment on "on the regulation of populations of mammals, birds, fish, and insects" II. Science 311, 1100.
Ross, J.V., 2009. A note on density dependence in population models. Ecol. Model. 220, 3472–3474.
Saha, B., Bhowmick, A.R., Chattopadhyay, J., Bhattacharya, S., 2013. On the evidence of an allee effect in herring populations and consequences for population survival: a model-based study. Ecol. Model. 250, 72–80.
Schwarz, G., 1978. Estimating the dimensions of a model. Ann. Stat. 6 (2), 461–464.
Sibly, R.M., Hone, J., Clutton-Brock, T.H., 2003. Introduction to wildlife population growth rates (Ed.) In: Sibly, R.M., Hone, J., Clutton-Brock, T.H. (Eds.), Wildlife Population Growth Rates. Cambridge University Press, Cambridge, UK, pp. 1–10.
Sibly, R.M., Barker, D., Denham, M.C., Hone, J., Pagel, M., 2005. On the regulation of populations of mammals, birds, fish, and insects. Science 309, 607–610.
Sibly, R.M., Barker, D., Hone, J., Pagel, M., 2007. On the stability of populations of mammals, birds, fish and insects. Ecol. Lett. 10, 970–976.
Smouse, P.E., Focardi, S., Moorcroft, P.R., Kie, J.G., Forester, J.D., Morales, J.M., 2010. Stochastic modelling of animal movement. Phil. Trans. R. Soc. B 365, 2201–2211.
Soetaert, K., Petzoldt, T., 2010. Inverse modelling, sensitivity and Monte Carlo analysis in R using package FME. J. Stat. Softw. 33 (3), 1–28.
Stephens, D.W., Krebs, J.R., 1986. Foraging Theory. Princeton University Press, Princeton NJ.
Stephens, P.A., Sutherland, W.J., 1999. Consequences of the Allee effect for behaviour, ecology and conservation. Trends Ecol. Evol. 14, 401–405.
Turchin, P., 1994. Wildlife Ecology and Management. Wiley.
Turchin, P., 2002. Population Viability Analysis. University of Chicago Press, Chicago, IL.
Turchin, P., 2003. Complex population dynamics: a theoretical/empirical synthesis. In: No. 35 in Monograph in Population Biology. Princeton University Press, Princeton.
Verhulst, P., 1838. Notice sur la loi que la population poursuit dans son accroissement. Corresp. Mathmati. Phys. 10, 113–121.
Zheng, Z., Yamasaki, J., Tenenbaum, B., Podobnik, Y., Tamura, H., 2012. Stanley, scaling of seismic memory with earthquake size. Phys. Rev. E 86 (1).
Ziebarth, N.L., Abbott, K.C., Ives, A.R., 2010. Weak population regulation in ecological time series. Ecol. Lett. 13 (1), 21–31.

Source details

Feedback > Compare sources >

Ecological Informatics

Scopus coverage years: from 2006 to Present

Publisher: Elsevier

ISSN: 1574-9541

Subject area: Mathematics: Applied Mathematics | Computer Science: Computational Theory and Mathematics | Mathematics: Modeling and Simulation | Agricultural and Biological Sciences: Ecology, Evolution, Behavior and Systematics | Environmental Science: Ecology View all

Source type: Journal

View all documents > Set document alert Save to source list

CiteScore 2022
6.1

SJR 2022
0.915

SNIP 2022
1.398

CiteScore | CiteScore rank & trend | Scopus content coverage

Journal of Theoretical Biology 478 (2019) 139–152

Contents lists available at ScienceDirect

Journal of Theoretical Biology

journal homepage: www.elsevier.com/locate/jtb

Impact of adult mosquito control on dengue prevalence in a multi-patch setting: A case study in Kolkata (2014–2015)

Abhishek Senapati[a,*], Tridip Sardar[b], Krishnendra Sankar Ganguly[c], Krishna Sankar Ganguly[d], Asis Kumar Chattopadhyay[e], Joydev Chattopadhyay[a]

[a] Agricultural and Ecological Research Unit, Indian Statistical Institute, 203, B. T. Road, Kolkata 700108, India
[b] Department of Mathematics, Dinabandhu Andrews College, Kolkata, West Bengal 700084, India
[c] National Informatics Centre, Kolkata, West Bengal, India
[d] Health Department, The Kolkata Municipal Corporation, Kolkata, West Bengal, India
[e] Department of Statistics, University of Calcutta, India

ARTICLE INFO

Article history:
Received 4 March 2019
Revised 17 June 2019
Accepted 19 June 2019
Available online 20 June 2019

Keywords:
Dengue
Multi-patch model
Adult mosquito control
Non-Autonomous system
Kolkata

ABSTRACT

Dengue is one of the deadliest mosquito-borne disease prevalent mainly in tropical and sub-tropical regions. Controlling the spread of this disease becomes a major concern to the public health authority. World Health Organization (WHO) adopted several mosquito control strategies to reduce the disease prevalence. In this work, a general multi-patch non-autonomous dengue model is formulated to capture the temporal and spatial transmission mechanism of the disease and the effectiveness of different adult mosquito control strategies in reducing dengue prevalence is evaluated. During the period (2014–2015) the dengue situation of Kolkata which is one of the most dengue affected city in India is considered in our study. Depending on geographical location, Kolkata is divided into five regions and our model is fitted to the monthly dengue cases of these five regions during the above-mentioned period. By considering control specific characteristics (e.g. efficacy, environment persistence) of the mosquito control strategies, we study the efficiency of three adult mosquito controls and their combined effect in reducing dengue prevalence. From our study, it is observed that control with higher environment persistence performs better in comparison to the controls having low environment persistence. It is also observed that, connectedness between the regions play a key role in the effectiveness of the control strategies.

1. Introduction

Human society is cursed with the burden of dengue. *Aedes* mosquitoes are the vectors responsible for this disease transmission. The number of dengue endemic country is gradually increasing. Dengue is widespread in more than hundred countries in tropical and sub-tropical regions (WHO, 2016). During the period 1990–2015, dengue appeared in the form of epidemic almost 262 times all over the world and consequently infected about 0.3 million individuals (Guo et al., 2017). Due to the fatality of this disease, dengue control becomes a great concern to the public health authorities and policy makers.

The transmission of dengue virus can be reduced either by adopting personal protection against mosquito bites or by controlling mosquito population. To acquire protection from mosquito bites, individuals generally cover their skin with full sleeve clothes, use mosquito-repellents on skin, and use bed-net etc. (WHO, 2009). On the other hand, several mosquito control techniques such as environmental control, chemical control, biological control etc. are employed to reduce the abundance of both larval and adult mosquito population (WHO, 2009). In environmental control technique, the habitats of mosquitoes such as large water containers, old tyres, septic tanks etc. are demolished or the water stored in these are emptied regularly (Baldacchino et al., 2015; Araújo et al., 2015). The chemical control techniques are used to kill the mosquitoes using various larvicides and insecticides (WHO, 2003; Araújo et al., 2015). Biological control strategy refers to the use of different species or organisms which reduce the *Aedes* mosquito population (Benelli et al., 2016). However, in terms of effectiveness, the adoption of adult mosquito control strategy is more fruitful than larval control especially in the situation where a faster depletion in disease prevalence is required (Gratz, 1991). Recently, the adult mosquito strategies like the use of materials

* Corresponding author.
E-mail address: abhishekiz4u04@gmail.com (A. Senapati).

https://doi.org/10.1016/j.jtbi.2019.06.021
0022-5193/

treated with insecticide, use of lethal ovitraps and ultra low volume (ULV) application of insecticides etc. are gaining considerable attentions (Perich et al., 2000; 2003; Kroeger et al., 2006).

Mathematical models have been utilized to observe the consequences of employing different control mechanisms in reducing the disease prevalence. A large number papers in the literature have been published which are devoted in describing disease dynamics and the outcomes of the control measures in the context of dengue disease using different mathematical models (see Andraud et al. (2012) and the references therein). The compartmental models describing the mechanisms of dengue transmission can be categorized broadly into two types: non-spatial models and spatial models. Non-spatial modeling approach assumes that the space under consideration is homogeneous and therefore no spatial variations across the space is incorporated into the models. However, the variability in different epidemiological and entomological factors of dengue across geographical locations are observed. Moreover, since the dengue transmission mechanism is two-fold in nature in the sense that human and mosquito both infect each other, the human mobility accelerates the disease propagation across distant parts of a particular city, province or country (Adams and Kapan, 2009; Stoddard et al., 2013; Wesolowski et al., 2015). Therefore, it becomes very essential to adopt spatial modeling approach which encompasses the different spatial features and explicit human migration to capture the disease dynamics more accurately. The transmission dynamics of dengue and its control in a multi-patch model setting are also well studied (see Wesolowski et al., 2015; Barrios et al., 2018; Nevai and Soewono, 2014; Hendron and Bonsall, 2016; Lee and Castillo-Chavez, 2015 etc.). But the above-mentioned studies did not consider the characteristics like efficacy and environment persistence of the available mosquito control strategies in evaluating the impact of controls. However, in the non-spatial framework, a few studies have incorporated the control specific characteristics while executing the efficiency of mosquito control strategies (Newton and Reiter, 1992; Burattini et al., 2008; Luz et al., 2009; 2011; Oki et al., 2011) to get more realistic insights. To our knowledge, in a spatially connected scenario, the quantification of the efficiency of different mosquito control strategies in lowering disease transmission and also the role of spatial coupling in the effectiveness of the controls by considering the control specific characteristics have not been studied yet.

In this present study, we propose a spatially explicit model for dengue transmission to evaluate the consequences of only the adult mosquito control strategies and also study the role spatial connectedness in the efficiency of the intervention strategies. Dengue cases of Kolkata for the period (2014–2015) is considered for the first time for validating the model and to evaluate the outcomes of applying different adult mosquito control strategies namely the use of materials treated with insecticide, use of lethal ovitraps and ultra low volume (ULV) application of insecticides to get practical insights from our study.

The paper is arranged in the following manner. Section 2 is alloted for the brief description and some mathematical analysis of the proposed model. A brief discussion on the three adult mosquito control strategies is given in Section 3. Section 4 is devoted to the description of model calibration. In Section 5 our proposed intervention settings and their effectiveness is discussed. The manuscript ends with a brief discussion (Section 6).

2. Model formulation and analysis

We use multi-patch modeling approach to describe the spatio-temporal evolution of dengue disease dynamics. The whole space of human residence is partitioned into n distinct regions (patch) based on the geographical locations connected through human migration. Depending on the range and duration, the human migration/mobility can be classified into different types of mobility patterns such as long-term, short-term, commuting etc. (Arino, 2017). However, in this study we consider the short term or commuting type of mobility (Cosner et al., 2009; Prosper et al., 2012). Differentiating on the basis of health status of human in each patch i $(1 \le i \le n)$, the human population is divided into five subclasses: susceptible, exposed, infectious, asymptomatic and recovered. Let $S_H^i(t)$, $E_H^i(t)$, $I_H^i(t)$, $A_H^i(t)$ and $R_H^i(t)$ denote the number of susceptible, exposed, infectious, asymptomatic and recovered human population in patch i at any instant of time t. Similarly, the mosquito population (adult female mosquitoes) in each patch is also categorized into two compartments: susceptible mosquito (S_M^i) and infected mosquito (I_M^i). The following assumptions on different demographical, epidemiological and entomological factors are made in formulating the model:

- The birth rate and death rate of human are assumed to be equal for each patch and denoted by μ_H. Therefore the total human population size in patch i remains constant over the time and we denote it by $H^i = S_H^i + E_H^i + I_H^i + A_H^i + R_H^i$.
- The rate of recovery of the people from both the compartments (infected and asymptomatic) are assumed to be same, γ_H.
- The biting rate of mosquito depends on different components of climate such as temperature and rainfall etc. of a particular region. Therefore, we choose the biting rate to be periodic with one year period. In the present study, month is considered to be the unit of time. Therefore, we consider the biting rate of mosquito in patch i as, $b_i(t) = b_{0i}(1 - \delta_i \cos(\frac{2\pi t}{12}))$, where b_{0i} and δ_i are the average number of bites per mosquito per month in patch i and amplitude of the oscillation respectively.
- We assume that the susceptible mosquito get infected by dengue infected human and move directly to infected mosquito class (I_M^i). We do not consider any exposed class for mosquito population.
- Since we consider a single-serotype dengue model, the disease-induced death is not incorporated into the model (Halstead, 2009).

The susceptible human in each patch increases due to the birth of the human population and decreases due to natural death of the human. People who are susceptible to dengue in a particular patch can get infected by the bites of infected *Aedes* mosquitoes and move to the exposed class (E_H^i). Since we consider a connected space where people can migrate between different patches, susceptible population belonging to a specified patch can get bites of mosquitoes in two ways: (i) while they reside in their patch of residence, and (ii) while they visit the remaining patches. We neglect the movement of mosquito as they have a limited flight range (McDonald, 1977; Muir and Kay, 1998). Therefore, the force of infection from mosquito to human in ith patch is given by,

$$\beta_H \frac{b_i(t)}{H^i} I_M^i + \beta_H \sum_{\substack{j=1 \\ j \neq i}}^{n} \epsilon_{ij} \frac{b_j(t)}{H^j} I_M^j.$$

The first term is due to the infection within the patch and the second term corresponds the infections coming from the remaining patches. The transmission probability of infection from mosquito to human is denoted by β_H. The intensities of the infections contributed from the visiting patches are assumed to be less than the infection from the patch of residence (Grenfell, 1998).

Table 1
Description of parameters for dengue model (2.1).

Parameters	Description	Value	Reference
μ_H	Birth/death rate of human population	0.0143–0.0167 year^{-1}	(Pinho et al., 2010; Derouich and Boutayeb, 2006)
Π^i_M	Recruitment rate of mosquito	$\mu_M(S^i_M(0)+E^i_M(0)+I^i_M(0))$	(Sardar et al., 2015)
μ_M	Mortality rate of female mosquitoes	0.6–7.5 month^{-1}	(Sardar et al., 2015; Andraud et al., 2012)
b_{0i}	Average bite per mosquito per month in patch i	Estimated	–
β_H	Transmission probability from mosquito to human	0.1–1	(Sardar et al., 2015; Andraud et al., 2012)
β_M	Transmission probability from human to mosquito	0.5–1	(Sardar et al., 2015; Andraud et al., 2012)
p	Fraction of exposed human move to dengue infected class	Estimated	–
η_1	Modification parameter	Estimated	–
η_2	Modification parameter	Estimated	–
γ_H	Recovery rate from dengue infection	2.14–10 month^{-1}	(Sardar et al., 2015; Andraud et al., 2012)
σ_H	Intrinsic incubation rate	2.1410 month^{-1}	(Pinho et al., 2010)
d_{ij}	Distance between the centroids of patch i and patch j	–	
θ	Scaling parameter	Estimated	–
α	Power that determines the strength of the dependence of migration rate on distance	Estimated	–
$\hat{H}_i$	Human population density in patch i	–	–

This situation is captured by introducing the coupling strength between the patches. The coupling strength between patch i and patch j is denoted by ϵ_{ij} with $0 \le \epsilon_{ij} \le 1$. Since the coupling between the patches is induced by human migration, we assume that the coupling strength follows so-called 'gravity-like' rule of migration (Lewer and Van den Berg, 2008). The coupling strength is given by the following expression:

$$\epsilon_{ij} = \theta \frac{\hat{H}^i \hat{H}^j}{d_{ij}^{\alpha}}.$$

The coupling strength is proportional to the product of human population density of patch i and patch j ($\hat{H}^i$ and $\hat{H}^j$) and inversely proportional to some exponent (α) of the distance (d_{ij}) between the patches. The exponent α governs the distance dependency of migration rate. The term θ is the proportional constant or scaling parameter.

The human exposed to dengue is transferred to the infected and asymptomatic human compartment at a rate σ_H. We assume that p portion of exposed human move to infected compartment and remaining $(1-p)$ portion move to asymptomatic compartment. The infected and asymptomatic human get recovery at a rate γ_H and move to the recovered class. On the other hand the susceptible mosquito is recruited at a constant rate Π^i_M. The mosquito population is decreased at a rate μ_M due to death. It is well established fact that susceptible mosquitoes can get infected and move to the infected class if they bite infected human as well as the human who are in exposed and asymptomatic state with certain probability (Wilder-Smith et al., 2004; Duong et al., 2015). Therefore, the force of infection from human to mosquito in a given patch i is given by:

$$b_i(t)\beta_M\left(\frac{(I^i_H+\eta_1E^i_H+\eta_2A^i_H)}{H^i}+\sum_{\substack{j=1\\ j\neq i}}^{n}\epsilon_{ij}\frac{(I^j_H+\eta_1E^j_H+\eta_2A^j_H)}{H^i}\right).$$

The transmission probability of infection from human to mosquitois denoted by β_M and the parameters η_1 and η_2 are incorporated to modify the transmission rate corresponding to exposed and asymptomatic classes of human. These modification parameters are taken to be less than or equal to unity. The above assumptions and considerations lead to the following dengue transmission model (2.1). The description of the model parameters is presented in Table 1.

$$\begin{aligned}
\frac{dS^i_H}{dt} &= \mu_H H^i - \beta_H S^i_H\left(\frac{b_i(t)}{H^i}I^i_M+\sum_{\substack{j=1\\ j\neq i}}^{n}\epsilon_{ij}\frac{b_j(t)}{H^j}I^j_M\right)-\mu_H S^i_H,\\
\frac{dE^i_H}{dt} &= \beta_H S^i_H\left(\frac{b_i(t)}{H^i}I^i_M+\sum_{\substack{j=1\\ j\neq i}}^{n}\epsilon_{ij}\frac{b_j(t)}{H^j}I^j_M\right)-(\sigma_H+\mu_H)E^i_H,\\
\frac{dI^i_H}{dt} &= p\sigma_H E^i_H-(\mu_H+\gamma_H)I^i_H,\\
\frac{dA^i_H}{dt} &= (1-p)\sigma_H E^i_H-(\mu_H+\gamma_H)A^i_H,\\
\frac{dR^i_H}{dt} &= \gamma_H(I^i_H+A^i_H)-\mu_H R^i_H,\\
\frac{dS^i_M}{dt} &= \Pi^i_M - b_i(t)\beta_M S^i_M\left(\frac{(I^i_H+\eta_1E^i_H+\eta_2A^i_H)}{H^i}\right.\\
&\qquad\left.+\sum_{\substack{j=1\\ j\neq i}}^{n}\epsilon_{ij}\frac{(I^j_H+\eta_1E^j_H+\eta_2A^j_H)}{H^i}\right)-\mu_M S^i_M,\\
\frac{dI^i_M}{dt} &= b_i(t)\beta_M S^i_M\left(\frac{(I^i_H+\eta_1E^i_H+\eta_2A^i_H)}{H^i}\right.\\
&\qquad\left.+\sum_{\substack{j=1\\ j\neq i}}^{n}\epsilon_{ij}\frac{(I^j_H+\eta_1E^j_H+\eta_2A^j_H)}{H^i}\right)-\mu_M I^i_M,\\
&\qquad i=1,2,\ldots,n.
\end{aligned} \tag{2.1}$$

Some dynamical properties of our model (2.1) have been studied by applying standard theory of nonlinear dynamics. The analytical results regarding the boundedness and persistence of the solution of our model have been carried out to ensure the biological relevance of our model (see Appendix A and Appendix D). The mathematical expression for basic reproduction number ($\mathcal{R}_0$), an important measure in epidemiology, has been derived and based on the threshold value of ($\mathcal{R}_0$), the stability of DFE and the global stability of the periodic solution have been examined (see Appendix B, Appendix C and Appendix E).

3. Adult mosquito control strategies

Dengue disease prevalence can be reduced in a region if proper control strategies are implemented. Mosquito control can be

accomplished by adopting larval control and adult mosquito control. However adult mosquito control is more effective than larval control in a region where dengue outbreak has already taken place, because the bite of the adult mosquito is responsible for the transmission of the disease. In this study we consider three adult mosquito control strategies and evaluate the efficiency of these controls in reducing the dengue cases. A brief description of different control strategies which we are going to follow is presented below.

C1. Ultra-low-volume (ULV) spray of insecticides: In this technique, a small amount of insecticides are used to create cold fog droplets which are used in controlling adult mosquito (Ditsuwan et al., 2012; WHO, 2003). The droplets can be produced by using ULV cold fogging machine. There are variations in the efficacy of ULV spray: high efficacy (90%), intermediate efficacy (60%) and low efficacy (30%) (Luz et al., 2009). The environment persistence of ULV spray is 1 day that means after 1 day the control method loses its efficiency (Luz et al., 2009; Perich et al., 2000).

C2. Insecticide treatment of surface and materials: Windows and door curtains, water container covers etc. in households are treated with insecticides to avoid the contact of adult mosquito. The environment persistence of this control strategy is 180 days and the efficacy is 25% (Luz et al., 2009; Kroeger et al., 2006).

C3. Lethal ovitraps: Lethal ovitraps is a container-type device used to kill female mosquito. Usually this type of traps are made black in colour and are filled with water and very small amount of lethal substances which kill the mosquito. These devices are usually placed in the breeding sites of mosquito where female mosquitoes are attracted to enter the container to lay eggs and get trapped and killed. The environment persistence of lethal ovitraps is 120 days and the efficacy is 25% (Luz et al., 2009; Perich et al., 2003).

The consequence of the application of the above mentioned adult mosquito controls would be an additional death of the mosquito. Since each control strategy has its own efficacy and environment persistence, the death rate of the mosquito population due to the application of the control strategy would be different. The death rate will be maximum at the beginning of the application and it is equals to the maximum efficacy of that particular control and decreases in the subsequent times and ultimately equals to zero at the end of its environment persistence. Therefore, we consider the death rate as follows (Luz et al., 2009):

$$\begin{aligned} d_i(t) &= \kappa_i\left(1-\frac{t^2}{T_i^2}\right), \ \ for\ 0 \le t \le T_i \\ &= 0, \qquad for\ t > T_i, \qquad i = C1, C2, C3. \end{aligned} \tag{3.1}$$

where, κ_i and T_i denotes the efficacy and the environment persistence of the ith control strategy respectively.

In the next section we evaluate how effectively the above said control strategies reduce the dengue cases in spatially coupled region. To address this query, we consider the dengue situation of Kolkata during the period (2014–2015) as case study. We first divide the whole city into five regions depending on the geographical location and apply the control strategies one at a time and also their combination only to the regions where dengue endemicity is high.

4. Case study: dengue scenario of Kolkata (2014–2015)

India is one of the most dengue affected country in the world. A large number of dengue outbreak has already taken place in India (Guo et al., 2017; Ganeshkumar et al., 2018). Several states of India like Delhi, Orissa, West Bengal etc. have been facing high dengue endemicity since last several decades (Guo et al., 2017). More specifically Kolkata, the capital of West Bengal faced several dengue outbreaks in recent times. A large number of dengue cases are confirmed every year. In this study, we consider the dengue scenario of Kolkata during the period 2014 – 2015. Monthly dengue cases data are collected from Kolkata Municipal Corporation (KMC) for 141 wards. Basically we have 24 data points (monthly dengue cases) for each of the 141 wards. Depending on the geographical location we group the 141 wards into five regions: Region 1 (West), Region 2 (South), Region 3 (East), Region 4 (North), Region 5 (Central) (see Fig. 1). We aggregate the dengue cases data of different wards under a particular region to produce the monthly cases data of that region.

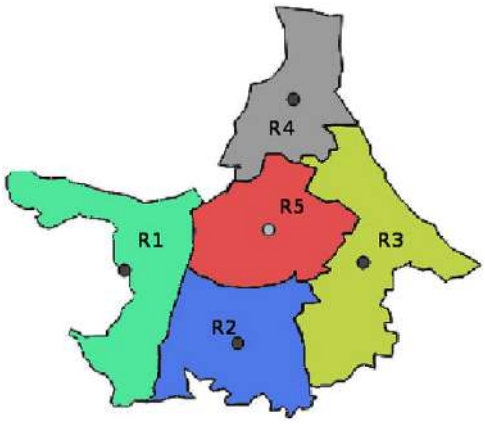

Fig. 1. Different regions of the Kolkata city. R1 denotes Region 1, R2 denotes Region 2, R3 denotes Region 3, R4 denotes Region 4,R5 denotes Region 5. The black dot in the region represents the centroid of that particular region.

4.1. Model calibration

We calibrated our multi-patch dengue model (2.1) to the monthly new Dengue cases for the five regions of Kolkata. Monthly dengue cases are obtained for the period January, 2014–December, 2015 from Kolkata Municipal Corporation (KMC). Since our model is formulated in a multi-patch setting, different coupling intensities (ϵ_{ij}) are involved in the model to connect the patches. Instead of assuming the values of the parameter ϵ_{ij}, we consider a gravity like form for estimating these parameters. The form of the coupling intensities ϵ_{ij} between ith patch and jth patch is given by $\epsilon_{ij} = \theta \frac{\hat{H}^i \hat{H}^j}{d_{ij}^{\alpha}}$. Here $\hat{H}^i$ denotes the population density in ith patch, which can be calculated by dividing the total population in the ith patch by the total area of that patch. In our study the total populations of the five regions and the total area of these regions are taken from KMC. In Table 2 total population, total area and population densities of the five regions are presented. The term d_{ij} denotes the distance between the ith and jth patches. We calculate the distances between the centroids of the five regions of Kolkata by using QGIS software (QGIS Development Team, 2009). The distance matrix is given in Table 3.

Table 2
Total population, total area and population density of the five regions of Kolkata. Region 1–Regions 5 are defined as in Fig. 1.

Regions	Total population(H^i)	Total area (in sq. km.)	Population density($\hat{H}^i$)
Region 1	774871	39.692	19522.095
Region 2	781226	37.297	20946.081
Region 3	619214	42.024	14734.770
Region 4	1274109	29.653	42967.288
Region 5	1059192	32.801	32291.45

Table 3
Distance matrix between the five regions obtained from QGIS software.

	Region 1	Region 2	Region 3	Region 4	Region 5
Region 1	0	201.17	360.84	363.55	225.73
Region 2	201.17	0	226.27	376.89	177.29
Region 3	360.84	226.27	0	267.31	152.05
Region 4	363.55	376.89	267.31	0	199.86
Region 5	225.73	177.29	152.05	199.86	0

4.2. Estimation procedure

Several model parameters are estimated by fitting our model (2.1) to the monthly dengue cases of Kolkata. The parameters which we have estimated from the data are: (*i*) fraction of human exposed to dengue move to infected class (p), (*ii*) average biting rate of mosquito in patch i (b_{0i}), (*iii*) amplitude of the oscillation (δ_i), (*iv*) scaling parameter (θ), (*v*) strength of the dependence of coupling on distance (α), (*vi*) modification parameters (η_1 and η_2).

The new dengue cases for jth region at tth month from the model (2.1) are given by,

$$N^j(t,\hat{\theta}) = \int_{t-1}^{t} p\sigma_H E_H^j(\tau)d\tau, \quad j = 1, 2, \ldots, 5. \tag{4.1}$$

where, $\hat{\theta}$ consists of all the unknown parameters of the model (2.1) which are to be estimated. The sum of square function is given by,

$$SS_j(\hat{\theta}) = \sum_{k=1}^{T}[N^j(t_k) - N^j(t_k,\hat{\theta})]^2, \quad j = 1, 2, \ldots, 5. \tag{4.2}$$

where $N^j(t_k)$ denotes the observed data at the t_k^{th} month and T is the number of data points. In our case $T = 24$.

The following procedure are used in estimating the unknown parameters:

1. Using Latin-Hypercube-Sampling technique, 1000 samples are drawn for the parameter set $\hat{\theta}$ from biologically feasible ranges of the parameters.
2. We use each sample as initial input to perform nonlinear least-square method to minimize the sum of square function defined in (4.2) and repeat this method 1000 times. Consequently, we obtain 1000 samples of $\hat{\theta}$ which minimize the sum of error function $SS_j(\hat{\theta})$. Nonlinear least-square is done by using MATLAB (Mathworks, R2015a) in-built optimizer function lsqcurvefit.
3. Out of these 1000 samples of the parameter $\hat{\theta}$ we select that $\hat{\theta}$ for which the sum of square function attains minimum value. Then we use this $\hat{\theta}$ as initial guess for obtaining 100,000 posterior MCMC samples by using Delayed Rejection Adaptive Metropolis Hastings (DRAM) algorithm (Haario et al., 2001; 2006). Gewekes Z-scores have been examined for the convergence of the MCMC chain.

The model fitting to the monthly dengue new cases data for the five regions of Kolkata is depicted in the Fig. 2. The estimated parameters values are listed in Table 4.

5. Intervention settings

As discussed in Section 3, we intend to apply the following three adult mosquito controls to reduce the dengue prevalence:

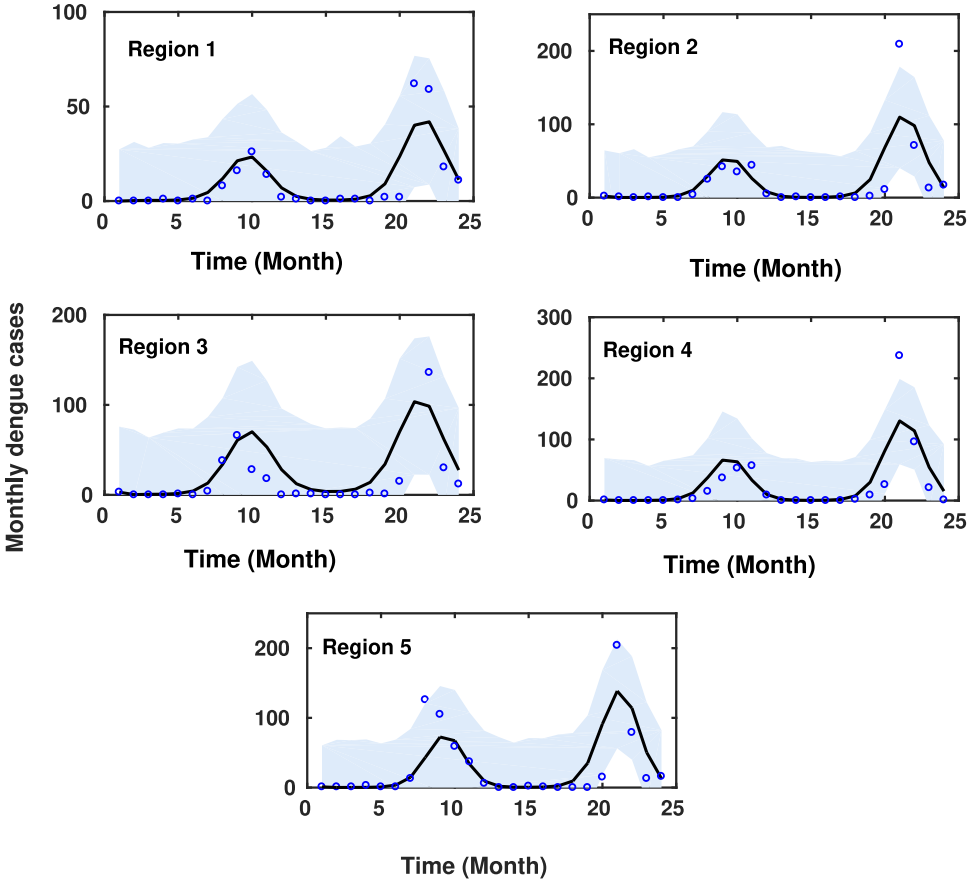

Fig. 2. Model fitting to monthly dengue cases from five regions of Kolkata. Blue circles are the discrete data points and solid black curve is the model solution. Shaded region represent 95% confidence interval.

Table 4
Estimated parameters of the model (2.1). Mean and their 95% confidence interval are given for each of the estimated parameter.

Estimated parameters	Mean	95% confidence interval
p	0.0056	(0.0030,0.0096)
b_{01}	14.4533	(11.5478,17.9077)
b_{02}	13.2803	(10.5869,16.6023)
b_{03}	16.4240	(13.3539,20.5016)
b_{04}	13.8725	(11.0177,17.3072)
b_{05}	13.7472	(10.8592,16.9563)
δ_{01}	0.5075	(0.3286,0.6785)
δ_{02}	0.578	(0.4005,0.6923)
δ_{03}	0.3493	(0.3049,0.4061)
δ_{04}	0.5741	(0.4026,0.6907)
δ_{05}	0.5965	(0.4387,0.6934)
θ	2.2778E-06	(1.2691E-06,2.9482E-06)
α	2.0931	(2.0061,2.2685)
η_1	0.2308	(0.0485,0.4372)
η_2	0.6296	(0.2878,0.9361)

C1. Use of ultra-low volume spray of insecticides.
C2. Treatment of surface and materials with insecticides.
C3. Use of lethal ovitraps.

In this study, we want to evaluate the efficiency of these three mosquito controls when they are applied separately as well as simultaneously. Therefore, we propose the following intervention settings:

I1. Application of **C1** only.
I2. Application of **C2** only.
I3. Use of **C3** only.
I4. Simultaneous application of **C1** and **C2**
I5. Simultaneous application of **C2** and **C3**.
I6. Simultaneous application of **C1** and **C3**.
I7. Simultaneous application of **C1, C2**, and **C3**.

Due to resource constraints, complications in implementing interventions strategies and other economic limitations, it is not always feasible to implement the control strategies in the whole space of a dengue prone region. Moreover, since the regions are connected through human migration and human population play a key role in spreading the disease over different parts of a city or country (Adams and Kapan, 2009), it becomes interesting and essential to study how the impact of intervention strategies is propagated over the regions in such a spatially connected scenario. More specifically, we want to study that if the intervention strategies are applied to a fewer regions instead of all, how much dengue prevalence would be reduced in the regions where interventions are applied and also in the regions where interventions are not applied. To study this, we first single out those regions where dengue endemicity is higher and apply the intervention strategies to these regions only. The regions for which the case fraction is higher than the population fraction, we consider those regions to have higher endemicity (Mubayi et al., 2010). For a particular region, the case fraction is obtained by dividing the cases reported in that region by the total cases reported in all the regions and in a similar manner population fraction can also be calculated. The case fraction and population fraction for the five regions of Kolkata for the first one year are presented in the Table 5, from where we can see that Region 3 and Region 5 are the regions where high endemicity is observed for the first one year. We now apply all the intervention settings to Region 3 and Region 5 at the beginning of the subsequent year and continue it throughout the year to study the consequences of the application of these interventions settings.

Table 5
Case fraction and population fraction for the five regions of Kolkata. The regions with high endemicity are marked bold.

Region	Case fraction	Population fraction
Region 1	0.074	0.140
Region 2	0.173	0.323
Region 3	**0.172**	**0.112**
Region 4	0.192	0.231
Region 5	**0.386**	**0.192**

5.1. Effectiveness of control strategies

In this section, the consequences of the intervention strategies are discussed.

5.1.1. Use of ultra-low volume spray of insecticides

The ultra-low-volume spray of insecticides (ULV) are applied to Region 3 and Region 5. Since this control looses its efficiency after one day, we consider a weekly application of this control which is indeed a practically feasible consideration. Therefore, the first application is done at the beginning of the second year and the next application is executed after 7 days of first application. Continuing this application process throughout the year, ULV is applied 52 times to reduce mosquito population (see Fig. 6A). We choose the ULV spray having high efficacy i.e the value of κ_1 is taken to be 0.9 in the numerical simulation. As a consequence of applying this intervention strategy, it reduces 2.9% and 3.1% cumulative dengue case the Region 3 and Region 5 (see Fig. 3A). For the remaining three regions (Region 1, Region 2 and Region 4), it reduces 2.5%, 2.8%, and 2.7% cumulative cases respectively. The impact of this intervention on dengue prevalence over time in the five regions of Kolkata is depicted in Fig. 5. This intervention reduces overall 2.9% cumulative cases when all the regions are taken into account (see Fig. 4).

5.1.2. Treatment of surface and materials with insecticides

The intervention is also applied to the high endemicity regions (i.e Region 3 and Region 5) at the beginning of the second year. Since it persists in the environment up to 6 months, the strategy is applied twice in a year in our study (see Fig. 6B). The first application is executed at the beginning of the first month and the second application is done at the beginning of the seventh month. It reduces 55% cumulative cases in Region 3 and 54.8% cases in Region 5 whereas the cases reduction in the remaining regions are 40.2%, 44.7%, and 43.7% respectively (see Fig. 3B). Overall cumulative cases reduction by this strategy is 49.1% (see Fig. 4). The time evolution of the cumulative cases with and without this control strategy in the five regions is presented in Fig. 5.

5.1.3. Use of lethal ovitraps

The environment persistence of this control is 4 months. Therefore it is applied thrice in a year (see Fig. 6C). The first application is done at the start of the first month and the next two applications are executed at the beginning of fifth and ninth month respectively. As a result this control reduces 53.6% and 53.1% cumulative cases in Region 3 and Region 5 respectively and 39.5%, 44.2%, and 43.1% cases reduction are observed in the remaining three regions (see Fig. 3C). However it reduces overall 48% dengue cases (see Fig. 4). The effect of this intervention strategy over the time is shown in Fig. 5.

5.1.4. Simultaneous application of ULV and treatment of surface and materials

In this intervention setting both the controls: ULV spray of insecticides and treatment of surface and materials are applied 52

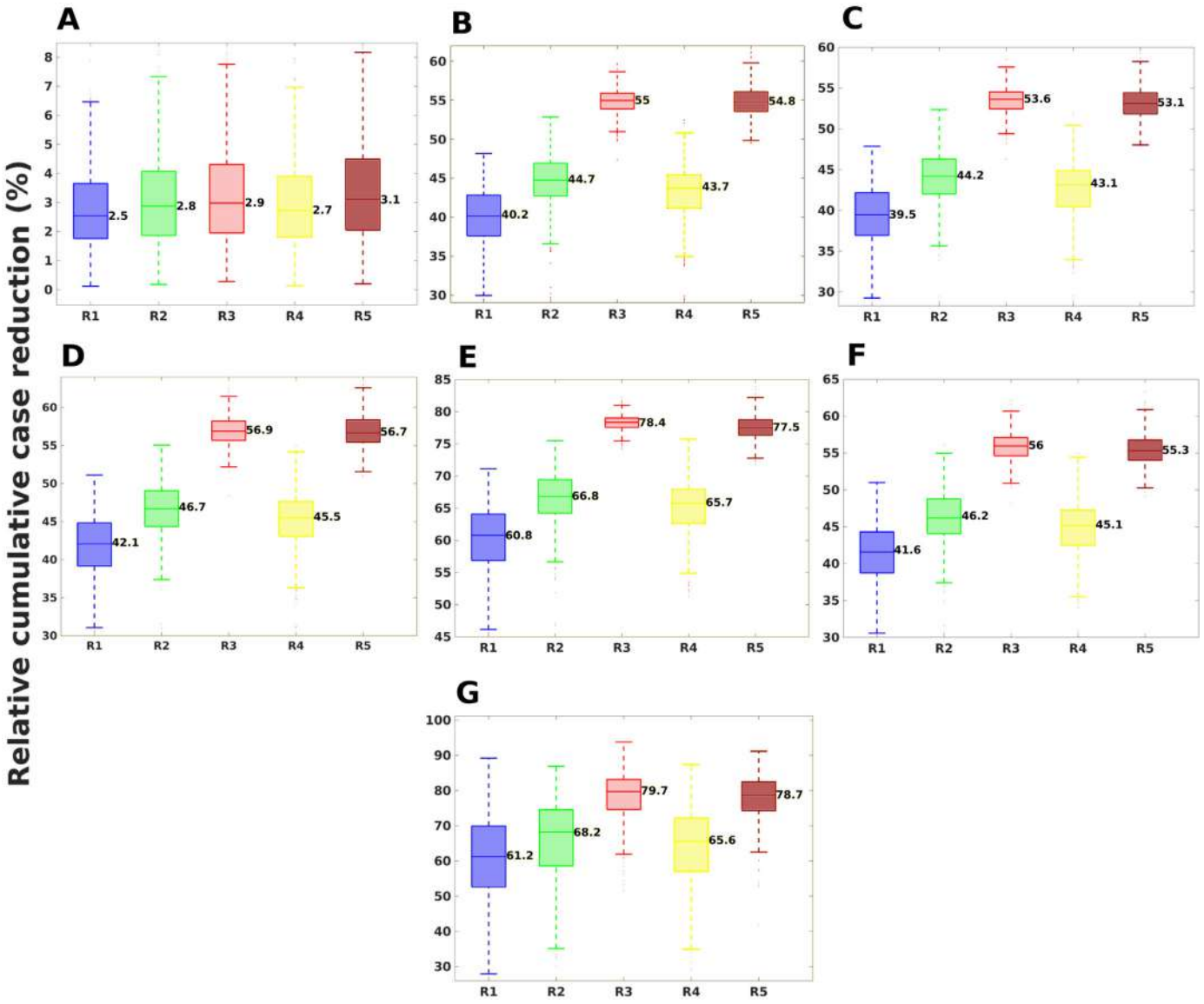

Fig. 3. (A–G) box-plot of Relative cumulative cases reduction in the different regions of Kolkata under different intervention settings I1-I7 respectively. The symbols R1, R2, R3, R4, R5 denote the same defined in Fig. 1. The number adjacent to each box-plot represent the median of that box-plot.

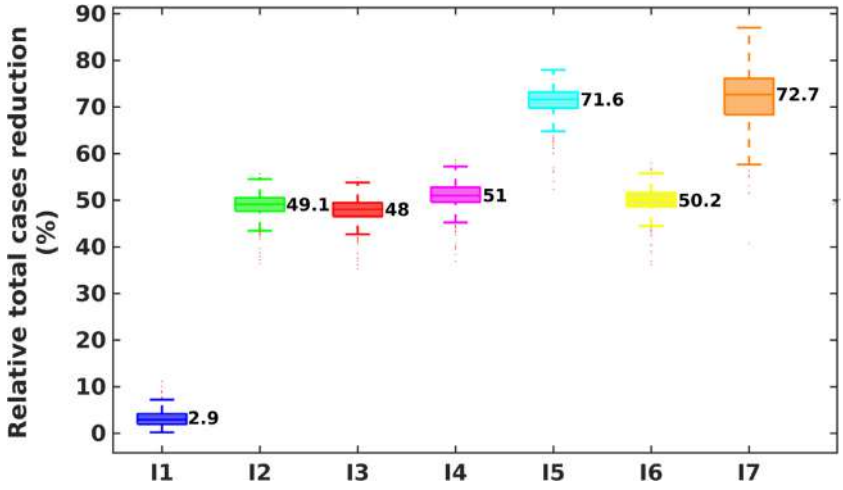

Fig. 4. Box-plot of relative total cumulative cases reduction under the intervention settings I1-I7. The number adjacent to each box-plot represent the median of that box-plot.

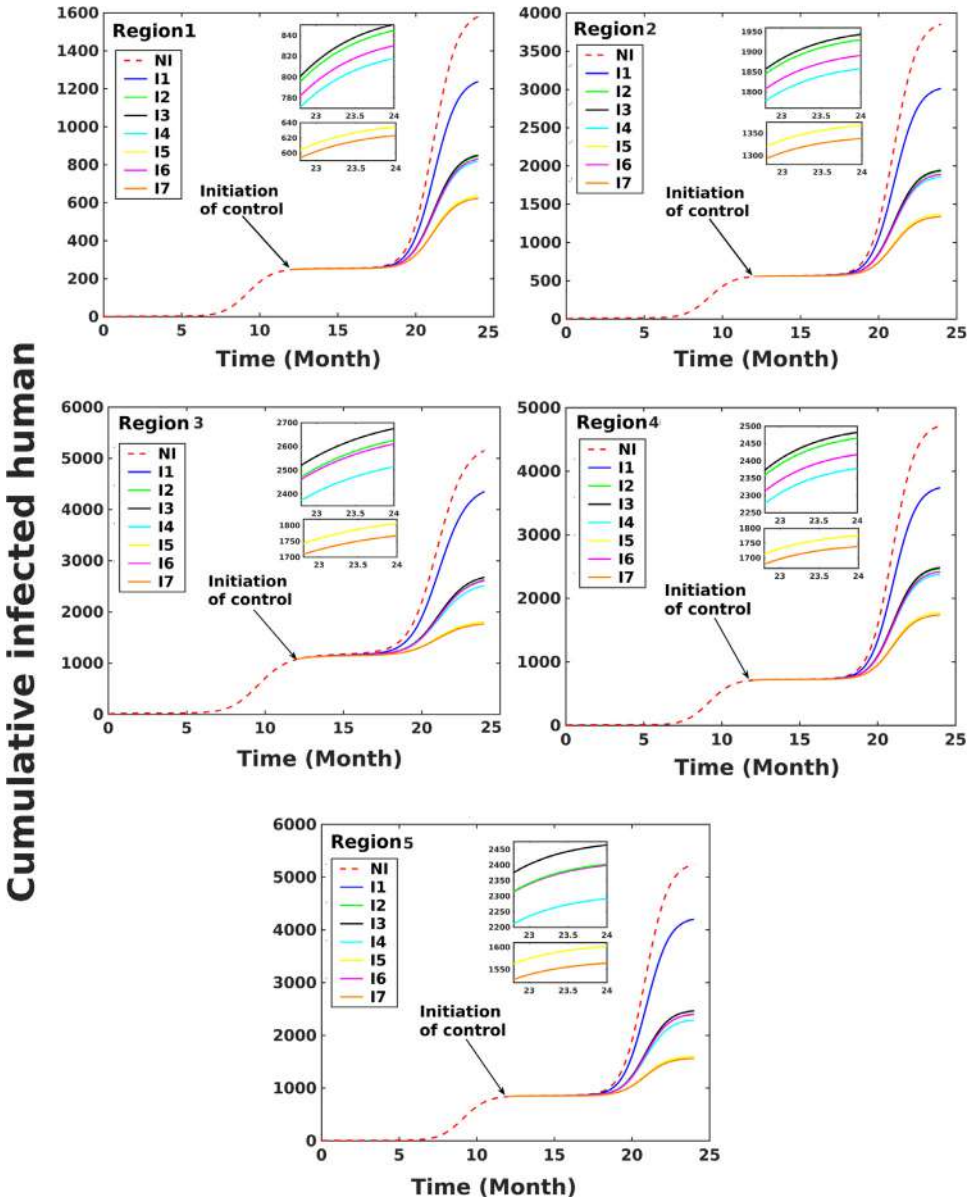

Fig. 5. Time evolution of cumulative infected cases in different regions. I1-I7 represent the different intervention settings. NI denotes No Intervention. The zoomed in figures are displayed in the insets.

times and 2 times respectively. The reduction of cases by applying this intervention setting in Region 3 and Region 5 are 56.9% and 56.7% respectively. It also reduces 42.1% cases in Region 1, 46.7% cases in Region 2, and 45.5% cases in Regions 4 (see Fig. 3D). The total cases reduction by this intervention setting is 51% (see Fig. 4). The dynamics of cumulative cases after and before applying this control in the five regions is given in Fig. 5.

5.1.5. Simultaneous application of surface & material treatment and lethal ovitraps

The treatment of surface and materials with insecticides is applied twice and lethal ovitraps are used thrice in this intervention setting. The outcome of applying this intervention setting is that it reduces by 71.6% the total cases in the five regions (see Fig. 4). It reduces by 78.4% the total cases in Region 3 and 77.5% the total cases in Region 5. The cases reductions in the remaining three regions are 60.8%, 66.8%, and 65.7% respectively (see Fig. 3E). The variation in cumulative cases over time in the five regions when this control strategy is applied is depicted in Fig. 5.

5.1.6. Simultaneous application of ULV and lethal ovitraps

The simultaneous application of ULV and lethal ovitraps reduces 56% cases in Region 3 and 55.3% cases in Region 5 respectively. In the remaining regions the reduction is appeared to be 41.6%, 46.2%, and 45.1% respectively (see Fig. 3F). Total cases reduction by this interventions setting is 50.2% (see Fig. 4). Fig. 5 shows the comparison between the dynamics of cumulative cases in the five regions after and before applying the intervention.

5.1.7. Simultaneous application of ULV, treatment with insecticides and lethal ovitraps

In this intervention setting, ULV spray, treatment of surface and materials and use of lethal ovitraps are applied 52 times, 2 times and 3 times respectively. This combined application reduces total 72.7% cumulative cases (see Fig. 4). The cases in the Region 3 and Region 5 are reduced by 79.7% and 78.7% after the application of this intervention setting (see Fig. 3G). In the regions: Region 1 and Region 2 and Region 4 the reductions in cases are 61.2%, 68.2% and 65.6% respectively (see Fig. 3G). The time series of cumula-

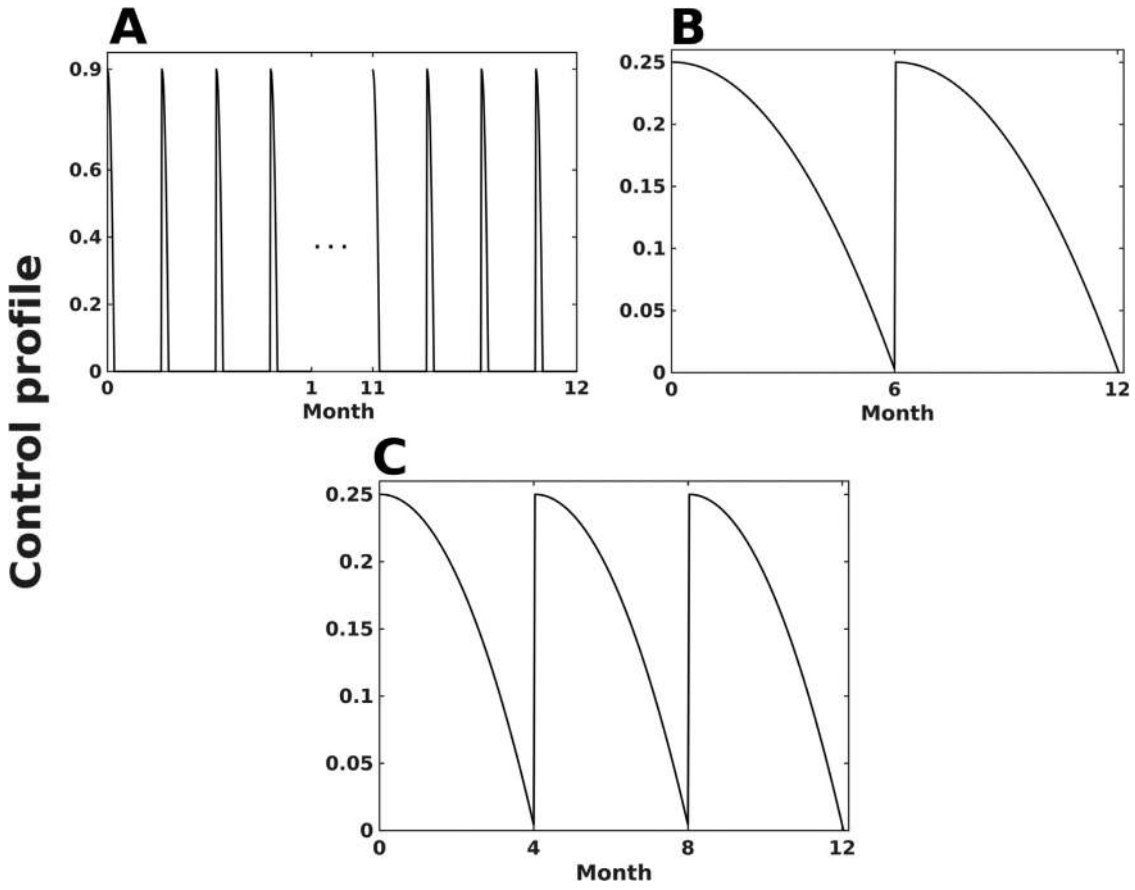

Fig. 6. (A) Control profile over time (only for first month and last month) of the intervention: application of ULV spray of insecticides. (B) Control profile over time of the intervention: insecticide treatment of surface and materials. (C) Control profile over time of the intervention: lethal ovitraps.

tive dengue cases after the application of this intervention setting in the five regions is presented in Fig. 5.

6. Discussion and conclusion

We formulated a general multi-patch non-autonomous transmission model to capture the temporal and spatial dynamics of dengue disease. Our model is fitted to the monthly dengue cases of Kolkata during the period January, 2014–December, 2015 and estimated several unknown model parameters. Using the estimated parameter values, the estimate of basic reproduction number ($\mathcal{R}_0$) (see Appendix B for detail formulation) is 1.106 (1.081–1.138) [mean(95%CI)], which implies that the endemic situation of Kolkata is well captured by our model. We considered three adult mosquito control strategies which are actually available and already applied in some dengue prone countries (Ditsuwan et al., 2012; Perich et al., 2000; Kroeger et al., 2006; Perich et al., 2003). We proposed intervention settings by considering the application of the strategies to the high dengue endemic regions, one at a time as well as simultaneously. To evaluate the impact and efficiency of the intervention settings, we considered an additional time-dependent death rate of mosquito population due to the application of the control, based on their efficacy and environment persistence.

We analyzed the influence of spatial coupling on the impact of the interventions settings considered in our study. It is observed that, though the intervention strategies are applied to Region 3 and Region 5 only, the spatial connectedness through human migration make it possible to reduce the cases significantly in those regions (i.e Region 1, Region 2 and Region 4) as well where interventions are not applied yet (see Fig. 3A–G). It is also observed that, among the three regions (Region 1, Region 2 and Region 4), reduction of cases in Region 1 is low in compared to the other two regions (see Fig. 3A–G). The Region 1 is not directly connected to both the regions (Region 3 and Region 5) (see Fig. 1) and this might be the reason behind the low reduction of cases in Region 1 compared to the other regions. Therefore, the role of spatial coupling in the effectiveness of interventions is well reflected from our study. Such utilization of spatial connectedness in dengue control was not studied previously.

From our study, it is observed that among the three control strategies, use of ULV spray has the least impact in reducing cases whereas the treatment of surface and materials reduces maximum cases (see Figs. 3A–C and 4). The performance of the use of lethal ovitraps is also better than that of ULV spray but slightly less than the treatment of surface and material. The observations regarding the performance of ULV spray are in accordance with the previous experimental and theoretical studies (Gratz, 1991; Luz et al., 2009; Newton and Reiter, 1992) where it has been shown that ULV spray is not so effective in reducing the abundance of *Aedes* mosquito population. The environment persistence of the ULV spray is very low (1 day) whereas the environment persistence of lethal ovitrap and treatment of surface and materials are 3 months and 4 months respectively. This provides the indication that higher environment persistence of a control strategy gives better performance in reducing cases. Among all the seven intervention settings, combined application of all the three control strategies (i.e Intervention setting 7 (I7)) naturally reduces maximum cases (see Figs. 3D–G and 4).

The implications of our study might help the public health departments of a dengue-prone region in implementing such inter-

vention strategies. We also recommend that the implementation of such adult mosquito control strategies should be initiated in the dengue endemic cities like Kolkata to prevent the further invasion of dengue disease.

Although our model captures the transmission dynamics of dengue in a spatially connected scenario, it would be more interesting to study the effect of control strategies if the temperature and rainfall are incorporated explicitly into the model additionally. We leave such extensions as future study.

Authors' contributions

AS, TS and JC constructed the model. AS, TS designed the study. AS executed mathematical calculation and performed the numerical simulations. AS edited the first draft and TS, JC participated in rewriting the manuscript. KSG, KSG and AKC contributed in collecting the data.

Acknowledgments

Abhishek Senapati is supported by the research fellowship from Council of Scientific & Industrial Research (Grant no: 09/093(0167)/2015/EMR-I), Government of India. The authors would like to thank the editors and anonymous reviewer for their valuable suggestions and constructive comments, which really helped to improve the presentation and quality of the paper.

Appendix A. Boundedness of the solution

Theorem 1. *For the solutions* $(S_H^i, E_H^i, I_H^i, A_H^i, R_H^i, S_M^i, I_M^i)$ *of the system (2.1) there exists* $L>0$ *and* $T_1>0$ *such that* $(S_H^i, E_H^i, I_H^i, A_H^i, R_H^i, S_M^i, I_M^i) \le (L, L, L, L, L, L, L)$ *(i.e the solutions are uniformly and ultimately bounded in* $\mathbb{R}_+^{7n}$*)*

Proof. We add all the equations related to human population which gives zero.

$\frac{d}{dt}(S_H^i + E_H^i + I_H^i + A_H^i + R_H^i) = 0$, for $i = 1, 2, \dots, n$, which gives $H^i(t) = H^i(0), \quad \forall t \ge 0$. This implies that the total human population in each patch is constant over the time. So, we have $S_H^i(t) \le H^i(0), E_H^i(t) \le H^i(0), I_H^i(t) \le H^i(0), A_H^i(t) \le H^i(0), R_H^i(t) \le H^i(0)$, for $i = 1, 2, \dots, n$ and $\forall t \ge 0$.

Now from the last two equations of the system (2.1) we get, $\frac{d}{dt}(M^i(t)) \le \Pi_M^i - \mu_M M^i(t)$, where $M^i(t) = S_M^i(t) + I_M^i(t)$ By using comparison theorem from Lakshmikantham et al. (1989), there exists $T_1 > 0$ such that $M^i(t) \le \frac{\Pi_M^i}{\mu_M}$, for all $t \ge T_1$ and for all i.

Let $L_i = \max_i\{H^i(0), \frac{\Pi_M^i}{\mu_M}\}$ and $L = \max\{L_i\}$. Then it follows that, $S_H^i(t) \le L, E_H^i(t) \le L, I_H^i(t) \le L, A_H^i(t) \le L, R_H^i(t) \le L,$ for $i = 1, 2, \dots, n$ and for all $t \ge T_1$. Hence the solutions of (2.1) are uniformly and ultimately bounded in $\mathbb{R}_+^{7n}$. □

Appendix B. Basic reproduction number and local stability of disease free equilibrium

Theorem 2. *If the basic reproduction number* $\mathcal{R}_0 < 1$*, then the disease free equilibrium* $\mathcal{E}_0$ *is locally asymptotically stable and it is unstable whenever* $\mathcal{R}_0 > 1$.

Proof. The model (2.1) has a unique disease free equilibrium (DFE). The equilibrium is given by,

$$\mathcal{E}_0 = \left(H^1, 0, 0, 0, 0, \frac{\Pi_M^1}{\mu_M}, 0, H^2, 0, 0, 0, 0, \frac{\Pi_M^2}{\mu_M}, 0, \dots, H^n, 0, 0, 0, 0, \frac{\Pi_M^n}{\mu_M}, 0\right)$$

In order to study the local stability of the disease free equilibrium $\mathcal{E}_0$, we first calculate the basic reproduction number ($\mathcal{R}_0$), an important epidemiological quantity in determining disease persistence. The basic reproduction number for our time-periodic compartmental model (2.1) is calculated following the procedure given by (Wang and Zhao, 2008). Here, the new infection matrix is denoted by $F(t)$ and given by,

$$F = \begin{bmatrix} \mathcal{O}_{n\times n} & \mathcal{O}_{n\times n} & \mathcal{O}_{n\times n} & \mathcal{A}_{n\times n} \\ \mathcal{O}_{n\times n} & \mathcal{O}_{n\times n} & \mathcal{O}_{n\times n} & \mathcal{O}_{n\times n} \\ \mathcal{O}_{n\times n} & \mathcal{O}_{n\times n} & \mathcal{O}_{n\times n} & \mathcal{O}_{n\times n} \\ \mathcal{B}_{n\times n} & \mathcal{C}_{n\times n} & \mathcal{D}_{n\times n} & \mathcal{O}_{n\times n} \end{bmatrix}$$

where, the matrices $\mathcal{A}, \mathcal{B}, \mathcal{C}, \mathcal{D}$ are given by the following matrices,

$$\mathcal{A} = \begin{bmatrix} b_1(t)\beta_H & b_2(t)\beta_H\epsilon_{12}\frac{H^1}{H^2} & \cdots & b_n(t)\beta_H\epsilon_{1n}\frac{H^1}{H^n} \\ b_1(t)\beta_H\epsilon_{21}\frac{H^2}{H^1} & b_2(t)\beta_H & \cdots & b_n(t)\beta_H\epsilon_{2n}\frac{H^2}{H^n} \\ \vdots & \vdots & \vdots & \vdots \\ b_1(t)\beta_H\epsilon_{n1}\frac{H^n}{H^1} & b_2(t)\beta_H\epsilon_{n2}\frac{H^n}{H^2} & \cdots & b_n(t)\beta_H \end{bmatrix}$$

$$\mathcal{B} = \begin{bmatrix} \frac{\eta_1 b_1(t)\beta_M\Pi_M^1}{H^1\mu_M} & \frac{\eta_1 b_1(t)\beta_M\epsilon_{12}\Pi_M^1}{H^1\mu_M} & \cdots & \frac{\eta_1 b_1(t)\beta_M\epsilon_{1n}\Pi_M^1}{H^1\mu_M} \\ \frac{\eta_1 b_2(t)\beta_M\epsilon_{21}\Pi_M^2}{H^2\mu_M} & \frac{\eta_1 b_2(t)\beta_M\Pi_M^2}{H^2\mu_M} & \cdots & \frac{\eta_1 b_2(t)\beta_M\epsilon_{2n}\Pi_M^2}{H^2\mu_M} \\ \vdots & \vdots & \vdots & \vdots \\ \frac{\eta_1 b_n(t)\beta_M\epsilon_{n1}\Pi_M^n}{H^n\mu_M} & \frac{\eta_1 b_n(t)\beta_M\epsilon_{n2}\Pi_M^n}{H^n\mu_M} & \cdots & \frac{\eta_1 b_n(t)\beta_M\Pi_M^n}{H^n\mu_M} \end{bmatrix}$$

$$\mathcal{C} = \begin{bmatrix} \frac{b_1(t)\beta_M\Pi_M^1}{H^1\mu_M} & \frac{b_1(t)\beta_M\epsilon_{12}\Pi_M^1}{H^1\mu_M} & \cdots & \frac{b_1(t)\beta_M\epsilon_{1n}\Pi_M^1}{H^1\mu_M} \\ \frac{b_2(t)\beta_M\epsilon_{21}\Pi_M^2}{H^2\mu_M} & \frac{b_2(t)\beta_M\Pi_M^2}{H^2\mu_M} & \cdots & \frac{b_2(t)\beta_M\epsilon_{2n}\Pi_M^2}{H^2\mu_M} \\ \vdots & \vdots & \vdots & \vdots \\ \frac{b_n(t)\beta_M\epsilon_{n1}\Pi_M^n}{H^n\mu_M} & \frac{b_n(t)\beta_M\epsilon_{n2}\Pi_M^n}{H^n\mu_M} & \cdots & \frac{b_n(t)\beta_M\Pi_M^n}{H^n\mu_M} \end{bmatrix}$$

$$\mathcal{D} = \begin{bmatrix} \frac{\eta_2 b_1(t)\beta_M\Pi_M^1}{H^1\mu_M} & \frac{\eta_2 b_1(t)\beta_M\epsilon_{12}\Pi_M^1}{H^1\mu_M} & \cdots & \frac{\eta_2 b_1(t)\beta_M\epsilon_{1n}\Pi_M^1}{H^1\mu_M} \\ \frac{\eta_2 b_2(t)\beta_M\epsilon_{21}\Pi_M^2}{H^2\mu_M} & \frac{\eta_2 b_2(t)\beta_M\Pi_M^2}{H^2\mu_M} & \cdots & \frac{\eta_2 b_2(t)\beta_M\epsilon_{2n}\Pi_M^2}{H^2\mu_M} \\ \vdots & \vdots & \vdots & \vdots \\ \frac{\eta_2 b_n(t)\beta_M\epsilon_{n1}\Pi_M^n}{H^n\mu_M} & \frac{\eta_2 b_n(t)\beta_M\epsilon_{n2}\Pi_M^n}{H^n\mu_M} & \cdots & \frac{\eta_2 b_n(t)\beta_M\Pi_M^n}{H^n\mu_M} \end{bmatrix}.$$

The transmission matrix is denoted by $V(t)$ and given by,

$$V = \begin{bmatrix} (\sigma_H + \mu_H)\mathcal{I}_{n\times n} & \mathcal{O}_{n\times n} & \mathcal{O}_{n\times n} & \mathcal{O}_{n\times n} \\ (-p\sigma_H)\mathcal{I}_{n\times n} & (\gamma_H + \mu_H)\mathcal{I}_{n\times n} & \mathcal{O}_{n\times n} & \mathcal{O}_{n\times n} \\ -(1-p)\sigma_H\mathcal{I}_{n\times n} & \mathcal{O}_{n\times n} & (\gamma_H + \mu_H)\mathcal{I}_{n\times n} & \mathcal{O}_{n\times n} \\ \mathcal{O}_{n\times n} & \mathcal{O}_{n\times n} & \mathcal{O}_{n\times n} & \mu_M\mathcal{I}_{n\times n} \end{bmatrix}$$

Let $Z(t, s)$, $t \ge s$ denote the evolution operator of the linear periodic system with period ω: $\frac{dz}{dt} = -V(t)z$. The evolution operator $Z(t, s)$ satisfies the following equation, $\frac{d}{dt}Z(t, s) = -V(t)Z(t, s)$ for all $t \ge s$ and $Z(s, s) = I$, where I is the identity matrix of order $4n$.

Let C_ω be the ordered Banach space of all ω-periodic functions from $\mathbb{R}$ to $\mathbb{R}^{4n}$ which is equipped with maximum norm $\|\cdot\|$. Now consider the linear operator L: $C_\omega \to C_\omega$ by,

$(L\phi)(t) = \int_0^{+\infty} Z(t, t-a)F(t-a)\phi(t-a)da$. We call the operator L, the next infection operator. The basic reproduction number $\mathcal{R}_0$ is defined as the spectral radius of L (Wang and Zhao, 2008), $\mathcal{R}_0 = \rho(L)$, where $\rho(A)$ denotes the spectral radius of the matrix A. We can calculate the numerical value of $\mathcal{R}_0$ for our model (2.1) using the following procedure:

Consider the linear ω periodic system $\frac{dw}{dt} = (-V(t) + \frac{F(t)}{\lambda})w$, $t \in \mathbb{R}$ with $\lambda \in (0, \infty)$. Let $W(t, \lambda)$ be the fundamental matrix of the above linear system. It is easy to observe that the two matrices $F(t)$ and $-V(t)$ are non-negative and cooperative respectively. As a

consequence, $\rho(W(\omega, \lambda))$ is continuous and non-increasing in λ in the interval $(0, \infty)$ and also $\lim_{\lambda\to\infty}\rho(W(\omega, \lambda)) < 1$. Before going to present the main result regarding the local stability of DFE, we first give two more results following (Wang and Zhao, 2008). First of all it can be easily verified that the system (2.1) satisfies all the assumptions $(A(1) - A(7))$ presented in (Wang and Zhao, 2008). Therefore, the following two results are valid for our system (2.1). □

Lemma 1. *(Theorem 2.1 in (Wang and Zhao, 2008)) Let all the assumptions $(A(1) - A(7))$ made in (Wang and Zhao, 2008) are satisfied by the system (2.1). Then the following three statements are true:*

(i) *If the equation $\rho(W(\omega, \lambda)) = 1$ has a positive solution $\bar{\lambda}$, then $\bar{\lambda}$ is an eigenvalue of the next infection operator L and hence $\mathcal{R}_0 > 0$.*
(ii) *If $\mathcal{R}_0 > 0$, then $\lambda = \mathcal{R}_0$ is the unique solution of $\rho(W(\omega, \lambda)) = 1$.*
(iii) *$\mathcal{R}_0 = 0$ if and only if $\rho(W(\omega, \lambda)) < 1$ for all $\lambda > 0$*

Lemma 1 is used to calculate the basic reproduction number $\mathcal{R}_0$ numerically.

Lemma 2. *(Theorem 2.2 in (Wang and Zhao, 2008)) Let all the assumptions $(A(1) - A(7))$ made in (Wang and Zhao, 2008) be satisfied by the system (2.1). Then the following three statements are true:*

(i) *$\mathcal{R}_0 = 1$ if and only if $\rho(\Phi_{F-V(\omega)}) = 1$.*
(ii) *$\mathcal{R}_0 > 1$ if and only if $\rho(\Phi_{F-V(\omega)}) > 1$.*
(iii) *$\mathcal{R}_0 < 1$ if and only if $\rho(\Phi_{F-V(\omega)}) < 1$.*

From Lemma 2, it follows that, If the basic reproduction number $\mathcal{R}_0 < 1$, then the disease free equilibrium $\mathcal{E}_0$ is locally asymptotically stable and it is unstable whenever $\mathcal{R}_0 > 1$.

Appendix C. Global stability of disease free state

Theorem 3. *If the basic reproduction number $\mathcal{R}_0 < 1$, then the disease free equilibrium $\mathcal{E}_0$ is globally asymptotically stable.*

Let us consider a system of linear non-autonomous ordinary differential equation

$$\frac{dz}{dt} = Z(t)z \tag{C.1}$$

where, $Z(t)$ is a $k \times k$ matrix function having the properties: continuous, irreducible, cooperative, and ω periodic. Let $\Phi_{Z(.)}(t)$ be the fundamental matrix of the system (C.1) and hence $\Phi_{Z(.)}(\omega)$ be the monodromy matrix with spectral radius $\rho(\Phi_{Z(.)}(\omega))$. By Perron-Frobenius, $\rho(\Phi_{Z(.)}(\omega))$ turns out to be the principal eigenvalue of $\Phi_{Z(.)}(\omega)$ (Aronsson and Kellogg, 1978; Hirsch, 1985). We state a result given by Zhang *et al.* (Zhang and Zhao, 2007) which is helpful to establish the global stability of the DFE, $\mathcal{E}_0$.

Lemma 3. *(Lemma 2.1 in (Zhang and Zhao, 2007)). Let $\bar{s} = \frac{1}{\omega} ln\rho(\Phi_{Z(.)}(\omega))$. Then there exists a function $f(t)$ which is positive, ω- periodic such that $e^{\bar{s}t} f(t)$ is a solution of the system (C.1).*

We now prove the main theorem:

Proof. We first consider the infected compartments from the system (2.1). Hence, taking 2nd, 3rd, 4th, and the last equations of (2.1) and considering the inequalities $S_H^i(t) \le H^i, S_M^i(t) \le \frac{\Pi_M^i}{\mu_M}$ $(i = 1, 2 \dots, n)$ for all $t \ge 0$, we have the following:

$$\begin{aligned}
\frac{dE_H^i}{dt} &= \beta_H S_H^i \left(\frac{b_i(t)}{H^i} I_M^i + \sum_{\substack{j=1\\ j\neq i}}^{n} \epsilon_{ij} \frac{b_j(t)}{H^j} I_M^j\right) - (\sigma_H + \mu_H) E_H^i, \\
&\le \beta_H \left(b_i(t) I_M^i + \sum_{\substack{j=1\\ j\neq i}}^{n} \epsilon_{ij} b_j(t) \frac{H^i}{H^j} I_M^j\right) - (\sigma_H + \mu_H) E_H^i, \\
\frac{dI_H^i}{dt} &= p\sigma_H E_H^i - (\mu_H + \gamma_H) I_H^i, \\
\frac{dA_H^i}{dt} &= (1-p)\sigma_H E_H^i - (\mu_H + \gamma_H) A_H^i, \\
\frac{dI_M^i}{dt} &= b_i(t)\beta_M S_M^i \left(\frac{(I_H^i + \eta_1 E_H^i + \eta_2 A_H^i)}{H^i} + \sum_{\substack{j=1\\ j\neq i}}^{n} \epsilon_{ij} \frac{(I_H^j + \eta_1 E_H^j + \eta_2 A_H^j)}{H^i}\right) \\
&\quad - \mu_M I_M^i, \\
&\le b_i(t)\beta_M \frac{\Pi_M}{\mu_M} \left(\frac{(I_H^i + \eta_1 E_H^i + \eta_2 A_H^i)}{H^i} + \sum_{\substack{j=1\\ j\neq i}}^{n} \epsilon_{ij} \frac{(I_H^j + \eta_1 E_H^j + \eta_2 A_H^j)}{H^i}\right) \\
&\quad - \mu_M I_M^i
\end{aligned} \tag{C.2}$$

We now consider the following auxiliary equations:

$$\begin{aligned}
\frac{dE_H^i}{dt} &= \beta_H \left(b_i(t) I_M^i + \sum_{\substack{j=1\\ j\neq i}}^{n} \epsilon_{ij} b_j(t) \frac{H^i}{H^j} I_M^j\right) - (\sigma_H + \mu_H) E_H^i, \\
\frac{dI_H^i}{dt} &= p\sigma_H E_H^i - (\mu_H + \gamma_H) I_H^i, \\
\frac{dA_H^i}{dt} &= (1-p)\sigma_H E_H^i - (\mu_H + \gamma_H) A_H^i, \\
\frac{dI_M^i}{dt} &= b_i(t)\beta_M \frac{\Pi_M}{\mu_M} \left(\frac{(I_H^i + \eta_1 E_H^i + \eta_2 A_H^i)}{H^i} + \sum_{\substack{j=1\\ j\neq i}}^{n} \epsilon_{ij} \frac{(I_H^j + \eta_1 E_H^j + \eta_2 A_H^j)}{H^i}\right) \\
&\quad - \mu_M I_M^i
\end{aligned} \tag{C.3}$$

The above system can be written as, $\frac{dZ}{dt} = (F(t) - V(t))Z$, where Z is a column vector containing the state variables, i.e $Z = [E_H^1, E_H^2, \dots, E_H^n, I_H^1, I_H^2, \dots, I_H^n, A_H^1, A_H^2, \dots, A_H^n, I_M^1, I_M^2, \dots, I_M^n]^t$.

Now Lemma 3 can be applied to the system (C.3) because the matrix $(F(t) - V(t))$ is continuous, irreducible, and cooperative. Therefore, by using Lemma 3, the existence of a ω-periodic function $\bar{Z}(t)$ such that $Z(t) = e^{\bar{s}t}\bar{Z}(t)$ is a solution of the system (C.3) is assured, where $\bar{s} = \frac{1}{\omega} ln\rho(\Phi_{F(.)-V(.)}(\omega))$. Now by Lemma 2, $\mathcal{R}_0 < 1$ implies that $\rho(\Phi_{F(.)-V(.)}(\omega)) < 1$. Therefore, it turns out that $\bar{s}$ is a negative quantity and as a consequence $Z(t) \to 0$ as $t \to \infty$. This means that the for $i = 1, 2, \dots, n$, $E_H^i \to 0$, $I_H^i \to 0$, $A_H^i \to 0$, $I_M^i \to 0$ as $t \to \infty$. It follows from the theory of asymptotic autonomous systems (Thieme, 1992) that the $S_H^i \to H^i$, $R_H^i \to 0$, $S_M^i \to \frac{\Pi_M^i}{\mu_M}$ as $t \to \infty$. Hence $\mathcal{E}_0$ is globally asymptotically stable whenever $\mathcal{R}_0 < 1$. □

Appendix D. Persistence of the solution of the model 2.1

Theorem 4. *The solution of the system (2.1) is uniformly persistent if $\mathcal{R}_0 > 1$. That means there exists $\kappa > 0$ such that the solution of the system (2.1) satisfies $\liminf_{t\to\infty} E_H^i(t) \ge \kappa$, $\liminf_{t\to\infty} I_H^i(t) \ge \kappa$, $\liminf_{t\to\infty} A_h^i(t) \ge \kappa$, and $\liminf_{t\to\infty} I_M^i(t) \ge \kappa$ for $i = 1, 2, \dots, n$, whenever the initial conditions are taken from the set $\mathcal{I} = \{(S_H^i(0), E_H^i(0), I_H^i(0), A_H^i(0), R_H^i(0), S_M^i(0), I_M^i(0)) \in \mathbb{R}_+^{7n} : E_H^i(0) > 0, I_H^i(0) > 0, A_H^i(0) > 0, I_M^i(0) > 0\}$.*

Proof. We first consider the following sets, $K = \mathbb{R}_+^{7n}$, $K_0 = \{(S_H^i, E_H^i, I_H^i, A_H^i, R_H^i, S_M^i, I_M^i) \in \mathbb{R}_+^{7n} : E_H^i > 0, I_H^i > 0, A_H^i > 0, I_M^i > 0\}$, and $\partial K_0 = K \backslash K_0$.

Consider a Poincarè map P: $K \to K$ which satisfies $P(x^0) = f(\omega, x^0)$, for all $x^0 \in K$, and $f(t, x^0)$ is the unique solution of (2.1) with $f(0, x^0) = x^0$.

From (2.1), it can be easily seen that K and K_0 are positively invariant and ∂K_0 is relatively closed in K. Also from Theorem 1, the solutions of the system (2.1) is uniformly and ultimately bounded. This implies that the Poincarè map P is point dissipative and compact on K. By using the Theorem 1.1.3 in (Zhao et al., 2003), the existence of a global attractor of P is confirmed.

Let us define the set K_∂ as:

$$K_\partial = \{(S_H^i(0), E_H^i(0), I_H^i(0), A_H^i(0), R_H^i(0), S_M^i(0), I_M^i(0)) \in \partial K_0 : P^k(X) \in \partial K_0, k \geq 0\}.$$

We claim that $K_\partial = \{(S_H^i, 0, 0, 0, R_H^i, S_M^i, 0) : S_H^i \geq 0, R_H^i \geq 0, S_M^i \geq 0\}$.

To prove this set equality, we have to show only that, $K_\partial \subseteq \{(S_H^i, 0, 0, 0, R_H^i, S_M^i, 0) : S_H^i \geq 0, R_H^i \geq 0, S_M^i \geq 0\}$.

Let $(S_H^i(0), E_H^i(0), I_H^i(0), A_H^i(0), R_H^i(0), S_M^i(0), I_M^i(0)) \in \partial K_0 \backslash \{(S_H^i, 0, 0, 0, R_H^i, S_M^i, 0) : S_H^i \geq 0, R_H^i \geq 0, S_M^i \geq 0\}$. Now if $E_H^i(0) = 0, I_H^i(0) > 0, A_H^i(0) > 0, I_M^i(0) > 0$, then from the 2nd equation of (2.1) we have, $\dot{E_H^i}(0) = \beta_H S_H^i(0)(\frac{b_{0i}}{H^i} I_M^i(0) + \sum_{j=1}^n \epsilon_{ij} \frac{b_{0j}}{H^j} I_M^j(0)) > 0$, this implies $E_H^i(0) > 0$, a contradiction. In a similar manner, we can get such contradictions for the remaining cases also. Therefore, if $(S_H^i(0), E_H^i(0), I_H^i(0), A_H^i(0), R_H^i(0), S_M^i(0), I_M^i(0)) \notin \{(S_H^i, 0, 0, 0, R_H^i, S_M^i, 0) : S_H^i \geq 0, R_H^i \geq 0, S_M^i \geq 0\}$ then $(S_H^i(0), E_H^i(0), I_H^i(0), A_H^i(0), R_H^i(0), S_M^i(0), I_M^i(0)) \notin \partial K_0$. This implies that $K_\partial \subseteq \{(S_H^i, 0, 0, 0, R_H^i, S_M^i, 0) : S_H^i \geq 0, R_H^i \geq 0, S_M^i \geq 0\}$ and thus $K_\partial = \{(S_H^i, 0, 0, 0, R_H^i, S_M^i, 0) : S_H^i \geq 0, R_H^i \geq 0, S_M^i \geq 0\}$.

Now $\mathcal{E}_0$ is a fixed point of P in K_∂. Any solution of the system (2.1) starting from K_∂ will remain in the set K_∂.

Our next job is to show $W^s(\mathcal{E}_0) \cap K_0 = \emptyset$, where $W^s(\mathcal{E}_0)$ is the stable set of $\mathcal{E}_0$ in order to show that $\{\mathcal{E}_0\}$ is isolated invariant subset of K_∂.

Let $x^0 = (S_H^i(0), E_H^i(0), I_H^i(0), A_H^i(0), R_H^i(0), S_M^i(0), I_M^i(0)) \in K_0$, then $\forall \epsilon_1 \in (0, \max\{\max\{H^i(0), \frac{\Pi_M^i}{\mu_M}\}\})$, $\exists \kappa_1 > 0$ such that $\forall x^0 \in K_0$ with $\| x^0 - \mathcal{E}_0 \| \leq \kappa_1, \| f(t, x^0) - f(t, \mathcal{E}_0) \| \leq \epsilon_1, \forall t \in [0, \omega]$. To show that $x^0 \in K_0 \Rightarrow x^0 \notin W^s(\mathcal{E}_0)$, we have to show $limsup_{k\to\infty} d(P^k(x^0), \mathcal{E}_0) \geq \kappa_1$ for some $k > 0$. If not, then there exist $x^0 \in K_0$ such that $limsup_{k\to\infty} d(P^k(x^0), \mathcal{E}_0) < \kappa_1$, for all $k > 0$, which implies that, $\| f(t, P^k(x^0)) - f(t, \mathcal{E}_0) \| \leq \epsilon_1$, for all $t \in [0, \omega]$.

For $t \geq 0$, let $t = k\omega + \hat{t}$, where $\hat{t} \in [0.\omega]$ and $k = [\frac{t}{\omega}]$. Thus, we get, $\| f(t, P^k(x^0)) - f(t, \mathcal{E}_0) \| = \| f(\hat{t}, P^k(x^0)) - f(\hat{t}, \mathcal{E}_0) \| < \epsilon_1$ for all $t \in [0, \omega]$.

In the above equation, we replace $f(t, x^0)$ by $(S_H^i(t), E_H^i(t), I_H^i(t), A_H^i(t), R_H^i(t), S_M^i(t), I_M^i(t))$. Then we have, $\forall t \geq 0$, $H^i(0) - \epsilon_1 \leq S_H^i(t) \leq H^i(0) + \epsilon_1, 0 \leq E_H^i(t) \leq \epsilon_1, 0 \leq I_H^i(t) \leq \epsilon_1, 0 \leq A_H^i(t) \leq \epsilon_1, 0 \leq R_H^i(t) \leq \epsilon_1, \frac{\Pi_M^i}{\mu_M} - \epsilon_1 \leq S_M^i(t) \leq \frac{\Pi_M^i}{\mu_M} + \epsilon_1, 0 \leq I_M^i(t) \leq \epsilon_1$. Using the above inequalities in (2.1), we have the following:

$$\begin{aligned}
\frac{dE_H^i}{dt} &\geq \beta_H (H^i(0) - \epsilon_1)\left(\frac{b_i(t)}{H^i} I_M^i + \sum_{\substack{j=1 \\ j\neq i}}^n \epsilon_{ij} \frac{b_j(t)}{H^j} I_M^j\right) - (\sigma_H + \mu_H) E_H^i, \\
\frac{dI_H^i}{dt} &= p\sigma_H E_H^i - (\mu_H + \gamma_H) I_H^i, \\
\frac{dA_H^i}{dt} &= (1-p)\sigma_H E_H^i - (\mu_H + \gamma_H) A_H^i, \\
\frac{dI_M^i}{dt} &\geq b_i(t)\beta_M \left(\frac{\Pi_M^i}{\mu_M} - \epsilon_1\right) \\
&\quad \times \left(d\frac{(I_H^i + \eta_1 E_H^i + \eta_2 A_H^i)}{H^i} + \sum_{\substack{j=1 \\ j\neq i}}^n \epsilon_{ij} \frac{(I_H^j + \eta_1 E_H^j + \eta_2 A_H^j)}{H^i}\right) \\
&\quad - \mu_M I_M^i, \qquad \text{(D.1)}
\end{aligned}$$

Now let,

$$\mathcal{M}^{\epsilon_1} = \begin{bmatrix} \mathcal{O} & \mathcal{O} & \mathcal{O} & \mathcal{A}^{\epsilon_1} \\ \mathcal{O} & \mathcal{O} & \mathcal{O} & \mathcal{O} \\ \mathcal{O} & \mathcal{O} & \mathcal{O} & \mathcal{O} \\ \mathcal{B}^{\epsilon_1} & \mathcal{C}^{\epsilon_1} & \mathcal{D}^{\epsilon_1} & \mathcal{O} \end{bmatrix}$$

where,

$$\mathcal{A}^{\epsilon_1} = \begin{bmatrix} \frac{\epsilon_1 b_1(t)\beta_H}{H^1} & \frac{\epsilon_1 b_2(t)\beta_H \epsilon_{12}}{H^2} & \cdots & \frac{\epsilon_1 b_n(t)\beta_H \epsilon_{1n}}{H^n} \\ \frac{\epsilon_1 b_1(t)\beta_H \epsilon_{21}}{H^1} & \frac{\epsilon_1 b_2(t)\beta_H}{H^2} & \cdots & \frac{\epsilon_1 b_n(t)\beta_H \epsilon_{2n}}{H^n} \\ \vdots & \vdots & \vdots & \vdots \\ \frac{\epsilon_1 b_1(t)\beta_H \epsilon_{n1}}{H^1} & \frac{\epsilon_1 b_2(t)\beta_H \epsilon_{n2}}{H^2} & \cdots & \frac{\epsilon_1 b_n(t)\beta_H}{H^n} \end{bmatrix}$$

$$\mathcal{B}^{\epsilon_1} = \begin{bmatrix} \frac{\epsilon_1 \eta_1 b_1(t)\beta_M}{H^1} & \frac{\epsilon_1 \eta_1 b_1(t)\beta_M \epsilon_{12}}{H^1} & \cdots & \frac{\epsilon_1 \eta_1 b_1(t)\beta_M \epsilon_{1n}}{H^1} \\ \frac{\epsilon_1 \eta_1 b_2(t)\beta_M \epsilon_{21}}{H^2} & \frac{\epsilon_1 \eta_1 b_2(t)\beta_M}{H^2} & \cdots & \frac{\epsilon_1 \eta_1 b_2(t)\beta_M \epsilon_{2n}}{H^2} \\ \vdots & \vdots & \vdots & \vdots \\ \frac{\epsilon_1 \eta_1 b_n(t)\beta_M \epsilon_{n1}}{H^n} & \frac{\epsilon_1 \eta_1 b_n(t)\beta_M \epsilon_{n2}}{H^n} & \cdots & \frac{\epsilon_1 \eta_1 b_n(t)\beta_M}{H^n} \end{bmatrix}$$

$$\mathcal{C}^{\epsilon_1} = \begin{bmatrix} \frac{\epsilon_1 b_1(t)\beta_M}{H^1} & \frac{\epsilon_1 b_1(t)\beta_M \epsilon_{12}}{H^1} & \cdots & \frac{\epsilon_1 b_1(t)\beta_M \epsilon_{1n}}{H^1} \\ \frac{\epsilon_1 b_2(t)\beta_M \epsilon_{21}}{H^2} & \frac{\epsilon_1 b_2(t)\beta_M}{H^2} & \cdots & \frac{\epsilon_1 b_2(t)\beta_M \epsilon_{2n}}{H^2} \\ \vdots & \vdots & \vdots & \vdots \\ \frac{\epsilon_1 b_n(t)\beta_M \epsilon_{n1}}{H^n} & \frac{\epsilon_1 b_n(t)\beta_M \epsilon_{n2}}{H^n} & \cdots & \frac{\epsilon_1 b_n(t)\beta_M}{H^n} \end{bmatrix}$$

$$\mathcal{D}^{\epsilon_1} = \begin{bmatrix} \frac{\epsilon_1 \eta_2 b_1(t)\beta_M}{H^1} & \frac{\epsilon_1 \eta_2 b_1(t)\beta_M \epsilon_{12}}{H^1} & \cdots & \frac{\epsilon_1 \eta_2 b_1(t)\beta_M \epsilon_{1n}}{H^1} \\ \frac{\epsilon_1 \eta_2 b_2(t)\beta_M \epsilon_{21}}{H^2} & \frac{\epsilon_1 \eta_2 b_2(t)\beta_M}{H^2} & \cdots & \frac{\epsilon_1 \eta_2 b_2(t)\beta_M \epsilon_{2n}}{H^2} \\ \vdots & \vdots & \vdots & \vdots \\ \frac{\epsilon_1 \eta_2 b_n(t)\beta_M \epsilon_{n1}}{H^n} & \frac{\epsilon_1 \eta_2 b_n(t)\beta_M \epsilon_{n2}}{H^n} & \cdots & \frac{\epsilon_1 \eta_2 b_n(t)\beta_M}{H^n} \end{bmatrix}.$$

Now, by Lemma 2, if $\mathcal{R}_0 > 1$, then $\rho(\Phi_{F-V(\omega)}) > 1$. We choose ϵ_1 sufficiently small such that $\rho(\Phi_{F-V-M^{\epsilon_1}(\omega)}) > 1$. By Lemma 3 and comparison theorem in (Smith and Waltman, 1995), there is function $g(t)$ which is positive and ω-periodic such that $X(t) \geq g(t)e^{st}$, where $X = [E_H^i, I_H^i, A_H^i, I_M^i]^t$ and $s = \frac{1}{\omega} ln\rho(\Phi_{F-V-M^{\epsilon_1}}(\omega)) > 0$. This immediately implies that $E_H^i(t) \to \infty, I_H^i(t) \to \infty, A_H^i(t) \to \infty, I_M^i(t) \to \infty$, which is a contradiction in K_∂ and hence $W^s(\mathcal{E}_0) \cap K_0 = \emptyset$. By Theorem 1.3.1 and Theorem 3.1.1 in (Zhao et al., 2003), P is uniformly persistent and hence the solution of the system (2.1) is uniformly persistent in K if $\mathcal{R}_0 > 1$. □

Appendix E. Existence and global stability of periodic solution

Theorem 5. *The system of non-autonomous differential Eq. (2.1) have a positive ω-periodic solution which is globally asymptotically stable if $\mathcal{R}_0 > 1$.*

Proof. It has already been proved that the Poincarè map P defined in Theorem 4 is point dissipative and compact, hence P is uniformly persistent with respect to $(K_0, \partial K_0)$. From Theorem 1.3.6 given in (Zhao et al., 2003), the Poincarè map P has a fixed point $(\bar{S}_H^i(t), \bar{E}_H^i(t), \bar{I}_H^i(t), \bar{A}_H^i(t), \bar{R}_H^i(t), \bar{I}_M^i(t), \bar{S}_M^i(t)) \in Int(\mathbb{R}_+^{7n})$.

This implies $f(t, (\bar{S}_H^i(t), \bar{E}_H^i(t), \bar{I}_H^i(t), \bar{A}_H^i(t), \bar{R}_H^i(t), \bar{S}_M^i(t), \bar{I}_M^i(t))) \in Int(\mathbb{R}_+^{7n})$, *for all* $t > 0$. Therefore, $(\bar{S}_H^i(t), \bar{E}_H^i(t), \bar{I}_H^i(t), \bar{A}_H^i(t), \bar{R}_H^i(t), \bar{S}_M^i(t), \bar{I}_M^i(t)) \in Int(\mathbb{R}_+^{7n})$ is a positive periodic solution of (2.1) of period ω.

Now the following Lyapunov function $\mathcal{L}(t)$ is constructed to prove the global stability of the periodic solution $(\bar{S}_H^i(t), \bar{E}_H^i(t), \bar{I}_H^i(t), \bar{A}_H^i(t), \bar{R}_H^i(t), \bar{S}_M^i(t), \bar{I}_M^i(t)) \in Int(\mathbb{R}_+^{7n})$.

$\mathcal{L}(t) = \sum_{i=1}^{n}[|S_H^i(t) - \bar{S}_H^i(t)| + |E_H^i(t) - \bar{E}_H^i(t)| + |I_H^i(t) - \bar{I}_H^i(t)| + |A_H^i(t) - \bar{A}_H^i(t)| + |R_H^i(t) - \bar{R}_H^i(t)| + |S_M^i(t) - \bar{S}_M^i(t)| + |I_M^i(t) - \bar{I}_M^i(t)|]$.

Taking Dini's derivative of $\mathcal{L}(t)$, we have

$$
\begin{aligned}
\mathcal{D}^+\mathcal{L}(t) = \sum_{i=1}^{n}\Bigg[& sgn(S_H^i(t) - \bar{S}_H^i(t))\Big\{\beta_H \bar{S}_H^i\Big(\frac{b_i(t)}{H^i}\bar{I}_M^i + \sum_{j=1}^{n}\epsilon_{ij}\frac{b_j(t)}{H^j}\bar{I}_M^j\Big) \\
& -\beta_H S_H^i\Big(\tfrac{b_i(t)}{H^i} I_M^i + \sum_{j=1}^{n}\epsilon_{ij}\frac{b_j(t)}{H^j} I_M^j\Big) - \mu_H(S_H^i - \bar{S}_H^i)\Big\} \\
& +sgn(E_H^i(t) - \bar{E}_H^i(t))\Big\{\beta_H S_H^i\Big(\tfrac{b_i(t)}{H^i} I_M^i + \sum_{j=1}^{n}\epsilon_{ij}\frac{b_j(t)}{H^j} I_M^j\Big) \\
& -\beta_H \bar{S}_H^i\Big(\tfrac{b_i(t)}{H^i}\bar{I}_M^i + \sum_{j=1}^{n}\epsilon_{ij}\frac{b_j(t)}{H^j}\bar{I}_M^j\Big) - (\mu_H + \sigma_H)(E_H^i - \bar{E}_H^i)\Big\} \\
& +sgn(I_H^i(t) - \bar{I}_H^i(t))\Big\{p\sigma_H(E_H^i - \bar{E}_H^i) - (\mu_H + \gamma_H)(I_H^i - \bar{I}_H^i)\Big\} \\
& +sgn(A_H^i(t) - \bar{A}_H^i(t))\Big\{(1-p)\sigma_H(E_H^i - \bar{E}_H^i) - (\mu_H + \gamma_H)(A_H^i - \bar{A}_H^i)\Big\} \\
& +sgn(R_H^i(t) - \bar{R}_H^i(t))\Big\{\gamma_H(I_H^i + A_H^i - \bar{I}_H^i - \bar{A}_H^i) - \mu_H(R_H^i - \bar{R}_H^i)\Big\} \\
& +sgn(S_M^i(t) - \bar{S}_M^i(t))\Big\{b_i(t)\beta_M\bar{S}_M^i\Big(\tfrac{(\bar{I}_H^i + \eta_1\bar{E}_H^i + \eta_2\bar{A}_H^i)}{H^i} \\
& + \sum_{j=1}^{n}\epsilon_{ij}\frac{(\bar{I}_H^i + \eta_1\bar{E}_H^i + \eta_2\bar{A}_H^i)}{H^i}\Big) - b_i(t)\beta_M S_M^i\Big(\frac{(I_H^i + \eta_1 E_H^i + \eta_2 A_H^i)}{H^i} \\
& + \sum_{j=1}^{n}\epsilon_{ij}\frac{(I_H^i + \eta_1 E_H^i + \eta_2 A_H^i)}{H^i}\Big) - \mu_M(S_M^i - \bar{S}_M^i)\Big\} \\
& +sgn(I_M^i(t) - \bar{I}_M^i(t))\Big\{b_i(t)\beta_M\bar{S}_M^i\Big(\tfrac{(I_H^i + \eta_1 E_H^i + \eta_2 A_H^i)}{H^i} \\
& + \sum_{j=1}^{n}\epsilon_{ij}\frac{(I_H^i + \eta_1 E_H^i + \eta_2 A_H^i)}{H^i}\Big) - b_i(t)\beta_M\bar{S}_M^i\Big(\frac{(\bar{I}_H^i + \eta_1\bar{E}_H^i + \eta_2\bar{A}_H^i)}{H^i} \\
& + \sum_{j=1}^{n}\epsilon_{ij}\frac{(\bar{I}_H^i + \eta_1\bar{E}_H^i + \eta_2\bar{A}_H^i)}{H^i}\Big) - \mu_M(I_M^i - \bar{I}_M^i)\Big\}\Bigg] \\
& \le -\mu_H|S_H^i(t) - \bar{S}_H^i(t)| - \mu_H|E_H^i(t) - \bar{E}_H^i(t)| - \mu_H|I_H^i(t) - \bar{I}_H^i(t)| \\
& -\mu_H|A_H^i(t) - \bar{A}_H^i(t)| - \mu_H|R_H^i(t) - \bar{R}_H^i(t)| \\
& -\mu_M|S_M^i(t) - \bar{I}_M^i(t)| - \mu_M|S_M^i(t) - \bar{I}_M^i(t)| \qquad \text{(E.1)}
\end{aligned}
$$

Let us define $B = \min\{\mu_H, \mu_M\}$. Then from the above inequality, $\mathcal{D}^+\mathcal{L}(t) \le -B(|S_H^i(t) - \bar{S}_H^i(t)| + |E_H^i(t) - \bar{E}_H^i(t)| + |I_H^i(t) - \bar{I}_H^i(t)| + |A_H^i(t) - \bar{A}_H^i(t)| + |R_H^i(t) - \bar{R}_H^i(t)| + |S_M^i(t) - \bar{I}_M^i(t)| + |S_M^i(t) - \bar{I}_M^i(t)|)$. This implies that $\mathcal{L}(t)$ is a non-increasing function on $[0, \infty)$.

Now by integrating we get,

$$
\begin{aligned}
& \mathcal{L}(t) + B\int_0^t(|S_H^i(\tau) - \bar{S}_H^i(\tau)| + |E_H^i(\tau) - \bar{E}_H^i(\tau)| + |I_H^i(\tau) - \bar{I}_H^i(\tau)| \\
& +|A_H^i(\tau) - \bar{A}_H^i(\tau)| + |R_H^i(\tau) - \bar{R}_H^i(\tau)| + |S_M^i(\tau) - \bar{S}_M^i(\tau)| \\
& +|I_M^i(\tau) - \bar{I}_M^i(\tau)|)d\tau \le \mathcal{L}(0) < \infty, \quad \textit{for all } t \ge 0. \qquad \text{(E.2)}
\end{aligned}
$$

Using Lemma 2.2 in (Zhu and Wang, 2011), we get $\lim_{t\to\infty}\mathcal{L}(t) = 0$. This implies for $i = 1, 2, \ldots, n$, $\lim_{t\to\infty}|S_H^i(t) - \bar{S}_H^i(t)| = 0$; $\lim_{t\to\infty}|E_H^i(t) - \bar{E}_H^i(t)| = 0$; $\lim_{t\to\infty}|I_H^i(t) - \bar{I}_H^i(t)| = 0$; $\lim_{t\to\infty}|A_H^i(t) - \bar{A}_H^i(t)| = 0$; $\lim_{t\to\infty}|R_H^i(t) - \bar{R}_H^i(t)| = 0$; $\lim_{t\to\infty}|S_M^i(t) - \bar{S}_M^i(t)| = 0$; $\lim_{t\to\infty}|I_M^i(t) - \bar{I}_M^i(t)| = 0$.

This proves that $(\bar{S}_H^i(t), \bar{E}_H^i(t), \bar{I}_H^i(t), \bar{A}_H^i(t), \bar{R}_H^i(t), \bar{S}_M^i(t), \bar{I}_M^i(t))$ is globally attracting.

To prove the uniqueness of the periodic solution, let us assume that $(\bar{S}_{H1}^i(t), \bar{E}_{H1}^i(t), \bar{I}_{H1}^i(t), \bar{A}_{H1}^i(t), \bar{R}_{H1}^i(t), \bar{S}_{M1}^i(t), \bar{I}_{M1}^i(t))$ be another solution of (2.1) with period ω. If this solution is not same with the previous solution then there exists at least one $\xi \in [0, \omega]$ such that $\bar{S}_H^1(\xi) \ne \bar{S}_{H1}^1(\xi)$ which means $|\bar{S}_H^1(\xi) - \bar{S}_{H1}^1(\xi)| = \epsilon_1 > 0$. Thus we get $\epsilon_1 = \lim_{n\to\infty}|\bar{S}_H^1(\xi + \eta\omega) - \bar{S}_{H1}^1(\xi + \eta\omega)| = \lim_{t\to\infty}|\bar{S}_H^1(t) - \bar{S}_{H1}^1(t)| > 0$, which contradicts the fact that $(\bar{S}_H^i(t), \bar{E}_H^i(t), \bar{I}_H^i(t), \bar{A}_H^i(t), \bar{R}_H^i(t), \bar{I}_M^i(t), \bar{S}_M^i(t))$ is globally attracting. Therefore, $\bar{S}_H^1(t) = \bar{S}_{H1}^1(t)$, *for all* $t \in [0, \omega]$. Similarly we can use the above argument for the remaining state variables. Thus, if $\mathcal{R}_0 > 1$, then the system (2.1) possesses a unique ω periodic solution which is globally asymptotically stable. □

References

Adams, B., Kapan, D.D., 2009. Man bites mosquito: understanding the contribution of human movement to vector-borne disease dynamics. PLoS One 4 (8), e6763.

Andraud, M., Hens, N., Marais, C., Beutels, P., 2012. Dynamic epidemiological models for dengue transmission: a systematic review of structural approaches. PLoS One 7 (11), e49085.

Araújo, H., Carvalho, D., Ioshino, R., Costa-da Silva, A., Capurro, M., 2015. Aedes aegypti control strategies in Brazil: incorporation of new technologies to overcome the persistence of dengue epidemics. Insects 6 (2), 576–594.

Arino, J., 2017. Spatio-temporal spread of infectious pathogens of humans. Infect. Dis. Model. 2 (2), 218–228.

Aronsson, G., Kellogg, R., 1978. On a differential equation arising from compartmental analysis. Math. Biosci. 38 (1–2), 113–122.

Baldacchino, F., Caputo, B., Chandre, F., Drago, A., della Torre, A., Montarsi, F., Rizzoli, A., 2015. Control methods against invasive Aedes mosquitoes in Europe: a review. Pest. Manag. Sci. 71 (11), 1471–1485.

Barrios, E., Lee, S., Vasilieva, O., 2018. Assessing the effects of daily commuting in two-patch dengue dynamics: a case study of Cali, Colombia. J. Theor. Biol. 453, 14–39.

Benelli, G., Jeffries, C., Walker, T., 2016. Biological control of mosquito vectors: past, present, and future. Insects 7 (4), 52.

Burattini, M.N., Chen, M., Chow, A., Coutinho, F., Goh, K., Lopez, L., Ma, S., Massad, E., 2008. Modelling the control strategies against dengue in Singapore. Epidemiol. Infect. 136 (3), 309–319.

Cosner, C., Beier, J.C., Cantrell, R.S., Impoinvil, D., Kapitanski, L., Potts, M.D., Troyo, A., Ruan, S., 2009. The effects of human movement on the persistence of vector-borne diseases. J. Theor. Biol. 258 (4), 550–560.

Derouich, M., Boutayeb, A., 2006. Dengue fever: mathematical modelling and computer simulation. Appl. Math. Comput. 177 (2), 528–544.

Ditsuwan, T., Liabsuetrakul, T., Ditsuwan, V., Thammapalo, S., 2012. Cost of standard indoor ultra-low-volume space spraying as a method to control adult dengue vectors. Trop. Med. Int. Health 17 (6), 767–774.

Duong, V., Lambrechts, L., Paul, R.E., Ly, S., Lay, R.S., Long, K.C., Huy, R., Tarantola, A., Scott, T.W., Sakuntabhai, A., et al., 2015. Asymptomatic humans transmit dengue virus to mosquitoes. Proc. Natl. Acad. Sci. USA 112 (47), 14688–14693.

Ganeshkumar, P., Murhekar, M.V., Poornima, V., Saravanakumar, V., Sukumaran, K., Anandaselvasankar, A., John, D., Mehendale, S.M., 2018. Dengue infection in india: a systematic review and meta-analysis. PLoS Negl. Trop. Dis. 12 (7), e0006618.

Gratz, N.G., 1991. Emergency control of Aedes aegypti as a disease vector in urban areas. J. Am. Mosq. Control Assoc. (7) 353–365.

Grenfell, B., 1998. Cities and villages: infection hierarchies in a measles metapopulation. Ecol. Lett. 1, 68–70.

Guo, C., Zhou, Z., Wen, Z., Liu, Y., Zeng, C., Xiao, D., Ou, M., Han, Y., Huang, S., Liu, D., et al., 2017. Global epidemiology of dengue outbreaks in 1990–2015: a systematic review and meta-analysis. Front. Cell. Infect. Microbiol. 7, 317.

Haario, H., Laine, M., Mira, A., Saksman, E., 2006. DRAM: efficient adaptive MCMC. Stat. Comput. 16 (4), 339–354.

Haario, H., Saksman, E., Tamminen, J., 2001. An adaptive Metropolis algorithm. Bernoulli 223–242.

Halstead, S., 2009. Antibodies determine virulence in dengue. Ann. N.Y. Acad. Sci. 1171 (s1), E48–E56.

Hendron, R.W.S., Bonsall, M.B., 2016. The interplay of vaccination and vector control on small dengue networks. J. Theor. Biol. 407, 349–361.

Hirsch, M.W., 1985. Systems of differential equations that are competitive or cooperative ii: convergence almost everywhere. SIAM J. Math Anal. 16 (3), 423–439.

Kroeger, A., Lenhart, A., Ochoa, M., Villegas, E., Levy, M., Alexander, N., McCall, P.J., 2006. Effective control of dengue vectors with curtains and water container covers treated with insecticide in Mexico and Venezuela: cluster randomised trials. Br. Med. J. 332 (7552), 1247–1252.

Lakshmikantham, V., Leela, S., Martynyuk, A.A., 1989. Stability Analysis of Nonlinear Systems. Springer.

Lee, S., Castillo-Chavez, C., 2015. The role of residence times in two-patch dengue transmission dynamics and optimal strategies. J. Theor. Biol. 374, 152–164.

Lewer, J.J., Van den Berg, H., 2008. A gravity model of immigration. Econ. Lett. 99 (1), 164–167.

Luz, P., Codeco, C., Medlock, J., Struchiner, C., Valle, D., Galvani, A., 2009. Impact of insecticide interventions on the abundance and resistance profile of Aedes aegypti. Epidemiol. Infect. 137 (8), 1203–1215.

Luz, P.M., Vanni, T., Medlock, J., Paltiel, A.D., Galvani, A.P., 2011. Dengue vector control strategies in an urban setting: an economic modelling assessment. Lancet 377 (9778), 1673–1680.

McDonald, P., 1977. Population characteristics of domestic Aedes aegypti (Diptera: Gulicidae) in villages on the Kenya coast II. Dispersal within and between villages. J. Med. Entomol. 14 (1), 49–53.

Mubayi, A., Castillo-Chavez, C., Chowell, G., Kribs-Zaleta, C., Siddiqui, N.A., Kumar, N., Das, P., 2010. Transmission dynamics and underreporting of Kala-azar in the Indian state of Bihar. J. Theor. Biol. 262 (1), 177–185.

Muir, L., Kay, B., 1998. Aedes aegypti survival and dispersal estimated by mark-release-recapture in Northern Australia. Am. J. Trop. Med. Hyg. 58 (3), 277–282.

Nevai, A.L., Soewono, E., 2014. A model for the spatial transmission of dengue with daily movement between villages and a city. Math. Med. Biol. 31 (2), 150–178.
Newton, E.A., Reiter, P., 1992. A model of the transmission of dengue fever with an evaluation of the impact of ultra-low volume (ULV) insecticide applications on dengue epidemics. Am. J. Trop. Med. Hyg. 47 (6), 709–720.
Oki, M., Sunahara, T., Hashizume, M., Yamamoto, T., 2011. Optimal timing of insecticide fogging to minimize dengue cases: modeling dengue transmission among various seasonalities and transmission intensities. PLoS Negl. Trop. Dis. 5 (10), e1367.
Perich, M.J., Davila, G., Turner, A., Garcia, A., Nelson, M., 2000. Behavior of resting Aedes Aegypti (Culicidae: Diptera) and its relation to ultra-low volume adulticide efficacy in Panama City, Panama. J. Med. Entomol. 37 (4), 541–546.
Perich, M.J., Kardec, A., Braga, I.A., Portal, I.F., Burge, R., Zeichner, B.C., Brogdon, W.A., Wirtz, R.A., 2003. Field evaluation of a lethal ovitrap against dengue vectors in Brazil. Med. Vet. Entomol. 17 (2), 205–210.
Pinho, S., Ferreira, C., Esteva, L., Barreto, F., e Silva, V., Teixeira, M., 2010. Modelling the dynamics of dengue real epidemics. Philos. Trans. A Math. Phys. Eng. Sci. 368 (1933), 5679–5693.
Prosper, O., Ruktanonchai, N., Martcheva, M., 2012. Assessing the role of spatial heterogeneity and human movement in malaria dynamics and control. J. Theor. Biol. 303, 1–14.
QGIS Development Team, 2009. QGIS Geographic Information System. Open Source Geospatial Foundation.
Sardar, T., Rana, S., Chattopadhyay, J., 2015. A mathematical model of dengue transmission with memory. Commun. Nonlinear Sci. Numer. Simul. 22 (1), 511–525.
Smith, H.L., Waltman, P., 1995. The Theory of the Chemostat: Dynamics of Microbial Competition, 13. Cambridge University Press.
Stoddard, S.T., Forshey, B.M., Morrison, A.C., Paz-Soldan, V.A., Vazquez-Prokopec, G.M., Astete, H., Reiner, R.C., Vilcarromero, S., Elder, J.P., Halsey, E.S., et al., 2013. House-to-house human movement drives dengue virus transmission. Proc. Natl. Acad. Sci. USA 110 (3), 994–999.
Thieme, H.R., 1992. Convergence results and a Poincaré-Bendixson trichotomy for asymptotically autonomous differential equations. J. Math. Biol. 30 (7), 755–763.
Wang, W., Zhao, X., 2008. Threshold dynamics for compartmental epidemic models in periodic environments. J. Dyn. Differ. Equ. 20 (3), 699–717.
Wesolowski, A., Qureshi, T., Boni, M.F., Sundsøy, P.R., Johansson, M.A., Rasheed, S.B., Engø-Monsen, K., Buckee, C., 2015. Impact of human mobility on the emergence of dengue epidemics in Pakistan. Proc. Natl. Acad. Sci. USA 112 (38), 11887–11892.
WHO, 2003. Space spray application of insecticides for vector and public health pest control: a practitioner's guide.
WHO, 2009. Dengue: Guidelines for Diagnosis, Treatment, Prevention and Control. World Health Organization.
WHO, 2016. Dengue and severe dengue. http://www.who.int/mediacentre/factsheets/fs117/en/. (Online Accessed- 15June 2018).
Wilder-Smith, A., Foo, W., Earnest, A., Sremulanathan, S., Paton, N.I., 2004. Seroepidemiology of dengue in the adult population of Singapore. Trop. Med. Int. Health 9 (2), 305–308.
Zhang, F., Zhao, X., 2007. A periodic epidemic model in a patchy environment. J. Math. Anal. Appl. 325 (1), 496–516.
Zhao, X., Borwein, J., Borwein, P., 2003. Dynamical Systems in Population Biology, 16. Springer.
Zhu, Y., Wang, K., 2011. Existence and global attractivity of positive periodic solutions for a predator–prey model with modified Leslie–Gower Holling-type II schemes. J. Math. Anal. Appl. 384 (2), 400–408.

Source details

Feedback > Compare sources >

Journal of Theoretical Biology

Scopus coverage years: from 1961 to Present

Publisher: Elsevier

ISSN: 0022-5193 E-ISSN: 1095-8541

Subject area: Mathematics: Statistics and Probability | Mathematics: Applied Mathematics | Agricultural and Biological Sciences: General Agricultural and Biological Sciences | Mathematics: Modeling and Simulation View all

Source type: Journal

View all documents > Set document alert Save to source list

CiteScore 2022
4.9

SJR 2022
0.566

SNIP 2022
0.784

CiteScore | CiteScore rank & trend | Scopus content coverage

PLOS | NEGLECTED TROPICAL DISEASES

RESEARCH ARTICLE

A realistic two-strain model for MERS-CoV infection uncovers the high risk for epidemic propagation

Tridip Sardar[1☯], Indrajit Ghosh[2☯], Xavier Rodó[3]*, Joydev Chattopadhyay[2]

1 Department of Mathematics, Dinabandhu Andrews College, Kolkata, India, **2** Agricultural and Ecological Research Unit, Indian Statistical Institute, Kolkata, India, **3** ICREA &CLIMA (Climate and Health Program), ISGlobal, Barcelona Institute for Global Health, Barcelona, Spain

☯ These authors contributed equally to this work.
* xavier.rodo@isglobal.org

OPEN ACCESS

Citation: Sardar T, Ghosh I, Rodó X, Chattopadhyay J (2020) A realistic two-strain model for MERS-CoV infection uncovers the high risk for epidemic propagation. PLoS Negl Trop Dis 14(2): e0008065. https://doi.org/10.1371/journal.pntd.0008065

Editor: Benjamin Althouse, Institute for Disease Modeling, UNITED STATES

Received: December 14, 2018

Accepted: January 15, 2020

Published: February 14, 2020

Data Availability Statement: The website containing all MERS-CoV dataset used is the following: http://empres-i.fao.org/eipws3g/

Funding: I.G. was supported by the research fellowship from University Grants Commission (https://www.ugc.ac.in/), Government of India. X. R. acknowledges the support of a fellowship by the PERIS PICAT project SLT002/16/00466 (peris@gencat.cat| http://canalsalut.gencat.cat) from the Catalan Ministry of Health. The funders had no role in study design, data collection and

Abstract

Middle East Respiratory Syndrome Coronavirus (MERS-CoV) causes severe acute respiratory illness with a case fatality rate (CFR) of 35,5%. The highest number of MERS-CoV cases are from Saudi-Arabia, the major worldwide hotspot for this disease. In the absence of neither effective treatment nor a ready-to-use vaccine and with yet an incomplete understanding of its epidemiological cycle, prevention and containment measures can be derived from mathematical models of disease epidemiology. We constructed 2-strain models to predict past outbreaks in the interval 2012–2016 and derive key epidemiological information for Macca, Madina and Riyadh. We approached variability in infection through three different disease incidence functions capturing social behavior in response to an epidemic (e.g. Bilinear, BL; Non-monotone, NM; and Saturated, SAT models). The best model combination successfully anticipated the total number of MERS-CoV clinical cases for the 2015–2016 season and accurately predicted both the number of cases at the peak of seasonal incidence and the overall shape of the epidemic cycle. The evolution in the basic reproduction number (R_0) warns that MERS-CoV may easily take an epidemic form. The best model correctly captures this feature, indicating a high epidemic risk ($1 \leq R_0 \leq 2{,}5$) in Riyadh and Macca and confirming the alleged co-circulation of more than one strain. Accurate predictions of the future MERS-CoV peak week, as well as the number of cases at the peak are now possible. These results indicate public health agencies should be aware that measures for strict containment are urgently needed before new epidemics take off in the region.

Author summary

There is currently no way to anticipate MERS-CoV epidemic outbreaks and strategies for disease prediction and containment are largely undermined by the limited knowledge of its epidemiological cycle. Not an effective treatment nor a vaccine for MERS-CoV exist to date. Instead, using three two-strain mathematical models that incorporate human social behavior as different disease incidence functions (e.g. bilinear, non-monotone and

analysis, decision to publish, or preparation of the manuscript.

Competing interests: No authors have competing interests.

saturated), the best model combinations successfully anticipate the occurrence of the peak week in the season and the incidence at the peak. Our results confirm there are currently 2 strains co-circulating in the most populated regions in Saudi Arabia and highlight the high risk for large epidemic outbreaks, while the role of super-spreaders appears irrelevant for disease spread.

Introduction

The first case of Middle East Respiratory Syndrome Coronavirus (MERS-CoV) infection was identified in Saudi Arabia in 2012[1–5]. Since then the country suffers from repeated outbreaks of MERS-CoV in different provinces (Fig 1A and 1B)[2]. There are two main routes of MERS-CoV transmission: animal-to-human and human-to-human[4–6]. It is suspected that dromedary camels are the source of human infections[1] but the transmission route of MERS-CoV to humans is yet not well understood (Fig 1C). However, transmission from camels to humans is confirmed from the isolation of near-identical strains of MERS-CoV from epidemiologically coexisting camels and humans[7]. The patients might be exposed to MERS-CoV by consumption of raw camel products[8] (e.g. milk and dairy products, raw meat, etc.). Meanwhile, human-to-human transmission has been reported in society and hospital settings[9–36] with the virus being transmitted between humans during close human-to-human contact through droplets of respiratory secretions. Potential propagation to nearby and more distant regions is also a high-risk possibility as an outbreak of MERS-CoV is likely to emerge in areas such as nearby countries in the Middle East and eastern Africa where the camel trade connects the different regions (Fig 1). Unfortunately, as for now, MERS-CoV vaccines are only at the preclinical phase[10], increasing our understanding of its epidemic potential and knowledge on the drivers of MERS-CoV variability might help to achieve better preparedness ahead of forthcoming epidemics.

The ability to predict disease outbreaks will provide a mechanism for policymakers and health-care services to respond to epidemics in a timely manner, reducing the impact and maximizing the limited resources available to be deployed[11]. The timing and severity of infectious disease outbreaks, two matters of considerable public-health relevance, are the main challenges when attempting to predict disease outbreaks[11–14]. Attempts to set up prediction frameworks for anticipating epidemics for other diseases such as dengue and influenza were pursued in the recent past with different degree of success, but clear added value[11–16]. These systems proved effective to better anticipate future outbreaks and increase our understanding on mechanisms driving disease variability. To this end, a threshold quantity that is most important to anticipate the risk of future outbreaks is the basic reproduction number (R_0). There are quite a few studies that estimated R_0 for the current MERS-CoV outbreak. Majumdar et al.[28] for instance, estimated R_0 for Jeddah and Riyadh using a function called Incidence Decay with Exponential Adjustments (IDEA). They found that the estimate of R_0 in Jeddah and Riyadh are in the ranges (3.5–6.7) and (2.0–2.8), respectively. A stochastic epidemiological model of MERS-CoV with zoonotic and human-to-human transmission was considered by Poletto et al.[29] to quantify the rates of generation of cases from those two transmission routes. They found that spring 2014 cases led to the increase in transmission rates, which brings R_0 to values above unity. Heishet al.[32] used a simple mathematical model to trace the temporal course of South Korea MERS-CoV outbreak. They estimated R_0 to be in the range of 7.0 to 19.3. Instead, Nishiura *et* al.[30] estimated the expected number of secondary cases following the importation of an index case (countries other than KSA, Qatar and

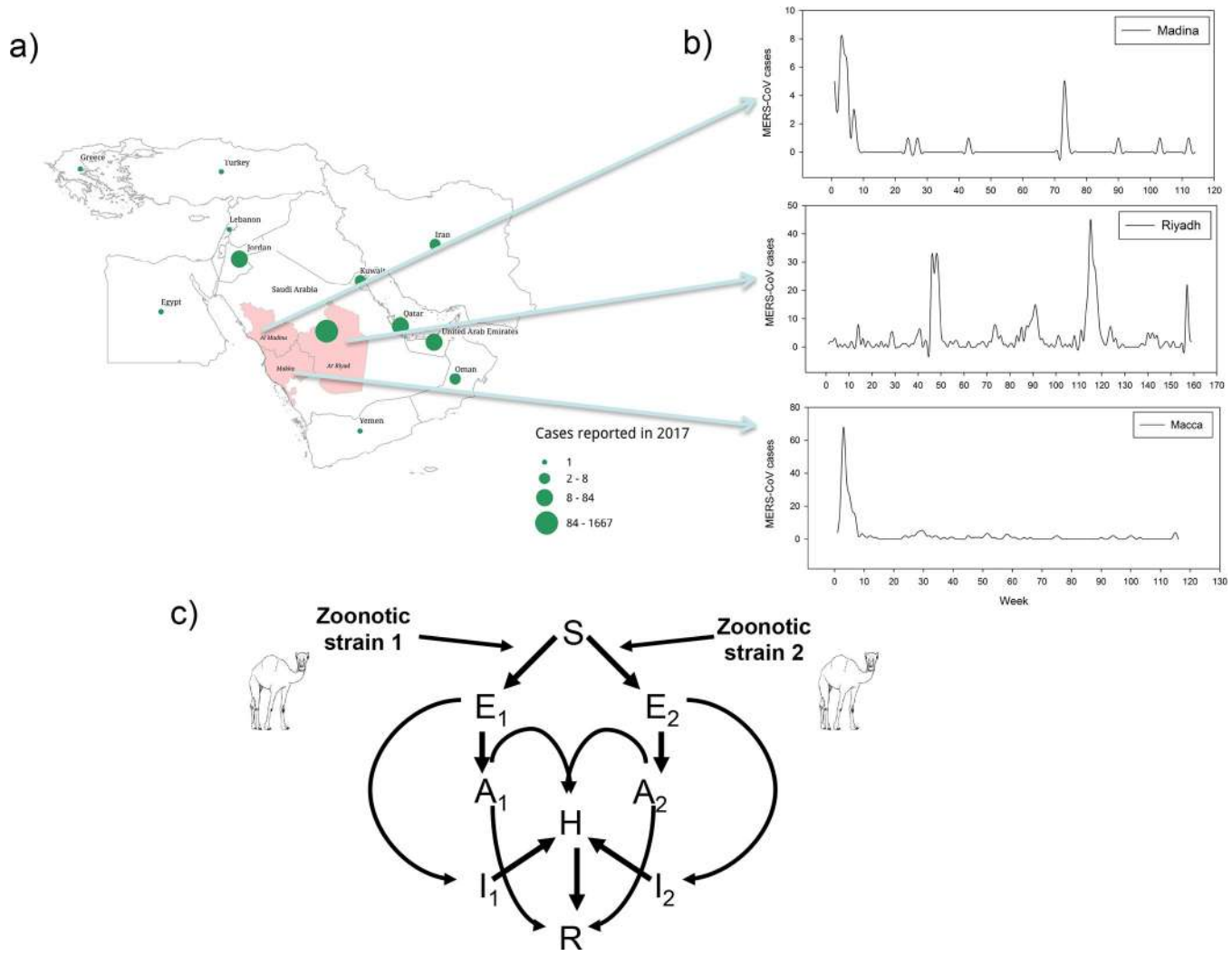

Fig 1. Distribution of MERS-CoV weekly cases in Riyadh, Macca and Madina provinces during July, 2013—June, 2016. (a) The geographic distribution of MERS-CoV cases reported in 2017 in the Middle East. (b) Time series of weekly incidence data of MERS-CoV in three major provinces, Riyadh, Maccaand Madina, respectively. (c) Two strain Models flow diagram considering asymptomatic, symptomatic, hospitalized, and Zoonotic transmission. Open source KML map for the Middle East was kindly obtained and redrawn by Josep-BoyardMicheau from https://community.qlik.com/t5/Qlik-Sense-Enterprise-Documents/GCC-Middle-East-country-boundary-KML-maps-KML-Shapefile/ta-p/1478595.

https://doi.org/10.1371/journal.pntd.0008065.g001

UAE), using a branching process type modelling approach. They also suggested that even if R_0 is below unity, a large cluster of cases with multiple generations might occur. The aforementioned studies indicated that the basic reproduction number is above unity, although there are few studies that suggest R_0 is less than one[4,17,18]. However, at the same time, intriguing differences in observed and predicted scenarios clearly suggested other important factors might be missing in previous models built for these MERS-CoV case studies. For instance, in a recent survey for Mers-CoV in over 1300 Saudi Arabian camels, Sabiret al.[1] found that camels share three coronaviruses (CoV) species with humans. Among them, one has been dominant in the region since December 2014 and led to the human MERS-CoV outbreaks occurring in 2015. The wide species range of CoVs and their propensity to cross species boundaries suggest that more MERS-CoV uncontained outbreaks may likely occur in the future. Zumlaet al.[19] also suggested that MERS-CoV species can mutate to have increased inter-human transmissibility. Cottenet al.[37] used MERS data from the period May to September 2013. They found

four Saudi Arabia MERS-CoV phylogenetic clades, with 3 clades apparently no longer contributing to current cases, therefore not appearing in the saliva of camels. They also show that the ancestors of most of the viral clades originated in Riyadh (See Cotten et al.[37]). Recently, strain variability in MERS-CoV infection was confirmed in 51 respiratory samples from 32 patients, confirming that more than one strain of human MERS-CoVis present[20]. The fact that more than one MERS-CoV strain is currently circulating in Saudi Arabia should be properly accounted for as this presence may have substantially contributed to amplify the transmission intensity producing repeated MERS-CoV changes in incidence through their periodic reintroduction into human populations[19]. Furthermore, Chan et al.[34] characterized MERS-CoV viruses from dromedaries in Saudi Arabia and Egypt and compared them with a human MERS-CoV reference strain. They isolated three dromedary strains, two from Saudi Arabia and one from Egypt. The human and dromedary MERS-CoV strains had similar viral replication competence in Vero-E6 cells and respiratory tropism in ex-vivo cultures of the human respiratory tract. They also suggested that dromedary viruses from Saudi Arabia and Egypt are probably infectious to human beings[34].

Methods

a) Disease incidence functions

We constructed three different 2-strain models for MERS-CoV that consider community human-human, hospital human-human, and passive zoonotic transmission (Fig 1C and see also S1–S18 Tables). Models derived also incorporate the effect of strain variability with strain-1 as the dominant strain (Fig 1C and S1–S18 Tables). Variability among models is based upon three different disease incidence functions (e.g. BL, NM and SAT models [21–23] and see formulation in Table 1A and Fig 2).

The top panel in Fig 2 represents the BL force of infection. Here, as the number of infected individuals increases the disease transmission also increases linearly. The bottom-left panel represents the NM incidence function. Biologically this incidence function can account for "psychological effects" [38–39]. In the presence of psychological effects, initially the disease transmission rate increases rapidly when the number of infected individuals is small. However, this rate falls also rapidly in the presence of a large number of infected persons in the community. As in the case of MERS-CoV infections the CFR is about 40%, psychological effects for this infection represents the effect in the community of fear of becoming infected. This fear effect reduces the transmission rate rapidly in the presence of a high number of infections in the community. The bottom-right panel of Fig 2 represents the SAT incidence function. Biologically this incidence function represents the crowding effect in disease transmission. This crowding effect explains how the number of new infections becomes constant as the number of infected individual increases. This effect is known to reproduce the awareness effect of the disease during the course of an epidemic.

b) Super-spreaders and 1-strain vs 2-strain models

Furthermore, we investigated the potential effects of super-spreading events by incorporating an additional compartment for super-spreaders to our 2-strain model. We also consider the effect of variable zoonotic transmission by incorporating dynamics of the camel population into our 2-strain model. Information about the calculation of the epidemiological parameter values for the newly proposed 2-strain models is provided in Table 1B. Data used corresponds to weekly cases of MERS-CoV for the three provinces in Saudi Arabia where most clinical cases for MERS-CoV occurred for the time intervals July, 6th 2013 till June, 28th 2016 (Riyadh), April, 7th2014 till June, 26th2016 (Macca), and April, 20th2014 till June, 26th2016 (Madina),

Table 1. (A)Description of the incidence functions for the three models considered. (B)Main parameters of the three 2-strain models.

A

Incidence functions	Description	Source
$f(I)=\frac{\beta_1 SI}{N}$	Bilinear incidence function	23
$f(I)=\frac{\beta_1 SI}{N(1+\alpha I^2)}$	Non-monotone incidence function	21, 22
$f(I)=\frac{\beta_1 SI}{N(1+\alpha I)}$	Saturated incidence function	21

B

Symbol	Description	Range/Fixed	Sources
μ	Natural birth/death rate of human	2.5924×10^{-4}Week^{-1}	24
β_1	Transmission coefficients of symptomatic and asymptomatic cases	*[0, 100]* Week^{-1}	Estimated
θ	Measure of variability of two strains	*[0,1]*	Estimated
ρ	Reduction in transmission due to less infectiousness of asymptomatic infected individuals	*[0,1]*	Estimated
β_2	Transmission rate from hospitalized to susceptible individuals	*[0, 100]* Week^{-1}	Estimated
β_3	Import rate of external zoonotic infection	*[0, 10]* Week^{-1}	Estimated
p_1	Proportion of susceptible that get infected from hospitalized individuals with strain-1	[0,1]	Estimated
p_2	Proportion of susceptible that get infected from zoonotic infection with strain-1	[0,1]	Estimated
p_3	Proportion of exposed individuals that become symptomatic infected	0.553	4
c_1	Undetected entry rate of strain-1 asymptomatic class to hospitalized class	[0,5]	Estimated
c_2	Undetected entry rate of strain-2 asymptomatic class to hospitalized class	[0,5]	Estimated
$\frac{1}{\sigma}$	Incubation period	0.7429 Week	19,25,26
K	Recovery rate of asymptomatic individuals	1.4 Week^{-1}	27
λ	Hospitalization rate of symptomatic individuals	4.4824 Week^{-1}	4
γ	Recovery rate of hospitalized individuals	1 Week^{-1}	4
δ_2	Disease induced death rate of hospitalized individuals	Data	2
α_1	Measure of inhibitory effect of strain-1 (only for non-monotone and saturated incidence models)	[0,500]	Estimated
α_2	Measure of inhibitory effect of strain-2 (only for non-monotone and saturated incidence models)	[0,500]	Estimated

https://doi.org/10.1371/journal.pntd.0008065.t001

respectively (Fig 1A). Main parameters of the different models are provided in Table 1B. Parameters estimates are obtained by fitting the models to new MERS-CoV hospitalized weekly data[40]. We also estimated from data itself some unknown initial conditions for the model. Delayed Rejection Adaptive Metropolis algorithm is used here to sample the 95% confidence.The goodness of fitsto compare among 2-strain and single strain models were tested by determining the respective AIC and BIC values (See S19 Table). To further compare among predictive capabilities of these models with regard to those of their single-strain versions, predictions of raw clinical cases were attempted. Albeit some discrepancies exist, fairly accurate results were obtained despite the low numbers and highly stochastic nature of the three datasets and the nearly operational capacity of these models (Fig 3). In fact, near-operational systems usually require a much longer training period than the scarce three years employed here. Differences arising from the comparison of simulated and observed cases may also be due to the fact that we are fitting the 2-strain and single strain models to cumulative MERS-CoV cases, rather than to new cases. The procedure for model adjustment is as follows: for approaching near-operational predictions in each province, we followed former initiatives (e.g. on influenza[14] and dengue[16]) and partitioned the whole clinical cases datasets into two parts. First part was used for calibrating the models and the remaining part (52 weeks) were left aside for out-of-fit prediction. For Riyadh, Macca and Madina prediction periods were, respectively, from weeks 105–156 (7th June, 2015 - 11th June, 2016), weeks 65–116 (11th July, 2015 - 2nd July, 2016), and weeks 63–114 (11th July, 2015 - 2nd July, 2016)(Fig 3). We generated predictions for three major characteristics of the epidemiological cycle similar to previous attempts made for cholera, dengue and influenza[15,41–43] namely: (a) peak week: the week during which the maximum number of clinical cases occurred in a season (comprising 52 weeks); (b) peak maximum: the number of cases occurring at the peak week, and (c) season totals: the total number of cases in the entire season. Prediction for each target variable was made every 4 weeks (i.e. week 0, 4, 8, . . ., 48), with week 0 corresponding to the first week of the prediction interval. In the case of predictions for week *N*, data up to week *N* was used to fit the model and the trajectory predicted for out-of-fit future weeks *N+1* through week 52

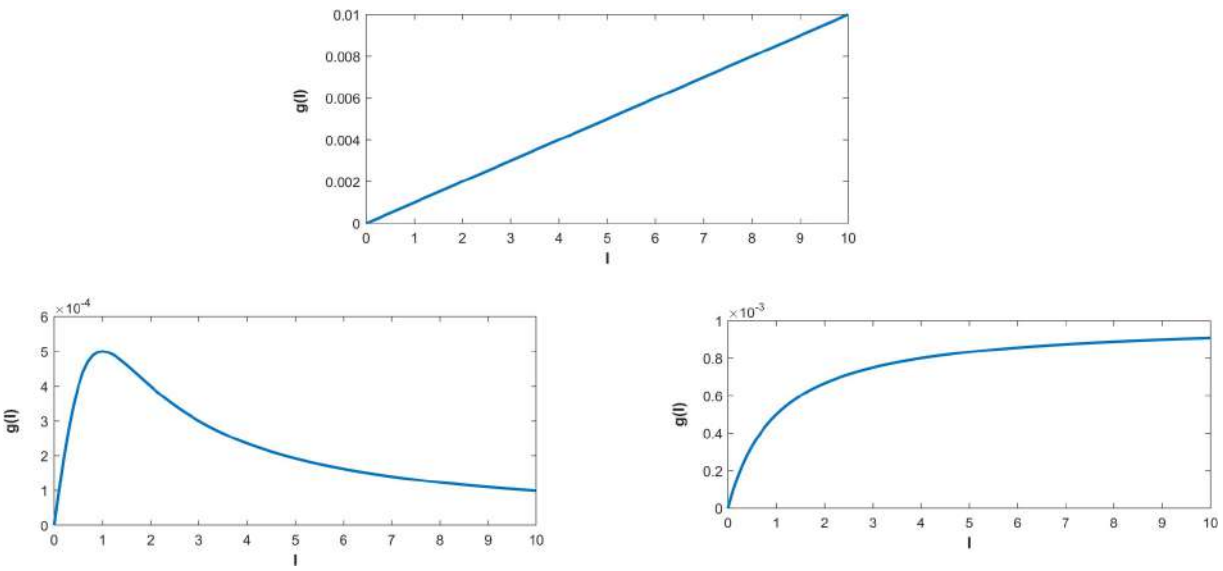

Fig 2. Representation of the three incidence functions, g(I). Top: g(I) = βI, bilinear incidence function. Bottom-left: g(I) = $\frac{\beta I}{N(1+\alpha I^2)}$, non-monotone incidence function and; bottom-right: g(I) = $\frac{\beta I}{N(1+\alpha I)}$, saturated incidence function. Here, N = 1000, α = 1 and β = 1.

https://doi.org/10.1371/journal.pntd.0008065.g002

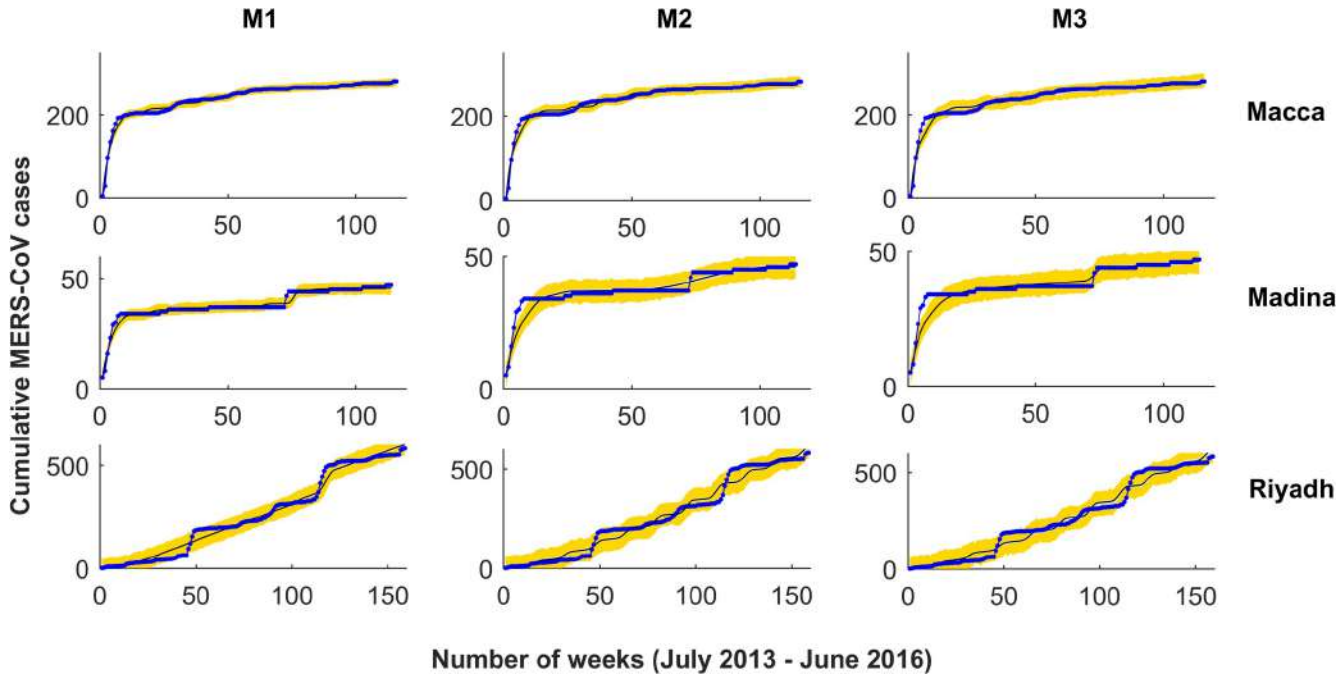

Fig 3. Model simulations fitted to accumulated MERS-CoV clinical cases in Macca, Madina and Riyadh. Observed data points are shown in blue and the solid line depicts the model solutions. The three two-strain models fitted to cumulative MERS-CoV cases are: M1: 2-strain model with bilinear incidence, M2: 2-strain model with non-monotone incidence, and M3: 2-strain model with saturated incidence.

https://doi.org/10.1371/journal.pntd.0008065.g003

(Fig 3). Indeed, the best models at predicting MERS-CoV incidence differed among regions (Fig 4), highlighting the complexity of the epidemiological situation, particularly in Riyadh. There, where at least there were two strains co-circulating, M2 stands up clearly as the best model function (see bottom panel in Fig 4), in comparison with Macca and Madina, with only one strain (Fig 4 top panels).

c) Estimation of R_0, R_C, and R_H and prediction framework

We estimated the basic reproduction number (R_0), the community reproduction number (R_C), and the hospital reproduction number (R_H) for the whole period of data for Riyadh, Macca and Madina (S1–S18 Tables; 44–45). We also estimated weekly values of R_0, R_C, and R_H for each prediction interval in the three provinces (i.e. weeks 105–156 in Riyadh, weeks 65–116 in Macca and weeks 63–114 in Madina, respectively). The predictions of R_0, R_C, and R_H are made for each 4-week time interval in the prediction period. The estimate of R_0, R_C, and R_H during 0^{th} week is obtained using the estimated parameter values for the training period of MERS-CoV data (i.e., in Riyadh week 1–104, in Macca week 1–64 and in Madina week 1–62). Afterwards, we keep on adding 4 data points to the previous data and re-estimate the parameters. These estimated parameters were then plugged into obtain values of R_0, R_C, and R_H in 4^{th} week to 48^{th} week of the prediction period. Thus in intervals of 4 weeks, we obtain an estimate of R_0, R_C, and R_H. Temporal evolution of R_0, R_C, and R_H for the three provinces is depicted in S1–S4 Figs, respectively.

Using the model that provides the best prediction for the season total cases in the three provinces (i.e., a 2-strain model with BL incidence for Macca and the 2-strain model with SAT incidence for both Madina and Riyadh), we predicted the total number of cases in the following year. Using the parameter estimates in the last prediction point (i.e. 48^{th} week) of the

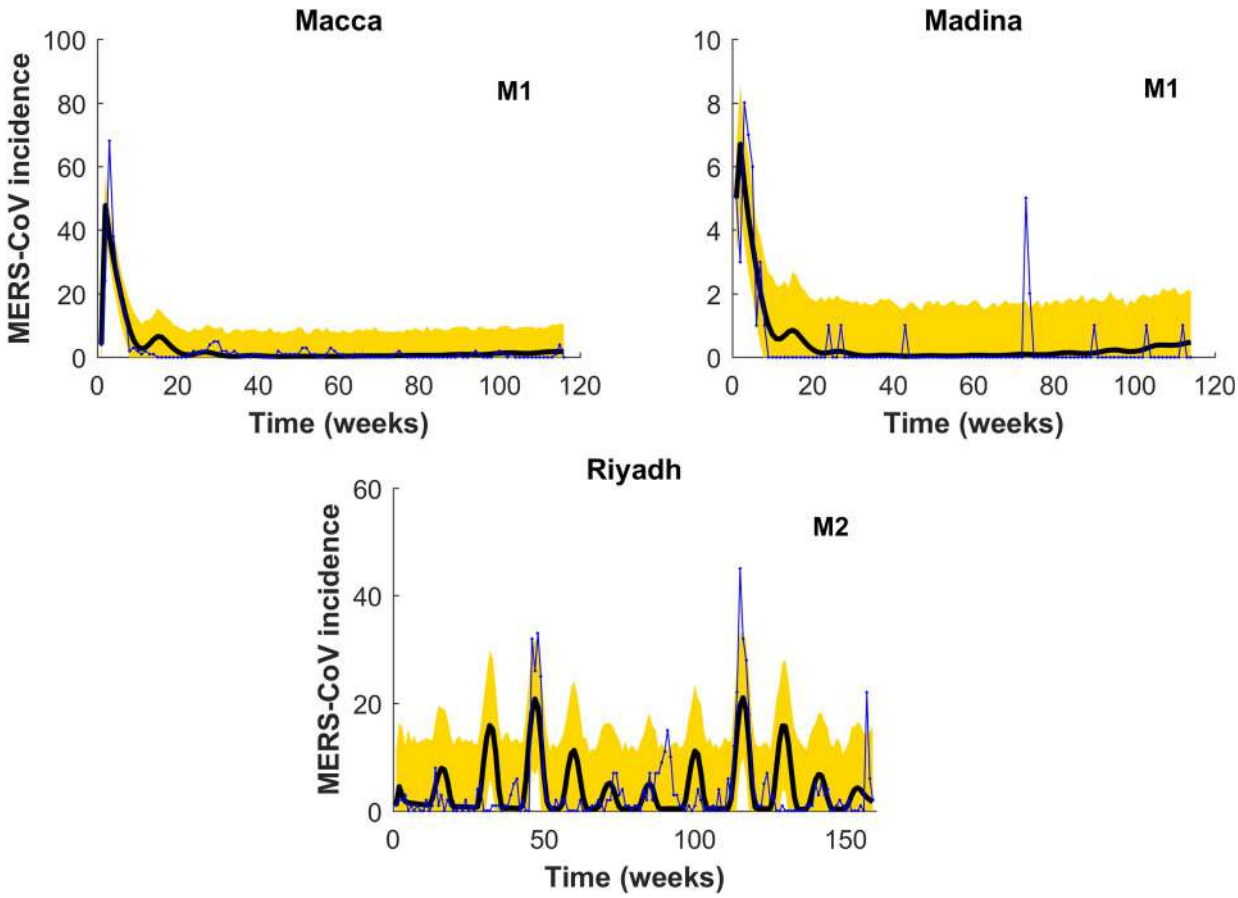

Fig 4. Same as for Fig 3 but predictions showing the best model for MERS-CoV incidence in each of the three regions. Notice that whereas M1 provides the best prediction for both Macca and Madina (top), M2 instead does it for the two-strain situation occurring in Riyadh. Blue line is MERS-CoV cases, solid black line predictions and yellow area denotes 95% confidence interval for predictions.

https://doi.org/10.1371/journal.pntd.0008065.g004

current season, we draw 1000 samples. Based on these parameter samples, we determined 1000 estimates of the season total cases in the next year[43]. We then defined a large outbreak in the forthcoming season in a particular region, as those events when cases exceeded the total number of cases in the previous season by more than one standard deviation (see Fig 5). Thus, the probability of a large outbreak (P_l) in those provinces isdetermined as the ratio of samples that exceed the total number of cases in a season divided by the total number of samples. We also considered the case when two strains of MERS-CoV may be co-circulating in the human population in Saudi Arabia. We also simulated the situation when one strain is assumed to be more active with a higher transmission rate, whilst the other is much less transmissible among individuals in the different provinces of Saudi-Arabia[37].Although we have considered two strains circulating in the community setting, we do not distinguish among strains in hospital premises. This is due to the lack of strain specific data in hospital settings. However, we are able to distinguish the contribution of infection from Community and Hospital setting by estimating the Community reproduction number (R_C) and the Hospital reproduction number (R_H). However, to account for this effect, we propose three different forces of infection (BL, NM and SAT) to model the MERS transmission in the three provinces. Saturated (SAT) functions describe "Crowding effects" in disease transmission, whereas Non-monotone (NM) functions are used to incorporate"psychological effects". As the CFR in MERS-CoV is about

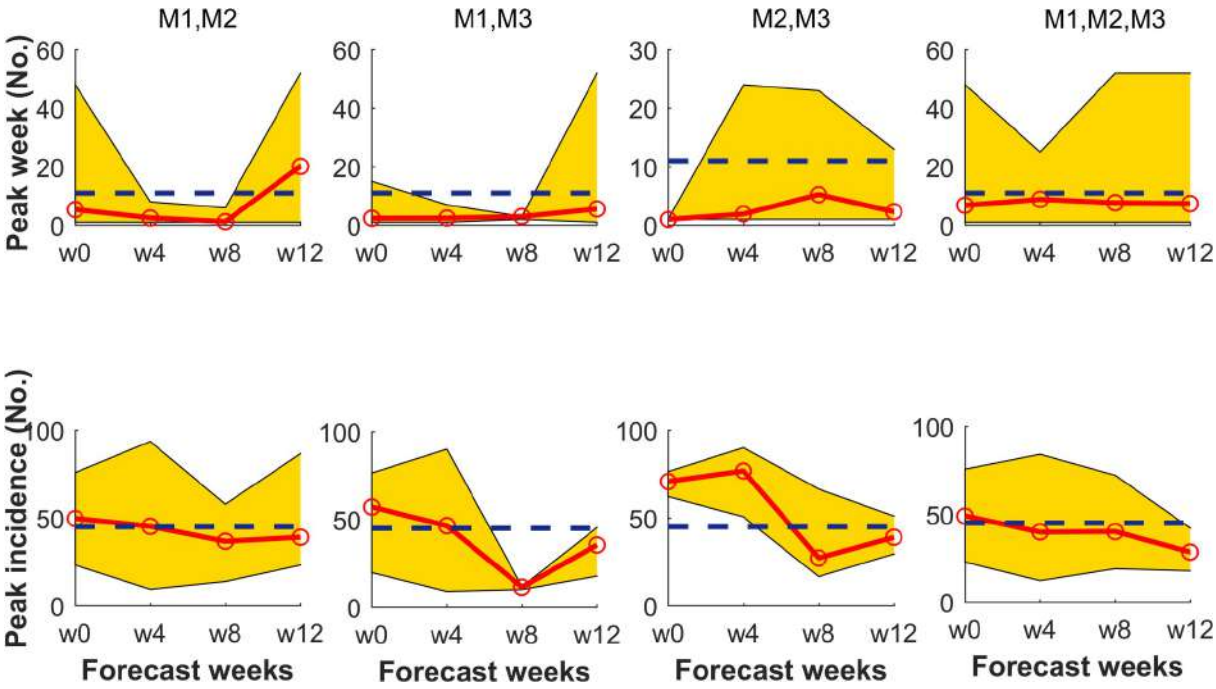

Fig 5. Best fit obtained from a combination of 2-strain models. Each model was aimed at predicting MERS-CoV epidemiological targets (top-peak week (No.), bottom-peak incidence (No.)) in Riyadh. Panels showing peak week and peak incidences are displayed up to the time of occurrence (11th week). Representations of the 2-strain models M1, M2, and M3 are the same as in Fig 2A. Dashed lines are observed values.

https://doi.org/10.1371/journal.pntd.0008065.g005

40%, it is easily expected that awareness in front of a MERS-CoV situation may play an important role during an epidemic[44–46]. Thus a model with such a crowding effect might seem a priori more realistic in comparison to the bilinear (BL) transmission (see also Fig 2). The crowding effect in disease transmission[38,39] can also be interpreted as the behavioral change of susceptible individuals when the number of infected individuals increases (Fig 2). This fact causes a lower number of new infections when a large number of infected individuals are already present in the community. This behavioral change in the susceptible population may occur due to, for instance, public health awareness campaigns and alerts raised by local or international authorities. The psychological effect is somewhat similar to the crowding effect, but with the effect of fear being added to the awareness. The psychological effect is stronger as the transmission rate decreases more rapidly with an increasing number of infected individuals (Fig 2) [40–42]. Recently, Kucharski et al.[35] suggested that MERS-CoV transmission is over dispersed and hence outbreaks can include super-spreading events. In a similar study, Nishiura et al.[33] concluded that super-spreaders who visited multiple healthcare facilities drove up the epidemic by generating larger number of secondary cases. Therefore, we also consider the role of potential super-spreaders in the context of a 2-strain model with BL incidence function.

Results and discussion

Estimates of the transmission rates for the 2-strain model with BL incidence suggest that MERS-CoV transmission in the three locations is dominated by community and hospital transmission (S1 Table to S9 Table). The former statement is in good agreement with a previous study that suggested that MERS-CoV infections are essentially produced through both hospital and community based human-human transmission[2]. This fact is well reflected in

the estimates of transmission rates obtained from the other two 2-strain models (e.g. NM and SAT incidence functions) for the three locations (S1–S9 Tables). Estimates of the parameter θ (a measure of variability within the two strains) in Riyadh and Macca (see S1–S3 Tables) suggest that both strains are currently active in these provinces (albeit strain 2 contributes with only 3% - 50% to community human-human transmission). In Madina instead, a majority of the models (BL and NM) point to only one active strain,with strain 2 contributing less than 1% to community human-human transmission, see S1–S9 Tables.

For each particular region in this study, two strain models are compared among themselves and also with regard to their single-strain counterparts in order to determine the best model (i.e. single, two-strain or a combination of other two-strain models). Results show that in the three locations, 2-strain models provide a better fitting to cumulative cases in comparison to their single strain counterparts (Fig 2). AIC and BIC values for the 2-strain models suggest that the best model is region specific (best model for Riyadh is a 2-strain model with BL incidence, whereas in Macca and Madina the best models are both the model with a NM incidence function and the one incorporating super-spreaders, respectively; see S19 Table). We also compare our 2-strain models with a 2-strain model with variable Zoonotic transmission (SI Eq. A2). Comparing AIC and BIC values, we found that the models with variable Zoonotic transmission (SI Eq. A2) did not improve all the previous results (see S19 Table). Therefore, the best model among all 2-strain models cannot be determined solely from their goodness-of-fit comparison. For this reason, we additionally compared all the two-strain models on the basis of their respective prediction skills. Forecasts for the three models in Riyadh suggest that, a majority of the times, the 2-strain model with SAT incidence can better predict the three targets in comparison to the other two competing 2-strain models (e.g. note that for SAT the average of the mean absolute error, MAE, for peak week is 11.6, whereas for peak maximum is 24.83 and for season totals 55.62) (Table 2A). For comparison, we also provide predictions in the province of Riyadh of the three targets using the model with super-spreaders. However, prediction with super-spreaders did not improve at all the former results obtained for Riyadh (see Table 2A). For Madina, both the peak week and season totals are better predicted by the same SAT 2-strain model (i.e. MAE average for peak week being 14.5 and 9.33 for season totals; see also S22 Table). However, when predicting the peak maximum in Madina, clearly the best model is the 2-strain model with the NM incidence function (i.e. MAE average for peak maximum being 2.62; see also S22 Table). For Macca, except for the peak week, the other two targets, namely peak maximum and season totals are better predicted with the 2-strain model with BL incidence (i.e. MAE average of 7.08 for peak maximum and of 63.42 for season totals, respectively; see S22 Table). For peak week in Macca, again a better prediction is achieved by the 2-strain model with SAT incidence (i.e. MAE average for peak week being 23.9, see S22 Table).

When comparing the three two strain models to their single-strain counterparts, composites of the mean absolute error (MAE) in Riyadh (Table 2A, and S23 Table) suggest that 2-strain models always outperform the single strain versions in predicting the three targets (i.e. peak week, peak maximum, and season totals). Averages of MAE for peak week, peak maximum and for season totals are 11.6, 24.83 and 55.62, respectively. This fact reinforces our earlier inference, confirming that there is more than one strain currently active in Riyadh. Among the single-strain models in Riyadh, the model with SAT incidence is found to have a better predictive capacity for the three targets in comparison to the other two single-strain models (S23 Table). In Macca instead, the single-strain model with SAT incidence provides better predictions of the peak week, the peak maximum and seasontotals in comparison to all the other models (see for instance MAE values in S22 Table; and values obtained for 1-strain and 2-strain models in S22 Table). Conversely, in Madina, both 1-strain and 2-strain models

Table 2. (A)Average predictions [Simple average of Mean Absolute Errors (MAE)] over all forecasts of the three 2-strain models and their different combinations for the Riyadh province. (B)Estimated values of the Basic reproduction number (R_0), the Hospital reproduction number (R_H), and the Community reproduction number (R_C)for the three provinces of Saudi Arabia using best model (two strain). The best two strain MERS model is with saturated incidence. The data are given as Mean (95% CI). *The MAE for the three models and their combinations during point prediction of peak week and peak incidence were calculated up-to the peak of the prediction season (11th Week) of the Riyadh province.

A Observed values (Data)	Peak week* (weeks)	Peak maximum* (cases)	Season totals (cases)
	11	**45**	**230**
Individual model forecasts			
M1	22.8 [19.5]	18.4 [32.94]	478.80 [69.33]
M2	28.7 [19.7]	16.5 [26.25]	216.60 [75.87]
M3	22.1 [11.6]	19.2 [24.83]	222.12 [55.62]
M1 with Superspreaders	44.1 [34.7]	68.9 [32.4]	533.71 [194.5]
Average model forecasts			
M1-M2	7.3 [12.1]	42.67 [18.06]	299.73 [69.92]
M1-M3	3.4 [9.5]	37.63 [22.19]	296.18 [68.31]
M2-M3	2.6 [9.4]	53.37 [21.74]	270.47 [42.79]
M1-M2-M3	7.7 [9.6]	39.37 [17.21]	306.90 [77.41]
B Provinces	R0 [Mean (95% CI)]	RH [Mean (95% CI)]	RC [Mean (95% CI)]
Riyadh	2.0706 [2.0629–2.0763]	2.0508 [2.0442–2.0543]	0.5657 [0.5587–0.5709]
Macca	4.5716 [2.8781–6.5899]	2.7239 [0.4281–4.9401]	2.0977 [0.1256–5.7307]
Madina	5.0661 [2.5264–9.3814]	4.7808 [0.7408–9.3132]	1.6506 [0.2116–2.9661]

https://doi.org/10.1371/journal.pntd.0008065.t002

with SAT incidence provide a similar performance in predicting the three targets (e.g. MAE for peak week 16.7 in comparison to 14.5, for peak maximum of 3.33 compared to 3.6 and for season totals of 5.87 against 9.33; see S22 and S23 Tables). The latter may likely represent the best choice of models to form the basis of a future early-warning system for MERS-CoV prediction in the region.

The best model, selected on the basis of its capacity to derive skillful predictions, is the model with the SAT incidence function. We used this model to estimate the basic reproduction number, R_0, the community reproduction number, R_C, and the hospital reproduction number, R_H, for the whole period of data available in those three provinces (Table 2B and S20 Table). In all three provinces, R_0 is estimated to be always greater than unity. In all three provinces, R_H is found out to be larger than R_C. This implies, MERS-CoV transmission triggered from the hospital setting (see Table 2B). These estimates agree with some previous values reported in the literature[4,17–18], while being a result well supported by other R_0 estimates [29–31, 33]. However, previous modeling attempts to model Saudi Arabia MERS-CoV clinical incidence used only a 1-strain model with BL transmission[4]. In our case, versions of R_0 were also estimated from our BL 1-strain model in those same three provinces (see S21 Table) and they are in good agreement with the previous values provided by Chowell et al.[4]. At the same time, though, 1-strain model show less predictive capacity than their similar two-strain counterparts. To further verify the robustness of these estimates, the temporal evolution of R_0, R_C, and R_H are displayed for different time intervals in the three provinces (S1–S4 Figs). Considering the best model configurations, we additionally computed the temporal evolution of R_0, R_C, and R_H in the three provinces. Temporal changes in R_0 (S1 Fig) indicate that in most of the predicted weeks, R_0 stays well above the epidemic threshold ($R_0 = 1$). This fact is well established from the temporal evolution of R_C, and R_H in those three provinces (S1 and S2 Figs).

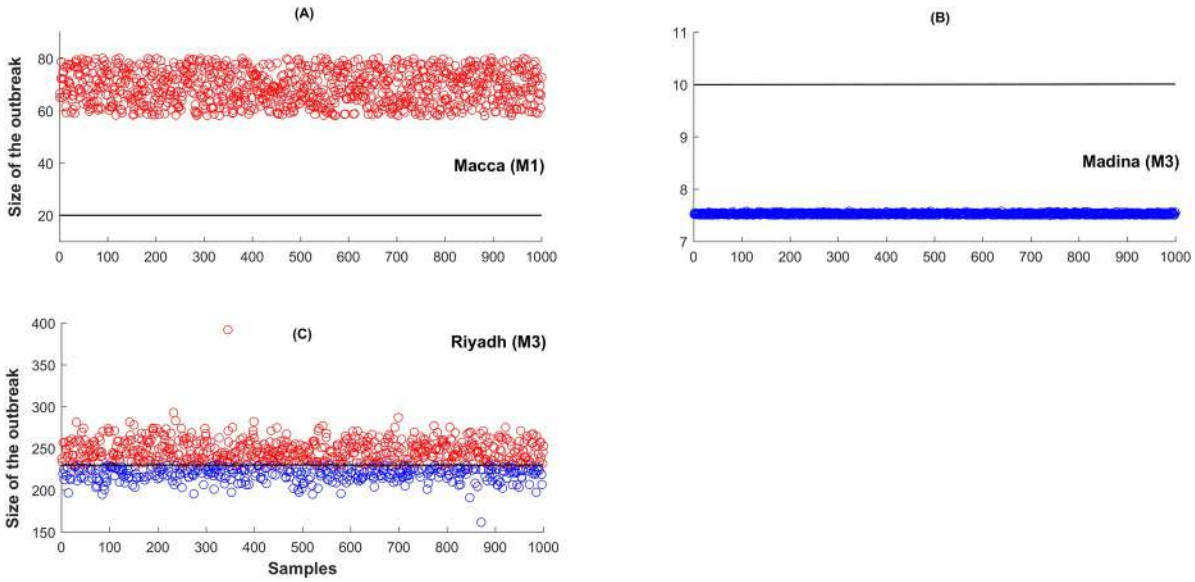

Fig 6. Out-of-fit prediction of large outbreaks in Macca, Madina and Riyadh in July 2016 to July 2017. Large outbreak size (red circles) are defined as those samples which exceeds previous year (July 2015 to July 2016) total season cases. Blue circles denote those samples that fall below previous year total cases. The black line denotes total cases during July 2015 to July 2016 of the data. M1: two strain model with bilinear incidence, M3: two strain model with saturated incidence.

https://doi.org/10.1371/journal.pntd.0008065.g006

As the basis for an operational EWS for the region, we predicted the total number of cases in the out-of-fit interval covering July 2016 to July 2017. We used the best individual model for the three provinces among all 2-strain and single strain models developed. Figs 6 and 7 and Table 3 clearly indicate the 2016–2017 season might be ripe for a larger outbreak in Macca and Riyadh. Instead, in Madina the likelihood of suffering a larger outbreak is very low (Fig 6 and Table 3). Fig 7 displays the single-strain model fitting to new MERS-CoV cases. Here M1 refers to the single strain model with BL force of infection, M2 to the single strain model with non-monotone incidence, and M3 to the single strain model with saturated incidence. Solid black curve represents model solution and yellow region denotes 95% confidence interval for predictions. Simulations for both Macca and Riyadh reflect quite appropriately the dynamics displayed in observations (Fig 7). Fig 8 shows All-season's predictions for the three consecutive years from July 6, 2013 to June 28, 2016, with each interval of 52 weeks fitted shown in panels S1-S3.

According to WHO reports, 249 MERS-CoV cases including 75 deaths (CFR 30%) were reported from Saudi Arabia between July 2016 and July 2017[44]. In the aforementioned period, at least 108 new cases[44] were reported from Riyadh province and at least 5 cases were reported from Madina. These values indicate that a larger epidemic did not occur in the last season (2016–2017), the risk for a larger one in the coming seasons still remains high.

Conclusions

Up to July 2018, 2237 new cases were reported, with 1861 only in KSA and 793 deaths[45] (CFR 35.5%). This is an alarming situation as previous predictions on MERS-CoV had instead suggested that MERS-CoV might not sustain as an epidemic in the Arabian Peninsula. The WHO report[44] suggests that MERS-CoV is still a relatively rare disease about which the medical personnel in health-care facilities have low awareness. Globally, MERS-CoV

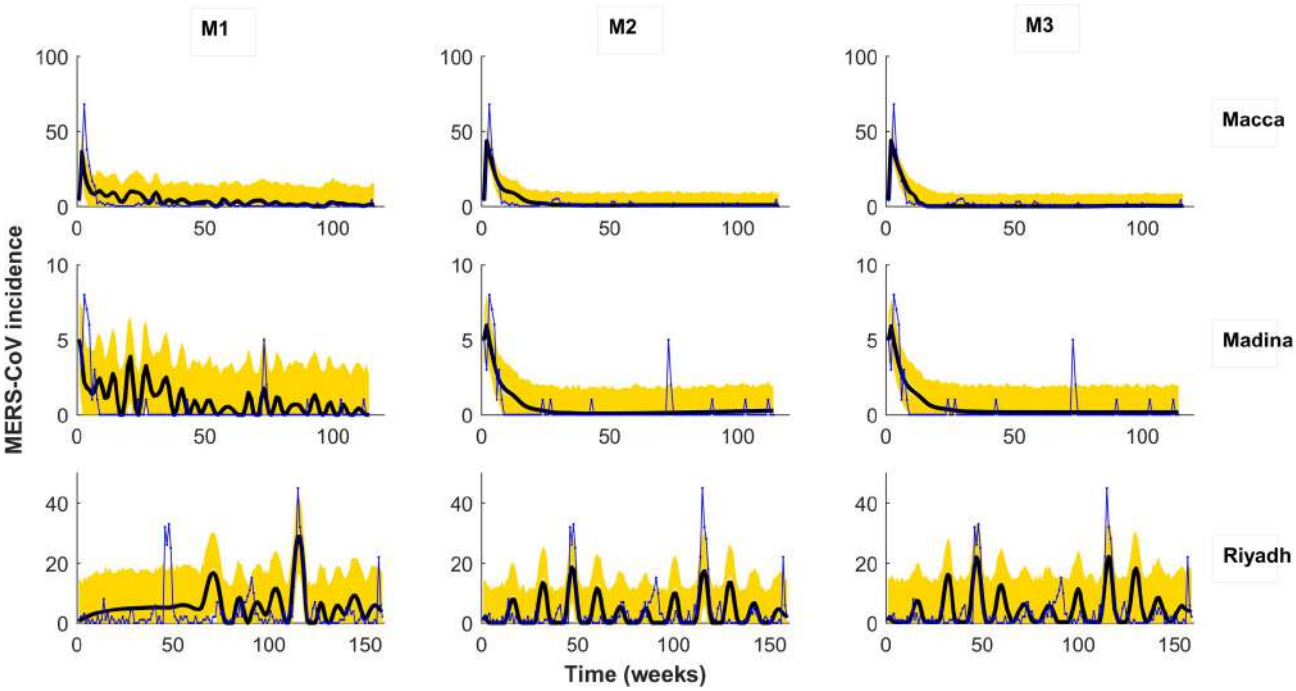

Fig 7. Single-strain model fitting to new MERS-CoV cases. Here M1: single strain model with BL force of infection, M2: single strain model with non-monotone incidence, and M3: single strain model with saturated incidence. Solid black curve represents model solution and yellow region denotes 95% confidence interval for predictions.

https://doi.org/10.1371/journal.pntd.0008065.g007

awareness is limited and because symptoms of MERS-CoV infection are non-specific, initial cases can be sometimes easily missed. With improved compliance in infection prevention and control, namely by stricter adherence to the standard precautions at all times, human-to-human transmission in health-care facilities can be reduced and even possibly eliminated with additional use of transmission-based precautions. In that regard, predictive mathematical models can help strengthen our understanding of both MERS-CoV transmission and control.

In this study, we addressed the capacity of predictive mathematical models based on two-strain MERS-CoV configurations having different transmission functions. The models differed from each other in their force of infection and in how they cope with heterogeneity in transmission. Estimates of transmission rates suggest that community and hospital transmission are dominant in the case of 2-strain models in Riyadh, Macca and Madina. The majority of the 2-strain models suggest that MERS-CoV transmission is dominated by community and hospital human-human transmissions, a fact that reflects the actual transmission scenario in Saudi Arabia [2–4]. Estimates of the parameter that measures transmission diversity between the two strains in the three provinces suggest that two strains are only active in Riyadh. This opposite trend in Riyadh in comparison to the other two provinces may be due to the fact that Riyadh is

Table 3. Hindcast prediction of season total MERS-CoV cases for July 2016 to July 2017 and probability of large outbreak. Prediction based upon the best two-strain model (in terms of season totals forecast) for the three provinces of the Saudi-Arabia.

Two strain models	MERS-CoV cases for July 2015 –July 2016	Predicted cases of MERS-CoV for the period July 2016 –July 2017 (Mean (95% CI))	Probability of larger outbreak ((No. of samples above 2015/2016 cases)/(total samples))
Riyadh (M3)	230	248.1724 (213.7383–268.26)	0.7150
Macca (M1)	20	69.0813(59.7604–78.9765)	1
Madina (M3)	10	7.5268 (7.5087–7.5598)	0

https://doi.org/10.1371/journal.pntd.0008065.t003

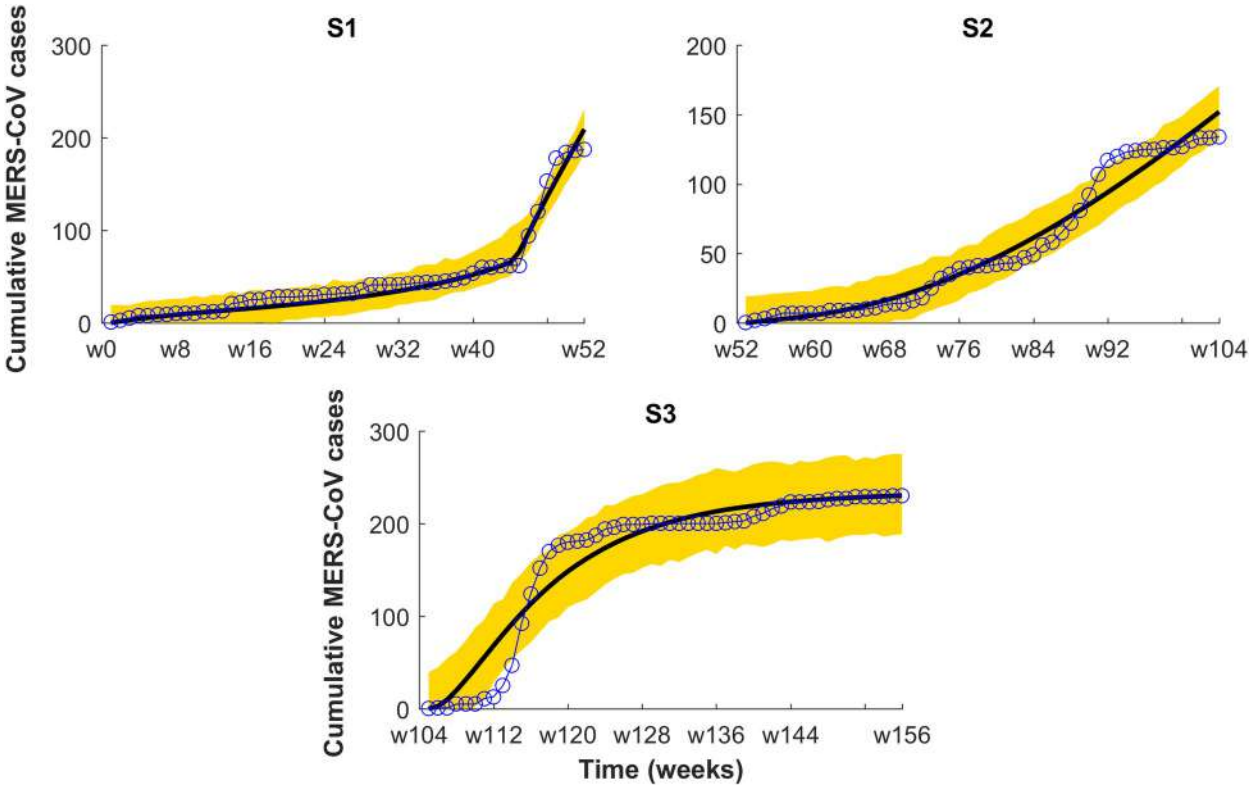

Fig 8. Season-wise model fitting to cumulative cases of Riyadh from July 6, 2013 to June 28, 2016. (Model fitted is a 2-strain model with saturated incidence. One year appears in each panel S1 to S3(S1 = S2 = S3 = 52 weeks). Line and circle line refers to observations and 95% confidence interval for cumulative predictions denoted by the yellow region.

https://doi.org/10.1371/journal.pntd.0008065.g008

the capital city with good large health care facilities and a majority of the MERS-CoV patients in Saudi Arabia come to Riyadh for treatment[2]. These patients may therefore carry different MERS strains, ultimately leading to multiple strains being presently co-circulating in Riyadh. Similarly, Cotten et al.[37] found that ancestors of most of the viral clades originated from Riyadh.

We compared among the 2-strain models according to their predictive performance with regard to three targets (i.e. peak week, peak maximum and season totals). Our results suggest that among the three 2-strain models, the model with SAT incidence provides consistently skillful predictions and may be used to date as the best predictive model for MERS-CoV in Riyadh. Riyadh iswhere most of the MERS-CoV cases occur, while for the provinces of Macca and Madina, with lower reported MERS cases, it is difficult to determine the best model among the three 2-strain models. This fact justifies our earlier finding that in Riyadh two different strains are currently active and therefore the performance of the 2-strain models is better there. As per our results for Macca and Madina, only one dominant strain is active in those provinces. Therefore, predictions based on single strain models are there more appropriate. Our results also suggest that among the single strain models, those with SAT incidence always accurately predict the three targets for these two provinces. Thus, a dynamical MERS model considering this crowding effect is the most appropriate configuration to cope with the nature of MERS-CoV transmission.

We estimated R_0 using the best 2-strain model in Riyadh and estimates are in good agreement with the findings of Majumdar et al. [28].The finding that R_0 is most of the time above 1

(S1 Fig) is well supported by some previous estimates in literature[28–30,32]. Lower contribution of community transmission in R_0 (See Table 2B) in Riyadh and Macca suggests that MERS-CoV transmission is triggered from hospital settings in those provinces. Most interestingly, in some forecasted periods, R_0 attains large values, a fact that denotes that a rapid propagation among the susceptible population is indeed possible. More worrisome is the range of values into which R_0 moves, most of the time above 1 and below 2,5, a fact that makes it a dangerous infection in terms of silent and constant potential population spread. Community reproduction number R_C well above unity (see S4 Fig) in most of the predictive weeks indicate that in a near future a large outbreak may be possible in those provinces. Out-of-fit predictions for the next season totals suggest that there is a high possibility of larger outbreaks in Macca and Riyadh. However, our results instead indicate that there is a very low possibility of larger outbreaks in Madina. The fact that this outbreak did not happen in 2017–2018 does not preclude what may occur in the forthcoming seasons. Under such a scenario, authorities and international health agencies should prepare and actively work towards the prompt implementation of cheap albeit efficient computational platforms ready to assist in the simulation of how a potential outbreak might evolve in the region. More so, given the high probability that another large MERS-CoV outbreak occurs in the Arabian Peninsula or nearby countries. Migration may also play a major role for increased transmission in the provinces of Saudi Arabia and this feature should be properly accounted for in future model configurations. In summary, our findings suggest that in a majority of provinces a single MERS-CoV strain is currently active, conversely to the situation in Riyadh. However, in the near future, it is also possible that more general MERS-CoV transmission occurs from multiple strains in other provinces of Saudi Arabia.

Supporting information

S1 Table. Estimated parameters for Model-(A) with bilinear incidence for the Riyadh province.
(DOCX)

S2 Table. Estimated parameters for Model-(A) with non-monotone incidence for the Riyadh province.
(DOCX)

S3 Table. Estimated parameters for Model-(A) with saturated incidence for the Riyadh province.
(DOCX)

S4 Table. Estimated parameters for Model-(A) with bilinear incidence for the Mecca province.
(DOCX)

S5 Table. Estimated parameters for Model-(A) with non-monotone incidence for the Mecca province.
(DOCX)

S6 Table. Estimated parameters for Model-(A) with Saturated incidence for the Mecca province.
(DOCX)

S7 Table. Estimated parameters for Model-(A) with bilinear incidence for the Madina province.
(DOCX)

S8 Table. Estimated parameters for Model-(A) with non-monotone incidence for the Madina province.
(DOCX)

S9 Table. Estimated parameters for Model-(A) with saturated incidence for the Madina province.
(DOCX)

S10 Table. Estimated parameters for the Model (B) with bilinear incidence for the Riyadh province.
(DOCX)

S11 Table. Estimated parameters for the Model (B) with non-monotone incidence for the Riyadh province.
(DOCX)

S12 Table. Estimated parameters for the Model (B) with saturated incidence for the Riyadh province.
(DOCX)

S13 Table. Estimated parameters for the Model (B) with bilinear incidence for the Macca province.
(DOCX)

S14 Table. Estimated parameters for the Model (B) with non-monotone incidence for the Macca province.
(DOCX)

S15 Table. Estimated parameters for the Model (B) with saturated incidence for the Macca province.
(DOCX)

S16 Table. Estimated parameters for the Model (B) with bilinear incidence for the Madina province.
(DOCX)

S17 Table. Estimated parameters for the Model (B) with non-monotone incidence for the Madina province.
(DOCX)

S18 Table. Estimated parameters for the Model (B) with saturated incidence for the Madina province.
(DOCX)

S19 Table. Multi-model inference quantities (AIC and BIC) for three two-strain and single-strain models. Model with smallest AIC and BIC value are given in bold.
(DOCX)

S20 Table. Estimated values of the Basic reproduction number (R0), the Hospital reproduction number (RH), and the Community reproduction number (RC), for the three provinces of Saudi Arabia for the two strain Model-1 and Model-2 (Equation (A) with bilinear incidence and non-monotone incidence). The data is given in the format (Mean [95%CI]).
(DOCX)

S21 Table. Comparison of estimated values of the Basic reproduction number (R0), the Hospital reproduction number (RH), and the Community reproduction number (RC), for

the three provinces of Saudi Arabia for the single strain Model-1, Model-2 and Model-3 (Equation (B) with bilinear, non-monotone and saturated incidence). The data is given in the format (Mean [95%CI]).
(DOCX)

S22 Table. Average predictions [Simple average of Mean Absolute Errors (MAE)] obtained over all the prediction weeks using Model -(A) with different incidence functions. Model -1 represents Model-(A) with bilinear incidence function. Model -2 represents Model-(A) with non-monotone incidence and Model -3 represents Model -(A) with saturated incidence.
(DOCX)

S23 Table. Aver.age predictions [Simple average of Mean Absolute Errors (MAE)] obtained over all the prediction weeks using a single-strain Model—(B) with different incidence functions. Model -1 represents Model-(B) with bilinear incidence function. Model -2 represents Model-(B) with non-monotone incidence and Model-3 represents Model-(B) with saturated incidence.
(DOCX)

S24 Table. Estimated parameters for Model-(A1) for Riyadh.
(DOCX)

S25 Table. Estimated parameters for Model-(A1) for Macca.
(DOCX)

S26 Table. Estimated parameters for Model-(A1) for Madina.
(DOCX)

S27 Table. Estimated parameters for the Model (B1) for Riyadh.
(DOCX)

S28 Table. Estimated parameters for the Model (B1) for Macca.
(DOCX)

S29 Table. Estimated parameters for the Model (B1) for Madina.
(DOCX)

S1 Fig. Temporal Evolution of R0 using the best predicted 2-strain model (Saturated incidence) in three provinces; Riyadh, Macca and Madina. R0 is estimated over different forecast weeks (0, 4, 8, . . ., 48).
(DOCX)

S2 Fig. Temporal Evolution of Hospital reproduction number (RH) using the best predicted 2-strain model (Saturated incidence) in three provinces; Riyadh, Macca and Madina. RH is estimated over different forecast weeks (0, 4, 8, . . ., 48). Dotted line represents the threshold of the epidemic potential (RH = 1).
(DOCX)

S3 Fig. Temporal Evolution of Community reproduction number (RC) using the best predicted 2-strain model (Saturated incidence) in three provinces; Riyadh, Macca and Madina. RC is estimated over different forecast weeks (0, 4, 8, . . ., 48).
(DOCX)

S4 Fig. Model simulations fitted to accumulated MERS-CoV clinical cases in Macca, Madina and Riyadh.
(DOCX)

Acknowledgments

The authors thank Joseph Boyard-Micheau for assistance with Fig 1 drawing.

Author Contributions

Conceptualization: Tridip Sardar, Xavier Rodó, Joydev Chattopadhyay.

Data curation: Tridip Sardar, Indrajit Ghosh, Joydev Chattopadhyay.

Formal analysis: Tridip Sardar, Indrajit Ghosh, Xavier Rodó.

Investigation: Tridip Sardar, Xavier Rodó, Joydev Chattopadhyay.

Methodology: Tridip Sardar, Indrajit Ghosh, Xavier Rodó, Joydev Chattopadhyay.

Software: Indrajit Ghosh.

Supervision: Xavier Rodó.

Validation: Tridip Sardar, Indrajit Ghosh, Xavier Rodó.

Writing – original draft: Tridip Sardar, Xavier Rodó, Joydev Chattopadhyay.

Writing – review & editing: Tridip Sardar, Indrajit Ghosh, Xavier Rodó, Joydev Chattopadhyay.

References

1. Sabir J.S.M. et al.Co-circulation of three camel coronavirus species and recombination of MERS-CoVs in Saudi Arabia. Science 351, 81–84 (2016). https://doi.org/10.1126/science.aac8608 PMID: 26678874
2. Ministry of Health (Saudi Arabia), Middle East Respiratory Syndrome Coronavirus (MERS-CoV); http://www.moh.gov.sa/en/CCC/PressReleases/Pages/default.aspx?PageIndex=1(2017).
3. World Health Organization (WHO), East Respiratory Syndrome Coronavirus (MERS-CoV)—Saudi Arabia; http://www.who.int/csr/don/06-july-2017-mers-saudi-arabia/en/ (2017).
4. Chowell G., Blumberg S., Simonsen L., Miller M.A. &Viboud C. Synthesizing data and models for the spread of MERS-CoV, 2013: key role of index cases and hospital transmission. Epidemics 9, 40–51 (2014). https://doi.org/10.1016/j.epidem.2014.09.011 PMID: 25480133
5. Zaki A.M., Van Boheemen S., Bestebroer T.M., Osterhaus A.D. &Fouchier R.A. Isolation of a novel coronavirus from a man with pneumonia in Saudi Arabia. N. Engl. J. Med. 367, 1814–1820 (2012). https://doi.org/10.1056/NEJMoa1211721 PMID: 23075143
6. Lee S.S. & Wong N.S. Probable transmission chains of Middle East respiratory syndrome coronavirus and the multiple generations of secondary infection in South Korea. Int. J. Infect. Dis. 38, 65–67 (2015). https://doi.org/10.1016/j.ijid.2015.07.014 PMID: 26216766
7. Omrani A.S., Al-Tawfiq J.A. &Memish Z.A. Middle East respiratory syndrome coronavirus (MERS-CoV): animal to human interaction. Pathog. Glob. Health 109(8), 354–362 (2015). https://doi.org/10.1080/20477724.2015.1122852 PMID: 26924345
8. Hemida M.G. et al. Lack of Middle East respiratory syndrome coronavirus transmission from infected camels. Emerg. Infect. Diseases 21(4), 699 (2015).
9. Cotten M. et al. Transmission and evolution of the Middle East respiratory syndrome coronavirus in Saudi Arabia: a descriptive genomic study. The Lancet 382(9909),1993–2002 (2013).
10. Lingshu W. et al. Evaluation of candidate vaccine approaches for MERS-CoV. Nat. Commun. 6(7712), (2015).
11. Myers M.F., Rogers D.J., Cox J., Flahault A. & Hay S.I. Forecasting disease risk for increased epidemic preparedness in public health. Adv.Parasitol. 47, 309–330 (2000). https://doi.org/10.1016/s0065-308x(00)47013-2 PMID: 10997211
12. Shaman J., Karspeck A., Yang W., Tamerius J. &Lipsitch M. Real-time influenza forecasts during the 2012–2013 season. Nat.Commun. 4, 2837 (2013). https://doi.org/10.1038/ncomms3837 PMID: 24302074

13. Biggerstaff M. et al. Results from the centers for disease control and prevention's predict the 2013–2014 Influenza Season Challenge. BMC Infect. Dis. 16(1), 357 (2016).

14. Shaman J. &Karspeck, A. Forecasting seasonal outbreaks of influenza. Proc. Natl. Acad. Sci. USA 109 (50), 20425–20430 (2012). https://doi.org/10.1073/pnas.1208772109 PMID: 23184969

15. Yamana T.K., Kandula S. & Shaman J. Superensemble forecasts of dengue outbreaks. J. R. Soc. Interface 13(123), 20160410 (2016). https://doi.org/10.1098/rsif.2016.0410 PMID: 27733698

16. Ray E.L. & Reich N.G. Prediction of infectious disease epidemics via weighted density ensembles. PLoSComput. Biol. 14(2), e1005910 (2018).

17. Breban R., Riou J. &Fontanet A. Interhuman transmissibility of Middle East respiratory syndrome coronavirus: estimation of pandemic risk. The Lancet 382(9893), 694–699 (2013).

18. Cauchemez S. et al. Unraveling the drivers of MERS-CoV transmission. Proc. Natl. Acad. Sci. USA 113(32), 9081–9086 (2016). https://doi.org/10.1073/pnas.1519235113 PMID: 27457935

19. Zumla A., Hui D.S. & Perlman S. Middle East respiratory syndrome. The Lancet 386(9997), 995–1007 (2015).

20. Muth D. et al. Infectious Middle East respiratory syndrome coronavirus excretion and serotype variability based on live virus isolates from patients in Saudi Arabia. J. Clin. Microbiol. 53(9), 2951–2955 (2015). https://doi.org/10.1128/JCM.01368-15 PMID: 26157150

21. Capasso V. &Serio, G. A generalization of the Kermack-McKendrick deterministic epidemic model. Math.Biosci. 42(1–2), 43–61 (1978).

22. Wang W. Epidemic models with nonlinear infection forces. Math.Biosci. Eng. 3(1), 267–279 (2006).

23. Xiao D. &Ruan, S. Global analysis of an epidemic model with nonmonotone incidence rate. Math.Biosci. 208(2), 419–29 (2007). https://doi.org/10.1016/j.mbs.2006.09.025 PMID: 17303186

24. Life expectancy, Saudi Arabia; http://countryeconomy.com/demography/ (2016).

25. Lessler J. et al. Incubation periods of acute respiratory viral infections: a systematic review. Lancet Infect. Dis. 9(5), 291–300 (2009). https://doi.org/10.1016/S1473-3099(09)70069-6 PMID: 19393959

26. Assiri A. et al. Hospital outbreak of Middle East respiratory syndrome coronavirus. N. Engl. J. Med. 2013(369), 407–16 (2013).

27. Xia Z.Q., Zhang J., Xue Y.K., Sun G.Q. &Jin Z. Modeling the transmission of Middle East respirator syndrome corona virus in the Republic of Korea. PloSOne 10(12), e0144778 (2015).

28. Majumder M.S., Rivers C., Lofgren E. &Fisman D. Estimation of MERS-coronavirus reproductive number and case fatality rate for the spring 2014 Saudi Arabia outbreak: insights from publicly available data. PLoSCurrents 6, (2014).

29. Poletto C., Colizza V. &Boëlle P.Y. Quantifying spatiotemporal heterogeneity of MERS-CoV transmission in the Middle East region: a combined modelling approach. Epidemics 15, 1–9 (2016). https://doi.org/10.1016/j.epidem.2015.12.001 PMID: 27266844

30. Nishiura H., Miyamatsu Y., Chowell G. &Saitoh M. Assessing the risk of observing multiple generations of Middle East respiratory syndrome (MERS) cases given an imported case. Eurosurveillance 20(27), 6–11 (2015).

31. Poletto C., Boëlle P.Y. &Colizza V. Risk of MERS importation and onward transmission: a systematic review and analysis of cases reported to WHO. BMC Infect.Dis. 16(1), 448 (2016). https://doi.org/10.1186/s12879-016-1787-5 PMID: 27562369

32. Hsieh Y.H. Middle East respiratory syndrome coronavirus (MERS-CoV) nosocomial outbreak in South Korea: insights from modeling. PeerJ 3, 1505 (2015).

33. Nishiura H. et al. Identifying determinants of heterogeneous transmission dynamics of the Middle East respiratory syndrome (MERS) outbreak in the Republic of Korea, 2015: a retrospective epidemiological analysis. BMJ Open 6(2), 009936 (2016).

34. Chan R.W. et al. Tropism and replication of Middle East respiratory syndrome coronavirus from dromedary camels in the human respiratory tract: an in-vitro and ex-vivo study. Lancet Respir. Med. 2(10), 813–822 (2014). https://doi.org/10.1016/S2213-2600(14)70158-4 PMID: 25174549

35. Kucharski A.J. &Althaus C. The role of superspreading in Middle East respiratory syndrome coronavirus (MERS-CoV) transmission. Eurosurveillance 20(25), 21167 (2015). https://doi.org/10.2807/1560-7917.es2015.20.25.21167 PMID: 26132768

36. Chowell G., Abdirizak F., Lee S., Lee J., Jung E., Nishiura H. &Viboud C. Transmission characteristics of MERS and SARS in the healthcare setting: a comparative study. BMC Med. 13(1), 210 (2015).

37. Cotten M. et al. Spread, circulation, and evolution of the Middle East respiratory syndrome coronavirus. MBio, 5(1), pii: e01062–13 (2014). https://doi.org/10.1128/mBio.01062-13 PMID: 24549846

38. Waters E.K. Modelling crowding effects in infectious disease transmission. B. Aust. Math. Soc. 92 (3),522–523 (2015).

39. Lloyd M. Mean crowding. J. Anim. Ecol. 1–30 (1967).

40. World Health Organization (WHO), WHO MERS-CoV Global Summary and Assessment of Risk;http://www.who.int/emergencies/mers-cov/risk-assessment-july-2017.pdf (2017).

41. Mukandavire Z.et al. Estimating the reproductive numbers for the 2008–2009 cholera outbreaks in Zimbabwe. Proc. Natl. Acad. Sci. USA 108(21), 8767–8772 (2011). https://doi.org/10.1073/pnas.1019712108 PMID: 21518855

42. Johnson L.R. et al. Phenomenological forecasting of disease incidence using heteroskedastic Gaussian processes: a dengue case study.Ann. Appl. Stat. 12(1), 27–66 (2018).

43. Haario H., Laine M., Mira A. &Saksman E. DRAM: efficient adaptive MCMC. Stat.Comput. 16(4), 339–54 (2006).

44. World Health Organization (WHO), Disease outbreak news MERS-CoV; http://www.who.int/csr/don/archive/disease/coronavirus_infections/en/ (2018).

45. World Health Organization (WHO), MERS-CoV situation; http://www.emro.who.int/pandemic-epidemic-diseases/mers-cov/mers-situation-update-july-2018.html (2018).

46. Lin Q., Chiu A.P.Y, Zhao S., & He D. Modeling the spread of Middle East respiratory syndrome coronavirus in Saudi Arabia. Stat Methods Med Res. 27(7), 1968–1978 (2018). https://doi.org/10.1177/0962280217746442 PMID: 29846148

Source details

Feedback > Compare sources >

PLoS Neglected Tropical Diseases

Open Access

Scopus coverage years: from 2007 to Present

Publisher: Public Library of Science

ISSN: 1935-2727 E-ISSN: 1935-2735

Subject area: Medicine: Public Health, Environmental and Occupational Health | Medicine: Infectious Diseases

Source type: Journal

View all documents > | Set document alert | Save to source list

CiteScore 2022
7.2

SJR 2022
1.298

SNIP 2022
1.335

CiteScore | CiteScore rank & trend | Scopus content coverage

SEE CORRECTION FOR THIS ARTICLE

An open challenge to advance probabilistic forecasting for dengue epidemics

Michael A. Johansson[a,b,1], Karyn M. Apfeldorf[c], Scott Dobson[c], Jason Devita[c], Anna L. Buczak[d], Benjamin Baugher[d], Linda J. Moniz[d], Thomas Bagley[d], Steven M. Babin[d], Erhan Guven[d], Teresa K. Yamana[e], Jeffrey Shaman[e], Terry Moschou[f], Nick Lothian[f], Aaron Lane[f], Grant Osborne[f], Gao Jiang[g], Logan C. Brooks[h], David C. Farrow[h], Sangwon Hyun[i], Ryan J. Tibshirani[h,i], Roni Rosenfeld[h], Justin Lessler[j], Nicholas G. Reich[k], Derek A. T. Cummings[l,m], Stephen A. Lauer[k], Sean M. Moore[n,o], Hannah E. Clapham[p], Rachel Lowe[q,r], Trevor C. Bailey[s], Markel García-Díez[t], Marilia Sá Carvalho[u], Xavier Rodó[r,v], Tridip Sardar[w], Richard Paul[x,y], Evan L. Ray[z], Krzysztof Sakrejda[k], Alexandria C. Brown[k], Xi Meng[k], Osonde Osoba[aa], Raffaele Vardavas[aa], David Manheim[bb], Melinda Moore[aa], Dhananjai M. Rao[cc], Travis C. Porco[dd], Sarah Ackley[dd], Fengchen Liu[dd], Lee Worden[dd], Matteo Convertino[ee], Yang Liu[ff], Abraham Reddy[ff], Eloy Ortiz[gg], Jorge Rivero[gg], Humberto Brito[gg,hh], Alicia Juarrero[gg,ii], Leah R. Johnson[jj], Robert B. Gramacy[kk], Jeremy M. Cohen[kk], Erin A. Mordecai[ll], Courtney C. Murdock[mm,nn], Jason R. Rohr[n,o], Sadie J. Ryan[m,oo,pp], Anna M. Stewart-Ibarra[qq], Daniel P. Weikel[rr], Antarpreet Jutla[ss], Rakibul Khan[ss], Marissa Poultney[ss], Rita R. Colwell[tt], Brenda Rivera-García[uu], Christopher M. Barker[vv], Jesse E. Bell[ww], Matthew Biggerstaff[xx], David Swerdlow[xx], Luis Mier-y-Teran-Romero[a,j], Brett M. Forshey[yy], Juli Trtanj[zz], Jason Asher[aaa], Matt Clay[aaa], Harold S. Margolis[a], Andrew M. Hebbeler[bbb,ccc], Dylan George[ccc,ddd], and Jean-Paul Chretien[ccc,eee]

Edited by Simon A. Levin, Princeton University, Princeton, NJ, and approved September 30, 2019 (received for review June 18, 2019)

A wide range of research has promised new tools for forecasting infectious disease dynamics, but little of that research is currently being applied in practice, because tools do not address key public health needs, do not produce probabilistic forecasts, have not been evaluated on external data, or do not provide sufficient forecast skill to be useful. We developed an open collaborative forecasting challenge to assess probabilistic forecasts for seasonal epidemics of dengue, a major global public health problem. Sixteen teams used a variety of methods and data to generate forecasts for 3 epidemiological targets (peak incidence, the week of the peak, and total incidence) over 8 dengue seasons in Iquitos, Peru and San Juan, Puerto Rico. Forecast skill was highly variable across teams and targets. While numerous forecasts showed high skill for midseason situational awareness, early season skill was low, and skill was generally lowest for high incidence seasons, those for which forecasts would be most valuable. A comparison of modeling approaches revealed that average forecast skill was lower for models including biologically meaningful data and mechanisms and that both multimodel and multiteam ensemble forecasts consistently outperformed individual model forecasts. Leveraging these insights, data, and the forecasting framework will be critical to improve forecast skill and the application of forecasts in real time for epidemic preparedness and response. Moreover, key components of this project—integration with public health needs, a common forecasting framework, shared and standardized data, and open participation—can help advance infectious disease forecasting beyond dengue.

forecast | dengue | epidemic | Peru | Puerto Rico

Infectious diseases pose a continuing and dynamic threat globally. The mosquito-transmitted dengue viruses, for example, are endemic throughout the tropical regions of the world and infect millions of people each year (1). In endemic areas, dengue incidence has a clear seasonal pattern but also, exhibits strong interannual variation, with major epidemics occurring every few years (2, 3). In San Juan, Puerto Rico, hundreds of confirmed cases may be reported over an entire interepidemic season, while hundreds of cases can be reported every week during the peak of epidemics (Fig. 1). Timely and effective large-scale interventions are needed to reduce the serious impacts of dengue epidemics on health, healthcare systems, and economies (4, 5). Unfortunately, these epidemics have proven difficult to predict, hindering efforts to prevent and control their impact.

Research on the determinants of dengue epidemics has included both statistical models incorporating historical incidence and climatological determinants (6) and dynamical,

Significance

Forecasts routinely provide critical information for dangerous weather events but not yet for epidemics. Researchers develop computational models that can be used for infectious disease forecasting, but forecasts have not been broadly compared or tested. We collaboratively compared forecasts from 16 teams for 8 y of dengue epidemics in Peru and Puerto Rico. The comparison highlighted components that forecasts did well (e.g., situational awareness late in the season) and those that need more work (e.g., early season forecasts). It also identified key facets to improve forecasts, including using multiple model ensemble approaches to improve overall forecast skill. Future infectious disease forecasting work can build on these findings and this framework to improve the skill and utility of forecasts.

Author contributions: M.A.J., B.R.-G., C.M.B., M.B., D.S., L.M.-y.T.-R., B.M.F., J.T., J.A., M.C., H.S.M., A.M.H., D.G., and J.-P.C. designed research; M.A.J., K.M.A., S.D., J.D., A.L.B., B.B., L.J.M., S.M.B., E.G., T.K.Y., J.S., T.M., N.L., A.L., G.O., G.J., L.C.B., D.C.F., S.H., R.J.T., R.R., J.L., N.G.R., D.A.T.C., S.A.L., S.M.M., H.E.C., R.L., T.C.B., M.G.-D., M.S.C., X.R., T.S., R.P., E.L.R., K.S., A.C.B., X.M., O.O., R.V., D.M., M.M., D.M.R., T.C.P., S.A., F.L., L.W., M.C., Y.L., A.R., E.O., J.R., H.B., A. Juarrero, L.R.J., R.B.G., J.M.C., E.A.M., C.C.M., J.R.R, S.J.R., A.M.S.-I., D.P.W., A. Jutla, R.K., M.P., and R.R.C. performed research; M.A.J., K.M.A., S.D., J.D., A.L.B., B.B., L.J.M., T.B., S.M.B., E.G., T.K.Y., J.S., T.M., N.L., A.L., G.O., G.J., L.C.B., D.C.F., S.H., R.J.T., R.R., J.L., N.G.R., D.A.T.C., S.A.L., S.M.M., H.E.C., R.L., T.C.B., M.G.-D., M.S.C., X.R., T.S., R.P., E.L.R., K.S., A.C.B., X.M., O.O., R.V., D.M., M.M., D.M.R., T.C.P., S.A., F.L., L.W., M.C., Y.L., A.R., E.O., J.R., H.B., A. Juarrero, L.R.J., R.B.G., J.M.C., E.A.M., C.C.M., J.R.R., S.J.R., A.M.S.-I., D.P.W., A. Jutla, R.K., M.P., R.R.C., and J.E.B. contributed new reagents/analytic tools; M.A.J., T.B., L.M.-y.-T.-R., B.M.F., J.A., and M.C. analyzed data; and M.A.J., K.M.A., A.L.B., T.K.Y., T.M., L.C.B., J.L., R.L., X.R., E.L.R., O.O., D.M.R., T.C.P., M.C., E.O., L.R.J., A. Jutla, B.R.-G., C.M.B., J.E.B., M.B., D.S., L.M.-y.-T.-R., B.M.F., J.T., J.A., M.C., H.S.M., A.M.H., D.G., and J.-P.C. wrote the paper.

The authors declare no competing interest.

This article is a PNAS Direct Submission.

Data deposition: The data are available at https://github.com/cdcepi/dengue-forecasting-project-2015 (DOI: 10.5281/zenodo.3519270).

[1]To whom correspondence may be addressed. Email: mjohansson@cdc.gov.

This article contains supporting information online at https://www.pnas.org/lookup/suppl/doi:10.1073/pnas.1909865116/-/DCSupplemental.

First published November 11, 2019.

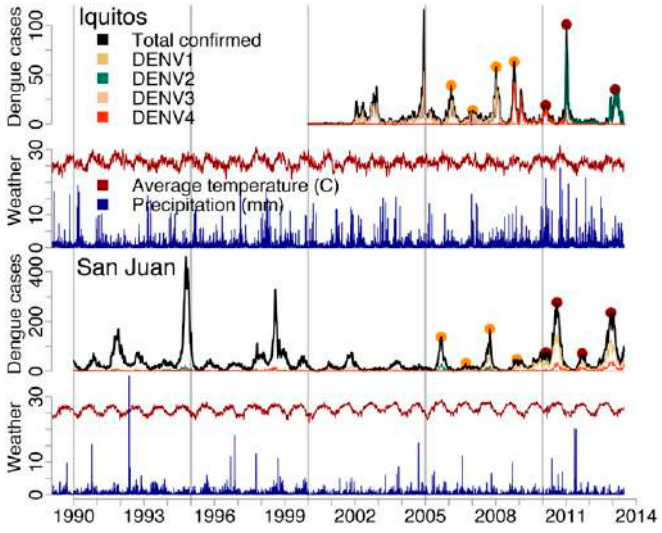

Fig. 1. Dengue and climate data for Iquitos, Peru and San Juan, Puerto Rico. The black and colored lines for dengue cases indicate the total and virus-specific weekly number of laboratory-confirmed cases. The yellow and red points indicate the peaks in the training and testing datasets, respectively. The climate data show the weekly rainfall (blue) and mean temperature (red) for Iquitos and San Juan, respectively, from the National Centers for Environmental Prediction Climate Forecast System Reanalysis.

mathematical models aimed at identifying both intrinsic and extrinsic drivers (7, 8). This body of research led to important insights, such as the putative influence of various climatological components (9), antibody-dependent enhancement (10, 11), serotype-specific cross-protection (12, 13), and spatial heterogeneity (14) on transmission dynamics.

Despite this substantial body of research, there are currently no operational dengue forecasts with documented prospective forecast skill, and challenges exist for both forecast development and assessment. First, the objectives of published forecasts and outcome metrics vary and are often not tied to specific public health needs. Second, there have been few accessible dengue datasets for forecasting research. Third, differences in data and metrics significantly complicate the comparison of forecasts from different research groups. Fourth, existing evaluations generally assess only point prediction accuracy, ignoring information on forecast confidence. Fifth, evaluations rarely incorporate out-of-sample testing (testing on either reserved or prospective data that were not used to develop and fit the models), the most important test for a forecasting model.

The need to systematically evaluate forecasting tools is widely recognized (15) and motivated multiple US government agencies within the Pandemic Prediction and Forecasting Science and Technology Working Group, coordinated by the White House Office of Science and Technology Policy, to launch an open forecasting challenge in 2015, the Dengue Forecasting Project. First, we worked with epidemiologists from dengue-endemic regions to identify 3 important epidemic forecasting targets: 1) the intensity of the epidemic peak (peak incidence), 2) the timing of that peak (peak week), and 3) the total number of cases expected over the duration of the season (season incidence). Reliable forecasts of these outcomes could improve the allocation of resources for primary prevention (e.g., risk communication, vector control) or secondary prevention (e.g., planning medical staffing, preparing triage units) (16). Additionally, because out-of-sample prediction is an important test of mechanistic causality, forecasts could also provide insight on key drivers of dengue epidemics and therefore, the expected impacts of interventions. Second, we identified 2 dengue-endemic cities, Iquitos, Peru (17, 18) and San Juan, Puerto Rico (19), with serotype-specific incidence data and local climate data that could be released publicly for enough seasons (13 and 23, respectively) to allow training of models and forecasting across multiple seasons (Fig. 1). Third, we established an a priori forecasting framework, including a specific protocol for submitting and evaluating out-of-sample probabilistic forecasts made at 4-wk intervals across 4 training and 4 testing seasons for each of the 3 targets in both locations.

Results

Sixteen teams submitted binned probabilistic forecasts generated using a variety of approaches, including statistical and mechanistic models and multimodel ensembles (*SI Appendix*, Table S1). All teams used the provided dengue data, 10 (63%) used matched climate data, 2 used serotype data, and 1 used additional data on global climate (e.g., Southern Oscillation Index). Three additional models were developed for comparison: a null model (equal probability assigned to each possible outcome), a baseline statistical time series model (a seasonal autoregressive integrated moving average [SARIMA] model), and a simple ensemble (an average of the probabilities of the 16 team and baseline forecasts).

After finalizing models and submitting forecasts for 4 training seasons (2005/2006 to 2008/2009), teams received additional data and had a maximum of 2 wk to submit forecasts for the testing seasons (2009/2010 to 2012/2013). Forecasts varied widely (Fig. 2 and *SI Appendix*, Figs. S1 and S2). For example, forecasts with data up to week 12 and week 24 predicted that the peaks in the 2012/2013 season might have been among the lowest or the highest on record. Confidence also varied: some forecasts were certain of an outcome being in a particular forecast bin, while others had broad 95% prediction intervals spanning the entire range of historical values, and some assigned 0 probability to the observed outcome.

We assessed forecast skill using the logarithmic score, a proper score incorporating probabilistic accuracy and precision. High logarithmic scores indicate consistent assignment of high probability to the eventually observed outcome. Forecast skill increased as seasons progressed for most models (Fig. 3). Some submitted forecasts outperformed both the null and baseline models for early time points, with numerous models showing increased skill around the time of the observed peak (median peak weeks: 22.5 for San Juan and 28 for Iquitos). The peak incidence target for Iquitos in 2011/2012 was not scored, as no distinct peak was identifiable. Forecast calibration (e.g., assigning 70% probability to events that occurred 70% of the time) varied across teams (*SI Appendix*, Fig. S3) and was strongly associated with forecast skill (*SI Appendix*, Fig. S4).

The highest skill early season forecasts (weeks 0 to 24) for each target–location pair were submitted by Team N (University of California, San Francisco, peak week, Iquitos), Team E (VectorBiTE, peak week, San Juan) (20), Team B (Breaking Bad Bone Fever, peak incidence and total incidence, Iquitos) (21), Team G (Areté, peak incidence, San Juan), and Team J (Delphi, total incidence, San Juan) (Figs. 3 and 4 and *SI Appendix*, Table S1). Many teams outscored both the null model and for each target except peak week, the baseline model. The ensemble forecast outperformed most individual models and was the only forecast to outperform the null model for every target. Training season forecasts showed similar patterns of low early season skill and overconfidence by some models, and numerous models outperformed the baseline and null models (*SI Appendix*, Fig. S5).The top teams differed for all targets except peak week in Iquitos (Fig. 4 and *SI Appendix*, Table S2), but the ensemble forecasts outperformed the majority of individual forecasts and the null forecast for all targets for all 8 seasons.

To assess extrinsic factors that may impact forecast skill, we fitted a series of regression models to target-, location-, and season-specific variables (*SI Appendix*). Scores were higher for forecasts made later in the season (0.043 per week, 95% confidence interval

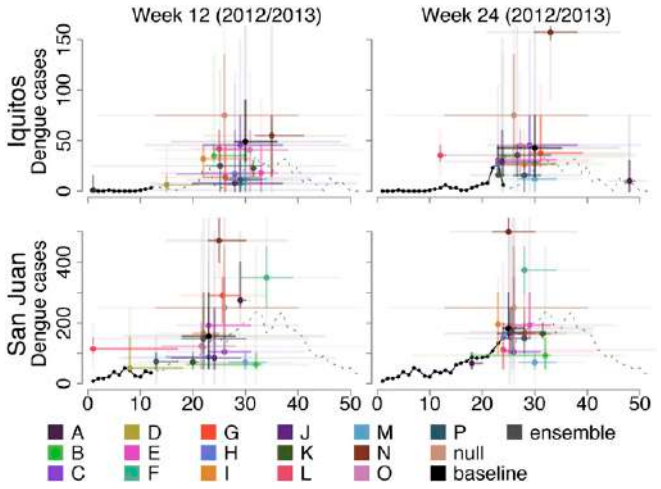

Fig. 2. Weeks 12 and 24 forecasts for the 2012/2013 dengue season in Iquitos and San Juan. The solid black lines indicate the most recent data that were available to teams to inform these forecasts, and the dashed lines indicate the data that became available later in the season. The colored points represent point estimates for each team, while the bars represent 50 and 95% prediction intervals (dark and light, respectively). Forecasts for additional time points and seasons as well as for seasonal incidence are shown in *SI Appendix*, Figs. S1 and S2, respectively.

[95% CI]: 0.039 to 0.046), seasons with lower peak incidence (0.43 per location-specific SD, 95% CI: 0.37 to 0.49), seasons with earlier peaks (0.048 per week prior to long-term location-specific mean, 95% CI: 0.040 to 0.057), San Juan (0.65, 95% CI: 0.54 to 0.76), and targets with fewer bins (peak and seasonal incidence, 0.0257 per bin, 95% CI: 0.0221 to 0.0293) (*SI Appendix*, Table S3).

Comparing high-level forecasting approaches across all targets and all 8 seasons while controlling for the differences by forecast week, season characteristics, location, and the numbers of bins (described above), we found that logarithmic scores were higher for teams using ensemble approaches (mean difference: 1.02, 95% CI: 0.91 to 1.13) (*SI Appendix*, Table S3). Forecasts from models incorporating mechanistic approaches (e.g., compartmental models or ensemble models with at least 1 mechanistic submodel) had lower logarithmic scores (−0.65, 95% CI: −0.80 to −0.49) than purely statistical approaches. Additionally, models using climate data had lower logarithmic scores (−0.14, 95% CI: −0.19 to −0.09). Relatedly, we found that forecasts using ensemble approaches tended to be better calibrated (−0.0010, 95% CI: −0.0034 to 0.0007) and that those using mechanistic approaches or climate data were less so (*SI Appendix*, Table S4). We did not compare models using serotype data or incorporating vector population dynamics, as only 2 models included serotype data (using them in different ways), and all but 1 mechanistic model included modeled vector populations (actual vector data were not available).

Discussion

Research aimed at forecasting epidemics and their impact offers tantalizing opportunities to prevent or control infectious diseases. Although many epidemic forecasting tools promise high accuracy, they have largely been fit to specific, nonpublic datasets and assessed only on historical data rather than future, unobserved outcomes. Here, we executed a multimodel assessment of out-of-sample probabilistic forecasts for key seasonal characteristics of dengue epidemics. Comparing these forecasts provides insight on current capabilities to forecast dengue, our understanding of the drivers of dengue epidemics, challenges to forecast skill, and avenues for improvement.

Good forecasts should identify possible outcomes relevant to decision makers and reliably assign probabilities to those outcomes (22). Proper scores (23, 24) of probabilistic forecasts, such as the logarithmic score used here, have distinct advantages over more common point prediction error metrics. Error only measures 1 dimension of forecast skill, the distance between the estimated and observed outcomes, and does not consider confidence, an essential characteristic for stochastic outcomes. Logarithmic scores for the submitted forecasts revealed low early season forecast skill, with many forecasts performing worse than a null forecast that assigned an equal probability to each possible outcome. Even in endemic areas with strong seasonal transmission patterns, epidemics are difficult to predict at time horizons of several months or more.

Nonetheless, several teams consistently outperformed the null model for each target–location pair, indicating that, even in early weeks, models provided some reliable information about what was likely to happen. Not surprisingly, forecasts improved substantially as seasons progressed and data accumulated. As more data are reported, the likely outcomes are reduced, and forecasting is easier (e.g., if 1,100 cases have been reported by week 40, it is impossible that the season total will be less than 1,000 and extremely unlikely that it would exceed 10,000). Despite this, some models had decreased or steady late season skill, possibly indicating that they did not fully account for data updates. Week-to-week incidence varies substantially, making peaks hard to identify in real time, and therefore, models with high midseason to late season skill may be very useful for situational awareness.

Overall scores varied by target, location, and season. Differences in target-specific scores were not associated with target-specific entropy, implying that target-specific differences were more likely due to study design than intrinsic differences in predictability. Specifically, the peak week target had more bins (52 vs. 11), and therefore, probabilities were distributed across more bins, leading to lower probabilities for the outcomes and lower scores. Higher scores for San Juan compared with Iquitos may reflect differences in dynamics, the availability of more historical data, or the location-specific bin selection. This difference was not related

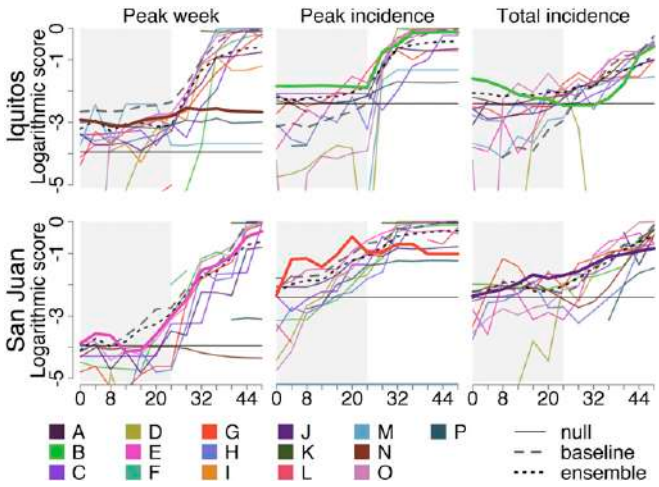

Fig. 3. Forecast skill by team, forecast week, and target in the testing seasons (2009/2010 to 2012/2013). Solid colored lines represent the scores of individual teams averaged across all testing seasons for the respective forecast week, target, and location. For each target, the top forecast for the first 24 wk (shaded) is indicated in bold (highest average early season score). The solid black lines indicate the null model (equal probability assigned to all possible outcomes), the dashed gray lines indicate the baseline model, and the dotted black lines indicate the ensemble model. Forecasts with logarithmic scores of less than −5 are not shown. Breaks in lines indicate a score of negative infinity in at least 1 of the testing seasons.

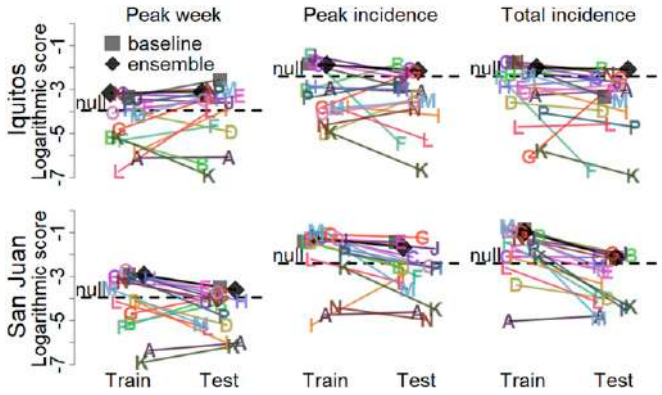

Fig. 4. Overall forecast scores for weeks 0 to 24 in the training (2005/2006 to 2008/2009) and testing (2009/2010 to 2012/2013) seasons. Each point is the average target- and location-specific log score for a model in the training (left side; light shading) and testing (right side; dark shading) seasons. The horizontal dispersion within training and testing scores is random to improve visualization. The null forecast for each target is represented by a horizontal line. Numerous forecasts assigned 0 probability to at least 1 observed outcome. Those individual forecast probabilities were changed to 0.001 before calculating the logarithmic scores.

to location-specific variability, as target-specific entropy was similar or higher for San Juan (peak week: 1.28 for Iquitos and 2.08 for San Juan; peak incidence: 1.75 and 1.73, respectively; and season incidence: 1.28 and 1.39, respectively). However, the long-term dynamics in the 2 locations were markedly different, with more recent introduction and serotype replacement in Iquitos vs. decades of hyperendemic transmission in San Juan. The effect of these differences and simply the availability of more historical data for San Juan are not distinguishable in this study. Finally, we found that forecast skill was lower for seasons with later and higher peaks. The association with later peaks may indicate a particular challenge of late seasons or a more general association with atypical peak timing rather than a late season per se, or it may simply reflect a higher proportion of forecasts being made before the peak, when there is more uncertainty. Influenza forecasts also tend to perform worse in late seasons (25). The association of low forecast skill with high incidence is also a key challenge; seasonal cycling is generally predictable, but high-incidence epidemics, the biggest challenge for public health, are the hardest to predict.

A wide variety of modeling approaches was used, including different criteria for data selection (e.g., climate data, lags), model frameworks (e.g., mechanistic, statistical), parameter assignment methods (e.g., fitting, specifying), and forecast generation procedures (e.g., model selection, combination). Because there are so many potential options for these components, the 17 models that we evaluated (teams and baseline) only represent a small subspace of all possible models. We, therefore, restricted our analysis to 3 high-level characteristics represented by multiple forecasts (climate data, a mechanistic model, or an ensemble approach), recognizing that even these findings may not be generalizable. Suitable climatic conditions are biologically necessary for dengue virus transmission, yet models including climate data had less skill than models that did not. One challenge is that climate forecasts may be more useful than historical data for dengue forecasts, but climate forecasts have their own uncertainty (26). Moreover, it is possible that better climate forecasts may not improve dengue forecasts. For example, climate may determine dengue seasonality, but models characterizing seasonality using historical dengue data alone (e.g., the baseline SARIMA model) may be able to provide equivalent information about expected future incidence (6). Incorporating additional data also increases model complexity in the form of variability in those data, parameters, and structural assumptions. Including estimated parameters or model structures that better match historical data or biological relationships may come at the expense of lower out-of-sample forecast skill.

Our finding that statistical models generally outperformed mechanistic models is another indicator of the potential downside of overly complex forecasting models. Statistical models may have performed slightly better because robust uncertainty estimates are easier to generate with standard statistical packages compared with tailored mechanistic models. For example, the relatively simple baseline SARIMA models (4 parameters for Iquitos, 5 for San Juan) were developed with a standard statistical package and generally performed well compared with more complex models, including having the best overall calibration and the highest skill forecasts for peak week. Although simple models have also performed well in other forecasting challenges (27, 28), mechanistic models should not be dismissed. Mechanistic models allow for the incorporation of biological interactions (e.g., serotype interaction, spatial heterogeneity) and are essential for estimating the impacts of potential interventions (29). Statistical models can be used to guide development of better mechanistic models, capturing key components of good forecasts, such as seasonality, short-term autocorrelation, and accurate characterization of uncertainty. Moreover, hybrid approaches such as ensemble models, including statistical and mechanistic submodels, may be able to leverage advantages of both approaches.

Ensemble approaches were used by almost half the teams (7 of 16) (20, 21, 30) and on average, had better calibration and higher forecast skill than forecasts generated from single models. Moreover, a simple ensemble of all of the forecasts was among the highest scoring forecasts for every target and time point and was the only forecast to outperform the null forecast for all targets. Despite being a simple average of many forecasts, most of which performed substantially worse on their own, the ensemble balanced uncertainty across competing models with different assumptions and parameters, improving calibration by hedging bets when submodels disagreed and consolidating them when there was agreement. This cross-model modulation of uncertainty leads to higher skill forecasts as seen here and in other challenges (25, 28) and highlights a key advantage of multimodel and multiteam forecasting: a suite of models is likely to outperform any single approach (31). It also points to an important future research area: optimization of ensembles with fitted and dynamic weights.

While these insights can drive future research, there were also key limitations. For example, 2 potentially important dengue drivers were not assessed: vector populations and dengue virus serotypes. Vector data were simply not available on a spatiotemporal scale commensurate with the dengue data used here. Because numerous studies have shown that the interactions between dengue virus serotypes and human immunity may be a critical driver of long-term dengue dynamics (32), we provided datasets, including serotype data. However, only 2 teams chose to use them: one as an indicator of recent introduction of a serotype and the other in a complex 4-strain mechanistic compartmental model. The importance of serotype data for forecasting remains an open and important question, particularly for long-term dengue-endemic areas, such as Southeast Asia, where these effects may be strongest. Datasets with such extensive historical data are rare but offer an opportunity to identify key epidemic drivers that could inform current and future surveillance strategies in areas with less comprehensive historical data. Additionally, the comparison of approaches was only among the limited set used by the teams, not a comprehensive library of approaches. Different data and models have the potential to improve forecasts, but additional evidence is needed to understand which data and relationships are most important for dengue forecasting. Those determinations will also be key to future surveillance strategies, identifying the most important data to capture.

The challenge structure also had some limitations. Forecasts were evaluated on probabilities that were binned according to prespecified bins. Because targets are on different scales, it is not clear how to objectively define these bins to enable between-target comparison. It is also unclear how closely the bins should be tied to very specific decision-making needs, such as identifying an "outbreak," a concept with a wide variety of definitions that are intrinsically dependent both on surveillance and a threshold selection algorithm (33). Binned forecasts enable more comprehensive comparison of forecasts without selection of a specific threshold and allow scaling to higher levels, such as the binary probability of incidence exceeding a particular threshold. The datasets differed in both amount of data (13 seasons for Iquitos, 23 for San Juan) and characteristics of local dengue (serotype replacement in Iquitos, hyperendemicity in San Juan). Yet, those only represent 2 locations of the many where dengue is endemic. More datasets will be needed to determine the generalizability of forecasting tools, but few datasets with this level of detail exist. To evaluate forecasts over multiple seasons, the project was designed to use retrospective data and therefore, was not truly prospective. To facilitate forecasting at 13 time points per season, some future data were shared. To assure appropriate use, all teams agreed to forecast using data exclusively from weeks prior to and including the forecast week, and testing data were only available for 2 wk and only after selection of a final model and submission of training forecasts. Another challenge posed by these retrospective datasets is that they do not represent real-time reporting with its intrinsic reporting delays, another key forecasting challenge. Short-term forecasts for seasonal influenza show promise at helping bridge this gap (25), but comparable data were not available for this challenge, and the problem is far from solved. The datasets also do not represent all infections or even all cases, as we focused on laboratory-confirmed cases. Some cases do not seek care, do not have access to care, or are misdiagnosed. This may impact forecast model inputs and outputs, as both the underlying transmission dynamics and the case burden are imperfectly captured by data on confirmed cases.

Nonetheless, this project highlights important lessons for the larger panorama of challenges to advance the research and application of epidemic forecasting for public health. First, to make forecasts relevant to decision making in outbreak responses, targets should be clearly and quantitatively defined, and they should directly address specific public health needs. To integrate forecasts into decision making, it will be vital to refine the way that forecasts are communicated and maximize their operational relevance. Second, more participation leads to more information gain both for improved forecast skill via ensembles and also, for characterizing the strengths and weakness of different modeling approaches (25, 28, 34). Opening new data, facilitating access, and presenting engaging problems can drive participation and enable this type of research. Third, forecast skill should be openly evaluated on out-of-sample data with prespecified metrics that consider uncertainty. Self-evaluation of point predictions on data that are not openly accessible does little to characterize the utility of a forecasting tool. Good forecasts should be able to 1) differentiate between possible out-of-sample outcomes and 2) accurately express confidence in those predictions. Together, these components can be the building blocks for future forecasting systems, such as those that have transformed weather and storm forecasting (35).

Dengue remains a major public health challenge, and decades of dengue research have led to little progress in prospective prediction of dengue epidemics. Here, we identified key challenges and established a framework with datasets to help advance this research specifically toward targets that would benefit public health and forecasting science. Next generation models by the participating teams and others should adopt the testing–training framework, data, and metrics to assess forecast performance using the scores of the forecasts published here as benchmarks to measure advances in forecasting skill. At the same time, it may be important to refine targets and identify new targets to maximize public health utility. Additional datasets to retrospectively and prospectively develop and validate forecasts will be critical for demonstrating forecast skill and reliability across multiple seasons (and multiple locations for broader implementation). The recent epidemics of chikungunya and Zika viruses have further complicated clinical and laboratory-based surveillance for dengue and created a more complex immunological landscape for flaviviruses, changes that create new challenges for interpreting surveillance data and forecasting. There is also a need for improved surveillance data systems to ensure that data are machine readable and available in real time to support truly prospective, real-time forecasts. Lastly, better forecasts will drive interventions, increasing the importance of better mechanistic models that can both forecast and estimate the impact of interventions. These are formidable challenges, but through probabilistic forecasting projects, such as the one reported here, the community can move this research forward, translating the research into public health tools that can transform the way that we prepare for and respond to epidemics.

Materials and Methods

Data. Weekly laboratory-confirmed and serotype-specific dengue surveillance data were provided for 2 endemic locations: Iquitos, Peru (17, 36) and San Juan, Puerto Rico (19). Data were time referenced starting with 1 January, and data from 31 December (30 December for leap years) were removed to ensure 52 wk/y. The week with the lowest average incidence over the training period was then selected as the end week for the transmission season (week 26 in Iquitos and week 17 in San Juan) such that each dengue season began on the following week. All data were final, reflecting all cases with onset in each week regardless of reporting delays that affected the availability of data in real time. The data were divided into training data (Iquitos: 2000/2001 to 2008/2009, San Juan: 1990/1991 to 2008/2009) and testing data (2009/2010 to 2012/2013 for both locations). Climate and environmental data were provided for both locations (*SI Appendix*). Complete datasets are available at https://predict.cdc.gov and ref. 37. Participants were permitted to use other data (e.g., social media or demographic data) but not data on dengue in the study locations or nearby locations unless those data were made available to all participants.

Forecast Targets. For each season and location, the following targets were forecasted: *Peak week*, the week with the highest incidence of dengue (or undefined if more than 1 wk had the highest number of cases); *Peak incidence*, the number of dengue cases reported in the peak week; and *Total incidence*, the total number of confirmed dengue cases reported over the season.

Each forecast included a point estimate and a binned probability distribution. For peak week, each bin represented a single week (i.e., 1, 2, . . ., 52). For peak and total incidence, 11 bins were chosen empirically by setting an upper bound ∼50% higher than the maxima observed in the training data. The maximum observed peak incidence in Iquitos was 116 cases, and we used bins of width 15 cases to cover up to 149 with 10 bins plus a final bin for 150 or more cases. For San Juan, with a maximum of 461 cases, we used bins of width 50 and 500 or more as the final bin. For total incidence, the maxima observed were 715 and 6,690 cases for Iquitos and San Juan, respectively. Bin widths were selected at 100 and 1,000 cases, respectively, with the last bin for >1,000 or >10,000 cases. Probabilities between 0 and 1 were assigned to each bin, summing to 1.0 for each specific forecast (e.g., the week 4 forecast for peak week in San Juan 2005/2006).

Forecasting. The forecasting project started on 5 June 2015, with public announcement of the challenge and online publication of the training datasets and forecast templates. Forecasting occurred in 2 stages. First, to participate, each team was required to submit a model description and a set of formatted forecasts for all 3 targets at both locations for the last 4 seasons of the training dataset (2005/2006 to 2008/2009) at 13 time points per season (weeks 0, 4, 8, . . ., 48) by email by 12 August 2015. Each team explicitly stated that these were out-of-sample forecasts using only the data from prior time points in all datasets used. The training forecasts and model descriptions were evaluated for adherence to the guidelines. Teams meeting those guidelines received the testing data on 19 August and had 2 wk to generate

and submit forecasts from the same model for the 4 testing seasons (2009/2010 to 2012/2013; deadline: 2 September 2015). The only incentives for participation were the provision of data, the opportunity to compare prospective forecasts, and the opportunity to participate in the development of this manuscript. Details are available at https://dengueforecasting.noaa.gov and https://predict.cdc.gov and in ref. 37.

We analyzed 3 additional models for comparison: a null model, a baseline model, and an ensemble model. The null model assigned equal probabilities to all bins (e.g., 1 of 52 for each possible peak week). The baseline models were SARIMA models, capturing seasonal trends and short-term autocorrelation [SARIMA(1, 0, 0)(4, 1, 0)$_{12}$ for San Juan and SARIMA(1, 0, 0)(3, 1, 0)$_{12}$ for Iquitos] (6). Finally, the ensemble model was created by averaging the probability bins from all team forecasts and the baseline forecast.

Evaluation. All forecasts were evaluated using the logarithmic score, a proper scoring rule based on probability densities (24, 38). The logarithmic score is the average logarithm of the probability assigned to the observed outcome bin (described above), p_i, over n predictions: $S_n = \frac{1}{n}\sum_{i=1}^{n}\log(p_i)$. We used Bayesian generalized linear models to identify season and model characteristics potentially related to forecast skill (*SI Appendix*). All analyses were performed in R (https://www.r-project.org/).

ACKNOWLEDGMENTS. T.K.Y. and J.S. were supported by National Institute of General Medical Sciences (NIGMS) Grant GM110748 and Defense Threat Reduction Agency Contract HDTRA1-15-C-0018. L.C.B., D.C.F., S.H., R.J.T., and R.R. were supported by NIGMS Award U54 GM088491 and NSF Graduate Research Fellowship Program Grant DGE-1252522. D.C.F. was a predoctoral trainee supported by NIH T32 Training Grant T32 EB009403 and the HHMI–National Institute of Biomedical Imaging and Bioengineering Interfaces Initiative. R.J.T. was supported by NSF Grant DMS-1309174. J.L., N.G.R., D.A.T.C., S.A.L., S.M.M., and H.E.C. were supported by National Institute of Allergy and Infectious Diseases (NIAID) Grant AI102939. N.G.R., E.L.R., K.S., A.C.B., and X.M. were supported by NIAID and NIGMS Grants R21AI115173, R01AI102939, and R35GM119582. R.L. was supported by a Royal Society Dorothy Hodgkin Fellowship. O.O., R.V., D.M., and M.M. were supported by the Forces and Resources Policy Center of the RAND National Defense Research Institute with discretionary US Department of Defense funds. T.C.P. and L.W. were supported by NIGMS Grant U01-GM087728. M.C., Y.L., and A.R. were supported by Global Institute for Collaborative Research and Education Big-Data and Cybersecurity Station and a Faculty in Industry Award at the University of Minnesota Informatics Institute. L.R.J., R.B.G., J.M.C., E.A.M., C.C.M., J.R.R., S.J.R., A.M.S.-I., and D.P.W. were supported by NIH–NSF–US Department of Agriculture Ecology of Infectious Diseases Grant 1R01AI122284. J.A. and M.C. were funded with federal funds from Office of the Assistant Secretary for Preparedness and Response, Biomedical Advanced Research and Development Authority Contract HHSO100201600017I.

[a]Division of Vector-Borne Diseases, Centers for Disease Control and Prevention, San Juan 00920, Puerto Rico; [b]Department of Epidemiology, Harvard T. H. Chan School of Public Health, Boston, MA 02115; [c]Data Analytics, Areté Associates, Northridge, CA 91324; [d]Systems Integration Branch, Johns Hopkins University Applied Physics Laboratory, Laurel, MD 20723; [e]Department of Environmental Health Sciences, Mailman School of Public Health, Columbia University, New York, NY 10032; [f]Data to Decisions Cooperative Research Center, Kent Town, SA 5067, Australia; [g]Heinz College Information System Management, Carnegie Mellon University, Adelaide, SA 5000, Australia; [h]School of Computer Science, Carnegie Mellon University, Pittsburgh, PA 15213; [i]Department of Statistics, Carnegie Mellon University, Pittsburgh, PA 15213; [j]Department of Epidemiology, Johns Hopkins Bloomberg School of Public Health, Baltimore, MD 21205; [k]Department of Biostatistics and Epidemiology, School of Public Health and Health Sciences, University of Massachusetts, Amherst, MA 01003; [l]Department of Biology, University of Florida, Gainesville, FL 32611; [m]Emerging Pathogens Institute, University of Florida, Gainesville, FL 32611; [n]Department of Biological Sciences, University of Notre Dame, Notre Dame, IN 46556; [o]Eck Institute for Global Health, University of Notre Dame, Notre Dame, IN 46556; [p]Hospital for Tropical Diseases, Oxford University Clinical Research Unit, Ho Chi Minh City, Vietnam; [q]Department of Infectious Disease Epidemiology, London School of Hygiene & Tropical Medicine, London WC1E 7HT, United Kingdom; [r]Climate and Health Program, Barcelona Institute for Global Health, 08003 Barcelona, Spain; [s]College of Engineering, Mathematics and Physical Sciences, University of Exeter, Exeter EX4 4QF, United Kingdom; [t]Predictia Intelligent Data Solutions, 39005 Santander, Spain; [u]Scientific Computation Program, Oswaldo Cruz Foundation, Rio de Janeiro 21040-900, Brazil; [v]Catalan Institution for Research and Advanced Studies, 08010 Barcelona, Spain; [w]Department of Mathematical Biology, Indian Statistical Institute, Kolkata, India 700108; [x]Pasteur Kyoto International Joint Research Unit for Integrative Vaccinomics, 606-8501 Kyoto, Japan; [y]Department of Global Health, Centre National de la Recherche Scientifique, 75016 Paris, France; [z]Department of Mathematics and Statistics, Mount Holyoke College, South Hadley, MA 01075; [aa]RAND Corporation, Santa Monica, CA 90401; [bb]Open Philanthropy, San Francisco, CA 94105; [cc]Department of Computer Science and Software Engineering, Miami University, Oxford, OH 45056; [dd]F. I. Proctor Foundation for Research in Ophthalmology, University of California, San Francisco, CA 94122; [ee]Information Science and Technology, Hokkaido University, Sapporo 060-0808, Japan; [ff]Division of Environmental Health Sciences, School of Public Health, University of Minnesota, Twin Cities, MN 55455; [gg]VectorAnalytica, Washington, DC 20007; [hh]Department of Aeronautical Engineering, Universidade de Sao Paolo, Sao Paolo 13566-590, Brazil; [ii]Department of Philosophy, University of Miami, Coral Gables, FL 33146; [jj]Department of Statistics, Virginia Tech, Blacksburg, VA 24060; [kk]Integrative Biology, University of South Florida, Tampa, FL 33620; [ll]Department of Biology, Stanford University, Stanford, CA 94305; [mm]Infectious Diseases, College of Veterinary Medicine, University of Georgia, Athens, GA 30602; [nn]Odum School of Ecology, University of Georgia, Athens, GA 30602; [oo]Department of Geography, University of Florida, Gainesville, FL 32608; [pp]School of Life Sciences, University of KwaZulu, Natal 3629, South Africa; [qq]Department of Medicine, State University of New York Upstate Medical University, Syracuse, NY 13421; [rr]Department of Biostatistics, University of Michigan, Ann Arbor, MI 48109; [ss]Department of Civil and Environmental Engineering, West Virginia University, Morgantown, WV 26505; [tt]Department of Cell Biology and Molecular Genetics, University of Maryland, College Park, MD 20742; [uu]Puerto Rico Department of Health, San Juan 00927, Puerto Rico; [vv]Department of Pathology, Microbiology, and Immunology, School of Veterinary Medicine, University of California, Davis, CA 95616; [ww]Department of Environmental, Agricultural, and Occupational Health, College of Public Health, University of Nebraska Medical Center, Omaha, NE 68198; [xx]Influenza Division, Centers for Disease Control and Prevention, Atlanta, GA 30329; [yy]Armed Forces Health Surveillance Branch, Department of Defense, Silver Spring, MD 20904; [zz]Climate Program Office, National Oceanic and Atmospheric Administration, Silver Spring, MD 20910; [aaa]Leidos supporting the Biomedical Advanced Research and Development Authority, Department of Health and Human Services, Washington, DC 20201; [bbb]Bureau of Oceans, International Environmental and Scientific Affairs, US Department of State, Washington, DC 20520; [ccc]Office of Science and Technology Policy, The White House, Washington, DC 20502; [ddd]BNext, In-Q-Tel, Arlington, VA 22201; and [eee]National Center for Medical Intelligence, Defense Intelligence Agency, Fort Detric, MD 21702

1. S. Bhatt *et al*., The global distribution and burden of dengue. *Nature* **496**, 504–507 (2013).
2. M. A. Johansson, D. A. Cummings, G. E. Glass, Multiyear climate variability and dengue–El Niño southern oscillation, weather, and dengue incidence in Puerto Rico, Mexico, and Thailand: A longitudinal data analysis. *PLoS Med.* **6**, e1000168 (2009).
3. W. G. van Panhuis *et al*., Region-wide synchrony and traveling waves of dengue across eight countries in Southeast Asia. *Proc. Natl. Acad. Sci. U.S.A.* **112**, 13069–13074 (2015).
4. D. Constenla, C. Garcia, N. Lefcourt, Assessing the economics of dengue: Results from a systematic review of the literature and expert survey. *Pharmacoeconomics* **33**, 1107–1135 (2015).
5. D. S. Shepard, E. A. Undurraga, Y. A. Halasa, J. D. Stanaway, The global economic burden of dengue: A systematic analysis. *Lancet Infect. Dis.* **16**, 935–941 (2016).
6. M. A. Johansson, N. G. Reich, A. Hota, J. S. Brownstein, M. Santillana, Evaluating the performance of infectious disease forecasts: A comparison of climate-driven and seasonal dengue forecasts for Mexico. *Sci. Rep.* **6**, 33707 (2016).
7. M. A. Johansson, J. Hombach, D. A. Cummings, Models of the impact of dengue vaccines: A review of current research and potential approaches. *Vaccine* **29**, 5860–5868 (2011).
8. R. C. Reiner Jr *et al*., A systematic review of mathematical models of mosquito-borne pathogen transmission: 1970-2010. *J. R. Soc. Interface* **10**, 20120921 (2013).
9. R. Lowe *et al*., Evaluating probabilistic dengue risk forecasts from a prototype early warning system for Brazil. *eLife* **5**, e11285 (2016).
10. N. Ferguson, R. Anderson, S. Gupta, The effect of antibody-dependent enhancement on the transmission dynamics and persistence of multiple-strain pathogens. *Proc. Natl. Acad. Sci. U.S.A.* **96**, 790–794 (1999).
11. D. A. Cummings, I. B. Schwartz, L. Billings, L. B. Shaw, D. S. Burke, Dynamic effects of antibody-dependent enhancement on the fitness of viruses. *Proc. Natl. Acad. Sci. U.S.A.* **102**, 15259–15264 (2005).
12. H. J. Wearing, P. Rohani, Ecological and immunological determinants of dengue epidemics. *Proc. Natl. Acad. Sci. U.S.A.* **103**, 11802–11807 (2006).
13. B. Adams *et al*., Cross-protective immunity can account for the alternating epidemic pattern of dengue virus serotypes circulating in Bangkok. *Proc. Natl. Acad. Sci. U.S.A.* **103**, 14234–14239 (2006).
14. J. Lourenço, M. Recker, Natural, persistent oscillations in a spatial multi-strain disease system with application to dengue. *PLoS Comput. Biol.* **9**, e1003308 (2013).
15. Pandemic Prediction and Forecasting Science and Technology Working Group, Towards epidemic prediction: Federal efforts and opportunities in outbreak modeling. https://obamawhitehouse.archives.gov/sites/default/files/microsites/ostp/NSTC/towards_epidemic_prediction-federal_efforts_and_opportunities.pdf. Accessed 22 October 2019.
16. World Health Organization and Special Programme for Research and Training in Tropical Diseases, *Dengue: Guideline for Diagnosis, Treatment, Prevention and Control* (World Health Organization, 2009).
17. B. M. Forshey *et al*.; NMRCD Febrile Surveillance Working Group, Arboviral etiologies of acute febrile illnesses in Western South America, 2000-2007. *PLoS Negl. Trop. Dis.* **4**, e787 (2010).

18. S. T. Stoddard *et al*., Long-term and seasonal dynamics of dengue in Iquitos, Peru. *PLoS Negl. Trop. Dis.* **8**, e3003 (2014).
19. T. M. Sharp *et al*., Virus-specific differences in rates of disease during the 2010 Dengue epidemic in Puerto Rico. *PLoS Negl. Trop. Dis.* **7**, e2159 (2013).
20. L. R. Johnson *et al*., Phenomenological forecasting of disease incidence using heteroskedastic Gaussian processes: A dengue case study. *Ann. Appl. Stat.* **12**, 27–66 (2018).
21. A. L. Buczak *et al*., Ensemble method for dengue prediction. *PLoS One* **13**, e0189988 (2018).
22. L. Held, S. Meyer, J. Bracher, Probabilistic forecasting in infectious disease epidemiology: The 13th Armitage lecture. *Stat. Med.* **36**, 3443–3460 (2017).
23. G. W. Brier, Verification of forecasts expressed in terms of probability. *Mon. Weather Rev.* **78**, 1–3 (1950).
24. T. Gneiting, A. E. Raftery, Strictly proper scoring rules, prediction, and estimation. *J. Am. Stat. Assoc.* **102**, 359–378 (2007).
25. M. Biggerstaff *et al*., Results from the second year of a collaborative effort to forecast influenza seasons in the United States. *Epidemics* **24**, 26–33 (2018).
26. R. Lowe *et al*., Climate services for health: Predicting the evolution of the 2016 dengue season in Machala, Ecuador. *Lancet Planet. Health* **1**, e142–e151 (2017).
27. J. Lega, H. E. Brown, Data-driven outbreak forecasting with a simple nonlinear growth model. *Epidemics* **17**, 19–26 (2016).
28. C. Viboud *et al*.; RAPIDD Ebola Forecasting Challenge group, The RAPIDD ebola forecasting challenge: Synthesis and lessons learnt. *Epidemics* **22**, 13–21 (2018).
29. D. Manheim, M. Chamberlin, O. A. Osoba, R. Vardavas, M. J. S. M. Moore, *Improving Decision Support for Infectious Disease Prevention and Control* (Rand Corporation, 2016).
30. T. K. Yamana, S. Kandula, J. Shaman, Superensemble forecasts of dengue outbreaks. *J. R. Soc. Interface* **13**, 20160410 (2016).
31. R. Polikar, Ensemble based systems in decision making. *IEEE Circuits Syst. Mag.* **6**, 21–45 (2006).
32. N. G. Reich *et al*., Interactions between serotypes of dengue highlight epidemiological impact of cross-immunity. *J. R. Soc. Interface* **10**, 20130414 (2013).
33. O. J. Brady, D. L. Smith, T. W. Scott, S. I. J. E. Hay, Dengue disease outbreak definitions are implicitly variable. *Epidemics* **11**, 92–102 (2015).
34. P. E. Tetlock, B. A. Mellers, N. Rohrbaugh, E. Chen, Forecasting tournaments: Tools for increasing transparency and improving the quality of debate. *Curr. Dir. Psychol. Sci.* **23**, 290–295 (2014).
35. D. R. Wernly, L. W. Uccellini, "Storm forecasting for emergency response" in *Storms*, R. A. Pielke, R. A. Pielke, Eds. (Routledge, London, UK, 2000), pp. 70–97.
36. R. C. Reiner Jr *et al*., Time-varying, serotype-specific force of infection of dengue virus. *Proc. Natl. Acad. Sci. U.S.A.* **111**, E2694–E2702 (2014).
37. M. A. Johansson, Dengue forecasting project data repository. Github. https://github.com/cdcepi/dengue-forecasting-project-2015. Deposited 25 October 2019.
38. R. Rosenfeld, J. Grefenstette, D. Burke, A proposal for standardized evaluation of epidemiological models. https://delphi.midas.cs.cmu.edu/files/StandardizedEvaluation_Revised_12-11-09.pdf. Accessed 20 October 2019.

Source details

Feedback > Compare sources >

Proceedings of the National Academy of Sciences of the United States of America

Scopus coverage years: from 1945 to 1951, from 1961 to Present

Publisher: National Academy of Sciences

ISSN: 0027-8424 E-ISSN: 1091-6490

Subject area: Multidisciplinary

Source type: Journal

View all documents > Set document alert Save to source list

CiteScore 2022
19.2

SJR 2022
4.026

SNIP 2022
2.765

CiteScore CiteScore rank & trend Scopus content coverage

International Journal of Engineering Science 152 (2020) 103277

Contents lists available at ScienceDirect

International Journal of Engineering Science

journal homepage: www.elsevier.com/locate/ijengsci

A thermodynamic analysis of an enhanced theory of heat conduction model: Extended influence of finite strain and heat flux

Soumen Shaw

Department of Mathematics Indian Institute of Engineering Science and Technology, Shibpur, Shibpur, Howrah - 711103 India

ARTICLE INFO

Article history:
Received 19 January 2019
Accepted 7 March 2020

Keywords:
Finite strain
Components of heat flux
Generalized thermoelasticity
Eulerian description
Integral transformation,

ABSTRACT

An Eulerian form of thermodynamically consistent generalized thermoelastic model capable of accounting for thermal signals is proposed. The heat flux is assumed to consist of both energetic and dissipative components. The constitutive relations for the stress, entropy and the heat fluxes are derived in the spatial coordinate system. Later on, a domain of dependence inequality for the proposed hyperbolic type heat conduction model is proved. The linearised form of this improved thermoelasticity theory of finite deformation is employed to study the thermoelastic interactions due a continuous source of heat in isotropic elastic solids. This newly developed model is also applied in a thermoelastic saturated porous medium. In order to obtain the exact analytical expressions of the field functions, appropriate integral transformations are employed in a convenient way.

1. Introduction

In mechanics and physics, invariance plays a significant role. There are some conservation laws in the all continuum theory; i.e., quantities that are constant in time, namely, mass and energy or balance laws such as balance of linear and angular momentum. There exist two ways to develop the continuum theory. In one hand building of continuum theory is to postulate those conservation or balance laws. On the other way, conservation laws and the balance laws can be obtained as a result of postulating invariance of a quantity such as energy or Lagrangian density, under some group of transformations.

In the classical theory of elasticity a deformation is termed as infinitesimal when the space derivatives of the components of the displacement vector of an arbitrary particle of the medium are so small that their squares and products may be neglected. Many attempts have been made to extend the classical theory of infinitesimal strain to the case of finite strains i.e., strains in which the fundamental hypothesis which serves to define an infinite strain is not legitimate. In the theory of finite strain, there is two essentially different perspectives which coalesce in the case of infinitesimal strain. We may use as the independent variables in terms of which the strains are described either in reference or spatial coordinate system. Most of the authors on the subject of finite strain have, probably for the reason of mathematical convenience, adopted the Lagrangian system. According to Seth (1935),*"Like the body-stress equation these (the components of strain) should be referred to the actual position of the material point in the strained condition, and not to the position of a point considered before strain. Apparently Coker and Filon (1931) were first to notice it and to stress its importance"*.

E-mail address: shaw_soumen@rediffmail.com

https://doi.org/10.1016/j.ijengsci.2020.103277
0020-7225/

From the principle of energy conservation, in the classical theory, the relation between stress and strain can be expressed as: *The stress tensor equals to the gradient of the elastic-energy-density with respect to the strain tensor*. In infinitesimal theory, for a virtual displacement of the strained elastic medium, the virtual work done by all the forces, both surface as well as body, acting upon the medium can be obtained by integrating the scalar product of the stress tensor and the variation of the strain tensor over the medium. This principle is merely an approximation, it is not holds good in the finite-strain theory. The exact principle is that the virtual work is obtained by integrating the scalar product of the stress tensor with the space-derivative of the virtual displacement vector over the medium (for details see Ref. Murnaghan, 1937). So in this view point domain of dependence of the proposed model is very significant.

In the small deformation, physical observations and results of the conventional coupled dynamic thermoelasticity theories, which were based on the mixed parabolic-hyperbolic governing equations of Biot (1956b), involved infinite speed of thermal signals. This paradoxical circumstances led many researchers to advance various generalizations on the coupled dynamic thermoelasticity theory. They are based on different modifications of the classical Fourier law of heat conduction. The refinements aim at derivations of hyperbolic partial differential equations of coupled thermoelasticity. Those are to simultaneously satisfy the following criteria: (i) Finiteness of heat signal propagation speed, (ii) Spatial propagation of thermoelastic waves without attenuation, and (iii) Existence of distortion less wave forms akin to the classical d'Alembert type waves. The first was due to Cattaneo (1958), in which a wave type heat equation was derived by postulating a new law of heat conduction to replace the classical Fourier law. Later on, Lord and Shulman (1967), Green and Lindsay (1972) and Green and Naghdi (1991, 1992, 1993) have proposed three different generalized heat conduction equations which are the most discussed hyperbolic type heat equations in the literature. All of these modifications, so called thermoelasticity with second sound, have been performed in the infinitesimal theory of elasticity.

In the context of non-linear continuum mechanics, after the pioneering work of Lee (1969), using the multiplicative decomposition of the deformation gradient into mechanical and thermal parts, several authors (Darijani & Naghdabadi, 2010; Imam & Johnson, 1998; Lubarda, 2004) have placed their articles for modeling the material behavior under various mechanical and geometrical boundary conditions in the context of elasto-plastic deformation.

In this article, based on the laws of conservation of thermodynamics, a spatial description of a fully non-linear coupled problem of non-classical thermoelasticity is proposed. There are two distinctions from the classical theory. The heat flux vector is additively decomposed into two components: dissipative and energetic. Secondly, the material derivative of the absolute temperature with respect to the time is assumed to be proportionate with the heat and the entropy of the system. Finally, the linearised form of the proposed model is applied successfully in elastic and poroelastic medium with various circumstances.

2. Kinematics

Kinematics is the study of the motion of bodies, without regard to the cause of the motion. It is purely a study of geometry and is an exact science within the hypothesis of continuum.

We consider $\mathbf{x} = (x_1, x_2, x_3)$ be a fixed coordinate system with respect to the fixed point $\mathbf{o}$ in R^3 and an orthogonal basis $e_i (i = 1, 2, 3)$ is defined there. When a physical body with its reference configuration Ω_0 at, say, $t = 0$, moves over a period of time and occupies a configuration Ω_t at time t, the material point $\mathbf{X} = X_i e_i$ in $\bar{\Omega}_0$ (the closer of Ω_0) is mapped into the position $\mathbf{x}$ in Ω_t by a smooth vector valued function:

$$\mathbf{x} = \xi(\mathbf{X}, t).$$

Thus, $\xi(\mathbf{X}, t)$ is the spatial position of the material point $\mathbf{X}$ at time t. The one parameter family $\{\xi(\mathbf{X}, t)\}$ of position is called the trajectory of $\mathbf{X}$. We assume that the function ξ be differentiable, injective, and orientation preserving. The function ξ is called the motion of the body.

Since $det(\frac{\partial \chi_i}{\partial X^j}) > 0$, so there exist another mapping $\Xi : \mathbf{X} \xrightarrow{t} \mathbf{x}$ i.e. $\mathbf{X} = \Xi(\mathbf{x}, t)$ for every material point in the spatial configuration $\mathbf{x}$ there is one point $\Xi(\mathbf{x}, t)$ in the reference configuration.

The displacement of the point $\mathbf{x}$ is

$$\mathbf{u} = \Xi(\mathbf{x}) - \mathbf{x}$$

and

$d\mathbf{X} = \nabla\Xi(\mathbf{x})d\mathbf{x}$ i.e. $dX_i = \frac{\partial \Xi_i}{\partial x^j} dx_j$

The tensor $\mathbf{E(x)} = \nabla\Xi(\mathbf{x})$ is called the deformation gradient.

Thus, $\mathbf{E(x)} = I + \nabla\mathbf{u(x)}$ where I is the identity tensor $\nabla\mathbf{u}$ is the displacement gradient.

3. Governing equations in generalized thermodynamic framework

3.1. Balance laws:

Balance of linear momentum yields the following equation

$$t_{ji,j} + \rho(f_j - \ddot{u}_j) = 0 \tag{1}$$

Balance of moment of momentum yields

$$t_{ij} = t_{ji} \tag{2}$$

where *tij* is the Cauchy stress tensor. ρ denotes the density of the material. f_j and u_j are the *j*th components of the body force density and displacement vector **u**. The superposed dot denotes the differentiation with respect to time *t* and 'comma' in the subscript denotes the differentiation with respect to spatial coordinates.

According to the first law of thermodynamics, balance of energy is given by

$$\dot{U} = t_{ij}\dot{e}_{ij} - div\mathbf{q} + Q \tag{3}$$

Here *U, q* and *Q* denote the internal energy, heat flux vector, and source of heat respectively. e_{ij} represents the strain tensor.

Second law of thermodynamics gives the balance of entropy inequality as follows:

$$\dot{\eta} \geq -div\mathbf{H} + S \tag{4}$$

where η, **H** and *S* are respectively the entropy, entropy flux vector, and source of entropy.

In Green-Naghdi Type-II and Type-III (for details see Refs. Green & Naghdi, 1992; Green & Naghdi, 1993) models of generalized thermoelasticity an extra thermal state variable, named thermal displacement, is defined by

$$\alpha(x,t) = \alpha_0(x) + \int_0^t \theta(x,s)ds \tag{5}$$

Here $\theta(x, t)$ is an empirical temperature scale, not necessarily the absolute one.

Now, assuming the summability of θ on R^-, we can extend the definition of thermal displacement as

$$\alpha(x,t) = \int_{-\infty}^t \theta(x,s)ds$$

If we consider $\alpha_0(x) = \alpha(x,0)$, in Eq. (5), summarizes the temperature history upto the initial time $t = 0$ i.e.

$$\alpha_0(x) = \int_{-\infty}^0 \theta(x,s)ds$$

Therefore, the temperature above the reference temperature i.e. the absolute temperature is defined by

$$\theta = \dot{\alpha} \quad and \quad \dot{\alpha} > 0. \tag{6}$$

Consequently,

$$\mathbf{H} = \frac{\mathbf{q}}{\dot{\alpha}} \quad and \quad S = \frac{Q}{\dot{\alpha}} \tag{7}$$

Now, substituting Eq. (7) in Eq. (4) we obtain,

$$\dot{\eta} \geq -div\left[\frac{\mathbf{q}}{\dot{\alpha}}\right] + \frac{Q}{\dot{\alpha}}$$

Using Eq. (6);

$$\frac{d}{dt}(U - \theta\eta) \leq -\dot{\theta}\eta - \frac{1}{\theta}\mathbf{q}.(\nabla\theta) + t_{ij}\dot{e}_{ij}$$

i.e.,

$$\dot{\psi} + \dot{\theta}\eta + \frac{1}{\theta}\mathbf{q}.(\nabla\theta) - t_{ij}\dot{e}_{ij} = -\theta\chi \leq 0 \tag{8}$$

where χ denotes the rate of entropy production and $\theta\chi$ represents the rate of energy dissipation. In which ψ denotes the Helmoltz's free energy function and Eq. (8) gives the balance of free energy.

3.2. Constitutive equations:

The modern research on thermodynamics to strengthening the hardening mechanisms for micro/nano structured materials indicate that the adaptation of only one type energetic or dissipative description may be insufficient to accurately describe the size effects exhibited in metallic components. therefore, in order to have a better understanding of the thermoelastic characteristics for micro/nano structured materials, it is important to incorporate more than one description of the thermodynamic processes into the modelling.

Without any loss of generality, as mentioned in the above motivation, we assume that the heat flux **q** is split additively as,

$$\mathbf{q} = \mathbf{q}_E + \mathbf{q}_D \tag{9}$$

where $\mathbf{q}_E$ and $\mathbf{q}_D$ are the energetic and dissipative components of the heat flux $\mathbf{q}$.

Consequently, the free energy balance Eq. (8) becomes,

$$\dot{\psi} - t_{ij}\dot{e}_{ij} + \dot{\theta}\eta + \frac{1}{\theta}\mathbf{q}_E.(\nabla\theta) + \frac{1}{\theta}\mathbf{q}_D.(\nabla\theta) = -\theta\chi \leq 0 \tag{10}$$

Here the function $\dot{\psi}$ and all other functions under consideration can be expressed in terms of the set of state variables $\{e_{ij}, \theta, \nabla\alpha, \nabla\theta\}$. Now by the chain rule of differentiation we get,

$$\dot{\psi} = \frac{\partial\psi}{\partial e_{ij}}\dot{e}_{ij} + \frac{\partial\psi}{\partial\theta}\dot{\theta} + \frac{\partial\psi}{\partial\Lambda}.\dot{\Lambda} + \frac{\partial\psi}{\partial\mathbf{G}}.\dot{\mathbf{G}} \tag{11}$$

where $\Lambda = \nabla\alpha, \mathbf{G} = \nabla\theta$.

Substitution of the time derivative of the free energy (11) into the Eq. (10) yields

$$\left(\frac{\partial\psi}{\partial e_{ij}} - t_{ij}\right)\dot{e}_{ij} + \left(\frac{\partial\psi}{\partial\theta} + \eta\right)\dot{\theta} + \left(\frac{\partial\psi}{\partial\Lambda} + \frac{1}{\theta}\mathbf{q}_E\right).\dot{\Lambda} + \frac{\partial\psi}{\partial\mathbf{G}}.\dot{\mathbf{G}} + \frac{1}{\theta}\mathbf{q}_D.(\nabla\theta) \leq 0 \tag{12}$$

which must be satisfied for all states.

As $\dot{e}_{ij}, \dot{\theta}, \dot{\Lambda}$ and $\dot{\mathbf{G}}$ can be chosen arbitrarily, it is sufficient to choose the constitutive equations as;

$$t_{ij} = \frac{\partial\psi}{\partial e_{ij}}, \quad \eta = -\frac{\partial\psi}{\partial\theta}, \quad \frac{1}{\theta}\mathbf{q}_E = -\frac{\partial\psi}{\partial\Lambda}, \quad \frac{\partial\psi}{\partial\mathbf{G}} = \mathbf{0} \quad \textit{and} \quad \mathbf{q}_D.(\nabla\theta) \leq 0 \tag{13}$$

in order to maintain the inequality (12). As a result, the rate of entropy production in any thermodynamically admissible process becomes

$$\chi = -\frac{1}{\theta^2}\mathbf{q}_D.(\nabla\theta) \tag{14}$$

Eq. (13) reveals that the free energy does not depend on $\nabla\theta$. Such a class of free energy function in the non-classical theory may be taken in the following form:

$$\psi = \psi_c + \frac{1}{2}K_1\nabla\alpha.\nabla\alpha$$

in which ψ_c represents the free energy function for classical thermoelasticity and K_1 is the non-classical symmetric, positive definite, second order conductivity tensor.

3.3. Field eqs. for heat conduction:

From the expressions obtained in the constitutive eqs. (13), the time derivative of the free energy function becomes

$$\dot{\psi} = t_{ij}\dot{e}_{ij} - \eta\dot{\theta} - \frac{1}{\theta}\dot{\mathbf{q}}_E.(\nabla\dot{\alpha})$$

or,

$$\dot{U} = t_{ij}\dot{e}_{ij} + \theta\dot{\eta} - \frac{1}{\theta}\dot{\mathbf{q}}_E.(\nabla\dot{\alpha})$$

Using Eq. (3);

$$-div\mathbf{q} + Q = \theta\dot{\eta} - \frac{1}{\theta}\dot{\mathbf{q}}_E.(\nabla\dot{\alpha}) \tag{15}$$

Now applying the constitutive relations (13) we obtain,

$$\rho C_e\dot{\theta} = -div\mathbf{q} + Q + \frac{2}{\theta}\dot{\mathbf{q}}_E.(\nabla\theta) + \theta\dot{e}_{ij}\frac{\partial t_{ij}}{\partial\theta} \tag{16}$$

where C_e denotes the specific heat and is defined by

$$\rho C_e = -\theta\frac{\partial^2\psi}{\partial\theta^2} \tag{17}$$

3.3.1. The linearised form:

In this section we summarize the initial boundary value problem (IBVP) for generalized thermoelasticity in linearised form.

The balance of linear momentum Eq. (1), the thermal displacement-temperature relation together with the balance of energy in the conservation form Eq. (15) lead to the system of PDEs governs the thermoelastic behaviour in the non-classical regime, given by

$$\begin{aligned} t_{ij,j} + \rho(f_i - \ddot{u}_i) &= 0, \\ \dot{\alpha} &= \theta, \\ T_0\dot{\eta} &= -div\mathbf{q} + Q, \end{aligned} \tag{18}$$

in which $\mathbf{u} = \dot{\mathbf{u}} = \mathbf{0}$, $\alpha = 0$, $\theta = T_0$ are assumed to be the natural state of the body.

The constitute equations can be derived from the classical Helmholtz free energy function, such that

$$t_{ij} = \frac{\partial\psi}{\partial e_{ij}}, \quad \eta = -\frac{\partial\psi}{\partial\theta}, \quad \mathbf{q} = \mathbf{q}_E + \mathbf{q}_D, \quad \mathbf{q}_E = -T_0\frac{\partial\psi}{\partial\Lambda}, \quad \mathbf{q}_D = -K_2\nabla\theta \tag{19}$$

and

$$\psi = \frac{1}{2}C_{ijkl} - T_0\beta_{ij}e_{ij} - \frac{\rho C_e}{2T_0}\theta^2 + \frac{1}{2}K_1(\nabla\alpha).(\nabla\alpha)$$

where C_{ijkl} is the forth order elasticity tensor, β_{ij} is the thermodynamic coupling tensor, K_2 is the classical heat conduction tensor and K_1 is the material constant characteristic of the body i.e., the non-classical conductivity tensor.

The linearised form of this theory has a wonderful similarity with Green-Naghdi Type-III model. In Green-Naghdi model if we substitute the non-classical conductivity tensor by T_0K_1 then this new model can be revealed.

3.4. Domain of dependence inequality:

Here we confine our attention on the statement and proof of the domain of dependence inequality for the solutions of the dynamic thermoelastic problem.

By a solution of the mixed initial boundary value problem in $\Omega = \Omega_t \times (0, \tau)$ we mean the pair $(\mathbf{u}, \theta)$ satisfy the Eqs. (18) in Ω together with initial conditions

$$\mathbf{u}(\mathbf{x}, 0) = \mathbf{u}_0(\mathbf{x}), \dot{\mathbf{u}}(\mathbf{x}, 0) = \dot{\mathbf{u}}_0(\mathbf{x}), \theta(\mathbf{x}, 0) = T_0(\mathbf{x}), \tag{20}$$

and boundary conditions

$$\mathbf{u}(\mathbf{x}, t)|_{\partial\Omega_t^{(1)}} = \mathbf{0}, t_{ij}(\mathbf{x}, t)|_{\partial\Omega_t^{(2)}} = 0, \quad \theta(\mathbf{x}, t)|_{\partial\Omega_t^{(3)}} = 0, \quad [\mathbf{q}(\mathbf{x}, t).\mathbf{n}(\mathbf{x})]|_{\partial\Omega_t^{(4)}} = 0 \tag{21}$$

in which $\mathbf{n}$ is the unit normal to $\partial\Omega_t$ and $\partial\Omega_t^{(i)}$ fixed subset of $\partial\Omega_t$ such that

$$\partial\bar{\Omega}_t^{(1)} \cup \partial\Omega_t^{(2)} = \partial\bar{\Omega}_t^{(3)} \cup \partial\Omega_t^{(4)} = \partial\Omega_t \ ;$$

$$\partial\bar{\Omega}_t^{(1)} \cap \partial\Omega_t^{(2)} = \partial\bar{\Omega}_t^{(3)} \cap \partial\Omega_t^{(4)} = \emptyset.$$

If $\partial\Omega_t^{(1)} = \emptyset$, then there exists a family of rigid motions which are the solutions of Eq. (18). To avoid the occurrence of the trivial solution in the case of such boundary conditions it is necessary to impose the following normalization restrictions on the initial data and boundary forces:

$$\begin{aligned} &\int_{\Omega_t} \mathbf{u}_0(\mathbf{x})d\mathbf{x} = \int_{\Omega_t} \dot{\mathbf{u}}_0(\mathbf{x})d\mathbf{x} = \int_{\Omega_t} \mathbf{u}_0(\mathbf{x}) \times \mathbf{x}d\mathbf{x} = \int_{\Omega_t} \dot{\mathbf{u}}_0(\mathbf{x}) \times \mathbf{x}d\mathbf{x} = \mathbf{0}, \\ &\int_{\Omega_t} \mathbf{f}(\mathbf{x}, t)d\mathbf{x} = \int_{\Omega_t} \mathbf{f}(\mathbf{x}, t) \times \mathbf{x}d\mathbf{x} = \mathbf{0}; \quad 0 < t < \tau. \end{aligned} \tag{22}$$

With the similar analogy, if $\partial\Omega_t^{(3)} = \emptyset$, we assume

$$\begin{aligned} &\int_{\Omega_t} \left[T_0\beta_{ij}e_{ij}(\mathbf{x}, 0) + \rho C_e T_0(\mathbf{x})\right]d\mathbf{x} = 0, \\ &\int_{\Omega_t} \rho Q(\mathbf{x}, t)d\mathbf{x} = 0, \quad 0 < t < \tau. \end{aligned} \tag{23}$$

To analyse the obtained solutions of the mixed initial boundary value problem including all possible boundary conditions defined in Eq. (21), here we define following spaces:

$$\tilde{\mathbf{H}}^1(\Omega_t) = \left\{\mathbf{u}(\mathbf{x}, t) \in \mathbf{H}^1(\Omega_t) : \mathbf{u}|_{\partial\Omega_t^{(1)}} = \mathbf{0} \quad or \quad if, \quad \partial\Omega_t^{(1)} = \emptyset \quad then \quad (22)_1 \quad holds\right\},$$

$$\tilde{H}^1(\Omega_t) = \left\{\theta(\mathbf{x}, t) \in H^1(\Omega_t) : \theta|_{\partial\Omega_t^{(3)}} = 0 \quad or \quad if, \quad \partial\Omega_t^{(3)} = \emptyset \quad then \quad (23)_1 \quad holds\right\},$$

$$\tilde{\mathbf{H}}^2(\Omega_t) = \mathbf{H}^2(\Omega_t) \cap \tilde{\mathbf{H}}^1(\Omega_t); \quad \tilde{H}^2(\Omega_t) = H^2(\Omega_t) \cap \tilde{H}^1(\Omega_t).$$

$$\tilde{\mathbf{L}}^1(\Omega_t) = \left\{\mathbf{f}(\mathbf{x}, t) \in \mathbf{L}^2(\Omega_t); \quad or \quad if, \quad \partial\Omega_t^{(1)} = \emptyset \quad then \quad (22)_2 \quad holds\right\},$$

$$\tilde{\mathbf{L}}^2(\Omega_t) = \left\{\mathbf{G}(\mathbf{x}, t) \in \mathbf{L}^2(\Omega_t); \quad or \quad if, \quad \partial\Omega_t^{(3)} = \emptyset \quad then \quad (23)_2 \quad holds\right\},$$

$$\mathscr{L}(\Omega_t) = \tilde{\mathbf{L}}^1(\Omega_t) \times \tilde{\mathbf{L}}^2(\Omega_t), \quad \mathscr{L}(0,\tau:\Omega_t) = \tilde{\mathbf{L}}^2(0,\tau;\mathscr{L}(\Omega_t)).$$

$$\mathscr{W}(0,\tau;\Omega_t) = \Big[H^2\big(0,\tau;\mathbf{L}^2(\Omega_t)\big) \cap H^1\big(0,\tau;\mathbf{H}^1(\Omega_t)\big) \cap L^2\big(0,\tau;\tilde{\mathbf{H}}^1(\Omega_t)\big)\Big]\Big[H^1\big(0,\tau;\mathbf{L}^2(\Omega_t)\big) \cap L^2\big(0,\tau;\tilde{\mathbf{H}}^2(\Omega_t)\big)\Big].$$

In which L^1, L^2, H^2, etc. represent the usual space of scalar functions, while $\mathbf{L}^1, \mathbf{L}^2, \mathbf{H}^1$ etc. the set of vectorial or tensorial functions.

Definition 1: A pair $(\mathbf{u},\theta)$ is said to be a strong solution of the IBVP (19)-(21) in Ω with the initial conditions $(\mathbf{u}_0,\theta_0,\dot{\mathbf{u}_0}) \in \tilde{\mathbf{H}}^2(\Omega_t) \times \tilde{H}^2(\Omega_t) \times \tilde{\mathbf{H}}^1(\Omega_t)$ and source $(\mathbf{f},\mathbf{G}) \in \mathscr{L}(0,\tau;\Omega_t)$, if $(\mathbf{u},\theta) \in \mathscr{W}(0,\tau;\Omega_t)$ and satisfy Eq. (19) almost everywhere in Ω and Eq. (21) almost everywhere in Ω_t.

Definition 2: If $(\mathbf{u},\theta)$ be a solution of (19)-(21), then for every domain $\mathscr{A} \subset \Omega_t$, we define the total energy

$$\mathscr{E}(\mathscr{A},t) = \int_{\mathscr{A}} \rho\Big[\frac{1}{2}|\dot{\mathbf{u}}(\mathbf{x},t)|^2 + \psi(\mathbf{x},t)\Big]d\mathbf{x} \tag{24}$$

We now employ the function $\mathscr{E}$ to state and proof the domain of dependence inequality for the solution of (19)-(21).

Lemma: Prove that

$$|\eta\dot{\theta}(t) + \frac{1}{\theta}\dot{\mathbf{q}}_E(t).(\nabla\theta(t))| \le \zeta\Big[\frac{1}{2}\dot{\mathbf{u}}^2 + \psi(t)\Big] \tag{25}$$

where ζ is a constant depends upon the material moduli.

Proof: The non-negativity of the entropy production defined in Eq. (14) is satisfied because of the inequality $(13)_4$ and it gives the insurance to satisfy the Eqs. (8) and (12). Hence, it follows that the temperature has to be strictly positive. Therefore,

$$\begin{aligned}|\eta\dot{\theta}(t) + \frac{1}{\theta}\dot{\mathbf{q}}_E(t).(\nabla\theta(t))| &\le |\dot{\psi} - t_{ij}\dot{e_{ij}}| \\ &\le |\frac{\partial\psi}{\partial\theta}\dot{\theta} + \frac{\partial\psi}{\partial\Lambda}.\dot{\Lambda} + \frac{\partial\psi}{\partial\mathbf{G}}.\dot{\mathbf{G}}| \\ &\le \frac{\partial}{\partial t}\Big(Total \quad energy \quad of \quad the \quad system\Big)\end{aligned}$$

Therefore, $|\eta\dot{\theta}(t) + \frac{1}{\theta}\dot{\mathbf{q}}_E(t).(\nabla\theta(t))| \le \zeta[\frac{1}{2}\dot{\mathbf{u}}^2 + \psi(t)]$. □

Theorem: Let $(\mathbf{u},\theta)$ be a solution of (19)-(21), then for every $(\mathbf{x}_0,t_0) \in \Omega$ we have

$$\mathscr{E}(\mathscr{B}(\mathbf{x}_0,a),t_0) \le \mathscr{E}(\mathscr{B}(\mathbf{x}_0,a+\zeta t_0),0) + \int_0^{t_0}\int_{\Omega_t \cap \mathscr{B}(\mathbf{x}_0,a+\zeta t_0)} \rho\Big[\dot{\mathbf{u}}.\ddot{\mathbf{u}} + t_{ij}\dot{e_{ij}}\Big]d\mathbf{x}dt \tag{26}$$

with $\mathscr{B}(\mathbf{x}_0,a) = \{\mathbf{x} \in \Omega_t; |\mathbf{x}-\mathbf{x}_0| < a\}$.

Proof: Without any loss of generality, let us consider a function ϕ defined in $C_0^\infty(\mathrm{R}^3,\mathrm{R})$ and $(\mathbf{u},\theta)$ be a solution of (19)-(21) such that

$$\mathscr{E}_\phi(\Omega_t,t) = \int_{\Omega_t} \rho\Big[\frac{1}{2}|\dot{\mathbf{u}}(\mathbf{x},t)|^2 + \psi(\mathbf{x},t)\Big]\phi(\mathbf{x},t)d\mathbf{x}$$

Therefore,

$$\dot{\mathscr{E}}_\phi(\Omega_t,t) = \int_{\Omega_t} \rho\Big[\dot{\mathbf{u}}.\ddot{\mathbf{u}} + \dot{\psi}(\mathbf{x},t)\Big]\phi(\mathbf{x},t)d\mathbf{x} + \int_{\Omega_t} \rho\Big[\frac{1}{2}|\dot{\mathbf{u}}(\mathbf{x},t)|^2 + \psi(\mathbf{x},t)\Big]\dot{\phi}(\mathbf{x},t)d\mathbf{x}$$

Let $\mathbf{x}_0$ be a fixed point in Ω_t for $\mathbf{x} \in \Omega_t$, $a > 0$, $t < T$. We define

$$\phi(\mathbf{x},t) = \phi_\delta\Big(|\mathbf{x}-\mathbf{x}_0| - a - \zeta(T-t)\Big)$$

with $\phi_\delta \in C^\infty(\mathrm{R}), \phi_\delta' < 0$ and

$$\begin{aligned}\phi_\delta(z) &= 1 \quad if \quad z \le -\delta \\ &= 0 \quad if \quad z \ge \delta\end{aligned}$$

So that

$$\begin{aligned}\dot{\phi}_\delta(\mathbf{x},t) &= \zeta\phi_\delta'(\mathbf{x},t) \\ \nabla\phi_\delta(\mathbf{x},t) &= \nabla|\mathbf{x}-\mathbf{x}_0|\phi_\delta'(\mathbf{x},t)\end{aligned}$$

Thus,

$$\dot{\mathscr{E}}_{\phi}(\Omega_t,t)=\int_{\Omega_t}\rho\Big[\dot{\mathbf{u}}.\ddot{\mathbf{u}}+t_{ij}\dot{e_{ij}}\Big]\phi_\delta(\mathbf{x},t)d\mathbf{x}-\int_{\Omega_t}\rho\Big\{\Big[\eta\dot{\theta}+\frac{1}{\theta}\mathbf{q}_E.(\nabla\theta)\Big]\phi_\delta(\mathbf{x},t)-\zeta\Big[\frac{1}{2}|\dot{\mathbf{u}}(\mathbf{x},t)|^2+\psi(\mathbf{x},t)\Big]\phi'_\delta(\mathbf{x},t)\Big\}d\mathbf{x}$$
$$\leq\int_{\Omega_t}\rho\Big[\dot{\mathbf{u}}.\ddot{\mathbf{u}}+t_{ij}\dot{e_{ij}}\Big]\phi_\delta(\mathbf{x},t)d\mathbf{x}$$

On integration over $(0,T)$ we obtain,

$$\mathscr{E}_{\phi_\delta}(\Omega_t,T)-\mathscr{E}_{\phi_\delta}(\Omega_t,0)\leq\int_0^T\int_{\Omega_t}\rho\Big[\dot{\mathbf{u}}.\ddot{\mathbf{u}}+t_{ij}\dot{e_{ij}}\Big]\phi_\delta(\mathbf{x},t)d\mathbf{x}dt$$

When δ tend to 0; $\phi_\delta(\mathbf{x},t)$ tends to the characteristic function of $\mathscr{B}(\mathbf{x}_0,a+\zeta(t-T))$, and the expression under the integral sign is given by Eq. (26). □

4. Applications

Thermo-acoustics in gases is a mechanism by which work done by the acoustic waves can be applied to transfer heat across the medium (Garrett, 2004; Swift, 1988; Wheatley, Hofler, Swift & Migliori, 1985). Though acoustic waves themselves do not transport heat on the average, it is possible to have such a transport if the phase angle between the particle velocity and temperature oscillations is altered by the presence of a thermal reservoir. The oscillation of fluid particles results in instantaneous heat transport. This transport can produce a heat transport if its time average at a given location is non-zero. Due to the intrinsic higher thermal conductivity, similar phenomenon is also exits in solids. In fact, given thermoelastic propagating waves in a homogeneous isotropic solid, the phase angle between the particle velocity and temperature oscillations enables motion-induced heat flux. This heat flux component is in addition to the Fourier conduction of heat flux.

4.1. Isotropic elastic solid

This section is devoted to analyse the thermoelastic interactions caused by a continuous heat source in a homogeneous and isotropic unbounded thermoelastic solid, by employing the proposed new thermoelasticity theory. The problem is solved by using suitable integral transformations. After some tedious mathematical manipulations, we have obtained the exact expressions of the temperature and stress fields in closed form.

4.1.1. Governing equations:

The governing equations (linear form) of the thermodynamically consistent generalized thermoelasticity at finite deformation are

$$\mu\nabla^2\mathbf{u}+(\lambda+\mu)\nabla(div\mathbf{u})-\beta\nabla\theta+\rho\mathbf{f}=\rho\ddot{\mathbf{u}} \tag{27}$$

$$T_0K_1\nabla^2\theta+K_2\nabla^2\dot{\theta}+\rho\dot{Q}=\rho C_e\ddot{\theta}+\beta T_0(\nabla.\ddot{\mathbf{u}}) \tag{28}$$

Here $\mathbf{u}$ is the displacement vector; θ is the temperature change with respect to the reference temperature T_0; $\mathbf{f}$ is the external force; and Q is the external rate of heat supply, both measured per unit mass; ρ is the mass density; C_e is the specific heat; λ and μ are the lame constants; $\beta=(3\lambda+2\mu)\alpha_t$; α_t being the coefficient of volume expansion.

The strain tensor $\mathbf{E}$ and the stress tensor $\mathbf{T}$ associated with $\mathbf{u}$ and θ are given by the following geometrical and constitutive relations, respectively, as

$$\mathbf{E}=\frac{1}{2}(\nabla\mathbf{u}+\nabla\mathbf{u}^T),$$
$$\mathbf{T}=\lambda(div\mathbf{u})\mathbf{I}+\mu(\nabla\mathbf{u}+\nabla\mathbf{u}^T)-\beta\theta\mathbf{I} \tag{29}$$

In all the above equations, the direct vector/tensor notation is employed. A superposed dot denotes the partial derivative with respect to the time variable t.

We suppose that the constants appearing in Eqs. (27) and (28) satisfy the inequalities:

$$\mu>0,\ \lambda+\mu>0,\ \rho>0,\ T_0>0,\ C_e>0,\ \beta>0,\ K_1>0,\ K_2>0$$

Then Eqs. (27) and (28) represent a fully hyperbolic system that permits finite speed for both elastic and thermal waves, which are coupled together in general.

In the problem of discussing a specific initial boundary value problem, it is convenient to rewrite the Eqs. (27–29) in non-dimensional form. For this we consider the transformations:

$$\mathbf{x}'=\frac{1}{l}\mathbf{x},\quad t'=\frac{v}{l}t,\quad \mathbf{u}'=\frac{\lambda+2\mu}{l\beta T_0}\mathbf{u},\quad \theta'=\frac{\theta}{T_0},\quad \mathbf{E}'=\frac{\lambda+2\mu}{\beta T_0}\mathbf{E},\quad \mathbf{T}'=\frac{1}{\beta T_0}\mathbf{T},$$
$$\mathbf{f}'=\frac{l(\lambda+2\mu)}{\beta T_0\rho v^2}\mathbf{f},\quad Q'=\frac{l}{\rho C_e v T_0}Q$$

Here l is a standard length and v is a standard speed.

Applying the above mentioned transformations and suppressing primes, Eqs. (27–29) can be recast in the following manner:

$$C_S^2\nabla^2\mathbf{u} + (C_P^2 - C_S^2)\nabla(div\mathbf{u}) - C_P^2\nabla\theta + \rho\mathbf{f} = \ddot{\mathbf{u}} \tag{30}$$

$$C_T^2\nabla^2\theta + C_D^2\nabla^2\dot{\theta} + \rho\dot{Q} = \ddot{\theta} + \epsilon(\nabla.\ddot{\mathbf{u}}) \tag{31}$$

$$\mathbf{E} = \frac{1}{2}(\nabla\mathbf{u} + \nabla\mathbf{u}^T)$$
$$\mathbf{T} = \left(1 - 2\frac{C_S^2}{C_P^2}\right)(div\mathbf{u})\mathbf{I} + \frac{C_S^2}{C_P^2}(\nabla\mathbf{u} + \nabla\mathbf{u}^T) - \theta\mathbf{I} \tag{32}$$

where $C_P^2 = \frac{\lambda+2\mu}{\rho v^2}$, $C_S^2 = \frac{\mu}{\rho v^2}$, $C_T^2 = \frac{T_0K_1}{\rho C_e v^2}$, $C_D^2 = \frac{K_2}{l\rho C_e v}$ and $\epsilon = \frac{\beta^2 T_0}{\rho C_e(\lambda+2\mu)}$.

Eqs. (30) and (31) represent the governing equations in coupled form for displacement and temperature fields. We observe that C_P and C_S, respectively, denote the speeds of purely elastic dilatational and shear waves. C_T represents the speed of the thermal waves without energy dissipation at finite deformation and C_D denotes the speed of the purely thermal waves in the material body. ϵ is the usual thermoelastic coupling parameter.

4.1.2. Statement of the problem:

Here we consider a homogeneous, isotropic unbounded thermoelastic medium and the conventional cylindrical polar coordinate system is adopted to characterise the position of the particles. With the assumption of axisymmetric condition, the non-dimensional governing equations, in absence of body forces, become

$$C_P^2\left(\nabla^2\phi - \theta\right) = \frac{\partial^2\phi}{\partial t^2} \tag{33}$$

$$\left(C_T^2 + C_D^2\frac{\partial}{\partial t}\right)\nabla^2\theta = \frac{\partial^2\theta}{\partial t^2} + \epsilon\frac{\partial^2}{\partial t^2}\left(\nabla^2\phi\right) - \rho\frac{\partial Q}{\partial t} \tag{34}$$

$$\sigma_r = \frac{1}{C_P^2}\frac{\partial^2\phi}{\partial t^2} - \frac{2}{r}\frac{C_S^2}{C_P^2}\frac{\partial\phi}{\partial r} \tag{35}$$

$$\sigma_\Phi = \frac{1}{C_P^2}\frac{\partial^2\phi}{\partial t^2} - \frac{2C_S^2}{C_P^2}\frac{\partial^2\phi}{\partial r^2} \tag{36}$$

where r is the radial distance measured from the axis of symmetry $(z - axis)$, ∇^2 is the Laplacian operator, ϕ is the thermoelastic potential, defined by

$$u = \frac{\partial\phi}{\partial r}.$$

In which u is the radial displacement, σ_r is the radial stress, σ_Φ is the circumferential stress.

Again we suppose that the medium was at rest in a undeformed and unstressed state at a uniform reference temperature. There was no body force acted upon the medium. The deformation occurred due to the presence of internal heat sources. The strength of the internal source of heat is given by

$$Q = \frac{Q_0}{r}\delta(r)H(t) \tag{37}$$

where $\delta(r)$ is the Dirac-delta function, $H(t)$ is the Heaviside unit step function and Q_0 is a constant.

4.1.3. Solution in integral transform domain:

Elimination of θ from Eqs. (33) and (34) gives

$$\left[\left(C_T^2 + C_D^2\frac{\partial}{\partial t}\right)C_P^2\nabla^4 - \left\{\left(C_T^2 + C_D^2\frac{\partial}{\partial t}\right) + (1+\epsilon)C_P^2\right\}\nabla^2\frac{\partial^2}{\partial t^2} + \frac{\partial^4}{\partial t^4}\right]\phi + C_P^2\rho\frac{\partial Q}{\partial t} = 0 \tag{38}$$

As, initially the medium was at rest with undeformed and unstressed state, so all the field functions satisfy homogeneous initial conditions. Taking Laplace transformation of the Eq. (38) under the homogeneous initial conditions we obtain

$$\left[\left(C_T^2 + C_D^2\, s\right)C_P^2\nabla^4 - \left\{\left(C_T^2 + C_D^2\, s\right) + (1+\epsilon)C_P^2\right\}s^2\nabla^2 + s^4\right]\bar{\phi} + \rho C_P^2\frac{Q_0}{r}\delta(r) = 0 \tag{39}$$

Here an over bar denotes the Laplace transformation of the field functions and s is the transform parameter.

Eq. (39) may be written in the following form:

$$\left(\nabla^2-\lambda_1^2\right)\left(\nabla^2-\lambda_2^2\right)\bar{\phi}=-\frac{Q_0\rho}{\left(C_T^2+C_D^2\,s\right)r}\delta(r) \tag{40}$$

where λ_1 and λ_2 are the roots of the bi-quadratic equation:

$$\lambda^4-\frac{s^2}{\left(C_T^2+C_D^2\,s\right)C_P^2}\left\{\left(C_T^2+C_D^2\,s\right)+(1+\epsilon)C_P^2\right\}\lambda^2+\frac{s^4}{\left(C_T^2+C_D^2\,s\right)C_P^2}=0 \tag{41}$$

Now, applying Hankel transformation in both sides of Eq. (40) we get

$$\left(\xi^2+\lambda_1^2\right)\left(\xi^2-\lambda_2^2\right)\tilde{\phi}=-\frac{Q_0\rho}{\left(C_T^2+C_D^2\,s\right)} \tag{42}$$

where

$$\tilde{\phi}(\xi,s)=H_0\left[\bar{\phi}(r,s);r\to\xi\right]=\int_0^\infty rJ_0(\xi r)\bar{\phi}(r,s)dr$$

in which J_0 is the Bessel function of 1st kind and of order zero.

Taking inverse Hankel transformation defined by

$$\bar{\phi}(r,s)=\int_0^\infty \xi J_0(\xi r)\tilde{\phi}(\xi,s)d\xi=H_0^{-1}\left[\tilde{\phi}(\xi,s);\xi\to r\right]$$

from Eq. (42) we obtain

$$\bar{\phi}(r,s)=\frac{Q_0\rho}{\left(C_T^2+C_D^2\,s\right)\left(\lambda_1^2-\lambda_2^2\right)}\left[K_0\left(\lambda_1 r\right)-K_0\left(\lambda_2 r\right)\right] \tag{43}$$

where $K_0(z)$ is the modified Bessel function of second kind and of order zero.

With the help of Eq. (43) from Eq. (33) we get

$$\bar{\theta}(r,s)=\frac{Q_0\rho}{\left(C_T^2+C_D^2\,s\right)\left(\lambda_1^2-\lambda_2^2\right)}\left[\left(\lambda_1^2-\frac{s^2}{C_P^2}\right)K_0\left(\lambda_1 r\right)-\left(\lambda_2^2-\frac{s^2}{C_P^2}\right)K_0\left(\lambda_2 r\right)\right] \tag{44}$$

and from Eqs. (35) and (36) we obtain the expressions of stresses in the Laplace transform domain

$$\bar{\sigma}_r(r,s)=\frac{Q_0\rho}{\left(C_T^2+C_D^2\,s\right)\left(\lambda_1^2-\lambda_2^2\right)}\sum_{\alpha=1}^{2}(-1)^{\alpha-1}\left[\frac{s^2}{C_P^2}K_0\left(\lambda_\alpha r\right)-\frac{2C_S^2}{C_P^2 r}\lambda_\alpha I_1\left(\lambda_\alpha r\right)\right] \tag{45}$$

$$\bar{\sigma}_\Phi(r,s)=\frac{Q_0\rho}{\left(C_T^2+C_D^2\,s\right)\left(\lambda_1^2-\lambda_2^2\right)}\sum_{\alpha=1}^{2}(-1)^{\alpha-1}\left[\left(\frac{s^2}{C_P^2}-\frac{2C_S^2}{C_P^2 r}\lambda_\alpha^2\right)K_0\left(\lambda_\alpha r\right)-\frac{2C_S^2}{C_P^2 r}\lambda_\alpha I_1\left(\lambda_\alpha r\right)\right] \tag{46}$$

where $I_1(z)$ denotes the modified Bessel function of 1st kind and of order one.

4.1.4. Special case:

Eqns. (44)–(46) represents the expressions of the temperature and stresses in the Laplace transform domain. Now, when there is no energy dissipating from the system i.e., $K_2=0$ we obtain the following exact solutions, in closed form, for θ, σ_r and σ_Φ :

$$\theta(r,t)=\frac{\rho Q_0 V_1^2 V_2^2}{C_T^2\left(V_1^2-V_2^2\right)}\sum_{\alpha=1}^{2}\left[(-1)^\alpha\left(\frac{1}{V_\alpha^2}-\frac{1}{C_P^2}\right)\left(t^2-\frac{r^2}{V_\alpha^2}\right)^{-1/2}H\left(t-\frac{r}{V_\alpha}\right)\right] \tag{47}$$

$$\sigma_r(r,t)=\frac{\rho Q_0 V_1^2 V_2^2}{C_T^2\left(V_1^2-V_2^2\right)}\sum_{\alpha=1}^{2}(-1)^\alpha\left[\frac{1}{C_P^2}\left(t^2-\frac{r^2}{V_\alpha^2}\right)^{-1/2}+\frac{2C_S^2}{C_P^2 r^2}\left(t^2-\frac{r^2}{V_\alpha^2}\right)^{1/2}\right]H\left(t-\frac{r}{V_\alpha}\right) \tag{48}$$

$$\sigma_\Phi(r,t)=\frac{\rho Q_0 V_1^2 V_2^2}{C_T^2\left(V_1^2-V_2^2\right)}\sum_{\alpha=1}^{2}(-1)^\alpha\left[\left(\frac{1}{C_P^2}-\frac{2C_S^2}{C_P^2 V_\alpha^2}\right)\left(t^2-\frac{r^2}{V_\alpha^2}\right)^{-1/2}-\frac{2C_S^2}{C_P^2 r^2}\left(t^2-\frac{r^2}{V_\alpha^2}\right)^{1/2}\right]H\left(t-\frac{r}{V_\alpha}\right) \tag{49}$$

where $V_\alpha=\frac{1}{\sqrt{2}}\left[\{C_T^2+(1+\epsilon)C_P^2\}+(-1)^{\alpha+1}\Delta\right]^{1/2}$ and

$\Delta=\left[\{C_T^2-(1+\epsilon)C_P^2\}^2+4\epsilon C_P^2 C_T^2\right]^{1/2}$

From the above expressions of temperature distribution and stress field it is observed that each of the solutions consist of two components corresponding to two distinct coupled waves propagating with the respective speeds V_1 and V_2. It is also noticed that the faster wave with speed V_1 is a predominantly elastic wave $(e-wave)$ or a predominantly thermal wave $(\theta-wave)$ according as $C_P > C_T$ or $C_P < C_P$. A Similar analysis holds for the slower wave with speed V_2 that is, elastic wave for $C_P < C_T$ and thermal wave for $C_P > C_T$.

4.2. Poroelastic solid

The theories of thermoelasticity as well as poroelasticity were established by Biot (1956a,b). He was very much aware of the isomorphism between thermoelastic continua and mechanics of porous media. Biot (1964) also shows that the theory of porous media applies immediately to thermoelasticity. Through the experimental study, Gurevich, Kelder and Smeulders (1999) confirms that the poroelasticity theory of Biot is adequate to describe the behaviour of porous material. There is another analogy, to translate the results from thermoelasticity in solving the problems of poroelasticity, in which the fluid pressure replaces the temperature and the relative fluid displacement is applied instead of the thermal displacement. In this section, the theory of Biot is adopted in a thermally conducting, isotropic porous solid saturated with a non-viscous fluid.

4.2.1. Governing equations:

The governing equations for isotropic thermally conducting fluid saturated porous medium is given by (in absence of body forces)

$$\mu\nabla^2\mathbf{u} + (\lambda+\mu+\alpha^2M)\nabla(div\mathbf{u}) + \alpha M\nabla(div\mathbf{w}) - \beta_s\nabla\theta = \rho\ddot{\mathbf{u}} + \rho_f\ddot{\mathbf{w}} \tag{50}$$

$$\alpha M\nabla(div\mathbf{u}) + M\nabla(div\mathbf{w}) - \beta_f\nabla\theta = \rho_f\ddot{\mathbf{u}} + q\ddot{\mathbf{w}} \tag{51}$$

$$T_0K_1\nabla^2\theta + K_2\nabla^2\dot{\theta} + \rho\dot{Q} = \rho C_e\ddot{\theta} + \beta T_0(\nabla.\ddot{\mathbf{u}} + \nabla.\ddot{\mathbf{w}}) \tag{52}$$

Here λ and μ are the Lame constants for porous medium; M is the elastic parameter for isotropic bulk coupling of fluid and solid particles; w_i denotes the component of the averaged fluid motion relative to solid frame and is defined as $w_i = f(U_i - u_i)$, in which f is the porosity of the solid, u_i and U_i are the displacement components in solid and fluid phases respectively. $\beta = \beta_s + \alpha\beta_f$; ρ and ρ_f are the densities of porous aggregate and pore-fluid respectively. q is the parameter represents inertial coupling between pore-fluid and solid matrix of porous aggregate.

As it was done in the previous section, the dimensionless form of the eqs. (50) - (52) are as follows:

$$C_S^2\nabla^2\mathbf{u} + (C_P^2 - C_S^2 + \alpha^2C_F^2)\nabla(div\mathbf{u}) + \alpha C_F^2\nabla(div\mathbf{w}) - \frac{\beta_s}{\beta}C_P^2\nabla\theta = \ddot{\mathbf{u}} + \frac{\rho_f}{\rho}\ddot{\mathbf{w}} \tag{53}$$

$$\alpha C_F^2\nabla(div\mathbf{u}) + C_F^2\nabla(div\mathbf{w}) - \frac{\beta_f}{\beta}C_P^2\nabla\theta = \frac{\rho_f}{\rho}\ddot{\mathbf{u}} + \frac{q}{\rho}\ddot{\mathbf{w}} \tag{54}$$

$$C_T^2\nabla^2\theta + C_D^2\nabla^2\dot{\theta} + \rho\dot{Q} = \ddot{\theta} + \epsilon(\nabla.\ddot{\mathbf{u}} + \nabla.\ddot{\mathbf{w}}) \tag{55}$$

where $C_F^2 = \frac{M}{\rho v^2}$.

Eqs. (53)–(55) represent the governing equations in coupled form of displacements of solid and fluid phases and the temperature field. C_F denotes the speed of the fluid motion relative to solid frame.

Similar to the previous section, due to axial-symmetric the above set of equations becomes;

$$\left(C_P^2 + (\alpha-f)\alpha C_F^2\right)\nabla^2\phi - \frac{\beta_s}{\beta}C_P^2\theta + f\alpha C_F^2\nabla^2\Phi = \left(1 - \frac{\rho_f}{\rho}f\right)\ddot{\phi} + f\frac{\rho_f}{\rho}\ddot{\Phi} \tag{56}$$

$$\left(\alpha - f\right)C_F^2\nabla^2\phi - \frac{\beta_s}{\beta}C_P^2\theta + fC_F^2\nabla^2\Phi = \left(\frac{\rho_f}{\rho} - \frac{q}{\rho}f\right)\ddot{\phi} + f\frac{q}{\rho}\ddot{\Phi} \tag{57}$$

$$\left(C_T^2 + C_D^2\frac{\partial}{\partial t}\right)\nabla^2\theta = \frac{\partial^2\theta}{\partial t^2} + \epsilon\frac{\partial^2}{\partial t^2}\left((1-f)\nabla^2\phi - f\nabla^2\Phi\right) - \rho\frac{\partial Q}{\partial t} \tag{58}$$

where r is the radial distance measured from the axis of symmetry $(z-axis)$, ∇^2 is the Laplacian operator, ϕ is the thermoelastic potential, defined by

$$u = \frac{\partial\phi}{\partial r}.$$

In which u is the radial displacement, and Φ is the potential function for fluid motion over the solid such that

$$U = \frac{\partial\Phi}{\partial r}.$$

Now from the eqs. (56) - (58) we obtain,

$$\left(A\nabla^6 + B\nabla^4 + C\nabla^2 + D\right)\phi = \left[\left\{fC_F^2\nabla^2 - \frac{q}{\rho}f\frac{\partial^2}{\partial t^2}\right\}\left\{f\alpha C_F^2\nabla^2 - \frac{\rho_f}{\rho}f\frac{\partial^2}{\partial t^2}\right\} - \frac{\beta_s\beta_f}{\beta^2}C_P^4\right]\rho\frac{\partial Q}{\partial t} \tag{59}$$

where

$$\begin{aligned}
A &= f\alpha C_F^4(\alpha - f)\left(C_D^2\frac{\partial}{\partial t} - C_T^2\right)\\
B &= C_F^2(\alpha - f)\left\{\frac{\rho_f}{\rho}f\left(C_T^2 - C_D^2\frac{\partial}{\partial t}\right)\frac{\partial^2}{\partial t^2} + f\left(\alpha C_F^2 + \frac{\beta_s}{\beta}\epsilon C_P^2\right)\frac{\partial^2}{\partial t^2}\right\} + f\alpha C_F^2\left(\frac{\rho_f}{\rho} - \frac{q}{\rho}f\right)\left(C_T^2 - C_D^2\frac{\partial}{\partial t}\right)\frac{\partial^2}{\partial t^2}\\
&\quad - fC_P^2C_F^2\epsilon(1-f)\left(\frac{\beta_s}{\beta} - \alpha\frac{\beta_f}{\beta}\right)\frac{\partial^2}{\partial t^2}\\
C &= \epsilon f(1-f)\left(\frac{q\beta_s}{\rho\beta} - \frac{\rho_f\beta_f}{\rho\beta}\frac{\partial^4}{\partial t^4}\right)\left(\frac{\rho_f}{\rho} - f\frac{q}{\rho}\right)\left\{f\frac{\rho_f}{\rho}\left(C_T^2 - C_D^2\frac{\partial}{\partial t}\right)\frac{\partial^2}{\partial t^2} - f\alpha C_F^2\frac{\partial^2}{\partial t^2} - f\epsilon C_P^2\frac{\beta_s}{\beta}\frac{\partial^2}{\partial t^2}\right\}\frac{\partial^2}{\partial t^2}\\
&\quad - fC_F^2\frac{\rho_f}{\rho}(\alpha - f)\frac{\partial^2}{\partial t^2}\\
D &= f\frac{\rho_f}{\rho}\left(\frac{\rho_f}{\rho} - f\frac{q}{\rho}\right)\frac{\partial^4}{\partial t^4}
\end{aligned}$$

This gives the governing equation for ϕ. Once ϕ is determined by solving this equation (with appropriate boundary conditions), then u, U and θ are follows from the eqs. (56) - (58).

4.2.2. Solution of the problem:

We suppose that initially the porous medium was at rest in an unstressed and unstrained state at a uniform reference temperature T_0. Also, we consider the strength of the heat source is given by

$$Q = \frac{Q_0}{r}\delta(r)H(t) \tag{60}$$

Now employing Laplace transformation with respect to the time variable t and after some mathematical manipulations eqs. (56) - (59) yields

$$\begin{aligned}
\bar{\phi}(r,s) &= Q_0\Big[A_3K_0(\lambda_3 r) + A_4K_0(\lambda_4 r) + A_5K_0(\lambda_5 r)\Big]\\
\bar{\Phi}(r,s) &= Q_0V\Big[A_3K_0(\lambda_3 r) + A_4K_0(\lambda_4 r) + A_5K_0(\lambda_5 r)\Big]\\
\bar{\theta}(r,s) &= Q_0\frac{\beta}{\beta_f C_P^2}\sum_{i=3}^{5}A_i\Big[\Big\{\alpha - (V-1)f\Big\}C_F^2\frac{1-\lambda_i}{r}K_1(\lambda_i r) + \Big\{\Big(\alpha - (V-1)f\Big)\lambda_3C_F^2 - \Big(\frac{\rho_f}{\rho} - (V-1)\frac{q}{\rho}\Big)s^2\Big\}K_0(\lambda_i r)\Big]
\end{aligned} \tag{61}$$

In which

$$\begin{aligned}
A_3 &= \frac{-1}{\left(\lambda_3^2 - \lambda_4^2\right)\left(\lambda_3^2 - \lambda_5^2\right)}\Big[\Big(\rho_f\beta_f - q\beta_s\Big)s^2 - \rho\lambda_3^2C_F^2\Big(\alpha\beta_f - \beta_s\Big)\Big]\frac{f}{\beta}C_P^2\\
A_4 &= \frac{-1}{\left(\lambda_3^2 - \lambda_4^2\right)\left(\lambda_3^2 - \lambda_5^2\right)}\Big[\Big(\rho_f\beta_f - q\beta_s\Big)s^2 - \rho\lambda_4^2C_F^2\Big(\alpha\beta_f - \beta_s\Big)\Big]\frac{f}{\beta}C_P^2\\
A_5 &= \frac{-1}{\left(\lambda_3^2 - \lambda_4^2\right)\left(\lambda_3^2 - \lambda_5^2\right)}\Big[\Big(\rho_f\beta_f - q\beta_s\Big)s^2 - \rho\lambda_5^2C_F^2\Big(\alpha\beta_f - \beta_s\Big)\Big]\frac{f}{\beta}C_P^2
\end{aligned}$$

$$V = \frac{C_P^2 + (\alpha - f)(\alpha - 1)C_F^2}{f(1-\alpha)C_F^2}$$

and λ_i^2 $(i = 3, 4, 5)$ are the roots of the equation

$$\bar{A}\lambda^6 + \bar{B}\lambda^4 + \bar{C}\lambda^2 + \bar{D} = 0 \tag{62}$$

The roots are given by

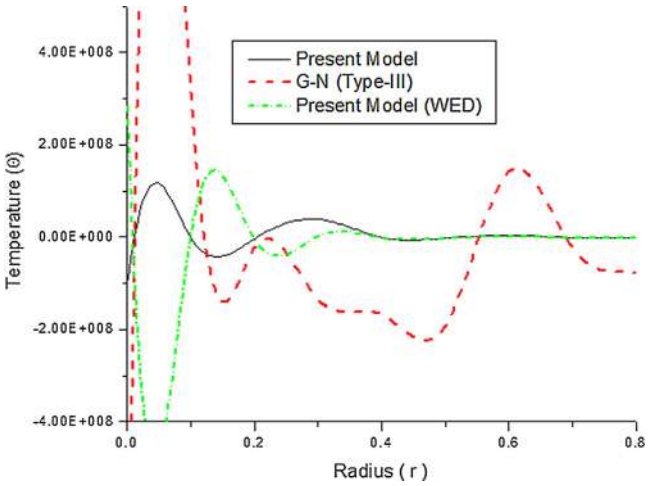

Fig. 1. Temperature distribution near the source of heat at $t = 0.25$.

$$\lambda_3^2 = \frac{1}{3}\left(2\bar{P}\sin(\bar{Q}) + \bar{A}\right)$$
$$\lambda_4^2 = -\frac{\bar{P}}{3}\left(\sqrt{3}\cos(\bar{Q}) + \sin(\bar{P})\right) + \frac{\bar{A}}{3}$$
$$\lambda_5^2 = \frac{\bar{P}}{3}\left(\sqrt{3}\cos(\bar{Q}) - \sin(\bar{P})\right) + \frac{\bar{A}}{3} \tag{63}$$

where
$\bar{P} = \frac{\sqrt{\bar{B}^2 - 3\bar{A}\bar{C}}}{\bar{A}}$, $\bar{Q} = \frac{1}{3}\sin^{-1}(\bar{R})$ and $\bar{R} = -\frac{2\bar{B}^3 - 9\bar{A}\bar{B}\bar{C} + 27\bar{A}^2\bar{D}}{2\sqrt{2}\bar{A}^3\bar{P}^3}$.

4.2.3. Numerical simulations:

With the view of illustrating the theoretical results obtained in the preceding sections and comparing those obtained in the context of Green-Naghdi (GN Type-III) (Green and Naghdi, 1993) model of generalized thermoelasticity theory, here in this section we now present some numerical simulating results on both elastic as well as poroelastic solids.

Isotropic elastic solid

To investigate the characteristics of the energetic and dissipative heat fluxes in solids, a quantitative example is set up. The medium is assumed to be made out of a material with the following properties: (i) Excellent heat conductivity, (ii) Excellent electric conductivity, (iii) Good corrosion resistance, (iv) Good machinability and (v) Retention of mechanical and electrical properties of cryogenic temperature. For numerical simulation, the copper type material is considered with the following physical data values:

$$\lambda = 77.6\ GPa, \quad \mu = 38.6\ GPa, \quad \alpha_t = 1.78 \times 10^{-5} m.K^{-1}, \quad \rho = 8945 Kg.m^{-3},$$
$$C_e = 381\ J.Kg^{-1}.K^{-1}, \quad K_1 = 300\ W.m^{-2}.K^{-2}, \quad K_2 = 400\ W.m^{-1}.K^{-1}, \quad T_0 = 298\ K.$$

Further we assume, $l = 1$ m, $v = 7.7 m.s^{-1}$ and $Q_0 = 1$.

In Fig. 1 we illustrate the nature of the temperature distribution in the vicinity of the source of heat applied. A comparison is made with the present analysis, proposed model including without energy dissipation (WED) and the Green-Naghdi Type-III model. Figs. 2–5 represent the variation of radial and hoop stresses near the applied heat source. In addition, comparisons are also made with the results obtained in absence of energy dissipation from the system. These plots were obtained maintaining all the parameters constant at the reference values above, expect the radial distance r that varies in predefined increments.

From Fig. 1, we note that, as expected, the temperature profiles of the proposed model, without energy dissipation theory and Green-Naghdi model are largely different. In Green-Naghdi theory as well as without energy dissipation cases the amplitudes of the temperature profile are abruptly very high near the origin. But, if both the heat fluxes are taken into account then we found a smooth wave form of the temperature. Thus, Green-Naghdi model and without energy dissipation theory of generalized thermoelasticity are not well appropriate in the vicinity of the applied heat source. Therefore, in order to obtain more accurate information about the temperature distribution into the solids in high temperature region we shall have to adopt both the aforementioned heat fluxes.

We also observe that the large temperature oscillation amplitude (as well as the corresponding heat fluxes) should be discarded because they violate the linearisation approximations. It is also of interest to note the physical principle of the energetic heat flux through the asymptotic behaviour of the material properties. (i) when $K_2 \to 0$, i.e. dissipative heat flux

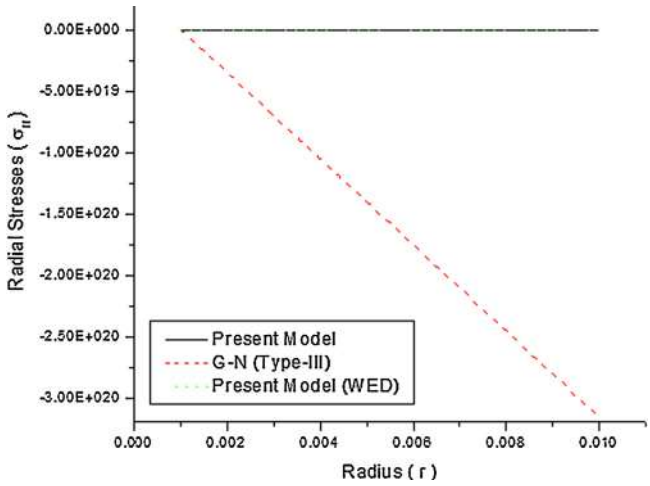

Fig. 2. Variation of radial stress near the source of heat at $t = 0.25$.

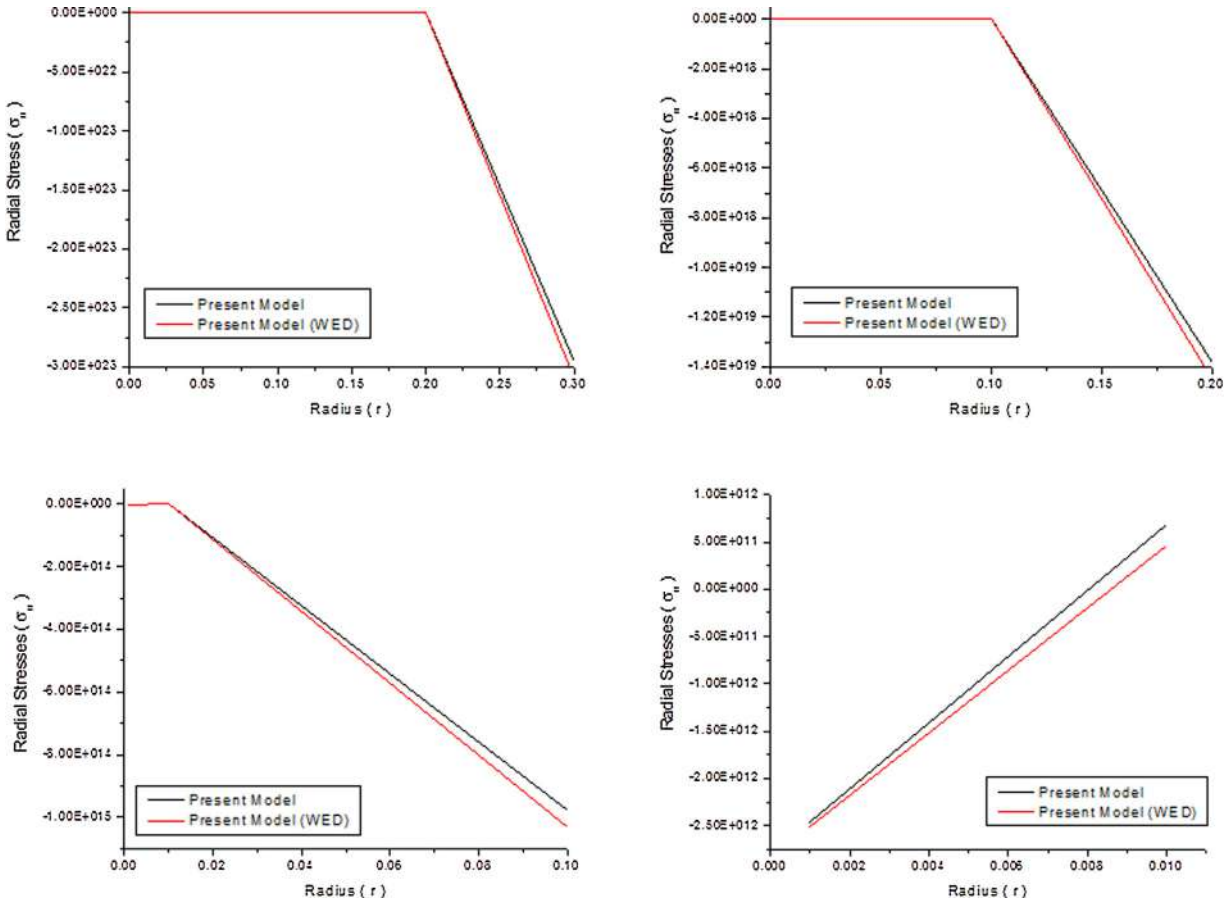

Fig. 3. Comparison of radial stresses for with (without) energy dissipation at $t = 0.25$.

is discarded, which gives the highest heat flux possible and consequently very large amplitude of the temperature profile. On the other hand (*ii*) when $K_2 \to \infty$, Eq. (28) shows that the amplitude of the temperature oscillation $\theta \to 0$ and $\mathbf{q}_E = \mathbf{0}$.

From the Eq. (19) it is clear that the energetic heat flux depends upon the material parameters β_{ij}, ρ, C_e and K_2. This relation suggest that it could be possible, in principle, to select the material properties and forcing conditions (input frequency) that produce large variation of the energetic heat fluxes. It is envisioned that the specific material properties could be properly tailored by engineering so to obtain desired heat flux performance.

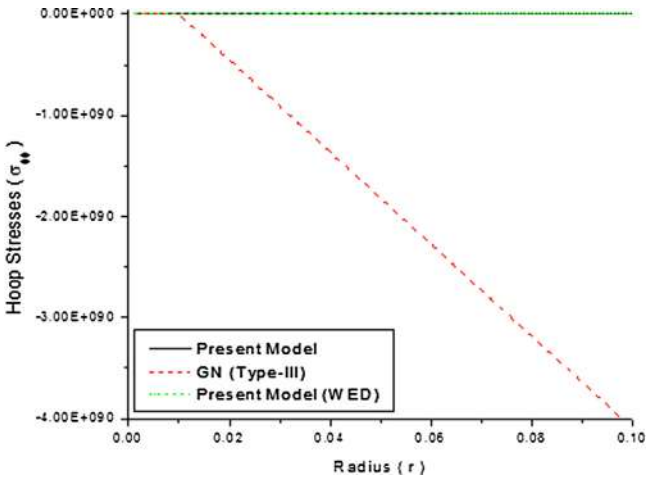

Fig. 4. Variation of hoop stress near the source of heat at $t = 0.25$.

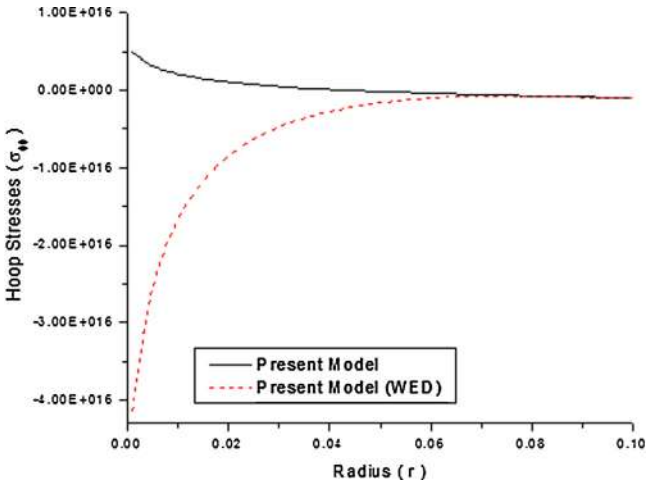

Fig. 5. Comparison of hoop stresses for with (without) energy dissipation at $t = 0.25$.

From Figs. 2 and 3, it is observed that the radial stress is decaying very rapidly with the distance from the origin. But there is a significant difference in stress profile with Green-Naghdi model. In Green-Naghdi model the generated stresses are started to decay from very first point, but the stresses due to the proposed model are increasing initially and then start to decay as distance goes. Moreover, in presence of the dissipative heat fluxes the produced stresses in the medium, in principle, should have been lesser. This phenomenon over stress distribution is confirmed by the Fig. 3.

Similar type of stress profiles are shown in hoop stresses (see Fig. 4) as it was observed in radial stress. Form Fig. 5, it is evident that impact of heat fluxes on the tangential stresses is energetic in the low-frequency region (i.e. far from the applied heat source) and predominantly dissipative at high frequency range.

Poroelastic Solid:

The effect of the heat fluxes upon the temperature distribution in a specific model of porous medium is considered here. A liquid-saturated reservoir rock (North-sea Sandstone) is chosen for the numerical computation purpose. The values of the elastic and dynamical constants for the porous rock are taken from the anisotropic constants in Rasolofosaon and Zinszner (2002). Those are given by,

$$\lambda = 3.7\ GPa, \quad \mu = 7.9\ GPa, \quad M = 6\ GPa, \quad \alpha = 0.4, \quad \rho = 2216 Kg.m^{-3}, \quad f = 0.16$$

The saturating fluid is assumed with the density $\rho_f = 950$ Kg.m^{-3} and $q = 1.05\frac{\rho_f}{f}$.

The numerical values

$$C_e = 381\ J.Kg^{-1}.K^{-1}, \quad K_1 = 150\ W.m^{-2}.K^{-2}, \quad K_2 = 170\ W.m^{-1}.K^{-1}, \quad T_0 = 298\ K,$$
$$\beta_f = 2.37 \times 10^{-3} GPa.K^{-1}, \quad \beta_s = 2\beta_f$$

define the thermoelastic characteristics of the porous aggregate.

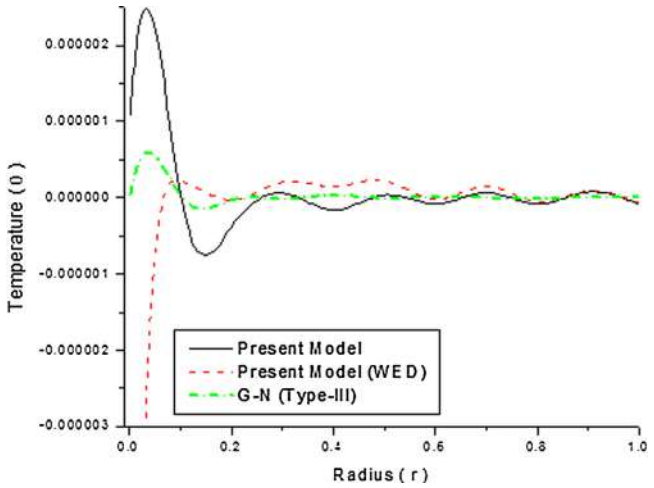

Fig. 6. Temperature distribution in poroelastic solid near the source of heat at $t = 0.25$.

In addition we consider, the characteristic length $l = 1$ m, to make the speed (non-dimensional) of the elastic dilatation wave $C_P = 1$ we assume $\nu = 7.7$ m.s^{-1} and the strength of the heat source $Q_0 = 1$.

In general, the thermal conductivity of a porous medium in a complex fashion on the geometry of the medium. In the case of a liquid-saturated porous medium temperature slip occurs in the fluid at the pore boundaries. In these circumstances one could expect that the fluid conductivity would tend to zero. Then in the case of external heating the heat would be be conducted almost entirely through the solid matrix. For internal heating in the fluid, the situation is reversed as the fluid phase becomes thermally isolated from the solid phase.

Thus the motion-induced heat fluxes are nominal and the average heat transfer occurred due to the dissipative heat fluxes. For this reason, the temperature profile for without energy dissipation is very low initially and the present model gives a high note near the heat sources (Fig. 6). Whereas, Green-naghdi model gives a moderate temperature distribution.

5. Conclusion

In this article, a spatial form of a coupled thermoelasticity theory at finite strain is proposed in thermodynamically consistent manner. Based on the Fourier's law of heat conduction, the overall heat flux is decomposed into two components: one is due to the motion of the particles (motion-induced heat fluxes) and other one for dissipation of heat energy. The domain of dependence inequality for the solution of the proposed dynamical thermoelastic problem is proved successfully. The linearised form of this newly developed theory at finite stain is applied in isotropic as well as poroelastic solids and the salient features are emphasized in throughout the application section. It has been observed that, in order to obtain more precise information about the temperature profile in solids (specially near the heat sources) both the heat fluxes are very much required. The energetic and dissipative heat fluxes have a great impact on stress distribution in solids. The stress profile is influenced by energetic heat transfer in the low-frequency region and predominantly dissipative at high frequency range.

In addition, a quantitative results have shown that the two characteristic thermoelastic modes can transfer a significant amount of heat. unlike in gases where de-phasing between the velocity and temperature oscillations is usually achieved by heat exchange with a thermal reservoir, in solids that effect is enabled due to thermal conduction. In fact, a large amount of heat flux may be obtained after certain combinations of material properties and input frequency.

References

Biot, M. A. (1956). Theory of propagation of elastic waves in a fluidsaturated porous solid. I. Lowfrequency range. *The Journal of the Acoustical Society of America, 28*(2), 168–178. doi:10.1121/1.1908239.

Biot, M. A. (1956). Thermoelasticity and irreversible thermodynamics. *Journal of Applied Physics, 27*(3), 240–253.

Biot, M. A. (1964). Theory of buckling of a porous slab and its thermoelastic analogy. *Journal of Applied Mechanics, 31*(2), 194–198. doi:10.1115/1.3629586. https://asmedigitalcollection.asme.org/appliedmechanics/article-pdf/31/2/194/5446030/194_1.pdf

Cattaneo, C. (1958). Sur une forme de l'equation de la chaleur eliminant le paradoxe d'ure propagation instantanee. *Comptes Rendus Mathematique, 2*, 431–433.

Coker, E. G., & Filon, L. N. G. (1931). *A treatise on photo-elasticity* p. 695-711. Cambridge: Cambridge University Press. Bibliography

Darijani, H., & Naghdabadi, R. (2010). Constitutive modeling of solids at finite deformation using a second-order stress–strain relation. *International Journal of Engineering Science, 48*(2), 223–236.

Garrett, S. L. (2004). Resource letter: Ta-1: Thermoacoustic engines and refrigerators. *American Journal of Physics, 72*(1), 11–17. doi:10.1119/1.1621034.

Green, A. E., & Lindsay, K. A. (1972). Thermoelasticity. *Journal of Elasticity, 2*(1), 1–7.

Green, A. E., & Naghdi, P. M. (1991). A re-examination of the basic postulates of thermomechanics. *Proceedings of the Royal Society of London A: Mathematical, Physical and Engineering Sciences, 432*(1885), 171–194. doi:10.1098/rspa.1991.0012. http://rspa.royalsocietypublishing.org/content/432/1885/171.full.pdf

Green, A. E., & Naghdi, P. M. (1992). On undamped heat waves in an elastic solid. *Journal of Thermal Stresses, 15*(2), 253–264. doi:10.1080/01495739208946136.
Green, A. E., & Naghdi, P. M. (1993). Thermoelasticity without energy dissipation. *Journal of Elasticity, 31*(3), 189–208. doi:10.1007/BF00044969.
Gurevich, B., Kelder, O., & Smeulders, D. M. J. (1999). Validation of the slow compressional wave in porous media: Comparison of experiments and numerical simulations. *Transport in Porous Media, 36*(2), 149–160. doi:10.1023/A:1006676801197.
Imam, A., & Johnson, G. (1998). Decomposition of the deformation gradient in thermoelasticity. *Journal of Applied Mechanics, 65*(2), 362–366.
Lee, E. H. (1969). *Elastic-plastic deformation at finite strains* (Vol. 36, pp. 1–6). ASME.
Lord, H. W., & Shulman, Y. (1967). A generalized dynamical theory of thermoelasticity. *Journal of the Mechanics and Physics of Solids, 15*(5), 299–309.
Lubarda, V. A. (2004). Constitutive theories based on the multiplicative decomposition of deformation gradient: Thermoelasticity, elastoplasticity, and biomechanics. *Applied Mechanics Reviews, 57*(2), 95–108.
Murnaghan, F. D. (1937). Finite deformations of an elastic solid. *American Journal of Mathematics, 59*(2), 235–260.
Rasolofosaon, P. N. J., & Zinszner, B. E. (2002). Comparison between permeability anisotropy and elasticity anisotropy of reservoir rocks. *Geophysics, 67*(1), 230–240. doi:10.1190/1.1451647.
Seth, B. (1935). Finite strain in elastic problems. *Philosophical Transactions of the Royal Society of London. Series A, Mathematical and Physical Sciences, 234*(738), 231–264.
Swift, G. W. (1988). Thermoacoustic engines. *The Journal of the Acoustical Society of America, 84*(4), 1145–1180. doi:10.1121/1.396617.
Wheatley, J., Hofler, T., Swift, G. W., & Migliori, A. (1985). Understanding some simple phenomena in thermoacoustics with applications to acoustical heat engines. *American Journal of Physics, 53*(2), 147–162. doi:10.1119/1.14100.

Source details

Feedback > Compare sources >

International Journal of Engineering Science

Incorporating: LETTERS IN APPLIED AND ENGNG. SCIENCES

Scopus coverage years: from 1963 to Present

Publisher: Elsevier

ISSN: 0020-7225

Subject area: Engineering: Mechanical Engineering | Engineering: General Engineering | Engineering: Mechanics of Materials | Materials Science: General Materials Science

Source type: Journal

View all documents > | Set document alert | Save to source list

CiteScore 2022
12.8

SJR 2022
2.082

SNIP 2022
1.849

CiteScore | CiteScore rank & trend | Scopus content coverage

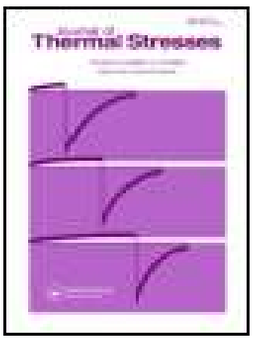

Journal of Thermal Stresses

ISSN: 0149-5739 (Print) 1521-074X (Online) Journal homepage: http://www.tandfonline.com/loi/uths20

Memory response on thermal wave propagation emanating from a cavity in an unbounded elastic solid

Santanu Banerjee, Soumen Shaw & Basudeb Mukhopadhyay

To cite this article: Santanu Banerjee, Soumen Shaw & Basudeb Mukhopadhyay (2018): Memory response on thermal wave propagation emanating from a cavity in an unbounded elastic solid, Journal of Thermal Stresses, DOI: 10.1080/01495739.2018.1461041

To link to this article: https://doi.org/10.1080/01495739.2018.1461041

Published online: 20 Jun 2018.

JOURNAL OF THERMAL STRESSES
https://doi.org/10.1080/01495739.2018.1461041

Taylor & Francis
Taylor & Francis Group

Memory response on thermal wave propagation emanating from a cavity in an unbounded elastic solid

Santanu Banerjee, Soumen Shaw, and Basudeb Mukhopadhyay

Department of Mathematics, Indian Institute of Engineering Science and Technology, Shibpur, West Bengal, India

ABSTRACT

The present paper deals with the thermal memory response of wave propagation in an unbounded, homogeneous, isotropic elastic body, emanating from a spherical cavity. To analyze the memory response, the generalized heat conduction model with the fractional order as well as memory-dependent-derivatives (MDDs) concepts are considered. The solution space is obtained in Laplace transform domain by using the eigenfunction expansion method to the vector-matrix form of the corresponding governing equations. Finally, a comparison study is furnished for thermal displacement, stresses, and temperature changes in the space-time domain and is presented graphically.

ARTICLE HISTORY
Received 7 February 2018
Accepted 2 April 2018

KEYWORDS
Eigenvalue approach; fractional derivative; generalized thermoelasticity; memory dependent derivatives; spherical symmetry

AMS SUBJECT CLASSIFICATION (2010)
65M; 74F; 74S; 80A

Introduction

Improving various shortcomings of classical uncoupled thermoelasticity theory, Biot [1] developed the coupled theory of thermoelasticity by assuming that the elastic deformations are depended on the temperature changes and vice-versa. Admitting this coupled theory of thermoelasticity, several works have been carried out on the mechanical wave propagation in an elastic medium while neglecting the interaction between coupled plasma and thermal effect. The physical observations and results considered the infinite speed for propagation of thermal waves. Experimental studies revealed that the conventional theory of thermoelasticity fails to be a suitable model in problems involving very large heat fluxes in short intervals of time. The relaxation time in thermal wave propagation plays a significant role in problems involving shock wave propagation, laser techniques, a rapidly propagating crack tip, etc. So to incorporate a thermal time delay into the thermoelastic theory, the development of a hyperbolic type heat conduction equation became essential. The first such change contrasting the conventional theory of thermoelasticity was due to Cattaneo [2], he derived a wave type heat equation by developing a new law of heat conduction replacing the classical Fourier's law. Later on, Lord-Shulman [3] and Green-Lindsay [4] brought into light the theories of generalized thermoelasticity considering hyperbolic type heat equation, which are based upon a modified thermomechanical inequality, admitting finite speed of thermal signals in elastic solids. The generalizations proposed by the Lord-Shulman theory and the Green-Lindsay theory involve one and two relaxation time parameters (respectively) in the heat flux-temperature gradient relaxation. Such generalized theories have aroused much interest during the last few decades and have many applications in several fields of applied sciences and mathematics, viz. modern engineering, earthquake prediction, soil dynamics, mineral exploration, etc.

CONTACT Santanu Banerjee santanubandopadhyay@gmail.com Department of Mathematics, Indian Institute of Engineering Science and Technology, Shibpur, West Bengal, India.
Color versions of one or more of the figures in the article can be found online at www.tandfonline.com/uths.

In recent years fractional calculus has been of tremendous use in applied mathematical and engineering problems. Oldham and Spanier [5] were the first to introduce the subject in book level. Later on Miller and Rose [6], Podlubny [7] were instrumental in developing the subject in solving fractional differential equations. Abel was probably the first to use fractional calculus for modifying and solving the existing mathematical model of a physical problem. He used fractional derivatives and integrals to obtain the solution of an integral equation in the Tautochrone problem. Since then many mathematicians have tried to link fractional calculus with existing models of physical processes.

It is an established fact that the next state of a physical system not only depends upon its present state but also on all of its historical states. Thus, in some recent studies fractional ordered derivatives come into account more frequently than integer ordered derivatives in various physical problems. This is because the integer ordered differential operator is a local operator whereas the fractional ordered differential operator is non-local. The non-local nature of the fractional derivative establishes its somewhat memory dependent nature, which is a more realistic fitting to the real world physical problems.

In the past few decades, various modifications and new extensions to the definitions of fractional ordered derivatives have become a topic of interest among many researchers. In various problems of thermoelasticity, instead of instantaneous response to physical stimuli, a retarded response suffices to be much more realistic. Thus the introduction of fractional ordered derivatives into several models of thermoelasticity comes into account. Caputo and Mainardi [8,9] have studied and found an agreement with the experimental and theoretical results. Recently, Ezzat et al. [10] and Sherief et al. [11] have introduced and developed the analytical studies on fractional ordered heat conduction equation in different coupled thermoelastic problems of solid mechanics. So far several mathematical algorithms and methods have been devised to solve time-fractional partial differential equations. Among other methods, in recent problems Ghosh-Kanoria [12], Shaw [13], and Bera et al. [14] have incorporated the eigenvalue approach to solve different spherical cavity problems in thermoelasticity.

In the present paper Caputo type fractional derivatives are considered. If we consider thermal diffusion using the Caputo and Riesz-Feller derivatives, the fractional index 'α' in the time derivative is related to memory whereas the fractional index in the space derivative is related to (extreme) non-locality in space. Here, we employ the theory formulated by Sherief et al. [11] to study spherically symmetric thermoelastic waves in a homogeneous and isotropic unbounded solid body containing a spherical cavity. We assume that the waves are generated due to the application of a constant step in temperature on the boundary of the cavity which is held in a stress-free state. Adopting the Laplace transform technique the governing equations are recast in the form of a vector matrix differential equation in the spherical polar coordinate system. The vector-matrix differential equation is then solved by an eigenvalue approach in the Laplace transform domain. Thermal displacement and temperature changes are depicted in various numerically computed figures with its memory.

Mathematical preliminaries

Till date several versions and modifications of the fractional derivative of order $\alpha > 0$, have been defined. The two most widely used versions are the Riemann-Liouville and Caputo sense, where both the definitions use Riemann-Liouville fractional integral and derivatives of the whole order.

Consider a function of two-variables $u(x, y)$. The Riemann-Liouville fractional partial integration of order ν with respect to x is defined as

$$D_x^{-\nu}u(x,y) = \frac{1}{\Gamma(\nu)}\int_0^x (x-\xi)^{\nu-1}u(\xi,y)\partial\xi, \qquad x > 0, 0 < \nu \leq 1,$$

and the Riemann-Loiuville fractional partial derivative of order α with respect to x is defined as

$$D_x^{\alpha}u(x,y)=\frac{\partial^m}{\partial x^m}D_x^{-m-\alpha}u(x,y),\qquad x>0,0<\alpha\le 1,$$

where m is a positive integer such that $m-1<\alpha\le m$.

The basic difference between the definitions is that in the Caputos definition we first compute the derivative followed by an integral whereas in Riemann-Liouvilles definition the computation is reversed. Therefore, in an initial value problem the Caputo fractional derivative operator permits the initial conditions in terms of integer ordered derivatives, but the Riemann-Liouville fractional derivative operator permits the initial conditions in terms of fractional integrals and their derivatives. In case of homogeneous initial condition, these two operators coincide. Hence for boundary value problems the most suited and widely used version of the fractional derivative is that of Caputo.

In the book of Diethelm [15], the kernel in Caputo definition has been modified into a generalized kernel form $K_{\alpha}(x-\xi)$ as follows,

$$D_a^{\alpha}u(x,y)=\int_a^x K_{\alpha}(x-\xi)\frac{\partial^m}{\partial\xi^m}u(\xi,y)\partial\xi,\qquad x>0,0<\alpha\le 1 \tag{1}$$

In 2011, Wang-Li [16] further modified and incorporated a time delay factor ω, into the definition as follows,

$$D_{\omega}^{(1)}u(x,t)=\frac{1}{\omega}\int_{t-\omega}^{t}K(t-\xi)u'(x,\xi)\partial\xi \tag{2}$$

The above modifications to the fractional derivatives introduced a new class of fractional derivatives, termed as memory dependent derivatives (MDD). Throughout this paper, for normal fractional derivatives, we shall use the definition in Caputo sense and the following definition in case of MDD.

The α order MDD of the function $f(t)$ relative to the time delay $\omega>0$ will be defined as

$$D_{\omega}^{\alpha}f(t)=\frac{1}{\omega}\int_{t-\omega}^{t}k(t,p)f^{(\alpha)}(p)dp \tag{3}$$

where $f^{(\alpha)}$ denotes the α^{th} order derivative of $f(t)$. In our problem, we shall consider the constant form of the kernel as $k(t,p)=1$.

Taking the Laplace transform of the MDD considering $k(t,p)=1$ we get,

$$L\left[D_{\omega}f(t)\right]=\frac{1}{\omega}(1-e^{-\omega s})\bar{f}(s) \tag{4}$$

where $\bar{f}(s)$ denotes the Laplace transform of $f(t)$ and $f(t-\omega)=0$ for $t<\omega$.

Fractional calculus in generalized thermoelasticity theory

For the past few years, fractional calculus has been successfully combined in several modified theories of generalized thermoelasticity by many researchers. In the year 2010, Sherief et al. [11], Youssef [16], and Ezzat [17] gave different modifications to the generalized theory of thermoelasticity by introducing fractional calculus into the thermoelastic models in their own manner. Sherief et al. developed a thermoelastic model by using fractional ordered derivatives in it. In his paper, he proved a uniqueness theorem and derived a variational principle and reciprocity theorem. Youssef used the Riemann-Liouville fractional integral operator to formulate a generalized heat conduction model. Similar to Sherief et al. he also proved a uniqueness theorem and further solved a one-dimensional problem. Ezzat, on the other hand, utilized the Taylors series expansion of time fractional order and gave a generalization to Fourier's law of heat conduction.

In the following year 2011, El-Karmany and Ezzat [18] developed a two temperature fractional order model for nonhomogeneous anisotropic elastic bodies. Ezzat and Fayik [19] introduced

another fractional order thermoelastic theory for elastic solids and proved an uniqueness and reciprocity theorem. Shaw and Mukhopadhyay [20] derived a new generalized theory of fractional micropolar thermoelasticity. Ezzat et al. [10] developed the field equations three-phase lag fractional model in linear thermoelasticity using time-fractional derivatives.

In recent works, many researchers contributed much to the theory of fractional order thermoelasticity and used the new theories to study various problems of fractional order, some of which can be found in the references [21–26]. Among them, Youssef [27] introduced a new modification to Duhamel-Newmanns stress-strain relation by developing a new thermoelastic theory with fractional order strain in it. Further, he proposed a generalized system that can govern seven different thermoelastic models. Shaw and Mukhopadhyay [28] introduced a new theory of fractional-ordered thermoelastic diffusion based upon the fractional Taylor series and fractional divergence theorem. In their work, they replaced the integer-order Taylor series approximation for flux with the fractional-order Taylor series approximation which eventually has removed the restriction that the flux has to be linear, or piece-wise linear and also the restriction that the control volume must be infinitesimal.

Below we provide a list of few models that may seem to prove instrumental in some recent and probable future developments of fractional thermoelasticity theory.

Heat conduction equation in Sherief's model of fractional order generalized thermoelasticity [10]:

$$q_i + \tau_0 \frac{\partial^\alpha}{\partial t^\alpha} q_i = -k_{ij} T_{,j} \qquad 0 < \alpha \leq 1$$

Heat conduction equation in Youssef's model of fractional order generalized thermoelasticity [16]:

$$q_i + \tau_0 \frac{\partial}{\partial t} q_i = -k_{ij} D^{-(\alpha-1)} T_{,j} \qquad 0 < \alpha \leq 2$$

Heat conduction equation in Ezzat's model of fractional order generalized thermoelasticity [17]:

$$q_i + \frac{\tau_0}{\Gamma(\alpha+1)} \frac{\partial^\alpha}{\partial t^\alpha} q_i = -k_{ij} T_{,j} \qquad 0 < \alpha \leq 1$$

The equation of mass flux vector in Ezzat and Fayik's thermoelastic diffusion model of fractional order generalized thermoelasticity [19]:

$$\eta_j + \frac{\tau_0}{\Gamma(\alpha+1)} \frac{\partial^\alpha}{\partial t^\alpha} \eta_j = -DP,j \qquad 0 < \alpha \leq 1$$

Heat conduction equation in Ezzat et al.'s model of fractional order generalized thermoelasticity with three-phase-lag [10]:

$$\left(1 + \frac{\tau_q^\alpha}{\Gamma(\alpha+1)} \frac{\partial^\alpha}{\partial t^\alpha} + \frac{\tau_q^{2\alpha}}{\Gamma(2\alpha+1)} \frac{\partial^{2\alpha}}{\partial t^{2\alpha}}\right) q_j = \left(\tau_\nu^* T_{,i} + k_{ij} \frac{\tau_T^\alpha}{\Gamma(\alpha+1)} \frac{\partial^\alpha}{\partial t^\alpha} + k_{ij}^* \nu_{,i}\right) \qquad 0 < \alpha \leq 1$$

where $\tau_\nu^* = k_{ij} + k_{ij}^* \frac{\tau_\nu^\alpha}{\Gamma(\alpha+1)} \frac{\partial^{\alpha-1}}{\partial t^{\alpha-1}}$

The stress-strain relation in Youssef's model of generalized thermoelasticity with fractional order strain [27]:

$$\sigma_{ij} = E^* \tau^{*\alpha} \frac{\partial^\alpha e_{ij}}{\partial t^\alpha} \qquad 0 < \alpha \leq 1$$

Heat conduction equation for isotropic solids in Shaw and Mukhopadhyay's thermoelastic diffusion model of fractional order generalized thermoelasticity [28]:

$$kD_{x_i}^\alpha D_{x_i}^\alpha \theta^\alpha = \left(1 + \tau_0 \frac{\partial^\beta}{\partial t^\beta}\right) \left(\frac{1}{2} \rho C_E \frac{\Gamma(2\alpha+1)}{(\Gamma(\alpha+1))^2} \frac{\partial \theta^\alpha}{\partial t} + \beta_1 T_0 \frac{\partial e_{kk}^\alpha}{\partial t} + a T_0 \frac{\partial C^\alpha}{\partial t} - W\right)$$

Thermal memory in the generalized thermoelasticity theory

Memory dependent thermoelasticity model without MDD

During last decade of the twentieth century, Green and Naghdi [29–32] developed new classes of heat conduction models. In their newly discussed theories, finite speed of thermal waves is established. Their models can be mainly classified into three types: Namely, type I, type II, and III.

Type I model: It is based on the classical theory of heat conduction equation due to Fourier's law:

$$q(x,t) = -K\nabla\theta(x,t); \qquad (x,t) \in \Omega \times \mathrm{R} \tag{5}$$

where $\Omega \in \mathrm{R}^n$, θ is the absolute temperature and $K>0$ is the thermal conductivity.

Type II model: This model is based on the extra thermal state variable named thermal displacement, defined as,

$$\alpha(x,t) = \alpha_0(x) + \int_0^1 \theta(x,s)ds \tag{6}$$

where $\theta(x,t)$ is an empirical temperature scale, not necessarily the absolute one.

Type III model: Similar to type II model, this model is also based on the thermal displacement variable $\alpha(x,t)$, defined as in (6).

This model is characterized by the heat flux law,

$$q(x,t) = -K\nabla\theta(x,t) - \varepsilon\nabla\alpha(x,t); \qquad \varepsilon > 0 \tag{7}$$

During the late sixties of the last century, Coleman and Gurtin [33] gave a generalization to the heat flux constitutive law in the form of a hereditary relation:

$$q(x,t) = -k_0\nabla\theta(x,t) - \int_{-\infty}^{t} k(t-s)\nabla\theta(x,s)ds \tag{8}$$

where $k_0 \geq 0$ and k is a convex summable function on the positive half line.

For $k_0 = 0$, the Coleman-Gurtin model reduces to the linear model by Gurtin and Pipkin [34].

Further, for $k_0 = 0$ with $k(s) = \frac{K}{\tau}e^{-\frac{s}{\tau}}$, Eq. (8) equalizes to the Maxwell-Catteno model, which is based upon a rate-type constitutive equation for the heat flux, ie.

$$\tau\dot{q}(x,t) + q(x,t) = -k_0\nabla\theta(x,t)$$

where, $\tau(>0)$ is a small value and the superposed dot stands for the material time derivative, the Coleman-Gurtin model can be specifically considered as a generalization to the Green-Naghdi type III model. Moreover, due to the presence of a time convolution integral, the Coleman-Gurtin theory is also referred to as the theory of heat conduction with a thermal memory.

Memory dependent thermoelasticity model with MDD

Apart from the presence of memory effects in thermoelastic theories being well established during the last quarter of the twentieth century, it was since 2010 that the memory components were introduced into the fractional thermoelastic models ([11], [16], and [19]). Recently in 2014, Yu et al. [35] introduced MDD into the heat conduction law in the following way:

$$q_i + \tau D_a q_i = -K\theta_{,i} \tag{9}$$

where $D_a q_i = D_a^{(1)} q_i = \frac{1}{a}\int_{t-a}^{t} k(t,p)q_i^{(1)}(p)dp$.

The kernel $k(t, p)$ and the time delay $a(>0)$ may be chosen in an arbitrary manner so that the material's real behavior can be understood more properly.

In common practice, the kernel function is considered in the following form:

$$k(t,p) = \left(\frac{p-t}{a} + 1\right)^b \tag{10}$$

The following are three different forms of kernels and the respective forms of Eq. (9):

1. Constant kernel ($b=0$): $q(x,t) + \frac{\tau}{a}\left[q(x,t) - q(x,t-a)\right] = -K\frac{\partial\theta}{\partial x}$
2. Linear kernel ($b=1$): $q(x,t) + \frac{\tau}{a^2}\int_{t-a}^{t} q(x,p)dp = -K\frac{\partial\theta}{\partial x}$
3. Parabolic kernel ($b=2$): $q(x,t) + \frac{2\tau}{a^3}\int_{t-a}^{t}(p-t+a)q(x,p)dp = -K\frac{\partial\theta}{\partial x}$.

In this regard, we can mention the work of Shaw [13], a note on generalized thermoelasticity with memory dependent derivatives, in which author showed how MDDs play a significant impact in thermoelasticity theory.

Basic equations

In the context of fractional-order-thermoelasticity theory, the field equations for a linear, homogeneous and isotropic thermoelastic solid body, in the absence of body forces and heat sources, are as follows

$$\begin{aligned} \mu\nabla^2\vec{u} + (\lambda+\mu)\vec{\nabla}(div\vec{u}) - \gamma\nabla\theta &= \rho\ddot{\vec{u}} \\ k\nabla^2\theta &= \left(\frac{\partial}{\partial t} + \tau\frac{\partial^{\alpha+1}}{\partial t^{\alpha+1}}\right)(\rho C_e\theta + \gamma T_0 div\vec{u}) \end{aligned} \tag{11}$$

in which $\vec{u}$ is the displacement vector; θ is the temperature change above a uniform reference temperature T_0; ρ is the mass density; C_e is the specific heat; λ and μ are the Lame' constant; $\gamma = (3\lambda + 2\mu)\alpha_t$, α_t being the coefficient of volume expansion and k is a material constant characteristic of the theory.

The stress tensor T associated with $\vec{u}$ and θ is given by

$$T = \lambda(div\vec{u})I + \mu(\nabla u + \nabla u^T) - \gamma\theta I \tag{12}$$

In all the above equations, the direct vector/tensor notation is employed. Also, an overdot denotes partial derivatives with respect to the time variable t.

We suppose that the constants appearing in Eq. (11) satisfy the inequalities:

$$\mu > 0, \quad \lambda + \mu > 0, \quad \rho > 0, \quad T_0 > 0, \quad C_e > 0, \quad \gamma > 0, \quad k > 0$$

Then Eq. (11) represent a fully hyperbolic system that permits finite speed for both elastic and thermal waves, which are coupled together in general.

Particular cases

Equations in (11) reduce to the equations of different theories of thermoelasticity as follows:

(1) If $\tau = 0$, they reduce to the equations of the classical coupled theory of thermoelasticity (CCTE).

(2) If $\alpha = 1$, they reduce to the equations of Lord Shulman theory of generalized thermoelasticity (LS Model).

Statement of the problem

We consider the model formulated Sherief et al. [11] to study spherically symmetric thermoelastic waves in a linear, homogeneous, and isotropic unbounded solid body containing a spherical

cavity. We assume the waves to be generated as a result of the application of a constant step in temperature on the boundary of the cavity which is held in a stress-free state. For spherical symmetric interactions, the displacement vector possesses only the radial component $u = u(r, t)$, where r is the radial distance measured from the origin (point of symmetry) and the stress tensor is determined by the radial stress σ_r and the circumferential stress (hoop stress) σ_ϕ. In this case, Eq. (11) yields the following governing equations for u and θ:

$$\begin{aligned}(\lambda+2\mu)\left[\frac{\partial}{\partial r}\left(\frac{\partial u}{\partial r}+\frac{2}{r}u\right)\right]-\gamma\frac{\partial\theta}{\partial r}&=\rho\frac{\partial^2 u}{\partial t^2}\\ k\left(\frac{\partial^2}{\partial r^2}+\frac{2}{r}\frac{\partial}{\partial r}\right)\theta&=\left(\frac{\partial}{\partial t}+\tau\frac{\partial^{\alpha+1}}{\partial t^{\alpha+1}}\right)\left(\rho C_e\theta+\gamma T_0\left(\frac{\partial u}{\partial r}+\frac{2}{r}u\right)\right)\end{aligned} \tag{13}$$

Also, the relation (12) yields

$$\begin{aligned}\sigma_r &= (\lambda+2\mu)\frac{\partial u}{\partial r}+2\lambda\frac{u}{r}-\gamma\theta\\ \sigma_\phi &= \lambda\frac{\partial u}{\partial r}+2(\lambda+\mu)\frac{u}{r}-\gamma\theta\end{aligned} \tag{14}$$

For mathematical analysis, it is convenient to have (13) and (14) rewritten in non-dimensional form. For this purpose, we consider the transformations

$$r'=\frac{r}{L},\quad t'=\frac{V}{L}t,\quad u'=\frac{\lambda+2\mu}{L\gamma T_0}u,\quad \tau'=\left(\frac{V}{L}\right)^{\alpha}\tau,\quad \theta'=\frac{\theta}{T_0},\quad {\sigma_r}'=\frac{\sigma_r}{\gamma T_0},\quad {\sigma_\phi}'=\frac{\sigma_\phi}{\gamma T_0}$$

where L is a standard length and V is a standard speed, using these transformations in (13) and (14) and suppressing primes for simplicity in the notations, we obtain the following equations, which are of the non-dimensional form:

$$\begin{aligned}C_P^2\left(\frac{\partial}{\partial r}\left(\frac{\partial u}{\partial r}+\frac{2}{r}u\right)-\frac{\partial\theta}{\partial r}\right) &= \frac{\partial^2 u}{\partial t^2}\\ C_T^2\left(\frac{\partial^2\theta}{\partial r^2}+\frac{2}{r}\frac{\partial\theta}{\partial r}\right)&=\left(\frac{\partial}{\partial t}+\tau\frac{\partial^{\alpha+1}}{\partial t^{\alpha+1}}\right)\left(\theta+\varepsilon\left(\frac{\partial u}{\partial r}+\frac{2}{r}u\right)\right)\end{aligned} \tag{15}$$

$$\sigma_r=\frac{\partial u}{\partial r}+2\eta\frac{u}{r}-\theta \tag{16}$$

$$\sigma_\phi=\eta\frac{\partial u}{\partial r}+(1+\eta)\frac{u}{r}-\theta \tag{17}$$

Here

$$C_P^2=\frac{\lambda+2\mu}{\rho V^2},C_T^2=\frac{k}{\rho C_e V},\varepsilon=\frac{\gamma^2 T_0}{\rho C_e(\lambda+2\mu)},\eta=\frac{\lambda}{\lambda+2\mu} \tag{18}$$

We note that C_P and C_T represent the non-dimensional speeds of purely elastic dilatational wave and purely thermal wave respectively, and ε is the usual thermoelastic coupling factor.

Boundary conditions

The body being considered for our analysis here is an unbounded thermoelastic solid with a spherical cavity. We chose the origin as the center of the cavity and denoted the dimensionless radius of the cavity by a. Initially if the body is at rest in an undeformed state and has its temperature-change and temperature-rate equal to zero, then the following initial conditions hold:

$$u=\frac{\partial u}{\partial t}=\theta=\frac{\partial\theta}{\partial t}=0\quad at\quad t=0\quad for\qquad r\geq a \tag{19}$$

If the thermoelastic interactions are caused by a uniform step in temperature applied to the boundary of the cavity which is held in the stress-free state, then the following boundary conditions hold:

$$\theta = \chi H(t), \sigma_r = 0 \qquad \text{for} \qquad r = a, t > 0 \tag{20}$$

where χ is a positive constant and $H(t)$ is the Heaviside unit step function with the aid of (16), these boundary conditions can be rewritten as

$$\frac{\partial u}{\partial r} + 2\eta \frac{u}{r} = \chi H(t) \qquad \text{for} \qquad r = a, t > 0 \tag{21}$$

Thus, for our problem here, (15) are the governing differential equations, (19) are the initial conditions, and (21) is the boundary condition. Once u and θ are determined by solving this initial-boundary value problem, then σ_r and σ_ϕ can be computed by using (16) and (17).

Solution in integral transform domain

We first employ Laplace transform upon the non-dimensional governing equations and then convert the basic transformed equations in the form of a vector matrix differential equation in spherical polar coordinates. Later the vector matrix differential equations shall be solved by an eigenvalue approach in the Laplace transform domain.

Solution using fractional ordered derivatives

Performing Laplace transform on Eq. (15) we respectively get,

$$\frac{d^2\bar{u}}{dr^2} + \frac{2}{r}\frac{d\bar{u}}{dr} - \frac{2}{r^2}\bar{u} = \frac{d\bar{\theta}}{dr} + \frac{s^2}{c_P^2}\bar{u} \tag{22}$$

and

$$c_T^2 \frac{d^2\bar{\theta}}{dr^2} + c_T^2 \frac{2}{r}\frac{d\bar{\theta}}{dr} = s_1\bar{\theta} + \varepsilon s_1 \frac{2}{r}\bar{u} + \varepsilon s_1 \frac{d\bar{u}}{dr} \tag{23}$$

where $s_1 = s + \tau s^{\alpha+1}, \ 0 < \alpha \leq 1$

Taking a differential operator $\mathbf{L}$ as:

$$\mathbf{L} \equiv \frac{d^2}{dr^2} + \frac{2}{r}\frac{d}{dr} - \frac{2}{r^2} \tag{24}$$

Equation (22) implies,

$$\mathbf{L}\bar{u} = \frac{d\bar{\theta}}{dr} + \frac{s^2}{c_P^2}\bar{u} \tag{25}$$

Differentiating Eq. (23) with respect to r and using Eq. (25) we get,

$$\mathbf{L}\frac{d\bar{\theta}}{dr} = \frac{s_1(1+\varepsilon)}{c_T^2}\frac{d\bar{\theta}}{dr} + \frac{\varepsilon s_1 s^2}{c_P^2 c_T^2}\bar{u} \tag{26}$$

Equations (25) and (26) can be written in the form of a vector matrix differential equation as:

$$\mathbf{L}\widetilde{v} = \widetilde{A}\widetilde{v} \tag{27}$$

where

$$\widetilde{A} = \begin{pmatrix} c_{11} & c_{12} \\ c_{21} & c_{22} \end{pmatrix}$$

$$\bar{v} = \begin{pmatrix} \bar{u} & \dfrac{d\bar{\theta}}{dr} \end{pmatrix}^T$$

Here,

$$c_{11}=\frac{s^2}{c_P^2}, c_{12}=1, c_{21}=\frac{\varepsilon s_1 s^2}{c_P^2 c_T^2}, c_{22}=\frac{s_1(1+\varepsilon)}{c_T^2} \tag{28}$$

The characteristic equation of matrix $\widetilde{A}$ can be written as:

$$\lambda^2-(c_{11}+c_{22})\lambda+(c_{11}c_{22}-c_{12}c_{21})=0 \tag{29}$$

We assume the eigenvalues of the matrix $\widetilde{A}$ to be of the form: $\lambda_1=m_1^2$ and $\lambda_2=m_2^2$
The right eigenvector $\widetilde{X}$, corresponding to the eigenvalue λ of the matrix $\widetilde{A}$ can be calculated as:

$$\widetilde{X}=\left(-c_{12}, c_{11}-\lambda\right)^T \tag{30}$$

Thus one can calculate the eigenvector corresponding to the eigenvalues $\lambda_i\,(i=1,2)$. We denote them as:

$$\begin{aligned}\widetilde{X}_1&=(-c_{12}, c_{11}-m_1^2)^T\\ \widetilde{X}_2&=(-c_{12}, c_{11}-m_2^2)^T\end{aligned} \tag{31}$$

Now,

$$\widetilde{v}=\sum_{i=1}^{2}\widetilde{X}_i y_i \tag{32}$$

where

$$y_i=A_i\left(\frac{(\mathrm{m}_i)}{r}+\frac{1}{r^2}\right)e^{-((m_i)r)} \tag{33}$$

Using Eqs. (32) and (33) and considering the boundary conditions taken in dimensionless form, we get,

$$\bar{u}(r,s)=-\frac{\chi\Omega_2}{T_0 s\Delta}e^{-m_1 r}\left(\frac{m_1}{r}+\frac{1}{r^2}\right)+\frac{\chi\Omega_1}{T_0 s\Delta}e^{-m_2 r}\left(\frac{m_2}{r}+\frac{1}{r^2}\right) \tag{34}$$

$$\bar{\theta}(r,s)=-\frac{\chi\Omega_2}{T_0 s\Delta}\frac{e^{-m_1 r}}{r}\left(c_{11}-m_1^2\right)+\frac{\chi\Omega_1}{T_0 s\Delta}\frac{e^{-m_2 r}}{r}\left(c_{11}-m_2^2\right) \tag{35}$$

$$\bar{\sigma}_r(r,s)=\frac{\chi\Omega_2}{T_0 s\Delta}e^{-m_1 r}\left[2(1-\eta)\left(\frac{m_1}{r^2}+\frac{1}{r^3}\right)+\frac{c_{11}}{r}\right]-\frac{\chi\Omega_1}{T_0 s\Delta}e^{-m_2 r}\left[2(1-\eta)\left(\frac{m_2}{r^2}+\frac{1}{r^3}\right)+\frac{c_{11}}{r}\right] \tag{36}$$

$$\begin{aligned}\bar{\sigma}_\phi(r,s)=&\frac{\chi\Omega_2}{T_0 s\Delta}e^{-m_1 r}\left[\left(2\eta m_1^2-(1+\eta)m_1\right)\frac{1}{r^2}+(\eta-1)\frac{1}{r^3}+\left(c_{11}+(\eta-1)m_1^2\right)\frac{1}{r}\right]\\&-\frac{\chi\Omega_1}{T_0 s\Delta}e^{-m_2 r}\left[\left(2\eta m_2^2-(1+\eta)m_2\right)\frac{1}{r^2}+(\eta-1)\frac{1}{r^3}+\left(c_{11}+(\eta-1)m_2^2\right)\frac{1}{r}\right]\end{aligned} \tag{37}$$

where

$$\Omega_i=e^{-am_i}\left[\frac{2m_i}{a^2}+\frac{2}{a^3}+\frac{m_i^2}{a}-\frac{2\eta}{a}\left(\frac{m_i}{a}+\frac{1}{a^2}\right)\right]+\xi_i$$

$$\xi_i=\frac{e^{-am_i}}{a}\left(c_{11}-m_i^2\right)$$

$$\Delta=\Omega_1\xi_2-\Omega_2\xi_1$$

$$m_i^2=\frac{2s^2 s_1}{\beta+(-1)^{i+1}\left(\beta^2-4s^2 s_1 c_P^2 c_T^2\right)^{\frac{1}{2}}}$$

$$\beta=c_T^2 s^2+s_1(1+\varepsilon)c_P^2$$

Solution using MDD

Considering the constant kernel form in the definition of MDD we get the following governing equations for u and θ:

$$\begin{aligned}(\lambda+2\mu)\left[\frac{\partial}{\partial r}\left(\frac{\partial u}{\partial r}+\frac{2}{r}u\right)\right]-\gamma\frac{\partial\theta}{\partial r}&=\rho\frac{\partial^2 u}{\partial t^2}\\ k\left(\frac{\partial^2}{\partial r^2}+\frac{2}{r}\frac{\partial}{\partial r}\right)\theta&=(1+\tau D_z)\frac{\partial}{\partial t}\left(\rho C_e\theta+\gamma T_0\left(\frac{\partial u}{\partial r}+\frac{2}{r}u\right)\right)\end{aligned}\tag{38}$$

Proceeding in a similar manner as discussed in the previous subsection we get the corresponding non-dimensional vector matrix differential equation as:

$$\mathbf{L}\widetilde{\nu}=\widetilde{A}\widetilde{\nu}\tag{39}$$

where

$$\widetilde{A}=\begin{pmatrix}d_{11} & d_{12}\\ d_{21} & d_{22}\end{pmatrix}$$
$$\bar{\nu}=\begin{pmatrix}\bar{u} & \dfrac{d\bar{\theta}}{dr}\end{pmatrix}^T$$

Here,

$$d_{11}=\frac{s^2}{c_P^2},d_{12}=1,d_{21}=\frac{\varepsilon s^3\xi}{c_P^2c_T^2},d_{22}=\frac{s\xi(1+\varepsilon)}{c_T^2}\tag{40}$$

where $\xi=1+\frac{\tau}{z}(1-e^{-sz})$

Further, proceeding in a similar way we get the following expressions for deformation, temperature, and stress considered in the non-dimensional form:

$$\bar{u}(r,s)=-\frac{\chi\Omega_2}{T_0s\Delta}e^{-m_1r}\left(\frac{m_1}{r}+\frac{1}{r^2}\right)+\frac{\chi\Omega_1}{T_0s\Delta}e^{-m_2r}\left(\frac{m_2}{r}+\frac{1}{r^2}\right)\tag{41}$$

$$\bar{\theta}(r,s)=-\frac{\chi\Omega_2}{T_0s\Delta}\frac{e^{-m_1r}}{r}(d_{11}-m_1^2)+\frac{\chi\Omega_1}{T_0s\Delta}\frac{e^{-m_2r}}{r}(d_{11}-m_2^2)\tag{42}$$

$$\bar{\sigma}_r(r,s)=\frac{\chi\Omega_2}{T_0s\Delta}e^{-m_1r}\left[2(1-\eta)\left(\frac{m_1}{r^2}+\frac{1}{r^3}\right)+\frac{d_{11}}{r}\right]-\frac{\chi\Omega_1}{T_0s\Delta}e^{-m_2r}\left[2(1-\eta)\left(\frac{m_2}{r^2}+\frac{1}{r^3}\right)+\frac{d_{11}}{r}\right]\tag{43}$$

$$\begin{aligned}\bar{\sigma}_\phi(r,s)=&\frac{\chi\Omega_2}{T_0s\Delta}e^{-m_1r}\left[\left(2\eta m_1^2-(1+\eta)m_1\right)\frac{1}{r^2}+(\eta-1)\frac{1}{r^3}+\left(d_{11}+(\eta-1)m_1^2\right)\frac{1}{r}\right]\\&-\frac{\chi\Omega_1}{T_0s\Delta}e^{-m_2r}\left[\left(2\eta m_2^2-(1+\eta)m_2\right)\frac{1}{r^2}+(\eta-1)\frac{1}{r^3}+\left(d_{11}+(\eta-1)m_2^2\right)\frac{1}{r}\right]\end{aligned}\tag{44}$$

where

$$\Omega_i=e^{-am_i}\left[\frac{2m_i}{a^2}+\frac{2}{a^3}+\frac{m_i^2}{a}-\frac{2\eta}{a}\left(\frac{m_i}{a}+\frac{1}{a^2}\right)\right]+\xi_i,$$
$$\xi_i=\frac{e^{-am_i}}{a}\left(d_{11}-m_i^2\right),\qquad\Delta=\Omega_1\xi_2-\Omega_2\xi_1,\qquad\beta=c_T^2s^2+s\xi(1+\varepsilon)c_P^2,$$
$$m_i^2=\frac{2s^3\xi}{\beta+(-1)^{i+1}\left(\beta^2-4s^3\xi c_P^2c_T^2\right)^{\frac{1}{2}}}.$$

Special cases

(i) ***Case I:*** Solutions for classical coupled thermoelasticity can be obtained by neglecting the thermal time delay (ie. $\tau = 0$) in Eqs. (34)–(37) and Eqs. (41)–(44).

In case of fractional ordered derivatives we get,

$$m_i^2 = \frac{2s^3}{\beta + (-1)^{i+1}(\beta^2 - 4s^3 c_P^2 c_T^2)^{\frac{1}{2}}} \tag{45}$$

and

$$\beta = c_T^2 s^2 + s_1(1+\varepsilon)c_P^2 \tag{46}$$

and for the case of MDD we get,

$$\xi = 1$$

and hence,

$$m_i^2 = \frac{2s^3}{\beta + (-1)^{i+1}(\beta^2 - 4s^3 c_P^2 c_T^2)^{\frac{1}{2}}} \tag{47}$$

and,

$$\beta = c_T^2 s^2 + s(1+\varepsilon)c_P^2 \tag{48}$$

(ii) ***Case II:*** Considering the fractional parameter $\alpha = 1$ in Eq. (13), the Eq. (34) and Eq. (35) gets reduced to the Lord-Shulman theory of generalized thermoelasticity;where,

$$m_i^2 = \frac{2\tau s^3(1+s)}{\beta + (-1)^{i+1}\{\beta^2 - 4\tau s^3(1+s)c_P^2 c_T^2\}^{\frac{1}{2}}} \tag{49}$$

and,

$$\beta = c_T^2 s^2 + \tau s(1+s)(1+\varepsilon)c_P^2 \tag{50}$$

which agrees with the results of Mukhopadhyay et al. [36]

(iii) ***Case III:*** Letting $z \to 0$ we see that the MDD $D_z f(t)$ tends to the normal derivative $\frac{d}{dt}f(t)$, and hence owing to such a case, Eqs. (41) and (42) transform into the Lord-Shulman theory of generalized thermoelasticity;
where

$$m_i^2 = \frac{2\tau s^3(1+\tau s)}{\beta + (-1)^{i+1}\{\beta^2 - 4\tau s^3(1+\tau s)c_P^2 c_T^2\}^{\frac{1}{2}}} \tag{51}$$

in which

$$\beta = c_T^2 s^2 + \tau s(1+s)(1+\varepsilon)c_P^2 \tag{52}$$

Numerical results and discussion

In order to obtain the physical nature of the field functions in the space-time domain, we must invert the transforms in Eqs. (41)–(44). We notice that the expressions for $m_i{}^2$ and Ω_i as given before are complicated functions of s. Consequently, the Laplace transform inversion of the expression $\bar{u}$ and $\bar{\theta}$, given by Eqs. (34), (35), (41), and (42) for all s values is a formidable task. We confine ourselves to the derivation of numerically approximate solutions for the field

functions. This can be done by adopting the algorithm given by Honig and Hirdes [37] (for details see Appendix).

For the computational purposes, we choose the parameters of copper-like materials with values of physical constants are as follows:

$$\lambda = 7.76 \times 10^{10}\ \mathrm{N/m^2}, \quad \mu = 3.86 \times 10^{10}\ \mathrm{N/m^2}, \quad \rho = 8954\ \mathrm{kg/m^3},$$
$$\varepsilon = 0.0168, \quad C_T = 2, \quad p_0 = 1, \quad \chi = 2$$

Numerical simulations are carried out for the displacement, temperature and radial stresses along the radius in context of both fractional ordered derivatives and MDD, which are demonstrated graphically in Figures 1–9 for different values of α. Figure 1 depicts the variations of displacement along the radius for different values of α. It is observed that the displacement is maximum near the surface of the cavity and it varies inversely with the radius. In Figure 2 we see that for $\tau = 0$ there is a uniform fall in displacement in accordance with the values of α. Figure 3 represents the variance of temperatures in two different scaling for different values of α. We see that in the response of memory effect in the heat conduction model the temperature increases slowly in a very small amount in the vicinity of the cavity. Similar to the nature of displacement, in Figure 4 we find that,

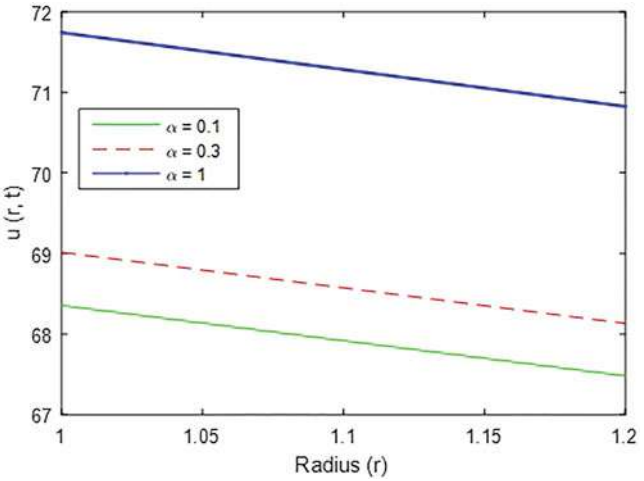

Figure 1. Comparison of displacement $u(r, t)$ for different values of α.

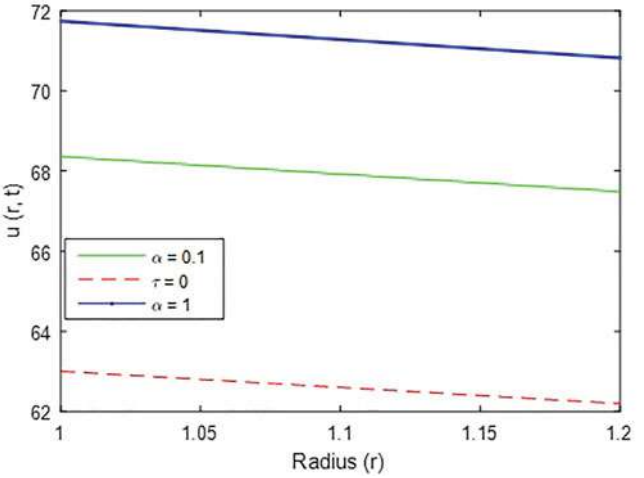

Figure 2. Comparison of displacement $u(r, t)$ for different values of α and $\tau = 0$.

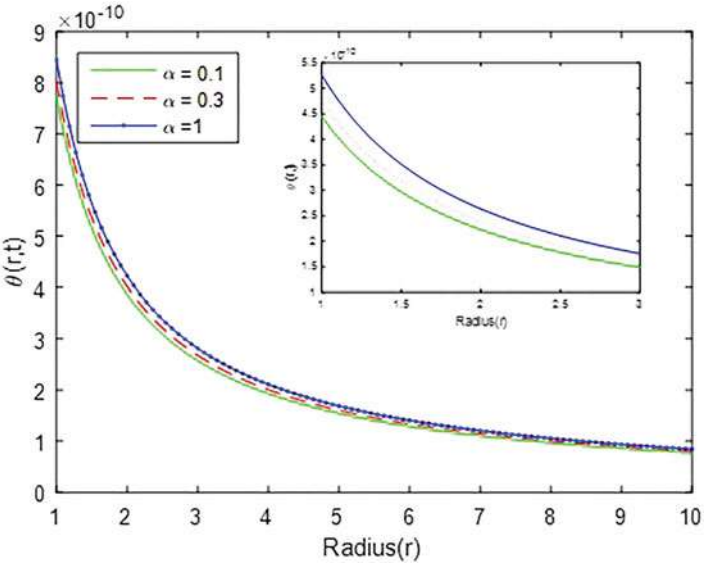

Figure 3. Comparison of temperature $\theta(r,t)$ for different values of α.

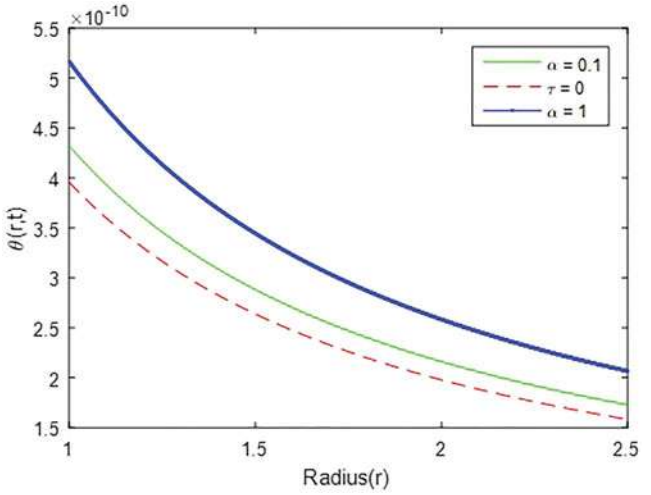

Figure 4. Comparison of displacement $u(r, t)$ for different values of α and $\tau = 0$.

although the temperature varies proportionally with the radius, there is a uniform fall in temperature when compared with the values of α for similar graphical studies. In Figures 5 and 6, variations of radial stresses have been compared for different values of α and for $\tau = 0$ respectively. Figures 7–9 shows the respective changes in displacement, temperature, and radial stress in the context of MDD as compared with fractional order generalized thermoelasticity with thermal time delay.

A uniform step in temperature is applied to the inner boundary of the cavity. Here we are concentrating on the impact of memory on the thermo-elastic phenomena into a homogeneous solid in very short time duration, such that the influence of thermal time delay is taken into account.

If we look at the temperature profile at a slightly faraway radial distance, then we observe that the temperature profile slowly decreases with radial distance from the cavity.

The similar nature is being followed by radial stresses with the variation of radial distance from the inner surface.

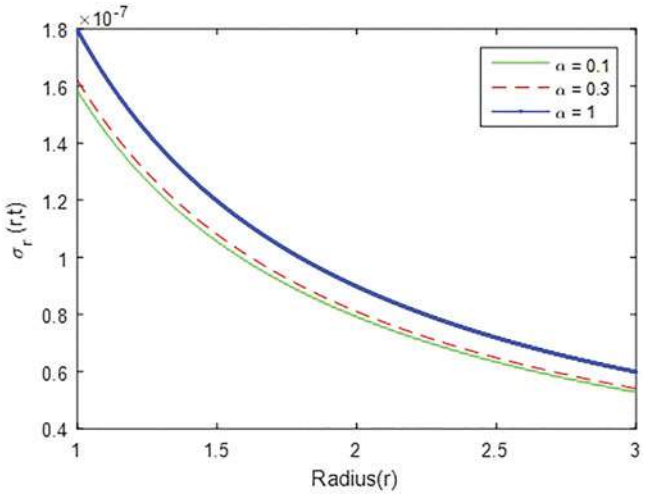

Figure 5. Comparison of radial stresses for different values of α.

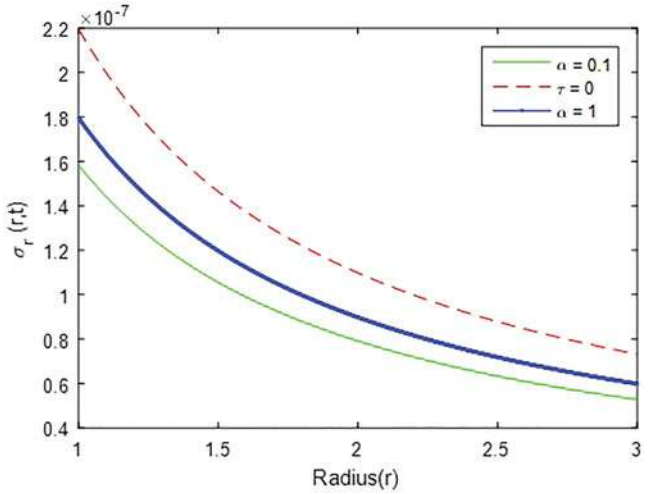

Figure 6. Comparison of radial stresses for different values of α and $\tau = 0$.

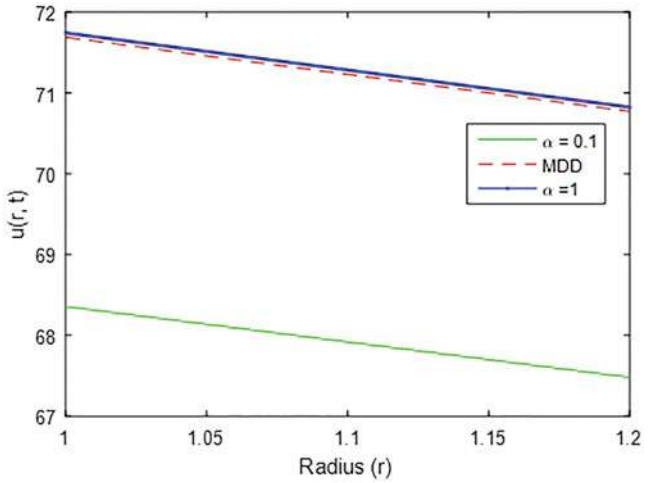

Figure 7. Comparison of displacement $u(r, t)$ for different values of α in context of MDD.

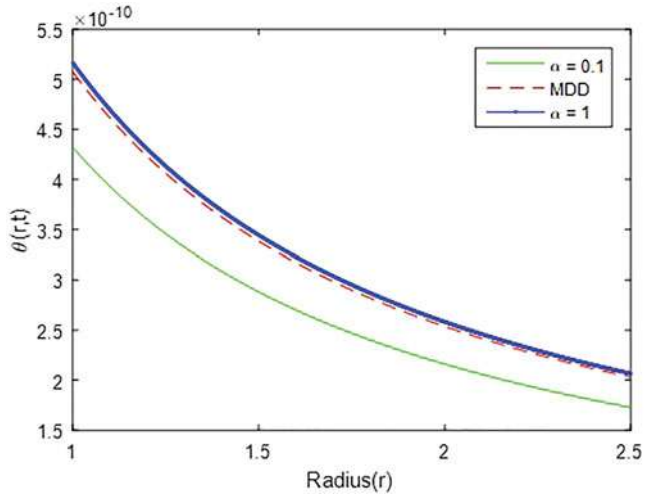

Figure 8. Comparison of temperature $\theta(r,t)$ for different values of α in context of MDD.

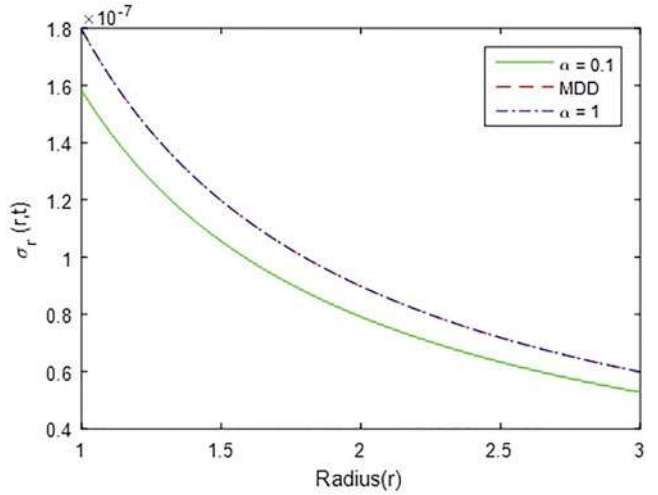

Figure 9. Comparison of radial stresses for different values of α in context of MDD.

A comparative study is being made with various values of fraction index in the time derivative with CCTE model and LS model in numerically simulated results. It is observed that with increasing values of the fractional index the aforementioned elastic medium experienced more deformation than the classical coupled thermoelasticity model. It implies that memory response plays a significant role in the deformation of thermoelastic media. In addition, the memory response on the amount of heat propagating into the medium is enhanced and this can be realized from the Figures 3 and 4. A similar nature of stress profile is observed with the radial distance from the boundary of the cavity. In contrary, for CCTE model the radial stresses experienced by the elastic body is much higher than that of for the other generalized hyperbolic thermoelastic models.

In the circumstance of the generalized thermoelastic model with memory dependent derivatives, the concerned thermoelastic medium experienced deformation, amount of heat propagating through the medium and the thermal stresses are almost identical with that for the maximum value of the fractional index.

Conclusion

With the view of theoretical analysis and numerical computation we can conclude the following phenomenon:

1. The present article provides a detailed analysis of thermal memory response on a thermoelastic disturbance in an unbounded elastic media in presence of a time-dependent thermal shock applied to the traction-free boundary of the cavity.
2. The theoretical analysis and computational results confirm that the memory response can increase the disturbance in the thermoelastic field with respect to the classical coupled thermoelasticity model.
3. One may select an appropriate kernel to enhance the memory effects in the theory of thermoelasticity. It is encouraging that MDD will also make sense in the comparison with other generalized thermoelasticity theories.
4. The influence of MDD with respect to the various generalized thermoelasticity theories with time delays is also revealed from this investigation. The MDD model with flat (constant) kernel shows identical results with the fractional order thermoelastic model.

The results presented in this article may be useful for researchers who are working on material science, mathematical physics, thermodynamics with low temperatures as well as on the development of the hyperbolic thermoelasticity theory.

Appendix

Inversion of the transforms

We can invert the above field functions in the space-time domain by the following inverse Laplace transform algorithm:

$$f(r,t) = L[\bar{f}(r,s)] = \frac{1}{2\pi i}\int_{\nu-i\infty}^{\nu+i\infty} e^{st}\bar{f}(r,s)ds \tag{A.1}$$

Let $s = \nu + iw \quad (\nu, w \in \mathrm{R})$. So Eq. (45) reduces to,

$$f(r,t) = \frac{e^{\nu t}}{2\pi}\int_{-\infty}^{+\infty} e^{iwt}\bar{f}(r,\nu+iw)dw \tag{A.2}$$

Expanding the function $h(r,t) = e^{-\nu t}f(r,t)$ in a Fourier series in the interval $[0,2T]$, Darbin derived the approximation formula,

$$\begin{aligned} f(r,t) = &-\frac{e^{\nu t}}{2T}Re\{\bar{f}(r,\nu)\} + \frac{e^{\nu t}}{T}\sum_{k=0}^{\infty}Re\left\{\bar{f}\left(r,\nu+i\frac{k\pi}{T}\right)\right\}\cos\left(\frac{k\pi}{T}t\right) \\ &-\frac{e^{\nu t}}{T}\sum_{k=0}^{\infty}Im\left\{\bar{f}\left(r,\nu+i\frac{k\pi}{T}\right)\right\}\sin\left(\frac{k\pi}{T}t\right) - F_1(r,\nu,t,T) \end{aligned} \tag{A.3}$$

where $F_1(r,\nu,t,T)$ is the discretization error.

As the series (47) can be summed upto a finite number N, hence the approximation value for $f(r, t)$ is,

$$\begin{aligned} f_N(r,t) = &-\frac{e^{\nu t}}{2T}Re\{\bar{f}(r,\nu)\} + \frac{e^{\nu t}}{T}\sum_{k=0}^{N}Re\left\{\bar{f}\left(r,\nu+i\frac{k\pi}{T}\right)\right\}\cos\left(\frac{k\pi}{T}t\right) \\ &-\frac{e^{\nu t}}{T}\sum_{k=0}^{N}Im\left\{\bar{f}\left(r,\nu+i\frac{k\pi}{T}\right)\right\}\sin\left(\frac{k\pi}{T}t\right) \end{aligned} \tag{A.4}$$

Now, to reduce the total error, first the Korrektur method and next the ε-algorithim are used to reduce the discretization error and hence to accelerate convergence.

References

[1] M. Biot, "Thermoelasticity and irreversible thermodynamics," *J. Appl. Phys.*, vol. 27, no. 3, pp. 240–253, 1956. DOI: 10.1063/1.1722351.

[2] C. Cattaneo, "Sur une forme de i'equation de la chaleur eliminant le paradoxe d'ure propagation instantanee," *Comptes. Rendus. Acad. Sci.*, vol. 2, pp. 431–433, 1958.

[3] H. Lord and Y. Shulman, "A generalized dynamic theory of thermoelasticity," *J. Mech. Phys. Solids*, vol. 15, no. 5, pp. 299–309, 1967. DOI: 10.1016/0022-5096(67)90024-5.

[4] A. E. Green and K. A. Lindsay, "Thermoelasticity," *J. Elasticity*, vol. 2, no. 1, pp. 1–7, 1972. DOI: 10.1007/BF00045689.

[5] K. B. Oldham and J. Spanier, *The Fractional Calculus-Theory and Application of Differentiation and Integration to Arbitrary Order*. Academic Press Inc., 1974.

[6] K. S. Miller and B. Ross, *An Introduction to Fractional Calculus and Fractional Differential Equations*. John Wiley and Sons, Inc., 1993.

[7] I. Podlubny, *Fractional Differential Equations*. Academic Press, Inc., 1999.

[8] M. Caputo and F. Mainardi, "A new dissipation model based on memory mechanism," *Pure. Appl. Geophys.*, vol. 91, no. 1, pp. 134–147, 1971. DOI: 10.1007/BF00879562.

[9] M. Caputo and F. Mainardi, "Linear models of dissipation in elastic solids, rivisita del," *Nuovo Cimento*, vol. 1, no. 2, pp. 161–198, 1971. DOI: 10.1007/BF02820620.

[10] M. A. Ezzat, A. S. El-Karamany and M. A. Fayik, "Fractional order theory in thermoelastic solid with three phase lag heat transfer," *Arch. Appl. Mech.*, vol. 82, no. 4, pp. 557–572, 2012. DOI: 10.1007/s00419-011-0572-6.

[11] H. H. Sherief, A. El-Sayed and A. A. El-Latief, "Fractional order theory of thermoelasticity," *Int. J. Solids Struct.*, vol. 47, no. 2, pp. 269–275, 2010. DOI: 10.1016/j.ijsolstr.2009.09.034.

[12] M. K. Ghosh and M. Kanoria, "Generalized thermoelastic functionally graded spherically isotropic solid containing a spherical cavity under thermal shock," *Appl. Math. Mech.-Engl. Ed*, vol. 29, no. 10, pp. 1263–1278, 2008. DOI: 10.1007/s10483-008-1002-2.

[13] S. Shaw, "A note on the generalized thermoelasticity theory with memory dependent derivatives," *J. Heat Transf.*, vol. 139, no. 9, pp. 092005, 2017. DOI: 10.1115/1.4036461.

[14] M. B. Bera, N. C. Das and A. Lahiri, "Thermoelastic wave with energy dissipation in an unbounded medium with a spherical cavity," *J. Therm. Stress.*, vol. 37, no. 12, pp. 1482–1494, 2014. DOI: 10.1080/01495739.2014.950527.

[15] K. Diethelm, *Analysis of Fractional Differential Equation: An Application Oriented Exposition Using Differential Operators of Caputo Type*. Berlin, Germany: Springer, 2010.

[16] H. M. Youssef, "Theory of fractional order generalized thermoelasticity," *J. Heat Transf.*, vol. 132, no. 6, pp. 061301–061307, 2010. DOI: 10.1115/1.4000705.

[17] M. A. Ezzat, "Thermoelectric MHD non-newtonian fluid with fractional derivative heat transfer," *Physica B*, vol. 405, no. 19, pp. 4188–4194, 2010. DOI: 10.1016/j.physb.2010.07.009.

[18] A. S. El-Karamany and M. A. Ezzat, "Convolutional variational principle, reciprocal and uniqueness theorems in linear factional two-temperature thermoelasticity," *J. Therm. Stress*, vol. 34, no. 3, pp. 264–284, 2011. DOI: 10.1080/01495739.2010.545741.

[19] M. A. Ezzat and M. A. Fayik, "Fractional order theory of thermoelastic diffusion," *J. Therm. Stress*, vol. 34, no. 8, pp. 851–872, 2011. DOI: 10.1080/01495739.2011.586274.

[20] S. Shaw and B. Mukhopadhyay, "Generalized theory of micropolar-fractional ordered thermoelasticity with two-temperature," *Int. J. Appl. Math. Mech*, vol. 7, pp. 32–48, 2011.

[21] Y. Z. Wang, D. Lieu, Q. Wang and J. Z. Zhou, "Fractional order theory of thermoelasticity for elastic medium with variable material properties," *J. Therm. Stress*, vol. 38, no. 6, pp. 665–676, 2015. DOI: 10.1080/01495739.2015.1015840.

[22] A. M. A. El-Latief and S. E. Khader, "Fractional model of thermoelasticity for a half-space overlaid by a thick layer," *Z. Angew. Math. Mech*, vol. 95, no. 5, pp. 511–518, 2015. DOI: 10.1002/zamm.201300174.

[23] E. M. Hussein, "Fractional order thermoelastic problem for infinitely long solid circular cylinder," *J. Therm. Stress*, vol. 38, no. 2, pp. 133–145, 2015. DOI: 10.1080/01495739.2014.936253.

[24] D. S. Mashat, A. M. Zenkour and A. E. Abouelregal, "Fractional order thermoelasticity theory for a half-space subjected to an axisymmetric heat distribution," *Mech. Adv. Mat. Struct*, vol. 22, no. 11, pp. 925–932, 2015. DOI: 10.1080/15376494.2014.882461.

[25] S. S. Sheoran, K. K. Kalkal and S. Deswal, "Fractional order thermo-viscoelastic problem with temperature dependent modulus of elasticity," *Mech. Adv. Mater. Struct*, vol. 23, no. 4, pp. 407–414, 2016. DOI: 10.1080/15376494.2014.981621.

[26] S. Deswal, K. K. Kalkal and S. S. Sheoran, "Axi-symmetric generalized thermoelastic diffusion problem with two-temperature and initial stress under fractionl order heat conduction," *Physica B*, vol. 496, pp. 57–68, 2016. DOI: 10.1016/j.physb.2016.05.008.

[27] H. M. Youssef, "Theory of generalized thermoelasticity with fractional order strain," *J. Vib. Cont.*, vol. 22, no. 18, pp. 3840–3857, 2016. DOI: 10.1177/1077546314566837.

[28] S. Shaw and B. Mukhopadhyay, "Theory of fractional-ordered thermoelastic diffusion," *Eur. Phys. J. Plus*, vol. 131, no. 6, pp. 1–10, 2016. DOI: 10.1140/epjp/i2016-16183-6.
[29] A. E. Green and P. M. Naghdi, "A re-examination of the basic postulates of thermomechanics," *Proc. R. Soc. Lond.*, vol. 432, no. 1885, pp. 171–194, 1991. DOI: 10.1098/rspa.1991.0012.
[30] A. E. Green and P. M. Naghdi, "On undamped heat waves in an elastic solid," *J. Therm. Stress*, vol. 15, no. 2, pp. 253–264, 1992. DOI: 10.1080/01495739208946136.
[31] A. E. Green and P. M. Naghdi, "Thermoelasticity without energy dissipation," *J. Elasticity*, vol. 31, no. 3, pp. 189–208, 1993. DOI: 10.1007/BF00044969.
[32] A. E. Green and P. M. Naghdi, "A unified procedure for construction of theories of deformable media. I. Classical continuum physics, II. Generalized continua, III. Mixture of interacting continua, proc," *R. Soc. Lond.*, vol. 448, no. 1934, pp. 335–388, 1995. DOI: 10.1098/rspa.1995.0020.
[33] B. D. Coleman and M. E. Gurtin, "Equipresence and constitutive equations for rigid heat conductors," *J. Appl. Math. Phys. and Physics (ZAMP)*, vol. 18, no. 2, pp. 199–208, 1967. DOI: 10.1007/BF01596912.
[34] M. E. Gurtin and A. C. Pipkin, "A general theory of heat conduction with finite wave speeds," *Arch. Rational Mech. Anal.*, vol. 31, no. 2, pp. 113–126, 1968. DOI: 10.1007/BF00281373.
[35] Y. J. Yu, W. Hu and X. G. Tian, "A novel generalized thermoelasticity model based on memory dependent derivatives," *Int. J. Eng. Sci.*, vol. 81, pp. 123–134, 2014. DOI: 10.1016/j.ijengsci.2014.04.014.
[36] B. Mukhopadhyay, R. Bera and L. Debnath, "On generalized thermoelastic disturbances in an elastic solid with a spherical cavity," *J. Appl. Math. Stoc. Anal*, vol. 4, no. 3, pp. 225–240, 1991. DOI: 10.1155/S1048953391000187.
[37] G. Honig and U. Hirdes, "A method for the numerical inversion of laplace transforms," *J. Comput. Appl. Math*, vol. 10, no. 1, pp. 113–132, 1984. DOI: 10.1016/0377-0427(84)90075-X.

Source details

Feedback > Compare sources >

Journal of Thermal Stresses

Scopus coverage years: from 1978 to Present

Publisher: Taylor & Francis

ISSN: 0149-5739 E-ISSN: 1521-074X

Subject area: Physics and Astronomy: Condensed Matter Physics | Materials Science: General Materials Science

Source type: Journal

View all documents > | Set document alert | Save to source list

CiteScore 2022
5.4

SJR 2022
0.567

SNIP 2022
1.247

CiteScore | CiteScore rank & trend | Scopus content coverage

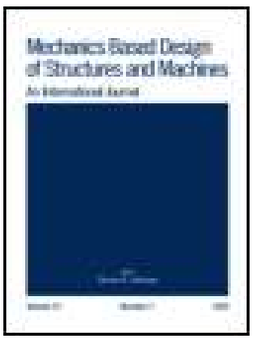

Mechanics Based Design of Structures and Machines

An International Journal

ISSN: 1539-7734 (Print) 1539-7742 (Online) Journal homepage: https://www.tandfonline.com/loi/lmbd20

Memory response on thermoelastic deformation in a solid half-space with a cylindrical hole

Santanu Banerjee, Soumen Shaw & Basudeb Mukhopadhyay

To cite this article: Santanu Banerjee, Soumen Shaw & Basudeb Mukhopadhyay (2019): Memory response on thermoelastic deformation in a solid half-space with a cylindrical hole, Mechanics Based Design of Structures and Machines, DOI: 10.1080/15397734.2019.1686989

To link to this article: https://doi.org/10.1080/15397734.2019.1686989

Published online: 10 Nov 2019.

MECHANICS BASED DESIGN OF STRUCTURES AND MACHINES
https://doi.org/10.1080/15397734.2019.1686989

Memory response on thermoelastic deformation in a solid half-space with a cylindrical hole

Santanu Banerjee, Soumen Shaw, and Basudeb Mukhopadhyay

Department of Mathematics, Indian Institute of Engineering Science and Technology, Shibpur, India

ABSTRACT

The present article deals with the memory response on thermal wave propagation emanating from a cylindrical hole in an unbounded thermoelastic solid. Here, we have theoretically demonstrated two aspects of thermal waves in elastic materials with memory. First, the characteristics of thermoelastic disturbances originated from the hole in an unbounded elastic solid under the light of generalized thermoelasticity theory with memory-dependent derivatives (MDDs). For numerical implementation, cylindrical polar coordinate system with radial symmetry is considered. An integral transform method and, while in inverse transformation, an efficient and pragmatic NILT (numerical inverse Laplace transform) is adopted. Second, a comparison study is being made on the memory response of thermal waves with and without energy dissipation into the medium. Finally, parameter studies are performed to evaluate the effect of the kernel function and time delay. For thermal wave, the results show appreciable differences with those in the usual thermoelasticity theory.

ARTICLE HISTORY
Received 26 November 2018
Accepted 28 October 2019

KEYWORDS
Thermal memory; memory-dependent derivatives; generalized thermoelasticity; energy dissipation; eigenfunction expansion method

1. Introduction

In the classical uncoupled theory of thermoelasticity developed by Duhamel (1837), there were no such terms involving elastic deformation and they were also of parabolic type. Two main paradoxes were raised in such a theory which was not compatible with the physical phenomena. First, elastic deformations produce no thermal effects and second, the heat conduction equation is of hyperbolic type predicting infinite speed of thermal signals. Over a century later, Biot (1956) came upon with a classical theory of coupled thermoelasticity, which overcame the first paradox inherent in Duhamel's uncoupled theory that elastic changes have no effect in temperature. Even after the introduction of Biot's coupled theory, the second paradox in Duhamel's uncoupled theory still remained unsolved. This was due to the fact that both the theories were of diffusion type predicting infinite speeds of propagation of thermal signals. To overcome this paradox, it was essential to obtain a wave-type heat equation instead of the conventional diffusion-type. In the late sixties of the twentieth century, the conventional classical theory was modified. Lord and Shulman (LS theory) (1967) were the first to introduce generalized thermoelasticity with one relaxation time by incorporating flux rate term into the Fourier's law of heat conduction. Later on, Green and Lindsay (GL theory) (1972) developed a temperature rate-dependent thermoelasticity with two relaxation times by including temperature rate among the constitutive equations. The heat conduction equations associated in both LS and GL theories are of hyperbolic type.

CONTACT Santanu Banerjee santanubandopadhyay@gmail.com Department of Mathematics, Indian Institute of Engineering Science and Technology, Shibpur, West Bengal, India.
Color versions of one or more of the figures in the article can be found online at www.tandfonline.com/lmbd.
Communicated by Seonho Cho.

Owing to such reason, the generalized theories are also labeled as theories of hyperbolic thermoelasticity.

During the final decade of the last century, three models (models I, II, and III) concerned to the generalized theory of thermoelasticity were developed by Green and Naghdi (GN) theory (1991, 1992, 1993, 1995). The three models of GN theory are in accordance with three types of constitutive equations depending upon the characteristics of material response for thermal phenomena. When the theory is linearized, type I converges to the Fourier's classical heat equation. Type II theory predicts finite speeds for propagation of thermal waves and involves no dissipation of thermal energy, whereas the type III theory predicts a finite speed of thermal propagation and involves a thermal damping term.

In applied science and engineering problems, mathematical modeling is an important and primary task before proceeding any further. Mathematical modeling comprises of constructing and introducing mathematical tools whose results and behaviors correspond in some way to a concerned physical system. Over the past few decades, it has now become an established fact that the next state of a physical system does not only depend upon its present state but also upon all of its historical states. The very introduction of memory-dependent derivatives (MDDs) by Wang and Li (2011) proved to be an useful mathematical tool and served a missing link to many physical problems. The integer order differential operator is a local operator whereas that fractional order differential operator is nonlocal. The nonlocal nature of the fractional derivative establishes its somewhat memory-dependent nature, which is a much more realistic fitting to the real-world physical problems. In various engineering structures, there may exist certain elastic materials such as amorphous, colloids, porous, polymers, etc. and physical situations like transient loading where classical theory and generalized theory of thermoelasticity may fail to fit perfect. In such cases, introduction of time-fractional derivatives or MDDs into the theory becomes relevant. Thus in some recent studies, fractional order derivatives come into account more frequently than integer order derivatives in various physical problems. Parallel to fractional order derivatives, MDDs serve as an important mathematical tool in describing many real-world phenomena. Even though not much have been explored regarding the applications of memory-dependent thermoelastic models, with the development of technologies we may see some in near future. In this context, it is worth mentioning that in several engineering structures, semiconducting materials are widely used. The study of thermal wave propagation in such materials by fitting the memory-dependent models into it may have an important academic significance and an application value.

In some recent works, Ezzat, El-Karamany, and Samaan (2001) and Ezzat, Othman, and El-Karamany (2002) investigated some generalized thermoelastic problems using the state-space approach. Abbas (2015, 2017) studied free vibration thermoelastic problems for both spherical and cylindrical bodies under the light of two-temperature generalized thermoelasticity theory. Othman and Eraki (2017) made a comparative study for the effect of initial stresses among Lord–Shulman, Green–Naghdi III, and three-phase-lag models, where the body was subjected to a magnetic field interaction. Biswas, Mukhopadhyay, and Shaw (2019) also analyzed a similar magneto-thermoelastic problem assuming the three-phase-lag model upon a transversely isotropic hollow cylindrical elastic body. Owing to the growing popularity of the MDDs upon fractional order derivatives, several works have been pursued using MDDs. Memory-dependent derivatives provide more possibilities to capture the material response of the physical problem under consideration. The main compatibility of MDDs lies upon its kernel and the time delay parameter. The kernel function and the memory parameters must be chosen in a way such that they are in harmony with the physical nature of the problem. In a recent study Banerjee, Shaw, and Mukhopadhyay (2018) analyzed the thermal effects upon a spherical body using both fractional and MDDs' model. They showed that in such process, a nonlocality effect plays a significant part in the theory of thermodynamics.

The present article deals with the memory response on thermal wave propagation, emanating from a cylindrical hole in an unbounded thermoelastic solid, under the purview of memory-dependent thermoelasticity theory. The dealt problem can be replicated with the situation of a drilled hole which is to be used as a calibration reflector for the purpose of nondestructive testing. This is primarily used to investigate the thermal wave scattering in the solid half-space by the cylindrical hole.

2. Time-dependent nonlocal thermoelasticity

2.1. Remembering memory in material modeling

In Scott–Blair's model (see Mainardi (2010)), basically a material modeling, we found a formula for memory phenomena in various disciplines. The model takes the form:

$$ {}_0D_t^{\alpha}\varepsilon(t) = \chi\sigma(t) \tag{1}$$

where ${}_0D_t^{\alpha}\varepsilon(t)$ is the fractional (fractional order) derivative which depends on the strain history from 0 to t, and χ is a positive constant. ${}_0D_t^{\alpha}\varepsilon(t) = D^n\varepsilon(t) = \frac{d^n}{dt^n}\varepsilon(t)$ if α is an integer n.

Fractional order derivative is a generalization of integer order derivative and integral. It was originated from the letter of L'Hôpital to Leibnitz in 1695 regarding the meaning of $\frac{1}{2}$ order derivative and is a promising tool for describing memory phenomena (see Rossikhin and Shitikova (2010) and Stiassnie (1979)). The kernel function of fractional derivative is termed as the memory function, but it does not replicate any physical process. Imprecise physical meaning has been a big obstacle that keeps fractional derivative lagging far behind the integer order calculus.

There are several definitions of fractional derivative. Riemann–Liouville derivative is one of most standard definitions, described by

$$ {}_0D_t^{\alpha}\varepsilon(t) = \frac{1}{\Gamma(m-\alpha)}\frac{d^m}{dt^m}\int_0^t \frac{\varepsilon(\tau)}{(t-\tau)^{\alpha+1-m}}\,d\tau \tag{2}$$

where $\Gamma(.)$ is Euler's gamma function and m is the integer satisfying $m-1 \le \alpha < m$. The important point is that a memory process generally consists of two stages. The former is short with permanent retention at the beginning and it cannot be neglected in general, while the later is governed by the fractional model (1). The critical point between the fresh stage and the working stage is usually not the origin. This observation is quite different from the traditional fractional models of one stage.

The key point of our observation is that the order of fractional derivative is an index of memory. The dimensionless form of solution of the Eq. (1) is

$$ E = \tau^{\alpha} - (\tau-1)^{\alpha} \tag{3}$$

where $\tau = \frac{t}{t_M}, E(\tau) = \frac{\varepsilon(t)}{\varepsilon_M}$, and ε_M is the strain at the end of time of creeping $t = t_M$. The dimensionless relation E increases with an increase of the value of α. The higher value of the index α indicates the slower the forgetting during the process. In particular, $E=0$ (nothing memorized) when $\alpha=0$ and $E=1$ (nothing forgotten) when $\alpha=1$. Therefore, we define the fractional order α as the index of memory.

For a standard creep and recovery process, the specimen is usually loaded under a constant stress $\sigma(t) = \sigma_0$ from 0 to t_M, and the load is removed at the instant $t = t_M$, then $\sigma(t) = 0$ for $t \ge t_M$.

Let $H(t)$ be the Heaviside function, then the Eq. (1) takes the following form

$$ {}_0D_t^{\alpha}\varepsilon(t) = \chi\sigma_0\Big(H(t) - H(t-t_M)\Big) \tag{4}$$

where ${}_0D_t^{\alpha}\varepsilon(t)$ is Riemann–Liouville fractional order derivative with zero initial condition.

The superposition method gives the solution of the above Eq. (4) as follows

$$\varepsilon(t) = \frac{\chi\sigma_0}{\Gamma(\alpha+1)}\Big(t^{\alpha}H(t) - (t-t_M)^{\alpha}H(t-t_M)\Big) \tag{5}$$

This is in agreement with the early observation of the behavior of some viscoelastic materials.

Second, we show that the Eq. (1) works not only in modeling viscoelastic materials, but also in modeling biological kinetics with memory, for example, for the protein adsorption kinetics, if the symbols σ and ε are replaced by the concentration c and the surface density Γ of fibronectin therein, respectively. Then,

$$\sigma(t) = \sigma_0\Big(H(t) - H(t-t_M) + H(t-t_N)\Big)$$

The absorbed density is found to be,

$$\sigma(t) = \sigma_0\Big(H(t) - H(t-t_M) + H(t-t_N) + (t-t_N)^{\alpha}H(t-t_N)\Big)$$

2.2. Thermal memory in the generalized thermoelasticity theory

Nonlocal continuum field theories are concerned with the physics of material bodies whose behavior at a material point is influenced by the state of all points of the body. The nonlocal theory generalizes the classical field theory in two respects: (i) the energy balance law is considered valid globally, and (ii) the state of the body at a material point is described by the response functional. In this description, nonlocality in time is known as memory dependence. The theory of heat conduction in continuous media with memory has drawn the attention of many researchers. Initially, the motivation was to avoid the unpleasant feature of the classical coupled heat conduction model that the thermal disturbance produced at some point in the body felt instantaneously at all other points. This contradicts the fact that energy cannot propagate at a speed exceeding the velocity of light. Gurtin and Pipkin (1968) first developed a general nonlinear heat conduction model for rigid body with memory for which thermal disturbances propagate with finite speed. They assumed that the response functional, namely the entropy, free energy, and heat flux, depends on the present value of the temperature and the integrated histories of the temperature and the temperature gradient.

It is an accepted fact that owing to a thermal disturbance, the instantaneous change rate of the physical quantities of any elastic body depends upon its past state. Thus, during the later half of the twentieth century, the introduction of Caputo-type fractional derivatives in thermoelastic models became fruitful step. Caputo defined fractional order derivatives in the form of an integral given by,

$$D_a^{\alpha}f(t) = \int_a^t \frac{(t-\xi)^{m-\alpha-1}}{\Gamma(m-\alpha)} f^{(m)}(\xi)d\xi$$

where $f^{(m)}$ denotes the mth order derivative.

Diethelm (2010) in his book modified the Caputo-type fractional derivative by generalizing the kernel in the integrand as follows:

$$D_a^{\alpha}f(t) = \int_a^t K_{\alpha}(t-\xi)f^{(m)}(\xi)d\xi$$

Jumarie (2010) developed a new Taylor series expansion of time fractional order and Ezzat (2010) used it to establish a new model of fractional heat conduction equation as,

$$q_i + \frac{\tau_0^{\alpha}}{a!}\frac{\partial^{\alpha}q_i}{\partial t^{\alpha}} = -K\theta_{,i} \tag{6}$$

Thus, due to their various applications in many engineering and scientific disciplines, since the last one decade, fractional order differential equations have gained considerably more attention.

As the mathematical models for the systems and processes, fractional differential equation has been successfully applied in various fields of physics and engineering, some of which can be found in the work of Shaw and Mukhopadhyay (2016). A rather detailed account of diverse recent theoretical advances and applications of fractional calculus in the various fields can be found in the books of Sabatier, Agrawal, and Tenreiro Machado (2007), Hilfer (2000), and Atanackovi et al. (2014).

One hindrance to the wider use of fractional order methods by engineers is, the absence of a simple geometric picture for the fractional order integral. Even though the definition of Caputo gained specific importance, there are other definitions of fractional derivatives (e.g., Riemann–Liouville, Reisz, and Grunwald–Letnikov), each of which has specific advantages and limitations, particularly when used to define a distribution of fluxes into a control volume or effects of fading memory on the forces applied in a free body diagram.

Wang and Li (2011) introduced a modification in the definition of fractional derivative, where the first-order derivative of a function $f(x, t)$ has been defined in an integral form, in terms of normal partial derivative of $f(x, t)$ with a kernel function on a slipping interval as follows:

$$D_{\omega}^{(1)} f(x,t) = \frac{1}{\omega}\int_{t-\omega}^{t} K(t-\xi) f_{\xi}'(x,\xi) d\xi \tag{7}$$

where ω is the time delay and $K(t-\omega)$ is the kernel function which can be chosen freely.

The above modifications to fractional order derivatives are denominated as MDDs. Due to the form of its integrand, MDDs resonate the memory effect better than the fractional order derivatives, thus showing better clairvoyance in understanding the physical nature of the material.

Even though the kernel function can be chosen freely, Wang and Li (2011) indicated that to reduce the memory effect better, the magnitude of MDD should be smaller than that of the common partial derivative, and for that the bounds of the kernel should be $0 \le K(t-\xi) \le 1$ for $\xi \in [t-\omega, t]$.

It should be noted that, following the definition of MDD, in case $K(t-\xi) = 1$,

$$D_{\omega}^{(1)} f(x,t) = \frac{1}{\omega}\int_{t-\omega}^{t} f_{\xi}'(x,\xi) d\xi = \frac{f(x,t) - f(x,t-\omega)}{\omega}$$

This indicates that, as $\omega \to 0$, MDD tends to common partial derivative of first order.

Recently, Yu, Hu, and Tian (2014) introduced MDD instead of factional derivative in the generalized heat conduction law. They inserted MDD into the Lord–Shulman generalized thermoelasticity theory in the rate of heat flux to indicate the memory reliance in the following manner:

$$q_i + \tau D_a q_i = -K\theta_{,i} \tag{8}$$

where $D_a q_i = D_a^{(1)} q_i = \frac{1}{a}\int_{t-a}^{t} k(t,p) q_i^{(1)}(p) dp$.

Nunziato (1971) proposed heat conduction model with memory response at slightly different way. He assumed the response functional can be memorized up to the present time of the temperature and the temperature gradient. In this model, heat conduction depends also on the present value of the temperature gradient so that Fourier's law of heat conduction is obtained as a particular case, if $k(0)$, the instantaneous conductivity, is nonzero. On the other hand, if $k(0) = 0$, Nunziato's (1971) heat conduction equation agrees with that of Gurtin and Pipkin (1968). Chen and Gurtin (1970) extended the theory presented by Gurtin and Pipkin (1968) to deformable media. They proposed with the constitutive assumptions that the response functional depends on the present values of the temperature and the deformation gradient and the integrated histories of the deformation gradient, temperature, and the temperature gradient.

Following the analysis of Lord and Shulman (1967), Green and Lindsay (1972), and Dhaliwal and Singh (1980) regarding generalized models of thermoelasticity and Nunziato (1971) in an isotropic medium, the linearized form of heat conduction equation can be expressed as:

$$\alpha(0)(\dot{\theta}+t_0\ddot{\theta})+\int_0^t\alpha'(s)\left[\dot{\theta}(x,t-s)+t_0\ddot{\theta}(x,t-s)\right]ds+\eta(0)\nabla.[\dot{\mathbf{u}}(x,t)+\delta_{mn}t_0\ddot{\mathbf{u}}(x,t)]$$
$$+\int_0^t\eta'(s)\nabla.[\dot{\mathbf{u}}(x,t-s)+\delta_{mn}t_0\ddot{\mathbf{u}}(x,t-s)]ds=k(0)\nabla^2\theta(x,t)+\int_0^t k'(s)\nabla^2\theta(x,t-s)ds \tag{9}$$

The stress–strain–temperature relation is,

$$\sigma_{ij}(x,t)=\lambda(0)e(x,t)\delta_{ij}-\beta(0)\left[\theta(x,t)+t_1\dot{\theta}(x,t)\right]\delta_{ij}+2\mu(0)e_{ij}(x,t)$$
$$+\int_0^t\left[\lambda'(s)e(x,t-s)\delta_{ij}-\beta'(s)(\theta(x,t-s)+t_1\dot{\theta}(x,t-s))\delta_{ij}+2\mu'(s)e_{ij}(x,t-s)\right]ds \tag{10}$$

Equations (9) and (10) correspond to that of LS theory if we take $t_1=0$ and $m=n$. Further, the above equation corresponds to that of GL theory for $m\neq n$. $\alpha(s)$ and $k(s)$ are the energy-temperature delay function and the heat conduction relaxation function, respectively. In thermoelastic materials, those functions correspond to, respectively, specific heat and conductivity of the material. $\lambda(s),\mu(s)$ may be called as the relaxation functions due to Lame. $\beta(s),\eta(s)$ are the relaxation functions corresponding to β and η where β is the coefficient of the temperature deviation in the stress--strain relation and η denotes the coupling parameter.

It should be remember that the relations

$$\beta(0)=(3\lambda(0)+2\mu(0))\alpha_T,\quad \eta(0)=T_0\beta(0) \tag{11}$$

where α_T is the coefficient of linear thermal expansion and T_0 is the reference temperature. Equation (11) holds for thermoelastic materials when $\alpha(s),\beta(s),\eta(s),\ k(s),\ \lambda(s),\mu(s)$ are all constants. Consequently, the Eqs. (9) and (10) reduce to the corresponding equations of usual linear thermoelasticity theory.

In the absence of body forces, the equation of motion in deformable body with memory becomes, using Eq. (10),

$$(\lambda(0)+2\mu(0))\nabla^2e(x,t)-\beta(0)(\nabla^2\theta(x,t)+t_1\frac{\partial}{\partial t}\nabla^2\theta(x,t))$$
$$+\int_0^\infty\left[(\lambda'(s)+2\mu'(s))\nabla^2e(x,t-s)-\beta'(s)(\nabla^2\theta(x,t-s)+t_1\frac{\partial}{\partial t}\nabla^2\theta(x,t-s))\right]ds=\rho\ddot{e}(x,t) \tag{12}$$

where $e(x,t)=div\mathbf{u}(x,t)$.

Later on, in the last decade of twentieth century, Green and Naghdi (1991, 1992, 1993, 1995) proposed a new class of heat conduction models for an elastic solid occupying a finite volume $\Omega\subset R^n$. The development was more general and the characterization of material response for the thermal phenomena was based on the three types of constitutive relations and they labeled as types I, II, and III.

Type I model: In this model, the constitute function consists of classical theory of heat conduction based on Fourier law:

$$q(x,t)=-K\nabla\theta(x,t);\quad (x,t)\in\Omega\times\mathbb{R} \tag{13}$$

where $\Omega\in\mathbb{R}^n$, θ is the absolute temperature and $K>0$ is the thermal conductivity.

Type II model: Contrary to type I model, one additional thermal state variable, namely thermal displacement, was adopted in type II and type III models, defined as

$$\alpha(x,t)=\alpha_0(x)+\int_0^t\theta(x,s)ds \tag{14}$$

where $\theta(x,t)$ is an empirical temperature scale, not necessarily the absolute one. More observations on the notion of thermal displacement, along with its history and use, can be found in the work of Podio-Guidugli (2009).

Type III model: Like type II model, the constitutive function of this model is also based on the thermal displacement variable $\alpha(x,t)$.

This model is characterized by the heat flux law:

$$q(x,t) = -k\nabla\theta(x,t) - k^*\nabla\alpha(x,t); \quad k^* > 0 \tag{15}$$

In the second half twentieth century, when Lord–Shulman (1967) and Green–Lindsay (1972) suggested several generalization of heat conduction laws with finite wave speed based on the heat flux rate-dependent terms, Coleman and Gurtin (1967) have also proposed one generalization to the heat flux constitutive law in the form of a hereditary relation given by,

$$q(x,t) = -k_0\nabla\theta(x,t) - \int_{-\infty}^{t} k(t-s)\nabla\theta(x,s)ds \tag{16}$$

where $k_0 \geq 0$, k is a convex summable function on the positive half-line.

For $k_0 = 0$, the Coleman–Gurtin model reduces to the linear model by Gurtin and Pipkin (1968). Further, if we substitute $k_0 = 0$ with $k(s) = \frac{K}{\tau}e^{-\frac{s}{\tau}}$, Eq. (13) reduces to the Maxwell–Cattaneo model, which is based upon a rate-type constitutive equation for the heat flux, that is,

$$\tau\dot{q}(x,t) + q(x,t) = -k_0\nabla\theta(x,t)$$

where $\tau(>0)$ is a small real positive quantity, termed as the thermal time delay and the superposed dot stands for the material time derivative.

The presence of memory in the generalized thermoelasticity theories, like GN models, became well established since the last decade of the twentieth century. The Coleman–Gurtin model can be specifically considered as a generalization to the Green–Naghdi type III model. Moreover, due to the presence of a time convolution integral, the Coleman–Gurtin (1968) theory is also referred to as the theory of heat conduction with a thermal memory.

In this regard, we can mention the work of Shaw (2017), a note on generalized thermoelasticity with MDDs, in which the author shown how MDDs play a significant impact in thermoelasticity theory.

The kernel $k(t, p)$ and the time delay $a(>0)$ in the definition of MDD should always be chosen in an arbitrary manner so that the material's real behavior can be understood more properly.

In common practice, the kernel function is considered in the following form:

$$k(t,p) = \left(\frac{p-t}{a} + 1\right)^b \tag{17}$$

The following are three different forms of kernels and the respective forms of heat conduction laws:

1. Constant kernel ($b=0$): $q(x,t) + \frac{\tau}{a}[q(x,t) - q(x,t-a)] = -K\frac{\partial\theta}{\partial x}$
2. Linear kernel ($b=1$): $q(x,t) + \frac{\tau}{a^2}\int_{t-a}^{t} q(x,p)dp = -K\frac{\partial\theta}{\partial x}$
3. Parabolic kernel ($b=2$): $q(x,t) + \frac{2\tau}{a^3}\int_{t-a}^{t}(p-t+a)q(x,p)dp = -K\frac{\partial\theta}{\partial x}$.

The kernel shows monotonic nature with $K=0$ for the past time $t-\xi$ and $K=1$ for the present time t.

In various thermoelastic investigations, Ezzat, El-Karamany, and El-Bary (2017) have proposed another form of the memory kernel as follows:

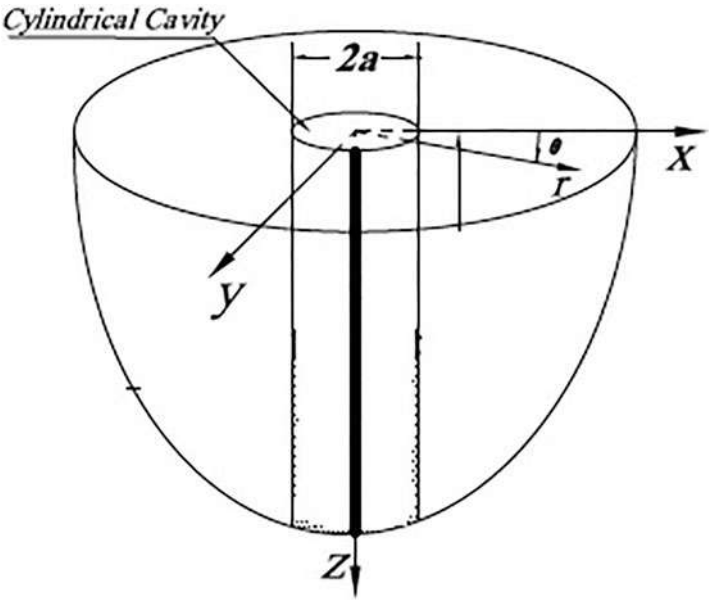

Figure 1. Schematic diagram of the problem.

$$k(t-p) = 1 - \frac{2b}{\omega}(t-p) + \frac{a^2(t-p)^2}{\omega^2} \tag{18}$$

where a, b, and ω are the parameters to be chosen.

Laplace transform of a function containing the MDD would have been a challenging task in our succeeding discussion. Thus, Laplace transform of any function $f(t)$ with first-order MDD is demonstrated here,

$$L[D_\omega f(t)] = \frac{\bar{f}(s)}{\omega}\left(\left(1 - \frac{2b}{\omega s} + \frac{2a^2}{\omega^2 s^2}\right) - e^{-\omega s}\left(1 - 2b^2 + a^2 + \frac{2(a^2-b)}{\omega s} + \frac{2a^2}{\omega^2 s^2}\right)\right) \tag{19}$$

If the kernel function in MDD is constant, that is, when $k(t,p) = 1$, then

$$L[D_\omega f(t)] = \frac{1}{\omega}(1 - e^{-\omega s})\bar{f}(s) \tag{20}$$

where $\bar{f}(s)$ denotes the Laplace transform of $f(t)$ and $f(t-\omega) = 0$ for $t < \omega$.

In the present article, our aim is to analyze the memory response on thermal disturbances in the context of Green–Naghdi (type III) theory of generalized thermoelasticity and as a special case, thermoelasticity without energy dissipation (type II). Later on, thermal disturbances due to GN models are meticulously compared with the recently proposed generalized thermoelasticity theory with MDDs. With these theoretical developments, we try to emphasize the fact that how memory-dependent generalized thermoelasticity model felt its impact on previously proposed thermoelasticity theory with memory?

3. Statement of the problem

Here, we consider a homogeneous, isotropic thermoelastic medium with a cylindrical hole (Fig. 1). Either the cylinder is full of a relatively hot fluid or a heat source is present inside the hole. Consequently, the heat will emanate from the hole into the considered elastic medium instantaneously. Moreover, the dimension of the radius of the hole $'a'$ is much lesser than that

of the whole medium. To analyze the considered thermoelastic problem, generalized theory of thermoelasticity due to Green and Naghdi (1993) and thermoelasticity theory with MDDs are adopted.

3.1. Basic equations

In the context of GN theory (type III model), the field equations for a linear, homogeneous, and isotropic thermoelastic solid body, in the absence of body forces and heat sources, with energy dissipation are as follows:

$$\mu\nabla^2\vec{u} + (\lambda+\mu)\vec{\nabla}\,(div\,\vec{u}) - \gamma\nabla\theta = \rho\ddot{\vec{u}}$$
$$k\nabla^2\dot{\theta} + k^*\nabla^2\theta = \rho C_e\ddot{\theta} + \gamma T_0 div\,\ddot{\vec{u}} \tag{21}$$

By adopting MDDs into the generalized thermoelasticity theory of Lord–Shulman type, the field equations for a linear, homogeneous, and isotropic thermoelastic solid body, in the absence of body forces and heat sources are given by,

$$\mu\nabla^2\vec{u} + (\lambda+\mu)\vec{\nabla}\,(div\,\vec{u}) - \gamma\nabla\theta = \rho\ddot{\vec{u}}$$
$$k\nabla^2\theta = (1+\tau D_\omega)\frac{\partial}{\partial t}(\rho C_e\theta + \gamma T_0 div\,\vec{u}) \tag{22}$$

in which $\vec{u}$ is the displacement vector; θ is the temperature change above a uniform reference temperature T_0; ρ is the mass density; C_e is the specific heat; λ and μ are the Lame's constant; $\gamma = (3\lambda+2\mu)\alpha_t$, α_t being the coefficient of linear thermal expansion and k, k^* are a material constants characteristic of the theory.

The stress matrix T associated with $\vec{u}$ and θ is given by

$$T = \lambda(div\,\vec{u})I + \mu(\nabla u + \nabla u^T) - \gamma\theta I \tag{23}$$

In all the above equations, the direct vector/tensor notation is employed. Also an over dot denotes partial derivatives with respect to the time variable t.

We suppose that the constants appearing in Eqs. (23)–(25) satisfy the inequalities:

$$\mu > 0, \quad \lambda+\mu > 0, \quad \rho > 0, \quad T_0 > 0, \quad C_e > 0, \quad \gamma > 0, \quad k > 0, \quad k^* > 0$$

Then, Eqs. (23) and (24) represent a fully hyperbolic system that permits finite speed for both elastic and thermal waves, which are coupled together in general.

3.2. Mathematical formulation

Mathematically, we assume that the thermal wave is generated due to an application of a constant step in temperature on the boundary of the hole which is held in a stress-free state. For radial symmetric interactions, the displacement vector possesses only the radial component $u = u(r,t)$, where r is the radial distance measured from the origin (point of symmetry) and the stress tensor is determined by the radial stress σ_{rr}, the circumferential stress (hoop stress) $\sigma_{\psi\psi}$, and the axial stress σ_{zz}. In this case, Eqs. (21) yield the following equations for u and θ:

$$\begin{aligned}
&(\lambda+2\mu)\left(\frac{\partial u}{\partial r}+\frac{1}{r}u\right)\frac{\partial u}{\partial r} - \gamma\frac{\partial\theta}{\partial r} = \rho\frac{\partial^2 u}{\partial t^2}\\
&k\frac{\partial}{\partial t}\left(\frac{\partial^2}{\partial r^2}+\frac{1}{r}\frac{\partial}{\partial r}\right)\theta + k^*\left(\frac{\partial^2}{\partial r^2}+\frac{1}{r}\frac{\partial}{\partial r}\right)\theta = \frac{\partial^2}{\partial t^2}\left(\rho C_e\theta + \gamma T_0\left(\frac{\partial u}{\partial r}+\frac{1}{r}u\right)\right)
\end{aligned} \tag{24}$$

Along with the following constitutive relations, which are obtained from Eq. (23):

$$\begin{aligned}\sigma_{rr} &= (\lambda+2\mu)\frac{\partial u}{\partial r}+\lambda\frac{u}{r}-\gamma\theta\\ \sigma_{\psi\psi} &= \lambda\frac{\partial u}{\partial r}+(\lambda+2\mu)\frac{u}{r}-\gamma\theta\\ \sigma_{zz} &= \lambda\left(\frac{\partial u}{\partial r}+\frac{u}{r}\right)-\gamma\theta\end{aligned} \tag{25}$$

It will be convenient for us to rewrite the Eqs. (24) in terms of e and θ, where e is the cubical dilatation given by

$$e=\frac{\partial u}{\partial r}+\frac{u}{r}.$$

Thus Eqs. (24) can be expressed as follows:

$$\begin{aligned}&(\lambda+2\mu)\left(\frac{\partial^2}{\partial r^2}+\frac{1}{r}\frac{\partial}{\partial r}\right)e-\gamma\left(\frac{\partial^2}{\partial r^2}+\frac{1}{r}\frac{\partial}{\partial r}\right)\theta=\rho\frac{\partial^2 e}{\partial t^2}\\ &k\frac{\partial}{\partial t}\left(\frac{\partial^2}{\partial r^2}+\frac{1}{r}\frac{\partial}{\partial r}\right)\theta+k^*\left(\frac{\partial^2}{\partial r^2}+\frac{1}{r}\frac{\partial}{\partial r}\right)\theta=\frac{\partial^2}{\partial t^2}(\rho C_e\theta+\gamma T_0 e)\end{aligned} \tag{26}$$

For mathematical analysis, it is convenient to have Eqs. (25) and (26) rewritten in nondimensional form. For this purpose, we consider the following transformations:

$$r'=\frac{r}{a_0},\quad t'=\frac{V}{a_0}t,\quad u'=\frac{\lambda+2\mu}{a_0\gamma T_0}u,\quad \theta'=\frac{\theta}{T_0},\quad \sigma'_{rr}=\frac{\sigma_{rr}}{\gamma T_0},\quad \sigma'_{\psi\psi}=\frac{\sigma_{\psi\psi}}{\gamma T_0},$$

$$\sigma'_{zz}=\frac{\sigma_{zz}}{\gamma T_0},\quad e'=\frac{\lambda+2\mu}{a_0\gamma T_0}e$$

where a_0 is a standard length and V is a standard speed, using these transformations in Eqs. (25) and (26) and suppressing primes for simplicity in the notations, we obtain the following equations in nondimensional form:

$$\begin{aligned}&C_P^2\left[\left(\frac{\partial^2}{\partial r^2}+\frac{1}{r}\frac{\partial}{\partial r}\right)e-\left(\frac{\partial^2}{\partial r^2}+\frac{1}{r}\frac{\partial}{\partial r}\right)\theta\right]=\frac{\partial^2 e}{\partial t^2}\\ &C_T^2\frac{\partial}{\partial t}\left(\frac{\partial^2\theta}{\partial r^2}+\frac{1}{r}\frac{\partial\theta}{\partial r}\right)+C_S^2\left(\frac{\partial^2\theta}{\partial r^2}+\frac{1}{r}\frac{\partial\theta}{\partial r}\right)=\frac{\partial^2}{\partial t^2}\left(\theta+\varepsilon\left(\frac{\partial u}{\partial r}+\frac{u}{r}\right)\right)\end{aligned} \tag{27}$$

$$\sigma_{rr}=\frac{\partial u}{\partial r}+\eta\frac{u}{r}-\theta \tag{28}$$

$$\sigma_{\psi\psi}=\eta\frac{\partial u}{\partial r}+\frac{u}{r}-\theta \tag{29}$$

$$\sigma_{zz}=\eta\left(\frac{\partial u}{\partial r}+\frac{u}{r}\right)-\theta \tag{30}$$

Here

$$C_P^2=\frac{\lambda+2\mu}{\rho V^2},C_T^2=\frac{k}{\rho C_e V a_0},C_S^2=\frac{k^*}{\rho C_e V^2},\varepsilon=\frac{\gamma^2 T_0}{\rho C_e(\lambda+2\mu)},\eta=\frac{\lambda}{\lambda+2\mu} \tag{31}$$

We note that C_P, C_T, and C_S, respectively, represent the nondimensional speeds of purely elastic dilatational wave and purely thermal wave and ε is the usual thermoelastic coupling factor.

3.3. Initial and boundary conditions

The body being considered for our analysis here is an unbounded thermoelastic solid with circular cylindrical hole. If initially the body is at rest in an undeformed state and has its temperature change and temperature rate equal to zero, then the following initial conditions hold:

$$u = \frac{\partial u}{\partial t} = \theta = \frac{\partial \theta}{\partial t} = 0 \ \ at \ \ t = 0 \ \ for \ \ r \geq 1 \tag{32}$$

If the thermoelastic interactions are caused by a uniform step in temperature applied to the boundary of the cylindrical hole which is held in the stress-free state, then the following boundary conditions hold:

$$\theta = T_0 H(t), \sigma_{rr} = 0 \ \ for \ \ r = 1, \ \ t > 0 \tag{33}$$

where $H(t)$ is the Heaviside unit step function.

Using Eqs. (28) and (33), these boundary conditions can be rewritten as

$$\frac{\partial u}{\partial r} + \eta \frac{u}{r} = T_0 H(t) \ \ for \ \ r = 1, \ \ t > 0 \tag{34}$$

Hence, for our concerned problem, the field equations together with the constitutive equations are given by Eqs. (27)–(30), and the initial and boundary conditions are provided in Eqs. (32) and (34), respectively. Once u and θ are determined by solving this initial boundary value problem, then σ_{rr}, $\sigma_{\psi\psi}$, and σ_{zz} can be computed by using Eqs. (28)–(30).

4. Solution in integral transform domain

Adopting Laplace transform technique, the dimensionless governing equations are expressed in the integral transform domain as a vector matrix differential equation in cylindrical polar coordinates. Later, the considered vector matrix differential equation shall be solved by an eigenvalue approach in the Laplace transform domain.

4.1. Solution using GN (type III) model

Performing Laplace transform on Eqs. (27), we obtain

$$\left(\frac{d^2}{dr^2} + \frac{1}{r}\frac{d}{dr}\right)(\bar{e} - \bar{\theta}) = \frac{s^2}{C_P^2}\bar{e} \tag{35}$$

and

$$(C_T^2 s + C_S^2)\left(\frac{d^2}{dr^2} + \frac{1}{r}\frac{d}{dr}\right)\bar{\theta} = s^2(\bar{\theta} + \varepsilon\bar{e}) \tag{36}$$

Using Eq. (36), Eq. (35) yields,

$$\mathbf{L}\bar{e} = s^2\left(\frac{1}{C_P^2} + \frac{\varepsilon}{C_T^2 s + C_S^2}\right)\bar{e} + \frac{s^2}{C_T^2 s + C_S^2}\bar{\theta} \tag{37}$$

where

$$\mathbf{L} \equiv \frac{d^2}{dr^2} + \frac{1}{r}\frac{d}{dr} \tag{38}$$

And using operator (38), Eq. (36) is represented as

$$\mathbf{L}\bar{\theta} = s^2\left(\frac{\varepsilon}{C_T^2 s + C_S^2}\bar{e} + \frac{1}{C_T^2 s + C_S^2}\bar{\theta}\right) \tag{39}$$

Equations (37) and (39) can be written in the form of a vector matrix differential equation as:

$$\mathbf{L}\tilde{v} = \tilde{A}\tilde{v} \tag{40}$$

where

$$\tilde{A} = \begin{pmatrix} c_{11} & c_{12} \\ c_{21} & c_{22} \end{pmatrix}$$
$$\bar{v} = \begin{pmatrix} \bar{e} & \bar{\theta} \end{pmatrix}^T$$

in which,

$$c_{11} = s^2\left(\frac{1}{C_P^2} + \frac{\varepsilon}{C_T^2 s + C_S^2}\right), c_{12} = c_{22} = \frac{s^2}{C_T^2 s + C_S^2}, c_{21} = \frac{s^2}{c_P^2} \tag{41}$$

The characteristic equation of matrix $\tilde{A}$ can be written as:

$$\lambda^2 - (c_{11} + c_{22})\lambda + (c_{11}c_{22} - c_{12}c_{21}) = 0 \tag{42}$$

Assuming the eigenvalues of the matrix $\tilde{A}$ to be of the form: $\lambda_1 = m_1^2$ and $\lambda_2 = m_2^2$, the right eigenvector $\tilde{X}$ corresponding to the eigenvalue λ of the matrix $\tilde{A}$ can be calculated as:

$$\tilde{X} = \begin{pmatrix} -c_{12}, c_{11} - \lambda \end{pmatrix}^T \tag{43}$$

Thus, one can calculate the eigenvector corresponding to the eigenvalues $\lambda_i \quad (i = 1, 2)$. We denote them as:

$$\begin{aligned} \tilde{X}_1 &= (-c_{12}, c_{11} - m_1^2)^T \\ \tilde{X}_2 &= (-c_{12}, c_{11} - m_2^2)^T \end{aligned} \tag{44}$$

In order to satisfy the regularity conditions at $r \to \infty$ of the field functions, solution of Eq. (40) can be taken in the following form:

$$\tilde{v} = \sum_{i=1}^{2} A_i \tilde{X}_i K_0(m_i r) \tag{45}$$

where $K_0(.)$ being the modified Bessel function of second kind of 0^{th} order.

Using Eqs. (40) and (45) and considering the boundary conditions taken in dimensionless form, we get

$$\bar{u}(r,s) = \frac{c_{12}}{\Delta s}\left[(\xi_2 - \Omega_2)\frac{K_1(m_1 r)}{m_1} - (\xi_1 - \Omega_1)\frac{K_1(m_2 r)}{m_2}\right] \tag{46}$$

$$\bar{\theta}(r,s) = \frac{1}{\Delta s}[(c_{11} - m_1)(\xi_2 - \Omega_2)K_0(m_1 r) - (c_{11} - m_2)(\xi_1 - \Omega_1)K_0(m_2 r)] \tag{47}$$

$$\begin{aligned} \bar{\sigma}_{rr}(r,s) = {} & \frac{c_{12}(\xi_2 - \Omega_2)}{\Delta s}\left(-K_0(m_1 r) + \frac{\eta - 1}{m_1 r}K_1(m_1 r) - (c_{11} - m_1)K_0(m_1 r)\right) \\ & - \frac{c_{12}(\xi_1 - \Omega_1)}{\Delta s}\left(-K_0(m_2 r) + \frac{\eta - 1}{m_2 r}K_1(m_2 r) - (c_{11} - m_2)K_0(m_2 r)\right) \end{aligned} \tag{48}$$

$$\begin{aligned} \bar{\sigma}_{\psi\psi}(r,s) = {} & \frac{\xi_2 - \Omega_2}{\Delta s}\left[c_{12}\left(\frac{1 - \eta}{m_1 r}K_1(m_1 r) - K_0(m_1 r)\right) - (c_{11} - m_1)K_0(m_1 r)\right] \\ & - \frac{\xi_1 - \Omega_1}{\Delta s}\left[c_{12}\left(\frac{1 - \eta}{m_2 r}K_1(m_2 r) - K_0(m_2 r)\right) - (c_{11} - m_2)K_0(m_2 r)\right] \end{aligned} \tag{49}$$

$$\bar{\sigma}_{zz}(r,s) = \frac{\xi_1 - \Omega_1}{\Delta s}[\eta c_{12} + (c_{11} - m_2)]K_0(m_2 r) - \frac{\xi_2 - \Omega_2}{\Delta s}[\eta c_{12} + (c_{11} - m_1)]K_0(m_1 r) \tag{50}$$

where

$$\Omega_i = (c_{11} - m_i)K_0(m_i)$$
$$\xi_i = c_{12}\left((\eta - 1)\frac{K_1(m_i)}{m_i} - K_0(m_i)\right)$$
$$\Delta = \Omega_1\xi_2 - \Omega_2\xi_1$$
$$m_i^2 = \frac{2s^2C_P{}^2\varepsilon}{(C_T{}^2s + C_S{}^2)\left[\beta + (-1)^{i+1}(\beta^2 - 4C_P{}^4\varepsilon)^{\frac{1}{2}}\right]}$$
$$\beta = C_T^2 s + C_S^2 + C_P^2(1 + \varepsilon)$$

Green–Naghdi model without energy dissipation:
At $k = 0$, the governing equations and the corresponding solutions illustrated in the preceding sections reduce the generalized thermoelasticity without energy dissipation theory due to Green and Naghdi.

4.2. Solution under the light of generalized thermoelasticity theory with MDD

Considering the time derivative to be memory dependent in the generalized heat conduction equation, we obtain the following dimensionless governing equations for u and θ:

$$C_P^2\left[\left(\frac{\partial^2}{\partial r^2} + \frac{1}{r}\frac{\partial}{\partial r}\right)e - \left(\frac{\partial^2}{\partial r^2} + \frac{1}{r}\frac{\partial}{\partial r}\right)\theta\right] = \frac{\partial^2 e}{\partial t^2}$$
$$C_T^2\left(\frac{\partial^2\theta}{\partial r^2} + \frac{1}{r}\frac{\partial\theta}{\partial r}\right) = (1 + \tau D_\omega)\frac{\partial}{\partial t}(\theta + \varepsilon e) \tag{51}$$

Proceeding in a similar way as in the previous section, we get the expressions for deformation, temperature and stresses as given in Eqs. (46)–(50), where the expressions for Ω_i, ξ_i, and Δ remain same, but

$$c_{11} = \frac{s^2}{C_P^2} + \frac{ss_1\varepsilon}{C_T^2}, c_{12} = c_{22} = \frac{ss_1}{C_T^2}, c_{21} = \frac{ss_1\varepsilon}{C_T^2} \tag{52}$$

where the expression for s_1 is:
$s_1 = 1 + \frac{\tau}{\omega}(1 - e^{-s\omega})$, when we consider the constant kernel form in MDD, and
$s_1 = 1 + \frac{\tau}{\omega}\left(\left(1 - \frac{2b}{\omega s} + \frac{2a^2}{\omega^2 s^2}\right) - e^{-\omega s}(1 - 2b^2 + a^2 + \frac{2(a^2-b)}{\omega s} + \frac{2a^2}{\omega^2 s^2})\right)$, when we consider the kernel form as mentioned in Eq. (18);
and

$$m_i^2 = \frac{2s^2 s_1}{\beta + (-1)^{i+1}(\beta^2 - 4ss_1C_P^2C_T^2)^{\frac{1}{2}}} \tag{53}$$

in which

$$\beta = s_1(1 + \varepsilon)C_P^2 + sC_T^2 \tag{54}$$

Special cases:
(i) ***Case I:*** Letting $a = 0$, $b = 0$, and $\omega \to 0$, we see that the MDD $D_\omega f(t)$ tends to the traditional derivative $\frac{d}{dt}f(t)$, and hence owing to such a case, the expressions for displacement, temperature, and stresses obtained under the light of generalized thermoelasticity theory with MDD are transformed to the expressions of the field functions for Lord–Shulman theory of generalized thermoelasticity:

where

$$m_i^2 = \frac{2s^2(1+\tau s)}{\beta + (-1)^{i+1}\left(\beta^2 - 4s(1+\tau s)C_P^2 C_T^2\right)^{\frac{1}{2}}} \tag{55}$$

in which

$$\beta = (1+\tau s)(1+\varepsilon)C_P^2 + sC_T^2 \tag{56}$$

(ii) ***Case II:*** Solutions for classical coupled thermoelasticity can be obtained by neglecting the thermal time delay (i.e., $\tau = 0$) in Eq. (51).

Consequently,

$$s_1 = 1$$

and hence,

$$m_i^2 = \frac{2s^2}{\beta + (-1)^{i+1}(\beta^2 - 4sC_P^2 C_T^2)^{\frac{1}{2}}} \tag{57}$$

and

$$\beta = (1+\varepsilon)C_P^2 + sC_T^2 \tag{58}$$

5. Numerical results and discussion

In order to obtain the final solutions of the physical quantities in space-time domain, we must invert the transforms given in Eqs. (46)–(50). Considering the fact that the expressions for m_i and Ω_i given in the preceding sections are complicated functions of s, the Laplace inversion for the expressions of $\bar{u}$ and $\bar{\theta}$ given in Eqs. (46) and (47) for all values of s becomes redoubtable in nature. Hence, we adopt the path of deriving the numerically approximate solutions for the field equations. For inverting the Laplace transforms in the required equations, we employ the algorithm for numerical inversion given by Honig and Hirdes (1984).

In this method, the Laplace transform $\bar{f}(r,s)$ has the inverse $f(r,t)$, which is given by the relation

$$f(r,t) = \frac{e^{\nu t}}{2\pi}\int_{-\infty}^{\infty} e^{i\omega t}\bar{f}(r,s)d\omega \tag{59}$$

where $s = \nu + i\omega \quad (\nu, \omega \in \mathbb{R})$

Darbin derived the approximated numerical inversion relation by expanding the function $h(r,t) = e^{-\nu t}f(r,t)$ in a Fourier series in the interval $[0, 2T]$. After summing the series up to a finite number N, we get the approximated value for $f(r,\ t)$ as,

$$\begin{aligned} f_N(r,t) = &-\frac{e^{\nu t}}{2T}Re\{\bar{f}(r,\nu)\} + \frac{e^{\nu t}}{T}\sum_{k=0}^{N} Re\left\{\bar{f}\left(r, \nu + i\frac{k\pi}{T}\right)\right\}\cos\left(\frac{k\pi}{T}t\right) \\ &-\frac{e^{\nu t}}{T}\sum_{k=0}^{N} Im\left\{\bar{f}\left(r, \nu + i\frac{k\pi}{T}\right)\right\}\sin\left(\frac{k\pi}{T}t\right) \end{aligned} \tag{60}$$

Now, for reducing the total error, we use the Korrektur method and then the $\epsilon - algorithim$ for reducing the discretizational error and hence to accelerate convergence.

For the purpose of numerical evaluation in the space-time domain, we choose the parameters of copper-like materials where the values of physical constants are as follows (for details, see Chandrasekharaiah and Srinath (1998) and Banerjee, Shaw, and Mukhopadhyay (2018)):

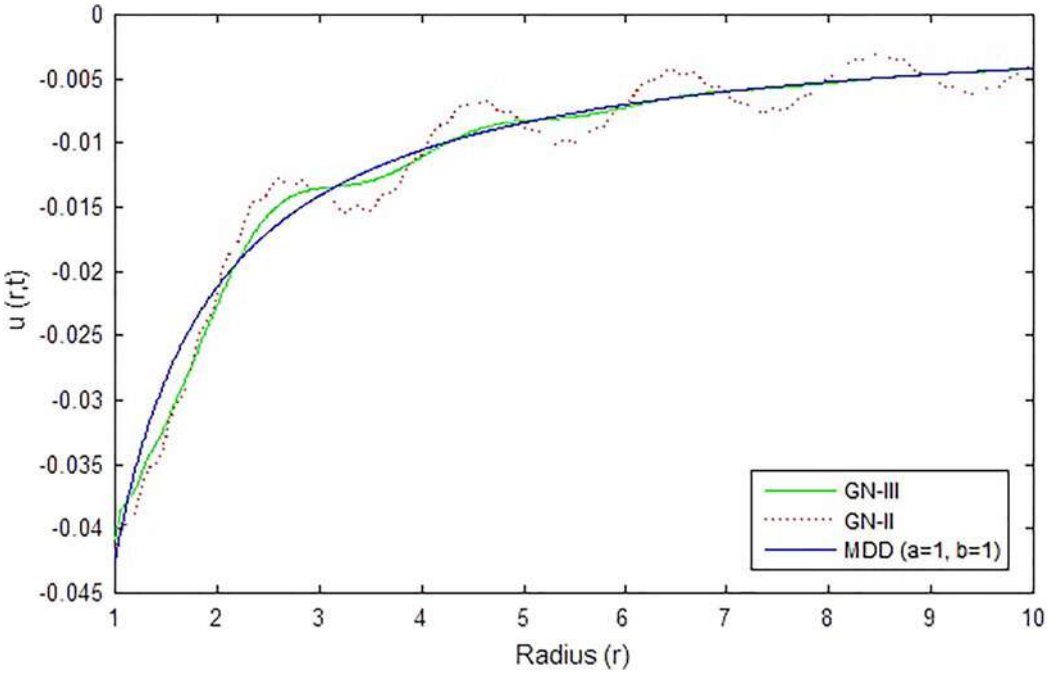

Figure 2. Comparison of displacement u(r, t) with MDD and GN models.

$$\lambda = 7.76 \times 10^{10} Nm^{-2}, \quad \mu = 3.86 \times 10^{10} Nm^{-2}, \quad \rho = 8954 kgm^{-3}, \varepsilon = 0.0168, \quad C_T = 2,$$
$$T_0 = 293K, \quad C_e = 381 Jkg^{-1}K^{-1}, \quad k = 400 Wm^{-1}K^{-1}, \quad k^* = 300 Wm^{-1}K^{-1}s^{-1}$$

Numerical computations were carried out comparing the displacement, temperature, radial, and axial stresses along the radius of the body in the context of both MDD model and Green–Naghdi models (with and without energy dissipation). The time moment for all graphically demonstrated physical phenomena is considered to be $t = 0.02$. The comparisons are demonstrated graphically in Figs. 2–13 for different values of a and b. Moreover, a graphical comparison of our results was carried out with reference to the work of Youssef (2005) (LS model).

Figures 2–4 represented the various displacements along the radius in comparison with the Green–Naghdi models, LS model, and MDD model for various values of a and b. In Figs. 2–4, we observed that the displacement is maximum near the surface of the cylindrical hole and it proportionately decreases along the radius of the elastic body. Further in Fig. 4, the displacement graph is noted to coincide for the LS, nonlinear MDD $(a = 1, b = 1)$, and the linear MDD models $(a = 0, b = 1/2)$.

Figures 5–7 showed that for all thermoelasticity models under consideration, the temperature is maximum at the surface of the hole and it gradually decreases as we move away radially from the hole. Similar to the nature of displacement, the rise in temperature is maximum for GN type III model followed by GN type II model and MDD model. From Figs. 5 and 6, we detected that near the vicinity of the cylindrical hole, the difference in the varying results of temperature distribution between the MDD model and GN models is greater in nonlinear MDD model when compared with the linear MDD model.

Figures 8–10 exhibited that the radial stress gets maximized near the inner surface of the hole. Although the radial stresses for different models gradually converge to a constant value as we move away from the center of the hole, the radial stress generated in the GN models is more near immediate vicinity of the surface of the hole when compared with MDD model. Figures 8

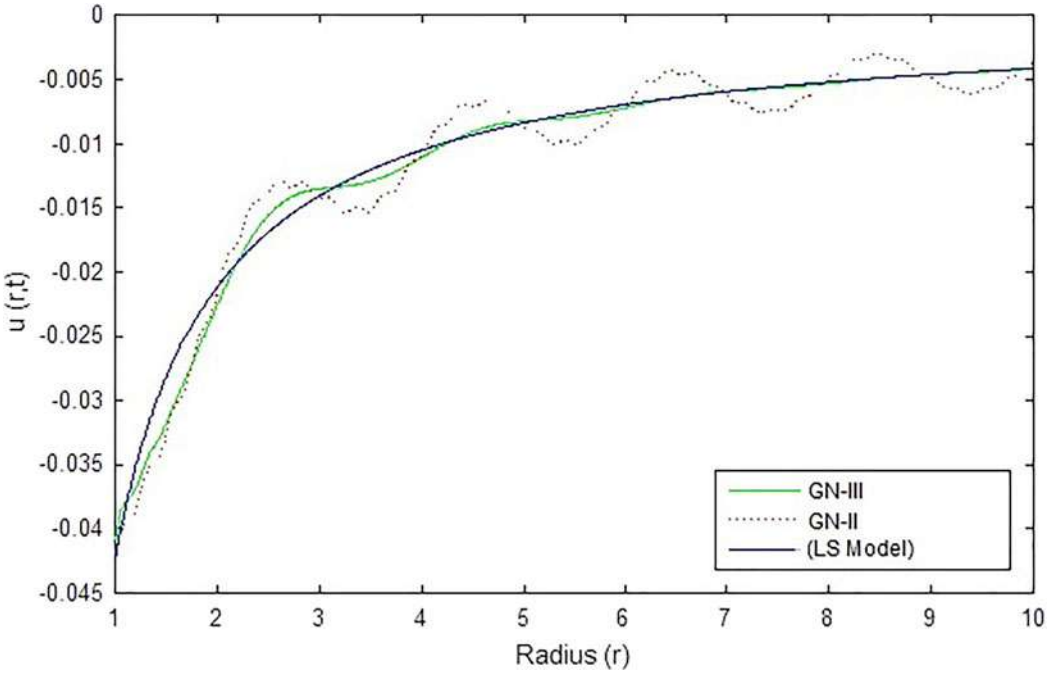

Figure 3. Comparison of displacement u(r, t) with LS model (Youssef 2005) and GN models.

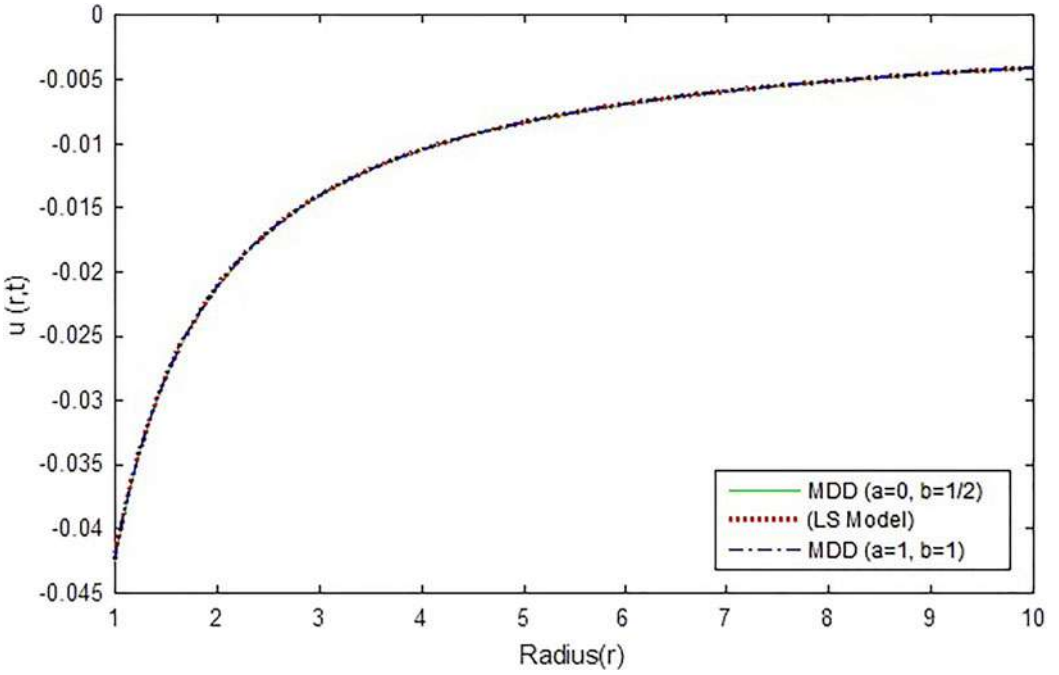

Figure 4. Comparison of displacement u(r, t) with LS model (Youssef 2005) and MDD models.

and 9 showed similar graphical traits for radial stresses among LS model (see Youssef (2005)) and the nonlinear MDD model.

Figures 11–13 displayed the graphical results for axial stress in the context of different thermoelastic models under consideration. In Figs. 11 and 12, the axial stress indicated proportionately

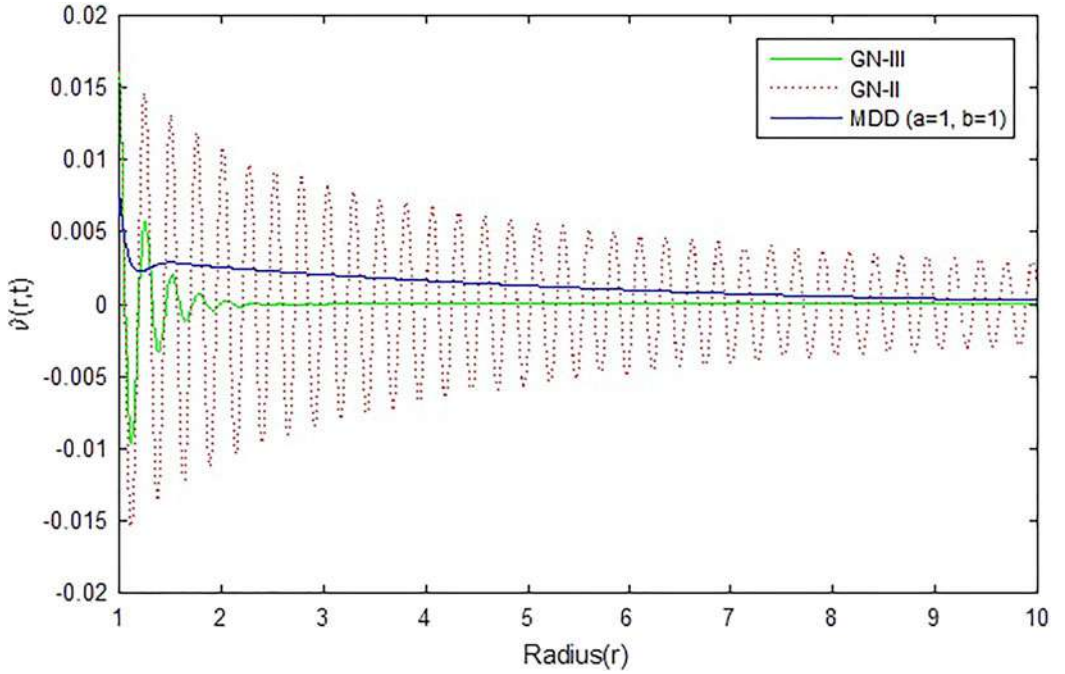

Figure 5. Comparison of temperature $\theta(r,t)$ with MDD and GN models.

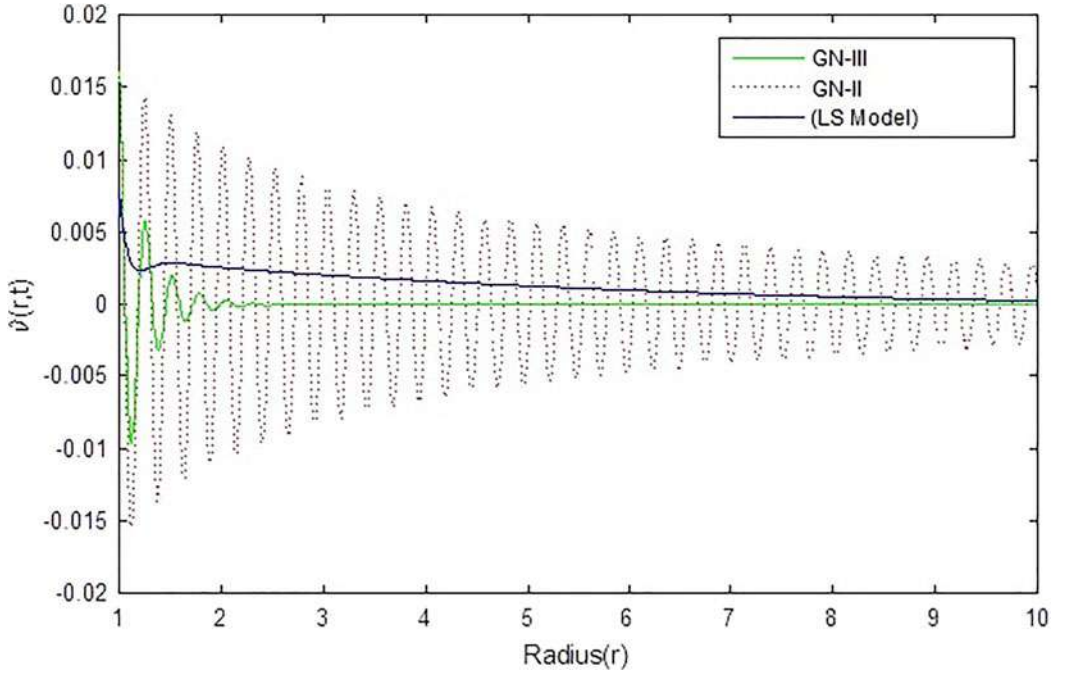

Figure 6. Comparison of temperature $\theta(r,t)$ with LS model (Youssef 2005) and GN models.

similar results like radial stress. Considering $a=0$, $b=0$, and $\omega \to 0$ in the expression of MDD, the memory-dependent thermoelasticity model converges with the Lord–Shulman model for generalized thermoelasticity. Owing to the effect of a constant heat source, Fig. 13 conveyed that the nature of the axial stress near the vicinity of the hole in the context of Lord–Shulman model

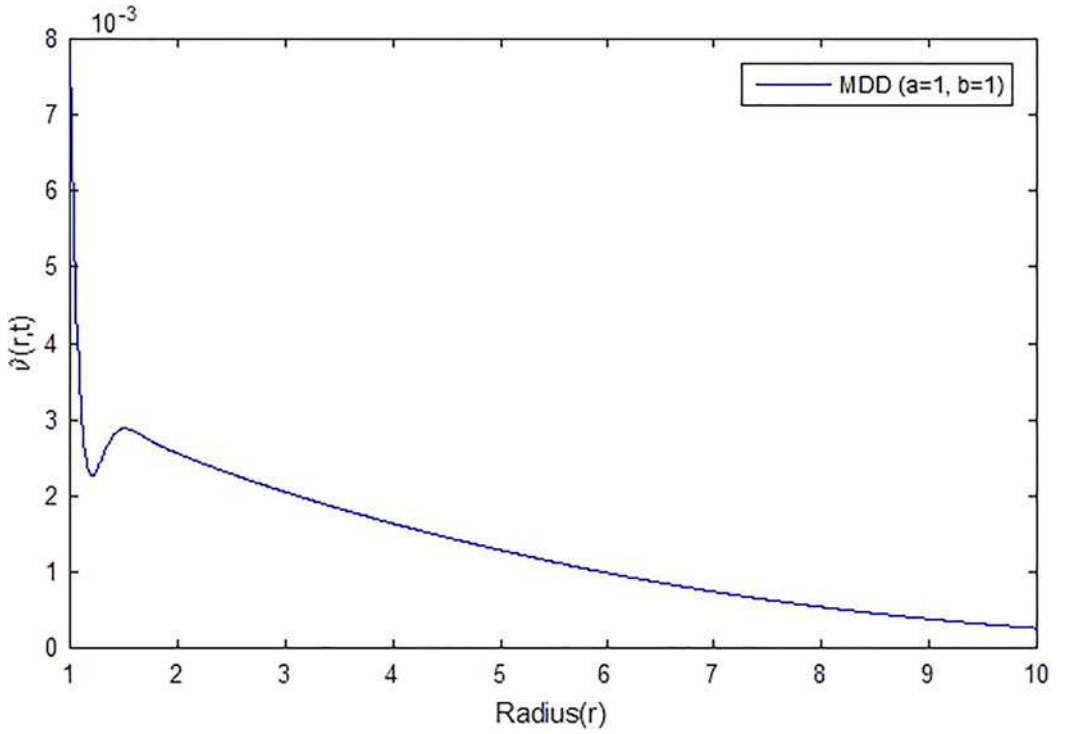

Figure 7. Variation of temperature $\theta(r,t)$ in nonlinear MDD model.

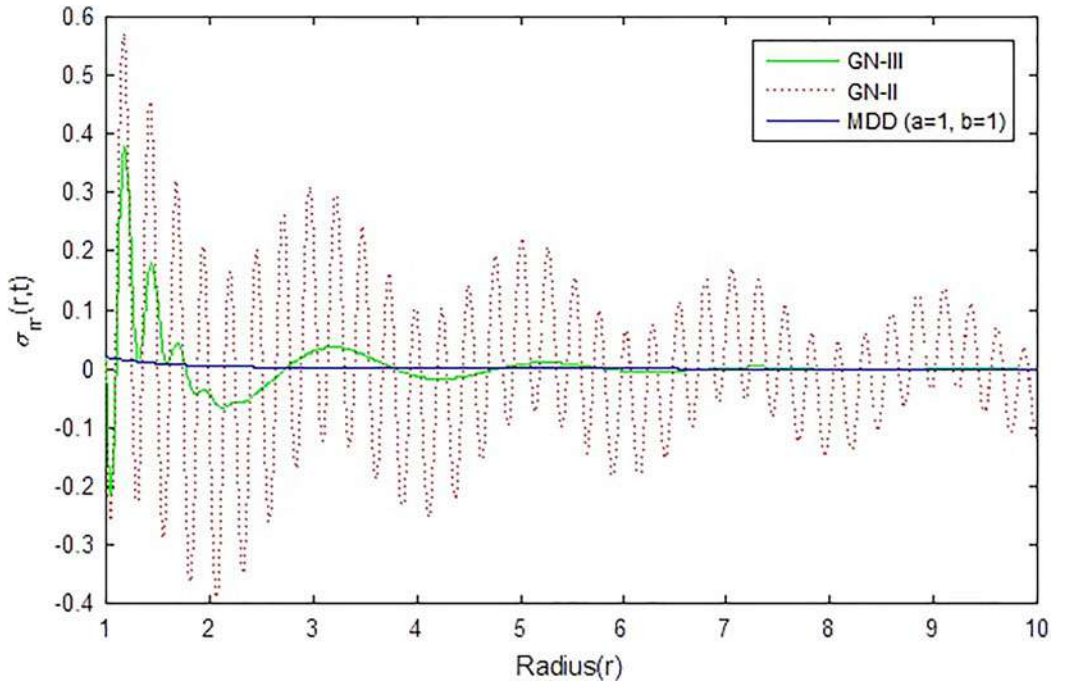

Figure 8. Comparison of radial stresses $\sigma_{rr}(r,t)$ with MDD and GN models.

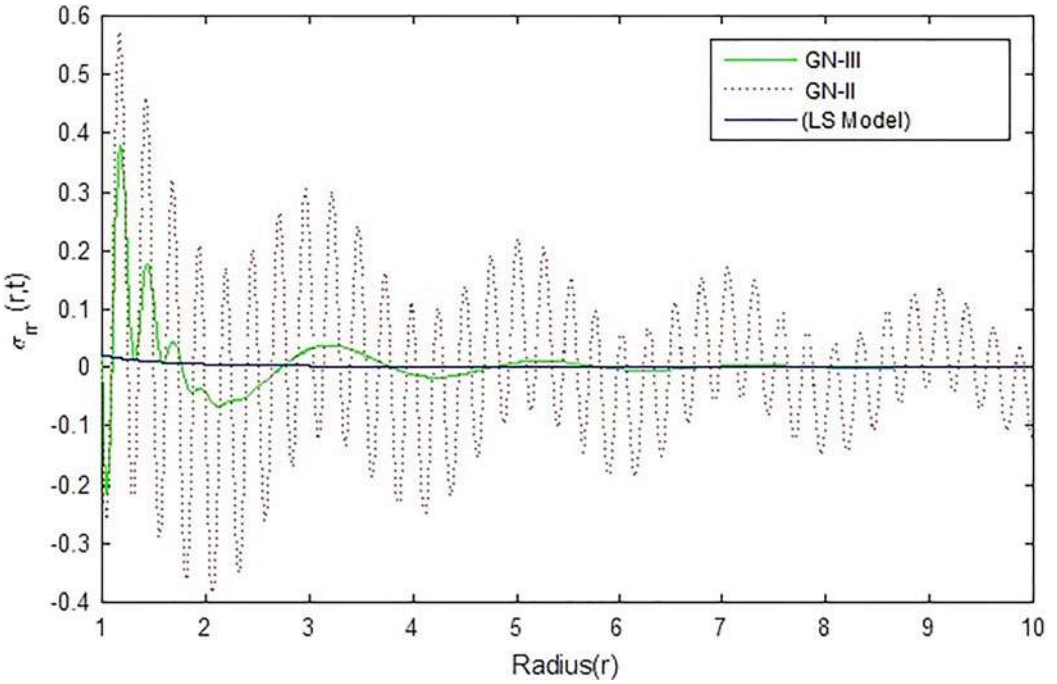

Figure 9. Comparison of radial stresses $\sigma_{rr}(r,t)$ with LS model (Youssef 2005) and GN models.

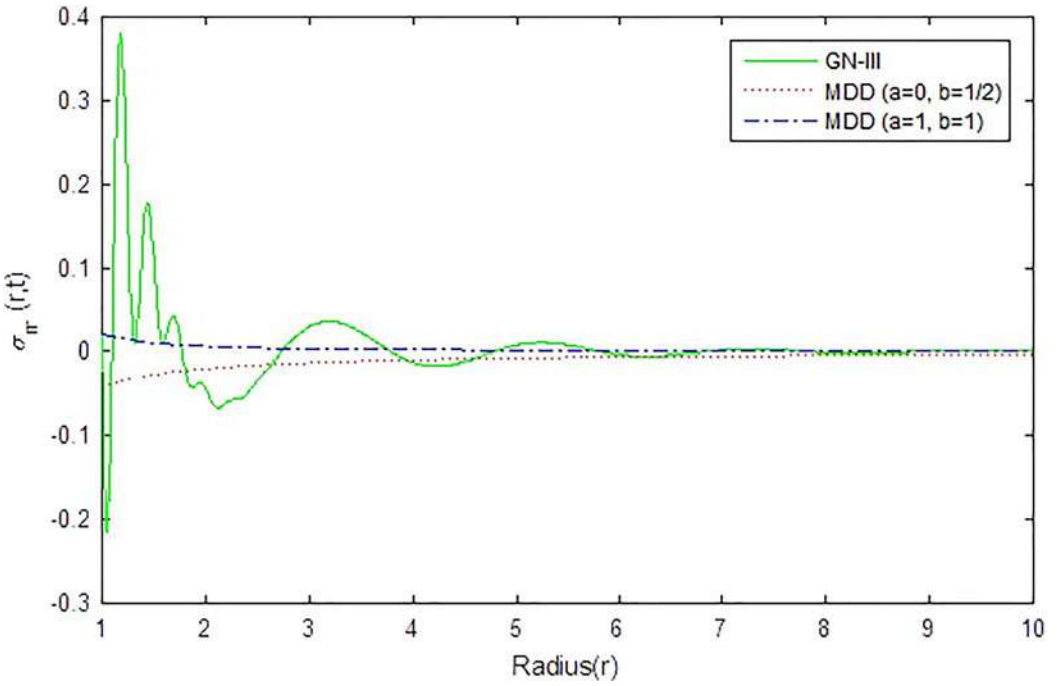

Figure 10. Comparison of radial stresses $\sigma_{rr}(r,t)$ with GN III and MDD models.

differs from GN models. The magnitude of the axial stress in LS model is significantly less than the stress generated by the GN models at the neighborhood of the hole but they gradually converge as we move away from the heat source.

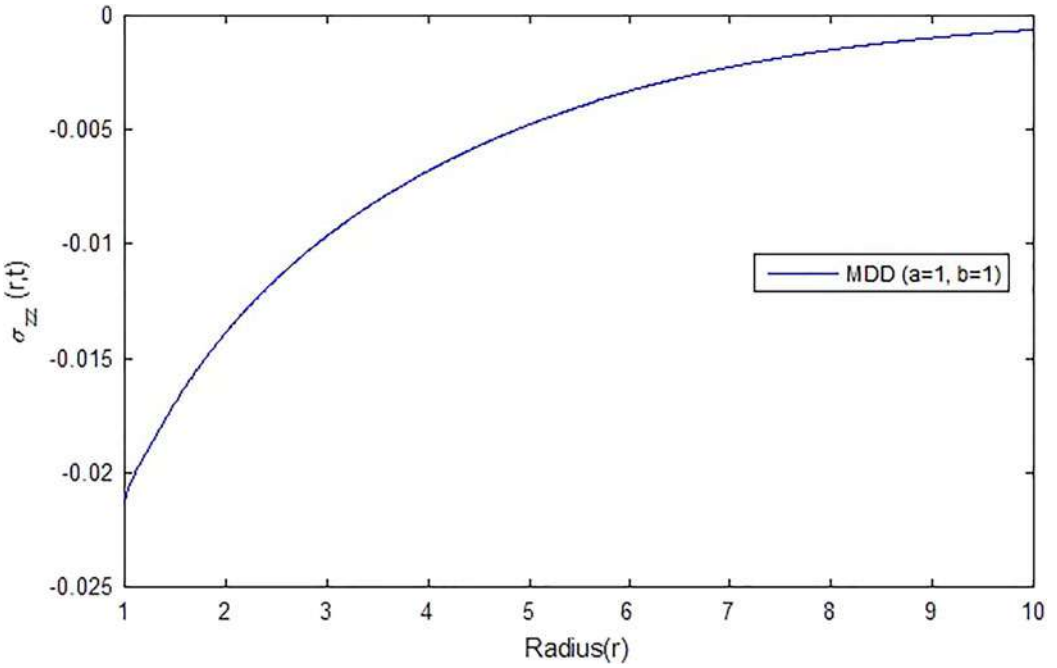

Figure 11. Variation of axial stress $\sigma_{zz}(r,t)$ in nonlinear MDD model.

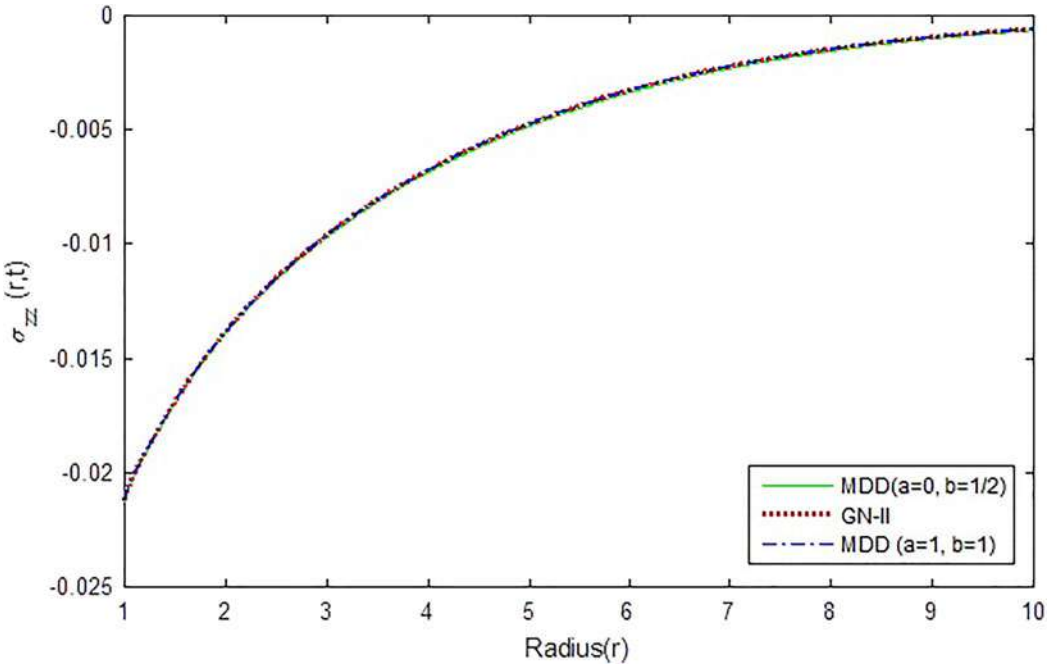

Figure 12. Comparison of axial stresses $\sigma_{zz}(r,t)$ with GN II and MDD models.

Comparing Figs. 2, 4, 5, 7, 8, and 10, we notice that for displacement, temperature, and radial stress, the graphs show almost similar nature for nonlinear MDD model and LS model for generalized thermoelasticity.

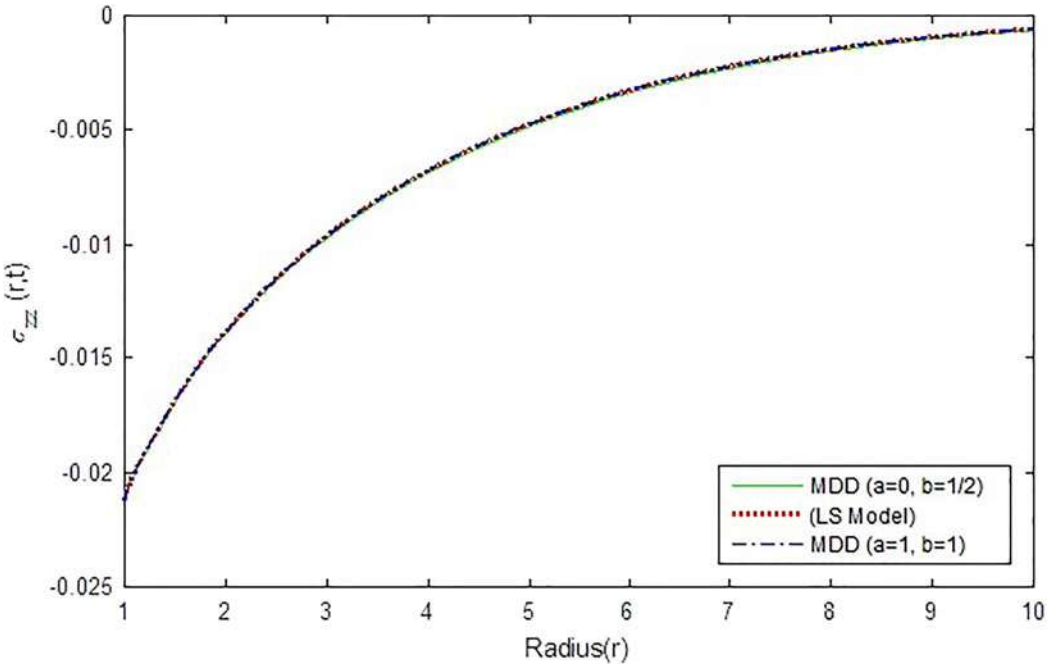

Figure 13. Comparison of axial stresses $\sigma_{zz}(r,t)$ with LS model (Youssef 2005) and MDD models.

In the presence of memory-dependent kernel in the generalized thermoelasticity, the observed values are significantly smaller than GN models in the context of infinitesimal theory of elasticity. Consequently, one can select an appropriate kernel to enhance the memory effect over thermal disturbances. It justified the fact that nonlocality has a remarkable impact over not only the thermoelasticity models with thermal time delay but also on the GN models. Thus, it has been revealed that the memory in the thermal displacement, which was incorporated in GN type II and type III models, is not enough to describe the exact memory of material response in the background of generalized thermoelasticity.

6. Conclusion

After analyzing the theoretical and computational aspects, we observe the following phenomena:

1. The present article provides a detailed comparative analysis of the memory response on thermal disturbances in the context of Green–Naghdi theories for generalized thermoelasticity (with and without energy dissipation) and the recently proposed generalized thermoelasticity theory with MDDs.
2. The theoretical developments and computational results showed that the memory-dependent generalized thermoelasticity model maintained an almost proportional difference throughout when compared with the Green–Naghdi theories for generalized thermoelasticities.
3. Upon selecting an appropriate kernel with the required values of the constants, one may enhance the memory effects in the theory of thermoelasticity. The influence of memory in thermoelastic models under consideration had a consequential effect over them. The graphical results suggested that the memory connected to thermal displacement was insufficient to cater the needs of nonlocality phenomenon in hyperbolic thermoelasticity.

4. The graphical results revealed that in all physical aspects (namely displacement, temperature, radial stress, and tangential stress), Green–Naghdi type III model gives an upper bound of the computed results among the considered generalized models.

The analysis and results exhibited in this article may prove to be functional for researchers who are working on material science, mathematical physics, thermodynamics with low temperatures, as well as on the evolution of the hyperbolic thermoelasticity theory.

References

Abbas, I. A. 2015. Analytical solution for a free vibration of a thermoelastic hollow sphere. *Mechanics Based Design of Structures and Machines* 43 (3):265–76. doi:10.1080/15397734.2014.956244.

Abbas, I. A. 2017. Free vibration of a thermoelastic hollow cylinder under two-temperature generalized thermoelastic theory. *Mechanics Based Design of Structures and Machines* 45 (3):395–405. doi:10.1080/15397734.2016.1231065.

Atanackovi, T. M., S. Pilipovi, B. Stankovi, and D. Zorica. 2014. *Fractional calculus with application in mechanics*. London: Wiley.

Banerjee, S., S. Shaw, and B. Mukhopadhyay. 2018. Memory response on thermal wave propagation emanating from a cavity in an unbounded elastic solid. *Journal of Thermal Stresses* 41:970–88. doi:10.1080/01495739.2018.1461041.

Biot, M. 1956. Thermoelasticity and irreversible thermodynamics. *Journal of Applied Physics* 27 (3):240–53. doi:10.1063/1.1722351.

Biswas, S., B. Mukhopadhyay, and S. Shaw. 2019. Effect of rotation in magneto-thermoelastic transversely isotropic hollow cylinder with three-phase-lag model. *Mechanics Based Design of Structures and Machines* 47 (2):234. doi:10.1080/15397734.2018.1545587.

Chandrasekharaiah, D. S., and K.S. Srinath. 1998. Thermoelastic interactions without energy dissipation due to a point heat source. *Journal of Elasticity* 50 (2):97–108. doi:10.1023/A:1007412106659.

Coleman, B. D., and M. E. Gurtin. 1967. Equipresence and constitutive equations for rigid heat conductors. *Zeitschrift Für Angewandte Mathematik Und Physik Zamp* 18 (2):199–208. doi:10.1007/BF01596912.

Chen, P. J., and M. E. Gurtin. 1970. On second sound in materials with memory. *Zeitschrift Für Angewandte Mathematik Und Physik Zamp* 21 (2):232–41. doi:10.1007/BF01590647.

Dhaliwal, R. S., and A. Singh. 1980. *Dynamic coupled thermoelasticity*. Delhi: Hindustan Publisher.

Diethelm, K. 2010. *Analysis of fractional differential equation: An application oriented exposition using differential operators of Caputo type*. Berlin: Springer-Verlag.

Duhamel, J. H. 1837. Second memoire, sur les phenomenes thermomechanique. *Journal de L'Ecole Polytechnique* 15:1–15.

Ezzat, M. A. 2010. Thermoelastic MHD non-Newtonian fluid with fractional derivative heat transfer. *Physica B: Condensed Matter* 405 (19):4188–94. doi:10.1016/j.physb.2010.07.009.

Ezzat, M. A., A. S. El-Karamany, and A. A. El-Bary. 2017. On dual-phase-lag thermoelasticity theory with memory-dependent derivative. *Mechanics of Advanced Materials and Structures* 24 (11):908–16. doi:10.1080/15376494.2016.1196793.

Ezzat, M. A., A. S. El-Karamany, and A. A. Samaan. 2001. State-space formulation to generalized thermoviscoelasticity with thermal relaxation. *Journal of Thermal Stresses* 24 (9):823–46. doi:10.1080/014957301750379612.

Ezzat, M. A., M. I. Othman, and A. S. El-Karamany. 2002. State space approach to generalized thermo-viscoelasticity with two relaxation times. *International Journal of Engineering Science* 40 (3):283–302. doi:10.1016/S0020-7225(01)00045-3.

Green, A., and K. Lindsay. 1972. Thermoelasticity. *Journal of Elasticity* 2 (1):1–7. doi:10.1007/BF00045689.

Green, A. E., and P. M. Naghdi. 1991. A re-examination of basic postulates of thermomechanics. *Proceedings of the Royal Society A* 432 (1885):171–94. doi:10.1098/rspa.1991.0012.

Green, A. E., and P. M. Naghdi. 1992. On undamped heat waves in an elastic solid. *Journal of Thermal Stresses* 15 (2):253–64. doi:10.1080/01495739208946136.

Green, A. E., and P. M. Naghdi. 1993. Thermoelasticity without energy dissipation. *Journal of Elasticity* 31 (3):189–208. doi:10.1007/BF00044969.

Green, A. E., and P. M. Naghdi. 1995. A unified procedure for construction of theories of deformable media. I. Classical continuum physics, II. Generalized continua, III. Mixture of interacting continua. *Proceedings of the Royal Society, London* 448 (1934):335–88. doi:10.1098/rspa.1995.00(20/21/22).

Gurtin, M.E., and A. C. Pipkin. 1968. A general theory of heat conduction with finite wave speeds. *Archive for Rational Mechanics and Analysis* 31 (2):113–26. doi:10.1007/BF00281373.

Hilfer, R. 2000. *Application of fractional calculus to physics*. Singapore: World Scientific.
Honig, G., and U. Hirdes. 1984. A method for the numerical inversion of Laplace transforms. *Journal of Computational and Applied Mathematics* 10 (1):113–32. doi:10.1016/0377-0427(84)90075-X.
Jumarie, G. 2010. Derivation and solutions of some fractional Black–Scholes equations in coarse-grained space and time, application to Merton's optimal portfolio. *Computers & Mathematics with Applications* 59 (3):1142–64. doi:10.1016/j.camwa.2009.05.015.
Lord, H., and Y. Shulman. 1967. A generalized dynamical theory of thermoelasticity. *Journal of the Mechanics and Physics of Solids* 15 (5):299–309. doi:10.1016/0022-5096(67)90024-5.
Mainardi, F. 2010. *Fractional calculus and waves in linear viscoelasticity*. London: Imperial College Press and Singapore, World Scientific.
Nunziato, J. W. 1971. On heat conduction in materials with memory. *Quarterly of Applied Mathematics* 29: 187–204. doi:10.1090/qam/295683.
Othman, M. I. A., and E. E. M. Eraki. 2017. Generalized magneto-thermoelastic half-space with diffusion under initial stress using three-phase-lag model. *Mechanics Based Design of Structures and Machines* 45 (2):145–59. doi:10.1080/15397734.2016.1152193.
Podio-Guidugli, P. 2009. A virtual power format for thermomechanics. *Continuum Mechanics and Thermodynamics* 20 (8):479–87. doi:10.1007/s00161-009-0093-5.
Rossikhin, A. Y., and M.V. Shitikova. 2010. Application of fractional calculus for dynamic problems of solid mechanics: Novel trends and recent results. *Applied Mechanics Reviews* 63 (1):010801. doi:10.1115/1.4000563.
Sabatier, J., O.P. Agrawal, and J.A. Tenreiro Machado. 2007. *Advances in fractional calculus. theoretical developments and applications in physics and engineering*. Dordrecht: Springer.
Shaw, S. 2017. A note on the generalized thermoelasticity theory with memory dependent derivatives. *Journal of Heat Transfer* 139 (9):092005. doi:10.1115/1.4036461.
Shaw, S., and B. Mukhopadhyay. 2016. Theory of fractional ordered thermoelastic diffusion. *European Physical Journal Plus* 131:183. doi:10.1140/epjp/i2016-16183-6.
Stiassnie, M. 1979. On the application of fractional calculus for the formulation of viscoelastic models. *Applied Mathematical Modelling* 3 (4):300–302. doi:10.1016/S0307-904X(79)80063-3.
Wang, J. L., and H.F. Li. 2011. Surpassing the fractional derivative: Concept of memory-dependent derivative. *Computers & Mathematics with Applications* 62 (3):1562–1567. doi:10.1016/j.camwa.2011.04.028.
Youssef, H. M. 2005. Generalized thermoelasticity of an infinite body with a cylindrical cavity and variable material properties. *Journal of Thermal Stresses* 28 (5):521–532. doi:10.1080/01495730590925029.
Yu, Y-J., W. Hu, and X-G. Tian. 2014. A novel generalized thermoelasticity model based on memory-dependent derivative. *International Journal of Engineering Science* 81:123–134. doi:10.1016/j.ijengsci.2014.04.014.

Source details

Feedback > Compare sources >

Mechanics Based Design of Structures and Machines

Formerly known as: Mechanics of Structures and Machines

Scopus coverage years: from 2003 to Present

Publisher: Taylor & Francis

ISSN: 1539-7734 E-ISSN: 1539-7742

Subject area: Mathematics: General Mathematics | Engineering: Ocean Engineering | Engineering: Aerospace Engineering | Engineering: Mechanical Engineering | Engineering: Civil and Structural Engineering | Engineering: Automotive Engineering | Engineering: Mechanics of Materials View all

Source type: Journal

View all documents > Set document alert Save to source list

CiteScore 2022
9.4

SJR 2022
0.646

SNIP 2022
1.433

CiteScore | CiteScore rank & trend | Scopus content coverage

Inorganica Chimica Acta 505 (2020) 119468

Contents lists available at ScienceDirect

Inorganica Chimica Acta

journal homepage: www.elsevier.com/locate/ica

Research paper

Schiff base triggering synthesis of copper(II) complex and its catalytic fate towards mimics of phenoxazinone synthase activity

Prafullya Kumar Mudi[a], Nilaj Bandopadhyay[a], Mayank Joshi[b], Madhusudan Shit[c], Suvendu Paul[d], Angshuman Roy Choudhury[b], Bhaskar Biswas[a,*]

[a] Department of Chemistry, University of North Bengal, Darjeeling 734013, India
[b] Department of Chemical Sciences, Indian Institute of Science Education and Research, Mohali, Sector 81, Knowledge City, S. A. S. Nagar, Manauli PO, Mohali, Punjab 140306, India
[c] Department of Chemistry, Dinobandhu Andrews College, Kolkata 700084, India
[d] Department of Chemistry, University of Kalyani, Kalyani 741235, India

ARTICLE INFO

Keywords:
Copper(II)
Schiff base
X-ray structure
Phenoxazinone synthase activity
DFT study

ABSTRACT

This research article reports the synthesis, structural characterization and phenoxazinone synthase activity of a new phenoxido-bridged dicopper(II)-Schiff base complex, $[Cu_2(\mathbf{L})_3]ClO_4$ **(1)**, [H**L** = (Z)-2-methoxy-6-(((2-methoxyphenyl)imino) methyl)phenol]. X-ray structure of the Cu(II) complex reveals that each of the two Cu(II) centres in **1** adopts different coordination geometries (distorted octahedral and distorted square planar) and phenoxido bridges couple two Cu(II) centres to form a dinuclear copper complex with Cu···Cu distance 3.182 Å. The dicopper(II) complex catalyzes the aerobic oxidation of 2-aminophenol (2-AP) to aminophenoxazinone species in acetonitrile with good turnover number, 78.14 h^{-1}. Electro-chemical and electrospray ionization mass spectrometry analysis of **1** in presence of 2-AP ensure the involvement and key role of the copper(II) centres in formation of enzyme-substrate adduct. Subsequently, electron paramagnetic resonance study confirms the generation of radical species in the course of catalysis. Finally, density functional theoretical calculations well reproduce the experimental geometrical parameters and spectroscopic behaviours of **1** and decisively argue in favour of the proposed catalytic pathways.

1. Introduction

Copper based coordination compounds containing Schiff base ligands have been widely employed in different organic transformations of laboratory and industrial significance [1–3]. In living system, copper ion has played a pivotal role as an essential bio-element. In addition, copper complexes have been widely distributed as the functional sites of various metal dependent enzymes like catechol and galactose oxidase, phenoxazinone synthase, superoxide dismutase, lysine oxidase, N_2O reductase etc [4–7]. Enormous efforts have been made by renowned research groups to mimic structural and functional sites of copper dependent enzymes aiming to develop better catalysts by tuning the electronic and geometric factors associated with the surrounding ligands [8–10]. It has commonly been observed that proper tuning of electronic and steric factors in ligand may lead to improve molecular properties for metal complexes [4–11].

Among the copper(II) complexes of varied nuclearities, dicopper compounds have played significant role in mimicking the functional activities of type-3 copper proteins with high efficiency [4–7]. Focusing on those structural and functional aspects, synthetic inorganic chemists have actively engrossed in designing and synthesizing coordination compounds aiming to explore the bio-functions of various metal-dependent enzymes [11]. Type-3 copper proteins have a dinuclear copper (II) active site and both the copper(II) centers are antiferromagnetically coupled that makes them EPR silent [12]. The magnetic interactions involving phenoxo-bridged dinuclear copper(II) complexes have been widely investigated in the scientific literature [13,14]. There are lots of examples where dinuclear copper complexes have formed by bridging phenolates and other atomic or molecular bridges (oxides, pyrazoles, phosphates, acetates etc) [15,16].

On the other hand, catalytic oxidative coupling from 2-aminophenol (2-AP) to 2-amino-3H-phenoxazine-3-one (2-APX) by copper(II) based coordination compounds has drawn considerable attention for its important mechanistic insights in the course of oxidative catalysis [17–21]. It has been experimentally observed that a naturally occurring antineoplastic agent, actinomycin D behaves as an inhibitor towards the

* Corresponding author.
E-mail address: bhaskarbiswas@nbu.ac.in (B. Biswas).

https://doi.org/10.1016/j.ica.2020.119468
Received 22 December 2019; Received in revised form 23 January 2020; Accepted 23 January 2020
Available online 28 January 2020
0020-1693/

preparation of DNA-directed RNA. Actinomycin D is related to questiomycin A which is familiar as 2-Amino-3H-phenoxazine-3-one [22]. This species is used clinically for the treatment of certain types of cancer [23]. It is well observed that in the final step of the biosynthesis of actinomycin D, the enzyme phenoxazinone synthase catalyzes the oxidative coupling of 2-aminophenol to the phenoxazinone chromophore [23–25]. On account of the significance of the oxidative catalysis, this research work presents the preparation, structural characterization and DFT study of a dinuclear copper(II)-Schiff base complex and its potential bio-mimicking activity towards catalytic oxidative coupling of 2-aminophenol under aerobic atmosphere.

2. Experimental

2.1. Preparation of the Schiff base and dinuclear copper(II) complex

(a) Chemicals, solvents and starting materials

Highly pure *o*-vanilin (Sigma Aldrich, USA), *o*-anisidine (Sigma Aldrich, USA), copper(II) perchlorate hexahydrate (E-Merck, India) and *o*-aminophenol (Sigma Aldrich, USA) were purchased from the respective concerns and used as received. All other chemicals and solvents were of analytical grade and were used as received without further purification.

Caution! Metal perchlorate salts are potentially explosive, especially in presence of organic ligands. Hence, metal perchlorate salts should only be handled with proper precautions (in small amount, avoid heat and fire).

(b) *Synthesis of the Schiff base and dicopper(II) complex*

The Schiff base ligand, H**L** was prepared following the reported procedure [26–28]. The Schiff base ligand was synthesised by refluxing *o*-anisidine (0.123 g, 1 mmol) with *o*-vanilin (0.152 g, 1 mmol) in 20 mL ethanol for 6 h. Thereafter, the reddish coloured solution was filtered and dried. Then, the compound was stored *in vaccuo* over $CaCl_2$ for use. Yield: 0.219 g (~85.2%). Anal. Calc. for $C_{15}H_{15}NO_3$ (H**L**): C, 70.02; H, 5.88; N, 5.44; Found: C, 70.09; H, 5.80; N, 5.93. IR (KBr, cm^{-1}; Fig. S1): 3432 (ν_{OH}), 1614 ($\nu_{C=N}$); UV–Vis (λ_{max}, nm; Fig. S2): 278, 340, 460; ^{1}H NMR (δ ppm, 400 Mz, $CDCl_3$; Fig. S3) δ = 14.46 (s, 1H), 8.70 (s, 1H), 7.26–6.82 (Ar-H, 7H), 5.94 (s, 1H), 3.93, 3.89 (d, 6H) ppm. ^{13}C NMR (400 MHz,$CDCl_3$; Fig. S4): 161.43 (HC=N); 153.19, 152.78 (Ar-OCH_3); 136.42 (Ar-N=C); 148.89 (Ar-OH); 128.15, 123.60, 121.03, 119.34, 119.25, 118.09, 114.40, 112.07 (Ar-C); 56.24, 55.97 (–OCH_3). ESI-MS (*m/z*; Fig. S5) 258.2663 (Calc. 258.28).

To prepare the dicopper(II) complex, initially a methanolic solution of $Cu(ClO_4)_2$ (0.730 g, 2 mmol) was added drop wise to the acetonitrile solution of H**L** (0.771 g, 3 mmol). Consequently, it was observed that the red coloured Schiff base solution was turned into green immediately. The, the reaction solution was kept in open atmosphere for slow evaporation. After 10–15 days, fine microcrystalline green coloured compound was separated out from the solution. Thereafter, the crystalline compound was washed with toluene and dried over silica gel to get pure crystals of **1**. Finally, different spectroscopic and analytical techniques were performed to characterize the compound. The results are as follows.

Yield of **1**: 0.630 g (~76% based on metal salt) Anal. calc. for $C_{45}H_{42}N_3O_{13}ClCu_2$ **(1)**: C, 54.30; H, 4.25; N, 4.22; Found: C, 54.35; H, 4.19; N, 4.28. IR (KBr pellet, cm^{-1}; Fig. S1): 1611 ($\nu_{C=N}$) & 1095(ν_{ClO4^-}); UV–Vis (1×10^{-4} M, λ_{max}(abs), nm, MeCN; Fig. S2): 240, 293, 400. ESI-MS (*m/z*; Fig. S6) 896.3281 (Calc. 896.15).

2.2. Physical measurements

IR spectra of the ligand and **1** were recorded with a FTIR-8400S SHIMADZU spectrophotometer (Shimadzu, Kyoto, Japan) in the range 400–3600 cm^{-1} with KBr pellet. ^{1}H and ^{13}C NMR spectra of the ligand (H**L**) were recorded on a Bruker Advance 400 MHz spectrometer (Bruker, Massachusetts, USA) in $CDCl_3$ at 298 K. Steady-state absorption and other spectral data were recorded with a JASCO V-730 UV–Vis spectrophotometer (Jasco, Tokyo, Japan). Electrospray ionization (ESI) mass spectrum of the ligand and **1** were recorded using a Q-tof-micro quadruple mass spectrometer. Operating parameters of the instrument like sample cone, source temperature, and pump flow were kept as fixed at 30 V, 80 °C and 20 μL/min respectively during the measurement of ESI-MS for this dicopper(II) complex. The pH values of different solutions were measured by Labman pH meter (Wensar, Chennai, India) at room temperature. Elemental analyses were performed on a Perkin Elmer 2400 CHN microanalyser (Perkin Elmer, Waltham, USA). X-band EPR spectra were recorded on a Magnettech GmbH MiniScope MS400 spectrometer (equipped with temperature controller TC H03, Magnettech, Berlin, Germany), where the microwave frequency was measured with an FC400 frequency counter.

2.3. Crystal structure determination and refinement

Single crystal X-ray diffraction data of **1** were collected using a Rigaku XtaLABmini diffractometer equipped with Mercury 375R (2 × 2 bin mode) CCD detector. The data were collected with graphite monochromated Mo-Kα radiation (λ = 0.71073 Å) at 100.0(2) K using ω scans. The data were reduced using CrysAlisPro 1.171.38.46 [29] and the space group determination was done using Olex2. The structure was resolved by dual space method using SHELXT-2015 [30a] and refined by full-matrix least-squares procedures using the SHELXL-2015 [30b] software package through OLEX2 suite [30c,30].

2.4. Hirshfeld surface calculations of dicopper(II) compound

Crystal Explorer 17.5 [31] program package was employed to generate Hirshfeld surfaces [31b] and 2D fingerprint plots [31c] of **1** using its single crystal X-ray diffraction data. It has already been established that Hirshfeld Surface analysis is a very important tool to study and locate intermolecular interactions within a crystal packing [31a,31c,31d]. The function d_{norm} is a ratio of the distances of any surface point to the nearest interior (d_i) and exterior (d_e) atom and the van der Waals radii of the atoms [32,33]. The normalized contact distance (d_{norm}) could be expressed as

$$d_{norm} = \frac{d_i - r_i^{vdw}}{r_i^{vdw}} + \frac{d_e - r_i^{vdw}}{r_e^{vdw}} \quad (1)$$

where, r_e^{vdW} and r_i^{vdW} denote the corresponding van der Waals radii of atoms. The negative value of d_{norm} indicates that the sum of d_i and d_e is shorter than the sum of the relevant van der Waals radii, which is considered to be a closest contact and is visualized in red colour. The white colour denotes intermolecular distances close to van der Waals contacts with d_{norm} equal to zero whereas contacts longer than the sum of van der Waals radii with positive d_{norm} values are coloured with blue. A plot of d_i versus d_e is a fingerprint plot that identifies the presence of different types of intermolecular interactions.

2.5. Phenoxazinone synthase activity of dicopper(II) complex **(1)**

Phenoxazinone Synthase like activity was examined by treating 1×10^{-4} M solution of **1** in MeCN medium with 10 equiv. of 2-aminophenol (2-AP) under aerobic conditions at room temperature. To study this activity, absorbance vs. wavelength (wavelength scans) of the solution was monitored spectrophometrically at a regular time interval of 5 min for 1 h in the wavelength range from 300 to 800 nm [6,19,26].

Kinetic experiments were also performed spectrophotometrically to enumerate the aminophenol oxidation efficacy with this dicopper(II) complex in presence of 2-AP in MeCN at 298 K [6,19,26]. 0.04 mL of the complex solution with a constant concentration of 1×10^{-4} M was added to 2 mL of 2-AP of a particular concentration (varying its concentration from 1×10^{-3} M to 1×10^{-2} M) to achieve the ultimate

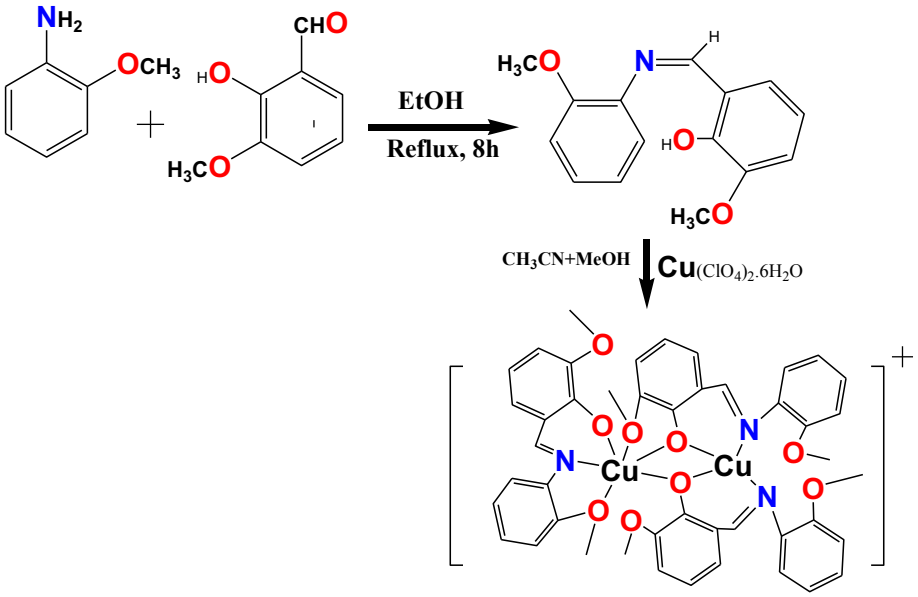

Scheme 1. Synthetic route for the formation of **1**.

concentration of the complex as 1×10^{-4} M. The conversion of 2-aminophenol to 2-aminophenoxazine-3-one was monitored with time at a wavelength 434 nm (time scan) in MeCN [6,19,26,34,35]. To determine the dependence of rate on substrate concentration, kinetic analyses were performed in triplicate.

Column chromatography was employed to extract the product, phenoxazinone in pure form from the catalytic oxidation of 2-AP. Neutral alumina was used as column support and benzene-ethyl acetate solvent mixture was treated as an eluant mixture in this chromatographic separation. The oxidation product was found in high yield (~77% for **1**). ^{1}H NMR spectral analysis helped to identify the species. ^{1}H NMR data for 2-amino-3*H*-phenoxazine-3-one (APX), ($CDCl_3$, 400 MHz,) δ_H: 7.62 (m, 1H), 7.44 (m, 3H), 6.47 (s, 1H), 6.39 (s, 1H), 6.28 (s, 1H). The identification of this phenoxazinone product was further consolidated in ESI-Ms spectrometry from the appearance of base peak at *m/z* 213.

2.6. Detection of presence of hydrogen peroxide in the catalytic oxidation of 2-aminophenol

To ensure the active participation of molecular oxygen in the course of catalysis, the formation of hydrogen peroxide was checked based on some previously reported literatures [34,35]. It is well known that molecular oxygen in oxidative catalytic reactions may convert itself to hydrogen peroxide or water as byproduct. In this course of oxidative catalytic reaction, the solution was acidified with H_2SO_4 to reach the pH of the solution at 2. After a certain time, an equal volume of water was added to stop further oxidation. The phenoxazinone species were extracted three times with dichloromethane. 1 mL of 10% solution of KI and three drops of a 3% solution of ammonium molybdate were added to the aqueous layer. The formation of I_3^- was monitored spectrophotometrically to check the development of the characteristic I_3^- band (λ_{max} = 353 nm) which is assignable to the production of hydrogen peroxide.

2.7. Electro-chemical analysis

The electro analytical instrument, BASi Epsilon-EC for cyclic voltammetric experiment in CH_2Cl_2 solutions containing 0.2 M tetrabutylammonium hexafluorophosphate as supporting electrolyte was used. The BASi platinum working electrode, platinum auxiliary electrode, Ag/AgCl reference electrode were used for the measurements.

2.8. Computational details

All the computational calculations were performed using Gaussian 09 W Programme Suite [36] avoiding symmetrical restrictions. Employing density functional theory (DFT), all the ground state calculations were performed with widely used B3LYP computational model and 6-311G basis set (for both metal and non-metallic elements) [37]. Initially, complex **1** was optimized in vacuum. Thereafter, to incorporate solvent effect, **1** was optimized in MeCN (ε = 35.668) employing integral equation formalism polar continuum model (IEFPCM) [38] solvent model. Global minimum of each structures were confirmed through stability calculations and IR frequency check-up with no imaginary frequency. All the optimized structures were stable under the perturbation considered. The images of frontier molecular orbitals (FMOs) were extracted from corresponding check point files. For further details of computational methods, readers might follow somewhere else [39]. To compare the XRD structure and computationally optimized structure visually, the structures were superimposed using PyMOL 1.3 software package [40].

3. Results and discussion

3.1. Synthesis and formulation of the Schiff base (HL) and dicopper(II) complex(1)

The reddish coloured Schiff base ligand, H**L** is synthesized by refluxing *o*-anisidine with *o*-vanilin in ethanol medium. Single crystals of the dicopper(II) complex are obtained by adding hydrated copper(II) perchlorate to polydentate Schiff base ligand in 2:3 mol ratio in methanol under slow stirring condition (Scheme 1). Different ratio between hydrated $Cu(ClO_4)_2$ and H**L** (1:1, 1:2) have also been applied to prepare the single crystals to divulge the mode of coordination of the Schiff base with Cu(II) ion. However no crystals are found. Different Cu (II) salts like bromide, acetate and sulfate have been combined with the polydentate Schiff base to prepare Cu(II) complexes of varied dimension and nuclearities but remains unsuccessful. This copper compound shows good solubility in common polar solvents as such methanol, acetonitrile, dichloromethane etc. This synthesis of Cu(II) complex may be successfully done using methanol-dichloromethane or methanol–acetonitrile medium.

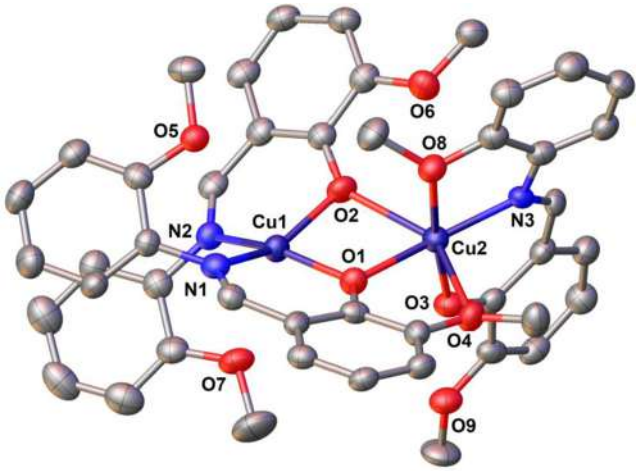

Fig. 1. An ORTEP plot of dicopper(II)-Schiff base complex with 30% ellipsoid probability (H atoms are removed to enhance clarity).

3.2. Description of crystal structure

X-ray structural analysis exhibits that the dinuclear copper(II) complex crystallizes in orthorhombic system with *Pbca* space group. Very interestingly, in this dinuclear copper(II)-Schiff base complex, each of the copper(II) centres adopts different coordination geometry – octahedral and square planar geometries. An ellipsoidal diagram of **1** is shown in Fig. 1. The structural refinement parameter for this Cu(II)-Schiff base complex is specified in Table 1. The bond angles as well as bond distances are given in Table S1. Three units of H**L** in coupling with two Cu(II) ions produce a monocationic dicopper(II)-Schiff base complex and the cationic charge is satisfied by perchlorate ion in the secondary zone of coordination. H**L** may be considered as a tetradentate chelator for consisting of four donor centres in its structure although it only coordinates using three donor centres and behaves as a flexidentate ligand system. The square planar geometry for Cu1 centre in **1** deviates slightly from ideal square planar geometry and it is evident from the measurements of bond angles (Table S1) [32]. The origin of distorted square planar geometry may be assigned to the presence of bond constraints in Schiff base ligand during coordination to copper ion. The Cu2 centre in **1** adopts a distorted octahedral geometry. The equatorial plane of the octahedron is effectively formed by the donor groups (O1, O2, N3, O4) those are closer to the Cu(II) center while the two oxygen atoms (O3,O8) are placed at longer distance giving a distorted octahedron (Fig. 1). This tetragonally flattened octahedral geometry of Cu2 centre about Z axis with two shorter and four longer bonds is caused by Jahn-Teller distortion and formally called as Z_{in} distortion [33]. Cu1 and Cu2 centres in the dinuclear copper(II) complex are interconnected by $\mu_{1,1}$-type phenoxo bridges with a separation distance of 3.182 Å.

Table 1
Crystallographic data and structure refinement parameters for **1**.

Parameters	**1**
Empirical formula	$C_{45}H_{42}N_3O_{13}C1Cu_2$
Formula weight	995.34
Temperature (K)	100
Crystal system	Orthorhombic
Space group	*Pbca*
a (Å)	20.6993(10)
b (Å)	15.1138(9)
c (Å)	26.913(2)
Volume (Å^3)	8419.6(9)
Z	8
ρ (gcm^{-3})	1.571
μ (mm^{-1})	1.146
Temperature (K)	100
F (0 0 0)	4096
R_{int}	0.088
θ ranges (°)	2.5–25.0
Number of unique reflections	7402
Total number of reflections	40,939
Final R indices	0.0685, 0.2393
Largest peak and hole (eÅ^{-3})	1.19, −1.24

The dicopper(II)-Schiff base complex is optimized in vacuum for ground state employing unrestricted density functional theory (DFT) and optimized structure is shown in Fig. S7. The DFT optimized structure is correlated with XRD structure to reveal the degree of similarity in structural connectivity and coordination geometries of copper(II) centres. The DFT computed geometrical parameters for the dicopper(II)-Schiff base complex are listed in Table S1. These bond lengths and bond angles data exactly reproduced the XRD data. These observations provide additional support in favour of the geometrical orientation of the ligand around the metal centres. Additionally, superimposition of the XRD structure (orange, Fig. S8) with DFT optimized structure (violet, Fig. S8) is performed using PyMOL 1.3 software [40]. The DFT optimized structure exactly reproduced the XRD structure which stands with the diverse coordination motif of Cu(II) at two different position within **1**. The crystal structure exhibits same degree of coordination linkages between Cu(II) and H**L** and coordination geometries of each of the copper(II) centres in dicopper(II)-Schiff base complex.

3.3. Hirshfeld analysis of dicopper(II) complex

Hirshfeld surface of Cu(II) complex (Fig. S9) over a definite d_{norm} has been calculated using Crystal Explorer software. The calculated surface volume is found as 963.85 Å^3 and surface area is determined as 687.91 Å^2. The red highlighted area shows the d_{norm} area and close non-covalent interactions of **1** with its surrounding analog within the 3D crystal. Percentage share of each element in close interaction with others is given in Table S2. In this d_{norm}, the blue area is showing the weak π···π interactions between aromatic rings of the ligands and most of area remains white which means there is no interaction. Red area presents weak C—H···O hydrogen bonding between C—H of benzene ring and O of ClO_4. This molecule is interacted by surrounding molecules through C—H···O hydrogen bond, C—H···π and π···π interactions as display in Fingerprint plots (Fig. 2). Quantitative information of different intermolecular interactions by each pair of elements is given in Table S2. In the fingerprint plot, the direction of interaction is towards weak interactions employing hydrogen atoms (inside and outside of hirshfeld surface centre peak) and carbon atoms of C—H···π interactions.

3.4. Solution property of the Schiff base and dicopper(II) complex

The electronic spectra of the Schiff base and its Cu(II) complex are recorded in acetonitrile medium (MeCN) from 200 to 900 nm at room temperature. The Schiff base, H**L** displays high intensity electronic bands at 278, 340 nm and a broad band at 460 nm while the dicopper (II)-Schiff base complex exhibits electronic transitions at 240, 293 and 400 nm. The optical bands for H**L** & **1** are displayed in Fig. S2. The highly intense electronic bands at 278, 340 nm in UV region for H**L** are assignable to π → π* and n → π* electronic transitions of ligand chromophore, however the development of optical band at 460 nm is assignable for charge transition of ligand origin [41]. The $^3A_{2g}(F) \rightarrow {}^3T_{2g}(F)$ transition that commonly appears above 700 nm is missing for this dicopper(II) complex [42]. The absorption at 400 nm corresponds to charge transfer transition and can be assignable to phenoxo to Cu(II) ion electron transfer transition [42b,42c]. The highly intense electronic bands at 240 and 293 nm for **1** may be attributed to π → π* and n → π* electronic transitions of ligand chromophore [41].

ESI-Ms spectra of H**L** and its Cu(II) compound is also measured in MeCN medium and the spectra are presented in Figs. S5 and S6. Presence of molecular ion peaks at *m/z* 258.6663 and 894.2371 for H**L** and

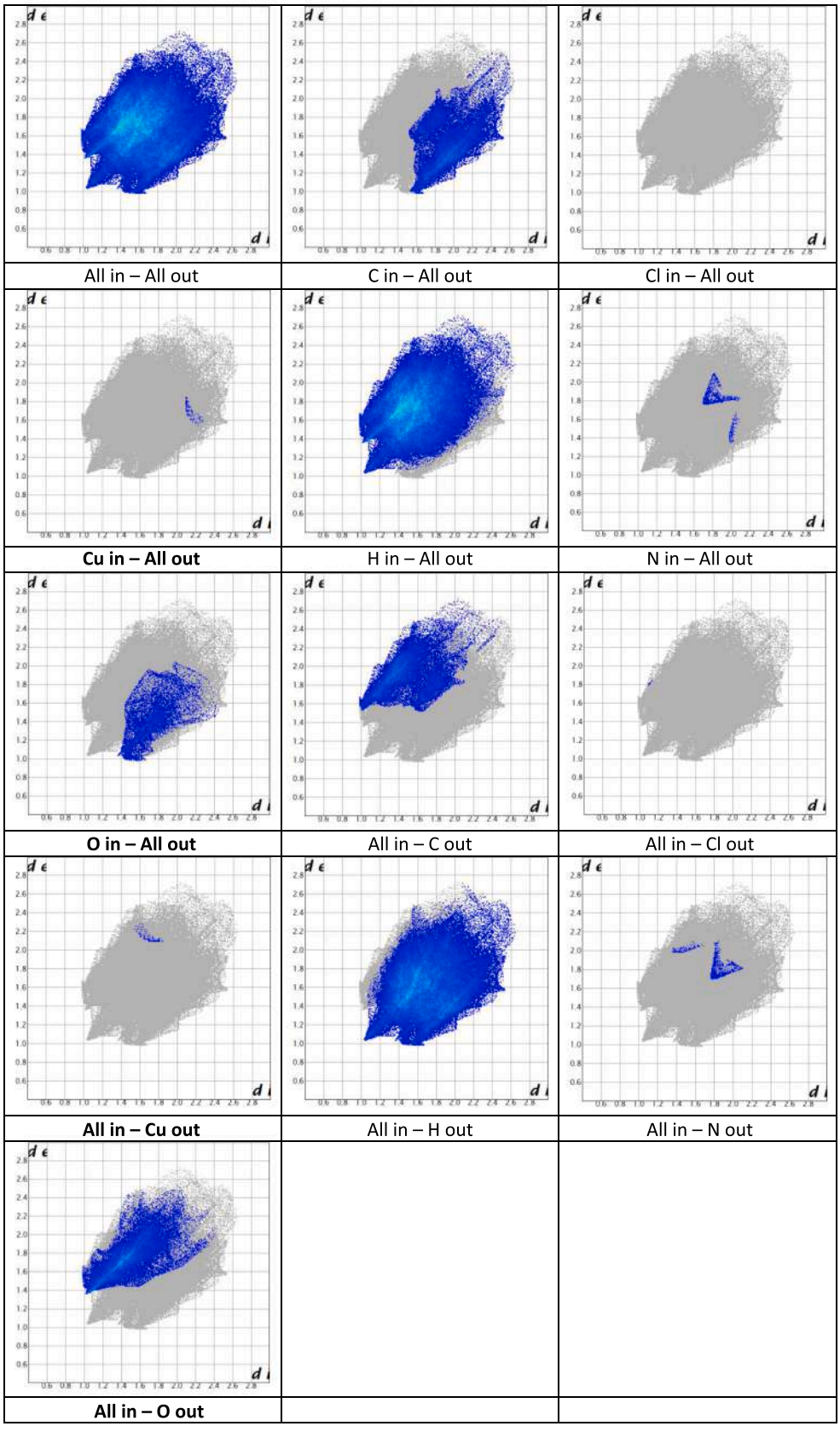

Fig. 2. Fingerprint plot of dicopper(II)-Schiff base complex.

1 justify the molecular integrity of the compounds in solution phase. The experimental *m/z* values agree very well with the calculated values of molecular mass for both the compounds.

The electrolytic nature of the dicopper(II) compound has also been examined through recording molar conductance values in MeCN medium at room temperature. The molar conductance values for

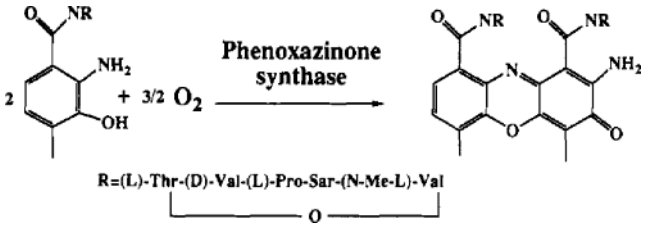

Scheme 2. Catalytic oxidation of 2-aminophenol by phenoxazinone synthase.

1.50×10^{-3} M solution of **1** produces 147 S m^2 mol^{-1} which certainly recommends the 1:1 electrolytic nature in MeCN medium. The electrolytic nature of **1** is attributed for the existence cationic dicopper(II) species with counter anionic perchlorate ion [43].

The fluorescence behaviour of the ligand and the dicopper(II) complex has been examined through recording of fluorescence spectra in MeCN medium and presented in Fig. S10. The Schiff base exhibits moderate intensity in fluorescence behaviour while dicopper(II) complex behaves as a non-fluorescent or poorly fluorescent compound at room temperature. The quenching of fluorescence intensity for Schiff base upon coordination of Cu(II) ion may be explained in terms of spin–orbit coupling or heavy atom effect [44]. Previously, Rathod *et al.* reported the similar kind of reduction of fluorescent intensity for highly fluorescent fluorescein-based Schiff base upon incorporation of Cu(II) ion in solution phase [44b].

To get an idea about the electronic transitions and molecular level reactivity, energy of frontier molecular orbitals of **1** have been computed and presented in Fig. S11. Electronic charge density of HOMO, HOMO–1 and HOMO–2 are located majorly both on the ligand and metal centres and electronic charge density of LUMO, LUMO + 1 and LUMO + 2 are exclusively located on the ligand. Besides, the transition energies or energy gap among the frontier molecular orbitals, HOMO − LUMO, (HOMO − 1)-(LUMO + 1) and (HOMO–2)-(LUMO + 2) are calculated as 2.69 eV (525 nm), 3.42 eV (473 nm) and 3.95 eV (435 nm) respectively. This transition energy values suggests the molecular level reactivity of the dicopper(II)-Schiff base complex.

3.5. Phenoxazinone synthase mimicking activity of the dicopper(II) complex (1)

The 2-aminophenol oxidation activity by the dicopper(II) complex **(1)** is examined using a model substrate 2-aminophenol (2-AP) under the aerobic condition in MeCN at room temperature (25 °C) (Scheme 2).

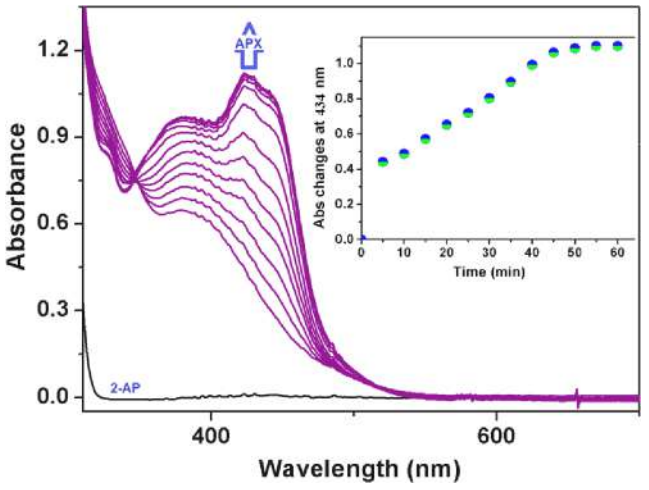

Fig. 3. Rise of optical band at 434 nm for the growth of APX in solution upon addition of copper complex to 100 equivalents of 2-AP in acetonitrile medium. (The spectra are recorded after every 5 min). Inset: Time vs Absorbance plot at defined wavelength.

Table 2
Comparison of k_{cat} (h^{-1}) values for catalytic oxidation of 2-AP by reported copper(II) compounds and **1**.

Complex	k_{cat} (h^{-1}) (Solvent)	CCDC No	Ref
$[L^1Cu(\mu\text{-}Cl)_2CuL^1]$	1065 (CH_3OH) 213 (CH3CN)	1,572,023	[46]
$[Cu_4(L^2)_4]$	86.3 (CH_3OH)	1,507,035	[47]
$[Cu_4(L^3)_4]$	340.26 (CH_3OH)	1,507,036	[47]
$[Cu_4(L^4)_4]$	1.21×10^5(CH_3OH)	1,455,999	[48]
[Cu(μ-Cl)(Phen)Cl]	1.69×10^4(CH_3OH)	1,524,680	[6]
$[(CH_3CN)Cu(L_s)_2Cu]^{2+}$	11.1 (CH_3OH)	1,940,162	[49]
$[Cu_2(L)_3]ClO_4$	78.14 (CH_3OH)	1,957,033	This work

L^1 = 2-(a-Hydroxyethyl)benzimidazole (Hhebmz), L^2 = (E)-4-Chloro-2-((thiazol-2-ylimino)methyl)phenol, L^3 = (E)-4-Bromo-2-((thiazol-2-ylimino) methyl)phenol, L^4 = N-(2-hydroxyethyl)-3-methoxysalicylaldimine.

To study the catalytic oxidation of 2-aminophenol, 1×10^{-4} M solution of Cu(II) complex is added to a 1×10^{-3} M solution of 2-AP in MeCN medium. The course of catalysis is monitored using UV–Vis spectrophotometer. The time-dependent scan is recorded at a time interval of 8 min for 2 h (Fig. 3). 2-AP in MeCN solution displays a single band at 267 nm which is an indication for its pure form in solution. On addition of dicopper(II) complex to 2-AP in MeCN, a new band at 434 nm with incremental absorbance is observed (Fig. 3) and concomitantly, solution in cuvette starts to turn brown. Appearance of this new electronic band at 434 nm in presence of dicopper(II) complex is a pure signature for the production of aminophenoxazinone species in MeCN [6,26,45]. The controlled experiment was also carried out to find out the role of Schiff base in this phenoxazinone synthase mimicking activity using 2-AP in MeCN solvent under the aerobic atmosphere at room temperature. Controlled experiment was also carried out using catalytic amount of Schiff base in 2-AP under identical reaction conditions (Fig. S12). Although, no considerable amount of growth for phenpxazinone species is noted up to 3 h. The titration curves got saturated after 1 h of catalysis by the dicopper(II) complex.

The details of kinetic investigations for the catalytic oxidation of 2-AP were performed to realize the efficacy for this copper(II) catalyst. The method of initial rates is followed to unveil the nature of kinetic for this catalytic oxidation of 2-AP. The growth of phenoxazinone species was monitored at 434 nm as a function of time (Fig. S13) [6,19,26,34,35]. The plot of rate constants versus concentration of the substrate displays the saturation kinetics (Fig. S13) where Michaelis–Menten equation looks to be appropriate (Fig. S13). The catalyst–substrate adduct (CS) that decomposes in a second step to release free catalyst (C) and product (P) is represented below.

The Michaelis–Menten equation may be written as:

$$V = \frac{V_{max}[S]}{K_M + [S]}$$

where, V is the reaction velocity (the reaction rate), K_m is the

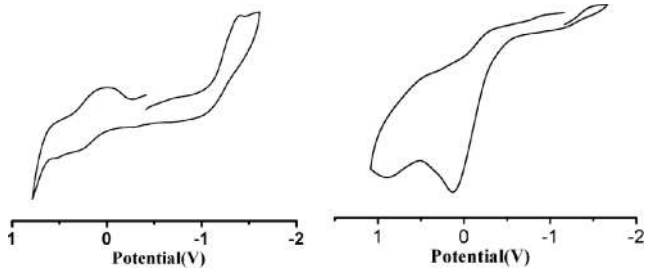

Fig. 4. Left: Cyclic voltammogram of the dicopper(II) compound in anhydrous DCM medium; Right: Cyclic voltammogram of the mixture of dicopper(II) compound and 2-AP under molecular oxygen atmosphere in anhydrous DCM in CH_2Cl_2 (0.20 M $[N(n - Bu)_4]PF_6$) at 295 K.

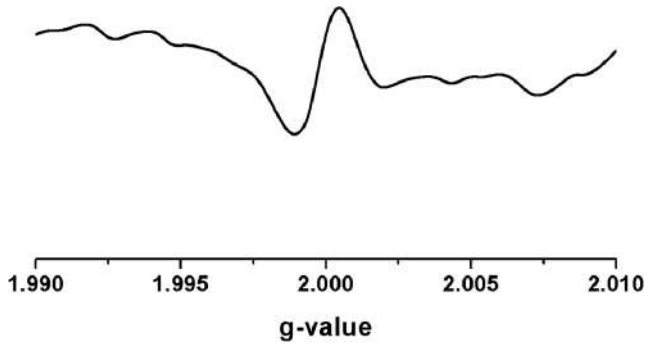

Fig. 5. X-band EPR spectra of the dicopper(II)-Schiff base in presence of 2-AP after 20 min in CH_3CN solution at 298 K.

Michaelis–Menten constant, V_{max} is the maximum reaction velocity, and [*S*] is the substrate concentration.

The values of kinetics parameters were determined from Michaelis-Menten approach of enzymatic kinetics **1** as V_{max} (MS^{-1}) = 2.17 × 10^{-6}; K_M = 4.40 × 10^{-4} [Std. Error for V_{max} (MS^{-1}) = 1.17 × 10^{-7}; Std. Error for K_m (M) = 1.40 × 10^{-5}].

A comparison of phenoxazinone synthase reactivity is drawn between this dicopper(II) complex and some other reported copper(II) and presented in Table 2 [46–49]. The catalytic efficiency for **1**, k_{cat}/K_M = 1.77 × 10^5 towards catalytic aminophenol oxidation is also encountered as high.

Electrochemical and electron paramagnetic resonance (EPR) analysis are also carried out to cope the catalytic efficiency of the dicopper (II) complex towards the catalytic oxidation of 2-AP in acetonitrile medium. The electrochemical behavior is recorded in dichloromethane medium at 298 K using cyclic voltammetry. *N*-tetrabutylammonium hexafluorophosphate is used to record the electrochemical data under aerobic condition and presented in Fig. 4. The electrochemical data in reference with ferrocenium/ferrocene (Fc + /Fc) couple are summarized in Table S3. This dicopper(II)-Schiff base complex exhibits one irreversible cathodic wave at −1.40 V which is assignable to electron transfer in Cu^{2+} to Cu^{+} redox couple in solution phase. Another irreversible peak is appeared at 0.0095 V which may probable for the deposition of Cu. The active participation of copper(II) centre in catalytic oxidation of 2-AP is confirmed by measurement of redox potentials of Cu(II) complex in presence of 2-AP under identical reaction conditions. The mixture of dicopper(II) complex in presence of 2-AP produces irreversible anodic peak at 0.134 V which strongly suggest the oxidation of 2-aminophenol to iminoquinone (Fig. 4). To view more insights of this dicopper(II) complex mediated oxidative coupling of 2-AP, EPR spectra of the Cu(II) complex in presence and absence of 2-AP are recorded in MeCN medium. The EPR spectrum of dicopper(II) complex **(1)** with X-band frequency at room temperature in MeCN medium displays silent nature of spectral profile and suggests the possibility of phenoxo-bridged magnetically coupled copper(II) centres through antiferromagnetic interactions. Bond angle measurements [∠Cu2-O1-Cu1, 107.66°; ∠Cu2-O2-Cu1, 95.82°] and literature reviews recommend further about the dominance of antiferromagnetic interactions between the copper(II) centres [13–15]. The EPR spectral analysis of the copper complex in presence of 2-AP in acetonitrile medium at room temperature strongly suggests the generation of radical species for the appearance of additional signal at g ca 2.057 (Fig. 5). The reported g value for oxidised 2-AP radical (iminobenzoquinone) is 2.0051 in 10^{-1} M Bu_4NPF_6 [6,10,26].

Furthermore, electrospray ionization (ESI) mass spectrum of the dicopper(II)-Schiff base complex in presence of 2-AP is recorded after mixing of 15 mins to reveal the binding aspects of the dicopper(II) complex and 2-AP in MeCN medium. It is observed that the ESI-Ms of the reaction mixture (Fig. S14) exhibits the base peak at *m/z* 214.56 which is attributed to the existence of aminophenoxazinone compound, [(2-amino-3*H*-phenoxazine-3-ones) + H^+] in the solution. Furthermore, another characteristics peak at *m/z* 1004.6951 is defined as the binding adduct between dicopper(II)-Schiff base complex and 2-AP, [[**1** + (2-AP)] + H^+]. It is supposed to consider that square planar copper centre facilitates the formation of adduct with 2-AP for its existence in less hindered coordinative environment. In this context, to view the chemical fate of molecular oxygen during the course of

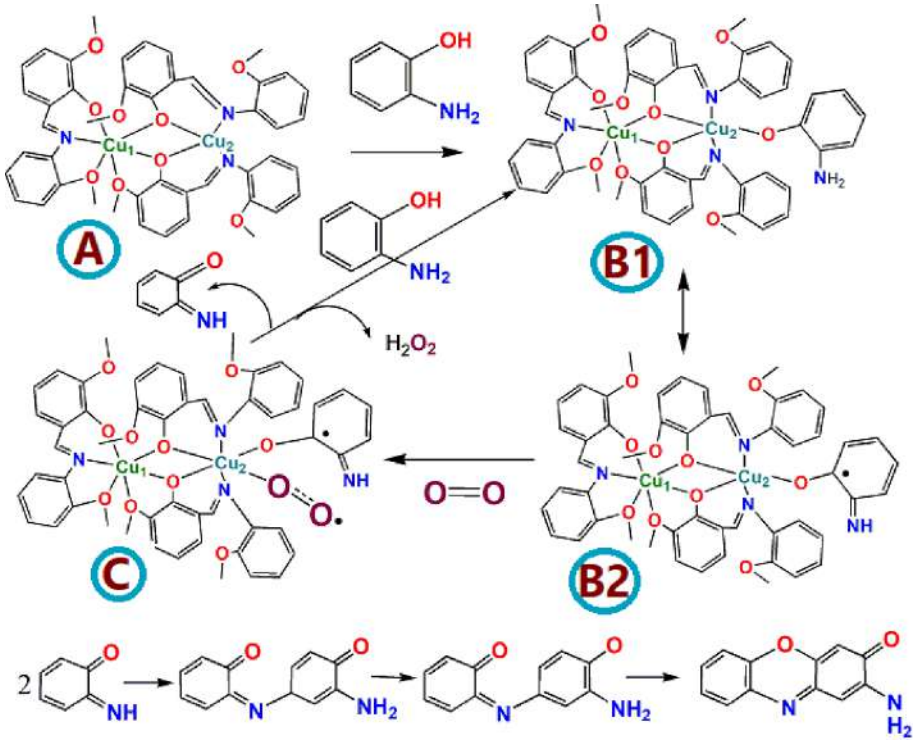

Scheme 3. Plausible mechanistic pathways for the catalytic oxidative coupling of 2-AP by this dicopper(II) complex.

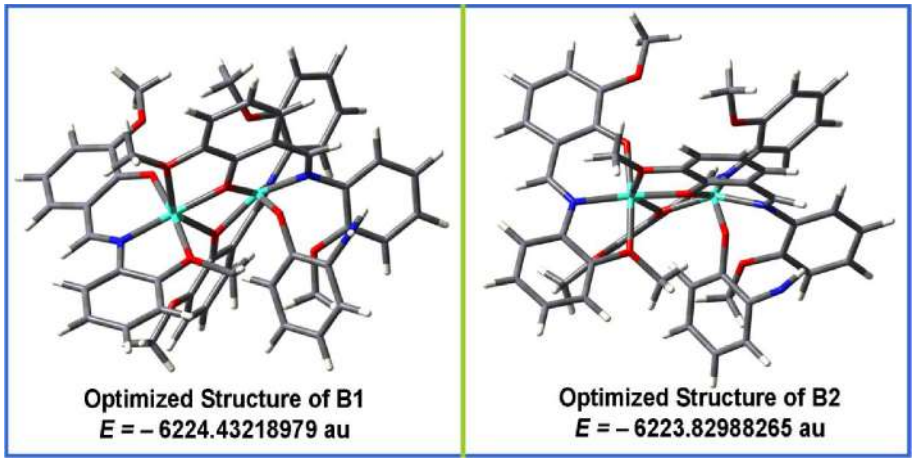

Fig. 6. Ground state optimized geometries of **B1** and **B2** with corresponding potential energy values employing DFT/B3LYP/6-311G theoretical method.

phenoxazinone mimics activity, the production of hydrogen peroxide has been examined following a reported procedure [34,35]. The production of hydrogen peroxide (Fig. S15) has been detected through rise of spectral band at λ_{max} 353 nm and this observation justifies the active involvement of molecular oxygen in this course of catalysis.

Previously study by P. Chaudhury and co-workers [50] about the bio-mimicking activities of the oxidation of 2-AP involving tetracopper complex strongly recommends and accounts on an "on–off" mechanism mediated via radical generation in active participation with the metal centers favouring 6e oxidative coupling of substrate. Another renowned scientist, T.P. Begley et al. [51] suggests the production of 2-aminophenoxazinone through a sequence of three consecutive 2e oxidation of 2-AP. The tautomerization reactions were the controlling unit in regeneration of the 2-Ap during this course of catalytic oxidation reaction.

Based upon important spectroscopic and electro-analytical methods, it may be proposed that the oxidation coupling of 2-AP (Scheme 3) undergoes through formation of catalyst-substrate intermediate (B1) in the primary stage. Later on, the Cu2 centre activates molecular oxygen (C) leading to production of hydrogen peroxide and iminobenzoquinone in the course of catalytic oxidation. Iminobenzoquinone undergoes coupling with another 2-AP and leads to aminophenoxazinone species.

To correlate the experimental observation, ground state geometries of both the **B1** and **B2** molecular adducts were optimized computationally and presented in Fig. 6. The potential energy of **B2** was found to be slightly higher ($E = -6223.82988265$ au) than **B1** ($E = -6224.43218979$ au). The theoretical calculation strongly supports the formation of enzyme-substrate adducts (**B1** and **B2**) and denoted that **B1** might easily be converted into **B2** by prevailing over slight potential energy difference. Therefore, it could be stated that **A** interacts with aminophenol to form **B1** which might be converted into **B2**. Then, **B2** might interact with molecular oxygen to form **C**. Hence, computational calculation moderately supports the plausible catalytic pathways in the oxidative coupling of 2-AP (Scheme 3).

4. Conclusions

A new dinuclear copper(II) complex, $[Cu_2(\mathbf{L})_3]ClO_4$ **(1)** has been developed based on a Schiff base ligand. The structural geometry of the dicopper(II) compound is confirmed principally by single crystal X-ray diffraction study with routine analytical techniques. The copper(II) complex crystallizes in orthorhombic system with *Pbca* space group. X-ray structure of **1** reveals that H**L** behaves as a tridentate chelator towards Cu(II) ion during chelation although H**L** is actually a tetradentate chelating ligand. Moreover, three Schiff base units with two Cu(II) ions build a dinuclear copper(II) complex through phenoxido bridges of Schiff base ligands. Interestingly, two Cu(II) centres in **1** adopts heterogeometries (octahedral and square pyramidal) in **1**. Evaluation of biomimetic efficiency of the Cu(II) compound towards 2-aminophenol (2-AP) as a model substrate in acetonitrile medium, it is observed that this Cu(II) complex catalyzes the oxidative coupling of 2-AP to aminophenoxazinone species with a significant turnover number, 78.14 h^{-1}. EPR, cyclic voltagram and ESI-MS strongly suggests the formation of enzyme-substrate adduct which subsequently produces iminibenzoquinone and the course of bio-oxidative catalysis undergoes through radical species along with the development of aminophenoxazinone species and hydrogenperoxide as products. Theoretical calculations employing DFT supports the structural aspects and observed reaction pathways of phenoxazinone synthase activity of the copper complex very well. This compound represents an example where two heterogeometric copper(II) centres are co-existed through phenoxo bridged. Magnetic aspect will be investigated in future and this compound may be a suitable candidate to exhibit potential biological activity.

CRediT authorship contribution statement

Prafullya Kumar Mudi: Conceptualization, Data curation, Formal analysis, Methodology, Investigation. **Nilaj Bandopadhyay:** Formal analysis, Investigation, Writing - original draft. **Mayank Joshi:** Visualization. **Madhusudan Shit:** Investigation. **Suvendu Paul:** Software. **Angshuman Roy Choudhury:** Validation. **Bhaskar Biswas:** Writing - review & editing, Supervision.

Declaration of Competing Interest

The authors declare the following financial interests/personal relationships which may be considered as potential competing interests: Prafullya Kumar Mudi – *University of North Bengal, Darjeeling-734013,* Nilaj Bandopadhyay –*University of North Bengal, Darjeeling-734013,* Bhaskar Biswas – *University of North Bengal, Darjeeling-734013,* Mayank Joshi – *Indian Institute of Science Education and Research, Mohali,* Angshuman Roy Choudhury – *Indian Institute of Science Education and Research, Mohali,* Madhusudan Shit – *Dinobandhu Andrews College, Kolkata 700084,* Suvendu Paul – *Department of Chemistry, University of Kalyani, Kalyani-741235, India*.

Acknowledgement

BB thanks SERB, India for financial support under the TEACHERS ASSOCIATESHIP for RESEARCH EXCELLENCE (TAR/000473/2018).

Appendix A. Supplementary data

Supplementary crystallographic data are available free of charge from The Director, CCDC, 12 Union Road, Cambridge, CB2 1EZ, UK (fax: +44-1223-336033; E-mail: deposit@ccdc.cam.ac.uk or www: http://www.ccdc.cam.ac.uk) upon request, quoting deposition number CCDC 1957033. Experimental information such FT-IR, UV-Vis, ^{1}H & ^{13}C NMR, Fluoresecence spectra, computational optimized structure, images of frontier orbitals, ESI mass spectra, rate vs. [substrate] plot, Hirshfeld surface plot bond distance & bond angle parameters, redox potential data etc are given here. Supplementary data to this article can be found online at https://doi.org/10.1016/j.ica.2020.119468.

References

[1] P.G. Cozzi, Chem. Soc. Rev. 33 (2004) 410–421.
[2] A.S. Smirnov, L.M.D.R.S. Martins, D.N. Nikolaev, R.A. Manzhos, V.V. Gurzhiy, A.G. Krivenko, K.O. Nikolaenko, A.V. Belyakov, A.V. Garabadzhiua, P.B. Davidovich, New J. Chem. 43 (2019) 188.
[3] W.A. Zoubi, Y.G. Ko, Appl. Organomett. Chem. 31 (2017) e3574.
[4] E.I. Solomon, D.E. Heppner, E.M. Johnston, J.W. Ginsbach, J. Cirera, M. Qayyum, M.T. Kieber-Emmons, C.H. Kjaergaard, R.G. Hadt, L. Tian, Chem. Rev. 114 (2014) 3659–3853.
[5] E.I. Solomon, M.J. Baldwin, M.D. Lowery, Chem. Rev. 92 (1992) 521–542.
[6] M. Garai, D. Dey, H.R. Yadav, A.R. Choudhury, M. Maji, B. Biswas, ChemistrySelect 2 (2017) 11040–11047.
[7] C. Mukherjee, U. Pieper, E. Bothe, V. Bachler, E. Bill, T. Weyhermu¨ller, P. Chaudhuri, Inorg. Chem. 47 (2008) 8943–8956.
[8] P. Chakraborty, J. Adhikary, B. Ghosh, R. Sanyal, S.K. Chattopadhyay, A. Bauzá, A. Frontera, E. Zangrando, D. Das, Inorg. Chem. 53 (2014) 8257–8269.
[9] G.C. Paul, K. Das, S. Maity, S. Begum, H.K. Srivastava, C. Mukherjee, Inorg. Chem. 58 (2019) 1782–1793.
[10] P. Mahapatra, S. Ghosh, S. Giri, V. Rane, R. Kadam, M.G.B. Drew, A. Ghosh, Inorg. Chem. 56 (2017) 5105–5121.
[11] K.D. Karlin, Z. Tyekla'r, A. Farooq, M.S. Haka, P. Ghosh, R.W. Cruse, Y. Gultneh, J.C. Hayes, P.J. Toscano, J. Zubieta, Inorg. Chem. 31 (1991) 1436–1451.
[12] (a) E.I. Solomon, R.K. Szilagyi, S. DeBeer George, L. Basumallick, Chem. Rev. 104 (2004) 419–458;
(b) D.J. Spira-Solomon, M.D. Allendorf, E.I. Solomon, J. Am. Chem. Soc. 108 (1986) 5318–5328;
(c) E.I. Solomon, U.M. Sundaram, T.E. Machonkin, Chem. Rev. 96 (1996) 2563–2605.
[13] (a) T. Mallah, O. Kahn, J. Gouteron, S. Jeannin, Y. Jeannin, C.J. O'Connor, Inorg. Chem. 26 (1987) 1375–1380;
(b) A. Benzekri, P. Dubourdeaux, J.-M. Latour, P. Rey, J. Laugierb, J. Chem. Soc., Dalton Trans. (1991) 3359–3365;
(c) A. Benzekri, P. Dubourdeaux, J.-M. Latour, J. Laugier, P. Rey, Inorg. Chem. 27 (1988) 3710–3716;
(d) A. Banerjee, R. Singh, E. Colacio, K.K. Rajak, Eur. J. Inorg. Chem. (2009) 277–284;
(e) P. Cheng, D. Liao, S. Yan, Z. Jiang, G. Wang, X. Yao, H. Wang, Inorg. Chim. Acta 248 (1996) 135–137.
[14] (a) P. Bhowmik, A. Bhattacharyya, K. Harms, S. Sproules, S. Chattopadhyay, Polyhedron 85 (2015) 221–231;
(b) A. Biswas, M.G.B. Drew, J. Ribas, C. Diaz, A. Ghosh, Eur. J. Inorg. Chem. (2011) 2405–2412.
[15] (a) S.S. Massoud, C.C. Ledet, T. Junk, S. Bosch, P. Comba, R. Herchel, J. Hoš ekZ. Trávníc ek, R.C. Fischer, F.A. Mautner, Dalton Trans. 45 (2016) 12933–12950;
(b) S.S. Massoud, A.A. Gallo, M.J. Dartez, J.G. Gautreaux, R. Vicente, J.H. Albering, F.A. Mautner, Inorg. Chem. Commun. 43 (2014) 35–38;
(c) S.S. Massoud, T. Junk, F.A. Mautner, RSC Adv. 5 (2015) 87139–87150.
[16] (a) S. Cao, R. Cheng, D. Wang, Y. Zhao, R. Tang, X. Yang, J. Chen, J. Inorg. Biochem. 192 (2019) 126–139;
(b) P. Kar, A. Franconetti, A. Frontera, A. Ghosh, Cryst. Eng. Comm. 21 (2019) 6886–6893;
(c) A. Shirvan, H. Golchoubian, E. Bouwman, J. Mol. Struct. 1195 (2019) 769–777;
(d) A. Hussain, M.F. AlAjmi, M.T. Rehman, S. Amir, F.M. Husain, A. Alsalme, M.A. Siddiqui, A.A. AlKhedhairy, R.A. Khan, Scientific Reports 9 (2019) 5237;
(e) Y.-X. Sun, Y.-Q. Pan, X. Xu, Y. Zhang, Crystals 9 (2019) 607.
[17] J. McLain, J. Lee, J. T. Groves, Biomimetic Oxidations Catalyzed by Transition Metal Complexes, In: Meunier, B. (Ed.), Imperial College Press, London.
[18] F. Benedini, G. Galliani, M. Nali, B. Rindone, S. Tollari, J. Chem. Soc. Perkin Trans. 2 (1985) 1963.
[19] L.I. Simandi, S. Nemeth, N. Rumlis, J. Mol. Catal. 42 (1987) 357.
[20] Z. Szeverenyl, E.R. Mileava, L.I. Simandi, J. Mol. Catal. 67 (1991) 251.
[21] (a) S. Roy, T. Dutta, M.G.B. Drew, S. Chattopadhyay, Polyhedron (2019), https://doi.org/10.1016/j.poly.2019.114311;
(b) N.C. Jana, M. Patra, P. Brandão, A. Panja, Inorg. Chim. Acta 490 (2019) 163–172;
(c) K. Ghosh, M.G.B. Drew, S. Chattopadhyay, Inorg. Chim. Acta 482 (2018) 23–33;
(d) S. Thakur, S. Banerjee, S. Das, S. Chattopadhyay, New J. Chem. 43 (2019) 18747–18759.
[22] S. Sakaue, T. Tsubakino, Y. Nishiyama, Y. Ishii, J. Org. Chem. 58 (1993) 3633.
[23] J. Kaizer, R. Csonka, G. Speier, J. Mol. Catal. A: Chem. 180 (2002) 91.
[24] T. Horvath, J. Kaizer, G. Speier, J. Mol. Catal. A: Chem. 215 (2004) 9.
[25] M.R. Maurya, S. Sikarwar, T. Joseph, S.B. Halligudi, J. Mol. Catal. A: Chem. 236 (2005) 132.
[26] M. Garai, A. Das, M. Joshi, S. Paul, M. Shit, A.R. Choudhury, B. Biswas, Polyhedron 156 (2018) 223–230.
[27] D. Dey, G. Kaur, A. Ranjani, L. Gayathri, P. Chakraborty, J. Adhikary, J. Pasan, D. Dhanasekaran, A.R. Choudhury, M.A. Akbarsha, N. Kole, B. Biswas, Eur. J. Inorg. Chem. (2014) 3350–3358.
[28] D. Dey, G. Kaur, M. Patra, A.R. Choudhury, N. Kole, B. Biswas, Inorg. Chim. Acta 421 (2014) 335–341.
[29] CrysAlisPro 1.171.39.35c, Rigaku Oxford Diffraction, Rigaku Corporation: Tokyo, Japan, 2017.
[30] (a) G.M. SheldrickSHELXT-,, Integrated space-group and crystal-structure determination, Acta Cryst, Acta Cryst. A 71 (2015) 3–8;
(b) G.M. Sheldrick, Crystal structure refinement with SHELXL, Acta Cryst. C71 (2015) 3–8;
(c) O.V. Dolomanov, L.J. Bourhis, R.J. Gildea, J.A.K. Howard, H. Puschmann, J. Appl. Cryst. 42 (2009) 339–341.
[31] (a) M.J. Turner, J.J. McKinnon, S.K. Wolff, D.J. Grimwood, P.R. Spackman, D. Jayatilaka, M.A. Spackman, Crystal Explorer, http://hirshfeldsurface.net17 University of Western Australia, 2017;
(b) M.A. Spackman, D. Jayatilaka, CrystEngCom. 11 (2009) 19;
(c) S.K. Seth, V.S. Lee, J. Yana, S.M. Zain, A.C. Cunha, V.F. Ferreira, A.K. Jordao, M.C.B.V. de Souza, S.M.S.V. Wardell, J.L. Wardellf, E.R.T. Tiekink, Cryst. Eng. Comm. 17 (2015) 2255–2266;
(d) M.N. Ahamad, M. Kumar, A. Ansari, I. Mantasha, M. Ahmad, M. Shahid, New J. Chem. 43 (2019) 14074–14083.
[32] (a) M.A. Spackman, D. Jayatilaka, Cryst. Eng. Comm. 11 (2009) 19–32;
(b) M.A. Spackman, J.J. McKinnon, Cryst. Eng. Comm. 4 (2002) 378–392.
[33] H. Yamatera, Acta Chem. Scand. A 33 (1979) 107–111.
[34] (a) C.K. Pal, S. Mahato, H.R. Yadav, M. Shit, A.R. Choudhury, B. Biswas, Polyhedron 174 (2019) 114156;
(b) D. Dey, S. Das, H.R. Yadav, A. Ranjani, L. Gyathri, S. Roy, P.S. Guin, D. Dhanasekaran, A.R. Choudhury, M.A. Akbarsha, B. Biswas, Polyhedron 106 (2016) 106–114.
[35] (a) A. De, M. Garai, H.R. Yadav, A.R. Choudhury, B. Biswas 31 (2017) e3551;
(b) B. Chowdhury, M. Maji, B. Biswas, J. Chem. Sci 129 (2017) 1627–1637.
[36] M. J. Frisch, G. W. Trucks, H. B. Schlegel, G. E. Scuseria, M. A. Robb, J. R. Cheeseman, G. Scalmani, V. Barone, B. Mennucci, G. A. Petersson, H. Nakatsuji, M. Caricato, X. Li, H. P. Hratchian, A. F. Izmaylov, J. Bloino, G. Zheng, J. L. Sonnenberg, M. Hada, M. Ehara, K. Toyota, R. Fukuda, J. Hasegawa, M. Ishida, T. Nakajima, Y. Honda, O. Kitao, H. Nakai, T. Vreven, J. A. Montgomery Jr, J. E. Peralta, F. Ogliaro, M. Bearpark, J. J. Heyd, E. Brothers, K. N. Kudin, V. N. Staroverov, R. Kobayashi, J. Normand, K. Raghavachari, A. Rendell, J. C. Burant, S. S. Iyengar, J. Tomasi, M. Cossi, N. Rega, J. M. Millam, M. Klene, J. E. Knox, J. B. Cross, V. Bakken, C. Adamo, J. Jaramillo, R. Gomperts, R. E. Stratmann, O. Yazyev, A. J. Austin, R. Cammi, C. Pomelli, J. W. Ochterski, R. L. Martin, K. Morokuma, V. G. Zakrzewski, G. A. Voth, P. Salvador, J. J. Dannenberg, S. Dapprich, A. D. Daniels, O. Farkas, J. B. Foresman, J. V. Ortiz, J. Cioslowski, D. J. Fox, Gaussian 09 (Revision A.02), Gaussian Inc., Wallingford, CT, 2009.
[37] T.H. Dunning, P.J. Hay, Modern Theoretical Chemistry, 3rd ed., H. F. Schaefer, Plenum, New York, 1976.
[38] (a) B. Mennucci, E. Cances, J. Tomasi, J. Phys. Chem. B. 101 (1997) 10506–10517;
(b) E. Cances, B. Mennucci, J. Tomasi, J. Chem. Phys. 107 (1997) 3032–3041;
(c) R. Cammi, J. Tomasi, J. Comput. Chem. 16 (1995) 1449–1458;
(d) S. Miertus, E. Scrocco, J. Tomasi, Chem. Phys. 55 (1981) 117–129.
[39] (a) M. Karar, S. Paul, B. Biswas, T. Majumdar, A. Mallick, Dalton Trans. 47 (2018) 7059–7096;
(b) N. Dutta, S. Haldar, G. Vijaykumar, S. Paul, A.P. Chattopadhyay, L. Carrella, M. Bera, Inorg. Chem. 57 (2018) 10802–10820;
(c) S. Paul, M. Karar, S. Mitra, S.A.S. Shah, T. Majumdar, A. Mallick, ChemistrySelect 1 (2016) 5547–5553;
(d) A. De, A. Sahu, S. Paul, M. Joshi, A.R. Choudhury, B. Biswas, J. Mol. Struct. 1167 (2018) 187–193.
[40] The PyMOL Molecular Graphics System, Version 1.3. Schrodinger, LLC, Mannheim, Germany.
[41] B. Chowdhury, M. Karar, S. Paul, M. Joshi, A.R. Choudhury, B. Biswas, Sens. Actuators B: Chem. 276 (2018) 560–566.
[42] (a) A. De, D. Dey, H.R. Yadav, M. Maji, V. Rane, R.M. Kadam, A.R. Choudhury, B. Biswas, J. Chem. Sci. 128 (2016) 1775–1782;
(b) S. Khan, S. Herrero, R. Gonzalez-Prieto, M.G.B. Drew, S. Banerjee, S. Chattopadhyay, New J. Chem. 42 (2018) 13512;
(c) T.M. Rajendiran, Transit. Met. Chem. 28 (2003) 447–454.
[43] W.J. Geary, Coord. Chem. Rev. 7 (1971) 81.
[44] (a) D. Dey, S. Pal, P.P. Bag, S. Saha, S. Chandraleka, D. Dhanasekaran, N. Kole, B. Biswas, J. Indian Chem. Soc. 92 (2015) 191–202;
(b) R.V. Rathod, S. Bera, M. Singh, D. Mondal, RSC Adv. 6 (2016) 34608–34615;
(c) J.R. Lakowicz (Ed.), Principles of Fluorescence Spectroscopy, Springer-Verlag U.S., 2006, , https://doi.org/10.1007/978-0-387-46312-4.
[45] B. Chowdhury, B. Bhowmik, A. Sahu, M. Joshi, S. Paul, A.R. Choudhury, B. Biswas, J. Chem. Sci. 130 (2018) 161.
[46] A.K. Ghosh, A. Ali, Y. Singh, C.S. Purohit, R. Ghosh, Inorg. Chim. Acta. 474 (2018)

156–163.
[47] S. Sagar, S. Sengupta, A.J. Mota, S.K. Chattopadhyay, A.E. Ferao, E. Riviere, W. Lewis, S. Naskar, Dalton Trans. 46 (2017) 1249–1259.
[48] M. Mitra, T.Y. Kundu, G. Kaur, G. Sharma, A.R. Choudhury, Y. Singhd, R. Ghosh, RSC Adv. 6 (2016) 58831–58838.
[49] T. Dutta, S. Mirdya, P. Giri, S. Chattopadhyay, Polyhedron 175 (2020) 114164.
[50] C. Mukherjee, T. Weyhermueller, E. Bothe, E. Rentschler, P. Chaudhuri, Inorg. Chem. 46 (2007) 9895–9905.
[51] (a) C.E. Barry III, P.G. Nayar, T.P. Begley, Biochemistry 28 (1989) 6323–6333;
(b) C.E. Barry III, P.G. Nayar, T.P. Begley, J. Am. Chem. Soc. 110 (1988) 3333–3334;
(c) J.C. Freeman, P.G. Nayar, T.P. Begley, J.J. Villafranca, Biochemistry 32 (1993) 4826–4830.

Source details

Feedback > Compare sources >

Inorganica Chimica Acta

See also: Inorganic Chemistry Communication

Incorporating: Inorganica Chimica Acta Reviews

Scopus coverage years: from 1967 to Present

Publisher: Elsevier

ISSN: 0020-1693 E-ISSN: 1873-3255

Subject area: Chemistry: Inorganic Chemistry | Materials Science: Materials Chemistry | Chemistry: Physical and Theoretical Chemistry

Source type: Journal

View all documents > | Set document alert | Save to source list

CiteScore 2022
5.6

SJR 2022
0.406

SNIP 2022
0.658

CiteScore | CiteScore rank & trend | Scopus content coverage

Journal Pre-proofs

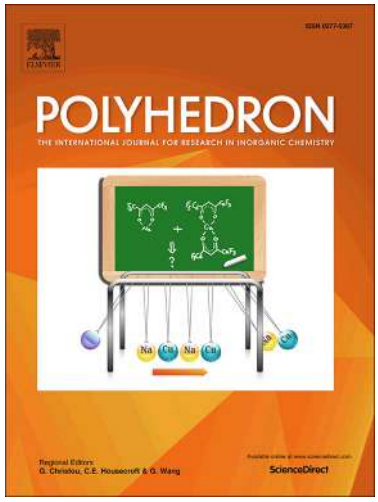

Bio-mimetic of Catecholase and Phosphatase Activity by a Tetra-iron(III) Cluster

Chanchal Kumar Pal, Shreya Mahato, Hare Ram Yadav, Madhusudan Shit, Angshuman Roy Choudhury, Bhaskar Biswas

PII: S0277-5387(19)30593-5
DOI: https://doi.org/10.1016/j.poly.2019.114156
Reference: POLY 114156

To appear in: *Polyhedron*

Received Date: 10 July 2019
Revised Date: 13 September 2019
Accepted Date: 15 September 2019

Please cite this article as: C. Kumar Pal, S. Mahato, H. Ram Yadav, M. Shit, A. Roy Choudhury, B. Biswas, Bio-mimetic of Catecholase and Phosphatase Activity by a Tetra-iron(III) Cluster, *Polyhedron* (2019), doi: https://doi.org/10.1016/j.poly.2019.114156

Bio-mimetic of Catecholase and Phosphatase Activity by a Tetra-iron(III) Cluster

Chanchal Kumar Pal,[a] Shreya Mahato,[a] Hare Ram Yadav,[b] Madhusudan Shit, [c] Angshuman Roy Choudhury, [b] Bhaskar Biswas[a,*]

[a]*Department of Chemistry, University of North Bengal, Darjeeling-734013, India*
[b]*Department of Chemical Sciences, Indian Institute of Science Education and Research, Mohali, Sector 81, Knowledge City, S. A. S. Nagar, Manauli PO, Mohali, Punjab 140306, India*
[c]*Department of Chemistry, Dinabandhu Andrews College, Kolkata 700084, India*

Abstract

An oxido- and acetato-bridged tetranuclear iron(III) cluster, $[Fe_4^{III}(\mu\text{-}O)_2(\mu\text{-}OAc)_6(phen)_2(H_2O)_2](NO_3)_2{\cdot}(H_2O)_3$ (**1**), [OAc = acetate; phen = 1,10-phenanthroline] has been prepared in the crystalline phase. X-ray structural analysis of the compound reveals that all the Fe(III) centres in **1** adopt an octahedral coordination geometry and the tetra-iron(III) core exists in an unusual asymmetric conformation. Bond valence sum (BVS) calculations recommend the existence of all iron ions in the +3 oxidation state in the crystalline phase. The tetra-iron(III) cluster elegantly catalyzes the oxidation of 3,5-di-*tert*-butylcatechol (DTBC), viz. catecholase-like activity, with a good turnover number, $k_{cat} = 9.28 \times 10^2\ h^{-1}$ in acetonitrile medium. Spectrophotometric titration shows the existence of two distinct isosbestic points, which unanimously proves the rarely observed enzyme-substrate binding phenomenon in solution. Electrochemical analysis recommends the production of Fe(II)-semiquinone species in the course of the catalytic oxidation of DTBC. Furthermore, the same iron(III) cluster displays phosphoester cleavage activity towards the disodium salt of p-nitrophenylphosphate (PNPP) in aqueous-methanol medium with rate of $7.20 \times 10^{-4}\ m^{-1}$. ESI-MS measurements of the tetra-iron(III) complex in the presence of PNPP indicate the formation of an organophosphorus intermediate in solution and solvent aqua molecules probably make a nucleophilic attack on the phosphorus centre, favouring the generation of the organophosphorus intermediate.

Keywords: Iron; X-ray structure; Electrochemistry; Catecholase activity; Phosphatase study

*Corresponding author. E-mail: bhaskarbiswas@nbu.ac.in / icbbiswas@gmail.com

1. Introduction

In nature, emergent biological processes often utilize 3d metal-based coordination compounds as functional sites for facilitating highly selective bio-chemical reactions [1-5]. Due to this, paramount interest has been shown by synthetic coordination chemists to design and synthesize bio-inspired catalysts in the pursuit of selective bond activation and organic transformations [6-16]. Nowadays, coordination compounds comprising of earth abundant transition metal ions in combination with different (N,N) and (N,O) donor ligands have received significant attention for their potential applications in biological and material science [17-24]. Iron is one of the most prevalent metal ions among the transition metal ions in living systems. The design of new catalytic systems based on abundant and inexpensive metal ions, particularly iron, for fundamental chemical transformations under environmentally benign conditions is an important paradigm in chemical synthesis [25-29]. In recent times, iron-based coordination compounds with varied nuclearities have shown unprecedented catalytic activity for different catalytic transformations of organic substrates [19,30-33]. Indeed, it has been demonstrated that the proper design of iron complexes by judiciously choosing ligands can aid in the development of novel catalysts [34-41].

Iron clusters bring additional importance for advances in the avenue of magnetism for metallo-clusters. Hence, considerable attention has been paid to synthetic approaches which may produce polymetallic coordination cores with promising magnetic properties [19,28,29]. A literature survey indicates the impact as well as the importance of the magnetic properties corresponding to the design and preparation of such tetra-iron(III) clusters. Previously, A.K. Boudalis et al, M.W. Wemple et al and J.K. McCusker et al [42-44] synthesized a similar type of tetra-iron(III) cluster, keeping azides as terminal ions to the iron centres. Recently, we also prepared a similar tetra-iron(III) cluster with bipyridine ligands and different counter anions [19]. However, catalytic performance, in relation to bio-mimics, by tetra-iron(III) clusters is limited. Based on the invaluable contribution of iron centric coordination compounds ranging from heme proteins to iron-sulfur clusters and redox-enzymes in the living world and focusing on industrial importance, we have designed and structurally characterised an oxido-acetato-

bridged tetra-iron(III)-phenanthroline cluster. Spectrophotometric titration shows the presence of two distinct isosbestic points in the course of the catalytic oxidation of DTBC and this remarkable phenomenon unanimously confirms the binding of the enzyme with the substrate in solution. Electrochemical analysis consolidates the production of Fe(II)-semiquinone species in the DTBC oxidation. This tetra-iron(III) cluster catalyzes the production of quinone species with a good turnover number, $k_{cat} = 9.28 \times 10^2\ h^{-1}$. This iron(III) cluster also effectively catalyses the cleavage of phosphoester linkages in PNPP and the rate of phosphatase activity is found to be as high as $7.20 \times 10^{-4}\ m^{-1}$. Experimental observations and ESI-MS analysis suggest that solvent aqua molecules make a nucleophilic attack on the phosphorus centre and the course of the catalysis proceeds through the formation of an organophosphorus intermediate in solution.

2. Experimental section

2.1. Preparation of the tetra-iron(III) cluster

(a) Chemicals, solvents and starting materials

High purity 1,10-phenanthroline (Lancaster, UK), iron(III) chloride hexahydrate (E. Merck, India), ceric ammonium nitrate (E. Merck, India) were purchased from commercial sources and used as received. All the other reagents and solvents were used of analytical grade (A.R. grade).

(b) *Synthesis of the tetra-iron(III) cluster*

An aqueous-acetic acid (40/60; v/v) solution (10 ml) of 1,10-phenanthroline (0.360 g, 2.0 mmol) was added to an aqueous solution of hydrated $FeCl_3$ (0.271 g, 1.0 mmol, 20 ml), followed by a solution of sodium acetate (0.164 g, 2.0 mmol). The reaction mixture was stirred slowly for 30 min, then solid ceric ammonium nitrate (CAN) (0.550 g, 1.0 mmol) was added and the resulting solution was stirred slowly for another 30 minutes. After that, the brown coloured solution obtained was filtered. The filtrate was kept in air for slow evaporation. After 12-15 days, a brown coloured compound (**1**) in the form of single crystals separated out. The tetra-iron compound was washed with hexane and dried in *vacuo* over

silica gel. Yield of the tetra-iron compound: 0.207 g (76.4% based on the metal salt) Spectroscopic results for $C_{36}H_{44}N_6O_{25}Fe_4$ (**1**); IR (KBr pellet, cm^{-1}): 3379 (ν_{OH}), 1592 ($\nu_{C=N}$), 1498, 1471($\nu_{M(\mu\text{-}OAc)}$), 1384($\nu_{(\text{-}NO3)}$); UV-Vis (1×10^{-4} M, λ_{max}, nm, MeCN): 249, 299, 353, 521.

2.2. Physical measurements

The infrared spectrum (KBr) was recorded with a FTIR-8400S SHIMADZU spectrophotometer in the range 4000–400 cm^{-1} with a KBr pellet. The ^1H NMR spectrum was obtained on a Bruker Advance 300 MHz spectrometer at 25 °C. Ground state absorption and all spectrophotometric analysis were recorded with a JASCO V-730 UV-Vis spectrophotometer. The electrospray ionization (ESI) mass spectrum was recorded using a Q-tof-micro quadruple mass spectrometer. The pH value of the solutions was measured using a Labman pH meter at room temperature.

2.3. X-ray diffraction analysis

Single crystal X-ray diffraction data of the oxido-acetato-bridged tetra-iron(III) complex was collected using a Rigaku XtaLABmini diffractometer equipped with a Mercury CCD detector. The data were collected with graphite monochromated Mo-Kα radiation (λ = 0.71073 Å) at 100.0(2) K, using ω scans. The data were reduced using Crystal Clear suite 2.0. [45] and the space group determination was done using Olex^2. The structure was resolved by the direct method and refined by full-matrix least-squares procedures using the SHELXL-2014/7 software package, using the OLEX^2 suite [46,47].

2.4. Catecholase activity of the tetra-iron(III) cluster

To examine the catechol oxidation activity of the iron(III) cluster, a 10^{-4} M solution of the tetra-iron compound in acetonitrile (ACN) medium was treated with 100 equiv. of 3,5-di-*tert*-butylcatechol (DTBC) at room temperature under an aerobic atmosphere. Absorbance vs. wavelength (wavelength scans) of these solutions were recorded at regular time intervals of 5 min in the wavelength interval 300–800 nm [48,49]. It may be noted that a control experiment

in the absence of this tetranuclear iron(III) catalyst was also performed, which showed very little development of the quinone species up to 6h in acetonitrile medium and thus can be ignored. Kinetic experiments were further performed spectrophotometrically with the iron(III) cluster and DTBC in ACN at 25 °C. A 0.04 ml solution of the tetra-iron(III) cluster, with a constant concentration of 1×10^{-4} M, was added to 2 ml of DTBC of a particular concentration (varying its concentration from 1×10^{-3} M to 1×10^{-2} M) to achieve an ultimate concentration of the tetra-iron(III) cluster of 1×10^{-4} M. The conversion of DTBC to DTBQ (quinone band maxima) was monitored with time at a wavelength of 400 nm (time scan) in ACN medium. The initial rate method [48,49] was applied to determine the rate constant value for each concentration of the substrate and each experiment was repeated thrice.

2.6. Electrochemical measurements

A BASi Epsilon−EC electro-analytical instrument was used for the cyclic voltammetric experiment in CH_3CN solutions containing 0.2 M tetrabutylammonium hexafluorophosphate as the supporting electrolyte. A BASi platinum working electrode, platinum auxiliary electrode and Ag/AgCl reference electrode were used for the measurements. The cyclic voltagrams were recorded for the tetra-iron(III) complex in the absence and presence of DTBC under molecular oxygen and molecular nitrogen atmospheres.

2.7. Phosphatase activity of the tetra-iron(III) cluster **(1)**

The disodium salt of 4-nitrophenylphosphate (PNPP) was used as a standard substrate to study the hydrolytic cleavage of the phosphoesterase linkage of PNPP in aqueous methanolic medium following a reported procedure [50,51]. An initial screening of the hydrolytic tendency of the tetra-iron(III) cluster was performed until 2% formation of 4-nitrophenolate was reached, and then its kinetic data were collected. The hydrolysis rate of PNPP in the presence of the iron(III) cluster was measured by the initial rate method, keeping the incremental band intensity in the absorption fixed at 412 nm for the release of the 4-nitrophenolate ion in aqueous H_2O-CH_3OH at 25 °C. For the wavelength scan, the spectrum was recorded on addition of the 1×10^{-4} M tetra-iron(III) complex solution to the 1×10^{-3} M

PNPP solution for 4 hours. A blank experiment with PNPP in the absence of the tetra-iron(III) complex under identical reaction conditions does not show any phosphatase activity.

Kinetics experiments for the phosphoester cleavage study were carried out by monitoring the growth of the 4-nitrophenolate species at 412 nm as a function of time under the condition of excess substrate in the presence of the tetra-iron(III) complex, keeping the other parameters constant. The kinetic experiment was performed with a 1×10^{-4} M concentration of the tetra-iron(III) cluster and PNPP (varying the concentration from 1×10^{-3} M to 1×10^{-2} M) in H_2O-CH_3OH, using a UV-Vis spectrophotometer. The visible absorption increase was recorded for a total period of 4 hours at 12 min intervals. All measurements were performed in triplicate.

3. Results and discussion

3.1. Synthesis and formulation of the tetra-iron(III) cluster (**1**)

The iron(III)-phenanthroline cluster was prepared by addition of 1,10-phenanthroline to hydrated ferric chloride, followed by a solution of sodium acetate and solid ceric ammonium nitrate (CAN) in aqueous-acetic acid solution. A control experiment was also carried out with the absence of CAN, under similar experimental conditions. It was observed that for the successful synthesis of this iron(III) cluster, the addition of CAN is a mandatory step. CAN helps to maintain the oxidation state of the iron ion, which facilitates the cluster formation of the iron ions by receiving molecular oxygen from the air and acetate ions in the presence of phenanthroline ligands in solution. CAN further supplies nitrate ions to stabilize the cationic tetra-iron(III) cluster in the crystalline state. The structural formulation of the iron(III) cluster is principally confirmed by X-ray diffraction analysis, along with different conventional spectroscopic methods.

3.2. Description of the crystal structure

Single crystal X-ray structural analysis reveals that the iron(III) cluster crystallizes in the monoclinic crystal system, with the *C*2/*c* space group. Each of the iron(III) centres in this cluster adopts an octahedral coordination geometry. Furthermore, two oxido-linkages (μ_3-O^{2-} ;

O1, O2) in association with six end-to-end type symmetric acetato bridges remain the driving force in assembling the four Fe(III) ions in close vicinity and producing a dicubane geometry. The phenanthroline ligand, a bidentate end-capper, in combination with aqua molecules help to saturate the coordination number of the iron(III) centres in this cluster. The cationic charges of the iron(III) centres are compensated by two units of nitrate ions, while three aqua molecules are also observed as water of crystallization. The ORTEP diagram of this tetra-iron(III) cluster is shown in Figure 1. The crystallographic refinement parameters, bond distance and bond angle data are tabulated in Tables 1 and S1 respectively.

The Fe–O–Fe linkages exhibit high non-linearity and display angles ranging from 84.25 to 134.40°. The Fe–μ_3-O distances [1.831(3) to 1.954(3) Å] show some similarity as well as dissimilarity with previously reported iron complexes [8,30]. The association of the non-linear bridges with strong Fe–μ-O bonding has a great impact on the production of inter-metallic (Fe…Fe) spacings from 3.251 to 3.483 Å. The C–N and C–C bond lengths in the phenanthroline ligands are found in a similar range to the literature values [8,18,23,26].

A comparison of the structural aspects is drawn between the crystal structures of the previously reported tetra-iron(III) cluster $[Fe_4^{III}(\mu\text{-}O)_2(\mu\text{-}OAc)_6(N_3)_2(phen)_2].3MeCN$ and our tetra-iron(IIII) cluster, $[Fe_4^{III}(\mu\text{-}O)_2(\mu\text{-}OAc)_6(phen)_2(H_2O)_2](NO_3)_2.(H_2O)_3$ (Table S2). From a crystallographic point of view, the molecular weights, cell dimensions (a, b, c, α, β, γ), volume and space group symmetry are entirely different. The relative torsion angles are different in both cases. The cationic charges of the iron centres in the reported structure are internally compensated by oxides, carboxylates and azide ions. Our tetra-iron(III) structure has similar types of oxides and carboxylates as bridging units, however two counter anionic nitrate ions are also present to satisfy the cationic charges of the iron(III) ions. The reported structure has no counter anions, which makes it a non-electrolyte, whilst our structure is a 1:2 type electrolyte. Both the tetra-iron(III) clusters crystallize in the monoclinic system, but the space groups are found to be different, as $P2_1/n$ and $C2/c$ (Table S2). The structural core, $[Fe_4(\mu_3\text{-}O)_2(\mu_3\text{-}OAc)_6]^{2+}$, for both the structures remain the same while the bridging linkages (oxido

and acetate bridges) are disposed in a slightly different arrangement in space. The solvents of crystallization are also different in the two structures.

Previously, it was observed by crystallography that $[Fe_4(\mu_3\text{-}O)_2]^{8+}$ core species may exist with either bent (butterfly) or planar dispositions of the tetra-iron core of A and B conformations (Scheme 1). Another type of asymmetric conformation of type C, a hybrid of types A and B (Scheme 1), for such a tetrametallic core may also be possible. For this case, both the structures exhibit a type C conformation, which had been previously only been observed in limited examples (Table S2) [19,52,53].

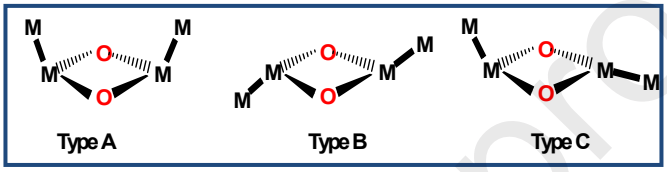

Scheme 1. Different conformations of the $[Fe_4(\mu_3\text{-}O)_2]^{8+}$ core

3.3. Bond Valence Sum (BVS) calculations

Bond Valence Sum (BVS) [54] is a highly useful theoretical method to quantify the oxidation level of metal ions in cluster/normal compounds in solids by employing bond distance values determined from X-ray crystallography. We have applied this method to identify the oxidation level for the iron ions in our iron cluster. All the iron ions present in the iron(III) cluster are found to be at the +3 oxidation level. The details of the calculations for finding out the oxidation states of the iron ions are presented in Table S3.

3.4. Catalytic oxidation of DTBC with mechanistic implications

The catecholase activity of this tetra-iron(III) cluster has been investigated with a model substrate, 3,5-di-*tert*-butylcatechol in acetonitrile (ACN) medium. DTBC contains two bulky *t*-butyl groups in the aromatic ring. The low quinone-catechol reduction potential makes DTBC a model substrate which undergoes easy oxidation to the corresponding *o*-quinone, DTBQ (Scheme 2). DTBQ is a stable compound and exhibits a maximum absorption in the wavelength range from 380 to 420 nm [14,18,22,23,48,49].

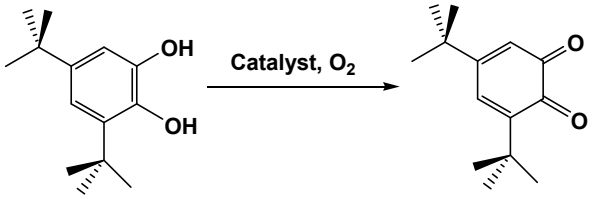

Scheme 2. Catalytic oxidation of DTBC to DTBQ in acetonitrile medium

The tetra-iron(III) cluster displays spectral bands at 249, 299, 353 and 521 nm in the electronic spectrum in acetonitrile medium. The high energy electronic bands at 249 and 299 nm correspond to π-π* or n-π* electronic transitions of phenanthroline origin. The low energy broad optical bands at 353 and 521 nm (ε_{max} = 1373 and 1227 M^{-1} cm^{-1} respectively) are assignable to O^{2-}→iron(III) charge transfers (LMCT). Previous scientific studies authenticate the characteristic electronic transitions for O^{2-}→iron(III) species as ligand to metal charge transfer (LMCT) transitions in oxido-acetato bridged iron(III) complexes, which are located in the range 350-520 nm with ε_{max} values of 930-1450 M^{-1} cm^{-1} [55-59].

The standard substrate, DTBC, displays an absorbance maximum at 284 nm in solution. Upon addition of the tetra-iron(IIII) cluster to DTBC, two new optical bands at 400 and 695 nm are developed with incremental absorbance (Fig. 2) and concomitantly a spectral band at 521 nm with a decrease in absorbance value is also observed during the spectrophotometric time scan. The growth of optical band at 400 nm is a definite signature for the generation of o-quinone species, while the decrement of the electronic band at 521 nm recommends the possibility of depletion of metal bound semiquinone species in solution [60-62]. Moreover, the gradual development of a broad band at 695 nm is indicative of a LMCT for the iron-catecholate adduct in solution [63-65]. Renowned scientist groups across the globe have explicitly proved the existence of dicatechoate adducts, metal bound quinone and ortho-quinone species in the solution phase [60-65].

Very significantly, two isosbestic points are observed at 469 and 550 nm during the course of the catalytic oxidation of DTBC (Fig. 2). The presence of isosbestic points, which are considered as reactive intermediates (ES1 and ES2), are rarely observed phenomenon in catechol oxidation studies. A few years back, we observed the existence of two isosbestic points in examining catecholase activity by a mono-iron(II) complex [18]. In a real sense,

limited examples are available where isosbestic points are observed during the course of catechol oxidation by iron complexes [8,18]. This experimental observation explicitly proves the catalytic transformation of DTBC to DTBQ under aerobic atmosphere and recommends the formation of DTBQ through enzyme-substrate binding. The produced DTBQ in solution was isolated by column chromatographic purification with hexane-ethyl acetate as the eluant mixture. The quinone was identified by ^{1}H NMR spectroscopy (Fig. S1). ^{1}H NMR ($CDCl_3$, 400 MHz) δ_H, ppm: 1.17 (s, 9H), 1.22 (s, 9H), 6.14 (d, J = 2.4 Hz, 1H), 6.87 (d, J = 2.4 Hz, 1H).

The development of the quinone band was monitored at 400 nm as a function of time and illustrates saturation kinetics where the Michaelis−Menten model seems to be very suitable (Fig. S2). We considered the mechanism to involve the formation of a catalyst–substrate complex (CS), which subsequently breaks down in a second step to form the free catalyst (C) and the product (P), as shown below.

$$C + S \underset{k_2}{\overset{k_1}{\rightleftharpoons}} CS \underset{k_4}{\overset{k_3}{\rightleftharpoons}} C+P$$

The above mechanism leads to the well known Michaelis–Menten equation:

$$V = \frac{V_{max}\,[S]}{K_M + [S]}$$

where V is the reaction velocity (the reaction rate), K_m is the Michaelis–Menten constant, V_{max} is the maximum reaction velocity and [S] is the substrate concentration.

The Michaelis–Menten equation can be transformed into different form, namely the Lineweaver–Burk Equation (Double reciprocal plot; Fig. S2), which is one of the most widely used equations, employing the reciprocal of both sides of the above equation and leading to the equation as follows:

$$\frac{1}{V} = \frac{K_M}{V_{max}} \cdot \frac{1}{[S]} + \frac{1}{V_{max}}$$

The kinetic parameters for the catechol oxidation by the tetra-iron(III) cluster are presented in

Table 2. The turn over number (TON) was also determined to evaluate the catalytic efficacy for transformation of a maximum number of substrate molecules to product per catalyst per time unit. The turnover number (k_{cat}) for the tetra-iron(III) cluster is $k_{cat} = 9.28\times10^2$ h^{-1} in ACN.

3.5. Electrochemical behavior of the Fe(III) complex in the presence of DTBC

Electrochemical analysis was employed to find out the mechanistic perspectives of the catechol oxidation studies by this iron(III) cluster in anhydrous acetonitrile medium. The iron(III) cluster undergoes two successive one-electron quasi-reversible diffusion controlled reductions, showing two peaks at -1.36 and -1.52 V vs. Ag/AgCl, saturated KCl (Fig. 3, Table 3). Chronocoulometry studies at a constant potential confirm that only one electron is involved in each reduction [66]. In this tetra-iron(III) cluster, two types of iron(III) centres are present where two Fe(III) ions are coordinated by a phenanthroline chelator (FeO_4N_2 environment) and the other two iron centres have oxido, acetato bridges and coordinated aqua molecules in their primary zone of coordination (FeO_6 environment). Thus, the two Fe(III) ions with the phenanthroline coordination in the tetra-iron(III) cluster are reduced to Fe(II) ions, thereby two waves are developed. The quasi-reversible nature of the reduction may be assigned to the greater stabilization of the Fe(II) ion in the presence of the phenanthroline ligand. The cyclic voltammogram of the tetra-iron(III) cluster in the presence of DTBC (Fig.3, Table 3) under molecular oxygen exhibits two reduction peaks at +0.153 and -0.314 V, along with three irreversible reduction peaks at -1.22, -1.35 and -1.510 V (Fig. 3, Table 3). The reduction peaks developed at -1.35 and -1.51 V are assignable to the reduction of the Fe1 and Fe2 centres in **1**, although a small peak at -1.22 V probably indicates the reduction of molecular oxygen to peroxide. Other important peaks appearing at +0.153 V (quasi-reversible) and -0.314 V (irreversible) focus on the production of semiquinone and quinone species in the reaction mixture. Previous investigations on the electrochemical nature of several quinones in organic polar media recommend that the peaks at +0.153 and -0.314 V appear solely for the development of semiquinone and quinone in the course of the catalysis [67, 68]. The electro-chemical behavior of the tetra-iron(III) cluster in the presence of DTBC under molecular N_2 was also examined to reveal the oxidizing nature of the cluster. Four

reversible peaks at -1.35, -1.7, -0.123 and -0.393 V (Fig. S3) are observed for the reaction mixture under the N_2 environment. The first two peaks with, potentials of -1.35 and -1.7 V, are assignable to the reduction of two iron centres in the cluster, however the peaks at -0.123 and -0.393 V authenticate the conversion of semiquinone to quinine and catechol to semiquinone, respectively (Fig. S3, Table 3). These observations indicate that this iron(III) cluster can also behave as an oxidizer for the conversion of catechol to quinone in the absence of a molecular oxygen atmosphere. A literature survey also reflects that the tetra-iron(III) cluster shows a good catalytic efficacy towards the oxidative conversion of DTBC to DTBQ [1,2,17,18].

3.6. Phosphatase activity of the tetra-iron(III) cluster (**1**) and its mechanistic inferences

Upon addition of a 10^{-4} M aq. methanolic solution of the tetra-iron(III) cluster to a 10^{-3} M PNPP solution, a new band with incremental absorbance at 412 nm is developed (Fig. 4). The rise of the optical band at λ_{max} = 412 nm may correspond to the evolution of the 4-nitrophenolate ion in solution during the course of the phosphatase activity [17,51,69]. The changes observed in the spectral features are displayed in Fig. 4.

The kinetic parameters are determined by employing the initial slope method. The initial first order rate constant, V (min^{-1}) = 7.20×10^{-4} (Error = 1.89×10^{-5}) is determined directly from a plot of the $\log[A_\alpha/(A_\alpha - A_t)]$ values versus time (Fig. 5) in this catalytic cleavage of PNPP. The nature of the plot maintains good linearity with R^2 = 0.989. Control experiments were also performed to validate the non-catalytic role of phenanthroline, and experiments under similar reaction conditions are found to be non-responsive towards phosphoesterase activity of PNPP. A literature survey on the rate of catalytic phosphatase activity of iron complexes was made to compare the level of activity of this tetra-iron(III) cluster with previously reported compounds (Table 4) [69-71].

The previous scientific observations helped us to unveil the mechanistic route for this phosphoesterase activity. Different modes of activation, namely Lewis acid activation, leaving group activation and metal-nucleophilic attack, including experimental observations, provide sufficient sources of information to propose a reasonable catalytic cycle of phosphoester

cleavage (Scheme 1) by this tetra-iron(III) cluster [72-75]. The presence of coordinated aqua molecules at the metal centres may also play a pivotal role in the phosphoester cleavage activity [76-78].

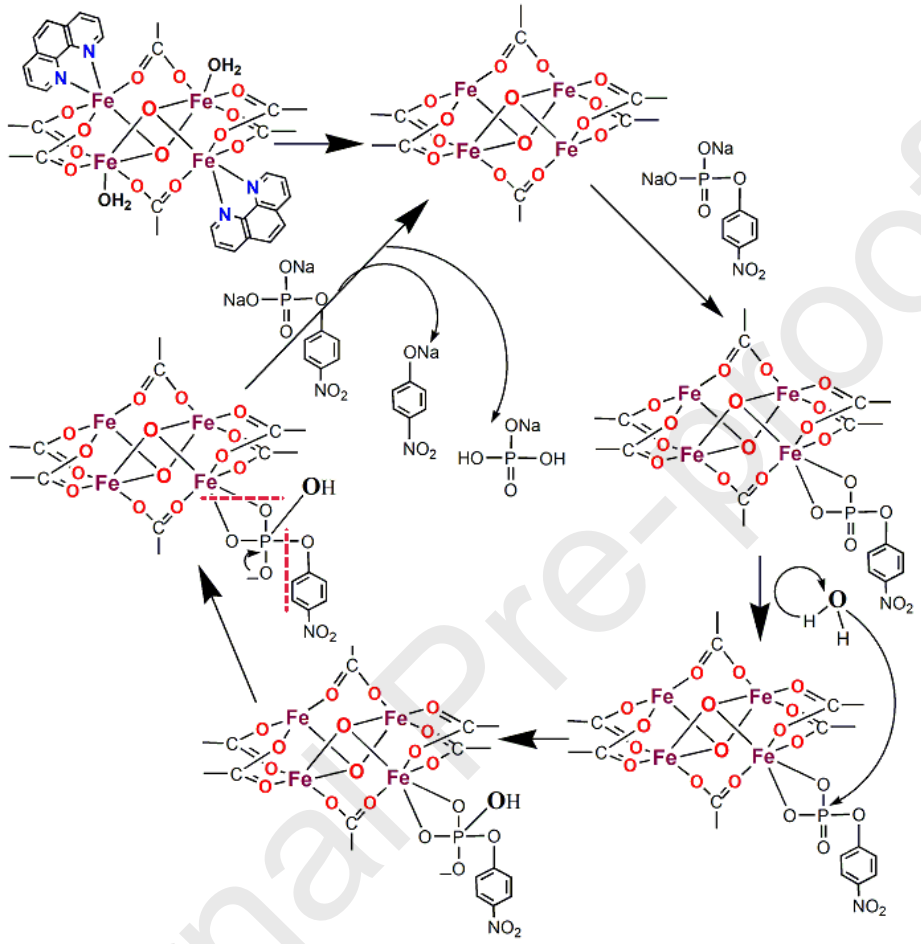

Scheme 1. Plausible catalytic cycle for phosphoester cleavage by the iron cluster

For this tetra-iron(III) cluster, at the primary stage, PNPP binds with the oxido-acetato-tetra-iron(III) core. The existence of an iron cluster-PNPP adduct ($[C_{18}H_{23}Fe_4NO_{19}P]^+$) is evidenced by the presence of a peak at 811.0634 m/z (Calcd. m/z 811.0121). The *in situ* development of organophosphorus intermediates is further confirmed by the appearance of the isotopic distribution pattern of the signal at m/z 827.0327 (Calcd. m/z 827.7221) and m/z 844.1074 (Calcd. m/z 844.4124) (Fig. S4). Important peaks at m/z 827.0327 (Calcd. m/z 827.7221) and

m/z 844.1074 (Calcd. m/z 844.4124) represent the existence of reactive intermediates as molecular species, $[C_{18}H_{23}Fe_4NO_{20}P]^+$ and $[C_{18}H_{24}Fe_4NO_{21}P]^+$ respectively. The presence of such peaks in the ESI mass spectrum provides sufficient evidence for the nucleophilic attack by aqua molecules to the P atom of PNPP, which actually facilitates hydrolytic cleavage of PNPP. High spin iron(III) ions always exhibit super acidic behaviour and this property assists in the generation of the hydroxide ion, which probably remains the driving force. This phenomenon leads to the construction of an organophosphorus intermediate developed by the nucleophilic substitution reaction and simultaneous eviction of the 4-nitrophenolate ion. Finally, it gradually breaks down into the active form of the tetra-iron(IIII) cluster and phosphoric acid.

4. Conclusion

In this present work, we report the synthesis and structural characterization of an oxido-acetato-bridged tetra-iron(III) cluster, $[Fe_4^{III}(\mu\text{-}O)_2(\mu\text{-}OAc)_6(phen)_2(H_2O)_2](NO_3)_2(H_2O)_3$ (**1**). Analysis of its X-ray structure reveals that the tetra-iron(III)-oxido core remains in a unusual asymmetric conformation, which will definitely enrich the molecular library of such a rare class of compounds. This iron(III) compound may be accessed as a precursor for facile incorporation of other monodentate ligands to iron(III) centres with the aim of achieving higher nuclearity iron clusters having good magnetic properties. The tetra-iron(III) cluster catalytically oxidizes DTBC to DTBQ in acetonitrile medium with a high turnover number, $k_{cat} = 9.28 \times 10^2\ h^{-1}$. Spectroscopic detection of two distinct isosbestic points at 469 and 550 nm in the course of DTBC oxidation recommends the formation of reactive intermediates, ES_1 and ES_2, which are very limited in scientific studies on the catecholase activity of iron(III) complexes. The iron(III) centres in the iron cluster in the presence of DTBC form Fe(II)-semiquinone and ortho-quinone species in solution, and this phenomenon is justified through electrochemical analysis of the iron cluster in the presence of DTBC under aerobic conditions. The rate of hydrolytic decomposition of the phosphoester linkage in the disodium salt of p-nitrophenylphosphate (PNPP) in aqueous-methanol medium is found to be as high as $7.20 \times 10^{-4}\ m^{-1}$. ESI-MS measurements of the iron(III) cluster in the presence of PNPP proves that

aqua molecules undergo a nucleophilic attack on the phosphorus centre, proceeding through an organo-phosphorus intermediate at one of the iron(III) centres to produce the 4-nitrophenolate ion. Bio-inspired catalysis by tetra-iron(III) clusters is very limited in the literature and these mimicking activities of the tetra-iron(III) cluster may be helpful in advancing investigations of this type to a good extent.

5. Supplementary data

Crystallographic data are available free of charge from The Director, CCDC, 12 Union Road, Cambridge, CB2 1EZ, UK (fax: +44-1223-336033; E-mail: deposit@ccdc.cam.ac.uk or www: http://www.ccdc.cam.ac.uk) upon request, quoting the deposition number CCDC 1939346 for the tetra-iron(III) complex.

Acknowledgements

BB thanks the Science and Engineering Research Board (SERB) for financial support under the FAST TRACK scheme, YOUNG SCIENTIST (No. CS-088/2013 dtd 21-5-2014). ARC thanks the X-ray facility of the Department of Chemical Sciences, IISER Mohali for single crystal X-ray diffraction data collection. *This work is dedicated to Dr. Indranil Kar, Principal, Surendranath College, Kolkata 700009 who remains a constant source of inspiration to me.*

References

[1] Biomimetic Oxidations Catalyzed by Transition Metal Complexes, B. Meunier (Ed.), Imperial College Press, London, 2000.

[2] A.-F. Miller, FEBS Lett., 586 (2012) 585-595

[3] Cytochrome P-450. Structure, Mechanism and Biochemistry, 2nd ed.; J.T. Groves, Y.Z. Han, P.R. Ortiz de Montellano, Eds. Plenum Press: New York, (1995) 3-48.

[4] W. Nam, Acc. Chem. Res. 40 (2007) 465.

[5] M. Costas, M.P. Mehn, M.P. Jensen, L. Que, Chem. Rev., 104 (2004) 939-986.

[6] J.P. Layfield, S. Hammes-Schiffer, Chem. Rev., 114 (2014) 3466-3494

[7] J.J.A. Cotruvo, J. Stubbe, Metallomics, 4 (2012) 1020-1036.

[8] D. Dey, A. De, H.R. Yadav, P.S. Guin, A.R. Choudhury, N. Kole, B. Biswas, ChemistrySelect 01 (2016) 1910-1916.

[9] B. Das, A. Al-Hunaiti, M. Haukka, S. Demeshko, S. Meyer, A.A. Shteinman, F. Meyer, T. Repo, E. Nordlander, Eur. J. Inorg. Chem., 21 (2015) 3590-3601.

[10] H.G. Jang, D.D. Cox, L. Que Jr, J. Am. Chem. Soc., 113 (1991) 9200-9204.

[11] M. Merkel, M. Pascaly, B. Krebs, J. Astner, S. P. Foxon, S. Schindler, Inorg. Chem., 44 (2005) 7582-7589.

[12] I. Ghosh, S. Banerjee, S. Paul, T. Corona, T.K. Paine, Angew. Chem. Int. Ed., (2019) 10.1002/anie.201906978.

[13] M. Bordeaux, A. Galarneau, J. Drone, Angew. Chem. Int. Ed., 51 (2012) 10712-10723.

[14] D. Dey, G. Kaur, A. Ranjani, L. Gyathri, P. Chakraborty, J. Adhikary, J. Pasan, D. Dhanasekaran, A.R. Choudhury, M.A. Akbarsha, N. Kole, B. Biswas, Eur. J. Inorg. Chem., (2014) 3350-3358.

[15] P.C.A. Bruijnincx, M. Lutz, A.L. Spek, W.R. Hagen, B.M. Weckhuysen, G. van Koten, R.J.M.K. Gebbink, J. Am. Chem. Soc., 129 (2007) 2275-2286.

[16] M.P. Valley, C.K. Brown, D.L. Burk, M.W. Vetting, D.H. Ohlendorf, J.D. Lipscomb, Biochemistry, 44 (2005) 11024-11039

[17] M. Garai, D. Dey, H.R. Yadav, A.R. Choudhury, N. Kole, B. Biswas, Polyhedron, 129 (2017) 114-122.

[18] A. De, M. Garai, H.R. Yadav, A.R. Choudhury, B. Biswas, Appl. Organomet. Chem., 31 (2017) e3551.

[19] D. Dey, M. Garai, S. Arar, A. Almherat, A. Al-Hunaiti, H.R. Yadav, M. Maji, A.R. Choudhury, B. Biswas, J. Mol. Struct., 1180 (2019) 220-226.

[20] A. De, D. Dey, C.K. Pal, S. Paul, B. Biswas, J. Mol. Struct., 1195 (2019) 293-301.

[21] R. Mayilmurugan, M. Sankaralingam, E. Suresh. Palaniandavar, Dalton Trans., 39 (2010) 9610-9625.

[22] S. Pal, B. Chowdhury, M. Patra, M. Maji, B. Biswas, Spectrochim. Acta Part A: Mol. Biomol. Spect., 144 (2015) 148-154.

[23] D. Dey, S. Das, H.R. Yadav, A. Ranjani, L. Gyathri, S. Roy, P.S. Guin, D. Dhanasekaran, A.R. Choudhury, M.A. Akbarsha, B. Biswas, Polyhedron, 106 (2016) 106-114.

[24] A. Al-hunaiti, M. Räisänen, T. Repo, Chem. Commun., 52 (2016) 2043-2046.

[25] R. Rahaman, B. Chakraborty, T.K. Paine, Angew. Chem. Int. Ed., 55 (2016) 13838-13842.

[26] B. Biswas, A. Al-Hunaiti, M. T. Räisänen, S. Ansalone, M. Leskelä, T. Repo, Y.-T. Chen, H.-L. Tsai, A.D. Naik, A.P. Railliet, Y. Garcia, R. Ghosh, N. Kole, Eur. J. Inorg. Chem., (2012) 4479-4485.

[27] B. Biswas, M. Mitra, J. Adhikary, G.R. Krishna, P.P. Bag, C.M. Reddy, N. Aliaga-Alcalde, T. Chattopadhyay, D. Das R. Ghosh, Polyhedron, 53 (2013) 264-268.

[28] W.H. Armstrong, S.J. Lippard, Inorg. Chem., 24 (1985) 981-982.

[29] K.T.V. Rao, P.S.N. Rao, P. Nagaraju, P.S. Sai Prasad, N. Lingaiah, J. Mol. Catal. A Chem., 303 (2009) 84-89.

[30] Y. Hitomi, Y. Iwamoto, A. Kashida, M. Kodera, Chem. Commun., 51 (2015) 8702.

[31] A.W. Nichols, S. Chatterjee, M. Sabat, C. W. Machan, Inorg. Chem., 57 (2018) 2111-2121.

[32] E. Balaraman, A. Nandakumar, G. Jaiswalab, M. K. Sahoo, Catal. Sci. Technol., 7 (2017) 3177.

[33] A. Taheri, L.A. Berben, Inorg. Chem., 55 (2016) 378-385

[34] J.R. Khusnutdinova, D. Milstein, Angew. Chem., Int. Ed., 54 (2015) 12236-12273.

[35] O.R. Luca, R.H. Crabtree, Chem. Soc. Rev., 42 (2013) 1440-1459.

[36] M. Bourrez, F. Molton, S. Chardon-Noblat, A. Deronzier, Angew. Chem., 2011, 123 (42), 10077-10080.

[37] K.T. Ngo, M. McKinnon, B. Mahanti, R. Narayanan, D.C. Grills, M.Z. Ertem, J. Rochford, J. Am. Chem. Soc., 139 (2017) 2604-2618.

[38] B. Biswas, P. Raghavaiah, N. Aliaga-Alcalde, J.-D. Chen, R. Ghosh, Polyhedron, 29 (2010) 2716-2721

[39] B. Biswas, A. Pal, G.R. Krishna, C.M. Reddy, F. Tuna, R. Ghosh, Polyhedron, 30 (2011) 2032-2037

[40] D. Dey, A. De, S. Pal, P. Mitra, A. Ranjani, L. Gayathri, S. Chandraleka, D. Dhanasekaran, M. A. Akbarsha, N. Kole, B. Biswas, Indian J. Chem., Sect. A, 54A (2015) 170-178.

[41] D. Dey, A. Basu Roy, C.-Y. Shen, H.-L. Tsai, A. Ranjani, L. Gayathri, S. Chandraleka, D. Dhanasekaran, M.A. Akbarsha, N. Kole, B. Biswas, J. Chem. Sci, 127 (2015) 649-661.

[42] A.K. Boudalis, V. Tangoulis, C.P. Raptopoulou, A. Terzis, J.-P. Tuchagues, S.P. Perlepes, Inorg. Chim. Acta, 357 (2004) 1345-1354.

[43] M.W. Wemple, D.A.K. Coggin, J.B. Vincent, J.K. McCusker, W.E. Streib, J.C. Huffman, D.N. Hendrickson, G. Christou, J. Chem. Soc., Dalton Trans., (1998) 719-725.

[44] J.K. McCusker, J.B. Vincent, E.A. Schmitt, M.L. Mino, K. Shin, D.A.K. Coggin, P.M. Hagen, J.C. Huffman, G. Christou, D.N. Hendrickson. J. Am. Chem. Soc., 113 (1991) 3012-3021.

[45] G.M. Sheldrick, SHELXT - Integrated space-group and crystal-structure determination Acta Cryst. A71 (2015) 3-8.

[46] O.V. Dolomanov, L.J. Bourhis, R.J. Gildea, J.A.K. Howard, H. Puschmann, J. Appl. Cryst., 42 (2009) 339.

[47] L.J. Farrugia. J. Appl. Cryst., 45 (2012) 849.

[48] S. Das, A. Sahu, M. Joshi, S. Paul, M. Shit, A. Roy Choudhury, B. Biswas, ChemistrySelect, 3 (2018) 10774-10781.

[49] M. Garai, D. Dey, H.R. Yadav, A.R. Choudhury, M. Maji, B. Biswas, ChemistrySelect, 2 (2017) 11040-11047

[50] M. Garai, A. Das, M. Joshi, S. Paul, M. Shit, A.R. Choudhury, B. Biswas, Polyhedron, 156 (2018) 223-230.

[51] M. Garai, D. Dey, M. Maji, H.R. Yadav, A.R. Choudhury, B. Biswas, J. Chem. Sci., 129 (2017) 1513-1520.

[52] B. Biswas, M. Mitra, A. Pal, A. Basu, S. Rajalakshmi, P. Mitra, N. Aliaga-Alcalde, G.S. Kumar, B.U. Nair, R. Ghosh, Indian J. Chem., 52A (2013) 1576-1583.

[53] Y.P. Tian, C.Y. Duan, X.X. Xu, X.Z. You, Acta Crystallogr. C, 51 (1995) 2309-2312.

[54] H.H. Thorp, Inorg. Chem., 31 (1992) 1585-1588.

[55] M. Kodera, H. Shimakoshi, K. Kano, Chem. Commun., (1996) 1737.

[56] K. Visvaganesan, E. Suresh, M. Palaniandavar, Dalton Trans., (2009) 3814.

[57] W.H. Armstrong, A. Spool, G.C. Papaefthymiou, R.B. Frankel, S.J. Lippard, J. Am. Chem. Soc., 106 (1984) 3653.

[58] P. Gomez-Romero, N. Casan-Pastor, A. Ben-Hussein, G.B. Jameson, J. Am. Chem. Soc., 110 (1988) 1988.

[59] M. Sankaralingam, M. Palaniandavar, Polyhedron, 67 (2014) 171-180

[60] L. Que, Jr., Iron Carriers and Iron Proteins, T.M. Loehr, ed.VCH: New York, (1989) 467-524.

[61] E.L. Spence, M. Kawamukai, J. Sanvoisin, H. Braven, T.D.H. Bugg, J. Bacteriol. 178 (1996) 5249.

[62] S. Chatterjee, D. Sheet, T.K. Paine, Chem. Commun., 49 (2013) 10251-20253.

[63] T. Kurahashi, K. Oda, M. Sugimoto, T. Ogura, H. Fujii, Inorg. Chem. 45 (2006) 7709.

[64] M. Balamurugan, P. Vadivelu, M. Palaniandavar, Dalton Trans., 43 (2014) 14653-14668.

[65] M.J. Sever, J.J. Wilker, Dalton Trans., (2004) 1061-1072.

[66] T. Shiga, H. Miyamoto, G.N. Newton, H. Oshio, Dalton Trans., 47 (2018) 13402-13407.

[67] P.S. Guin, S. Das, P.C. Mandal, Int. J. Electrochem., (2011) Article ID 816202.

[68] S. Roy, P.S. Guin, J. Electrochem. Soc., 162 (2015) 124 -131.

[69] N. Dutta, S. Haldar, G. Vijaykumar, S. Paul, A.P. Chattopadhyay, L. Carrella, M. Bera, Inorg. Chem., 57 (2018) 10802-10820.

[70] A. Kantacha, R. Buchholz, S.J. Smith, G. Schenk, L.R. Gahan, J. Biol. Inorg. Chem., 16 (2011) 25-32.

[71] C. Pathak, M.K. Gangwar, P. Ghosh, Polyhedron, 145 (2018) 88-100.

[72] (a) P. Hendry, A.M. Sargeson, Inorg. Chem., 29 (1990) 92-7; (b) P. Hendry, A.M. Sargeson, Aust. J. Chem., 39 (1986) 1177.

[73] S. Benkovic, L. Dunikoski, J. Am. Chem. Soc., 93 (1971) 1526.

[74] Y. Murakami, J. Sunamoto, Bull. Chem. Soc. Japan, 44 (1971) 1827.

[75] T. Fife, M. Pujari, J. Am. Chem. Soc., 110 (1988) 7790-7797.

[76] F. Mancin, P. Scrimina, P. Tecilla, Chem. Commun., 48 (2012) 5545-5559.

[77] N.H. Williams, B. Takasaki, M. Wall, J. Chin, Acc. Chem. Res., 32 (1999) 485-493.

[78] Y. Ren, J. Lu, B. Cai, D. Shi, H. Jiang, J. Chen, D. Zheng, B. Liu, Dalton Trans., 40 (2011) 1372-1381.

Table 1 Crystallographic data and structure refinement parameters for the tetra-iron(III) cluster

Parameters	**1**
Empirical formula	$C_{36}H_{44}N_6O_{25}Fe_4$
Formula weight	1184.17
Temperature (K)	100
Crystal system	Monoclinic
Space group	*C*2/*c*
a (Å)	27.9634(14)
b (Å)	12.7441(6)
c (Å)	27.6727(13)
α, β, γ (º)	90, 104.878(5), 90
Volume (Å^3)	9531.1(8)
Z	8
ρ (g cm^{-3})	1.651
μ (mm^{-1})	1.287
F (000)	4848
θ ranges (º)	2.7-32.9
R_{int}	0.086
Number of unique reflections	16607
Total number of reflections	57573
Final R indices	0.0984, 0.2993
Largest peak and hole (e Å^{-3})	5.17, -1.53

Table 2. Kinetic parameters for the oxidation of DTBC catalyzed by the tetra-iron(III) cluster

Complex	**V_{max} (M s^{-1})**	**K_m (M)**	**k_{cat}(h^{-1})**	**Ref**
1	1.469×10^{-5}	2.10×10^{-4}	9.28×10^{2}	Present

Std. Error: V_{max} (M s^{-1}) = 5.35×10^{-7} ; K_m (M) = 1.55×10^{-5}

Table 3. Electrochemical data of the tetra-iron(III) complex in ACN

Compound	Ep,c (CV)(V)	Redox processes
Tetra-iron(III) cluster (**1**)	-1.36	$Fe_1(III) \rightarrow Fe_1(II)$
	-1.52	$Fe_2(III) \rightarrow Fe_2(II)$
Tetra-iron(III) cluster (**1**) in the presence of DTBC	-1.22	$O_2 \rightarrow O_2^{2-}$
	-1.35 (-1.35 in N_2)*	$Fe_1(III) \rightarrow Fe_1(II)$
	-1.51 (-1.7 in N_2)*	$Fe_2(III) \rightarrow Fe_2(II)$
	-0.314 (-0.123 in N_2)*	DTBSQ→DTBQ (semiquinone to quinone)
	+0.153 (-0.393 in N_2)*	H_2DTBC→DTBSQ (Cat to Semiquinone)

*CV value in parenthesis indicates the potential value obtained under an N_2 environment

Table 4. Kinetic parameters for the hydrolysis of the phosphoester linkage in PNPP catalyzed by the tetra-iron(III) cluster in aqueous methanol

Complex	V_{max} (M s^{-1})	K_m (M)	k_{cat} (S^{-1})	Ref
1	6.54×10^{-7}	8.30×10^{-5}	6.44×10^{-3}	Present
$[Fe_4(cpdp)_2(phth)_2(OH)_2]$	6.83×10^{-9}	4.80×10^{-3}	2.73×10^{-5}	26
$[Fe_4(cpdp)_2(terephth)_2(OH)_2]$	2.66×10^{-9}	4.08×10^{-3}	1.06×10^{-5}	26
$[Fe_4(HPBA)_2(\mu\text{-}OAc)_2(\mu\text{-}O)\text{-}(\mu\text{-}OH)(OH_2)_2]^{2+}$	-	-	1.6×10^{-3}	27

$\{[(Fe_2^{III}(\mu\text{-OAc}))]L\}^+$	-	-	2.94×10^{-3}	28

Std. Error: V_{max} ($M\ s^{-1}$) = 5.036×10^{-8}; K_m (M) = 3.634×10^{-6}

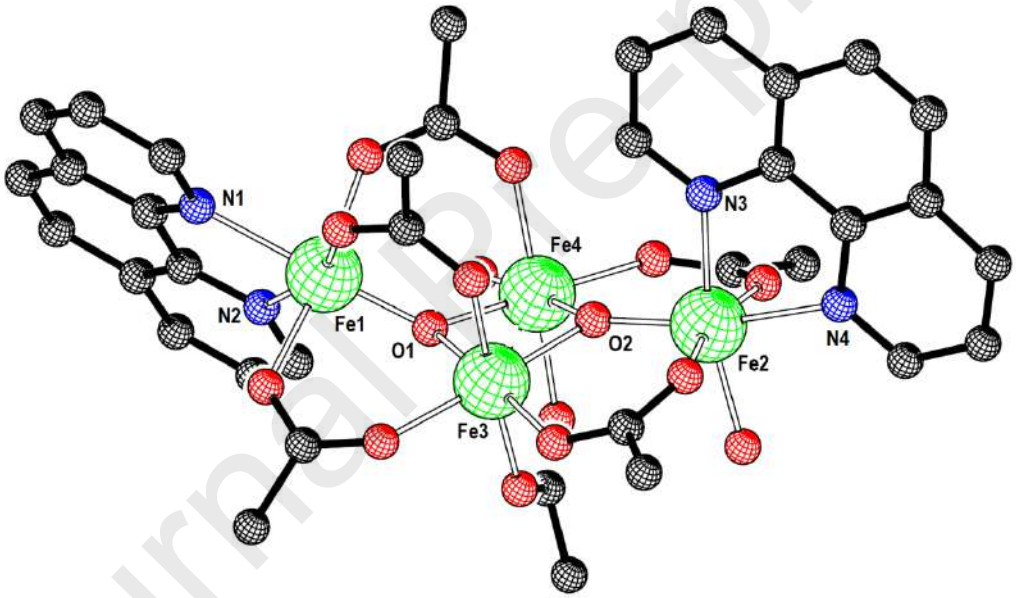

Fig. 1. X-ray

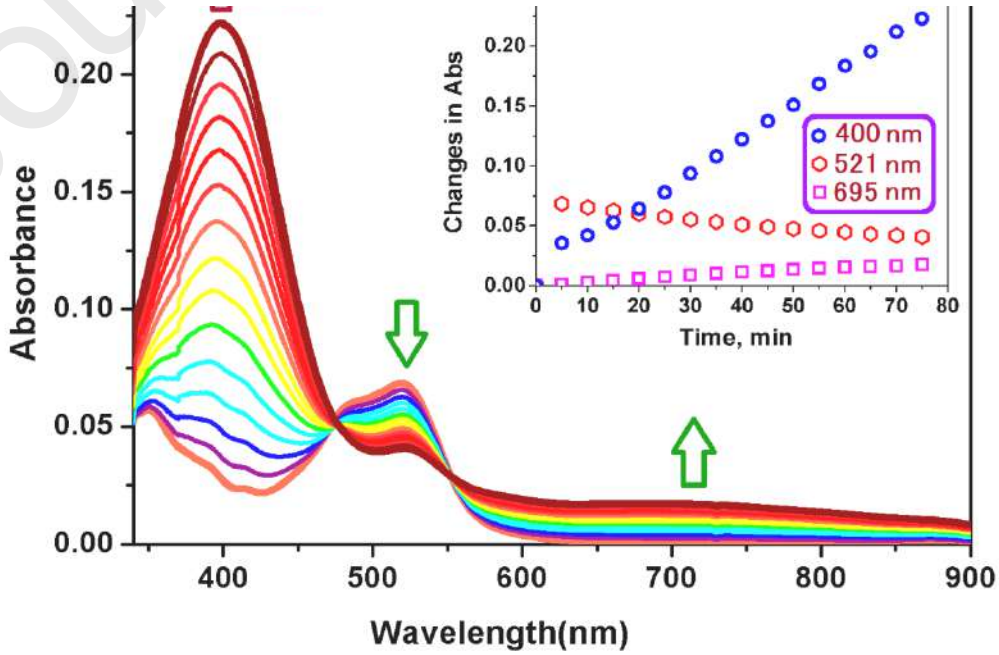

structure of the cationic tetra-iron(III) cluster (**1**) with 30% ellipsoid probability. H atoms are removed for clarity

Fig 2. Rise of the DTBQ band at 400 nm upon addition of **1** (10^{-4} M) to 100 equivalents of DTBC in acetonitrile. The spectra were recorded after every 5 min.

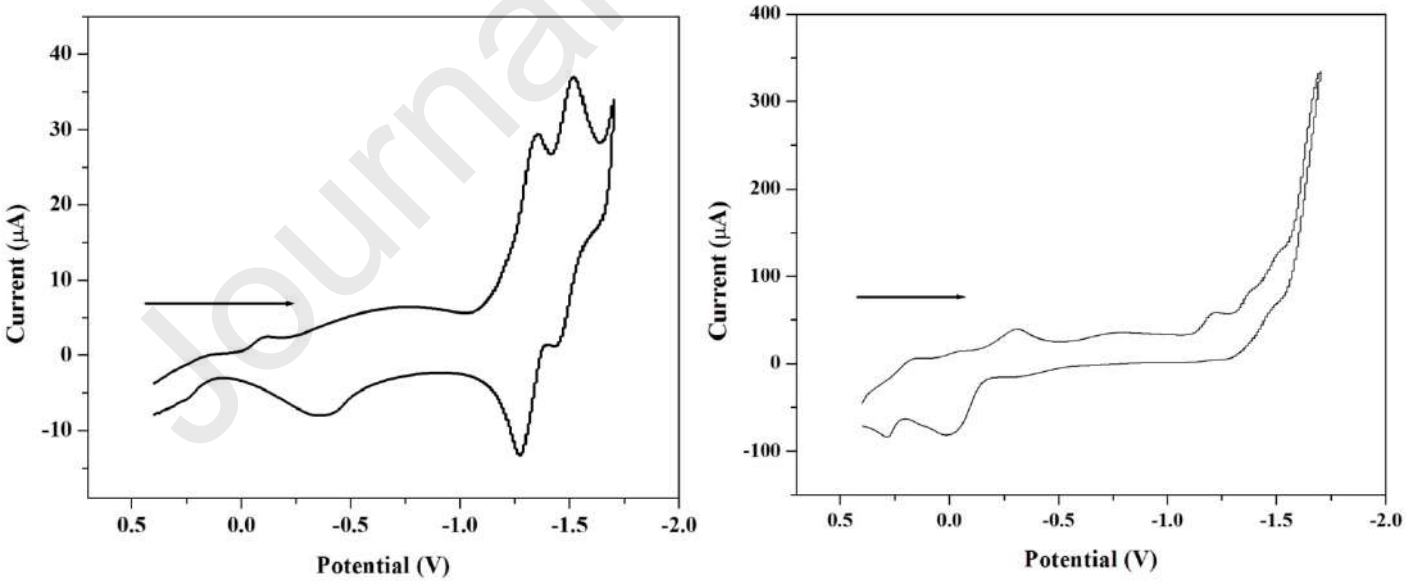

Fig 3. Left: Cyclic voltammogram of the tetra-iron(III) cluster in anhydrous acetonitrile media; **Right:** Cyclic voltammogram of the mixture of the tetra-iron(III) cluster and DTBC under a molecular oxygen atmosphere in anhydrous acetonitrile media.

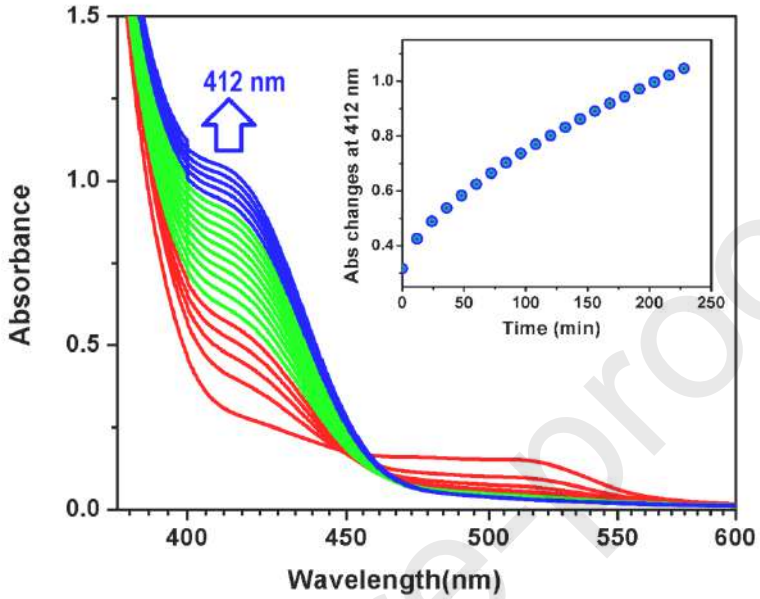

Fig 4. Increase of the 4-nitrophenolate band at 412 nm after addition of the tetra-iron(III) cluster to 100 equivalents of PNPP in aq. methanolic solution. (The spectra were recorded after every 12 min). Inset: Time vs Absorbance plot at the defined wavelength

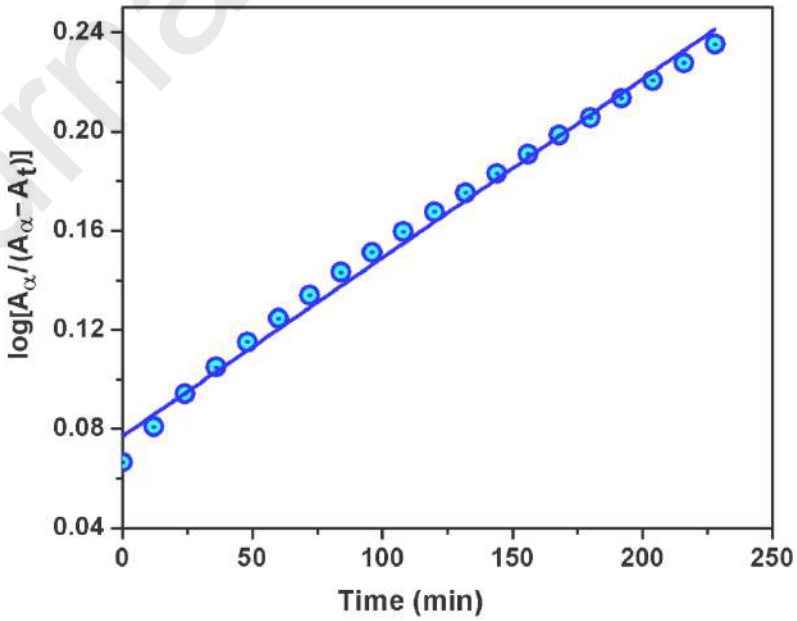

Fig 5. Initial rate determination for phosphoester cleavage activity by the tetra-iron(III) cluster towards PNPP using a plot of time vs $\log[A_\alpha/(A_\alpha-A_t)]$ for the same solution

Bio-mimetic of Catecholase and Phosphatase Activity by a Tetra-iron(III) Cluster

Chanchal Kumar Pal,[a] Shreya Mahato,[a] Hare Ram Yadav,[b] Madhusudan Shit, [c] Angshuman Roy Choudhury, [b] Bhaskar Biswas[a,*]

[a]*Department of Chemistry, University of North Bengal, Darjeeling-734013, India*
[b]*Department of Chemical Sciences, Indian Institute of Science Education and Research, Mohali, Sector 81, Knowledge City, S. A. S. Nagar, Manauli PO, Mohali, Punjab 140306, India*

[c]*Department of Chemistry, Dinabandhu Andrews College, Kolkata 700084, India*

This paper highlights the catalytic aspects of a tetra-iron(III) cluster, $[Fe_4^{III}(\mu\text{-}O)_2(\mu\text{-}OAc)_6(phen)_2(H_2O)_2](NO_3)_2.(H_2O)_3$ [phen = 1,10-phenanthroline], towards catechol oxidation and phosphoesterase activity, showing significant catalytic efficacy.

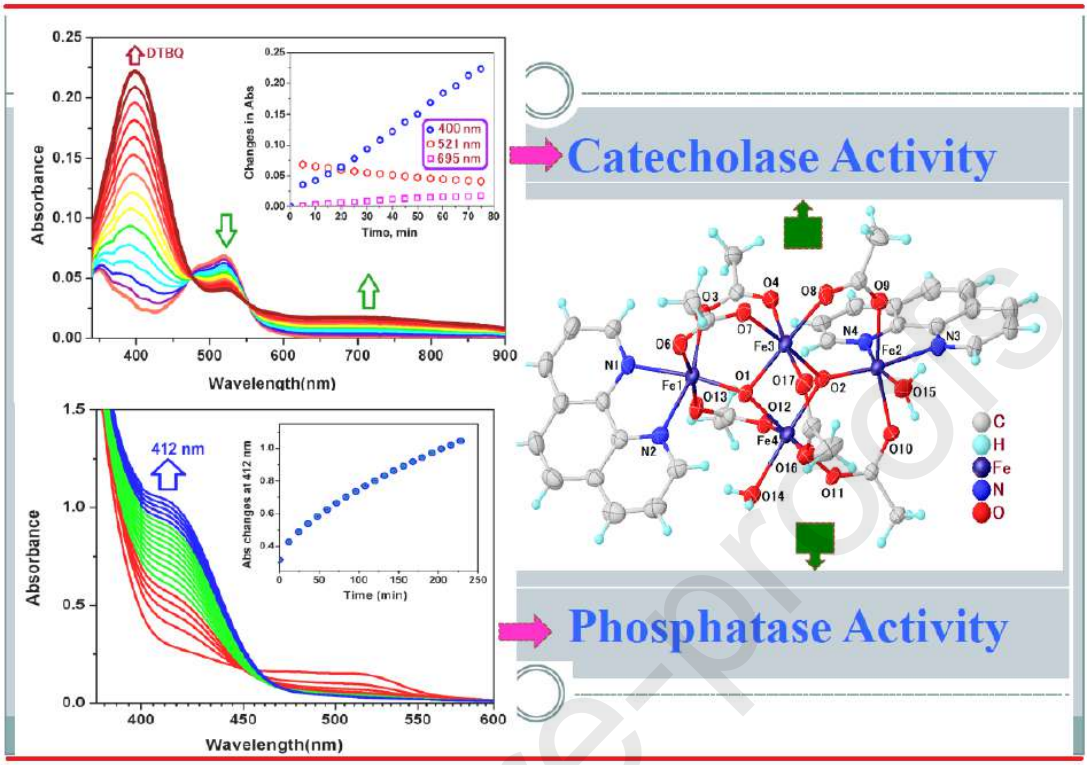

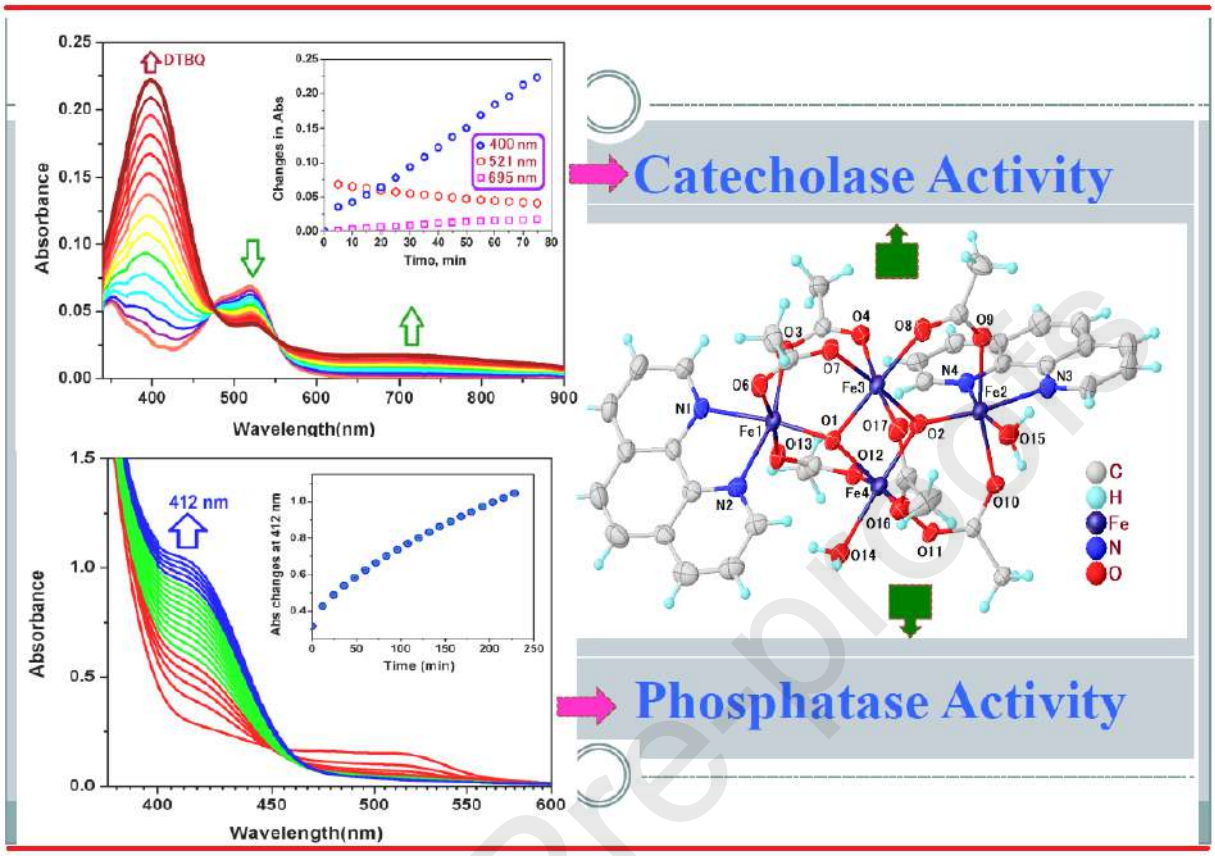

Source details

Feedback > Compare sources >

Polyhedron

Formerly known as: Journal of Inorganic and Nuclear Chemistry

Formerly known as: Inorganic and Nuclear Chemistry Letters

Scopus coverage years: from 1982 to Present

Publisher: Elsevier

ISSN: 0277-5387

Subject area: Chemistry: Inorganic Chemistry | Materials Science: Materials Chemistry | Chemistry: Physical and Theoretical Chemistry

Source type: Journal

View all documents > | Set document alert | Save to source list

CiteScore 2022
5.4

SJR 2022
0.400

SNIP 2022
0.635

CiteScore | CiteScore rank & trend | Scopus content coverage

J. Indian Chem. Soc.,
Vol. 97, June 2020, pp. 839-848

Synthesis, characterisation, DFT computation and DNA binding study of Ir(III)-dichloro bis[1-alkyl-2-(tolylazo)]imidazoles complexes

Dibakar Sardar*[a] and Chittaranjan Sinha[b]

[a]Department of Chemistry, Dinabandhu Andrews College, Garia, Kolkata-700 084, India

[b]Department of Chemistry, Jadavpur University, Kolkata-700 032, India

E-mail: dibakardac@gmail.com

Manuscript received online 18 January 2020, revised and accepted 07 May 2020

Ir(III) complexes of 1-alkyl-2-(tolylazo)imidazoles (TaiR, **1**; R = Me (**a**), Et (**b**), CH_2Ph (**c**)), $[Ir(TaiR)_2Cl_2](ClO_4)$ (**2**) have been synthesized. All the complexes have been characterized by elemental and spectral (IR, UV-Vis, Mass and ^1H NMR) analysis. The DNA binding property of the complexes has been studied by spectroscopic methods. Density functional theory (DFT) computation technique has been performed to interpret the electronic structures and spectral properties of the complexes.

Keywords: 1-Alkyl-2-(tolylazo)imidazoles, DFT calculation, DNA binding study, Ir(III) complex, synthesis and characterisation.

Introduction

The study of interaction of transition metal complexes with DNA has received much attention over the past few decades because of its subsequent utility in the field of cancer chemotherapy research[1–16]. DNA is the primary target of the synthetic anti-tumor complexes[17–19]. The interaction of metal complexes with DNA affects both replication and transcription of DNA which ultimately leads to the cell death[16]. After the discovery of anticancer activity of cisplatin, a large number of platinum metal complexes have been synthesized and used against different tumor cells[21–25]. Narrow range of activity, rapid development of drug resistance and nephrotoxicity of platinum complexes limit their widespread use[26,27] and enforce to explore safer complexes. Over the past few years, an intensive effort has been dedicated to develop metal-based drugs with improved clinical effectiveness, reduced toxicity and broader spectrum of activity[28–35]. Many of them are very promising, and have already reached for clinical trials[31,32].

We have been engaged for the last several years to synthesize arylazoheterocycles belong to azoimine function, -N=N-C=N-, and this is isoelectronic to diimine (-N=C-C=N-) function. The transition and nontransition metal coordination chemistry of this ligand is studied by us[36–43]. These ligands are pH-responsive, photochromic, redox active and exhibit photo-electron communication and non-linear optical property[41–43]. Recently we have become interested to study the DNA-binding property of metal complexes[44,45] and the present work is the continuation of that. In this article, the synthesis and the spectral characterization of iridium(III) complexes of 1-alkyl-2-(tolylazo)imidazoles are described. The DNA binding ability of complexes is established by absorption and fluorescence spectroscopic studies and the electronic properties are correlated with DFT calculation.

Experimental

Materials and physical measurements:

$IrCl_3.3H_2O$ was procured from Arora Matthey, India. The required solvents and $NaClO_4$ were purchased from E. Merck, India. The ligands, 1-alkyl-2-(tolylazo)imidazoles (TaiR, **1**) used in this work were prepared by reported procedure[46]. Chemicals used for syntheses were of analytical grade. Spectroscopic grade solvents obtained from Lancester, UK were utilized for spectral studies.

Caution! Perchorate salts are generally explosive. Although no detonation tendencies have been observed, care is advised and handling of only small quantities recommended.

Microanalyses (C, H, N) were carried out with Perkin-Elmer 2400 CHN elemental analyzer. Spectroscopic measurements were studied using the following instruments: UV-Vis spectra, Lambda 25 Perkin-Elmer; the IR spectra, Perkin-

Elmer L120-00A FTIR spectrophotometer (KBr disk); ^{1}H NMR spectra in $CDCl_3$, Bruker 300 MHz FT-NMR spectrometers in presence of TMS as internal standard.

Synthesis:

The following common procedure was used to synthesis all the complexes. Yield varied 60–70%.

*Synthesis of $[Ir(TaiMe)_2Cl_2](ClO_4)$ (**2a**):*

The mixture $IrCl_3.3H_2O$ (150 mg, 0.425 mmol) and 1-alkyl-2-(tolylazo)imidazoles (TaiMe) (175 mg, 0.85 mmol) in methanol was refluxed for 8 h under stirring condition and was allowed to cool to room temperature. Then addition of saturated aqueous solution of $NaClO_4$ afforded a brown precipitate. The product was filtered, washed with methanol and ether, and dried under vacuum. The dried product was dissolved in dichloromethane and was subjected to chromatographed. A brown band was eluted with acetonitrile-toluene (1:3, v/v). The evaporation of the solution afforded analytically pure product **2a**. Yield was 242 mg (61%).

Anal. Calcd. for $[Ir(TaiMe)_2Cl_2](ClO_4)$ (**2a**): C, 34.62; H, 3.15; N, 14.69. Found: C, 34.56; H, 3.19; N, 14.62%. TOF-MS: *m/z* 663.88 $(M\text{-}ClO_4^-)^+$, 628.5 $(M\text{-}ClO_4^-\text{-}Cl)$, 592 $(M\text{-}ClO_4^-\text{-}2Cl)$. IR (KBr disk): $\nu_{N=N}$, 1368 cm^{-1}; $\nu_{C=N}$, 1596 cm^{-1}; $\nu_{ClO_4^-}$, 1100 cm^{-1}; $\nu_{Ir\text{-}Cl}$, 319. UV (λ_{max}, nm (ε, M^{-1} cm^{-1}), CH_3CN): 500 (4340), 421 (15034), 415 (15007), 272 (9900), 264 (11024).

Anal. Calcd. for $[Ir(TaiEt)_2Cl_2](ClO_4)$ (**2b**): C, 36.43; H, 3.54; N, 14.17. Found: C, 36.52; H, 3.47; N, 14.11%. TOF-MS: *m/z* 690.86 $(M\text{-}ClO_4^-)^+$, 655.27 $(M\text{-}ClO_4^-\text{-}Cl)$. IR (KBr disk): $\nu_{N=N}$, 1361 cm^{-1}; $\nu_{C=N}$, 1597 cm^{-1}; $\nu_{ClO_4^-}$, 1101 cm^{-1}; $\nu_{Ir\text{-}Cl}$, 318. UV (λ_{max}, nm (ε, M^{-1} cm^{-1}), CH_3CN): 500 (5332), 421 (16368), 416 (16338), 272 (14084), 264 (15736).

Anal. Calcd. for $[Ir(TaiCH_2Ph)_2Cl_2](ClO_4)$ (**2c**): C, 44.61; H, 3.50; N, 12.25. Found: C, 44.55; H, 3.56; N, 12.17%. TOF-MS: *m/z* 816 $(M\text{-}ClO_4^-)^+$, 781 $(M\text{-}ClO_4^-\text{-}Cl)$, 745 $(M\text{-}ClO_4^-\text{-}2Cl)$. IR (KBr disk): $\nu_{N=N}$, 1362 cm^{-1}; $\nu_{C=N}$, 1584 cm^{-1}; $\nu_{ClO_4^-}$, 1100 cm^{-1}; $\nu_{Ir\text{-}Cl}$, 322. UV (λ_{max}, nm (ε, M^{-1} cm^{-1}), CH_3CN): 503 (6090), 408 (15764), 275 (10442), 267 (12174).

Computational methods:

All computations were performed using the Gaussian 09 program package[45]. The Becke's three-parameter hybrid exchange functional and the Lee-Yang-Parr nonlocal correlation functional (B3LYP) was used throughout this computation[48]. Elements except iridium were assigned a 6-31G basis set in our calculations. For iridium the Los Alamos effective core potential plus double zeta (LanL2DZ) basis set were employed[49]. The geometric structures of the ligand and the complexes in the ground state (S_0) were fully optimized at the B3LYP level. In all cases, vibrational frequencies were calculated to ensure that optimized geometries represented local minima. Using the respective optimized S_0 geometries we employed time dependent density functional theory (TD-DFT) at the B3LYP level to predict their absorptions characteristics[50].

DNA binding study:

Preparation of the complex solutions for DNA binding study:

The stock solutions of complexes (2 mM) were prerpared in acetone free methanol and diluted with Tris-HCl buffer to get required concentration before each set of experiments.

Preparation of calf thymus and pUC19 plasmid DNA:

The solution of calf thymus (CT) DNA (Bangalore Genei, India) was prepared in 5 mM Tris-HCl/50 mM NaCl buffer, pH 7.2 using deionised and sonicated HPLC grade water (Merck). The CT-DNA used in the experiments was sufficiently free from protein (UV absorption ratio A_{260nm}/A_{280nm} ~1.9). The DNA concentration was determined with the help of its extinction coefficient, ε of 6600 M^{-1} cm^{-1} at 260 nm. The DNA stock solution was stored at 4°C and used within 4 days after preparation.

Ethidium bromide (EB) stock solution preparation:

Ethidium bromide (EB) dust (Sigma-Aldrich, USA) was dissolved in double distilled water at a concentration of 1 mM. Stored stocks (at 4°C in dark) were diluted freshly before each experiment.

Absorption spectroscopic studies of the complexes in presence of CT-DNA:

Absorption spectroscopic studies were done on a spectrophotometer (Perkin-Elmer, Lambda-25). The interaction between the metal complexes and CT-DNA was observed by adding increasing concentrations of CT-DNA (2 μM to 20 μM) to a fixed concentration of complex (40 μM) and increasing concentrations of complex (2 μM to 20 μM) to fixed concentration of CT-DNA (100 μM). After each addition, the

DNA and complex mixtures were incubated at room temperature for 15 min and scanned from 290 nm to 700 nm. The self-absorption of DNA was eliminated in each set of experiments. Each sample was scanned for a cycle number of 2, cycle time of 5 s at a scan speed of 100 nm/min. Modified Benesi-Hildebrand[51] plot was used for the determination of ground state binding constant between the complexes and CT-DNA. The binding constant "*K*" was determined by using the following relation:

$$A_0/\Delta A = A_0/\Delta A_{max} + (A_0/\Delta A_{max})\times 1/K\times 1/L_t$$

where $\Delta A = A_0 - A$, ΔA_{max} = maximum change in reduced absorbance,

A_0 = maximum absorbance of receptor molecules (without any ligand),

A = reduced absorbances of the receptor molecules (in presence of ligand),

L_t = ligand concentration.

Fluorescence spectroscopic studies of the complexes with EB bound DNA:

Fluorescence spectroscopic studies of EB bound CT-DNA with varing concentrations of the complexes (0–100 μM) were done by using by LS 55 Perkin-Elmer spectrofluorimeter at room temperature (298 K). The EB bound CT-DNA was prepared freshly before each experiment by treating with 10^{-5} *M* DNA solution with 10^{-5} *M* of EB solution and it was incubated for 30 min.

The experiments was carried out with gradual addition of the complexes (10 μM) into EB bound DNA mixture, incubated for 15 min and the fluorescence spectra were taken. The excitation wavelength was 500 nm and the emission spectra were scanned from 510 nm to 750 nm, spectral response of 2 s, along with a scanning speed of 60 nm/min[52].

The study is based on the competitive binding of the complex to DNA by replacing EB from EB bound DNA and this is observed by the quenching of the fluorescence intensity. The fluorescence quenching of EB bound DNA is expressed by the Stern-Volmer equation[53,54]

$$I_0/I = 1 + K_{SV}[Q] = 1 + kq\tau_0[Q]$$

where I_0 and I are the fluorescence intensities of BSA in the absence and in the presence of the quencher (i.e. the metal complex), respectively, K_{SV} is the Stern-Volmer quenching constant, [Q] is the concentration of the quencher, kq is the quenching rate constant of the biomolecule and τ_0 is the average lifetime of the molecule in the absence of the quencher. A linear I_0/I vs [Q] plot indicates that a single type of quenching mechanism is involved, either static or dynamic, while a deviation from linearity suggests a mixed quenching mechanism[55].

Results and discussion

Synthesis and formulation:

1-Alkyl-2-(tolylazo)imidazoles (TaiR, **1**; R = Me (**a**) (Scheme 1: TaiR, **1**; R = CH_3 (**a**), CH_2-CH_3 (**b**), CH_2Ph (**c**)) are N,N′-bidentate chelator where N and N′ refer to N(imidazole) and N(azo) donor centers respectively. The ligand, TaiR reacts with $IrCl_3.3H_2O$ in 2:1 mole ratio in methanol under refluxing condition to result a red colour solution which upon treatment with a saturated aqueous solution of $NaClO_4$ isolates a brown precipitate of $[Ir(TaiR)_2Cl_2]ClO_4$ (**2**). The composition has been supported by elemental analysis and FAB mass data. The conductance of the complexes in acetonitrile (Λ_M, 115–125 Ω^{-1} cm^2 mol^{-1}) proposes 1:1 electrolyte nature for them. $[Ir(TaiR)_2Cl_2]^+$ can exist in five isomeric forms out of them three are *cis*-MCl_2 (I-III, Scheme 1) and two are *trans*-$IrCl_2$ (IV and V, Scheme 1) configuration (Scheme 1). Because of unavailability of good quality crystals of **2** the spectral (UV-Vis, IR and ^{1}H NMR, Mass) techniques have been used to characterize the structure of the compounds. The spectral characterization shows that the configuration of the isolated complex **2** is *cis-cis-trans* (*cct*) fashion with respect to N(imidazole), N(azo) and Cl respectively.

Spectral characterization:

The FT-IR spectra of the complexes have been studied in KBr disc. The azo ($\nu_{N=N}$) and imine ($\nu_{C=N}$) stretching frequencies of the complexes are significantly shifted to lower frequencies compared to free ligand values and appear at 1361–1368 cm^{-1} and 1584–1597 cm^{-1} respectively[46]. The lowering of these frequencies establishes the coordination of ligand to the metal centre through azo (-N=N-) and imine (-C=N-) nitrogens. The IR spectra of the complexes also show one $\nu_{Ir\text{-}Cl}$ stretch at 318–322 cm^{-1} (Supplementary Material, Fig. S1). This fact implies that two Ir-Cl bonds are similar and proposes the *trans*-MCl_2 type configuration for the complexes. The presence of ClO_4^- as a counter ion is observed

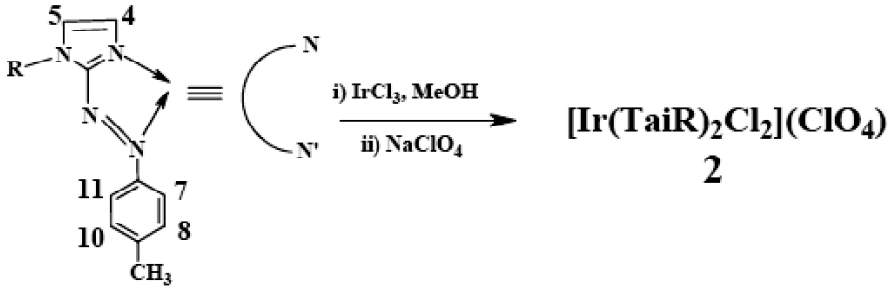

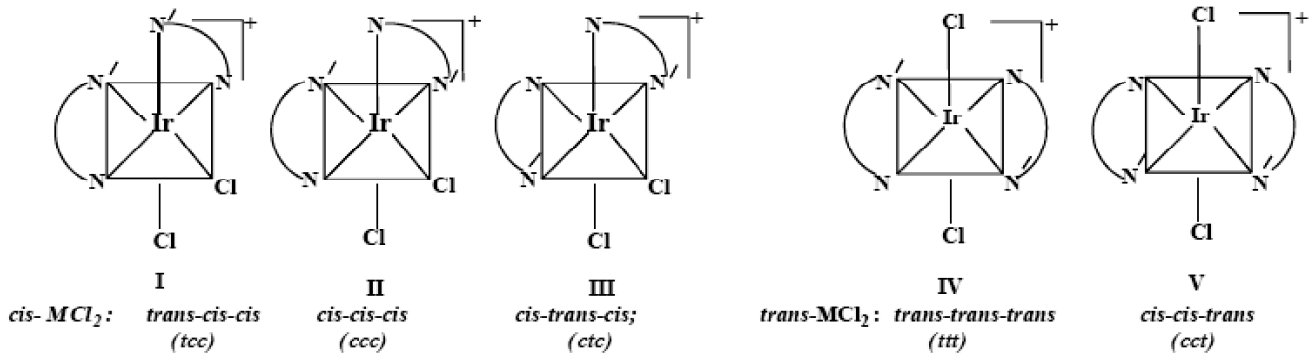

Scheme 1. The ligands and the complexes.

at 1100 cm^{-1} along with a comparatively weak band at 625 cm^{-1}.

The mass fragmentations by ESI-MS (QTOF) of the complexes show expected fragmentation pattern. The spectra of the complexes recorded $(M\text{-}ClO_4^-)^+$ ion peak as base peak at (Supplementary Material, Fig. S2) *m/z* 664.88 for **2a**, 690.86 for **2b** and 816.12 for **2c**.

The ^1H NMR spectra of the complexes in $CDCl_3$ recorded the downfield shifting of proton signals compared to free ligand data[46] which may be the outcome of the electron withdrawing effect of the coordinated iridium(III) (Table 1). The imidazole proton, 4-H suffers maximum downfield shifting by 0.5–0.6 ppm and appear as a broad singlet at ~7.6–7.8 ppm while 5-H suffers downfield shifting by 0.2–0.3 ppm and appear at 7.26 ppm. These observations support the coordination of imine-N to the metal centre. The ^1H NMR spectra also recorded the appearance of every different type of protons of both the coordinated ligands of a complex at a same δ value. For example, the N(1)-CH_3 protons of **2a** appear as singlet at 4.06 ppm and N(1)-CH_2- protons of **2b** and **2c** appear as quartets at 4.52 ppm and 5.7 ppm respectively (Table 1 and Supplemetary Material, Fig. S3). This fact strongly indicates that the two coordinated ligands of the each complex are equivalent. Therefore, the expected geometry of isolated isomer should be *cis-cis-trans* (*cct*) with respect to N(imidazole), N(azo) and Cl respectively[56–58].

Table 1. ^1H NMR spectral data of Ir(III)-TaiR complexes in $CDCl_3$ at 300 K

Compd.	δ (ppm) (*J* (Hz))								
	4-H[a]	5-H[a]	7, 11-H[b]	8,10-H[b]	9-R[c]	1- CH_3[c]	1-CH_2	(1-CH_2)CH_3[d]	Ph-H
Ir-TaiMe	7.59	7.26	7.83(7.2)	7.34(7.0)	2.43	4.06			
Ir-TaiEt	7.63	7.26	7.89(7.2)	7.36(7.2)	2.47	4.52[e](7.5)	1.53(7.0)		
Ir-TaiBz	7.75	7.26	7.91(7.4)	7.39(7.2)	2.51		5.7[c]		7.26–7.61

[a]Broad singlet, [b]doublet [c]singlet, [d]triplet, [e]quartet.

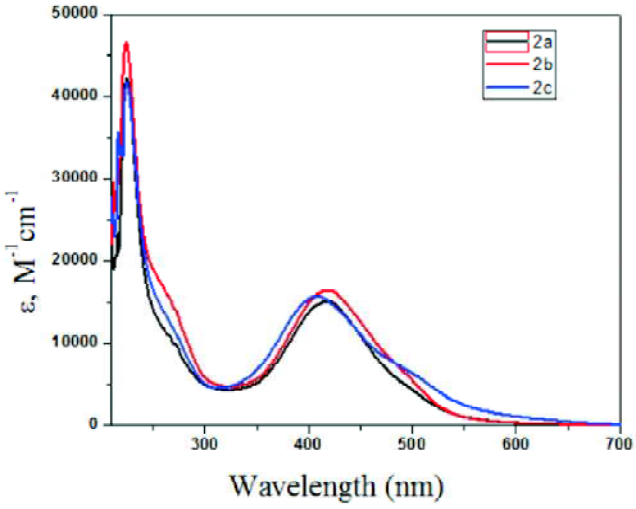

Fig. 1. UV-Visible spectra of the complexes (**2a, 2b and 2c**) in acetonitrile.

The absorption spectra of the complexes in acetonitrile solution (Fig. 1) shows one high intense transitions (ε ~10^4 M^{-1} cm^{-1}) at ~420 nm along with a weak at 500 nm (ε ~10^3 M^{-1} cm^{-1}) in the visible region and two moderately intense transitions (ε ~103 M^{-1} cm^{-1}) within 265–275 nm in the UV region. The high energy transitions (< 400 nm) region may be assigned ligand centred transitions and those in the visible region (> 400 nm) may be regarded as metal-to-ligand charge transfer transitions as these are not present in free ligands. These assignments of absorption bands are further discussed by TDDFT calculations.

DFT calculation and electronic structure:

As we have failed to determine the single crystal structure, a theoretical structure of **2b** has been optimized in gas phase to get information about the structural parameters. The optimized structure is shown in Fig. 2 and the figure showing that iridium(III) is surrounded by two Cl (*trans* to each other) and four N (two azo-N and two imine-N from two coordinated ligands) forming a distorted-octahedral coordination

Table 2. Selected bond lengths (Å) and angles (°) for the $[Ir(TaiEt)_2Cl_2]ClO_4$ (**2b**) (from DFT calculation)

Bond length (Å)	Theoretical value	Bond angle (°)	Theoretical value
Ir(55)-N(1)	2.049	N(1)-Ir(55)-N(9)	76.10083
Ir(55)-N(16)	2.049	N(16)-Ir(55)-N(27)	76.10097
Ir(55)-N(9)	2.099	N(1)-Ir(55)-N(27)	176.20552
Ir(55)-N(27)	2.099	N(16)-Ir(65)-N(9)	176.20463
Ir(55)-Cl(22)	2.421	N(1)-Ir(55)-N(16)	101.75566
Ir(55)-Cl(23)	2.421	N(16)-Ir(65)-N(9)	106.21215
N(3)-N(9)	1.283	Cl(22)-Ir(55)-Cl(23)	176.84603
N(26)-N(27)	1.283		

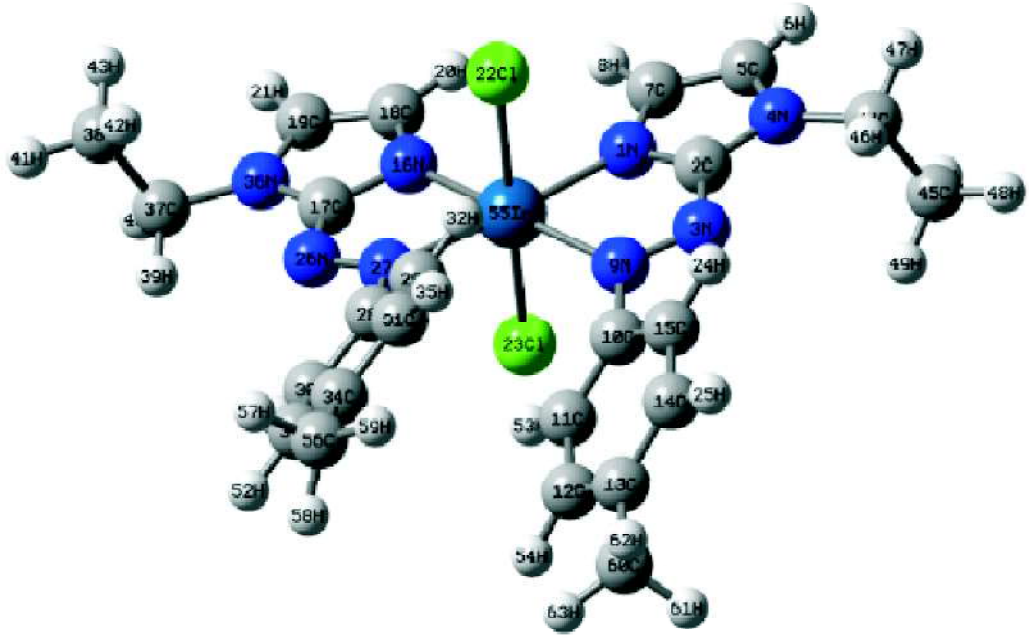

Fig. 2. Optimised structure of $[Ir(TaiEt)_2Cl_2]ClO_4$ (**2b**).

environment. The relevant bond parameters are given in Table 2. These theoretical bond parameters show good agreement with the reported values[44,59].

The energy and the composition of some selected molecular orbitals are given in the Supplementary Material, Table S1 and surface plots of some frontier orbitals are shown in Fig. 3.

The energies of HOMO and LUMO are –8.65 eV and –6.07 eV respectively. The highest occupied molecular orbital, HOMO is composed of 41% ligand, 31% Cl and 28% metal. The occupied frontier orbitals H-1, H-3, H-4 and H-5 are mainly constituted (65–95%) with ligand pπ orbitals while in case of H-2, 68% contribution come from Cl and 25% contribution metal d-orbitals. The LUMO and L+1 are mostly delocalized on ligand π* orbitals (95%, and 91% respectively). The LUMO+2 is constituted by metal (Ir, 50%) and Cl (39%) while LUMO+3 is carrying 52% metal and 39% Cl contribution.

To gain an insight about the nature of electronic transitions and to explain the electronic spectra, the TD-DFT calculations were performed. The experimental spectrum of **2a** correlates well with the theoretical spectrum (Supplementary Material, Fig. S4). The experimental spectrum shows a transition at 501 nm which appears at 510 in theoretical spectrum is mainly due to the transitions HOMO-1→LUMO and can be regarded as admixture of intraligand charge transfer

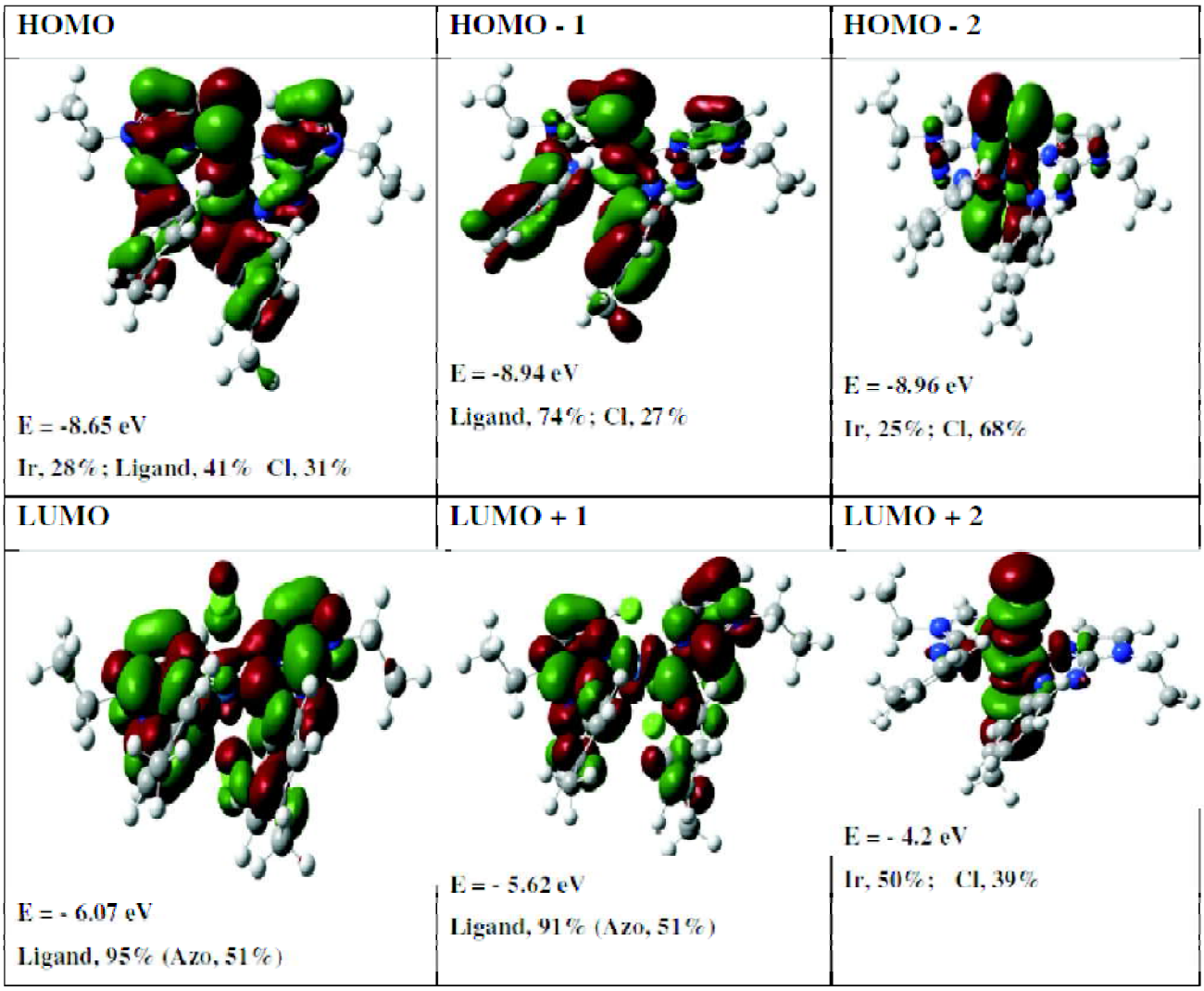

Fig. 3. Surface plots of some frontier orbitals of $[Ir(TaiEt)_2Cl_2]ClO_4$ (**2b**).

transition, ILCT [Im, Ph→Azo] and chloride-to-ligand, (XLCT: Cl →Azo, Im) and metal-to ligand (MLCT: Ir→Azo) charge transfer transitions (Supplementary Material, Table S2). The transition in the experimental spectrum of **2b** at ~420 nm is result of the transitions HOMO-3, HOMO-6→LUMO+1 and is assigned to the transition mainly originated from ILCT [Im, Ph→Azo]. The other transitions at shorter wavelengths are mixture of ILCT [Im, Ph→Azo], XLCT [Cl →Azo, Im], MLCT [Ir→Azo] transitions.

Interaction of complexes with DNA:

Absorption spectroscopic studies of the complexes in presence of CT-DNA:

The study of interaction of the complexes with CT-DNA was observed by recording the changes in UV-Vis absorption spectra. Any change in absorption spectra due to the mixing of DNA and complexes is the one of indication of interaction between them[60]. Upon addition of increasing concentrations of complexes to 100 μM CT-DNA (100 μM), the absorption of DNA at 260 nm was decreasing successively and while the addition of increasing concentrations of CT-DNA to fixed concentration of complexes recorded a steady decrease in absorption with a slight red shift (Fig. 4 and Supplementary Material, Figs. S5-6). Such changes in absorbance indicate the specific interaction between the DNA and the complex molecules. In order to compare the binding ability of the complexes, we have calculated the ground state binding constant (K_b) between the complexes and DNA at the absorption maximum of DNA by using modified Benesi-Hildebrand (BH) plot (Fig. 4 and Supplementary Material, Figs. S5-6). The calculated binding constants are 7.8×10^4 M^{-1} (**2a**), 5.296×10^4 (**2b**), and 3.44×10^5 (**2c**). These observed values reveal a decreasing tendency of the binding constant with the increasing size of the complexes which may be due to the better interchalating ability of the smaller positive ions into the adjacent base pairs of DNA. Thus the complex **2a** binds strongly with CT-DNA than the other complexes.

Fluorescence spectroscopic studies of the complexes with ethidium bromide (EB) bound DNA:

To further verify the interaction of the complexes with DNA, we studied the ability of the complexes to displace ethidium bromide (EB) from EB bound DNA by fluorescence quenching method. Either DNA or EB do not have fluorescence property alone but being a fluorescence probe, EB emits intense fluorescent light in presence of DNA due to its strong intercalation between adjacent base pairs. The studies showed that the gradual addition of complexes to EB bound DNA solution caused quenching in fluorescence intensity. The fluorescence quenching of EB bound DNA upon gradual addition of complexes follow the classic linear Stern-Volmer equation (Fig. 5 and Supplementary Material, Figs. S7-8). The Stern-Volmer quenching constants (K_{sv}) obtained from the slope of the plot [*Q*] vs I_0/I are 1.2935×10^4 M^{-1} (**2a**), 1.1×10^4 M^{-1} (**2b**) and 4.086×10^3 M^{-1} (**2c**). These values indicate the strong interaction of the complexes with the DNA[60,61]. The

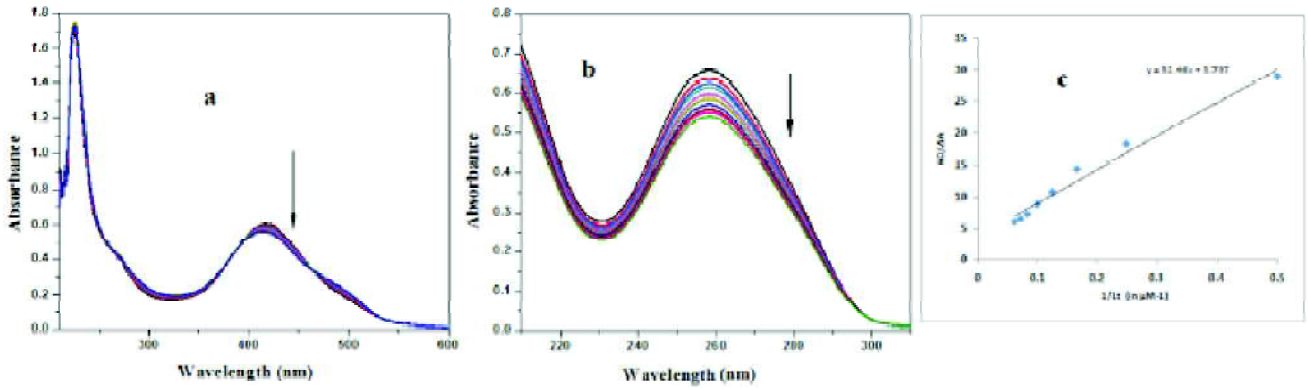

Fig. 4. (a) Absorption spectroscopic study of 40 μM complex **2a** with increasing concentrations of CT-DNA (0, 1, 2, 4, 6, 8, 10, 12, 14, 16, 18 and 20 μM) respectively; (b) absorption spectroscopic study of CT-DNA (100 μM) with increasing concentrations of complex **2a** (0, 2, 4, 6, 8, 10, 12, 14, 16, 18 and 20 μM) respectively; (c) modified Benesi-Hildebrand plot for the determination of ground state binding constant between CT-DNA and rhodium complex **2a**.

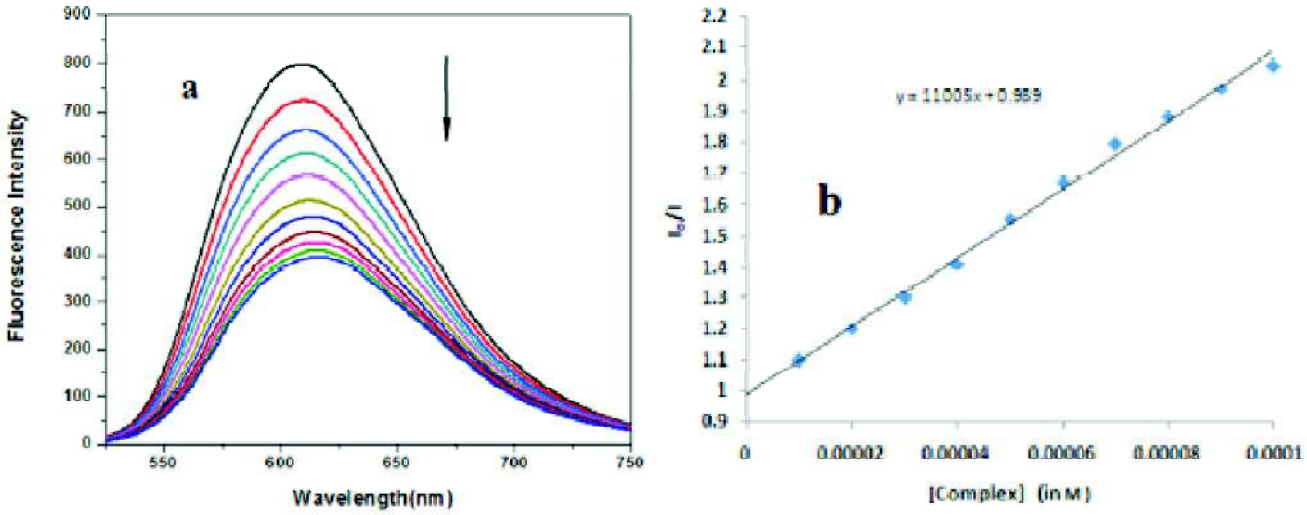

Fig. 5. (a) Fluorescence spectroscopic study of EB bound DNA with increasing concentrations of complex **2b** (0, 10, 20, 30 40, 50, 60, 70, 80, 90 and 100 μM) respectively; (b) Stern-Volmer plot for complex **2b**.

apparent binding constant (K_{app}) was also calculated from the equation K_{EB}[EB] = K_{app}[complex], where K_{EB} = 1.0×10^7 M^{-1}, [EB] = 50 μM; and [complex] is the concentration that causes a 50% quenching of the initial EB fluorescence[62]. The K_{app} values of the complexes are 6.4035×10^5 M^{-1} (**2a**), 5.4426×10^5 M^{-1} (**2b**) and 2.11×10^5 M^{-1} (**2c**) which also suggest the strong interaction between DNA and complex molecules[60–62].

Conclusion

The Ir(III) complexes of 1-alkyl-2-(tolylazo)imidazoles have been synthesized and characterized by elemental and spectroscopic techniques. The spectral characterization suggest octahedral geometry for the Ir(III) complexes with *cis-cis-trans* (*cct*) configuration respect to N(imidazole), N(azo) and Cl respectively. Density functional theory (DFT) study interprets the electronic structures and their spectral properties. The DNA binding study by absorption and fluorescence spectroscopic methods show the DNA binding ability of the complexes. The complex **2a** binds most strongly while the least binding ability was observed in case of complex **2c**.

Supplemetary material

Supplemetary Material includes the energy and composition of the selected frontier molecular orbitals calculated by DFT, electronic transition data from TD-DFT calculation, ^{1}H NMR and IR spectra, and some figures regarding DNA binding study.

Acknowledgements

Financial support from University Grant Commission (Reference No. F.: PSW-044/14-15 (ERO)) New Delhi is gratefully acknowledged.

References

1. J. K. Barton and A. L. Raphael, *J. Am. Chem. Soc.,* 1984, **106**, 2466.
2. H. Y. Mei and J. K. Barton, *Proc. Natl. Acad. Sci. USA*, 1988, **85**, 1339.
3. V. W.-W. Yam, K. K.-W. Lo, K.-K. Cheung and R. Y.-C. Kong, *J. Chem. Soc., Dalton Trans.*, 1997, 2067.
4. M. Komiyama and J. Sumaoka, *Curr. Opin. Chem. Biol*., 1998, **2**, 751.
5. A. Sreedhara and J. A. Cowan, *J. Biol. Inorg. Chem*., 2001, **6**, 337.
6. J. A. Cowan, *Curr. Opin. Chem. Biol*., 2001, **5**, 634.
7. I. Kostova, *Curr. Med. Chem.,* 2006, **13(4)**, 1085.
8. R. W. –Y. Sun, D.-L. Ma, E. L.-M. Wong and C.-M. Che, *Dalton Trans.,* 2007, **43**, 4884.
9. E. Meggers, *Chem. Commun*., 2009, **9**, 1001.
10. N. Chavain and C. *Biot, Curr. Med. Chem*., 2010, **17**, 2729.
11. G. Gasser, I. Ott and N. Metzler-Nolte, *J. Med. Chem*., 2010, **54**, 3.
12. C. G Hartinger, A. D Phillips and A. A Nazarov, *Curr. Top.*

Med. Chem., 2011, **11**, 2688.

13. F. Ahmadi, M. Saberkari, R. Abiri, H. M. Motlagh and H. Saberkari, *Appl. Biochem. Biotech.*, 2013, **170(4)**, 988.
14. D.-L. Ma, D. S.-H. Chan and C.-H. Leung, *Acc. Chem. Res.*, 2014, **47**, 3614.
15. J. Nagaj, P. KoBkowska, A. Bykowska, U. K. Komarnicka, A. KyzioB and M. Je|owska-Bojczuk, *Med. Chem. Res.,* 2015, **24(1)**, 115.
16. M. Heydari, M. E. Moghadam, A. Tarlani and H. Farhangian, *Appl. Biochem. Biotech.,* 2017, **182(1)**, 110.
17. B. K. Keppler (Ed.), "Metal Complexes in Cancer Chemotherapy", VCH, Weinheim, 1993.
18. M. J. Clarke, F. Zhu and D. R. Frasca, *Chem. Rev.*, 1999, **99**, 2511.
19. E. D. A. Stemp and J. K. Barton, *Metal Ions Biol. Syst.*, 1996, **33**, 325.
20. T. C. Johnstone, K. Suntharalingam and S. J. Lippard, *Chem. Rev.,* 2016, **116(5)**, 3436.
21. L. D. Dale, J. H. Tocher, T. M. Dyson, D. I. Edwards and D. A. Tocher, *Anti-cancer Drug Des.*, 1992, **7**, 3.
22. J. Suh, *Acc. Chem. Res.*, 2003, **33**, 562.
23. W. H. Ang, S. Pilet, R. Scopelliti, F. Bussy, L. Juillerat-Jeanneret and P. J. Dyson, *J. Med. Chem.*, 2005, **48**, 8060.
24. H. M. Pineto and J. H. Schornagel, "Platinum and Other Metal Coordination Compounds in Cancer Chemotherapy", Plenum, New York, 1996.
25. M. A. Fuertes, C. Alonso and J. M. Perez, *Chem. Rev.*, 2003, **103**, 645.
26. V. Cepeda, M. A. Fuertes, J. Castilla, C. Alonso, C. Quevedo and J. M. Perez, *Anti-Cancer Agents Med. Chem.*, 2007, **7**, 3.
27. G. Giaccone, R. S. Herbst, C. Manegold, G. Scagliotti, R. Rosell and V. J. Miller, *Clin. Oncol.*, 2004, **22**, 777.
28. A. Dorcier, W. H. Ang, S. Bolaño, L. Gonsalvi, L. Juillerat-Jeannerat, G. Laurenczy, M. Peruzzini, A. D. Phillips, F. Zanobini and P. J. Dyson, *Organometallics*, 2006, **25**, 4090.
29. C. B. Spillane, J. L. Morgan, N. C. Fletcher, J. G. Collins and F. R. Keene, *Dalton Trans.*, 2006, 3122.
30. P. U. Maheswari, V. Rajendiran, H. Stoeckli-Evans and M. Palaniandavar, *Inorg. Chem.*, 2006, **45**, 37.
31. G. H. Christian, A. J. Michael, S. Z.-Seifried, M. Groessl, A. Egger, W. Berger, H. Zorbas, J. D. Paul and K. K. Bernhard, *Chem. Biodivers.*, 2008, **5(10)**, 2140.
32. I. Bratsos, S. Jedner, T. Gianferrara and E. Alessio, *Chimia Int. J. Chem.*, 2007, **61**, 692.
33. S. J. Lucas, R. M. Lord, R. L. Wilson, R. M. Phillips, V. Sridharan and P. C. McGowan, *Dalton Trans.*, 2012, **41**, 13800.
34. N. Cutillas, G. S. Yellol, C. de Haro, C. Vicente, V. Rodríguez and J. Ruiz, *Coord. Chem. Rev.*, 2013, **257**, 2784.
35. R.-R. Ye, J.-J. Cao, C.-P. Tan, L.-N. Ji and Z.-W. Mao, *Chem. Eur. J.*, 2017, **23**, 15166.
36. B. K. Ghosh and A. Chakravorty, *Coord. Chem. Rev.*, 1989, **95**, 239.
37. N. Bag, A. Pramanik, G. K. Lahiri and A. Chakravorty, *Inorg. Chem.*, 1992, **31**, 40.
38. T. K. Misra, D. Das. C. Sinha, P. Ghosh and C. K. Pal. *Inorg. Chem.*, 1998, **37**, 1672.
39. P. Byabartta, Sk. Jasimuddin, B. K. Ghosh, C. Sinha, A. M. Z. Slawin and J. D. Woollins, *New J. Chem.*, 2006, **26**, 1415.
40. P. Byabartta, J. Dhinda, P. K. Santra, C. Sinha, K. F. Panneerselvam, -L. Liao and T.-H. Lu, *J. Chem. Soc., Dalton Trans.*, **2001**, 2825.
41. Q. W. Pan, Z. Y. Zhang, C. H. Fang, W. Shi, Q. T. Gu and X. W. Wu, *Mater. Lett.*, 2001, **50**, 284.
42. E. C. Constable and P. J. Steel, *Coord. Chem. Rev.*, 1989, **93**, 205.
43. T. Yamamoto, Z.-h. Zhou, T. Kanbara, M. Shimura, K. Kizu, T. Maruyama, Y. Nakamura, T. Fukuda, B.-L. Lee, N. Ooba, S. Tomaru, T. Kurihera, T. Kaino, K. Kubota and S. J. Sasaki, *J. Am. Chem. Soc.*, 1996, **118**, 10389.
44. D. Sardar, P. Datta, S. Das, B. Saha, S. Samanta, D. Bhattacharya, P. Karmakar, C.-D. Chen, C.-J. Chen and C. Sinha, *Inorg. Chemica Acta*, 2013, **394**, 98.
45. P. Dutta, S. Mondal, S. Roy, E. L.-Torres and C. Sinha, *Polyhedron*, 2015, **89**, 203.
46. D. Banerjee, U. Ray, SK. Jasimuddin, J.-C. Liou, T.-H. Lu and C. Sinha, *Polyhedron,* 2006, **25**, 1299.
47. H. B. Schlegel *et al.*, Gaussian 09, Revision A.02, Gaussian, Inc., Wallingford CT, 2009.
48. C. Lee, W. Yang and R. G. Parr, *Phys. Rev. B,* 1988, **37**, 785.
49. P. J. Hay and W. R. Wadt, *J. Chem. Phys.*, 1985, **82**, 270
50. EMSL, basis set library available http:/www.emsl.pnl.gov/forms/basisform.html.
51. H. A. Benesi and J. H. Hildebrand, *J. Am. Chem. Soc.*, 1949, **71**, 2703.
52. C. Lee, C. W. Yang and R. G. Parr, *Phys. Rev. B*, 1988, **37**, 785.
53. J. R. Lakowicz, "Principles of Fluorescence Spectroscopy", 2nd ed., Kluwer Academic/Plenum Publishers, New York, 1999.
54. B. Valeur, "Molecular Fluorescence, Principles and Applications", Wiley, Weinheim, 2001.
55. M. R. Eftink and C. A. Ghiron, *Anal. Biochem.*, 1981, **114**, 199.
56. S. Mondal, S. P. Rath, S. Dutta and A. Chakravorty, *J. Chem. Soc., Dalton Trans.*, 1996, 99.

57. M. Panda, C. Das, G.-H. Lee, S.-M. Peng and S. Goswami, *J. Chem. Soc., Dalton Trans*., 2004, 26.

58. D. Sardar, P. Datta, R. Saha, P. Raghavaiah and C. Sinha, *Polyhedron*, 2019, **171**, 542.

59. D. Sardar, P. Datta, P. Mitra and C. Sinha, *Polyhedron*, 2010, **29**, 3170.

60. S. Mathur and S. Tabassum, *Biometals*, 2008, **21**, 299.

61. J. L. García-Giménez, M. González-Álvarez, M. Liu-González, B. Macías, J. Borrás and G. Alzuet, *J. Inorg. Biochem.*, 2009, **103**, 923.

62. X. Sheng, X. Guo, X.-M. Lu, G. Y Lu, Y. Shao, F. Liu and Q. Xu, *Bioconjugate Chem*., 2008, **19**, 490.

Source details

Feedback > Compare sources >

Journal of the Indian Chemical Society

Scopus coverage years: from 1973 to 1985, from 1987 to 1991, from 1996 to Present

Publisher: Elsevier

ISSN: 0019-4522

Subject area: Pharmacology, Toxicology and Pharmaceutics: Drug Discovery | Chemistry: Physical and Theoretical Chemistry | Chemistry: Inorganic Chemistry | Chemistry: Organic Chemistry | Chemistry: Electrochemistry

Source type: Journal

View all documents > | Set document alert | Save to source list

CiteScore 2022
1.3

SJR 2022
0.242

SNIP 2022
0.371

CiteScore | CiteScore rank & trend | Scopus content coverage

Polyhedron 171 (2019) 542–550

Contents lists available at ScienceDirect

Polyhedron

journal homepage: www.elsevier.com/locate/poly

Rhodium(III) supported amination reaction of a pendant naphthyl group: Structure, electrochemistry and theoretical interpretation

Dibakar Sardar [a,b], Papia Datta [a,c], Rajat Saha [d], Raghavaiah Pallepogu [e], Chittaranjan Sinha [a,*]

[a] Department of Chemistry, Jadavpur University, Kolkata 700 032, India
[b] Department of Chemistry, Dinabandhu Andrews College, Garia, Kolkata 700084, India
[c] Department of Applied Science, RCC Institute of Information Technology, Canal South Road, Kolkata 700015, India
[d] Department of Chemistry Kazi Nazrul University Asansol, 713340, India
[e] Department of Chemistry, Dr. Harisingh Gour University, Sagar, MP 470003, India

ARTICLE INFO

Article history:
Received 18 May 2019
Accepted 29 July 2019
Available online 8 August 2019

Keywords:
Rhodium(III)-naphthylazoimidazoles
C—N coupling reaction
X-ray structure
Electrochemistry
DFT calculations

ABSTRACT

[Rh(α-NaiR)$_2$Cl$_2$]ClO$_4$ (**2**) (α-NaiR (**1**), 1-alkyl-2-(naphthyl-α-azo)imidazoles, R = Me (**a**), Et (**b**)) complexes react with ArNH$_2$ (where Ar = X—C$_6$H$_4$—, X = H (**3**), Me (**4**), Cl (**5**)) to synthesize the naphthyl appended C—N fused bis-[1-alkyl-2-{(7-imidoaryl)naphthyl-α-azo}imidazole-N,N′,N″]rhodium(III)perchlorate complexes [Rh(α-NaiR—N—Ar)$_2$]ClO$_4$ (**3**–**5**). The single crystal X-ray diffraction measurements of one of the complexes, [Rh(α-NaiEt—N—C$_6$H$_5$)$_2$]ClO$_4$ (**3b**), confirms the structure. The absorption spectra of the complexes **3**–**5** show high intense broad multiple transitions at 650–800 nm compared to the transition of the precursor **2** at 500 nm and DFT computations have assigned this transition to an admixture of LLCT (ligand-to-ligand charge transfer, imidoaryl → azonaphthyl) and LMCT transitions. The cyclic voltammogram shows a quasireversible oxidation at >0.8 V, which is assigned by DFT computation to oxidation of the imidoaryl chelate, along with azo reductions at <−0.4 V.

1. Introduction

Transition metals have played an important role in organic synthesis [1] and metal mediated C—X coupling reactions (C—C, C—N, C—O, C—S etc.) are a success of this program [2–20]. The N atom is a component of proteins and the amide bond (—CONH—) has significance to living molecules; thus reactions involving C—N bond formation underpin the inspiration of innovative chemical reactions. Metal-catalyzed C—N coupling reactions have been considered as a promising synthetic tool under the green chemistry protocol [4–12]. The coordination of organic molecules to metal ions has provided a beautifully designed platform, stereochemical orientation and electronic requirement of ligands that are responsible for chemical reactions. It is observed that arylazoheterocycles do not show any nucleophilic reaction in the free ligand state, while metallated-arylazoheterocycles show easy reactions *viz.*, hydroxylation [16,17], thiolation [18–20] and aryl-amination [2–12] reactions. The coordination of an azoheterocycle to a metal centre provides a chemical platform for holding the ligands in close proximity, alters the electrophilic character of the ligand and provides a fascinating route [13–15] for metal-assisted organic transformation.

The pendant aryl group of an arylazoheterocycle in metal complexes (e.g., Fe(III), Ni(II), Co(II), Rh(III), Ir(III), Pd(II), Pt(II) etc.) shows a C—N coupling reaction with aromatic amines and has been used to synthesize tridentate monoanionic N, N′, N″ (N: heterocycle-N; N′: azo-N; N″: anilide-N) chelated complexes [10,11,13,15,21–23]. Thus, the reaction is not at all metal ion specific; rather, the Lewis acid character of the metal ions increase the acidity of the C—H bond at the *ortho*-position of the pendant aryl ring; aromatic amines are being attracted by non-covalent forces to the C—H function and may initiate substitution, followed by C—N bond formation. The terminal oxidizing agent in the reaction is air oxygen. The C—H activation of the naphthyl group of a naphthylazoimodazolyl-Rh(III) complex was reported by us in 2013 [24]. In this work, the Rh(III) mediated C—N coupling reaction of the Rh(III)-coordinated 1-alkyl-2-(naphthyl-α-azo)imidazole (α-NaiR) ligand with arylamine (ArNH$_2$) is reported. The complexes thus produced have been characterized by spectral data. The structure of one of the C—N coupled products has been established by a single crystal X-ray diffraction study and the redox properties were examined and have been correlated with theoretical calculations.

* Corresponding author. Fax: +91 033 2413 7121.
E-mail address: crsjuchem@gmail.com (C. Sinha).

https://doi.org/10.1016/j.poly.2019.07.045
0277-5387/

2. Experimental

2.1. Materials

$RhCl_3{\cdot}3H_2O$ was obtained from Arora-Mathy, India and used as received. Triphenylphosphine, triethylamine and the solvents used were obtained from E. Merck, India. The ligands used in this work were 1-alkyl-2-(naphthyl-α-azo)imidazole (α-NaiR, R = CH_3 and CH_2—CH_3) (Scheme 1) and they were prepared by a reported procedure [24]. The chemicals used for the syntheses were of analytical grade and solvents were dried before use [25]. The solution spectral studies were carried out with spectroscopic grade solvents obtained from Sigma–Aldrich.

2.2. Physical measurements

Microanalytical data (C, H, N) were collected on Perkin-Elmer 2400 CHNS/O elemental analyzer. Spectroscopic data were obtained using the following instruments: UV–Vis spectra, Perkin Elmer Lambda 25; IR spectra, Perkin Elmer L120-00A FT IR spectrophotometer (KBr disk, 4000–225 cm^{-1}); ^1H NMR spectra, Bruker (AC) 300 MHz FTNMR spectrometer. FAB-MS spectra were collected on a Jeol-AX 500 instrument. The molar conductance was measured using a Systronics conductivity meter, 304 model, using *ca.* 10^{-3} M solutions in acetonitrile. Electrochemical measurements were performed using a CHI 600 computer-controlled electrochemical workstation with Pt-disk electrodes. All measurements were carried out under a nitrogen environment at 298 K with reference to the Ag/AgCl electrode in acetonitrile, using $[nBu_4N][ClO_4]$ as a supporting electrolyte. The reported potentials are uncorrected for junction potentials. The emissions were examined with a LS 55 Perkin Elmer spectrofluorimeter at room temperature (298 K) in acetonitrile solution under degassed conditions. The fluorescence quantum yield of the complexes was determined using phenanthrene as a reference [26]. The complex and the reference dye were excited at the same wavelength, maintaining nearly equal absorbance (~0.1), and the emission spectra were recorded. The area of the emission spectrum was integrated using the software available in the instrument and the quantum yield was calculated according to the following equation:

$$\phi_S/\phi_R = [A_S/A_R] \times [(Abs)_R/(Abs)_S] \times [\eta_S^2/\eta_R^2]$$

Here, ϕ_S and ϕ_R are the fluorescence quantum yield of the sample and reference, respectively. A_S and A_R are the area under the fluorescence spectra of the sample and the reference respectively, $(Abs)_S$ and $(Abs)_R$ are the respective optical densities of the sample and the reference solution at the wavelength of excitation, and η_S and η_R are the refractive index values for the respective solvent used for the sample and reference.

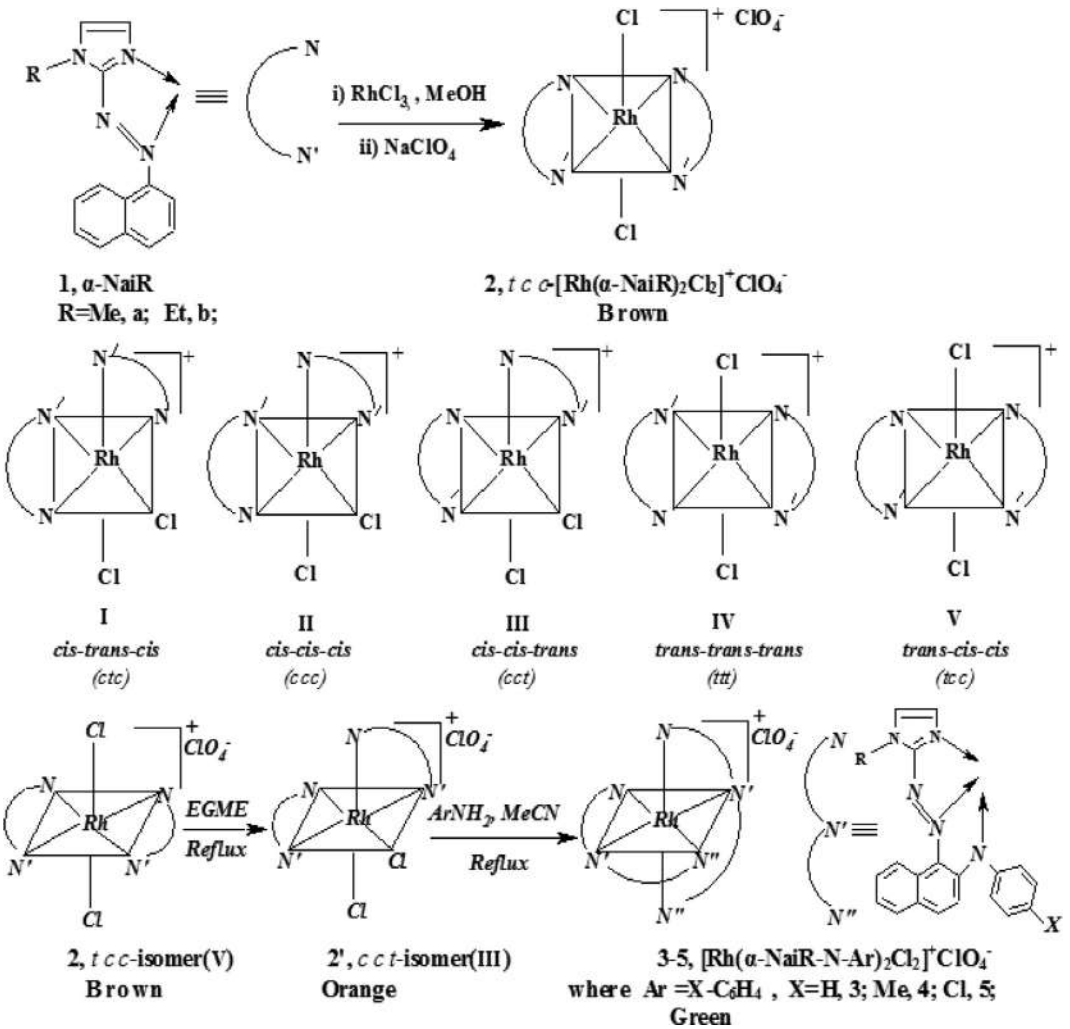

Scheme 1. The ligands (α-NaiR, **1**), the complexes ($[Rh(\alpha\text{-NaiR})_2Cl_2]^+$, **2**), plausible isomers (**I**–**V**) and the C—N fused products ($[Rh(\alpha\text{-NaiR—N—Ar})_2]^+$, **3**–**5**).

2.3. Preparation of the complexes

2.3.1. Preparation of [Rh(α-NaiMe)$_2$Cl$_2$]ClO$_4$ (**2a** and **2′a**)

$RhCl_3{\cdot}3H_2O$ (0.1 g, 0.315 mmol) and 1-methyl-2-(naphthyl-α-azo)imidazole, α-NaiMe (0.149 g, 0.63 mmol) (1:2 mole-ratio) were refluxed in methanol for 6 h; the mixture was left at room temperature for slow evaporation to half of the original volume. A saturated aqueous solution of $NaClO_4$ was then added, which afforded a brown precipitate. The product was collected by filtration, washed with methanol and ether, and dried under vacuum. The dried product was dissolved in CH_2Cl_2 and subjected to chromatography. A brown band was eluted with an acetonitrile–toluene mixture (1:5, v/v), whilst an orange band was eluted with an acetonitrile–toluene mixture (1:3, v/v). A small amount of an orange-red band was eluted with acetonitrile from the column and this band has not been characterized. The yields were 0.12 g (51%) for the brown isomer (**2a**) and 0.04 g (17%) for the orange isomer (**2′a**).

The other complexes of the series were prepared by the same procedure.

2a. Microanalytical data, Found: C, 45.12; H, 3.27; N, 12.10%. Calc. for $C_{28}H_{24}N_8O_4Cl_3Rh$: C, 45.07; H, 3.22; N, 12.02%. MS(FAB) *m/z*: 645 $(M-ClO_4^-)^+$. FT-IR (KBr disc, cm^{-1}): $\nu(ClO_4^-)$ 624(m), 1091(vs); ν(N=N) 1370(s); ν(C=N) 1556(w); ν(Rh—Cl) 333(w).

2b. Microanalytical data, Found: C, 46.50; H, 3.67; N, 14.87%. Calc. for $C_{30}H_{28}N_8O_4Cl_3Rh$: C, 46.54; H, 3.62; N, 14.84%. MS(FAB) *m/z*: 673 $(M-ClO_4^-)^+$. FT-IR (KBr disc, cm^{-1}): $\nu(ClO_4^-)$ 625(m), 1092(vs); ν(N=N) 1370(m); ν(C=N) 1547(w); ν(Rh—Cl) 333(w).

2′a. Microanalytical data, Found: C, 45.09; H, 3.25; N, 12.09%. Calc. for $C_{28}H_{24}N_8O_4Cl_3Rh$: C, 45.07; H, 3.22; N, 12.02%. MS(FAB) *m/z*: 645 $(M-ClO_4^-)^+$. FT-IR (KBr disc, cm^{-1}): $\nu(ClO_4^-)$ 626(w), 1092(vs); ν(N=N) 1348(s); ν(C=N) 1561(m); ν(Rh—Cl)(w) 314, 331.

2′b. Microanalytical data, Found: C, 46.57; H, 3.61; N, 14.87%. Calc. for $C_{30}H_{28}N_8O_4Cl_3Rh$: C, 46.54; H, 3.62; N, 14.84%. MS(FAB) *m/z*: 673 $(M-ClO_4^-)^+$. FT-IR (KBr disc, cm^{-1}): $\nu(ClO_4^-)$ 624(m), 1101(vs); ν(N=N) 1361(s); ν(C=N) 1543(w); ν(Rh—Cl)(w) 312, 334. (w = weak; s = strong; vs = very strong; m = medium)

*2.3.1.1. Conversion of the brown isomer (**2a**) to the orange isomer (**2′a**).* The brown isomer (**2a**) was suspended in ethylene glycol monomethyl ether (EGME) and heated to reflux for 4 h (conversion was tested by TLC paper). It was then treated with a saturated aqueous solution of $NaClO_4$, affording an orange precipitate. The products were collected by filtration, washed with methanol and ether, and dried under vacuum. The dried product was dissolved in CH_2Cl_2 and was chromatographed as before. A very small brown band eluted with an acetonitrile–toluene mixture (1:5, v/v), followed by an orange band with an acetonitrile–toluene mixture (1:3, v/v). The yield was 90%.

2.3.2. Preparation of [Rh(α-NaiMe—N—C_6H_5)$_2$]ClO$_4$ (**3a**)

*2.3.2.1. From **2a** (brown red isomer).* To an acetonitrile solution (20 ml) of [Rh(α-NaiMe)$_2$Cl$_2$]ClO$_4$ (**2a**) (0.112 g, 0.15 mmol), aniline (0.033 g, 0.35 mmol) and triethylamine (0.2 ml) were added and the mixture was refluxed for 6 h under stirring conditions. The red color of the solution gradually turned to green. Evaporation of this solution gave a dark green solid, which was subjected to purification by column chromatography in a silica gel column, prepared in petroleum–ether (60–80 °C fraction). A green portion was eluted with acetonitrile–toluene (1:3, v/v), which upon evaporation afforded the analytically pure product **3a**. The yield was 0.065 g (51%).

The other complexes were prepared by the same procedure. The yields varied from 45% to 55%. **3a.** Microanalytical data, Found: C, 56.19; H, 3.70; N, 16.35%. Calc. for $C_{40}H_{32}N_{10}O_4ClRh$: C, 56.17; H, 3.74; N, 16.38%. MS(FAB) *m/z*: 755$(M-ClO_4^-)^+$. FT-IR (KBr disc, cm^{-1}): $\nu(ClO_4^-)$ 626(m), 1095(vs); ν(N=N)1349(s); ν(C=N) 1537 (w).

3b. Microanalytical data, Found: C, 57.15; H, 4.07; N, 15.83%. Calc. for $C_{42}H_{36}N_{10}O_4ClRh$: C, 57.11; H, 4.08; N, 15.86%. MS(FAB) *m/z*: 783 $(M-ClO_4^-)^+$. FT-IR (KBr disc, cm^{-1}): $\nu(ClO_4^-)$ 626(m), 1089(vs); ν(N=N) 1345(s); ν(C=N) 1553(w).

4a. Microanalytical data, Found: C, 57.18; H, 4.01; N, 15.80%. Calc. for $C_{42}H_{36}N_{10}O_4ClRh$: C, 57.11; H, 4.08; N, 15.86%. MS(FAB) *m/z*: 783 $(M-ClO_4^-)^+$. FT-IR (KBr disc, cm^{-1}): $\nu(ClO_4^-)$ 623(m), 1100(vs); ν(N=N) 1362(s); ν(C=N) 1544(m).

4b. Microanalytical data, Found: C, 57.89; H, 4.51; N, 15.45%. Calc. for $C_{44}H_{40}N_{10}O_4ClRh$: C, 57.99; H, 4.39; N, 15.37%. MS(FAB) *m/z*: 811 $(M-ClO_4^-)^+$. FT-IR (KBr disc, cm^{-1}): $\nu(ClO_4^-)$ 624(m), 1093(vs); ν(N=N) 1354(m); ν(C=N) 1548(w).

5a. Microanalytical data, Found: C, 52.12; H, 3.34; N, 15.09%. Calc. for $C_{40}H_{30}N_{10}O_4Cl_3Rh$: C, 52.03; H, 3.25; N, 15.17%. MS(FAB) *m/z*: 823 $(M-ClO_4^-)^+$. FT-IR (KBr disc, cm^{-1}): $\nu(ClO_4^-)$ 622(m), 1098(vs); ν(N=N) 1368(m); ν(C=N) 1543(m).

5b. Microanalytical data, Found: C, 53.09; H, 3.45; N, 14.80%. Calc. for $C_{42}H_{34}N_{10}O_4Cl_3Rh$: C, 53.02; H, 3.58; N, 14.73%. MS(FAB) *m/z*: 851 $(M-ClO_4^-)^+$. FT-IR (KBr disc, cm^{-1}): $\nu(ClO_4^-)$ 625(m) 1093 (vs); ν(N=N) 1357(m); ν(C=N) 1545(m); (w = weak; s = strong; vs = very strong; m = medium).

*2.3.2.2. From **2′a** (orange isomer).* Aniline (0.033 g, 0.35 mmol) and triethylamine (0.2 ml) were added to an EGME solution of **2′a** (0.112 g, 0.15 mmol). The reaction mixture was refluxed for 5 h under stirring conditions. The orange color of the solution gradually became green. Evaporation of this solution gave a dark green solid, which was subjected to purification by column chromatography as before.

2.4. X-ray diffraction study

Crystals were grown by slow diffusion of a dichloromethane solution of **3b** in hexane. Crystal parameters and refined data are listed in Table 1. The data were collected with a fine focus sealed tube at 298(2) K using a graphite monochromator Bruker Smart CCD Area Detector (Mo Kα radiation, (λ = 0.71073 Å). Unit cell

Table 1
Selected crystallographic data for [Rh(α-NaiEt—N—C_6H_5)$_2$]ClO$_4$ (**3b**).

	[Rh(α-NaiEt—N—C_6H_5)$_2$]ClO$_4$ (**3b**)
Chemical_formula_sum	$C_{42}H_{36}ClN_{10}RhO_4$
Chemical Formula weight	883.17
Crystal system	triclinic
space group	$P\bar{1}$
Unit cell dimensions	
a (Å)	12.1941(18)
b (Å)	12.7781(18)
c (Å)	14.726(2)
α (°)	75.004(2)
β (°)	83.896(2)
γ (°)	65.941(2)
V (Å^3)	2023.9(5)
Z	2
D_{Calc} (Mg m^{-3})	1.449
Absorption coefficient (mm^{-1})	0.543
Total reflection collected	14,596
Unique reflections (R_{int})	7852
Refined parameters	524
Goodness-of-fit on F^2	1.263
R (F_o)[a] [$I > 2\sigma(I)$]	0.0669
wR (F_o)[b] [$I > 2\sigma(I)$]	0.1124

[a] $R = \Sigma|F_0 - F_c|/\Sigma F_0$.
[b] $wR = [\Sigma w(F_0^2 - F_c^2)/\Sigma wF_0^4]^{1/2}$ where $w = 1/[\sigma^2(F_0^2) + (0.0263P)^2 + 0.8373P]$, where $P = (F_0^2 + 2F_c^2)/3$.

parameters were determined from least-squares refinement of setting angles with θ in the range $1.43 \leq \theta \leq 26.06°$. The *hkl* range was $-14 \leq h \leq 15$; $-15 \leq k \leq 15$; $-17 \leq l \leq 18$. Reflection data were recorded using the ω scan technique. Data were corrected for Lorentz polarization effects and for linear decay. Semi-empirical absorption corrections based on ψ-scans were applied. Data reduction was carried out with the Bruker SAINT program. The structure was solved by direct method using SHELXS-97 [27] and successive difference Fourier syntheses. All non-hydrogen atoms were refined anisotropically. The hydrogen atoms were fixed geometrically and refined using the riding model. All calculations were carried out using SHELXL-97 [27], ORTEP-32 [28] and PLATON-99 [29] programs.

2.5. Computational details

All computations were performed using the GAUSSIAN 09 program package [30]. The Becke's three-parameter hybrid exchange functional and the Lee–Yang–Parr non-local correlation functional (B3LYP) were used throughout this computation [31]. Elements, except rhodium, were assigned to the 6-31G basis set in the calculations. For rhodium, the Los Alamos effective core potential plus double zeta (LanL2DZ) basis set were employed [32]. The geometric structures of the ligand and the complexes in the ground state (S_0) were fully optimized at the B3LYP level. Geometry optimization was carried out from the geometry obtained from the crystal structure without any symmetry constraints. In all cases, vibrational frequencies were calculated to ensure that the optimized geometries represented local minima. Using the respective optimized S_0 geometries, we employed time dependent density functional theory (TD-DFT) at the B3LYP level to predict their absorption characteristics [33].

3. Results and discussion

3.1. Synthesis and formulation

The reaction of $RhCl_3{\cdot}3H_2O$ with α-NaiR (**1**) in methanol under refluxing conditions isolated brown $[Rh(\alpha\text{-NaiR})_2Cl_2]ClO_4$ (**2**) upon adding $NaClO_4$. The composition of this product has been supported by elemental analysis. The conductance measurement in acetonitrile (Λ_M, 120–140 Ω^{-1} cm^2 mol^{-1}) suggests a 1:1 electrolytic nature of the complexes. $[Rh(\alpha\text{-NaiR})_2Cl_2]^+$ may exist in five isomeric forms (Scheme 1); three have a *cis*-MCl_2 (i–iii) and two a *trans*-MCl_2 (iv, v) configuration. On refluxing the brown complex (**2**) in a high boiling solvent, like EGME, for a period of 4 h, an orange colored product is isolated (**2′**). We could not isolate good quality crystals of **2** for X-ray diffraction studies and spectral (UV–VIS, IR and ^{1}H NMR, Mass; ESI†, Figs S1–S4) techniques have been used to characterize the structure of the compounds. The infra-red spectra of the brown isomer of $[Rh(\alpha\text{-NaiR})_2Cl_2]ClO_4$ (**2**) shows an intense band at 1095 cm^{-1}, along with a weak band at 625 cm^{-1}, that are assigned to $\nu(ClO_4)$ (ESI†, Fig. S1). A single weak stretch for the brown isomer at 330 cm^{-1} is assigned to one ν(Rh—Cl), while the orange isomer shows two ν(Rh—Cl) stretches within the range 310–340 cm^{-1} in the complexes. This stretching information sustains the *trans*-MCl_2 and *cis*-MCl_2 type configuration for the brown and orange isomer, respectively. The sharp band at 1400–1405 cm^{-1} corresponding to ν(N=N) in the free ligand, is shifted to 1365–1370 cm^{-1} in the complexes and the reason for the lowering (~30–35 cm^{-1}) of frequency characterizes the coordination of the azo-N atom to the Rh(III) ion. The FAB-MS spectra of the complexes show the expected fragmentation patterns and the $(M-ClO_4^-)^+$ (ESI†, Fig. S2) ion peak appears as the base peak. This information establishes that the configuration of the isolated complex **2** is the *trans*-MCl_2 type, *i.e. trans–cis–cis* (*tcc*) fashion with respect to Cl, N(imidazolyl) and N(azo) donors, respectively. Upon refluxing in ethanol, the color of the solution changes from brown to orange and converts to the *cis–trans–cis* (*ctc*) isomer, *i.e.* to a *cis*-MCl_2 type isomer (**2′**). The *cis*-MCl_2 type isomer has been isolated and characterized by the spectral techniques.

On boiling the brown solution of **2** in acetonitrile in the presence of $ArNH_2$, a green product was isolated, which has been identified as the amine coupled product, bis-[1-alkyl-2-{(7-imidoaryl)naphthyl-α-azo}imidazole-N,N′,N″]rhodium(III) perchlorate, $[Rh(\alpha\text{-NaiR—N—Ar})_2]ClO_4$ (**3**–**5**) (where Ar = X—C_6H_4—, X = H, **3**; Me, **4**; Cl, **5**). The C—N fusion takes place at the *ortho* position to the azo function in the pendant naphthyl ring of both the coordinated α-NaiR ligands and forms Rh(III) complexes of tridentate-N,N′,N″ chelating ligands (α-NaiR—N—C_6H_5; *N,N′,N″* refer to *N*(imidazolyl), *N*(azo) and *N*(anilide), respectively) [24]. The X-ray structure of $[Rh(\alpha\text{-NaiEt—N—}C_6H_5)_2]ClO_4$ (**3b**) confirms the above observation (Fig. 1a). The C—N fusion reaction has been also carried out directly with the orange isomer (**2′**) and aniline under refluxing conditions and a similar observation was recorded. The infra-red spectra of **3** show a noteworthy shifting of ν(N=N) to lower frequencies by 50–60 cm^{-1} in the coupled products **3**, with ν(N=N) occurring at 1340–1350 cm^{-1}. The significant decrease in the azo frequency may be due to charge delocalization from the N—Ar fragment to the azo function intramolecularly [21–24].

3.2. Molecular structure of $[Rh(\alpha\text{-NaiEt—N—}C_6H_5)_2]ClO_4$ (**3b**)

The molecular structure of bis-[1-ethyl-2-{(7-imidophenyl)-naphthyl-α-azo}imidazole-N,N′,N″]rhodium(III)perchlorate, $[Rh(\alpha\text{-NaiEt—N—}C_6H_5)_2]ClO_4$ (**3b**), is shown in Fig. 1a and relevant bond parameters are given in Table 2. Two tridentate donor ligands constitute the RhN_6 coordination sphere, where the ligands bind in a meridional fashion and their relative orientations with reference to N(imidazolyl), N′(azo) and N″(anilido) are *cis*, *trans* and *cis*, respectively. There are three pairs of Rh—N bonds and among them the Rh—N(azo) [Rh(1)—N(1), 1.990(3); Rh(1)—N(2), 1.985(3) Å] bonds are shorter than the Rh—N(imidazolyl) [Rh(1)—N(3), 2.035 (3); Rh(1)—N(6), 2.056(3) Å] bonds and the Rh—N(anilide) [Rh (1)—N(4), 2.020(3); Rh(1)—N(5), 2.030(3) Å] bonds.

Thus, the coordination arrangement is distorted octahedral. These experimental bond parameters of **3b** also show good agreement with the theoretical values (Table 2) and values reported in the literature [15]. DFT computations of the two complexes **2′b** and **3b** have been performed with optimized geometries. The calculated structures well reproduce the experimental structures. In

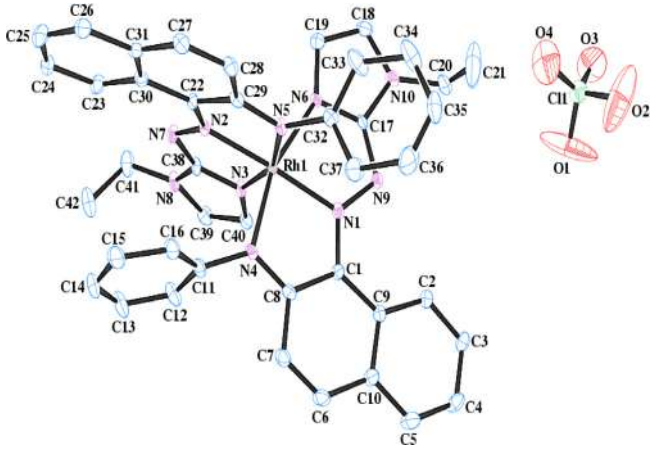

Fig. 1a. ORTEP diagram of $Rh(\alpha\text{-NaiEt—N—}C_6H_5)_2]ClO_4$ (**3b**).

Table 2
Selected bond lengths (Å) and angles (°) for the complex [Rh(α-NaiEt—N—C_6H_5)$_2$]ClO_4 (**3b**) (from X-ray and DFT calculations) and [Rh(α-NaiEt)$_2Cl_2$]ClO_4 (**2′b**) (from DFT calculation).

[Rh(α-NaiEt—N—C_6H_5)$_2$]ClO_4 (**3b**)

Bond lengths (Å)	Experimental value	Theoretical value	Bond angles (°)	Experimental value	Theoretical value
Rh(1)—N(1)	1.990(3)	2.03	N(1)—Rh(1)—N(3)	101.35(13)	99.53
Rh(1)—N(2)	1.985(3)	2.03	N(1)—Rh(1)—N(4)	80.55(14)	80.37
Rh(1)—N(3)	2.035(3)	2.08	N(1)—Rh(1)—N(5)	99.54(13)	100.88
Rh(1)—N(6)	2.056(3)	2.08	N(1)—Rh(1)—N(6)	79.16(13)	79.21
Rh(1)—N(4)	2.020(3)	2.059	N(3)—Rh(1)—N(4)	89.56(13)	90.37
Rh(1)—N(5)	2.030(3)	2.059	N(3)—Rh(1)—N(6)	94.38(12)	92.45
N(1)—N(9)	1.317(4)	1.342	N(4)—Rh(1)—N(5)	93.85(13)	93.98
N(2)—N(7)	1.337(4)	1.342	N(1)—Rh(1)—N(2)	176.31(13)	178.21
N(6)—C(17)	1.330(5)	1.366	N(3)—Rh(1)—N(5)	159.11(13)	159.57

[Rh((α-NaiEt)$_2Cl_2$]ClO_4 (**2′b**)

Bond lengths (Å)	Theoretical value	Bond angles (°)	Theoretical value
Rh(1)—N(3)	2.135	N(3)—Rh(1)—N(4)	77.49
Rh(1)—N(4)	2.023	N(3)—Rh(1)—N(19)	102.69
Rh(1)—N(19)	2.135	N(3)—Rh(1)—N(20)	103.08
Rh(1)—N(20)	2.023	N(3)—Rh(1)—Cl(35)	83.27
Rh(1)—Cl(34)	2.412	N(4)—Rh(1)—Cl(34)	92.35
Rh(1)—Cl(35)	2.412	N(4)—Rh(1)—N(5)	87.12
N(2)—N(3)	1.312	N(20)—Rh(1)—Cl(34)	87.03
N(18)—N(19)	1.311	N(20)—Rh(1)—Cl(35)	92.40
N(4)—C(6)	1.359	N(3)—Rh(1)—Cl(34)	169.08
N(3)—C(38)	1.359	N(4)—Rh(1)—N(20)	179.21

3b, the calculated Rh—N distances are about 0.01–0.04 Å longer than that of the experimental data, while the bond angles vary by 0–1° (Table 2).

The packing view shows the presence of a π···π network among three aromatic rings: the imidazolyl (Imz), naphthyl (Naph) and anilide—phenyl (anil—Ph) groups. The supramolecular interaction generates a 1D chain (Fig. 1b). The Imz-A···Naph-B interactions (Cg(6)···Cg(8), 3.64 Å) (A refers to one molecule and B refers to the neighbouring molecule) and *vice-versa*, *i.e.* Imz-B···Naph-A, generate a supramolecular dimer. The pendant naphthyl groups (Naph) of the dimeric motif exhibit a π···π interaction (Cg(10)···Cg(11), 3.54 Å) with a neighbouring partner to constitute the 1D chain. Additionally, interactions between Imz and anil-Ph of neighbouring partners (Cg(6)—Cg(12), 4.262(8) Å) increase the robustness of the network.

3.3. The solution spectral characterization

Methanol solutions of the complexes show multiple transitions of moderately high intensity (ε, 10^4 M^{-1} cm^{-1}) in the range 250–500 nm (Table 3). Complexes **3**–**5** show some transitions in the longer wavelength region (650–800 nm), which are absent in **2** (Fig. 2 and ESI†, Fig. S3). The transitions in the UV region may be assigned as intraligand transitions (ILCT) (ππ* type) and those in the visible region are probably due to metal-to-ligand charge transfer (MLCT) transitions. However, the d-level splitting of 4d and 5d-block metal ions in a high oxidation state is less acceptable to interpret multiple charge transfer transitions. It is recommended that the lower symmetry splitting of the metal level in such mixed-ligand complexes may result from the mixing of singlet and triplet configurations in the excited state through spin–orbit coupling [34]. Thus, high intense charge transfer transitions are mostly applicable in these complexes.

The geometries of the *ctc*, *cct*, *ttt* and *tcc* isomers have been optimized to compare the ground state energies and ligand orientations (Fig. 3); unfortunately the geometry of the *ccc* isomer failed to converge. The calculations have revealed that the *ttt* isomer is most stable, while under the reaction conditions, *i.e.,* in boiling methanol, the *tcc* isomer is stabilized by 13.2 kJ mol^{-1} more than the *cct* isomer.

The orbital energies along with the contributions from the coordinated ligands of **2′b** and **3b** are tabulated in Table S1 (ESI†) and Fig. 4 depicts the energy correlation diagram between **2′b** and **3b**. The energies of the HOMO and LUMO of **3b** are comparatively higher (E_{HOMO} = −7.51 eV; E_{LUMO} = −5.16 eV; ΔE = 2.35 eV) than those of **2′b** (E_{HOMO} = −8.61 eV; E_{LUMO} = −6.22 eV; ΔE = 2.39 eV) and the energy difference between the HOMO and the LUMO is slightly decreased on going from **2′b** → **3b**. The compositions of the MOs show the ligand dominating (70–95%), with a small contribution from the metal component in **3b**.

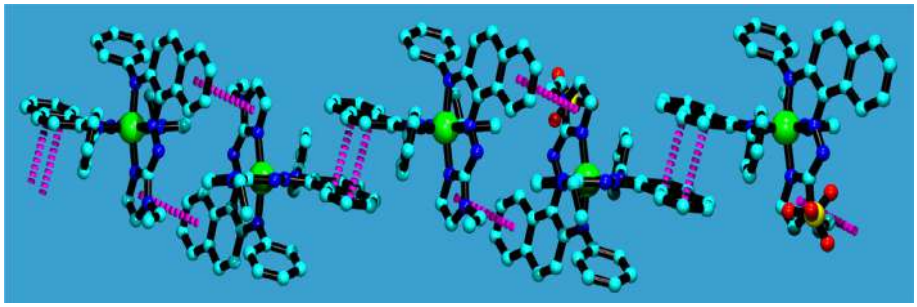

Fig. 1b. The π…π interactions of the complex [Rh(α-NaiEt—N—C_6H_5)$_2$]ClO_4 (**3b**).

Table 3
UV–Vis[a], fluorescence[a] spectral data of the complexes.

Complex	Absorption[a] λ_{max} (nm) ($10^{-3}\varepsilon/M^{-1}$ cm^{-1})	λ_{ex} (nm)[a]	λ_{em} (nm)[a]	Quantum yield (φ)[a]
$[Rh(\alpha\text{-NaiMe})_2Cl_2]ClO_4$ (**2a**)	478(14.37), 409(14.52), 305(13.02), 260(17.36)	–		
$[Rh(\alpha\text{-NaiEt})_2Cl_2]ClO_4$ (**2b**)	489(19.88), 356(11.43), 265(41.48)	–		
$[Rh(\alpha\text{-NaiMe})_2Cl_2]ClO_4$ (**2′a**)	448(17.34), 381(14.99), 307(13.77), 260(21.04)			
$[Rh(\alpha\text{-NaiEt})_2Cl_2]ClO_4$ (**2′b**)	461(23.41), 360(21.03), 274(50.12)			
$[Rh(\alpha\text{-NaiMe—N—}C_6H_5)_2]ClO_4$ (**3a**)	790(12.89), 713(17.14), 573(13.02), 431(22.89), 346(41.15), 297(47.877)	297	343	0.0055
$[Rh(\alpha\text{-NaiEt—N—}C_6H_5)_2]ClO_4$ (**3b**)	771(13.28), 678(14.9), 431(19.45), 346(36.44), 295(42.13), 244(68.45)	296	344	0.0057
$[Rh(\alpha\text{-NaiMe—N—}C_6H_4\text{—Me-}p)_2]ClO_4$ (**4a**)	775(8.983), 713(12.56), 643(11.13), 503(18.24), 298(36.22), 253(64.72)	298	347	0.0056
$[Rh(\alpha\text{-NaiEt—N—}C_6H_4\text{—Me-}p)_2]ClO_4$ (**4b**)	770(10.16), 707(14.22), 635(12.37), 498(18.70), 300(33.60)	300	346	0.0059
$[Rh(\alpha\text{-NaiMe—N—}C_6H_4\text{—Cl-}p)_2]ClO_4$ (**5a**)	812(9.32), 747(12.76), 677(10.15), 434(10.97), 383(13.70), 304(26.91), 260(36.53)	304	348	0.0051
$[Rh(\alpha\text{-NaiEt—N—}C_6H_4\text{—Cl-}p)_2]ClO_4$ (**5b**)	815(13.4), 740(14.34), 678(9.47), 438(13.64), 389(16.70), 295(31.4)	295	346	0.0050

[a] In MeOH solvent; λ_{ex} = Excitation wavelength, λ_{em} = Emission wavelength, φ = Quantum yield.

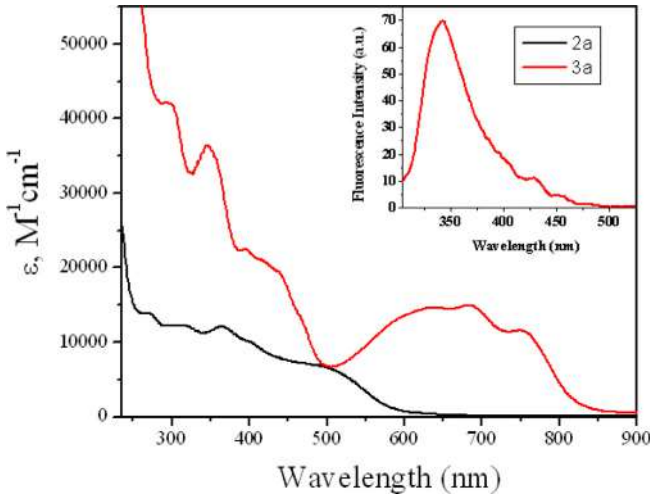

Fig. 2. UV–Vis spectra of **2a** and **3a**; inset picture shows the fluorescence spectrum of **3a**.

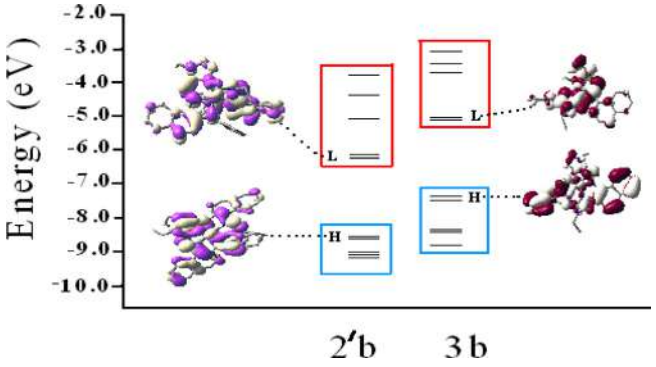

Fig. 4. Energy correlation diagram between *tcc*-$[Rh(\alpha\text{-NaiEt})_2Cl_2]ClO_4$, **2′b** (orange isomer) and $[Rh(\alpha\text{-NaiEt—N—}C_6H_5)_2]ClO_4$, **3b**.

To gain detailed insight into the charge transitions, TD-DFT calculations were performed. The calculated absorption spectra of the complexes are shown in Fig. S6 (ESI†) and the theoretical excitation wavelengths and their assignments are given in Table S2 (ESI†). In

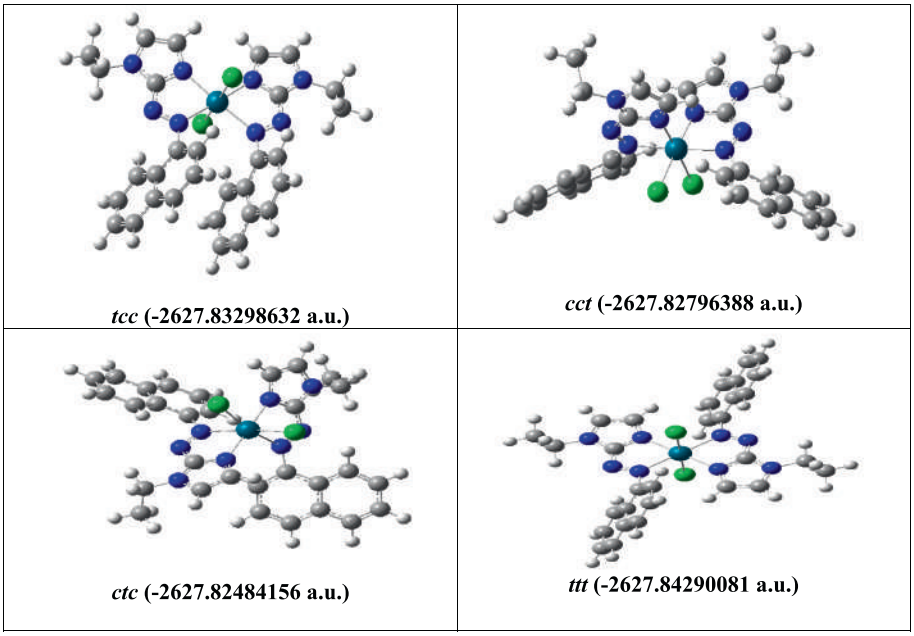

Fig. 3. Optimized geometries and energies of the possible isomers of $[Rh(\alpha\text{-NaiEt})_2Cl_2]ClO_4$, **2b**.

the gas phase, **2′b** shows a reasonably intense (oscillator strength *f*, 0.1124) transition at 634 nm followed by a band at 590 nm (*f*, 0.1279). Longer wavelength transitions (634 nm) are referred to the HOMO−4, HOMO−2 and HOMO−1 → LUMO transitions and may be assigned to a mixture of intra-ligand charge transfer (ILCT), metal to ligand charge transfer (MLCT) and chlorine to ligand charge transfer (XLCT) transitions. The TD-DFT results of **3b** determine the absorption at 731 nm (*f*, 0.0135), that signifies the HOMO → LUMO transition, mainly to be an intra-ligand charge transfer transition. Transitions in the range 450 to 600 nm, are reasonably intense (*f*, 0.15 → 0.25) (H-2, H-1 → LUMO), these are referred to a mixture of ILCT, YLCT (aniline to ligand) and MLCT transitions. Similarly, the 405.3 nm transition (*f*, 0.054) is calculated as a mixture of ILCT, XLCT and MLCT. High energy transitions <300 nm are mainly ILCT. The energy correlation between the MOs of **2′b** and **3b** (Fig. 4) imply destabilization of the HOMO of **3b** by 1.10 eV compared to the HOMO of **2′b**. Thus, the energy separation between the HOMO–LUMO in **3b** appears at a lower energy (2.35 eV) than that of **2′b** (2.39 eV). This may be one of the reasons for the appearance of the longer wavelength transition in **3b** than **2′b**.

Although α-NaiR and the precursor complex **2** are non-emissive, interestingly the ammine coupled products **3**–**5** are emissive at room temperature when excited in the 300 nm region (Fig. 2). The fluorescence quantum yields of the complexes lie in the range 0.0056–0.006 (Table 3). The photo-inactivity of the ligands and the complex **2** may be due to energy loss by vibrational relaxation and the heavy-atom effect of Rh, along with photo-induced electron transfer (PET) to the pendent naphthyl group in the excited state [35]. In the C—N fused product **3**, the structural rigidity and deletion of PET may be one of the reasons for luminescence efficiency.

The ^{1}H NMR spectra of all the complexes were assigned by a comparison with the free ligand data [36] and the intensity measurement of the signals corresponds to the total number of protons in the respective complexes (Table 4). In the brown isomer of **2**, the N(imidazolyl)—CH_3 protons appear as a singlet signal at δ 4.30 ppm; the —CH_2— and —CH_3 protons of N(imidazolyl)—CH_2-—CH_3 emerge as a quartet at *δ* 4.56 ppm and a triplet at *δ* 1.60 ppm, respectively. The ^{1}H NMR spectra of the orange isomer (**2′**) are different from those of the brown isomer and show complexity in the aromatic region (ESI†, Fig. S4). In the orange isomer, the N(1)—CH_3 protons appear as two equally intense signals at *ca.* *δ* 3.98 and 4.13 ppm. The —CH_2 protons of the N—CH_2—CH_3 groups appear as AB type quartets [37] of equal intensities. The above experimental observations imply that the two ligands in **2** (brown) are equivalent, but they are not equivalent in **2′** (orange) isomer. Therefore, the expected geometry of brown isomer should be *trans* with respect to chloride and *cis* with respect to both imidazolyl and azo pairs of nitrogen atoms [38], while that of the orange (**2′**) isomer should be the *cis*-MCl_2 type where the imidazolyl and azo nitrogen pairs are in *cis* and *trans* fashions or *vice-versa*. Like in isomer **2′**, the N(imidazolyl)—CH_3 protons of the coupled product (**3**–**5**) appear as two equally intense signals (*δ*/ppm) at 4.20 and 4.31 for **3**[a], 4.20 and 4.30 for **4a** and 4.21 and 4.33 for **5**[a], and the —CH_2 protons of the N(1)—CH_2—CH_3 group appear as AB type multiplets (*δ*/ppm) at 4.15 and 4.25 for **3b**, 4.13 and 4.31 for **4b** and 4.23 and 4.32 for **5b**. [Rh(α-NaiR—N—Ar)$_2$]ClO_4 (**3**–**5**) show complex NMR spectra in the aromatic region. Due to the large number of protons in the aromatic region, the NMR signals of the amine coupled products become complex in this region, but the expected effects of the substituent X were observed in the signals. The electron donating substituent (Me) in **4** results in a lower *δ* value for the coupled amine protons in **4** compared to **3**, whereas the reverse is observed in **5** due to the electron withdrawing substituent (Cl).

These observations infer that the coordination of α-NaiR to the Rh(III) ion increases the acidity of the *ortho* C—H (C(β)—H), which may undergo a hydrogen bonding (non-covalent) interaction with added Ar—NH_2. This binding may initiate electron transport (Scheme 2), followed by C—N bond formation where the terminal electron acceptor is air O_2.

3.4. Electrochemistry

The complexes exhibit two reductive responses in the −0.40 to −0.60 and −0.80 to −1.00 V potential ranges (Fig. 5; Table 5 and ESI†, Fig. S5) when the CV has been drawn in acetonitrile (0.1 TBAP)

Table 4
^{1}H NMR spectral data of the complexes in $CDCl_3$.

Compd.	*δ* (ppm) (J/Hz) academy										
	4-H[c]	5-H[b]	7-H[c]	8,9-H[f]	10-12-H[f]	13-H[c]	15,19-H[c]	16,18-H[f]	17-H[d]	N(1)—R	17-CH_3[a]
(**2a**)	7.94	7.26	8.44	7.63	7.35	8.13				4.09[a]	
(**2b**)	7.92	7.26	8.43	7.59	7.36	8.14				1.65[d]	
										4.52[e]	
(**2′a**)	7.93;	7.20	8.43	7.52–7.72	7.36–7.48	8.11;				3.98[a]	
	7.98	7.26	8.47			8.17				4.13[a]	
(**2′b**)	7.90;	7.22	8.40	7.64–7.75	7.36–7.55	8.12;				1.46[d]; 1.67[d]	
	7.97	7.26	8.48			8.19				4.20[e]; 4.49[e]	
(**3a**)	7.93;	7.20		7.51–7.67	7.36–7.47	8.11;	7.77;	7.70	7.73	4.20[a]	
	7.98	7.26				8.18	7.81			4.31[a]	
(**3b**)	7.92;	7.20;		7.49–7.65	7.36–7.48	8.11;	7.78;	7.70	7.74	1.57[d]; 1.42[d]	
	7.98	7.25				8.19	7.81			4.15[e]; 4.25[e]	
(**4a**)	7.94;	7.20;		7.51–7.61	7.31–7.40	8.13;	7.78;	7.43–7.46		4.20[a]	2.30
	8.00	7.25				8.20	7.83			4.30[a]	2.46
(**4b**)	7.92;	7.20;7.24		7.55–7.65	7.30–7.39	8.12;	7.76;	7.45–7.50		1.49[d]; 1.63[d]	2.31
	7.98					8.19	7.83			4.13[e]; 4.31[e]	2.49
(**5a**)	7.93;	7.21;		7.56–7.70	7.36–7.48	8.10;	7.84	7.78		4.21[a]	
	7.99	7.26				8.19				4.33[a]	
(**5b**)	7.93;	7.22;		7.57–7.68	7.36–7.51	8.12;	7.84	7.78		1.41[d]; 1.50[d]	
	8.00	7.25				8.19				4.23[e]; 4.32[e]	

[a] Singlet.
[b] Broad singlet.
[c] Doublet (*J* = 7.0–8.0 Hz).
[d] Triplet (*J* = 7.5–8.5).
[e] Quartet (*J* = 8.0–9.0 Hz).
[f] Multiplet.

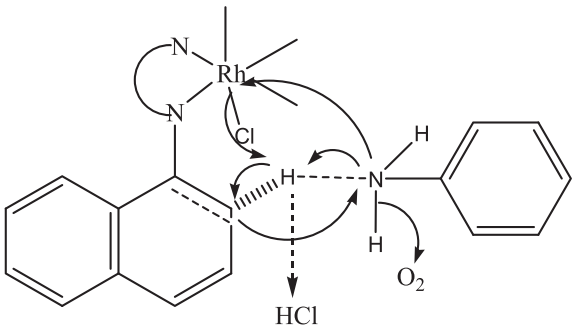

Scheme 2. Plausible charge flow and C—N fusion of Ar—NH_2 with the *ortho* C—H (pendant naphthyl group) function.

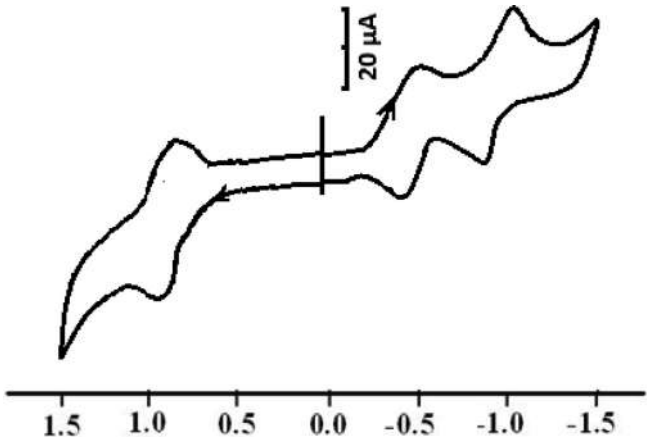

Fig. 5. Cyclic voltammogram of **3a** in acetonitrile solution.

Table 5
Cyclic voltametric data of the complexes.

Complex	Cyclic voltammetric data[a]		
	Ligand reduction E (V), (ΔE_p, mV)		Oxidation E (V), (ΔE_p, mV)
[Rh(α-NaiMe)$_2$Cl$_2$]ClO$_4$ (**2a**)	−0.93 (140)	−0.53 (160)	–
[Rh(α-NaiEt)$_2$Cl$_2$]ClO$_4$ (**2b**)	−0.96 (160)	−0.54 (150)	–
[Rh(α-NaiMe—N—C$_6$H$_5$)$_2$]ClO$_4$ (**3a**)	−0.93 (200)	−0.47 (90)	0.92 (80)
[Rh(α-NaiEt—N—C$_6$H$_5$)$_2$]ClO$_4$ (**3b**)	−0.95 (170)	−0.48 (160)	0.88 (90)
[Rh(α-NaiMe—N—C$_6$H$_4$—Me-*p*)$_2$]ClO$_4$ (**4a**)	−0.97 (180)	−0.55 (140)	0.97(100)
[Rh(α-NaiEt—N—C$_6$H$_4$—Me-*p*)$_2$]ClO$_4$ (**4b**)	−0.92 (140)	−0.43 (120)	0.95 (120)
[Rh(α-NaiMe—N—C$_6$H$_4$—Cl-*p*)$_2$]ClO$_4$ (**5a**)	−0.91 (130)	−0.44 (140)	1.00 (100)
[Rh(α-NaiEt—N—C$_6$H$_4$—Cl-*p*)$_2$]ClO$_4$ (**5b**)	−0.84 (170)	−0.48 (120)	1.03 (100)

[a] Solvent: dry CH_3CN; Pt-working electrode, Ag/AgCl reference, Pt-auxiliary electrode; [*n*-Bu_4N](ClO_4) supporting electrolyte, scan rate 50 mV/s; metal oxidation E = 0.5 (E_{pa} + E_{pc}) V, $\Delta E_p = |E_{pa} - E_{pc}|$ mV, where E_{pa} (anodic-peak-potential) and E_{pc} (cathodic-peak-potential).

in the potential range 2.0 to −2.0 V. The nature of the voltammogram does not change with scan rate (50–200 mV S^{-1}). The reductive responses may be regarded as electron accommodation of the azoimine function of the naphthylazoimidazole ligand. One oxidative response is obtained for complexes **3**–**5** in the potential region 0.95–1.1 V. Since the Rh(III) ion is hard to oxidize in this region, an oxidative response is not observed in the case of complexes **2**, so this oxidative response may be referred to the oxidation of the ligand at the easily oxidisable azonaphthyl-imidazolylamine chelated center [21,24]. The redox property of the complexes may be explained in terms of DFT calculations. Oxidation involves electron abstraction from occupied MOs and reduction involves electron addition to unoccupied MOs. Since the LUMO of the complexes are mainly (>95%) contributed of ligand orbitals, the reduction is referred to the reduction of the naphthylazoimidazole ligands. The oxidation may be defined as electron extraction from the HOMO. Interestingly the HOMO is mainly contributed (90%) by ligand orbitals, hence the oxidation in this case may be treated as a ligand centered oxidation.

4. Conclusion

1-Alkyl-2-(naphthyl-α-azo)imidazoles are N,N′-bidentate chelators and are used in the synthesis of the rhodium(III) complexes [Rh(α-NaiR)$_2$Cl$_2$]ClO$_4$, which react with $ArNH_2$ to give [Rh(α-NaiR—N—Ar)$_2$]ClO$_4$ where α-NaiR—N—Ar is a monoanionic tridentate N,N′,N″-chelating ligand. The arylamination takes place at the *ortho* position to the azo function in the pendant aryl ring of both α-NaiR ligands. The C—N coupling reactions are confirmed by a single crystal X-ray diffraction study in one case of a coupled product. The complexes are characterized by IR, UV–VIS and ^{1}H NMR spectral data. The precursor, [Rh(α-NaiR)$_2$Cl$_2$]ClO$_4$, is photoinactive, but the amine coupled products [Rh(α-NaiR—N—Ar)$_2$]ClO$_4$ exhibit emission upon excitation at ~300 nm and the solution spectra of [Rh(α-NaiR—N—Ar)$_2$]ClO$_4$ show structured absorptions in the red to NIR region which are absent in [Rh(α-NaiR)$_2$Cl$_2$]ClO$_4$.

Acknowledgements

Financial support from the University Grant Commission (Reference No. F.: PSW-044/14-15 (ERO)) New Delhi is gratefully acknowledged. One of the Authors (C.S.) thanks the Council of Scientific and Industrial Research (CSIR, Sanction no. 01(2814)/17/EMR-II), New Delhi, India for financial sanction.

Appendix A. Supplementary data

CCDC 1853241 contains the supplementary crystallographic data. These data can be obtained free of charge via http://www.ccdc.cam.ac.uk/conts/retrieving.html, or from the Cambridge Crystallographic Data Centre, 12 Union Road, Cambridge CB2 1EZ, UK; fax: (+44) 1223-336-033; or e-mail: deposit@ccdc.cam.ac.uk. Supplementary data (the energy and composition of selected frontier molecular orbitals calculated by DFT and electronic transition data from the TDDFT calculations) to this article can be found online at https://doi.org/10.1016/j.poly.2019.07.045.

References

[1] M. Kannan, M. Sengoden, T. Punniyamurthy, Arene chemistry, in: J. Mortier (Ed.), Transition Metal-Mediated Carbon-Heteroatom Cross-Coupling ... : An Overview. Arene Chemistry: Reaction Mechanisms and Methods for Aromatic Compounds, Wiley Onlines Books, 2015, pp. 547–586.
[2] M.J. Mphahlele, M.M. Maluleka, Molecules 19 (2014) 17435.
[3] H. Kim, S. Chang, ACS Catal. 6 (2016) 2341.
[4] D. Sengupta, P. Ghosh, T. Chatterjee, H. Datta, D.N. Paul, S. Goswami, Inorg. Chem. 53 (2014) 12002.
[5] P. Ruiz- Castillo, S.L. Buchwald, Chem. Rev. 116 (2016) 12564.
[6] D. Sengupta, N. Saha Chowdhury, S. Samanta, P. Ghosh, S.K. Seth, S. Demeshko, F. Meyer, S. Goswami, Inorg. Chem. 54 (2015) 11465.
[7] D. Oyama, B. Mun, T. Takase, J. Organomet. Chem. 799–800 (2015) 173.
[8] I. Chatterjee, P. Ghosh, H. Datta, S. Goswami, Indian J. Chem., Sec. A 53A (2014) 27.
[9] F.F. Khan, S.K. Sinha, G.K. Lahiri, D. Maiti, Chem. Asian J. 13 (2018) 2243.

[10] A.K. Ghosh, P. Majumdar, L.R. Falvello, G. Mostafa, S. Goswami, Organometallics 18 (1999) 5086.
[11] M. Panda, C. Das, G.-H. Lee, S.-M. Peng, S. Goswami, Dalton Trans. 17 (2004) 2655.
[12] M. Panda, S. Das, G. Mostafa, A. Castineiras, S. Goswami, Dalton Trans. 7 (2005) 1249.
[13] K.K. Kamar, S. Das, C.-H. Hung, A. Castineiras, M.D. Kuz'min, C. Rillo, J. Bartolomé, S. Goswami, Inorg. Chem. 42 (2003) 5367.
[14] K.K. Kamar, A. Saha, S. Goswami, Proc. Indian Acad. Sci. (Chem. Sci.) 114 (2002) 339.
[15] A. Saha, P. Majumdar, S.-M. Peng, S. Goswami, Eur. J. Inorg. Chem. (2000) 2631.
[16] A. Bharath, B.K. Santra, P. Munshi, G.K. Lahiri, J. Chem. Soc., Dalton Trans. 16 (1998) 2643.
[17] C.K. Pal, S. Chattopadhyay, C. Sinha, D. Bandyopadhyay, A. Chakravorty, Polyhedron 13 (1994) 999.
[18] B.K. Santra, G.K. Lahiri, Proc. Indian Acad. Sci. Chem. Sci. 111 (1999) 509.
[19] B.K. Santra, P. Munshi, G. Das, P. Bharadwaj, G.K. Lahiri, Polyhedron 18 (1999) 617.
[20] S.K. Roy, S. Samanta, N.S. Chowdhury, T.K. Mondal, S. Goswami, Chem. Eur. J. 20 (2014) 2712.
[21] P.K. Santra, P. Byabartta, S. Chattopadhyay, L.R. Falvello, C. Sinha, Eur. J. Inorg. Chem. (2002) 1124.
[22] P. Pratihar, T.K. Mondal, P. Raghavaiah, C. Sinha, Inorg. Chim. Acta 363 (2010) 831.
[23] S. Senapoti, S.K. Jasimuddin, G. Mostafa, T.-H. Lu, C. Sinha, Polyhedron 25 (2006) 1571.
[24] D. Sardar, P. Datta, R. Saha, P. Raghavaiah, C. Sinha, J. Organomet. Chem. 732 (2013) 109.
[25] Arthur I. Vogel (Ed.), A Text – Book of Quantitative Inorganic Analysis, 3rd ed., Longmans, 1961.
[26] W.R. Dawson, M.W. Windsor, J. Phys. Chem. 72 (1968) 3251.
[27] G.M. Sheldrick, shelxs-97, Program for the Solution of Crystal Structure, University of Gottingen, Germany, 1997.
[28] L.J. Farrugia, ORTEP-3 for windows, J. Appl. Crystallogr. 30 (1997) 565.
[29] A.L. Spek, PLATON, Molecular Geometry Program, University of Utrecht, The Netherlands, 1999.
[30] M.J. Frisch, G.W. Trucks, H.B. Schlegel, G.E. Scuseria, M.A. Robb, J.R. Cheeseman, G. Scalmani, V. Barone, B. Mennucci, G.A. Petersson, H. Nakatsuji, M. Caricato, X. Li, H.P. Hratchian, A.F. Izmaylov, J. Bloino, G. Zheng, J.L. Sonnenberg, M. Hada, M. Ehara, K. Toyota, R. Fukuda, J. Hasegawa, M. Ishida, T. Nakajima, Y. Honda, O. Itao, H. Nakai, T. Vreven, J.A. Montgomery Jr., J.E. Peralta, F. Ogliaro, M. Bearpark, J.J. Heyd, E. Brothers, K.N. Kudin, V.N. Staroverov, R. Kobayashi, J. Normand, K. Raghavachari, A. Rendell, J.C. Burant, S.S. Iyengar, J. Tomasi, M. Cossi, N. Rega, J.M. Millam, M. Klene, J.E. Knox, J.B. Cross, V. Bakken, C. Adamo, J. Jaramillo, R. Gomperts, R.E. Stratmann, O. Yazyev, A.J. Austin, R. Cammi, C. Pomelli, J.W. Ochterski, R.L. Martin, K. Morokuma, V.G. Zakrzewski, G.A. Voth, P. Salvador, J.J. Dannenberg, S. Dapprich, A.D. Daniels, Ö. Farkas, J.B. Foresman, J.V. Ortiz, J. Cioslowski, D.J. Fox, Gaussian 09, Revision D.01, Gaussian, Inc., Wallingford CT, 2009.
[31] C. Lee, W. Yang, R.G. Parr, Phys. Rev. B 37 (1988) 785.
[32] P.J. Hay, W.R. Wadt, J. Chem. Phys. 82 (1985) 270.
[33] EMSL, basis set library available http:/www.emsl.pnl.gov/forms/basisform.html.
[34] E.M. Kober, T.J. Meyer, Inorg. Chem. 21 (1982) 3967.
[35] B. Valeur, Molecular Fluorescence: Principles and Applications, Wiley-VCH, Weinheim, NY, 2002.
[36] J. Dinda, P.K. Santra, C. Sinha, L.R. Falvello, J. Organomet. Chem. 629 (2001) 28.
[37] S. Mondal, S.P. Rath, S. Dutta, A. Chakravorty, J. Chem. Soc., Dalton Trans. (1996) 99.
[38] M. Panda, C. Das, G.-H. Lee, S.-M. Peng, S. Goswami, J. Chem. Soc., Dalton Trans. (2004) 26.

Source details

Feedback > Compare sources >

Polyhedron

Formerly known as: Journal of Inorganic and Nuclear Chemistry

Formerly known as: Inorganic and Nuclear Chemistry Letters

Scopus coverage years: from 1982 to Present

Publisher: Elsevier

ISSN: 0277-5387

Subject area: Chemistry: Inorganic Chemistry | Materials Science: Materials Chemistry | Chemistry: Physical and Theoretical Chemistry

Source type: Journal

View all documents > | Set document alert | Save to source list

CiteScore 2022
5.4

SJR 2022
0.400

SNIP 2022
0.635

CiteScore | CiteScore rank & trend | Scopus content coverage

Polyhedron 176 (2020) 114277

Contents lists available at ScienceDirect

Polyhedron

journal homepage: www.elsevier.com/locate/poly

The role of methyl and benzyl substituted dithiocarbazate of 2-acetyl pyridine for the formation of bridged dimeric and unbridged monomeric copper(II) complexes and catecholase mimetic activity of the complexes

Ananyakumari Santra [a], Paula Brandao [b], Gopinath Mondal [a], Pradip Bera [a,c], Abhimanyu Jana [a], Indranil Bhattacharyya [a], Chandana Pramanik [a,d], Pulakesh Bera [a,*]

[a] Department of Chemistry, Panskura Banamali College (Autonomous), Panskura R.S, Midnapore (East), West Bengal 721152, India
[b] CICECO, University of Aveiro, 3810-193 Aveiro, Portugal
[c] Kandi College, Murshidabad, West Bengal 742137, India
[d] Department of Chemistry, Dinabandhu Andrews College, Garia, Kolkata, West Bengal 700084, India

ARTICLE INFO

Article history:
Received 7 September 2019
Accepted 1 December 2019
Available online 16 December 2019

Keywords:
Cu(II) complex
X-ray crystallography
London dispersion
DFT
Catecholase activity

ABSTRACT

Monomeric $[Cu(L_1)Cl]$ (**1**) and dimeric $[Cu(L_2)Cl]_2$ (**2**) copper(II) complexes, where HL_1 = methyl-2-(1-(pyridine-2-yl)ethylidene)-hydrazine-1-carbodithioate and HL_2 = benzyl-2-(1-(pyridine-2-yl)ethylidene)hydrazine-1-carbodithioate, have been synthesized and characterized by X-ray crystallography, TGA and spectral methods. Complex **1** crystallizes in a space group *P*21/n and adopts a square planar environment surrounding the Cu ion, and complex **2** is a triclinic crystal system with space group Pī. Complex **2** is a centrosymmetric dimer where each copper atom forms two chloro bridges and completes five coordination with the tridentate NNS donor. Density functional calculations demonstrate that chloro-unbridged structure of **1** is favored by London dispersion between its layers. It is noticed that the layers are usually packed closely in the solid phase, such attractive interactions are sterically hindered between the layers of **2.** Due to the presence of large phenyl group that extend from one layer to the other, the layers cannot slide on top of each other. This leads to the chloro-bridged structure of **2** stabilized by electrostatic interactions between Cu and Cl atoms located at different layers. Both complexes exhibit prominent catecholase activity in methanol following the oxidation of 3,5-di-*tert*-butyl catechol (DTBC) to the corresponding quinone. Based on the observed turn over frequency of **1** (25.19 h^{-1}) and **2** (10.76 h^{-1}), the monomeric complex demonstrates more catechol mimetic oxidation than the dimer. A plausible mechanism of catecholase activity has been discussed.

1. Introduction

Schiff bases derived from S-alkyl/aryl dithiocarbazates are a very important class of NSS chelating agents which allow the formation of stable complexes with a wide range of transition and non-transition metal ions [1–5]. These metal complexes have been shown to exhibit interesting electronic behaviors like non-linear optics [6,7], magnetic [8], electrochemical properties [9] and chemotherapeutic properties [10]. Among the reported complexes, the monomeric complexes are numerous whereas the polynuclear complexes are particularly rare. Recently, dinuclear copper(II) complexes of Schiff bases 2-benzoylpyridine S-methyldithiocarbazate and di-2-pyridyl ketone N(4),N(4)-(butane-1,4-diyl) thiosemicarbazone have been synthesized and structurally characterized [5,11,12]. M. R. P. Kurup reported the synthesis and structural characterization of a dinuclear copper(II) complex of di-2-pyridyl ketone N(4),N(4)-(butane-1,4-diyl) thiosemicarbazone [13]. Very recently Koo reported the structure and chemistry of a dinuclear copper(II) complex derived from mixed ligand of benzoic acid and 2-acetylpyridine/2-benzoylpyridine based benzhydrazide [14]. Both monomer and dinuclear copper(II) entities of 2-pyridinecarbaldehyde thiosemicarbazone have been reported to show antiferromagnetism and nuclease activity [8]. G. Fenteany et al. reported the synthesis and structure activity relationship in the cancer cell proliferation study of both monomer and dimeric complexes of M(II) (M = Cu and Zn)-Schiff's bases derived from 2-acetyl pyridine and S-alkyl dithiocarbazates [2]. The reports on several biological applications such as antimicrobial activity [4], cytotoxicity effect [15,16], biocatalytic [17–19], and antiproliferative [20] have been shown by these class of compounds. Design and synthesis of efficient bio-inspired, environ-

* Corresponding author.
E-mail address: pbera.pbc.chem@gmail.com (P. Bera).

https://doi.org/10.1016/j.poly.2019.114277
0277-5387/

ment friendly catalysts that mimic enzymatic activities are also very crucial in synthetic and supramolecular chemistry. The enzymes active sites are modeled with the metal complexes using the knowledge of redox behavior and coordination chemistry. S-alkyl/aryl derived metal complexes are not frequently modeled though these are bioactive compounds [1–5]. The geometry and the structural features of enzyme active sites and the choice of metal binding can be helpful to establish the structure–function activities in the model experiments [21,22]. Several copper based mononuclear and dinuclear complexes have been modeled to study insight about the mechanism of the biological oxidation process of 3,5-di-*tert*-butylcatechol (DTBC) to 3,5-di-*tert*-butylquinone (DTBQ) [23–26]. Herein, we report the synthesis, characterization and theoretical interpretation in relative stability of a mononuclear copper(II) complex of deprotonated methyl-2-(1-(pyridin-2-yl)ethylidene)hydrazine-1-carbodithioate (HL_1) and a dinuclear dichloro bridged copper(II) complex of deprotonated benzyl-2-(1-(pyridin-2-yl)ethylidene)hydrazine-1-carbodithioate (HL_2), and investigate their ability to catalyze catechol oxidase mimetic activity. The stability of the complexes and their tendency toward chloro-bridged and chloro-unbridged structures were investigated by B3LYP-D3 calculations [27–29].

2. Experimental section

2.1. Materials

Reagent grade metal salts $CuCl_2{\cdot}2H_2O$ was purchased from Merck India and used without further purification. Hydrazine hydrate (99%), carbon disulfide, benzyl chloride, methyl iodide, and 2-acetyl pyridine were purchased from Merck chemical company and used without further purification. Solvent ethanol (Changshu Yangyuan Chemical, China), methanol (Merck, India) and dichloromethane (Merck, India) were dried and distilled before use in the experiment.

2.2. Synthesis of methyl-2-(1-(pyridine-2-yl)ethylidene)hydrazine-1-carbodithioate (HL_1) and benzyl-2-(1-(pyridine-2-yl)ethylidene) hydrazine-1-carbodithioate (HL_2)

The HL_1 and HL_2 were prepared by the condensation of 2-acetyl pyridine with corresponding hydrazine carbodithioate [2,30]. Methyl hydrazine carbodithioate and benzyl hydrazine carbodithioate were synthesized from 99% pure hydrazine hydrate, carbon disulfide, and methyl iodide. The freshly prepared methyl hydrazine carbodithioate (10 mmol, 1.22 g) was refluxed with 2-acetyl pyridine (10 mmol, 1.21 g) in dry methanol for half an hour to obtain methyl-2-(1-(pyridin-2-yl)ethylidene)hydrazine-1-carbodithioate (HL_1). The crude product of HL_1 was crystallized from 1:1 ethanol–water. Yield: 2.01 g (89%). Elemental analyses (%) for $C_9H_{11}N_3S_2$ are C, 47.97; H, 4.92; N, 18.65; S, 28.46%. Found C, 47.69; H, 4.89; N, 18.56; S, 28.48%. Similarly, benzyl-2-(1-(pyridin-2-yl)ethylidene)hydrazine-1-carbodithioate (HL_2) was prepared following the condensation of benzyl hydrazine carbodithioate (10 mmol, 1.98 g) and 2-acetyl pyridine (10 mmol, 1.21 g) in methanol. The crude product thus obtained was crystallized from 1:1 ethanol–water. Yield: 2.57 g (73.79%). Elemental analyses (%) for $C_{15}H_{15}N_3S_2$ are C, 59.77; H, 5.02; N, 13.94; S, 21.27%. Found C, 59.62; H, 4.91; N, 13.85; S, 21.30%.

2.3. Synthesis of copper complexes

Copper(II) complexes **1** and **2** were synthesized by the reaction of the methanolic solution of HL_1 and HL_2 with copper chloride, respectively [2]. Separately HL_1 (10 mmol, 2.25 g) and HL_2 (10 mmol, 3.01 g) were allowed to react with $CuCl_2{\cdot}2H_2O$ (10 mmol, 1.70 g) in methanol. The reaction mixture in each case was stirred for 3 h at room temperature and then refluxed for 2 h in a water bath. In both the cases, solid deep green product was separated out which is filtered and washed with dry methanol. The solid products were dried over silica-gel. A pinch of solid products was taken in 1:1 methanol-DMF and placed the solution in the open air for slow evaporation. Deep blue micro crystals suitable for single crystal X-ray analysis were grown. Yield for **1** is 2.50 g (77.4%). Elemental analyses (%) for $C_9H_{10}N_3S_2ClCu$ (**1**) are C, 33.43; H, 3.12; N, 13.0; S, 19.83%. Found C, 33.39; H, 3.10; N, 13.01; S, 19.88%. Yield for **2** is 6.2 g (77.52%). Elemental analyses (%) for $C_{30}H_{28}N_6S_4Cl_2CuN_6S_4$ (**2**) are C, 45.11; H, 3.53; N, 10.52; S, 16.05%. Found C, 45.01; H, 3.47; N, 10.45; S, 16.08%.

2.4. Characterization

FISONS EA-1108 CHN analyzer was used for elemental analysis (C, H, N, and S) of the ligands and complexes. The FTIR spectra (4000–500 cm^{-1}) were recorded on a Perkin Elmer Spectrum Two FT-IR Spectrophotometer with sample prepared as KBr pellets. Mass spectra of ligands were obtained using a Waters HRMS XEVO-G2QTOF#YCA351. Thermogravimetric analysis was performed using Perkin Elmer Thermal Analyzer TGA4000 instrument at a heating rate 20 °C/min under nitrogen atmosphere. The X-band electron paramagnetic resonance (EPR) spectrum was recorded in a Bruker EMX X-band spectrometer operating at a field modulation of 100 kHz, modulation amplitude of 7 G and microwave radiation power of 10 mW at room temperature. The single crystal X-ray diffractions of complex **1** and **2** were carried out on a Bruker SMART APEX II X-ray diffractometer equipped with graphite-monochromated Mo-Kα radiation (λ = 0.71073 Å) and 16 CCD area detector. The intensity data were collected in the π and ω scan mode, operating at 50 kV, 30 mA at 296 K [31]. The data reduction was performed using the SAINT and SADABS programs [32]. All calculations in the structural solution and refinement were performed using the Bruker SHELXTL program [33]. The structure was solved by the heavy atom method and refined by full-matrix least-squares methods. All the non-hydrogen atoms were refined anisotropically; the hydrogen atoms were geometrically positioned and fixed with isotropic thermal parameters. The final electron density maps showed no significant difference.

The catecholase activities of **1** and **2** were examined by the reaction of 100 equivalents of 3,5-di-*tert*-butylcatechol (DTBC) with 1×10^{-5} M solutions of the complexes under aerobic conditions at ambient temperature in methanol. The reaction was followed spectrophotometrically by monitoring the growth of the absorbance as a function of time at *ca.* 400 nm which is characteristic of 3,5-di-*tert*-butylquinone chromophore. To determine the dependence of the rate of the reaction on substrate concentration and to evaluate various kinetic parameters, 1×10^{-5} M solutions of the complexes were mixed with at least 10 equivalents of the substrate to maintain pseudo-first order condition. To check the rate dependency on catalyst concentrations similar set of experiments were performed at a fixed concentration of substrate with various catalyst concentrations. The rate of a reaction was determined by the initial rate method, and the average initial rate over three independent measurements was recorded.

2.5. Computational details

All calculations were performed with the ORCA 4.0 program package [34,35] by using def2-TZVP and its matching auxiliary basis sets [36,37]. The structures were fully optimized at the unrestricted Kohn-Sham B3LYP [27–29] level of density functional theory (DFT) calculations incorporating the atom-pairwise dispersion

correction (D3) with Becke–Johnson damping (BJ) [38], i.e., UB3LYP-D3(BJ), within the resolution of identity (RI) approach RIJ-COSX [39,40]. The effect of methylene solution on the energetics was assessed implicitly at the same level of theory through the conductor-like polarizable continuum model (C-PCM) [41].

The molecular docking was carried out using AUTODOCK 4.0 software as accomplished by the graphical user interface AUTODOCK TOOLS 4.0 (AD4.1_bound.dat). The macro cyclic receptor was choosing as PDB formed of three dimensional x-ray crystals structure of a Truncated ErbB2 Ectodomain Reveals an Active Conformation (entry 2A91 in the Protein Data Bank). The graphical user interface AUTODOCK TOOLS was devoted to setup the protein: water molecule was deleted from the crystal of protein, only polar hydrogen were added, computed gasteigers charge was calculated as −10.998 and non polar hydrogen were merged to carbon atom. Complexes 3D structures were saved in PDB format with the aid of the program MERCURY. The AUTODOCK TOOLS program was used to make docking input file. A grid box size for complex **1** is 83 × 85 × 83 and complex **2** is 74 × 74 × 82 with grid spacing 1 Å. Both receptor and complex were save pdbqt format. A distances-dependent functions of the dielectric constant were used for the calculation of the energetic map. Ten runs were generated by using Lamarckian genetic algorithm searches. Default settings were used with an initial population of 50 randomly placed individuals, a maximum number of $2.5x10^6$ energy evaluations [42]. Final docking was run with autogrid4.exe and autodock4.exe function to generate glg and dlg files respectively. The graphical interactions picture were found using Schrodinger software.

3. Result and discussion

3.1. Chemistry

Ligands have a proton adjacent to the thiocarbonyl group and consequently can exhibit thione-thiol tautomerism (Scheme 1). Mostly the structure of the reported complexes derived from Schiff bases of S-alkyl/aryl dithiocarbazate adopted monomeric structure [1–5]. The formation of the monomer from methyl ester (HL_1) and dimer from benzyl ester (HL_2) of dithiocarbazic acid suggest that SR group has a pronounced effect on nuclearity and structure of the complexes. Mass spectra of **1** and **2** show *m*/*z* value 286.96 and 363.02, respectively, which correspond to a highly unsaturated $[ML]^+$ species (Fig. S1 for **1** and Fig. S2 for **2**). The $[CuL_1]^+$ from **1** is further attached with another NNS donor (L_1) to satisfy its maximum coordination number (6) forming $[Cu(L_1)_2]^+$ giving *m*/*z* value 509. In the mass spectrum of **2**, no peak equivalent to the dichloro-bridged complex is obtained but a peak *m*/*z* value 763.21 is observed which can be assigned as the chloro-bridged complex, $[Cu_2(L_2)_2Cl]^+$. Solid state FTIR spectra analysis was performed to determine the coordination mode of the ligand with the copper (II) ion (Fig. S3). The FTIR spectra do not display any ν_{S-H} band at *ca.* 2600 cm^{-1}, but exhibit ν_{NH} bands in the range 3100–3200 cm^{-1} indicating that the ligands remain in the thio-keto tautomer in the solid state. The significant differences in spectral data were analyzed by comparing the spectra of the complexes with the corresponding ligand shown in Table S1. The $\nu_{NH/NH2}$ stretching vibrations of the ligand HL_1 and HL_2 appeared at 3138 and 3154 cm^{-1}, respectively. These higher frequency peaks are not observed in the complex indicating the involvement of primary or secondary amine during the complexation. The observed ν_{C-N}, $\nu_{C=N}$ and $\nu_{C=S}$ stretching frequencies of the corresponding ligand and complexes appear at the range of 1408–1496 cm^{-1}, 1585–1708 cm^{-1} and 770–784 cm^{-1}, respectively. The characteristic stretching frequencies of $\nu_{C=N}$ and $\nu_{C=S}$ shifted to higher frequencies upon complexation indicating the coordination of nitrogen and sulfur atoms to the copper(II) ion [43].

3.2. TGA analysis

As can be seen in Fig. 1, the decomposition profile of the ligand HL_1 and HL_2 are very similar. Both are stable up to 150 °C and major decomposition occurs between 150 °C and 330 °C. The first step of decomposition is attributed to the loss of the SR unit. Almost all the organics evaporates completely at 300 °C. The decomposition profile proves that ligands are quite suitable for the formation of stable complexes. Complexes (**1** and **2**) also decomposed following very similar decomposition pattern. Both **1** and **2** are stable up to 250 °C. A weight loss about 14.5% and 15.4% correspond to the loss of one unit of SCH_3 and one unit SCH_2-Ph in **1** and **2**, respectively. Complex **1** starts decomposition at 220 °C. In the first step of decomposition 15 unit mass loss corresponds to a loss of CH_3 from SCH_3 of the ligand. The major loss of organics and coordinate Cl atom occur between 250 °C and 350 °C. If heating is continued more than 800 °C the gradual weight loss will happen until CuS (29.53%) is obtained i.e., leading to the formation of CuS. The analysis indicated that complex **1** is a suitable single-source precursor for CuS particle synthesis.

3.3. EPR spectroscopy

The EPR spectroscopy is a powerful tool to study the electronic and magnetic properties of the metal center. Generally Cu(II) complexes are distorted octahedral geometry (tetragonal or rhombic). An axially symmetric more intense peak at higher field ($g_{\|}$) and

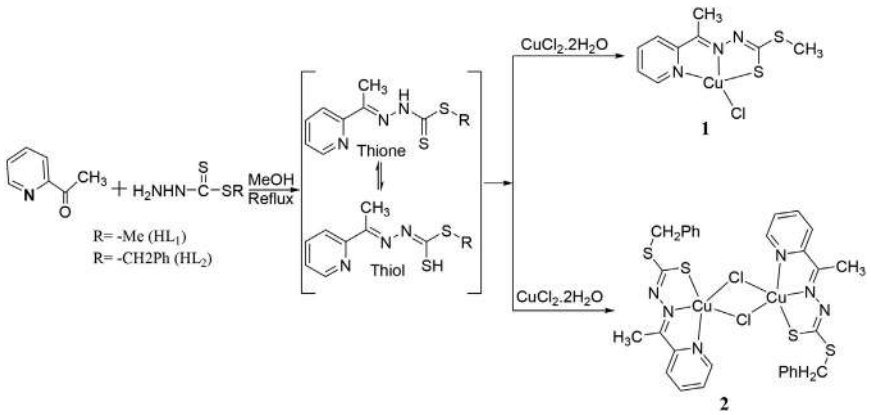

Scheme 1. Formation pathway of HL_1, HL_2, 1 and 2.

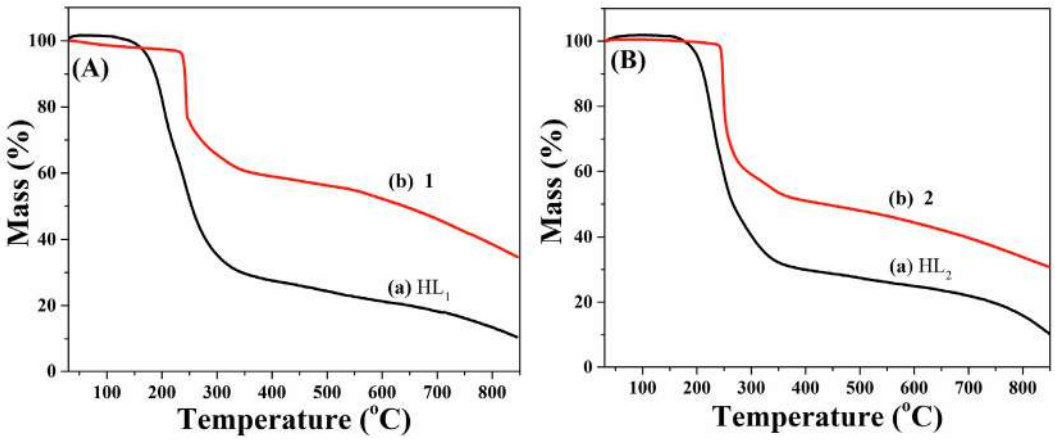

Fig. 1. Thermogravimetry analysis of HL_1 and **1** (A); HL_2 and **2** (B).

low intense peak at lower field ($g^{\perp}$) are observed for Cu(II) complexes [44]. The X-band EPR spectrum of the solid SP1 sample at RT shows classical resonance bands of axial symmetry with $g_{\parallel}$ = 2.097 (A = 91 G) and $g^{\perp}$ = 2.047 as shown in Fig 2.

A rhombic distorted EPR spectrum is observed for the solid SP2 sample at RT with $g_{\parallel}$ = 2.12 and $g^{\perp}$ = 2.06 without any signature of nuclear coupling between two copper(II) ions. So, it can be concluded that the unpair electron is highly localized in d_{x2-y2} orbital of Cu(II) ion. The similar results are also found in the literature [45,46].

3.4. Single crystal X-ray analysis

To establish the structure and coordination environment of the synthesized complexes single crystal X-ray analysis of the complexes were performed. The crystal refinement data of the reported complexes are given in Table 1. An ORTEP view of **1** with atom leveling scheme of the independent past is shown in Fig. 3 and a selection of bond angles and length is given in Table 2 and Table 3. The metal ion in **1** possesses approximate square planer geometry with pyridinyl nitrogen donor, an imine nitrogen donor and sulfur atom of cabodithioate unit, and a chloride ion. Complex **1** is a monomeric complex and crystallizes in the monoclinic P 21/n space group in approximate square planer geometry. Bond angles N1–Cu–N2, N2–Cu–S1, N1–Cu–Cl1 and Cl1–Cu–S1 are 80.06(4)°, 84.69(3)°, 97.32(3)° and 97.81(2)°, respectively (Table 2) whereas N1–Cu–S1 and Cl1–Cu–N2 angles are 176.53(3)° and 164.50(3)°, respectively. The measured dihedral angle 3.24° corresponds to Cu-S1-C8-N3-N2 and Cu-N2-C6-C5-N1 planes to a planer geometry

Table 1
Crystal refinement parameters of the complexes **1** and 2.

	1	**2**
CCDC	1833374	1833376
Moiety formula	$C_9H_{10}ClCuN_3S_2$	$C_{30}H_{28}Cl_2Cu_2N_6S_4$
Mr	323.31	798.82
a(Å)	8.1368(11)	7.9812(11)
b(Å)	8.7126(10)	8.4000(11)
c(Å)	17.106(2)	13.8741(18)
α(°)	90	93.512(4)
β(°)	101.547(4)	106.006(4)
γ(°)	90	113.715(4)
Crystal system	monoclinic	Triclinic
Volume (Å^3)	1188.2(3)	802.77(19)
Space group	*P*21/n	P ī
Z	4	1
F (0 0 0)	652.0	406.0
Dcalc (g cm^{-3})	1.807	1.652
Absorption coefficient / μ(mm^{-1})	2.387	1.784
h,k,l	11,12,24	10,11,19
2θ	61.15	58.58
Reflections I > 2σ(I)	3349	3595
Total reflections I > 2σ(I)	3645	4332
R1(I > 2σ(I))	0.0206	0.0444
w*R2*(all reflections)	0.0551	0.1192
goodness_of_fit	1.057	1.079
Residuals (e.Å3)	0.471/-0.585	1.288/-0.972

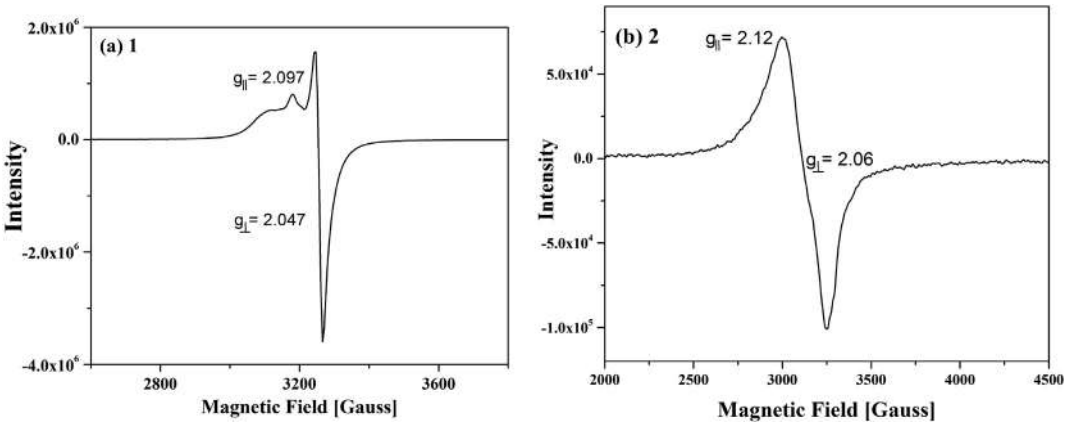

Fig. 2. Soilid state EPR spectrum of 1 (a) and 2 (b).

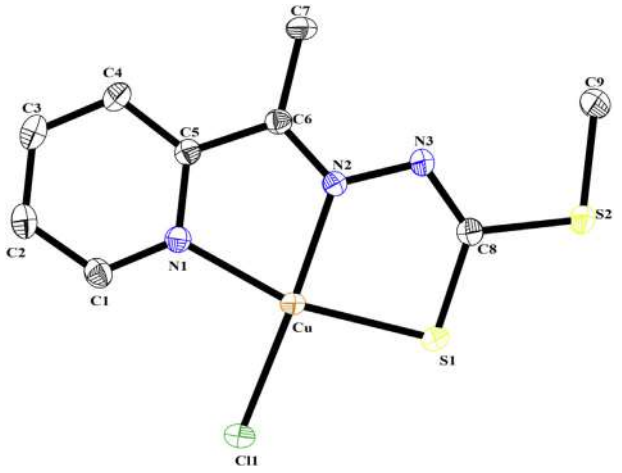

Fig. 3. ORTEP picture of the complex **1**. Thermal ellipsoids are drawn at the 55% probability label. For the clarity of the structure hydrogen atoms have been omitted. Structure truncated to highlight the ligand–metal bonding geometry.

Table 2
Selected bond lengths of **1** and **2**.

Atoms	**1** Length (Å)	**2** Length(Å)
Cu–Cl1	2.2166(5)	2.2595(8)
Cu–S1	2.2615(4)	2.2659(7)
Cu–N1	2.031(1)	2.032(2)
Cu–N2	1.960(1)	1.966(2)
Cu–Cl1′	–	2.711(1)
S1–C8	1.737(1)	1.734(3)
S2–C8	1.744(1)	1.747(3)
S2–C9	1.801(1)	1.830(3)
N1–C1	1.337(2)	1.337(4)
N1–C5	1.357(2)	1.359(3)
N2–N3	1.384(1)	1.391(3)
N2–C6	1.296(1)	1.299(3)
N3–C8	1.305(1)	1.311(3)

Symmetry code for Cl1′ = 1 − x, 2−y, 1−z.

Table 3
Selected bond angles of **1** and **2**.

Atoms	**1** Angle (°)	**2** Angle (°)
Cl1–Cu–S1	97.81(2)	96.63(3)
Cl1–Cu–N1	97.32(3)	97.08(7)
Cl1–Cu–N2	176.53(3)	171.69(8)
S1–Cu–N1	164.50(3)	162.35(7)
S1–Cu–N2	84.69(3)	84.73(7)
N1–Cu–N2	80.06(4)	80.1(1)
Cu–S1–C8	94.16(4)	94.0(1)
Cu–N1–C1	127.89(9)	128.0(2)
Cu–N1–C5	112.86(8)	112.6(2)
Cu–N2–N3	122.93(8)	122.8(2)
C8–S2–C9	102.59(6)	–
S1–Cu–Cl1	–	101.26(3)
N1–Cu–Cl1	–	89.62(7)
N2–Cu–Cl1	–	96.97(7)
Cu–N2–C6	118.60(8)	
Cu–Cl1–Cu	–	89.19(3)
N3–N2–C6	118.4(1)	–
Cl1–Cu–Cl1	–	90.81(3)

which confirms nearly square planar geometry of the complex with τ4 value 0.9. There is no H-bonding interaction but strong aromatic-π and chelate-π (3.432 Å/3.567 Å) interaction form a supramolecular arrangement (Fig. 4). The calculated offset angle between two centroids planes is 2.12°. The selective bond lengths Cu–N1, Cu–N2, Cu–Cl1 and Cu–S1 are 2.031(1)°, 1.960(1)°, 2.2166 (5)° and 2.2615(4)°, respectively, as shown in Table 3. The similar length and angle of bis-chelated complexes of a dithiocarbazate N, S Schiff base ligand were observed [47]. The relatively shorter bond lengths of copper-nitrogen i.e., Cu–N1 (2.031 Å) and Cu–N2 (1.960 Å) than the reported copper(I) complexes are strongly suggesting the presence of copper in +2 state in the reported complexes [48]. The corresponding Cu^{+2}–N bond lengths (2.073 and 2.019 Å) of **1** calculated presently at the UB3LYP-D3 level are also quite consistent with the X-ray values. The corresponding BVS (Bond Valence Sum) calculation is also supportive to planar structure with 2.26 (Table S2).

In the presence of copper(II) chloride salt ligand HL_2 furnished a chloro-bridged binuclear Cu(II) complex. Fig. 5 shows the single crystal X-ray structure of the complex **2**. It has a triclinic crystal system with Pī space group. In complex 2, the two symmetry related copper atoms exhibit a penta coordinated bridged environment. The uninegative L2 ligand coordinate the copper atom through the pyridinyl N, imine N and thiolato sulfur donors and the two copper atoms are connected by a pair of chloride bridge. Of the doubly bridging Cl atoms, one occupies the basal plane and the other is located at the apical position of the square pyramidal geometry, indicated by the index τ5 value 0.2 [49,50]. The Cu–N1 and Cu–N2 bond lengths of **2** are 2.032(2) Å and 1.966(2) Å, respectively. These are analogous to the respective bond lengths of **1**, and thus are consistent with the + 2 oxidation state of copper atoms. The higher value of Cu–Cl1 bond (2.2595Å) in **2** is due to the Jhan-Teller distortion in d^9 system. The UB3LYP-D3 calculations on the dimeric **2** find the corresponding Cu^{+2}–N bond lengths as 2.064 and 2.006 Å, which are consistent with the X-ray values revealing oxidation state + II. The BVS value (2.17) of **2** is also supportive the + 2 oxidation state of copper (Table S2). In the complex, strong aromatic-π ↔ chelate-π (3.558 Å) and chelate-π ↔ chelate-π (3.618 Å) interaction make a stable supramolecular array shown in Fig. 6. The calculated offset angle between two centroids planes is 6.08°.

3.5. Computational results

1 and **2** have monomeric and dimeric chloro-bridged structures in their single crystals, respectively. Computationally, both the monomeric and dimeric structures for both complexes in the gas phase and in the solution can be obtained to access the experimen-

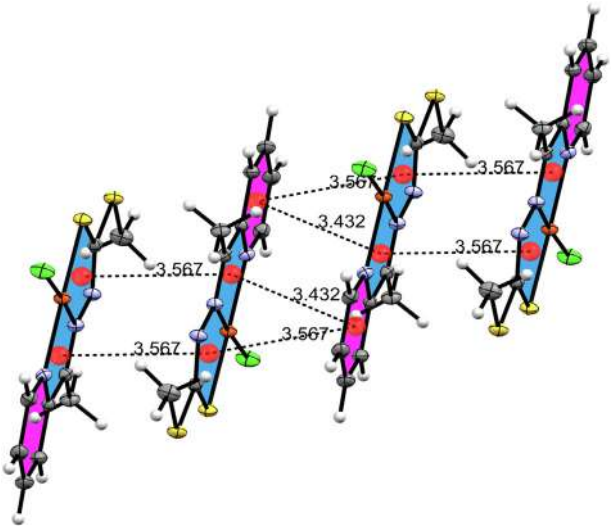

Fig. 4. Aromatic-π and chelate-π interactions in complex **1**.

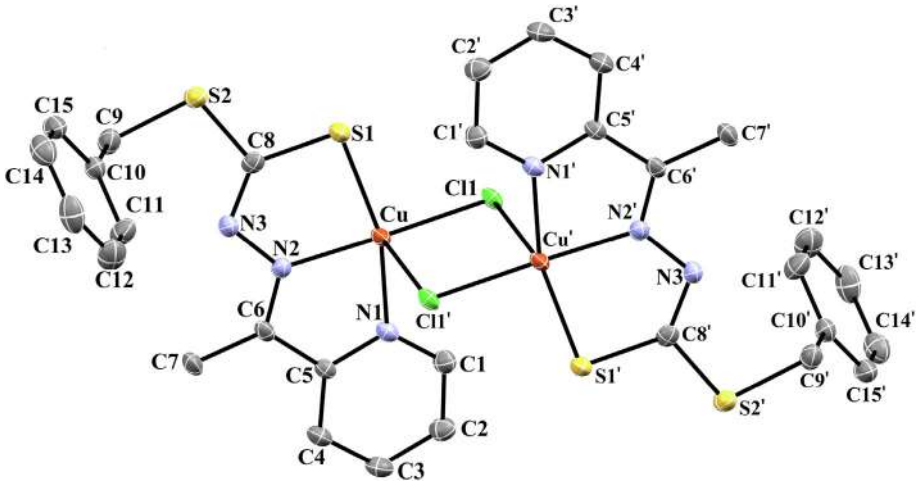

Fig. 5. ORTEP diagram of **2**. Thermal ellipsoids are drawn at the 55% probability label. For the clarity of the structure hydrogen atoms have been omitted. Structure truncated to highlight the ligand–metal bonding geometry.

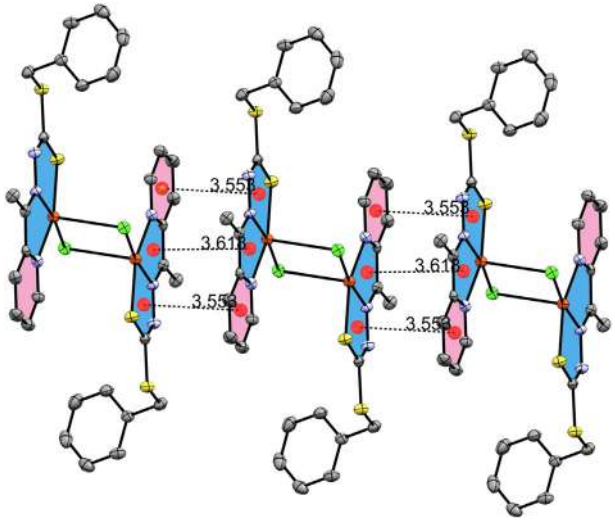

Fig. 6. Aromatic-π and chelate-π interactions in **2**.

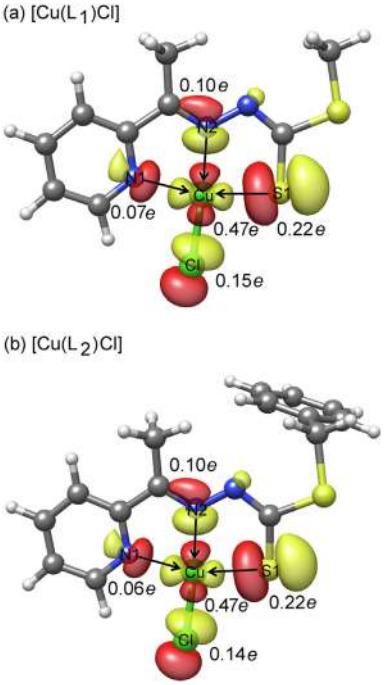

Fig. 7. Singly-occupied orbital of monomeric **1** and **2** and the associated atomic Mulliken spin densities calculated at the UB3LYP.

tal preference of one structure over the other. In this study, the stability of the monomeric and dimeric complexes of **1** and **2** has been investigated by the UB3LYP-D3 calculations. As shown in Fig. 7, the monomeric structures of **1** and **2** have one-unpaired electron (doublet state), which is primarily located on the $CuCl^{+}$ moiety (with largest spin density on the Cu^{+2} ion), consistent with the results on analogous Cu(II) complexes [51]. The coordinating atoms S1, N1, and N2 have also noticeable spin densities.

The single unpaired electron of monomeric **1** and **2** can couple in the dimeric structures in parallel and anti-parallel configurations, yielding triplet and open-shell singlet spin states, respectively. The triplet states of the dimers of both **1** and **2** (1 kcal/mol) are more stable than the singlet states at the UB3LYP level. The smallness of the singlet–triplet energy gap is consistent with the previous studies on analogous Cu(II) complexes [52]. The spin density distributions of all dimeric structures are identical to those of the monomeric structures. However, as expected, in the open-shell singlet state of the dimeric structures, atomic spin densities have opposite signs on both fragments. Therefore, we do not provide them additionally in Fig. 7. As seen in Table 4, the gas-phase UB3LYP calculations find almost the same binding energies with both ligands (~−255 kcal/mol). The stabilizing dispersive interaction components of the binding energy are noticeable (~−10 kcal/mol) but much smaller than the overall binding energy. Although methanol weakens the interaction greatly (~115 kcal/mol), the coordination of the ligands to $CuCl^{+}$ is still strong in solution (~−152 kcal/mol). As the ligands coordinate to the $CuCl^{+}$ ion with nearly the same energies, their preference to monomeric and dimeric structure formation cannot be assigned to the differences in their electronic structure.

To shed light on the dimerization process of [Cu(L_1)Cl] and [Cu(L_2)Cl] complexes, first we optimized the geometry of the chloro-bridged [Cu(L_2)Cl]$_2$ complex at the UB3LYP-D3 level by taking the initial coordinates from the present X-ray structure. It should be noted here that other stable dimeric structures can be obtained when the initial orientations of the two layers are different. However, our aim is not to explore conformational space of the dimers

Table 4
The calculated binding energies (ΔE, kcal/mol) for the interaction of the $CuCl^+$ ion with the anionic L_1 and L_2 ligands and for the interaction of the two identical $[Cu(L_1)Cl]$ and $[Cu(L_2)Cl]$ complexes together with their individual components for UB3LYP level bare gas-phase interaction (ΔE_{UB3LYP}), its D3-level dispersion correction ($\Delta E_{D3\text{-}disp}$), and UB3LYP level solvent effect ($\Delta E_{UB3LYP\text{-}solv}$).

	ΔE	ΔE_{UB3LYP}	$\Delta E_{D3\text{-}disp}$	$\Delta E_{UB3LYP\text{-}solv}$
Doublet monomer				
$[L1^-\cdots CuCl^+]$	−151.7	−258.3	−10.0	116.5
$[L2^-\cdots CuCl^+]$	−151.4	−255.4	−10.9	114.9
Triplet dimer				
$[Cu(L_1)Cl]\cdots[Cu(L_1)Cl]$	−21.0	0.2	−33.1	11.9
$[Cu(L_2)Cl]\cdots[Cu(L_2)Cl]$	−16.6	−10.8	−19.0	13.2
Singlet dimer				
$[Cu(L_1)Cl]\cdots[Cu(L_1)Cl]$	−18.4	1.4	−31.0	11.2
$[Cu(L_2)Cl]\cdots[Cu(L_2)Cl]$	−16.7	−11.7	−17.3	12.2

but to assess the factors that differentiate the preference of the ligands towards chloro-bridged and chloro-unbridged structures when the layers are initially oriented parallel as in the X-ray structure of $[Cu(L_2)Cl]_2$. The optimized coordinates of $[Cu(L_2)Cl]_2$ are consistent with the X-ray coordinates. As can be seen in Fig. 8(a), the chloro-bridged crystal structure of $[Cu(L_2)Cl]_2$ is preserved.

By replacing the two SCH_2Ph moieties of the X-ray structure of $[Cu(L_2)Cl]_2$ with the SCH_3 moieties, we obtained initial coordinates for the chloro-bridged $[Cu(L_1)Cl]_2$ complex. However, the two layers in the initial coordinates of the $[Cu(L_1)Cl]_2$ complex slide over each other during geometry optimization due to strong attraction between Cl atom and methyl group of 2-acetyl pyridine belonging to different $[Cu(L_1)Cl]$ layers, as seen in Fig. 8(b). Therefore, the chloro-bridged structure is not preserved for the $[Cu(L_1)Cl]$ dimer. The resulting computational structure of this dimer is consistent with the X-ray structure shown in Fig. 5. Since SCH_3 moiety of L_1 is small, the $[Cu(L_1)Cl]$ layers can slide on top of each other easily.

The same type of strong interaction is also expected for $[Cu(L_2)Cl]$ dimer. However, the size of the phenyl moiety is larger than the distance between the $[Cu(L_2)Cl]$ layers. Therefore, the $[Cu(L_2)Cl]$ layers cannot slide on top of each other despite the strong attraction between Cl atom and methyl group of 2-acetyl pyridine, which leads chloro-bridged $[Cu(L_2)Cl]_2$ structure. Methanol solution

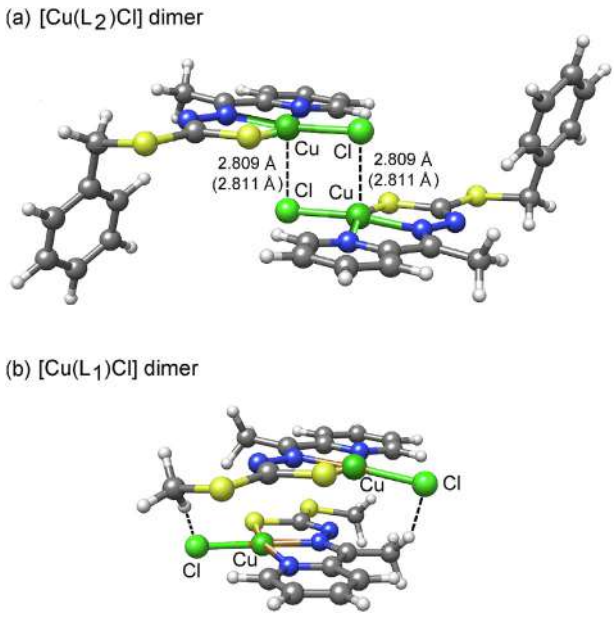

Fig.8. B3LYP-D3 optimized structure of $[Cu(L_2)Cl]_2$ starting from its X-ray coordinates, and of $[Cu(L_1)Cl]_2$ starting from the X-ray coordinates of $[Cu(L_2)Cl]_2$ after replacing both SCH_2Ph moieties with SCH_3 moieties.

weakens the interaction energy of the two layers of the dimeric structures by ~12 kcal/mol. In the absence of solution, the gas-phase UB3LYP-D3 interaction energy of the layers with both ligands are ~−30 kcal/mol (the sum of UB3LYP and D3 contributions in Table 4). The interaction between the two layers of $[Cu(L_1)Cl]_2$ is slightly repulsive without dispersion contribution. Therefore, the chloro-unbridged $[Cu(L_1)Cl]_2$ structure is driven mainly by the favored London dispersion in addition to the stabilizing electrostatic interaction between the Cl and CH_3 moieties of the two layers. Methyl group is already well known as a dispersion energy donor [53].

The interaction between the two layers of the chloro-bridged $[Cu(L_2)Cl]_2$ is already strong (~−12 kcal/mol) without dispersion contribution at the UB3LYP-D3 level, owing to the strong electrostatic interaction between the two CuCl moieties. The dispersion contribution in the chloro-bridged $[Cu(L_2)Cl]_2$ is also significant but ~10 kcal/mol smaller than that in the chloro-unbridged $[Cu(L_1)Cl]_2$.

These indicate that the stabilities of both chloro-bridged and chloro-unbridged structures are governed largely by the electrostatics and London dispersion. When the layers cannot slide on top of each other due to the large size of the SCH_2Ph tail of the L_2 ligand, electrostatic interaction between the two layers becomes the main stabilizing effect through the formation of the chloro-bridged structure, followed by London dispersion. However, with L_1 ligand having small SCH_3 tail, the Cl and CH_3 moieties of the two layers are attracted to each other due to strong dispersion interaction, which breaks the chloro-bridge.

3.6. Catechol oxidase mimetic activity

Catechol oxidases are ubiquitous plant enzymes containing a dinuclear copper center. To study the catalytic mechanism model complexes **1** and **2** catalyze the oxidation of 3,5-di-^{t}butyl catechol (DTBC) to 3,5-di-*tert*-butyl-*o*-quinone (DTBQ) coupled with the reduction of oxygen to hydrogen peroxide. DTBC has lower redox potential that facilitates the oxidation of DTBC and the bulky substituent prevents further reactions such as ring-opening process. Here we introduced analogous copper complexes of NNS donor ligands (**1** and **2**) to check the catecholase activity in the air. The presence of the labile group (Cl) makes metal centre susceptible to ligand's substitution. Various approaches have been reported by a different group to investigate the mechanism pathway of DTBC oxidation by model copper complexes [54,55]. The product DTBQ is quite stable in air and has a characteristic transition at about 400 nm and therefore the catalytic study can be monitored by UV–Vis spectrophotometry. Reactivity and kinetic studies were performed in methanol because of the good solubility of the complexes, substrate and their product in this solvent. Before going to the detailed kinetic investigation, it is first necessary to check the

ability of the complexes to behave as catalysts for the catechol oxidase mimetic activity. Accordingly, 1.0×10^{-5} M solutions of the complexes were treated with a 200-fold concentrated solution of DTBC, and the spectra were recorded up to 1.5 h in dioxygen saturated methanol at room temperature. The time dependent spectral changes for a period of 1.5 h after the addition of DTBC are displayed in Fig. 9 for **1** and **2**. The spectral scan reveals the increase of the band intensity at *ca.* 400 nm characteristic of quinine chromophore for both complexes although a blank experiment using copper chloride salt instead of the complexes did not show significant spectral growth. These results suggest that **1** and **2** are active towards the catecholase activity.

The initial rate of reactions versus concentration of the substrate data show a first-order rate dependence on the substrate concentration at lower concentrations of DTBC but almost zero order at the higher concentrations (Fig. 10). This observation suggests that quinone formation proceeds through a relatively stable intermediate, a complex-substrate adduct, followed by the irreversible redox transformation of the intermediate at the rate determining step. In this regard, the Michaelis-Menten model is helpful to explain the rate saturation kinetics on the concentration of the substrate. The observed initial rates versus substrate concentration plot and the Lineweaver–Burk plot for both complexes are shown in Fig. 11. Analysis of the experimental data produced Michaelis binding constant (K_M) values of 1.733×10^{-4} M for **1** and 1.01×10^{-3} for **2** and V_{max} values of 6.999×10^{-8} M s^{-1} and 2.991×10^{-8} M s^{-1} for **1** and **2**, respectively (Table 5). The turnover frequency (K_{cat}) value is obtained by dividing the V_{max} by the concentration of the catalyst used and is found to be 25.19 and 10.76 h^{-1} for **1** and **2**, respectively. Previous studies on catecholase activities of copper complexes showed wide range of k_{cat} values 1 to 9471 h^{-1} [44]. The observed k_{cat} values of 25.19 h^{-1} for **1** and 10.76 h^{-1} for **2** are comparable to those with moderate catecholase activities [54–56].

The mass spectra of complexes with DTBC are performed to establish the possible mechanism catalytic oxidation. The plausible catalytic cycle is given in Scheme 2. Mass spectra of monomer (**1**) and dimer (**2**) in $CDCl_3$ show the existence of $[ML]^+$ species which can be attributed to the formation of the highly solvated intermediate product following a dissociative mechanism. The peaks corresponding to $[CuL]^+$ are observed at *m*/*z* 287.5 (Fig. S1) and *m*/*z* 363.91 (Fig. S2) for **1** and **2**, respectively. An intense peak with *m*/*z* value 509 in **1** is also observed which can be assigned as $[Cu(L_1)_2]^+$. The formation of stable $[Cu(L_1)_2]^+$ is the result of the reorganization of $[CuL]^+$ with another ligand unit through solvent displacement mechanism. The intermediate $[CuL]^+$ activates

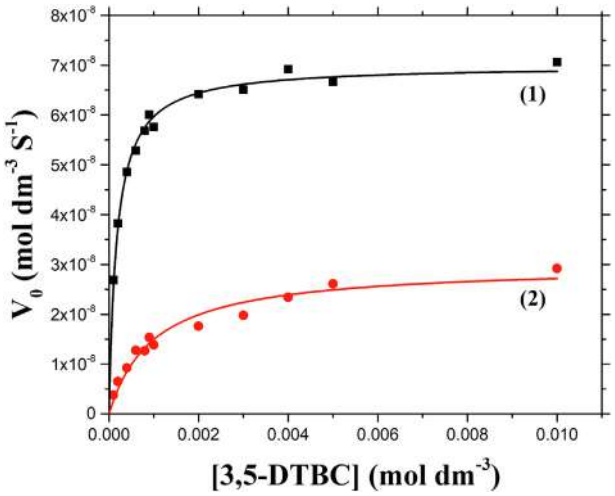

Fig. 10. Initial rate versus substrate concentration plot for the oxidation of 3.5-DTBC in air-saturated methanol catalyzed by the complexes at room temperature. Symbols and solid lines represent the experimental and simulated profiles, respectively.

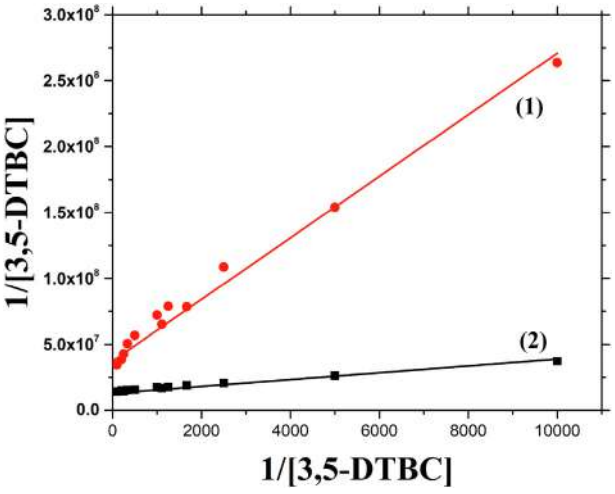

Fig. 11. Line weaver–Burk plots for the oxidation of 3,5-DTBC catalyzed by **1** and **2** in methanol. Symbols and solid lines represent the experimental and simulated profiles, respectively.

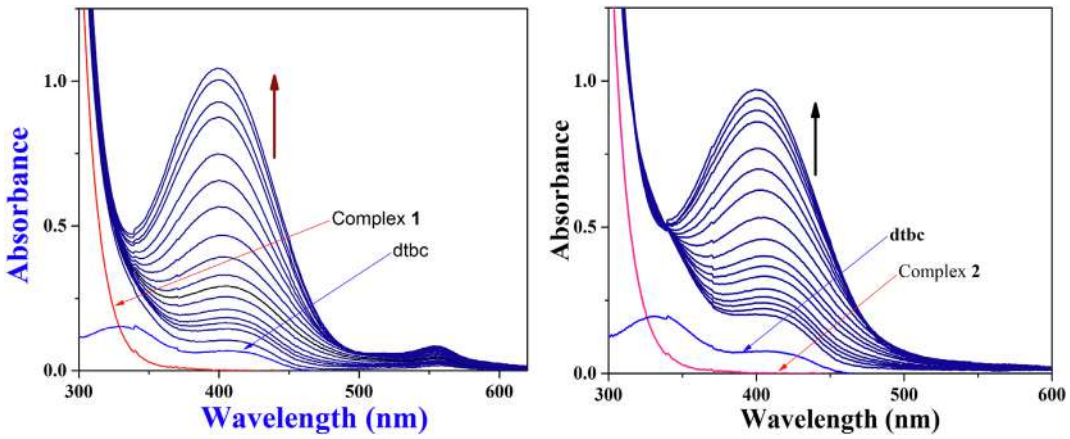

Fig. 9. The spectral profile showing growth of 3,5-DTBQ at 400 nm upon addition of 0.001 M 3,5-DTBQ to a solution containing **1** (1×10^{-5} M) in methanol. The spectra were recorded in 5 min time interval in aerobic condition at room temperature.

Table 5
Kinetics data and k_{cat} values of **1** and **2.**

Substrate	Catalyst	V_{max}	K_m	Slope	Intercept	$k_{cat}(h^{-1})$
3,5-Di-tButyl catechol [3,5-DTBC]	1	6.9999×10^{-8}	1.733×10^{-4}	2581.535	1.28699×10^{7}	25.19
	2	2.991×10^{-8}	1.01×10^{-3}	23346.928	3.73406×10^{7}	10.76

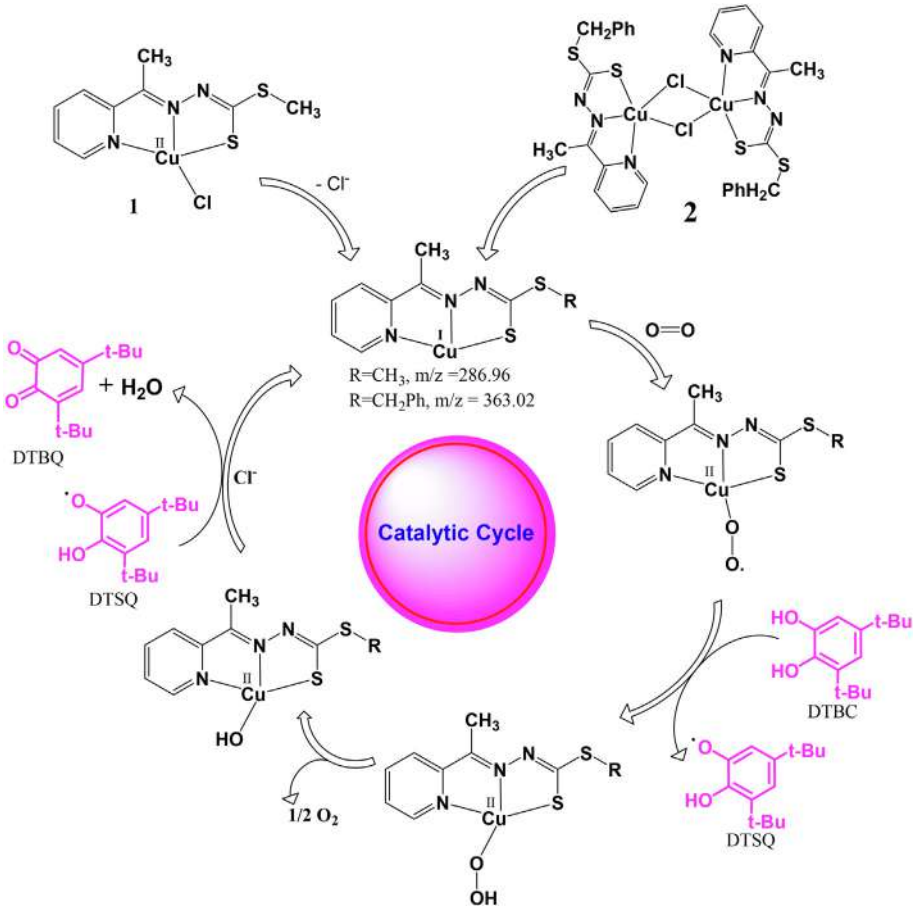

Scheme 2. Plausible mechanistic pathway for the oxidation of 3,5-DTBC by dioxygen in presence of catalyst complex **1** or complex **2**.

molecular oxygen. In the process of oxygen activation DTBC is transform to DTSQ (ditertiary butyl semiquinone) (Scheme 2). The peak corresponding to intermediate adduct [Cu(L)(DTBC)(O_2)] in the course of catalytic transformation are observed in the mass spectra of **1** and **2** in DTBC at *m*/*z* 539.12 (Fig. S4) and *m*/*z* + Na 639.40 (Fig. S5), respectively indicating the adduct formation between substrate, catalyst, and molecular oxygen. The catecholase activity of **1** is 2.5 times greater than the **2**. The low activity of **2** may be due to the high activation energy required to form $[CuL]^+$ intermediate breaking a dichloro dimeric structure. This fact is also supported by the weak dispersion interaction in the [Cu(L_2)Cl] layers due to the largeness of the phenyl moiety of L_2.

3.7. Molecular docking study

The binding mode of **1** and **2** with protein surface are shown in Figs. 12 and 13, respectively where the interactions of **1** and **2** with protein surface model are shown in Figs. 14 and 15 , respectively. The results indicate that complexes under investigation are well fitted in the active pocket of the protein molecule. Complex **1** exerts hydrophobic interaction with THR269, ARG267, VAL251, ALA249, CYS247, ASP286, VAL287, GLY288 and one hydrogen bonding interaction with LEU250 base pair of protein chain [57]. The free binding energy with protein is −5.52 kcal/mole and inhibition constant, Ki = 90.23 μM [at 298.15 K]. The calculated

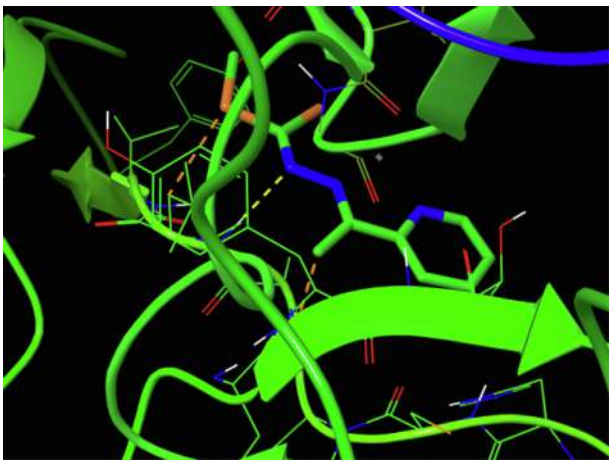

Fig. 12. Binding mode of **1** with Truncated ErbB2 Ectodomain. The protein was shown in surface. Complex was shown in sticks.

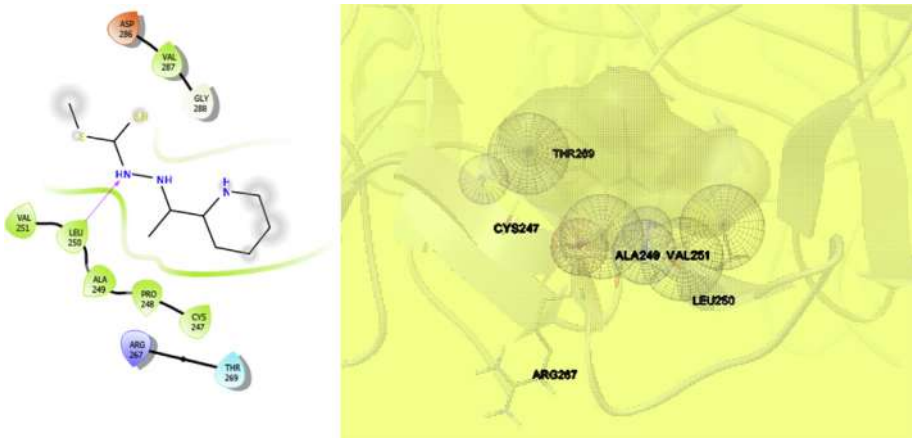

Fig. 13. Binding mode of **1** with Truncated ErbB2 Ectodomain. The protein was shown in surface. Complex was shown in solid sphere.

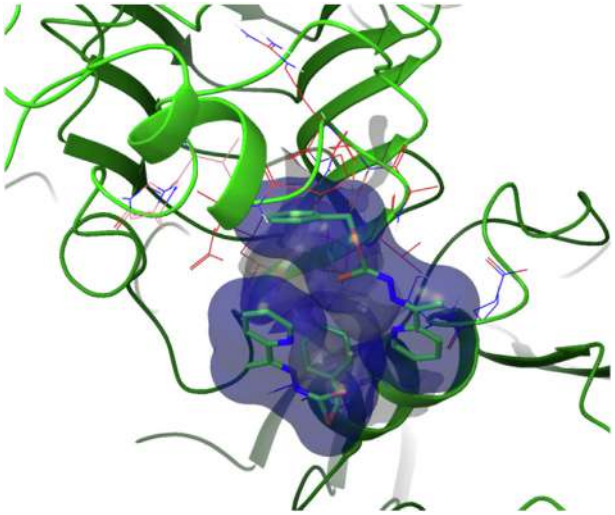

Fig. 14. Hydrophobic and hydrogen bond interaction of **1** with truncated ErbB2 Ectodomain protein.

intermolecular energy is −5.82 kcal/mole and summation of vdW, H-bond and dissolved energy is −5.77 kcal/mol. The electrostatic energy is calculated to −0.05 kcal/mol where the total internal energy is −0.04 kcal/mol and the torsional free energy is + 0.30 kcal/mole with unbound system's energy is −0.04 kcal/-mole. Complex **2** also forms hydrophobic interaction with GLU480, PRO449, ARG478, ASN477, ALA476, THR475, HIS474 and GLU19 base pair of protein chain. The values of different computed weak interactions e.g., binding energy with protein (−8.04 Kcal/-mol), inhibition constant (Ki = 1.28 μM at 298.15 K), intermolecular energy (−9.83 Kcal/mol), internal energy (−1.3 Kcal/mol), torsional energy (−1.79 Kcal/mole), and unbound extended energy (−1.3 Kcal/mole) are found in complex 2 with cluster RMS = 0.0 and reference RMS = 73.35. The docking evaluation of **1** and **2** with the target enzyme showed that weak interactions like hydrogen bonding and van der Waals forces are mainly responsible. The docking study could explain the potency of the complexes as an effective model of catecholase activity.

4. Conclusion

Copper(II) complexes with methyl-2-(1-(pyridin-2-yl)ethylidene)hydrazine-1-carbodithioate (HL_1) and benzyl-2-(1-(pyridin-2-yl)ethylidene)hydrazine-1-carbodithioate (HL_2) were synthesized and characterized by IR spectroscopy, X-ray crystallography, TGA. The stabilities of the monomeric and dimeric structures of these complexes were investigated computationally at the UB3LYP-D3 level. The mono nuclear structure of the [Cu(L_1)Cl] layers was found due to strong dispersion interaction between Cl and CH_3 moieties located at different layers. However, this interaction

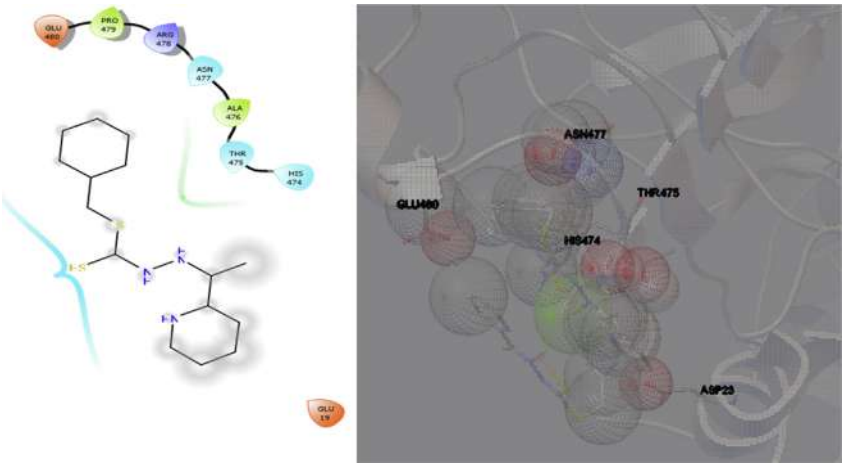

Fig. 15. Hydrophobic interactions of **2** with base pair of Truncated ErbB2 Ectodomain protein chain.

is hindered in the [Cu(L_2)Cl] layers due to the largeness of the phenyl moiety of L_2 than the separation between the layers that prevents slide of the layers on top of each other. As a result, the strong electrostatic interaction between Cu and Cl atoms located at different layers results in chloro-bridged [Cu(L_2)Cl]$_2$ structure. Both monomeric [Cu(L_1)Cl] and dimeric [Cu(L_2)Cl]$_2$ complexes act as a good catalyst to show catechol oxidase mimetic activity in methanol medium, through a fraction of [CuL]$^+$ species in methanol medium.

Acknowledgments

We gratefully acknowledge to Council for Scientific and Industrial Research (CSIR), Government of India for the project grant [No. 1 (2858)/16/EMR–II]. Panskura Banamali College (Autonomous) acknowledges the grants received from the Department of Science and Technology (SR/FST/College–295 dated 18/11/2015), Govt. of India through FIST program. We thank Syam Sengupta, IISER, Kolkata for EPR spectral analysis.

Conflict of interest

The authors declare that they have no conflict of interest.

Appendix A. Supplementary data

CCDC 1833374 and 1833376 for compound **1** and **2**, respectively. Crystallographic data can be obtained free of charge on application to CCDC, 12 Union Road, Cambridge CB2 1EZ, UK, fax: (+44) 1223 336033, e-mail: deposit@ccdc.cam.ac.uk. The computational structures are provided. Supplementary data to this article can be found online at https://doi.org/10.1016/j.poly.2019.114277.

References

[1] M.T.H. Tarafder, A.M. Ali, D.J. Wee, K. Azahari, S. Silong, K.A. Crouse, Transition Met. Chem. 25 (2000) 456.
[2] A.B. Beshir, S.K. Guchhait, J.A. Gascon, G. Fenteany, Bioorg. Med. Chem. Letters 18 (2008) 498.
[3] M.T.H. Tarafder, A. Kasbollah, K.A. Crouse, A.M. Ali, B.M. Yamin, H.K. Fun, Polyhedron 20 (2001) 2363.
[4] N.C. Kasuga, K. Sekino, M. Ishikawa, A. Honda, M. Yokoyama, S. Nakano, N. Shimada, C. Koumo, K. Nomiya, J. Inorg. Biochem. 96 (2003) 298.
[5] M.X. Li, L.Z. Zhang, C.L. Chen, J.Y. Niu, B.S. Ji, J. Inorg. Biochem. 106 (2012) 117.
[6] M. Shahid, M. Salim, M. Khalid, M.N. Tahir, M.U. Khan, A.A.C. Braga, J. Mol. Struct. 1161 (2018) 66.
[7] H. Zhou, D. Li, P. Wang, L. Cheng, Y. Gao, Y. Zhu, J. Wu, Y. Tian, Z. Tao, M. Jiang, H.K. Fun, J. Mol. Struct. 826 (2007) 205.
[8] P. Gómez-Saiz, R. Gil-García, M.A. Maestro, J.L. Pizarro, M.I. Arriortua, L. Lezama, T. Rojo, M. González-Álvarez, J. Borrás, J. García-Tojal, Inorg. Biochem. 102 (2008) 1910.
[9] D.X. West, A.E. Liberta, S.B. Padhye, R.C. Chikate, P.B. Sonawane, A.S. Kumbhar, R.G. Yerande, Coord. Chem. Rev. 123 (1993) 49.
[10] R. Vafazadeh, R. Esteghamat-Panaha, A.C. Willis, A.F. Hill, Polyhedron 48 (2012) 51.
[11] T.S. Lobana, R.J. Butcher, A. Castineiras, E. Bermejo, P.V. Bharatam, Inorg. Chem. 45 (2006) 1535.
[12] S. Walia, S. Kaur, J. Kaur, A.K. Sandhu, T.S. Lobana, G. Hundal, J.P. Jasinski, ZAAC 641 (2015) 1728.
[13] V. Philip, V. Suni, M.R.P. Kurup, M. Nethaji, Polyhedron 25 (2006) 1931.
[14] B.K. Koo, J. Korean Chem. Soc. 59 (2015) 103.
[15] P. Vijayan, P. Viswanathamurthi, K. Velmurugan, R. Nandhakumar, M.D. Balakumaran, P.T. Kalaichelvan, J.G. Malecki, RSC Adv. 5 (2015) 103321.
[16] M.A. Ali, A.H. Mirza, R.J. Butcher, M.T.H. Tarafder, T.B. Keat, A.M. Ali, J. Inorg. Biochem. 92 (2002) 141.
[17] A. Biswas, L.K. Das, M.G.B. Drew, G. Aromí, P. Gamez, A. Ghosh, Synth. Inorg. Chem. 51 (2012) 7993.
[18] L.K. Das, A. Biswas, J.S. Kinyon, N.S. Dalal, H. Zhou, A. Ghosh, Inorg. Chem. 52 (2013) 11744.
[19] K.S. Banu, T. Chattopadhyay, A. Banerjee, S. Bhattacharya, E. Suresh, M. Nethaji, E. Zangrando, D. Das, Inorg. Chem. 47 (2008) 7083.
[20] D. Kovala-Demertzi, P.N. Yadav, J. Wiecek, S. Skoulika, T. Varadinova, M.A. Demertzis, J. Inorg. Biochem. 100 (2006) 1558.
[21] K.M. Deck, T.A. Tseng, J.N. Burstyn, Inorg. Chem. 41 (2002) 669.
[22] L. Zhu, O. Santos, C.W. Koo, M. Rybstein, L. Pape, J.W. Canary, Inorg. Chem. 42 (2003) 7912.
[23] A. Biswas, L.K. Das, M.G.B. Drew, C. Diaz, A. Ghosh, Inorg. Chem. 51 (2012) 10111.
[24] S.K. Dey, A. Mukharjee, Coord. Chem. Rev. 310 (2016) 80.
[25] S. Dasgupta, I. Majumder, P. Chakraborty, E. Zangrando, A. Bauza, A. Frontera, D. Das, Eur. J. Inorg. Chem. (2017) 133.
[26] S. Dolai, K. Das, A. Bhunia, V. Bertolasi, S.C. Manna, Appl. Org. Chem. 32 (2018) 4506.
[27] A.D. Becke, J. Chem. Phys. 98 (1993) 5648.
[28] C. Lee, W. Yang, R.G. Parr, Phys. Rev. B 37 (1988) 785.
[29] A.D. Becke, Phys. Rev. A 38 (1988) 3098.
[30] P. Bera, C.-H. Kim, S.I. Seok, Polyhedron 27 (2008) 3433.
[31] Bruker, SMART (Version 5.625) Data Collection Program, Bruker AXS Inc., Madison, Wisconsin, USA (2001).
[32] Bruker, SAINT (Version 6.28a) and SADABS (Version 2.03) Data Reduction and Absorption Correction Program, Bruker AXS Inc., Madison, Wisconsin, USA (2001).
[33] G.M. Sheldrick, SHELXTL (Version 6.12) Structure Analysis Program, Bruker AXS Inc., Madison, Wisconsin, USA, 2001.
[34] F. Neese, The ORCA Program System, Wiley Interdiscip. Rev. Comput. Mol. Sci. 2 (2012) 73.
[35] F. Neese, Software Update: The ORCA Program System, Version 4.0, Wiley Interdiscip. Rev. Comput. Mol. Sci. 8 (2018) 1327.
[36] F. Weigend, Phys. Chem. Chem. Phys. 8 (2006) 1057.
[37] F. Weigend, R. Ahlrichs, Phys. Chem. Chem. Phys. 7 (2005) 3297.
[38] S. Grimme, S. Ehrlich, L. Goerigk, J. Comput. Chem. 32 (2011) 1456.
[39] F. Weigend, M. Häser, H. Patzelt, R. Ahlrichs, Chem. Phys. Lett. 294 (1998) 143.
[40] K. Eichkorn, O. Treutler, H. Öhm, M. Häser, R. Ahlrichs, Chem. Phys. Lett. 240 (1995) 283.
[41] V. Barone, M. Cossi, J. Phys. Chem. A 102 (1998) 1995.
[42] Z.L. You, Y.M. Cui, Y.P. Ma, C. Wang, X.S. Zhou, K. Li, Inorg. Chem. Comm. 14 (2011) 636.
[43] P.R. Reddy, A. Shilpa, N. Raju, P. Raghavaiah, Synthesis, structure, J. Inorg. Biochem. 105 (2011) 1603.
[44] S. Sarkar, A. Sim, S. Kim, H.I. Lee, J. Mol, Catal. A: Chem. 410 (2015) 149.
[45] A. Jana, P. Brandão, G. Mondal, P. Bera, A. Santra, A.D. Jana, R.B. Mokhamatam, S.K. Manna, P. Bera, Inorg. Chim. Acta 482 (2018) 621.
[46] L. Rigamonti, A. Forni, R. Pievo, J. Reedjijk, A. Pasini, Dalton Trans 40 (2011) 3381.
[47] M.S. Begum, E. Zangrando, M.C. Sheikh, R. Miyatake, M.B.H. Howlader, M.N. Rahman, A. Ghosh, Transition Met. Chem. 42 (2017) 553.
[48] J.-L. Chen, Z.-H. Guo, H.-G. Yu, L.-H. He, S.-J. Liu, H.-R. Wena, J.-Y. Wang, Dalton Trans. 45 (2016) 696.
[49] M.F. Haddow, H. Kara, G.R. Owen, Inorg. Chim. Acta 362 (2009) 3502.
[50] Y. Acar, H. Kara, E. Gungor, M.B. Coban, Mol. Cryst. Liq. Cryst. 664 (2018) 165.
[51] M. Atanasov, P. Comba, B. Martin, V. Müller, G. Rajaraman, H. Rohwer, S. Wunderlich, J. Comput. Chem. 27 (2006) 1263.
[52] S. Kundu, A. Mondal, T. Weyhermüller, S. Sproules, P. Ghosh, Inorg. Chim. Acta 451 (2016) 23.
[53] S. Grimme, R. Huenerbein, S. Ehrlich, Chem. Phys. Chem. 12 (2011) 1258–1261.
[54] P. Chakraborty, I. Majumder, H. Kara, S.K. Chattopadhyay, E. Zangrando, D. Das, Inorg. Chim. Acta 436 (2015) 139.
[55] I. Majumder, P. Chakraborty, J. Adhikary, H. Kara, E. Zangrando, A. Bauza, A. Frontera, D. Das, Chemistry Select 3 (2016) 615.
[56] A. Jana, P. Brandão, H. Jana, A.D. Jana, G. Mondal, P. Bera, A. Santra, A.K. Mahapatra, P. Bera, J. Coord, Chem. 72 (2019) 2636.
[57] M.M. Abd-Elzaher, A.A. Labib, H.A. Mousa, S.A. Moustafa, M.M. Ali, A.A. El-Rashedy, Beni-suef Univ. J. Basic Appl. Sci. 5 (2016) 85.

Source details

Feedback > Compare sources >

Polyhedron

Formerly known as: Journal of Inorganic and Nuclear Chemistry

Formerly known as: Inorganic and Nuclear Chemistry Letters

Scopus coverage years: from 1982 to Present

Publisher: Elsevier

ISSN: 0277-5387

Subject area: Chemistry: Inorganic Chemistry | Materials Science: Materials Chemistry | Chemistry: Physical and Theoretical Chemistry

Source type: Journal

View all documents > | Set document alert | Save to source list

CiteScore 2022
5.4

SJR 2022
0.400

SNIP 2022
0.635

CiteScore | CiteScore rank & trend | Scopus content coverage

Inorganica Chimica Acta 501 (2020) 119315

Contents lists available at ScienceDirect

Inorganica Chimica Acta

journal homepage: www.elsevier.com/locate/ica

Research paper

Monomeric and dimeric cadmium(II) complexes of S-alkyl/aryl dithiocarbazate as single-source precursors for cadmium sulfide nanoparticles: An experimental, theoretical interpretation in the stability of precursor and visible light dye degradation study

Ananyakumari Santra[a], Paula Brandao[b], Gopinath Mondal[a], Pradip Bera[a,c], Abhimanyu Jana[a], Indranil Bhattacharyya[a], Chandana Pramanik[a,d], Pulakesh Bera[d,*]

[a] Post Graduate Department of Chemistry, Panskura Banamali College (Autonomous), Panskura R.S, Midnapore (East), West Bengal 721152, India
[b] Department of Chemistry, CICECO, University of Aveiro, 3810 – 193 Aveiro, Portugal
[c] Department of Chemistry, Kandi College, Murshidabad, West Bengal 42137, India
[d] Department of Chemistry, Dinabandhu Andrews College, Garia, Kolkata, West Bengal 700084, India

ARTICLE INFO

Keywords:
Pyridinyl dithiocarbazates
Single-source precursor
X-ray crystallography
Solvothermal
CdS nanocrystals
Photocatalytic activity

ABSTRACT

The reaction of S-alkyl/aryl dithiocarbazate functionalized with 2-acetyl pyridine ligands and cadmium chloride in ethanol leads to the formation of a mono nuclear cadmium(II) complex, $[Cd(\mathbf{L^1})_2]$ (SP**1**), ($\mathbf{HL^1}$ is S-methyl-2-(1-(pyridine-2-yl)ethylidene)hydrazine-1-carbodithioate) and a dinuclear dichloro bridged complex, $[(\mathbf{L^2})Cd(\mu\text{-}Cl)_2Cd(\mathbf{L^2})]$ (SP**2**), ($\mathbf{L^2}$ is S-benzyl-2-(1-(pyridine-2-yl)ethylidene)hydrazine-1-carbodithioate). The complexes are characterized by FTIR, single X-ray crystallography and thermogravimetry analysis. Density functional calculations indicate that different coordination patterns of the complexes with $\mathbf{HL^1}$ and $\mathbf{HL^2}$ ligands relate with the available space of the dissociation of $CdCl_2$ in their solutions. Thermochemical destruction of the precursor complexes at the molecular level fabricated hexagonal CdS nanoparticles where the morphology is guided by the precursor. In situ generated thiols e.g., CH_3SH in case of SP**1**, and $PhCH_2SH$ in case of SP**2**, internally stabilized the flower-like and rod shaped CdS structures, respectively. The synthesized nanoparticles were characterized by powder X-ray diffraction (XRD), scanning electronic microscope (SEM) and energy-dispersive X-ray spectroscopy (EDAX). The UV–Vis spectroscopic study shows a prominent quantum confinement effect in CdS with a band gap energy of 2.4 eV and 2.5 eV for SP**1** and SP**2**, respectively. The CdS nanocrystals under investigation degrade Rose Bengal (RB) dye (96%) under visible light irradiation. A reusability study shows that the CdC nanoparticles retain their catalytic activity (86%).

1. Introduction

Dithiocarbazate [1–5] and dithiocarbamate (esters of dithioic acid) [6,7] derivatives are successfully used as single-source precursors (SP) for the preparation of binary and ternary nanoparticles. The effect of nuclearity, 3D network arrangements, and different strong and weak forces in the SP structure might have definite influence on the quality (shape, size, crystallinity and dispersibility) of the nanoparticles. The tuning of size and shape of the nanoparticles can be controlled by the intrinsic structural properties of SP [8,9] in the solvothermal decomposition method. S-Methyl/benzyl dithiocarbazates have been successfully utilized earlier by us to synthesize binary CuS [10,6], PbS [11,12] and CdS [13–15] and ternary $CuInS_2$ [16,17] nanoparticles with various morphologies. In order to study the effect of *N*-heterocycle rings such as pyridine etc. in the dithiocarbazate unit various metal complexes are reported [18,19]. Introduction of an *N*-heterocycle into the dithocarbazate unit enhances the flexibility and coordinating properties of the ligand that might improve the quality of the SP in the particle formation. Dithocarbazates are a class of compounds that have sufficient flexibility to form monomeric and dimeric compounds. Monomer formation is very common but dimer formation with dithiocarbazates is rarely reported in the literature [20]. The stabilization of a chloro-bridged dimer over the monomer is quite interesting and a quantum mechanical analysis is opted to understand the SP structure. In an attempt to obtain hierarchical CdS nanoparticles, we synthesized two new pyridinyl dithiocarbazate single-source precursors as building

* Corresponding author.
E-mail address: pbera.pbc.chem@gmail.com (P. Bera).

https://doi.org/10.1016/j.ica.2019.119315
Received 16 August 2019; Received in revised form 26 November 2019; Accepted 27 November 2019
Available online 30 November 2019
0020-1693/

blocks, namely SP**1** [a mono nuclear cadmium(II) complex of methyl-2-(1-(pyridine-2-yl)ethylidene)hydrazine-1-carbodithioate, $[Cd(\mathbf{L^1})_2]$ and SP**2,** [a dinuclear dichloro bridged complex with benzyl-2-(1-(pyridine-2-yl)ethylidene)hydrazine-1-carbodithioate, $[(\mathbf{L^2})Cd(\mu\text{-}Cl)_2Cd(\mathbf{L^2})]$]. Here we describe the complete structural characterization of the complexes in both solid and solution phase. L^1 and L^2 tend to include and exclude the Cl atom from their Cd-complex, respectively. The reason behind this tendency was investigated through density functional theory (DFT) calculations. A reasonable explanation for monomer or dimer formation has been estimated on the basis of the DFT study. We also report the facile synthesis and characterization of CdS nanoparticles obtained from $[Cd(\mathbf{L^1})_2]$ and $[(\mathbf{L^2})Cd(\mu\text{-}Cl)_2Cd(\mathbf{L^2})]$ in a solvothermal process. The as synthesized CdS nanocrystals show excellent photocatalytic activity for the degradation of RB dyes under visible light irradiation.

2. Materials and methods

2.1. Chemicals

Cadmium chloride (Merck), 2-acetyl pyridine (Merck), ethylene diamine (Himedia), ethylene glycol (Himedia), oleic acid (Merck) were all of analytical grade and used without further purification. The solvent ethanol (Changshu Yangyuan Chemical, China) was dried and distilled before use.

2.2. Synthesis of cadmium complexes

HL1 and HL2 were synthesized following a method reported earlier [21]. To prepare the cadmium complex of the ligand $H\mathbf{L^1}$ and $H\mathbf{L^2}$, 5 mmol (0.92 g) of $CdCl_2$ in ethanolic solution were mixed with 10 mmol (2.25 g) of $H\mathbf{L^1}$ and 10 mmol (3.01 g) of $H\mathbf{L^2}$ separately in methanol. The mixtures were refluxed for 3 h and then cooled to room temperature, which resulted in the precipitation of yellow solid products. The products were filtered and washed using dry ethanol. The filtrate parts were kept for crystallization and after several days light yellow crystalline products were obtained. Chemical Formula for SP**1**: $C_{18}H_{20}CdN_6S_4$, Formula Weight: 561.05, Elemental Analysis, found: C, 38.53; H, 3.59; N, 14.98; S, 22.86. Calculated: C, 38.49; H, 3.56; N, 14.97; S, 22.81. Yield 78%, MP (decomposition temperature) 195 °C, Λ_m = 16 $\Omega^{-1}cm^2$ $mole^{-1}$. ^1H NMR (d_6-DMSO) δ (in ppm): 8.83 (doublet, 2H at C1 & C19), 8.15 (triplet, 2H at C3 and C12 in pyridine ring), 7.85 (doublet, 2H at C4 & C13), 7.60 (triplet, 2H at *C*2, C11) in aromatic pyridine ring, 2.65–2.70 (singlet, 3H at CH_3 attached to C═N) and 2.41–2.49 (singlet, 3H at SCH_3). IR frequencies (KBr pellets, in cm^{-1}): 1421 for $\nu_{(C-N)}$, 1578 for $\nu_{(C=N)}$, 1417 for $\nu_{(N-N-C)}$, 1507 for $\nu_{(C-N)}$ & $\nu_{(N-N)}$ mixing and 744 for $\nu_{(C=S)}$.

Chemical Formula for SP**2**: $C_{30}H_{28}Cd_2Cl_2N_6S_4$, Formula Weight: 896.56, Elemental Analysis, found: C, 40.19; H, 3.15; N, 9.37; S, 14.30. Calculated: C, 40.15; H, 3.12; N, 9.36; S, 14.27. Yield 72%, MP (decomposition temperature) 220 °C, Λ_m = 19 $\Omega^{-1}cm^2$ $mole^{-1}$. ^1H NMR (d_6-DMSO) δ (in ppm): 8.84 (doublet, 1H at C1), 8.40 (triplet 2H at C3) 7.91 (doublet, 1H at C4), 7.68 (triplet, 2H at *C*2) in aromatic pyridine ring, 2.60 (singlet, 3H at SCH_2-) and 2.51 (singlet, 3H at CH_3 attached to C═N). IR frequencies (KBr pellets, in cm^{-1}): 1376 for $\nu_{(C-N)}$, 1600 for $\nu_{(C=N)}$, and 760 for $\nu_{(C=S)}$.

2.3. Synthesis of CdS nanoparticles

0.5 mmol (0.28 g) of the respective precursor complex were taken in 20 mL of organic solvent and stirred for 30 min to form a homogeneous mixture. Ethylene glycol (EG) and ethylene diamine (EN) were used as solvent in the synthesis procedure. Then the mixture was transferred into a 50 mL three-necked round bottom flask with a thermo adaptor and condenser. The reaction vessel was filled with N_2 gas and heated at 180 °C with constant stirring. After the reaction time (1 h), yellow suspended particles were obtained. The reaction was immediately paused by adding cold ethanol. The particles were separated by centrifugation followed by washing with ethanol 3–4 times. The CdS nanoparticles were dried in vacuum at 100 °C for 1 h. A similar experiment was performed with oleic acid (OA) at 180 °C to compare the morphology of nanoparticles (Table 1).

Table 1
Reaction parameters of CdS nanoparticles synthesis from SP1 and SP2.

SP	Solvent	Size	Shape	JCPDS
SP1	EG	15.30 nm	Flower like architecture	0041–1049
	EN	15.35 nm		
	OA	15.31 nm		
SP2	EG	11.16 nm	Rod	0041–1049
	EN	11.11 nm		
	OA	11.15 nm		

3. Experimental

The elemental analysis (C, H, N, and S) of the complex was performed using a FISONS EA-1108 CHN analyzer. The molar conductance of the complexes was measured in ethanolic solution with a systronics model 304 digital conductivity meter. ^1H NMR spectra of the ligands and the complexes were recorded in $CDCl_3$ and d_6-DMSO solvent, respectively on a Bruker 300 MHz NMR spectrometer using tetramethylsilane (δ = 0) as an internal standard. The FTIR spectra (4000–500 cm^{-1}) were recorded on a Perkin Elmer Spectrum Two spectrophotometer. The single-crystal X-ray diffraction data of SP**1** and SP**2** was recorded on a Bruker SMART APEX II X-ray diffractometer equipped with graphite-monochromated Mo-Kα radiation (λ = 0.71073 Å) and 16 CCD area detector. The intensity data were collected in the π and ω scan mode, operating at 50 kV, 30 mA at 296 K [22]. The data reduction was performed using the SAINT and SADABS programs [23]. All calculations in the structural solution and refinement were performed using the Bruker SHELXTL program [24]. The structure was solved by the heavy atom method and refined by full-matrix least-squares methods. All non-hydrogen atoms were refined anisotropically; the hydrogen atoms were geometrically positioned and fixed with isotropic thermal parameters. The final electron density maps showed no significant difference. The thermogravimetry analysis of the precursors was carried out on a Thermogravimetric Analyzer, TGA 4000 (Perkin Elmer) at a heating rate 10 °C/min under nitrogen. UV–Visible absorption spectra were recorded on a Perkin Elmer Lambda 35 spectrophotometer from 200 to 800 nm at room temperature and the photocatalytic activity was observed under a 250 W electric lamp. Powder X-ray diffraction (XRD) data of the NCs was recorded using a Seifert XDAL 3000 diffractometer using graphite-monochromated Cu-Kα radiation (λ = 1.5418 Å) with a scan rate of 5°/min over a range of 20° < 2θ < 60° with steps of 0.02° and a scintillation detector operating at 40 kV and 40 mA. The SEM and FESEM of the particles were analysed with a JEOL JSM 7600F field emission scanning electron microscope (FESEM). The EDAX plots were obtained using an AMETEK Energy Dispersive Analysis System operating at 200 kV at a tilt angle of 15°. All quantum mechanical calculations were performed with the ORCA 4.0 program package [25,26]. The structures were optimized with the B3LYP [27–29] density functional by including the D3 dispersion correction with Becke–Johnson damping (BJ) [30] and the effect of methylene solution implicitly through the conductor-like polarizable continuum model (C-PCM) [31]. The def2-TZVP and its matching auxiliary basis sets were used within the RIJCOSX approach [32,33]. The photocatalytic activity of the cadmium sulfide nanoparticles was investigated by various groups [34–36]. As a model dye, Rose Bengal (RB), was used to study the photocatalytic activity in visible light irradiation. 50 mL of a 5×10^{-5} M aqueous solution of RB

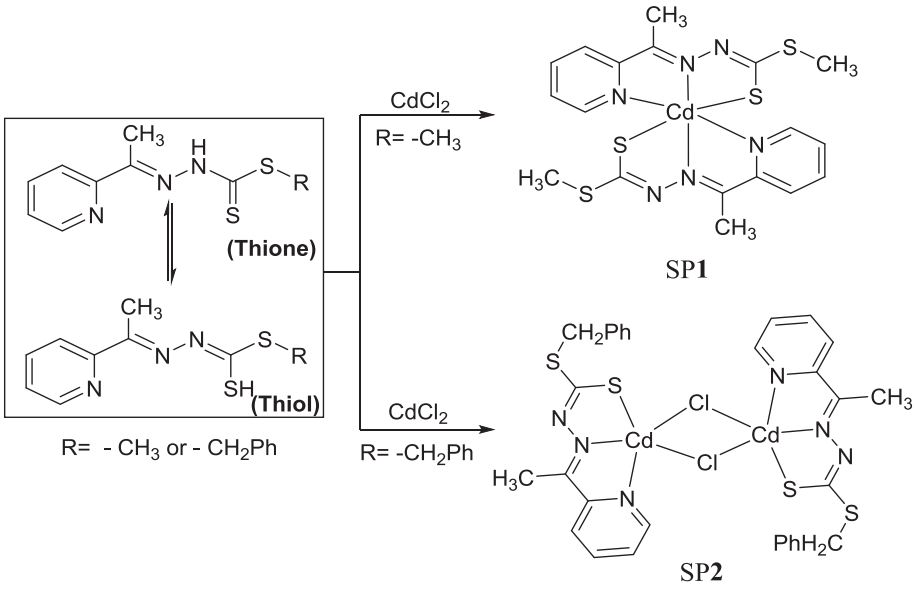

Scheme 1. Reaction path for the formation of SP1 and SP2.

in a 100 mL beaker were used for the photo degradation with 15 mg CdS. A 200 W indoor fluorescent lamp was used as the light source. The concentration of the dye after photocatalytic degradation was determined with a Perkin Elmer Lambda 35 UV–Vis spectrophotometer. The reusability studies were performed with CdS collected and washed from previous experiments.

4. Results and discussion

4.1. General

The ^{1}H NMR spectra of HL^1 (Fig. S2) and HL^2 (Fig. S3) clearly demonstrate that the ligand undergoes a thione-thiol tautomerism in solution (Scheme 1). The peak at about 1.70 ppm in both HL^1 and HL^2 corresponds to the thiol proton. The disappearance of this peak in the ^{1}H NMR spectrum of the cadmium complexes (Figs. S3 and S4) reveals that the coordination occurs through the S atom of the ligand. The aromatic ring protons peaks are mostly observed in the range between 7.70 and 8.70 ppm, and the methyl protons are found at 2.45 ppm in HL^1. The methyl proton of the SCH_3 group in HL^1 gives a peak at 2.70 ppm and the CH_2 moiety of the benzyl group in HL^2 appears at 4.60 ppm. The other aromatic protons in both ligands are shifted downfield, attesting a coordination through the nitrogen atom of the pyridine ring. A ligand-shared or bridged dimer is formed when the disposition of the donor atoms on a rigid frame does not allow the formation of a monomer [36]. Formation of both monomer and dimer can be possible with sufficient flexibility in the structure of the ligand. Under identical experimental conditions, cadmium(II) chloride reacts with HL^1 and HL^2 producing a monomer and a chloro-bridged dimer, respectively (Scheme 1). Reported complexes with a similar backbone furnished mostly monomeric species irrespective of the substitution of the thiol sulfur atom [37]. S-alkylated dithiocarbazate without any anchored *N*-heterocycle produced a dichloro-bridged dimeric cadmium complex [39]. Isolation of the dichloro-bridged complex with ligand HL^2 containing a large SR group certainly relates to the fact that the complexes are solid and sufficiently air stable at room temperature. The decomposition of the reported complexes started near 200 °C. The complexes are suitable single source precursors to synthesize CdS nanocrystals in a solvothermal process. The conductance values of the complexes are very low, supporting the non-ionic and first order inner metallic nature of the complexes. Studies on the preferential monomer and dimer formation might provide meaningful information about the structure and stability of the complexes. A similar observation was also made in the reaction of HL^1 and HL^2 with copper(II) chloride. Earlier it was observed that the cadmium(II) complex of S-methyl dithiocarbazate produced spherical nanoparticles irrespective of the solvent, and the cadmium(II) complex of S-benzyl dithiocarbazate produced rod-shaped CdS nanocrystals.

The isolated ligands and their cadmium(II) complexes were characterized using FTIR spectroscopy and mass spectrometry. The FTIR spectra of the free ligands and the corresponding cadmium complex are shown in Fig. S1 and Table S1.

4.2. Thermogravimetric analysis

A thermogravimetric analysis (TGA) of SP**1** and SP**2** was performed to check their suitability as single-source molecular precursors for CdS nanoparticles. The TGA curves of HL^1, HL^2, SP**1** and SP**2** are given in Fig. 1. Both the ligands decompose earlier than the corresponding complexes. Two steps of decomposition occur both in HL^1 and HL^2 involving a huge mass loss, which amounts to about 70% in the first step of decomposition and be attributed to the loss of the dithiocarbazate unit of the ligand. The precursor complex has a higher decomposition temperature than the corresponding ligands. The decomposition patterns of SP**1** and SP**2** are very similar. The decomposition of SP**1** starts at 250 °C and about 34.5% of the mass loss occurs between 250 and 350 °C, which is due to the loss of two units of NHC(S)SMe (calcd. 212.3). The remaining organics attached to the central atom evaporate in the last step of decomposition (39.3%) between 400 and 850 °C, accompanied by the formation of CdS (26.2%). Similarly, a two-step decomposition of SP2 is observed, in which the first step mass loss (about 35.3%) is due to the combined loss of SCH_2Ph and Cl from each ligand.

The residual mass at 850 °C corresponds to 2CdS (37.2%) and is little bit higher than the calculated value of 33%. This suggests that small organic molecules are still embedded at 850 °C. On the basis of the TGA results, it is quite reasonable that both the precursors are suitable for the preparation of CdS nanocrystals. Depending on the TGA results, the solution decomposition temperature was adjusted at 160 °C using coordinating solvents such that the stability of the coordinate bonds decreases significantly towards the nucleation of the CdS particle. Qualitatively, it can be inferred that the multistep decomposition of the precursor generally facilitated an anisotropic growth of crystallites where a single step clean decomposition favors an isotropic growth

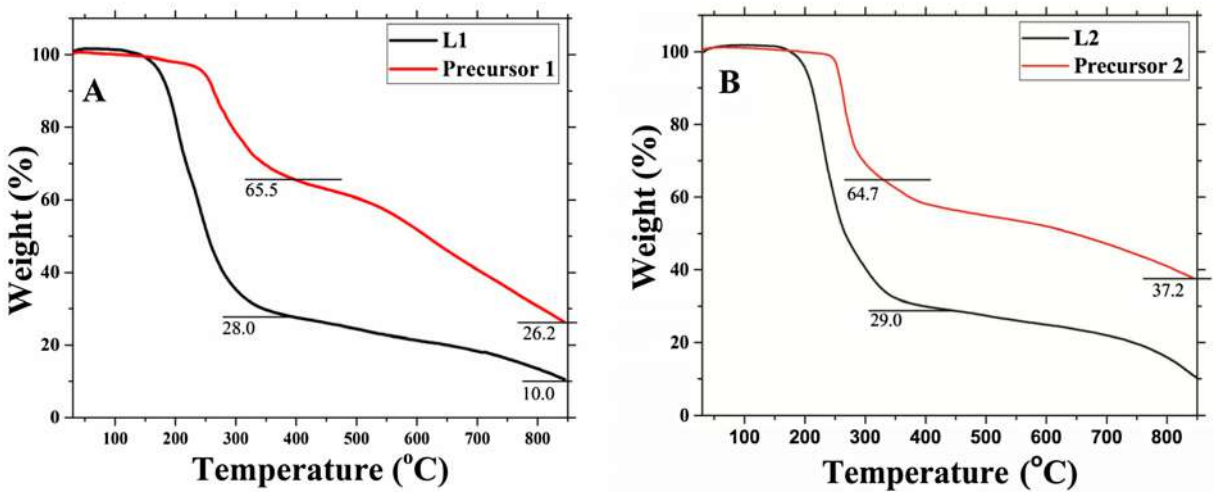

Fig. 1. Thermal decomposition pattern of SP**1** and HL^1 [A]; SP**2** and HL^2 [B].

of the particles [7]. In the present study, both SPs follow a multistep thermal decomposition, which might lead to an anisotropic growth of crystallites.

4.3. Single crystal X-ray crystallography

The solid-state structures of the complexes were characterized by single crystal X-ray crystallography to confirm the molecular structures of precursor complexes. The ORTEP diagrams with atom numbering scheme of SP**1** and SP**2** are shown in Figs. 2 and 3, respectively. Precursor SP**1** is monomeric whereas SP**2** is a dimeric chloro-bridged complex crystallizing in the triclinic Pī space group. The coordination geometry around the Cd-atom is octahedral with an $N_2N_2S_2$ chromophore of deprotonated L^1 with the participation of two ligands in complex SP**1**. Ligand **HL^1** acts as uninegative point charge *via* thiolato-S bonding to the cadmium center. Cadmium(II) is coordinating as a tridentate donor through its *N*-atoms the and thiolato-S, resulting in the neutral complex $[Cd(L1)_2]$. In SP**1**, the chelate bite angles N(1)–Cd–N(2), S(1)–Cd–N(2), S(3)–Cd–N(5) and N(4)–Cd–N(5) are 74.87(4)°, 67.96(5)°, 73.23(4)° and 67.55(5)°, respectively. These angles are much smaller than the ideal octahedral angle (90°). The other two angles, i.e. N(1)–Cd–N(4) [90.17(5)°] and S(1)–Cd–N(4) [94.01(4)°] are close to the ideal octahedral angle. The low bites angles in the complex may be due to the closeness of the coordinating N and S atoms to facilitate the formation of 5–membered chelate rings. The bite angles S(1)–Cd–S(3) [101.59(2)°], N(2)–Cd–N(4) [110.02(5)°] and S(1)–Cd–N(5) [137.98(4)] reveal an out-of-plane position of the two pyridine rings from two adjacent ligands, exerting less steric crowding. In SP**2**, two Cd (II) centers are doubly bridged with Cl atoms and five coordinated with each unit of deprotonated L^2 (Fig. 3). The distance between the Cd centers is found to be 3.664 Å. The bite angles N(1)-Cd-N(2) and S(1)-Cd-N(2) are 69.77(5) and 76.52(4), respectively. The bridged chlorido

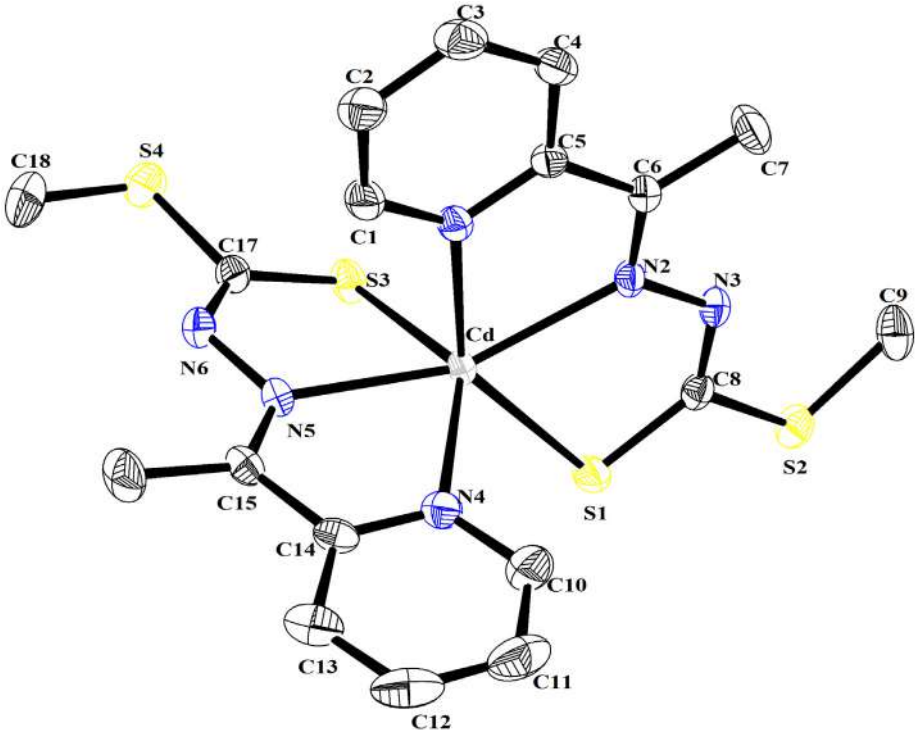

Fig. 2. ORTEP diagram of precursor SP**1**.

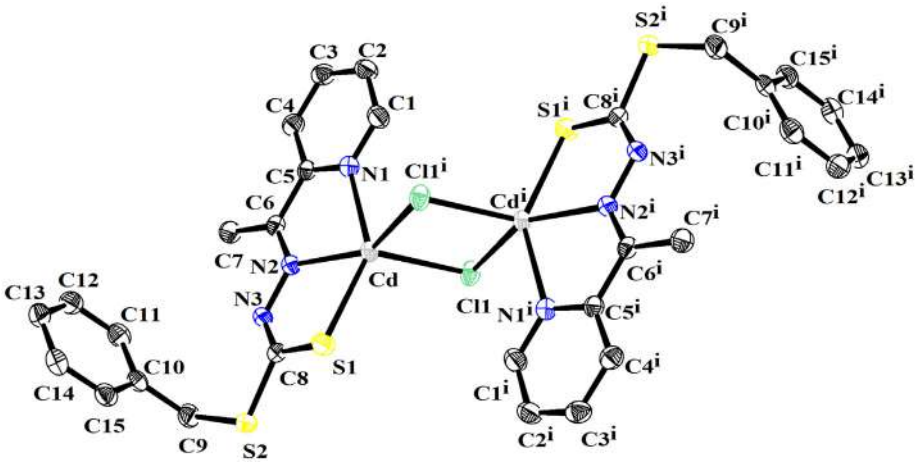

Fig. 3. ORTEP diagram of precursor SP**2**.

Table 2
Crystal refinement parameters of SP1 and SP2.

	SP1	SP2
CCDC	1,833,373	1,833,375
Moiety formula	$C_{18}H_{20}CdN_6S_4$	$C_{30}H_{28}Cd_2Cl_2N_6S_4$
Mr	561.05	896.52
a(Å)	7.6582(4)	9.1658(5)
b(Å)	10.6878(5)	9.2721(5
c(Å)	13.9776(6)	10.7922(6)
α(°)	99.199(2)	72.562(2)
β(°)	95.857(2)	74.696(2)
γ(°)	97.625(2)	72.819(2)
Crystal system	Triclinic	Triclinic
Temperature	150 K	150 K
Volume (Å^3)	1110.44(9)	820.36(8)
Space group	Pī	Pī
Z	2	1
F (0 0 0)	564.0	444.0
Dcalc (g cm^{-3})	1.678	1.815
Absorption coefficient/μ(mm^{-1})	1.377	1.746
h,k,l	10,14,19	12,12,14
2θ	58.38	58.42
Reflections I > 2σ(I)	5289	4126
Total reflections I > 2σ(I)	5998	4436
R1(I > 2σ(I))	0.0210	0.0180
w*R*2(all reflections)	0.0502	0.0442

ligands are perpendicular to the basal ligand metal plane, where the Cl (1)-Cd-Cl(1) angle is 89.23(1), which is very close to 90°. The two benzyl groups of two adjacent ligands are out of plane with respect to the remaining part, resulting in a decreased steric effect. The complex crystallizes in the centro-symmetric space group Pī in a triclinic unit cell. The crystal parameters and selected bond length/angles are presented in Tables 2 and 3, respectively.

4.4. Computational study

As seen in Scheme 1, two deprotonated ligands (HL^1) coordinate directly to a single Cd atom ($[L_1CdL_1]$) while the Cd complex of deprotonated ligand HL^2 is the dimeric CdCl-bridged $[L_2CdCl]_2$. To shed light into the difference in the complex formation mechanisms of the deprotonated HL^1 and HL^2 ligands with Cd, we considered the model $[L_1(CdCl)_2]^{2+}$ and $[L_2(CdCl)_2]^{2+}$ complexes and investigated the first step in the dissociation of $CdCl_2$ from these structures. For this purpose, we scanned the relaxed potential energy surfaces of these complexes in methanol by taking the Cd1–Cl1 bond (Fig. 4) as a reaction coordinate at the B3LYP-D3/def2-TZVP level. The structures of the reactant, transition state, and product are shown in Fig. 4. In the reactant complex (see left panel of Fig. 4), Cd1 atom is coordinated to deprotonated HL^1 and deprotonated HL^2 through the two N atoms and one sulfur atom (S1), as in SP**1** and SP**2**. The increase in the distance between this

Table 3
Selected bond angles (in °) and bond lengths (in Å) of the complexes.

SP**1**		SP**2**		SP**1**		SP**2**	
Atoms	Angle(°)	Atoms	Angle(°)	Atoms	Length(Å)	Atoms	Length(Å)
S1–Cd–S3	101.59(2)	Cl1-Cd-S1	110.10(2)	Cd–S1	2.5821(6)	Cd–Cl1	2.5711(4)
S1–Cd–N1	141.67(4)	Cl1-Cd-N1	99.44(4)	Cd–S3	2.6207(5)	Cd–S1	2.5125(5)
S1–Cd–N2	74.87(4)	Cl1-Cd-N2	117.59(4)	Cd–N1	2.425(1)	Cd–N1	2.340(2)
S1–Cd–N4	94.01(4)	Cl1-Cd-Cl1	89.23(1)	Cd–N2	2.359(2)	Cd–N2	2.316(1)
S1–Cd–N5	132.35(4)	S1-Cd-N1	142.74(4)	Cd–N4	2.401(1)	Cd–Cl1	2.5766(4)
S3–Cd–N1	100.43(3)	S1-Cd-N2	76.52(4)	Cd–N5	2.361(2)	Cl1–Cd	2.5766(4)
S3–Cd–N2	111.66(4)	S1-Cd-Cl1	107.27(2)	S1–C8	1.727(2)	S1–C8	1.736(1)
S3– Cd–N4	137.98(4)	N1-Cd-N2	69.77(5)	S2–C8	1.756(2)	S2–C8	1.759(2)
S3–Cd–N5	73.23(4)	N1-Cd-Cl1	95.00(4)	S2–C9	1.804(2)	S2–C9	1.820(2)
N1–Cd–N2	67.96(5)	N2-Cd-Cl1	150.41(4)	S3–C17	1.729(2)	N1–C1	1.340(2)
N1–Cd–N4	90.17(5)	C8-S2-C9	103.71(8)	S4–C17	1.755(2)	N1–C5	1.355(2)
N1–Cd–N5	84.12(5)	C1-N1-C5	119.0(1)	S4–C18	1.795(2)	N2–N3	1.384(2)
N2–Cd–N4	110.02(5)	N3-N2-C6	118.2(1)	N1–C1	1.333(2)	N2–C6	1.290(2)
N2–Cd–N5	152.06(5)	N2-N3-C8	112.9(1)	N1–C5	1.354(2)	N3–C8	1.307(2)
N4–Cd–N5	67.55(5)	N1-C1-C2	122.9(2)	N2–N3	1.386(2)	C1–C2	1.388(3)
C1–N1–C5	118.5(1)	N1-C5-C4	121.0(1)	N2–C6	1.291(2)	C2–C3	1.382(2)
N3–N2–C6	116.2(1)	N1-C5-C6	117.3(1)	N3–C8	1.305(2)	C3–C4	1.393(3)
N2–N3–C8	114.0(1)	C4-C5-C6	121.6(1)	N4–C10	1.333(2)	C4–C5	1.392(3)

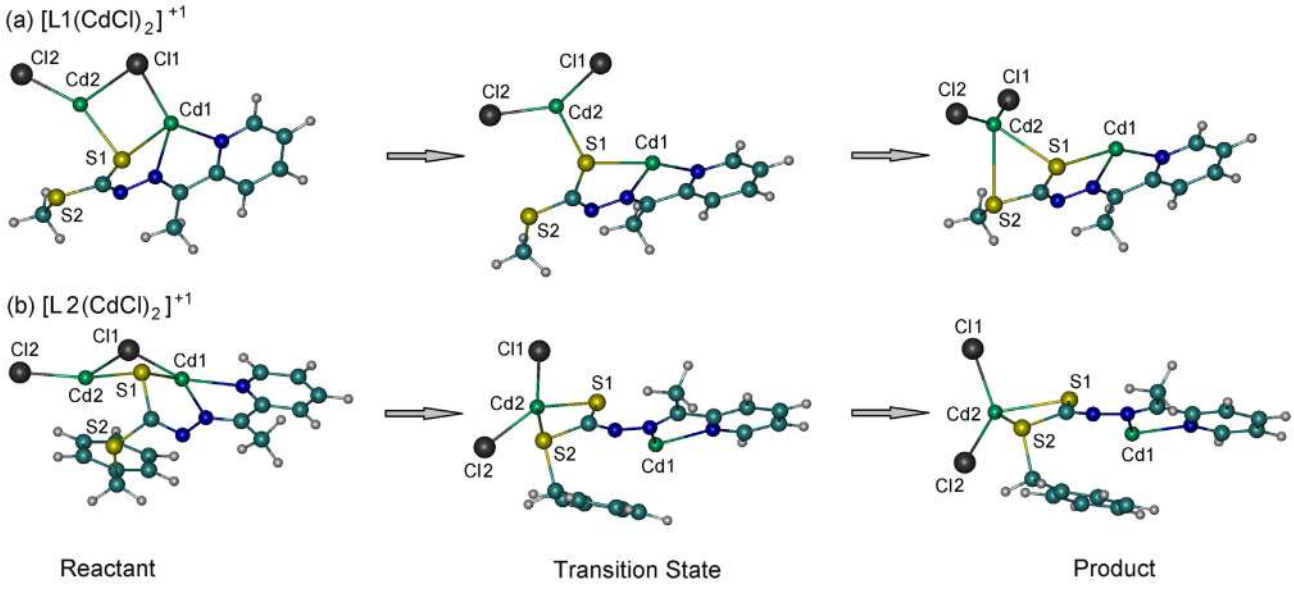

Fig. 4. Cleavage of the CdCl bond in the model complexes of deprotonated (a) HL^1 (b) HL^2 coordinated to $[(CdCl)_2]^{+2}$ in methanol.

Cd1 atom and its bound Cl1 atom is associated to the cleavage of this bond and to the rotation of the $CdCl_2$ plane by about 90° such that the Cd2–S2 bond is formed and the environment around the Cd2 atom, coordinated to S1, S2, Cl1 and Cl2, becomes distorted tetrahedral in the product complex. The transition state connecting the reactant and product is only 15.4 and 16.0 kcal/mol above the reactant for the complexes with deprotonated HL^1 and deprotonated HL^2, respectively. Therefore, the cleavage of the Cd1–Cl1 bond is energetically facile in methanol with both HL^1 and HL^2. However, the Cd1–Cl1 distance of the transition state structure is smaller with HL^1 (4.3 Å) than with HL^2 (5.9 Å). Therefore, the rotation of the $CdCl_2$ moiety starts at a shorter distance in the Cd complex of HL^1 having a small-sized S2-Me moiety. The large S2-Ph moiety of HL^2 prevents rotation of the closely-positioned $CdCl_2$ moiety.

Therefore, $CdCl_2$ must move away from the bulky body of the phenyl ring of HL^2 to be able to rotate for the formation of the product complex. Considering that the solution contains several other L^2 ligands, $CdCl_2$ could not be such flexible. These computational experiments in methanol solution indicate that $CdCl_2$ can effectively dissociate from the structure containing HL^1 to form the $[L^1CdL^1]$ complex while the bulky phenyl group of HL^2 is more protected against removal of $CdCl_2$ from the structure. Therefore, with HL^2, the $[L^2CdCl]_2$ complex is formed. The computational study proves that the ligand substitution plays a major role in the formation of the dinuclear complex.

4.5. XRD study

Thermogravimetric analyses give a direction about the suitability of the complexes to act as precursors for the synthesis of CdS nanocrystals. Using these precursors, CdS nanocrystals were synthesized in a solvothermal synthesis process using the solvents ethylene glycol and ethylene diamine. The crystalline phase of the prepared CdS nanocrystals was characterized by powder X-ray diffraction (XRD) as shown in Fig. 5. The diffraction patterns of the samples are indexed to the Wurtzite (hexagonal) phase of CdS with characteristic (1 0 0), (0 0 2), (1 0 1), (1 0 2), (1 1 0), (1 0 3), (1 1 2), and (2 0 1) peaks (JCPDS number 041–1049). The sharp peaks in the XRD patterns of the samples obtained from EG and oleic acid (OA) at 160 °C growth temperature reveal the crystallinity and narrow size distribution of the particles [8,15–17]. The strong and sharp diffraction peak at $2\theta = 23°$ corresponding to the (1 0 0) plane has been used to determine the grain diameter using the Debye–Scherrer equation, $D = 0.9\lambda/\beta\cos\theta$, where D is the grain size, λ is X-ray wavelength (1.5418 Å), β is the full width at half maximum (FWHM) in radian and θ is the Bragg's angle in degree. The calculated grain diameter of the CdS nanocrystals are 15.3 nm and 11.16 nm for the samples prepared from precursors SP**1** and SP**2**, respectively, using OA.

4.6. SEM and EDX analysis

The morphology and size of the CdS nanoparticles prepared from SP**1** and SP**2** using different solvents were investigated by SEM. As shown in Fig. 6, the monomer SP**1** produced an irregular rod-shaped architecture of CdS nanoparticles in EG (Fig. 6a) and EN (Fig. 6c). The rods are quite agglomerated into a flower-like structure comprising of numerous hollow spaces which may be responsible for their efficient catalytic properties. The CdS nanoparticles derived from SP**1** in OA are distinctly rod-shaped with a diameter of 50–60 nm. The distinct dispersibility of the nanorods in the present case might be due to the higher surface-passivating property of OA than EG/EN. The morphology of the CdS nanoparticles obtained from SP**2** in EG (Fig. 6b) is quite interesting and the low magnification SEM image shows that the nanoparticles consist of a well-dispersed irregular array of nanorods with a diameter range of 20–30 nm. A 3D hexagonal disk architecture with a width range 25–30 nm is observed in the sample obtained from SP**2** in OA (Fig. 6f). The dimension of the CdS discs from OA is quite high compare to the hexagonal rods from EG. Interestingly, the thermolysis of SP**2** in EN produced a flower-like nano architecture with a high level of porosity. It is interesting to note that both SP**1** and SP**2** produce anisotropic CdS nanoparticles with irregular arrangements. The quality arrangement of anisotropic CdS is obtainable in the presence of an external capping agent (OA) which suggests that the metal-chalcogen bond template is a softer structure-directing agent than OA. In our previous report, the dimeric SP of S-benzyl dithiocarbazate produced distinct CdS rods [38]. Incorporation of the pyridyl group in S-benzyl dithiocarbazate forming dimeric SP**2** might have a different effect on particle nucleation and growth. Notably, the particles in all cases have a high level of porosity to act as catalyst. Furthermore, an increase in the hydrothermal synthesis temperature to 200 °C results in products whose morphology is nearly the same as that obtained at 160 °C. These observations suggest that there is no prominent effect of temperature on CdS growth.

A rational formation mechanism of CdS has been proposed on the basis of the experimental results (Scheme 2). Generally, isotropic

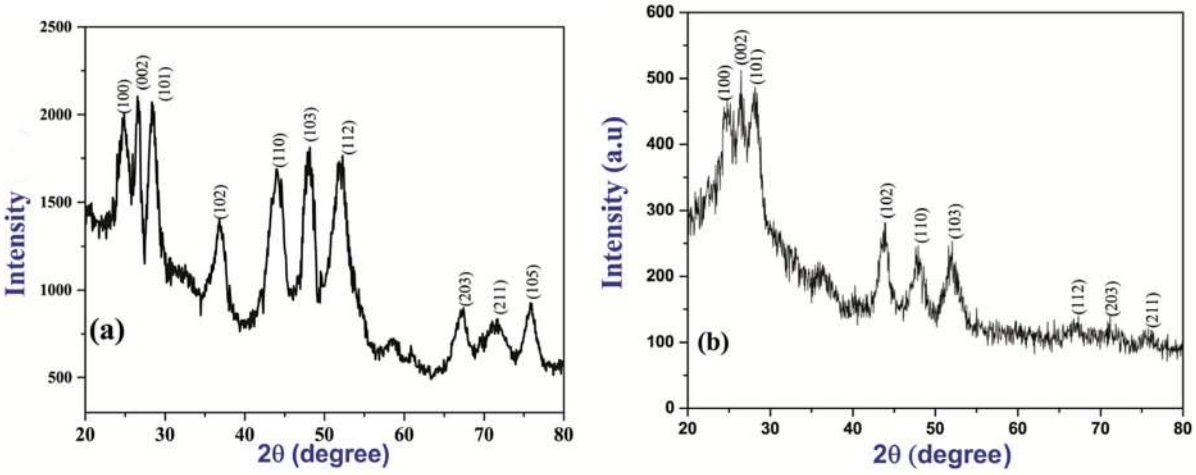

Fig. 5. XRD patterns of the CdS nanoparticals prepared from SP**1** (a) and SP**2** (b) using OA.

growth occurs in the SP method using an additional structure-directing agent (e.g., HPA etc.) [7]. Later on, it has been shown that the SP itself has the inherent property to control the shape of the particle [8,40–42]. In the present method, the SP can be regarded as a microreactor for the CdS synthesis. In the process, thermal energy weakens the bonds in the coordination sphere and a structural rearrangement occurs without dissolution. The seed nanocrystals of CdS are formed following the direction of the metal-sulfur template in the nucleation stage. Being a dimer, SP**2** provides sufficient space in the lattice domain of the molecule to orient or attach internally a seeded CdS particle in a fashion similar to the Cd–S bond template. Further growth of the nanoparticles follows the oriented attachment, which forms a 1D rod-like structure progressively as shown in Scheme 2. On the other hand, in SP**1** the localization of the Cd and S atoms in the unit lattice provides an orientation of CdS seeds in such a way that the seeded nanoparticles attache themselves to grow further in all directions (x, y and z axes), forming a 3D flower-like architecture (Scheme 2).

In addition, to determine the crystallinity and the atomic ratio, an energy-dispersive X-ray spectroscopy (EDX) analysis of CdS NCs was performed. The EDX results confirm that the elemental composition of Cd:S ≈ 1:1 and no precursor element or impurity remains after the reaction [Fig. 7].

4.7. UV–VIS spectral analysis

The optical properties of the CdS nanoparticles are illustrated by a UV–Vis absorption spectra analysis. Dispersed CdS nanoparticles in ethanol, grown from SP**1** in EG, show an absorbance throughout the entire visible region [Fig. 8(a)]. A similar feature is also observed for the sample obtained from SP**2** in EG [Fig. 8(b)]. The band gap plots of $(\alpha h\upsilon)^2$ *vs.* E(= $h\upsilon$) show the band gaps between the conduction and valence band appearing at 2.4 eV and 2.5 eV in SP**1** and SP**2**, respectively, [inset of Fig. 8] indicating an absorptivity in the solar spectrum and a quantum confinement effect in the structure.

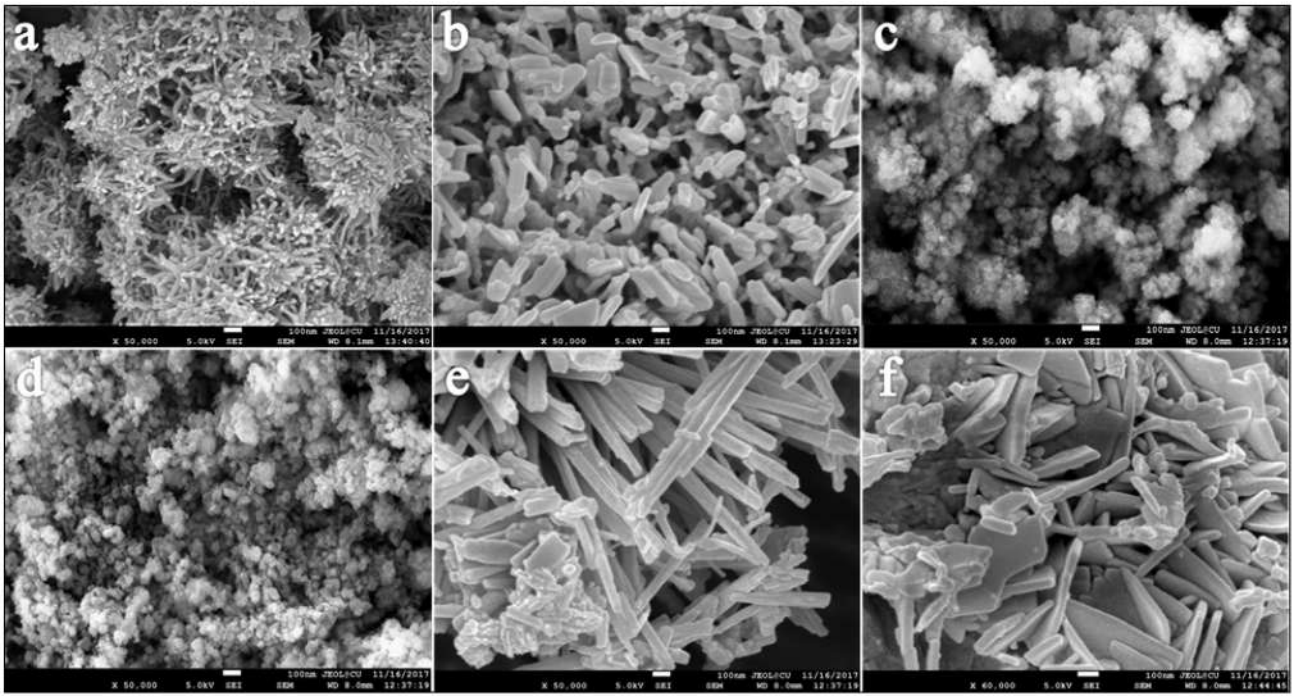

Fig. 6. SEM images of the prepared CdS nanocrystals [a and b from SP**1** and SP**2** using EG, respectively, c and d from SP**1** and SP**2** using EN, respectively, and e and f from SP**1** and SP**2** using OA, respectively.]

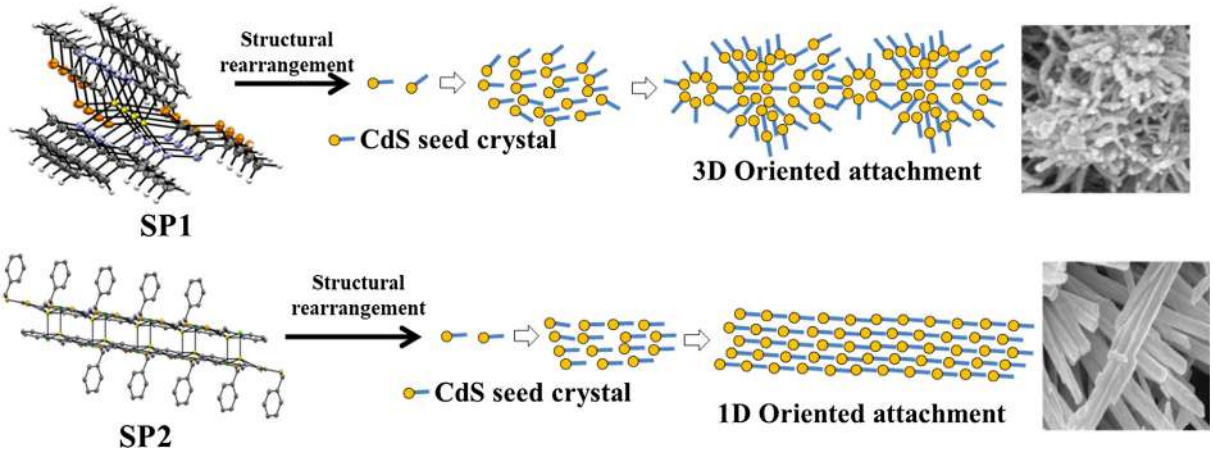

Scheme 2. Different modes of oriented attachment.

4.8. Photocatalytic activity

The synthesized semiconducting CdS NCs have been used as catalysts for photodegradation under visible light. The catalytic performance was examined by photo degradation of RB under visible light illumination. We have chosen Rose Bengal (RB) as a model dye to test the photocatalytic activity. This dye is used largely by textile industries.

The time-dependent VU-VIS spectral change of an RB solution in the presence of CdS nanocrystals under the irradiation of visible light for 90 min is given in Fig. 9. The solutions were stored in the dark to attend the adsorption/desorption equilibrium for 40 min. Next, the solutions were exposed to visible light with magnetic stirring. At a certain time interval, 3 mL of solution were centrifuged and the supernatants adsorption was measured in a UV–Vis spectrophotometer. The characteristic absorption peaks at 540 nm for the RB solution gradually decreased with irradiation time. After 90 min reaction time, no new absorption peaks appeared, but the characteristic absorption bands of the dyes disappeared, suggesting a complete photo degradation of RB. In order to determine the kinetics of the photo degradation, we plotted $\ln(C_t/C_o)$ *vs.* irradiation time according to the equation $\ln(C_o/C_t) = kt$, where C_o is the initial concentration of the aqueous solution, C_t is the concentration at time t and k is rate constant for the reaction (Figs. 10 and 11). The measured k value is 3.5×10^{-3} min^{-1} for the photo degradation of RB, indicating pseudo first order kinetics.

5. Conclusion

Both dichloro-bridged and chloro-unbridged Cd^{II} complexes of pyridinyl dithiocarbazate were synthesized varying the substitution in the ligand's arm. The molecular structures of the complexes were studied by single crystal X-ray analysis. The ligand bearing a bulky benzyl prefers to form a chlorido-bridged dimer structure whereas the unbridged structure is stabilized with a methyl substitution of the ligand. Different coordination patterns of the Cd complexes with HL^1 and HL^2 ligands were investigated through DFT model studies. DFT calculations indicate that the $[L^1CdL^1]$ complex can be effectively formed through the dissociation of $CdCl_2$ from the structure while the bulky body of the phenyl group in the HL^2 ligand hinders a dissociation of $CdCl_2$ from the structure, leading to the formation of the $[L^2CdCl]_2$ complex. The complexes are suitable for the production of high quality CdS nanoparticles as evidenced by their low decomposition temperature. The particle growth is governed by the metal-chalcogen bond template of the SPs. The dichloride-bridged dimer produces rod-shaped anisotropic CdS, whereas the unbridged monomer produces isotopic a 3D cluster of CdS. The synthesized CdS nanoparticles profoundly degrade Rose Bengal dye (96%) under visible light irradiation. A reusability study shows that the catalytic activity of the CdS nanoparticles is retained up to two cycles (86%).

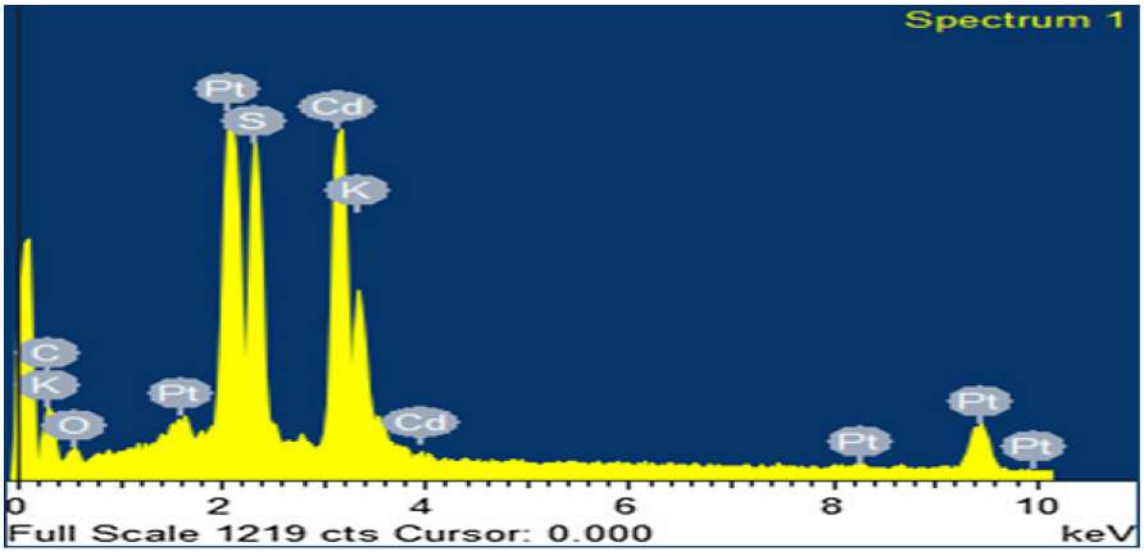

Fig. 7. EDX analysis of CdS NCs prepared from SP**1**.

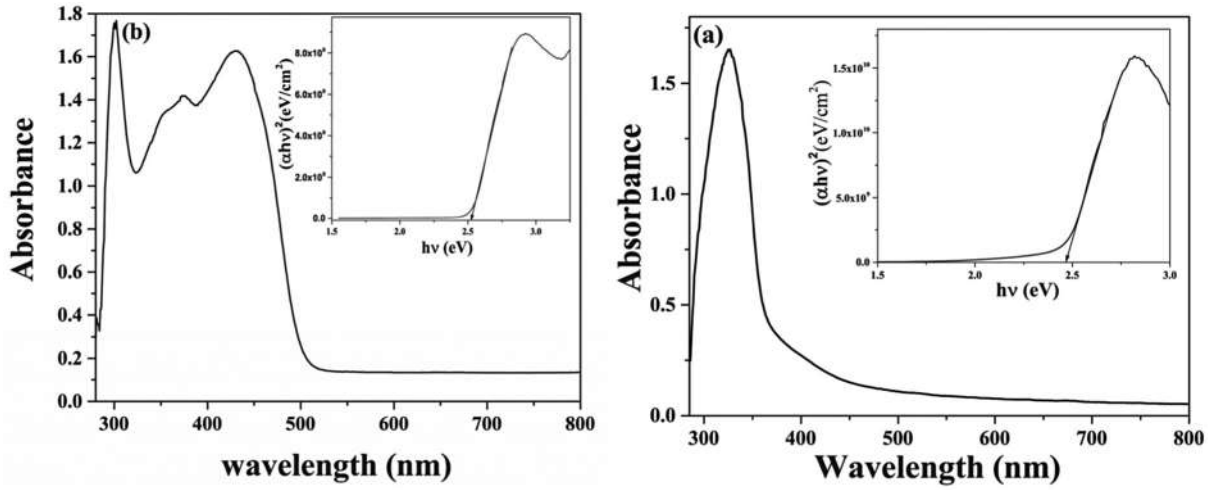

Fig. 8. UV–Vis spectra of CdS NCs prepared from SP**1** (a) and SP**2** (b); inset band gap $(\alpha h\nu)^2$ *vs.* hν plot of the respective samples.

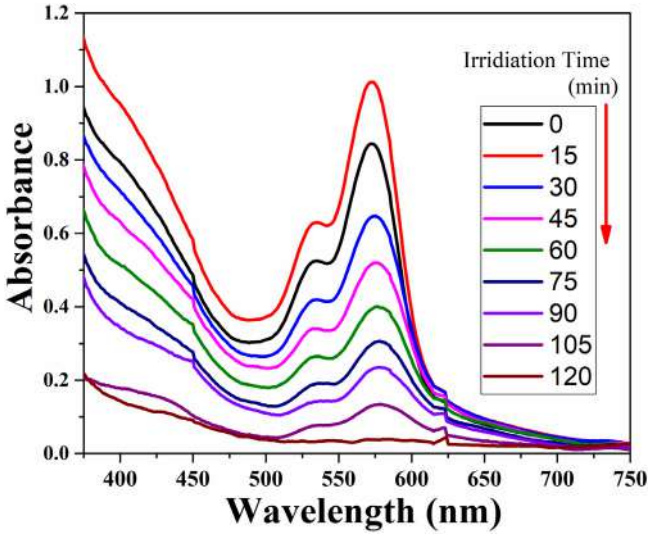

Fig. 9. UV–Vis spectral changes during the photodegradation of Rose Bengal dye in the presence of CdS nanoparticles prepared from SP**1**.

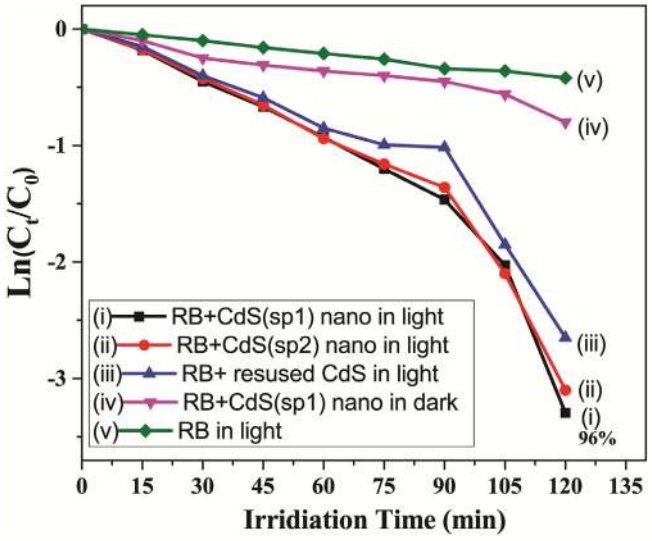

Fig. 10. Photodegradation of Rose Bengal dye [$Ln(C_t/C_0)$ *vs* Irradiation time] under different conditions.

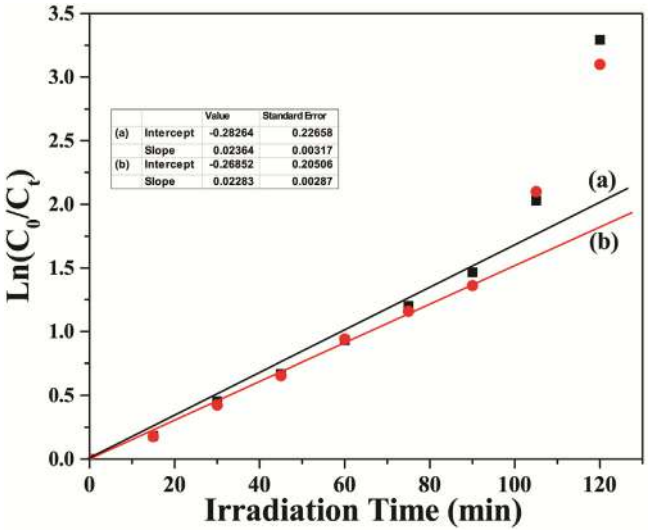

Fig. 11. Logarithmic change of the relative concentration of Rose Bengal dye with catalyst CdS from SP**1** (a) and CdS from SP**2** (b) as a function of irradiation time under different conditions.

Declaration of Competing Interest

The authors declare that they have no known competing financial interests or personal relationships that could have appeared to influence the work reported in this paper.

Acknowledgements

We gratefully acknowledge to Council for Scientific and Industrial Research (CSIR), Government of India for financial support [grant no. 1(2858)/16/EMR–II]. Panskura Banamali College acknowledges the grants received from Department of Science and Technology (DST), Govt. of India through FIST program (No.SR-FIST-COLLEGE-295-dt 18/11/2015). Also thanks to all members of CRNN, Kolkata and IIEST, Shibpur for their help ~~to~~ in characterization.

Appendix A. Supplementary data

CCDC 1833373 and 1833375 for compound SP**1** and SP**2,** respectively. Crystallographic data can be obtained free of charge on application to CCDC, 12 Union Road, Cambridge CB2 1EZ, UK, fax: (+44) 1223 336033, e-mail: deposit@ccdc.cam.ac.uk. The computational

structures are provided.

Supplementary data to this article can be found online at https://doi.org/10.1016/j.ica.2019.119315.

References

[1] M.A. Malik, N. Revaprasadu, P. Obrien, Air-stable single-source precursors for the synthesis of chalcogenide semiconductor nanoparticles, Chem. Mater. 13 (2001) 913–920.

[2] B. Ludolph, M.A. Malik, P. O'Brien, N. Revaprasadu, Novel single molecule precursor routes for the direct synthesis of highly monodispersed quantum dots of cadmium or zinc sulfide or selenide, Chem. Commun. (1998) 1849–1850.

[3] P.S. Nair, T. Radhakrishnan, N. Revaprasadu, G.A. Kolawole, P. O'Brain, Cadmium ethylxanthate: a novel single-source precursor for the preparation of CdS nanoparticles, J. Mater. Chem. 12 (2002) 2722–2725.

[4] M.A. Malik, M. Afzaal, P. O'Brien, Precursor chemistry for main group elements in semiconducting materials, Chem. Rev. 110 (2010) 4417–4446.

[5] L.D. Nyamen, N. Revaprasadu, R.V.S.R. Pullabhotla, A.A. Nejo, P.T. Ndifon, M.A. Malik, P. Obrien, Synthesis of multi-podal CdS nanostructures using heterocyclic dithiocarbamato complexes as precursors, Polyhedron 56 (2013) 62–70.

[6] G. Mondal, P. Bera, A. Santra, S. Jana, T.N. Mondal, S.I. Seok, A. Mondal, P. Bera, Precursor-driven selective synthesis of hexagonal chalcocite (Cu_2S) nanocrystals: structural, optical, electrical and photocatalytic properties, New J. Chem. 38 (2014) 4774–4782.

[7] P. Bera, S.I. Seok, Nanocrystalline copper sulfide of varying morphologies and stoichiometries in a low temperature solvothermal process using a new single-source molecular precursor, Solid State Sci. 14 (2012) 1126–1132.

[8] P.S. Nair, G.D. Scholes, Thermal decomposition of single source precursors and the shape evolution of CdS and CdSe nanocrystals, J. Mater. Chem. 16 (2006) 467–473.

[9] T. Mondal, G. Piburn, V. Stavila, I. Rusakova, T.O. Ely, A.C. Colson, K.H. Whitmire, New mixed ligand single-source precursors for PbS nanoparticles and their solvothermal decomposition to anisotropic nano- and microstructures, Chem. Mater. 23 (2011) 4158–4169.

[10] G. Mondal, A. Santra, P. Bera, M. Acharjya, S. Jana, D. Chattopadhyay, A. Mondal, S.I. Seok, P. Bera, A pyrazolyl-based thiolato single-source precursor for the selective synthesis of isotropic copper-deficient copper(I) sulfide nanocrystals: synthesis, optical and photocatalytic activity, J. Nanopart Res. 18 (2016) 311.

[11] G. Mondal, A. Santra, S.I. Seok, P. Bera, Synthesis of isotropic PbS nanoparticles from the single precursor, highly coordinative lead complex of S-methyl dithiocarbazate, [Pb{S=C(SCH3)NHNH2}(NO3)2], J. Nanosci. Lett. 4 (2014) 35 http://www.cognizure.com/abstract.aspx?p=200638328.

[12] A. Santra, G. Mondal, M. Acharjya, P. Bera, A. Jana, S.I. Seok, P., Bera, New pyrazole based single precursor for the surfactantless synthesis of visible light responsive PbS nanocrystals: Synthesis, X-ray crystallography of ligand and photocatalytic activity, Nano-Struct. Nano-Objects 10 (2017) 91–99.

[13] G. Mondal, M. Acharjya, A. Santra, P. Bera, S. Jana, N.C. Pramanik, A. Mondal, P. Bera, A new pyrazolyl dithioate function in the precursor for the shape controlled growth of CdS nanocrystals: optical and photocatalytic activities, New J. Chem. 39 (2015) 9487–9496.

[14] P. Bera, C.H. Kim, S.I. Seok, High-yield synthesis of quantum-confined CdS nanorods using a new dimeric cadmium(II) complex of S-benzyldithiocarbazate as single-source molecular precursor, Solid State Sci. 12 (2010) 532–535.

[15] P. Bera, C.H. Kim, S.I. Seok, Synthesis of nanocrystalline CdS from cadmium(II) complex of S-benzyl dithiocarbazate as a precursor, Solid State Sci. 12 (2010) 1741–1747.

[16] G. Mondal, A. Santra, S. Jana, N.C. Pramanik, A. Mondal, P. Bera, Enhanced photocatalytic activity of ternary $CuInS_2$ nanocrystals synthesized from the combination of a binary Cu(I)S precursor and $InCl_3$, J. Nanopart Res. 20 (2018) 108.

[17] P. Bera, S.I. Seok, Facile synthesis of nanocrystalline wurtzite Cu–In–S by amine-assisted decomposition of precursors, J. Solid State Chem. 183 (2010) 1872–1877.

[18] M.A. Ali, A.H. Mirza, M.H.S.A. Hamid, P.V. Bernhardt, O. Atchade, X. Song, G. Eng, L. May, Synthesis, spectroscopic and structural characterization of diphenyltin(IV) complexes of acetone Schiff bases of S-alkyldithiocarbazates, Polyhedron 27 (2008) 977–984.

[19] M.T.H. Tarafder, A.M. Ali, D.J. Wee, K. Azahari, S. Silong, K.A. Crouse, Complexes of a tridentate ONS Schiff base-Synthesis and biological properties, Transition Met. Chem. 25 (2000) 456–460.

[20] B.K. Koo, Synthesis and crystal structures of copper(II) complexes with Schiff base ligands, J. Korean Chem. Soc. 59 (2015) 103.

[21] A.B. Beshir, S.K. Guchhait, J.A. Gascon, G. Fenteany, Bioorgan. Med. Chem. Lett. 18 (2008) 498–504.

[22] Bruker, (2001) SMART (Version 5.625) Data Collection Program, Bruker AXS Inc., Madison, Wisconsin, USA.

[23] Bruker, (2001) SAINT (Version 6.28a) and SADABS (Version 2.03) Data Reduction and Absorption Correction Program, Bruker AXS Inc., Madison, Wisconsin, USA.

[24] G.M. Sheldrick, 2001, SHELXTL (Version 6.12) Structure Analysis Program, Bruker AXS Inc. Madison, Wisconsin, USA.

[25] F. Neese, The ORCA program system, Wiley Interdiscip. Rev. Comput. Mol. Sci. 2 (2012) 73–78.

[26] F. Neese, Software update: the ORCA program system, version 4.0, Wiley Interdiscip. Rev. Comput. Mol. Sci. 8 (2018) 1327.

[27] A.D. Becke, Density-functional thermochemistry. III. The role of exact exchange, J. Chem. Phys. 98 (1993) 5648.

[28] C. Lee, W. Yang, R.G. Parr, Development of the Colle-Salvetti correlation-energy formula into a functional of the electron density, Phys. Rev. B 37 (1988) 785.

[29] A.D. Becke, Density-functional exchange-energy approximation with correct asymptotic Behavior, Phys. Rev. A 38 (1988) 3098.

[30] S. Grimme, S. Ehrlich, L. Goerigk, Effect of the damping function in dispersion corrected density functional theory, J. Comput. Chem. 32 (2011) 1456–1465.

[31] V. Barone, M. Cossi, Quantum calculation of molecular energies and energy gradients in solution by a conductor solvent model, J. Phys. Chem. A 102 (1998) 1995–2001.

[32] F. Weigend, Accurate coulomb-fitting basis sets for H to Rn, Phys. Chem. Chem. Phys. 8 (2006) 1057–1065.

[33] F. Weigend, R. Ahlrichs, Balanced basis sets of split valence, triple zeta valence and quadruple zeta valence quality for H to Rn: design and assessment of accuracy, Phys. Chem. Chem. Phys. 7 (2005) 3297–3305.

[34] N.E. Fard, R. Fazaeli, R. Ghiasi, Band gap energies and photocatalytic properties of CdS and Ag/CdS nanoparticles for azo dye degradation, Chem. Eng. Technol. 39 (2016) 149–157.

[35] X. Wang, H. Tian, Y. Yang, H. Wang, S. Wang, W. Zheng, Y. Liu, Reduced graphene oxide / CdS for efficiently photocatalystic degradation of methylene blue, J. Alloys Compd. 524 (2012) 5–12.

[36] C. Peng, X. Cheng, S. Chen, X. Li, T. Li, D. Zhang, Z. Huang, A. Zhang, A Facile method to Prepare Monodispersed CdS / SiO_2 Composite Microspheres and Investigation on Their Photocatalytic Properties, Photochem. Photobiol. 88 (2012) 1433–1441.

[37] J.M. Rowland, M.M. Olmstead, P.K. Mascharak, Monomeric and Dimeric Copper(II) complexes of a novel tripodal peptide ligand: structures stabilized via hydrogen bonding or ligand sharing, Inorg. Chem. 39 (2000) 5326–5332.

[38] A. Mitra, T. Banerjee, P. Roychowdhury, S. Chaudhuri, P. Bera, N. Saha, Synthesis and spectroscopic characterisation of cobalt(III) complexes with S-benzyl dithiocarbazate of 5-methyl-3-formyl pyrazole (HMPzSB): X-ray crystal structure of [Co(MPzSB)2]Cl, Polyhedron 16 (1997) 3735–3742.

[39] P. Bera, C.H. Kim, S.I. Seok, High-yield synthesis of quantum-confined CdS nanorods using a new dimeric cadmium(II) complex of S-benzyldithiocarbazate as single-source molecular precursor, Solid State Sci. 10 (2010) 532–535.

[40] C. Li, J. Yuan, B. Han, W. Shangguan, Synthesis and photochemical performance of morphology-controlled CdS photocatalysts for hydrogen evolution under visible light, Int. J. Hydrog. Energy 36 (2011) 4271–4279.

[41] J.F.A. Oliveira, T.M. Milão, V.D. Araújo, M.L. Moreira, E. Longo, M.I.B. Bernardi, Influence of different solvents on the structural, optical and morphological properties of CdS nanoparticles, J. Alloy Compd. 509 (24) (2011) 6880–6883.

[42] S.L. Cumberland, K.M. Hanif, A. Javuer, G.A. Khitrov, G.F. Strouse, S.M. Woessner, C.S. Yun, Inorganic clusters as single-source precursors for preparation of CdSe, ZnSe, and CdSe/ZnS Nanomaterials, Chem. Mater. 14 (2002) 1576–1584.

Source details

Feedback > Compare sources >

Inorganica Chimica Acta

See also: Inorganic Chemistry Communication

Incorporating: Inorganica Chimica Acta Reviews

Scopus coverage years: from 1967 to Present

Publisher: Elsevier

ISSN: 0020-1693 E-ISSN: 1873-3255

Subject area: Chemistry: Inorganic Chemistry | Materials Science: Materials Chemistry | Chemistry: Physical and Theoretical Chemistry

Source type: Journal

View all documents > | Set document alert | Save to source list

CiteScore 2022
5.6

SJR 2022
0.406

SNIP 2022
0.658

CiteScore | CiteScore rank & trend | Scopus content coverage

Chemosphere 238 (2020) 124647

Contents lists available at ScienceDirect

Chemosphere

journal homepage: www.elsevier.com/locate/chemosphere

Arsenic-induced immunomodulatory effects disorient the survival-death interface by stabilizing the Hsp90/Beclin1 interaction

Zarqua Jamal [a], Joydeep Das [a], Sayan Ghosh [b], Anasuya Gupta [a], Sreya Chattopadhyay [b], Urmi Chatterji [a, *]

[a] Cancer Research Laboratory, Department of Zoology, University of Calcutta, 35 Ballygunge Circular Road, Kolkata, 700 019, India
[b] Department of Physiology, University of Calcutta, 92 Acharya Prafulla Chandra Road, Kolkata, 700 009, India

HIGHLIGHTS

- Arsenic causes cellular disorganization of thymocytes and splenocytes.
- ROS has a key role in mediating the cytotoxicity of sodium arsenite in the immune organs.
- High level of ROS stimulates autophagic/apoptotic pathways responsible for inducing cell death.
- Hsp90 protein plays a crucial role in Beclin-1 stabilization and upregulation of autophagy upon arsenic exposure.

GRAPHICAL ABSTRACT

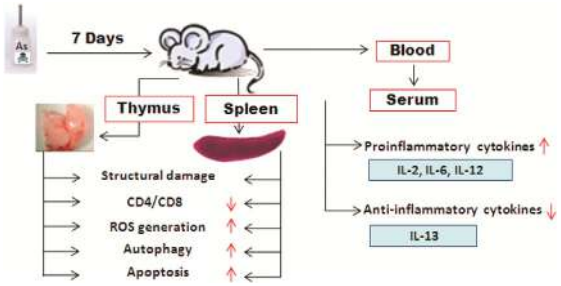

ARTICLE INFO

Article history:
Received 7 May 2019
Received in revised form
19 August 2019
Accepted 21 August 2019
Available online xxx

Handling Editor: Willie Peijnenburg

Keywords:
Arsenic
Immunophenotyping
Cytokines
ROS
Autophagy
Apoptosis

ABSTRACT

Ground water arsenic contamination is a global menace. Since arsenic may affect the immune system, leading to immunesuppression, we investigated the effects of acute arsenic exposure on the thymus and spleen using Swiss albino mice, exposed to 5 ppm, 15 ppm and 300 ppm of sodium arsenite for 7 d. Effects on cytokine balance and cell survivability were subsequently analyzed. Our data showed that arsenic treatment induced debilitating alterations in the tissue architecture of thymus and spleen. A dose-dependent decrease in the ratio of $CD4^{+}$-$CD8^{+}$ T-cells was observed along with a pro-inflammatory response and redox imbalance. In addition, pioneering evidences established the ability of arsenic to induce an up regulation of Hsp90, eventually resulting in stabilization of its client protein Beclin-1, an important autophagy-initiating factor. This association initiated the autophagic process, confirmed by co-immunoprecipitation assay, acridine orange staining and Western blot, indicating the effort of cells trying to survive at lower doses. However, increased arsenic assault led to apoptotic cell death in the lymphoid organs, possibly by increased ROS generation. There are several instances of autophagy and apoptosis taking place either simultaneously or sequentially due to oxidative stress. Since arsenic is a potent environmental stress factor, exposure to arsenic led to a dose-dependent increase in both autophagy and apoptosis in the thymus and spleen, and cell death could therefore possibly be induced by

Abbreviations: ppm, parts per million; WHO, World Health Organization; ATSDR, Agency of Toxic Substance and Disease Registry; IARC, International Agency for Research on Cancer; ELISA, Enzyme-linked immune sorbent assay; IL, interleukin; GSH, glutathione; SOD, superoxide dismutase; CAT, catalase; ROS, reactive oxygen species; PAGE, polyacrylamide gel electrophoresis; RIPA, radioimmunoprecipitation assay; SDS, sodium dodecyl sulphate; PVDF, polyvinylidene fluoride; SEM, scanning electron microscopy; TEM, transmission electron microscopy; AVOs, acidic vesicular organelles.

* Corresponding author.
E-mail address: urmichatterji@gmail.com (U. Chatterji).

https://doi.org/10.1016/j.chemosphere.2019.124647

autophagy. Therefore, exposure to arsenic leads to serious effects on the immune physiology in mice, which may further have dire consequences on the health of exposed animals.

1. Introduction

An interminable conflict exists within cells while they respond to different kinds of stress, which range from activation of components that promote cell survival to eliciting programmed death pathways to eliminate damaged cells (Kasprowska-Liśkiewicz, 2017). While the initial cellular response to a stress is to defend against and recover from the insult, the cells are eventually coerced to activate death signaling pathways if the magnitude of stress is unresolved (Navarro-Yepes et al., 2014). Therefore, survival of a cell critically depends on its ability to construe an appropriate response towards an environmental or intracellular stress stimuli and the adaptive capacity of a cell will ultimately determine its fate (Orrenius et al., 2011). The concerted mechanisms by which a cell may eventually die, that is, apoptosis, necrosis, or autophagy-induced apoptosis, often depends on its ability to cope with the conditions to which it is exposed (Chatterjee et al., 2014). Molecular epidemiologic studies have substantiated that several environmental factors, such as tobacco, infections, radiation and most prominently, heavy metal pollution, are the major causes of human diseases and disorders (Anand et al., 2008; Ren et al., 2011). The risk of being affected by these factors depends on an individual's genetic makeup and acquired susceptibility to environmental factors, specifically heavy metal pollution (Ahsan et al., 2007; Faita et al., 2013). It is nevertheless debatable if exposure to heavy metals would cause curable physiological disorders or lead to something more critical like cancer, and the precise activation of intracellular components controlling such a decision is yet to be discerned. This also raises questions regarding the molecular mechanisms involved in a switch from pro-survival to pro-death signaling. Therefore, whether a cell affected by heavy metal toxicity will die or acquire changes that will lead to its unregulated proliferation is an unrequited question and challenges a fine balance between components which control the cell survival and death pathways.

Arsenic, a heavy metal toxicant known to cause organ toxicity (Chatterjee and Chatterji, 2010; Noman et al., 2015; Chen et al., 2001), may trigger malignant transformation either by inducing the expression of proinflammatory chemokines (Li et al., 2017; Shao et al., 2018) or by inducing ROS generation (Chatterjee and Chatterji, 2017). Under heavy metal-induced stress conditions, cells initially adopt several adaptive alternatives, such as autophagy, to protect against cell death (So et al., 2018). In normal cells, basal levels of autophagy help the cells adapt to the environment; however, excessive autophagy eventually triggers autophagy-induced cell death (Das et al., 2012). The molecules associated with autophagy and apoptosis are regulated by molecular chaperones, which prevent protein unfolding, and regulate diverse biological processes by maintaining the stability of its client proteins (Cattaneo et al., 2012). Exposure to arsenic is known to trigger heat shock proteins (HSPs), which play important roles in immunomodulation and apoptosis (Banerjee et al., 2015). A critical balance in the interactions of autophagy-inducing proteins with molecular chaperones may play an important role in skewing the survival versus death response in cells exposed to arsenic. However, the role of Beclin 1 in heavy metal toxicity and the interaction between Hsp 90 and Beclin 1 is yet to be elucidated. Several studies have demonstrated that arsenic induces apoptosis in different tissues (Chatterjee and Chatterji, 2017; Choudhury et al., 2016; Htike et al., 2016); however, the mechanism involving autophagy and autophagy-induced apoptosis in the thymus and spleen, which regulates the pro- and anti-inflammatory cytokine balance in the body, needs to be discerned. The present study intends to determine the toxic effects of arsenic exposure on immune-organs and delineate the critical resolution of cell survival versus death mechanisms in response to arsenic-mediated stress. This study will identify that arsenic-induced toxicity stimulates an immuno-inflammatory change due to modulation of the T-cell population, and although activation of the Hsp90-mediated autophagic machinery occurs as an initial survival mechanism, finally the thymic and splenic cells progressed towards apoptosis. Eventually, new insights into the mechanistic basis of response to heavy metals like arsenic will generate novel perspectives for the development of targeted treatment approaches and specific drug discovery.

2. Materials and methods

2.1. Chemicals and kits

Natrium-*meta*-arsenite ($NaAsO_2$) was obtained from Merck (Germany). FITC Annexin Apoptosis Detection kit was purchased from Bio Legend (USA), Acridine Orange, DCFDA from Abcam, (UK). Multianalyte ELISArray kit from Qiagen (USA), Cleaved PARP, Akt, Akt1 (phospho T450), mTOR antibodies were procured from Abcam (UK). Hsp90, Beclin1, LC3, Bax, Bcl2, p53 and phospho-mTOR antibodies and horseradish peroxidase-conjugated secondary antibodies were obtained from Santa Cruz Biotechnologies (USA). DTNB, reduced glutathione (GSH), pyrogallol, Trizma, glycine, sodium chloride, sodium dodecyl sulphate were all obtained from Sigma Aldrich (USA). Protein A/G plus Agarose was obtained from Santa Cruz Biotechnologies (USA). Optiblot ECL detect kit was purchased from Abcam (UK). Cedarwood oil and D.P.X. mountant for microscopy were bought from Merck (Germany). Paraplast high melt tissue embedding medium was obtained from Leica biosystems (Netherlands). Prism ultra protein ladder was obtained from Abcam (UK).

2.2. Animals

All animal experiments were done in accordance with Principles of Laboratory Animal Care (NIH Publication No 85-23, revised in 1985) and approval of the of the Institutional Animal Ethical Committee, Government of India (Registration Number 885/ac/05/CPCSEA). Specific Indian Laws of Animal Protection (ILAP) were followed throughout the experimental schedule. Swiss albino mice (male) were maintained under controlled conditions ($25 \pm 2\,^{\circ}C$ temperature, $50 \pm 15\%$ RH and normal photoperiod of 12 h dark and 12 h light) throughout the experiment. The animals were fed with food pellets and water *ad libitum* and allowed to acclimatize to the laboratory environment a week prior to the commencement of the experiments.

2.2.1. Selection of the dose of arsenic

Sodium arsenite was administered via drinking water. The mice were randomly divided into different groups, each containing six

animals (n = 6). The groups were treated as follows: Group I (control group, received arsenic-free water), Group II (5 ppm arsenic), Group III (15 ppm arsenic), Group IV (300 ppm arsenic). Animals were exposed to arsenic for 7d, after which they were euthanized. Tissues and blood were harvested for subsequent experiments.

2.2.2. Tissue and blood collection

Tissues were collected and washed in 0.9% (w/v) cold normal saline. Small representative tissue slices were processed for histological studies, scanning electron microscopy (SEM), transmission electron microscopy (TEM) and protein purification. Serum was isolated for ELISA.

2.3. Histology and morphometric analysis

Spleen and thymus from control and treated animals were fixed in Bouins' fluid. For histological studies, 5μ paraffin sections were stained by hematoxylin-eosin double staining procedure (Chatterjee and Chatterji, 2011) and observed under a light microscope (Dewinter Optical Inc., India). The stained sections were subjected to morphometric analysis using the Dewinter Caliper Pro software.

2.4. Scanning electron microscopy

Spleen and thymus were dissected, cut into small pieces (1 mm × 1 mm) and fixed by immersion in 2.5% glutaraldehyde with 0.2 M phosphate buffer for 2 h at 4 °C. Tissues were cut into small pieces and fixed overnight. Fixed tissues were washed three times with 0.2 M phosphate buffer. Tissues were subsequently dehydrated through ascending grades of ethanol, placed in chilled acetone, and air dried overnight. After critical point drying, the tissues were coated with gold in a Sputter Coater (Quorum Q150TES) and finally viewed by SEM (Choudhury et al., 2016) (Zeiss EVO-18-Special edition, Germany).

2.5. Transmission electron microscopy

This study focused on alterations in arsenic exposed and control spleen and thymus tissues of mice, with particular reference to the sub-cellular organelles *viz* lysosomes, endoplasmic reticulum, mitochondria and nucleus. Small pieces of tissues (thymus/spleen) were cut and the tissue samples fixed in 2.5% glutaraldehyde and 2% paraformaldehyde in 0.1 M sodium phosphate buffer (pH 7.3) for 12 h at 4 °C. After washing, the samples were fixed in 1% OsO_4 for 1 h at 4 °C. The samples were dehydrated in ascending grades of acetone, infiltrated and embedded in araldite CY 212 (TAAB, UK). Thin Sections (1 μm) were cut with an ultramicrotome, mounted on to glass slides, stained with aqueous toluidine blue and observed under a light microscope for gross observation of the area and quality of the tissue fixation. To have a random, unbiased, and global view of the thymus and spleen samples studied, several small pieces of tissue were prepared from each block, and finally one sample was selected at random for embedding. Ultrathin sections were cut from each of the blocks and placed on copper grids. For electron microscope examination, thin sections of grey-silver colour interference (70–80 nm) were cut and mounted onto 300 mesh-copper grids. Sections were stained with alcoholic uranyl acetate and alkaline lead citrate, washed gently with distilled water and observed under a Morgagni 268 D transmission electron microscope (Fei Company, The Netherlands) at an operating voltage of 80 kV. Images were digitally acquired by a CCD camera (Megaview III, Fei Company) using iTEM software (Sift Imaging System, Münster, Germany) attached to the microscope.

2.6. Flow cytometric detection of cell surface receptors

The thymus and spleen were harvested and single cell suspensions were prepared by gently teasing the respective tissues in sterile PBS. The single cells were passed through a nylon mesh (pore size 40 μm) and washed thrice. For determination of the surface receptors $CD4^+$ and $CD8^+$, the cells were incubated with corresponding antibodies at a concentration of 1 μg/ml in PBS containing 1% BSA for 1 h. After incubation, the cells were washed and analyzed by flow cytometry (BD FACS Verse, USA). A total of 10,000 events were acquired (Choudhury et al., 2016). The experiment was repeated thrice for statistical significance.

2.7. Cytokine analysis

Analyses of cytokines in serum of arsenic-treated and control mice were carried out using the Multi-analyte ELISArray Kit, according to the manufacturer's protocol (Qiagen MEM-004A, USA), using the standard sandwich-based ELISA technique. Briefly, samples were prepared, added to each well of the ELISArray plate and incubated for 2 h. Plates were incubated with antibody solution for 1 h, followed by 30 min in Avidin-HRP conjugate. The wells were washed and incubated for 15 min in the dark with development solution. Finally, the stop solution was added and OD measured in an ELISA plate reader (Biorad iMark Microplate Reader, USA) at 450 nm and 595 nm.

2.8. Estimation of intracellular ROS generation

Intracellular ROS was measured using the oxidation sensitive fluorescence probe, 2′,7' -dichlorofluorescein diacetate (DCFDA). DCFDA is deacetylated by intracellular esterase, which is further oxidized by ROS to the fluorescent compound 2′, 7′- dichlorofluorescein (DCF). Cells from the thymus and spleen of arsenic-exposed and unexposed mice were resuspended in PBS. 20 μM DCFDA was added and incubated for 30 min at 37 °C. The cells were placed on ice for 10 min. DCF fluorescence was detected by FACS scan flow cytometer at 530 nm (BD Accuri, BD Biosciences, USA) and analyzed using the BD ACCURI C6 software (Chatterjee and Chatterji, 2017).

2.9. Estimation of ROS scavenging enzymes

Catalase (CAT) activity in thymocytes and splenocytes was evaluated spectrophotometrically from cell lysates at 240 nm, based on the decomposition of H_2O_2 to H_2O and O_2 by CAT present in the cell lysates at 240 nm and was expressed as U/mg of protein (Claiborne, 1985). Superoxide dismutase (SOD) activity was assayed from cell lysates of splenocytes and thymocytes, based on the auto-oxidation rate of pyrogallol at 420 nm and inhibition of this auto-oxidation by SOD where 50% inhibition corresponded to one unit of enzyme activity (Marklund and Marklund, 1974). Reduced glutathione (GSH) content of and thymocytes was determined from cell lysates, based on the reduction of DTNB at 412 nm (Jollow et al., 1974). GSH content was measured with reference to a GSH standard curve, and expressed in μmoles/mg of protein.

2.10. Acridine orange staining

Cellular acidic compartments were examined by acridine orange staining. Acridine orange (Abcam, UK) was diluted to 1 mg/ml with PBS. Cells were isolated and stained with acridine orange at 37 °C for 15 min in the dark. After washing with PBS, the cells were immediately visualized by the Olympus laser-scanning confocal microscope (FV-10 ASW 3.0 viewer image browser) at 450 nm and

593 nm for the detection of acidic vesicular organelles. Data were analyzed from several cells of one sample. For the quantitation analysis, fluorescent intensity was quantified using Image-J software. Data were analyzed from several cells of one sample, and there were five samples for each group. Acridine orange emits in the red range determined by flow cytometry (BD ACCURI) using BD-Accuri C6 software.

2.11. Immunoblotting

Proteins were extracted from cells of the thymus and spleen in RIPA buffer (150 mM NaCl, 50 mm Tris, 0.1% Triton X-100 and 0.1% SDS) containing protease inhibitors (Chatterjee and Chatterji, 2017). For evaluation of the status of autophagic and apoptotic markers, 30 μg protein was separated by SDS-PAGE, transferred onto a PVDF membrane and immunoblotted with antibodies to p53, Bcl-2, Bax, cleaved caspase-3, cleaved-PARP, LC-3, Beclin-1, Akt, p-Akt, mTOR and p-mTOR. β-tubulin was used as loading control. After incubation with horseradish peroxidase-conjugated secondary antibodies, antibody binding was detected using 3, 3′-diaminobenzidine (DAB) in 50 mM Tris (pH 7) containing 0.2% H_2O_2 or chemiluminescence. Bands were analyzed using a Gel Documentation System (Gel Doc XR, Bio-Rad laboratories, USA). Band intensities were quantified with Image J software and were normalized using β-tubulin, the internal loading control. Antibodies and sample concentrations for Western blot were titrated to ensure that band intensities were in linear range.

2.12. Co-immunoprecipitation

Cell lysates were incubated with Hsp90 antibody along with 50 μl of Agarose-protein A/G beads at 4 °C overnight to form immunocomplexes. After washing with lysis buffer, the immunocomplexes were analyzed by immunoblotting with Beclin 1 antibody. The amount of Hsp90 that co-immunoprecipitated with Beclin1 was documented using the Gel Doc XR type imaging system. The intensities of the bands were quantified using Image J software.

2.13. Analysis of apoptotic cells by flow cytometry

The cells from thymus and spleen of control and exposed mice were collected, washed twice with Ca^{2+}-free PBS, and stained with Annexin V-FITC and propidium iodide (PI). Cells were eventually analyzed on a BD ACCURI flow cytometer (BD Biosciences, USA). The percentages of apoptotic cells were calculated by BD ACCURI C6 software (Das et al., 2019).

2.14. Statistical analysis

Each experimental group comprised six mice ($n = 6$). Experiments were repeated 3 times and data was expressed as mean ± standard deviation, using a statistical software package (Graphpad Prism, Version 6.0). The significance of differences between the group mean values were evaluated by Students' t-test, and confirmed by one-way ANOVA, as all data sets were normally distributed. Each arsenic treated group was compared to the control and p values less than 0.05 were considered statistically significant.

3. Results

3.1. Arsenic induces histopathological alterations in the thymus and spleen

Hematoxylin and eosin sections of the thymus of the unexposed group (Fig. 1A and E) showed normal capsular structure and well-demarcated cortical region with distinct trabeculae. The medulla is well-defined and compact with normal lymphocytes. Thymus from mice exposed to arsenic (Fig. 1B–D and F-H) depicted significant alterations as compared to control mice. The average cortico-medullary ratio of the control group was approximately 2. However, upon arsenic exposure, the ratio reduced to 1.6 in 5 ppm, 0.79 in 15 ppm and 0.73 in the 300 ppm ($p < 0.05$) arsenic-treated groups (Fig. 1B–D). Moreover, the cortical capsule appeared to be disintegrated, and the trabeculae were distinctly missing with increasing doses of arsenic. Apoptotic bodies characterized by pyknotic nuclei (Fig. 1C and D) and focal areas of tingible body macrophages (defined as macrophages containing stainable cellular debris) were evident (Fig. 1F–H). The cellular organization of the cortex was disintegrated (Fig. 1G and H). Scanning electron microscopy images revealed that the thymus of the control group showed a compact arrangement of spherical lymphocytes with well-defined microprocesses (Fig. 1I). Epithelial cells forming a well-defined reticular meshwork dividing the thymus into compartments was observed. Presence of large macrophages without any deformities was also seen (Fig. 1I). However, after arsenic treatment the structural integrity of the thymus was markedly compromised. Exposure to arsenic led to loss of the reticular meshwork, along with loss of distinctive architecture of thymocytes and flattening of the villous microprocesses in the arsenic-treated mice (Fig. 1J-L). Transmission electron microscopic studies of the thymus resected from control mice showed lymphocytes with intact nucleus and peripherally-arranged and normal organelles in a compact cytoplasm (magnification: ×3500) with mitochondria showing compact ultrastructure. An abnormal nucleus with heterochromatinization and degeneration of mitochondria were observed in thymocytes of mice exposed to 5 ppm, 15 ppm and 300 ppm arsenic. Dose-specific (1.15-fold, $p < 0.05$; 2.5-fold, $p < 0.01$; and 3.24-fold, $p < 0.001$) reduction in the nuclear diameter was also evident. The mice exposed to 300 ppm arsenic showed complete fragmentation of nuclear and cytoplasmic components and increased number of vacuoles (indicated by arrows). In addition, numerous lipofuscin granules were also observed (Fig. 1P).

The spleen from unexposed mice (Fig. 2A and E) displayed compact white (wp) and red (rp) pulp, with an intact capsule, from which extended trabeculae divided the splenic parenchyma into incomplete lobules. The spleens of arsenic-treated mice (Fig. 2B–D) demonstrated reduced to the control, increased pyknotic nuclei and tingible body macrophages were also visible in the marginal zones (Fig. 2F–H) and varied degrees of connective tissue fibrosis was observed in the capsular and arteriolar region of 15 and 300 ppm arsenic treated mice (Fig. 2G and H). SEM micrographs of control spleen showed structural integrity with normal, well-defined lymphocytes bearing surface microvilli; fibroblastic reticular cells (RCs) and interdigitating cells (IDCs) were also intact (Fig. 2I). A common feature observed for all three doses of arsenic exposure was ballooning of the cells accompanied by the loss of cellular compactness and lymphocyte-surface microvilli (Fig. 2J- L). Formation of membrane blebs and dents were also visible in the Presence of well-defined epithelial cells and IDCs indicated normal overall structure in the control spleen (Fig. 2M). A dose-dependent increase in the size of the splenocytes was also seen in all the groups of arsenic treatment which increased by 1.8-fold ($p < 0.05$)

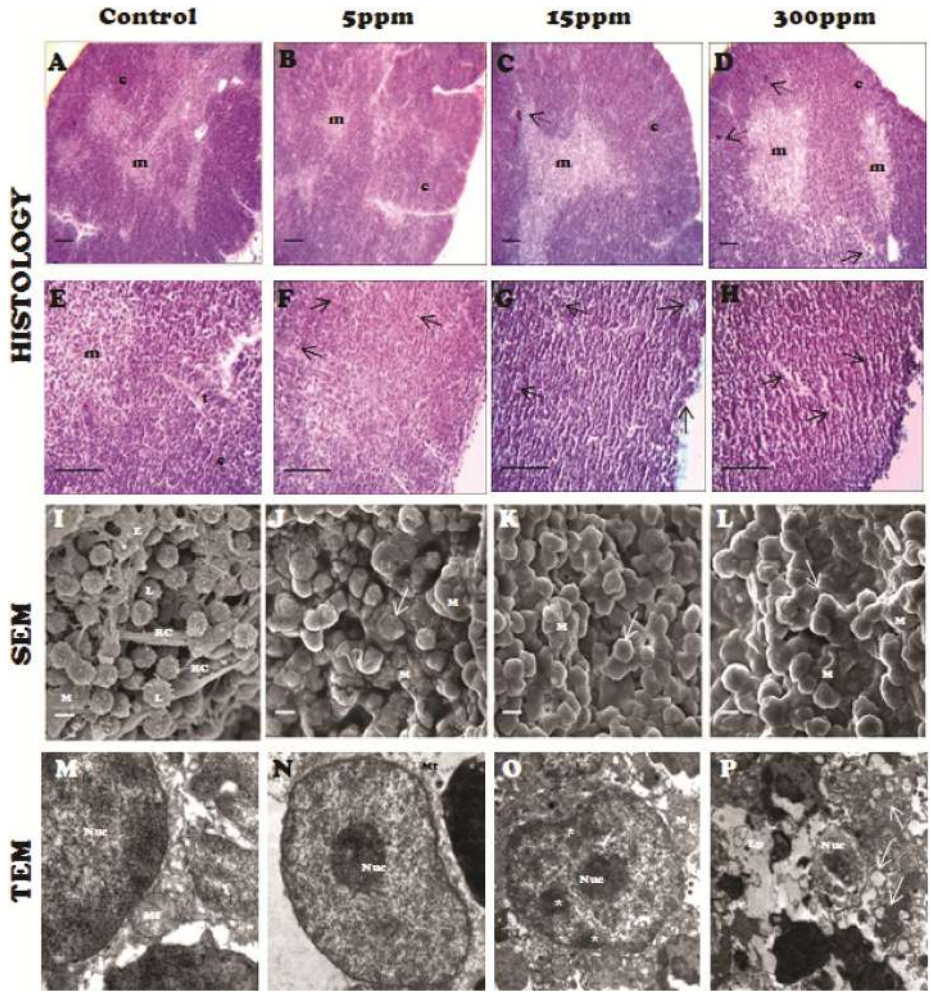

Fig. 1. Effects of arsenic on morphological changes of thymus. **(A-H)** Representative hematoxylin and eosin-stained cross-sections of thymus from all experimental groups at the end of 7 d, (n = 6). **A, B, C, D** (magnification 10×) and **E, F, G, H** (magnification 40×). **(A&E)** Control sections; **(B-D & F-H)** arsenic treated sections. **(B-D)** A significant decrease in cortex: medulla ratio of the arsenic-treated thymus was observed in the treated sections as compared to the untreated one **(A)**. Broken arrows indicate pyknotic nuclei; solid arrows indicate tingible bodies; c, cortex; m, medulla; t, trabaculae; scale bar 10 μm. Panels **I-L** represents the ultrastructural images of thymus by scanning electron microscopy (n = 6) at a magnification of 10KX. L, lymphocytes; RC, reticular cells; E, epithelial cells; M, macrophages; Loss of microprocesses from lymphocytes, marked by arrows; scale bar 2 μm. **(M-P)** Transmission electron micrographs of thymus (n = 6) of control **(M)** and arsenic treated groups **(N, O & P)** showing a dose dependent decrease in the nuclear size compared to the control. Mt, mitochondria; *, heterochromatinization; arrow, vacuoles; Lp, lipofuscin granules. Magnification 3500×; data are representative of three independent experiments.

in 5 ppm, 2.04-fold ($p < 0.01$) in 15 ppm, and 2.71-fold ($p < 0.001$) in 300 ppm arsenic-treated groups (Fig. 2N-P). Furthermore, there was a marked dose-dependent increase in the intercellular spaces, along with irregularly shaped nucleus and branched cytoplasmic projections. Heterochromatinization and chromatin margination was clearly observed, along with presence of lipofucsin granules in the 300 ppm arsenic-exposed group (Fig. 2O and P).

3.2. Arsenic reduced the $CD4^+/CD8^+$ T-cell ratio and induced cytokine imbalance

Immunophenotyping was performed using specific monoclonal antibodies against $CD4^+$ and $CD8^+$ cell surface markers to determine if exposure to arsenic altered immune homeostasis in the thymus and spleen. Fig. 3A and B indicated a dose-dependent reduction in the $CD4^+/CD8^+$ T-cell ratio of both thymus and spleen in the arsenic-exposed mice. The ratio of $CD4^+/CD8^+$ in the thymus of control group (2.112) reduced to 2.025, 2.09 and 1.75 ($p < 0.05$) in the mice exposed to 5 ppm, 15 ppm and 300 ppm arsenic, respectively (Fig. 3 A and C). Similarly, the ratio of $CD4^+/CD8^+$ T-cell (2.75) in spleen of the control group reduced to 2.24 in mice receiving 5 ppm of arsenic, 2 in 15 ppm arsenic-treated mice, and 1.9 ($p < 0.05$) in the 300 ppm arsenic-treated mice (Fig. 3B and D).

In order to determine whether the imbalance in immune homeostasis triggered by arsenic exposure led to alterations in the cytokine levels, ELISA for both pro- and anti-inflammatory cytokines was carried out (Fig. 3E). The levels of IL-2 increased by 1.08 fold in 5 ppm group, 1.4 fold ($p < 0.001$) in 15 ppm group and 1.54-fold ($p < 0.001$) in 300 ppm group. The levels of IL-6 and IL-12 increased by 1.08-fold and 1.35-fold ($p < 0.05$), respectively, in the 5 ppm treatment group. It further increased by 1.4-fold ($p < 0.01$) and 1.75-fold ($p < 0.001$) at 15 ppm (Fig. 3E), after which the levels declined. Interestingly, it was seen that the level of IL-13 decreased by 1.15-, 1.25- ($p < 0.05$) and 1.35- ($p < 0.01$) fold in 5 ppm, 15 ppm and 300 ppm groups, respectively (Fig. 3E).

3.3. Arsenic induced a redox imbalance in immune organs

Estimation of relative fluorescence intensity of DCF, monitored using 2′, 7′-dichlorofluorescin diacetate (DCFDA) is a direct parameter to measure the redox status of a cell. As observed in

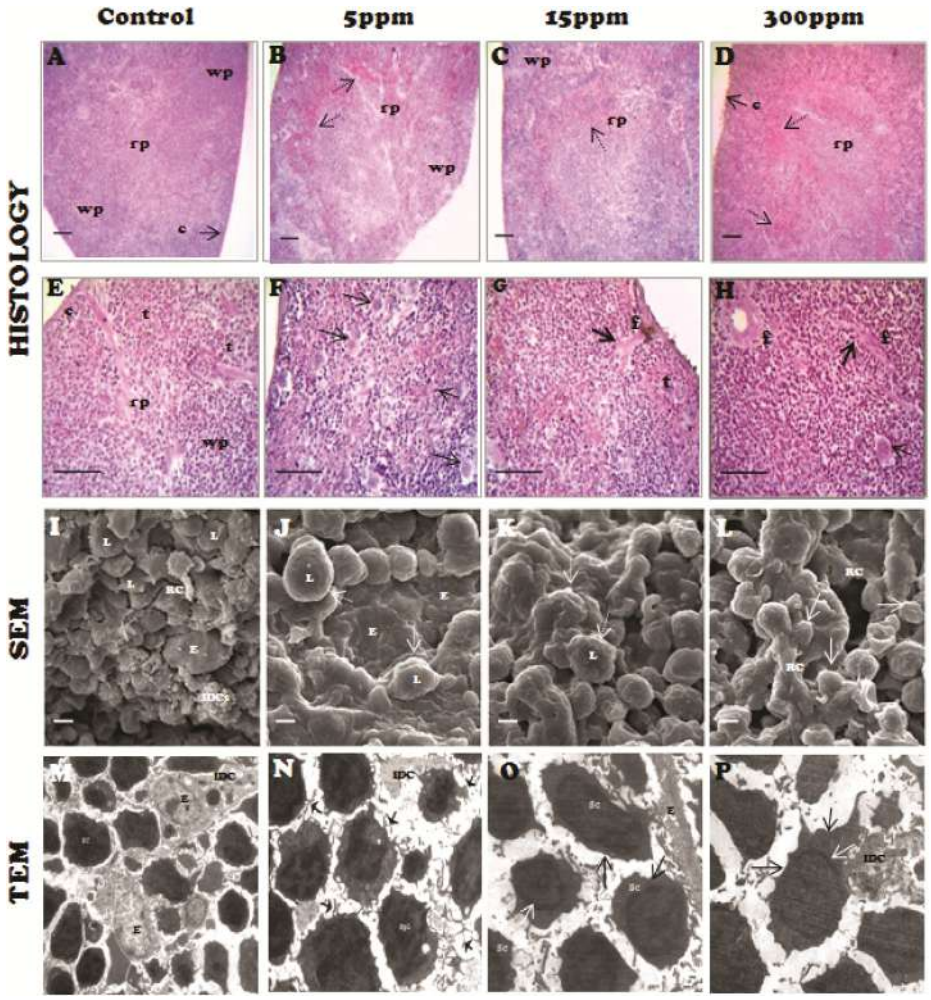

Fig. 2. Effects of arsenic on morphological changes of spleen. (A-H) Histopathological changes in mouse spleen (n = 6) following 7 d of arsenic exposure via drinking water. **A, B, C & D** (magnification 10×) and **E, F, G & H** (magnification 40×). wp, white pulp; rp, red pulp; t, trabaculae; c, capsule and f, fibrosis; broken arrows mark areas of hemolysed RBCs and solid arrows mark tingible bodies; scale bar 10μm. **(I, J, K & L)** Scanning electron micrographs of arsenic treated spleen (n = 6) at magnification 10KX. Broken arrows indicate splenocytes with increased diameters and solid arrows mark cell shrinkage. L, lymphocytes; RC, reticular cells; E, epithelial cells; IDCs, interdigitating cells; scale bar 2μm. **(M, N, O & P)** reveal the ultrastructural images of spleen (n = 6) by transmission electron microscope at 3500×. Black arrows mark dose dependent increase in the size of splenocytes. White arrows indicate chromatin marginalization in splenocytes of arsenic treated groups. Sc, splenocytes; E, epithelial cells; IDCs, interdigitating cells; Data are representative of three independent experiments. (For interpretation of the references to colour in this figure legend, the reader is referred to the Web version of this article.)

Fig. 4A, exposure to 5 ppm arsenic for 7 d led to a significant increase in ROS generation in the thymus of arsenic treated mice, increasing to 40% as compared to 2.1% in the control mice; $p < 0.001$. ROS accumulation further increased to 52.9%; $p < 0.001$, in 15 ppm and to 72.4%; $p < 0.001$, in 300 ppm arsenic treated groups. Concomitant dose-dependent obliteration of the activities of ROS scavenging enzymes were also seen (Fig. 4B). The activity of CAT in thymus decreased by almost 2-fold ($p < 0.01$) in the 5 ppm treated group and reduced further by 2.8-fold ($p < 0.001$) and 2.9-fold ($p < 0.001$) in the 15 and 300 ppm treatment groups. The SOD activity in thymus of mice receiving arsenic was registered to decrease by 1.3-fold ($p < 0.05$) in the 5 ppm, by 1.5-fold ($p < 0.05$) in the 15 ppm and by 2.5-fold ($p < 0.001$) in the 300 ppm arsenic-treated groups. Arsenic further aggravated oxidative stress by depleting intracellular GSH levels which were reduced by 1.24-fold ($p < 0.05$) in the thymus of 15 ppm and by 1.35-fold ($p < 0.05$) in 300 ppm arsenic-treated mice (Fig. 4B).

Similar results were observed in the spleen of arsenic-exposed mice. ROS generation as measured by DCF fluorescence was 62.3% in 5 ppm arsenic treated group compared to 11% in control mice ($p < 0.001$), which further increased to 68.8% in the 15 ppm ($p < 0.001$) and 81% ($p < 0.001$) in the 300 ppm groups (Fig. 4C). Simultaneously, in comparison to the control, the activity of CAT in arsenic exposed spleen reduced in a dose-dependent manner in 5 ppm, 15 ppm and 300 ppm arsenic treated mice decreasing by 1.14-, 1.66- and 1.7-folds ($p < 0.05$, $p < 0.01$, $p < 0.01$; Fig. 4D). Activity of SOD was also seen to reduce by 1.16-fold ($p < 0.05$), 1.46-fold ($p < 0.05$) and 1.92-fold ($p < 0.01$) in the groups exposed to 5, 15 and 300 ppm arsenic. Similarly, a dose-dependent reduction in the levels of GSH was observed for all the three doses of arsenic but the change was significant for 15 and 300 ppm arsenic groups where it reduced by 1.17 and 1.25-fold ($p < 0.05$) with respect to the control.

3.4. Exposure to arsenic triggered autophagy in the thymus and spleen

In an attempt to determine whether cells of the thymus and spleen were striving to survive during arsenic-induced oxidative stress, we evaluated the cellular and molecular changes related to autophagy, a well known cytoprotective process, in the immune organs. We observed a dose-dependent increase in the formation of

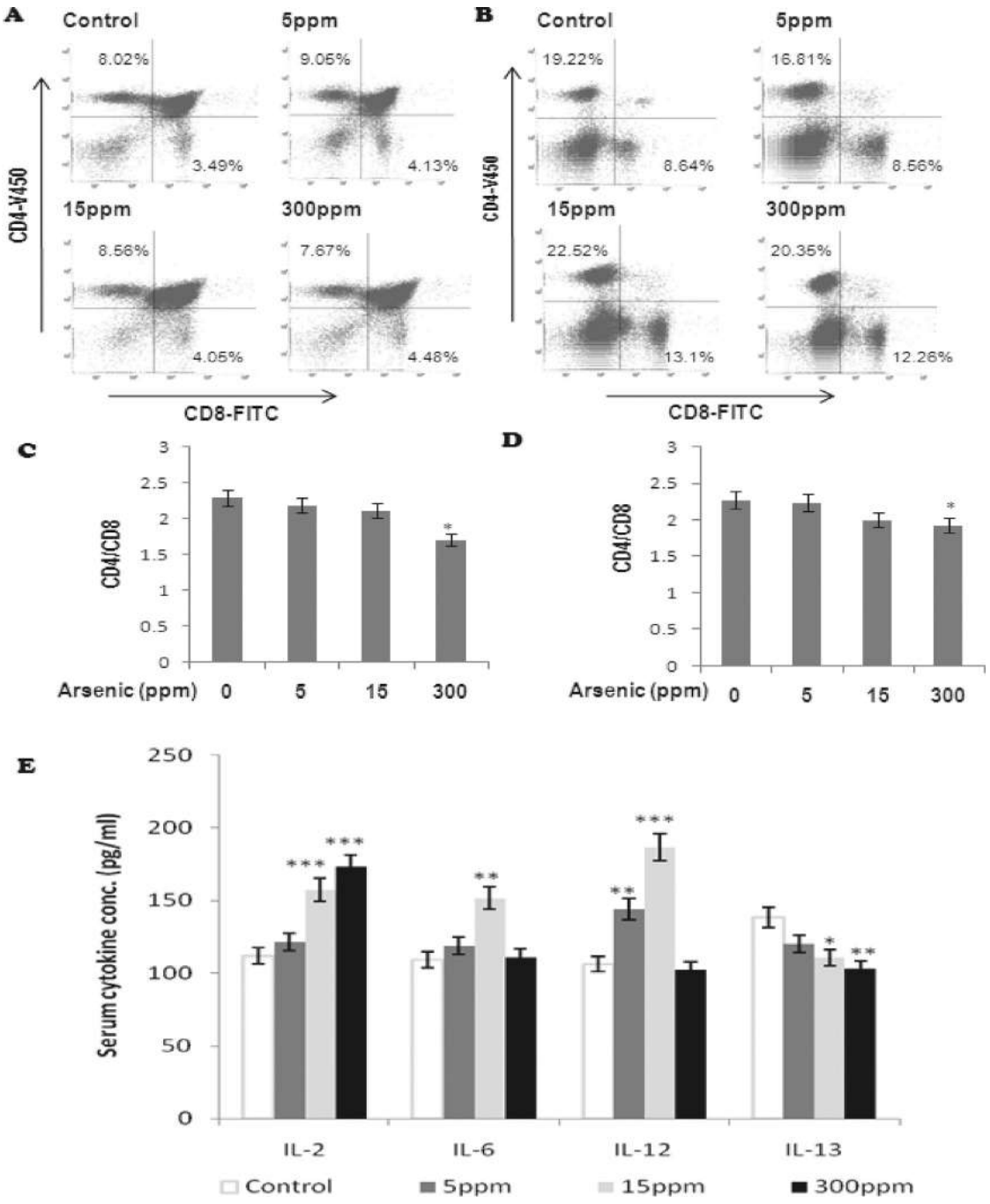

Fig. 3. Effects of arsenic on lymphocyte populations of thymus and spleen in Swiss albino mice. (A & B) Flow cytometric analysis of $CD4^+$ and $CD8^+$ T cells from arsenic treated and untreated thymus (n = 6) **(A)** and spleen (n = 6) **(B)** of Swiss albino mice at 7 d post-treatment. Data are represented as percent $CD4^+$ and $CD8^+$ T-cell populations. **(C & D)** are graphical representation of $CD4^+/CD8^+$ ratios in thymus and spleen. **(E)** Graphical representation of pro and anti-inflammatory cytokine profile of arsenic treatment versus control groups. Serum IL-2 levels show a significant dose dependent increase, IL-6 and IL-12 levels show an increase at the dose of 5 ppm and 15 ppm but a steep decline at the dose of 300 ppm. Serum levels of IL-13 shows a significant dose dependant decrease. Error bars represent S.D. from the mean of three independent experiments. *$p < 0.05$, **$p < 0.01$, ***$p < 0.001$ compared with control.

acidic vesicular organelles (AVOs; autophagosomes) in arsenic-treated thymocytes when stained with the lysomotropic agent, acridine orange (Fig. 5A), as confirmed by confocal microscopy. Exposure to 5 ppm arsenic led to a 2.39-fold ($p < 0.05$) increase in the fluorescence intensity and exposure to 15 ppm and 300 ppm caused a 4-fold ($p < 0.01$) and 6.9-fold ($p < 0.001$) increase in fluorescence intensity. This was further authenticated by flow cytometry which confirmed enhanced accumulation of AVOs, increasing to 6.4% ($p < 0.01$), 24.6% ($p < 0.001$) and 50.5% ($p < 0.001$) in 5 ppm, 15 ppm and 300 ppm groups, respectively, with respect to the control (3.5%). The PI3K/Akt/mTOR signaling pathway is a major pathway that negatively regulates autophagy. Expressions of pathway components in arsenic-exposed groups significantly reduced ($p < 0.001$). Immunoblot was also performed to estimate the major autophagy related markers, Beclin-1 and LC3-II, correlated with the extent of autophagosome formation and

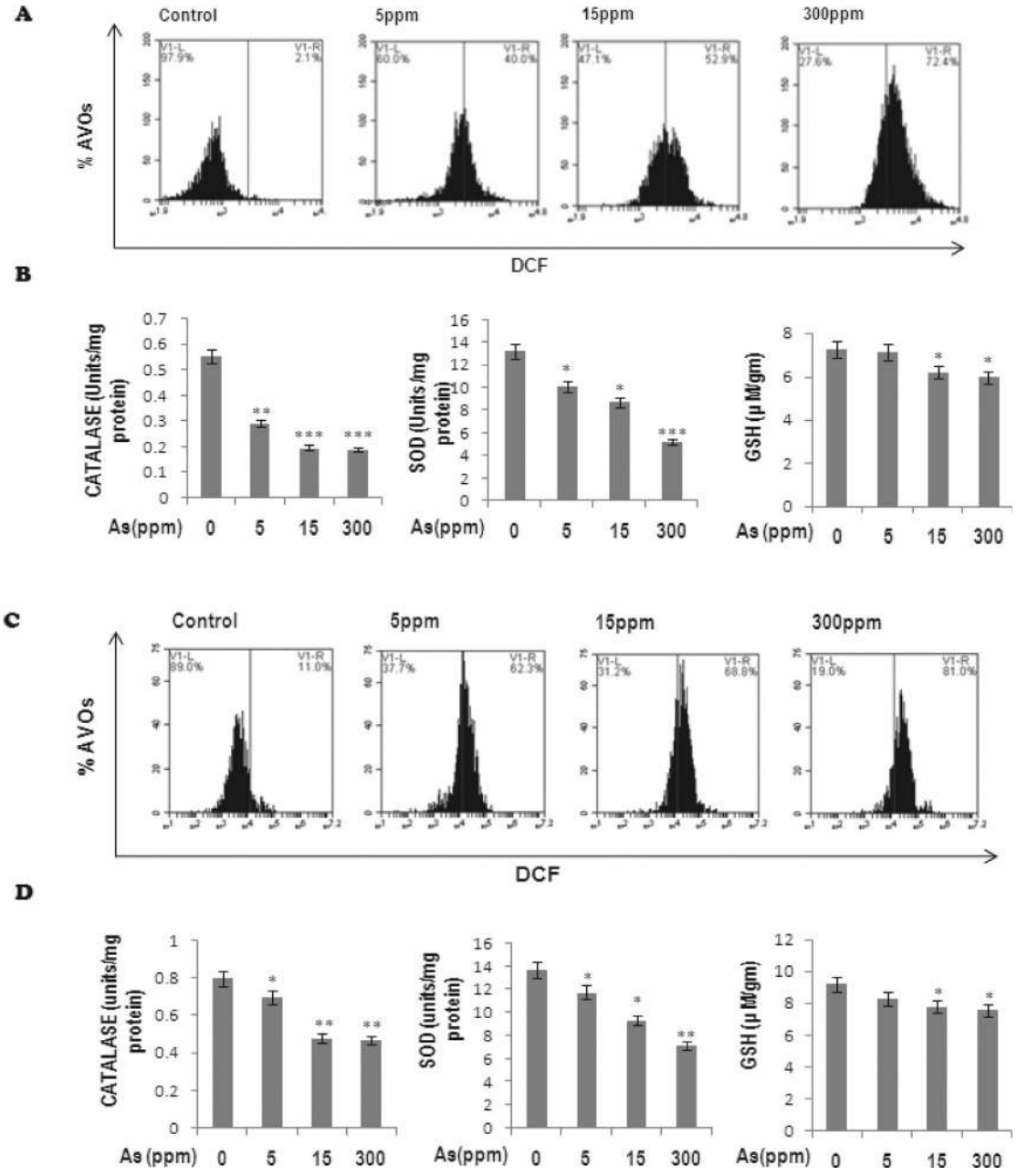

Fig. 4. Effects of arsenic induced ROS accumulation in thymus and spleen. **(A & C)** Representative histogram profile of DCF fluorescence from thymus (n = 6) **(A)** and spleen (n = 6) **(C)** illustrating a dose dependent increase in ROS generation upon exposure to acute arsenic for 7 d **(B & D)** ROS scavenging enzyme assays from thymus (n = 6) **(B)** and spleen (n = 6) **(D)** shows a significant dose dependent decrease in the activities of superoxide dismutase (SOD), catalase (CAT) and a reduction in the level of glutathione (GSH) compared to untreated controls. Error bars represent S.D. from the mean of three independent experiments. *p < 0.05; **p < 0.01; ***p < 0.001 compared with control.

hence serving as a measure of autophagic activity. Beclin-1 and LC3-II expression levels were markedly increased ($p < 0.001$) in the arsenic-exposed thymuses compared to the unexposed groups (Fig. 5B). To understand the effect of arsenic on the interaction of Hsp90 and Beclin 1, a Co-IP assay was performed. The result indicated a dose-dependent increase in Hsp90/Beclin1 complex formation in 5 ppm ($p < 0.05$), 15 ppm and 300 ppm arsenic treated groups ($p < 0.01$) compared to the untreated group. Evidence of autophagy was more vivid in the TEM micrographs which confirmed a dose-dependent increase in autophagy upon arsenic treatment. Compared to the control thymus with well-defined nucleus and intact organelles, there was an abundance of autophagosomes in 5 ppm group. The sections of the 15 ppm experimental group revealed maturing autophagolysosomes, where fusion of vesicles and accumulation of intracellular components were evident. The 300 ppm group showed damage of mitochondrial membrane integrity, expansion of acidic vesicles and a large number of autophagolysosomes of different sizes (Fig. 5D).

Strong induction of autophagy was also observed in the spleen of arsenic exposed mice. The confocal findings were positive for the results of AVO development. The strength of fluorescence increased by 2.1- ($p < 0.05$), 4.6- ($p < 0.01$), and 6.05- ($p < 0.05$) folds with increased doses of arsenic. Although the intensity was considerably less in the spleen compared to the thymus, the flow cytometry results for AVO accumulation was consistent with that of confocal studies. As shown in Fig. E, arsenic exposure increased the

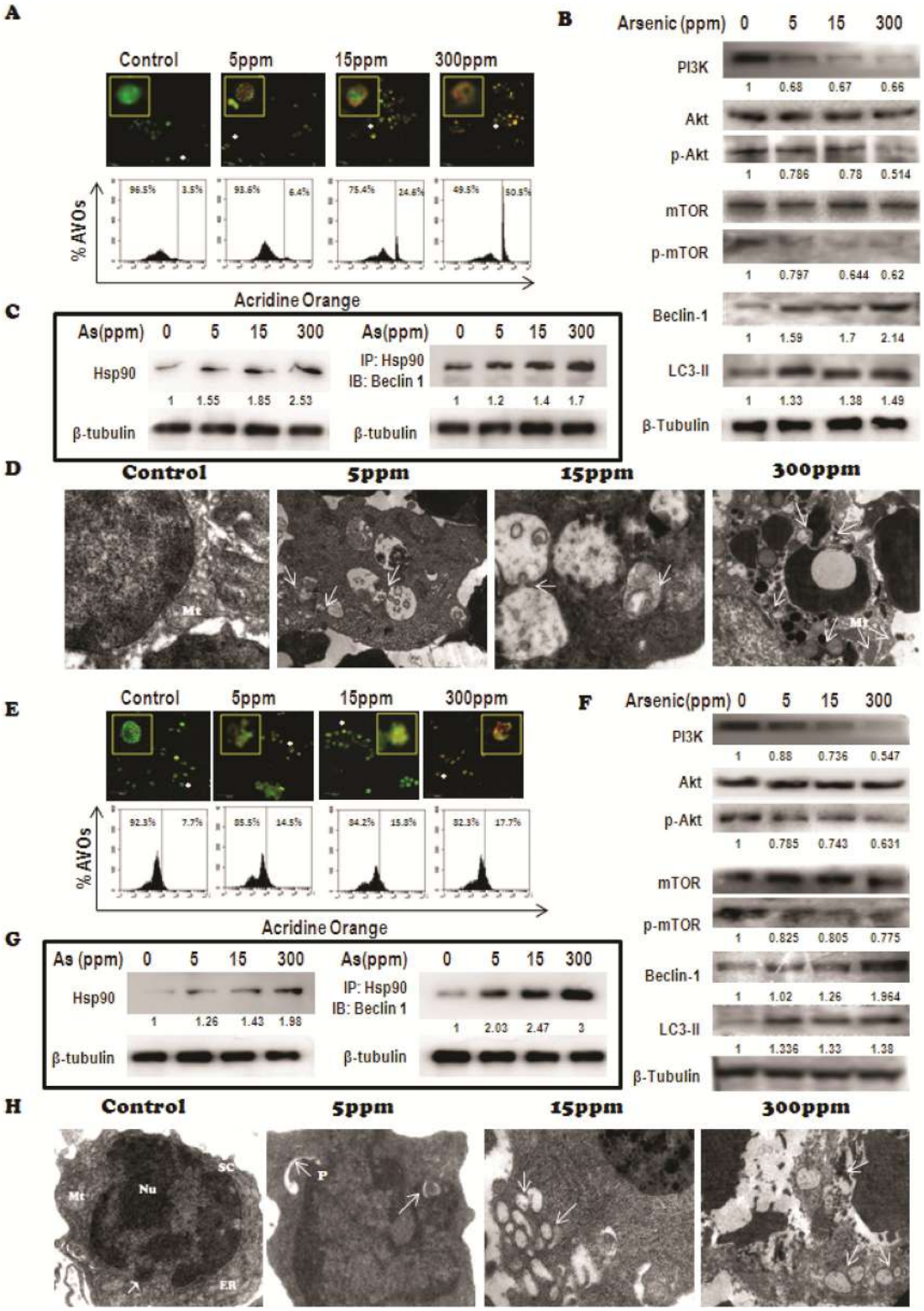

Fig. 5. Effects of arsenic on autophagic induction in thymus and spleen. **(A & E)** Cellular autophagy in thymus (n = 6) **(A)** and spleen (n = 6) **(E)** measured by AO staining. The presence of acridine orange stained intracellular vesicles by confocal microscopy (upper panels; scale bars 10 μm and 20 μm) and flow cytometry (lower panels), showing an increase in red fluorescence intensity (upper panels) with a concomitant increase of AO^{+ve} cells (lower panels) upon arsenic exposure. **(B & F)** Western blots showing expression of autophagic protein markers in thymus (n = 6) **(B)** and spleen (n = 6) **(F)** following treatment with sodium arsenite for 7 d **(C & G)** Expression of endogenous Hsp90 and co-immunoprecipitates of Hsp90/Beclin1 was detected by immunoblotting from proteins retrieved from thymus (n = 6) **(C)** and spleen (n = 6) **(G)** of treated and untreated groups. β-tubulin was used as loading control and respective fold changes are represented as ratio of net band pixel density of arsenic treated groups to the control. **(D & H)** Transmission electron micrographs of thymus (n = 6) **(D)** and spleen (n = 6) **(H)** of control and arsenic treated mice at magnification 3500×. Autophagosomes, maturing autophagolysosomes fusing with lysosomes and disintegrated mitochondria are marked by arrows. P, phagophore; Mt, mitochondria; Nu, nucleus; ER, endoplasmic reticulum. Data are representative of three independent experiments. (For interpretation of the references to colour in this figure legend, the reader is referred to the Web version of this article.)

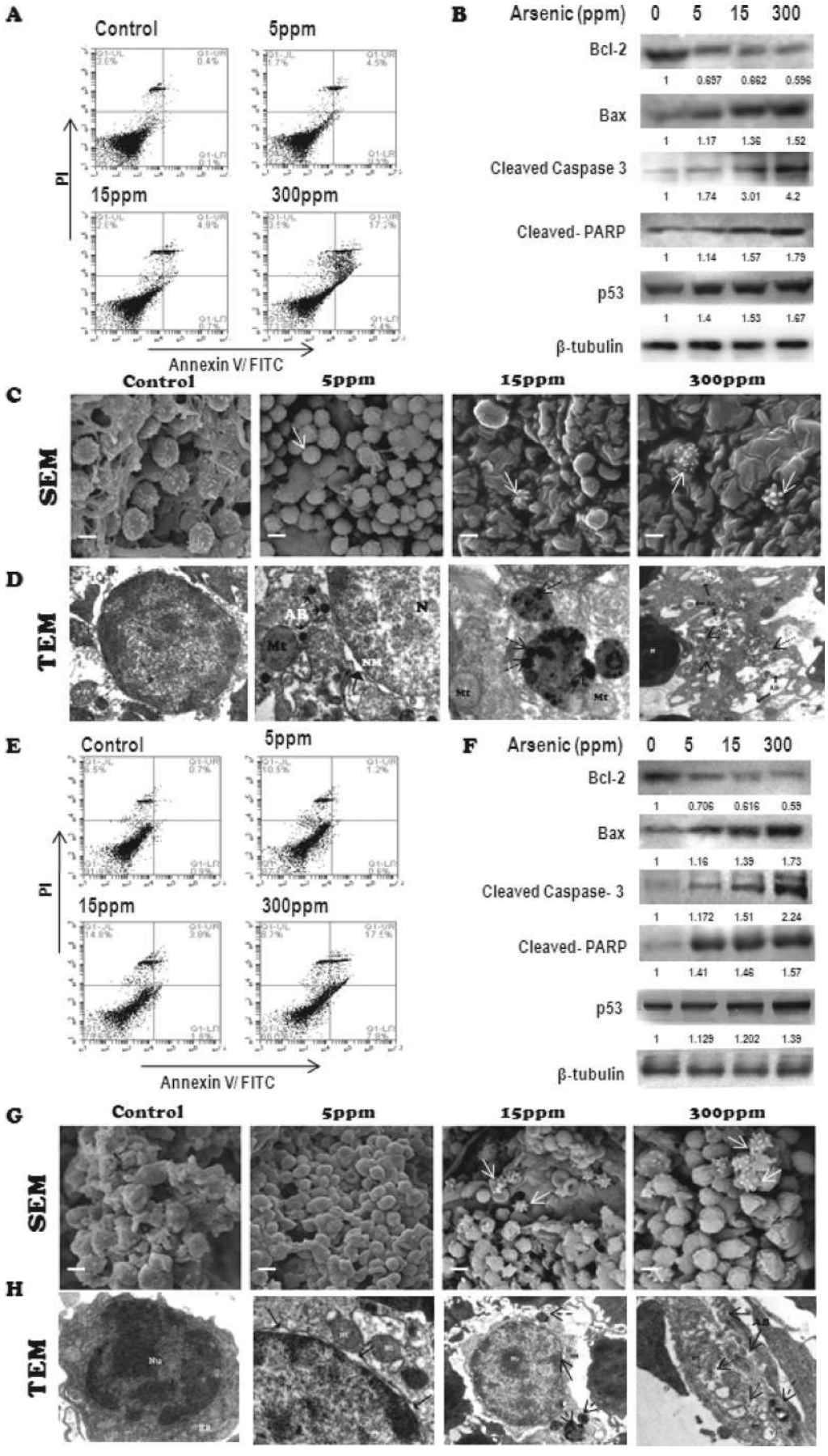
A
Control
5ppm
15ppm
300ppm
PI
Annexin V/ FITC
B
Arsenic (ppm) 0 5 15 300
Bcl-2
1 0.657 0.662 0.596
Bax
1 1.17 1.36 1.52
Cleaved Caspase 3
1 1.74 3.01 4.2
Cleaved- PARP
1 1.14 1.57 1.79
p53
1 1.4 1.53 1.67
β-tubulin
C
Control
5ppm
15ppm
300ppm
SEM
D
TEM
AB
N
Mt
NM
E
Control
5ppm
15ppm
300ppm
PI
Annexin V/ FITC
F
Arsenic (ppm) 0 5 15 300
Bcl-2
1 0.706 0.616 0.55
Bax
1 1.16 1.35 1.73
Cleaved Caspase- 3
1 1.172 1.51 2.24
Cleaved- PARP
1 1.41 1.46 1.57
p53
1 1.129 1.202 1.38
β-tubulin
G
Control
5ppm
15ppm
300ppm
SEM
H
TEM

percentage of AVOs from 7.7% in control mice to 14.5% (5 ppm; $p < 0.001$), 15.8% (15 ppm; $p < 0.001$) and 17.7% (300 ppm; $p < 0.001$). Reduced expressions of PI3K, phospho-Akt, phospho-mTOR, and elevated expressions of Beclin-1 and LC3-II ($p < 0.001$) further confirmed ensuing autophagy in the splenocytes following arsenic treatment (Fig. 5F).

The co-immunoprecipitation assay for Hsp90 and Beclin 1 confirmed 2-fold ($p < 0.001$), 2.47-fold ($p < 0.001$) and 3-fold ($p < 0.001$) increase in the interaction of the proteins (Fig. 5G). TEM images of spleen exposed to arsenic revealed gross changes in the morphological features, exhibiting initiation of phagophore formation and vacuolation, engulfing and fusion of autophagosome and lysosomes and an increased number of autophagolysosomes (Fig. 5H).

3.5. Arsenic induced apoptosis in the immune organs of mice

The histopathological evidences of gross tissue damage caused by arsenic, as observed in Fig. 1, necessitated probing into the effect of varying concentrations of arsenic on the viability of thymo-cytes and splenocytes. Consequently, our next aim was to detect apoptosis, if any, in the mice thymus and spleen after exposure to arsenic. Annexin V-FITC^{+ve} population increased from 0.4% in the control thymus to 4.5% ($p < 0.05$) in 5 ppm, 4.9% ($p < 0.05$) in 15 ppm and 17.2% ($p < 0.001$) in 300 ppm arsenic-treated groups (Fig. 6A). Results indicated a significant dose-dependent decrease in the expression of Bcl-2 ($p < 0.001$), and a concomitant upregulation of Bax, cleaved caspase-3 and cleaved PARP ($p < 0.001$) in a dose-dependent manner (Fig. 6B). Since the major underpinning cause of arsenic toxicity is ROS generation and DNA damage, p53 activation was also observed. SEM images displayed shrinkage of thymocytes and loss of membrane structures in thymus exposed to arsenic insult (5 ppm), as compared to the control (Fig. 6C). A loss in the cellular integrity and septa was observed in 15 ppm and 300 ppm arsenic-treated groups accompanied with appearance of membrane projections of the thymocytes undergoing apoptosis. The TEM images indicated blebbing of the nuclear membrane, swollen mitochondria and formation of apoptotic bodies; condensed chromatin bodies were also visible in the nucleus. A dose-dependent increase in apoptotic bodies accompanied with disruption of cytoplasmic organelles was also prominent in arsenic-treated groups (Fig. 6D).

Apoptosis in spleen was similar when mice were subjected to arsenic exposure. The Annexin V-FITC^{+ve} population increased from 0.7% in the control mice to 1.2% in 5 ppm, 3.8% in 15 ppm ($p < 0.05$), and 17.5% in 300 ppm ($p < 0.01$) arsenic-treated mice respectively (Fig. 6E). Significant increase in the expression of pro-apoptotic markers was observed in the spleen (Fig. 6F; $p < 0.001$). Major morphological changes like loss of compactness and membrane protrusions, simulating apoptosis in spleen following arsenic administration, were also demonstrated (Fig. 6G). Apoptosis was further confirmed by TEM images which depicted mitochondrial swelling, shrinkage of nucleus along with prominent blebbing of the nuclear membrane, extensive vacuolation, accumulation of apoptotic bodies and finally, complete disruption of the cellular architecture and cytoplasmic matrix (Fig. 6H).

4. Discussion

Arsenic is well known for its intricate and convoluted biological effects. Innumerable reports from all over the world have provided ample evidence on the toxic effects of arsenic ingestion (Chatterjee and Chatterji, 2017, 2011, 2010; Choudhury et al., 2016; Htike et al., 2016). One of the crucial questions yet to be completely addressed is the effect of arsenic on the host immune system which is responsible for spearheading host defenses against all sorts of physiological stresses. The immune system is essential to fight invading pathogens but it is also crucial for repair of tissue damages (Julier et al., 2017). When the immune system itself is functionally impaired, it results in gross deregulation of immune responses (Stoecklein et al., 2012). In order to demarcate arsenic as an immune-homeostasis disrupter, the effects of arsenic on the immune organs and cell death were delineated, and the extent of damage induced by arsenic on the thymus and spleen at the structural and molecular level were also evaluated.

Both the thymus and spleen are the major T cell repertoires and drive immune responses against invading agents. Therefore, the structure-function integrity of the lymphocytes is extremely essential for maintaining the immune physiology. Immune-modulation is best detected by the ratio of $CD4^+$ and $CD8^+$ T-cells (Wei et al., 2015). Exposure to arsenic led to a dose dependent decrease in the $CD4^+/CD8^+$ ratio which possibly caused immune-suppression in the animals. There are alternating reports on the effect of arsenic on the partitioning of immune cells into different subtypes (Dangleben et al., 2013). However, a common observation is that high doses arsenic (0.1 mg/ml) or prolonged exposure (30 d) results in an immune-suppressed phenotype (Choudhury et al., 2016). In an interesting study (Pournara et al., 2016), arsenic exposure led to alterations in the global histone modification pattern of $CD4^+$ but not $CD8^+$ cells. This corroborates with our data where we observe a decrease in the CD4 to CD8 positive T-cell ratio, implying that the CD8 responses are aggravated in response to the loss of immune balance. In addition, arsenic-induced balance of the pro- and anti-inflammatory cytokines was inconsistent and the results were found to vary with time and dose of arsenic exposure (Duan et al., 2017). Our results, however, indicate a definitive inflammatory response after arsenic exposure, since it was preceded by an uncontrolled increase in dose-dependent ROS generation.

Cytokines are important mediators of cell mediated immune response, and when expressed in a deregulated fashion, may lead to either immunodeficient or immunopathologic conditions. It has become increasingly lucid that there are important dose, time, and tissue-specific differences in the effects of arsenic, as well as important gene-environment and co-exposure interactions, which determine how arsenic alters disease risk under any particular exposure circumstance (Markowski et al., 2011; Platanias, 2009). Since the integrity of the immune system is necessary to guarantee adequate immunosurveillance and response to external agents (Ichim, 2005; Theron et al., 2012), the effect of environmental pollutants like arsenic on immune organs and cytokine balance is thus of immense importance for designing therapeutic strategies in future.

The damages inflicted upon different tissues by arsenic are mostly due to increased ROS generation, as confirmed by earlier

Fig. 6. Effects of arsenic on apoptosis of thymus and spleen. **(A & E)** Mice were treated with sodium arsenite for 7 d and cell apoptosis in thymus **(A)** and spleen **(E)** was quantified by Annexin V-FITC and PI double staining. **(B & F)** Immunoblot analysis of apoptotic protein markers in thymus ($n = 6$) **(B)** and spleen ($n = 6$) **(F)** following arsenic treatment. β-tubulin was used as loading control and respective fold changes are represented as ratio of net band pixel density of arsenic treated groups to the control. **(C & G)** SEM micrographs of thymus ($n = 6$) **(C)** and spleen ($n = 6$) **(G)** at magnification 10KX, showing an increase of apoptotic thymocytes and splenocytes (arrows) upon arsenic exposure. Scale bar 2μm. **(D & H)** TEM images of thymus **(D)** and spleen **(H)** at magnification 3500×, showing a marked increase in nuclear membrane blebbing (arrows), chromatin marginalization (broken arrows), disintegrated cytoplasmic organelles (dotted arrows) mitochondrial swelling (Mt) and apoptotic bodies (AB) upon arsenic exposure. Data are representative of three independent experiments.

studies (Chatterjee and Chatterji, 2017). Increased levels of ROS within immune cells can result in hyperactivation of inflammatory responses resulting in tissue damage and pathological phenotypes (Mittal et al., 2014). If cells are not able to control their ROS levels, then they are susceptible to oxidative stress-induced cell death. Together with increased inflammatory response and uncontrolled ROS production, severe damage to the primary and secondary immune organs was observed. Structural deterioration leading to morphological alterations in the immune organs was apparent from our results, and was presumed to affect the functional integrity of the organs. Concomitantly, the balance between cell survival and cell death was investigated, since it would reflect on the possibility and severity of occurrence of a more drastic disease in the animals. Autophagy can be stimulated by various stress situations, including nutrient depletion and oxidative stress. Autophagy has diversified functionality and has both beneficial and harmful effects on the physiology of an organism, since it is both self-protective (Green and Levine, 2014) and self-destructive (Berry and Baehrecke, 2007; Cutler and Somerville, 2005). If cells are severely damaged, autophagy drives cells towards apoptosis either by active degradation of cellular components or by passive non-selective destruction of cellular components unto a point that a cell can no longer survive. In our study, we unraveled a dose-dependent increase in the accumulation of autophagosomes and autophagolysosomes, concomitant with downregulation of PI3K/Akt/mTOR pathway and an upregulation of Beclin 1 and LC3-II, suggesting an increase in autophagy in the respective lymphoid organs of our experimental model.

Initiation of autophagy is induced by formation of an isolation membrane or phagophore through expression of Beclin 1 (Tam et al., 2017). Beclin 1 has been reported to be a client protein of Hsp90 and it is targeted for degradation via the ubiquitin-proteasome pathway if it is dissociated from Hsp90. Hsp90 on the other hand is a heat shock protein that maintains the functionality and stability of cellular proteins (Li and Buchner, 2013). It has been suggested that increase in autophagy influences the development and progression of cancer by formation of a complex with Hsp90 (Wang et al., 2014). Given the crucial role of Hsp90 in Beclin 1 stabilization and its contribution in increase in autophagy, we speculated that arsenic led to an upregulation in the expression of Hsp90, which in turn led to an increased stability of Beclin 1, culminating in an increase in autophagy. Our results corroborated our hypothesis as co-immunoprecipitation assay for Hsp90 and Beclin 1 re-established the importance of Hsp90 in arsenic-induced autophagy.

Stress-inducing stimuli that promote autophagy may also activate apoptotic cell death (Zhang et al., 2009; Liu and Levine, 2015). However, it is only up to a point of continuous insult from external factors that autophagy acts as a survival process, beyond which the cell is destined to die due to the scarcity of metabolic needs. This cell death is often induced by autophagy itself, since if the levels of autophagy are very high, then it may interfere in the normal homeostatic mechanisms of the ER and disrupts its structure and function. The outer nuclear membrane is physically in close proximity with the ER, but under normal physiological conditions, the autophagic machinery usually avoids using the outer nuclear membrane as a source for the formation of autophagosomes. However, at the onset of high levels of autophagy, the ER membrane may become exhausted as a source of autophagosomes, inducing the use of the outer nuclear membrane for the same and perhaps triggers some undefined signal that the cell should self-destruct.

In our experiments, we have observed that there is an increase in autophagy right at the lower dose of arsenic, which does not change very dramatically at higher doses. However, there is progressive increase in apoptosis with increasing doses of arsenic. This leads us to believe that at lower doses, when there is no significant cell death, cells stimulate autophagy in order to survive. On the other hand, at higher doses, where both autophagy and apoptosis are high, it is plausible that cells lose their survival capacity, succumb to cell death, and eventually undergo autophagy-induced apoptosis. Additionally, in our study, swollen mitochondria, and perinuclear space dilation is clearly visible in the TEM images of thymus and spleen of arsenic exposed mice, along with the presence of autophagosomes and autophagolysosomes. Thus, stress-inducing stimuli that promote autophagy may also activate apoptotic cell death (Zhang et al., 2009; Liu and Levine, 2015). Moreover, there are instances of autophagy and apoptosis taking place either simultaneously or sequentially due to oxidative stress (Zhang et al., 2009; Knaapen et al., 2001). Since arsenic is regarded as a potent environmental stress factor (Bernstam and Nriagu, 2000), exposure to arsenic led to a dose-dependent increase in apoptosis in the thymus and spleen, as evident from molecular and ultrastructural changes.

5. Conclusion

Therefore, arsenic-induced toxicity may be implicated to stimulate an immuno-inflammatory change due to modulation of the T-cell population, eventually overcoming cell survival mechanisms and leading to thymic and splenic cell death. Although activation of the Hsp90-mediated autophagic machinery occurs as an initial survival mechanism, activation of apoptotic genes renders the organs damaged beyond repair. It is thus imperative to devise strategies that will reduce oxidative stress in the organs, overcome immune suppression and avoid cell death, so that the normal physiology of the organs can be restored.

Conflicts of interest

The authors declare no conflict of interest.

Acknowledgement

We acknowledge University Grants Commission (UGC), for grant [41-128/2012(SR)] and fellowship support. We would also like to acknowledge the central instrument facility of CRNN (University of Calcutta) for flow cytometry and SEM, and All India Institute of Medical Sciences (AIIMS), New Delhi, for TEM. We are also thankful to DST-FIST, UGC-SAP and DST-PURSE for infrastructure support.

Appendix A. Supplementary data

Supplementary data to this article can be found online at https://doi.org/10.1016/j.chemosphere.2019.124647.

References

Ahsan, H., Chen, Y., Kibriya, M.G., Slavkovich, V., Parvez, F., Jasmine, F., Gamble, M.V., Graziano, J.H., 2007. Arsenic metabolism, genetic susceptibility, and risk of premalignant skin lesions in Bangladesh. Cancer Epidemiol. Biomark. Prev. 16, 1270–1278.

Anand, P., Kunnumakkara, A.B., Sundaram, C., Harikumar, K.B., Tharakan, S.T., Lai, O.S., Sung, B., Aggarwal, B.B., 2008. Cancer is a preventable disease that requires major lifestyle changes. Pharm. Res. 25, 2097–2116.

Banerjee, S., Mitra, T., Purohit, G.K., Mohanty, S., Mohanty, B.P., 2015. Immunomodulatory effect of arsenic on cytokine and HSP gene expression in Labeo rohita fingerlings. Fish Shellfish Immunol. 44, 43–49.

Bernstam, L., Nriagu, J., 2000. Molecular aspects of arsenic stress. J. Toxicol. Environ. Health B Crit. Rev. 3, 293–322.

Berry, D.L., Baehrecke, E.H., 2007. Growth arrest and autophagy are required for salivary gland cell degradation in Drosophila. Cell 131, 1137–1148.

Cattaneo, M., Dominici, R., Cardano, M., Diaferia, G., Rovida, E., Biunno, I., 2012.

Molecular chaperones as therapeutic targets to counteract proteostasis defects. J. Cell. Physiol. 227, 1226–1234.
Chatterjee, A., Chatterji, U., 2010. Arsenic abrogates the estrogen-signaling pathway in the rat uterus. Reprod. Biol. Endocrinol. 8, 80.
Chatterjee, A., Chatterji, U., 2011. All-trans retinoic acid protects against arsenic-induced uterine toxicity in female Sprague-Dawley rats. Toxicol. Appl. Pharmacol. 257, 250–263.
Chatterjee, A., Chatterji, U., 2017. All-Trans retinoic acid ameliorates arsenic induced oxidative stress and apoptosis in the rat uterus by modulating MAPK signaling proteins. J. Cell. Biochem. 118, 3796–3809.
Chatterjee, S., Sarkar, S., Bhattacharya, S., 2014. Toxic metals and autophagy. Chem. Res. Toxicol. 27, 1887–1900.
Chen, F., Vallyathan, V., Castranova, V., Shi, X., 2001. Cell apoptosis induced by carcinogenic metals. Mol. Cell. Biochem. 222, 183–188.
Choudhury, S., Ghosh, S., Mukherjee, S., Gupta, P., Bhattacharya, S., Adhikary, A., Chattopadhyay, S., 2016. Pomegranate protects against arsenic-induced p53-dependent ROS-mediated inflammation and apoptosis in liver cells. J. Nutr. Biochem. 38, 25–40.
Claiborne, A., 1985. Catalase Activity, vol. 1. CRC Press, Boca Raton, FL, pp. 283–284.
Cutler, S.R., Somerville, C.R., 2005. Imaging plant cell death: GFP-Nit1 aggregation marks an early step of wound and herbicide induced cell death. BMC Plant Biol. 5, 4.
Dangleben, N.L., Skibola, C.F., Smith, M.,T., 2013. Arsenic immunotoxicity: a review. Environ. Health 12, 73.
Das, G., Shravage, B.V., Baehrecke, E.H., 2012. Regulation and function of autophagy during cell survival and cell death. Cold. Spring. Harb. Perspect. Biol. 4.
Das, S., Mukherjee, P., Chatterjee, R., Jamal, Z., Chatterji, U., 2019. Enhancing chemosensitivity of breast cancer stem cells by down regulating SOX2 and ABCG2 using Wedelolactone-encapsulated nanoparticles. Mol. Cancer Ther. 18, 680–692.
Duan, X., Gao, S., Li, J., Wu, L., Zhang, Y., Li, W., Zhao, L., Chen, J., Yang, S., Sun, G., Li, B., 2017. Acute arsenic exposure induces inflammatory responses and $CD4^{+}$ T-cell subpopulations differentiation in spleen and thymus with the involvement of MAPK, NF-kB, and Nrf2. Mol. Immunol. 81, 160–172.
Faita, F., Cori, L., Bianchi, F., Andreassi, M.G., 2013. Arsenic induced Genotoxicity and genetic susceptibility to arsenic-related pathologies. Int. J. Environ. Res. Public Health 10, 1527–1546.
Green, D.R., Levine, B., 2014. To be or not to be? How selective autophagy and cell death govern cell fate. Cell 157, 65–75.
Htike, N.T., Maekawa, F., Soutome, H., Sano, K., Maejima, S., Aung, K.H., Tokuda, M., Tsukahara, S., 2016. Arsenic exposure induces unscheduled mitotic S phase entry coupled with cell death in mouse cortical astrocytes. Front. Neurosci. 10, 297.
Ichim, C.V., 2005. Revisiting immunosurveillance and immunostimulation: implications for cancer immunotherapy. J. Transl. Med. 3, 8.
Jollow, D.J., Mitchell, J.R., Zampaglione, N., Gillette, J.R., 1974. Bromobenzene-induced liver necrosis. Protective role of glutathione and evidence for 3, 4-bromobenzene oxide as the hepatotoxic metabolite. Pharmacology 11, 151–169.
Julier, Z., Park, A.J., Briquez, P.S., Martino, M.M., 2017. Promoting tissue regeneration by modulating the immune system. Acta Biomater. 53, 13–28.
Kasprowska-Liśkiewicz, D., 2017. The cell on the edge of life and death: crosstalk between autophagy and apoptosis. Postepy Hig. Med. Dosw. 71, 825–841.
Knaapen, M.W., Davies, M.J., De Bie, M., Haven, A.J., Martinet, W., Kockx, M.M., 2001. Apoptotic versus autophagic cell death in heart failure. Cardiovasc. Res. 51, 304–312.
Li, J., Buchner, J., 2013. Structure, function and regulation of the hsp90 machinery. Biomed. J. 36, 106–117.
Li, J., Zhao, L., Zhang, Y., Li, W., Duan, X., Chen, J., Guo, Y., Yang, S., Sun, G., Li, B., 2017. Imbalanced immune responses involving inflammatory molecules and immune-related pathways in the lung of acute and sub-chronic arsenic-exposed mice. Environ. Res. 159, 381–393.
Liu, Y., Levine, B., 2015. Autosis and autophagic cell death: the dark side of autophagy. Cell Death Differ. 22, 367–376.
Marklund, S., Marklund, G., 1974. Involvement of superoxide anion radical in the autoxidation of pyrogallol and a convenient assay for superoxide dismutase. Eur. J. Biochem. 47, 469–474.
Markowski, V.P., Currie, D., Reeve, E.A., Thompson, D., Wise, J.P. Sr, 2011. Tissue-specific and dose related accumulation of arsenic in mouse offspring following maternal consumption of arsenic-contaminated water. Basic Clin. Pharmacol. Toxicol. 108, 326–332.
Mittal, M., Siddiqui, M.R., Tran, K., Reddy, S.P., Malik, A.B., 2014. Reactive oxygen species in inflammation and tissue injury. Antioxidants Redox Signal. 20, 1126–1167.
Navarro-Yepes, J., Burns, M., Anandhan, A., Khalimonchuk, O., del Razo, L.M., Quintanilla-Vega, B., Pappa, A., Panayiotidis, M.I., Franco, R., 2014. Oxidative stress, redox signaling and autophagy: cell death versus survival. Antioxidants Redox Signal. 21, 66–85.
Noman, A.S., Dilruba, S., Mohanto, N.C., Rahman, L., Khatun, Z., Riad, W., Al Mamun, A., Alam, S., Aktar, S., Chowdhury, S., Saud, Z.A., Rahman, Z., Hossain, K., Haque, A., 2015. Arsenic-induced histological alterations in various organs of mice. J. Cytol. Histol. 6, 323.
Orrenius, S., Nicotera, P., Zhivotovsky, B., 2011. Cell death mechanisms and their implications in toxicology. Toxicol. Sci. 119, 3–19.
Platanias, L.C., 2009. Biological responses to arsenic compounds. J. Biol. Chem. 284, 18583–18587.
Pournara, A., Kippler, M., Holmlund, T., Ceder, R., Grafström, R., Vahter, M., Broberg, K., Wallberg, A.E., 2016. Arsenic alters global histone modifications in lymphocytes in vitro and in vivo. Cell Biol. Toxicol. 32, 275–284.
Ren, X., McHale, C.M., Skibola, C.F., Smith, A.H., Smith, M.T., Zhang, L., 2011. An emerging role for epigenetic dysregulation in arsenic toxicity and carcinogenesis. Environ. Health Perspect. 119, 11–19.
Shao, Y., Zhao, H., Wang, Y., Liu, J., Li, J., Chai, H., Xing, M., 2018. Arsenic and/or copper caused inflammatory response via activation of inducible nitric oxide synthase pathway and triggered heat shock protein responses in testis tissues of chicken. Environ. Sci. Pollut. Res. Int. 25, 7719–7729.
So, K.Y., Lee, B.H., Oh, S.H., 2018. The critical role of autophagy in cadmium-induced immunosuppression regulated by endoplasmic reticulum stress-mediated calpain activation in RAW264.7 mouse monocytes. Toxicology 393, 15–25.
Stoecklein, V.M., Osuka, A., Lederer, J.A., 2012. Trauma equals danger—damage control by the immune system. J. Leukoc. Biol. 92, 539–551.
Tam, S.Y., Wu, V.W., Law, H.K., 2017. Influence of autophagy on the efficacy of radiotherapy. Radiat. Oncol. 12, 57.
Theron, A.J., Tintinger, G.R., Anderson, R., 2012. Harmful interactions of non-essential heavy metals with cells of the innate immune system. J. Clin. Toxicol. S3, 005.
Wang, B., Chen, L., Ni, Z., Dai, X., Qin, L., Wu, Y., Li, X., Xu, L., Lian, J., He, F., 2014. Hsp90 inhibitor 17-AAG sensitizes Bcl-2 inhibitor (−)-gossypol by suppressing ERK-mediated protective autophagy and Mcl-1 accumulation in hepatocellular carcinoma cells. Exp. Cell Res. 328, 379–387.
Wei, Y., An, Z., Zou, Z., Sumpter, R., Su, M., Zang, X., Sinha, S., Gaestel, M., Levine, B., 2015. The stress-responsive kinases MAPKAPK2/MAPKAPK3 activate starvation-induced autophagy through Beclin 1 phosphorylation. Elife 4.
Zhang, H., Kong, X., Kang, J., Su, J., Li, Y., Zhong, J., Sun, L., 2009. Oxidative stress induces parallel autophagy and mitochondria dysfunction in human glioma U251 cells. Toxicol. Sci. 110, 376–388.

Source details

Feedback > Compare sources >

Chemosphere

Incorporating: Chemosphere - Global Change Science

Scopus coverage years: from 1972 to Present

Publisher: Elsevier

ISSN: 0045-6535 E-ISSN: 1879-1298

Subject area: Medicine: Public Health, Environmental and Occupational Health | Environmental Science: Environmental Engineering | Environmental Science: Health, Toxicology and Mutagenesis | Chemistry: General Chemistry | Environmental Science: Pollution View all

Source type: Journal

View all documents > Set document alert Save to source list

CiteScore 2022
13.3

SJR 2022
1.727

SNIP 2022
1.624

CiteScore CiteScore rank & trend Scopus content coverage

Altered expressions of DNA methyltranferases in biomass using rural women in West Bengal

Banani Bindhani[1], Hirak Saha[2], Bidisha Mukherjee[2], Manas Ranjan Ray[2]

Abstract-- **Unprocessed solid biomass such as wood, coal, dung and agricultural residues are still being used in many rural households in India as main source of domestic energy for cooking, boiling and heating of water. Combustion of biomass releases a considerable amount of particulate matters (PM) and toxic pollutants. Therefore, use of biomass as fuels cause very high level of indoor air pollution (IAP) in rural households and the women who do most of the daily household cooking with these fuels, receive the maximum exposure. Thus, the cells of the nasopharynx, oral cavity, airways and the lungs in these women get severely affected and undergo harmful changes. The present study is conducted to appraise the effects of IAP generated PMs and/or carcinogens on epigenetic changes in airway epithelial cells as little information is known and available about it. In the present study LPG using rural women were used as control against biomass using rural women and both these groups comprise of non-smokers and non-chewer of tobacco and betel nut. Significantly enhanced production of ROS was evident in biomass fuel users with depletion of SOD, a major scavenger enzyme for oxidants in comparison to LPG using control women. Furthermore, Immunocytochemical evaluation showed significantly increased expressions of DNMT1 and DNMT3a enzymes and reduced expression of SET7, an inhibitor of DNMT1, in airway epithelial cells of biomass-using rural women in comparison to LPG using control women. The findings indicate major epigenetic changes in airway epithelial cells of biomass users due to long-term exposure to particulate pollution which also increases the risk of lung cancer in these women.**

Key words - Indoor Air Pollution (IAP), Particulate Pollution, Biomass fuel, DNA methyltransferases, SET7, Epigenetic Changes, Reactive Oxygen Species (ROS)

I. INTRODUCTION

Air pollution is one of the most important causes of various respiratory diseases including different types of cancer. It is generally perceived as an urban problem associated with toxic pollutants emitted from motor vehicles and industries (Zhang and Smith 2003). However, developing nations of Asia, Africa and Latin America have another major source of air pollution (Smith 2002). Around 50% of the world's population, particularly in developing countries, uses solid fuels, including biomass (wood, dung and agricultural residues) and coal, to meet their most basic energy needs: cooking, boiling water and heating (Bruce et al., 2000). According to the report of the World Health Organization, a significant portion of the population of rural areas in India still uses unprocessed solid biomass such as wood, dung and agricultural residues as their primary source of domestic energy (Bruce et al., 2000). Recent studies have shown that indoor biomass combustion causes very high level of indoor air pollution (IAP) by releasing a considerable amount of pollutants, including carbon monoxide (CO), nitric oxides (NO_x), sulphur dioxide (SO_2), formaldehyde (HCHO), volatile organic compounds (VOC), particulate matter (PM) and polycyclic aromatic hydrocarbons (PAHs) (Rehfuess 2006; Gennarro et al., 2015). Moreover, several factors such as occupant's behavior, microclimatic and ventilation condition and outdoor intrusion can also influence indoor pollution levels.
[1]

IAP resulted from combustion of biomass in rural households often exceeds the level of ambient (outdoor) air pollution in the cities (Balachandran et al., 2000; Ramachandran et al., 2003).

Like cigarette smoke, biomass smoke also contains a number of harmful chemicals including oxides of nitrogen and sulphur, thousands of organic compounds such as volatile organic compounds (VOCs) like benzene, benzene 1, 3-butadiene, benzo(a)pyrene which itself is a well-established carcinogen, transition metals, coarse (diameter <10 µm, PM_{10}), fine (diameter < 2.5 µm , $PM_{2.5}$) and ultra fine particles (UFP) (diameter < 0.1 µm) (Zhang and Smith, 2003; Danielsen et al., 2009).

Poverty and easy availability are the main reasons behind dependence on biomass for cooking. Biomass fuels are not energy-efficient, and incomplete combustion of biomass emits a very high level of smoke that remains in the cooking area for a longer time because of poor kitchen ventilation in most poor households. In many cases, kitchens are altogether absent and women cook in a place adjacent to the living room (Gennaro et al., 2015). As a result, every member of the family is exposed to high levels of indoor air pollution, and women, who bear the burden of daily household cooking with these fuels, receive the maximum exposure. It is reasonable to assume therefore that cumulative exposures to biomass smoke may cause harmful changes especially in cells that are present at the direct route of exposure such as cells of the

[1] * Corresponding Author: Smt. Banani Bindhani, Asst. Prof., Dept. of Zoology, Dinabandhu Andrews College, Garia, Kolkata – 700084; Email: bindhanibanani@gmail.com, Mobile: +918478822525

nasopharynx, oral cavity, airways and the lung (Zhang and Smith 2003; Rehfuess 2006).

Genomic DNA is often methylated at the fifth position of the cytosine base in CpG sequences (Ehrlich et al., 1982). DNA methylation is a common mechanism for gene silencing and plays a crucial role in development, genome stability, genomic imprinting, X-chromosome inactivation, and silencing of retrotransposons (Reik and Lewis 2005; Goll and Bestor 2005). DNA methyltransferases (DNMTs) catalyze the transfer of a methyl group to the fifth position of cytosine bases in DNA. Mammalian genomes carry three distinct active Dnmt genes. Dnmt3a and Dnmt3b are highly expressed in embryonic tissues and undifferentiated ES cells and down regulated in differentiated cells. Two of the three genes, Dnmt3a and Dnmt3b, encode enzymes that show activity toward unmethylated DNA (Okano et al 1998; Aoki et al 2001) and are responsible for creating global DNA methylation patterns during embryogenesis and gametogenesis (Okano et al., 1999; Kaneda et al., 2004). Once the DNA methylation patterns are established, they are maintained by DNMT1 encoded by the Dnmt1 gene, which ensures the transmission of lineage-specific DNA methylation patterns during replication (Li et al., 1992). DNMT1 preferentially methylates the hemimethylated state of DNA that appears just after replication or repair & plays a crucial and major role in epigenetic changes in mammals (Takeshita et al., 2011).

DNA methylation is a potential mechanism linking indoor air pollution to adverse health effects. Recent studies have established associations between DNA methylation and PM exposure. ROS generated by transitional metals or other PM-contents can damage DNA. PM- containing chemical components may exert direct or indirect influences on DNA methylation patterns (Wang et al., 2012). Oxidative DNA damage can interfere with the ability of DNMT to interact with the DNA, thus resulting in a generalized altered methylation of cytosine residues at CpG sites (Wang et al., 2012). Exposure to ambient PM leads to a consistently reduced global DNA methylation in both human and experimental animal (Baccarelli et al., 2009; Tarantini et al., 2009).

Fetal and early-life environmental exposures have been associated with altered DNA methylation and play a critical role in progression of various diseases in adulthood (Tao et al., 2014). Furthermore, DNA methylation has emerged as a promising biomarker for environmental-related diseases, including lung cancer (Hou et al., 2014).

SET7 is a methyltransferase that methylates lysine residues in its target proteins. SET7 mediated methylation of mammalian DNMT1 at Lys142 leads to its proteasomal degradation. Therefore, the enzyme SET7 act as a negative regulator of DNA methyltransferase-1 (DNMT1) activity in mammalian cells by promoting degradation of DNMT1 and thus allows epigenetic changes to occur via DNA demethylation (Estève et al., 2011). Thus SET7 plays a critical role as a regulator of gene expression by controlling the stability of DNMT1.

Presence of high level of DNMT1 can hypermethylate the promoter regions of different genes thereby leading to transcriptional inactivation of these genes. For example, presence of high amount of particulate matters in air may lead to DNMT1 mediated hypermethylation of p16 promoter resulting its subsequent inactivation (Soberanes et al., 2012). Moreover, studies have shown that exposure to tobacco specific carcinogen NKK also leads to high level of DNMT1 expression in cells and causes hypermethylation of various cancer-critical genes in lung cancer patients (Lin et al., 2010). Several studies have documented altered expression of DNMTs following the exposure of test subjects to high level of particulate matters (Wang et al., 2012; Soberanes et al., 2012). Benzo(a)pyrene also regulates the expression level of DNMTs (Ye and Xu 2010). Smoke resulted from incomplete combustion of biomass contributes particulate matter and several carcinogens like benzo(a)pyrene in breathing air. However, very little information has been generated about the effects of IAP generated PMs and/or carcinogens on epigenetic changes through regulation of DNMTs in airway epithelial cells. In view of this, the current study has been undertaken to appraise the changes in the expressions of DNMT1, DNMT3a, DNMT3b and SET7 in airway epithelial cells of biomass users exposed to IAP in contrast to LPG users.

II. MATERIALS & METHODOLOGY

Participants

For the study, a total number of 128 premenopausal women aged between 27 and 42 years from rural areas of West Bengal were enrolled. Among the participants, 83 women (age 27–42 years, median 34 years) used to cook daily about 5 hours exclusively with wood, cow dung and agricultural wastes, such as bamboo, jute stick, paddy husk, hay and dried leaves for the past 5 years or more. They were considered as biomass users. The remaining 45 women were aged 27–41 years [median age 32 years] from same locality and cooked with cleaner fuel LPG and were considered as control.

Inclusion and Exclusion criteria

The inclusion criteria were apparently healthy premenopausal married women with husbands, actively engaged in daily household cooking for the past 5 years or more, non-smoker and non- chewer of tobacco and betel nut and having a body mass index > 15 and < 30 kg/m^2. Exclusion criteria were mixed fuel (biomass + LPG/kerosene) users, pregnant or breastfeeding, using oral contraceptive pills, had recent or past history of malignancy and currently under medication. Information about age, habits, education, family size and income, number of smokers in family, cooking time per day, years of cooking, fuel and oven type, and location of kitchen, was obtained during personal interview with female researchers of the study team. The Ethics Committee of Chittaranjan National Cancer Institute, Kolkata approved the study protocol.

Collection of background data

During personal interview, each participant was requested to furnish information about age, education, family size and income, habit, cooking time per day, years of cooking, fuel and oven type, location and ventilation of kitchen, health problems in past 3 months and last one year. As most of the participants were poorly educated, the researchers entered their responses in structured questionnaire forms on their behalf. The Ethics Committee of Chittaranjan National Cancer Institute, Kolkata approved the study protocol.

Measurement of air pollution

The concentrations of particulate matter with a diameter of less than 10 and 2.5 □m (PM_{10} and $PM_{2.5}$, respectively) were measured by real-time aerosol monitor (DustTrak™, model 8520, TSI Inc., MN, USA). The instrument contains 10-mm nylon Dor-Oliver cyclone, operates at a flow rate of 1.7 L/min and measures particle load in the concentration range of 1 mg-100 mg/m^3. The monitor was calibrated to the standard ISO 12103-1 A1 test dust. Monitoring was carried out for 3 consecutive days, 8 hours/day (07:00-15:00 hours). For biomass-using women who cook in a sitting position 2-3 ft away from the open chullah (oven), the monitor was placed in the breathing zone of the cook, 2.5 ft above floor level on a wooden stool, 3 ft away from the chullah. LPG users, on the other hand, cook in a standing position and the monitor was placed accordingly at a height of 4.5 ft.

Collection of Sputum sample

For the collection of sputum sample, the participants were instructed to cough vigorously after awakening in the morning and to collect the expectorated sputum in sterile plastic cups given to them. For better collection of cells from the deeper airways, early morning sputum samples of each participant were collected for three consecutive days (Erkilic et al., 2003). Highly viscous parts of the sputa were collected in 30 ml of PBS that contained 0.1% dithiotheritol. Collected samples were transported from the villages to the laboratory under dry ice.

Flow cytometric measurement of ROS (Reactive Oxygen Species) generation

Flow cytometric measurement of ROS Generation of reactive oxygen species (ROS) was measured in cells present in expectorated sputum by flow cytometry following the procedure of Rothe and Valet (1990) with some modifications. In brief, an aliquot of 200 µl of sputum cell suspension was diluted with 1 ml of HBSS containing 0.15 M NaCl and 5 mM HEPES, pH 7.35. Thereafter, 20 µl of 0.5 mM 2, 7-dichlorofluorescein diacetate (DCF-DA, Sigma Chem, USA) solution in dimethyl formamide was added to the cell suspension and incubated at 37^0C for 30 min in darkness. After that, 10,000 events were acquired immediately in flow cytometer (FACS Calibur with sorter, Becton Dickinson [BD], San Jose, CA, USA) using Cell Quest software (BD, USA). Respiratory burst and generation of ROS by cells present in sputum resulted in green fluorescence that was recorded in fluorescence channel and was expressed as mean fluorescence intensity (MFI) in arbitrary unit.

Spectrophotometric measurement of SOD (Superoxide dismutase)

The activity of the antioxidant enzyme superoxide dismutase (SOD) was assayed in whole sputum cell lysates spectrophotometrically following the procedure of Paoletti et al. (1986). Presence of SOD in sample was reflected by proportionate inhibition of the rate of NADH oxidation. This was calculated after measuring the absorbance of the samples and standard at 340 nm in a UV-spectrophotometer (Shimadzu, Japan) at 1 min intervals up to 5 min. The absorbance (OD) values were graphically plotted against time after mercaptoethanol addition (at 0, 1, 2, 3, 4, and 5 min). SOD activity in lysates was calculated from the standard curve and was expressed as U/ml.

Collection of sputum samples for Immunocytochemistry

The participants were asked to cough vigorously and the expectorated sputum was collected in sterile plastic cup for three consecutive days. The thick viscous parts of the sputa were smeared on clean glass slides. Ten slides were prepared from sputa of each participant. Slides containing airway cells were air dried and then fixed with cold methanol at the site of collection for immunocytochemistry.

Immunocytochemical detection of DNMT1, DNMT3a, DNMT3b and SET7 in airway epithelial cells

Expressions of DNMT1, DNMT3a, DNMT3b and SET7 proteins, actively involved in epigenetic changes were detected by immunocytochemistry (ICC) using the primary antibody by Abcam, UK following the established staining protocol (Ghosh et al, 2009).

Reagents used

For preparation of 1x phosphate buffered saline (PBS, pH 7.2), chemicals like NaCl (Merck, Mumbai, India), KCl (Merck, Mumbai, India), $Na_2HPO_4.7H_2O$ (Merck, Mumbai, India), KH_2PO_4 (Merck, Mumbai, India) were used. BSA solutions (Sigma–Aldrich Chemicals, Saint Louis, MO, USA) for making of 3% (w/v) BSA in 1X PBS 1% (w/v) BSA in 1X PBS were required for non-specific site blocking and for antibody dilution respectively. Primary antibodies, Rabbit polyclonal DNMT1 (dilution 1:50) (ab19905) and Mouse monoclonal SET7 (dilution 1:50) (ab14820) were purchased from Abcam, UK; and Rabbit polyclonal DNMT3a (dilution 1:50) (sc20703) and Rabbit polyclonal DNMT3b (dilution 1:50) (sc130740) were purchased from Santacruz, USA. Secondary antibodies, Goat anti-rabbit IgG, $F(ab')_2$- HRP (dilution 1:500) (sc3837) was purchased from Santa Cruz Biotechnology, Inc., USA) and Rabbit anti-mouse IgG, $F(ab')_2$- HRP (dilution 1:500) (ab6728) was purchased from Abcam, UK. Tris powder was purchased from SISCO Research Laboratories, India, for preparation of Tris-HCl

solution (pH 7.6). HRP substrate mixture was prepared by using DAB (Santa Cruz Biotechnology, Inc., USA), 50% H_2O_2 (Merck, Mumbai, India) and 1M Tris-HCl.

Procedure

The slides containing exfoliated airway epithelial cells (AEC) in spontaneously expectorated sputum, after fixation, were air dried, washed in PBS thrice and blocked in 3% bovine serum albumin (BSA) for 1 hour at room temperature. Thereafter, rabbit polyclonal DNMT1, DNMT3a and DNMT3b and mouse monoclonal SET7 primary antibodies (diluted both 1:50 in 1% BSA) were added separately to each slide. The slides were placed in a humid box at 4^{o}C and kept overnight in darkness. After washing with PBS, both anti-rabbit IgG, F(ab')$_2$- HRP and anti-mouse IgG , F(ab')$_2$- HRP secondary antibodies (diluted 1:500 in 1% BSA) was added to the respected slides and kept for 90 min. After washing with PBS the HRP substrate mixture was added to the slides and kept for 60 min in darkness. Then the slides were washed with distilled water and counterstained with hematoxylin, dehydrated in graded ethanol and mounted in distrene plasticizer xylene (DPX) and examined under light microscope (model BX50, Olympus, Japan). Slides were evaluated for the presence of DAB-stained golden brown nuclei. At least 300 AEC were scored from each slide and the results were expressed as percentage of positive (stained) cells.

Statistical evaluation of data

Results were expressed as mean ± standard deviation (SD). Data were processed and analyzed in EPI info 6.0 and SPSS 10.0 (IL, USA) statistical software. The collected data were statistically analyzed by Chi-square test and Student's t-test and $p<0.05$ was considered significant. Logistic regression analysis for odds ratios (OR) at 95% confidence interval (CI) and Spearman's rank correlation test was done to examine the relationship between respiratory symptoms, spirometric lung function measurements, cellular lung responses and air pollution exposure. Then, the cumulative impact of these factors on the expression of DNA methylation proteins was evaluated by stepwise multivariate logistic regression analysis. Statistical significance was assigned at $p < 0.05$.

III. RESULTS

Demographic characteristics

Demographic and socio-economic characteristics of rural women exposed to biomass smoke have been compared with LPG using control women from same locality, with respect to age, body mass index, cooking years, cooking hours per day, having separate kitchen, food habit, use of mosquito repellent, number of family members and environmental tobacco smoke for the presence of smokers in the family. However, the three groups differed significantly with respect to education ($p<0.0002$), family income ($p< 0.0001$) which were lower in biomass users, and lack of a separate kitchen ($p=0.0477$) which was more prevalent among biomass users. The findings are tabulated in Table 1.

TABLE 1
Demographic and socio-economic characteristics of biomass and LPG-using rural women

Variable	LPG-using control (n = 45)	Biomass user (n = 83)	P value
Age in years, median (range)	32.0 (27-41)	34.0 (27- 42)	=0.2173
Body mass index (kg/m^2), median (range)	23.1 (19.4-25.5)	22.7 (18.2-25.4)	=1.0000
Cooking years, median (range)	9 (5-21)	10 (5-27)	=0.1750
Cooking hours per day, median (range)	3.0 (2-5)	4.0 (3-6)	=0.4804
Cooking hours per day, (mean ± SD)	3.3 ± 1.1	3.8 ± 1.2	=0.4804
Years of schooling, median (range)	10(5–16)	2(0–8)	<0.0002**
Homes with separate kitchen (%)	84.5	66.3	=0.0477*
Smoker in family (%)	42.3	42.2	=0.1213
Use of mosquito repellent at home (%)	57.8	57.8	=1.000
Food habit, mixed (%)	100	100	
Members in family, median (range)	5 (3-6)	5 (4-6)	=0.0842
Family income per month in US $ (mean ± SD)	104 ±16	54 ± 12	< 0.0001***

n, number of subjects; NS, statistically not significant; Significantly different from control in *, Chi-square test; **,Mann-Whitney U test' ***, Student's t-test

Indoor air quality of the biomass using households

Concentrations of particulate pollutants in cooking areas during cooking and non-cooking time are presented in Table 2 and Figure 1. During cooking hours, the mean concentration of PM_{10} in biomass-using kitchen was 482±112 (SD) □g/m^3 in contrast to 134±39 □g/m^3 in LPG-using kitchen. Thus, 3.6 times more PM_{10} was recorded in indoor air of biomass-using kitchen when compared to that of LPG-using kitchen ($p<0.0035$). Even in non-cooking hours, PM_{10} level in indoor air of biomass-using kitchen was 1.8 times higher than that of LPG-using kitchen (134±42vs. 73±29, $p<0.0035$).

Like PM_{10}, the concentration of $PM_{2.5}$ in indoor air of biomass-using kitchen was significantly higher than LPG-using kitchen (Table 2, Figure 1). During cooking time, $PM_{2.5}$ level in indoor air of biomass-using kitchen was 272±69 μg/m^3 against 74±21 μg/m^3 in LPG-using kitchen, showing 3.7 times more fine particulate matter in kitchen where biomass is used as cooking fuel ($p<0.001$). In non-cooking time also, $PM_{2.5}$ level in indoor air of biomass-using kitchen was 2 times higher than that of LPG-using kitchen (78±39 μg/m^3 vs. 39±14 μg/m^3, $p<0.0217$).

TABLE 2
Comparison of particulate pollution in indoor air of cooking areas between LPG and biomass using Households

	LPG-using Households	Biomass-using Households
PM_{10} (µg/m^3)		
Cooking time	134±39	482±112*
Non-cooking time	73±29	134±42*
$PM_{2.5}$ (µg/m^3)		
Cooking time	74±21	272±69*
Non-cooking time	39±14	78±39*

Significantly different from control in *, Student's t-test

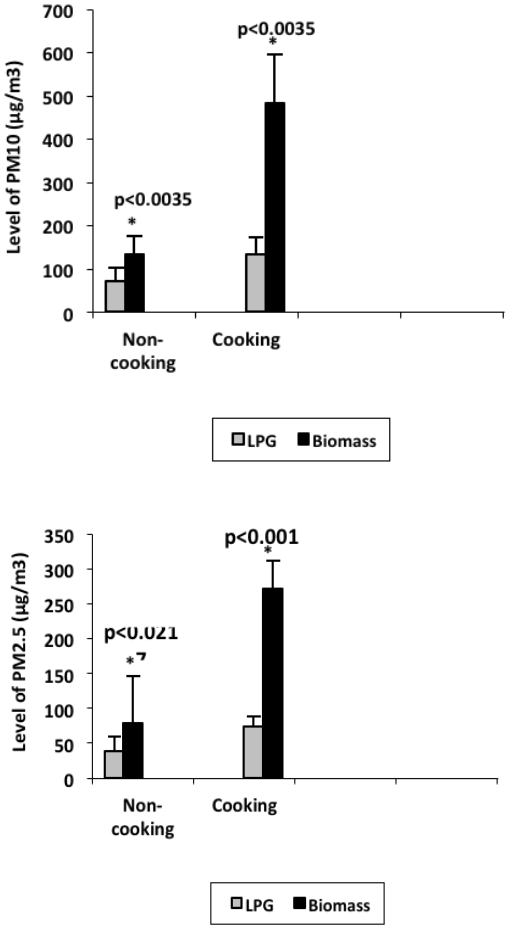

Fig. 1 The levels of particulate pollution in cooking areas of biomass- and LPG-using households during cooking and non-cooking hours

Generation of ROS in Airway Epithelial cells of Biomass Users

Flow cytometric analysis showed appreciable rise in ROS generation ($p<0.0001$) in airway epithelial cell exfoliated in sputum of biomass using women than LPG users. The MFI of DCFH-DA was increased by 36% in airway epithelial cells (62.5 ± 13.2 vs. 31.7 ± 8.5 in control, $p<0.0001$, Figure 2).

Depletion of SOD level in Airway Epithelial cells of Biomass Users

Since, air pollutants elicits oxidative stress that could be harmful for the body, antioxidant defense state was evaluated by measuring the activity of antioxidant enzyme superoxide dismutase (SOD). Significant decline ($p<0.0011$) in antioxidant enzyme levels ($p<0.0011$) was recorded in indoor air pollution-exposed subjects (859.8 ± 45.9 in LPG user vs. 706.5 ± 96.7 U/ml in biomass smoke-exposed), implying greater oxidative stress that may lead to cellular damage (Figure 3).

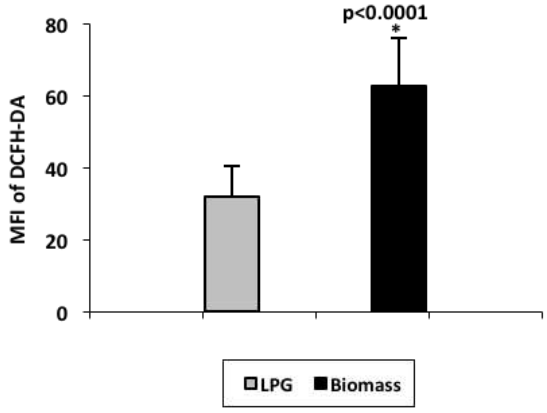

Fig. 2 Significant generation of ROS in Airway epithelial cells of Biomass user women

Association between Particulate Matter Exposure and Generation of ROS

Particulate matter exposure during cooking with Biomass fuel was significantly correlated with generation of Reactive Oxygen Species in Airway Epithelial cells. The value of Pearson Correlation was 0.851, $p<0.0001$ was highly significant. Kendall's tau-b value was 0.782, $p=0.001$ was significant and Spearman ρ value was 0.94, $p<0.0001$ was highly significant.

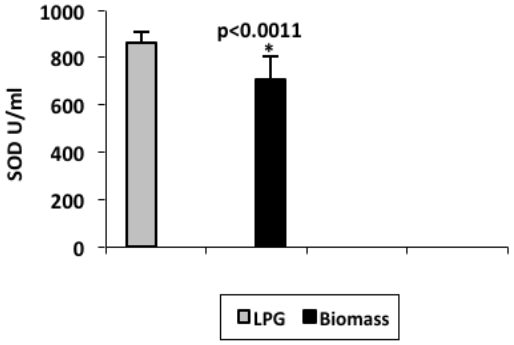

Fig. 3 Significant decline antioxidant enzyme levels in women chronically exposed to indoor air pollution compared with age and sex-matched controls.

Concentration of trans, trans–muconic acid (t, t-MA) in urine

The concentration of t, t-MA in urine, a biomarker of benzene exposure, was 8.24 ± 6.74mg/l in biomass-using women in contrast to 1.19 ± 0.8 mg/l in control subjects (Figure 4, p<0.0001 in Student's t-test). The range of urinary t, t-MA was 0.3-2.9 mg/l with a median of 0.9 mg/l in control women whereas biomass using women had a range of 2.4-20.5 mg/l with a median of 6.8 mg/l (p<0.0001 in Mann-Whitney U-test).

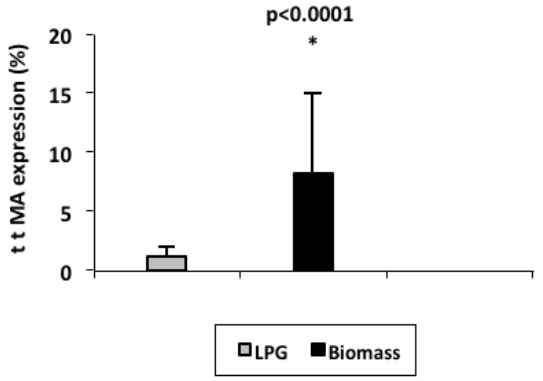

Fig. 4 Histogram showing increase level of t,t-MA in exposed group

Expression of DNMT1 and SET7 in airway epithelial cells

In ICC, the expressions of DNMT1 and SET7 proteins were found mainly in the nuclei of airway epithelial cells, especially in the basal and parabasal cells (Plate 1 & 2, Table 3, Figure 5). The percentages of airway epithelial cells expressing DNMT1 and SET7 were significantly higher and lower respectively in women who were chronically exposed to biomass smoke (Table 3). For instance, as the frequencies of DNMT1 expressing epithelial cells exfoliated in sputam varied considerably between biomass users and control women, we converted the relative (%) values to absolute ones (cells/hpf). Still, expression of DNMT1 (67.6 ± 7.3 vs. 28.6 ± 4.2 cells/hpf in control, p<0.0001) was significantly higher in biomass users than LPG users. However, SET7 expressing cells (15.7 ± 6.3 vs. 28.8 ± 9.2cells/hpf in control, p<0.0001) in biomass-using women were significantly lower than the control.

Expressions of DNMT1 and SET7 in Airway epithelial cells of Biomass users

Expressions of DNMT1 and SET7 in Airway epithelial cells of biomass user women show negative correlation. DNMT1 expression was significantly higher whereas SET7 expression was diminished in the nuclei of Airway epithelial cells of biomass users. The value of Pearson Correlation was -0.581, p=0.04 was significant. But Kendall's tau-b value was -0.492, p=0.055 was not significant and Spearman ρ value was -0.54, p=0.062 was not significant.

TABLE 3
Immunocytochemical expression of DNMT1 and SET7 in airway epithelial cells (AEC) of biomass- and LPG-using women (mean±SD)

Parameters	LPG using control (n = 45)	Biomass users (n = 83)	P value
Percentage of DNMT1-expressing cells			
Mean ± SD	28.6 ± 4.2	67.6 ± 7.3	<0.0001*
Median (range)	30 (24-32)	66.5 (52-83)	<0.0001**
Percentage of SET7-expressing cells			
Mean ± SD	28.8 ± 9.2	15.7 ± 6.3	<0.0001*
Median (range)	26 (19-43)	15.5 (8-27)	<0.0001**

Significantly different from control in **, Mann-Whitney U test and *, Student's t-test

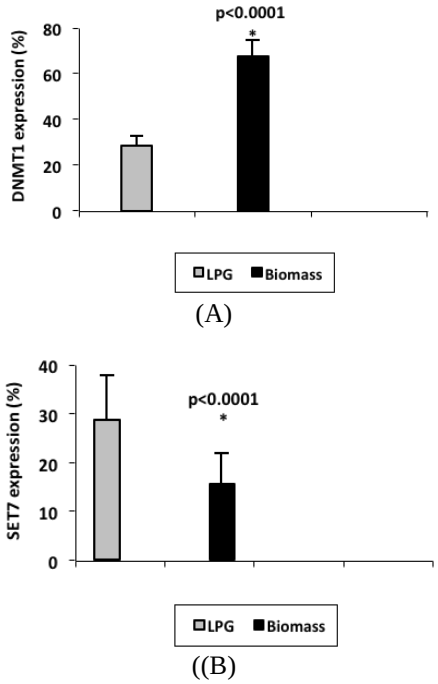

Fig. 5 Immunocytochemical expression of DNMT1 (A) and SET7 (B) in Airway Epithelial cells of LPG and Biomass - users rural women

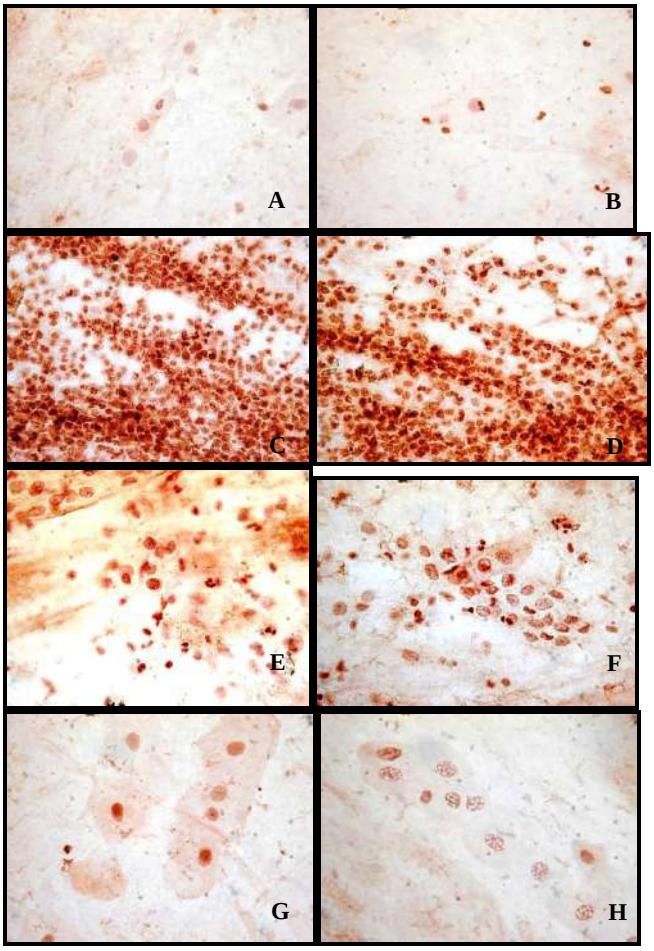

Plate 1 Immunocytochemical expression of DNMT1 – Airway Epithelial cells of LPG users showing very low expression (A,B); Airway Epithelial cells of Biomass users showing very high expression (C,D); Strong expression in nucleus of epithelial cell of Biomass users (E,F,G,H). The cell nuclei were counterstained with hematoxylin, original magnification, 1000x.

Generation of ROS and Expression of DNMT1

Generation of ROS due to chronic exposure of particulate matter in indoor air pollution was highly correlated with DNMT1 expression in Airway epithelial cells of Biomass user women. The value of Pearson Correlation was 0.871, $p<0.0001$ was highly significant. Also Kendall's tau-b value was 0.776, $p=0.001$ was significant and Spearman ρ value was 0.90, $p<0.0001$ was highly significant.

Depletion of SOD and Expression of DNMT1

Depletion of SOD was negatively correlated with high level of DNMT1 expression in airway epithelial cells of Biomass user women. The value of Pearson Correlation was -0.591, $p=0.043$ was significant. Also Kendall's tau-b value was -0.492, $p=0.039$ was significant but Spearman ρ value was -0.563, $p=0.057$ was not significant.

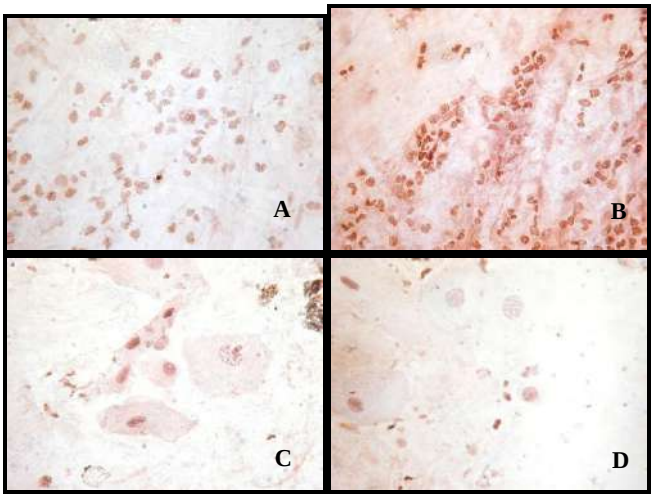

Plate 2 Immunocytochemical expression of SET7 – Airway Epithelial cells of LPG users showing very high expression (A,B); Strong expression in nucleus of epithelial cell of LPG users (C); Airway Epithelial cells of Biomass users showing low expression (D). The cell nuclei were counterstained with hematoxylin, original magnification 1000x.

Expression of DNMT3a and DNMT3b in airway epithelial cells

In ICC, the expressions of DNMT3a and DNMT3b proteins were found mainly in the nuclei of airway epithelial cells, especially the basal and parabasal cells (Plate 3, 4; Table 4, Figure 6). The percentages of airway epithelial cells expressing DNMT3a and DNMT3b were significantly higher and lower respectively in women who were chronically exposed to biomass smoke (Table 4). For instance, as the frequencies of DNMT3a expressing epithelial cells exfoliated in sputam varied considerably between biomass users and control women, we converted the relative (%) values to absolute ones (cells/hpf). Still, expression of DNMT3a (32.9 ± 7.3 vs. 14.3 ± 3.7 cells/hpf in control, $p<0.0001$) was significantly higher in biomass users than LPG users. However, DNMT3b expressing cells (11.8 ± 2.9 vs. 11.2 ± 2.2 cells/hpf in control, $p=0.2282$) in biomass-using women were not significantly higher than the control.

TABLE 4
Immunocytochemical expression of DNMT3a and DNMT3b in airway epithelial cells (AEC) of biomass- and LPG-using women (mean ± SD)

Parameters	LPG using control (n = 45)	Biomass users (n = 83)	P value
Percentage of DNMT3a-expressing cells			
Mean ± SD	14.3 ± 3.7	32.9 ± 7.3	<0.0001*
Median (range)	14.1 (11-34)	32.7 (31-64)	<0.0001**
Percentage of DNMT3b expressing cells			
Mean ± SD	11.2 ± 2.2	11.8 ± 2.9	0.2282
Median (range)	11 (4-18)	11.3 (6-19)	0.2282

Significantly different from control in **, Mann-Whitney U test and *, Student's t-test

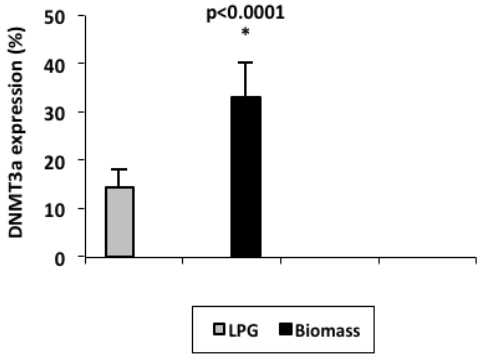

(A)

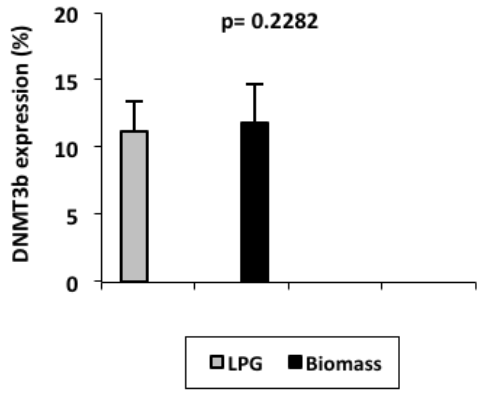

(B)

Fig. 6 Immunocytochemical expression of DNMT3a (A) and DNMT3b (B) in Airway Epithelial cells of LPG and Biomass - users rural women

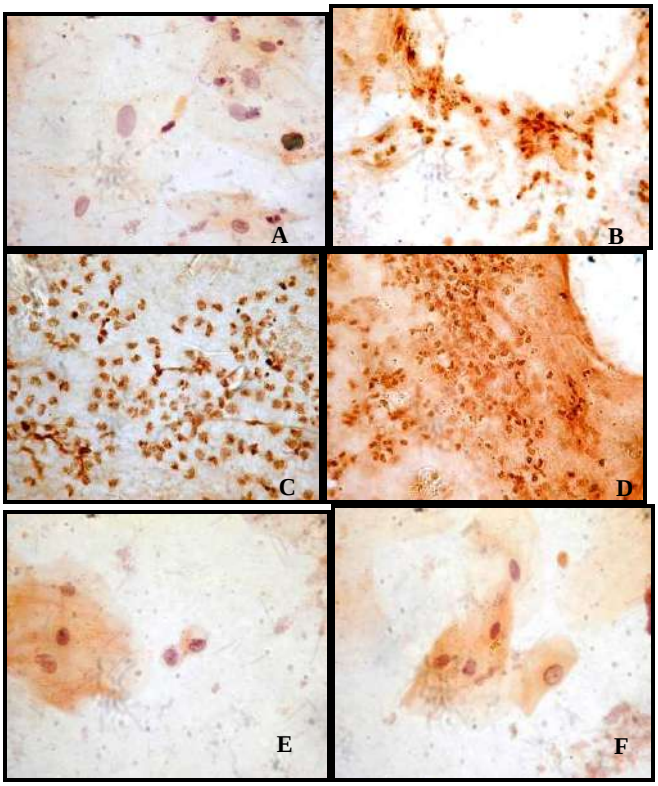

Plate 3 Immunocytochemical expression of DNMT3a – Airway Epithelial cells of LPG users showing very low expression (A); Airway Epithelial cells of Biomass users showing very high expression (B,C,D); Strong expression in nucleus of epithelial cell of Biomass users (E,F). The cell nuclei were counterstained with hematoxylin, original magnification, 1000x.

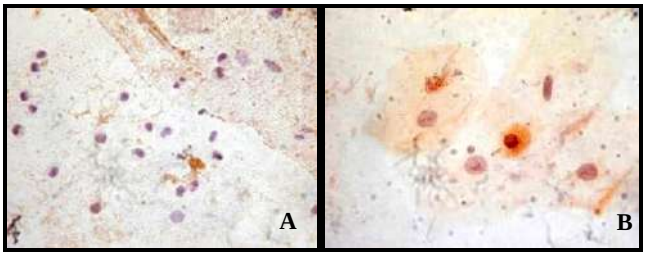

Plate 4 Immunocytochemical expression of DNMT3b – Airway Epithelial cells of LPG users showing low expression (A); Airway Epithelial cells of Biomass users showing nuclear expression (B). The cell nuclei were counterstained with hematoxylin, original magnification, 1000x.

Generation of ROS and Expression of DNMT3a

Generation of ROS due to chronic exposure of particulate matter in indoor air pollution, was well correlated with DNMT3a expression in Airway epithelial cells of Biomass user women. The value of Pearson Correlation was 0.714, $p<0.01$ was highly significant, Kendall's tau-b value was 0.654, $p<0.05$ was significant and Spearman ρ value was 0.651, $p<0.05$ was highly significant.

Depletion of SOD and Expression of DNMT3a

Depletion of SOD was negatively correlated with DNMT3a expression in airway epithelial cells of Biomass user women. The value of Pearson Correlation was -0.782, $p<0.01$ was significant, Kendall's tau-b value was -0.659, $p<0.05$ was significant and Spearman ρ value was -0.664, $p>0.05$ was not significant.

Association between ROS, SOD, t, t-MA and methylation protein expression

In univariate analysis, the reduction in the percentages of DNMT1 and DNMT3a-positive cells was positively associated with lower education and family income, increasing age and exposure years to biomass smoke, tobacco smoking habit of the husband, and cooking in a space adjacent to living room due to lack of separate kitchen. Even after controlling the influence of the confounders in multivariate logistic regression analysis, significant association was found between higher expression of DNMT1 and DNMT3a proteins and ROS generation, urinary t, t-MA and depletion of SOD (Table 5).

TABLE 5
Association between oxidative stress, expression of SOD, benzene exposure and lower expression of methylation proteins in airway epithelial cells of biomass-using women

Parameters	Higher expression of DNMT1 in cells	Higher expression of DNMT3a in cells
ROS generation	2.29 (1.46-4.59)	3.24 (1.83-5.61)
Depletion of SOD	2.04 (1.03-3.92)	1.74 (1.09-3.47)
t, t-MA in urine	1.71 (1.04-3.06)	1.75 (1.02-2.94)

Results are expressed as odds ratio with 95% confidence interval in parentheses after controlling education, family income, age, exposure years, husband's smoking habit and adjacent kitchen as potential confounders in multivariate logistic regression analysis.

IV. Discussion

Many families living in rural areas in India still use unprocessed solid biomass such as wood, coal, dung and agricultural residues as their main source of domestic energy for cooking, boiling water and heating. Biomass combustion releases a considerable amount of toxic pollutants, including carbon monoxide (CO), nitric oxides (NO_x), sulphur dioxide (SO_2), formaldehyde (HCHO), thousands of volatile organic compounds (VOC), particulate matters (PM) and polycyclic aromatic hydrocarbons (PAHs). Therefore, use of biomass as fuels causes very high level of indoor air pollution (IAP) in rural households. In these families usually it is the women who do most of the daily household cooking with these fuels and therefore receive the maximum exposure. Therefore, the cells that are present at the direct route of exposure of these harmful chemicals, such as cells of the nasopharynx, oral cavity, airways and the lungs in these women get severely affected and undergo harmful changes.

Little information is known about the effects of IAP generated PMs and/or carcinogens on epigenetic changes in airway epithelial cells. DNA methylation is one of the major epigenetic mechanisms exist in cells. DNA methyltransferases methylate cytosine residues in CpG sequences in promoter regions of different genes and thereby inhibit their expressions. Therefore, expressions of different genes can be controlled by regulating the stability and expressions of DNA methyltransferases. In view of this, the present study has been undertaken to evaluate the changes in the expression profiles of DNA methyltransferases [DNMT1, DNMT3a and DNMT3b] and SET7 in airway epithelial cells of biomass users exposed to IAP in contrast to LPG users.

The results show significantly high levels of DNMT1 and DNMT3a enzymes in airway epithelial cells of biomass-using rural women in comparison to LPG using women. Furthermore, the expression of another enzyme, SET7, an inhibitor of DNMT1, decreases significantly in airway epithelial cells of biomass-using rural women whereas its expression increases in LPG using control women. DNMT1 is involved in DNA methylation process and its elevated level in cells cause hypermethylation of DNA in airway cells. SET7 plays a key role in regulating the stability and function of DNMT1 by methylating Lys142 of DNMT1 and thereby leading to proteasomal degradation of DNMT1 (Estève et al 2009). Hence, reduced expression of SET7 enzyme in airway epithelial cells of biomass-using rural women corroborates well with the high expression of DNMT1 enzyme found in these cells of biomass users.

High levels of DNMT1 and DNMT3a enzymes in cells may lead to hypermethylation of the promoter regions of different genes resulting in transcriptional inactivation of these genes and thus leading to drastic changes in gene expression profiles of the cells.

Participants in this study, both LPG and biomass users were non-smokers and non-chewer of tobacco and betel nut. Therefore, increased expression of DNMT1 and reduced expression of SET7 in airway epithelial cells of biomass-using rural women cannot be explained by smoking or tobacco chewing habit. All participants are from same rural areas of West Bengal and in those rural areas effects of pollutants emitted from motor vehicles and industries are negligible due to absence of highway and industries within 5 km range of the study area. Here the LPG using control women as well as the biomass users are exposed in same ambient air, so ambient air pollution is not responsible for the changes in expressions of DNMT1, DNMT3a and SET7 enzymes. Both LPG and biomass users were apparently healthy and premenopausal women with very little variation and their lifestyle, food habit were more or less same. Therefore, it can be assumed that significant changes observed in the expressions of DNMT1, DNMT3a and SET7 enzymes in biomass users in contrast to LPG using women are not due to variations in physiological conditions.

The major difference between the control and the test groups was exposure to particulate matters generated from combustion of biomass fuels. One group of participants i.e. the biomass users were very much exposed to PM_{10} and $PM_{2.5}$ due to incomplete combustion of biomass fuels they used during cooking and these particulate matters, especially ultrafine particles which are abundant in biomass smoke, can produce ROS directly because of the presence of free radicals and oxidants adsorbed on their surface (Fubini et al., 2004). Thus, in the present investigation excess amount of ROS production in airway epithelial cells of biomass-using rural women can be explained as a result of higher exposure to particulate pollution due to incomplete combustion of biomass fuels they are using during household activities. Furthermore, reduced expression of antioxidant enzyme superoxide dismutase was recorded in indoor air pollution-exposed subjects indicating even greater oxidative stress that may lead to severe cellular damage. Finally, in multivariate logistic regression analysis, significant association was found between higher expression of DNMT1 and DNMT3a proteins and ROS generation, urinary t, t-MA [a biomarker of benzene exposure] and depletion of SOD in biomass using rural women.

In essence, our study has shown that exposure to particulate matter released into the breathing air during combustion of biomass fuel is associated with increase level of DNMT1 that can cause hypermethylation in sputum cells, and the action is probably mediated by oxidative stress. Participated women, same as rural women, became involved in cooking in their late teens when they started helping their mothers in the kitchen and after marriage they took the major role in cooking. As a result, they were more and more exposed in particulate matter during cooking with biomass fuel and the probability of epigenetic changes may increase. The consequences can be disastrous, if hypermethylation by DNMT1 occur in promoter region of necessary genes like DNA repair genes or may be in tumor suppressor gene then it should be lethal to health and increase the chances of cancer (White et al., 2015; Jacinto et al 2007; Lin et al 2010; Zhou et al 2012).

Recent *in vitro* and *in vivo* studies have demonstrated that exposure to PM significantly increased ROS production with enhanced expression of the DNA methyltransferase 1 (DNMT1) leading to hypermethylation of the p16 promoter. Furthermore, increased transcription of DNMT1 and methylation of the p16 promoter were inhibited by a mitochondrially targeted antioxidant and a JNK inhibitor (Soberanes et al., 2012). These previous results corroborate well with the current findings and provide a potential mechanism by which PM exposure increases the risk of lung cancer.

The present study may provide an epidemiological link to high incidence of lung cancer recorded among never-smokers and biomass user women in eastern India. In agreement with current study, a high incidence of lung cancer has been recorded among women in eastern India (where the present work was carried out) who were overwhelmingly never-smokers and biomass users (Nandakumar et al., 2004).

V. References

Aoki A et al. Enzymatic properties of de novo-type mouse DNA (cytosine-5) methyltransferases. Nucleic Acids Res 29:3506–3512, 2001.

Baccarelli A, Wright RO, Bollati V, et al. Rapid DNA methylation changes after exposure to traffic particles. Am J Respir Crit Care Med.; 179(7):572–578; 2009. [PubMed: 19136372]

Balachandran S, Meena BR, Khillare PS. Particle size distribution and its elemental composition in the ambient air of Delhi. Environ Int, 26, 49-54, 2000.

Bruce N, Perez-Padilla R, Albalak R. Indoor air pollution in developing countries: a major environmental and public health challenge for the new millennium. Bull. World Health Org. 78, 1078–1092, 2000.

Danielsen PH, Loft S, Kocbach A, et al. Oxidative damage to DNA and repair induced by Norwegian wood smoke particles in human A549 and THP-1 cell lines. Mutat. Res. 674, 116-122, 2009.

Ehrlich M, Gama-Sosa MA, Huang LH, et al. Amount and distribution of 5- ethylcytosine in human DNA from different types oftissues of cells. Nucleic Acids Res. Apr 24;10 (8):2709-21, 1982.

Erkilic, S., Coskun-Ozsarac, M.D., Kullu, S. Sputum cytology for the diagnosis of lung cancer. Acta Cytol. 47, 1023–1027, 2003.

Estève PO, Chang Y, Samaranayake M, et al. A methylation and phosphorylation switch between an adjacent lysine and serine determines human DNMT1 stability, Nat Struct Mol Biol. Jan;18(1):42-8. doi: 10.1038/nsmb.1939. Epub 2010 Dec 12, 2011.

Estève PO, et al. Regulation of DNMT1 stability through SET7-mediated lysine methylation in mammalian cells. Proc. Natl. Acad. Sci. USA;106:5076–5081, 2009. [PubMed: 19282482]

Estève PO, Chin HG, Benner J, et al. Regulation of DNMT1 stability through SET7- mediated lysine methylation in mammalian cells, Proc Natl Acad Sci U S A. Mar 31;106(13):5076-81. doi: 10.1073/pnas.0810362106. Epub 2009 Mar 12, 2009.

Fubini B, Fenoglio I, Ceschino R, et al. Relationship between the state of the surface of four commercial quartz flours and their biological activity in vitro and in vivo. Int. J. Hyg. Environ. Health 207: 89–104, 2004.

Gennaro DG, Dambruoso PR, Di Gilio A, et al. Discontinuous and Continuous Indoor Air Quality Monitoring in Homes with Fireplaces or Wood Stoves as Heating System, Int J Environ Res Public Health. Dec 24;13(1). pii: E78. doi: 10.3390/ijerph13010078, 2015.

Ghosh A, Ghosh S, Maiti GP, et al. SH3GL2 and CDKN2A/2B loci are independently altered in early dysplastic lesions of head and neck: correlation with HPV infection and tobacco habit. J Pathol, 217, 408–419, 2009.

Goll MG, Bestor TH. Eukaryotic cytosine methyltransferases. Annu Rev Biochem 74:481–514, 2005.

Jacinto FV, Esteller M. Mutator pathways unleashed by epigenetic silencing in human cancer. Mutagenesis. Jul; 22 (4):247–253, 2007.

Hou L, Zhang X, Zheng Y, et al. Altered methylation in tandem repeat element and elemental component levels in inhalable air particles, Abstract Environ Mol Mutagen. Apr;55(3):256-65. doi: 10.1002/em.21829. Epub 2013 Nov 23, 2014.

Kaneda M, et al. Essential role for de novo DNA methyltransferase Dnmt3a in paternal and maternal imprinting. Nature 429:900–903, 2004.

Li E. Chromatin modification and epigenetic reprogramming in mammalian development. Nat Rev Genet 3:662–673, 2002.

Lin RK, Hsieh YS, Lin P, et al. The tobacco-specific carcinogen NNK induces DNA methyltransferase 1accumulation and tumor suppressor gene hypermethylation in mice and lung cancer patients, J Clin Invest. Feb; 120 (2):521-32. doi: 10.1172/JCI40706. Epub 2010 Jan 19, 2010.

Lin RK, Wu CY, Chang JW, et al. Dysregulation of p53/Sp1 control leads to DNA methyltransferase-1 overexpression in lung cancer, Cancer Res, Jul 15;70(14):5807-17. doi: 10.1158/0008-5472.CAN-09-4161. Epub 2010 Jun 22, 2010.

Liu F, Zhou Y, Zhou D, et al. Whole DNA methylome profiling in lung cancer cells before and afterepithelial-to-mesenchymal transition, Diagn Pathol. Mar 20;9:66. doi: 10.1186/1746-1596-9-66; 2014.

Nandakumar A, Gupta PC, Gangadharan P, Visweswara RN. Development of an atlas of cancer in India. First all India report- 2001-2002. *National cancer registry programme (ICMR)*, Bangalore, India, pp 15–17, 2004.

Okano M, Bell DW, Haber DA, et al. DNA methyltransferases Dnmt3a and Dnmt3b are essential for de novo methylation and mammalian development. Cell 99:247–257, 1999.

Okano M, Xie S, Li E. Cloning and characterization of a family of novel mammalian DNA (cytosine-5) methyltransferases. Nat Genet 19:219–220, 1998.

Paoletti, F., Aldinucci, D., Mocali, A, et al. A sensitive spectrophotometric method for the determination of superoxide dismutase activity in tissue extracts. Analyt. Biochem. 154, 536–541, 1986.

Ramachandran TV, Kamakshi G, Shruti BV. Bioresource status in Karnataka.doi:10.1016/j.rser.2003.09.001.2Published by Elsevier Science Ltd., 2003.

Rehfuess E. Fuels for Life: Household Energy and Health. World Health Organization: Geneva, 2006.

Reik W, Lewis A. Co-evolution of X-chromosome inactivation and imprinting in mammals. Nat Rev Genet 6:403–410, 2005.

Rothe, G., Valet, G. Flow cytometric analysis of respiratory burst activity in phagocytes with hydroethidine and 2, 7-dichlorofluorescein. J. Leukoc. Biol. 47, 440–448, 1990.

Smith KR. Indoor air pollution in developing countries: recommendations for research. Indoor Air 12: 198–207, 2002.

Soberanes S, Gonzalez A, Urich D, et al. Particulate matter Air Pollution induces hypermethylation ofthe p16 promoter Via amitochondrial ROS-JNK-DNMT1 pathway, Sci Rep. 2012;2:275. doi: 10.1038/srep00275. Epub 2012 Feb 17, 2012.

Takeshita K, Suetake I, Yamashita E, et al. Structural insight into maintenance methylation by mouse DNA methyltransferase 1(Dnmt1). Proc Natl Acad Sci U S A. May 31; 108(22):9055-9. doi: 10.1073/pnas.1019629108. Epub 2011 Apr 25, 2011.

Tao MH, Zhou J, Rialdi AP, et al. Indoor air pollution from solid fuels and peripheral blood DNA methylation: findings from a population study in Warsaw, Poland, Environ Res. Oct;134:325-30. doi: 10.1016/j.envres.2014.08.017. Epub 2014 Sep 7, 2014.

Tarantini L, Bonzini M, Apostoli P, et al. Effects of particulate matter on genomic DNA methylation content and iNOS promoter methylation. Environ Health Perspect. 2009; 117(2):217–222. [PubMed: 19270791]

Wang T, Garcia JG, Zhang W., Epigenetic Regulation in Particulate Matter-Mediated Cardiopulmonary Toxicities: A Systems Biology Perspective, Curr Pharmacogenomics Person Med. 2012 Dec;10 (4):314-321.

White AJ, Chen J, Teitelbaum SL, et al. Sources of polycyclic aromatic hydrocarbons are associated with gene-specific promoter methylation in women with breast cancer, Environ Res. Dec 6; 145:93-100. doi: 10.1016/j.envres.2015.11.033. [Epub ahead of print], 2015.

Zhang J, Smith KR. Indoor air pollution: a global health concern. Br. Med. Bull. 68, 209–225, 2003.

Zhou ZH, Lei YX, Wang CX. Analysis of aberrant methylation in DNA repair genes during malignant transformation of human bronchial epithelial cells induced by cadmium. Toxicol Sci. Feb;125(2):412-7. doi: 10.1093/toxsci/kfr320. Epub 2011 Nov 23, 2012.

ASIAN JOURNAL OF PHARMACEUTICAL AND CLINICAL RESEARCH

INNOVARE ACADEMIC SCIENCES
Knowledge to Innovation

Vol 12, Issue 7, 2019

Online - 2455-3891
Print - 0974-2441

Research Article

GREEN SYNTHESIS OF SILVER NANOPARTICLES USING MANGROVE FRUIT POLYSACCHARIDE FOR BACTERIAL GROWTH INHIBITION

GAJENDRA NATH MAITY[1¥], JOY SARKAR[2,3¥], SOMANJANA KHATUA[2,4], SOUMITRA MONDAL[5], KRISHNENDU ACHARYA[2,6*]

[1]Department of Microbiology, Panskura Banamali College, Purba Medinipur, West Bengal, India. [2]Department of Botany, Molecular and Applied Mycology and Plant Pathology Laboratory, Centre of Advanced Study, University of Calcutta, Kolkata, West Bengal, India. [3]Department of Botany, Dinabandhu Andrews College, Kolkata, West Bengal, India. [4]Department of Botany, Krishnagar Government College, Krishnagar, Nadia, West Bengal, India. [5]Department of Chemistry, Panskura Banamali College, Panskura R.S., Purba Medinipur, West Bengal, India. [6]Center for Research in Nanoscience and Nanotechnology, Technology Campus, University of Calcutta, Kolkata, West Bengal, India. *Email: krish_paper@yahoo.com

[¥]These authors have contributed equally to this work.

Received: 21 April 2019, Revised and Accepted: 21 May 2019

ABSTRACT

Objective: The objective of this study was to find out the antibacterial activity of the silver nanoparticles (Ag-NPs) using a low-cost green synthesis approach for the formulation of Ag-NPs applying polysaccharide extracted from the fruits of a mangrove plant of Sundarban.

Methods: Fresh and healthy fruits were collected from *Ceriops decandra* plant. Sufficient amount of carbohydrates was extracted from those fruits and the physicochemical characterization of the polysaccharide was analyzed by gas chromatography–mass spectrometry and Fourier-transform infrared spectrophotometry. The respective polysaccharide was further applied to generate the Ag-NPs which were characterized by UV visible, dynamic light scattering, transmission electron microscopy, EDAX, and X-ray diffraction. The antibacterial efficacy of the Ag-NPs was also determined against some pathogenic Gram-negative and Gram-positive bacteria using the microdilution method.

Results: Glucose and galactose are the major monomers among the extracted carbohydrates. Various types of spectral analysis confirmed the formation of Ag-NPs. The green synthesized Ag-NPs have the average diameter of about 28 nm. Furthermore, the green synthesized Ag-NPs exhibited strong antibacterial activity against some pathogenic Gram-positive (*L. cytomonogenes, Bacillus Subtilis,* and *Staphylococcus aureus*) and Gram-negative (*Salmonella typhimurium* and *Escherichia coli*) bacteria.

Conclusion: The green synthesis of Ag-NPs using plant polysaccharide was an environment-friendly and cost-effective method as compared to the conventional physical and chemical synthesis techniques.

Keywords: Green synthesis, *Ceriops decandra*, Polysaccharide, Silver nanoparticle, Bacterial growth.

 DOI: http://dx.doi.org/10.22159/ajpcr.2019.v12i7.33681

INTRODUCTION

Since 1000 B.C., Ag has been applied for the treatment of burns, wounds, and several bacterial infections in the form of metallic silver, silver nitrate ($AgNO_3$), as well as silver sulfadiazine. However, the use of silver compounds in medicinal systems declined to a great extent after the introduction of penicillin during the 1940s [1]. However, over the recent past, the field of nanotechnology has introduced a new era of science which involves the creation of materials near-atomic scale with unique chemical, physical, thermal, and optical properties [2]. As a consequence, metallic silver made a remarkable comeback in the form of Ag-NP with powerful antimicrobial effects. Investigations have revealed that after exposure to bacteria, the nano-silver gets attached to the cell membrane, penetrates inside, and attacks respiratory chain that ultimately leads to cell death. In addition, these particles release silver ions inside cells which inhibit bacterial replication ability and cause the deactivation of proteins containing thiol groups [1,3]. This has unfolded novel strategies to use pure silver against a wide range of antibiotic-resistant microorganisms, and as a result, it has been adopted in many commercial products such as topical ointments, toothpaste, soap, and socks [4,5]. In addition, Ag-NP has also emerged up as a promising agent for wastewater purification system [6]. In recent work, the use of silver compounds as antimicrobial compounds against coliform bacteria found in wastewater has been reported [7].

So far, a number of techniques are available for Ag-NP synthesis; although most of them are expensive, complicated, and involve the use of hazardous chemicals [8]. Conversely, the biological techniques are considered as an alternative and advancement over other methods as it involves natural reagents such as sugars, biodegradable polymers, plant extracts, and microorganisms [4,9-19]. In this context, the mangrove plant, *Ceriops decandra* (Griff.) W. Theob., could be an effective alternative as it was scientifically proved to contain several bioactive components. It has been traditionally used as remedial measures for hepatitis, diabetes, wounds, ulcers, boils, angina, dysentery, and diarrhea [20-23]. Recent investigations have reported that *C. decandra* possesses antioxidant [24], antinociceptive [25], antidiabetic [26], and antimicrobial properties [27-30]. Thus, the present work was aimed for the synthesis of Ag-NP by a greener method using polysaccharide extracted from fruits of *C. decandra*, characterization of the particles, and assessment of antibacterial efficacy against some pathogenic microorganisms.

MATERIALS AND METHODS

Plant material

The plant parts of *C. decandra* (Griff.) W. Theob. were collected from the mangrove forest of Sundarban (21.9497° N, 89.1833° E) of the district South 24 Parganas, West Bengal, India. The respective plant specimen was self-identified and binomially jointly by the Department of Botany,

University of Calcutta, West Bengal - 700 019, India and Department of Botany, Dinabandhu Andrews College, Garia, Kolkata - 700 084, West Bengal, India. Voucher specimens were made from the collected specimen and further deposited at the Herbarium of the Botany Department, Dinabandhu Andrews College.

Isolation of polysaccharide from fruits of *C. decandra*

Fresh and healthy fruits were collected from the respective mangrove plant. To remove all noticeable unwanted as well as dust particles, the fruits were washed carefully with tap water followed by distilled water. After that, they were dried at room temperature and cut into small pieces. About 750 g of these finely incised fruits were steeped into 250 ml distilled water and boiled for 5 h. The resultant solution was maintained at 4°C for overnight and then filtered through nylon cloth. Polysaccharides were precipitated by adding five volume of absolute ethanol and incubated overnight at 4°C. After centrifugation at 8000 rpm for 10 min, the precipitate was again dissolved in distilled water and dialyzed through DEAE cellulose bag for 2 h to remove low-molecular-weight polysaccharides. Further, the lyophilized extract was subjected to Sephadex G-100 gel permeation column (50 cm × 1.5 cm) using water as eluent (flow rate: 0.5 ml/min). The eluate was collected (2 ml/tube) and carbohydrates were determined by the phenol-sulfuric acid method [31,32]. Finally, polysaccharide was pooled from test tube number 15–30 and vacuum freeze-dried.

Physicochemical characterization of polysaccharide

The total quantity of sugar was measured by the phenol-sulfuric acid method using glucose as standard. The protein content was estimated by Bradford using bovine serum albumin as a reference. Gallic acid was considered as a standard to quantify the total amount of phenolic compounds present in the polysaccharide using Folin–Ciocalteu reagent. All values were presented as a gram of standard equivalents per 100 g of dry polysaccharide [33]. For determination of monosaccharide composition, 2 mg polysaccharide was hydrolyzed with 2 M TFA at 100°C for 2 h in screw cap vial. TFA was eliminated by evaporation at 55°C under reduced pressure (Rota vapor R3, Buchi, Switzerland). About 50% ethanol (1 ml) was included in the vial to dissolve hydrolysate. The solution was centrifuged (5 min, 12,000 rpm) to remove non-hydrolyzed polysaccharide and further analyzed by gas chromatography–mass spectrometry (GC–MS) as described in our previous publication [34].

Green synthesis of silver nanoparticles (Ag-NPs)

$AgNO_3$ (>99.9% pure) was purchased from Merck, India. For Ag-NP synthesis, 20 ml of 0.5 mg/ml of isolated polysaccharide was mixed with 20 ml of 1 mM $AgNO_3$ solution and stirred with a magnetic stirrer for 90 min at room temperature. Change of color from pale yellow to brown specified the production of the Ag-NP due to the reaction of polysaccharide with the silver metal ion. Simultaneously, both the positive control (polysaccharide solution without any addition of $AgNO_3$) and the negative control (only the $AgNO_3$ solution) sets were kept under the same conditions, in which the reaction mixture was maintained.

Characterization of synthesized Ag-NPs

Generation of Ag-NP was established by UV-visible (UV-Vis) spectrophotometer (Hitachi 330 spectrophotometer) with plasmon peaks at different regions of the spectral range 200–900 nm which corresponded to different signature marks for the production of different nanoparticles (NPs), respectively. Particle size was determined using Zen 1600 Malvern nanosize particle analyzer ranging between 0.6 nm and 6.0 µm. For X-ray diffraction (XRD) measurement of the reaction mixture, the spectra were recorded in a PW 3040/60 PANalytical X-ray Diffractometer (Cu Kα radiation, λ 1.54443) running at 45 kV and 30 mA. The diffracted intensities were documented from 35° to 90° 2 θ angles. Energy-dispersive X-ray (EDX) analysis of the dried sample of Ag-NP was carried out by the Hitachi S 3400N instrument. For Fourier transform infrared (FTIR) analysis, the dried Ag-NP was mixed with potassium bromide (KBr) at a ratio of 1:100. Furthermore, the prepared pellet was observed using a diffuse reflectance accessory in the spectral range between 4000 and 400/cm with a Shimadzu 8400S FTIR spectrophotometer. In addition, the synthesized particles were studied and visualized by transmission electron microscopy (TEM) using Tecnai G2 spirit Biotwin instrument (FP 5018/40), operating at around 80 kV accelerating voltage.

Analysis of the effect of synthesized Ag-NPs on some pathogenic bacteria

Bacillus subtilis ATCC® 6633™ (MTCC 736), *Listeria monocytogenes* ATCC® 19111™ (MTCC 657), *Staphylococcus aureus* ATCC® 700699™, *Escherichia coli* ATCC® 25922™, and *Salmonella typhimurium* ATCC® 23564™ (MTCC 98) were utilized for the experiment. The antibacterial effect was estimated by determining minimum inhibitory concentration (MIC) values according to the microdilution method [35]. The six investigating bacteria were cultured freshly and 1 × 10^5 CFU/ml concentrated dilutions were prepared separately. Reactions were performed in 96-well plates consisting of 200 µl of NB, 20 µl of inoculum, and different dilutions of NPs. Following incubation for 1 day at 37°C, 40 µl of INT dye (0.2 mg/ml) was added and incubated for another 30 min. The concentration that inhibited 50% growth of bacteria as compared with positive control was calculated as MIC value. Streptomycin was used as a standard drug.

RESULTS AND DISCUSSION

Physicochemical characterization of isolated polysaccharide

The extractive yield of polysaccharide from fruits of *C. decandra* was 0.002% of dry matter. Total carbohydrate and protein content of the polysaccharide was 53.06 ± 2.73 g/100 g and 5.04 ± 0.31 g/100 g of dry polysaccharide, respectively. A very negligible amount of phenolics was detected (0.005 ± 0.001 g/100 g of dry polysaccharide). Further, the composition of molecular components was determined by GC–MS where two monosaccharides such as glucose as well as galactose were detected in a molar ratio of 3.64:1 (Fig. 1).

Green synthesis of Ag-NP

The characteristic brown color of the reaction mixture, a signature mark for the production of Ag-NP in the solution, arose due to the collective vibration of free electrons of Ag-NP in resonance with a light wave. The surface plasmon resonance absorption band of the reaction solution in the visible spectral region of electromagnetic radiation further confirmed the claim of the formation of Ag-NP [36]. The synthesis of Ag-NP by reduction of the metal ions during exposure of 20 ml of 0.5 mg/ml of the polysaccharide isolated from *C. decandra* into 20 ml of 1 mM $AgNO_3$ solution detected by brown color formation (Fig. 2).

UV/Vis spectrophotometric analysis of biosynthesized Ag-NP

The reduction of silver from Ag + ions to Ag^0 state was subjected to spectral analysis. The surface plasmon band of the reaction mixture

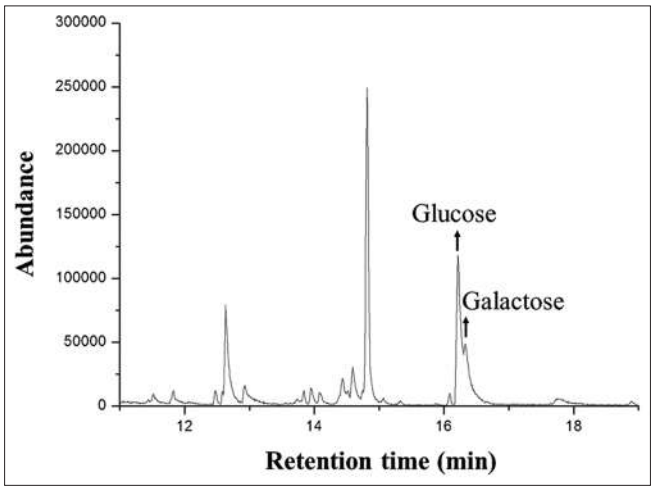

Fig. 1: Gas chromatography–mass spectrometry of polysaccharide extracted from fruits of *Ceriops decandra*

was obtained in the visible region at 426 nm, which was specific for Ag-NP (Fig. 3). Furthermore, this spectral analysis suggested that the NPs were well dispersed in the solution as well as there was not any type of indication for the aggregation of the NPs.

Analysis of particle size of the Ag-NP by dynamic light scattering (DLS) analyzer

The DLS measurement was performed to measure the particle size of the Ag-NP (Fig. 4). Observations revealed the homogeneous nature of the dispersed Ag-NP, with a size distribution between 20 and 58 nm.

Analyses of the crystallinity of Ag-NP by XRD

Crystalline nature of the NPs was confirmed by the XRD analysis. XRD measurement often proves to be a useful analytical tool for newly formed compounds and their phases. The XRD spectra of Ag-NP displayed four identical appearing at 2 θ = 38°, 44°, 64°, and 78° conforming to the (111), (200), (220), and (311) facets of silver, respectively (JCPDS card file no. 04-0783) [10] (Fig. 5).

Investigation of elemental compositions of synthesized Ag-NP by EDX

The analysis of the elemental composition of the green synthesized Ag-NP was made by EDX. As presented in Fig. 6, a sharp wide peak characteristic of silver was observed around 3–4 keV. The occurrence of a sturdy signal from Ag atoms (81.54%) specified that the NPs were solely made by silver. Other EDX peaks such as U and O also suggested that they were mixed precipitates of the polysaccharide and silver salt. XRD analysis also agreed with the generation of nanosilver.

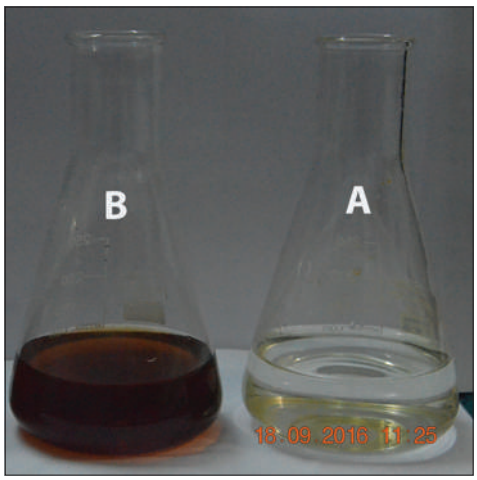

Fig. 2: (A) Only silver nitrate ($AgNO_3$) solution and (B) color change of the reaction mixture of the polysaccharide with $AgNO_3$ solution after 24 h

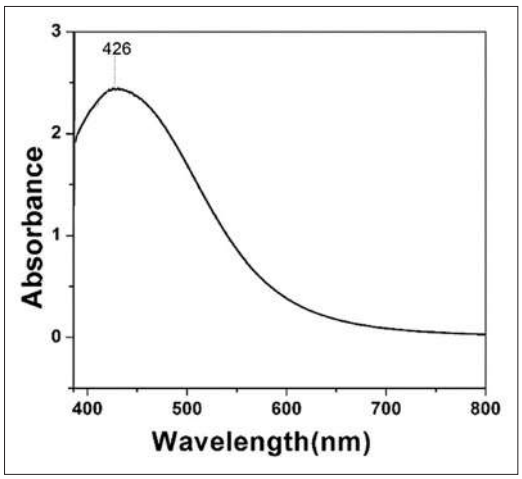

Fig. 3: UV-visible spectrum of the synthesized silver nanoparticles

FTIR analysis of isolated polysaccharide and biosynthesized Ag-NP

Fig. 7 shows the FTIR absorption spectra for the polysaccharide and the synthesized Ag-NP, respectively. Both the spectra exhibited the occurrence of bands around 3430/cm, 2,910/cm, 1600/cm, 1450/cm, and 1070/cm signifying the O-H stretching, aldehydic C-H stretching, C = C group, -COO stretching, and -C-O-C- stretching, respectively [37-40]. These peaks designated the existence of proteins and other organic

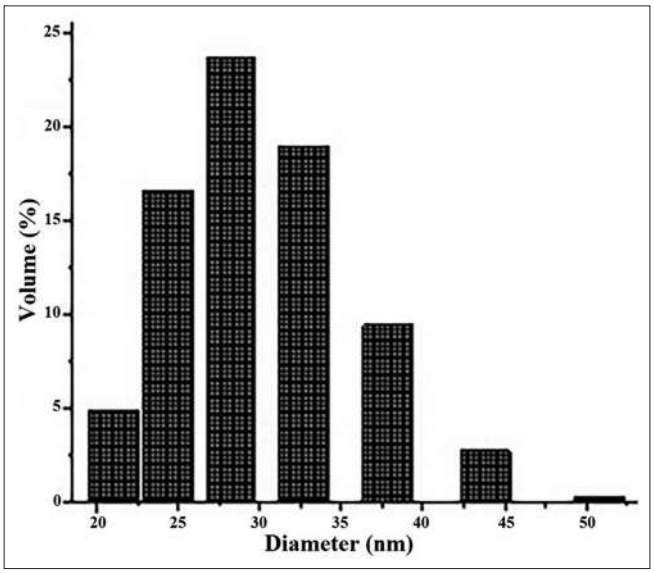

Fig. 4: The particle size distribution of bioreduced silver nanoparticles

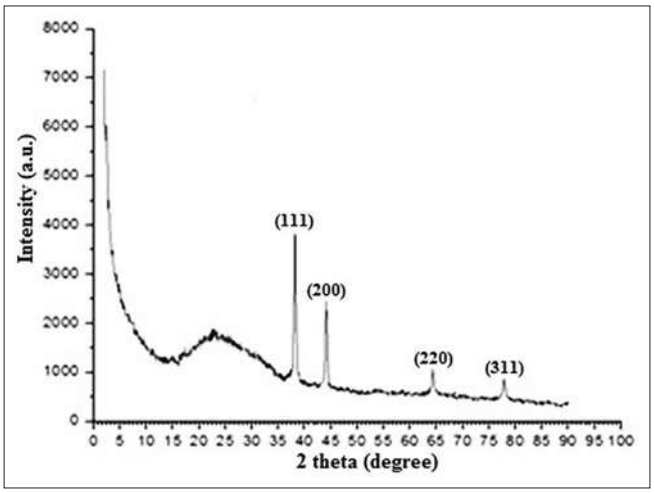

Fig. 5: Representative X-ray diffraction pattern of silver nanoparticles

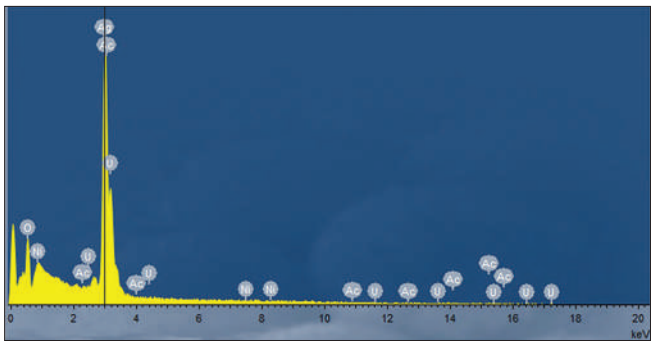

Fig. 6: Energy-dispersive X-ray spectrum of silver nanoparticles

residues. Bands at around 1650, 1550, and 1250/cm indicated the amide I, II, and III linkages between the amino acid residues in proteins, which provided an indication in infrared regions of the electromagnetic spectrum [38,39,41]. Symmetric and antisymmetric modes of C–H stretching were observed in the spectral region around 2920 and 2850/cm, respectively [38]. The bands observed in the 500–750/cm spectral region indicated the occurrence of R-CH group [42].

Transmission electron microscopic study of the Ag-NP

Fig. 8a displays the TEM image of the Ag-NP with a diverse range of their sizes which were produced after the bioreduction of the $AgNO_3$ solution by the polysaccharides. These findings inferred that the synthesized Ag-NPs were homogeneous and monodisperse in nature and most of them were spherical in shape. The diameters of these Ag-NPs were in the range of 20–45 nm. The average diameter was found to be 28 ± 4 nm. It was thought-provoking to note that majority of the NPs in the TEM image were not in physical contact but were separated by a fairly undeviating interparticle distance. Due to the developmental course of the sample preparation, the data obtained from the TEM and DLS measurements were quite different from each other. Although the particles were measured in the dry state in the TEM image, the actual diameter of the NPs was found in this analysis, whereas the size measured by the DLS experiment was in the hydrated state of the NPs. Therefore, the NPs had a higher hydrodynamic volume due to solvent effects in the hydrated state. The bright circular spots in the selected area electron diffraction pattern further confirmed the single crystalline nature of the Ag-NP (Fig. 8b) [43].

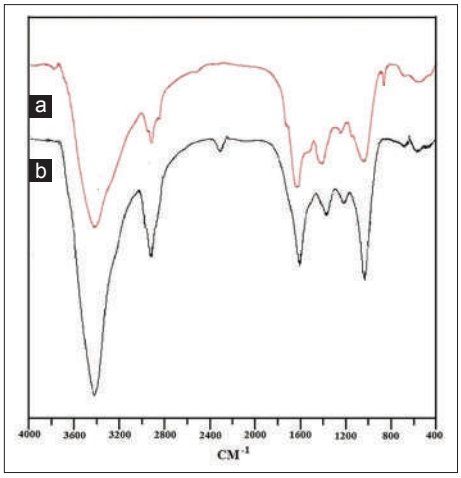

Fig. 7: Fourier-transform infrared absorption spectra of (a) isolated polysaccharide and (b) synthesized silver nanoparticles

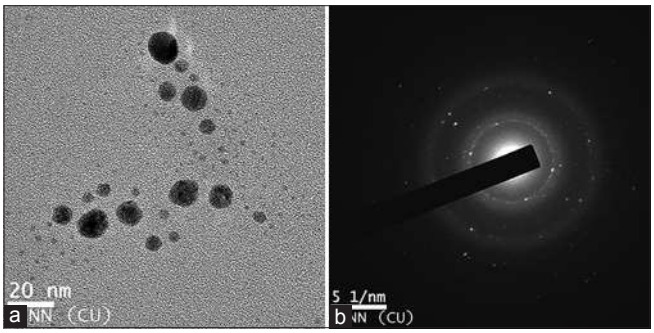

Fig. 8: (a) Transmission electron microscopic image of silver nanoparticles (Ag-NPs) (b) selected area electron diffraction patterns of crystalline Ag-NPs

Table 1: Antibacterial activity of synthesized silver nanoparticles as determined by minimum inhibitory concentration value (µg/ml) (mean±standard deviation; n=3)

Type of bacteria	Name of bacteria	Silver nanoparticles	Streptomycin
Gram-positive	*Listeria monocytogenes*	62.77±11.74	4.68±0.17
	Staphylococcus aureus	179.24±29.38	6.29±0.16
	Bacillus subtilis	174.05±33.56	5.61±0.01
Gram-negative	*Escherichia coli*	153.02±46.18	5.41±0.11
	Salmonella typhimurium	123.42±10.69	5.09±0.03

Streptomycin was considered as a positive control

Analysis of the effect of polysaccharide-based Ag-NP on some pathogenic bacteria

The antibacterial activity of biosynthesized Ag-NP was observed against both Gram-negative and Gram-positive bacteria using the microdilution method. As presented in Table 1, the growth of all experimental strains was found to be affected in the presence of the NPs as compared to the negative control. In the case of *L. monocytogenes*, a Gram-positive bacterium, introduction of 50 µg/ml of polysaccharide Ag-NP caused 47.93 ± 5.98% of reduction of bacterial density. Interestingly, growth of all examined Gram-negative bacteria was also detected to be inhibited in the presence of similar doses of the nanomaterials. Treatment of 50 µg/ml of synthesized nano inhibited 10.11 ± 0.18 and 28.17 ± 5.97% in the case of *E. coli* and *S. typhimurium,* respectively. These observations suggested strong antibacterial potentiality of synthesized Ag-NP.

CONCLUSION

The present study described biosynthesis of stable Ag-NP using polysaccharide from fruits of *C. decandra* plant. The production of biosynthesized nanomaterial was established by UV-Vis, XRD, and FTIR. The green synthesized Ag-NP presented strong antibacterial activity against some pathogenic Gram-positive (*L. cytomonogenes, B. subtilis,* and *S. aureus*) and Gram-negative (*S. typhimurium* and *E. coli*) bacteria. Thus, the green synthesis of Ag-NP using plant polysaccharide was an environment-friendly and cost-effective method as compared to the conventional physical and chemical synthesis techniques.

AUTHORS' CONTRIBUTIONS

Gajendra Nath Maity, Joy Sarkar, Somanjana Khatua, Soumitra Mondal, and Krishnendu Acharya have equally contributed to the construction and editing of the manuscript.

CONFLICTS OF INTEREST

The authors confirm that they have no conflicts of interest.

REFERENCES

1. Rai M, Yadav A, Gade A. Silver nanoparticles as a new generation of antimicrobials. Biotechnol Adv 2009;27:76-83.
2. Mohammadlou M, Maghsoudi H, Jafarizadeh-Malmiri H. A review on green silver nanoparticles based on plants: Synthesis, potential applications and eco-friendly approach. Int Food Res J 2016;23:446-63.
3. Ydollahi M, Ahari H, Anvar AA. Antibacterial activity of silver-nanoparticles against *Staphylococcus aureus*. Afr J Microbiol Res 2016;10:850-5.
4. Ahmed S, Ahmad M, Swami BL, Ikram S. A review on plants extract mediated synthesis of silver nanoparticles for antimicrobial applications: A green expertise. J Adv Res 2016;7:17-28.
5. Zhao HQ, Aisa HA, Rasulov B, Rustamova N, Yili AR. Synthesis of Ag-NP on the basis of low and high molar mass exopolysaccharides of *Bradyrhizobium japonicum* 36 and its antimicrobial activity against some pathogens. Folia Microbiol 2016;61:283-93.
6. Bora T, Dutta J. Applications of nanotechnology in wastewater treatment – a review. J Nanosci Nanotechnol 2014;14:613-26.
7. Jain P, Pradeep T. Potential of silver nanoparticle-coated polyurethane foam as an antibacterial water filter. Biotechnol Bioeng 2005;90:59-63.

8. Rajeshkumar SR. Synthesis of Ag-NP using fresh bark of *Pongamia pinnata* and characterization of its antibacterial activity against gram positive and gram negative pathogens. Resour Technol 2016;2:30-5.
9. Railean-Plugaru V, Pomastowski P, Wypij M, Szultka-Mlynska M, Rafinska K, Golinska P, *et al.* Study of silver nanoparticles synthesized by acidophilic strain of actinobacteria isolated from the of *Picea sitchensis* forest soil. J Appl Microbiol 2016;120:1250-63.
10. Saha S, Sarkar J, Chattopadhyay D, Patra S, Chakraborty A, Acharya K, *et al*. Production of silver nanoparticles by a phytopathogenic fungus *Bipolaris nodulosa* and its antimicrobial activity. Dig J Nanomater Biostruct 2010;5:887-95.
11. Sarkar J, Dey P, Saha S, Acharya K. Mycosynthesis of selenium nanoparticles. Micro Nano Lett 2011;6:599-602.
12. Sarkar J, Ray S, Chattopadhyay D, Laskar A, Acharya K. Mycogenesis of gold nanoparticles using a phytopathogen *Alternaria alternata*. Bioprocess Biosyst Eng 2012;35:637-43.
13. Sarkar J, Ghosh M, Mukherjee A, Chattopadhyay D, Acharya K. Biosynthesis and safety evaluation of ZnO nanoparticles. Bioprocess Biosyst Eng 2014;37:165-71.
14. Sarkar J, Acharya K. *Alternaria alternata* culture filtrate mediated bioreduction of chloroplatinate to platinum nanoparticles. Synth React Inorg Met Nano Metal Chem 2017;47:365-9.
15. Sarkar J, Mollick MM, Chattopadhyay D, Acharya K. An eco-friendly route of γ-Fe2O3 nanoparticles formation and investigation of the mechanical properties of the HPMC-γ-Fe2O3 nanocomposites. Bioprocess Biosyst Eng 2017;40:351-9.
16. Dasgupta A, Sarkar J, Ghosh M, Bhattacharya A, Mukherjee A, Chattopadhyay D, *et al*. Green conversion of graphene oxide to graphene nanosheets and its biosafety study. PLoS One 2017;12:e0171607.
17. Acharya K, Sarkar J. Bryo-synthesis of gold nanoparticles. Int J Pharm Sci Rev Res 2014;29:82-6.
18. Kanchana R, Zantye P. Plant-mediated synthesis of silver nanoparticles with diverse applications. Asian J Pharm Clin Res 2016;9:124-8.
19. Joshi SC, Kaushik U, Upadhyaya A, Sharma P. Green technology mediated synthesis of silver nanoparticles from *Momordica charantia* fruit extract and its bactericidal activity. Asian J Pharm Clin Res 2017;10:196.
20. Watt J, Breyer-Brandwijk M. The Medicinal and Poisonous Plants of Southern and Eastern Africa. 2nd ed. Edinburgh and London: E & S. Livingstone Ltd.; 1962.
21. Kathiresan K, Ramanathan T. Medicinal Plants of Parangipettai Coast, Monograph. Parangipettai, India: Annamalai University; 1997.
22. Bandaranayake WM. Traditional and medicinal uses of mangroves. Mangroves Salt Marshes 1998;2:133-48.
23. Duke J, Wain K. Computer Index with more than 85,000 Entries. In: Medicinal Plants of the World. Vol. 3. Beltsville, Maryland: Plants Genetics and Germplasm Institute, Agriculture Research Service; 1981.
24. Banerjee D, Chakrabarti S, Hazra AK, Banerjee S, Ray J, Mukherjee B. Antioxidant activity and total phenolics of some mangroves in Sundarbans. Afr J Biotechnol 2008;7:805-10.
25. Uddin SJ, Shilpi JA, Barua J, Rouf R. Antinociceptive activity of *Ceriops decandra* leaf and pneumatophore. Fitoterapia 2005;76:261-3.
26. Nabeel MA, Kathiresan K, Manivannan S. Antidiabetic activity of the mangrove species *Ceriops decandra* in alloxan-induced diabetic rats. J Diabetes 2010;2:97-103.
27. Sakagami H, Kashimata M, Toguchi M, Satoh K, Odanaka Y, Ida Y, *et al.* Radical modulation activity of lignins from a mangrove plant, *Ceriops decandra* (Griff.) Ding Hou. *In vivo* 1998;12:327-32.
28. Vadlapudi V, Naidu K. *In vitro* antimicrobial activity *Ceriops decandra* against selected aquatic, human and phytopathogens. Int J Chem Tech Res 2009;1:1236-8.
29. Ravikumar S, Gnanadesigan M, Suganthi P, Ramalakshmi A. Antibacterial potential of chosen mangrove plants against isolated urinary tract infectious bacterial pathogens. Int J Med Med Sci 2010;2:94-9.
30. Chandrasekaran M, Kannathasan K, Venkatesalu V, Prabhakar K. Antibacterial activity of some salt marsh halophytes and mangrove plants against methicillin resistant *Staphylococcus aureus*. World J Microbiol Biotechnol 2009;25:155-60.
31. Mecozzi M. Estimation of total carbohydrate amount in environmental samples by the phenol-sulphuric acid method assisted by multivariate calibration. Chemometr Intell Lab Syst 2005;79:84-90.
32. Masuko T, Minami A, Iwasaki N, Majima T, Nishimura S, Lee YC, *et al.* Carbohydrate analysis by a phenol-sulfuric acid method in microplate format. Anal Biochem 2005;339:69-72.
33. Saha S, Khatua S, Paloi S, Acharya K. Antioxidant and nitric oxide synthase activation properties of water soluble polysaccharides from *Pleurotus florida*. Int J Green Pharm 2013;7:182-8.
34. Khatua S, Acharya K. Influence of extraction parameters on physico-chemical characters and antioxidant activity of water soluble polysaccharides from *Macrocybe gigantea* (Massee) Pegler & Lodge. J Food Sci Technol 2016;53:1878-88.
35. Stojković D, Reis FS, Ferreira IC, Barros L, Glamočlija J, Ćirić A. *Tirmania pinoyi*: Chemical composition, *in vitro* antioxidant and antibacterial activities and in situ control of *Staphylococcus aureus* in chicken soup. Food Res Int 2013;53:56-62.
36. Sarkar J, Chattopadhyay D, Patra S, Deo SS, Sinha S, Ghosh M. *Alternaria alternata* mediated synthesis of protein capped silver nanoparticles and their genotoxic activity. Dig J Nanomater Biostruct 2011;6:563-73.
37. Jin L, Bai R. Mechanisms of lead adsorption on chitosan/PVA hydrogel beads. Langmuir 2002;18:9765-70.
38. Sanghi R, Verma P. Biomimetic synthesis and characterisation of protein capped silver nanoparticles. Bioresour Technol 2009;100:501-4.
39. Sathyavathi R, Krishna MB, Rao SV, Saritha R, Rao DN. Biosynthesis of silver nanoparticles using *Coriandrum sativum* leaf extract and their application in nonlinear optics. Adv Sci Lett 2010;3:1-6.
40. Socrates G. Infrared and Raman Characteristic Group Frequencies. 3rd ed. Wiley Publisher; 2004.
41. Barth A. Infrared spectroscopy of proteins. Biochim Biophys Acta 2007;1767:1073-101.
42. Singh AK, Talat M, Singh DP, Srivastava ON. Biosynthesis of gold and silver nanoparticles by natural precursor clove and their functionalization with amine group. J Nanopart Res 2010;12:1667-75.
43. Mollick MM, Bhowmick B, Maity D, Mondal D, Roy I, Sarkar J, *et al*. Green synthesis of silver nanoparticles-based nanofluids and investigation of their antimicrobial activities. Microfluid Nanofluidics 2014;16:541-51.

Source details

Feedback > Compare sources >

International Journal of Nano and Biomaterials

Scopus coverage years: from 2007 to 2012, from 2014 to 2021, 2023

Publisher: Inderscience Publishers

ISSN: 1752-8933 E-ISSN: 1752-8941

Subject area: Chemistry: Physical and Theoretical Chemistry | Physics and Astronomy: Atomic and Molecular Physics, and Optics | Engineering: Biomedical Engineering | Materials Science: Biomaterials

Source type: Journal

View all documents > | Set document alert | Save to source list

CiteScore 2022
0.9

SJR 2022
0.126

SNIP 2022
0.180

CiteScore | CiteScore rank & trend | Scopus content coverage

Digest Journal of Nanomaterials and Biostructures Vol. 14, No. 2, April - June 2019, p. 479 - 490

A GREEN APPROACH FOR THE SYNTHESIS OF ANTIMICROBIAL BIO-SURFACTANT SILVER NANOPARTICLES BY USING A FERN

A. CHATTERJEE[a], S. KHATUA[c,d], K. ACHARYA[c,e], J. SARKAR[b,c,*]
[a]*Department of Botany, University of Kalyani, Kalyani, Nadia, West Bengal, India, Pin—741235.*
[b]*Department of Botany, Dinabandhu Andrews College, Garia, Kolkata, West Bengal, India, Pin—700084.*
[c]*Molecular and Applied Mycology and Plant Pathology Laboratory, Centre of Advanced Study, Department of Botany, University of Calcutta, Kolkata, West Bengal, India, Pin—700019.*
[d]*Department of Botany, Krishnagar Govt. College, Krishnagar, Nadia, West Bengal, India, Pin-741101.*
[e]*Center for Research in Nanoscience & Nanotechnology, Technology Campus, University of Calcutta, Kolkata, West Bengal, India, Pin—700098.*

Advancement of an environment-friendly, trustworthy, and speedy route for the generation of Ag-NP using natural system is an essential urge in nanotechnology. This study accounts for the efficacy of liquid extract of *Adiantum lunulatum* Burm. f. for the synthesis of Ag-NP. This is the first attempt of introducing the biosynthesis mechanism of Ag-NP using the extract of this plant along with the antimicrobial evaluation of the Ag-NP. All the detailed features of the fabricated nanoparticles were well documented by UV-Vis, DLS, Zeta Potential, FTIR, EDX, XRD, and TEM. The mean diameter of Ag-NP was about 28±2 nm. Antibacterial proficiency of Ag-NP was also determined against various gram natured pathogenic bacteria.

(Received April 4, 2019; Accepted June 14, 2019)

Keywords: Adiantum lunulatum, Biosynthesis, Silver Nanoparticles, Antimicrobial

1. Introduction

Nanotechnology is an imperative tool for the expansion of science in the present era. It is the competence to produce and design structure at nano-metric range [1] and a stimulus for the expansion of several other fields like physiochemical [2], optical [3], electrical [4], sensing [5], catalysis [6], photochemical [7], etc. due their exclusive feature of sizeable surface area to volume ratio.

Silver is one of the safe inorganic elements which is projected as “next-gen” antimicrobial agent [8]. As consequences metallic silver made an incredible response in the form of Ag-NP. This has unfolded novel strategies to use metallic silver. Ag-NP has extensive angles of application concerning bio-labeling [9], [10], antibiotics [11], antibacterial [12], [13], antifouling & anti-parasitic [14] properties, drug delivery mechanisms [15] etc. They are also highly effectual in triggering of inflammation & apoptosis than bulk silver material. It also acts as a catalyst for the reduction of dye like methylene blue [16], enhances radiation therapy [17], used in ESR dosimetry [18], glyconano sensors for diseases diagnosis [19]. But still, there are many lacunas regarding the appliance of Ag-NP on the evaluation of the risk of human health and environment and human health [20].

Various protocols are known to date for developing metallic nanoparticles. They are mainly parted into two approaches- (i) top-down and (ii) bottom up [21]. The former one defines to be a reduction in the size of bulk material by means of mechanical methods, and later one is a

*Corresponding author: jsarkar80@gmail.com

process of assembling smaller particle into a larger entity. Production of nanoparticles by chemical means is one such example [22]. However, the nanoparticles synthesized via chemical means are hazardous as for the utilization of various toxic and corrosive chemicals during the production process [23]. Moreover, the process is not so cost-effective [11]. Therefore, an urge to develop an eco-friendly and a non-hazardous route to manufacture nanoparticles which can meet both cost & energy demands [24] has become an urgent need.

Consequently, the biological performances are considered as an alternative and advancement over former approaches as it involves natural compounds such as sugars, biodegradable polymers, plants extracts [3], [25]–[28]. Metallic nanoparticles manufactured by fungi [11], [29], [30], bacteria [31], algae [27] and plants [26], [32] are well known. Furthermore, the rate of plant synthesized nanoparticles is much faster [26], [32], stable [24] and are highly mono-dispersive [33] in relation to supplementary biological methods.

Among cryptograms, the use of algae [24] & bryophytes [34] to fabricate nanoparticles are quite popular. Unlike that of pteridophytes (fern & fern allies) for forging of nanoparticles are less investigated. Till date only few of the pteridophytes like *Adiantum capillus-veneris* [35], *Adiantum caudatum* [36], *Adiantum philippense* [37], [38], *Azolla microphylla* [39], [40], *Pteris tripartita* [41], *Asplenium scolopendrium* [42], *Actinopteris radiata* [43], *Christella dentata*, *Cyclosorus interruptus*, *Nephrolepis cordifolia* [44] have been used so far.

Adiantum lunulatum Burm. f. is recognized for it's antioxidant [45], antimicrobial [46] & medicinal properties like anti-hyperglycemic action [47] against influenza and tuberculosis [48]. The plant is enriched with carbohydrates, terpenoids, phenols, and flavonoids [45], [49], [50]. These versatile features of this plant made it our choice in the first place to fulfill our goals. Thus, this current study was designed with an intention of synthesis of Ag-NP by a greener route by using the fern *Adiantum lunulatum* and assessment of the antibacterial nature of these Ag-NP against various pathogenic microorganisms.

2. Experimental

2.1. Chemicals

The chemical silver nitrate ($AgNO_3$) was procured from Sigma, St. Louis, MO, USA.

2.2. Plant material

The plant was collected from different areas of West Bengal like Kalyani (22.9751° N, 88.4345° E) of the district Nadia, West Bengal, Kalingpong district (27.066668° N, 88.466667° E) and Rajpur-Sonarpur Municipality area (22.4491° N, 88.3915° E) of the district South 24 Parganas, West Bengal, India. The respective plant specimen was self-identified and binomially jointly by Pteridology & Paleobotany Lab, Department of Botany, University of Kalyani, Kalyani, Nadia, West Bengal, India, Pin-741235 and Department of Botany, Dinabandhu Andrews College, Garia, Kolkata, West Bengal, India, Pin-700084. Voucher specimens were made from the collected specimen and further deposited both at the Herbarium of the Botany Department, University of Kalyani as well as Herbarium of the Botany Department, Dinabandhu Andrews College.

2.3. Preparation of plant extract

At first, the whole plant was washed entirely by tap water and distilled water respectively. The superficial water was dried from the plant body by proper desiccation. Then, 5 gm of that desiccated plant material was crushed in mortar & pestle into a paste. After that hundred ml of distilled water was mixed to that paste [37]. Filtration of the crude solution was done thrice by Whatman filter paper no.1. Finally, the filtrate was collected all together for future reference.

2.4. Synthesis of Ag-NP

Hundred ml of 1mM $AgNO_3$ solution was mixed to the liquid extract (1:5v/v) and stirred constantly for 1 hour [11], [13]. Both, positive (plant extract) and negative control ($AgNO_3$ solution only) were conserved under similar environments.

Centrifugation was followed to separate out the Ag-NP (at 12000 g for 15 min), and the settled nanoparticles were washed (three times) in deionized water. The purified Ag-NP were re-suspended in deionized water and ultra-sonicated by Piezo-u-sonic ultrasonic cleaner (Pus-60w) and kept at normal room temperature (37°C) [30].

2.5. UV–Vis absorption spectroscopy analysis

Adiantum lunulatum mediated biosynthesized nanoparticles had been observed under Hitachi 330 Spectrophotometer with plasmon peaks at varied regions of the spectral range 300 to 700 nm which resembled different signature marks for the production of different nanoparticles respectively [51], [52]. Deionized water was selected for reference.

2.6. Particle size measurement by DLS experiment

Particle size was found out by using Zen 1600 Malvern nanosize particle analyzer ranging between 0.6 nm and 6.0 μm under such conditions particle having an absorption coefficient of 0.01, particle refractive index 1.590, water refractive index 1.33, viscosity –cP, Temperature-25°C and a broad calculation model for irregular particles. About 10−15 measurement cycles of 10 s each was taken in account. The acquired data were averaged by the preloaded software (DTS, version 5.00 from Malvern) of the respective instrument [53].

2.7. Zeta potential measurement

Using Beckman Coulter DelsaTM Nano Particle Analyser (USA) zeta potential (Charge distribution) of the nanoparticles was investigated by revealing the solution with He–Ne laser in a sample cell (658 nm). Using Phase Analysis Light Scattering mode measurements were taken with an Ag electrode [54].

2.8. EDS analysis

A small amount of sample was taken in glass slide creating a reedy layer of the sample. An additional sample was blotted off and then the sample was permitted to dry for overnight [55]. Hitachi S 3400N instrument was the automatic choice for us to carry out the analysis of the samples. The spectra were recorded for future analysis.

2.9. XRD- measurement

The crystallinity of forged Ag-NP was confirmed and determined by XRD analysis. The XRD sample was all set on a microscopic glass slide by depositing the centrifuged sample and thereafter dried at 45ºC in a vacuum drying oven overnight. The vacuum dried Ag-NP were then used for powder X-ray diffraction analysis.

The diffractogram was documented from PANalytical, XPERTPRO diffractometer using Cuk (Cu Kα radiation, λ 1.54443) as X-ray source running at 45 kV and 30 mA [56]. The diffracted intensities were noted from 35° to 99° 2θ angles [53], [57], [58].

2.10. FTIR analysis

The vacuum dried inorganic metal nanoparticles were mixed up individually with KBr, alkali halide at a ratio of 1:100 (weight/weight). The two materials were then grounded to a fine powder in a mortar and pestle separately. Then the mixture was converted into a pellet press consisting of two pistons in a smooth cylindrical chamber. The pressure of up to 25000 psi was then applied for different measures of time in a vacuum. After that, the pistons were removed and the clear pellet was placed in a holder of the spectrophotometer. Since the KBr did not absorb infrared radiation in the region 4,000 and 400 cm^{-1} a complete spectrum of the solid was obtained [59]. The spectra were viewed by Shimadzu 8400S FTIR spectrophotometer. The spectral domain was set down in between four thousand and four hundred cm^{-1} [56].

2.11. TEM inspection of nanoparticles

Morphological and topographical characterization of the nanoparticles had been well established by the TEM studies [21]. On a carbon-coated copper grid thin films of the synthesized Ag-NP were prepared (30 μm × 30 μm mesh size) and a droplet of the Ag-NP suspension was

spotted on the grid. With the help of blotting paper, the excess sample was blotted off and then it was kept for drying off under a mercury lamp for five minutes. The synthesized particles were examined and visualized by TEM using a Tecnai G2 spirit Biotwin instrument (FP 5018/40), operating at around 80 kV accelerating voltage [60].

2.12. Estimation of antibacterial potentiality

Bacillus subtilis MTCC Code 736, *Listeria monocytogenes* MTCC Code 657, *Staphylococcus aureus* MTCC Code 96, *Escherichia coli* MTCC Code 68, *Klebsiella pneumoniae* MTCC Code 109 and *Salmonella typhimurium* MTCC Code 98 were obtained from MTCC, Institute of Microbial Technology, Chandigarh, India. Antibacterial nature was estimated by determining minimum inhibitory concentration (MIC) values according to the microdilution method [61], [62]. The six investigating bacteria were freshly cultured and 1×10^5 CFU/ml concentrated dilutions were constructed separately. Reactions were performed in ninety-six well plate consisting of 200 µl of NB, 20 µl of inoculum and different dilutions of polymers. Following incubation for one day at 37°C, 40 µl of INT dye (0.2 milligrams/milliliter) was mixed and incubated for the next round of thirty min. The concentration that inhibited 50% progression of bacteria growth as compared with positive control was calculated as MIC value. Streptomycin was cast-off as a standard drug.

3. Results and discussion

3.1. Characterization and identification of the plant specimen

The plant is rhizomatous, sub-erect to erect in posture, Entire body appears to be shiny and glabrous. Plant body ranges between 9–18 inches and are non-articulate (Fig. 1A). The mature stem appears to be brownish to dark in colour. Lamina is simply pinnate, lanceolate. Pinnae is finely leathery which is deep green or pale in colour, glabrous above and below, up to 10 pairs, stalked, alternate, fan-shaped (Fig. 1C) [63]–[65]. Venation pattern of the pinnae is dichotomous (Fig. 1D)[63]. Sporophylls are not grouped in strobili, whereas sporangia are enclosed in sporocarps. Sori is not dorsal and have false indusium, sporangia formed in definite groups [66]. T.S of the stem shows sclerenchymatous ground tissue and are 3–4 layered followed by parenchymatous cells. The xylem appears to be V-shaped with two arms that are turned inwards (Fig. 1B). Xylems are also both exarch and diarch [63], [67], [68]. The outer wall of spore appears to be rugulate under SEM which is an enlisted characteristic of the species [69] (Fig. E-G). Hence, the observation made from the above evidence identifies the specimen to be *Adiantum lunulatum* Burm.f. (*A. Philippense* Linn.) of the family Pteridaceae.

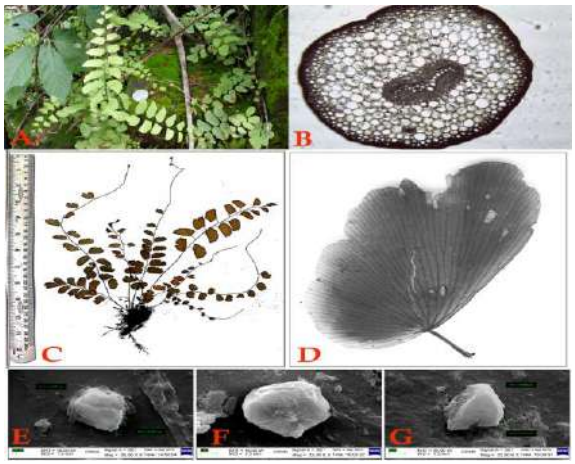

Fig. 1. (A) Digital photograph of the sporophyte of Adiantum lunulatum Burm. f. used in the biosynthesis of Ag-NP, (B) Transverse Section of the stem of Adiantum lunulatum, (C) Photograph of the Herbarium Specimen of Adiantum lunulatum Burm. f., (D) Venation pattern of the leaf of Adiantum lunulatum, (E–G) Scanning Electron Microscopic images of the spores of Adiantum lunulatum.

3.2. Production and characterization of Ag-NP

Ag-NP exhibits dark brown colour in liquid solution due to excitation of SPR in Ag-NP. Reduction of the Ag ions to Ag-NP at the time of contact to the liquid extract of *Adiantum lunulatum* could be followed by colour change. The liquid extract mediated synthesis of Ag-NP was validated by visually monitoring three flasks containing the $AgNO_3$ solution, a liquid extract of *Adiantum lunulatum* and the reaction mixture of the liquid plant extract with $AgNO_3$ solution respectively. An instantaneous and immediate turn over in the colour of the reaction mixture from colourless solution to brown colour signified the formation of Ag-NP (Fig. 2B) [70], whereas the liquid plant extract (Fig. 2A) and the $AgNO_3$ solution (Fig. 2C) were observed to retain their original colour. The colour of the control samples showed no change with cumulative incubation time. The appearance of a prominent brown colour designated the occurrence of the reaction and the development of the Ag-NP [53].

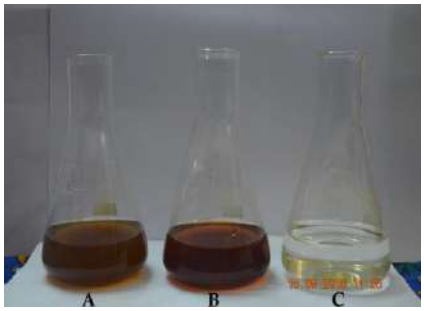

Fig. 2. Three flasks containing (A) only the liquid plant extract, (B) reaction mixture of liquid plant extract and $AgNO_3$ solution and (C) Only $AgNO_3$ solution, respectively.

3.3. UV–Visible spectroscopic analysis of Ag-NP

The evolution of silver from Ag^+ ions to Ag^0 state was categorized for spectral analysis. A broad and strong SPR band of the reaction solution was obtained in the visible spectrum at 420 nm, which was specific for Ag-NP (Fig. 3). Furthermore, this spectral analysis advocated that the Ag-NP were not in aggregated form. They scattered very well in the suspension [43], [53].

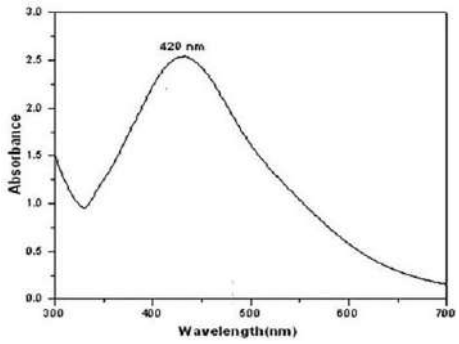

Fig. 3. UV–VIS spectrum of the synthesized silver nanoparticles.

3.4. Particle size measurement of Ag-NP

The DLS measurement was performed to get the knowledge of the size of the Ag-NP. Laser diffraction had shown that particle size found in the between 30–98 nm range (Fig. 4) The average diameter of these $AgNO_3$ nanoparticles was calculated to be 65±2 nm [71].

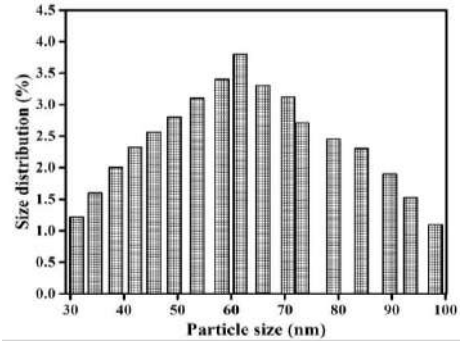

Fig. 4. The particle size distribution of bioreduced silver nanoparticles.

3.5. Zeta potential of Ag-NP

As displayed in Fig. 5, the zeta potential obtained from the Ag-NP showed a surface charge with a value of –84.11 mv [72]. The particles repel each other in suspension either having a negative or a positive zeta potential and also there shall be a very less tendency for the particles to come along. The slightly negative charge on the nanoparticles was probably resulting in the high stability of the Ag-NP without forming any aggregates when kept for an extended episode of time of more than a month [73]. Even the samples were retained their characteristic nature for more than a year (data not shown).

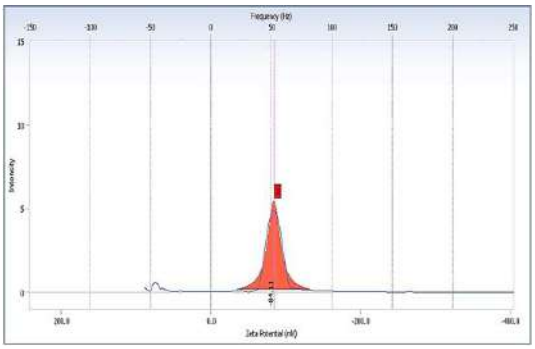

Fig. 5. Zeta potential of the biosynthesized silver nanoparticles.

3.6. EDX observation of Ag-NP

Fig. 6 illustrates the spot-profile mode of the EDX spectrum recorded from one of the densely-populated Ag-NP areas. In EDX spectra of Ag-NP, a sharp wide peak was detected in between 3–4 keV spectral region. The peak around 3–4 keV spectral region associated with the binding energies of silver [74]. The incident of that sturdy signal from Ag atoms (87.76%) itemized that the nanoparticles were solely made by silver. Therefore, EDX spectra of the Ag-NP established the presence of silver in the nanoparticles without any impurity of peaks [34]. However, there were other peaks of EDX for Cl and P, signifying that they were mixed precipitates from the plant extracts.

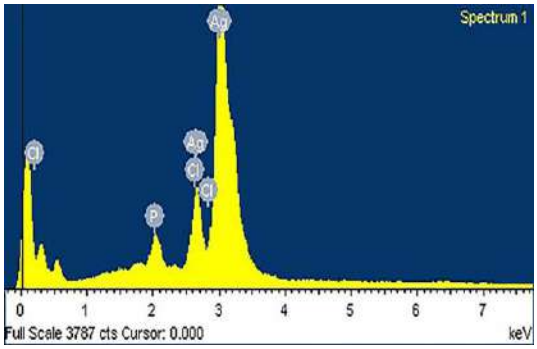

Fig. 6. EDX spectrum of silver nanoparticles.

3.7. Analyses of the crystallinity of Ag-NP by XRD

XRD measurement often proves to be a useful analytical gizmo for the identification of the crystalline nature of the newly formed compounds and their respective phases. XRD patterns of the dried Ag-NP revealed the subsistence of sharp diffraction lines at low angles (2° to 99°). The Ag-NP pointed out four sharp peaks of Ag at 2θ = 38°, 44°, 64° and 78° that could be indexed to the (111), (200), (220) and (311) facets of Ag, respectively (JCPDS card file no. 04-0783) [Fig. 7] [75]–[79]. Thus, the XRD-spectrum measurement, answered in four strong peaks agreed to the Bragg's reflection of silver nanocrystals, finalized the crystalline nature of the Ag-NP [80]. The unambiguous background noise was undoubtedly due to the shell of protein around the nanoparticles [56].

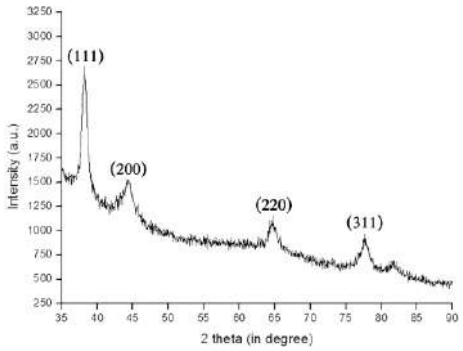

Fig. 7.XRD pattern of silver nanoparticles.

3.8. FTIR analysis of Ag-NP

FTIR absorption spectra of biosynthesized vacuum-dried Ag-NP have presented in Fig. 8. The spectra exhibited an extensive and strong absorption band corresponding to the O–H stretching vibration at around ~3,066 cm^{-1}. Symmetric and anti-symmetric modes of C–H stretching vibration were observed in the spectral region around ~2,889 cm^{-1} and ~2,820 cm^{-1} respectively [81]–[83]. Taraschewski et al. [84] reported earlier that the peak at around ~2,360 cm^{-1} was observed due to CO_2 vibration that might not be necessarily from the sample. Peaks at around ~1,567, ~1,380, and ~1,070 cm^{-1} were attributed to C=C stretching, $–NH_2$ symmetric stretch, and CO vibrations, respectively [34], [82], [85]–[87]. The band at around ~1,567 cm^{-1}, which commensurate to bending vibration movements in amides II, was earlier reported during the synthesis of Ag-NP [34]. The bands are visible in between the range of 500 to 750 cm^{-1} which confirmed the presence of R-CH group which might come from the liquid plant extract [88]. From this result, it could be stated that the soluble polypeptides present in the liquid plant extract may have acted as a capping agent to prevent the aggregation of Ag-NP in solution, and thus playing a

relevant role in their extracellular synthesis and shaping of the quasi-spherical Ag-NP [11], [30], [89].

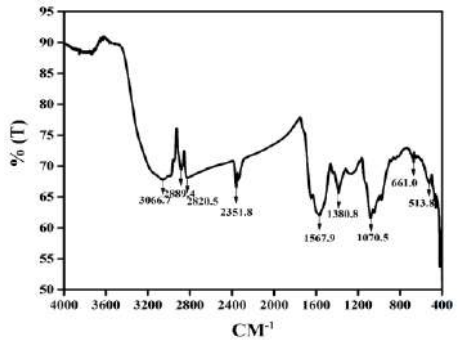

Fig. 8. FTIR absorption spectra of biosynthesized Ag-NP.

3.9. TEM of Ag-NP

TEM image, shown in Fig. 9, recorded dissimilar dimensions of Ag-NP which arose from the bio-reduction of the silver solution by liquid plant extract at room temperature (30ºC). The particles were found to be hexagonal, quasi-spherical as well as monodisperse in nature (Fig. 9 A-C) [11]. The measured diameter of these Ag-NP was in the domain of about 10–60 nm [90]. The average diameter of these Ag-NP was calculated to be 28±2 nm. The SAED pattern showed bright circular spots which further confirmed the single crystalline property of the Ag-NP (Figure 8D) [71]. It was thought-provoking to note that most of the Ag-NP in the TEM images were not in physical contact but were separated by a fairly undeviating inter-particle distance. Due to the developmental course of the sample preparation, the observed diameter of the Ag-NP during TEM analysis was quite unlike from that of the results obtained from DLS measurement as because Ag-NP were in a dry state in TEM whereas in the hydrated state in DLS experiment [91].

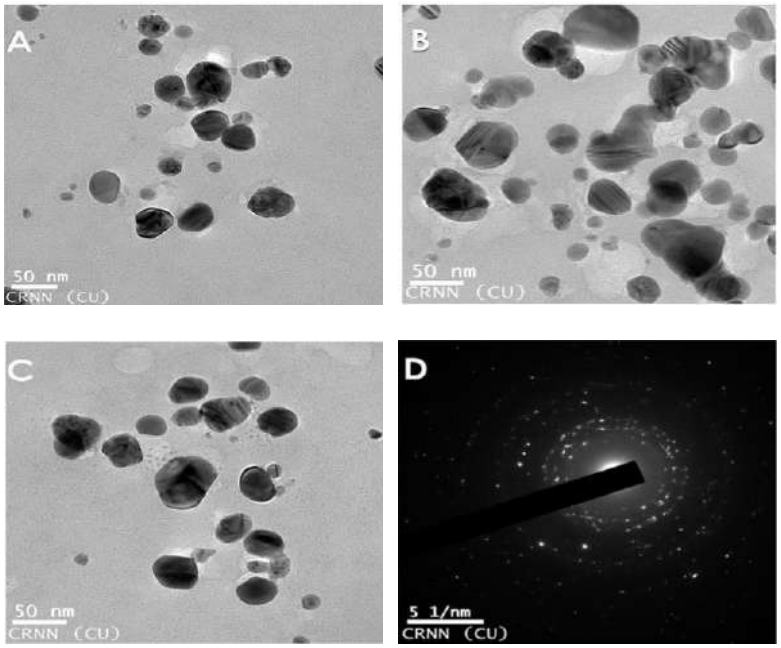

Fig. 9. (A–C) TEM images of Ag-NP (D) Selected area electron diffraction (SAED) patterns of crystalline Ag-NP.

3.10. Analysis of the effect of synthesized Ag-NP on some pathogenic bacteria

The biosynthesized Ag-NP was studied in 96 well plates for determining its antibacterial activity against both Gram-positive and Gram-negative bacteria. As presented in Table 1, the growth of all experimental strains was found to be subdued by the treatment of the Ag-NP as compared to Gram-negative control. In the case of *Listeria monocytogenes*, a Gram-positive bacterium, introduction of 25 μg/ml of Ag-NP caused 72.64±4.58% of reduction of bacterial density. Interestingly, growth of all examined Gram-negative bacteria were also noticed to be affected in the presence of a similar dose of the nanomaterials. Treatment of 25 μg/milliliter of synthesized Ag-NP showed maximum inhibition 48.45±2.87 and 88.7±5.62% with reference to *S. typhimurium* and *E. coli* respectively. These findings recommended strong antibacterial potentiality of synthesized Ag-nano.

Table 1. Antibacterial activity of synthesized silver nanoparticles as determined by the minimum inhibitory concentration value (μg/ml) (mean ± standard deviation; n = 3).

Type of bacteria	Name of bacteria	Nanoparticles	Streptomycin
Gram positive	*Listeria monocytogenes*	17.55 ± 3.57	4.68 ± 0.17
	Staphylococcus aureus	17.85 ± 1.71	6.29 ± 0.16
	Bacillus subtilis	105.41 ± 14.23	5.61 ± 0.01
Gram negative	*Escherichia coli*	12.36 ± 2.68	5.41 ± 0.11
	Salmonella typhimurium	28.77 ± 1.47	5.09 ± 0.03
	Klebsiella pneumoniae	17.84 ± 0.58	5.29 ± 0.14

4. Conclusions

The current work described biosynthesis of stable Ag-NP using liquid plant extract of *Adiantum lunulatum*. The production of biosynthesized nanomaterial was established by UV-Vis, DLS, EDX, XRD, FTIR and TEM analysis. The green synthesized Ag-NP presented strong antibacterial potentiality against pathogenic Gram-positive (*Listeria monocytogenes*, *Staphylococcus aureus*, and *Bacillus subtilis*) and Gram-negative (*Escherichia coli*, *Salmonella typhimurium* and *Klebsiella pneumoniae*) bacteria. Thus, the green synthesis of antimicrobial Ag-NP using liquid plant extract was an environment-friendly method as compared to the conventional physical and chemical synthesis techniques.

Acknowledgements

The authors thank Dr. Sudha Gupta, Assistant Professor, Pteridology & Paleobotany Lab, Department of Botany, University of Kalyani, Kalyani, Nadia, West Bengal, India, Pin-741235 for her entire effort in plant specimen identification and encouragement regarding this work. We also acknowledge Sinha Institute of Medical Science and Technology for providing us with the centrifugation and -20°C refrigeration facility.

Conflict of interest

On behalf of all listed authors, the corresponding author declares that there is not any sort of financial and non-financial conflict of interests in the subject materials mentioned in this manuscript.

References

[1] V. Filipe, A. Hawe, W. Jiskoot, Pharm. Res. **27**(5), 796 (2010).
[2] S. Galindo-Rodriguez, E. Allémann, H. Fessi, E. Doelker, Pharm. Res. **21**(8), 1428 (2004).
[3] A. Vilchis-Nestor, V. Sánchez-Mendieta, Mater. Lett. **62**(17–18), 3103 (2008).
[4] P. Magudapathy, P. Gangopadhyay, Phys. B Condens. **299**(1–2), 142 (2001).
[5] F. Frederix, J. Friedt, K. Choi, W. Laureyn, Anal. Chem. **75**(24), 6894 (2003).
[6] N. Jana, T. Sau, T. Pal, J. Phys. Chem. B **103**(1), 115 (1999).
[7] N. Chandrasekharan, P. Kamat, J. Phys. **104**(46), 10851 (2000).
[8] A. Gade, A. Ingle, C. Whiteley, M. Rai, Biotechnology Letters **32**(5), 593 (2010).
[9] M. Hayat, Colloidal gold: principles, methods, and applications. Academic Press INC, 2012.
[10] V. Filipe, A. Hawe, W. Jiskoot, Pharm. Res. **27**(5), 796 (2010).
[11] J. Sarkar et al., Dig. J. Nanomater. Biostructures **6**(2), 563 (2011).
[12] D. Maity et al., J. Appl. Polym. Sci. **122**, 2189 (2011).
[13] M. M. R. Mollick et al., Int. J. Green Nanotechnol. **4**(3), 230 (2012).
[14] S. K. Srikar, D. D. Giri, D. B. Pal, P. K. Mishra, S. N. Upadhyay, Green Sustain. Chem. **6**(1), 34 (2016).
[15] S. Mann, G. A. Ozin, Nature **382**(6589), 318 (1996).
[16] T. J. I. Edison, M. G. Sethuraman, Process Biochem. **47**(9), (2012).
[17] R. Lu, D. Yang, D. Cui, Z. Wang, L. Guo, Int. J. Nanomedicine **7**, 2101 (2012).
[18] E. J. Guidelli, A. P. Ramos, M. E. D. Zaniquelli, P. Nicolucci, O. Baffa, Radiat. Phys. Chem. **81**(3), 301 (2012).
[19] C. L. Schofield, A. H. Haines, R. A. Field, D. A. Russell, Langmuir **22**(15), 6707 (2006).
[20] V. Colvin, Nat. Biotechnol. **21**(10), 1166 (2003).
[21] G. Cao, Nanostructures and nanomaterials: synthesis, properties and applications. 2004.
[22] V. Rotello, Nanoparticles: building blocks for nanotechnology. Springer, Boston, MA, 2004.
[23] W. De Jong, P. Borm, Int. J. Nanomedicine, 2008.
[24] S. Saif, A. Tahir, Y. Chen, Nanomaterials **6**(11), 209 (2016).
[25] K. Mukunthan, S. Balaji, Int. J. Green **4**(1), 54 (2012).
[26] V. V Makarov et al., Acta Naturae **6**(1), 35 (2014).
[27] S. Iravani, "Green synthesis of metal nanoparticles using plants," Green Chem., 2011.
[28] S. S. Shankar, A. Rai, A. Ahmad, M. Sastry, J. Colloid Interface Sci. **275**(2), 496 (2004).
[29] J. Sarkar, M. Ghosh, A. Mukherjee, D. Chattopadhyay, K. Acharya, Bioprocess Biosyst. Eng. **37**(2), 165 (2014).
[30] J. Sarkar, S. Ray, D. Chattopadhyay, A. Laskar, K. Acharya, Bioprocess Biosyst. Eng. **35**(4), 637 (2012).
[31] N. Friis, P. Myers- Keith, Biotechnol. Bioeng. **28**(1), 21 (1986).
[32] S. Ahmed, M. Ahmad, B. L. Swami, S. Ikram, Journal of Advanced Research **7**(1), 17 (2016).
[33] G. Dhillon, S. Brar, S. Kaur, Crit. Rev. **32**(1), 49 (2012).
[34] K. Acharya, J. Sarkar, Int. J. Pharm. Sci. Rev. Res. **29**(1), 82 (2014).
[35] S. Santhoshkumar, K. Arts, T. Nadu, "No Title," **5**(12), 5511 (2014).
[36] A. J. De Britto, D. H. S. Gracelin, P. B. Jeya, R. Kumar, P. Molecular, T. Nadu, Int. J. Univers. Pharm. Life Sci. **2**(4), 92 (2012).
[37] D. G. Sant et al., J. Nanoparticles **2013**, 1 (2013).
[38] S. Kalita, R. Kandimalla, K. K. Sharma, A. C. Kataki, M. Deka, J. Kotoky, Mater. Sci. Eng. C **61**, 720 (2016).
[39] A. K. Jha, K. Prasad, Int. J. Nanosci. **15**(1–2), 1 (2016).
[40] B. Ch, S. Kunjiappan, C. Bhattacharjee, R. Chowdhury, Nanomed. J. **2**(1), 88 (2015).
[41] X. Baskaran, A. V. G. Vigila, T. Parimelazhagan, D. Muralidhara-Rao, S. Zhang, Int. J. Nanomedicine **11**, 5789 (2016).
[42] N. A. Şuţan, I. Fierăscu, R. C. Fierăscu, D. Ş. Manolescu, L. C. Soare, Ind. Crops Prod. **83**, 379 (2016).
[43] B. Koteswaramma, J. Kamakshamma, S. Varalaksmi, Int. J. Pharma Bio Sci. **8**(1), 121 (2017).
[44] N. John, "of the ferns Cyclosorous," **9**(2), 125 (2016).

[45] M. S. Ali, M. R. Amin, C. M. I. Kamal, M. A. Hossain, Asian Pac. J. Trop. Biomed. **3**(6), 464 (2013).
[46] M. Johnson, J. Microbiol. Exp. **4**, (41), (2017).
[47] T. Paul, B. Das, K. G. Apte, S. Banerjee, R. C. Saxena, J. Diabetes Metab. **3**(9), (2012).
[48] R. Sikarwar, B. Pathak, A. Jaiswal, Int. J. Tradit. Knowl. **7**(4), 613 (2008).
[49] C. Pan, Y. G. Chen, X. Y. Ma, J. H. Jiang, F. He, Y. Zhang, Tropical Journal of Pharmaceutical Research **10**(5), 681 (2011).
[50] M. Mithraja, J. Marimuthu, M. Mahesh, Z. Paul, Trop. Biomed. **2**(1), S40 (2012).
[51] A. Henglein, J. Phys. Chem. **97**(21), 5457 (1993).
[52] M. Sastry et al., Curr. Sci. **85**(2), 162 (2003).
[53] S. Saha, J. Sarkar, D. Chattopadhyay, S. Patra, A. Chakraborty, K. Acharya, Dig. J. Nanomater. Biostruc. **5**(4), 887 (2010).
[54] M. Behera, G. Giri, Mater. Sci. **32**(4), 702 (2014).
[55] S. M. Mukhopadhyay, Sample Preparation for Microscopic and Spectroscopic Characterization of Solid Surfaces and Films. 2003.
[56] N. Vigneshwaran, A. A. Kathe, P. V. Varadarajan, R. P. Nachane, R. H. Balasubramanya, Langmuir **23**(13), 7113 (2007).
[57] Y. Sun, Y. Xia, Science (80-.). **298**(5601), 2176 (2002).
[58] S. Pal, Y. Tak, J. Song, Appl Env. Microbiol. **73**, 1712 (2007).
[59] T. Bonnal, G. Foray, E. Prud, S. Tadier, European Journal of Environmental and Civil Engineering 1 (2017).
[60] B. Schaffer, U. Hohenester, A. Trugler, F. Hofer, Phys. Rev. B - Condens. Matter Mater. Phys. **79**(4), (2009).
[61] D. Stojković et al., Food Res. Int. **53**(1), 56 (2013).
[62] D. Stojković, J. Petrović, M. Soković, J. Glamočlija, J. Kukić-Marković, S. Petrović, J. Sci. Food Agric. **93**(13), 3205 (2013).
[63] V. G. K. L. C. V. A. Pallavi, Int J Pharm. Biol. Arch. **2**(6), 1668 (2011).
[64] D. M. Hillis, Annu. Rev. Ecol. Syst. **18**(1), 23 (1987).
[65] B. Verdcourt, "Flora of Tropical East Africa," 2002.
[66] K. U. Kramer, P. S. (Peter S. Green, and E. Götz, Pteridophytes and gymnosperms. Springer-Verlag, 1990.
[67] S. Resmi, T. Vp, S. Vk, in Kerala **2**(1), 115 (2016).
[68] A. B. Hungarica **58**(1909), 199 (2016).
[69] A. F. Tryon, B. Lugardon, Spores of the Pteridophyta, New York, NY: Springer New York, 1991, pp. 1–26.
[70] G. Singhal, R. Bhavesh, K. Kasariya, A. R. Sharma, R. P. Singh, J. Nanoparticle Res. **13**(7), 2981 (2011).
[71] M. M. R. Mollick et al., Microfluid. Nanofluidics **16**(3), 541 (2014).
[72] M. Gohel, T. Soni, L. Hingorani, A. Patel, N. Patel, Curr. Res. Drug Discov. **1**(2), 29 (2014).
[73] J. Sarkar, P. Dey, S. Saha, K. Acharya, Micro Nano Lett. **6**(8), 599 (2011).
[74] S. Kunjiappan, R. Chowdhury, C. Bhattacharjee, Front. Mater. Sci. **8**(2), 123 (2014).
[75] G. Li et al., Int. J. Mol. Sci. **13**(1), 466 (2012).
[76] K. Selvi, T. Sivakumar, Int. J. Curr. Microbiol. App. Sci. **1**(1), 56 (2012).
[77] D. R. Patil, Int. J. Res. Stud. Biosci. **3**(10), 146(2015).
[78] B. V. Bhimba, S. Gurung, S. U. Nandhini, Int. J. ChemTech Res. **7**(1), 68 (2015).
[79] K. Jyoti, M. Baunthiyal, A. Singh, J. Radiat. Res. Appl. Sci. **9**(3), 1 (2016).
[80] H. W. Lu, S. H. Liu, X. L. Wang, X. F. Qian, J. Yin, Z. K. Zhu, Mater. Chem. Phys. **81**, 104, (2003).
[81] N. Sundaramurthy, C. Parthiban, Int. Res. J. Eng. Technol. **2**(6), 332 (2015).
[82] S. Chandra, N. Chakraborty, A. Dasgupta, J. Sarkar, K. Panda, K. Acharya, Sci. Rep. **5**, 15195 (2015).
[83] R. Sanghi, P. Verma, Bioresour Technol. **100**(1), 501 (2009).
[84] M. Taraschewski, H. K. Cammenga, R. Tuckermann, S. Bauerecker, J. Phys. Chem. A **109**(15), 3337 (2005).
[85] R. M. Silverstein, F. X. Webster, D. J. Kiemle, Microchemical Journal **21**, 496 (2005).

[86] C. Y. Kim, T. Sekino, K. Niihara, J. Am. Ceram. Soc. **86**(9), 1464 (2003).
[87] Y. F. Zhang, J. X. Zhang, Q. M. Lu, Q. Y. Zhang, Mater. Lett. **60**(20), 2443 (2006).
[88] A. K. Singh, M. Talat, D. P. Singh, O. N. Srivastava, J. Nanoparticle Res. **12**, 1667 (2010).
[89] J. Sarkar, K. Acharya, Synth. React. Inorganic, Met. Nano-Metal Chem. **47**(3), 365 (2017).
[90] K. P. Bankura et al., Carbohydr. Polym. **89**(4), 1159 (2012).
[91] R. M. M. Mollick et al., RSC Adv. **4**(71), 37838 (2014).

Source details

Feedback > Compare sources >

Digest Journal of Nanomaterials and Biostructures

Open Access

Scopus coverage years: from 2009 to Present

Publisher: S.C. Virtual Company of Physics S.R.L

ISSN: 1842-3582

Subject area: Materials Science: General Materials Science | Physics and Astronomy: Condensed Matter Physics | Chemistry: Physical and Theoretical Chemistry | Physics and Astronomy: Atomic and Molecular Physics, and Optics | Engineering: Biomedical Engineering View all

Source type: Journal

View all documents > Set document alert Save to source list

CiteScore 2022
1.4

SJR 2022
0.188

SNIP 2022
0.341

CiteScore | CiteScore rank & trend | Scopus content coverage

Polysaccharide capped antibacterial silver nanoparticles synthesis using green chemistry

Joy Sarkar

Department of Botany,
Dinabandhu Andrews College,
Garia, Kolkata, West Bengal, Pin-700084, India
and
Molecular and Applied Mycology and Plant Pathology Laboratory,
Centre of Advanced Study, Department of Botany,
University of Calcutta,
Kolkata, West Bengal, Pin-700019, India
Email: jsarkar80@gmail.com

Gajendra Nath Maity

Department of Microbiology,
Panskura Banamali College,
Panskura R.S., Purba Medinipur,
West Bengal, Pin-721152, India
and
Department of Microbiology, Asutosh College,
Shyamaprasad Mukherjee Road,
Kolkata, West Bengal, Pin-700026, India
Email: mailme.gajendramaity@gmail.com

Somanjana Khatua

Molecular and Applied Mycology and Plant Pathology Laboratory,
Centre of Advanced Study, Department of Botany,
University of Calcutta,
Kolkata, West Bengal, Pin-700019, India
and
Department of Botany,
Krishnagar Government College,
Krishnagar, Nadia, West Bengal, Pin-741101, India
Email: somanjana.khatua4@gmail.com

Soumitra Mondal

Department of Chemistry,
Panskura Banamali College,
Panskura R.S., Purba Medinipur,
West Bengal, Pin-721152, India
Email: mondalsoumitra78@yahoo.com

Krishnendu Acharya*

Molecular and Applied Mycology and Plant Pathology Laboratory,
Centre of Advanced Study, Department of Botany,
University of Calcutta,
Kolkata, West Bengal, Pin-700019, India
and
Center for Research in Nanoscience & Nanotechnology,
Technology Campus, University of Calcutta,
Kolkata, West Bengal, Pin-700098, India
Fax: +091-033-24764419
Email: krish_paper@yahoo.com
*Corresponding author

Abstract: Advancement of an environment friendly, trustworthy, and speedy route for the production of Ag-NP using natural system is an essential urge in nanotechnology. Biological synthetic techniques are considered as a better alternative over other conventional methods. Silver is a safe inorganic element that is projected as 'next-gen' antimicrobial agent and had been extensively used against several bacterial strains from the ancient times. Here, we document a low-cost green synthesis approach for construction of Ag-NP using fruit extracted polysaccharide of *Bruguiera cylindrica*, a mangrove plant of Sundarban. During the investigation of GC-MS an adequate amount of glucose was found as major carbohydrate molecule in the extracted polysaccharide. Synthesised Ag-NP were also characteristically described by UV-Vis, DLS, TEM, EDAX, XRD and FTIR. The average diameter of the Ag-NP was 4.5 ± 1 nm. Additionally, antibacterial nature of Ag-NP was also find out against some of the pathogenic gram-positive and gram-negative bacteria.

Keywords: green synthesis; *Bruguiera cylindrica*; polysaccharide; silver nanoparticle; bacterial growth.

Reference to this paper should be made as follows: Sarkar, J., Maity, G.N., Khatua, S., Mondal, S. and Acharya, K. (2020) 'Polysaccharide capped antibacterial silver nanoparticles synthesis using green chemistry', *Int. J. Nano and Biomaterials*, Vol. 9, Nos. 1/2, pp.80–94.

Biographical notes: Joy Sarkar is an Assistant Professor and the previous Head of the Department of Botany, Dinabandhu Andrews College, Garia, Kolkata, India. He has successfully completed his PhD degree from the University of Calcutta. He has published more than 25 research papers in peer reviewed journals. His areas of interests are green nanotechnology, carbohydrate biology, medical biology, botany, mycology, etc.

Gajendra Nath Maity presently is an Assistant Professor of the Department of Microbiology, Asutosh College, Shyama Prasad Mukherjee Road, Kolkata, India. Formerly, he has served for Pashkura Banamali College, Purba Medinipur, West Bengal, India. He has successfully completed his MSc degree from the University of Kalyani. He has published four research papers in peer reviewed journals. His areas of interests are green nanotechnology, carbohydrate biology, microbiology, etc.

Somanjana Khatua is an Assistant Professor of the Department of Botany, Krishnagar Government College, Krishnagar, Nadia, West Bengal, India. She is pursuing her PhD degree from the University of Calcutta. She has published more than 45 research papers in peer reviewed journals. Her areas of interests are green nanotechnology, carbohydrate biology, medical biology, cell biology, botany, mycology, etc.

Soumitra Mondal presently is an Assistant Professor of the Department of Chemistry, Pashkura Banamali College, Purba Medinipur, West Bengal, India. He has successfully completed his PhD degree from the Vidyasagar University. He has published 24 research papers in peer reviewed journals. His areas of interests are green nanotechnology, carbohydrate biology, microbiology, etc.

Krishnendu Acharya is the Head of the Department of Botany, University of Calcutta, Kolkata, India. He has successfully completed his MTech and PhD degree from the Jadavpur University. He has received several awards from different institutions and organisations. He has published more than 350 research papers in peer reviewed journals. His areas of interests are green nanotechnology, carbohydrate biology, medical biology, botany, mycology, etc.

1 Introduction

In nanotechnology, when a particle performs the similar characteristic features and transports properties like the whole unit then it is indicated as a small object. Depending on the size, it is furthermore categorised into three classes such as fine particles, ultrafine particles and nanoparticles (Taylor et al., 2013). In respect of diameter, the fine particles are specified in between the scale of 100–2,500 nanometres, while for both ultrafine particles and nanoparticles; it is ranged in between 1–100 nanometres. But the nanoparticles probably be or not be revealed the same size-related characteristic features that diverged considerably from those detected in fine particles or bulk materials (Taylor et al., 2012, 2013; Hewakuruppu et al., 2013). Like the nanoparticles, when the distribution of size of any clustered material ranges in single dimension between 1–10 nanometres, it is specified as nanoclusters whereas the assembling of these nanoclusters is recognised as nano-powders. In a similar way, the single nano-sized crystals or ultrafine single-domain particles are recognized as nanocrystals (Fahlman, 2011). Over the recent past, the field of nanotechnology has introduced a new age of science which involves creation of materials near atomic scale with unique optical, chemical, physical and thermal features (Mohammadlou et al., 2016).

Silver is a safe inorganic element that has the capability to kill more than 650 variants of disease causing microorganisms (Jeong et al., 2005). The observed antimicrobial feature of Ag-NP is a growing interest in the arena of microbiology (Choi et al., 2008). This Ag-NP have been projected as ‘next-gen’ antimicrobial representatives (Rai et al., 2009b). As a consequence, metallic silver made a significant recovery in form of Ag-NP with powerful antimicrobial effects. Investigations have revealed that after exposure to bacteria, the nano-silver gets adhered to cell membrane, penetrates inside and attacks respiratory chain that finally causes to cell death. In addition, these particles discharge silver ions inside cells which hinder the ability of bacterial DNA synthesis and causes

deactivation of proteins containing thiol groups (Rai et al., 2009a; Ydollahi et al., 2016). This has unfolded novel strategies to use pure silver against many antibiotic resilient microorganisms and due to this, it has been adopted in many commercial products like topical ointments, toothpaste, soap, socks etc. (Ahmed et al., 2016; Zhao et al., 2016). In addition, Ag-NP has also emerged up as a promising agent for waste water disinfection system (Bora and Dutta, 2014). In a recent work, the use of antimicrobial silver compounds against coliform bacteria of waste water has been well established (Jain and Pradeep, 2005).

So far, a number of conventional physical and chemical techniques are available for Ag-NP synthesis; although majority of them are expensive, complicated, energy generative and involve use of hazardous chemicals (Ayyub et al., 2001; Backman, 2005; Kimling et al., 2006; Dong et al., 2010; Rajeshkumar, 2016). Conversely, the biological techniques are recognised as an advance and better replacement over other methods as it involves natural reagents like sugars, biodegradable polymers, plant extracts, microorganisms (Saha et al., 2010; Sarkar et al., 2011b, 2012, 2014, 2017; Acharya and Sarkar, 2014; Railean-Plugaru et al., 2016; Sarkar and Acharya, 2017). Previously, several attempts have been made to synthesise Ag-NP by using polysaccharide extracted from different plants (El-Rafie et al., 2013; Sathiyanarayanan et al., 2013; Sanyasi et al., 2016; Vasquez et al., 2016; Maity et al., 2019). But we have first time made this attempt to synthesis Ag-NP by using the polysaccharide extracted from a mangrove plant. Polysaccharides from mangrove plants such as *Bruguiera cylindrica* (L.) Blume can be used as a bio-factory for synthesis of nanoparticles because these are extremely stable, benign, non-toxic and with known biological activities (Maity et al. 2019). In this context, the mangrove plant, *Bruguiera cylindrica* (L.) Blume, could be a better substitute as it was scientifically proved that it has numerous bioactive components. It has been traditionally used as remedial measures for hepatitis, diabetes, wounds, ulcers, boils, diarrhoea, angina and dysentery (Kathiresan and Ramanathan, 1997; Bandaranayake, 1998). Recent investigations have reported that *Bruguiera cylindrica* possesses antioxidant (Banerjee et al., 2008), antinociceptive (Uddin et al., 2005), antidiabetic (Nabeel et al., 2010) and antimicrobial properties (Sakagami et al., 1998; Ravikumar et al., 2010). Thus, the recent work was aimed to produce Ag-NP by a greener method using the fruit extracted polysaccharide of *Bruguiera cylindrica* (L.) Blume, characterisation of the particles and appraisal of antibacterial nature.

2 Materials and methods

2.1 Separation of polysaccharide from fruit extract of B. cylindrica

Fresh and healthy fruits were accumulated from the mangrove forest of Sundarban, West Bengal. To remove all noticeable unwanted dust particles, the fruits were carefully washed with tap water and distilled water respectively. After that, they were desiccated and sliced into small pieces. 750 gm of these finely sliced fruits were steeped into distilled water (volume 250 millilitres) and simmered for five hours. The subsequent suspension was retained at 4°C for nightlong and then filtration was achieved by nylon cloth. Precipitation of the polysaccharide was made by the inclusion of five volumes of ethanol (99% alcohol). The precipitate was retained nightlong at 4°C. After centrifugation at 8,000 rpm for ten minutes, the precipitate was again liquefied in distilled

water and dialysed through DEAE cellulose bag for two hours to remove low molecular weight polysaccharides. Further, the lyophilised extract was exposed to sephadex G-100 gel permeation column (50 × 1.5 cm) using water as eluent (flow rate 0.5 millilitres/min). The eluate was accumulated (2 millilitres/tube) and carbohydrates were unveiled by phenol-sulphuric acid method (Masuko et al., 2005; Mecozzi, 2005). Finally, polysaccharide was pooled from test tube number 15–30 and freeze-dried.

2.2 Physical and chemical characterisation of fruit extracted polysaccharide

The entire content of sugar was calculated by phenol sulphuric acid method. Glucose was provided as standard. The sum total of protein was estimated by Bradford using BSA as reference. Gallic acid was defined as a reference to enumerate the total amount of phenolic amalgam from the polysaccharide using Folin-Ciocalteau reagent. All the data were presented as gram of standard equivalents per 100 gram of dry polysaccharide (Saha et al., 2013). To establish the monosaccharide composition, 2 milligrams polysaccharide was hydrolysed with 2M TFA at 100°C for two hours in screw cap vial. TFA was eliminated by desiccation at 55°C by bringing down the pressure (Rotavapor R3, Butchi, Switzerland). To dissolve hydrolysate, 50% ethanol (1 millilitre) was included to the vial. The centrifugation was performed for five minutes at 12,000 rpm to remove non-hydrolysed polysaccharide and further scrutinised by GC-MS as conveyed in our earlier publication (Khatua and Acharya, 2016).

2.3 Synthesis of Ag-NP

$AgNO_3$ (> 99.9% pure) was procured from Merck, India. For Ag-NP synthesis, 20 millilitres of 0.5 milligrams/millilitre of isolated polysaccharide was mixed with 20 millilitres of 1 mM $AgNO_3$ solution and stirred with magnetic stirrer for 90 min at room temperature. The colour change from pale yellow to brown specified the generation of the Ag-NP due to reaction of polysaccharide with silver metal ion. Simultaneously, the polysaccharide solution without any addition of $AgNO_3$ (positive control) and only the $AgNO_3$ solution (negative control) were kept by following the similar environment of reaction solution.

2.4 Characterisation of synthesized Ag-NP

The generation of Ag-NP was established by UV-Vis spectrophotometer (Hitachi 330 spectrophotometer) with plasmon peaks at various regions of the spectral range 200–900 nm which corresponded to different signature marks for different nanoparticles respectively. The particle size was find out by using Zen 1600 Malvern nano-size particle analyser ranging between 0.6 nm and 6.0 μm. For XRD measurement, the spectra were logged in a Panalytical X'Pert Pro X-ray Diffractometer (Cu Kα radiation, λ 1.54) running at 40 mA and 45 kV. The diffracted intensities were documented from 35° to 90° 2θ angles. EDX analysis of Ag-NP was performed by the Hitachi S 3400N instrument. For FTIR analysis, the dried Ag-NP were mixed with KBr at a ratio of 1:100. Furthermore, the prepared pellet was viewed by Shimadzu 8400S FTIR spectrophotometer. The spectral range was set down in between 4,000 cm^{-1} and

400 cm^{-1}. In addition, the synthesised particles were examined and visualised by TEM using Tecnai G2 spirit Biotwin instrument (FP 5018/40), operating at around 80 kV accelerating voltage.

2.5 Analysis of effect of synthesised Ag-NP on some pathogenic bacteria

Staphylococcus aureus ATCC® 700699™, *Bacillus subtilis* ATCC® 6633™ (MTCC 736), *Listeria monocytogenes* ATCC® 19111™ (MTCC 657), *Escherichia coli* ATCC® 25922™ and *Salmonella typhimurium* ATCC® 23564™ (MTCC 98) were utilised for the experiment. The antibacterial effect was estimated by determining MIC values according to microdilution method (Stojković et al., 2013). The five investigating bacteria were cultured freshly and 1×10^5 CFU/millilitre concentrated dilutions were constructed separately. Reactions were performed in 96 well plates consisting of 200 µl of NB, 20 µl of inoculum and different dilutions of nanoparticles. Following incubation for one day at 37°C, 40 µl of INT dye (0.2 milligrams/millilitre) was mixed and incubated for a next round of 30 min. The concentration that inhibited 50% progression of bacteria growth as compared with positive control was calculated as MIC value. Streptomycin was cast-off as a standard drug.

3 Results and discussion

3.1 Physical and chemical characterisation of isolated polysaccharide

The extractive yield of polysaccharide from fruit extract of *B. cylindrica* was 0.026 ± 0.006% of dry matter. Total carbohydrate content was 51±5 gm/100 gm of the dried polysaccharide whereas the total estimated protein content was 4±0.06 gm/100 gm of the respective sample. Very negligible percent of phenol was detected (0.5±0.05 gm/100 gm of dry polysaccharide). Further, the molecular contents were finalised by GC-MS where glucose was detected as the dominant monomer (Figure 1).

Figure 1 GC-MS of polysaccharide extracted from fruits of *Bruguiera cylindrica*

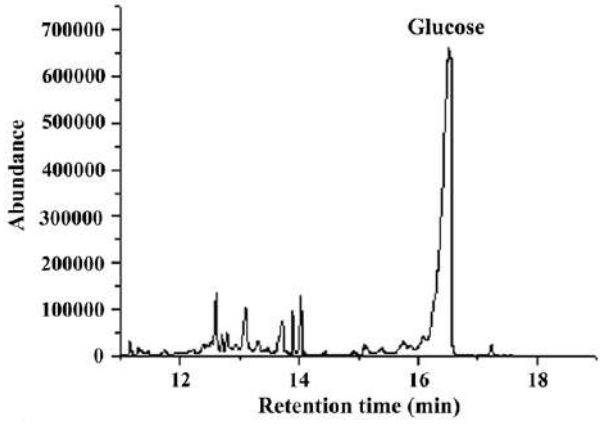

3.2 Synthesis of Ag-NP

The characteristic brown colour of reaction mixture, a signature mark for the generation of Ag-NP in the solution, arose due to the collective vibration of free electrons of Ag-NP in resonance with light wave. The SPR absorption band of reaction solution in the visible spectral region of electromagnetic radiation further confirmed the claim of the formation of Ag-NP (Sarkar et al., 2011a). The generation of Ag-NP by reduction of the metal ions during exposure of 20 millilitres of 0.5 milligrams/millilitre of the polysaccharide isolated from *Bruguiera cylindrica* into 20 millilitres of 1 mM $AgNO_3$ solution, was detected by brown colour formation (Figure 2 inset).

Figure 2 UV-Vis spectrum of the synthesised silver nanoparticles (see online version for colours)

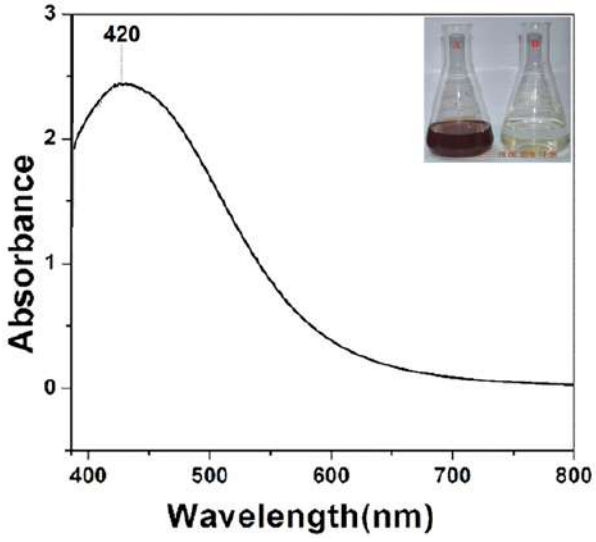

Notes: Inset: represents (A) colour change of reaction mixture of the polysaccharide with $AgNO_3$ solution after 24 hours and (B) only $AgNO_3$ solution.

3.3 UV-Vis spectrophotometric analysis of biosynthesised Ag-NP

The evolution of silver from Ag^+ ions to Ag^0 state was categorised for spectral analysis. Broad and strong SPR band of reaction solution was obtained in the visible spectrum at 420 nm, which was specific for Ag-NP (Figure 2). Furthermore, this spectral analysis advocated that the Ag-NP were not in aggregated form. They scattered very well in the suspension (Sarkar et al., 2011a).

3.4 Analysis of size distribution of the Ag-NP by DLS analyser

The DLS measurement was performed to get the knowledge of size of the Ag-NP [Figure 3(a)]. Observations revealed the heterogeneous nature of the dispersed Ag-NP, with a size distribution between 1–10 nm.

3.5 Analysis of the crystallinity of Ag-NP by X-ray diffraction

The XRD measurement often proves to be a useful investigative device for newly formed compounds and their phases. Crystallinity of Ag-NP was established by this analysis. The XRD spectra of Ag-NP displayed four identical appearing at 2θ = 38°, 44°, 64° and 78° conforming to the (111), (200), (220) and (311) facets of silver, respectively (JCPDS card file no. 04-0783) (Saha et al., 2010) [Figure 3(b)].

Figure 3 (a) Particle size distribution of bioreduced silver nanoparticles (b) representative XRD pattern of silver nanoparticles (see online version for colours)

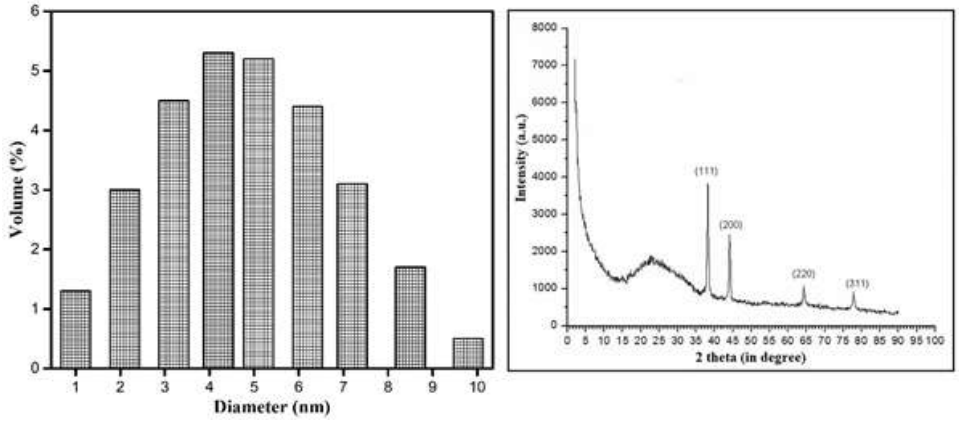

(a) (b)

Figure 4 EDX spectrum of silver nanoparticles (see online version for colours)

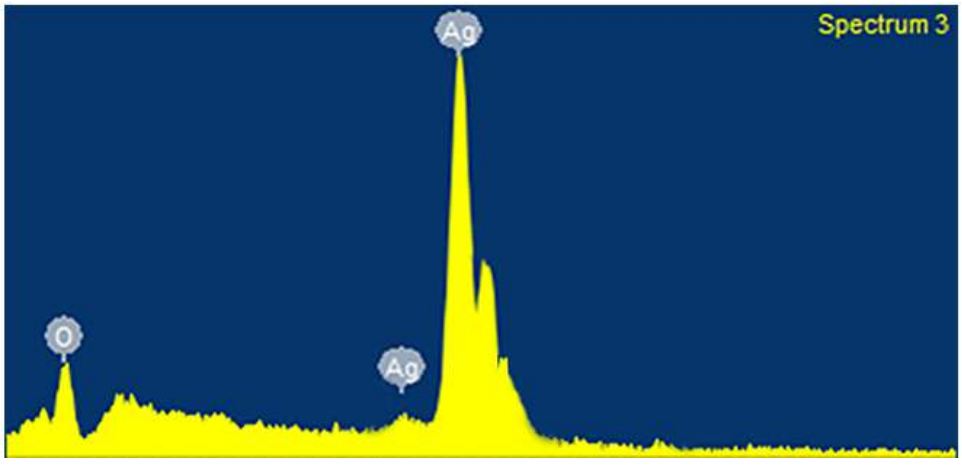

3.6 Investigation of elemental framework of the produced Ag-NP by EDX

In Figure 4, a sharp wide peak characteristic to silver was observed around 3–4 keV (Magudapathy and Gangopadhyay, 2001; Durán et al., 2005; Jaidev and Narasimha,

2010; Banu et al., 2011). The existence of a sturdy signal from Ag atoms (85.29%) finalised that the produced nanoparticles were solely made by silver. Other EDX peaks like the peaks of oxygen also advocated that they were mixed precipitates of the polysaccharide and silver salt. XRD analysis also agreed with the generation of nano silver.

3.7 FTIR study of isolated polysaccharide and bio-synthesised Ag-NP

Figure 5 shows the FTIR absorption spectra for the synthesised Ag-NP [Figure 5(a)] and untreated polysaccharide [Figure 5(b)] respectively. Both the spectra exhibited the existence of bands around 3,430 cm^{-1} and 1,620 cm^{-1} signifying the O-H stretching and C=C group respectively (Jin and Bai, 2002; Socrates, 2004; Sanghi and Verma, 2009; Sathyavathi et al., 2010). The intensity of these peaks was revealed the chief role of O_2-containing functional groups in the reduction of Ag^+ ions in contrast to untreated polysaccharide [Figure 5(a)] where the peak of the –COOH (carboxyl) group was shortened due to interaction with the surface of the Ag-NP (Ebrahiminezhad et al., 2016b). In the 5B spectrum, bands observed at around 2,920, 1,450 and 1,250 cm^{-1} indicated the aldehydic C-H stretching, –COO stretching and C-C stretching vibration respectively (Barth, 2007; Sathyavathi et al. 2010). Due to diminution of Ag^+ to Ag^0, the peaks at around 2,920, 1,450, 1,250 and 1,070 cm^{-1} were eliminated from the 5A spectrum (Ebrahiminezhad et al., 2016b). A new peak visible only at 1,380 cm^{-1} in Figure 5(a) showed the existence of $–NO_3$ which was derived from $AgNO_3$ (Sarkar et al., 2011a; Ebrahiminezhad et al., 2016b). The bands noticed in the 500 to 750 cm^{-1} spectral region indicated the existence of R-CH group (Singh et al., 2010). The characteristic peaks for C=O stretching vibration appeared at 1,745 cm^{-1} was shifted to 1,760 cm^{-1} in the spectrum of Ag-NP which framed that the carbohydrates performed a major role both as a diminishing as well as capping agent of the Ag-NP (Dasgupta et al., 2017). Majority of the carbohydrates have variety of O_2-containing functional groups, like carbonyl, phenolic, hydroxyl and carboxylic groups. Silver ions displays a powerful attraction to these functional moieties via coordination or electrostatic interactions. These interactions allow electrons to pass to the Ag^+ ions resulting in nucleation and growth of Ag-NP (Ebrahiminezhad et al., 2016a).

$$R-CH_2OH \underset{Ag^+}{\rightarrow} R-CHO \underset{Ag^+}{\rightarrow} R-COOH \quad (1)$$

$$R_2-CHOH \underset{Ag^+}{\rightarrow} R_2-CO. \quad (2)$$

In lieu of the above explanation it can be itemised that the carbohydrates present over the Ag-NP surface may also acts as capping agent for their stabilisation. The result of this spectroscopic analysis established that the carbohydrates extracted from the plant, *Bruguiera cylindrica*, has the capability to perform the function regarding the stability of the Ag-NP over long period.

3.8 TEM analysis of the Ag-NP

Figure 6(a) displays the TEM image of the Ag-NP with a diverse range of their sizes which were produced after the bioreduction of the $AgNO_3$ solution by the

polysaccharides. These findings inferred that the produced Ag-NP were homogeneous and polydisperse in nature and majority of them were spherical in shape. The diameters of these Ag-NP were in the range of 1–10 nm. The mean diameter was observed to be 4.5±1 nm. The bright circular spots in the SAED pattern further confirmed the single crystalline nature of the Ag-NP [Figure 6(b)].

Figure 5 FTIR absorption spectra of, (a) synthesised silver nanoparticles (b) untreated polysaccharide

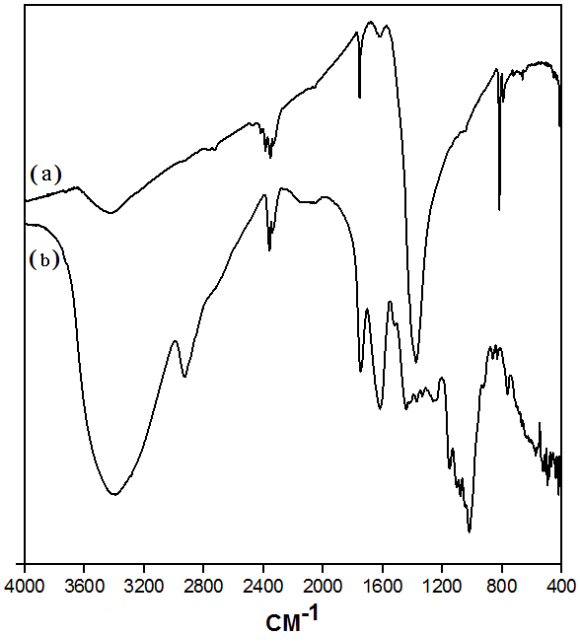

Figure 6 (a) Transmission electron microscopic image of silver nanoparticles (b) SAED patterns of crystalline silver nanoparticle (see online version for colours)

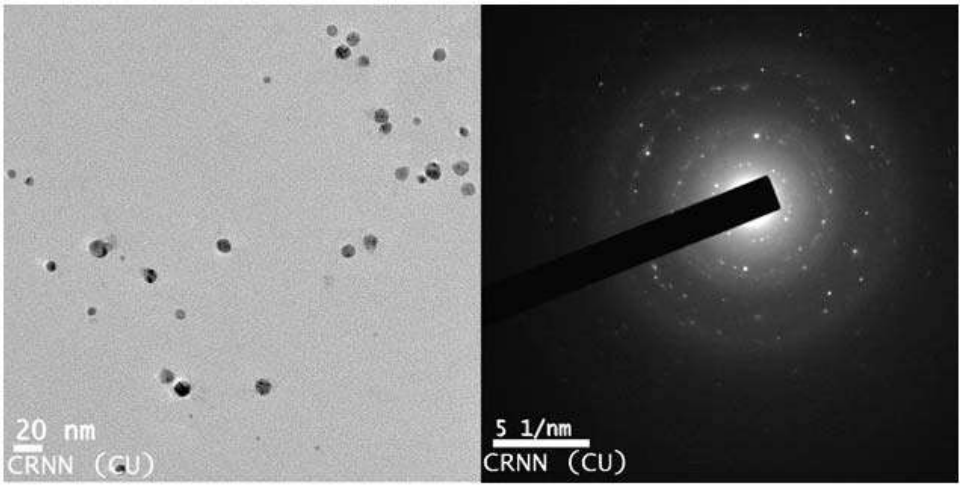

(a) (b)

Table 1 Antibacterial activity of synthesised silver nanoparticles as determined by minimum inhibitory concentration (MIC) value (µg/ml) (mean ± SD; n = 3)

Type of bacteria	*Name of bacteria*	*Minimum inhibitory concentration by*	
		Silver nanoparticles	*Streptomycin*
Gram-positive	*Listeria monocytogenes*	28.31 ± 2.4	4.68 ± 0.17
	Bacillus subtilis	30.14 ± 5.43	5.61 ± 0.01
Gram-negative	*Escherichia coli*	32.72 ± 9.53	5.41 ± 0.11
	Salmonella typhimurium	42.83 ± 0.08	5.09 ± 0.03
	Klebsiella pneumoniae	39.69 ± 1.67	5.294 ± 0.143

Note: Streptomycin was considered as a positive control.

3.9 Analysis of effect of polysaccharide based Ag-NP on some pathogenic bacteria

The antibacterial nature of Ag-NP was studied against both gram-positive and gram-negative bacteria using microdilution method. As unveiled in Table 1, the growth of all experimental strains was affected in appearance of the Ag-NP in contrast to negative control. In case of *B. subtilis*, a gram-positive bacterium, introduction of 25 µg/millilitre of polysaccharide capped Ag-NP caused 50.74 ± 3.56% of reduction of bacterial density. Interestingly, growth of all examined gram-negative bacteria were also inhibited in presence of similar doses of the nanomaterials. The treatment of 50 µg/millilitre of synthesised Ag-NP showed maximum inhibition 62.32 ± 2.86 and 65.98 ± 6.57% with reference to *E. coli* and *K. pneumoniae* respectively. The antibacterial activity was not represented by inhibitory zone, rather by determination of minimum inhibitory concentration (MIC). Thus, the value was higher in case of experimental sample which means superior concentration was required for the sample to inhibit bacterial growth in comparison with the standard drug. These findings indicated the strong antibacterial potentiality of synthesised Ag-nano.

4 Conclusions

This study described biosynthesis of stable Ag-NP using polysaccharide from fruit extract of *B. cylindrica* plant. The generation of biosynthesised nanomaterials was established by UV-Vis, XRD, FTIR. The green synthesised Ag-NP presented a dynamic antibacterial nature antagonistic towards some pathogenic gram-positive (*L. cytomonogenes*, *B. subtilis* and *S. aureus*) and gram-negative (*S. typhimurium* and *E. coli*) bacteria. Thus, the green approach for the production of Ag-NP using plant polysaccharide was an environment friendly and low cost method in contrast to the conventional physical and chemical synthesis techniques.

Acknowledgements

Joy Sarkar and Gajendra Nath Maity have equal contribution.

References

Acharya, K. and Sarkar, J. (2014) 'Bryo-synthesis of gold nanoparticles', *International Journal of Pharmaceutical Sciences Review and Research*, Vol. 29, No. 1, pp.82–86.

Ahmed, S., Ahmad, M., Swami, B.L. and Ikram, S. (2016) 'A review on plants extract mediated synthesis of silver nanoparticles for antimicrobial applications: a green expertise', *Journal of Advanced Research*, Vol. 7, pp.17–28, DOI: 10.1016/j.jare.2015.02.007.

Ayyub, P., Chandra, R., Taneja, P. et al (2001) 'Synthesis of nanocrystalline material by sputtering and laser ablation at low temperatures', *Applied Physics A: Materials Science Processing*, Vol. 73, pp.67–73, DOI: 10.1007/s003390100833.

Backman, U. (2005) *Studies on Nanoparticle Synthesis Via Gas-to-Particle Conversion*, VTT Publications, pp.3–45.

Bandaranayake, W.M. (1998) 'Traditional and medicinal uses of mangroves', *Mangroves Salt Marshes*, Vol. 2, pp.133–148, DOI: 10.1023/A:1009988607044.

Banerjee, D., Chakrabarti, S., Hazra, A. et al. (2008) 'Antioxidant activity and total phenolics of some mangroves in Sundarbans', *African Journal of Biotechnology*, Vol. 7, No. 6, pp.805–810, DOI: 10.5897/AJB07.911.

Banu, A., Rathod, V. and Ranganath, E. (2011) 'Silver nanoparticle production by *Rhizopus stolonifer* and its antibacterial activity against extended spectrum β-lactamase producing (ESBL) strains of Enterobacteriaceae', *Materials Research Bulletin*, Vol. 46, No. 9, pp.1417–1423, DOI: 10.1016/j.materresbull.2011.05.008.

Barth, A. (2007) 'Infrared spectroscopy of proteins', *Biochimica et Biophysica Acta (BBA) – Bioenergetics*, Vol. 1767, No. 9, pp.1073–1101, DOI: 10.1016/j.bbabio.2007.06.004.

Bora, T. and Dutta, J. (2014) 'Applications of nanotechnology in wastewater treatment – a review', *Journal of Nanoscience and Nanotechnology*, Vol. 14, No. 1, pp.613–626, DOI: 10.1166/jnn.2014.8898.

Choi, O., Deng, K.K., Kim, N.J. et al. (2008) 'The inhibitory effects of silver nanoparticles, silver ions, and silver chloride colloids on microbial growth', *Water Research*, Vol. 42, No. 12, pp.3066–3074, DOI: 10.1016/j.watres.2008.02.021.

Dasgupta, A., Sarkar, J., Ghosh, M. et al. (2017) 'Green conversion of graphene oxide to graphene nanosheets and its biosafety study', *PLoS One*, Vol. 12, No. 2, p.e0171607, DOI: 10.1371/journal.pone.0171607.

Dong, X., Ji, X., Jing, J. et al. (2010) 'Synthesis of triangular silver nanoprisms by stepwise reduction of sodium borohydride and trisodium citrate', *The Journal of Physical Chemistry C*, Vol. 114, No. 5, pp.2070–2074, DOI: 10.1021/jp909964k.

Durán, N., Marcato, P.D., Alves, O.L. et al. (2005) 'Mechanistic aspects of biosynthesis of silver nanoparticles by several *Fusarium oxysporum* strains', *Journal of Nanobiotechnology*, Vol. 3, No. 8, DOI: 10.1186/1477-3155-3-8.

Ebrahiminezhad, A., Bagheri, M., Taghizadeh, S-M. et al. (2016a) 'Biomimetic synthesis of silver nanoparticles using microalgal secretory carbohydrates as a novel anticancer and antimicrobial', *Advances in Natural Sciences: Nanoscience and Nanotechnology*, Vol. 7, No. 1, p.15018, DOI: 10.1088/2043-6262/7/1/015018.

Ebrahiminezhad, A., Taghizadeh, S., Berenjian, A. et al. (2016b) 'Synthesis and characterization of silver nanoparticles with natural carbohydrate capping using *Zataria Multiflora*', *Advanced Materials Letters*, Vol. 7, No. 11, pp.939–944, DOI: 10.5185/amlett.2016.6458.

El-Rafie, H.M., El-Rafie, M.H. and Zahran, M.K. (2013) 'Green synthesis of silver nanoparticles using polysaccharides extracted from marine macro algae', *Carbohydrate Polymers*, Vol. 96, No. 2, pp.403–410, DOI: 10.1016/j.carbpol.2013.03.071.

Fahlman, B.D. (2011*) Materials Chemistry*, 2nd ed., Springer Nature, Spain.

Hewakuruppu, Y.L., Dombrovsky, L., Chen, C. et al. (2013) 'Plasmonic 'pump-probe' method to study semi-transparent nanofluids', *Applied Optics*, Vol. 52, No. 24, pp.6041–50, DOI: 10.1364/AO.52.006041.

Jaidev, L.R. and Narasimha, G. (2010) 'Fungal mediated biosynthesis of silver nanoparticles, characterization and antimicrobial activity', *Colloids and Surfaces B: Biointerfaces*, Vol. 81, No. 2, pp.430–433, DOI: 10.1016/j.colsurfb.2010.07.033.

Jain, P. and Pradeep, T. (2005) 'Potential of silver nanoparticle-coated polyurethane foam as an antibacterial water filter', *Biotechnology and Bioengineering*, Vol. 90, No. 1, pp.59–63, DOI: 10.1002/bit.20368.

Jeong, S.H., Yeo, S.Y. and Yi, S.C. (2005) 'The effect of filler particle size on the antibacterial properties of compounded polymer/silver fibers', *Journal of Materials Science*, Vol. 40, No. 20, pp.5407–5411.

Jin, L. and Bai, R. (2002) 'Mechanisms of lead adsorption on chitosan/PVA hydrogel beads', *Langmuir*, Vol. 18, No. 25, pp.9765–9770, DOI: 10.1021/la025917l.

Kathiresan, K. and Ramanathan, T. (1997) *Medicinal Plants of Parangipettai Coast*, Monograph, Annamalai University, Parangipettai, India.

Khatua, S. and Acharya, K. (2016) 'Influence of extraction parameters on physico-chemical characters and antioxidant activity of water soluble polysaccharides from *Macrocybe gigantea* (Massee) Pegler & Lodge', *Journal of Food Science and Technology*, Vol. 53, No. 4, pp.1878–1888, DOI: 10.1007/s13197-015-2145-0.

Kimling, J., Maier, M., Okenve, B. et al. (2006) 'Turkevich method for gold nanoparticle synthesis revisited', *The Journal Physical Chemistry B*, Vol. 110, pp.15700–15707, DOI: 10.1021/jp061667w.

Magudapathy, P. and Gangopadhyay, P. (2001) 'Electrical transport studies of Ag nanoclusters embedded in glass matrix', *Physica B: Condensed Matter*, Vol. 299, Nos. 1/2, pp.142–146, DOI: 10.1016/S0921-4526(00)00580-9.

Maity, G.N., Sarkar, J., Khatua, S. et al. (2019) 'Green synthesis of silver nanoparticles using mangrove fruit polysaccharide for bacterial growth inhibition', *Asian Journal of Pharmaceutical Clinical Research*, Vol. 12, No. 7, pp.179–183.

Masuko, T., Minami, A., Iwasaki, N. et al. (2005) 'Carbohydrate analysis by a phenol-sulfuric acid method in microplate format', *Analytical Biochemistry*, Vol. 339, No. 1, pp.69–72, DOI: 10.1016/j.ab.2004.12.001.

Mecozzi, M. (2005) 'Estimation of total carbohydrate amount in environmental samples by the phenol-sulphuric acid method assisted by multivariate calibration', *Chemometrics and Intelligent Laboratory Systems*, Vol. 79, Nos. 1/2, pp.84–90, DOI: 10.1016/j.chemolab. 2005.04.005.

Mohammadlou, M., Maghsoudi, H. and Jafarizadeh-Malmiri, H. (2016) 'A review on green silver nanoparticles based on plants: synthesis, potential applications and eco-friendly approach', *International Food Research Journal*, Vol. 23, No. 2, pp.446–463.

Nabeel, M.A., Kathiresan, K. and Manivannan, S. (2010) 'Antidiabetic activity of the mangrove species Ceriops decandra in alloxan-induced diabetic rats', *Journal of Diabetes*, Vol. 2, No. 2, pp.97–103, DOI: 10.1111/j.1753-0407.2010.00068.x.

Rai, M., Yadav, A. and Gade, A. (2009a) 'Silver nanoparticles as a new generation of antimicrobials', *Biotechnology Advances*, Vol. 27, No. 1, pp.76–83.

Rai, M., Yadav, P., Bridge, P. and Gade, A. (2009b) 'Myconanotechnology: a new and emerging science', in Rai, M. and Bridge, P. (Eds.): *Applied Mycology*, pp.258–267, CABI Publication, UK.

Railean-Plugaru, V., Pomastowski, P., Wypij, M. et al. (2016) 'Study of silver nanoparticles synthesized by acidophilic strain of *Actinobacteria* isolated from the of *Picea sitchensis* forest soil', *Journal of Applied Microbiology*, Vol. 120, pp.1250–1263, DOI: 10.1111/jam.13093.

Rajeshkumar, S.R. (2016) 'Synthesis of Ag-NP using fresh bark of *Pongamia pinnata* and characterization of its antibacterial activity against gram positive and gram negative pathogens', *Resource-Efficient Technologies*, Vol. 2, No. 1, pp.30–35.

Ravikumar, S., Gnanadesigan, M., Suganthi, P. and Ramalakshmi, A. (2010) 'Antibacterial potential of chosen mangrove plants against isolated urinary tract infectious bacterial pathogens', *International Journal of Medicine and Medical Sciences*, Vol. 2, No. 3, pp.94–99.

Saha, S., Khatua, S., Paloi, S. and Acharya, K. (2013) 'Antioxidant and nitric oxide synthase activation properties of water soluble polysaccharides from *Pleurotus florida*', *International Journal of Green Pharmacy*, Vol. 7, pp.182–188, DOI: 10.4103/0973-8258.120190.

Saha, S., Sarkar, J., Chattopadhyay, D. et al. (2010) 'Production of silver nanoparticles by a phytopathogenic fungus *Bipolaris nodulosa* and its antimicrobial activity', *Digest Journal of Nanomaterials and Biostructures*, Vol. 5, No. 4, pp.887–895.

Sakagami, H., Kashimata, M., Toguchi, M. et al. (1998) 'Radical modulation activity of lignins from a mangrove plant, Ceriops decandra (Griff.) Ding Hou', *In Vivo (Brooklyn)*, Vol. 12, No. 3, pp.327–332.

Sanghi, R. and Verma, P. (2009) 'Biomimetic synthesis and characterisation of protein capped silver nanoparticles', *Bioresource Technology*, Vol. 100, No. 1, pp.501–504, DOI: 10.1016/j.biortech.2008.05.048.

Sanyasi, S., Majhi, R.K., Kumar, S. et al. (2016) 'Polysaccharide-capped silver nanoparticles inhibit biofilm formation and eliminate multi-drug-resistant bacteria by disrupting bacterial cytoskeleton with reduced cytotoxicity towards mammalian cells', *Scientific Reports*, Vol. 6, DOI: 10.1038/srep24929.

Sarkar, J. and Acharya, K. (2017) '*Alternaria alternata* culture filtrate mediated bioreduction of chloroplatinate to platinum nanoparticles', *Synthesis and Reactivity in Inorganic Metal-Organic and Nano-Metal Chemistry*, Vol. 47, No. 3, pp.365–369, DOI: 10.1080/15533174.2016.1186062.

Sarkar, J., Chattopadhyay, D., Patra, S. et al. (2011a) '*Alternaria alternata* mediated synthesis of protein capped silver nanoparticles and their genotoxic activity', *Digest Journal of Nanomaterials and Biostructures*, Vol. 6, pp.563–573.

Sarkar, J., Dey, P., Saha, S. and Acharya, K. (2011b) 'Mycosynthesis of selenium nanoparticles', *Micro & Nano Letters*, Vol. 6, No. 8, pp.599–602, DOI: 10.1049/mnl.2011.0227.

Sarkar, J., Ghosh, M., Mukherjee, A. et al. (2014) 'Biosynthesis and safety evaluation of ZnO nanoparticles', *Bioprocess and Biosystems Engineering*, Vol. 37, No. 2, pp.165–171, DOI: 10.1007/s00449-013-0982-7.

Sarkar, J., Mollick, M.M.R., Chattopadhyay, D. and Acharya, K. (2017) 'An eco-friendly route of γ-Fe_2O_3 nanoparticles formation and investigation of the mechanical properties of the HPMC-γ-Fe_2O_3 nanocomposites', *Bioprocess and Biosystems Engineering*, Vol. 40, No. 3, pp.351–359, DOI: 10.1007/s00449-016-1702-x.

Sarkar, J., Ray, S., Chattopadhyay, D. et al. (2012) 'Mycogenesis of gold nanoparticles using a phytopathogen *Alternaria alternata*', *Bioprocess and Biosystems Engineering*, Vol. 35, No. 4, pp.637–643, DOI: 10.1007/s00449-011-0646-4

Sathiyanarayanan, G., Seghal Kiran, G. and Selvin, J. (2013) 'Synthesis of silver nanoparticles by polysaccharide bioflocculant produced from marine Bacillus subtilis MSBN17', *Colloids Surfaces B: Biointerfaces*, Vol. 102, pp.13–20, DOI: 10.1016/j.colsurfb.2012.07.032.

Sathyavathi, R., Krishna, M.B., Rao, S.V. et al. (2010) 'Biosynthesis of silver nanoparticles using coriandrum sativum leaf extract and their application in nonlinear optics', *Advanced Science Letters*, Vol. 3, No. 2, pp.1–6, DOI: 10.1166/asl.2010.1099.

Singh, A.K., Talat, M., Singh, D.P. and Srivastava, O.N. (2010) 'Biosynthesis of gold and silver nanoparticles by natural precursor clove and their functionalization with amine group', *Journal of Nanoparticle Research*, Vol. No. 5, pp.1667–1675, DOI: 10.1007/s11051-009-9835-3.

Socrates, G. (2004) *Infrared and Raman Characteristic Group Frequencies*, Wiley, USA.

Stojković, D., Reis, F.S., Ferreira, I.C.F.R. et al. (2013) '*Tirmania pinoyi:* Chemical composition, in vitro antioxidant and antibacterial activities and in situ control of *Staphylococcus aureu*s in chicken soup', *Food Research International*, Vol. 53, No. 1, pp.56–62, DOI: 10.1016/j.foodres.2013.03.046.

Taylor, R., Otanicar, T. and Rosengarten, G. (2012) 'Nanofluid-based optical filter optimization for PV/T systems', *Light: Science & Applications*, Vol. 1:e34, DOI: 10.1038/lsa.2012.34.

Taylor, R.A., Otanicar, T.P., Herukerrupu, Y. et al. (2013) 'Feasibility of nanofluid-based optical filters', *Applied Optics*, Vol. 52, No. 7, pp.1413–1422, DOI: 10.1364/AO.52.001413.

Uddin, S.J., Shilpi, J.A., Barua, J. and Rouf, R. (2005) 'Antinociceptive activity of *Ceriops decandra* leaf and pneumatophore', *Fitoterapia*, Vol. 76, No. 2, pp.261–263, DOI: 10.1016/j.fitote.2004.12.015.

Vasquez, R.D., Apostol, J.G., De Leon, J.D. et al. (2016) 'Polysaccharide-mediated green synthesis of silver nanoparticles from *Sargassum siliquosum* J.G. Agardh: assessment of toxicity and hepatoprotective activity', *Open Nano*, Vol. 1, pp.16–24, DOI: 10.1016/j.onano.2016.03.001.

Ydollahi, M., Ahari, H. and Anvar, A.A. (2016) 'Antibacterial activity of silver-nanoparticles against *Staphylococcus aureus*', *African Journal of Microbiology Research*, Vol. 10, No. 23, pp.850–855, DOI: 10.5897/AJMR2016.7908.

Zhao, H-Q., Aisa, H.A., Rasulov, B. et al. (2016) 'Synthesis of Ag-NP on the basis of low and high molar mass exopolysaccharides of *Bradyrhizobium japonicum* 36 and its antimicrobial activity against some pathogens', *Folia Microbiologica*, Vol. 61, No. 4, pp.283–293, DOI: 10.1007/s12223-015-0436-5.

Abbreviations

Ag	Silver
Ag-NP	Silver nanoparticles
$AgNO_3$	Silver nitrate
BSA	Bovine serum albumin
DLS	Dynamic light scattering
EDX	Energy dispersive X-ray
FTIR	Fourier transform infrared,
GC-MS	Gas chromatography-mass spectrometry
MIC	Minimum inhibitory concentration
KBr	Potassium bromide
SAED	Selected area electron diffraction
SPR	Surface plasmon resonance
TEM	Transmission electron microscopy
XRD	X-ray diffraction
UV-Vis	UV-Visible

Source details

Feedback > Compare sources >

Asian Journal of Pharmaceutical and Clinical Research

Scopus coverage years: from 2009 to 2018

(coverage discontinued in Scopus)

Publisher: Asian Journal of Pharmaceutical and Clinical Research

ISSN: 0974-2441 E-ISSN: 2455-3891

Subject area: Pharmacology, Toxicology and Pharmaceutics: Pharmaceutical Science | Medicine: Pharmacology (medical) | Pharmacology, Toxicology and Pharmaceutics: Pharmacology

Source type: Journal

View all documents > | Set document alert | Save to source list

CiteScore 2017
0.6

SJR 2019
0.139

SNIP 2021
0.520

CiteScore | CiteScore rank & trend | Scopus content coverage

nanomaterials

MDPI

Article

Green Synthesized Copper Oxide Nanoparticles Ameliorate Defence and Antioxidant Enzymes in *Lens culinaris*

Joy Sarkar [1,†], Nilanjan Chakraborty [2,†], Arindam Chatterjee [3], Avisek Bhattacharjee [2], Disha Dasgupta [2] and Krishnendu Acharya [4,*]

1 Department of Botany, Dinabandhu Andrews College, Garia, Kolkata 700084, India; jsarkar80@gmail.com
2 Department of Botany, Scottish Church College, Kolkata 700006, India; nilanjanchak85@gmail.com (N.C.); avisek0007@gmail.com (A.B.); dishadasgupta5@gmail.com (D.D.)
3 Department of Botany, University of Kalyani, Kalyani, Nadia 741235, India; arindamchatterjee206@gmail.com
4 Molecular and Applied Mycology and Plant Pathology Laboratory, Centre of Advanced Study, Department of Botany, University of Calcutta, Kolkata 700019, India
* Correspondence: kabot@caluniv.ac.in or krish_paper@yahoo.com; Tel.: +91-801-316-7310
† These authors contributed equally to this work.

Received: 26 December 2019; Accepted: 16 January 2020; Published: 12 February 2020

Abstract: Biosynthesis of copper oxide nanoparticles (CuONPs) in a cost-effective and eco-friendly way has gained its importance. CuONPs has been prepared from copper sulfate by using *Adiantum lunulatum* whole plant extract. CuONPs have been characterized by X-ray diffraction, Fourier transform infrared spectroscopic, transmission electron microscope, etc. Mono-disperse, spherical, pure, and highly stable CuONPs have formed with an average diameter of 6.5 ± 1.5 nm. Biosynthesized CuONPs at different concentrations were applied to seeds of *Lens culinaris*. Physiological characteristics were investigated in the germinated seeds. Roots obtained from the seeds treated with 0.025 mgmL^{-1} concentration of CuONPs showed highest activity of different defence enzymes and total phenolics. However, at higher concentration it becomes close to control. It showed gradual increase of antioxidative enzymes, in accordance with the increasing dose of CuONPs. Likewise, lipid peroxidation and proline content gradually increased with the increasing concentration. Reactive oxygen species and nitric oxide generation was also altered due to CuONPs treatment indicating stress signal transduction. Finally, this study provides a new approach of the production of valuable CuONPs, is a unique, economical, and handy tool for large scale saleable production which can also be used as a potent plant defence booster instead of other commercial uses.

Keywords: *Adiantum lunulatum*; antioxidative enzymes; copper oxide nanoparticles; defence enzymes; reactive oxygen species; nitric oxide; transmission electron microscope

1. Introduction

Copper (Cu) is one of the indispensable microelements obligatory for the growth and development of plant. It can be present as Cu^{2+} and Cu^{+} under natural conditions. Optimum concentration is regularly involved in the plants, ranging from 10^{-14} to 10^{-16} M. In addition to many of its important functions such as cell wall metabolism and protein regulation, it also acts as secondary signaling molecule in plant cells. It takes part in the mitochondrial respiration, photosynthetic electron transport, iron mobilization, hormone signaling, oxidative stress response, and also acts as cofactor for many enzymes [1,2]. However, a higher dose of Cu leads to oxidative stress generation, growth inhibition, cellular malfunctioning, and photosynthesis retardation [2–4].

Though, nanotechnology is considered to be the next industrial revolution, the search is still ongoing for better nontoxic, hazard free, and eco-friendly approach for synthesis of nanomaterials [5]. In comparison to chemically synthesized nanoparticles, green synthesized nanoparticles are more effective and eco-friendly [6]. Until now various biological organisms are reported to have their potentiality for the production of metallic nanoparticles. However, the rate of metal nanoparticle synthesis with the help of plant extract is stable [7], much faster [8,9], and extremely mono-dispersive [10] in respect to other biological methods. Moreover, in the case of copper, different organisms suchas microbes [11,12], algae [13], fungi [14,15], and angiosperm plant extracts [16,17], are utilized for the nanoparticles production.

Among other cryptograms, algae [7] and bryophytes [18] are quite popular to fabricate metal nanoparticles. However, potentiality of different pteridophytes (fern and fern allied species) for the production of nanoparticles is less surveyed. Until now only few species such as *Pteris tripartite* [19], *Adiantum capillus-veneris* [20], *A. caudatum* [21], *A. philippense* [22,23], *Asplenium scolopendrium* [24], *Actinopteris radiata* [25], *Azolla microphylla* [26], etc. have been used.

Although previously there are some reports where some ferns are considered to be poisonous and carcinogenic for the animals [27]. However, our choice of interest, *Adiantum lunulatum* Burm. f. is popular due to its antimicrobial [28], antioxidant [29], and other medicinal properties. The plant extract may act as an anti-hyperglycemic [30] and also have some curative role against influenza and tuberculosis [31]. The plant is a rich source of various terpenoids, carbohydrates, phenols, and flavonoids [29,32,33].

On the other hand, despite other inorganic applications, nanomaterials are utilized as an antimicrobial agent and defence booster in the field of agriculture. Recently, we have reported the effect of chitosan nanoparticles as an inducer of innate immunity in tea [34]. Recent research on nanoparticles in a number of crops such as corn, wheat, ryegrass, alfalfa, soybean, tomato, radish, lettuce, spinach, onion, pumpkin, bitter melon, and cucumber have provided evidence of enhanced seedling growth, germination, photosynthetic activity, nitrogen metabolism, protein level, mRNA expression, and changes in gene expression indicating their potential use for crop improvement.

In this context, here, an attempt has been made to synthesize copper oxide nanoparticles in an eco-friendly, greener route by using the important fern *Adiantum lunulatum*. The potentiality of this CuONPs in the induction of defence and generation of stress has also been checked in a model plant *Lens culinaris*.

2. Materials and Methods

2.1. Collection and Identification of Plant Material

The fresh plant was collected from the Rajpur-Sonarpur Municipality area (22.4491° N, 88.3915° E) of the district South 24 Parganas, West Bengal, India. The respective plant specimen was self-identified and binomially jointly by Pteridology and Paleobotany Lab, Department of Botany, University of Kalyani, Kalyani, Nadia, West Bengal, India, Pin-741235 and Department of Botany, Dinabandhu Andrews College, Garia, Kolkata, West Bengal, India, Pin-700084. Voucher specimens were prepared from the collected specimens and further deposited both at the Herbarium of the Botany Department, University of Kalyani, as well as Herbarium of the Botany Department, Dinabandhu Andrews College, Kolkata.

2.2. Preparation of Plant Extract

The whole plant was rinsed with tap water and distilled water, respectively. The superficial water was soaked from the plant surface. Fiveg of the desiccated plant material was homogenized in mortar and pestle into a paste. After that, 100 mL of distilled water was mixed to that paste [22]. Filtration of the crude solution was done thrice by Whatman filter paper no.1. Finally, the filtrate was collected all together for future reference.

2.3. Green Synthesis of Copper Oxide Nanoparticles

For the production of copper oxide nanoparticles, the plant extract was used to reduce copper sulfate ($CuSO_4$-1 mM). The substrate was mixed with the plant extract (ratio: 1:5, *v*/*v*) and stirred constantly for at least 1 h [35,36]. Simultaneously, a positive control set (only the plant extract of *A. lunulatum*) and a negative control set (only the copper sulfate solutions without plant extract) was also maintained at a similar experimental condition. The reaction mixtures were regularly monitored and the color change was recorded properly. The reactions were performed under normal room temperature (37 °C) at pH 9 (optimum).

The whole preparation was centrifuged at 12,000× *g* for 15 min and the pellet containing nanoparticles were washed (three times) with deionized water. The purified CuONPs were resuspended in deionized water and ultra-sonicated by a Piezo-u-sonic ultrasonic cleaner (Pus-60w) and kept at normal room temperature (37 °C) [35].

2.4. Characterization of Copper Nanoparticles

2.4.1. UV–Visible Spectroscopy of Synthesized Nanoparticles

Plant extract mediated biosynthesized nanoparticles had been observed under a Hitachi 330 spectrophotometer with plasmon peaks at different regions of the spectral range 200–900 nm, which corresponded to different signature marks for the production of different nanoparticles, respectively [37]. Deionized water was used as reference.

2.4.2. Particle Size Measurement by Dynamic Light Scattering (DLS) Experiment

By laser diffractometry, particle size was measured using a nano-size particle analyzer (Zen 1600 Malvern USA) in the range between 0.6 and 6.0 µm, under such conditions such as having particle refractive index 1.590, particle absorption coefficient 0.01, water refractive index 1.33, viscosity—cP, Temperature-25 °C and general calculation model for irregular particles. About 10−15 measurement cycles of 10 s each were taken and the data obtained were averaged by the respective instrument preloaded software (DTS, version 5.00 from Malvern) [38].

2.4.3. Transmission Electron Microscopic (TEM) Observation of Nanoparticles

Morphological and topographical characterization of the nanoparticles had been well established by the electron microscopic studies [39]. On a carbon coated copper grid thin films of the synthesized nanoparticles were prepared (30 × 30 µm mesh size) and a drop of the nanoparticle suspension was spotted on the grid. Excess solution was removed by using blotting paper. It was allowed to dry under a mercury lamp for 5 min. The micrographs were obtained by Tecnai G2 spirit Biotwin (FP 5018/40) instrument, operating at around 80 kV accelerating voltage [14].

2.4.4. Zeta Potential Measurement

Using Beckman Coulter DelsaTM Nano Particle Analyzer (USA) zeta potential (Charge distribution) of the nanoparticles was investigated by illuminating the solution with He–Ne laser (658 nm) in a sample cell. Using phase analysis light scattering mode measurements were taken with an Ag electrode [40].

2.4.5. Investigation of Elemental Compositions of the Nanoparticles by Energy Dispersive Spectroscopy (EDX)

A small amount of the sample was taken in glass slide creating a thin layer of sample. Extra solution was rinsed using a blotting paper and then the sample was allowed to dry overnight [41]. This analysis of the samples was carried out by using the Hitachi S 3400N instrument. The spectra were recorded.

2.4.6. XRD Measurement

Crystallinity of forged CuONP was confirmed and determined by XRD analysis. The XRD sample was all set on a microscopic glass slide by depositing the centrifuged sample and thereafter dried at 45 °C in a vacuum drying oven overnight. The vacuum dried CuONPs were then used for powder X-ray diffraction analysis.

The diffractogram was documented from PANalytical, XPERTPRO diffractometer using Cuk (Cu Kα radiation, λ 1.54443) as X-ray source running at 45 kV and 30 mA [42]. The diffracted intensities were noted from 35 to 99° 2θ angles [43].

2.4.7. Fourier Transform Infrared Spectroscopic (FTIR) Analysis

The vacuum dried inorganic metal nanoparticles of culture filtrate were mixed up separately with potassium bromide (KBr), alkali halide at a ratio of 1:100 (*w*/*w*). The two materials were ground to a fine powder in a mortar and pestle separately. Then, the mixture was poured into a pellet press consisting of two pistons in a smooth cylindrical chamber. Pressure of up to 25,000 psi was then applied for different amounts of time in a vacuum. After that the pistons were removed and the clear pellet was placed in a holder of the spectrophotometer. Since the KBr did not absorb infrared radiation in the region 4000 and 400 cm^{-1} a complete spectrum of the solid was obtained [44]. The spectra were recorded with a Shimadzu 8400SFourier transform infrared spectrophotometer using a diffuse reflectance accessory. The scanning data were obtained from the average of 50 scans in the range between 4000 and 400 cm^{-1} [45,46].

2.5. Effects of CuONP on Seedling Germination and Seedling Development

Lens culinaris Medik was selected as a model plant system to investigate the effects of CuONPs. Seeds of *Lens culinaris* were washed with tap water to remove dirt from seed coats. Then, those seeds were soaked in separate petri-dishes containing water (Control) and three different concentrations of CuONPs (viz. 0.01, 0.025, and 0.05 $mgmL^{-1}$, and kept in the dark for 72 h at 30 ± 2 °C. All the dilutions of CuONPs were prepared from the 1 $mgmL^{-1}$ stock. For each petridish 50 seeds were incubated. After the incubation of three days the seedlings root length and germination percentage was calculated of all the samples [40].

Vigor index of each experimental setup was calculated using the following formula:

$$\text{Vigor index (VI)} = \text{Germination percent (\%)} \times \text{Seedling growth (mm)}.$$

2.6. Determination of Water Content (WC) and Relative Water Content (RWC)

After four days of germination, fresh weights (FW) of roots from different sets were taken. Then, the roots were immersed in water overnight for turgid weight (TW). It was then ovendried at 100 °C to constant weight and reweighed for the dry weight (DW).

WC was estimated on the FW basis. RWC was determined using the method of [47] and calculated using the following formula:

$$\text{RWC} = [(\text{FW} - \text{DW})/(\text{TW} - \text{DW})] \times 100$$

Roots of the samples were taken for biochemical and molecular determinations as described below.

2.7. Enzyme Extraction and Assays

Fresh root samples (500 mg) were homogenized with 2 mL of 0.1 M sodium phosphate buffer (pH 7.0) containing 0.1% of polyvinyl pyrrolidone (PVP) and 20 µL of 0.05 mM phenyl methane sulfonyl fluoride (PMSF). The extract was centrifuged at 10,000× *g* for 15 min at 4 °C and the supernatant was used to assay the enzyme.

2.7.1. Peroxidase Assay (PO)

The peroxidase (PO) activity was determined by the method of Hemada and klein [48] with few changes. The reaction mixture was prepared with 2.99 mL of substrate (adding 5 mL of 1% guaiacol, 5 mL of 0.3% H_2 O_2 mixing, and 50 mL of 0.05 M sodium phosphate buffer) and 0.01 mL of enzyme extract, and the absorption change was measured at 470 nm in a UV–Vis spectrophotometer (Intech, India) for 0–2 min at 30 s interval. The peroxidase activity was determined by the increase in absorbance and expressed as $\mu molmin^{-1}mg^{-1}$ protein.

2.7.2. Polyphenol Oxidase Assay (PPO)

The polyphenol oxidase (PPO) activity was determined by the method of Kumar and Khan [49] with slight modifications. The reaction mixture was prepared by adding 2 mL of 0.1 M sodium phosphate buffer (pH 6.5), 1 mL of 0.1 M catechol, 0.5 mL of crude enzyme extract and incubated for 10 minat room temperature, and the reaction was ceased by adding 1 mL of 2.5 N H_2SO_4. The absorption was measured at 495 nm against a blank set. The PPO activity was taken in U $min^{-1}mg^{-1}$ protein. (U = change in 0.1 absorbance $min^{-1}mg^{-1}$ tissue).

2.7.3. Phenylalanine Ammonia Lyase (PAL)

Following the same tissue homogenizing procedure for phenylalanine ammonia lyase (PAL) assay a sodium borate buffer (pH 8.7) with PVP and PMSF was used. The method of Dickerson et al. [50] was used for PAL activity to determine the rate of conversion of L-phenylalanine to Transcinnamic acid at 290 nm. The reaction mixture was prepared by adding substrate (1.3 mL of 0.1 M borate buffer, pH 8.7 and 0.5 mL of 12 mM L-phenyl alanine) with 0.2 mL of enzyme and incubated for 30 min at room temperature. The amount of Transcinnamic acid synthesized was measured at 290 nm. Enzyme activity was expressed as nmol of transcinnamic acid $min^{-1}g^{-1}$ protein.

2.7.4. β-1,3 glucanase Assay

β-1,3 glucanase activity was assayed using the laminarin dinitrosalicylate method of Pan et al. [51] with minor changes. Root tissues were homogenized in 2 mL of 0.05 M sodium acetate buffer and centrifuged at 10,000× *g* for 15 min at 4 °C. Fifty µL of enzyme and an equal amount of laminarin (1%) was mixed and incubated for 30 min in a 2 mL microcentrifuge tube and at the end of 30 min 0.3 mL of dinitrosalicylic acid reagent was added and boiled for 5 min in water bath. Blank set was prepared in a similar way without mixing of any enzyme in the reaction mixture. Finally, the volume of all the heated microcentrifuge tubes was made to 2 mL by adding distilled water. The microcentrifuge tubes were inverted to mix well and absorption was measured at 520 nm. The enzyme activity was expressed as µmol of glucose released $min^{-1}g^{-1}$ protein.

2.7.5. Ascorbate Peroxidase Assay (APX)

Ascorbate peroxidase (APX) activity was determined by following the method of Nakano and Asada [52]. The reaction mixture was prepared by adding 2.9 mL of substrate (containing 50 mM potassium phosphate buffer with pH 7.0, 0.5 mM ascorbic acid, 0.2 mM EDTA, and 2% H_2O_2), and 0.1 mL of enzyme extract in a final volume of 3 mL.A decrease in absorbance at 290 nm for 1 min was recorded and using extinction coefficient (ϵ = 2.8 mM^{-1}APX was defined as 1 $mmolmL^{-1}min^{-1}cm^{-1}$) the amount of oxidized ascorbate was calculated as $\mu molmin^{-1}g^{-1}$ protein.

2.7.6. Catalase Assay (CAT)

Catalase (CAT) assay was determined spectrophotometrically using the method of Cakmak and Horst [53]. The reaction mixture contains 50 µL of H_2O_2 (0.3%) with 0.1 mL of enzyme extract and the final volume was made up to 3 mL by adding 50 mM phosphate buffer (pH 7.0). The decrease in

absorbance was taken for 0–2 min at 240 nm. The CAT activity was expressed as nmol $min^{-1}g^{-1}$ of protein using Molar extinction coefficient, ϵ = 39,400 $mM^{-1}cm^{-1}$.

2.7.7. Superoxide Dismutase Assay (SOD)

Activity of superoxide dismutase (SOD) was determined by measuring its ability to inhibit photochemical reduction of nitro blue tetrazolium (NBT) [54]. The reaction mixture contains 0.7 mL of 0.2 M sodium phosphate buffer (pH 7.8), 390 µL of methionine, 300 µL of EDTA (1 mM), 1.2 mL of water, 100 µL of crude enzyme extract, 250 µL of nitroblue tetrazolium (NBT), and 6 µL of riboflavin. Blank was prepared without any enzyme. Two sets were taken and one was incubated in bright light for 10 min and other one was incubated in the dark· After incubation readings were taken at 560 nm, enzyme activity was expressed as percentage of color inhibition mg protein g^{-1}.

2.8. Estimation of Total Protein Content

Total protein content of the sample was determined using the method of Lowry et al. [55]. The reaction mixture contains 100 µL of extract and volume was made to 1 mL by adding distilled water. Then, 5 mL of Lowry's reagent was added and incubated for 15 min at room temperature. After this 500 µL of Folinciocalteu reagent was added and incubated in the dark for 30 min, blank sets were taken similarly as absorption was measured at 680 nm. Using the standard curve of BSA solution the amount of protein was calculated and estimated protein was expressed as mg protein g^{-1} of the fresh root sample.

2.9. Estimation of Total Phenol Content

Total phenol content was estimated using the method of Zieslin and Benzaken [56] with minor changes. Fresh tissues were homogenized in 2 mL of 80% methanol and maintained for 15 min in water bath at 65 °C, then centrifuged at 10,000× *g* for 10 min at room temperature. The supernatant was used to estimate phenol. The reaction mixture contains 1 mL of extract, 5 mL of distilled water, and 250 µL of 1N Folinciocalteu reagent was added and incubated for 30 min at room temperature. Phenol content was measured spectrophotometrically at 725 nm using gallic acid as standard. The amount of total phenol content was expressed as µg gallic acid produced g^{-1} tissue.

2.10. Estimation of Flavonoid Content

The amount of total flavonoid content of the root material was determined using the method of Chang et al. [57]. Fresh tissues were homogenized in 2 mL of 80% ethanol and maintained for 30 min in the dark, then it was centrifuged at 10,000× *g* for 5 min at room temperature. The reaction mixture was prepared with 1 mL of crude extract mixed with 4.3 mL of 80% aqueous ethanol, 0.1 mL of 10% aluminium nitrate, and 0.1 mL of 1 M aqueous sodium acetate and kept in the dark for 30 min. The absorption of the coloured sample was measured at 415 nm against blank sample in a spectrophotometer. The amount of total flavonoid was expressed as µg quercetin g^{-1} fresh tissue.

2.11. Determination of Lipid Peroxidation Rate

Using the method of Cakmak and Horst [53], the rate of lipid peroxidation was determined by estimating 2-thiobarbituric acid reactive substances (TBARS) with some modifications. Root samples were grounded in 5 mL of 0.1% (*W*/*V*) trichloroacetic acid (TCA) at 4 °C and centrifuged at 12,000 rpm for 5 min. An aliquot of 1 mL from the supernatant was mixed with 4 mL of 0.5% (*W*/*V*) thiobarbituric acid (TBA) in 20% (*W*/*V*) TCA. Blank set was prepared using distilled water instead of extract. All the reaction mixtures were heated at 90 °C for 30 min. The reactions were stopped in an ice bath and the mixtures were centrifuged at 10,000× *g* for 5 min and the absorbance was taken at 532 nm on a spectrophotometer and corrected for nonspecific turbidity by subtracting the absorbance at 600 nm.

The formula was applied to calculate malondialdehyde content using its absorbent coefficient (ϵ) and using the following formula nmolmalondialdehyde g^{-1} fresh mass was calculated.

$$\text{MDA (nmol } g^{-1} \text{ FM)} = [(A532 - A600) \times V \times 1000/\epsilon] \times W$$

Here, ϵ is the specific extinction coefficient (=155 $mMcm^{-1}$), V is the volume of crushing medium, W is the fresh weight of sample, and A532, A600 are the absorbance at 532 and 600 nm, respectively.

2.12. Estimation of Total Proline Content

Using the protocol of Bates et al. [58], the free proline content of samples was determined. Three hundred and fiftymg of root tissues was grounded in 3.5 mL of 3% sulphosalicylic acid in chilled mortar pestle and centrifuged at 11,000× *g* for 15 min at 4 °C. The reaction mixture was prepared with 1 mL of crude extract, 1 mL of 0.5% ninhydrin reagent, and 1 mL of glacial acetic acid. The mixture was boiled for 30 min in a water bath. After cooling it down, 3 mL of toluene was added and shaken. The mixture and upper layer of toluene was collected using a separating funnel. The absorption of the sample was taken at 520 nm against toluene. The amount of proline was determined using standard curve and expressed as μg of proline g^{-1} of tissue.

2.13. Estimation of Nitric Oxide (NO)

Real time NO production was visualized using a DAF-2DA membrane permeable fluorochrome dye [59]. Thin sections of roots were taken in loading buffer and 50 μL of 10 mM KCl and 50 μL of 10 mM TrisHCl (pH 7.2) with final concentration of DAF-2DA 10 mM were added and incubated in the dark for 20 min. Fluorescence was observed and high resolution images were taken using Floid Cell Imaging station microscope by Life technologies. Green fluorescence indicates the production of NO.

2.14. Measurement of Reactive Oxygen Species (ROS)

ROS generation was monitored according to the method of Gupta et al. [60]. To measure ROS, thin transverse sections of treated roots were immersed in the 1 mL of detection buffer DB (2.5 mM HEPES, pH 7.4) containing 10 μM DCF-2DA fluorescent dye (Invitrogen, Carlsbad, CA, USA), and it was kept for 10 min in dark incubation. The high-resolution images were checked using Floid Cell Imaging station microscope by Life technologies.

2.15. In Vivo Detection of H_2O_2

In vivo detection of H_2O_2 of root samples was carried out using DAB by following the method of Thordal-Christensen et al. [61]. After one week of germination the roots were excised and immersed in a solution containing 1 mg/mL diaminobenzidine (DAB) solution (pH 3.8) and incubated for 8 h in the dark. After that sectioning of roots were performed and the section is immersed in 3:1 (*V*/*V*) ethanol and glacial acetic acid mixture for bleaching. After that it was cleaned with water and for 24 h the sections were dipped in lactoglycerol (1:1:1, lactic acid: glycerol:water *V*/*V*). High-resolution images were taken using Floid Cell Imaging station microscope by Life technologies.

2.16. Statistics

All data presented were means ± standard deviation (SD) of three replicates. Statistical analyses were performed by an analysis of variance (ANOVA) using SPSS software version 20. Differences between treatments were separated by the least significant difference (LSD) test at a 0.05 probability level.

3. Results and Discussion

3.1. Characterization and Identification of the Plant Specimen

The plant is sub-erect to erect and rhizomatous in nature. Rachis and the body seem to be glabrous and lustrous. Entire loftiness of the plant ranges between 9–18 inches and are nonarticulated (Figure 1a). Lamina is simply pinnate, lanceolate. The stem when mature appears as brownish to dark in colour. Pinnae is finely rubbery which is deep green or pale in colour, glabrous on both sides, and counts up to 10 pairs, alternate, stalked, fan-shape [62,63] (Figure 1b). Pattern of the pinnae venation is dichotomous [63] (Figure 1d). Sporophylls are not grouped in strobili, whereas sporangia are enclosed in sporocarps. Sori are not dorsal and have false indusium, sporangia formed in definite groups [64]. Transverse section of the stem reveals 3–4 layered sclerenchymatous ground tissue followed by parenchymatous cells. Xylems are of exarch and diarch type and it also appears to be V-shaped with two arms that are turned inwards [63,65,66] (Figure 1c). The SEM images of outer wall of spore appear to be rugulate which confirmed the species [67] (Figure 1e–g). Hence, conclusion made from the above recommendations identifies the specimen to be *Adiantum lunulatum* Burm. f. (*A. philippense* Linn.) of the family *Pteridaceae* [68].

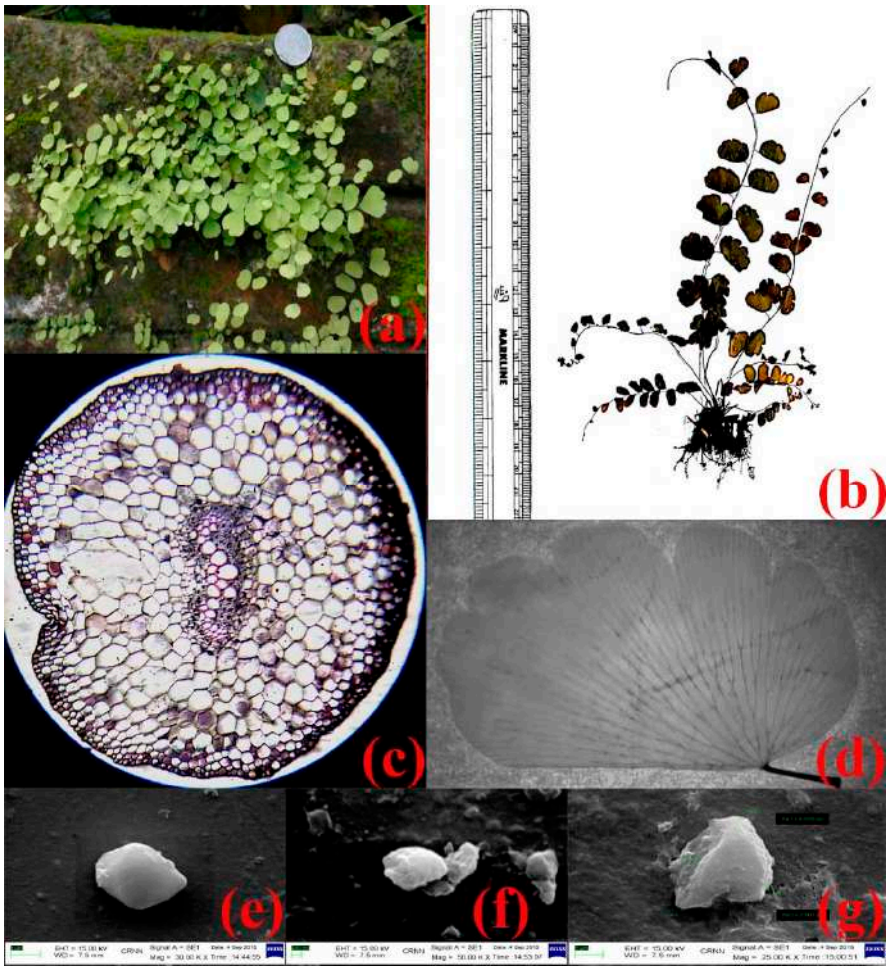

Figure 1. (**a**) Digital photograph of the sporophyte of *Adiantum lunulatum* Burm. f., (**b**) Photograph of the Herbarium Specimen of *A. lunulatum*, (**c**) transverse section of the stem of *A. lunulatum*, (**d**) venation pattern of the leaf of *A. lunulatum*, (**e**–**g**) scanning electron microscopic images of the spores of *A. lunulatum*.

3.2. Production and Characterization of Copper Oxide Nanoparticles

The plant extract mediated synthesis of copper oxide nanoparticles was validated by visually monitoring three flasks containing the copper sulfate solution, plant extract of *A. lunulatum*, and the reaction mixture of the plant extract with copper sulfate solution, respectively. An instantaneous change in the colour of the reaction mixture from brown to green indicated the formation of copper-containing nanoparticles [69], whereas the plant extract and the copper sulfate solution were observed to retain their original colour (Figure 2). The colour did not change further with cumulative incubation time. The appearance of intense green colour designated the incidence of the reaction and the development of the copper oxide nanoparticles [69].

(**a**) (**b**) (**c**)

Figure 2. Three conical flasks containing (**a**) only the *A. lunulatum* extract (ALE), (**b**) reaction mixture of ALE and $CuSO_4$ solution and (**c**) only $CuSO_4$ solution, respectively.

3.3. UV–Visible Spectroscopic Analysis Copper Oxide Nanoparticles

The characteristic green colour of the reaction solution was due to the excitation of the surface plasmon vibration of copper oxide particles and provided a convenient spectroscopic signature of their formation. Both the control set showed no significant color change in the same experimental conditions. The reduction of copper sulfate was subjected to spectral analysis by using the UV–Visible spectrophotometer. This showed an absorbance peak at around 270 nm (Figure 3a), which was specific for copper oxide nanoparticles [7]. The optical density at around 270 nm was 1.5 for copper oxide nanoparticles. Simultaneously, the UV–Vis spectra of plant extract (Figure 3b) did not show such type of excitation in the said region mentioned for the copper oxide nanoparticles.

3.4. Particle Size Measurement of Copper Oxide Nanoparticles

To find out the particle size of the nanoparticles the dynamic light scattering measurement was performed. Laser diffraction had shown that particle size was found in the range of 1.5–20 nm (Figure 4). The average diameter of these copper oxide nanoparticles was calculated to be 6.5 ± 1.5 nm [70].

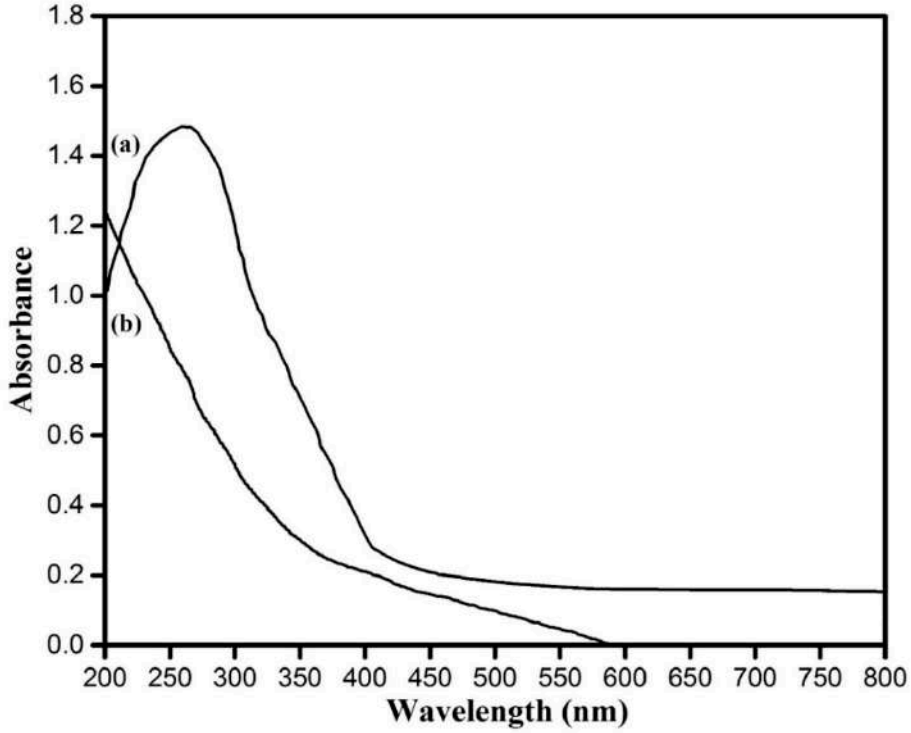

Figure 3. (a) UV–Visible spectra recorded as a function of reaction time of an aqueous solution of 1 mM $CuSO_4$ with the *A. lunulatum* extract (ALE) and (b) only *A. lunulatum* extract (ALE).

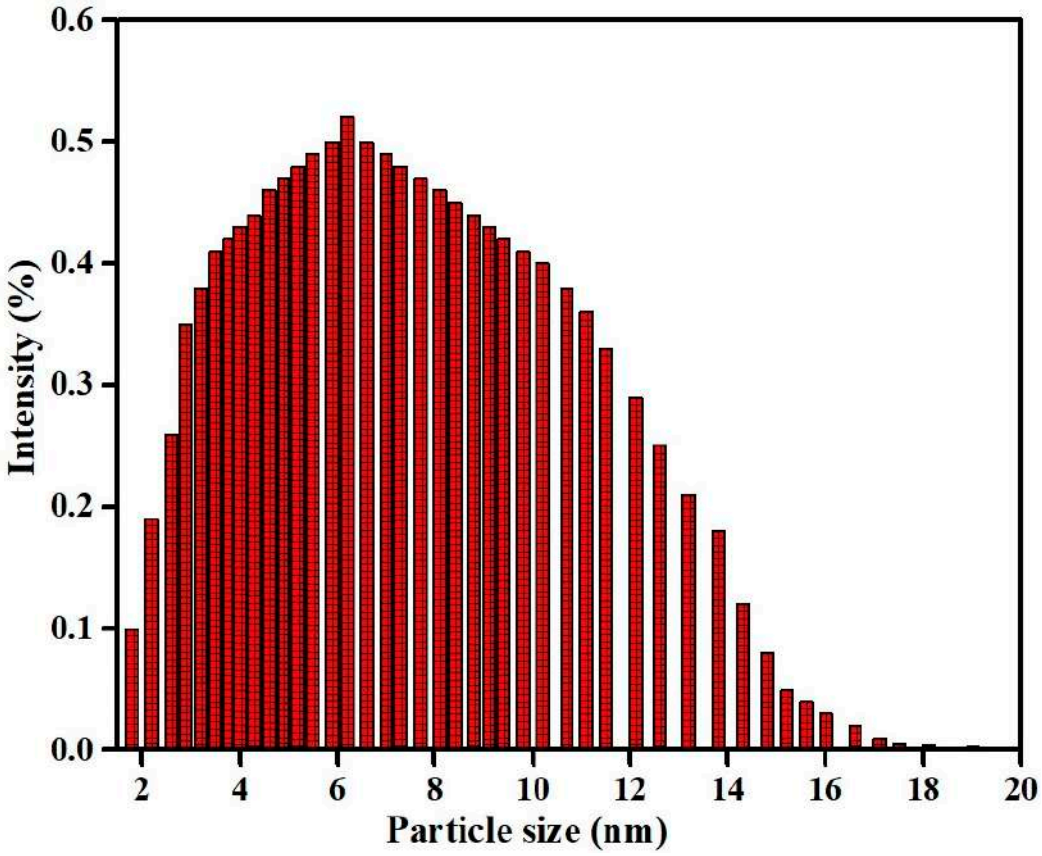

Figure 4. Histogram of particle size distribution as obtained from light scattering of the copper oxide nanoparticles produced by *A. lunulatum* extract (ALE).

3.5. Zeta Potential of Copper Oxide Nanoparticles

As shown in Figure 5, the zeta potential obtained from the copper oxide nanoparticles showed a negative surface charge with a value of −2.67 mV [71]. If all the particles in suspension have a negative or positive zeta potential, then they will tend to repel each other and there is little tendency for the particles to come together. The slightly negative charge on the nanoparticles was probably resulting in the high stability of the copper oxide nanoparticles without forming any aggregates when kept for an extended period of time for more than a month [6,72].

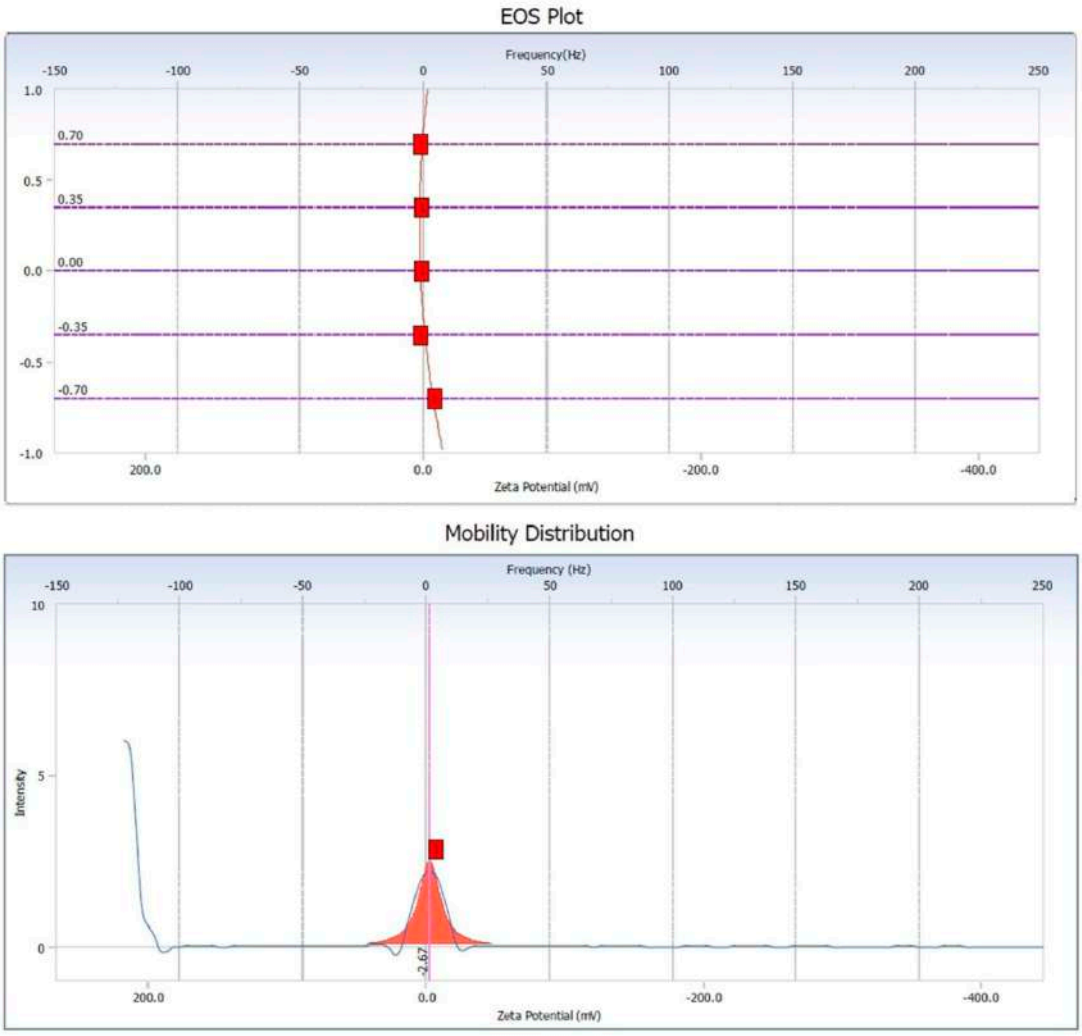

Figure 5. Zeta potential measurement of the copper oxide nanoparticles.

3.6. EDX Observation of Copper Oxide Nanoparticles

Figure 6 shows the EDX spectrum recorded in the spot-profile mode from one of the densely-populated copper oxide nanoparticles area. In EDX spectra of copper oxide nanoparticles, two separate strong signals were observed in between 0–1 keV spectral region. The peak around 0.9 keV associated with the binding energies of copper and the peak around 0.5 keV signified with the binding energies of oxygen [73]. Therefore, the EDX spectra for the copper oxide nanoparticles confirmed the presence of copper and oxygen in the nanoparticles without any impurity of peaks [73]. However, there was other EDX peak for C and S, suggesting that they were mixed precipitates from the culture filtrate [74]. The EDX spectrum also indicates the presence of chlorine (2.6 keV) for the reason that it is usually present in nanomaterials synthesized using plant extracts [75].

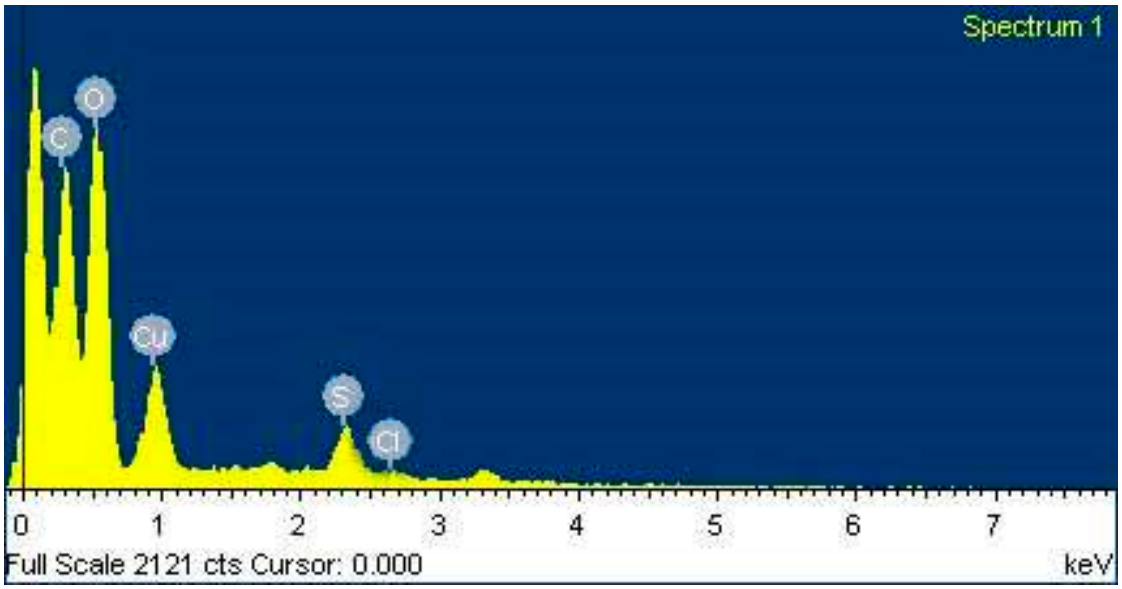

Figure 6. Energy dispersive spectrum of copper oxide nanoparticles.

3.7. XRD Study of Copper Oxide Nanoparticles

XRD measurement often proves to be a useful analytical gizmo for the identification of the crystalline nature of the newly formed compounds and their respective phases. In this present work, the XRD diffraction patterns were detected to be at 2θ = 32.35, 35.62, 38.69, 48.72, 53.49, 58.33, 61.57, and 66.31 were assigned to (110), (111), (200), (−202), (020), (202), (−113), and (022) reflection lines, respectively of monoclinic CuO nanoparticles (JCPDS-05-0661). Thus, the XRD spectrum evidently recommended the crystalline nature of the CuONP synthesized from the plant extract of *A. lunulatum* (Figure 7) [42,76]. In this measurement, a series of diffraction peaks were observed which agreed to the Bragg's reflection pattern of copper nanocrystals. The unambiguous background noise was undoubtedly due to the shell of protein around the nanoparticles [77].

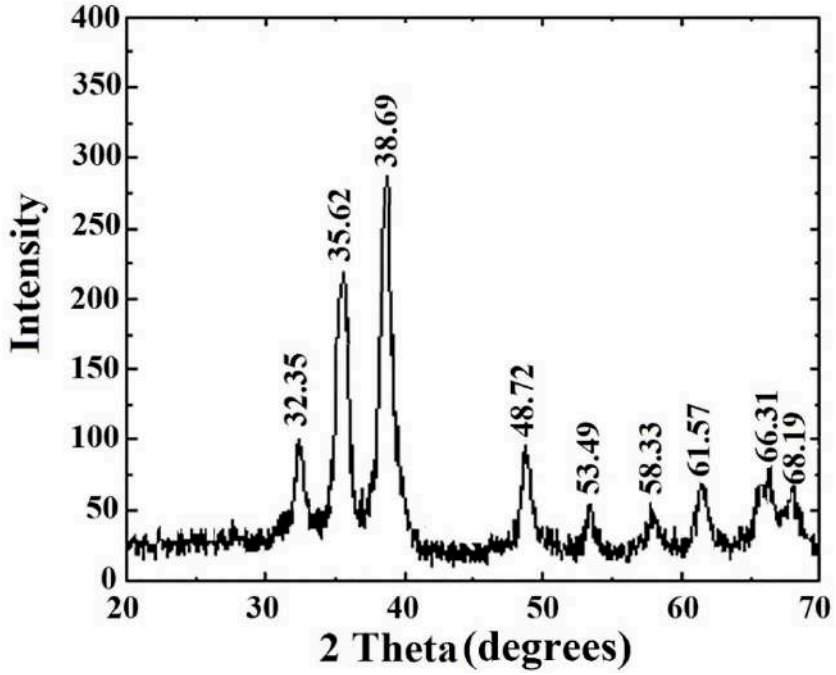

Figure 7. XRD spectrum of copper oxide nanoparticles.

3.8. FTIR Analysis of Copper Oxide Nanoparticles

FTIR absorption spectra of biosynthesized vacuum-dried copper oxide nanoparticles are shown in the Figure 8. The spectra found at around the region of 3253 and 2948 cm^{-1} presented the bonds dueto the type movements of stretching vibrations in primary and secondary amines, respectively [71]. The broad and strong absorption band at 2356 cm^{-1} corresponded to the C–H stretching aldehydes [73]. The peaks at 1439, 1538,and 1651 cm^{-1} indicated the C–C groups derived from aromatic rings, phenols, and the conjugated carbonyl (–C=O) group stretching vibration, respectively which might come from the pteridophyte cell to the plant extract [69]. The shift of the peak near the 1600 cm^{-1} spectrum was attributed to the binding of a C=O group with the nanoparticles [78]. Simultaneously, the FTIR peaks in between 1240–1280 cm^{-1} indicated amide III band of the random coil of protein [79]. A band at 1076 cm^{-1}, which corresponds to bending vibration movements in amides II, was earlier reported during the synthesis of CuS nanoparticles [80]. Three IR absorption peaks revealed the vibrational modes of CuO nanostructures in the range 700–400 cm^{-1} [81]. The foremost peaks were detected to be 525, 580, and 675 cm^{-1}, respectively. The peak at 525 cm^{-1} should be a stretching of Cu–O, which matches up to the B_{2u} mode [70,81]. The peaks at 525 and 580 cm^{-1} indicated the formation of the CuO nanostructure [6]. Absorption peaks in between 900–700 cm^{-1} were also assigned to the aromatic bending vibration of C–H group [70].

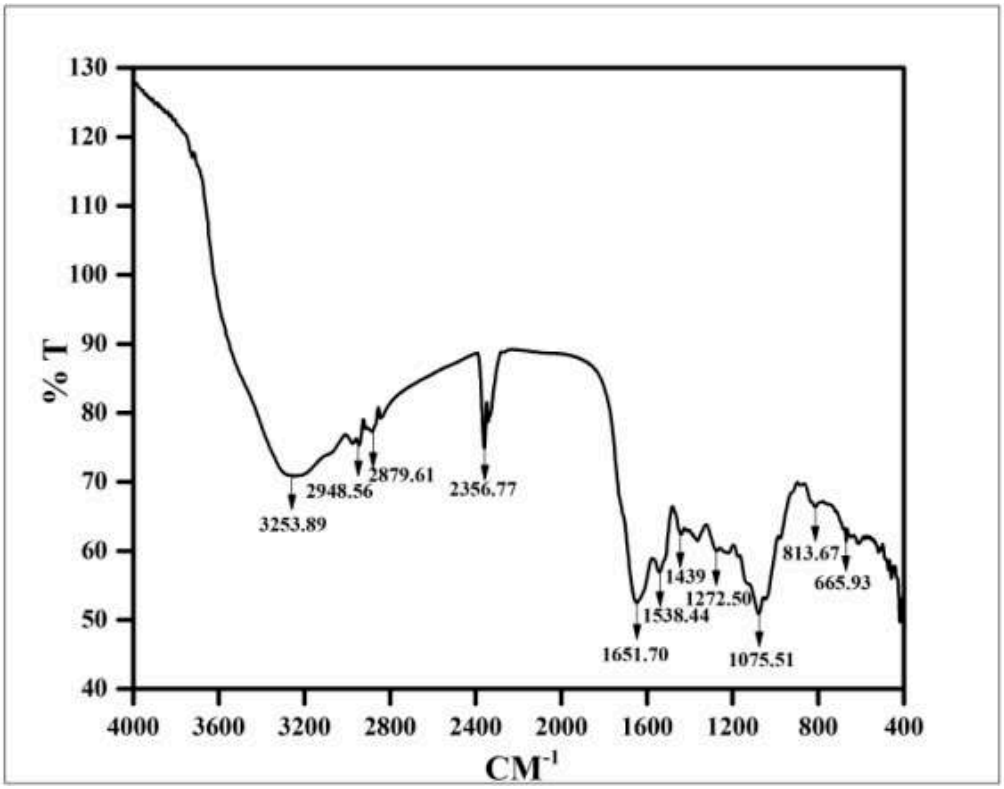

Figure 8. FTIR absorption spectra of copper oxide nanoparticles.

From this result, it could be stated that the soluble elements present in *A. lunulatum* extract (ALE) could have acted as capping agents preventing the aggregation of nanoparticles in solution, and thus playing a relevant role in their extracellular synthesis and shaping of the quasi-spherical copper oxide nanoparticles [40,42,46,76,82,83]. In addition to that *A. lunulatum* extract (ALE) could generate different extracellular nanoparticles by a process involving the enzyme [84].

3.9. Transmission Electron Microscopy of Copper Oxide Nanoparticles

The TEM image, shown in Figure 9, recorded different sizes of copper oxide nanoparticles which arose from the bio-reduction of copper sulfate solution by *A. lunulatum* extract (ALE) at room temperature (30 °C). Particles were found to be quasi-spherical, as well as mono-disperse in nature [40,71]. The measured diameter of these copper oxide nanoparticles was in the range of 1 to 20 nm [40,71]. The average diameter of these copper oxide nanoparticles was calculated to be 6.5 ± 1.5 nm. The SAED pattern showed bright circular spots which further confirmed the single crystalline property of the CuONP (Figure 9b). It was interesting to note that most of the CuONP in the TEM images were not in physical contact but were separated by a properly undeviating inter-particle distance. Due to the evolving course of the sample preparation, the detected diameter of the CuONP during TEM analysis was quite unlike from that of the results obtained from DLS measurement because CuONP were in dry state in TEM whereas in the hydrated state in DLS experiment [83,84].

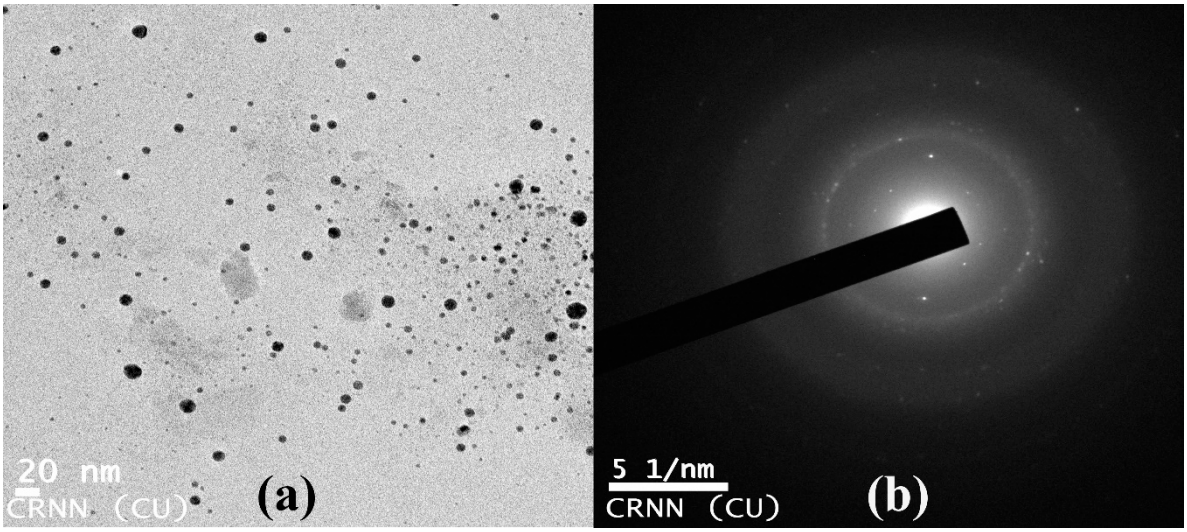

Figure 9. (**a**) TEM image of copper oxide nanoparticles (CuONPs). (**b**) Selected area electron diffraction (SAED) patterns of crystalline CuONPs.

3.10. Effects of CuONPs on Seed Germination and Growth

Significant changes were observed in seed germination percentage, root length, and seedling vigor index (Table 1). The percentage of seed germination increased in up to 1.16 and 1.13-fold in 0.01 and 0.025 mgmL^{-1} CuONPs treated seeds than control. However, it decreased slightly in 0.05 mgmL^{-1} CuONPs indicating its toxic nature. According to Nair et al. [39] seed germination percentage of *Vigna radiata* becomes significantly reduced due to toxic effects of CuONPs which was observed in our case also.

Table 1. Effect of CuONPson seed germination, seedling vigor index, and relative water content in *Lens culinaris*. Values represent mean ± SD of three separate experiments, each in triplicate.

Sets	% Seed Germination	Seedling Vigor Index	RWC (%)
Control	80.77 ± 1.82 ^{b}	3661.04 ± 46.41 ^{c}	87.39 ± 4.37 ^{a}
CuONP-0.01 mgmL^{-1}	93.96 ± 1.75 ^{a}	4269.4 ± 71.26 ^{a}	88.38 ± 3.81 ^{a}
CuONP-0.025 mgmL^{-1}	91.26 ± 1.31 ^{a}	4168.43 ± 48.15 ^{b}	84.37 ± 5.33 ^{b}
CuONP-0.05 mgmL^{-1}	75.98 ± 2.41 ^{c}	2541.36 ± 61.31 ^{d}	81.28 ± 3.71 ^{c}

Different letters within the row indicate significant difference ($p < 0.05$) from the control set using Duncan's multiple range test. Same letter within the row denotes no significant difference between the groups.

Furthermore, root length was increased in CuONPs (0.025 mgmL^{-1}) treated seedlings compared to control (Table 1). Retardation of primary root growth (Figure 10) was observed upon exposure to higher concentrations of CuONPs (0.05 mgmL^{-1}) as it was observed by Nair et al. [39].

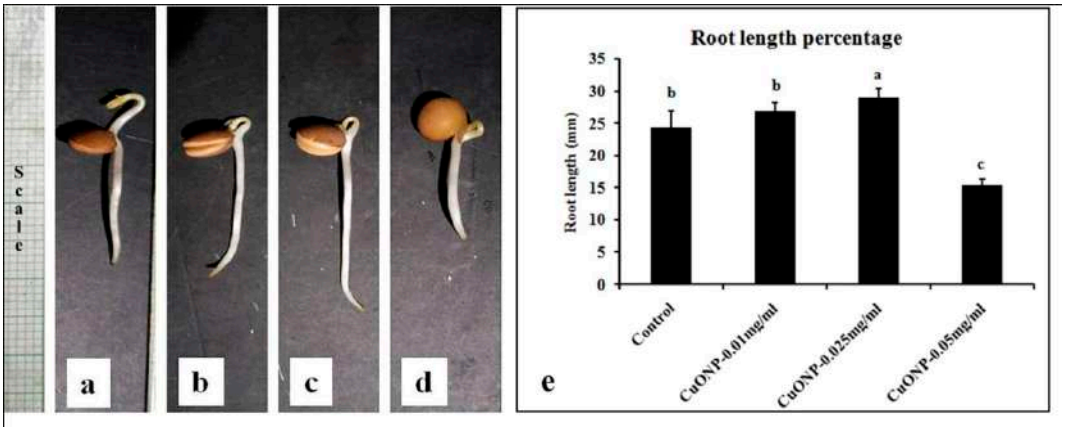

Figure 10. Representative samples after 72 h germination in water: (**a**) Control; (**b**) CuONP-0.01; (**c**) CuONP-0.025, and (**d**) CuONP-0.05 mgmL^{-1}. (**e**) Graphical representation of root length percentage of 50 seeds in triplicate. Different letters above the bar indicate significant difference ($p < 0.05$), using Duncan's multiple range test. Same letter above the bar denotes no significant difference between the groups.

A similar trend was observed in case of vigor index of seedlings. Significant increase was found in the seeds treated with 0.01 and 0.025 mgmL^{-1} CuONPs (Table 1). However, significant reduction of vigor was observed in the seeds treated with higher concentration of CuONPs (0.05 mgmL^{-1}) compared to control, indicating its toxic effects to the plants. Nair and Chung [85], also reported that the higher concentration of copper oxide nanoparticles reduced the shoot growth, weight, and total chlorophyll content in soybean.

Relative water content (RWC) of the treated roots remains close to control plants (Table 1).

3.11. Effects of CuONPs on Defence Related and Antioxidative Enzymes

In the present study, the expression of different defence related, as well as the antioxidative enzymes were demonstrated. All the activity of enzymes was studied and compared with the control set for inspection of the efficiency of CuONPs in the model plant system.

PO and PPO play a crucial role in triggering the hypersensitive reaction regarding cross-linking and lignifications of the cell wall and in transducing signals to adjacent unaffected cells [86–89]. On the other hand, PAL is the prime enzyme of the phenyl-propanoid pathway which initiates the biosynthesis of phenolics, phytoalexins, and lignins [90,91]. Therefore, the increased activity of PAL may contribute to the reduced percentage of disease incidence. β-1,3 glucanase is a type of PR-protein encoded by the host, that has a direct role against the fungal cell wall compounds including glucans [88].

CuONPs at a concentration of 0.025 mgmL^{-1} showed higher inductive ability of all the defence enzymes tested. However, at higher concentration (0.05 mgmL^{-1}), enzyme production becomes significantly lower. Nair and Chung [85], reported that the copper oxide nanoparticles increased the peroxidase activity and lignin contents in soybean. The copper oxide exposure enhanced the lignification of root cells, which leads to the changes in root developmental process in soybean seedlings [85].

PO, PPO, PAL, and β-1,3 glucanase activity was found 1.49, 1.88, 1.56, and 2.04-fold higher in the roots treated with CuONPs (0.05 mgmL^{-1}), respectively (Figure 11). A similar kind of increase in the defence related enzymes were observed by Chandra et al. [34] where tea leaves were treated with

chitosan nanoparticles [34]. Higher production of defence enzymes activity may confer higher disease resistance to plants.

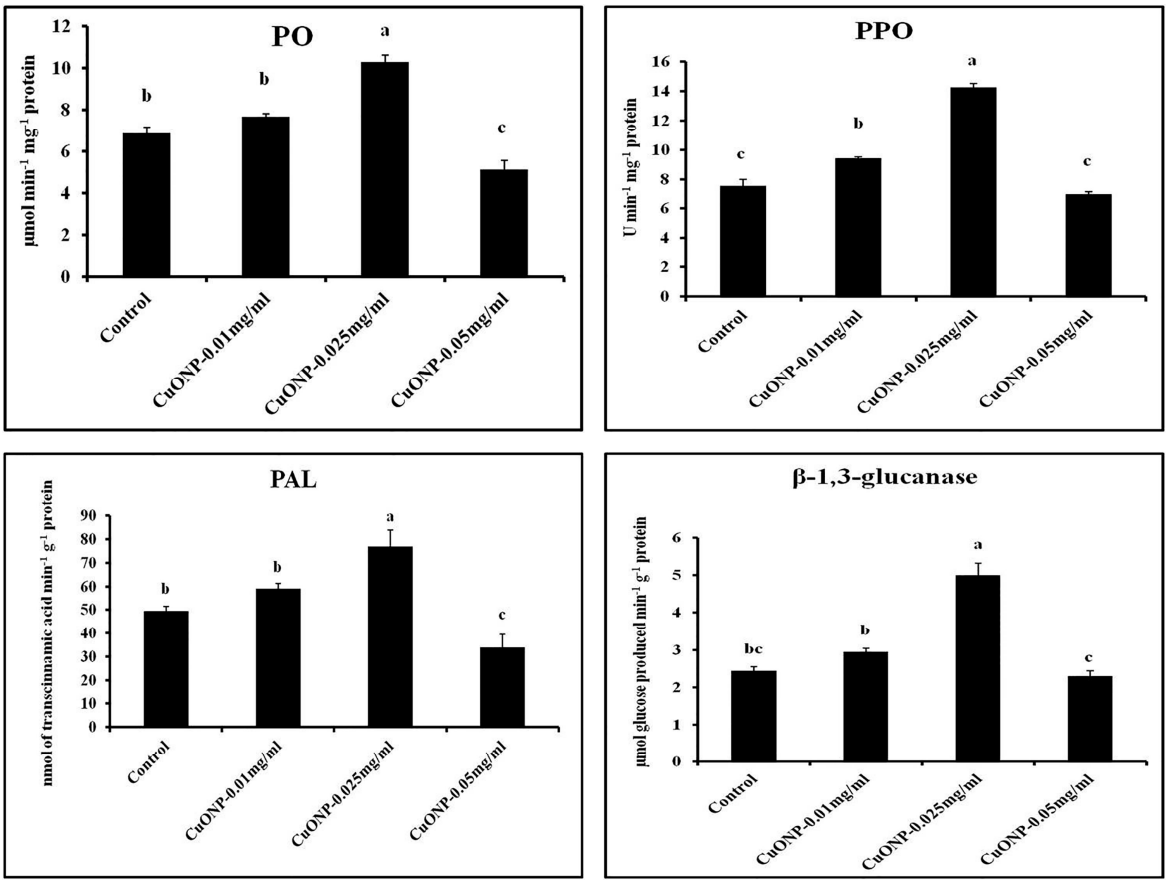

Figure 11. Effect of CuONPs on the production of defence enzymes in treated roots. Values represent mean ± SE of three separate experiments, each in triplicate. Sharing the same letter are not significantly different ($p < 0.05$) using Duncan's multiple range test.

CAT, APX, and SOD are the most essential components of the antioxidant system, which play a key role in removal of H_2O_2 from the sub-cellular compartments of plants [92]. Our results demonstrated that CAT, APX, and SOD activities have also steadily increased according to the increasing concentration of CuONPs (Figure 12). In some previous works, APX and CAT activity was found to be significantly increased in 1.0 and 1.5 mM CuONPs treatments [93,94]. The highest increase of APX, CAT, and SOD was observed in the roots treated with CuONPs (0.05 mgmL^{-1}) as 2.09, 2.13 and 1.46-fold higher than control, respectively. The higher amount of antioxidative enzymes indicate a higher degree of resistance from oxidative stress. Furthermore, roots treated with CuONPs (0.025 mgmL^{-1}) showed moderate level of increase for all the antioxidative enzymes.

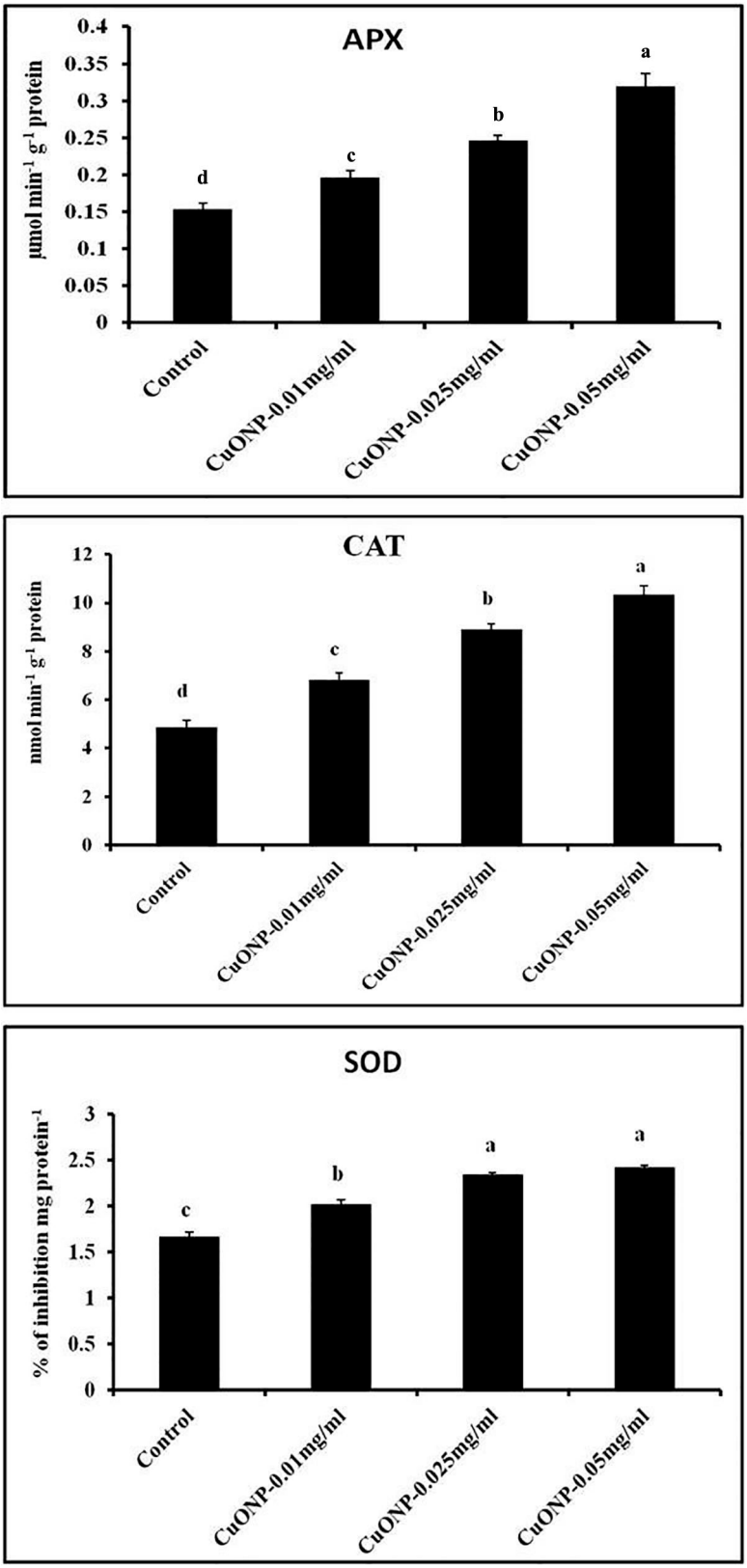

Figure 12. Effect of CuONPs on the production of antioxidative enzymes in treated roots. Values represent mean ± SE of three separate experiments, each in triplicate. Sharing the same letter are not significantly different ($p < 0.05$) using Duncan's multiple range test.

3.12. Effects of CuONPs on Phenol and Flavonoid Production

Phenols are involved in disease resistance in many ways suchas lignification of cell walls, hypersensitive cell death, etc. [95]. So, an increase of phenolic contents may give greater protection against impending pathogens. In our study, optimum concentration of CuONPs was found 0.025 mgmL^{-1}, which shows higher production of phenol and flavonoid. A similar kind of observation was found in the case of tea plants when elicited with chitosan nanoparticles [34]. However, a higher concentration was found to be toxic as the production of phenolic substances become significantly lower than control (Figure 13). The highest, 1.76 and 2.33-fold increase of total phenol and flavonoid was observed in the roots treated with CuONPs (0.025 mgmL^{-1}).

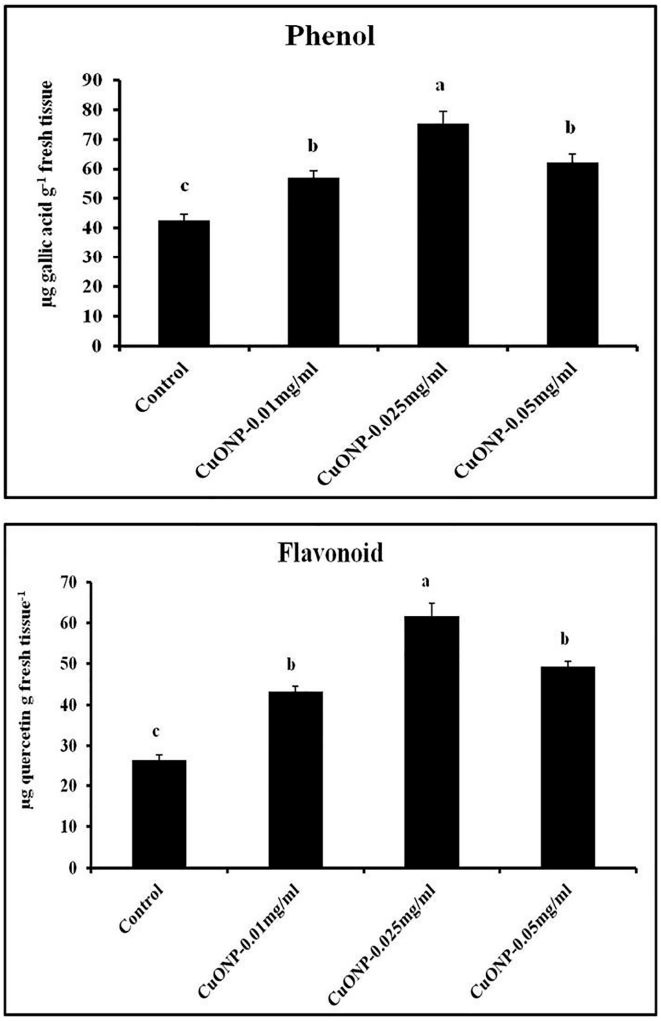

Figure 13. Effect of CuONPs on the production of total phenol and flavonoid in treated roots. Values represent mean ± SE of three separate experiments, each in triplicate. Sharing the same letter are not significantly different ($p < 0.05$) using Duncan's multiple range test.

3.13. Effects of CuONPs on Lipid Peroxidation Rate and Proline Content

Assessment of malondialdehyde (MDA) and the oxidation product of polyunsaturated fatty acid, is widely used to determine the level of lipid peroxidation [96]. An increase in proline in the plant tissue occurs in response to several abiotic stresses including salinity, drought, and frost, as well as biotic stresses [97,98]. In our case we have studied both the parameters to know whether the application of CuONPs on the roots of *Lens* generates stress or not. From the results it was evident that the higher dose of CuONPs may cause stress generation to the roots as both the parameters become significantly

higher in the roots treated with CuONPs (0.05 mgmL^{-1}). However, in other cases both the parameters remain as low as control. CuONPs (0.05 mgmL^{-1}) showed 1.49 and 1.74-fold higher lipid peroxidation and proline content than control (Figure 14). In *Vigna radiata*, similar kinds of responses were observed by Nair et al. [39].

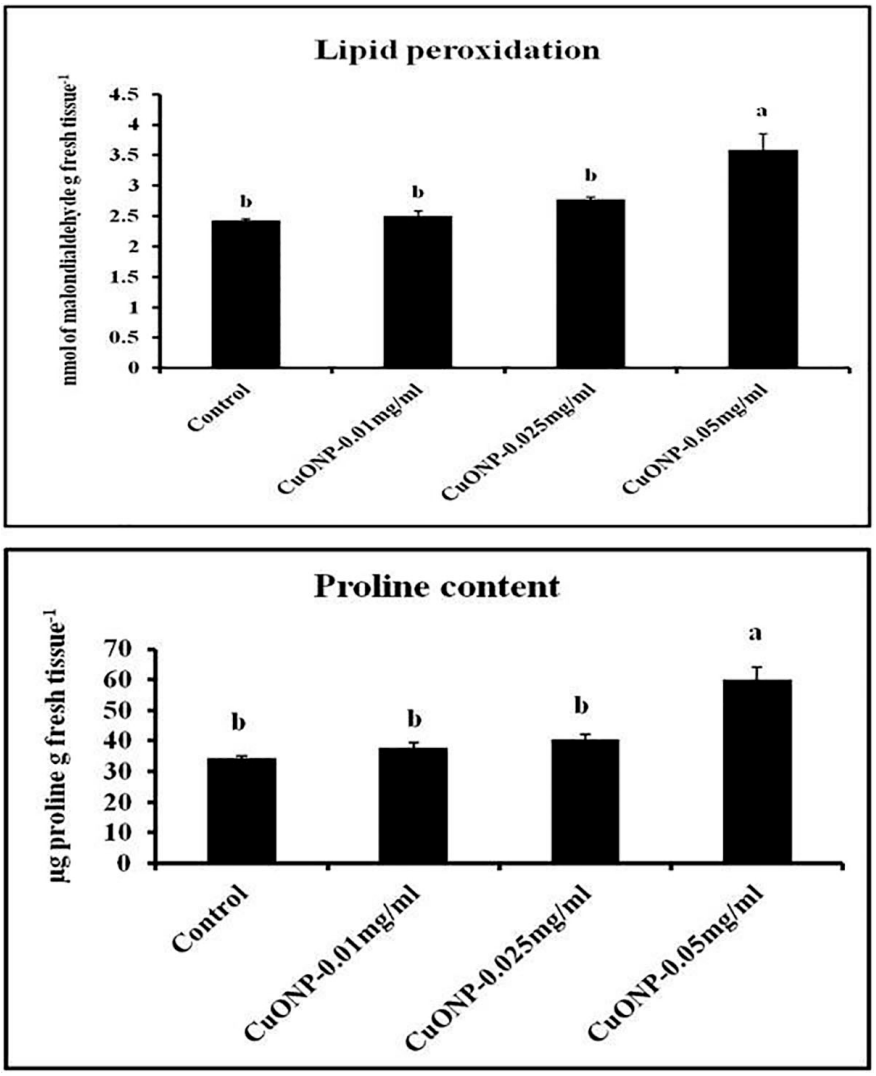

Figure 14. Effect of CuONPs on lipid peroxidation and proline content in treated roots. Values represent mean ± SE of three separate experiments, each in triplicate. Sharing the same letter are not significantly different ($p < 0.05$) using Duncan's multiple range test.

3.14. Effects of CuONPs on Nitric Oxide (NO) Production

Furthermore, a gaseous signaling molecule nitric oxide (NO) besides many of its valuable functions in plants appears to be activated after elicitor perception [99–102]. It is also believed that NO is positively involved in regulating plant defence cascades in response to various types of elicitors [103–106]. In this connection, we had tested for NO generation in our system. It was interesting to note that the production of NO in the treated roots were significantly higher than control (Figure 15). Furthermore, the higher NO production, as observed by higher green fluorescence in the root tissue, was found in CuONPs (0.025 mgmL^{-1}) treated roots and was also positively correlated with higher production of defence molecules. Though, CuONPs (0.05 mgmL^{-1}) showed greater fluorescence that was not correlated with higher induction of defence enzymes.

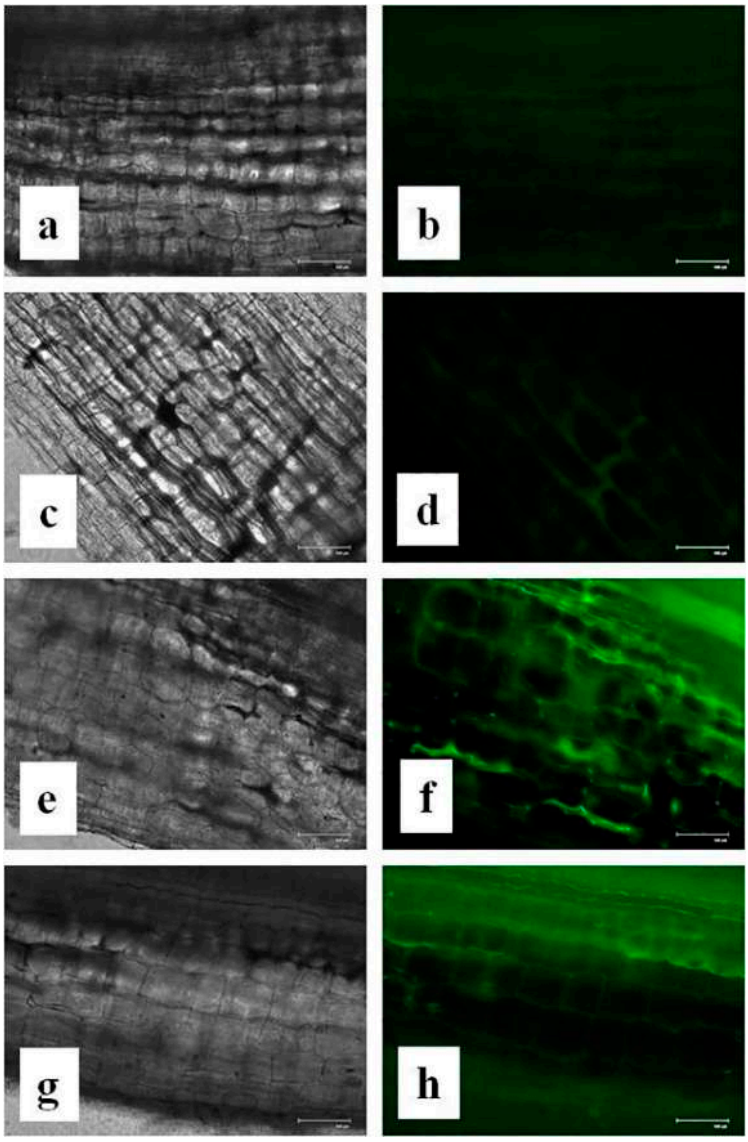

Figure 15. Effect of CuONPs on NO production in treated roots. (**a**,**b**) Control; (**c**,**d**) CuONPs-0.01; (**e**,**f**) CuONPs-0.025; (**g**,**h**) CuONPs-0.05 mgmL^{-1}. Left column (black and white image) and right column (no generation was detected by green fluorescence).

3.15. Effects of CuONPs on Reactive Oxygen Species (ROS) and H_2O_2 Production

Though past reports suggest that assembly of hydrogen peroxide (H_2O_2) from the oxidative burst was a prerequisite for defence gene activation [107], increased accumulation of H_2O_2 becomes injurious to the cells, resulting in lipid peroxidation and membrane injury [104]. To investigate whether the application of CuONPs generate oxidative stress we had also examined the ROS and H_2O_2 production in treated roots (Figures 16 and 17). As expected, increasing concentrations of CuONPs (0.05 mgmL^{-1}) showed a higher amount of ROS and H_2O_2 generation in treated roots, indication stress generation. However, CuONPs at a concentration of 0.01 and 0.025 mgmL^{-1}, showed a moderate level of ROS and H_2O_2 production.

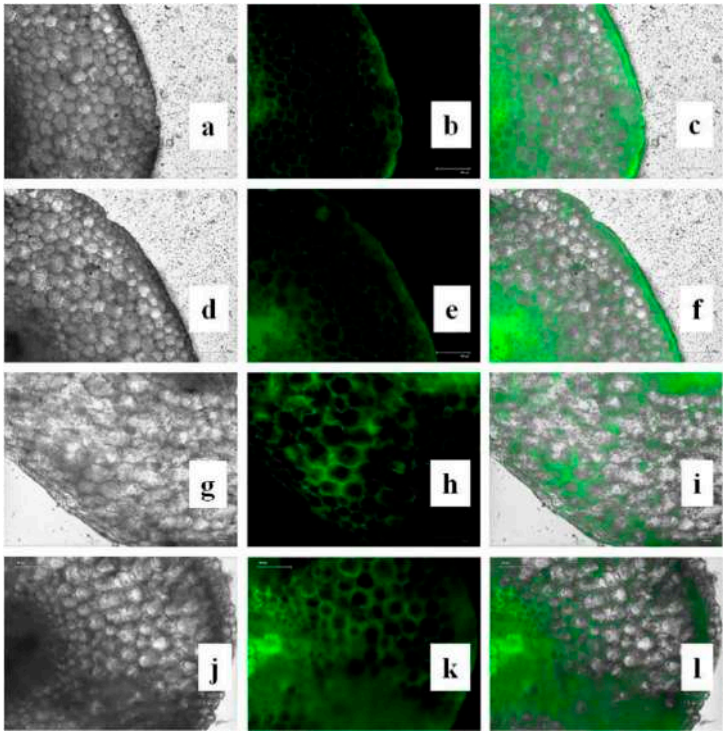

Figure 16. Effect of CuNPs on ROS production in treated roots. (**a**–**c**) Control; (**d**–**f**) CuONPs-0.01; (**g**–**i**) CuONPs-0.025; (**j**–**l**) CuONPs-0.05 mgmL^{-1}. Left column (black and white image), middle column (green fluorescence showing ROS production) and right column (merging of white field and fluorescence figure to point out the location of ROS production in the root cells).

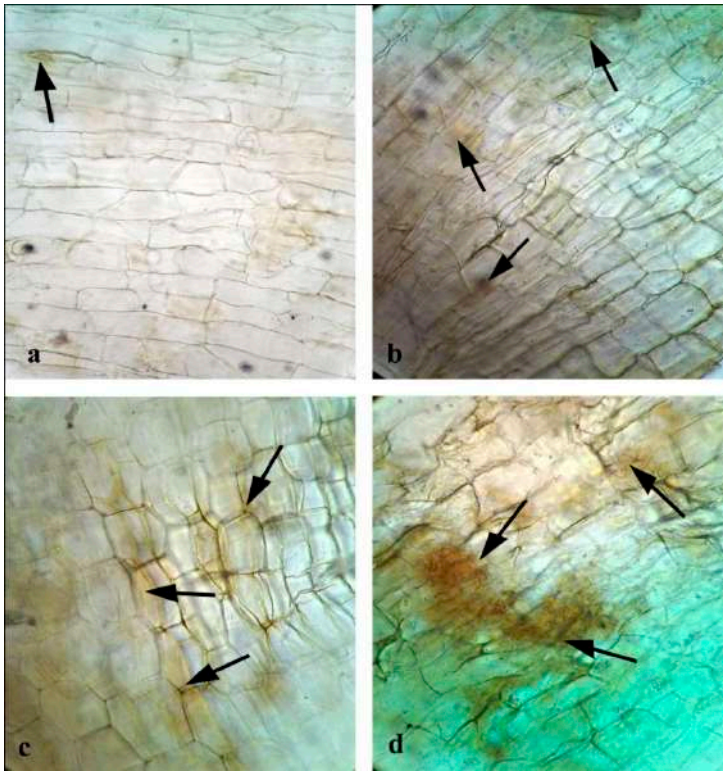

Figure 17. Effect of CuONPs on H_2O_2 production in treated roots: (**a**) Control; (**b**) CuONPs-0.01; (**c**) CuONPs-0.025; (**d**) CuONPs-0.05 mgmL^{-1}.

4. Conclusions

Green synthesis of CuONPs by using pteridophyte extract is one of the new approaches in the field of nanotechnology. From the extensive characterization it can be stated that the pteridophyte *Adiantum lunulatum* is very much efficient to produce mono-disperse CuONPs through a nontoxic way. Overall experimental results depicted that the growth of the plant is significantly altered by application of CuONPs. At the moderate concentration (0.025 mgmL^{-1}), the root length was found to be increased but at higher concentration there was decrease in the length that may be due to excess CuONPs. The defence enzyme activity also becomes influenced by the application of CuONPs. At the moderate concentration (0.025 mgmL^{-1}), defence enzymes such as PO, PPO, PAL, and β-1,3 glucanase activity become increased. It indicates that CuONPs at an optimum concentration has the potentiality to trigger innate immunity of plants. However, at higher concentration it becomes toxic to the plants as all the enzyme production becomes downregulated. Phenol and flavonoid levels were also induced by the application of CuONPs (0.025 mgmL^{-1}). Furthermore, antioxidative enzymes such as CAT, APX, and SOD were also induced by the application of CuONPs. The higher amount of antioxidative enzymes production indicates a higher degree of resistance from oxidative stress. On the other hand, the rate of membrane lipid peroxidation and proline content remain increased with the increasing concentration of CuONPs application. However, at optimum dose (0.025 mgmL^{-1}), all those parameters become close to the basal level. These results indicate lower stress generation in plants. The higher amount of ROS and H_2O_2 production was found in the roots treated with CuONPs (0.05 mgmL^{-1}), which further validate the previous results. Interestingly, production of NO was increased up to a certain level by the application of optimum dose of CuONPs (0.025 mgmL^{-1}) than control. In this connection, the higher amount of NO might influences the defence enzyme production and also checks ROS production in the treated plants. However, to establish NO as a potent mediator in this process needs further investigation.

Taken together, it can be concluded that at the optimum concentration (0.025 mgmL^{-1}) innate immunity and plant vigor was induced. However, the higher concentration (0.05 mgmL^{-1}) retards all the parameters instead of stress markers, ROS generation, and H_2O_2 production. Overall, observation suggests that, CuONPs at an optimum concentration not only have the potentiality to affect the physiological condition but also it can modulate the innate immune system of model plants such as *Lens*.

Author Contributions: Conceptualization, J.S., N.C., and K.A.; methodology, A.C., A.B., and D.D.; software, J.S. and N.C.; validation, K.A., J.S., and N.C.; formal analysis, A.C.; investigation, A.B. and D.D.; resources, K.A.; data curation, N.C. and J.S.; writing—original draft preparation, A.C. and A.B.; writing—review and editing, N.C. and J.S.; visualization, K.A.; supervision, K.A.; project administration, J.S.; funding acquisition, J.S. All authors have read and agreed to the published version of the manuscript.

Funding: This research received no external funding.

Acknowledgments: The authors thank Sudha Gupta, Pteridology & Paleobotany Lab, Department of Botany, University of Kalyani, Kalyani, Nadia, West Bengal, India, Pin-741235 for her entire effort in plant specimen identification and encouragement regarding this work. We also acknowledge the Sinha Institute of Medical Science and Technology for providing us with the centrifugation and −20 °C refrigeration facility.

Conflicts of Interest: On behalf of all listed authors, the corresponding author declares that there is not any sort of financial and non-financial conflict of interests in the subject materials mentioned in this manuscript.

References

1. Passam, H.C.; Karapanos, I.C.; Bebeli, P.J.; Savvas, D. A Review of Recent Research on Tomato Nutrition, Breeding and Post-Harvest Technology with Reference to Fruit Quality. *Eur. J. Plant Sci. Biotechnol.* **2007**, *1*, 1–21.
2. Shobha, G.; Moses, V.; Ananda, S. Biological Synthesis of Copper Nanoparticles and its impact—A Review. *Int. J. Pharm. Sci. Invent.* **2014**, *3*, 28–38.
3. Yruela, I. Copper in plants. *Braz. J. Plant Physiol.* **2005**, *17*, 145–156. [CrossRef]
4. Manceau, K.L.; Nagy, M.A.; Marcus, M.; Lanson, N.; Geoffroy, T.J.; Kirpichtchikova, T. Formation of metallic copper nanoparticles at the soil-root interface. *Environ. Sci. Technol.* **2008**, *1*, 1766–1772. [CrossRef]

5. Filipe, V.; Hawe, A.; Jiskoot, W. Critical evaluation of Nanoparticle Tracking Analysis (NTA) by NanoSight for the measurement of nanoparticles and protein aggregates. *Pharmaceut. Res.* **2010**, *27*, 796–810. [CrossRef]
6. Yedurkar, S.M.; Maurya, C.B.; Mahanwar, P.A. A Biological Approach for the Synthesis of Copper Oxide Nanoparticles by *Ixora coccinea* Leaf Extract. *J. Mater. Environ. Sci.* **2017**, *8*, 1173–1178.
7. Saif, S.; Tahir, A.; Chen, Y. Green Synthesis of Iron Nanoparticles and Their Environmental Applications and Implications. *Nanomaterials* **2016**, *6*, 209. [CrossRef]
8. Makarov, V.V.; Love, A.J.; Sinitsyna, O.V.; Makarova, S.S.; Yaminsky, I.V.; Taliansky, M.E.; Kalinina, N.O. "Green" nanotechnologies: Synthesis of metal nanoparticles using plants. *Acta Nat.* **2014**, *6*, 35–44. [CrossRef]
9. Ahmed, S.; Ahmad, M.; Swami, B.L.; Ikram, S. A review on plants extract mediated synthesis of silver nanoparticles for antimicrobial applications: A green expertise. *J. Adv. Res.* **2016**, *7*, 17–28. [CrossRef]
10. Küünal, S.; Rauwel, P.; Rauwel, E. Plant extract mediated synthesisof nanoparticles. In *Emerging Applications of Nanoparticles and Architecture Nanostructures*, 1st ed.; Barhoum, A., Makhlouf, A.S.H., Eds.; Elsevier: Cambridge, MA, USA, 2018; pp. 411–446. [CrossRef]
11. Singh, V.; Patil, R.; Ananda, A.; Milani, P.; Gade, W. Biological Synthesis of Copper Oxide Nano Particles Using *Escherichia coli*. *Curr. Nanosci.* **2010**, *6*, 365–369. [CrossRef]
12. Usha, R.; Prabu, E.; Palaniswamy, M.; Venil, C.K.; Rajendran, R. Synthesis of metal oxide nanoparticles by *Streptomyces* sp. for development of antimicrobial textiles. *Glob. J. Biotechnol. Biochem.* **2010**, *5*, 153–160.
13. Abboud, Y.; Saffaj, T.; Chagraoui, A.; Bouari, E.; Tanane, K.B.; Ihssane, O. Biosynthesis, characterization and antimicrobial activity of copperoxide nanoparticles (CONPs) produced using brown alga extract (*Bifurcaria bifurcata*). *Appl. Nanosci.* **2013**, *4*, 571–576. [CrossRef]
14. Honary, S.; Barabadi, H.; Fathabad, E.G.; Naghibi, F. Green synthesis of copper oxide nanoparticles using *Penicillium aurantiogriseum*, *Penicillium citrinum* and *Penicillium wakasmanii*. *Digest J. Nanomater. Biostruct.* **2012**, *7*, 999–1005.
15. Salvadori, M.R.; Lepre, L.F.; Ando, R.A.; do Nascimento, C.A.O.; Corrêa, B. Biosynthesis and Uptake of Copper Nanoparticles by Dead Biomass of *Hypocrea lixii* isolated from the Metal Mine in the Brazilian Amazon Region. *PLoS ONE* **2013**, *8*, e80519. [CrossRef] [PubMed]
16. Harne, S.; Sharma, A.; Dhaygude, M.; Joglekar, S.; Kodam, K.; Hudlikar, M. Novel route for rapid biosynthesis of copper nanoparticles using aqueous extract of *Calotropis procera* L. latex and their cytotoxicity on tumor cells. *Colloids Surf. B* **2012**, *15*, 284–288. [CrossRef] [PubMed]
17. Lee, H.-J.; Song, J.Y.; Kim, B.S. Biological synthesis of copper nanoparticles using *Magnolia kobus* leaf extract and their antibacterial activity. *J. Chem. Technol. Biotechnol.* **2013**, *8*, 1971–1977.
18. Acharya, K.; Sarkar, J. Bryo-synthesis of gold nanoparticles. *Int. J. Pharmaceut. Sci. Rev. Res.* **2014**, *29*, 82–86.
19. Baskaran, X.; Vigila, A.V.G.; Parimelazhagan, T.; Muralidhara-Rao, D.; Zhang, S. Biosynthesis, characterization, and evaluation of bioactivities of leaf extract-mediated biocompatible silver nanoparticles from an early tracheophyte, *Pteristripartita* Sw. *Int. J. Nanomed.* **2016**, *11*, 5789–5805. [CrossRef]
20. Santhoshkumar, S.; Nagarajan, N. Biological synthesis of silver nanoparticles of *Adiantum capillusveneris* L. and their evaluation of antibacterial activity against human pathogenic bacteria. *Int. J. Pharm. Sci. Res.* **2014**, *5*, 5511–5518. [CrossRef]
21. Britto, A.J.; Gracelin, D.H.S.; Jeya, P.B.; Kumar, R.; Molecular, P.; Nadu, T. Biogenic silver nanoparticles by *Adiantum caudatum* and their antibacterial activity. *Int. J. Univer. Pharm. Life Sci.* **2012**, *2*, 92–98.
22. Sant, D.G.; Gujarathi, T.R.; Harne, S.R.; Ghosh, S.; Kitture, R.; Kale, S.; Chopade, B.K.; Pardesi, K.R. *Adiantum philippense* L. Frond Assisted Rapid Green Synthesis of Gold and Silver Nanoparticles. *J. Nanopart.* **2013**, 1–9. [CrossRef]
23. Kalita, S.; Kandimalla, R.; Sharma, K.K.; Kataki, A.C.; Deka, M.; Kotoky, J. Amoxicillin functionalized gold nanoparticles reverts MRSA resistance. *Mater. Sci. Eng. C.* **2016**, *61*, 720–727. [CrossRef] [PubMed]
24. Şuţan, N.A.; Fierăscu, I.; Fierăscu, R.C.; Manolescu, D.Ş.; Soare, L.C. Comparative analytical characterization and in vitro cytogenotoxic activity evaluation of *Asplenium scolopendrium* L. leaves and rhizome extracts prior to and after Ag nanoparticles phytosynthesis. *Ind. Crops Prod.* **2016**, *83*, 379–386. [CrossRef]
25. Koteswaramma, B.; Kamakshamma, J.; Varalaksmi, S. Biological synthesis of silver nanopartical from liquid extract of *Actiniopteris radiata* and evaluation of their antimicrobial activity. *Int. J. Pharm. Biol. Sci.* **2017**, *8*, 121–125.

26. Ch, B.; Kunjiappan, S.; Bhattacharjee, C.; Chowdhury, R. Hepatoprotective and antioxidant effects of *Azolla microphylla* based gold nanoparticles against acetaminophen induced toxicity in a fresh water common carp fish (*Cyprinus carpio* L.) Biological activity of *Azolla microphylla*-based gold nanoparticles. *Nanomed. J.* **2015**, *2*, 88–110.
27. Potter, D.M.; Baird, M.S. Carcinogenic effects of ptaquiloside in bracken fern and related compounds. *Br. J. Cancer.* **2000**, *83*, 914–920. [CrossRef]
28. Johnson, M. Antibacterial Potentials of *Adiantum* Species against the UTI Pathogens. *J. Microbiol. Exp.* **2017**, *4*, 00104. [CrossRef]
29. Ali, M.S.; Amin, M.R.; Kamal, C.M.I.; Hossain, M.A. In vitro antioxidant, cytotoxic, thrombolytic activities and phytochemical evaluation of methanol extract of the *A. philippense* L. leaves. *Asian Pac. J. Trop. Biomed.* **2013**, *3*, 464–469. [CrossRef]
30. Paul, T.; Das, B.; Apte, K.G.; Banerjee, S.; Saxena, R.C. Evaluation of Anti-Hyperglycemic Activity of *Adiantum philippense* Linn, a Pteridophyte in Alloxan Induced Diabetic Rats. *J. Diab. Metabol.* **2012**, *3*, 1000226. [CrossRef]
31. Sikarwar, R.; Pathak, B.; Jaiswal, A. Some unique ethnomedicinal perceptions of tribal communities of Chitrakoot, Madhya Pradesh. *Int. J. Trad. Knowl.* **2008**, *7*, 613–617.
32. Pan, C.; Chen, Y.G.; Ma, X.Y.; Jiang, J.H.; He, F.; Zhang, Y. Phytochemical constituents and pharmacological activities of plants from the genus *Adiantum*: A review. *Trop. J. Pharmaceut. Res.* **2011**, *10*, 681–692. [CrossRef]
33. Mithraja, M.; Marimuthu, J.; Mahesh, M.; Paul, Z. Inter–specific variation studies on the phyto–constituents of *Christella* and *Adiantum* using phytochemical methods. *Asian Pac. J. Trop. Biomed.* **2012**, *2*, S40–S45. [CrossRef]
34. Chandra, S.; Chakraborty, N.; Dasgupta, A.; Sarkar, J.; Panda, K.; Acharya, K. Chitosan nanoparticles: A positive modulator of innate immune responses in plants. *Sci. Rep.* **2015**, *5*, 15195. [CrossRef] [PubMed]
35. Sarkar, J.; Chattopadhyay, D.; Patra, S.; Singh Deo, S.; Sinha, S.; Ghosh, M.; Mukherjee, A.; Acharya, K. *Alternaria alternata* Mediated Synthesis of Protein Capped Silver Nanoparticles And Their Genotoxic Activity. *Digest J. Nanomat. Biostruct.* **2011**, *6*, 563–573.
36. Mollick, M.M.R.; Bhowmick, B.; Maity, D.; Mondal, D.; Bain, M.K.; Bankura, K.; Sarkar, J.; Rana, D.; Acharya, K.; Chattopadhyay, D. Green Synthesis of Silver Nanoparticles Using *Paederia foetida* L. Leaf Extract and Assessment of Their Antimicrobial Activities. *Int. J. Green Nanotechnol.* **2012**, *4*, 230–239. [CrossRef]
37. Viet, P.V.; Nguyen, H.T.; Cao, T.M.; Hieu, L.V. *Fusarium* Antifungal Activities of Copper Nanoparticles Synthesized by a Chemical Reduction Method. *J. Nanomat.* **2016**. [CrossRef]
38. Shi, J.; Peng, C.; Yang, Y.; Yang, J.; Zhang, H.; Yuan, X.; Chen, Y.; Hu, T. Phytotoxicity and accumulation of copper oxide nanoparticles to the Cu-tolerant plant *Elsholtzia splendens*. *Nanotoxicology* **2014**, *8*, 179–188. [CrossRef]
39. Nair, P.M.G.; Kim, S.-H.; Chung, I.M. Copper oxide nanoparticle toxicity in mung bean (*Vignaradiata* L.) seedlings: Physiological and molecular level responses of in vitro grown plants. *Acta. Physiol. Plant.* **2014**, *36*, 2947–2958. [CrossRef]
40. Behera, M.; Giri, G. Green synthesis and characterization of cuprous oxide nanoparticles in presence of a bio-surfactant. *Mat. Sci.-Pol.* **2014**, *32*, 702–708. [CrossRef]
41. Henglein, A. Physichochemical Properties of Small Metal Particles in Solution: "Microelectrode" Reactions, Chemisorption, Composite Metal Particles, and the Atom-to-Metal Transition. *J. Phys. Chem.* **1993**, *97*, 5457–5471. [CrossRef]
42. Vigneshwaran, N.; Ashtaputre, N.M.; Varadarajan, P.V.; Nachane, R.P.; Paralikar, K.M.; Balasubramanya, R.H. Biological synthesis of silver nano particles using the fungus *Aspergillus flavus*. *Mat. Lett.* **2007**, *61*, 1413–1418. [CrossRef]
43. Pal, S.; Tak, Y.; Song, J. Does the antibacterial activity of silver nanoparticles depend on the shape of the nanoparticle? A study of the Gram-negative bacterium *Escherichia coli*. *Appl. Environ. Microbiol.* **2007**, *73*, 1712–1720. [CrossRef]
44. Saha, S.; Sarkar, J.; Chattopadhyay, D.; Patra, S.; Chakraborty, A.; Acharya, K. Production of silver nanoparticles by a phytopathogenic fungus *Bipolaris nodulosa* and its antimicrobial activity. *Dig. J. Nanomater. Biostruc.* **2010**, *5*, 887–895.
45. Sastry, M.; Ahmad, A.; Khan, I.; Kumar, R. Biosynthesis of metal nanoparticles using fungi and actinomycete. *Curr Sci.* **2003**, *85*, 162–170.

46. Sadowski, Z.; Maliszewska, I.H.; Grochowalska, B.; Polowczyk, I.; Kozlecki, T. Synthesis of silver nanoparticles using microorganisms. *Mater. Sci.* **2008**, *26*, 419–424.
47. Balestri, M.; Bottega, S.; Spanò, C. Response of *Pteris vittata* to different cadmium treatments. *Acta Physiol. Plant.* **2014**, *36*, 767–775. [CrossRef]
48. Hemada, H.M.; Klein, B.P. Effects of naturally occurring antioxidants on peroxidase activity of vegetable extracts. *J. Food Sci.* **1990**, *55*, 184–185. [CrossRef]
49. Kumar, K.B.; Khan, P.A. Peroxidase and Polyphenoloxidase in excised ragi (*Eleusine coracana* cv PR 202) leaves during senescence. *Ind. J. Exp. Bot.* **1982**, *20*, 412–416.
50. Dickerson, D.P.; Pascholati, S.F.; Gagerman, A.E.; Butler, L.G.; Nicholson, R.L. Phenylalanine ammonia-lyase and hydroxycinnamate, CoA ligase in maize mesocotyls inoculated with *Helminthosporium maydis* or *Helminthosporium carbonum*. *Physol. Plant Pathol.* **1984**, *25*, 111–123. [CrossRef]
51. Pan, S.Q.; Ye, X.S.; Kuc, J. Association of β-1,3-glucanase activity and isoform pattern with systemic resistance to blue mould in tobacco induced by stem injection with *Peronospora tabacina* or leaf inoculation with tobacco mosaic virus. *Physiol. Mol. Plant Pathol.* **1991**, *39*, 25–39. [CrossRef]
52. Nakano, Y.; Asada, K. Hydrogen peroxide is scavenged by ascorbate-specific peroxidase in spinach chloroplasts. *Plant Cell Physiol.* **1981**, *22*, 867–880.
53. Cakmak, I.; Horst, J. Effect of aluminium on lipid peroxidation, superoxide dismutase, catalase, and peroxidase activities in root tips of soybean (*Glycine max*). *Physiol. Plant.* **1991**, *83*, 463–468. [CrossRef]
54. Dhindsa, R.H.; Plumb-Dhindsa, R.; Thorpe, T.A. Leaf senescence correlated with increased level of membrane permeability, lipid peroxidation and decreased level of SOD and CAT. *J. Exp. Bot.* **1981**, *32*, 93–101. [CrossRef]
55. Lowry, O.H.; Rosebrough, N.J.; Farr, A.L.; Randall, R.J. Protein measurement with the Folin phenol reagent. *J. Biol. Chem.* **1951**, *193*, 265–275. [PubMed]
56. Zieslein, N.; Ben-Zaken, R. Peroxidase activity and presence of phenolic substances in peduncles in rose flowers. *Plant Physiol. Biochem.* **1993**, *31*, 333–339.
57. Chang, C.; Yang, M.; Wen Hand Chem, J. Estimation of total flavonoid content in propolis by two complementary colorimetric methods. *J. Food Drug Anal.* **2002**, *10*, 178–182.
58. Bates, L.S. Rapid determination of free proline for water-stress studies. *Plant Soil.* **1973**, *39*, 205–207. [CrossRef]
59. Bartha, B.; Kolbert, Z.; Erdei, L. Nitric oxide production induced by heavy metals in *Brassica juncea* L. Czern and *Pisum sativum* L. *Acta Biol. Szeged.* **2005**, *49*, 9–12.
60. Gupta, K.J.; Brotman, Y.; Mur, L.A. Localisation and Quantification of Reactive Oxygen Species and Nitric Oxide in *Arabidopsis* Roots in Response to Fungal Infection. *Bio-Protocol* **2014**, *4*, e1259. [CrossRef]
61. Thordal-Christensen, H.; Zhang, Z.; Wei, Y.; Collinge, D.B. Subcellular localization of H_2O_2 in plants. H_2O_2 accumulation in papillae and hypersensitive response during the barley powdery mildew interaction. *Plant J.* **1997**, *11*, 1187–1194. [CrossRef]
62. Hillis, D.M. Molecular Versus Morphological Approaches to Systematics. *Ann. Rev. Eco. Syst.* **1987**, *18*, 23–42. [CrossRef]
63. Pallavi, G.; Virupaksha, G.K.L.; Chate, V.A. An Ethno-Pharmaco-Botanical Review of Hamsapadi—*Adiantum lunulatum* Burm. F. (*A. Philippense* Linn.). *Int. J. Pharm. Biol. Arch.* **2011**, *2*, 1668–1676.
64. Kramer, K.U.; Green, P.S.; Peter, S.; Götz, E. *Pteridophytes and Gymnosperms*, 1st ed.; Springer: Berlin/Heidelberg, Germany, 2014; p. 404.
65. Van den Boom, P.P.G. lichens and lichenicolous fungi of the azores (portugal), collected on sãomiguel and terceira with the descriptions of seven new species. *Acta Bot. Hung.* **2016**, *58*, 199–222. [CrossRef]
66. Resmi, S.; Thomas, V.; Sreenivas, V.K. Anatomical studies of selected species of *Adiantum* L. in Kerala. *South Ind. J. Biol. Sci.* **2016**, *2*, 115–118. [CrossRef]
67. Tryon, A.F.; Lugardon, B. Introduction. In *Spores of the Pteridophyta*; Springer: New York, NY, USA, 1991; pp. 1–26. [CrossRef]
68. Chatterjee, A.; Khatua, S.; Acharya, K.; Sarkar, J. A green approach for the synthesis of antimicrobial bio-surfactant silver nanoparticles by using a fern. *Dig. J. Nanomater. Biostruct.* **2019**, *14*, 479–490.
69. Kulkarni, V.D.; Kulkarni, P.S. Green Synthesis of Copper Nanoparticles Using *Ocimum*. *Int. J. Chem. Stud.* **2013**, *1*, 1–4.
70. Padil, V.V.T.; Černík, M. Green Synthesis of Copper Oxide Nanoparticles Using Gum Karaya as a Biotemplate and Their Antibacterial Application. *Int. J. Nanomed.* **2013**, *8*, 889–898. [CrossRef]

71. Cuevas, R.; Durán, N.; Diez, M.C.; Tortella, G.R.; Rubilar, O. Extracellular biosynthesis of copper and copper oxide nanoparticles by *Stereumhirsutum*, a native white-rot fungus from Chilean forests. *J. Nanomater.* **2015**, *2015*, 7. [CrossRef]
72. Sarkar, J.; Dey, P.; Saha, S.; Acharya, K. Mycosynthesis of Selenium Nanoparticles. *Micro Nano Lett.* **2011**, *6*, 599–602. [CrossRef]
73. Sundaramurthy, N.; Parthiban, C. Biosynthesis of Copper Oxide Nanoparticles Using *Pyrus pyrifolia* Leaf Extract and Evolve the Catalytic Activity. *Int. Res. J. Eng. Technol.* **2015**, *2*, 332–338.
74. Sarkar, J.; Ray, S.; Chattopadhyay, D.; Laskar, A.; Acharya, K. Mycogenesis of gold nanoparticles using a phytopathogen *Alternari aalternata*. *Bioproc. Biosys. Eng.* **2012**, *35*, 637–643. [CrossRef]
75. Okaiyeto, K.; Ojemaye, M.O.; Hoppe, H.; Mabinya, L.V.; Okoh, A.I. Phytofabrication of Silver/Silver Chloride Nanoparticles Using Aqueous Leaf Extract of *Oederagenistifolia*: Characterization and Antibacterial Potential. *Molecules* **2019**, *24*, 4382. [CrossRef]
76. Kumar, P.P.N.V.; Shameem, U.; Kollu, P.; Kalyani, R.L.; Pammi, S.V.N. Green Synthesis of Copper Oxide Nanoparticles Using *Aloe vera* Leaf Extract and Its Antibacterial Activity Against Fish Bacterial Pathogens. *BioNanoScience* **2015**, *5*, 135–139. [CrossRef]
77. Sanghi, R.; Verma, P.; Puri, S. Enzymatic formation of gold nanoparticles using *Phanerochaete chrysosporium*. *Adv. Chem. Eng. Sci.* **2011**, *1*, 154–162. [CrossRef]
78. Kannan, R.R.; Stirk, W.A.; Van Staden, J. Synthesis of Silver Nanoparticles Using the Seaweed *Codium capitatum* P.C. Silva (Chlorophyceae). *S. Afr. J. Bot.* **2013**, *86*, 1–4. [CrossRef]
79. Cai, S.; Singh, B.L. A Distinct Utility of the Amide III Infrared Band for Secondary Structure Estimation of Aqueous Protein Solutions Using Partial Least Squares Methods. *Biochemistry* **2004**, *43*, 2541–2549. [CrossRef] [PubMed]
80. Hosseini, M.R.; Schaffie, M.; Pazouki, M.; Darezereshki, E.; Ranjbar, M. Biologically synthesized copper sulfide nanoparticles: Production and characterization. *Mater. Sci. Semicond. Process.* **2012**, *15*, 222–225. [CrossRef]
81. Karthik, K.; Victor Jaya, N.; Kanagaraj, M.; Arumugam, S. Temperature-Dependent Magnetic Anomalies of CuO Nanoparticles. *Solid State Commun.* **2011**, *151*, 564–568. [CrossRef]
82. Dwivedi, S.; AlKhedhairy, A.A.; Ahamed, M.; Musarrat, J. Biomimetic Synthesis of Selenium Nanospheres by Bacterial Strain JS-11 and Its Role as a Biosensor for Nanotoxicity Assessment: A Novel Se-Bioassay. *PLoS ONE* **2013**, *8*, e57404. [CrossRef]
83. Mollick, M.M.R.; Bhowmick, B.; Mondal, D.; Maity, D.; Rana, D.; Dash, S.K.; Chattopadhyay, S.; Roy, S.; Sarkar, J.; Acharya, K.; et al. Anticancer (in vitro) and antimicrobial effect of gold nanoparticles synthesized using *Abelmoschus esculentus* (L.) pulp extract via a green route. *RSC Adv.* **2014**, *4*, 37838–37848. [CrossRef]
84. Sarkar, J.; Mollick, M.M.R.; Chattopadhyay, D.; Acharya, K. An eco-friendly route of c-Fe_2O_3 nanoparticles formation and investigation of the mechanical properties of the HPMC-γ-Fe_2O_3 nanocomposites. *Bioprocess Biosyst. Eng.* **2017**, *40*, 351–359. [CrossRef]
85. Nair, P.M.G.; Chung, I.M. Impact of copper oxide nanoparticles exposure on *Arabidopsis thaliana* growth, root system development, root lignification, and molecular level changes. *Environ. Sci. Pol. Res.* **2014**, *21*, 12709–12722. [CrossRef] [PubMed]
86. Lamb, C.; Dixon, R.A. The oxidative burst in plant disease resistance. *Annu. Rev. Plant Physiol. Plant Mol. Biol.* **1997**, *48*, 251–275. [CrossRef] [PubMed]
87. Acharya, K.; Chakraborty, N.; Dutta, A.K.; Sarkar, S.; Acharya, R. Signaling role of nitric oxide in the induction of plant defense by exogenous application of abiotic inducers. *Arch. Phytopathol. Plant Prot.* **2011**, *44*, 1501–1511. [CrossRef]
88. Chandra, S.; Chakraborty, N.; Chakraborty, A.; Rai, R.; Bera, B.; Acharya, K. Abiotic elicitor mediated improvement of innate immunity in *Camellia sinensis*. *J. Plant Growth Regul.* **2014**, *33*, 849–859. [CrossRef]
89. Chakraborty, N.; Chandra, S.; Acharya, K. Biochemical basis of improvement of defense in tomato plant against *Fusarium* wilt by $CaCl_2$. *Physiol. Mol. Biol. Plants* **2017**, *23*, 581–596. [CrossRef]
90. Pellegrini, L.; Rohfritsch, O.; Fritig, B.; Legrand, M. Phenylalanine ammonia-lyase in tobacco. Molecular cloning and gene expression during the hypersensitive reaction to tobacco mosaic virus and the response to a fungal elicitor. *Plant Physiol.* **1994**, *106*, 877–886. [CrossRef]

91. Whan, J.A.; Dann, E.K.; Smith, L.J.; Aitken, E.A.B. Acibenzolar-S-methyl-induced alteration of defence gene expression and enzyme activity in cotton infected with *Fusarium oxysporum* f. sp. *vasinfectum*. *Physiol. Mol. Plant Pathol.* **2008**, *73*, 175–182. [CrossRef]
92. Najami, N.; Tibor, J.; Barriah, W.; Kayam, G.; Moshe, T.; Guy, M.; Volokita, M. Ascorbate peroxidase gene family in tomato: Its identification and characterization. *Mol. Genet. Genom.* **2008**, *279*, 171–182. [CrossRef]
93. Shaw, A.K.; Hossain, Z. Impact of nano-CuO stress on rice (*Oryza sativa* L.) seedlings. *Chemosphere* **2013**, *93*, 906–991. [CrossRef]
94. Trujillo-Reyes, J.; Majumdar, S.; Botez, C.E.; Peralta-Videa, J.R.; Gardea-Torresdey, J.L. Exposure studies of core–shell Fe/Fe_3O_4 and Cu/CuO NPs to lettuce (*Lactuca sativa*) plants: Are they a potential physiological and nutritional hazard? *J. Hazard. Mate.* **2014**, *267*, 255–263. [CrossRef] [PubMed]
95. Biswas, S.K.; Pandey, N.K.; Rajik, M. Inductions of defense response in tomato against fusarium wilt through inorganic chemicals as inducers. *J. Plant Pathol. Microbiol.* **2012**, *3*, 1–7.
96. Lin, C.; Kao, C. Effect of NaCl stress on H_2O_2 metabolism in rice leaves. *Plant Growth Regul.* **2000**, *30*, 151–155. [CrossRef]
97. Hare, P.; Cress, W. Metabolic implications of stress- induced proline accumulation in plants. *Plant Growth Regul.* **1997**, *21*, 79–102. [CrossRef]
98. Slama, I.; Ghnaya, T.; Hessini, K.; Messedi, D.; Savouré, A.; Abdelly, C. Comparative study of the effects of mannitol and PEG osmotic stress on growth and solute accumulation in *Sesuvium portulacastrum*. *Environ. Exp. Bot.* **2007**, *61*, 10–17. [CrossRef]
99. Corpas, F.J.; Leterrier, M.; Valderrama, R.; Airaki, M.; Chaki, M.; Palma, J.M.; Barroso, J.B. Nitric oxide imbalance provokes a nitrosative response in plants under abiotic stress. *Plant Sci.* **2011**, *181*, 604–611. [CrossRef]
100. Leterrier, M.; Valderrama, R.; Chaki, M.; Airaki, M.; Palma, J.M.; Barroso, J.B.; Corpas, F.J. Function of nitric oxide under environmental stress conditions. In *Phytohormones and Abiotic Stress Tolerance in Plants*, 1st ed.; Khan, N.A., Nazar, R., Iqbal, N., Anjum, N.A., Eds.; Springer: Berlin/Heidelberg, Germany, 2012; pp. 99–113. [CrossRef]
101. Chakraborty, N.; Chandra, S.; Acharya, K. Sublethal Heavy Metal Stress Stimulates Innate Immunity in Tomato. *Sci. World J.* **2015**, *2015*, 208649. [CrossRef]
102. Chakraborty, N.; Mukherjee, K.; Sarkar, A.; Acharya, K. Interaction between Bean and *Colletotrichum gloeosporioides*: Understanding Through a Biochemical Approach. *Plants* **2019**, *8*, 345. [CrossRef]
103. Laspina, N.V.; Groppa, M.D.; Tomaro, M.L.; Benavides, M.P. Nitric oxide protects sunflower leaves against Cd-induced oxidative stress. *Plant Sci.* **2005**, *169*, 323–330. [CrossRef]
104. Hasanuzzaman, M.; Nahar, K.; Alam, M.M.; Fujita, M. Exogenous nitric oxide alleviates high temperature induced oxidative stress in wheat (*Triticum aestivum* L.) seedlings by modulating the antioxidant defense and glyoxalase system. *Aust. J. Crop Sci.* **2012**, *6*, 1314–1323.
105. Chakraborty, N.; Ghosh, S.; Chandra, S.; Sengupta, S.; Acharya, K. Abiotic elicitors mediated elicitation of innate immunity in tomato: An ex vivo comparison. *Physiol. Mol. Biol. Plants.* **2016**, *22*, 307–320. [CrossRef] [PubMed]
106. Chakraborty, N.; Acharya, K. "NO way"! Says the plant to abiotic stress. *Plant Gene* **2017**, *11*, 99–105. [CrossRef]
107. Repka, V. Elicitor-stimulated induction of defense mechanisms and defense gene activation in grapevine cell suspension cultures. *Biol. Plant.* **2001**, *44*, 555–565. [CrossRef]

Source details

Feedback > Compare sources >

Nanomaterials

Open Access

Scopus coverage years: from 2011 to Present

Publisher: Multidisciplinary Digital Publishing Institute (MDPI)

E-ISSN: 2079-4991

Subject area: Chemical Engineering: General Chemical Engineering | Materials Science: General Materials Science

Source type: Journal

View all documents > | Set document alert | Save to source list

CiteScore 2022
7.4

SJR 2022
0.811

SNIP 2022
1.065

CiteScore | CiteScore rank & trend | Scopus content coverage

ZINC ENRICHMENT IN MAIZE GROWN IN SOIL DRESSED WITH NEEM FERTILIZER

[1]Rupa Chakraborty, [2]Anish Pyne

[1]Assistant Professor, [2]Research Student
[1]Department of Botany,
[1]Dinabandhu Andrews College, Kolkata-84, India.

Abstract: A large part of reclaimed wetland in the Eastern fringe of Kolkata is being used for maize farming. Fertilizers are frequently being added to the soil by maize growers in order to obtain better yield as well as to improve the soil quality in many cases. In this study, effect of supplementation of urea and neem fertilizer in wetland soil on zinc uptake by maize leaves and grains were investigated, as maize is one of the staple crops consumed by all irrespective of economic standards in our country and also throughout the world.

Key words: Maize, Neem fertilizer, Urea, Wetland, Zinc, Immunity, Anti-Oxidant.

I. INTRODUCTION:-

India is an agro-based country. As until 2018, agriculture employed more than 50% of the Indian work force and contributed 17–18% to country's GDP. Across seasons, varieties of crops are grown throughout the country going in accordance with the quality of the soil, fertilizers and other allied factors. Quality of the soil, where a particular crop is grown plays a very crucial role in deciding not only the yield but also the nutritional index of the crop itself. This depends on a number of factors like the ability of the soil to make essential nutrients available to the crops, aeration, percentage of heavy metals in the soil etc. The number of heavy metals found in any soil plays a pivotal role in estimating the quality of the soil. Heavy metals like copper, zinc and arsenic can prove to decisive weather a particular soil can be used for farming or not. The use of fertilizers for better yield of crops are a must nowadays given the demand and supply ratio throughout the country and even in the export relations abroad.

The wetland located in the Eastern fringe of Kolkata is famous for dumping wastes. At the same time, these wetlands are also being used for agricultural purposes. Maize is a very important crop due to its nutritional values (Nuss and Tanumihardjo, 2010) and also because it acts as an important raw material in several industrial applications. Maize farming is a popular practice in these wetland areas. Maize farmers supply different fertilizers in their field regularly for better yield. Urea is frequently being used by maize growers as it is an inexpensive form of nitrogen fertilizer. In addition to it, farmers are now using organic fertilizers in their field also.

Several studies have confirmed the presence of different heavy metals in wetland soil (Chattopadhyay et al., 2002; Khatun et al., 2016; Dutta et al., 2016). Zinc, a heavy metal, also found to be present in the wetland soil (Das et al., 2014), proves to be a very important one for human body as it has anti-oxidant properties and acts both as a co-factor for enzymes like carbonic anhydrase and inhibitor for enzymes like NADPH Oxidase. At the same time, excessive concentrations of zinc can lead to unwanted toxicity in the body. Maize plant is a significant accumulator of zinc (Lu et al., 2015). During the present investigation, a field experiment was conducted to study the effect of supplementation of urea and neem fertilizer in wetland soil on zinc uptake by maize leaves and grains. Our study is based on the effect of some fertilizers in supplementing the uptake of heavy metal (in our case, zinc). The study was carried forward with the following objectives:-

- To improve the yield of maize, an inexpensive staple crop available to all irrespective of socio-economic standards in an eco-friendly manner
- To test whether the incorporation of organic fertilizers increase the zinc uptake in maize plants, which is a natural accumulator of zinc.
- To exploit the anti-oxidant property of zinc at a non-toxic concentration which helps us to reduce oxidative stress and boost our immunity, which is the need of the hour.

II. Materials and Methods:

2.1. Growing plants in the field:

Three plots (33 sq. m each) were selected in reclaimed wetland in the eastern fringe of Kolkata (Latitude - 22.572645, Longitude - 88.363892). One plot was used as control while the other two were used for urea and neem fertilizer treatment separately. Maize seeds (Cv. MSF 56) were disinfected with 0.1% HgCl2 solution for 5 minutes , washed thoroughly with sterile distilled water , soaked in water for overnight and then sown in rows (60- 75 cm apart) in the field (wetland soil).

2.2. Supplementation of urea and neem fertilizer in the soil:

Maize seeds (Cv. MSF 56) sown in wetland soil was supplemented with urea and neem fertilizer at the rate of 150 and 500kg / ha respectively. Leaves and cobs of 88 old day plants were collected and the amount of zinc was estimated.

2.3. Estimation of zinc:

Zinc content in the sample was estimated using Atomic Absorption Spectrophotometer (Perkin Elmer 2380).

III. Results:-

3.1. Effect of supplementation of urea and neem fertilizer (Neem shield) on zinc uptake by maize leaves

The results of Zinc uptake by leaves of maize plants (Cv. MSF 56) are given in Table 1.

Table 1. Effect of supplementation of urea and neem fertilizer (Neem shield) on zinc uptake by maize leaves

Treatment		Average zinc content (µg /g dry wt.) in leaves
Untreated (control)		13.93 ± 0.467
Treated (fertilizer)	Urea	12.97 ± 0.467
	Neem fertilizer	34.50 ± 0.467

Results show that addition of neem fertilizer to wetland soil increased zinc uptake significantly by maize leaves when it is compared to untreated set and urea treatment too. In case of neem fertilizer treatment, 147.66 % enhancement in zinc uptake was noticed in relation to control. A decrease (6.89 %) in zinc uptake has been noted in case of urea treatment when it is compared to untreated control set.

3.2. Effect of supplementation of urea and neem fertilizer (Neem shield) on zinc uptake by maize grains

The results of zinc uptake by cobs of treated maize plants (Cv. MSF 56) are given in Table 2.

Table 2. Effect of supplementation of urea and neem fertilizer on zinc uptake by maize grains

Treatment		Average zinc content (µg /g dry wt.) in grains
Untreated (control)		10.13 ± 0.467
Treated (fertilizer)	Urea	26.50 ± 0.467
	Neem fertilizer	27.30 ±0.467

Results reveal that addition of fertilizer to wetland soil enhanced zinc uptake by maize grains. Urea and neem fertilizer treatment showed 161.6 % and 169.49 % increase in zinc uptake respectively. Supplementation of neem fertilizer showed a slight increase in zinc uptake in comparison to urea.

IV. Discussions:-

Maize plant is responsive to zinc sources (Ruffo et al. 2016). Lu et al., 2015 also proved that presence of heavy metal in the soil resulted in the accumulation of heavy metal content specially zinc in maize plant. A great effect of nitrogen fertilizer on zinc absorption by winter wheat has been established by Zhao et al, 2016. They showed that nitrogen application increased total Zn accumulations and Zn concentrations of each plant part of winter wheat. Furthermore, it was also noted that appropriate N application increased Zn content in grains. The results obtained from our study shows the increase in the amount of zinc uptake via supplementation with fertilizers as nitrogen sources which automatically uplifts the nutritional value of these cobs as the anti-oxidant property of zinc allows reduction of oxidative stress in our body and builds up immunity which is the need of the hour amidst the deadly pandemic situation the world is stuck in today. These advantages acquired from zinc can be extracted from the maize grown in fertilized soil and owing to the fact that maize is an inexpensive staple crop consumed all around the world irrespective of the socio-economic status of people employed in varied sectors, this study can be our key to boost immunity in such a handy way amidst the COVID-19 crisis. The concentration of zinc accumulated in both the maize leaves and cobs, are well below the toxicity level but provides us with the added advantage that can be accumulated from zinc uptake whose mechanism is well explained by Gupta et al., 2016.

V. Conclusion:

Present experiment indicates that supplementation of fertilizer (urea and neem fertilizer) in wetland soil plays an important role in zinc uptake by maize plants. Addition of neem fertilizer showed higher increase in zinc uptake in both maize leaves and grains (cobs) when it was compared to untreated control set which boosted the nutritional index of the maize and hence may lead to the improvement of the socio-economic status of the maize farmers.

VI. Acknowledgement

Author is thankful to Department of Metallurgical Engineering, Jadavpur University for heavy metal estimation.

Author is also thankful to Sri Bihari Yadav for rendering help in maize field.

VII. References:

[1] Das, D. K. Bandopadhyay, P. K. Jee, A. Karmakar. “Geochemistry of sediments and water with a health risk assessment of heavy metal contaminated vegetables grown in Dhapa, a waste disposal site in Kolkata, India”. World Review of Science Technology and Sustainable Development. 11(3/4): pp 248 – 268, 2014. DOI: 10.1504/WRSTSD.2014.066817

[2] Khatun , S. Pal , A. K. Mukherjee , P. Samanta1, S. Mondal , D. Kole , P. Chandra , A. R. Ghosh. “Evaluation of metal contamination and phytoremediation potential of aquatic macrophytes of East Kolkata Wetlands, India” .Environmental Health and Toxicology, Vol.31, Article ID: e2016021, 7 pages. 2016 https://doi.org/10.5620/eht.e2016021 eISSN: 2233-6567

[3] Chattopadhyay, A. Chatterjee, S. K. Mukhopadhyay . “Bioaccumulation of metals in the East Calcutta wetland ecosystem”. Aquatic Ecosystem Health & Management, 5(2): pp 191-203, 2002.

[4] E. T. Nuss, S. A. Tanumihardjo.” Maize: a paramount staple crop in the context of global nutrition”. Compr. Rev. Food Sci. F. 9, pp 417–436. 2010. doi: 10.1111/j.1541-4337.2010.00117.x

[5] J. Dutta, A. Saha, A. Mitra. “Impact of acidification on heavy metal levels in a bheri of East Kolkata Wetlands (EKW), a Ramsar Site in the Indian sub-continent”. Int. J. Adv. Res. Biol. Sci. 3(11): pp154-159, 2016. DOI: http://dx.doi.org/10.22192/ijarbs.2016.03.11.018

[6] M. Ruffo, R. Olson, I. Daverede.” Maize yield response to zinc sources and effectiveness of diagnostic indicators”. Communications in Soil Science and Plant Analysis .47 (2):pp. 137–41. 2016 doi:10.1080/00103624.2015.1108433.

[7] Y. Lu, H. Yao, D. Shan, Y. Jiang, S. Zhang, and J. Yang. “Heavy Metal Residues in Soil and Accumulation in Maize at Long-Term Wastewater Irrigation Area in Tongliao, China”. Journal of Chemistry. vol. 2015, Article ID 628280, 9 pages, 2015. https://doi.org/10.1155/2015/628280.

[8] P. Zhao,F.Yang,F. Sui,Q. Wang & H. Liu."Effect of nitrogen fertilizers on zinc absorption and translocation in winter wheat"Journal of Plant Nutrition .39 (9) : pp. 1311-1318.2016 https://doi.org/10.1080/01904167.2015.1106560

[9] Gupta, N., Ram, H. & Kumar, B. Mechanism of Zinc absorption in plants: uptake, transport, translocation and accumulation. Rev Environ Sci Biotechnol 15, 89–109 (2016). https://doi.org/10.1007/s11157-016-9390-1

[10] Zou CQ, Zhang YQ, Rashid A, Ram H, Savasli E, Arisoy RZ, Ortiz-Monasterio I, Simunj S, Wang ZH, Sohu V, Hassan M et al (2012) Biofortification of wheat with zinc through zinc fertilization in seven countries. Plant Soil 361:119–130

[11] Vymazal J, Brezinova T (2015) Heavy metals in plants in constructed and natural wetlands: concentration, accumulation and seasonality. Water Sci Tecchnol 71:268–276

Endophytism in Zingiberaceae: Elucidation of Beneficial Impact

Chapter · June 2019

DOI: 10.1007/978-3-319-90484-9_31

4 authors:

Avijit Chakraborty
Ramakrishna Mission Vivekananda Centenary College
14 PUBLICATIONS **80** CITATIONS
SEE PROFILE

Subrata Kundu
Ramakrishna Mission Vivekananda Centenary College
20 PUBLICATIONS **280** CITATIONS
SEE PROFILE

Swapna Mukherjee
28 PUBLICATIONS **391** CITATIONS
SEE PROFILE

Biswajit Ghosh
Ramakrishna Mission Vivekananda Centenary College
155 PUBLICATIONS **2,130** CITATIONS
SEE PROFILE

Endophytism in Zingiberaceae: Elucidation of Beneficial Impact

Avijit Chakraborty, Subrata Kundu, Swapna Mukherjee, and Biswajit Ghosh

Contents

Abstract

Endophytism is a unique relationship between plant and endosymbiotic microorganism wherein the microbes colonize within plant tissues without producing any disease etiology. Various groups of endophytes isolated from different medicinal plants are extremely significant in this respect for their ability to synthesize novel bioactive compounds as well as for the modulation of productivity. Endophytes also play various crucial roles in growth, biotic and abiotic stress tolerance, and adaptation. With the implementation of "state-of-the-art" technologies in molecular biology, the specific identification of associated microorganism as well as their relationship with corresponding host plants has been explicitly deciphered in

A. Chakraborty · S. Kundu · B. Ghosh (✉)
Plant Biotechnology Laboratory, Department of Botany, Ramakrishna Mission Vivekananda Centenary College, Kolkata, India
e-mail: avijit.microbio@gmail.com; subratakundu83@gmail.com; ghosh_b2000@yahoo.co.in

S. Mukherjee
Department of Microbiology, Dinabandhu Andrews College, Kolkata, India
e-mail: swamuk15@gmail.com

S. Jha (ed.), *Endophytes and Secondary Metabolites*,
Reference Series in Phytochemistry, https://doi.org/10.1007/978-3-319-76900-4_31-1

recent years. Zingiberaceae, generally recognized as ginger family, comprises of rhizomatous medicinal and aromatic plants and is characterized by the presence of plethora of bioactive compounds along with volatile oils. They are widely cultivated in tropical and subtropical regions of Asia. This chapter aims to explore the endophytic relationship between medicinally important species of Zingiberaceae and the corresponding microbes, for improved production of imminent natural products and their role in protection of host plants from pathogens as well as in stress tolerance, thus helping the plants, indirectly, to grow better.

Keywords
Endophytism · Zingiberaceae · Plant natural products · Antimicrobial activity · Plant growth-promoting bacteria · Medicinal plants

1 Introduction

Endophytism is an exclusive relationship between plant and bacterial or fungal microorganism wherein the microbes colonize within healthy plant tissues without producing any disease symptom. This complex association can be either mutualistic or antagonistic and is almost ubiquitous among most of the plants examined till date. The term "endophyte" was first coined about 150 years ago for pathogenic fungi infecting the plants [1]. It originates from Greek, "endo" denoting within and "phyte" meaning plant. Since the introduction of the term, many scientists have been involved to redefine it. Galippe was the first scientist to hypothesize that numerous vegetable plants host microbes within it, and these microbes are originated from soil [2]. Although scientist di Vestea agreed with this postulate, most of the renowned scientists including Pasteur, Chamberland, Fernbach, and Laurent were against Galippe's proposal and established that the plants are free of any kind of microbes [3, 4]. However, it is well established that the plants generally host a wide range of phylogenetically distinct endophytes in various organs [5] and that almost all of these microbes are derived from the soil environment [4, 6–8]. Nevertheless, endophytes were considered as "any microorganism if it can be isolated or extracted from inside surface of disinfected plant tissue and it does not seemingly harm the plant" [9]. Conversely, due to the lack of suitable techniques for removal of nucleic acids after sterilization of plant surfaces, this definition appeared to be less suitable for non-cultured species upon the exclamation of molecular biology techniques in endophyte research. Therefore, the improved definition of endophytes was proposed by Coombs and Franco as "ubiquitous colonizers of the interior tissues of host plants and can constitute a range of different relationships such as symbiotic, mutualistic, and commensalistic where they do not usually cause any substantial morphological changes and disease symptoms" [10].

The Zingiberaceae family includes about 52 genera and more than 1300 species that are dispersed throughout tropical Africa, Asia, and the America. This family is enriched with aromatic perennial herbs with creeping horizontal or tuberous

rhizomes, and many species are economically important as ornamental plants, spices, or folk medicine. It also includes vital groups of medicinal plants with volatile essential oils and oleoresins of export quality. The secondary metabolites extracted from different genera of Zingiberaceae including *Curcuma*, *Kaempferia*, *Hedychium*, *Amomum*, *Zingiber*, *Alpinia*, and *Elettaria* have antimicrobial, anti-arthritic, antioxidant, anticancer, anti-inflammatory, and antidiabetic properties. The essential oil of the rhizome of *Kaempferia galanga* has been reported to constitute over 54 components including derivatives of cyclohexene oxide and diterpenes that have insecticidal properties [11–14]. Saponin, an essential bioactive compound synthesized by the plant species *Costus speciosus*, was found to have anti-conidial germinal effect on the most effective pathogen, i.e., *Botrytis cinerea* and *Alternaria* sp. [15]. *Alpinia* is the genus under Zingiberaceae family and an important medicinal herb that stimulates digestion, blood purification, and antifungal activity [16–19]. *Zingiber officinale*, an important aromatic medicinal plant, contains essential oil with versatile biological potential including antirhinoviral activity [20, 21]. The root of *Hedychium spicatum* is useful in asthma, pains, inflammations, foul breath, vomiting, bronchitis, and "tridosha" diseases of the blood [22]. *Kaempferia angustifolia* is an aromatic medicinally important rhizomatous plant and has potential in the treatment of fever, cold, coughs, diarrhea, stomach ache, and dysentery [23, 24].

The endophytes associated with different family members of Zingiberaceae play pivotal roles in growth, development, fitness, as well as induction of several bioactive secondary metabolites. There are several such reports on the existence and beneficial roles of diverse endophytic microorganism within different genera of Zingiberaceae. To the best of our knowledge, limited cumulative information are available regarding the endosymbiotic microorganisms associated with the entire family of Zingiberaceae. The comprehensive information on endophytes provides understanding into the complex nature of the microbiome connected with Zingiberaceae family. Therefore, the objective of the present chapter was to explore different types of endophytes and their multipartite interactions with host plants along with favorable impression within the entire family of Zingiberaceae.

2 Decoding the Molecular Interaction in Endophytism

Knowingly, a complex interaction exists between host and endophytes although suitable methods to study *in planta* mechanisms are unavailable. Only limited reports are there elucidating comprehensive mechanisms of plant-endophyte interactions [25–27]. The phenomenon of endophytism primarily depends upon the genotype of plant and the corresponding strain of endophyte [28, 29]. It has been reported that chemoperception systems within the plants sense the existence of secretory molecules from endophytes [30]. This interaction activates a cascade of signal transduction pathway that induces the expression of defense-related genes within the host plants [29]. Thus, endophytism produces reactive oxygen species (ROS) within the plants and stimulates the synthesis of antioxidant

enzymes [31, 32]. Nevertheless, some endophytes also modulates host metabolism by altering the nutrient uptake and homeostasis [25, 33]. During endophytism, the magnitude of induction of pathogenesis-related genes in the absence of pathogenic determinants is relatively lower [34]. However, these are the preliminary research works on the mechanistic feature of endophytism; comprehensive molecular events can be explored through the application of "omics" technologies including metagenomics, metabolomics, and transcriptomics. Thus cumulative approaches have increased potential for analyzing total microbial community in endophytic relationship with host plants. Nevertheless, functional assay of the whole microbiome also offers novel opportunity to explore biogeochemical environments, multifaceted ecosystems related to host organisms, metabolism, and interactions between them. These aforementioned systematic approaches accompanied with progressive computational tools (system biology) are the crucial tactics to elucidate comprehensive biochemical and environmental interactions happening within host plants and associated microbial community.

3 Impact of Endophytic Microorganisms on Plants

The endophytes can induce growth of the plants by fixing atmospheric nitrogen, producing phytohormones, regulating the growth of phytopathogens by accumulating secondary metabolites or through enhanced uptake of minerals [6, 35, 36]. Beneficial properties of different types of endophytes were represented in Fig. 1. The magnitude of growth enhancement by endophytic community is highly dependent on the soil that encourages colonization and compatibility between plant and endophytes [37–39]. Furthermore, endophytes produce various bioactive compounds including benopyranones, alkaloids, flavonoids, chinones, phenolics, steroids, and terpenoids that have immense potential in medicine and agrochemical industries as well as in biotechnological applications [40–44]. The endophytes also play pivotal role in the maintenance of soil nutrients and make them accessible to each component of the ecosystem. They have the potential to degrade complex compounds into simpler compatible form that can be assimilated by plants [45]. Nevertheless, endophytes secrete several enzymes including amylase, pectinase, cellulase, lipase, and proteinase that are associated with biodegradation and hydrolytic processes during plant-pathogen interaction as well as for the biodegradation of litter of the host plant [46, 47].

4 Diversity of Endophytes Associated with the Family Zingiberaceae

The endophytic organisms associated with Zingiberaceae family have been isolated from different parts including midrib segment leaf, meristem, roots, stem, leaf blade, and petiole. They are generally isolated by surface sterilization followed by culturing from crushed tissue extract or through culturing of plant tissues on suitable media [48, 49]. The identification of endophytes was executed based on

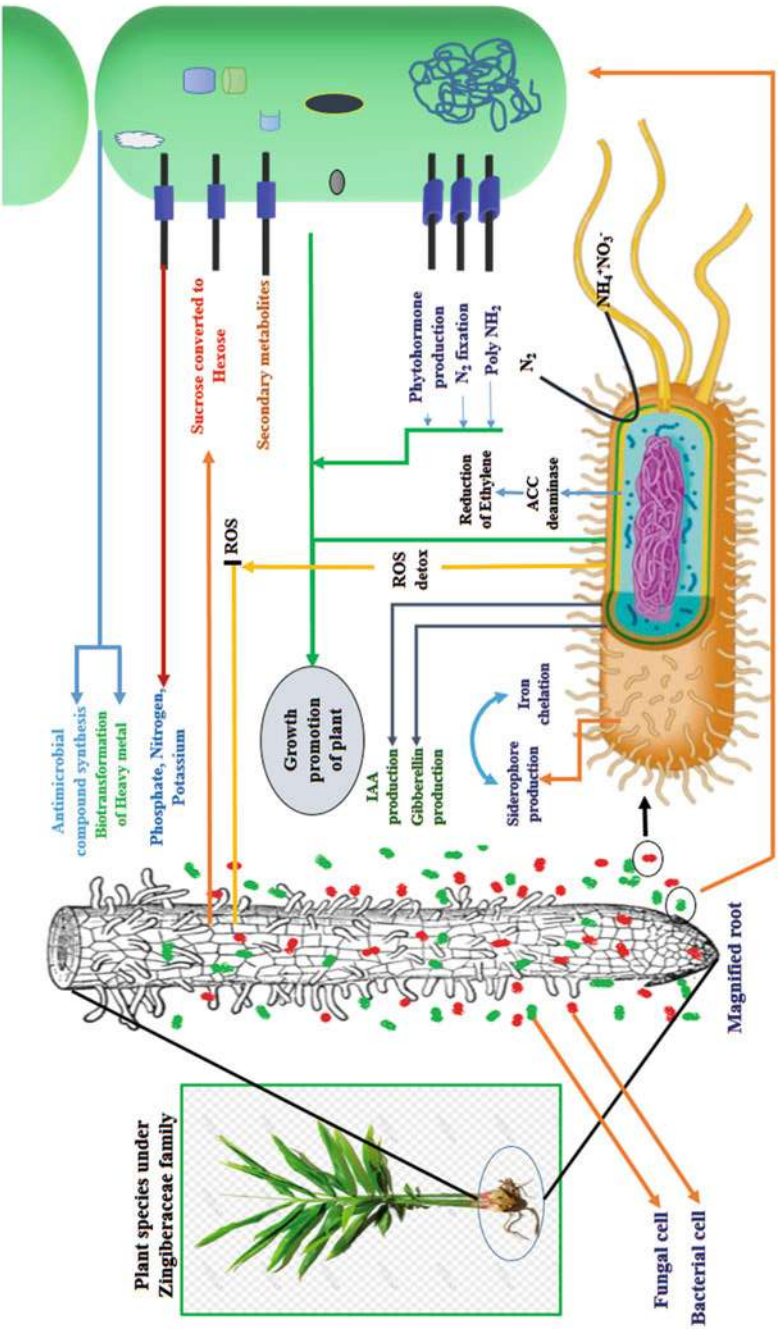

Fig. 1 Schematic representation of beneficial impact of different types of endophytes

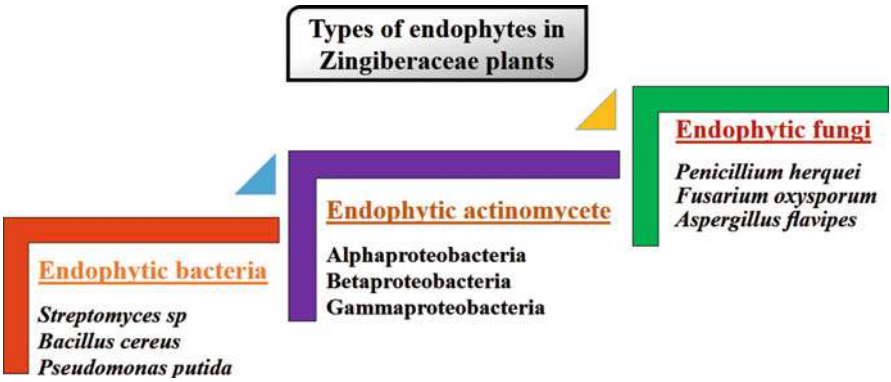

Fig. 2 Different types of endophytes associated with Zingiberaceae family

morphological characteristics corroborated with biochemical tests. The modern molecular biological techniques including ribosomal DNA internal transcribed spacer (ITS) sequence analysis have also been explored in identification of microorganisms as well as their phylogenetic relationships. The endophytes associated with Zingiberaceae are highly diverse (Fig. 2). Different types of endophytes including fungus and bacteria within Zingiberaceae family are represented in Table 1. Fourteen bacterial endophytes, isolated from the rhizome of *Curcuma longa*, were characterized through 16S rRNA sequence analysis [50]. In another study, 11 endophytic fungal strains have been reported from *Curcuma longa* plant [51]. Different parts of the plant including leaf, rhizome, root, and stem of *Zingiber officinale* Rosc., an important plant with medicinal properties, are also associated with various types of endophytes [52–54]. Different types of endophytic bacteria were also identified from *Alpinia galanga*, another important member of this family [55–57].

5 Advantageous Imprint Within the Zingiberaceae Family due to Endophytism

The diverse groups of endophytes associated with Zingiberaceae family are responsible for different types of advantageous functions including growth promotion, synthesis of unique medicinally important bioactive compounds, biocontrol agent, antimicrobial activity, and protection against different types of biotic stress (Fig. 3).

5.1 Plant Growth Promotion by Endophytes

The microorganisms that are capable of providing different types of benefits to the plants are known as plant growth-promoting microorganism [58]. Among different types of microorganism, several genera of bacteria are proficient to encourage plant

Table 1 Diversity of endophytes associated with the plants belonging to the family Zingiberaceae

Plant	Associated endophytes		Reference
	Bacteria	Fungi	
Alpinia galanga	*Streptomyces* sp. Tc022; *Nocardia*; *Microbispora*; *Micromonospora*; *Streptomyces* sp. LJK109		[55–57]
Alpinia officinarum		*Marasmius* sp.; *Penicillium herquei*; *Fusarium oxysporum*; *Colletotrichum siamense*; *Pestalotiopsis* sp.; *Sebacina vermifera*; *Exserohilum* sp.; *Mycoleptodiscus* sp.; *Mycoleptodiscus indicus*; *Scopulariopsis hibernica*; *Meyerozyma guilliermondii*; *Exserohilum* sp.	[92]
Alpinia malaccensis		*Aspergillus flavipes*; *Cladosporium* sp.; *Cladosporium oxysporum*; *Colletotrichum boninense*; *Exophiala* sp.; *Exophiala lecanii-corni*; *Guignardia mangiferae*; *Penicillium citrinum*; *Pyricularia costina*; *Ochroconis gallopava*; *Colletotrichum cliviae*; *Colletotrichum gloeosporioides*; *Diaporthe gardeniae*	[93]
Boesenbergia rotunda	*Streptomyces* sp.; *Asanoa endophytica* sp.		[85, 86]
Curcuma longa	*Bacillus cereus*; *Bacillus thuringiensis*; *Bacillus* spp.; *Bacillus pumilus*; *Pseudomonas putida*; *Clavibacter Michiganensis*; *Stenotrophomonas maltophilia*; *Bacillus safensis*; *Brevibacterium halotolerans*; *Bacillus pumilus*	*Arthrobotrys foliicola*; *Cochliobolus kusanoi*; *Daldinia eschscholzii*; *Fusarium oxysporum*; *Fusarium proliferatum*; *Fusarium solani*; *Fusarium verticillioides*; *Phaeosphaeria ammophilae*; *Phanerochaete chrysosporium*	[50, 51, 94]

(*continued*)

Table 1 (continued)

Plant	Associated endophytes		Reference
	Bacteria	Fungi	
Curcuma heyneana	*Agrobacterium larrymoorei*; *Sphingomonas* sp.; *Herbaspirillum* sp.; *Sphingomonas paucimobilis*; *Agrobacterium tumefaciens*; *Bacillus aerophilus*; *Enterobacter asburiae*; *Brevundimonas* sp.; *Chromobacterium aquaticum*; *Enterobacter cancerogenus*; *Microbacterium testaceum*; *Enterobacter asburiae*; *Curtobacterium plantarum*; *Microbacterium laevaniformans*; *Rhizobium alamii*; *Agrobacterium larrymoorei*		[95]
Curcuma xanthorrhiza		*Fusarium* cf. *oxysporum*; *Fusarium* cf. *solani*; *Eupenicillium* sp.; *Actinomycetes*; *Xylaria* sp.	[96, 97]
Hedychium coronarium		*Trichoderma* sp.; *Mycelia sterilia*; *Penicillium* sp.; *Alternaria* sp.; *Penicillium* sp.; *Fusarium* sp.; *Aspergillus* sp.; *Bipolaris* sp.; *Nigrospora* sp.	[93]
Hedychium acuminatum		*Fusarium oxysporum*; *Rhizoctonia* sp.; *F. solani*; *Colletotrichum alienum*; *C. aotearoa*; *Aspergillus parasiticus*; *Hansfordia biophila*; *F. semitectum*; *C. coccodes*; *C. gloeosporioides*	[84]
Hedychium flavescens		*Colletotrichum* sp.; *Fusarium* sp.; *Bipolaris* sp.; *Pithomyces* sp.; *Mucor* sp.; *Alternaria* sp.; *Mycelia sterilia*; *Rhizopus* sp.; *Fusarium* sp.; *Cladosporium* sp.	[93]
Hornstedtia conica		*Aspergillus flavipes*; *Cladosporium* sp.; *Colletotrichum boninense*; *Diaporthe* sp.; *Diaporthe anacardii*; *Exophiala* sp.; *Exophiala lecanii-corni*; *Penicillium citrinum*; *Pyricularia costina*;	[93]

(*continued*)

Table 1 (continued)

Plant	Associated endophytes		Reference
	Bacteria	Fungi	
		Arthrinium malaysianum; *Colletotrichum cliviae*; *Sydowiellaceae*; *Ochroconis gallopava*	
Kaempferia rotunda	*Actinobacteria*		[96]
Stahlianthus campanulatus	*Nonomuraea stahlianthi*		[98]
Zingiber officinale	*Streptomyces aureofaciens*	*Acremonium macroclavatum*; *Cochliobolus geniculatus*; *Colletotrichum gloeosporioides*; *Curvularia affinis*; *Fusarium oxysporum*; *Fusarium solani*; *Glomerella cingulata*; *Lecanicillium kalimantanense*; *Leiosphaerella lycopodina*; *Myrothecium verrucaria*; *Neonectria punicea*; *Periconia macrospinosa*; *Rhizopycnis vagum*; *Talaromyces assiutensis*; *Ascomycota* sp.; *Fusarium* sp.; *Gliocladiopsis*; *Acremonium furcatum*; *Trichothecium* sp.; *Colletotrichum crassipes*; *Aspergillus niger*; *Phlebia* sp.; *Fusarium oxysporum*; *Earliella scabrosa*; *Pseudolagarobasidium* sp.; *Cerrena* sp.	[52–54]
Zingiber montanum	*Pseudomonas baetica*		[99]

growth through plentiful independent or interconnected pathways [4]. The endophytic bacteria, associated with Zingiberaceae family, can stimulate growth by synthesizing phytohormones, modulating the uptake of minerals from soil, maintaining iron homeostasis, and increasing availability of phosphorus (Table 2).

5.1.1 Production of Phytohormone Indole-3-Acetic Acid

The plant growth-promoting phytohormone indole-3-acetic acid (IAA) is responsible for the induction of root growth in plant. It has been reported that the bacteria including *Bacillus cereus*, *Bacillus thuringiensis*, *Bacillus pumilus*, *Pseudomonas putida*, and *Clavibacter michiganensis* isolated from *Curcuma longa* are capable of synthesizing IAA in associative condition with the plant [59]. In another study, IAA

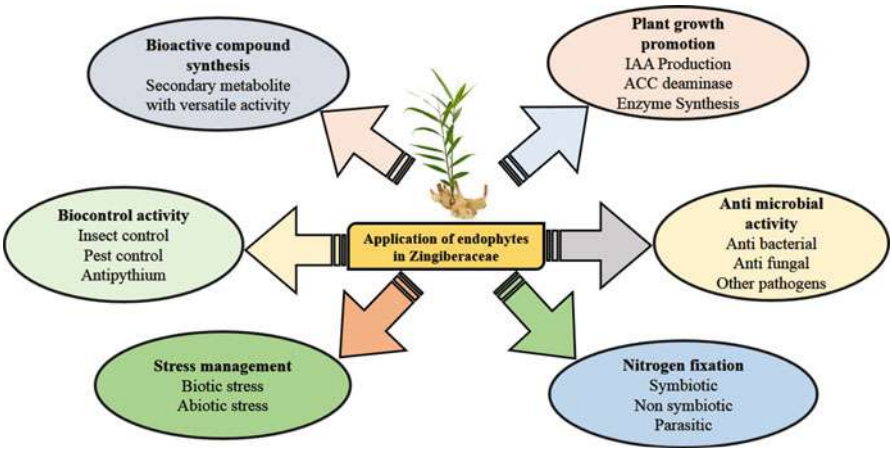

Fig. 3 Advantageous roles of endophytes within Zingiberaceae family

producing bacteria including *Pseudomonas aeruginosa*, *Enterobacter* sp., and *Acinetobacter* sp. were also isolated from *C. longa* [60]. The bacteria of *Paenibacillus* sp., found in *C. longa* rhizome, also have the ability to synthesize IAA and have been reported to promote the growth of the plant species [61]. The endophytic bacteria of *Pseudomonas* sp. isolated from *Z. officinale* were also found responsible for the production of IAA [62]. Nineteen endophytic bacteria, including *P. putida*, *L. adecarboxylata*, *S. nematodiphila*, *Pantoea ananatis*, *A. pasteurianus*, *S. maltophilia*, *A. trotsa*, and *A. larrymoorei*, were reported to be able to produce IAA and could promote the growth in ginger plant [63]. In another study, about 57 endophytic bacteria, isolated from ginger rhizome and identified through 16S rDNA PCR-RFLP fingerprinting, 14 bacteria of genera including *Agrobacterium*, *Ochrobactrum*, *Bacillus*, *Serratia*, *Acinetobacter*, *Pseudomonas*, *Stenotrophomonas*, *Enterobacter*, and *Tetrathiobacter* were found to be capable of synthesizing IAA [64]. Another study showed that one of the *Klebsiella* spp., present in the rhizome of the same plant, also helps in the production of the important hormone IAA [65].

5.1.2 Maintenance of Iron Homeostasis Through Production of Siderophore

Iron acts as an essential element for the growth of all living organisms due to its diverse biological activities including electron transfer, oxygen metabolism, enzymatic reactions, etc. [66]. Under low bioavailability condition, different types of microorganisms follow some specific iron uptake strategies such as the production of siderophores [67, 68]. The extracellular chelating compounds, siderophores, are divided into four major categories: rhodotorulic acid, fusarinines, coprogens, and ferrichromes. Although its primary function is to convert soil iron into a soluble form under iron starvation, its complex forming ability with other essential elements of siderophores is also reported [67, 68]. It has also been recommended that these

Table 2 Plant growth-promoting activity of endophytes associated with Zingiberaceae family

Plant Name	Associated Endophytes		PGPR activity	Reference
	Bacteria	Fungi		
Alpinia malaccensis		*Aspergillus flavipes*; *Cladosporium* sp.; *Cladosporium oxysporum*; *Colletotrichum boninense*; *Exophiala* sp.; *Exophiala lecanii-corni*; *Guignardia mangiferae*; *Penicillium citrinum*; *Pyricularia costina*; *Ochroconis gallopava*; *Colletotrichum cliviae*; *Colletotrichum gloeosporioides*; *Diaporthe gardenia*	Amylase, cellulase, pectinase, and asparaginase activity	[93]
Amomum siamense		*Eupenicillium crustaceum*; *Fusarium* spp.; *Glomerella* spp.; *Phomopsis* spp.; *Phyllosticta* spp.; *Pyricularia* spp.; *Talaromyces flavus*; *Xylariaceae taxa*; *Mycelia sterilia*	Absorption of soil nutrients including phosphorus	[75]
Curcuma longa	*Stenotrophomonas maltophilia*; *Bacillus safensis*; *Brevibacterium halotolerans*; *Bacillus pumilus*		Nitrate reduction, H_2S production, starch hydrolysis, IAA production, phosphorus solubilization, siderophore production,	[59]

(*continued*)

Table 2 (continued)

Plant Name	Associated Endophytes		PGPR activity	Reference
	Bacteria	Fungi		
Curcuma heyneana	*Agrobacterium larrymoorei*; *Sphingomonas* sp.; *Herbaspirillum* sp.; *Sphingomonas paucimobilis*; *Agrobacterium tumefaciens*; *Bacillus aerophilus*; *Enterobacter asburiae*; *Brevundimonas* sp.; *Chromobacterium aquaticum*; *Enterobacter cancerogenus*; *Microbacterium testaceum*; *Enterobacter asburiae*; *Curtobacterium plantarum*; *Microbacterium laevaniformans*; *Rhizobium alamii*; *Agrobacterium larrymoorei*		Nitrogen fixation	[95]
Hedychium coronarium		*Trichoderma* sp.; *Mycelia sterilia*; *Penicillium* sp.; *Mycelia sterilia*; *Alternaria* sp.; *Penicillium* sp.; *Fusarium* sp.; *Aspergillus* sp.; *Bipolaris* sp.; *Nigrospora* sp.	Amylase, cellulase, pectinase, and asparaginase activity	[93]
Hedychium flavescens		*Colletotrichum* sp.; *Fusarium* sp.; *Bipolaris* sp.; *Pithomyces* sp.; *Mucor* sp.; *Alternaria* sp.; *Mycelia sterilia*; *Rhizopus* sp.; *Fusarium* sp.; *Cladosporium* sp.	amylase, cellulase, pectinase, and asparaginase activity	[93]
Stahlianthus campanulatus	*Nonomuraea stahlianthi* sp.		Nitrate reduction, carbon utilization	[98]

compounds play pivotal role in the induction of systemic resistance against bacterial, fungal, and viral diseases [69–71]. The endophytic bacteria *Pseudomonas putida* were able to synthesize siderophore in the plant *C. longa* and could be able to provide protection against other pathogenic microbes [59]. In another study, it has been reported that the synthesis of siderophore protects turmeric against rot and leaf blight diseases caused by *Pythium aphanidermatum* (Edson) Fitzp. and *Rhizoctonia solani* Kuhn. [72]. Siderophore production, in the root of *Zingiber officinale* by different species of *Pseudomonas* and *Stenotrophomonas*, has also been reported by Jasim et al. 2014 [62].

5.1.3 Phosphate Solubilization

Insoluble phosphate is often present in the soil, but plant is unable to take up this form of phosphate. The soluble form is most important mineral for the growth of the plants and enhances crop productivity [73, 74]. Bacterial and fungal endophytes, associated with plant root, can help to solubilize the phosphate and convert insoluble phosphate to the common soluble form, so that plant can take up easily [64]. *Bacillus cereus*, *Bacillus* sp., *Bacillus pumilus*, and *Pseudomonas putida*, present in the roots and associated area of the important medicinal *C. longa*, promote the growth of the plant by inducing availability of phosphate [50, 59]. It has also been reported that the strain of *Klebsiella* sp., present in the rhizome of the turmeric plant, can also promote the growth of the plant by transforming insoluble phosphate into soluble form [65]. The endophytes associated with *Amomum siamense* were found to help the host plant in absorption of soil nutrients, such as phosphorus and other essential molecules that can stimulate the growth of the plant [75].

5.1.4 ACC Deaminase Production

It is well accepted that the plant growth-promoting bacteria (PGPB) that produce the enzyme 1-aminocyclopropane-1-carboxylic acid (ACC) deaminase facilitates plant growth by lowering the plant ethylene levels that, when present in high concentrations, can be detrimental to plants. The enzyme ACC deaminase actually catalyzes the cleavage of 1-aminocyclopropane-1-carboxylic acid (ACC), the ethylene precursor, into ammonia and α-ketobutyrate. Thus, the ACC deaminase-producing bacteria help the plant growth by reducing a portion of ethylene biosynthesis. Many members of the genera *Azospirillum*, *Rhizobium*, *Agrobacterium*, *Achromobacter*, *Burkholderia*, *Ralstonia*, *Pseudomonas*, and *Enterobacter*, along with various endophytic strains, produce ACC deaminase [76]. Some strains of *Pseudomonas* sp., found in association with *Zingiber officinale*, can produce ACC deaminase and hence can suppress the effect of the hormone ethylene and can enhance the growth of the plant [62]. Pseudomonas-related production of ACC deaminase is also reported by another group of researchers [77]. Ethylene-mediated plant growth inhibition decreases with the decrease of the level of ACC and ethylene. Endophytic microbes increase the plant growth by residing inside the host plants with these capabilities and can promote the growth of the host plant by reducing ethylene-inducing stresses [7, 78].

Table 3 Endophyte associated with the plants belonging to family Zingiberaceae and their bioactive compounds

Plant	Associated Endophytes		Active compound	Reference
	Bacteria	Fungi		
Alpinia galanga	*Streptomyces* sp. Tc022; *Nocardia*; *Microbispora*; *Micromonospora*; *Streptomyces* sp. LJK109		Kaempferol, scutellarin, umbelliferone, ctinomycin D	[55, 56]
Boesenbergia rotunda	Strain BO-07 *Streptomyces* sp.		3′-Hydroxy-5-methoxy-3,4-methylenedioxybiphenyl and 3′-hydroxy-5,5′-dimethoxy-3,4-methylenedioxybiphenyl	[85]
Curcuma xanthorrhiza		*Fusarium* cf. *oxysporum*; *Fusarium* cf. *solani*; *Eupenicillium* sp.; *Actinomycetes*; *Xylaria* sp.	$C_{17}H_{16}O$, xylarugosin, and resacetophenone	[97]
Hedychium acuminatum		*Fusarium oxysporum*; *Rhizoctonia* sp.; *F. solani*; *Colletotrichum alienum*; *C. aotearoa*; *Aspergillus parasiticus*; *Hansfordia biophila*; *F. semitectum*; *C. coccodes*; *C. gloeosporioides*	Secondary metabolite	[84]
Zingiber officinale		*Ascomycota* sp.; *Fusarium* sp.; *Gliocladiopsis*; *Acremonium furcatum*; *Trichothecium* sp.; *Colletotrichum crassipes*; *Aspergillus niger*; *Phlebia* sp.; *Fusarium oxysporum*; *Earliella scabrosa*; *Pseudolagarobasidium* sp.; *Cerrena* sp.	Tyrosol, benzene acetic acid, ergone, dehydromevalonic lactone, N-aminopyrrolidine, and many bioactive fatty acids and their derivatives which included linoleic acid, oleic acid, myristic acid, n-hexadecanoic acid, palmitic acid methyl ester, and methyl linoleate	[53]

(*continued*)

Table 3 (continued)

Plant	Associated Endophytes		Active compound	Reference
	Bacteria	Fungi		
Zingiber officinale	*Streptomyces aureofaciens*		5,7-Dimethoxy-4-phenylcoumarin (51b), 5,6-dimethoxy-4-(p-methoxyphenyl) coumarin (51c) vanillin 3-methoxy-4-hydroxytoluene	[55]
Zingiber spectabile	*Streptomyces omiyaensis* NBRC 13449T		prolyl (3S, 8aR)-3-(1H-indol-3-ylmethyl) hexahydropyrrolo [1, 2-a], pyrazine-1, 4-dione CAP 2,2-dichloro-*N*-[(1R, 2R)-2-hydroxy-1-(hydroxymethyl)-2-(4-nitrophenyl) ethyl]-acetamide	[87]

5.2 Synthesis of Bioactive Compounds

Bioactive natural products represent the class of compounds synthesized by living organisms with high therapeutic value. These compounds are secondary metabolites and produced mostly by plants and microbes – alone or in association with each other. Different endophytic microbes including fungi, bacteria, and actinomycetes produce varied types of bioactive compounds like terpenoids, alkaloids, flavonoids, steroids, peptides, quinols, and phenols. These bioactive secondary metabolites, produced by endophytes, are usually used by plants for defense against abiotic and biotic stresses. Nevertheless, a plethora of these compounds has been confirmed to be valuable for novel drug synthesis in pharmaceutical industry. It has been reported that hundreds of these natural products serve as important sources of anticancer, antioxidant, antibacterial, antidiabetic, antifungal, immunosuppressive, insecticidal, and antiviral agents [79–81]. It is also established that these secondary metabolites are associated with cell signaling, alleviation of biotic and abiotic stress, and establishment of symbiosis [82]. Recently, it has also been reported that apart from the production of secondary metabolites, endophytes are also able to modulate the secondary metabolism within their host plant [83]. There are reports of production of several important secondary metabolites by various endophytic microorganisms in different members of Zingiberaceae (Table 3; Fig. 4). In the medicinal plant *Alpinia galanga*, the important secondary metabolites including kaempferol, scutellarin, umbelliferone, and actinomycin D were found to be synthesized by different endophytic bacteria [55, 56]. In another plant, *Hedychium accuminatum*, 11 endophytic fungi were found to be responsible for the production of various metabolites including alkaloids, flavonoids, terpenoids, and tannins [84]. The endophytic species

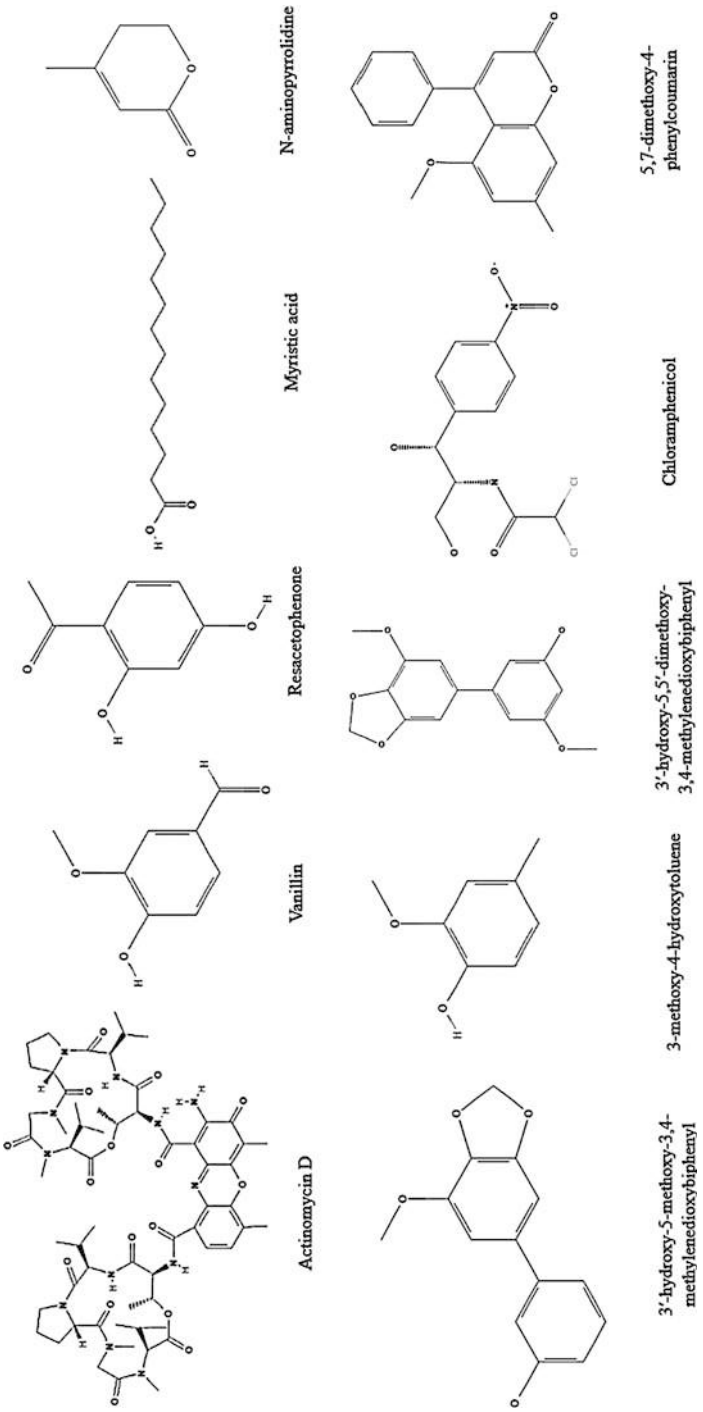

Fig. 4 The chemical structure of different secondary metabolites associated with various endophytic microorganisms

of *Streptomyces* (strain BO-07), isolated from the root tissue of *Boesenbergia rotunda*, was found to contain two biphenyls, 3′-hydroxy-5-methoxy-3,4-methylenedioxybiphenyl and 3′-hydroxy-5,5′-dimethoxy-3,4-methylenedioxy-biphenyl, with antibacterial, antioxidant, and anticancer activities [85]. Fifteen fungal strains including the genera of *Acremonium*, *Gliocladiopsis*, *Fusarium*, *Colletotrichum*, *Aspergillus*, *Phlebia*, *Earliella*, and *Pseudolagarobasidium* were found to be associated with *Z. officinale* [53]. The fungal bodies extracted from this plant were subjected to metabolite profiling and found to contain many bioactive compounds including tyrosol, dehydromevalonic lactone, ergone, *N*-aminopyr-rolidine, benzene acetic acid, linoleic acid, oleic acid, myristic acid, n-hexadecanoic acid, palmitic acid, and methyl ester. In another report, *Streptomyces aureofaciens* CMUAc130 was isolated from *Z. officinale* root [54], and compounds like 5,7-dimethoxy-4-p-methoxylphenylcoumarin and 5,7-dimethoxy-4-phenylcoumarin, with antifungal activity, were isolated from the bacterial extract. The bacterial strain of *Streptomyces* BT01, isolated from *Boesenbergia rotunda* (L.), was identified through 16S rDNA sequencing [86]. Two important flavonoids with antibacterial activity, namely, 7-methoxy-3,3′,4′,6-tetrahydroxyflavone and 2′,7-dihydroxy-4′,5′-dimethoxyisoflavone, were identified by thin-layer chromatography. The secondary metabolites like cyclo-(L-tryptophanyl-L-prolyl) (3S, 8aR)-3-(1H-indol-3ylmethyl) hexahydropyrrolo [1, 2-a] pyrazine-1, 4-dione, CAP 2,2-dichloro-*N*-[(1R, 2R)-2-hydroxy-1-(hydroxymethyl)-2-(4-nitrophenyl) ethyl]-acetamide (diketopiperazine cyclo-(tryptophanyl-prolyl), and chloramphenicol, isolated from *Streptomyces* sp., an endophytic association of rhizomatous root of *Zingiber spectabile* [87], showed anti-methicillin resistance against *S. aureus* activity.

Several endophytic bacteria are capable of synthesizing a vast range of uncharacterized secondary metabolites. There are limited information regarding the amount and conditions under which these metabolites are produced. The revolution in the field of genomics along with expansion of modern analytical techniques will definitely hasten the detection of such cryptic compounds and will assist to explore the wide spectrum of secondary metabolites with novel chemical structures encoded by the genomes of endophytic microorganisms of the entire Zingiberaceae family.

5.3 Antimicrobial Activity of Endophytes

The diverse groups of endophytes isolated from plants of Zingiberaceae family are recognized for their antimicrobial properties (Table 4). The crude extract of bacterial strain of *Streptomyces* sp. LJK109, isolated from root tissues of *Alpinia galanga* [88], showed antifungal potential against pathogenic fungi *Alternaria porri*, *Colletotrichum gloeosporioides*, *Colletotrichum musae*, *Curvularia* sp., *Drechslera* sp., *Exserohilum* sp., *Fusarium oxysporum*, *Verticillium* sp., and *Sclerotium rolfsii*. The endophytic fungi, isolated and identified via internal transcribed spacer (ITS) region of ribosomal DNA from *Curcuma longa*, have antibacterial potential against

Table 4 Antimicrobial activity of endophytes associated with plants belonging to family Zingiberaceae

Plant	Associated Endophytes		Antimicrobial activity	Reference
	Bacteria	Fungi		
Alpinia galanga	*Streptomyces* sp. Tc022; Nocardia; Microbispora; Micromonospora; *Streptomyces* sp. LJK109		Antifungal activity	[56, 88]
Boesenbergia rotunda	*Streptomyces* sp.; *Asanoa endophytica* sp.		Antibacterial activity	[86]
Curcuma longa	*Bacillus cereus*; *Bacillus thuringiensis*; *Bacillus* sp.; *Bacillus pumilus*; *Pseudomonas putida*; *Clavibacter Michiganensis*; *Stenotrophomonas maltophilia*; *Bacillus safensis*; *Brevibacterium halotolerans*; *Bacillus pumilus*	*Arthrobotrys foliicola*; *Cochliobolus kusanoi*; *Daldinia eschscholzii*; *Fusarium oxysporum*; *Fusarium proliferatum*; *Fusarium solani*; *Fusarium verticillioides*; *Phaeosphaeria ammophilae*; *Phanerochaete chrysosporium*	Antibacterial and antifungal activity	[51, 94]
Curcuma xanthorrhiza		*Fusarium* cf. *oxysporum*; *Fusarium* cf. *solani*; *Eupenicillium* sp.; *Actinomycetes*; *Xylaria* sp.;	Antibacterial activity	[97]
Kaempferia rotunda	*Actinobacteria*		Antibacterial activity	[96]

histamine-producing bacteria *Morganella morganii* [51]. Several endophytic actinomycetes were isolated from *Zingiber officinale* rhizome among which Nocardiopsis sp. ZoA1 was found to be highly active against phytopathogen and human clinical pathogens [89].

5.4 Biocontrol Activity of Endophytes

Some of the microbes often prevent the deleterious effects of the potent plant pathogens including bacteria, fungi, and nematodes. This is considered as biocontrol activity. In agriculture, biocontrol microorganisms have appeared as harmless replacements of chemical pesticides. They also cause indirect promotion of plant

Table 5 Biocontrol activity of endophytes associated with Zingiberaceae family

Plant	Associated endophytes		Effects	Reference
	Fungi	Bacteria		
Alpinia galanga		*Streptomyces* sp. Tc022	Effective against pathogen *Colletotrichum musae* and *Candida albicans*	[55]
Amomum siamense	*Eupenicillium crustaceum*; *Fusarium* spp.; *Glomerella* spp.; *Phomopsis* spp.; *Phyllosticta* spp.; *Pyricularia* spp.; *Talaromyces flavus*; *Xylariaceae taxa*; *Mycelia sterilia*		Protect from insect attack	[75]
Curcuma longa	*Trichoderma harzianum*		Antagonistic activity against *Pythium aphanidermatum*	[72]
		Bacillus cereus	Inhibit growth of *Rhizoctonia solani*	
	Arthrobotrys foliicola; *Cochliobolus kusanoi*; *Daldinia eschscholzii*; *Fusarium oxysporum*; *Fusarium proliferatum*; *Fusarium solani*; *Fusarium verticillioides*; *Phanerochaete chrysosporium*, *Phaeosphaeria ammophilae*		Inhibit growth of the histamine-producing bacteria	[51]
	Fungal isolates		Leaf spot disease	[90]
		Bacillus; *Pseudomonas*; *Klebsiella*; *Citrobacter*	*Pythium aphanidematum*	[91]

(*continued*)

Table 5 (continued)

Plant	Associated endophytes		Effects	Reference
	Fungi	Bacteria		
Zingiber officinale	*Acremonium macroclavatum*; *Cochliobolus geniculatus*; *Colletotrichum gloeosporioides*; *Curvularia affinis*; *Fusarium oxysporum*; *Fusarium solani*; *Glomerella cingulata*; *Lecanicillium kalimantanense*; *Leiosphaerella lycopodina*; *Myrothecium verrucaria*; *Neonectria punicea*; *Periconia macrospinosa*; *Rhizopycnis vagum*, *Talaromyces assiutensis*		Inhibitory activity against *F. oxysporum*	[52]
	Ascomycota sp.; *Fusarium* sp.; *Gliocladiopsis*; *Acremonium furcatum*; *Trichothecium* sp.; *Colletotrichum crassipes*; *Aspergillus niger*; *Phlebia* sp.; *Fusarium oxysporum*; *Earliella scabrosa*; Pseudolagarobasidium sp.; Cerrena sp.		Anti-*Pythium* activity	[53]

growth by limiting the damage caused by their phytopathogens. The endophytes associated with different members of Zingiberaceae can efficiently remove plant pathogens (Table 5). There is a potent pathogen *Colletotrichum gloeosporioides* that causes leaf spot on turmeric and is responsible for major economic damage in cultivation of turmeric. It has been reported that about 200 endophytic fungal strains, isolated from *Curcuma longa*, have antagonistic effect on this pathogen [90]. In another study, five endophytic fungi isolated from turmeric have been found to have biocontrol activity against *Morganella morganii* [51]. Thirty-one endophytes from the rhizome of *C. longa*, isolated and identified by morphological and ITS analysis and by rDNA sequencing, were found to be active against *Pythium aphanidermatum* (Edson) Fitzp, the causal agent of turf rot blights [72]. In another report, 154 endophytes were identified from turmeric with anti-*Pythium* activity [91]. The endophytic strain isolated from *Zingiber officinale* was very much effective against *Fusarium oxysporum*, a potent phytopathogen that causes excessive loss in

agriculture [52]. Streptomyces sp. Tc022, associated with root of *Alpinia galanga*, showed inhibitory effect on the fungal pathogens, *Colletotrichum musae* and *Candida albicans* [55].

6 Conclusion

Comprehensive studies on endophytism in different important members of Zingiberaceae suggest that endophytic microorganisms could find a direct application on the improvement of productivity and protection of plants against biotic and abiotic stresses. The endophytes isolated from different members of this family can also be considered as a novel source of bioactive molecules. Several endophytes of this family are potential source of secondary metabolites that have enormous industrial and pharmaceutical applications. However, *in planta* synthesis of these medicinally important natural products is very much challenging due to involvement of multiple genes and complex nature of biosynthetic pathways. Consequently, identification and isolation of specific genes in endophyte genome associated with the synthesis of bioactive molecule and subsequent metabolic engineering can ultimately result in enhanced production of the desired metabolites, at industrial level. Therefore, the identification of holobiont (host and its associated microorganisms) is a major and fascinating field of research that reveals symbiotic relationship between plant and microbes. The involvement of contemporary molecular biological tools and improved techniques of isolation along with an application of efficient genomic data mining techniques and identification of uncharacterized endophytes within Zingiberaceae family, for the purpose of comprehensive analysis of endophytic microorganisms and plant holobiome, is quite an achievable target. Nevertheless, implementation of multidisciplinary "omics" science and methods is inevitable to decipher the endophytism within Zingiberaceae family for human welfare. These approaches, corroborated with the system biology, will definitely explore the comprehensive physiological and biochemical processes associated with the host-endophyte symbiotic relationship, stress tolerance displayed by endophytes, and their pivotal role in growth promotion.

Acknowledgments The authors are thankful to Swami Kamalasthananda, Principal, Ramakrishna Mission Vivekananda Centenary College, Rahara, Kolkata (India), for the facilities provided during the present study and acknowledge DST-FIST program for infrastructural facilities.

References

1. Bary A (1866) Morphologie und Physiologie Pilze, Flechten, und myxomyceten, Hofmeister's Handbook of Physiological Botany. Engelmann, Leipzig
2. Galippe V (1887) Note sur la pr é sence de micro-organismes dans les tissus végétaux. C R Hebd Sci Mem Soc Biol 39:410–416
3. Di Vestea A (1888) De l'absence des microbes dans les tissus végétaux. Annales de l'lnstitut Pasteur 670e671

4. Compant S, Clément C, Sessitsch A (2010) Plant growth-promoting bacteria in the rhizo- and endosphere of plants: their role, colonization, mechanisms involved and prospects for utilization. Soil Biol Biochem 42:669–678. https://doi.org/10.1016/j.soilbio.2009.11.024
5. Bacon CW, White JFJ (2000) Physiological adaptations in the evolution of endophytism in the Clavicipitaceae. In: Bacon CW, White JFJ (eds) Microbial endophytes. Marcel Dekker Inc, New York, pp 237–263
6. Rosenblueth M, Martínez-Romero E (2006) Bacterial endophytes and their interactions with hosts. Mol Plant-Microbe Interact 19:827–837
7. Hardoim PR, van Overbeek LS, van Elsas JD (2008) Properties of bacterial endophytes and their proposed role in plant growth. Trends Microbiol 16:463–471
8. Ryan RP, Germaine K, Franks A, Ryan DJ, Dowling DN (2008) Bacterial endophytes: recent developments and applications. FEMS Microbiol Lett 278:1–9
9. Hallmann J, Quadt-Hallmann A, Mahaffee WF, Kloepper JW (1997) Bacterial endophytes in agricultural crops. Can J Microbiol 43:895–914
10. Coombs JT, Franco CMM (2003) Isolation and identification of *Actinobacteria* from surface-sterilized wheat roots. Appl Environ Microbiol 69:5603–5608
11. Wong KC, Ong KS, Lim CL (1992) Composition of the essential oil of rhizomes of *Kaempferia galanga* L. Flavour Fragr J 7:263–266
12. Pandji C, Grimm C, Wray V, Witte L, Proksch P (1993) Insecticidal constituents from four species of Zingiberaceae. Phytochemistry 34:415–419
13. Orasa P, Yenhatai N, Pittaya T, Taylor W (1994) Cyclohexane oxide derivatives and diterpenes from the genus *Kaempferia*. ASOMPS, VIII, Malaysia
14. Parwat U, Tuntiwachwuttikul P, Taylor WC, Engelhardt LM, Skelton BW, White AH (1993) Diterpenes from *Kaempferia* species. Phytochemistry 32:991–997
15. Singh UP, Srivsastava BP, Singh KP, Pandey VB (1992) Antifungal activity of steroid saponins and sapogenins from *Avena sativa* and *Costus speciosus*. Nat Sao Paulo 17:71–77
16. Husain A (1992) Dictionary of Indian medicinal plants. Central Institute of Medicinal and Aromatic Plants, Lucknow
17. Warrier PK, Nambiar VPK, Ramankutty C (1993–1995) Indian medicinal plants, vol 1–5. Orient Longman Ltd. Madras
18. Chunekar KC (1982) Bhavaprakashanighantu of Sri Bhavamishra. Commentary, Varanasi (in Hindi)
19. Gurib-Fakim A (2006) Medicinal plants: traditions of yesterday and drugs of tomorrow. Mol Asp Med 27:1–93
20. Denyer CV, Jackson P, Loakes DM, Ellis MR, Young AB (1994) Isolation of antirhinoviral sesquiterpenes from ginger (*Zingiber officinale*). J Nat Prod 57:658–662
21. Xiuzhen C, Dejian Q, Hexing D (1992) Studies on the constituents of the essential oil of *Zingiber officinale*. Guihaia 12:129–132
22. Kirtikar KR, Basu BD (1987) Indian medicinal plants, vol vol I-IV. International Book Distributors, Dehradun
23. Sukari MA, Neoh BK, Lajis NH, Ee GCL, Rahmani M, Ahmad FH, Yusof UK (2004) Chemical constituents of *Kaempferia angustifolia* (Zingiberaceae). Orient J Chem 20:451–456
24. Yeap YSY, Kassim NK, Ng RC, Ee GCL, Saiful Yazan L, Musa KH (2017) Antioxidant properties of ginger (*Kaempferia angustifolia* Rosc.) and its chemical markers. Int J Food Prop 20:1158–1172
25. Sherameti I, Shahollari B, Venus Y, Altschmied L, Varma A, Oelmüller R (2005) The endophytic fungus Piriformospora indica stimulates the expression of nitrate reductase and the starch-degrading enzyme glucan-water dikinase in tobacco and Arabidopsis roots through a homeodomain transcription factor that binds to a conserved motif in their promoters. J Biol Chem 280:26241–26247
26. Mathys J, De Cremer K, Timmermans P, Van Kerkhove S, Lievens B, Vanhaecke M, Cammue B, De Coninck B (2012) Genome-wide characterization of ISR induced in

Arabidopsis thaliana by Trichoderma hamatum T382 against Botrytis cinerea infection. Front Plant Sci 3:108
27. Straub D, Rothballer M, Hartmann A, Ludewig U (2013) The genome of the endophytic bacterium H. frisingense GSF30T identifies diverse strategies in the Herbaspirillum genus to interact with plants. Front Microbiol 4:168
28. Gundel PE, Martínez-Ghersa MA, Omacini M, Cuyeu R, Pagano E, Ríos R, Ghersa CM (2012) Mutualism effectiveness and vertical transmission of symbiotic fungal endophytes in response to host genetic background. Evol Appl 5:838–849
29. Qawasmeh A, Obied HK, Raman A, Wheatley W (2012) Influence of fungal endophyte infection on phenolic content and antioxidant activity in grasses: interaction between Lolium perenne and different strains of Neotyphodium lolii. J Agric Food Chem 60:3381–3388
30. Boller T (1995) Chemoperception of microbial signals in plant cells. Annu Rev Plant Biol 46:189–214
31. Tanaka A, Christensen MJ, Takemoto D, Park P, Scott B (2006) Reactive oxygen species play a role in regulating a fungus–perennial ryegrass mutualistic interaction. Plant Cell 18:1052–1066
32. White JF Jr, Torres MS (2010) Is plant endophyte-mediated defensive mutualism the result of oxidative stress protection? Physiol Plant 138:440–446
33. Singh D, Rathod V, Ninganagouda S, Herimath J, Kulkarni P (2013) Biosynthesis of silver nanoparticle by endophytic fungi *Penicillium* sp. isolated from *Curcuma longa* (turmeric) and its antibacterial activity against pathogenic gram negative bacteria. J Pharm Res 7:448–453
34. Conn VM, Walker AR, Franco CMM (2008) Endophytic *Actinobacteria* induce defense pathways in Arabidopsis thaliana. Mol Plant-Microbe Interact 21:208–218
35. Nair DN, Padmavathy S (2014) Impact of endophytic microorganisms on plants, environment and humans. Sci World J 2014:e250693
36. Xin G, Zhang G, Kang JW, Staley JT, Doty SL (2009) A diazotrophic, indole-3-acetic acid-producing endophyte from wild cottonwood. Biol Fertil Soils 45:669–674
37. Joseph B, Mini Priya R (2011) Bioactive compounds from endophytes and their potential in pharmaceutical effect: a review. Am J Biochem Mol Biol 1:291–309
38. Gaiero JR, McCall CA, Thompson KA, Day NJ, Best AS, Dun field KE (2013) Inside the root microbiome: bacterial root endophytes and plant growth promotion. Am J Bot 100:1738–1750
39. Nair DN, Padmavathy S (2014) Impact of endophytic microorganisms on plants, environment and humans. Sci World J 2014:1–11
40. Tan RX, Zou WX (2001) Endophytes: a rich source of functional metabolites. Nat Prod Rep 18:448–459
41. Pimentel MR, Molina G, Dionisio AP, Maróstica MR, Pastore GM (2011) Use of endophytes to obtain bioactive compounds and their application in biotransformation process. Biotechnol Res Int 2011:1–11. https://doi.org/10.4061/2011/576286
42. Schulz B, Boyle C, Draeger S, Rommert A-K, Krohn K (2002) Endophytic fungi: a source of novel biologically active secondary metabolites. Mycol Res 106:996–1004
43. Strobel GA (2003) Endophytes as sources of bioactive products. Microbes Infect 5:535–544
44. Prado S, Buisson D, Ndoye I, Vallet M, Nay B (2013) One-step enantioselective synthesis of (4S)-isosclerone through biotransformation of juglone by an endophytic fungus. Tetrahedron Lett 54:1189–1191
45. Müller MM, Valjakka R, Suokko A, Hantula J (2001) Diversity of endophytic fungi of single Norway spruce needles and their role as pioneer decomposers. Mol Ecol 10:1801–1810
46. Gunatilaka AAL (2006) Natural products from plant-associated microorganisms: distribution, structural diversity, bioactivity, and implications of their occurrence. J Nat Prod 69:505–526
47. Fouda AH, El-Din Hassan S, Eid AM, El-Din Ewais E (2015) Biotechnological applications of fungal endophytes associated with medicinal plant *Asclepias sinaica* (Bioss). Ann Agric Sci 60:95–104
48. Rai R, Dash PK, Prasanna BM, Singh A (2007) Endophytic bacterial flora in the stem tissue of a tropical maize (Zea mays L.) genotype: isolation, identification and enumeration. World J Microbiol Biotechnol 23:853–858

49. Hata K, Sone K (2008) Isolation of endophytes from leaves of Neolitsea sericea in broadleaf and conifer stands. Mycoscience 49:229–232
50. Kumar A, Singh R, Yadav A, Giri DD, Singh PK, Pandey KD (2016) Isolation and characterization of bacterial endophytes of *Curcuma longa* L. 3 Biotech 6:60. https://doi.org/10.1007/s13205-016-0393-y
51. Septiana E, Sukarno N, Simanjuntak P (2017) Endophytic fungi associated with turmeric (*Curcuma longa* L.) can inhibit histamine-forming bacteria in fish. HAYATI J Biosci 24:46–52. https://doi.org/10.1016/j.hjb.2017.05.004
52. Ginting RCB, Sukarno N, Widyastuti U, Darusman LK, Kanaya S (2013) Diversity of endophytic fungi from red ginger (*Zingiber officinale* Rosc.) plant and their inhibitory effect to *Fusarium oxysporum* plant pathogenic fungi. HAYATI J Biosci 20:127–137. https://doi.org/10.4308/hjb.20.3.127
53. Anisha C, Radhakrishnan EK (2017) Metabolite analysis of endophytic fungi from cultivars of *Zingiber officinale* Rosc. identifies myriad of bioactive compounds including tyrosol. 3 Biotech 7:1–10. https://doi.org/10.1007/s13205-017-0768-8
54. Taechowisan T, Lu C, Shen Y, Lumyong S (2005) Secondary metabolites from endophytic *Streptomyces aureofaciens* CMUAc130 and their antifungal activity. Microbiology 151:1691–1695
55. Taechowisan T, Wanbanjob A, Tuntiwachwuttikul P, Taylor WC (2006) Identification of *Streptomyces* sp. Tc022, an endophyte in *Alpinia galanga*, and the isolation of actinomycin D. Ann Microbiol 56:113–117
56. Taechowisan T, Chuaychot N, Chanaphat S, Wanbanjob A, Shen Y (2008) Biological activity of chemical constituents isolated from *Streptomyces* sp. Tc052, and endophyte in *Alpinia galanga*. Int J Pharm 4:95–101
57. Thongchai T, Srisakul C, Wanwikar R, Waya SP (2012) Antifungal activity of 3-methylcarbazoles from *Streptomyces* sp. LJK109; an endophyte in *Alpinia galanga*. J Appl Pharm Sci 02:124–128
58. Bashan Y, Holguin G (1998) Proposal for the division of plant growth-promoting rhizobacteria into two classifications: biocontrol-PGPB (plant growth-promoting bacteria) and PGPB. Soil Biol Biochem 30:1225
59. Kumar A, Singh M, Singh PP, Singh SK, Singh PK, Pandey KD (2016) Isolation of plant growth promoting rhizobacteria and their impact on growth and curcumin content in *Curcuma longa* L. Biocatal Agric Biotechnol 8:1–7
60. Vinayarani G, Prakash HS (2018) Growth promoting rhizospheric and endophytic bacteria from *Curcuma longa* L. as biocontrol agents against rhizome rot and leaf blight diseases. Plant Pathol J 34:218
61. Aswathy AJ, Jasim B, Jyothis M, Radhakrishnan EK (2013) Identification of two strains of *Paenibacillus* sp. as indole 3 acetic acid-producing rhizome-associated endophytic bacteria from *Curcuma longa*. 3 Biotech 3:219–224
62. Jasim B, Joseph AA, John CJ, Mathew J, Radhakrishnan EK (2014) Isolation and characterization of plant growth promoting endophytic bacteria from the rhizome of *Zingiber officinale*. 3 Biotech 4:197–204
63. Chen T, Chen Z, Ma GH, Du BH, Shen B, Ding YQ, Xu K (2014) Diversity and potential application of endophytic bacteria in ginger. Genet Mol Res 13:4918–4931
64. Zhang Y, Kang X, Liu H, Liu Y, Li Y, Yu X, Chen Q (2018) Endophytes isolated from ginger rhizome exhibit growth promoting potential for *Zea mays*. Arch Agron Soil Sci 64:1302–1314
65. Anisha C, Mathew J, Radhakrishnan EK (2013) Plant growth promoting properties of endophytic *Klebsiella* sp. isolated from *Curcuma longa*. Int J Biol Pharm Allied Sci 2:593–601
66. Aguado-Santacruz GA, Moreno-Gomez B, Jimenez-Francisco B, Garcia-Moya E, Preciado-Ortiz RE (2012) Impact of the microbial siderophores and phytosiderophores on the iron assimilation by plants: a synthesis. Rev Fitotec Mex 35:9–21
67. Bellenger JP, Wichard T, Kustka AB, Kraepiel AML (2008) Uptake of molybdenum and vanadium by a nitrogen-fixing soil bacterium using siderophores. Nat Geosci 1:243

68. Braud A, Jézéquel K, Bazot S, Lebeau T (2009) Enhanced phytoextraction of an agricultural Cr-and Pb-contaminated soil by bioaugmentation with siderophore-producing bacteria. Chemosphere 74:280–286
69. Berg G, Hallmann J (2006) Control of plant pathogenic fungi with bacterial endophytes. In: Microbial root endophytes. Springer, Berlin/Heidelberg, pp 53–69
70. Sturz AV, Christie BR, Nowak J (2000) Bacterial endophytes: potential role in developing sustainable systems of crop production. CRC Crit Rev Plant Sci 19:1–30. https://doi.org/10.1080/07352680091139169
71. Van Loon LC, Bakker PAHM, van der Heijdt WHW, Wendehenne D, Pugin A (2008) Early responses of tobacco suspension cells to rhizobacterial elicitors of induced systemic resistance. Mol Plant-Microbe Interact 21:1609–1621
72. Vinayarani G, Prakash HS (2018) Fungal endophytes of turmeric (*Curcuma longa* L.) and their biocontrol potential against pathogens *Pythium aphanidermatum* and *Rhizoctonia solani*. World J Microbiol Biotechnol 34:1–17. https://doi.org/10.1007/s11274-018-2431-x
73. Pandey A, Trivedi P, Kumar B, Palni LMS (2006) Characterization of a phosphate solubilizing and antagonistic strain of *Pseudomonas putida* (BO) isolated from a Sub-Alpine location in Himalaya. Curr Microbiol 53:102–107
74. Forchetti G, Masciarelli O, Alemano S, Alvarez D, Abdala G (2007) Endophytic bacteria in sunflower (*Helianthus annuus* L.): isolation, characterization, and production of jasmonates and abscisic acid in culture medium. Appl Microbiol Biotechnol 76:1145–1152
75. Bussaban B, Lumyong S, Lumyong P, McKenzie EH, Hyde KD (2001) Endophytic fungi from *Amomum siamense*. Can J Microbiol 47:943–948. https://doi.org/10.1139/w01-098
76. Blaha D, Prigent-Combaret C, Mirza MS, Moënne-Loccoz Y (2006) Phylogeny of the 1-aminocyclopropane-1-carboxylic acid deaminase-encoding gene acdS in phytobeneficial and pathogenic Proteobacteria and relation with strain biogeography. FEMS Microbiol Ecol 56:455–470
77. Alizadeh O, Sharafzadeh S, Firoozabadi AH (2012) The effect of plant growth promoting rhizobacteria in saline condition. Asian J Plant Sci 11:1–8
78. Glick BR, Cheng Z, Czarny J, Duan J (2007) Promotion of plant growth by ACC deaminase-producing soil bacteria. Eur J Plant Pathol 119:329–339
79. Brader G, Compant S, Mitter B, Trognitz F, Sessitsch A (2014) Meta-bolic potential of endophytic bacteria. Curr Opin Biotechnol 27:30–37. https://doi.org/10.1016/j.copbio.2013.09.012
80. Strobel G, Daisy B (2003) Bioprospecting for microbial endophytes and their natural products. Microbiol Mol Biol Rev 67:491–502. https://doi.org/10.1128/MMBR.67.4.491-502.2003
81. Verma VC, Kharwar RN, Strobel GA (2009) Chemical and functional diversity of natural products from plant associated endophytic fungi. Nat Prod Commun 4:1511–1532
82. Schulz B, Boyle C (2005) The endophytic continuum. Mycol Res 109:661–686. https://doi.org/10.1017/S095375620500273X
83. Zhang HW, Song YC, Tan RX (2006) Biology and chemistry of endophytes. Nat Prod Rep 23:753–771. https://doi.org/10.1039/b609472b
84. Hastuti US, Asna PMA, Rahmawati D (2018) Histologic observation, identification, and secondary metabolites analysis of endophytic fungi isolated from a medicinal plant, *Hedychium accuminatum* Roscoe. AIP Conf Proc 2002:0200701-8. https://doi.org/10.1063/1.5050166
85. Taechowisan T, Chaisaeng S, Phutdhawong WS (2017) Antibacterial, antioxidant and anticancer activities of biphenyls from *Streptomyces sp*. BO-07: an endophyte in *Boesenbergia rotunda* (L.) Mansf A. Food Agric Immunol 28:1330–1346. https://doi.org/10.1080/09540105.2017.1339669
86. Taechowisan T, Chanaphat S, Ruensamran W, Phutdhawong WS (2014) Antibacterial activity of new flavonoids from *Streptomyces* sp. BT01; an endophyte in *Boesenbergia rotunda* (L.) Mansf. J Appl Pharm Sci 4:8–13. https://doi.org/10.7324/JAPS.2014.40402
87. Alshaibani MM, Jalil J, Sidik NM, Edrada-Ebel R, Zin NM (2016) Isolation and characterization of cyclo-(tryptophanyl-prolyl) and chloramphenicol from *Streptomyces* sp. SUK 25 with

antimethicillin-resistant *Staphylococcus aureus* activity. Drug Des Devel Ther 10:1817–1827. https://doi.org/10.2147/DDDT.S101212
88. Taechowisan T, Chanaphat S, Ruensamran W, Phutdhawong WS (2012) Antifungal activity of 3-methylcarbazoles from *Streptomyces* sp. LJK109; an endophyte in *Alpinia galangal*. J Appl Pharm Sci 2:124
89. Sabu R, Soumya KR, Radhakrishnan EK (2017) Endophytic *Nocardiopsis sp.* from *Zingiber officinale* with both antiphytopathogenic mechanisms and antibiofilm activity against clinical isolates. 3 Biotech 7:115
90. Gupta A, Mahajan S, Sharma R (2015) Evaluation of antimicrobial activity of *Curcuma longa* rhizome extract against Staphylococcus aureus. Biotech Rep 6:51–55
91. Nandini MLN, Rasool SN, Ruth CH, Gopal K (2018) Antagonistic activity of endophytic microorganisms against rhizome rot disease of turmeric. J Pharmacogn Phytochem 7:3736–3741
92. Shubin L, Juan H, RenChao Z, ShiRu X, YuanXiao J (2014) Fungal endophytes of *Alpinia officinarum* rhizomes: insights on diversity and variation across growth years, growth sites, and the inner active chemical concentration. PLoS One 9:1–21. https://doi.org/10.1371/journal.pone.0115289
93. Uzma F, Konappa NM, Chowdappa S (2016) Diversity and extracellular enzyme activities of fungal endophytes isolated from medicinal plants of Western Ghats, Karnataka. Egypt J Basic Appl Sci 3:335–342. https://doi.org/10.1016/j.ejbas.2016.08.007
94. Deshmukh AG, Patil VB, Kale SK, Dudhare MS (2018) Isolation, characterization and identification of endophytes from *Curcuma longa*. Int J Curr Microbiol App Sci 6:1040–1050
95. Sulistiyani TR, Lisdiyanti P (2016) Diversity of endophytic bacteria associated with (*Curcuma heyneana*) and their potency for nitrogen fixation. Widyariset 2:106–117. https://doi.org/10.14203/widyariset.2.2.2016.106–117
96. Praptiwi KDP, fathoni A, wulansari D, ilyas M, agusta A (2016) Evaluation of antibacterial and antioxidant activity of extracts of endophytic fungi isolated from Indonesian Zingiberaceous plants. Nusant Biosci 8:306–311. https://doi.org/10.13057/nusbiosci/n080228
97. Hammerschmidt L, Ola A, Mueller WE, Lin W, Mándi A, Kurtán T et al (2015) Two new metabolites from the endophytic fungus *Xylaria* sp. isolated from the medicinal plant *Curcuma xanthorrhiza*. Tetrahedron Lett 56:1193–1197. https://doi.org/10.1016/j.tetlet.2014.12.120
98. Niemhom N, Chutrakul C, Suriyachadkun C, Thawai C (2017) *Nonomuraea stahlianthi* sp. nov., an endophytic *Actinomycete* isolated from the stem of *Stahlianthus campanulatus*. Int J Syst Evol Microbiol 67:2879–2884. https://doi.org/10.1099/ijsem.0.002045
99. Nongkhlaw FM, Joshi SR (2015) Investigation on the bioactivity of culturable endophytic and epiphytic bacteria associated with ethnomedicinal plants. J Infect Dev Ctries 9:954–961

Source details

Feedback > Compare sources >

Reference Series in Phytochemistry

Scopus coverage years: from 2017 to Present

Publisher: Springer Nature

ISSN: 2511-834X E-ISSN: 2511-8358

Subject area: Agricultural and Biological Sciences: Plant Science | Chemistry: Organic Chemistry | Pharmacology, Toxicology and Pharmaceutics: Toxicology | Biochemistry, Genetics and Molecular Biology: Biochemistry

Source type: Book Series

View all documents > Set document alert Save to source list

CiteScore 2022
2.2

SJR 2022
0.159

SNIP 2022
0.330

CiteScore | CiteScore rank & trend | Scopus content coverage

Research Journal of Agricultural Sciences An Understanding of Fungal Diversity of Cereal and Oil Seed Crops Particularly in Coastal Region Composed to Indo-Gangetic Areas and their…

Article · March 2020

CITATIONS
0

READS
21

4 authors, including:

Tanmay Ghosh
Dinabandhu Andrews College university of calcutta
74 PUBLICATIONS **211** CITATIONS

SEE PROFILE

Res. Jr. of Agril. Sci. **11**(2): 413-419

ISSN: 0976-1675

www.rjas.org

Research Journal of Agricultural Sciences

Research Paper

© Centre for Advanced Research in Agricultural Sciences

DI: 5909-1402-079

An Understanding of Fungal Diversity of Cereal and Oil Seed Crops Particularly in Coastal Region Composed to Indo-Gangetic Areas and their Eco-friendly Management

Tanmay Ghosh*[1], Joydip Ghosh[2], Maitreyee Mondal[3] and Subhasree Roy[4]

[1,3,4]Department of Microbiology,
Dinabandhu Andrewas College, Deparrshnabghata, 24 Parganas (South), Kolkata - 700 084, West Bengal, India
[2]Department of Microbiology, Rabindra Mahavidyalaya, Champadanga, Hooghly, W.B. 712401

Received: 14 February 2020; Revised accepted: 22 March 2020

A B S T R A C T

This study deals with the isolation of fungal communities and comparison seed borne mycoflora between Coastal zone seeds (Digha; West Bengal) and Indo-gangetic areas (Burdwan, Hooghly, Howrah; West Bengal) and to identify and classify them by standard blotter method and agar plate technique. Coastal areas seed samples were collected from the sea side of Bay of Bengal, Digha, West Bengal and the Indo-gangetic areas seed samples were collected from Burdwan, Hooghly, Howrah; West Bengal. The seeds were stored in sterile screw cap bottles for further analysis. Phenotypic and genotypic characterization of fungal isolates were done using above tow methods. Six fungal genera including *Aspergillus sp., Penicillium sp., Rhizopus sp., Mucor sp., Alternaria sp., Macrophomina sp.* Of them *Aspergillus sp.* and *Alternaria sp.* are the most frequent members. It was found that the rate of germination of coastal zone seeds were more than the rate of germination of Indo-gangetic zones seeds. Whereas the fungal community of coastal areas were appeared more frequent and destructive than indo-gangetic region. The germination percentage of oil seeds of indo-gangetic areas appeared respectively 92% and 96% where the germination percentage of oil seeds of coastal region appeared respectively 64% and 72%, and the germination percentage of cereal crops of indo-gangetic areas (Pratiksha, Swarna, Khas, Minikit, Kalma) appeared respectively 88%, 92%, 84%, 96%, 80%. Whereas the germination percentage of all those cereal crops (Protiksha, Swarna, Khas, Minikit, Kalma) of coastal region appeared respectively 60%, 68%, 56%, 72% and 52%. In the other hand the appearance of fungal community were more frequent of coastal areas than indo-gangetic region. The percentage of fungal growth of oil seed of indo-gangetic region (oil seeds) were respectively 35% and 20%. Whereas in coastal areas it was respectively 50% and 45%. The fungal growth of different cereal crops (Protiksha, Swarna, Khas, Minikit, Kalma) of indo-gangetic and coastal areas were respectively (20%, 18%, 25%, 15%, 28%) and (38%, 35%, 40%, 30%, 44%).

Key words: Standard blotter method, Fungal community, Phenotypic, Agar plate technique, Destructive, Genotypic

India is one of the major cereal crops and oil seeds grower and importer. The diverse agro ecological conditions in the country are favorable for growing annual cereal crops and oil seeds. Ninety percent of food crops are propagated by seed. A most widely grown crops in agriculture zone (wheat, rice, maize, sesame, nut, mustard) are affected by various seed-borne diseases. A seed-borne pathogen present externally or internally or associated with the seed as contaminant may cause seed abortion, seed necrosis, reduction or elimination of germination capacity as

***Corresponding author:** Tanmay Ghosh, Department of Microbiology, Dinabandhu Andrews College, Baishnabghata, South 24 Parganas, Kolkata - 700 084, West Bengal
e-mail: tanmay.tanmay.ghosh780@gmail.com | **Contact:** +91- 9732188299

well as seedling damage resulting in development of disease at later stages of seed growth (Fakhrunnisa *et al*. 2006). The literature on seed mycoflora of species was revealed and observed by several workers. Fungi including *Aspergillus sp., Penicillium sp., Rhizopus sp.,Mucor sp., Alternaria sp., Macrophomina sp.* have been found associated with the seeds of cereal crop and oil seeds. Among these, *Alternaria sp.* as well as *Aspergillus sp.* are known to be the most destructive pathogen of those seeds. Fungi are fundamental organisms in our ecological systems and will be found anywhere where the environment will support their growth, both on Indo-gangetic area and Coastal zone. However our understanding of fungal diversity particularly in marine environment (Digha, West Bengal) compared to Indo-gangetic areas (Burdwan, Hooghly, Howrah).

Mechanism of seed infection by fungi

Fungal infection of seed borne pathogens may reach the ovule of the seed at any stage from the initiation of ovule formation to the mature seed. The fungal plant pathogens vary in their modes of multiplication and attack on the lost plant (Chernin and Chet 2002, Ping and Boland 2004, Wei *et al*. 1991, Zhang and Birch 1996) fungal propagules / spores germinate and the growing hyphae determine the entry of the pathogens in plant tissue including the fruit and seed. The ovule and the seed develop in the pistil which is enclosed by other floral appendages in the flower and seed. The position and structure of seed, including the physical environment during seed development, determines the successful seed infection. The physiological and biochemical factors inside the fruit and seed further control the establishment of successful infection. Fungi may be biotroph (obligate parasite) or necrotroph (saprophytic). Biotroph cause minimal damage to the host seed, have a narrow host range, while necrotrophs cause apparent damage to the host cell and have a wide host range. The fungi, depending upon the time of infection and environment condition cause superficial or deep infection. Biotrophs usually establish deeper into the tissues including embryo. Necrotroph which degrade tissues through their enzymatic activity, as they spread, are rarely transmitted to the embryo through the mother plant. The mechanism of infection of the ovule and seed is also dependent upon the nature of disease in the plant and the mechanism of transmission of infection into the seed (Van *et al*. 1998, Kushi and Khare 1978).

Important seed borne disease of oil seeds and cereal crops

Any infectious agent associated with the seed, having the potential of causing a disease of a seedling or a plant, is termed as seed borne pathogens. In this case seed may or may not exhibit disease symptoms. This term includes all plant pathogenic microorganisms (fungi, bacteria, nematode) and the viruses which are carried in, on or with the seed (Limonard 1968).

Crop	Disease	Pathogens
Wheat	Loose smut	*Ustilago segetum* var. *tritici*
	Black point	*Alternaria tritici*
	Head blight	*Fusarium senitectum*
Rice	Brown spot	*Bipolaris oryzae*
	False smut	*Ustilaginoidea virens*
	Blast of rice	*Pyricularia oryzae*
Maize	Leaf blight	*Bipolaris maydis*
	Downy mildew	*Peronosclerospora maydis*
	Loose smut	*Ustilago zeae*
Groundnut	Collor rot	*Macrophomina phaseolina*
	Seed rot	*Aspergillus flavus & niger*
Mustard	Downy mildew	*Peronospora parasitica*
	Pod spot	*Alternaria drassicae*
Sesame	Leaf blight	*Alternaria sesamicola*
	Sesame blight	*Corynespora cassiicola*

MATERIALS AND METHODS

Various microorganisms have been reported as causative agent of seed borne disease. Fungi and bacteria are most important pathogens among them. Scientists are able to discover methods to detect and identified. There are various techniques to detect the presence of pathogens associated with infection of seeds. Methods are described as follows:

Collection of various oilseeds and cereal crops samples
Seed samples of Indo-gangetic areas

For studying mycoflora associated with oilseeds (sesame, mustard, nut) and cereal crops (wheat, rice, maize) were collected from various region of Indo-gangetic area (Burdwan, Hooghly, Howrah; West Bengal, India).

Seed samples of coastal zone

For studying mycoflora associated with oilseeds (sesame, mustard, nut) and cereal crops (wheat, rice, maize) were collected from coastal zone of the Digha, West Bengal. The collected seed samples were shade dried and stored in paper bags at room temperature for further studies. All the seed samples were examined by visual seed inspections and occurrence of seed mycoflora was analyzed by standard blotter method and agar plate method.

Surface sterilization of seed

Surface sterilization of the seed was done by one percent sodium hypochlorite for 30 seconds. The seeds were then washed with three changes of sterile water.

Detection of seed mycoflora

For isolation of seed mycoflora associated with oilseeds the two detection methods viz. Standard Blotter Method and Agar Plate Method (ISTA 1996) were employed.

Standard blotter method

Three pieces of filter paper (Lantos *et al*. 2002, Agarwal 1976), were properly soaked in sterilized water and were placed at the bottom of a 9 cm well labelled plastic Petri dishes. Twenty (20) seeds per Petri dish were placed using a pair of forceps and making sure that seeds are placed equidistantly under aseptic conditions. The lids of each Petri dish were held in place with gummy cello tape. The Petri

dishes containing seeds were incubated at room temperature (25°± 2°C) for 7 days under alternating cycles of light and darkness of 12 hours each.

Fig 1 Standard Blotter Method

Fig 2 Agar plate method

Agar plate method

PDA was prepared and sterilized in an autoclave. In agar plate method (Barnet and Hunter 1999), 20 ml of potato dextrose agar was distributed to each of the sterile Petri plates under aseptic conditions. After cooling, crop seed samples were transferred (ISTA 2005) to the plate containing PDA medium. Twenty seeds per Petri plate were kept at equidistance in a circle and incubated at room temperature (25 ± 2 degree C) under 12 hours alternating cycles of light and darkness for 7 days and observed everyday for the growth of fungi (Warham 1990). The per cent seed mycoflora and percentage frequency of various fungal species were calculated. The incidence of fungi on seed performed under these methods were calculated as follows:

$$\text{Percent incidence} = \frac{\text{Number of infected seeds}}{\text{Number of plated seeds}} \times 100$$

Identification of seed mycoflora

The identification of fungi was done based on the morphological and colony characteristic of the pathogens. Ten fungi were noticed on the oilseed samples and cereal crop seed samples collected from the different region of Indo-gangetic and coastal zone of West Bengal. *Aspergillus niger, Aspergillus flavus* often appeared in many samples along with species of *Rhizopus sp.*, *Fusarium sp.* and *Mucor sp. Alternaria sp.* were found mostly in the seed samples. Spore morphology and colony characteristic are as under:

Aspergillus niger

Colony of *Aspergillus niger* on seed grows slowly, consisting of a compact to fairy loose white to faintly yellow basal mycelium, which bears abundant erect and initially crowed conidial structures. Conidial heads are typically large and black, compact at first, spherical or split into two or looser to reasonably well defined columns. Conidiophores are smooth, hyaline or faintly brownish near the apex. Two series conidia bearing the cells (supporting cells and phialides) are produced but in some heads only phialides are present. Conidia are typically spherical at maturity. Often very rough or spiny, mostly 4-5 µm diameter and very dark in colour or with conspicuous longitudinal striations.

Aspergillus flavus

Colony of *Aspergillus flavus* on seed is usually spreading and very light. Yellow to deep yellow-green, olive-brown. Conidiophores are swollen apically with numerous conidia bearing cells in long chains. Conidiophores are heavily walled, hyaline coarsely and rough end. They can be one or two series of conidia bearing cells (Phialides and supporting cells). Conidia are typically spherical to sub-spherical, conspicuously spiny, variably 3-6 µm in diameter.

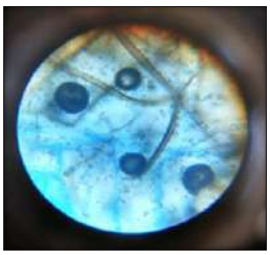

Fig 3 *Aspergillus sp.*

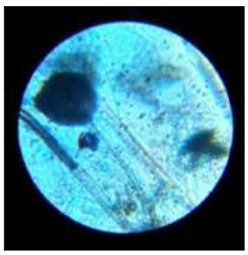

Fig 4 *Mucor sp.*

Mucor sp.

Colonies grow rapidly at the temperature of 25-30°C. It resembles cotton candy. From the front the colour is white initially and becomes greyish brown. Conidia are generally globose to ellipsoidal, yellowish brown and slightly rough-walled and are produced in sporangia that are developed around pin form columella. Mycelium are generally shiny, hyaline, greyish white to milky white. Conidiophore are Pin form columella and are found which bears the sporangia around it.

Rhizopus sp.

Colony of *Rhizopus sp.* on seed grows slowly, consisting of a compact to fairy loose pink mycelium, sporangiophores grow in cluster they are stout and stiff, the characteristic features is rhizoids present at the base of the sporangium, vegetative body is highly branched coenocytic in nature. The sporangium contain either one or both type of sporangiospore.

Fig 5 *Rhizopus sp.*

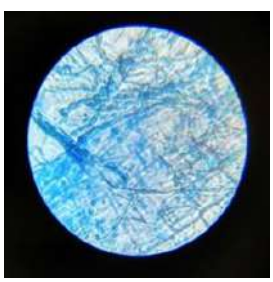

Fig 6 *Penicillium sp.*

Penicillium sp.

Penicillium spp. are commonly known as contaminants. The colonies of *Penicillium sp.* are rapid growing, flat, filamentous and velvety, woolly or cottony in structure. The colonies are initially white and become blue green, gray green, olive gray, yellow or pinkish in time. Colonies of *Penicillium sp.* are often dominated by copious clear to

yellow or brown exudates at the centres. Hyphae are septate, hyaline measuring 1.5 to 5 µm in diameter with simple or branched conidiophores. Metulae are secondary branches that form on conidiophores. The metulae carries the flasks shaped phialides. The organisation of the phialides and the conidiophores are very typical. They form brush like clusters, which are also referred as "penicilli". The conidia (2.5–5 µm in diameter) are round, unicellular and visualized as unbranching chains at the tip of phialides.

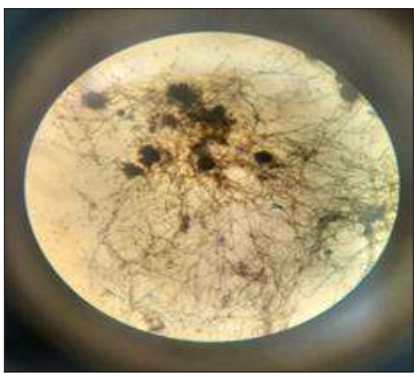

Fig 7 *Macrophomina sp.*

Macrophomina sp.

Conidia are aseptate, hyaline, ellipsoidal to obovoid. Pycnidia are larger than sclerotia, dark brown to black and scattered throughout the surface. Hyphae are thick, grey to brown to black or dull white to light brown. Produces a profuse aerial mycelium with pycnidia and sclerotia. Sclerotia are black, shiny, and irregular shaped. Pycnidia are larger than sclerotia, dark brown to black and scattered throughout the surface.

RESULTS AND DISCUSSION

The results of *in-vitro* studies conducted at the Department of microbiology; Rabindra Maha Vidyalaya; Champadanga; Hooghly,West Bengal, India during 2018.

Germination percentage of oil seeds of Indo-gangetic and coastal areas under in-vitro condition

The data obtained from (Table 1) indicated that the germination percentage of sesame (black) and nut were respectively 64% and 72%.

Table 1 Germination percentage of different oil seeds of coastal area under *in-vitro* condition (Agar Plate Method)

Oil seeds	Germination percentage (%)
Sesame (black)	64.00
Nut	72.00

Table 2 Germination percentage of different oil seeds of indo-gangetic area under *in-vitro* condition (Agar Plate Method)

Oil seeds	Germination percentage (%)
Sesame (black)	92.00
Nut	96.00

The data obtained from (Table 2) indicated that the germination percentage of sesame (black) and nut were respectively 92% and 96%.

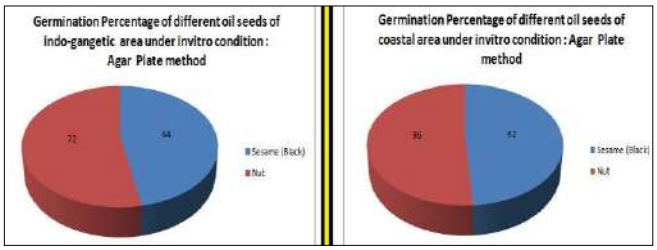

Fig 8 Comparing germination rate different oil seeds between Indo-gangetic seed and coastal area seed

Fungal growth of oil seeds of Indo-gangetic and coastal areas under in-vitro condition

The data obtained from (Table 3) indicated that the fungal growth of sesame (black) and nut were respectively 50% and 45%.

Table 3 Fungal growth of different oil seeds of Indo-gangetic area under in-vitro condition (Agar Plate Method)

Oil seeds	Fungal growth
Sesame (black)	35.00
Nut	20.00

Table 4 Fungal growth of different oil seeds of coastal area under *in-vitro* condition (Agar Plate Method)

Oil seeds	Fungal growth
Sesame (black)	50.00
Nut	45.00

The data obtained from (Table 4) indicated that the fungal growth of sesame (black) and nut were respectively 35% and 20%.

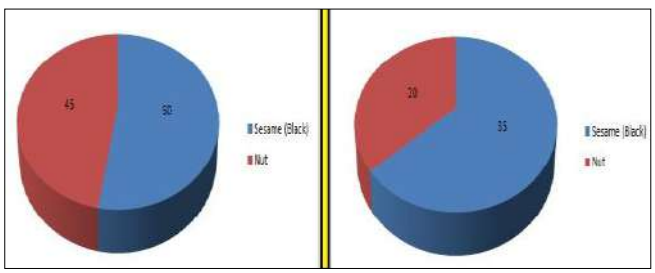

Fig 9 Comparing fungal growth of different oil seeds of Indo-gangetic area and coastal area under in-vitro condition

Table 5 Germination percentage of different cereal crop seeds of coastal area under *in-vitro* condition

Cereal crop seeds	Germination percentage
Protiksha	60.00
Swarna	68.00
Khas	56.00
Minikit	72.00
Kalma	52.00

Germination percentage of cereal crops of Indo-gangetic and Coastal areas under in-vitro condition

The data obtained from (Table 7) indicated that the germination percentage of Pratiksha, Swarna, Khash, Minikit, Kalma were respectively 60%, 68%, 56%, 72% and 52%.

Table 6 Germination percentage of different oil seeds of indo-gangetic area under *in-vitro* condition

Cereal crop seeds	Germination percentage
Pratiksha	88.00
Swarna	92.00
Khas	84.00
Minikit	96.00
Kalma	80.00

The data obtained from (Table 8) indicated that the germination percentage of Pratiksha, Swarna, Khash, Minikit, Kalma were respectively 88%, 92%, 84%, 96% and 80%.

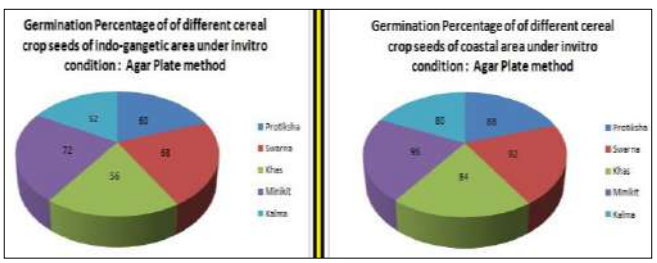

Fig 10 Comparing germination percentage between cereal crop seeds of Indo-gangetic area and coastal area

Fungal growth of cereal crops of Indo-gangetic and coastal areas under in-vitro condition

Table 7 Fungal growth of different oil seeds of Coastal area under *in-vitro* condition

Cereal crop seeds	Fungal growth
Pratiksha	38.00
Swarna	35.00
Khas	40.00
Minikit	30.00
Kalma	44.00

Table 8 Fungal growth of different oil seeds of indo-gangetic area under *in-vitro* condition

Cereal crop seeds	Fungal growth
Pratiksha	20.00
Swarna	18.00
Khas	25.00
Minikit	15.00
Kalma	28.00

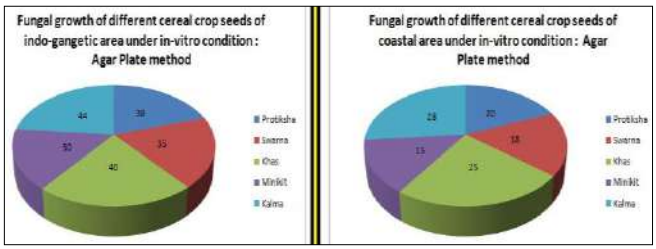

Fig 11 Comparing fungal growth between cereal crop seeds of Indo-gangetic and coastal area

The data obtained from (Table 10) indicated that the fungal growth of Pratiksha, Swarna, Khash, Minikit, Kalma were respectively 38%, 35%, 40%, 30% and 44%.

The data obtained from (Table 11) indicated that the fungal growth of Pratiksha, Swarna, Khash, Minikit, Kalma were respectively 20%, 18%, 25%, 15% and 28%.

Evaluation of plant extract under in-vitro condition

Various plant extracts such as leaf extract of Neem, Tulsi, Bisalyakarani, Thankuni, Basak, Sajne, Bon tulsi, Garlic, Ginger, Datura, Nilgiri have been used for seed treatment of different varieties of oilseeds and cereal crops by soaking methods. Extract of botanicals has been applied at two concentrations, 500ppm and 1000 ppm made. Fresh plant materials are collected and washed first in tap water and then three times in distilled water. The botanical samples was chopped and then crushed in a surface sterilized mortar and pestle by adding 100 ml of sterile distilled water (1:1 w/v). The phyto- extracts are filtered with double layered muslin cloth and filtrate is used as stock solution. Seeds were dipped in plant extract for one hour and then kept in sterilized moist chamber of plastic petriplates for seven days incubation. Observation regarding seed germination and mycoflora associated with seed have been recorded in percentage.

Evaluation of plant extract on basis of fungal growth of cereal crop seeds of Indo-gangetic areas under in-vitro condition

Table 9 Evaluation of plant extract on basis of fungal growth of cereal crop seeds of Indo-gangetic areas

Cereal crops	Plant extracts																				Control
	Tulsi		Bisalyakarani		Neem		Thankuni		Basak		Sajne		Garlic		Ginger		Datura		Nilgiri		
	500 ppm	1000 ppm	500 ppm	1000 ppm	500 ppm	1000 ppm	500 ppm	1000 ppm	500 ppm	1000 ppm	500 ppm	1000 ppm	500 ppm	1000 ppm	500 ppm	1000 ppm	500 ppm	1000 ppm	500 ppm	1000 ppm	
Pratiksha	75	80	90	96	50	60	35	46	85	96	40	47	40	44	45	50	40	48	81	89	30
Swarna	70	74	89	94	55	63	45	50	88	94	50	56	32	40	50	59	50	57	50	60	29
Khas	55	62	75	87	50	62	55	64	86	91	30	43	40	47	35	40	37	45	31	40	27
Minikit	60	67	80	90	36	44	30	40	70	78	33	45	45	56	37	43	30	45	50	60	25
Kalma	110	130	46	53	60	68	65	76	115	140	58	63	61	70	60	67	77	84	95	100	35

Table 10 Evaluation of plant extract on basis of fungal growth of cereal crop seeds of coastal areas

Cereal crops	Plant extracts																				Control
	Tulsi		Bisalyakarani		Neem		Thankuni		Basak		Sajne		Garlic		Ginger		Datura		Nilgiri		
	500 ppm	1000 ppm	500 ppm	1000 ppm	500 ppm	1000 ppm	500 ppm	1000 ppm	500 ppm	1000 ppm	500 ppm	1000 ppm	500 ppm	1000 ppm	500 ppm	1000 ppm	500 ppm	1000 ppm	500 ppm	1000 ppm	
Pratiksha	55	60	70	76	30	35	20	28	60	67	23	33	20	30	25	30	20	28	60	66	17
Swarna	50	54	55	64	35	40	28	36	65	72	27	37	20	25	20	28	30	36	35	42	16
Khas	35	43	57	62	30	33	37	42	55	61	18	22	24	30	25	32	20	26	20	26	12
Minikit	39	45	40	50	20	27	19	26	50	55	27	33	30	35	28	37	20	28	30	34	15
Kalma	65	75	37	44	40	45	35	39	40	48	70	76	36	42	49	55	40	47	70	75	20

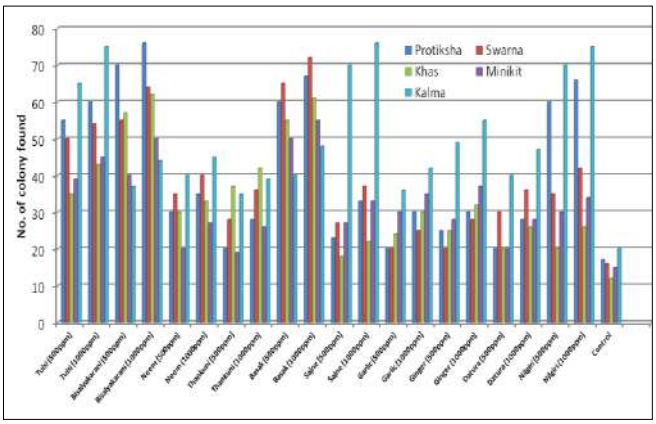

Fig 12 Evaluation of plant extract on the basis of fungal growth of different cereal crop seeds of indo-gangetic area under *in-vitro* condition : Agar Plate method

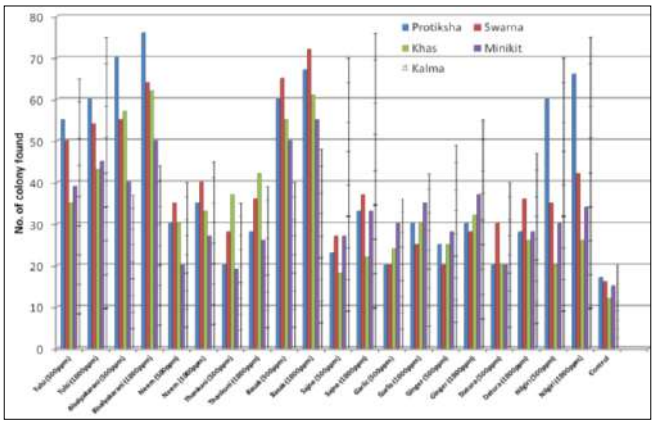

Fig 13 Evaluation of plant extract on the basis of fungal growth of different cereal crop seeds of coastal area under *in-vitro* condition : Agar Plate method

Table 11 Evaluation of plant extract on basis of fungal growth of oil seeds of Indo-gangetic areas

Cereal crops	Plant extracts																				Control
	Tulsi		Bisalyakarani		Neem		Thankuni		Basak		Sajne		Garlic		Ginger		Datura		Nilgiri		
	500 ppm	1000 ppm	500 ppm	1000 ppm	500 ppm	1000 ppm	500 ppm	1000 ppm	500 ppm	1000 ppm	500 ppm	1000 ppm	500 ppm	1000 ppm	500 ppm	1000 ppm	500 ppm	1000 ppm	500 ppm	1000 ppm	
Sesame (black)	75	85	96	100	76	86	24	30	45	50	37	42	65	70	70	75	86	90	40	50	27
Nut	55	64	65	70	80	86	70	80	47	57	45	50	65	69	68	77	65	70	75	79	35

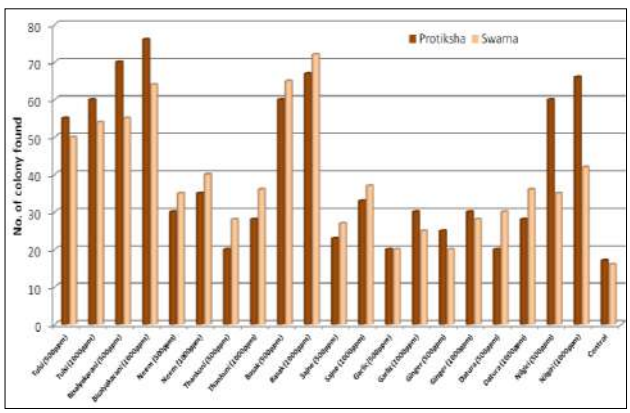

Fig 14 Evaluation of plant extract on the basis of fungal growth of different oil seeds of Indo-gangetic area under *in-vitro* condition : Agar plate method

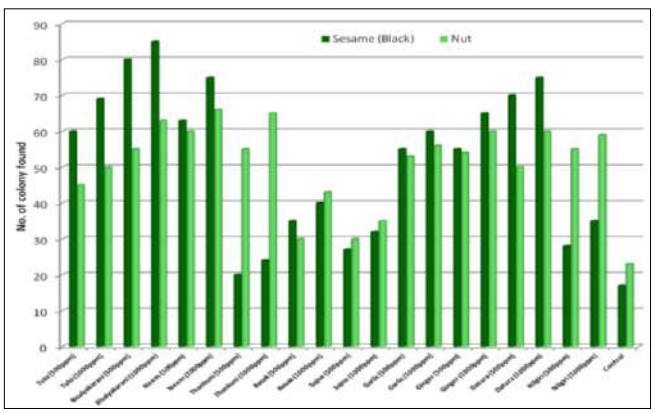

Fig 15 Evaluation of plant extract on the basis of fungal growth of different oil seeds of coastal area under *in-vitro* condition : Agar Plate method

This present work deals with the comparative study of fungal growth and germination percentage of different oil and cereal crop seed of coastal area and Indo-gangetic area. It was found that the rate of germination of indo-gangetic areas seeds were more than the rate of germination of Coastal zones seeds. Whereas the fungal community were appeared more frequently and distractive in Coastal region. Environmental factors are the most decisive factor for

growth of fungal species. In case of coastal area the temperature range is 25°-30° and the relative humidity is 50-79%. All the environmental factors of coastal area were found more suitable for the growth of microflora than indo-gangetic region. Wind speed and sunshine hours have a positive effect on the growth of microflora. The wind speed of coastal region range from 11-15 KpH, which were found most appropriate for faster multiplication and spread of the pathogen. All the meteorological factors were responsible for the development of the disease of coastal regions seeds and thus their germination percentages were decreases. Among 10 plant extracts of Bisalyakaruni, Neem, Basak and tulsi showed more efficient result than others. Whereas in case of coastal and indo-gangetic regions seeds. Thus these 4 plant extracts can be used as biofertilizer and biostimulants to treat both indo-gangetic and coastal regions seed crops. Biostimulants are product that reduces the need for fertilizers and increase plant growth. The above mentioned information are very useful for the farmers involved in oil and cereal crop cultivation. They also can take their decision in time of sowing of crop and enhance their profitability by proper management of disease. Here more research work is required to detect, identify, isolate those bacterial and fungal pathogens. Institutions have to cooperate with researchers and scientists to carry on this type of research work. From present review we can identify and control seed-borne pathogenic fungi and still now science is unable to identify those pathogenic microorganisms like bacteria, virus etc. So more research work is needed to detect and control them. If we can detect them, then it will be easier to decrease infections caused by them.

Table 12 Evaluation of plant extract on basis of fungal growth of oil seeds of coastal areas

Cereal crops	Plant extracts																				Control
	Tulsi		Bisalyakarani		Neem		Thankuni		Basak		Sajne		Garlic		Ginger		Datura		Nilgiri		
	500 ppm	1000 ppm	500 ppm	1000 ppm	500 ppm	1000 ppm	500 ppm	1000 ppm	500 ppm	1000 ppm	500 ppm	1000 ppm	500 ppm	1000 ppm	500 ppm	1000 ppm	500 ppm	1000 ppm	500 ppm	1000 ppm	
Sesame (black)	60	69	80	85	63	75	20	24	35	40	27	32	55	60	55	65	70	75	28	35	17
Nut	45	50	55	63	60	66	55	65	30	43	30	35	53	56	54	60	50	60	55	59	23

LITERATURE CITED

Fakhrunnisa, Hashmi M H and Ghaffar A. 2006. Seed-borne mycoflora of wheat, sorghumand and barley. *Pakistan Journal of Botany* **38**(1):185-192.

Chernin L and Chet I. 2002. *Enzymes in the Environment: Activity, Ecology, and Applications.* Marcel Dekker, New York. pp 171-225.

Ping L and Boland W. 2004. Signals from the underground: Bacterial volatiles promote growth in Arabidopsis. *Trends Plant Science* **9**: 263-269.

Wei G, Kloepper J W and Tuzun S. 1991. Induction of systemic resistance of cucumber to *Colletotrichum orbiculare* by select strains of plant growth promoting Rhizobacteria. *Phytopathology* **81**: 1508-1512.

Zhang L and Birch R G. 1996. Biocontrol of sugar cane leaf scald disease by an isolate of *Pantoea dispersa* which detoxifies albicidin phytotoxins. *Letters in Applied Microbiology* **22**: 132-136.

Van, Loon L C, Bakker P A H M and Pieterse C M J. 1998. Systemic resistance induced by rhizosphere bacteria. *Annual Review of Phytopathology* **36**: 453-483.

Kushi K K and Khare M N. 1978. Comparative efficacy of five methods to detect Macrophomina Phaseolina associated with sesamum seeds. *Indian Phytopathology* **31**: 258-259.

Limonard J. 1968. Ecological aspects of seed health testing. *International Proceedings of Seed Testing Association* **33**: 1-8.

Lantos F, Lantos J and Lantos E. 2002. An unusual twist to the blotter test - the Lantos Method. Practicing Oil Analysis Magazine. Houston, July-August. pp 46-50.

Agarwal V K. 1976. Techniques for the detection of seed borne fungi. *Seed Research* **4**: 24-31.

Barnet H L and Hunter B B. 1999. Illustrated genera of imperfect fungi. *The American Psychopathological or Phytopathological Society*. pp 273.

ISTA. 2005. Seed health testing methods and the germination test. *In*: International Rules for Seed Testing. Published by International Seed Testing Association Bassersdorf, Switzerland spring wheat. *Journal of Phytopathology* **149**: 185-188.

Warham E J. 1990. Effect of *Tilletia indica* infection on viability, germination and vigour of wheat seed. *Plant Disease* **74**: 130-135.

UGC-CARE List

UGC-CARE List

You searched for "**Research Journal of Agricultural Sciences**". Total Journals : **1**

Search:

Sr.No.	Journal Title	Publisher	ISSN	E-ISSN	UGC-CARE coverage years	Details
1	Research Journal of Agricultural Sciences- An International Journal	Centre for Advanced Research in Agricultural Sciences	0976-1675	2249-4538	from September-2019 to Present	View

Showing 1 to 1 of 1 entries

Previous 1 Next

Research Journal of Agricultural Sciences An Understanding of Fungal Diversity of Cereal and Oil Seed Crops Particularly in Coastal Region Composed to Indo-Gangetic Areas and their…

Article · March 2020

CITATIONS
0

READS
24

4 authors, including:

Tanmay Ghosh
Dinabandhu Andrews College university of calcutta
74 PUBLICATIONS **211** CITATIONS

SEE PROFILE

Res. Jr. of Agril. Sci. **11**(2): 413-419

ISSN: 0976-1675

www.rjas.org

Research Journal of Agricultural Sciences

Research Paper

© Centre for Advanced Research in Agricultural Sciences

DI: 5909-1402-079

An Understanding of Fungal Diversity of Cereal and Oil Seed Crops Particularly in Coastal Region Composed to Indo-Gangetic Areas and their Eco-friendly Management

Tanmay Ghosh*[1], Joydip Ghosh[2], Maitreyee Mondal[3] and Subhasree Roy[4]

[1,3,4]Department of Microbiology,
Dinabandhu Andrewas College, Deparrshnabghata, 24 Parganas (South), Kolkata - 700 084, West Bengal, India
[2]Department of Microbiology, Rabindra Mahavidyalaya, Champadanga, Hooghly, W.B. 712401

Received: 14 February 2020; Revised accepted: 22 March 2020

A B S T R A C T

This study deals with the isolation of fungal communities and comparison seed borne mycoflora between Coastal zone seeds (Digha; West Bengal) and Indo-gangetic areas (Burdwan, Hooghly, Howrah; West Bengal) and to identify and classify them by standard blotter method and agar plate technique. Coastal areas seed samples were collected from the sea side of Bay of Bengal, Digha, West Bengal and the Indo-gangetic areas seed samples were collected from Burdwan, Hooghly, Howrah; West Bengal. The seeds were stored in sterile screw cap bottles for further analysis. Phenotypic and genotypic characterization of fungal isolates were done using above tow methods. Six fungal genera including *Aspergillus sp., Penicillium sp., Rhizopus sp., Mucor sp., Alternaria sp., Macrophomina sp.* Of them *Aspergillus sp.* and *Alternaria sp.* are the most frequent members. It was found that the rate of germination of coastal zone seeds were more than the rate of germination of Indo-gangetic zones seeds. Whereas the fungal community of coastal areas were appeared more frequent and destructive than indo-gangetic region. The germination percentage of oil seeds of indo-gangetic areas appeared respectively 92% and 96% where the germination percentage of oil seeds of coastal region appeared respectively 64% and 72%, and the germination percentage of cereal crops of indo-gangetic areas (Pratiksha, Swarna, Khas, Minikit, Kalma) appeared respectively 88%, 92%, 84%, 96%, 80%. Whereas the germination percentage of all those cereal crops (Protiksha, Swarna, Khas, Minikit, Kalma) of coastal region appeared respectively 60%, 68%, 56%, 72% and 52%. In the other hand the appearance of fungal community were more frequent of coastal areas than indo-gangetic region. The percentage of fungal growth of oil seed of indo-gangetic region (oil seeds) were respectively 35% and 20%. Whereas in coastal areas it was respectively 50% and 45%. The fungal growth of different cereal crops (Protiksha, Swarna, Khas, Minikit, Kalma) of indo-gangetic and coastal areas were respectively (20%, 18%, 25%, 15%, 28%) and (38%, 35%, 40%, 30%, 44%).

Key words: Standard blotter method, Fungal community, Phenotypic, Agar plate technique, Destructive, Genotypic

India is one of the major cereal crops and oil seeds grower and importer. The diverse agro ecological conditions in the country are favorable for growing annual cereal crops and oil seeds. Ninety percent of food crops are propagated by seed. A most widely grown crops in agriculture zone (wheat, rice, maize, sesame, nut, mustard) are affected by various seed-borne diseases. A seed-borne pathogen present externally or internally or associated with the seed as contaminant may cause seed abortion, seed necrosis, reduction or elimination of germination capacity as

***Corresponding author:** Tanmay Ghosh, Department of Microbiology, Dinabandhu Andrews College, Baishnabghata, South 24 Parganas, Kolkata - 700 084, West Bengal
e-mail: tanmay.tanmay.ghosh780@gmail.com | **Contact:** +91- 9732188299

well as seedling damage resulting in development of disease at later stages of seed growth (Fakhrunnisa *et al*. 2006). The literature on seed mycoflora of species was revealed and observed by several workers. Fungi including *Aspergillus sp., Penicillium sp., Rhizopus sp.,Mucor sp., Alternaria sp., Macrophomina sp.* have been found associated with the seeds of cereal crop and oil seeds. Among these, *Alternaria sp.* as well as *Aspergillus sp.* are known to be the most destructive pathogen of those seeds. Fungi are fundamental organisms in our ecological systems and will be found anywhere where the environment will support their growth, both on Indo-gangetic area and Coastal zone. However our understanding of fungal diversity particularly in marine environment (Digha, West Bengal) compared to Indo-gangetic areas (Burdwan, Hooghly, Howrah).

Mechanism of seed infection by fungi

Fungal infection of seed borne pathogens may reach the ovule of the seed at any stage from the initiation of ovule formation to the mature seed. The fungal plant pathogens vary in their modes of multiplication and attack on the lost plant (Chernin and Chet 2002, Ping and Boland 2004, Wei *et al*. 1991, Zhang and Birch 1996) fungal propagules / spores germinate and the growing hyphae determine the entry of the pathogens in plant tissue including the fruit and seed. The ovule and the seed develop in the pistil which is enclosed by other floral appendages in the flower and seed. The position and structure of seed, including the physical environment during seed development, determines the successful seed infection. The physiological and biochemical factors inside the fruit and seed further control the establishment of successful infection. Fungi may be biotroph (obligate parasite) or necrotroph (saprophytic). Biotroph cause minimal damage to the host seed, have a narrow host range, while necrotrophs cause apparent damage to the host cell and have a wide host range. The fungi, depending upon the time of infection and environment condition cause superficial or deep infection. Biotrophs usually establish deeper into the tissues including embryo. Necrotroph which degrade tissues through their enzymatic activity, as they spread, are rarely transmitted to the embryo through the mother plant. The mechanism of infection of the ovule and seed is also dependent upon the nature of disease in the plant and the mechanism of transmission of infection into the seed (Van *et al*. 1998, Kushi and Khare 1978).

Important seed borne disease of oil seeds and cereal crops

Any infectious agent associated with the seed, having the potential of causing a disease of a seedling or a plant, is termed as seed borne pathogens. In this case seed may or may not exhibit disease symptoms. This term includes all plant pathogenic microorganisms (fungi, bacteria, nematode) and the viruses which are carried in, on or with the seed (Limonard 1968).

Crop	Disease	Pathogens
Wheat	Loose smut	*Ustilago segetum* var. *tritici*
	Black point	*Alternaria tritici*
	Head blight	*Fusarium senitectum*
Rice	Brown spot	*Bipolaris oryzae*
	False smut	*Ustilaginoidea virens*
	Blast of rice	*Pyricularia oryzae*
Maize	Leaf blight	*Bipolaris maydis*
	Downy mildew	*Peronosclerospora maydis*
	Loose smut	*Ustilago zeae*
Groundnut	Collor rot	*Macrophomina phaseolina*
	Seed rot	*Aspergillus flavus & niger*
Mustard	Downy mildew	*Peronospora parasitica*
	Pod spot	*Alternaria drassicae*
Sesame	Leaf blight	*Alternaria sesamicola*
	Sesame blight	*Corynespora cassiicola*

MATERIALS AND METHODS

Various microorganisms have been reported as causative agent of seed borne disease. Fungi and bacteria are most important pathogens among them. Scientists are able to discover methods to detect and identified. There are various techniques to detect the presence of pathogens associated with infection of seeds. Methods are described as follows:

Collection of various oilseeds and cereal crops samples
Seed samples of Indo-gangetic areas

For studying mycoflora associated with oilseeds (sesame, mustard, nut) and cereal crops (wheat, rice, maize) were collected from various region of Indo-gangetic area (Burdwan, Hooghly, Howrah; West Bengal, India).

Seed samples of coastal zone

For studying mycoflora associated with oilseeds (sesame, mustard, nut) and cereal crops (wheat, rice, maize) were collected from coastal zone of the Digha, West Bengal. The collected seed samples were shade dried and stored in paper bags at room temperature for further studies. All the seed samples were examined by visual seed inspections and occurrence of seed mycoflora was analyzed by standard blotter method and agar plate method.

Surface sterilization of seed

Surface sterilization of the seed was done by one percent sodium hypochlorite for 30 seconds. The seeds were then washed with three changes of sterile water.

Detection of seed mycoflora

For isolation of seed mycoflora associated with oilseeds the two detection methods viz. Standard Blotter Method and Agar Plate Method (ISTA 1996) were employed.

Standard blotter method

Three pieces of filter paper (Lantos *et al*. 2002, Agarwal 1976), were properly soaked in sterilized water and were placed at the bottom of a 9 cm well labelled plastic Petri dishes. Twenty (20) seeds per Petri dish were placed using a pair of forceps and making sure that seeds are placed equidistantly under aseptic conditions. The lids of each Petri dish were held in place with gummy cello tape. The Petri

dishes containing seeds were incubated at room temperature (25°± 2°C) for 7 days under alternating cycles of light and darkness of 12 hours each.

Fig 1 Standard Blotter Method

Fig 2 Agar plate method

Agar plate method

PDA was prepared and sterilized in an autoclave. In agar plate method (Barnet and Hunter 1999), 20 ml of potato dextrose agar was distributed to each of the sterile Petri plates under aseptic conditions. After cooling, crop seed samples were transferred (ISTA 2005) to the plate containing PDA medium. Twenty seeds per Petri plate were kept at equidistance in a circle and incubated at room temperature (25 ± 2 degree C) under 12 hours alternating cycles of light and darkness for 7 days and observed everyday for the growth of fungi (Warham 1990). The per cent seed mycoflora and percentage frequency of various fungal species were calculated. The incidence of fungi on seed performed under these methods were calculated as follows:

$$\text{Percent incidence} = \frac{\text{Number of infected seeds}}{\text{Number of plated seeds}} \times 100$$

Identification of seed mycoflora

The identification of fungi was done based on the morphological and colony characteristic of the pathogens. Ten fungi were noticed on the oilseed samples and cereal crop seed samples collected from the different region of Indo-gangetic and coastal zone of West Bengal. *Aspergillus niger, Aspergillus flavus* often appeared in many samples along with species of *Rhizopus sp.*, *Fusarium sp.* and *Mucor sp. Alternaria sp.* were found mostly in the seed samples. Spore morphology and colony characteristic are as under:

Aspergillus niger

Colony of *Aspergillus niger* on seed grows slowly, consisting of a compact to fairy loose white to faintly yellow basal mycelium, which bears abundant erect and initially crowed conidial structures. Conidial heads are typically large and black, compact at first, spherical or split into two or looser to reasonably well defined columns. Conidiophores are smooth, hyaline or faintly brownish near the apex. Two series conidia bearing the cells (supporting cells and phialides) are produced but in some heads only phialides are present. Conidia are typically spherical at maturity. Often very rough or spiny, mostly 4-5 µm diameter and very dark in colour or with conspicuous longitudinal striations.

Aspergillus flavus

Colony of *Aspergillus flavus* on seed is usually spreading and very light. Yellow to deep yellow-green, olive-brown. Conidiophores are swollen apically with numerous conidia bearing cells in long chains. Conidiophores are heavily walled, hyaline coarsely and rough end. They can be one or two series of conidia bearing cells (Phialides and supporting cells). Conidia are typically spherical to sub-spherical, conspicuously spiny, variably 3-6 µm in diameter.

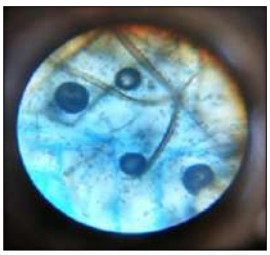

Fig 3 *Aspergillus sp.*

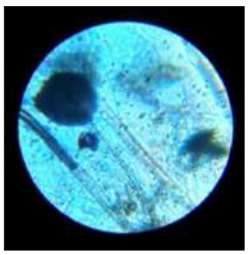

Fig 4 *Mucor sp.*

Mucor sp.

Colonies grow rapidly at the temperature of 25-30°C. It resembles cotton candy. From the front the colour is white initially and becomes greyish brown. Conidia are generally globose to ellipsoidal, yellowish brown and slightly rough-walled and are produced in sporangia that are developed around pin form columella. Mycelium are generally shiny, hyaline, greyish white to milky white. Conidiophore are Pin form columella and are found which bears the sporangia around it.

Rhizopus sp.

Colony of *Rhizopus sp.* on seed grows slowly, consisting of a compact to fairy loose pink mycelium, sporangiophores grow in cluster they are stout and stiff, the characteristic features is rhizoids present at the base of the sporangium, vegetative body is highly branched coenocytic in nature. The sporangium contain either one or both type of sporangiospore.

Fig 5 *Rhizopus sp.*

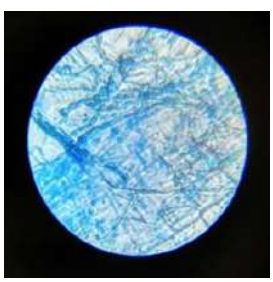

Fig 6 *Penicillium sp.*

Penicillium sp.

Penicillium spp. are commonly known as contaminants. The colonies of *Penicillium sp.* are rapid growing, flat, filamentous and velvety, woolly or cottony in structure. The colonies are initially white and become blue green, gray green, olive gray, yellow or pinkish in time. Colonies of *Penicillium sp.* are often dominated by copious clear to

yellow or brown exudates at the centres. Hyphae are septate, hyaline measuring 1.5 to 5 µm in diameter with simple or branched conidiophores. Metulae are secondary branches that form on conidiophores. The metulae carries the flasks shaped phialides. The organisation of the phialides and the conidiophores are very typical. They form brush like clusters, which are also referred as "penicilli". The conidia (2.5–5 µm in diameter) are round, unicellular and visualized as unbranching chains at the tip of phialides.

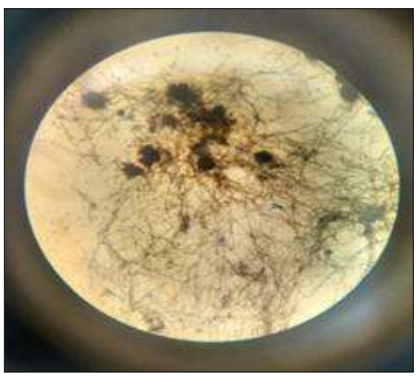

Fig 7 *Macrophomina sp.*

Macrophomina sp.

Conidia are aseptate, hyaline, ellipsoidal to obovoid. Pycnidia are larger than sclerotia, dark brown to black and scattered throughout the surface. Hyphae are thick, grey to brown to black or dull white to light brown. Produces a profuse aerial mycelium with pycnidia and sclerotia. Sclerotia are black, shiny, and irregular shaped. Pycnidia are larger than sclerotia, dark brown to black and scattered throughout the surface.

RESULTS AND DISCUSSION

The results of *in-vitro* studies conducted at the Department of microbiology; Rabindra Maha Vidyalaya; Champadanga; Hooghly,West Bengal, India during 2018.

Germination percentage of oil seeds of Indo-gangetic and coastal areas under in-vitro condition

The data obtained from (Table 1) indicated that the germination percentage of sesame (black) and nut were respectively 64% and 72%.

Table 1 Germination percentage of different oil seeds of coastal area under *in-vitro* condition (Agar Plate Method)

Oil seeds	Germination percentage (%)
Sesame (black)	64.00
Nut	72.00

Table 2 Germination percentage of different oil seeds of indo-gangetic area under *in-vitro* condition (Agar Plate Method)

Oil seeds	Germination percentage (%)
Sesame (black)	92.00
Nut	96.00

The data obtained from (Table 2) indicated that the germination percentage of sesame (black) and nut were respectively 92% and 96%.

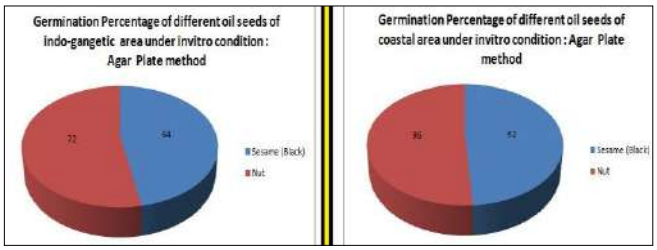

Fig 8 Comparing germination rate different oil seeds between Indo-gangetic seed and coastal area seed

Fungal growth of oil seeds of Indo-gangetic and coastal areas under in-vitro condition

The data obtained from (Table 3) indicated that the fungal growth of sesame (black) and nut were respectively 50% and 45%.

Table 3 Fungal growth of different oil seeds of Indo-gangetic area under in-vitro condition (Agar Plate Method)

Oil seeds	Fungal growth
Sesame (black)	35.00
Nut	20.00

Table 4 Fungal growth of different oil seeds of coastal area under *in-vitro* condition (Agar Plate Method)

Oil seeds	Fungal growth
Sesame (black)	50.00
Nut	45.00

The data obtained from (Table 4) indicated that the fungal growth of sesame (black) and nut were respectively 35% and 20%.

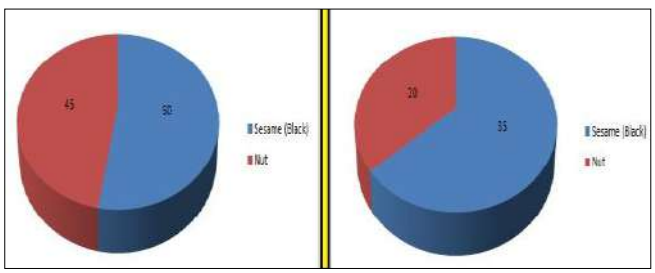

Fig 9 Comparing fungal growth of different oil seeds of Indo-gangetic area and coastal area under in-vitro condition

Table 5 Germination percentage of different cereal crop seeds of coastal area under *in-vitro* condition

Cereal crop seeds	Germination percentage
Protiksha	60.00
Swarna	68.00
Khas	56.00
Minikit	72.00
Kalma	52.00

Germination percentage of cereal crops of Indo-gangetic and Coastal areas under in-vitro condition

The data obtained from (Table 7) indicated that the germination percentage of Pratiksha, Swarna, Khash, Minikit, Kalma were respectively 60%, 68%, 56%, 72% and 52%.

Table 6 Germination percentage of different oil seeds of indo-gangetic area under *in-vitro* condition

Cereal crop seeds	Germination percentage
Pratiksha	88.00
Swarna	92.00
Khas	84.00
Minikit	96.00
Kalma	80.00

The data obtained from (Table 8) indicated that the germination percentage of Pratiksha, Swarna, Khash, Minikit, Kalma were respectively 88%, 92%, 84%, 96% and 80%.

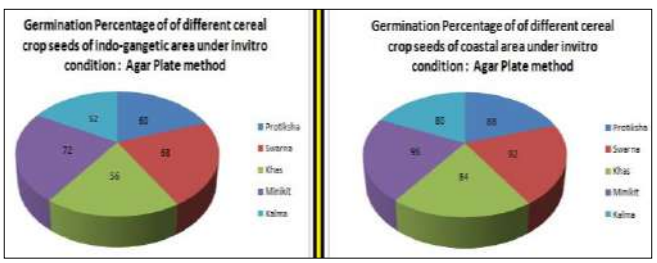

Fig 10 Comparing germination percentage between cereal crop seeds of Indo-gangetic area and coastal area

Fungal growth of cereal crops of Indo-gangetic and coastal areas under in-vitro condition

Table 7 Fungal growth of different oil seeds of Coastal area under *in-vitro* condition

Cereal crop seeds	Fungal growth
Pratiksha	38.00
Swarna	35.00
Khas	40.00
Minikit	30.00
Kalma	44.00

Table 8 Fungal growth of different oil seeds of indo-gangetic area under *in-vitro* condition

Cereal crop seeds	Fungal growth
Pratiksha	20.00
Swarna	18.00
Khas	25.00
Minikit	15.00
Kalma	28.00

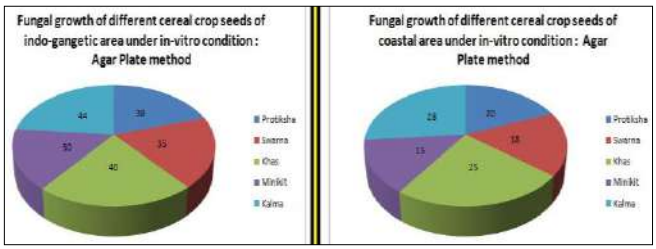

Fig 11 Comparing fungal growth between cereal crop seeds of Indo-gangetic and coastal area

The data obtained from (Table 10) indicated that the fungal growth of Pratiksha, Swarna, Khash, Minikit, Kalma were respectively 38%, 35%, 40%, 30% and 44%.

The data obtained from (Table 11) indicated that the fungal growth of Pratiksha, Swarna, Khash, Minikit, Kalma were respectively 20%, 18%, 25%, 15% and 28%.

Evaluation of plant extract under in-vitro condition

Various plant extracts such as leaf extract of Neem, Tulsi, Bisalyakarani, Thankuni, Basak, Sajne, Bon tulsi, Garlic, Ginger, Datura, Nilgiri have been used for seed treatment of different varieties of oilseeds and cereal crops by soaking methods. Extract of botanicals has been applied at two concentrations, 500ppm and 1000 ppm made. Fresh plant materials are collected and washed first in tap water and then three times in distilled water. The botanical samples was chopped and then crushed in a surface sterilized mortar and pestle by adding 100 ml of sterile distilled water (1:1 w/v). The phyto- extracts are filtered with double layered muslin cloth and filtrate is used as stock solution. Seeds were dipped in plant extract for one hour and then kept in sterilized moist chamber of plastic petriplates for seven days incubation. Observation regarding seed germination and mycoflora associated with seed have been recorded in percentage.

Evaluation of plant extract on basis of fungal growth of cereal crop seeds of Indo-gangetic areas under in-vitro condition

Table 9 Evaluation of plant extract on basis of fungal growth of cereal crop seeds of Indo-gangetic areas

Cereal crops	Plant extracts																				Control
	Tulsi		Bisalyakarani		Neem		Thankuni		Basak		Sajne		Garlic		Ginger		Datura		Nilgiri		
	500 ppm	1000 ppm	500 ppm	1000 ppm	500 ppm	1000 ppm	500 ppm	1000 ppm	500 ppm	1000 ppm	500 ppm	1000 ppm	500 ppm	1000 ppm	500 ppm	1000 ppm	500 ppm	1000 ppm	500 ppm	1000 ppm	
Pratiksha	75	80	90	96	50	60	35	46	85	96	40	47	40	44	45	50	40	48	81	89	30
Swarna	70	74	89	94	55	63	45	50	88	94	50	56	32	40	50	59	50	57	50	60	29
Khas	55	62	75	87	50	62	55	64	86	91	30	43	40	47	35	40	37	45	31	40	27
Minikit	60	67	80	90	36	44	30	40	70	78	33	45	45	56	37	43	30	45	50	60	25
Kalma	110	130	46	53	60	68	65	76	115	140	58	63	61	70	60	67	77	84	95	100	35

Table 10 Evaluation of plant extract on basis of fungal growth of cereal crop seeds of coastal areas

Cereal crops	Plant extracts																				Control
	Tulsi		Bisalyakarani		Neem		Thankuni		Basak		Sajne		Garlic		Ginger		Datura		Nilgiri		
	500 ppm	1000 ppm	500 ppm	1000 ppm	500 ppm	1000 ppm	500 ppm	1000 ppm	500 ppm	1000 ppm	500 ppm	1000 ppm	500 ppm	1000 ppm	500 ppm	1000 ppm	500 ppm	1000 ppm	500 ppm	1000 ppm	
Pratiksha	55	60	70	76	30	35	20	28	60	67	23	33	20	30	25	30	20	28	60	66	17
Swarna	50	54	55	64	35	40	28	36	65	72	27	37	20	25	20	28	30	36	35	42	16
Khas	35	43	57	62	30	33	37	42	55	61	18	22	24	30	25	32	20	26	20	26	12
Minikit	39	45	40	50	20	27	19	26	50	55	27	33	30	35	28	37	20	28	30	34	15
Kalma	65	75	37	44	40	45	35	39	40	48	70	76	36	42	49	55	40	47	70	75	20

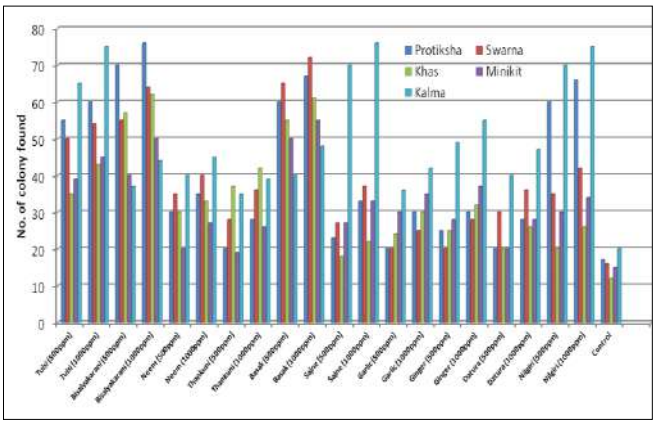

Fig 12 Evaluation of plant extract on the basis of fungal growth of different cereal crop seeds of indo-gangetic area under *in-vitro* condition : Agar Plate method

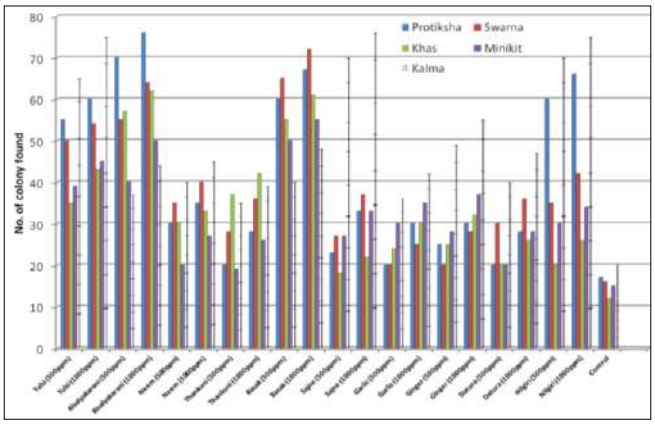

Fig 13 Evaluation of plant extract on the basis of fungal growth of different cereal crop seeds of coastal area under *in-vitro* condition : Agar Plate method

Table 11 Evaluation of plant extract on basis of fungal growth of oil seeds of Indo-gangetic areas

Cereal crops	Plant extracts																				Control
	Tulsi		Bisalyakarani		Neem		Thankuni		Basak		Sajne		Garlic		Ginger		Datura		Nilgiri		
	500 ppm	1000 ppm	500 ppm	1000 ppm	500 ppm	1000 ppm	500 ppm	1000 ppm	500 ppm	1000 ppm	500 ppm	1000 ppm	500 ppm	1000 ppm	500 ppm	1000 ppm	500 ppm	1000 ppm	500 ppm	1000 ppm	
Sesame (black)	75	85	96	100	76	86	24	30	45	50	37	42	65	70	70	75	86	90	40	50	27
Nut	55	64	65	70	80	86	70	80	47	57	45	50	65	69	68	77	65	70	75	79	35

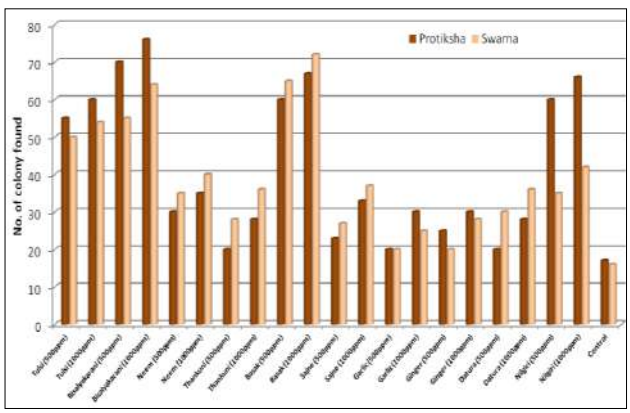

Fig 14 Evaluation of plant extract on the basis of fungal growth of different oil seeds of Indo-gangetic area under *in-vitro* condition : Agar plate method

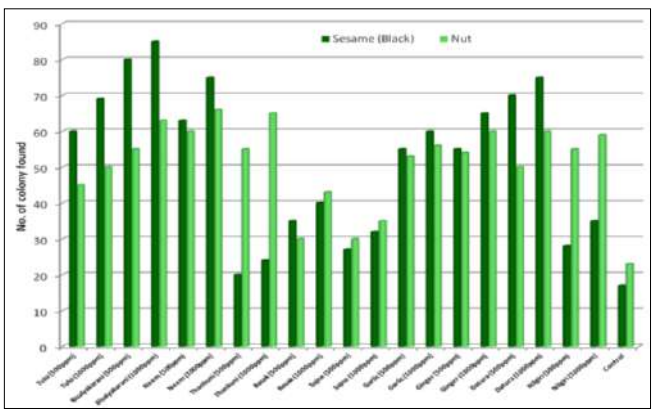

Fig 15 Evaluation of plant extract on the basis of fungal growth of different oil seeds of coastal area under *in-vitro* condition : Agar Plate method

This present work deals with the comparative study of fungal growth and germination percentage of different oil and cereal crop seed of coastal area and Indo-gangetic area. It was found that the rate of germination of indo-gangetic areas seeds were more than the rate of germination of Coastal zones seeds. Whereas the fungal community were appeared more frequently and distractive in Coastal region. Environmental factors are the most decisive factor for

growth of fungal species. In case of coastal area the temperature range is 25°-30° and the relative humidity is 50-79%. All the environmental factors of coastal area were found more suitable for the growth of microflora than indo-gangetic region. Wind speed and sunshine hours have a positive effect on the growth of microflora. The wind speed of coastal region range from 11-15 KpH, which were found most appropriate for faster multiplication and spread of the pathogen. All the meteorological factors were responsible for the development of the disease of coastal regions seeds and thus their germination percentages were decreases. Among 10 plant extracts of Bisalyakaruni, Neem, Basak and tulsi showed more efficient result than others. Whereas in case of coastal and indo-gangetic regions seeds. Thus these 4 plant extracts can be used as biofertilizer and biostimulants to treat both indo-gangetic and coastal regions seed crops. Biostimulants are product that reduces the need for fertilizers and increase plant growth. The above mentioned information are very useful for the farmers involved in oil and cereal crop cultivation. They also can take their decision in time of sowing of crop and enhance their profitability by proper management of disease. Here more research work is required to detect, identify, isolate those bacterial and fungal pathogens. Institutions have to cooperate with researchers and scientists to carry on this type of research work. From present review we can identify and control seed-borne pathogenic fungi and still now science is unable to identify those pathogenic microorganisms like bacteria, virus etc. So more research work is needed to detect and control them. If we can detect them, then it will be easier to decrease infections caused by them.

Table 12 Evaluation of plant extract on basis of fungal growth of oil seeds of coastal areas

Cereal crops	Plant extracts																				Control
	Tulsi		Bisalyakarani		Neem		Thankuni		Basak		Sajne		Garlic		Ginger		Datura		Nilgiri		
	500 ppm	1000 ppm	500 ppm	1000 ppm	500 ppm	1000 ppm	500 ppm	1000 ppm	500 ppm	1000 ppm	500 ppm	1000 ppm	500 ppm	1000 ppm	500 ppm	1000 ppm	500 ppm	1000 ppm	500 ppm	1000 ppm	
Sesame (black)	60	69	80	85	63	75	20	24	35	40	27	32	55	60	55	65	70	75	28	35	17
Nut	45	50	55	63	60	66	55	65	30	43	30	35	53	56	54	60	50	60	55	59	23

LITERATURE CITED

Fakhrunnisa, Hashmi M H and Ghaffar A. 2006. Seed-borne mycoflora of wheat, sorghumand and barley. *Pakistan Journal of Botany* **38**(1):185-192.

Chernin L and Chet I. 2002. *Enzymes in the Environment: Activity, Ecology, and Applications.* Marcel Dekker, New York. pp 171-225.

Ping L and Boland W. 2004. Signals from the underground: Bacterial volatiles promote growth in Arabidopsis. *Trends Plant Science* **9**: 263-269.

Wei G, Kloepper J W and Tuzun S. 1991. Induction of systemic resistance of cucumber to *Colletotrichum orbiculare* by select strains of plant growth promoting Rhizobacteria. *Phytopathology* **81**: 1508-1512.

Zhang L and Birch R G. 1996. Biocontrol of sugar cane leaf scald disease by an isolate of *Pantoea dispersa* which detoxifies albicidin phytotoxins. *Letters in Applied Microbiology* **22**: 132-136.

Van, Loon L C, Bakker P A H M and Pieterse C M J. 1998. Systemic resistance induced by rhizosphere bacteria. *Annual Review of Phytopathology* **36**: 453-483.

Kushi K K and Khare M N. 1978. Comparative efficacy of five methods to detect Macrophomina Phaseolina associated with sesamum seeds. *Indian Phytopathology* **31**: 258-259.

Limonard J. 1968. Ecological aspects of seed health testing. *International Proceedings of Seed Testing Association* **33**: 1-8.

Lantos F, Lantos J and Lantos E. 2002. An unusual twist to the blotter test - the Lantos Method. Practicing Oil Analysis Magazine. Houston, July-August. pp 46-50.

Agarwal V K. 1976. Techniques for the detection of seed borne fungi. *Seed Research* **4**: 24-31.

Barnet H L and Hunter B B. 1999. Illustrated genera of imperfect fungi. *The American Psychopathological or Phytopathological Society*. pp 273.

ISTA. 2005. Seed health testing methods and the germination test. *In*: International Rules for Seed Testing. Published by International Seed Testing Association Bassersdorf, Switzerland spring wheat. *Journal of Phytopathology* **149**: 185-188.

Warham E J. 1990. Effect of *Tilletia indica* infection on viability, germination and vigour of wheat seed. *Plant Disease* **74**: 130-135.

UGC-CARE List

UGC-CARE List

You searched for "**0976-1675**". Total Journals : **1**

Search:

Sr.No.	Journal Title	Publisher	ISSN	E-ISSN	UGC-CARE coverage years	Details
1	Research Journal of Agricultural Sciences- An International Journal	Centre for Advanced Research in Agricultural Sciences	0976-1675	2249-4538	from September-2019 to Present	View

Showing 1 to 1 of 1 entries

Previous 1 Next

Journal of Critical Reviews

ISSN- 2394-5125 Vol 7, Issue 1, 2020

Review Article

A Eco-friendly management of seed borne mycoflora of Mustard (Brassica sp.) through botanicals and determination of antifungal activity by SEM.

Tanmay Ghosh[1*], M. K. Biswas[2] and Kaustav Aikat[3]

Department of Biotechnology, NIT Durgapur, Burdwan, W.B., India.
Department of Plant Protection, P. S. B., Visva-Bharati , Sriniketan, W. B. 731236, India.
Department of Biotechnology, NIT Durgapur, Burdwan, W.B., India. [*Corresponding Author]

Received: 20.11.2019 ***Revised: 21.12.2019*** ***Accepted: 17.01.2020***

ABSTRACT

The study was planned to investigate the efficiency of Plant extract of Moringa oleifera against, Datura stramonium , Azadirachta indica and Corton bonplandianum against some seed born fungi (Aspergillus sp., Rhizopus sp., Fusarium sp., Alternaria sp., Cochleobolus sp., Rhizoctonia sp.) isolated from oil seed (Jhumi) using standard microbiological procedures and to investigate effectiveness of plant extract on seed borne mycoflora by SEM study. The process well diffusion method is used to study the efficacy of Plant extract. The extracts were poured into the wells at different concentrations like 50mg/ml, 100mg/ml, 200mg/ml and 400mg/ml. After incubation zones of inhibition was carried out by agar plate observed. As the concentrations of extracts increased the activity also increased and thus the zones of inhibition too increase. Hence Moringa oleifera, Datura stramonium, Azadirachta indica and Corton bonplandianum can be used against various seed born fungal disease.

Keywords: Mycoflora, Seed treatment, Aspergillus sp., Rhizopus sp., Fusarium sp., Alternaria sp., Cochleobolus sp., Rhizoctonia sp., Antifungal activity

DOI: http://dx.doi.org/10.31838/jcr.07.01.107

INTRODUCTION

Oilseeds are raised in almost all the parts of the country. Interestingly, in some regions of the country, they are considered as important oil-seeds. Oilseeds are the source of oil-cake as well as vegetable oil. However, the export of oilseeds has been curtailed to meet the increasing demands of the country. The oilseed accounts for 13% of the Gross Cropped Area, 3% of the Gross National Product and 10% value of all agricultural commodities. This sector has recorded annual growth rate of area, production and yield @ 2.44%, 5.47% and 2.96% respectively during last decade (1999-2009). During the last few years, the domestic consumption of edible oils has increased substantially and has touched the level of 18.90 million tonnes in 2011-12 and is likely to increase further. With per capita consumption of vegetable oils at the rate of 16kg/year/person for a projected population of 1276 million, the total vegetable oils demand is likely to touch 20.4 million tonnes by 2017. This oil-seed is generally cultivated in light soils and are grown as a Rabi crop. It is grown in Gujarat and Andhra Pradesh. The oil extracted from these seeds is used in the manufacture of hydrogenated oil. India is of the biggest producers of this particular oil seed. Thus, it can be said that India is a huge producer of oil seeds and most of its states produce one form of oil seed or the other. Despite the rapid spread of the crop, a disheartening trend is that the productivity is going down in recent years. Several diseases are known to cause yield loss in the oilseed crops and many of these diseases are caused by seed borne mycoflora *viz., Aspergillus niger, Rhizopus sp., Fusarium sp., Alternaria sp., Colletotrichum sp., Rhizoctonia sp. Among these, Alternaria sp., Aspergillus sp.* has been considered as a potentially destructive on many oilseed crops in different countries. The loss in yield varies from 25- 60percent depending on the stage and the extent of infection [1]. Hence, it is imperative that the seeds must be tested before they are sown in the field. The uses and expectations of seed treatments with chemicals are greater today but due to the impact of environment regulations they have either banned or restricted the use of older chemicals like organo mercurial fungicides, because of their residual toxicity. Bio protectants applied to seeds may not only protect the seeds but also may colonize and protect roots and increase the plant growth. However, biological agents have tended to be somewhat less effective and more variable than chemical seed treatments. The study was planned to investigate the efficiency of Plant extract of *Moringa oleifera*, *Datura stramonium, Azadirachta indica* and *Corton bonplandianum* against some seed born fungi (*Aspergillus sp., Rhizopus sp., Fusarium sp., Alternaria sp., Cochleobolus sp., Rhizoctonia sp.*) isolated from oil seed (Jhumi) using standard microbiological procedures and to investigate effectiveness of plant extract on seed borne mycoflora by SEM study.

Historical background of the pathogen:

Alternaria blight is a destructive disease of rapeseed-mustard throughout the world and appears each year in crop fields. The disease is caused by different species of *Alternaria viz. A. brassicae* (Berk) Sacc, *A. brassicicola* (Schw.), *A. raphani* Grows and Skolo and *A.alternata* (Fr) Keisskr. Among than *A. brassicae* is much more destructive and occurs more frequently than *A. brassicicola* on *B. Juncea* [2]. The literature on the disease is voluminous, however, in the present review, only those aspects which have a direct bearing on the investigation, have been included. The genus *Alternaria* was first described by Neesin 1817 with type species *A. tenius*; which was later renamed as *A. alternata*. Berkeley, noticed fungal infection on plant belonging to the family Brassicaceae and indentified the fungus as *Macrosporium brassicae* (Berk) which was later renamed as *A. Brassicae* (Berk) Sacc by Saccardo in 1886. In India, *Altenaria* blight was first observed on sarson from Tirhoot in 1901 but the fungus was thought to be new and described as *Sporodochium brassicae*. Later Mason, first observed the *Alternaria* species from aherbarium material of sarson from Pusa (Bihar) India.

Mechanism of seed infection by fungi:

Fungal infection of seed borne pathogens may reach the ovule of the seed at any stage from the initiation of ovule formation to the mature seed. The fungal plant pathogens vary in their modes of multiplication and attack on the lost plant [3,4,5,6] fungal propagules / spores germinate and the growing hyphae determine the entry of the pathogens in plant tissue including the fruit and seed. The physiological and biochemical factors inside the fruit and seed further control the establishment of successful infection. The mechanism of transmission of infection into the seed [7, 8, 9, 10].

MATERIALS AND METHOD:

Site of experiment:

The experiments were carried out in the department of Biotechnology, NIT Durgapur, Burdwan, W.B, India.

Collection of oil seed sample:

For studying mycoflora associated with oil seed (variety-Jhumi) are collected from various region of oil seed grower. Mainly seeds are collected from different Indo-Gangatic areas (Burdwan, Hooghly, Howrah) of West Bengal. The collected seed samples are shade dried and stored in paper bags at room temperature for further studies.

Detection of seed Mycoflora:

International Seed Testing Association (ISTA) techniques (1966, 1973, and 1976) were used for the detection and isolation of seed-borne mycoflora of oil seed (Jhumi). The methods used for seed health testing were: Inspection of dry seeds or visual examination; Incubation method, rolled paper towel method, standard blotter method, Agar Plate method; Deep freeze method, pathogenicity test. Brief account of the methods employed during the course of the present investigation is given below.

Surface Sterilization of Seed:

Surface sterilization of the seeds are done by one percent sodium hypochlorite for 30 seconds. The seeds are then washed with three changes of sterile water.

Standard blotter method:

As per available literature reports three pieces of filter paper [11, 12] should be properly soaked in sterilized water and are placed at the bottom of a 9 cm well labelled plastic Petri dishes. Generally Twenty Five (25) seeds per Petri dish are placed using a pair of forceps and making sure that seeds are placed equidistantly under aseptic conditions. The lids of each Petri dish should be held in place with gummy cello tape. The Petri dishes containing seeds are incubated at room temperature ($25^{o}\pm 2^{o}C$) for 7 days under alternating cycles of light and darkness of 12 hours each.

Fig no: 1 Standard blotter method

Agar plate method:

As described in the literature in the agar plate method [13] 20 ml of potato dextrose agar are distributed to each of the sterile Petri plates under aseptic conditions. After cooling, crop seed samples are transferred [14] to the agar plate. Twenty Five seeds per Petri plate are to kept at equidistance in a circle and incubated at room temperature ($25^{o}\pm 2^{o}$ C) under 12 hours alternating cycles of light and darkness for 7 days and has to be observed everyday for the growth of fungi [15].

Fig no: 2 Agar plate method

Rolled towel method:

It is another process described by researchers to study the germinability of the seeds in the laboratory at room temperature (30º±2ºC). A total of 200 seeds are recommended to be randomly taken from each variety and 50 seeds are placed between a pair of moist paper towels [16]. The towels are rolled and the ends are closed by robber band and covered by polyethylene paper to prevent drying. First observation is recommended to take after 5 days and final count has to be taken after 14 days of incubation period pertaining to (a) % germination, (b) non germinated seed (hard seed and rotten seed), (c) shoot length and, (d) root length. For determination of seed mycoflora the fungal growth on infected seed are taken with the needle and observed under compound microscope.[17].

Deep freeze method:

This method is developed by scientists to detect slow growing pathogens. According to researchers three hundred seeds by moderately infected pathogens, are generally placed at the rate of 25 seeds per plate on moistened blotters in the way as described under Standard blotter method. The Petri plates are incubated at 20º± 2ºC for 24 h under alternate cycles of 12 h NUV light and darkness, for next 24 hours the plates are incubated at –20ºC in dark and then kept back under original conditions for next five days. After eight days of incubation, the seeds are examined under stereobinocular microscope [30]. The frequency of the fungus is calculated by the following formula: No. of seeds containing a particular fungus

$$\frac{}{\text{Total seeds used}} \times 100$$

METHODOLOGY FOR MANAGEMENT STUDIES:

Evaluation of Seed Priming:

Seed priming is a process to increase the germination rate of crops. Priming is one of the most important physiological methods which improves the seed performance and provides faster and synchronized germination. This technique helps in the germination rate by giving some biological and physiological advantage such as enzyme activation which help in rapid synthesis of nucleic acid and any other essential component of cell division. There are various methods of seed priming such as osmopriming, halopriming, hydropriming, hormonalpriming etc. Seed priming is a process where seeds are soaking in priming agents before its germination. Thus the germination rate of the seed will be increased.

Technique of seed priming	Priming agent
Halopriming	Solution of inorganic salts i.e. NaCl, KNO3 CaCl2, CaSO4
Osmopriming	Solutions of sugar, polyethylene glycol (PEG), glycerol, sorbitol, or mannitol
Hormonalpriming	salicylic acid, ascorbate, kinetin

Table no: 1 -List of Seed priming agent.

EVALUATION OF PLANT EXTRACT:

Four plant are used to study the evaluation of plant extract on seed borne mycoflora.Those are Neem, Datura, Sajne, and Bon Tulsi. Several concentration are made (400 mg/ml; 200mg/ml; 100mg/ml; and 50mg/ml) to study the efficacy of plant extract.

Solvents used for Plant extract:

I. Hexane
II. Ethyl acetate
III. Benzene
IV. Chloroform

Figure 3: Different plant extracts

Preparation of different plant extract:

There are four types of plant extract prepared to evolution of plant extract are 1.Benzene extract 2.Hexane extract 3.Chloroform extract 4.Ethyl acetate extract. 5gm of air-dried powder of leaves was mixed with 25ml of benzene in a conical flask and then kept on a rotary shaker for 10mints. Then they were bind with tissue paper and rubber band.

Some holes were made so that air can pass through it and then take room temperature for 3-5 days for evaporate.

Table no:2 -List of plant extract and recommended doses.

Sl. No	Common name	Plant part used	Half Recommended dose	Recommended dose
1	Bon Tulsi	Leaf	5%	10%
2	Neem	Leaf	5%	10%
3	Sajne	Leaf	5%	10%
4	Datura	Leaf	5%	10%

Evaluation of Bio-agents :

Three bio- agents i.e. *Trichoderma viride* (Parbham) and *Pseudomonas fluorescens* and *Bacillus subtilis* were used to control the seed borne mycoflora associated with the oilseed cultivars on PDA medium. Three species of seven days old cultures of *Trichoderma viride* (Parbham) and *Pseudomonas fluorescens* and *Bacillus subtilis* were used for seed treatment of oilseed cultivars. Every 5 and 10 gm. *Trichoderma* cultures were mixed with 100 gm (W/W) fine charcoal powder to increase total volume and adhesive vortex was added for better sticking with the oilseeds. The oilseed seeds were moist with sterilized distilled water and coated with *Trichoderma viride* (Parbham) and *Pseudomonas fluorescens* culture. Plating of oilseeds was done on agar plates. Observations regarding mycoflora associated with the seeds and seed germination per cent were recorded after seven days.

Table no:3 List of Bio-agent and recommended doses.

Sl No.	Bio-agent	Half Recommended dose	Recommended dose
1	*Trichoderma viride*	0.5%	1.0%
2	*Psudomonas fluorescens*	0.5%	1.0%
3	*Bacillus subtilis*	0.5%	1.0%

Detection of effectiveness of plant extract on seed borne mycoflora by SEM study:

Fungi samples (1 × 1 cm), collected from seedlings, were pre-fixed in 3% glutaraldehyde plus 2% paraformaldehyde in a 0·1 M sodium cacodylate (CAC) buffer (pH 7·2) for 2 h at room temperature and then stored at 4°C until further processing. Samples were washed twice in the CAC buffer for 30 min and then postfixed in 0·1% w/v osmium tetroxide in the same buffer for 2–3 h at room temperature. After fixation, samples were washed (2 × 30 min) with distilled water and dehydrated with a graded ethanol series (20, 40, 60, 70, 80, 90, 95 and 99·5%) consisting of 10 min steps for each ethanol concentration followed by a graded ethanol–acetone series with 30 min steps. Specimens were subsequently dried in a critical-point drier (Agar Scientific Ltd) with liquid CO_2 as the transition fluid, mounted on SEM stubs with double-sided sticky tape and coated. Observations of plant and fungal structures were made using a *ZEISS* Sigma FE scanning electron microscope operated at 15.00 kV and equipped with a camera for digital micrographs.

Statistical Analysis:

Statistical values were analysed using SIGMAPLOT software (Version – 14.0). The 'ANOVA test' were used to analysis of resulting data. The data represents as mean and standard deviation (SD) with Probability value (p).

RESULT:

Morphological Identification of different seed borne mycoflora associated with the oilseed samples by light microscopy:

The identification of fungi was done based on spore morphology and colony character.Ten fungi were noticed on the oilseed samples collected from the different oilseed growing areas of Birbhum district, West Bengal. *Aspergillus niger, Aspergillus flavus* often appeared in many samples along with species of *Rhizopus sp., Fusarium sp., Mucor sp.* and

Alternaria sp. were found mostly. Spore morphology and colony characters are given below.

Aspergillus sp.

Colony of *Aspergillus niger*on seed grows slowly, consisting of a compact to fairy loose white to faintly yellow basal mycelium, which bears abundant erect and initially crowed conidial structures. Conidial heads are typically large and black, compact at first, spherical or split into two or more loose to reasonably well defined columns. Conidiophores are smooth, hyaline or faintly brownish near the apex. Two series of conidia bearing the cells (supporting cells and phialides) are produced but in some heads only phialides are present. Conidia are typically spherical at maturity. Often very rough or spiny, mostly 4-5 µm diameter and very dark in colour or with conspicuous longitudinal striations.

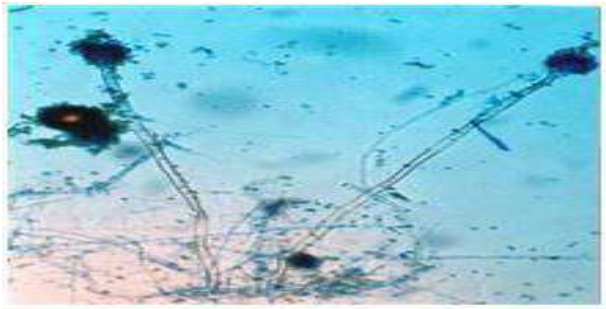

Plate 1: *Aspergillus sp*

Fusarium sp.

The fungus produces abundant loose, aerial white mycelium on incubated seed. In this mycelium several shiny, hyaline, transparent to milky white spherical droplets are seen hanging at the tip of long thin stalks. These stalks are primary conidiophores, which arise laterally from the hyphae in the aerial mycelium. Microconidia are hyaline, 1-2 septate oval, ellipsoidal to sub- cylindrical and measure 5-20 x 2.8-7 µm. Macroconidia are hyaline, stout, measured 22-75 x 35- 7 µm, subcylindrical (or) slightly curved, with short blunt and rounded apical cells and indistinctly pedicillate basal cells. They are glubose to subglubose, smooth (or) rough- walled and 6-11 µm in diameter (Kraft, 1969, Ram Nath *et al.*, 1970; Booth, 1971).

Plate 2: *Fusarium sp*

Rhizopus sp.

Colonies are greyish white in colour. Mycellium are filamentous, branching. Three types of hyphae are found stolons, rhizoids and usually unbranching Sporangiophores. Sporangiophores are rounded and produce numerous nonmotile multinucleate spores for asexual reproduction. Sporangia are black in colour.

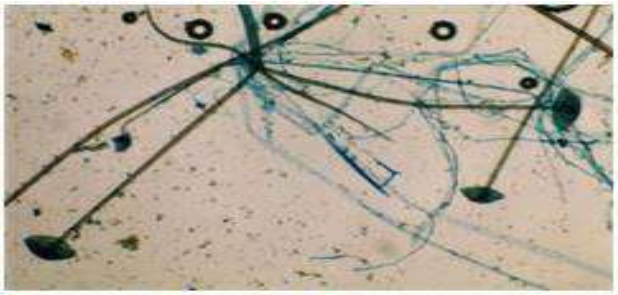

Plate 3: *Rhizopus sp*

Alternaria sp.

Colonies are usually gray, dark blackish brown and black. Mycelium all are immersed or partly superficial, hyphae colourless, olivaceous brown or brown. The conidiophores of the pathogen are pale brown, cylindrical, erect and not rigid and arise singly with a size of 34- 54 x 4-7 µm. Conidiophores produces conidia at the apex which are in chains of one or two. The conidia are straight or slightly curved, obclavate, yellowish brown to dark brown in colour and measures 30- 120- x 4-7 µm. The conidia have 4- 12 transverse septa and 0- 6 longitudinal septa. The conidia have long beak which may be simple or branched and about 24 to 220 x 2-4 µm in size (Ellis and Holiday, 1970).

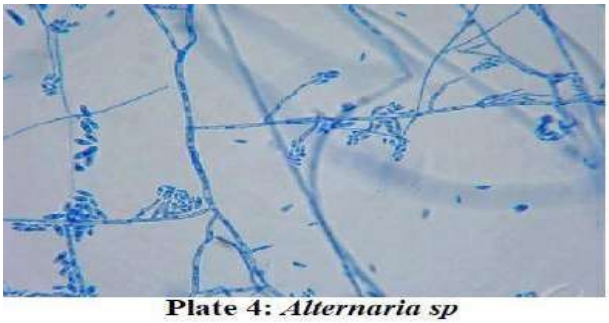

Plate 4: *Alternaria sp*

Rhizoctonia sp.

The pathogen is not currently known to produce any asexual spores. Colonies are distinguishing right angles. Conidia are hyaline basidiospores are borne. Conidiophores forms club shaped basidia with four apical sterigmata on which oval.

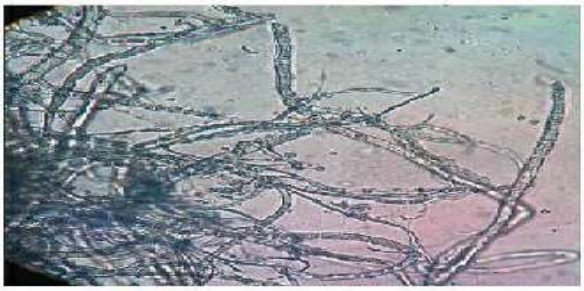

Plate 5: *Rhizoctonia sp*

Cochleobolus sp.

These fungi are able of showing different interaction with their host and different life style depending on their interaction. Shape various from small circular to oval. Colonies are oblong, chocolate coloured sports. Conidia are reddish brown to tan lesions and over time more greyish.

Plate 6: *Cochliobolus sp*

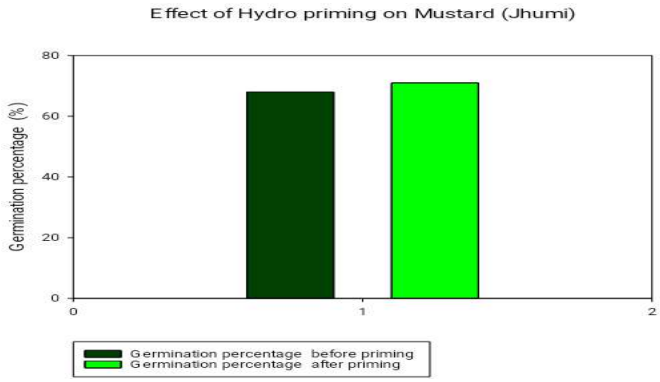

Fig No.-4 Evaluation of Hydro priming on the germination of Oil seed

Seed priming plays an important role on the germination percentage of seeds. In Hydro priming it was shown that the germination percentage of mustard increased from 68% to 71% (Table no: 4)

Evaluation of Halo priming on the germination percentage of oil seed:

Table no:-4 Effect of Halo priming on Mustard (Jhumi)

Sl No.	Name of Priming Salt	Germination percentage before Priming.	Germination percentage after Priming.
		Mustard (Jhumi)	Mustard (Jhumi)
1.	NaCl	69	73
2.	KNO3	65	68
3.	$CaCl_2$	68	73
4.	$CaSO_4$	63	68
S.D		2.387	1.924
Mean		65.130	72.130

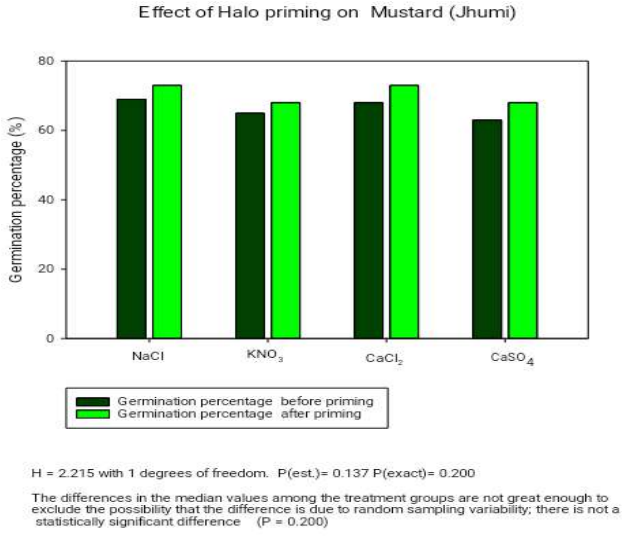

Fig No.-5 Evaluation of Halo priming on the germination percentage of oil seed

In Halo priming it was shown that Nacl increased the germination percentage of mustard from 69% to 73%. KNO_3 increased the germination percentage of mustard from 65% to 68%. $Cacl_2$ increased the germination percentage of mustard from 68% to 73% and $caso_4$ increased the germination percentage of mustard from 63% to 68 %.(Table no: 5).

Evaluation of Osmo priming on the germination percentage of oil seed:

Table no:-5 Effect of Osmo priming on Rice (Khas) and Mustard (Jhumi)

SL.	Name of Priming agent	Germination percentage before Priming.	Germination percentage after Priming.
1.	Sugar	68	71
2.	PEG (Poly ethelene glycol)	66	70
3.	Glycerol	65	69
4.	Sorbitol	69	73
5.	Manitol	63	68
	S.D	2.387	1.924
	Mean	66.200	70.200

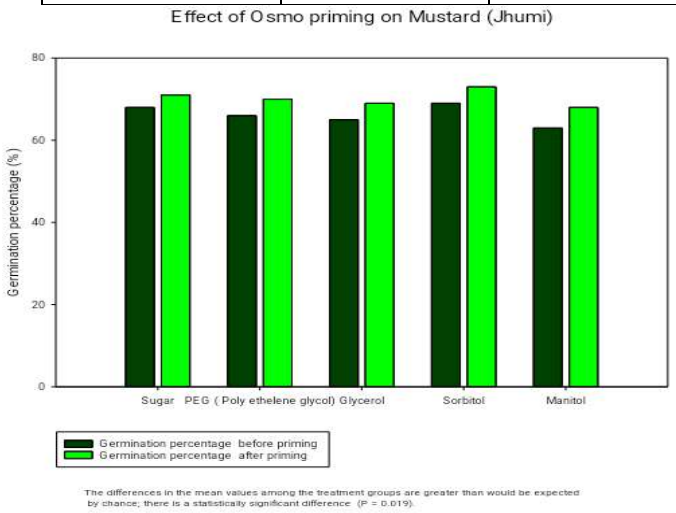

Fig No.-6 Evaluation of Osmo priming on the germination percentage of oil seed

In case of Osmo priming it was shown that Sugar increased the germination percentage of mustard from 68% to 71%. PEG increased the germination percentage of mustard from 66% to 70%. Glycerol increased the germination percentage of mustard from 65% to 69%. Sorbitol increased the germination percentage of mustard from 69% to 73%. NaCl increased the germination percentage of rice mustard from 63% to 68%. (table no:6)

Evaluation of Hormonal priming on the germination percentage of oil seeds:

Table no :-6 Effect of Hormonal priming on Mustard.

SL. No.	Name of Priming agent	Germination percentage before Priming.	Germination percentage after Priming.
		Mustard (Jhumi)	Mustard (Jhumi)
1	Salicylic acid	64	73
2	Ascorbic acid	66	75
3	Kinetin	68	76

S.D	2.000	1.528
Mean	66.000	74.667

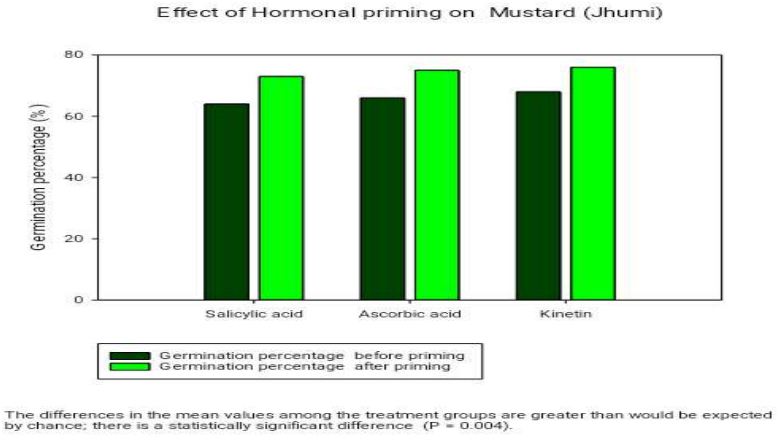

Fig No.-7 Evaluation of Hormonal priming on the germination percentage of oil seeds

In Hormonal priming Salicylic acid increased the germination percentage of mustard from 64% to 73%. Ascorbic acid increased the germination percentage of mustard from 66% to 75%. Kinetin increased the germination percentage of mustard from 68% to 76%.

Evaluation of Bio-agents on the basis of germination percentage of oil seeds:

Three bio- agents i.e., *Trichoderma viride* and *Pseudomonas fluorescens* and *Bacillus subtilis* were used as seed treating agents to assess their efficacy on seed germination. Soaking method which was described under materials methods was followed for the experiment. Data pertaining to the various parameters are presented in Table no (7) The results revealed the positive effects of most of the bio- agents against the infection of seed mycoflora which reduced the infection percentage considerably and enhanced the germination percentage of different seeds of oilseed crops. All the treatments differ significantly over control. *Trichoderma viride* showed good for all the seeds of oilseeds with the germination percent increasing 68%(before treatment) to 79%(after treatment) Followed by *Pseudomonas fluorescens 65%(*before treatment) to *70%* (after treatment)and *Bacillus subtilis* 65% (before treatment) to 69% (after treatment).

Table No:7 Evaluation of Bio-agent (*Trichoderma viridae, Pseudomonas fluorescens, Bacillus subtilis)* on oil seed (Jhumi).

SL No.	**Bio-Agent**	**Germination percentage before treatment**	**Germination percentage after treatment**
1.	***Trichoderma viridae***	68	79
2.	***Pseudomonas fluorescens***	65	70
3.	***Bacillus subtilis***	65	69
SD		1.732	5.508
Mean		66.000	72.667

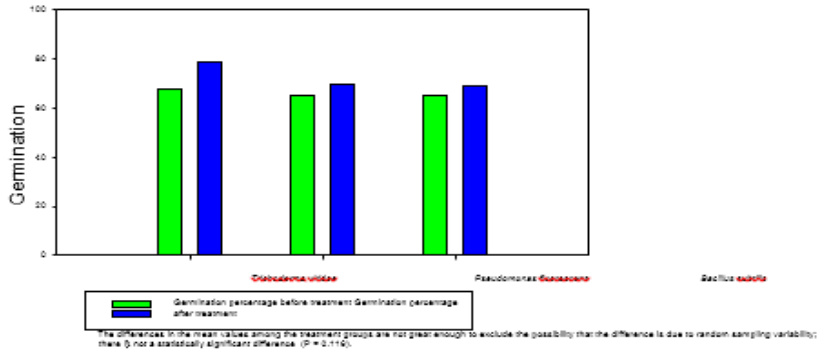

Fig no:8 Evaluation of Bio-agent (*Trichoderma viridae, Pseudomonas fluorescens, Bacillus subtilis)* on oil seed (Jhumi).

Evaluation of plant extracts on the basis of germination percentage of oil seed (Standard Blotter Method and Agar Plate method):

Four plants extracts viz. leaf extract of Ban Tulsi, Neem, Datura and Sajne were used as seed treating agents to assess their effect on seed germination. Soaking method which was described under materials methods was followed for the experiment. Data pertaining to the various parameters are presented in Table no (9) and Fig. no (9). All the treatments differ significantly over control. However, the extract of Tulsi showed 72% (500ppm), and 76% (1000ppm) germination percentage against the seed mycoflora. The Datura leaf extract showed maximum germination on Jhumi 96% (1000ppm) followed by Sajne 84% (1000ppm)and Neem 80% (1000ppm).

Table No –8 Evaluation of plant extracts on the basis of germination percentage of different oil seeds under in-vitro condition (Standard Blotter method

Sl. No.	Oil Seeds	Plant Extracts								Control	
		TULSI		**NEEM**		**SAJNE**		**DATURA**			
		500 ppm	**1000 ppm**	**500 ppm**	**1000 ppm**	**500 ppm**	**1000 ppm**	**500 ppm**	**1000 ppm**		
1.	Jhumi (large)	72.00	76.00	72.00	80.00	80.00	84.00	92.00	96.00	52.00	54.00
	SD	11.588	12.362	11.588	12.362	11.588	12.362	11.588	12.362	11.588	12.362
	Mean	73.600	78.000	73.600	78.000	73.600	78.000	73.600	78.000	73.600	78.000

Evaluation of plant extracts on the basis of germination percentage of different oil seeds under in-vitro condition (Standard Blotter method)

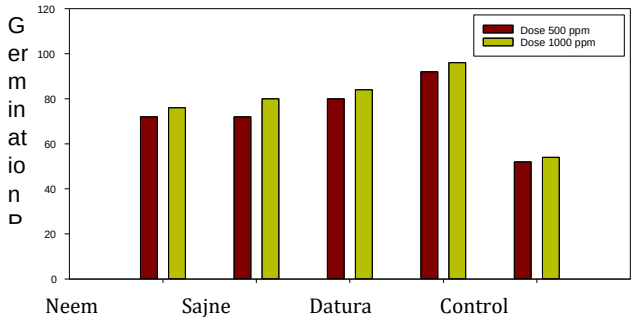

FIG NO:9 Evolution of plant extracts on the basis of germination percentage of different oil seeds under in-vitro condition (standard Blotter method)

Table No – 9 Evaluation of plant extracts on the basis of germination percentage of Oil seed under invitro condition (Agar pate method)

Sl. No.	Oil Seeds	Plant Extracts								Control	
		TULSI		NEEM		SAJNE		DATURA			
		500 ppm	1000 ppm	500 ppm	1000 ppm	500 ppm	1000 ppm	500 ppm	1000 ppm		
1.	Jhumi (large)	40.00	48.00	36.00	40.00	40.00	44.00	52.00	56.00	20.00	22.00
SD		11.524	12.198	11.524	12.198	11.524	12.198	11.524	12.198	11.524	12.198
Mean		37.600	40.400	37.600	40.400	37.600	40.400	37.600	40.400	37.600	40.400

Table No – 9 Evaluation of plant extracts on the basis of germination percentage of Oil seed under invitro condition (Agar pate method)

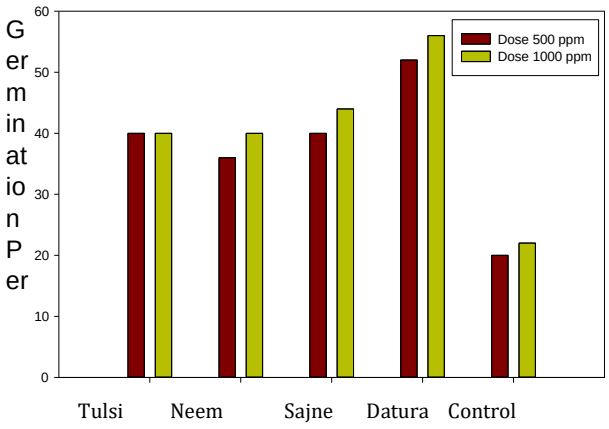

FIG NO:10 -Evolution of plant extracts on the basis of germination percentage of different oil seeds under invitro condition (Agar plate method)

Evaluation of plant extracts on the basis of inhibition of fungal growth of different oilseeds under invitro condition: (Standard Blotter method and Agar plate method:

Four plant extracts viz. leaf extract of Ban Tulsi, Neem, Datura, Sajne were used as seed treating agents to assess their effect on seed germination. Soaking method which was described under materials methods was followed for the experiment. Data pertaining to the various parameters are presented in Table no. (11) and Fig no. (11). All the treatments differ significantly over control. The Datura leaf extract showed maximum inhibition of seed mycoflora on Jhumi 67% (500ppm) followed by Bon Tulsi 62% (500ppm) and Sajne 59% (500ppm).

Table No. 10 – Evaluation of plant extracts on the basis of fungal growth inhibition of Oil seed under invitro condition (Agar plate method)

Sl. No.	Oil Seeds	Plant Extracts								Control	
		BONTULSI (*Croton bonplandianum*)		NEEM (*Azadirachta indica*)		SAJNE (*Moringa oleifera*)		DATURA (*Datura Stramonium*)			
		500 ppm	1000 ppm	500 ppm	1000 ppm	500 ppm	1000 ppm	500 ppm	1000 ppm		
1.	Jhumi (large)	62.00	56.00	54.00	49.00	59.00	53.00	67.00	65.00	95.00	94.00
	SD	16.134	18.091	16.134	18.091	16.134	18.091	16.134	18.091	16.134	18.091
	Mean	67.400	63.400	67.400	63.400	67.400	63.400	67.400	63.400	67.400	63.400

Evaluation of plant extracts on the basis of fungal growth inhibition of Oil seed under invitro condition (Agar plate method)

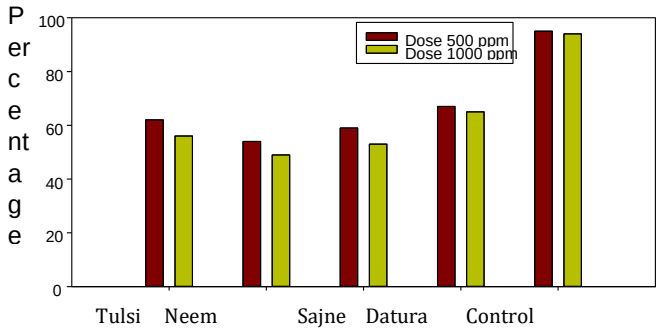

The differences in the mean values among the treatment groups are not great enough to exclude the possibility that the difference is due to random sampling variability; there is not a statistically significant difference (P = 0.722).

Fig No:11- Evaluation of plant extracts on the basis of fungal growth inhibition of Oil seed under in-vitro condition (Agar plate method)

Table No.-11 Evaluation of plant extracts on the basis of fungal growth inhibition of Oil seed under invitro condition (Standard Blotter method)

Sl. No.	Oil Seeds	Plant Extracts								Control	
		BONTULSI (*Croton bonplandianum*)		NEEM (*Azadirachta indica*)		SAJNE (*Moringa oleifera*)		DATURA (*Datura Stramonium*)			
		500 ppm	1000 ppm	500 ppm	1000 ppm	500 ppm	1000 ppm	500 ppm	1000 ppm		
1.	Jhumi (large)	85.00	79.00	83.00	79.00	87.00	81.00	95.00	88.00	110.00	100.00
	SD	11.045	08.961	11.045	08.961	11.045	08.961	11.045	08.961	11.045	08.961
	Mean	92.000	85.400	92.000	85.400	92.000	85.400	92.000	85.400	92.000	85.400

Evaluation of plant extracts on the basis of fungal growth inhibition of Oil seed under in-vitro condition (Standard Blotter method)

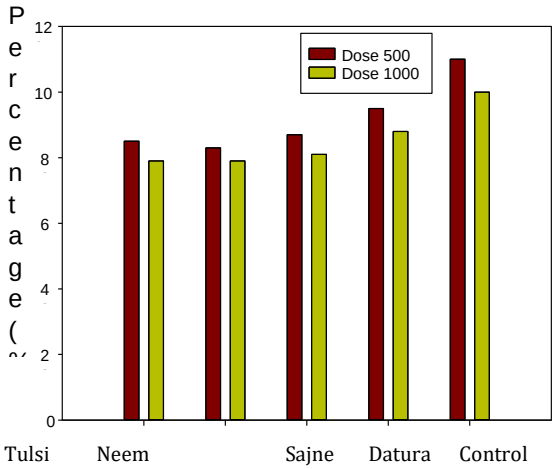

Fig No:12 – Evaluation of plant extracts on the basis of fungal growth inhibition of Oil seed under in-vitro condition (Standard Blotter method)

The differences in the mean values among the treatment groups are not great enough to exclude the possibility that the difference is due to random sampling variability; there is not a statistically significant difference (P = 0.330).

Detection of level of effectiveness of plant extract on seed bone mycoflora by SEM study:

The seed borne fungi, *Rhizopus sp., Aspergullis sp., Fusarium sp., Cochliobolus sp., Alternaria sp.* and *Rhizoctonia sp.* growing over the seed of Rice and Mustard were observed under Light microscope. Then the microscopically identified samples of each plate was marked, thereafter treatment via plant extracts it supplied for SEM identification The Scanning Electron Microscopy showed different rapture stages of these fungi.. The result of each plate is below-

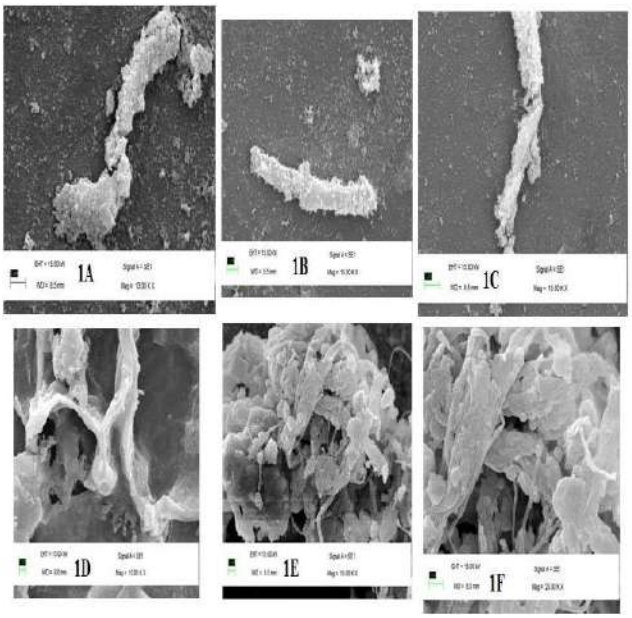

Figure-13 : Effect of Ethyl acetate extract of *Moringa oleifera* and the raptureness occurred in those seed borne fungi (*Rhizopus sp.* {1A}, *Aspergullis sp.* {1B}, *Fusarium sp.* {1C}, *Cochliobolus sp.* {1D}, *Alternaria sp.* {1E} and *Rhizoctonia sp.* {1F}) respectively.

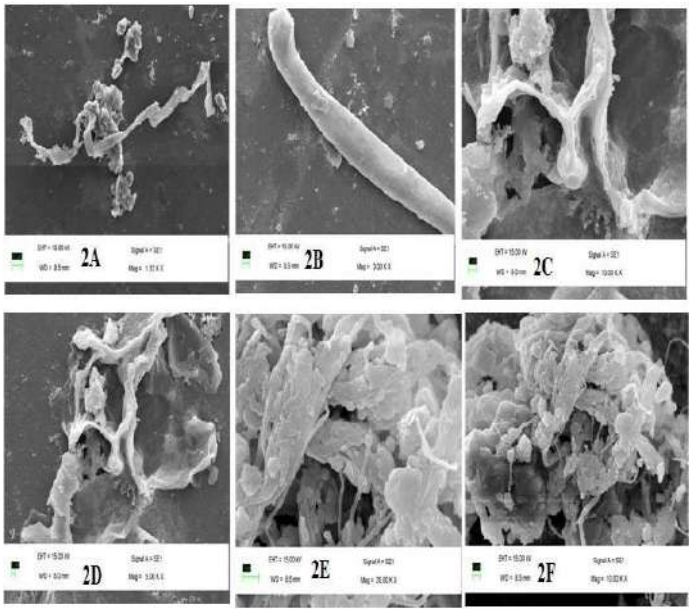

Figure-14 : Effect of Ethyl acetate extract of *Croton bonplandianum* and the raptureness occurred in those seed borne fungi (*Rhizopus sp.* {2A}, *Aspergullis sp.* {2B}, *Fusarium sp.* {2C}, *Cochliobolus sp.* {2D}, *Alternaria sp.* {2E} and *Rhizoctonia sp.* {2F}) respectively.

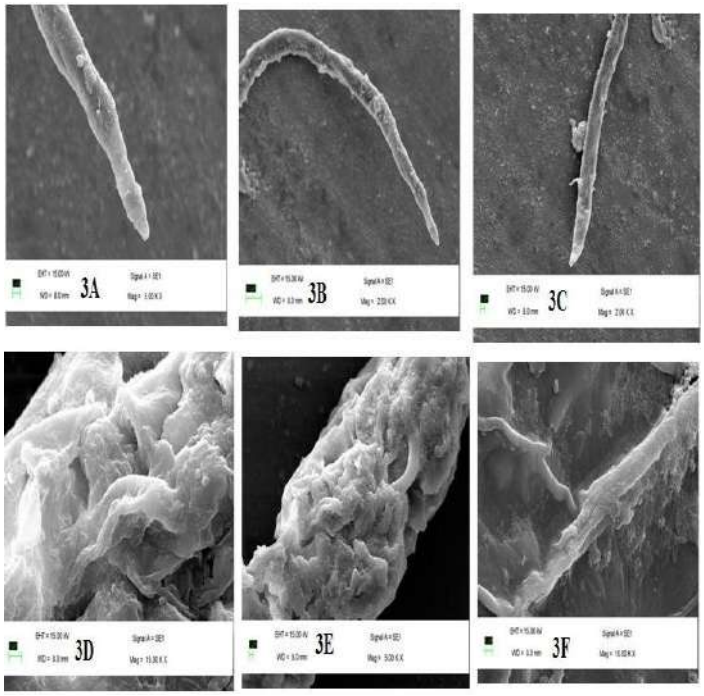

Figure-15 : Effect of Ethyl acetate extract of *Datura stramonium* and the raptureness occurred in those seed borne fungi (*Rhizopus sp.*{3A}, *Aspergullis sp.*{3B}, *Fusarium sp.*{3C}, *Cochliobolus sp.*{3D}, *Alternaria sp.*{3E} and *Rhizoctonia sp.*{3F}) respectively.

Figure-16 : Effect of Ethyl acetate extract of *Azadirachta indica* and the raptureness occurred in those seed borne fungi (*Rhizopus sp.*{4A}, *Aspergullis sp.*{4B}, *Fusarium sp.*{4C}, *Cochliobolus sp.*{4D}, *Alternaria sp.*{4E} and *Rhizoctonia sp.*{4F}) respectively.

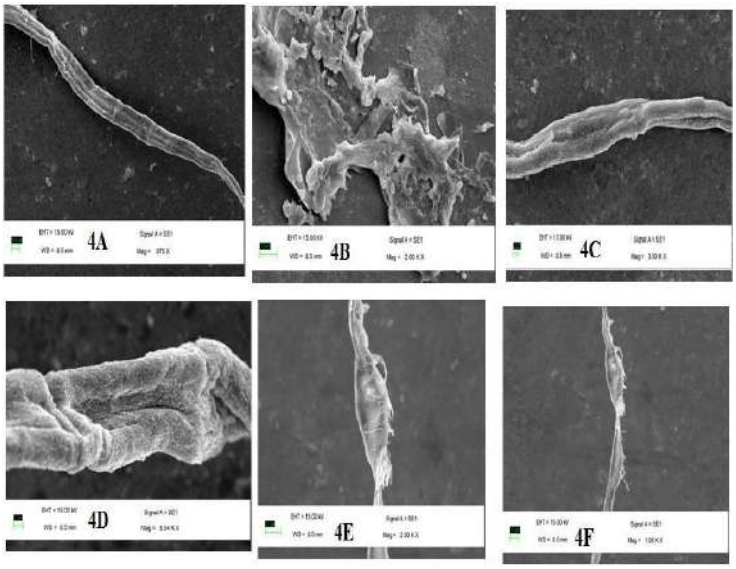

DISCUSSION AND CONCLUSION:

The findings pertaining to the investigations carried out on detection and identification of seed mycoflora of mustard isolation of predominant mycoflora *i.e. Aspergillus sp., Rhizopus sp.*, *Fusarium sp.*, *Cochleobolus sp.*, *Rhizoctonia sp.* and *Alternaria sp.*, *in- vitro* evaluation of botanicals, biocontrol agents and chemical on the basis of germination and infection percentage are summarized as below. Occurrence of *Aspergillus sp.*, *Alternaria sp.* was found predominant. The mycofloral species viz. *Rhizopus sp.*, *Fusarium sp.*, *Aspergillus sp.*, *Alternaria sp.* were found associated with all the tested genotypes while species of *Cochleobolus sp., Rhizoctonia sp.* were not detected in some of the genotypes. Among the methods adopted for detection of seed mycoflora, agar plate method proved to be better than the other methods as the number of colonies of the seed mycoflora were more in agar plate method. Four plants extracts viz. leaf extract of Ban Tulsi, Neem, Datura, Sajne were used as seed treating agents to assess their effect on seed germination. Four botanical formulations evaluated against the seed borne mycoflora associated with the oilseed by soaking method. Leaf extract of Tulsi and Neem showed maximum inhibition of mycoflora infestation followed by leaf extract of datura and whereas leaf extract of Sajne showed poor result of inhibition against the seed borne mycoflora. In Agar plate method of Mustard the data revealed the positive effects of most of the plant extracts against the infection of seed mycoflora which reduced the infection percentage considerably and enhanced the germination percentage of different seeds of oilseed crops. However, the extract of Tulsi showed 40% (500ppm), and 48% (1000ppm) germination percentage against the seed mycoflora. The Datura leaf extract showed maximum germination on Jhumi 56% (1000ppm) followed by Tulsi 48% (1000ppm) and Neem 40% (1000ppm). The Datura leaf extract showed maximum inhibition of seed mycoflora on Jhumi 67% (500ppm) followed by Bon Tulsi 62% (500ppm) and Sajne 59% (500ppm). Among the three bio- agents tested for their efficacy against the pathogens by soaking method, maximum percentage of seed germination with less infection was noticed in *Trichoderma viride,* which was found on par with *Pseudomonas fluorescens.* Among the four priming agent viz. Hydro priming, Halopriming, Osmopriming and Hormonal priming, the Hormonal priming showed maximum germination percentage. In Hormonal priming Salicylic acid increased the germination percentage of mustard from 64% to 73%.Ascorbic acid increased the germination percentage of mustard from 66% to 75%. Kinetin increased the germination percentage of mustard from 68% to 76%.

FUTURE ASPECT:

Microbial contamination of seed become in a growing concerned of the farmers as it affect directly and indirectly with germination percentage viability of the seed heath and vigour and also on nutritional property. It is quite obvious that considerable amount of seeds destroyed or rotted every year due to the infection of various mycoflora the quantum of losses is under great threat owing to the fluctuating environmental condition which contributing tremendously towards the multiplication and development of seeds mycoflora is considerable amount of research have been done on the aspect of seed pathology which include identification of seed borne mycoflora, interaction between post pathogens, seed resistance , seed priming use of different indigenous and technological knowhow to Combat seed infection. But till today there is a considerable gap between the proper identification and managements of seed mycoflora under diverse eco-system best on the present research work some emphasis has to be given further on the following aspect-Bio pesticides i.e. botanicals, bio-organism, medicinal plane extract, having an anti microbial property must best utilize in a broad manner. For increase the detection efficacy, alternation in detection methods to be done at regular intervals on all the oilseed crops. For effective detection of bacterial species, special methods need to be developed. Efficacy of various type of indigenous methods to control the seed borne mycoflora associated with the can be practised. Relation with epidemiological factors.

REFERENCES:

1. Indi, D.V., Lukade, G.M., Patil, P S and Shambharkar, DA., Yield losses due to*Alternaria* leaf spot in safflower under dry land condition. Pesticides. 22(1): 41-43(1987).
2. Chohan, and Saharan, A review of deterioration of oil-seeds by fungi withspecial reference to India (2003).
3. Chernin, L. and Chet, I., Enzymes in the Environment: Activity, Ecology, andApplications,Marcel Dekker, NY, pp 171- 225 (2002).
4. Ping, L. and Boland, W*Trends Plant Sci* 9 263-269 (2004).
5. Wei, L., Kloepper, J.W. and Tuzun SPhytopathol81: 1508-1512 (1991).
6. Zhang, L. and Birch, R.G., Lett Appl Microbiol22: 132-136 (1996).
7. Van, Loon L.C., Bakker, P.A.H.M. and Pieterse CMJ *Annu Rev Phytopathol* 36:453-483 (1998).
8. Thomashow LS and Weller DM, PlantMicrobe Interactions, Chapman and Hill, New York, pp 236-271 (1996).
9. Thomashow LS, Weller DM, Bonsall RF. Appl Environ Microbiol56: 908-912(1990).
10. Kushi,K.K and Khare,M,N, comparative efficacy of five methods to detect*Macrophomina Phaseolina* associated with sesamum seeds.Indian Phytopath. 31: 258-259 (1978).
11. Lantos F, Lantos J, Lantos E, *Practicing Oil Analysis*, 7 (2002).
12. Agarwal V.K., Techniques for the detection of seed borne fungi. Seed Research. 4:24-31 (1976).
13. Barnet H.L., Hunter BB. Illustrated genera of imperfect fungi. The American Psychopathological or Phytopathological Society. 273. U.S.A (1999).
14. ISTA. Seed health testing methods and the germination test. In. International Rulesfor Seed Testing. Pub. by Intl. Seed Test. Assoc. Bassersdorf, Switzerland. Spring wheat. J. Phytopathol. 149: 185-188 (2005).
15. Warham, E.J., Effect of Tilletia indica Infectionon Viability, Germination andVigour of Wheat Seed. Plant Disease, 74: 130-135 (1990).
16. Baki, A.A. and J.D. Anderson, Physiological and Biological Deteriorationof Seeds. In Seed Biology, Vol. II.
17. Academic press, New York, pp: 283-315 (1972).
18. Habib A., Sahi ST, Ghazanfar MU, Ali S, *Int J Agric Biol*, 9: 514–516 (2007)

Source details

Feedback > Compare sources >

Journal of Critical Reviews

Scopus coverage years: from 2019 to 2020

(coverage discontinued in Scopus)

Publisher: Innovare Academics Sciences Pvt. Ltd

E-ISSN: 2394-5125

Subject area: Pharmacology, Toxicology and Pharmaceutics: General Pharmacology, Toxicology and Pharmaceutics

Biochemistry, Genetics and Molecular Biology: General Biochemistry, Genetics and Molecular Biology

Source type: Journal

View all documents > Set document alert Save to source list

CiteScore 2019
0.6

SNIP 2022
0.361

CiteScore CiteScore rank & trend Scopus content coverage

Plant Cell Biotechnology and Molecular Biology 20(23&24):1408–1419; 2019 ISSN: 0972-2025

DETERMINATION OF LEVEL OF SEED INFECTIVITY CAUSED BY RICE (*Oryza sativa*) SEED BORNE MYCOFLORA: AN *in-vitro* STUDY

TANMAY GHOSH*, M. K. BISWAS AND KAUSTAV AIKAT
Department of Biotechnology, NIT Durgapur, Burdwan, W.B., India [TG,KA].
Department of Plant Protection, P. S. B., Visva-Bharati, Sriniketan, W. B. 731236, India [MKB].
[*For Correspondence: E-mail: tanmay.tanmay.ghosh780@gmail.com]

Received: 09 November 2019
Accepted: 19 January 2020
Published: 22 January 2020

Original Research Article

ABSTRACT

The study aimed to isolate and determine seed-borne fungi associated with Cereal crop- Rice .The seeds sample were procured from Burdwan, W.B, India. The seed sample was hold on in artifact bag. Total 5 used to were wont to identification of seed borne fungi. The four flora genera, *Rhizopus, Fusarium, Alternaria, Rhizoctonia, Cochlioboplus* was found to be conspicuously related to totally different seeds of rice. Among them the share of incidence of *Rhizopus sp.* is predominently high all methods, used in isolation. The 18S rRNA sequence based molecuar methodology performed for phylogenetically determine the foremost pathogenic *Rhizopus oryzae*. Histopathology of apparently in infected seeds confined to plant structure fragments by *Rhizopus oryzae* in episperm and reproductive structure, embryonic region of Rice.

Keywords: Seed infectivity; seed borne mycoflora; *Rhizopus oryzae*; phylogenetic identification; histopathological study.

INTRODUCTION

India is one in every of the key oilseeds granger and bourgeois of edible oils. India's oil economy is world's fourth largest when USA, China & Brazil. the various agro-ecological conditions within the country are favorable for growing annual seed crops. Oilseeds cultivation is undertaken across the country in concerning twenty seven million hectares principally on marginal lands, of that seventy two is confined to rainfed farming. The area of science coping with the interactive relationship between seed and unwellness inflicting agents is Seed Pathology. it's conjointly thought-about because the second most vital cereal within the world, that provides concerning ninety five you look after food needs of the planet population [1,2]. Created in roughly one hundred ten countries, together with in variable degrees, it doesn't solely establish the cause however conjointly includes the role of the seed as supply of inoculant, the survival of the infective agent and also the actions taken to regulate the diseases related to seed. Seed mycoflora play a significant role in crucial the quality and longevity of seed. Contaminated seeds can usually finish in poor germination and poor spermatophyte vigor, resulting in academic degree un-healthy crop. Field flora related to seeds causes deterioration of seed quality, have an effect on viability and reduces germination [3]. Frequent and serious rain and floods significantly close to harvest within the completely different parts of the country wet the crop and build panicles additional prone invasion by plant life species [4]. Fungi are a serious reason for reduction within the quality of rice because of high wetness and temperature conditions before its harvest. India stands initial in

rice space and second in production within which virtually tripled from thirty. 4 million tons in 2001-02. Seed is thought to be the first basis of crop production and is one in every of the foremost necessary on the market input factors for acres farmers [5]. Species of *Alternaria*, *Aspergillus*, *Ceratobasidium*, *Cercospora*, *Cochliobolus*, *Curvularia*, *Dreschslera*, *Fusarium*, *Gaeumannomyces*, *Microdochium*, *Penicillium*, *Pyricularia*, *Pythium*, *Rhizoctonia*, *Rhizopus*, *Sclerophthora*, *Trichoderma* and *Tricoconella* are commonest associates in paddy everywhere the planet inflicting pre and post-infections and wide quality losses viz., seed abortion, seed rot, seed sphacelus, reduction or elimination of germination capability, seed plant injury and their alimental price are according Miller, and Kavitha et al. [6,7]. The fungi the embryos reproductive structure and seed coats of the Kernels [8]. The *C. lunata* is one in every of the key grain mould of sorghum, the flora causes black discoloration of seed, degradation of reproductive structure and infect the embryo. Histopathologically sorghum seed consist and natural covering testa, reproductive structure and embryo [9,10,11]. This studies were conducted to determine the infectivity of seed borne fungi and their seed transmission in seed of rice (Variety- Khas).

MATERIALS AND METHODS

Site of Experiments

The experiments were carried out in the department of Biotechnology, National Institute of Technology (NIT), Burdwan, W.B, India.

Collection of Seed Samples

For study Rice seeds (Khas) were collected from Burdwan, W.B, India.

Methods used for Isolation of Mycoflora Using ISTA Technique

Surface Sterilization of Seed: Surface sterilization of the seed are done by one percent sodium hypochlorite for 30 seconds. The seeds are then washed with three changes of sterile water.

Standard blotter method: As per available literature reports three pieces of filter paper should be properly soaked in sterilized water and are placed at the bottom of a 9 cm well labeled plastic Petri dishes. Generally Twenty Five (25) seeds per Petri dish are placed using a pair of forceps and making sure that seeds are placed equidistantly under aseptic conditions. The lids of each Petri dish should be held in place with gummy cello tape. The Petri dishes containing seeds are incubated at room temperature (25°± 2°C) for 7 days under alternating cycles of light and darkness of 12 hours each.

Agar plate method: As described in the literature in the agar plate method 20 ml of potato dextrose agar are distributed to each of the sterile Petri plates under aseptic conditions. After cooling, crop seed samples are transferred to the agar plate. Twenty Five seeds per Petri plate are to kept at equidistance in a circle and incubated at room temperature (25°±2°C) under 12 hours alternating cycles of light and darkness for 7 days and has to be observed everyday for the growth of fungi.

The percent seed mycoflora and percentage frequency of various fungal species should be calculated.

Rolled towel method: It is another process described by researchers to study the germ inability of the seeds in the laboratory at room temperature (30°±2°C). A total of 200 seeds are recommended to be randomly taken from each variety and 50 seeds are placed between a pair of moist paper towels. Generally four replications are used by researchers for each variety. The towels are rolled and the ends are closed by robber band and covered by polyethylene paper to prevent drying. First observation is recommended to take after 5 days and final count has to be taken after 14 days of incubation period pertaining to (a) % germination, (b) non germinated seed (hard seed and rotten seed), (c) shoot length and, (d) root length. For determination of seed mycoflora the fungal growth on infected seed are taken with the needle and observed under compound microscope. For determinations of seedling vigor ten seedlings (normal/abnormal) are randomly selected from each paper and their individual shoot and root length is measured.

Deep freeze method: This method is developed by scientists to detect slow growing pathogens. According to researchers three hundred seeds by

moderately infected pathogens, are generally placed at the rate of 25 seeds per plate on moistened blotters in the way as described under Standard blotter method. The Petri plates are incubated at 20°± 2°C for 24 h under alternate cycles of 12 h NUV light and darkness, for next 24 hours the plates are incubated at –20°C in dark and then kept back under original conditions for next five days. After eight days of incubation, the seeds are examined under stereo binocular microscope. For the surface sterilization the seed in all methods are recommended to sterilize by 0.1% mercuric chloride solution to 1 to 2 min then has to be to behed by sterilized water.

The frequency of the fungus is calculated by the following formula:

{(No. of seeds containing a particular fungus/ Total seeds used) × 100}

NaOH Seed Soak Method: Rice seeds were collected from central Agriculture Research Farm of O.U.A.T. Each sample was replicated twice (1000 seeds each). The bunt incidence was determined by sodium hydroxide method (Agarwal and Shrivastava 1981). Rice seeds of each variety were soaked separately in a plastic Petri dish containing 250 ml of 0.2% sodium hydroxide solution (2 g NaOH/1000 ml of water) for 24 hr at 20-30°C. The solution was decanted after 24 hours of incubation and the seeds were thoroughly washed in tap water then spread over blotter paper so that excess water on the surface of seeds was absorbed. Then the seeds were examined visually and under stereo binacular microscope. The seeds which exhibited shiny jet black, were separated and then ruptured in a drop of water by puncturing with needle. The punctured seeds were observed visually for the release of stream of fungal spores. The numbers of seeds which released stream of fungal spores were counted as infected seeds and the result was recorded in percentage.

Methods Used to Identify Seed Borne Mycoflora

Preliminary Identification of seed borne mycoflora: The identification of fungi was done based on the morphological and colony characters of the pathogens. Various staining methods such as Gram staining, simple staining, lactophenol cotton blue staining was done to identify the mycoflora associated with different seed.

Identification by 18S rRNA gene based molecular method: 18s rRNA /ITS gene sequencing and Phylogenetic tree analysis methods are commonly used for molecular identification of Eukaryotes. It helps in classification and quantitation of microbes within complex biological mixture such as environmental samples. These genes have very high degree of variation even between closely related species. The experimental methods carried out by following steps-

1. DNA was isolated from the culture provided by the scientist. Its quality was evaluated on 1.0% Agarose Gel, a single band of high-molecular weight DNA has been observed.
2. Fragment of ITS region was amplified by PCR. A single discrete PCR amplicon band of ~700 bp was observed when resolved on agarose
3. The PCR amplicon was purified to remove contaminants.
4. Forward and reverse DNA sequencing reaction of PCR amplicon was carried out with ITS1 and ITS4 primers using BDT v3.1 Cycle sequencing kit on ABI 3730xl Genetic Analyzer.
5. Consensus sequence of the PCR amplicon was generated from forward and reverse sequence data using aligner software.
6. The ITS region sequence was used to carry out BLAST with the database of NCBI Genbank. Based on maximum identity score first ten sequences were selected and aligned using multiple alignment software program Clustal W. Distance matrix was generated and the phylogenetic tree was constructed using MEGA 7.

Detection of Infectivity on Infected Seed by Histopathological Study

Fifty seeds of Jhumi, Khas from infected seed lot having characteristics symptoms of seed borne fungi were boiled in distilled water for 30 min at 60°C. Later, seeds were soaked in 70% ethanol for 48 hours. The seed become soft and was ready to

give a cut. Seed of Jhumi and Khas were cut transversely into two pieces at the center of seed to ensure better dehydration, infiltration and embedding. The fixed seeds were dehydrated through acetone I, II, III, IV series for 40 minutes per treatment and benzene I, II for 20 min/treatment and infiltrated using paraffin wax at 52°C for 2 hours. The solid paraffin wax was liquidified and poured in the blocks, cut seeds were placed at the centre of per block, so that the seeds were embedded in the solid wax and the blocks were cooled overnight. Next day, blocks were cut into squares. The blocks were used for serial microtome sections of 7-15 µm thickness by using hand rotary microtome. The ribbon of sections were uplifted, kept floating in water bath having 40°C temperature to deparaffinise the wax and the sections were lifted on the slides. The slides were heated on spirit lamp to make ready for staining and mounted in DPX.

RESULTS AND DISCUSSION

Isolation and Percentage of Incidence of Different Mycoflora Associated with Cereal Crop (Rice-Khas)

Seeds which were collected were tested with five different methods. Those were Standard blotter method Agar plate method, Rolled Towel method, Deep Freeze method and NaOH seed soak method. The data obtained in Table 1 and Fig. 1.

The data are indicate the association of four fungal species viz., *Rhizopus sp.*, *Alternaria sp.*, *Fusarium sp.*, *Cochliobolus sp.*, *Rhozoctonia sp.*, *Macrophomina sp.*, *Mucor sp.* and *Aspergillus sp.* Out of these whole of all methods *Rhizopus sp.* was found predominant with association of *Alternaria sp.*, *Fusarium sp.*, *Cochliobolus sp.*, *Rhozoctonia sp.* respectively that indicates the association of those four fungal species are predominantly present with the seed samples ,and the other fungi enlisted from review of literature is absent as those fungi seems like to normal mycoflora. The total infection percentage varied from approx 40.00 to 50.00%.

Identification of Different Seed Borne Mycoflora Associated with the and Cereal Crop:

Morphological Identification by light microscopy: The seed samples were tested initially by Different methods as described in materials and methods and the results are presented in Table 2 and Fig. 2. Totally Five fungi including both saprophytic as well as pathogenic were encountered. The fungi recorded in these five methods were *Aspergillus sp, Rhizopus sp.*, *Fusarium sp.*, *Alternaria sp., Cochleobolus sp., Rhizoctonia sp., Macrophomina sp.* and *Mucor sp.* The identification of fungi was done based on the morphological and colony characters of the pathogens. *Rhizopus sp.* often appeared with many samples along with *Rhizopus sp.*, *Fusarium sp. Cochleobolus sp., Rhizoctonia sp.* and *Alternaria sp.* Spore morphology and colony characters of mycoflora are given Table 2.

Identification by 18S rRNA Gene Based Molecular Method

Identification of *Rhizopus sp.* using: As the percentage of incidence of *Rhizopus sp.* is dominantly high in each Standard Blotter and Agar Plate method, so, we identified this fungi up to species level by 18s rRNA sequencing and Phylogenetic tree analysis technique. Here the results screening below.

Table 1. Percentage of incidence of mycoflora in different methods

Mycoflora	Percentage of incidence of mycoflora in different methods				
	Standard blotter method	Agar plate method	Rolled towel method	Deep freeze method	NaOH seed soak method
Rhizopus sp.	10.12	15.00	10.00	10.00	10.00
Alternaria sp.	10.00	10.00	10.00	10.00	5.00
Fusarium sp.	10.00	10.00	5.00	10.00	5.00
Conchliobolus sp.	05.00	10.00	10.00	5.00	5.00
Rhizoctonia sp.	05.00	05.00	5.00	5.00	5.00
Macrophomina sp.	0.00	0.00	0.00	0.00	0.00
Mucor sp.	0.00	0.00	0.00	0.00	0.00
Aspergillus sp.	0.00	0.00	0.00	0.00	0.00
Total Percentage	**40.12%**	**50.00 %**	**40.00%**	**40%**	**30%**

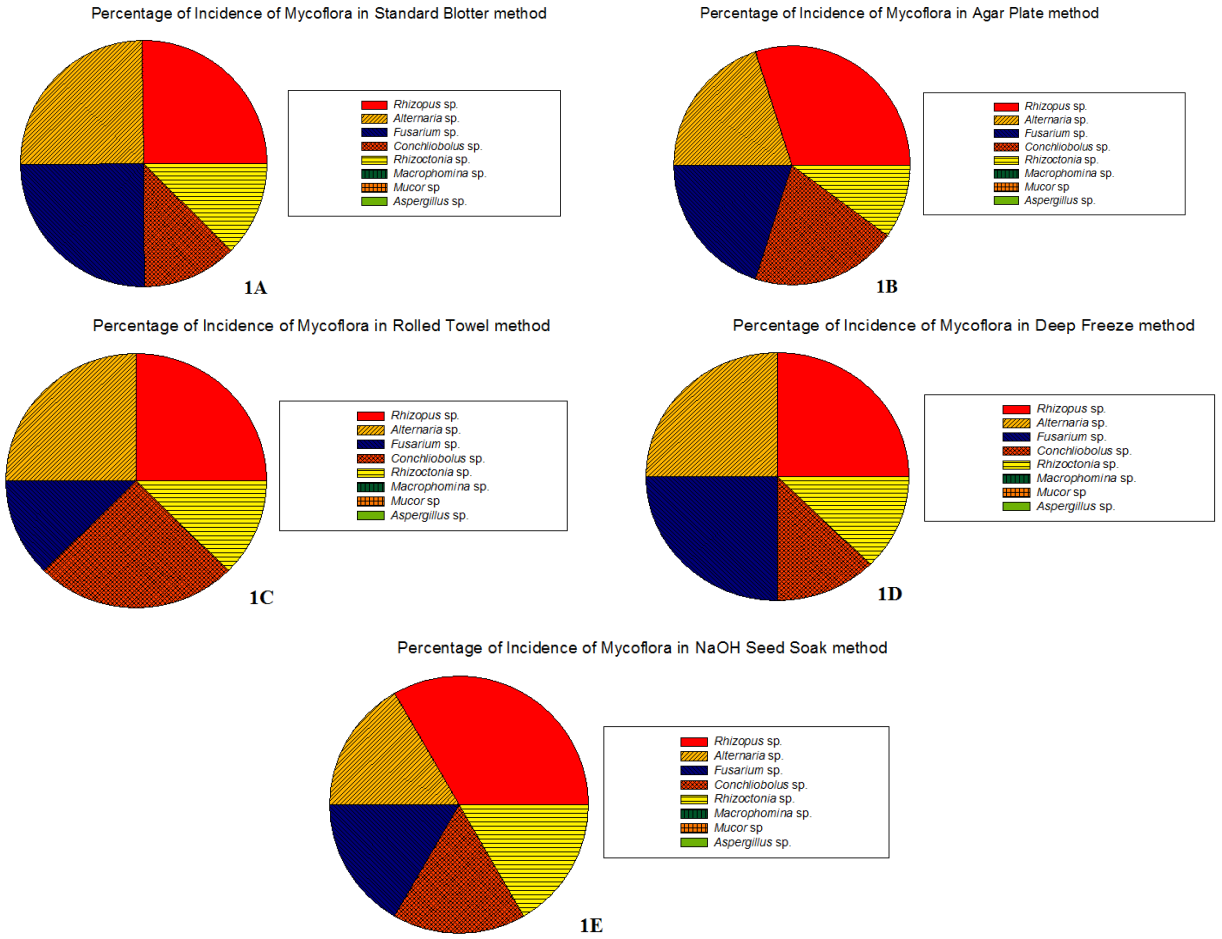

Fig. 1. 1A indicates the percentage (%) of incidence of mycoflora in standard blotter method, 1B indicates the percentage (%) of incidence of mycoflora in agar plate method, 1C indicates the Percentage (%) of incidence of mycoflora in rolled towel method, 1D indicates the percentage (%) of incidence of mycoflora in deep freeze method, 1E indicates the percentage (%) of incidence of mycoflora in NaOH seed soak method

Table 2. Spore morphology and colony characters of seed borne mycoflora

Mycoflora	Colony	Mycelium	Conidiophore	Conidia
Rhizopus sp.	Colonies are greyish white in colour	Filamentous, branching. Three types of hyphae are found stolons, rhizoids and usually unbranching Sporangiophores	Sporangiophores are rounded and produce numerous nonmotile multinucleate spores for asexual reproduction	Sporangia are black in colour.
Alternaria sp.	Usually gray, dark blackish brown and black.	Immersed or partly superficial, hyphae colourless, olivaceous brown or brown.	Pale brown, cylindrical, erect, not rigid and arise singly	Straight or slightly curved, obclavate, yellowish brown to dark brown in colour. Conidia have 4- 12 transverse septa and 0- 6 longitudinal septa with a long beak.
Fusarium sp.	Sporodocia are found	several shiny, hyaline, transparent to milky white	very long and slender	Microconidia are hyaline, 1-2 septate oval, ellipsoidal to sub- cylindrical. Macroconidia are hyaline, stout, subcylindrical or slightly curved
Cochliobolus sp.	Oblong, chocolate coloured sports.	The fungi showing different interaction with their host and different life style depending their interaction	Small circular to oval.	Reddish brown to tan lesions and over time more greyish.
Rhizoctonia sp.	Distinguishing right angles.	The pathogen is not currently known to produce any asexual spores	Forms club shaped basidia with four apical sterigmata on which oval	Hyaline basidiospores are borne.

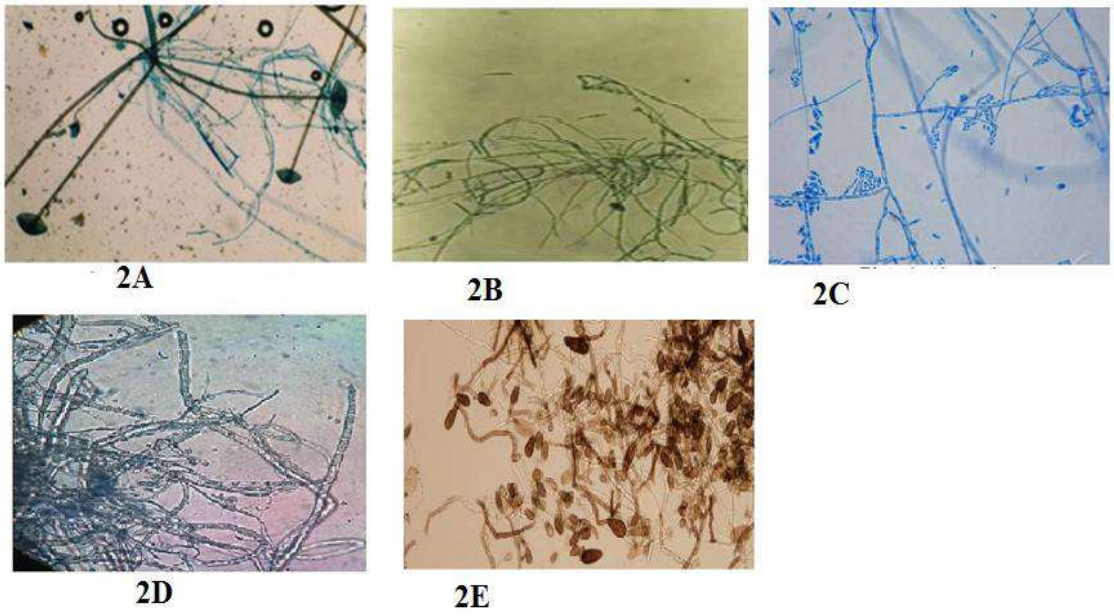

Fig. 2. Direct microscopic view of 2A-*Rhizopus sp.*, 2B-*Fusarium sp.*, 2C-*Alternaria sp.*, 2D-*Rhizoctonia sp.*, 2E-*Cochliobolus sp.*

Data and Result: Fungi which was suspected as *Rhizopus sp.* by morphological identification was identified as *Rhizopus oryzae* based on nucleotide homology and phylogenetic analysis (Fig. 3).

Analysis

gDNA and ITS Amplicon QC data

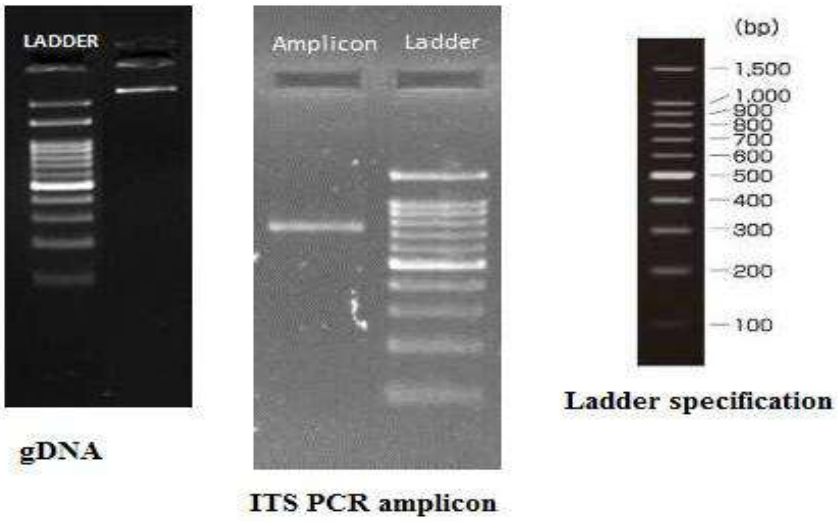

Sanger Seq Chromatogram data file Data

- **Forward Seqdata**

GATTGCTTCTACACTGTGAAAATTTGGCTGAGAGACTCAGACTGGTCATGGGTAGACCTATCT
GGGGTTTGATCGATGCCACTCCTGGTTTCAGGAGCACCCTTCATAATAAACCTAGAAATTCA
GTTATAAAGTTTAATAAAAAACAACTTTTAACAATGGATCTCTTGGTTCTCGCATCGATGAAG
AACGTAGCAAAGTGCGATAACTAGTGTGAATTGCATATTCAGTGAATCATCGAGTCTTTGAA
CGCGTTGCACTCTATGGTTTTTCTATAGAGTACGCCTGCTTCAGTATCATCACAAACCCACAC
ATAACATTTGTTTATGTGGTAATGGGTCGCATCGCTGTTTTATTACAGTGAGCACCTAAGATG
TGTTGTTTTCTGTCTGGCTTGCTAGGCAGGAATATTACGCTGGTCTCAGGATCTTTTTCTTTGG
TTCGCCCAGGAAGTAAAGTACAAGAGTATAATCCAGCAACTTTCAAACTATGATCTGAAGTC
AGGGGGTTACCCGCTGAACTTAAGCATATCATAAACGGAGGAAAAAAAAA

- **Reverse SeqData**

ATCATAGTTTGAAAGTTGCTGGATTATACTCTTGTACTTTACTTCCTGGGCGAACCAAGAAAA
AGATCCTGAGACCAGCGTAATATTCCTGCCTAGCAAGCCAGACAGAAAATCACACACATTTT
AGGCTCACTGTAATAAAACAGCGATGCGACCCATTACCACATAAACAAATGTTATGTGTGGG
TTTGTGATGATACTGAAGCAGGCGTACTCTATAGAAAAACCATAGAGTGCAAGCTGCGTTCA
AAGATGATGATTCACTGAATATGCAATTCACACTAGTTATCGCACTTTGCTACGTTCTTCATC
GATGCGAGAACCAAGAGATCCATTGTTAAAAGTTGTTTTTTATTAAACTTTATAATACTGAAT
TTCTGGTTATTATGAAGGGTGCTCCTGAAACCAGGAGTGGCATCGATCAAACCCCAGATAGG
TCTACCCATGACCAGTCTGAGTCTCTCAGCCAAATTTTCACAGTGTAGAAGCAATCACTTACC
CCAGAGAACCCTAAGAGGTAAGGCGCTTTAACATAATTAATGATCCTTCCGCAGGTTCACCT
ACGGAAACCTTGTTACGACTTTTACTTCCTCTAATTGACCCAAAAGAAA

- **Reverse complement**

TTTCTTTTGGGTCAATTAGAGGAAGTAAAAGTCGTAACAAGGTTTCCGTAGGTGAACCTGCG
GAAGGATCATTAATTATGTTAAAGCGCCTTACCTCTTAGGGTTTCCTCTGGGGTAAGTGATTG
CTTACACTGTGAAAATTTGGCTGAGAGACTCAGACTGGTCATGGGTAGACCTATCTGGGGTT
TGATCGATGCCACTCCTGGTTTCAGGAGCACCCTTCATAATAAACCTAGAAATTCAGTATTAT
AAATTAATAAAAAACAACTTTTAACAATGGATCTCTTGGTTCTCGCATCGATGAAGAACGTA
GCAAAGTGCGATAACTAGTGTGAATTGCATATTCAGTGAATCATCGAGTCTTTGAACGCAGC
TTGCATCATGGTTTTTCTATAGAGTACGCCTGCTTCAGTATCATCACAAACCCACACATAACA
TTTGTTTATGTGGTAATGGGTCGCATCGCTGTTTTATTACAGTGAGCACCTAAAATGTGTGTG
ATTTTTGTTGGCTTGCTAGGCAGGAATATTACGCTGGTCTCAGGATCTTTTTCTTGGTTCGCCC
AGGAAGTAAAGTACAAGAGTATAATCCAGCAACTTTCAAACTATGAT

- **Consensus data**

GGAAGTAAAAGTCGTAACAAGGTTTCCGTAGGTGAACCTGCGGAAGGATCATTAATTATGTT
AAAGCGCCTTACCTCTTAGGGTTTCCTCTGGGGTAAGTGATTGCTTCTACACTGTGAAAATTT
GGGAGAGACTCAGACTGGTCATGGGTAGACCTATCTGGGGTTTGATCGATGCCACTCCTGGT
TTCAGGAGCACCCTTCATAATAAACCTAGAAATTCAGTATTATAAAGTTTAATAAAAAACAA
CTTTACAATGGATCTCTTGGTTCTCGCATCGATGAAGAACGTAGCAAAGTGCGATAACTAGT
GTGAATTGCATATTCAGTGAATCATCGAGTCTTTGAACGCAGCTTGCACTCTATGGTTTTTCT
ATAGATAGCCTGCTTCAGTATCATCACAAACCCACACATAACATTTGTTTATGTGGTAATGGG
TCGCATCGCTGTTTTATTACAGTGAGCACCTAAGATGTGTGTGATTTTCTGTCTGGCTTGCTA
GGCAGAATTTACGCTGGTCTCAGGATCTTTTTCTTTGGTTCGCCCAGGAAGTAAAGTACAAGA
GTATAATCCAGCAACTTTCAAACTATGATCTGAAGTCAGGTGGGATTACCCGCTGAACTTAA
GCATATATAA

DATA: (Alignment view using combination of NCBI GenBank)

Distribution of 100 Blast Hits on the Query Sequence

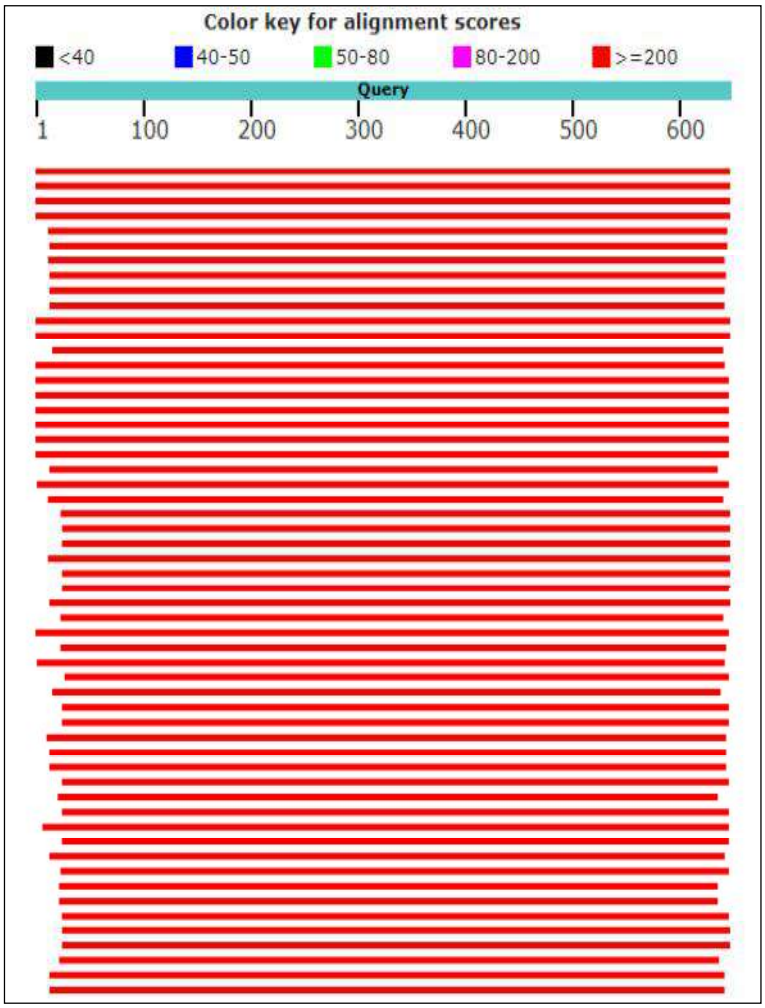

Sequences producing significant alignments

Table 3.

Description	Max score	Total score	Query cover	E value	Ident	Accession
Rhizopus oryzae genes for 18S rRNA, ITS1, 5.8S rRNA, ITS2, 28S rRNA, partial and complete sequence, strain:PCNB1276	1179	1179	99%	0	99%	AB109754.1
Rhizopus oryzae genes for 18S rRNA, ITS1, 5.8S rRNA, ITS2, 28S rRNA, partial and complete sequence, strain:PCNB1280	1173	1173	99%	0	99%	AB109757.1
Rhizopus oryzae genes for 18S ribosomal RNA, internal transcribed spacer 1, 5.8S ribosomal RNA, internal transcribed spacer 2, 28S ribosomal RNA, partial and complete sequence, strain:1289	1170	1170	99%	0	99%	AB126323.1
Rhizopus oryzae genes for 18S rRNA, ITS1, 5.8S rRNA, ITS2, 28S rRNA, partial and complete sequence, strain:PCNB1278	1168	1168	99%	0	99%	AB109755.1

Description	Max score	Total score	Query cover	E value	Ident	Accession
Rhizopus delemar isolate AR14 small subunit ribosomal RNA gene, partial sequence; internal transcribed spacer 1, 5.8S ribosomal RNA gene, and internal transcribed spacer 2, complete sequence; and large subunit ribosomal RNA gene, partial sequence	1157	1157	97%	0	99%	MF445161.1
Rhizopus delemar isolate AR9 small subunit ribosomal RNA gene, partial sequence; internal transcribed spacer 1, 5.8S ribosomal RNA gene, and internal transcribed spacer 2, complete sequence; and large subunit ribosomal RNA gene, partial sequence	1153	1153	97%	0	99%	MF445156.1
Rhizopus delemar isolate AR8 small subunit ribosomal RNA gene, partial sequence; internal transcribed spacer 1, 5.8S ribosomal RNA gene, and internal transcribed spacer 2, complete sequence; and large subunit ribosomal RNA gene, partial sequence	1153	1153	97%	0	99%	MF445155.1
Rhizopus delemar isolate AR13 small subunit ribosomal RNA gene, partial sequence; internal transcribed spacer 1, 5.8S ribosomal RNA gene, and internal transcribed spacer 2, complete sequence; and large subunit ribosomal RNA gene, partial sequence	1151	1151	97%	0	99%	MF445160.1
Rhizopus oryzae strain NB31 small subunit ribosomal RNA gene, partial sequence; internal transcribed spacer 1, 5.8S ribosomal RNA gene, and internal transcribed spacer 2, complete sequence; and large subunit ribosomal RNA gene, partial sequence	1149	1149	99%	0	99%	MF685318.1
Rhizopus oryzae genes for 18S rRNA, ITS1, 5.8S rRNA, ITS2, 28S rRNA, partial and complete sequence, strain: IFM 62202	1149	1149	99%	0	99%	LC317754.1

Phylogenetic Tree

The evolutionary history was inferred by using the Maximum Likelihood method based on the Kimura 2-parameter model [12]. The bootstrap consensus tree inferred from 1000 replicates is taken to represent the evolutionary history of the taxa analyzed. Branches corresponding to partitions reproduced in less than 50% bootstrap replicates are collapsed. The percentage of replicate trees in which the associated taxa clustered together in the bootstrap test (1000 replicates) are shown next to the branches. Initial tree(s) for the heuristic search were obtained automatically by applying Neighbor-Join and BioNJ algorithms to a matrix of pairwise distances estimated using the Maximum Composite Likelihood (MCL) approach and then selecting the topology with superior log likelihood value. The analysis involved 11 nucleotide sequences. Codon positions included were 1st+2nd+3rd+Noncoding. All positions containing gaps and missing data were eliminated. There were a total of 624 positions in the final dataset. Evolutionary analyses were conducted in MEGA7 [13].

Distance Matrix

The number of base substitutions per site from between sequences are shown. Standard error estimate(s) are shown above the diagonal. Analyses were conducted using the Kimura 2-parameter model [12]. The analysis involved 11 nucleotide sequences. Codon positions included were 1st+2nd+3rd+Noncoding. All positions containing gaps and missing data were eliminated. There were a total of 624 positions in the final dataset. Evolutionary analyses were conducted in MEGA7 [13].

Screening Infectivity by Histopathological Study

Histopathological examinations of transverse sections of asymptomatic (control seed) seed under Phase contrast microscope were observed. The mature rice (Khas) seed consist of a seed coat cotyledon and embryo. The seed coat with prominent air-spaces and parenchyma cell Asymptomatic seeds (healthy) were free from fungal infections and tissues of seed components were well developed and compacted under Phase contrast microscope. The seeds are infected with *Rhizopus oryzae.* Transverse sections of infected seeds using Phase contrast microscope showed the presence of fungal mycelia on the seed surface and internal tissues of the seed coat. Mycelial growth was more abundant in the hourglass layer of the seed coat where large intercellular spaces were present.

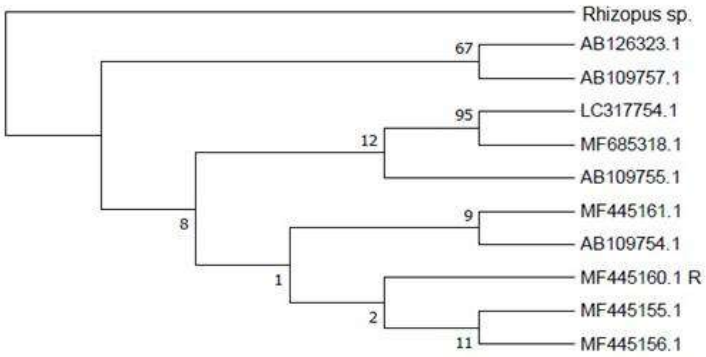

Fig. 3. Molecular phylogenetic analysis by maximum likelihood method

Table 4. Estimates of evolutionary divergence between sequences

Rhizopus sp		0.002	0.002	0.002	0.003	0.002	0.002	0.002	0.002	0.003	0.003
AB109754.1	0.002		0.002	0.002	0.002	0.000	0.000	0.000	0.000	0.003	0.003
AB109757.1	0.003	0.002		0.000	0.003	0.002	0.002	0.002	0.002	0.003	0.003
AB126323.1	0.003	0.002	0.000		0.003	0.002	0.002	0.002	0.002	0.003	0.003
AB109755.1	0.005	0.003	0.005	0.005		0.002	0.002	0.002	0.002	0.003	0.003
MF445161.1	0.002	0.000	0.002	0.002	0.003		0.000	0.000	0.000	0.003	0.003
MF445156.1	0.002	0.000	0.002	0.002	0.003	0.000		0.000	0.000	0.003	0.003
MF445155.1	0.002	0.000	0.002	0.002	0.003	0.000	0.000		0.000	0.003	0.003
MF445160.1_R	0.002	0.000	0.002	0.002	0.003	0.000	0.000	0.000		0.003	0.003
MF685318.1	0.006	0.005	0.006	0.006	0.008	0.005	0.005	0.005	0.005		0.000
LC317754.1	0.006	0.005	0.006	0.006	0.008	0.005	0.005	0.005	0.005	0.000	

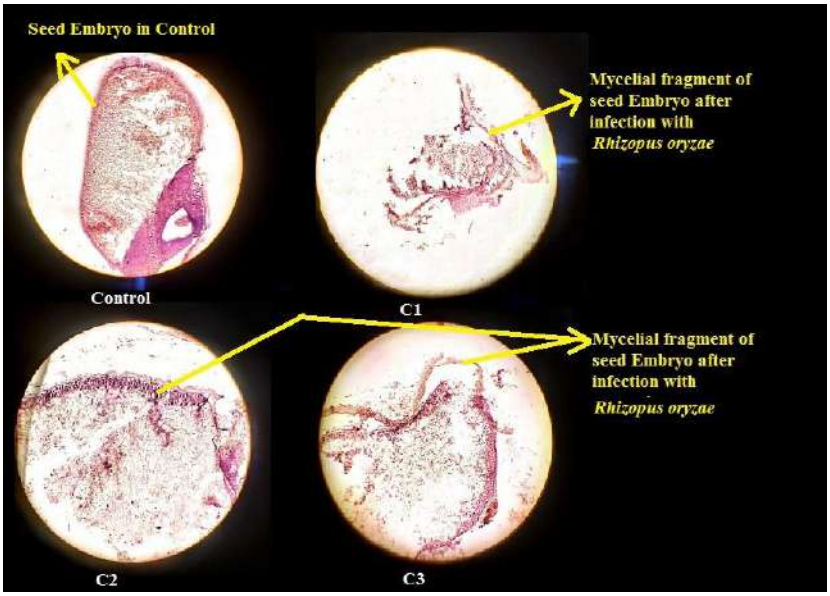

Fig. 4. Histopathological studies of cereal crop seed (Rice-Khas) [C1,C2,C3 indicated the infected seeds confined to plant structure fragments of *Rhizopus oryzae* in episperm and reproductive structure, embryonic region]

The Fungi were found colonize in seed coat, pericarp and endosperm and embryo region. Thus histopathological study revealed that, *Rhizopus oryzae* infected the seed and colonized in various seed tissues and damage the embryo and effect seed viability.

CONCLUSION

In conclusion, the current study reveals the presence of varied fungi related to rice seeds from Burdwan, W.B. and indicates the likelihood of illness incidence once such infected seeds are planted. Though the results of the current study could also be thought of preliminary, the recommend fungi related to rice seeds are potential threat to its production. Histopathology of infected seed showed the distribution of fungi within the covering, seed coat, reproductive structure and embryo. The body part, brown, thick and knotty *Rhizopus sp.* invaded the varied seed components. The fungi, phylogenetically referred to as *Rhizopus oryzae* was found colonize in episperm, pericarp and reproductive structure and embryo region. Thus, histopathological studies discovered that, *Rhizopus oryzae* infect the seed, colonize in numerous seed tissues and harm the embryo and have an effect on seed viability.

COMPETING INTERESTS

Authors have declared that no competing interests exist.

REFERENCES

1. Juliano BO. Rice in human nutrition. FAO/IRRI. FAO Food and Nutrition Series No 26, FAO Rome; 1993.
2. Boumas G. Grain handling and storage. Elsevier Science Publisher B.V., De Datta, S. K. 1985;9-10.
3. Shrivastava RN, Gupta JS. Seed mycoflora from Indian seed lots from *Cosmos bipinatus* and their control. Indian Phyotopath. 1981;34(3):383-385.
4. Reddy CS, Reddy KRN, Kumar RN, Laha GS, Muralidharan K. Exploration of aflatoxin contamination and its management in rice. J. Mycol. Pl. Pathol. 2004;34(3):816-820.
5. Subramanian M. Pulses production strategies in Tamil Nadu. Centre for Plant Breeding and Genetics Tamil Nadu Agricultural University, Coimbatore. India; 2000.
6. Miller JD. Fungi and mycotoxins in grain implications for stored product research. J. Stored Prod. Res. 1995;31(1):1-16.
7. Kavitha R, Umesha S, Shetty HS. Dose dependent impact of dominant seed-borne fungi on seed germination and seedling vigour of cotton seeds. Seed Sci. Res. 2005; 33(2):187-194.
8. Ozer Nuray. Determination of fungi responsible for black point in bread wheat and effects of the disease on emergence and seedling vigour. Trakya Univ. J. Sci. 2005; 6(1):35-40.
9. Deshmukh RN, Raut JG. Sites of *Curvularia lunata* infection in sorghum seed. Indian Phytopathology. 1993;251.
10. Girish AG, Deepti S, Rao VP, Thakur RP. Detection of seed borne grain mold fungi in sorghum and their control with fungicidal seed treatment. ISMN. 2004;45:31-33.
11. Singh DP, Agrawal VK. Effect of different degrees of grain molds infection on yield and quality of sorghum seed. Indian J. Plant Pathol. 1989;7(2):103-108.
12. Kimura M. A simple method for estimating evolutionary rate of base substitutions through comparative studies of nucleotide sequences. Journal of Molecular Evolution. 1980;16:111-120.
13. Kumar S, Stecher G, Tamura K. MEGA7: Molecular evolutionary genetics analysis version 7.0 for bigger datasets. Molecular Biology and Evolution (submitted); 2015.

Source details

Feedback > Compare sources >

Plant Cell Biotechnology and Molecular Biology

Scopus coverage years: from 2002 to 2012, from 2014 to 2021

(coverage discontinued in Scopus)

Publisher: Society for Biology and Biotechnology

ISSN: 0972-2025

Subject area: Agricultural and Biological Sciences: Horticulture | Biochemistry, Genetics and Molecular Biology: Biotechnology

Source type: Journal

View all documents > | Set document alert | Save to source list

CiteScore 2020
0.2

SJR 2020
0.132

SNIP 2022
0.244

CiteScore | CiteScore rank & trend | Scopus content coverage

EFFECTS OF FUNGAL FILTRATES ON MAIZE PLANT ANATOMY AND SEEDLINGS AND TREATMENT WITH DATURA STRAMONIUM BY ITS PHYTOCHEMICALS PROPERTIES

Article · June 2020

CITATIONS
0

READS
29

2 authors:

Tanmay Ghosh
Dinabandhu Andrews College university of calcutta
77 PUBLICATIONS **214** CITATIONS
SEE PROFILE

Mohan Kumar Biswas
Visva Bharati University
118 PUBLICATIONS **525** CITATIONS
SEE PROFILE

Journal of the Maharaja Sayajirao University of Baroda
ISSN : 0025-0422

EFFECTS OF FUNGAL FILTRATES ON MAIZE PLANT ANATOMY AND SEEDLINGS AND TREATMENT WITH *DATURA STRAMONIUM* BY ITS PHYTOCHEMICALS PROPERTIES

Tanmay Ghosh Department of Microbiology, Dinabandhu Andrews College, Baishnabghata, South 24 Parganas (South), Kolkata - 700 084, West Bengal, India
Mohan Kumar Biswas Department of Plant Protection, Palli Siksha Bhavana, Visva - Bharti, Sriniketan, Birbhum, West Bengal.

Abstracts:
Zea mays are one of the very important cereal crops that cultivated in almost all over the India. Under temperature 21^0C – 27^0C and rainfall 50-100nm maize plants are growth well. Maize seed treated with fungal filtrates of *Aspergillus niger* and *Penicillium chrysogenum* effects on percentage of seed germination, morphological and anatomical structures of maize seedlings. The percentage of germination of maize seed treated with *Aspergillus niger* and *Penicillium chrysogenum* were 66.3% and 78.7% and the stomatal index of seed leaf surface treated with that filtrate was 44.16% and 30.46%. *Datura stramonium* is well known plants having antifungal effects. After applying Datura extract against fungal filtrates the anatomical structure as well as seed quality improve by inhibiting fungal activity. There are several phytochemical compounds which were responsible for antifungal activities of *Datura stramonium*.

Key-words: Anatomical, Aadaxial, Diabetic, Germination.

Introduction:

Maize is one of the important cereal crops and also an important food crops belong to *Poaceae* (*Graminae*) family (1) (2). Maize plants often height 2.5 m (8ft.) and sometime this height cross over more than 12 m (40ft.) in some natural strains. Maize seeds or corn seeds also called kernel and Maize plants known as caryopsis in plants environment (3) (4). Normally maize grows well in the varying temperature from 21°C to 27°C though it can be tolerate 35°C temperature as high temperature. 50-100 mm rainfall is requires for its growth. The crop is irrigated in lesser rainfall area (5) (6) (7). Through maize is an important cereal crop through all over the world, its production does not fulfill the need. According to the report, in 1988 75% fungi causes various types of seed disease like – rot, discoloration, necrosis and blight. Other than that few fungi created fungal disease like – kernel rot (*Aspergillus flavus),* Banded leaf and sheath leaf (*Rhizoctonia solani),* Anthracnose leaf blight (*Colletotrichum graminicala*), Black kernel rot (*Botryodiplodia theobromal).* The seedlings of maize seeds are susceptible for soil and seed borne disease because many seeds may disappear before or after germination. Maize plants also affected various types of fungal disease and the affected plants may have to be suffered from little growth, reduce ear size, may die as a result of poor root system (7) (8) (9). Fungi of the various genera *Aspergillus* sp., *Fusarium* sp., *Penicillium* sp. and *Rhizoctonia* sp. are known to produce mycotoxin. These mycotoxins have been slow down or degrade the seed quality. Culture filtrates of *Aspergillus* sp. culture filteres reduced seed germination and reduce spread in root-shoot and *A. niger* was filtrates as found as inhibitor. Seed borne disease plays important role in the agricultural product in this quality and quantity. Seed rot, seedling blight, culvularia leaf spot and bipolaris leaf spot are etiologically caused by *Aspergillus* sp., *Bipolaris maydis* and *Cuvularia lunata* respectively. Plant age, plant species and environmental factors affect these symptoms (10) (11) (12) (13) (14). The foliage attack and infection structures, developed by the fungi, may consider stomatal as their penetration route. Stomatal, the pores on leaf surface control the water vapor between plant and atmosphere and CO_2 exchange and it also plays important role in maintaining immunity by controlling pathogens in their entry level (15) (16) (17). The *Datura stramonium* uses antifungal activity against pathogenic fungi such as *Aspergillus niger* and *Penicillium chrysogenum.* The ethanol and ethyl acetate extract of *Datura stramonium* uses antifungal activities against *A. niger* and *P. chrysogenum.* The collected leaf samples were powdered with mixed grinder. The well diffusion method was used to determine antifungal activity (18) (19)

(20) (21). This study is for finding the effects of the filtrates of *Aspergillus niger* and *Penicillium chrysogenum* on leaf anatomy and seed germination of maize seedling and control the fungal disease by uses of *Datura stramonium* plant extract (22) (23).

Methods and Materials:

Seed sample collection:

Zea mays seeds were collected from the market on Jangipara, Hooghly, West Bengal, India.

Taxonomical position of *Zea mays*:-

Kingdom: plantae
Clade: Tracheophytes
Clade: Angiosperms
Clade: Monocots
Clade: commelinids
Order: poales
Family: poaceae
Genus: Zea
Species: *mays*

The Datura plant is chosen for the study of effects of plant extract on antifungal activity. The Datura plant was collected from Jangipara near our house garden.

Taxonomical position of *Datura stramonium*:-

Kingdom : Plantae
Clade : Tracheophytes
Clade : Angiosperms
Clade : Eudicots
Clade : Asterids
Order : Solanales
Family : Solanaceae
Subfamily : Solanoideae
Tribe : Datureae
Genus : Datura
Species : *stramonium.*

Plant extracts preparation:

At first distilled water was used to wash the collected seed samples, after soaking the excess amount of water was removed by filter papers, then incubated at 37°C for 4-5 days. The dried leaf was powdered with the help of an engraver or mix grinder.

Preparation of different plants extract:

Ethyl Acetate extract:

5gm of air dried powder of leaf extract was mixed with 25ml of chloroform in a conical flask and then kept on a rotary shaker for 10min. Then they bind with tissue paper and rubber band. Some holes were made so that air can pass through it and then take it at room temperature for 3-5 days for evaporates.

Ethanol extract:

5gm of air dried powder of leaf extract was mixed with 25ml of ethanol in a conical flask and then kept on a rotary shaker for 10 min. Then they bind with tissue paper and rubber band. Some holes were made so that air can pass through it and then take it at room temperature for 3-5 days for evaporates.

Preparation of extract concentration:

Four concentrations (25mg/ml, 50mg/ml, 150mg/ml, and 200mg/ml) were made from each of the two extracts (ethyl acetate, ethanol). In every case 2gm of extract was mixed with 15ml DMSO (Dimethyl sulfoxide) to prepare 200 mg/ml stock concentration. Then other three concentrations were made by adding extra DMSO with the stock in other test tube.

Viability test of the seeds:-

After collection of seeds their physical assessment was done and the defected seeds (cracked or broken) were rejected. The perfect one put into the water in a bowl. The seeds (*Zea mays)* with living embryo drowned and were used for this research work while the floated ones were discarded.

Fungal filtrates preparation:

The pure cultures of *Aspergillus niger* and *Penicillium chrysogenum* were collected from Microbiology Department, Rabindra Mahavidyalaya, Champadanga, Hooghly, West Bengal, India. Every fungus was grown in 250ml conical flask containing 100ml potato dextrose broth and incubated at 25 ± 2°C for 14 days. After incubation, the culture filtrates were filtered into sterilized with filter paper into conical flasks and then stored in a refrigerator at 4 ± 2°C.

Determination of effects of fungal filtrates on seed germination:

The two hundred (200) viable maize seeds were surface sterilized with 70% ethanol and then rinsed three sequent times with distilled water and sixty (60) seeds were soaked in every fungal filtrate for 12 hours. After soaking the seeds were removed and rinsed with distilled water separately. Each treatments was done in three replicates and control the experiment was treat and maintain with distilled water in the same number of replicates. The seedlings were determined after seven days of incubation, percentage of germination as well as length of plumule and length of radical. The vigor index was calculated using the following mathematical expression.

Vigor index (V. I) = {(length of plumule (cm) + length of radical (cm)} percentage of germination.

Determination of effects of fungal filtrates morphology:

The used soil in the experiment was bolstered to separate stones and large particles. During 1 hour they were sterilized at 121^0C. Four kingdom of sterilized soil was in 7×7 sterilized pots. These treated seeds were planted in pots and they were watered. The pots were watered in two times daily throughout the experimental period.

Isolation of leaf epidermal layers:

Leaf segment of an area of 1 cm square from every specimen was cut and immersed in concentrated solution of nitric acid for maceration. The upper and lower layers were separated with needle and forceps. Picking the samples from acid they were rinsed with distilled water.

Determination of frequency of stomatal complex types:

Different types of stomatal complex present in each specimen were also observed using 35 fields of view at x40 objectives as quadrants. The number of conducive cells per stomatal was noted and recorded to determine the frequency of the different stomatal complex types in each specimen.

Determination of stomatal density (SD) and stomatal Index (SI):-

The stomatal density was determined as number of stomatal per square millimeter.

The stomatal index was determined as follows: SI =SD/SD +E

Where, SD =numbers of stomatal per square millimeter, E = number of ordinary epidermal cells per square millimeter.

Determination of stomatal size (SS) and epidermal cell size (ECS):

The stomatal size of the plant was determined as product of length and breadth of ward cells using eye piece micrometer. Epidermal cell size was determined as product of length and breadth of a cell based on a sample size of 35.

Phytochemical analysis:

Phytochemical analysis of all the evaporated solvent extracts was conducted following the procedure of Indian Pharmacopoeia.

Test for alkaloids:

For testing of alkaloids first we take 200 mg plant material in 10 ml methanol, (filtered) and a 2ml filtrate + 1% HCl + steam mixed and then 1 ml filtrate + 6 drops of Mayer's reagents or Wagner's reagent added then the ceramic precipitate/brownish-red precipitate/ orange precipitate found that indicated the presence of respective alkaloids.

Test for tannins:

For testing of tannins 200mg plant material in 10 ml distilled water added (filtered), a 2ml filtrate + 2ml $FeCl_3$ mixed then blue-black precipitate that indicated found the presence of tannins.

Test for flavonoids:

For testing of flavonoids 200mg plant material in 10 ml ethanol (filtered), a 2ml filtrate + conc. HCl + magnesium mixed and then ribbon pink-tomato red color indicated the presence of flavonoids.

Test for steroids:

For testing of steroids we follow the Liebermann – Burchard reaction and there we take 200 mg plant material in 10 ml chloroform, (filtered), a 2 ml filtrate + 2 ml acetic anhydride + conc. H_2SO_4 was added then the founded Blue-green ring indicated the presence of steroids.

Test for phenols:

For testing of phenols first 1ml of each solvent extracts dissolved in alcohol or water was separately treated with a few ml of neutral ferric chloride solution. The change in color indicated the presence of phenols.

Microbiological assay:

Medium:

The potato dextrose agar (PDA) is used as base medium of antifungal activity and used for the preparation of inoculums.

Preparation of fungal inoculums:

The fungal inoculums were prepared by 0.1ml of cultures was transferred to the agar plates and incubated at 37°C for 4-5 hours.

Agar plate well diffusion method:

Agar plate well diffusion method is widely used to estimate the antifungal activity of plant. The plate count method was carried on potato dextrose agar (PDA) Plates. Petri plates were prepared by 20ml of potato dextrose agar and allowed to solidify for the use in susceptibility test against fungi. The Petri plates were dried and 0.1ml of fungal inoculums was poured and spread to allow dry. After the PDA agar well made on agar plates and poured into different concentration of extract into the well. The plates were incubated at 37°C for 1day. The zone of inhibition were observed and measured on agar plates. The agar plates were incubated at 4°C for 1-2 hours and were then incubated at 37°C. After 1-2 days of incubation the antifungal activity was evaluated by measuring the width of zone of inhibition of growth.

Table: Display the presence /absence of different Phytochemical in the leaf of *Datura stramonium.*

Photochemical	**Ethyl acetate**	**Ethanol**
Tannin	-	+
Alkaloid	+	-
Flavonoid	-	+
Phenolic	-	+
Steroid	+	-

Results:

We used both polar and non polar solvents for the extraction of ethyl acetate and ethanol from the leaves of *Datura stramonium.* The percentage of seed germination of *Zea mays* soaked in *P. chrysogenum* filtrate (78.7%) was significantly different from its counterparts seed that soaked in *A. niger*(66.03%).*A. Niger* and *P. chrysogenum* were found to be seed borne fungi. The pathogenic fungi *A. niger* and *A. flavus* are produced mycotoxin. These mycotoxin are found in different parts of the plants like the seed coat, endosperm. The fungal filtrates of *A. niger* inhibited the seed germination. The fungal cultures of *A. niger* reduced epidermal cell, stomatal size and stomatal density. Stomatal help in photosynthesis, moisture regulation and temperature control. The vigor indices of experimental plants were significantly different from each other at $P< 0.05$ as shown in Table 1.

TABLE :1 Percentage of germination and vigor indices of maize seeds				
	Seed Germination	**Radicle length**	**Plumule length**	**Vigor index**
Control	100.00	8.27	10.17	18.43
Aspergillus niger	67.30	6.00	6.26	7.37
Penicillium chrysogenum	80.12	7.27	8.80	11.22
Mean	82.47	7.00	9.00	15.00
Standard Error	5.00	0.59	0.65	1.57
P – value	0.00	0.003	0.002	0.00

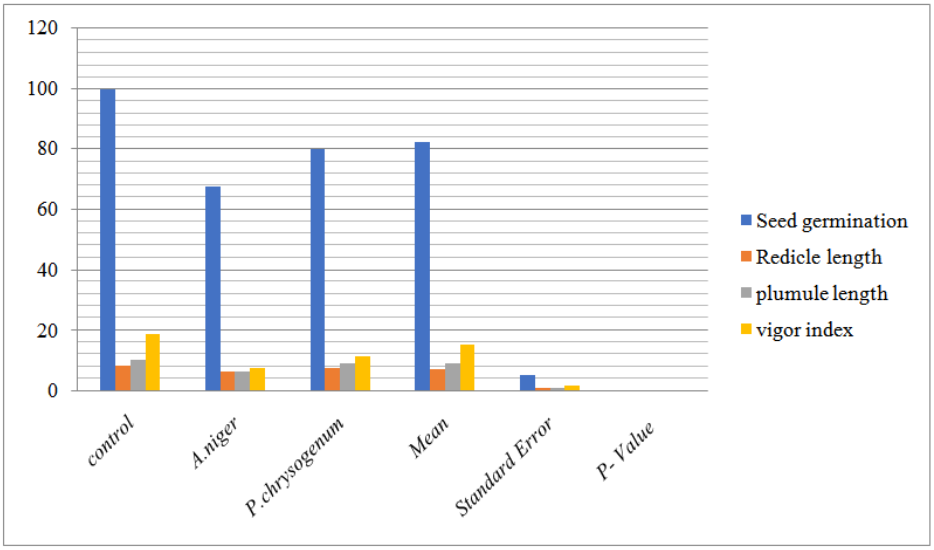

Fig 1: Percentage of germination and vigor indices of maize seeds.

TABLE :2 Morphological response of maize seedlings to fungal filtrates				
	Seed Germination	**Radicle length**	**Plumule length**	**Vigor index**
Control	100.00	8.27	10.17	18.43
Aspergillus niger	67.30	6.00	6.26	7.37
Penicillium chrysogenum	80.12	7.27	8.80	11.22
Mean	82.47	7.00	9.00	15.00
Standard Error	5.00	0.59	0.65	1.57
P – value	0.00	0.003	0.002	0.00

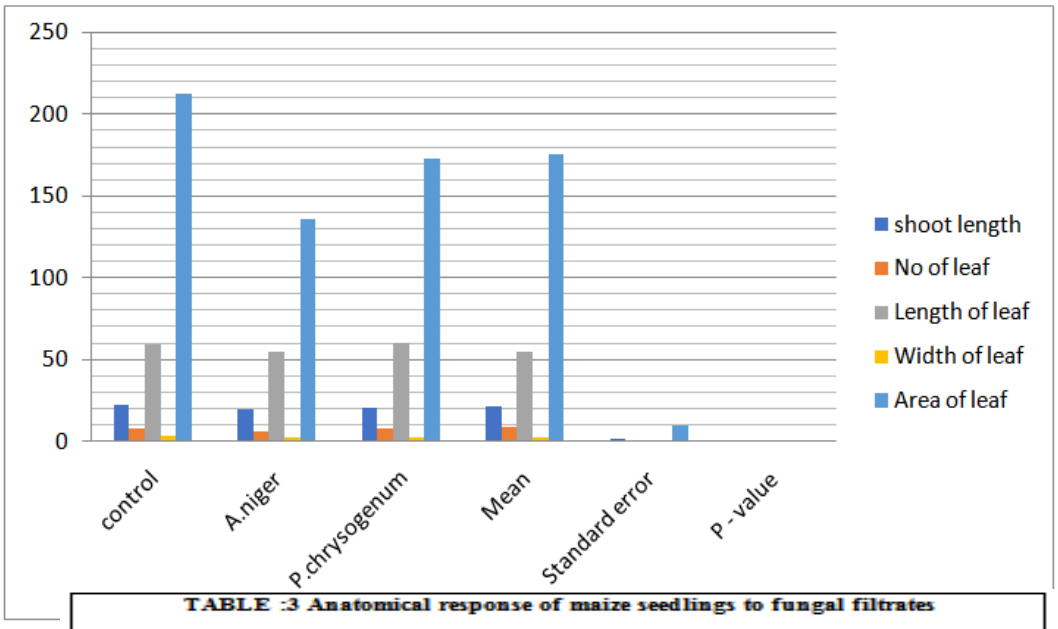

TABLE :3 Anatomical response of maize seedlings to fungal filtrates

	Stomatal Index (%)	**Stomatal Density (mm-2)**	**Stomatal size (micrometer)**	**Epidermal cell size**
Control	45.09	14.57	145.57	470.18
Aspergillus niger	40.41	15.00	70.35	495.40
Penicillium chrysogenum	36.87	10.41	65.68	235.55
Mean	40.40	10.33	90.52	400.23
Standard Error	0.35	1.27	5.00	19.45
P-value	0.005	0.004	0.003	0.00

Fig 2: Morphological response of maize seedlings to fungal filtrates.

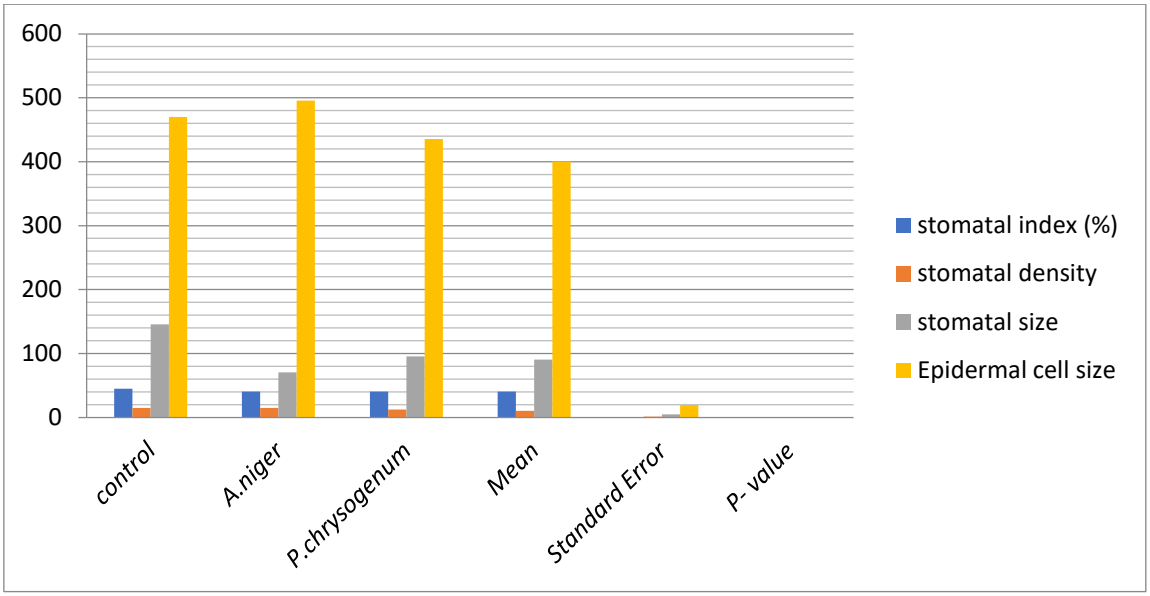

Fig 3: Anatomical response of maize seedlings to fungal filtrates.

TABLE 4: Antifungal activity of Ethyl acetate extract of leaf of *Datura stramonium.*

Concentration of Ethyl acetate (mg/ml)	Zone of inhibition	
	A. niger	***P. chrysogenum***
200	**18.0 ± 2.0**	**21.3 ± 1.0**
100	**16.5 ± 1.0**	**17.4 ±1.0**
50	**14.3 ± 1.0**	**14.0 ±2.0**
25	**13.0 ±2.0**	**12.4 ±1.0**

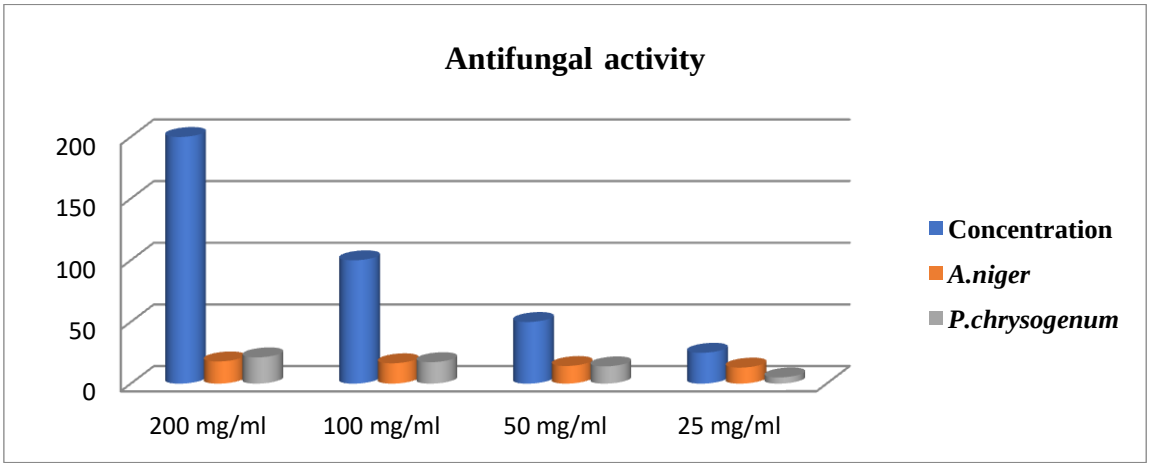

Fig 4: Antifungal activity of Ethyl acetate extract of leaf of *Datura stramonium.*

TABLE 5: Antifungal activity of Ethanol extract of leaf of *Datura stramonium.*		
Concentration of Ethanol (mg/ml)	**Zone of inhibition**	
	A. niger	***P. chrysogenum***
200	**16.0 ±2.0**	**16.5 ± 1.0**
100	**14.3 ±1.0**	**13.3 ±1.0**
50	**12.0 ±1.0**	**12.6 ±2.0**
25	**11.3 ±2.0**	**11.0 ±1.0**

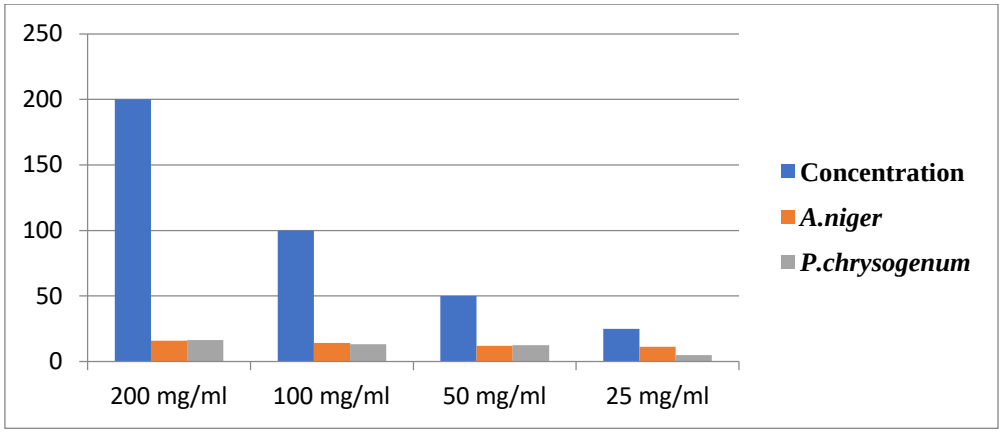

Fig 5: Antifungal activity of Ethanol extract of leaf of *Datura stramonium*.

Discussion:-

The morphological response of maize seedlings, to the fungal filtrates *A. niger* and *P. chrysogenum* did not affect any significant difference in Shoot length but inhibit the leaf area when compared with the control (Table – 2). The Anatomical response of maize seedlings to the fungal filtrates of *A. niger* reduced the epidermal cell size to 300.46 micrometer at leaf surface and higher than the epidermal cell size value gained from the seedlings treated with *P. chrysogenum* filtrate (235.55 micrometer). But both cultures filtrates *A. niger* and *P. chrysogenum* are significantly different from the value obtained from control (485.44 micrometer) as shown in Table 3. In this study the fungal filtrates affected both the stomatal density and stomatal index. *P. chrysogenum* are known to decreased percentage of seed germination. The fungus had shown poisonous effect on the maize seedlings. The culture filtrate *A. niger* and *P. chrysogenum* produced toxic metabolites which reduced the germination and seedling development. The two solvent based extract of ethyl acetate extract of 200mg/ml concentration shows highest antifungal activity against *P. chrysogenum* the zone of inhibition was 21.3 ± 1.0 mm and the lowest activity shows on *A. niger* at 25mg/ml zone of inhibition 13.0 ± 1.0 mm. The other solvent extract of ethanol extract of 200mg/ml concentration shows highest antifungal activity against *P. chrysogenum* the zone of inhibition was 16.5 ± 2.0 and the lowest activity shows on *A. niger* at 25mg/ml zone of inhibition 11.3 ± 0.0 (Table 4).

Future aspects:-

There has an important future aspect of research work with *Zea mays*. The *Zea mays* have a great beneficial and economical role in our human society. The three solvents based extract of maize seedlings that methanol based extract is higher sensitivity. The methanol extracts best in antimicrobial activity of maize seedlings. The stomatal on *Zea mays* play an important role in plant innate immunity by limiting pathogen entry into leaves. The medicinal purpose from *Zea mays* stigmas are used the most. The antioxidants effect is a very important feature of maize plants. The Flavonoid extracts using microwaves to harness them as natural food antioxidant and used in natural medicine. The other medicinal features of maize plants are – Antitumor and Antidiabetic effect. The polysaccharide extracted from maize plants, significantly inhibits tumor growth and prolonged survived. The maize polysaccharide reduced the body weight loss, reduced blood glucose level and insulin levels. The *Datura stramonium* plant work on antifungal activity, so it is future used in medicinally as well as antioxidants.

Conclusion:-

The fungal filtrates of both *A. niger* and *P. chrysogenum* not only affected percentage of seed germination, it also affected the morphology and anatomy of maize seedlings. It also affected the epidermal cells and stomata. The two solvent based extract of *Datura stramonium* extract based on ethyl acetate and ethanol shows highest antifungal activity on *P. chrysogenum* not only at 200mg/ml zone of inhibition and lowest activity shows on *A. niger* at 25mg/ml zone of inhibition.

References:-

1) Agrawal, M.K., Goyal, S.K., Varma, A.K. and Varma, A. 2014. Antibacterial and anticandidalScreening of certain traditionally used Indian medicinal plants against multi-drug resistant Human pathogens. International Journal of Science and Nature, 5: 423-432.
2) Bauer, A.W., Kirby, W.M., Sherris, J.C. and Turck, M. 1966. Antibiotic susceptibility testing by a Standardized single disk method. American Journal of Clinical Pathology, 45: 493-496.
3) Caster, L and Frederikson ;R. A (1980).Fusarium head Blight, occurance of effects on Sorghum yield and Grain characteristics in Texas. Journal of plant disease. 64: 1017-1017. In Jalander n V. and Gachande, B. D (2012). Effect of culture Filtrates of FusariumOxysporum on seed Germination AND seedling Growth of Pigeon Pea (Caianuscaian). Bioscience Discovery 02 (2) :185 – 188.
4) Debnath, M., Sultana, A. and Rashid, A. Q. M. B. (2012). Effect of Seed-borne Fungi on the Germinating Seeds And their Bio-control in Maize. J. Environ. Sci. &Natural Resources, 5(1): 117 – 120.
5) Aberg E, Akerberg E. 1958. Cool tolerance studies in maize Grown under northern conditions. Annals of the Royal Collegeof Sweden 24, 477-94.
6) Baker NR. 1994. Chilling stress and photosynthesis. In: FoyerCH, Mullineaux PM, eds. Causes of photo-oxidative stress and amelioration of defense systems in plants. Boca Raton :CRC Press. 127-54.
7) Baker NR, Bradbury M, Farage PK, Ireland CR, Long SP.1989. Measurements of the quantum yield of carbon assimilation and chlorophyll fluorescence for assessment of photosynthetic performance of crops in the field. Philosophical Transection of the Royal Society London B 323, 295-308.
8) Devash, Y., Okin, Y. and Henis, Y. (1980). Survival of Pseudomonas tomato in the Soil and Seeds of Tomato. Phytopathology 99:175-185.
9) Dilcher, D. L. (1974). Approaches to the Identification of Angiosperm Leaf Remains. Botanical Review, 40(1): 1-57.
10) Fazilatun, N., Zhari, I. and Nornisah, M. 2001. Phytochemicals from corn silk (Zeamays). Journal Of Tropical Medicinal Plants, 2: 189-192.
11) Gomez, K.A. and Gomez, A.A. 1984. Statistical Procedures for Agricultural Research (2nd edn.).John Wiley & sons, New York, USA.
12) Grosvenor, P.W., Supriono, A. and Gray, D.O. 1995. Medicinal plants from Riau province, Sumatra, Indonesia. Part 2: Antibacterial and antifungal activity. Journal of Ethno-Pharmacology, 45: 97-111.
13) Gopinath, A. and Shetty, H.S. (1988). Role of Volatile Metabolites Produced by Seed-borne growth of Fusariummoniliforme. Geobios.15: 10-1
14) Gudesblat, G. E., Torres, P. S. and Vojnov, A. A. (2009). Stomatal and Pathogens: Warefare at the Gate. Plant Signal Behav. : 4(12): 1114–1116.
15) Jones HG (2014) Plants and Microclimate, Ed 3. Cambridge University Press, New York
16) KenzoT, Yoneda R, Azani MA, Majid NM (2008) Changes in leaf waterUse after removal of leaf lower surface hairs on Mallotusmacrostachyus(Euphorbiaceae) in a tropical secondary forest in Malaysia. J For Res 13:137–142.
17) Lawson T, James W, Weyers J (1998) A surrogate measure of stomatalAperture. J Exp Bot 49: 1397–1403.
18) Parekh, J., D. Jadeja and S. Chanda., 2005. Efficacy of Aqueous and Methanol Extracts of Some Medicinal Plants for Potential Antimicrobial Activity. Turkey Journal of Biology, 29 :203 – 210.
19) Ali Rehman, Latif and Adam.,2002. Antimicrobial activity of leaf extract of Acalyphaindica. Journal of India Medicinal Plant, 1 :503 -508.
20) Sahu, D.K.; Khare, C.P; Patel, R. Eco friendly management of Early blight of tomato using botanical plant extracts, Journal of Industrial Pollution Control, 30., 2., 215-218, 2014.
21) Rastogi, R.P and B.N. Mehrotra. 2002. Glossary of Indian Medicinal Plants. National Institute of science communication, New Delhi, India.
22) Vincelli, P. (2008). Seed and Seedling Diseases of Corn: Plant Pathology Fact Sheet university of Kentucky-College of Agriculture PPFS-AG-C-02
23) Zeng, W., Melotto, M. and He, S. Y. (2010). Plant Stomata: A Checkpoint of Host Immunity and Pathogen Virulence. Curr. Opin.Biotechnol. 21(5): 599-603.

Home

UGC

Search

UGC-CARE List

You searched for "**0025-0422**". Total Journals : **1**

Search:

Sr.No.	Journal Title	Publisher	ISSN	E-ISSN	UGC-CARE coverage years	Details
1	Journal of the Maharaja Sayajirao University of Baroda	Maharaja Sayajirao University of Baroda	0025-0422	NA	from June-2019 to Present	View

Showing 1 to 1 of 1 entries

Previous 1 Next

Article

The Effect of Non-pecuniary-based Incentive Mechanisms to Reduce Water Usage at the Household Level and to Achieve Positive Environmental Outcomes

Global Business Review
1–17

DOI: 10.1177/0972150919857013
journals.sagepub.com/home/gbr

Jhumur Sengupta[1]

Abstract

There has been a sixfold increase in global water use over the twentieth century. The study answers the question, 'how can scarce water be saved in an efficient manner?' The current study uses the non-pecuniary incentive, 'neighbourhood comparison', as a tool for giving signals to water users. This study stresses on the negative linkage between water usage by households and 'neighbourhood comparison' in the Indian context. The field survey of this study considers household-level data related to water usage. In the present study, it is revealed that 'neighbourhood comparison' message causes significant reductions in water consumption per capita.

Keywords

Water resources, environmental outcome, water conservation, impact evaluation, randomized control trials

Introduction

The diamond-water paradox in economics is cited to explain the concept of scarcity. The famous economist Adam Smith used the comparison between water and diamonds to make a distinction between the two concepts, 'value in use' and 'value in exchange'. Although water is essential to sustain life, a low price is paid for getting enough water. Whereas, diamond has a price because it is scarce in nature. In today's context, the paradox has less relevance. Water is no more available in plenty. With reckless use of water and increasing demand due to growing human population, this resource is overexploited and it is becoming a scarce resource.

There has been a sixfold increase in global water use over the twentieth century. Availability of freshwater has been identified as one of the most critical issues by policymakers. According to an

[1] Dinabandhu Andrews College, Kolkata, West Bengal, India.

Corresponding author:
Jhumur Sengupta, Dinabandhu Andrews College, Raja S. C. Mallick Road, Kolkata, West Bengal 700084, India.
E-mail: jhumursengupta@yahoo.com

estimate by the United Nations, over two-thirds of the world population will reside in water-stressed regions by 2025. A series of factors such as population growth, urbanization and climate change are responsible for the water scarcity problem around the world (Ferraro & Price, 2013; UNESCO, 2012).

Water resources are unevenly distributed across different continents. Asia has 36 per cent of freshwater reserves with over 60 per cent of the world population. In Africa, 13 per cent of the world population has 11 per cent of freshwater reserves. Australia and Oceana have 5 per cent of freshwater reserves with 1 per cent of the world population. In North and Central America, 15 per cent of freshwater reserves are used by 8 per cent of the global population. South America has 26 per cent of freshwater reserves with 6 per cent of the world population. As industrialization and urbanization have taken place over the years, the use of water resources is likely to rise in the years to come. It has been estimated that water use per capita terms in India will increase to 167 litres per day in 2050 as compared to 88.9 litres per day per capita in 2000. In contrast, per capita water consumption in the USA will reduce by 2050 from its current level. In India, due to growth in population and overexploitation of water resources, it is gradually becoming a scarce resource.

Now, the question arises, 'how can scarce water be saved in an efficient manner?' Water conservation by way of reduction in water use can be done by adopting pecuniary or non-pecuniary approaches. The pecuniary approaches involve financial or tariff-related measures to motivate households in reducing water usage and thereby conserving water. Although traditionally, economists and policymakers have focused on pecuniary approaches involving price or tax increases as the primary force driving water demand, in the absence of assured and regular water supply to households, any increase in tariffs is socially and politically unacceptable. Advances in applied behavioural economics suggest that non-pecuniary approaches may have a useful role to play in reducing water consumption. Further, non-pecuniary information-based strategies are inexpensive and have been found to be effective in changing environmentally related behaviours such as electricity consumption (Alcott, 2011). Non-pecuniary, information-based environmental policy strategies have long been used to influence individual decision-making. Policymakers are increasingly using norm-based messages to influence individual decision-making (Ferraro & Miranda, 2013).

A number of studies (Alcott, 2011; Ayres, Raseman, & Shih, 2009) find that sending pro-social messages and social comparison which involves a comparison between own consumption and peer-group consumption can reduce water and energy consumption. Although reduction in water use has become a policy priority around the world, a study on behavioural interventions such as social comparison or sending pro-social messages for reducing water consumption remains relatively under researched. This is especially true of developing countries. A small number of studies estimate the effects of pro-social and social comparison messages on energy and water use (Ferraro & Miranda, 2013). Only three studies (Alcott, 2011; Ferraro & Price, 2013) have examined heterogeneous treatment responses on energy use.

Therefore, the current study uses the non-pecuniary incentive, 'neighbourhood comparison', as a tool for giving signals to the users. The present study examines the effectiveness of non-pecuniary strategies to manage residential water demand. The analysis is focused on residential water demand for two reasons. First, policymakers frequently rely upon non-pecuniary measures rather than market-based approaches to promote conservation efforts and manage water resources. Second, during the twentieth century, the availability of freshwater will be difficult. The United Nation's Environmental Programme estimates that by 2025 over two-thirds of the world's population will reside in regions considered water stressed. Similar concerns abound in the United States where a recent government survey suggests that at least 36 states anticipated some form of water shortage by 2013 (Ferraro & Price, 2013).

The scheme of the article is as follows. The second section discusses the literature review. Objectives are given in the third section. The theoretical framework is explained in the fourth section. The

methodology used in the study is discussed in the fifth section. The sixth section presents the analysis of the article. In the seventh section, discussions are presented. The eighth section concludes and managerial implications are discussed in the final section.

Literature Review

One new tool to reduce energy consumption is the use of social norms, particularly a 'strong' signal of social norms that shows a customer how her consumption compares to her peers (Ferraro & Miranda, 2013). These comparisons leverage motivations that have been extensively studied by psychologists and behavioural economists. Social comparisons have been widely used in the electricity sector by OPOWER. Alcott (2011) examines the impact of the non-price energy conservation programme run by a company called OPOWER. The study assesses the impact evaluation of average treatment effects (ATEs) in the treatment and control group. OPOWER has done 17 experiments in this study. The treatment is in the form of home energy reports (HERs) which consist of several-page letters with the social comparison module. This module consists of the 'descriptive norm' by comparing households to the mean and 20th percentile of its comparison group. The HERs also include the 'injunctive norm' to combat the 'boomerang effect', an effect which causes households that used less than the norm to use more energy when social comparison is made. Under the 'injunctive norm', households are labelled as 'great' if they use less than 20th percentile of their neighbour with whom the comparison is made, 'below average' if they use more than the mean and 'good' if they are in-between. The year of study by OPOWER is 2009. The monthly, bimonthly and quarterly HERs were sent to the treatment group and a control group was made to whom the HERs were not sent. The results of the study show that ATEs are clustered around -2.7 per cent and -2.3 per cent for monthly and quarterly treatment, respectively. In 17 experiments done by OPOWER, estimated ATEs range from -1.37 per cent in experiment three to -3.32 per cent in experiment eight.

Ferraro and Miranda (2013) studied heterogeneity in a large-scale field experiment done in 2007 along with water utility in metropolitan Atlanta, GA, and the USA. Three types of treatments were sent: (a) a tip sheet which consists of information about reducing water consumption, (b) a weak social norm message which consists of a tip sheet and a personalized letter promoting pro-social behaviour and (c) a tip sheet, a personalized letter promoting pro-social behaviour and a social comparison of households' water consumption with median county consumption. The third treatment is called a strong social norm message and the first treatment is called pure information message. The study finds little evidence of heterogeneous responses to treatment one and treatment two and strong evidence of heterogeneous responses to the strong social norm message. The study proposes testing of a null hypothesis which is relevant for treatment one. The null hypothesis states that the conditional ATE is zero (zero CATE). The other null hypothesis corresponding to treatment two and three is that conditional ATE is constant (constant CATE). To test the null hypotheses, the study runs ordinary least square regression with treated and control groups controlling for covariates. The results of the study show that the null hypothesis for some subgroups is rejected for treatment one. For treatment two, the null hypothesis is never rejected. For treatment three, the null hypothesis of constant CATE is always rejected. Therefore, it can be inferred from the study that the effect of the social norm message (treatment three) on subpopulation is always strong enough to reject the null hypothesis of constant CATE.

Ayres et al. (2009) conducted two field experiments on 85,000 consumers of Sacramento Municipal Utility District (SMUD) and Puget Sound Energy (PSE). Their study covers the period from April 2008 to April 2009. The samples in the treatment group received 'HERs'. This report consists of four components. These are (a) current period comparison between neighbours, (b) 12-month neighbour comparison, (c) personal historical comparison, it compares household's use of energy in the current

month with the energy use in the same month of the previous year, and (d) targeted energy efficiency advice. Data on energy consumption were provided by SMUD. The study examines the impact of treatment on the log of monthly average energy consumption by using regression analysis. The study finds that energy use by treatment group lowers the energy use significantly relative to the control group after the 'HER' was mailed. After controlling the hose characteristics, the result shows that there is a significant drop in the energy consumption of the treatment group relative to the control group. The study also estimates the impact of 'HER' on energy conservation and money saved by the households. The results show that reduction is by 2.35 per cent for monthly recipients and a reduction in consumption of energy by 211 kWH per year per household and it would save US$31 per year per household. For quarterly recipients, that is, households who received 'HERs' on a quarterly basis, it was estimated that energy consumption would decrease by 130 kWH per year per household for a saving of US$13. The PSE data were also analysed in the same manner as the SMUD data and it shows that the treatment households reduced energy usage relative to the control group after 'HERs' were sent to the treatment group.

The role of ideology on energy conservation has been examined with the help of a randomized field experiment undertaken in California Utility district. In the field experiment, households were sent HERs which consist of information on own electricity consumption on a monthly basis relative to neighbour's usage. The article shows that energy conservation depends on an individual's ideology. Using regression, the study finds that liberals who purchase electricity from renewable sources, who donate to environmental groups and who live in a census block group receive an HER which leads to a reduction in electricity use by 3.6 per cent. On the other hand, for conservatives who do not donate to environmental causes and who live in the census block group, receiving an HER leads to a reduction in electricity usage by 1.1 per cent. The result of the study shows that a conservative will decrease mean daily kWH by 1.7 per cent following the treatment and a liberal will decrease consumption of electricity by 2.4 per cent following the HERs that were sent. The analysis suggests that the effect of treatment on home energy consumption is more in liberal communities.

Shahbaz, Islam, and Butt (2016) show the relationship between financial development and energy consumption. Using data on economic growth, on Pakistan, over 1972–2011, the article finds both way causality between financial development and energy consumption and between modern sector growth and energy consumption. It shows that energy consumption causes agriculture growth. The findings give valuable insights for policymakers in designing appropriate energy policies for Pakistan.

Sualihu and Rahman (2014) argue that electricity companies are typically businesses with significant credit sales. But, payment of bills on time by customers has been very poor especially in the case of the developing world. The study aims to identify a set of organizational and behavioural factors that influence bill payment behaviour of customers of the Electricity Company of Ghana. The study is based on a survey of households in the Greater Accra Region of Ghana. The results of the study suggest that electricity utilities must reduce the transaction time of customers at the bill collection centres and improve the quality of service and customer satisfaction to reduce customer bill payment period.

Objectives

On the basis of the literature review presented above, this study seeks to examine the following objectives. The first objective is to show the negative linkage between water usage by household and 'neighbourhood comparison' in the Indian context. The second objective is to show the effectiveness of non-pecuniary incentives like peer group comparison in reducing water usage by households.

Theoretical Framework

The study develops a conceptual framework to show that pro-social messages may influence household water consumption.

The present study is based on 'neighbourhood comparison' among households. It consists of social comparison module which compares households to the mean water user. The neighbourhood comparisons are influenced by academic work showing that providing social norm information induces people to conserve energy (Schultz, Nolan, Cialdini, Goldstein, & Griskevicius, 2007). Recent research on psychology suggests that peer comparisons can be a potential alternative tool for changing household behaviour of energy consumption. A series of field experiments have been conducted to demonstrate that low cost persuasion strategies can change the behavior of an individual by making the individual aware of the actions of others. Policymakers can avoid wasting money by sending information-based pro-social messages and by making neighbourhood comparisons.

Methodology

The field survey of this study considers household-level data related to water usage in summer, winter, average water usage and covariates which may have a considerable effect on household water usage. In this study, a randomized experimental design has been undertaken to show the effectiveness of non-pecuniary incentives like peer-group comparison in reducing water usage by households. The rationale for using randomized experimental design which is based on peer-group comparison is as follows. Social psychologists emphasize that attention of households to reduce water use can be drawn most effectively through social comparisons. Randomized experimental design takes the form of neighbourhood comparison which compares the household's water use to the mean water user. A growing body of work in social psychology examines the use of social-norm information-based campaigns to promote environmental conservation.

A field survey of 480 households (respondents) was randomly chosen from the residential area of Kasba under the Kolkata Municipal Corporation, West Bengal, India. A random sampling method has been applied to choose the respondents for the survey. While selecting the respondents randomly, a function $f(x) = 1/n$ (where x can take n possible values, $X_1, X_2, \ldots, X_n$) has been assigned to each respondent. Here X_i represents choosing of the ith individual. A field survey questionnaire has been used to undertake the survey.

The survey was undertaken in two different time periods with a time gap. In the first stage (which was conducted in March 2016), 480 respondents were interviewed and a strong social norm message about the mean usage of water resources was given to 50 per cent, that is, 240 of the total respondents. The selection of 240 respondents out of 480 was completely random. This 240 sample unit constitutes an experimental group in which the treatment in the form of peer-group comparison was given. The rest 50 per cent of the respondents was not given any strong social norm message in the form of peer-group comparison. They were given only general information on the availability of water resources and depletion of this resource because of excessive usage and pollution. This subgroup of respondents constitutes the control group for the experimental design. First, a mail containing general information on the availability of water was sent to all the 480 respondents and subsequently, a treatment mail was sent out to each of the 240 respondents chosen randomly as the treatment group on the same day. The treatment mails were sent to the treatment group via registered speed post in envelopes. This ensures that the

control group was not exposed to the information that the treatment group was exposed to. After a time gap of one year (March 2017), the same set of 480 respondents were again approached and usage of water by each of them was re-estimated. The layout for randomized design has been furnished in the Appendix section.

The study examines the impact of treatment in the form of neighbourhood comparison with 240 households in the treatment group. Out of 480 households, 240 households constitute the treatment group which receives 'neighbourhood comparison' treatment. The control group received no 'neighbourhood comparison' during the experiment.

'Neighbourhood comparison' (Figure 1) consists of the social comparison module, which compares household to the mean water user. In order to remove 'boomerang effect' (an effect which causes households that used less water previously than the mean to use more as a result of neighbourhood comparison), the present study includes injunctive norms. Under injunctive norms, households are labelled 'great' if they use less than the mean water user and 'below average' if they use more water than the mean.

To estimate the impact of 'neighbourhood comparison' on household's water use, the present study uses variables that are important modifiers of treatment, 'neighbourhood comparison'. In line with the studies by Mansur and Olmstead (2011), Davis (2010), and Ferraro and Miranda (2013), the present study uses the house's fair market value, ownership status and age of house as important determinants of water usage. The study by Mansur and Olmstead (2011) shows that high-income households with high fair market values of houses are less price sensitive to changes in water prices. For them, the non-pecuniary approach such as neighbourhood comparison may be more effective in reducing water usage. The present study uses fair market value of house acts as an important covariate. Davis (2010) argues that the owner occupant households possess greater social capital and therefore, they may have greater social connections to neighbours. Hence, they may be more responsive to the 'neighbourhood comparison' module. In the same manner, the present study uses the status of households (owner occupants or renters) as one of the covariates along with the 'neighbourhood comparison' message which may have an impact on the water use pattern of households. Another important covariate for the present study is the age of the house in which the household resides. As per the study done by Ferraro and Miranda (2013), older homes have, for example, older-fashioned toilets which are more cost effective to replace and water conservation goals may be achieved more easily.

While considering the impact of treatment on the use of water per capita, the following linear equation is considered. The linear regression equation is:

$$\text{DiffwaterPC} = a_0 + a_1\ \text{TREATDUM} + a_2\ \text{Ownership status} + a_3\ \text{Age of house} + a_4\ \text{Fair market value} + \epsilon \quad (1)$$

where DiffwaterPC is defined as the modulus difference in water use per capita between before the treatment period and after the treatment period. TREATDUM is a dummy variable which takes the value 1 if 'neighbourhood comparison' treatment is given to the household and 0 if the household does not get any treatment. Ownership status is a binary variable which takes the value 1 if the household resides in his or her own house and 2 if the household resides in a rented house. Age of house and fair market value represent the age of the house in which the household resides and fair market value of the house. The variable fair market value is a proxy for the standard of living of households. A high fair market value of the house corresponds to a rich household and fair market value at the lower side corresponds to a poor household. The dependent variable DiffwaterPC is measured by three different categories—difference in water use per capita on average, difference in water use per capita during the summer season (from March to October) and difference in water use per capita during the winter season (from November to

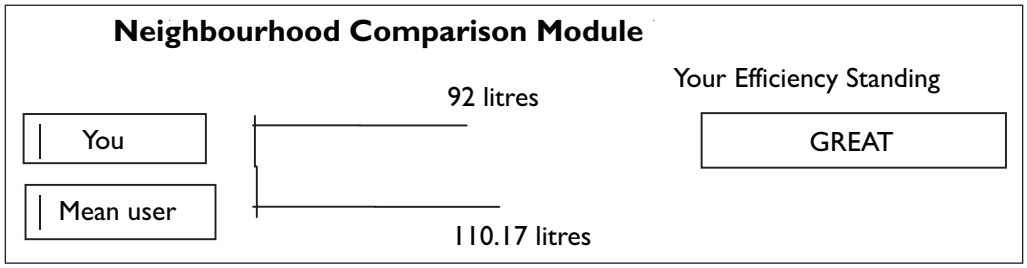

Figure 1. Neighbourhood Comparison Module

Source: Alcott (2011).

January). The primary regression of DiffwaterPC is run on TREATDUM. Afterward, in addition to TREATDUM, the control variables are included one by one. The relationship between DiffwaterPC and TREATDUM is assumed to be positive.

In the next specification of the regression equation, the impact of treatment on water use per capita is estimated. WaterusePC by households has been measured for three different time periods in a year—average water use, water use during summer and water use during winter. This procedure of estimation of water use per capita has been used for each of the rich households, poor households separately and then by combining both types of households together. The relationship between waterusePC and TREATDUM is assumed to be negative.

$$\text{WaterusePC} = a_0 + a_1\text{TREATDUM} + \epsilon \tag{2}$$

Analysis

Table 1 presents descriptive statistics by treatment and control group for pre-treatment data. Columns 1 and 2 of Table 1 display mean water use by households assigned to treatment 'neighbourhood comparison' and mean water use by the control group, respectively. Column 3 shows the *F*-statistics and column 4 shows the *p*-values. Here, we test the null hypothesis that mean values of treatment and control groups are equal. The result shows that with the exception of age of house, there are no statistically significant differences in pre-treatment variables. The result supports the fact that randomization has been effective.

Table 2 presents descriptive statistics by treatment and control group for post-treatment water use. Columns 1 and 2 of Table 2 display mean values for treatment and control groups. Columns 3 and 4 display differences with respect to the control group and the statistical significance of these differences, respectively. It is observed from the table that mean differences are statistically significant for all types of water use in per capita terms, that is, for average water use per capita, summer water use per capita and winter water use per capita.

Table 1. Descriptive Statistics of Pre-treatment Data

	Social Comparison	Control	*F*-test	*p*-Value
Average water consumption	92.87951119	90.81010582	0.216	0.642
Summer water consumption	93.99625423	92.01835979	0.172	0.678

(Table 1 Continued)

(Table 1 Continued)

	Social Comparison	Control	*F*-test	*p*-Value
Winter water consumption	81.94421199	78.50518519	0.666	0.415
Age of house	4.970833333	9.604166667	(361.728)**	0.001
Ownership status	1.216666667	1.345833333	(8.124)*	0.062
House's fair market value	2812124.167	3988680.417	(4.033)*	0.055

Source: The author.

Note: ** and * represent that *F* values are significant at 1% and 10% levels, respectively.

Table 2. Post-treatment Water Use Descriptive Statistics

Variables	Treatment	Control	Difference	*t*-Test	*p*-Value
Average water use per capita	81.92	91.56	–9.64	(–2.36)*	0.0092
Summer water use per capita	68.94	77.85	–8.91	(–2.48)*	0.0136
Winter water use per capita	68.94	77.85	–8.91	(–2.48)*	0.0068

Source: The author.

Note: *Represents that *t* values are significant at the 1% level.

Table 3.1 represents the estimation of 'neighbourhood comparison' treatment on the difference in average water use per capita. The estimation results of Equation (1) are presented in model 4 of Table 3.1. In the primary regression model (model 1), TREATDUM is the only independent variable affecting DiffwaterusePC. Afterward, the number of independent variables has been increased gradually along with TREATDUM. Models 2–4 of Table 3.1 measure the extent of difference in water usage per capita between the pre-treatment and post-treatment period of two input variables (TREATDUM, ownership status), three input variables (TREATDUM, ownership status and age of house) and four input variables (TREATDUM, ownership status, age of house and fair market value), respectively. Table 3.1 shows that the coefficients of TREATDUM are of positive signs as expected and become significant variables, the level of significance being at the 1 per cent level in all models. The control variable, age of house, has an effect on DiffwaterusePC. It has been observed that older homes have older toilets, which are more cost effective to replace and therefore DiffwaterusePC would be higher with the increase in age of house. The second control variable, ownership status, also has an effect on DiffwaterusePC. Owner occupants have greater incentives to invest in cost-saving water conservation innovations. According to the study by Davis, as ownership status changes from 1 to 2 (1 for owner occupants and 2 for renters), the DiffwaterusePC falls. The other control variable in the present study is the fair market value of the house. Mansur and Olmstead (2012) find that households having houses whose market values are on the higher side are generally rich households. The effect of non-pecuniary approaches such as neighbourhood comparison on rich households is high as compared to poor households whose house's fair market values are generally low. Therefore, the effect of the fair market value of the house on DiffwaterusePC should be positive. As per the results in Table 3.1, the coefficients of control variables do not always show correct signs in the models. However, the findings suggest that TREATDUM is an important determinant for DiffwaterusePC outcome. As regards adjusted R^2 is concerned, the values of adjusted R^2 in models 1–4 are low and lie between 0.2512 and 0.2873. The results suggest that treatment in the form of

'neighbourhood comparison' matters for an increase in the difference in water use per capita in a significant manner. In a similar way, the effect of treatment on the difference in summer water use per capita and the difference in winter water use per capita are presented in Table 3.2 and Table 3.3, respectively. The results presented in these two tables are very much similar to the findings of the effect of treatment on the difference in average water use per capita (Table 3.1).

Table 3.1. Effect of Treatment on Difference in Average Water Use Per Capita

RHS Variables	1	2	3	4
TREATDUM	17.85193	16.6484	15.75817	16.46037
	(12.72)***	(8.95)***	(8.58)**	(8.92)***
p-Value	0	0	0	0
Age of house		–0.2597539	–0.2629967	–0.1993984
		(–0.99)	(–1.02)	(–0.77)
p-Value		0.325	0.310	0.44
Ownership status			–6.775843	–6.197246
			(–4.38)***	(–3.99)***
p-Value			0	0
Fair market value				2.83E-07
				(2.61)**
p-Value				0.009
Adjusted R^2	0.2512	0.2543	0.2786	0.2873
No. of observations	480	480	480	480

Source: The author.

Note: *** and ** represent that t values are significant at 1% and 5% level respectively.

Table 3.2. Effect of Treatment on Difference in Summer Water Use Per Capita

RHS Variables	1	2	3	4
TREATDUM	4.687328	4.789891	4.460864	4.572712
	(4.25)***	(3.27)***	(3.04)***	(3.08)***
p-Value	0	0.001	0.003	0.002
Age of house		0.0221358	0.0209373	0.0310674
		(0.11)	(0.1)	(0.15)
p-Value		0.915	0.919	0.881
Ownership status			–2.504313	–2.412152
			(–2.02)*	(–1.93)
p-Value			0.044	0.054

(Table 3.2 Continued)

(Table 3.2 Continued)

RHS Variables	1	2	3	4
Fair market value				4.51E-08
				(0.52)
p-Value				0.606
Adjusted R^2	0.0344	0.0364	0.0446	0.0371
No. of observations	480	480	480	480

Source: The author.

Note: *** and * represent that t values are significant at 1% and 10% levels respectively.

Table 3.3. Effect of Treatment on Difference in Winter Water Use Per Capita

RHS Variables	1	2	3	4
TREATDUM	6.836376	5.556974	5.253273	5.406465
	(6.61)***	(4.06)***	(3.82)***	(3.89)***
p-Value	0	0	0	0
Age of house		–0.2761299	–0.2772362	–0.2633617
		(–1.42)	(–1.43)	(–1.35)
p-Value		0.156	0.153	0.176
Ownership status			–2.311545	–2.18532
			(–2)*	(–1.87)
p-Value			0.047	0.063
Fair market value				6.17E-08
				(0.76)
p-Value				0.450
Adjusted R^2	0.0817	0.0837	0.0894	0.0886
No. of observations	480	480	480	480

Source: The author.

Note: *** and * represent that t values are significant at 1 % and 10% levels respectively.

The results of the estimation of water use per capita (WaterusePC) have been displayed in Table 4 for each of the rich households, poor households and for both types of households together. The results of Table 4 are as follows. First, for rich households, all coefficients of TREATDUM related to all regressions are significant and are of expected signs. For poor households, the coefficients of TREATDUM show correct negative signs for all types of water use, such as, average water use, summer water use and winter water use but it loses statistical significance in some cases. The result of estimation of WaterusePC for both rich and poor households taken together also corroborates the previous findings of Table 4. Though in all cases adjusted R^2 possesses low values, these results seem to suggest that 'neighbourhood

comparison' treatment matters for lower water use per capita for all types of households. In order to establish the robustness of the results obtained in Table 4, the control variables, namely, age of house, ownership status, house fair market value, number of family members, education level in terms of years of schooling and race, have been considered along with the treatment of the dummy variable, TREATDUM. It is evident from Tables 5–7 that after inclusion of the abovementioned control variables, the coefficient of TREATDUM does not lose the level of statistical significance and it shows correct negative signs in each case. Moreover, the values of adjusted R^2 have been improved as the explanatory power of regression has been increased due to the inclusion of control variables. This study considers the education level of respondents and race as control variables which act as a proxy for environmental preference. Ferraro and Miranda (2013) argue that environmental preference varies with education level and race. Here, we measure the education level in terms of years of schooling. For measuring race, this study considers three categories—general, scheduled caste and scheduled tribe. The variable race takes the value 1 if the respondent belongs to the general category, 2 if the respondent belongs to the scheduled caste category and 3 if the respondent belongs to the scheduled tribe category. It is assumed that people belonging to scheduled caste and scheduled tribe categories are generally poor and the majority of them reside in a rented house. Hence, they have less incentive to reduce water consumption. The number of family members acts as another control variable as water use per capita generally rises as the number of family members increases. The rationale behind including other control variables has already been explained above in the present article.

Table 4. Effect of Treatment on Water Use Per Capita

	RHS Variables	For Rich Households	For Poor Households	For Rich and Poor Household Taken Together
Average water use per capita	TREATDUM	–41.64667	–7.083968	–24.36532
		(–13.58)***	(–2.28)*	(–6.84)***
	p-Value	0	0	0
	Adj. R^2	0.4342	0.0173	0.0872
	No. of observations	240	240	480
Summer water use per capita	TREATDUM	–20.45778	–3.41418	–11.93598
		(–6.54)***	(–0.98)	(–2.94)***
	p-Value	0	0.326	0
	Adj. R^2	0.1489	0.0041	0.0158
	No. of observations	240	240	480
Winter water use per capita	TREATDUM	–22.55222	–3.128624	–12.84042
		(–8.29)***	(–0.95)	(–3.55)***
	p-Value	0	0.344	0
	Adj. R^2	0.224	0.0038	0.0236
	No. of observations	240	240	480

Source: The author.

Note: *** and * represent that t values are significant at 1% and 10% levels.

Table 5. Effect of Treatment on Average Water Use Per Capita

	RHS Variables	For Rich Households	For Poor Households	For Rich and Poor Households Taken Together
Average water use per capita	TREATDUM	–41.6467	–7.0839	–24.3653
		(–19.86)***	(–3.57)***	(–13.28)***
	p-Value	0	0	0
	Education level	1.04	1.1628	1.2037
		(3.05)***	(3.45)***	(5.12)***
	p-Value	0.003	0.001	0
	Race	5.5987	–1.6069	2.3134
		(3.86)***	(–1.14)	(1.87)
	p-Value	0	0.256	0.062
	Age of house	2.3842	2.5463	–0.3342
		(5.03)***	(4.95)***	–0.80
	p-Value	0	0	0.423
	No. of family members	10.94	10.6838	11.8706
		(9.5)***	(15.57)***	(16.16)***
	p-Value	0	0	0
	Ownership status	–9.6642	–6.9349	1.9685
		(–1.13)	(–3.27)***	(0.79)
	p-Value	0.260	0.001	0.431
	House fair market value	2.22×10^{-6}	–0.0001	6.03×10^{-6}
		(3.85)***	(–1.39)	(15.16)***
	p-Value	0	0.164	0
	Adjusted R^2	0.7354	0.5973	0.7580
	No. of observations	240	240	480

Source: The author.

Note: *** represents that t values are significant at 1% level.

Table 6. Effect of Treatment on Summer Water Use Per Capita

	RHS Variables	For Rich Households	For Poor Households	For Rich and Poor Households Taken Together
	TREATDUM	–20.4577	–3.4142	–11.9359
		(–10.06)***	(–1.57)	(–6.92)***
	p-Value	0	0.117	0
	Education level	0.1886	1.5061	2.0861
		(0.57)	(4.08)***	(9.43)***
	p-Value	0.570	0	0
	Race	5.0109	4.0069	1.7588

(Table 6 Continued)

(Table 6 Continued)

	RHS Variables	For Rich Households	For Poor Households	For Rich and Poor Households Taken Together
Summer water use per capita		(3.56)***	(2.60)***	(1.51)
	p-Value	0	0.01	0.130
	Age of house	–0.1061	3.3605	1.9357
		(–0.23)	(5.97)***	(4.94)***
	p-Value	0.818	0	0
	No. of family members	15.2872	11.7718	13.6156
		(13.7)***	(15.57)***	(19.72)***
	p-Value	0	0	0
	Ownership status	–3.7926	–8.6330	2.9418
		(–0.46)	(–3.72)***	(1.25)
	p-Value	0.468	0	0.211
	House fair market value	3.19×10^{-6}	–0.0001	6.49×10^{-6}
		(5.70)***	(–1.90)	(17.37)***
	p-Value	0	0.058	0
	Adjusted R^2	0.6402	0.6074	0.8218
	No. of observations	240	240	480

Source: The author.

Note: *** represents that t values are significant at 1% level.

Table 7. Effect of Treatment on Winter Water Use Per Capita

	RHS Variable	For Rich Households	For Poor Households	For Rich and Poor Households Taking Together
Winter water use per capita	TREATDUM	–22.5522	–3.1286	–12.8404
		(–12.15)***	(–1.44)	(–7.86)***
	p-Value	0	0.151	0
	Education level	0.2595	1.6100	1.8757
		(0.86)	(4.36)***	(8.96)***
	p-Value	0.392	0	0
	Race	4.1128	3.78	1.1774
		(3.20)***	(2.45)***	(1.07)
	p-Value	0.002	0.02	0.285
	Age of house	–0.6025	3.5112	2.1548
		(–1.44)	(6.24)***	(5.80)***

(Table 7 Continued)

(Table 7 Continued)

RHS Variable	For Rich Households	For Poor Households	For Rich and Poor Households Taking Together
p-Value	0.152	0	0
No. of family members	12.9019	11.7583	11.7583
	(12.67)***	(17.9)***	(17.99)***
p-Value	0	0	0
Ownership status	7.0375	–8.7016	4.4584
	(0.93)	(–3.750***	(2)
p-Value	0.354	0	0.046
House of fair market value	3.02×10^{-6}	–0.0001	5.81×10^{-6}
	(5.91)***	(–2.37)**	(16.42)***
p-Value	0	0.018	0
Adjusted R^2	0.6375	0.5666	0.8014
No. of observations	240	240	480

Source: The author.

Note: *** and ** represent that t values are significant at 1% and 5% levels respectively.

Discussion

In the present study, it is revealed that the 'neighbourhood comparison' message causes significant reductions in water consumption per capita. The results are in line with the studies done by Ayres et al. (2009), Alcott (2011), Costa and Khan (2010) and Ferraro and Miranda (2013). The present experimental study shows that the effect of social comparison treatment is strong on households' water consumption. The experiment also reveals how different demographics were affected by the treatment. In the experiment, households in the treatment group with higher house values saved more water than households with lower fair market values of houses. Thus, the 'neighbourhood comparison' message had a strong and significant effect on water use and high-income households are the most responsive to the message.

Conclusion

Economists have only recently started to explore the effect of non-pecuniary strategies, such as appeals to pro-social behaviour or the use of social comparisons, as a means to influence individual decision-making and promote pro-social behaviours. This study seeks to further our understanding of such strategies by exploring whether they influence household-level consumption decisions.

The objective of this article is to show the negative linkage between water usage by household and 'neighbourhood comparison' in the Indian context and to show the effectiveness of non-pecuniary incentives like peer-group comparison in reducing water usage by households. Accordingly, this research sought to assess the use of the non-pecuniary incentive, 'neighbourhood comparison', as a tool for giving a signal to

water users in lowering water consumption. This study is a departure from traditional energy-efficiency programmes as it is a non-price intervention study based on behavioural science. In the case of water conservation programmes based on pecuniary incentives, the average responses of households are slow and high-income households are least responsive. Thus, the present work is a remarkable departure from the price mechanism and it uses randomized control trials. The study suggests that behavioural intervention can supplement price-based tools to tackle the issue of water conservation at the household level.

Managerial Implications

This article examines the effect of a social comparison–based programme on households' water usage. The study provides information on (a) current water usage, (b) comparison to the previous usage and (c) comparison to similar nearby households. This article contributes to a substantial body of research in the water sector and in social comparison programmes in water resource management by households.

Acknowledgement

The author is grateful to anonymous referees of the journal for their extremely useful suggestions to improve the quality of the article. The author would like to thank the people of the residential area of Kasba under Kolkata Municipal Corporation, West Bengal, India, who have participated in the survey and were interviewed.

Declaration of Conflicting Interests

The author declared no potential conflicts of interest with respect to the research, authorship and/or publication of this article.

Funding

The author received no financial support for the research, authorship and/or publication of this article.

Appendix A

Randomized Experimental Design

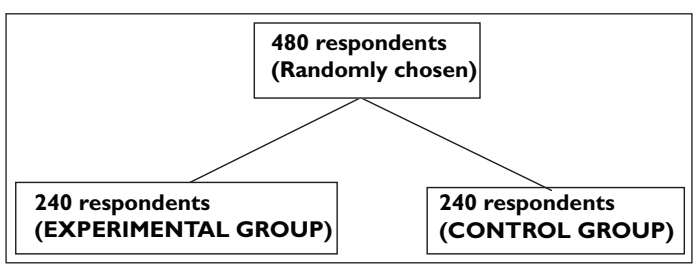

Survey Questionnaire on Water Usage Pattern at the Household Level

Water is life because plants and animals cannot survive without water. A total of 70 per cent of the Earth's surface is covered with water. Freshwater availability is only 35 cubic kilometres and only 40 per cent of this can be used by human beings. But due to the growing human population, severe neglect and over-exploitation of this resource, water is becoming a scarce commodity.

In the above context, I would like to undertake a study on *Effect of Non-pecuniary based Incentive Mechanism to Reduce Water usage at Household Level and to Achieve Positive Environmental Outcome*.

General Information on Availability of Water Resources and Recent Trends

The following table gives you a comprehensive overview of the existing water resources available in India and the recent trends in a very brief manner.

Information About Existing Water Resources Available in India

Items	Quantity (Cubic km)
Annual precipitation (including snow fall)	4,000
Average annual availability	1,869
Per capita water availability (2001) in cubic metres	1,820
Estimated utilizable water resources	1,122
a. Surface-water resources	690
b. Ground-water resources	431
Recent trends	• Water pollution is on the rise. • 70% of the surface-water resources and growing percentages of ground-water reserves are contaminated by toxic organic and inorganic pollutants. • Depletion and contamination of ground-water level.

Source: Report on Water Resources, 2011, Central Water Commission, India.

The purpose of this survey is to learn your water usage pattern in general. Your response will be kept confidential and used only for academic purpose.

1. Name of the respondent: ……
2. Gender of the respondent: ……..
3. Occupation of the respondent:
4. Family's water consumption per day (in litres or in buckets):
   a. Bathing ……..
   b. Washing utensils ……
   c. Washing of clothes ……..
   d. Washing the house ……
   e. Toilet flushing ……..
   f. Usage for any other purpose ……
5. Family's current water consumption level in a day (in litres or in number of buckets) …… ……
6. Water consumption level in summer (March to October) [in litres or in buckets] …… ……
7. Water consumption in winter (November to January) [in litres or in buckets]…… ……..
8. Given that the water usage by an average household per day is 150–200 litres, do you think your usage is more.

completely disagree neutral agree completely agree
disagree (1) (2) (3) (4) (5)

9. Age of the house in which the family is residing ……..
10. The ownership status of the family [please put a tick]:
    Owner occupants / Renters
11. House's fair market value (in `): …….
12. Number of family Members: ……
13. Number of adult members (above 18 years of age) ……...
14. Number of teenagers in the family ……..
15. The family belongs to which caste group [please put a tick]
    Scheduled Caste/Scheduled Tribe/general
16. The family belongs to which Religious Group [please specify] ……..

After one year we will come back to you!

Residential Address: …….
…….
…….
…….
……..

References

Alcott, H. (2011). Social norms and energy conservation. *Journal of Public Economics, 95*(9), 1082–1095.

Ayres, I., Raseman, S., & Shih, A. (2009). Evidence from two large field experiments that peer comparison feedback can reduce residential energy use (NBER Working Paper No. 15386). Cambridge, MA: National Bureau of Economic Research.

Costa, D. L., & Khan, M. E. (2010). Energy conservation 'nudges' and environmental ideology: Evidence from a randomized residential electricity field experiment (NBER Working Paper No. 15939). Cambridge, MA: National Bureau of Economic Research.

Davis, L. W. (2010). Evaluating the slow adoption of energy efficient investments: Are renters less likely to have energy efficient appliances? (NBER Working Paper No. 16114). Cambridge, MA: National Bureau of Economic Research.

Ferraro, P., & Miranda, J. J. (2013). Heterogeneous treatment effects and mechanisms in information-based environmental policies: Evidence from a large-scale field experiment. *Resource and Energy Economics, 35*(3), 356–379.

Ferraro, P. J., & Price, M. K. (2013). Using non pecuniary strategies to influence behavior: Evidence from a large scale field experiment. *Review of Economics and Statistics, 95*(1), 64–73.

Mansur, E. T., & Olmstead, S. M. (2011). The value of scarce water: Measuring the inefficiency of municipal regulations (Working Paper). New Hampshire, US: Dartmouth College.

———. (2012). The value of scarce water: Measuring the inefficiency of municipal regulations. *Journal of Urban Economics, 71*(3), 332–346.

Schultz, P. W., Nolan, J. M., Cialdini, R. B., Goldstein, N. J., & Griskevicius, V. (2007). The constructive, destructive, and reconstructive power of social norms. *Psychological Science, 18*(5), 429–434.

Shahbaz, M., Islam, F., & Butt, M. S. (2016). Finance–growth–energy nexus and the role of agriculture and modern sectors: Evidence from ARDL bounds test approach to cointegration in Pakistan. *Global Business Review, 17*(5), 1037–1059.

Sualihu, M. A., & Rahman, M. A. (2014). Payment behaviour of electricity consumers: Evidence from the greater Accra region of Ghana. *Global Business Review, 15*(3), 477–492.

UNESCO. (2012). *The United Nations world water development report 4: Managing water under uncertainty and risk*. Paris: UNESCO.

Source details

Feedback > Compare sources >

Global Business Review

Scopus coverage years: from 2000 to Present

Publisher: SAGE

ISSN: 0972-1509 E-ISSN: 0973-0664

Subject area: Business, Management and Accounting: Business and International Management

Source type: Journal

View all documents > Set document alert Save to source list

CiteScore 2022
4.3

SJR 2022
0.459

SNIP 2022
0.964

CiteScore CiteScore rank & trend Scopus content coverage

Man & Development
Vol. XLII No. 2, June 2020,
http://www.crrid.res.in/journal/
ISSN 0258-0438

GROWTH AND PRODUCTIVITY OF ORGANISED MANUFACTURING SECTOR IN INDIA: A DISAGGREGATED ANALYSIS USING ASI DATA

Sajal Jana[1] and Maniklal Adhikary[2]

Abstract: The manufacturing sector is one of the engines of economic growth and India has a huge industrial potential. India adopted economic reforms to augment the efficiency of Indian manufacturing sector and make the manufacturing industries more competitive in the international market. The present study is an attempt to analyse the growth performance of organised manufacturing sector in India at disaggregated state level during 1980-81 to 1990-91 (pre-reform period) and 1991-92 to 2007-08 (post-reform period). The comparative analysis of the growth rate in the pre-reform period and post-reform period provides the validity of the basic policy change adopted in 1991. The empirical disaggregated analysis of productivity trends establishes the fact that of the 22 two-digit level industries, three followed S-curve pattern, eight followed J-curve pattern and ten followed a hybrid of S-J curve pattern. Only one industry followed the pattern of falling productivity. The empirical findings disclose the existence of huge variation in the growth rates of selected key variables under evaluation among major states. Reforms failed to bring significant improvement in the performance of overall Indian manufacturing sector. So, use of appropriate technology and optimum allocation of resources becomes a pre- requisite to achieve greater economies of scale in Indian manufacturing sector during post-reform era. In addition, technologically vibrant and internationally competitive manufacturing sector needs to be encouraged to make a sustainable contribution to national output and employment in the reformed era.

Key words: Manufacturing, Interstate, Growth, Productivity, India

[1]Assistant Professor, Dept. of Economics, Dinabandhu Andrews College, Baishnabghata, Kolkata-700084 Email: janasajal78@yahoo.com

[2]Professor, Dept. of Economics, Burdwan University, Burdwan,
Email ID: drmaniklaladhikary@gmail.com

Growth and Productivity of Organised Manufacturing Sector in India: A Disaggregated Analysis using Annual Survey of Industries (ASI) Data

1. Introduction

The manufacturing sector of a country is generally considered as an engine of growth. The performance of the manufacturing sector in India has become a central issue during the post-reform period which needs to be assessed empirically. The share of employment, output, Gross Value Added (GVA) and capital of the industrially developed states such as Maharashtra, Gujarat and Tamil Nadu is high in the organised manufacturing sector compared to the other small states such as Uttarakhand, Jammu and Kashmir and Himachal Pradesh. Industrially developed states showed less concentration of industries in their manufacturing sectors while industrially less developed states such as Odisha, Jharkhand, Chhattisgarh and Goa registered high concentration over the period. The assessment of the factor intensity of the states reveal that the industrially developed states made higher use of the capital-intensive techniques. Over the period of the study, the states have exhibited shifts in their factor intensities used in the production process. Differences in the extent of industrialisation are one of the most glaring aspect of the variations in the levels and structure of state economies. The probable reasons for interstate variations in industrial growth may be the factors, like, infrastructure, human development and expanding market. More industrialised states had a more diversified industrial structure than those of lower level of industrialisation.

In recent period, the productivity growth has been recognised as the dominant determinant of the economic growth. Productivity growths in the manufacturing sector have been considered as the most significant policy variable in the formation of growth oriented industrial strategy. Productivity growth is essential not only to increase output, but also to improve the competitiveness of an industry both in the domestic and international markets. The growth of an economy is governed by two distinct sources – productivity driven growth and input growth through the increase in factors of production which is certainly subjected to diminishing returns and is not sustainable in the long run. The productivity-driven growth is the growth in output that cannot be explained by the growth in total inputs. It is normally credited to the improvement in knowledge, organisational structure, human resources management, skills attainment, information technology and efficient use of factors of production. Productivity growth is accepted as a key characteristic of economic dynamism. Economic performance of a unit is generally supposed to be reflected in its productivity which is measured by the ratio of its output to its inputs. Alternatively, Total Factor Productivity Growth (TFPG) is output growth less the sum total of input share weighted input growth. It is often argued that the economic liberalisation promotes industrial productivity and input use efficiency

(Goldar, 2000). It becomes pertinent to analyse the productivity performance of the industrial sector which is facing stiff competition from outside world in the era of globalisation and liberalisation where the role of government is restricted. The sole objective of highly liberalised policies was to augment productivity and efficiency in Indian industries by creating a competitive environment.

Over the years, there are significant numbers of studies that examine performance of manufacturing industries in India. Some of the studies are done by Desai (1981), Patnaik (1981), Rangarajan (1982), Ahluwalia (1985), Goldar and Seth (1989), Nagaraj (1989), Albin (1990), Sengupta (1993), Upendranath et.al. (1994), Burange (1999), Unni et. al. (2001), Das (2004). Although some of the earlier studies make a comparative analysis on the interstate variation in growth performance of manufacturing sector in India but there is a dearth of literature that incorporates the recent time series dataset.

At the very outset, the present study examines the growth performance of manufacturing industry by taken into account 16 major states in India. The study is an endeavour to analyse the growth performance of various important variables affecting Indian manufacturing sector before and after economic reforms at disaggregated state levels. The comparative analysis of the growth rate in the pre-reform period and post-reform period provides the validity of the basic policy change adopted in 1991. Besides the Introduction in Section 1, this paper has been organised as follows: Section 2 presents regional distribution of industries in India. Section 3 highlights the database and measurement of variables. Section 4 reports the methodology adopted for empirical estimation. Section 5 reports the empirical results. Section 6 reports a disaggregated analysis of productivity trends across industries. Section 7 concludes and draws policy measures.

2. Regional Distribution of Industries across States in India

This section begins with analysing the regional distribution of manufacturing industries across 16 states and 4 major regions in India. Table 2.1 reports the share of regions and states in organised sector manufacturing employment during the years: 1987-88, 1997-98 and 2010-11 respectively. Table 2.2 shows the share of states in terms of gross output. It is obvious that the southern region has gained employment share from about 29 per cent in 1987/88 to 34.8 per cent in 1997/98, whereas the eastern region has considerably lost their share from 17.7 to 14.4 per cent during the same period. The employment share of the central region remains more or less same during the period of study and that of the north-west region fluctuates over the years. A state level analysis of the employment share corresponding to the eastern region shows that the sharp decline in the share of employment share is largely due to sharp decline in the share of West Bengal and to some extent Bihar. While the share of Assam and Odisha remains more or less the same. On the other hand, the insignificant fall in the employment share of

central region between 87/88 and 97/98 is mainly due to decline in the share of Maharashtra while the share of Gujarat and Madhya Pradesh decline marginally and that of Rajasthan remains more or less the same. Empirical results showing the share of states in terms of gross output is reported in Table 2.2 as mentioned above. The share of the eastern region has significantly declined from about 16 per cent in 1987/88 to 8 per cent in 2010/11 whereas that of the southern region has increased marginally between the same time points. The share of the north-west region has consistently declined in the respective years 1997/98 and 2010/11.

Table-2.1
Share of States in Total Employment of Organised Manufacturing Sector

(per cent)

States/ Regions	Share of States/ Regions			Absolute change	
	1987-88	1997-98	2010-11	1987-88 to 1997-98	1997-98 to 2010-11
Assam	1.31	1.55	1.31	0.24	-0.24
Bihar	4.93	2.75	0.84	-2.18	-1.91
Orissa	2.06	1.80	2.23	-0.26	0.43
West Bengal	9.36	8.34	5.01	-1.02	-3.33
Eastern Region	17.66	14.44	9.39	-3.22	-5.05
Delhi	1.75	1.37	0.96	-0.38	-0.41
Haryana	3.04	3.16	4.30	0.12	1.14
Punjab	4.96	4.59	4.84	-0.37	0.25
Uttar Pradesh	9.66	9.73	8.64	0.07	-1.09
North- West Region	19.41	16.85	18.74	-2.56	1.89
Gujarat	8.67	8.80	10.20	0.13	1.4
Madhya Pradesh	4.82	4.67	4.86	-0.15	0.19
Maharashtra	15.66	14.76	13.38	-0.9	-1.38
Rajasthan	3.01	2.94	3.40	-0.07	0.46
Central Region	32.16	31.17	31.84	-0.99	0.67
Andhra Pradesh	9.17	12.09	10.25	2.92	-1.84
Karnataka	4.98	6.28	6.16	1.3	-0.12
Kerala	3.14	3.60	3.00	0.46	-0.6
Tamilnadu	11.45	12.85	15.31	1.4	2.46
Southern Region	28.74	34.82	34.72	6.08	-0.1
Total of 16 States	97.97	97.28	94.69	-0.69	-2.59
Other States	2.03	2.72	5.31	0.69	2.59
All India	100	100	100		

Source: Based on ASI data, provided by CSO

Table-2.2
Share of States in Gross output of Organised Manufacturing Sector

(per cent)

States/Regions	Share of States/ Regions			Absolute change	
	1987-88	1997-98	2010-11	1987-88 to 1997-98	1997-98 to 2010-11
Assam	1.25	0.91	0.91	-0.34	0
Bihar	5.26	3.51	0.77	-1.75	-2.74
Orissa	1.90	1.81	1.97	-0.09	0.16
West Bengal	7.20	5.08	4.41	-2.12	-0.67
Eastern Region	15.61	11.31	8.06	-4.30	-3.25
Delhi	2.10	1.86	1.04	-0.24	-0.82
Haryana	3.50	3.94	4.60	0.44	0.66
Punjab	5.00	3.88	3.18	-1.12	-0.7
Uttar Pradesh	8.88	8.70	8.51	-0.18	-0.19
North- West Region	19.48	18.38	17.33	-1.10	-1.05
Gujarat	10.65	12.87	17.25	2.22	4.38
Madhya Pradesh	5.20	5.36	4.56	0.16	-0.8
Maharashtra	21.32	21.00	16.79	-0.32	-4.21
Rajasthan	2.83	3.45	3.21	0.62	-0.24
Central Region	40.00	42.68	41.81	2.68	-0.87
Andhra Pradesh	5.93	6.88	7.35	0.95	0.47
Karnataka	4.26	5.17	6.11	0.91	0.94
Kerala	2.71	2.42	1.75	-0.29	-0.67
Tamilnadu	10.62	10.01	10.10	-0.61	0.09
Southern Region	23.52	24.48	25.31	0.96	0.83
Total of 16 States	98.61	96.85	92.51	-1.76	-4.34
Other States	1.39	3.15	7.49	1.76	4.34
All India	100	100	100		

Source: Based on ASI data, provided by CSO

Viewed in terms of gross output, the eastern regions' declining share is mainly due to the decline in the share of output in West Bengal and Bihar. The increasing share of the southern region is attributed to the share of Andhra Pradesh and Karnataka in contrast to the state, Tamil Nadu that has consistently shown lower share during the time points as considered in the present analysis. Individually, West Bengal, Maharashtra, Bihar and Tamil Nadu have significantly lost their share in gross output, while Gujarat, Andhra Pradesh, Haryana and Karnataka have improved their position in the years 1997/98 and 2010/11 respectively. It is remarkable to note that though Tamil Nadu has improved its share in terms of employment over the years, it has a stable position in terms of gross output throughout the years.

3. Database and Measurement of Variables

3.1 Database

The present study emphasises on organised manufacturing sector. The basic data source for the time series data on variables such as value added, capital, employment for the organised manufacturing industries is Annual Survey of

Industries (ASI) published by Central Statistical Organisation (CSO) and Economic and Political Weekly Research Foundation (EPWRF). For the present study, the consistent and comparable time-series database is prepared based on NIC-87 by using the available two-digit concordance tables.

3.2 Period of the Study

The study covers the period from 1980-81 to 2007-08. To ascertain the impact of alternative policies of trade and technology on industrial growth, we have divided the whole period in to two sub-periods: 1980-81 to 1990-91 (pre-reform period) and 1991-92 to 2007-08 (post-reform period).

3.3 Measurement of Variables

The present study has considered two output variables namely, GVA at constant prices and gross output and three input variables namely, gross fixed capital at constant prices, number of employees and total emoluments at constant prices for 16 major states. Appropriate price deflators have been used to deflate the dataset at constant prices. The standard practice of perpetual inventory method (Appendix-1) has been followed to generate the series of gross fixed capital stock at constant prices. The figures of total persons engaged provided by ASI consists of both non-production and production workers, and it has been as the measure of labour input. The variable, namely, total emoluments can be defined as the sum of wages and salaries, employers' contribution as provident fund and other funds, and workmen and staff welfare expenses. After converting GVA at constant price, gross fixed capital at constant price we have divided these variables by the number of factories in each state following Ray (2002) and Kumar (2001). This step results GVA at constant prices per factory, gross fixed capital at constant prices per factory and total person engaged per factory in a state.

4. Methodology

4.1 Model Specification for estimation of Sub Period Growth Rate

We have applied linear spline function developed by Poirier (1974) to obtain the growth rates of more than one period in single regression estimation. The use of such a regression model becomes relevant when a significant structural break exists in the time series under evaluation. Although, the periods of estimated growth rates differ according to the availability of the data, the structural break is common in the year 1990-91. To calculate the growth rate of selected key variables for the entire study period (1980-81 to 2007-08), semi-log trend equation has been used as follows.

$$\ln Y_t = \theta + \lambda t + \varepsilon_t \qquad (4.1.1)$$

The estimated value of λ represents an average annual growth rate of the variable under evaluation. Assuming that there are two sub-periods, two equations are needed to be formulated which takes the following forms:

Sub-Period 1:

$$\ln Y_t = \theta_1 + \lambda_1 t + \varepsilon_t \quad \text{When } t < t_1 \tag{4.1.2}$$

Sub-Period 2:

$$\ln Y_t = \theta_2 + \lambda_2 t + \varepsilon_2 \quad \text{When } t < t_2 \tag{4.1.3}$$

To tackle the discontinuities in the sub-period wise growth rate, the reparametrised form of linear spline function is as follows.

$$\ln Y_t = \theta_2 + \gamma_1 \omega_{1t} + \gamma_2 \omega_{2t} + \varepsilon_2 \tag{4.1.4}$$

Where**,**

$$\omega_{1t} = \text{t and } \omega_{2t} = \begin{cases} 0 & \text{if} \quad t < t_1 \\ t\text{-}t_1 & \text{if} \quad t < t_2 \end{cases}$$

The value (γ_1 x100) is the measure of pre-reforms average annual growth rate where as, $(\gamma_1+\gamma_2)\times 100$ provides an average annual growth rate during the post-reforms period. To check significance of the estimated growth rates during pre-reforms period, simple *t*-statistics has been used. However, to test the significance of post-reforms period, a restriction $(\gamma_1+\gamma_2)=0$ is tested using F-statistics.

5. Empirical Results

Estimation of linear spline function as given by equations (4.1.1) and (4.1.4) provides the estimated growth rate of the relevant key variables considered for the present study. The estimated results are reported in the following sub sections.

5.1 Analysis of Interstate variation in growth rate of GVA

Table 5.1 summarises the growth scenario of GVA in the manufacturing sector of various states during pre and post reform period and Fig. 5.1 graphically presents the results. It has been observed that GVA in the manufacturing sector of three states namely, Gujarat, Haryana and Karnataka follow higher growth rate during post-reform period in comparison to pre-reform period. Thus, the reform process has a positive impact on income generation among manufacturing sector of these states. Except these three states negative impact of economic reforms has been observed in the remaining states. It is remarkable to note that Rajasthan has witnessed a negative growth rate during the entire study period. Considering the

entire period of study, it is interesting to note that Andhra Pradesh has grown at highest annual growth rate of 12.07 per cent per annum.

The growth rate calculated for the entire period shows that the states, Andhra Pradesh and Assam rank at top positions among all states considered under present study.

Table-5.1
Growth rate of GVA in Indian Manufacturing Per Factory

(in per cent)

States	Pre-Reform (1980/81-1990/91)	Post-Reform (1991/92-2007/08)	Entire Period (1980/81-2007/08)
Andhra Pradesh	13.00***	11.50	12.07***
Assam	16.00***	9.40***	12.05***
Bihar	19.2***	-7.12***	3.32**
Delhi	7.00***	0.80***	3.25***
Gujarat	5.80***	9.80	2.56***
Haryana	2.70***	5.90***	4.65***
Karnataka	5.10***	5.80	2.95***
Kerala	2.80***	-1.80***	0.030
Madhya Pradesh	16.20***	7.30***	0.98***
Maharashtra	14.25***	9.30**	1.38***
Orissa	8.24***	3.50*	1.83***
Punjab	16.75***	6.40***	0.69***
Rajasthan	13.12***	6.90*	-0.72***
Tamil Nadu	2.72*	2.08	0.83***
Uttar Pradesh	15.80***	7.42***	0.70***
West Bengal	11.2***	7.00***	4.16***

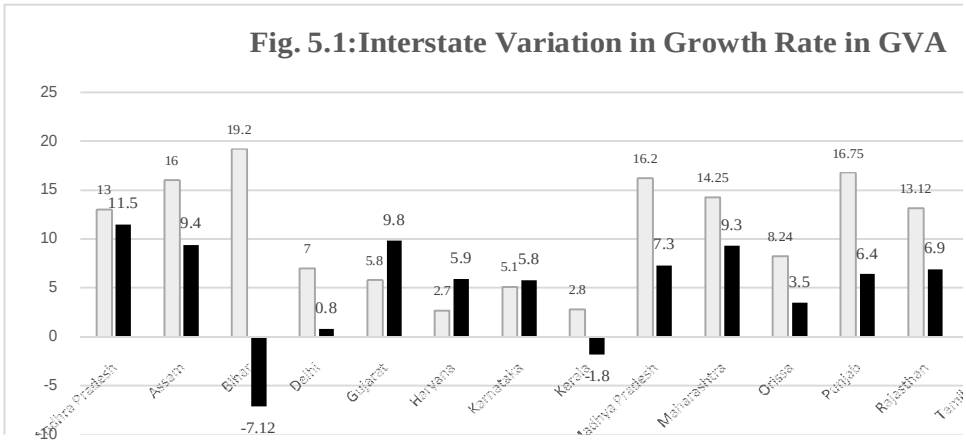

Source: Based on Table 5.1

5.2 Analysis of Interstate variation in growth rate of gross output

Table 5.2 presents inter-state variations in growth summary of manufacturing output in the states. Here also acceleration in the growth rates has been observed

among manufacturing sector of five states namely, Gujarat, Haryana, Karnataka, Tamil Nadu and Kerala. Except these states deceleration has been observed in the remaining eleven states. Hence, in majority of states negative impact of economic reforms has been observed in the growth of output variables as shown in Fig. 5.2. The growth analysis over the entire study period reveals that output in seven states namely; Andhra Pradesh, Madhya Pradesh, Maharashtra, Punjab, Rajasthan, Uttar Pradesh and West Bengal is rising at a rate above 10 per cent per annum. Among these states except Andhra Pradesh the growth of value added had been observed at a very slow rate. High growth of output is coupled with low growth of GVA represents that the cost of raw material has been increased at a very high rate.

Table-5.2
Growth Rate of Output in Indian Manufacturing Per Factory

(in percentage)

States	Pre-Reform (1980/81-1990/91)	Post-Reform (1991/92-2007/08)	Entire Period (1980/81-2007/08)
Andhra Pradesh	11.20***	9.50	10.12***
Assam	12.20***	9.70	8.55**
Bihar	15.00***	4.80***	8.85***
Delhi	4.90***	2.50***	3.52***
Gujarat	4.40***	8.00***	6.70***
Haryana	4.90***	6.10	5.58***
Karnataka	5.40*	7.40*	6.70***
Kerala	-0.10	3.80	2.74***
Madhya Pradesh	17.30***	9.80***	12.82***
Maharashtra	13.30***	11.30**	12.15***
Orissa	7.30***	3.10**	4.77***
Punjab	15.90***	8.00***	11.16***
Rajasthan	14.30***	8.10***	10.62***
Tamil nadu	4.50**	4.20*	3.25***
Uttar pradesh	15.10***	10.10***	12.13***
West Bengal	10.90***	9.80	10.31***

Notes: *, **, and *** represent significance at 10%, 5% and 1% respectively.
Source: Authors' own calculation.

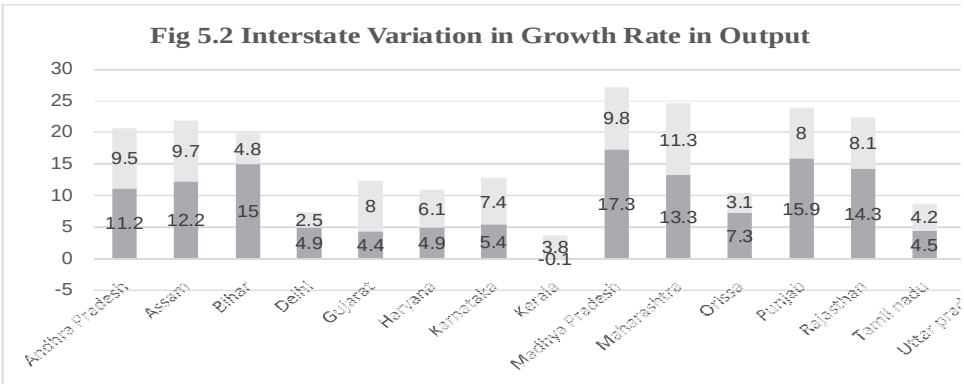

Source: Based on Table 5.2

5.3 Analysis of Interstate variation in the growth rate of Fixed Capital

Table 5.3 represents the growth rate of capital among the selected states over the study period under evaluation. The highest growth of capital has been observed in Kerala followed by Assam, Gujarat and Andhra Pradesh and the value is significant at one per cent level of significance. We have considered the analysis of the growth rate of fixed capital in order to capture the trend of investment in the manufacturing sector across states. Bihar has witnessed negative growth rate during post-reform period. The interstate variation in growth rate of fixed capital is graphically presented in Fig. 5.3.

Table-5.3
Growth Rate of Fixed Capital in Indian Manufacturing Per Factory

(in percentage)

States	Pre-Reform (1980/81-1990/91)	Post-Reform (1991/92-2007/08)	Entire Period (1980/81-2007/08)
Andhra Pradesh	8.30***	4.30***	5.87***
Assam	6.00***	9.00**	7.67***
Bihar	2.40**	-4.70***	1.92***
Delhi	1.50*	1.70*	1.62***
Gujrat	8.20***	7.10***	7.53***
Haryana	4.00***	3.60***	3.78***
Karnataka	5.80***	6.80***	6.40***
Kerala	4.10***	0.20	11.68***
Madhya Pradesh	7.70***	3.70***	2.93***
Maharashtra	7.40***	2.50***	5.23***
Orissa	10.20***	5.30***	5.54***
Punjab	5.90***	0.000	2.28***
Rajasthan	5.10***	0.60***	2.45***
Tamil Nadu	6.70***	2.80***	4.35***
Uttar Pradesh	6.00***	0.80***	2.87***
West Bengal	7.80***	1.60***	4.17***

Notes: *, **, and *** represent significance at 10%, 5% and 1% respectively.
Source: Authors' calculation

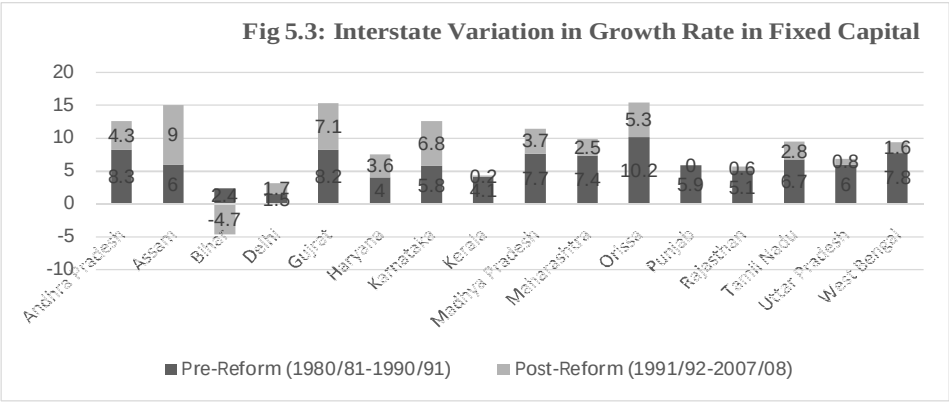

A close look to the Fig.5.3 highlights the fact that Odisha has achieved highest growth rate of above 10 per cent among all the states during pre-reform period and Punjab has achieved least growth rate during post-reform period. Bihar has achieved negative growth rate of capital during the post-reform period among all the states considered for the present study. Again, Punjab has witnessed almost zero growth rate of fixed capital during post-reform period. In contrast, the same state has achieved significantly positive growth rate during the entire study period. The states, Gujarat, Karnataka and Haryana maintained positive growth rate of fixed capital consistently during the pre-reform as well as post-reform period.

5.4 Analysis of Interstate variation in the growth rate of emoluments

Table 5.4 provides estimated growth summary of emoluments among the manufacturing sector of the Indian states. The highest emolument growth has been observed in the manufacturing sector of Assam followed by Andhra Pradesh. However, growth of emolument in Kerala is the lowest one. The manufacturing sector of Kerala has been noticed with the highest growth rate of capital but, least growth of emolument. The causes behind such evidence seem to be the knowledge spillovers and capital-intensive nature of the manufacturing sector of Kerala. Given the highest literacy rate, people prefer to use capital intensive techniques to reap the benefits of the capital deepening and have an aversion to the use of labour-intensive technology. Hence, given the high demand for capital, the price of capital is high and that of labour is low consequently, the emoluments growth is least in the manufacturing sector of Kerala.

Table-5.4
Growth Rate of Emoluments in Indian Manufacturing per Factory

(in percentage)

States	Pre-Reform (1980/81-1990/91)	Post-Reform (1991/92-2007/08)	Entire Period (1980/81-2007/08)
Andhra Pradesh	6.00***	8.30***	7.42***
Assam	8.90***	8.30***	8.54***
Bihar	7.00***	-12.80***	4.93***
Delhi	1.80**	1.50	1.62***
Gujrat	2.80***	2.40***	2.58***
Haryana	4.10***	2.90***	3.40***
Karnataka	3.50***	2.60***	2.98***
Kerala	2.20***	-1.40***	0.0308
Madhya Pradesh	4.80***	-1.50***	0.982***
Maharashtra	2.60***	0.60*	1.42***
Orissa	4.00***	0.40**	1.83**
Punjab	8.20***	-4.20***	0.689
Rajasthan	2.60***	-2.90***	0.724*
Tamil Nadu	0.30	1.20	0.828***
Uttar Pradesh	1.90**	0.000	0.697***
West Bengal	4.60***	-9.90*	4.18

Notes: *, **, and *** represent significance at 10%, 5% and 1% respectively.
Source: Authors' own estimate

The interstate variation in growth rate of emoluments is graphically presented in Fig. 5.4. The Fig. 5.4 reflects the fact that the states, namely, Bihar, Kerala, Uttar Pradesh, Punjab, Rajasthan, Madhya Pradesh, West Bengal have witnessed negative growth rate during the post-reform period. Assam has achieved highest growth rate during the post-reform period as well as for the entire study period.

Fig 5.4: Interstate Variation in Growth Rate of Emoulments

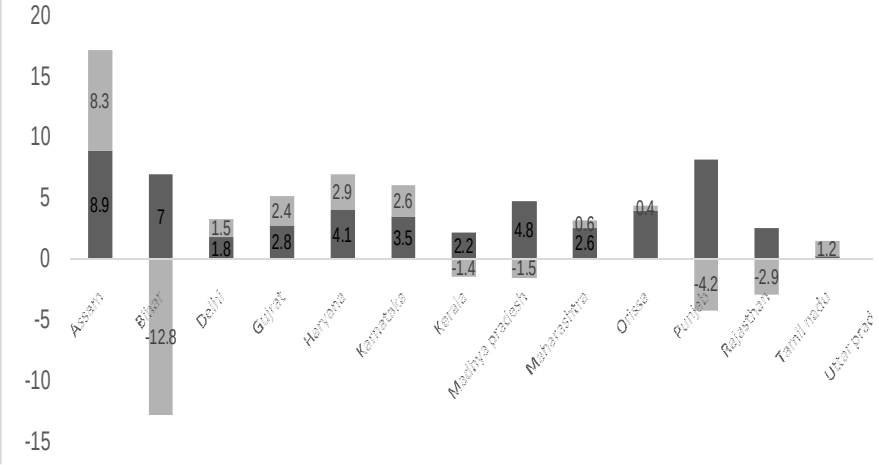

The overall analysis of growth performance of Indian manufacturing reveals the presence of significant interstate variation among the states in India. The impact of economic reforms on the growth performance of important variables have not resulted in favourable changes as was expected. In majority of the states, negative impact of economic reform has been observed, however, there are only few states in which reforms have been affected positively.

6. Disaggregated Analysis of Productivity trends in Indian manufacturing sector

The present section attempts to make an assessment towards the success of policy measures undertaken during reform period. At the very outset, we have attempted to make a comparative study of relative growth of output and inputs during the pre-reform and post reform period. The impact of economic reforms has been assessed on the basis of comparison of estimated growth rate of key variables during the two sub periods. Before starting the comparative analysis, it becomes necessary to estimate growth rate of selected variables during the entire study period as well as for the two sub periods. The following section presents the estimates of growth rate of relevant key variables.

Table-6.1
Total Factor Productivity (TFP) Growth in Indian Manufacturing Sectors

(per cent)

Industries	Phase I (1991-92 to 1997-98)	Phase II (1998-99 to 2001-2002)	Phase III (2002-03 to 2007-08)	1991/92 to 2007/08
15. Food products & beverages	-0.56	-0.24	0.95	0.05
16. Tobacco products	0.54	-1.55	-1.14	-0.54
17. Textiles	0.49	1.20	1.78	1.12
18. Apparel & dyeing fur	-0.78	1.11	1.71	0.55
19. Leather products & tanning	1.31	-0.08	1.08	0.90
20. Wood & wood products	-10.03	1.13	1.13	-3.46
21. Paper & paper products	-1.30	0.32	1.86	0.20
22. Publishing & printing	-2.12	-4.62	3.12	-0.86
23. Coke & petroleum products	-3.99	-0.47	2.39	0.91
24. Chemicals & chemical products	-1.25	-0.33	1.71	0.01
25. Rubber & plastic products	0.16	0.92	0.07	0.31
26. Non-Metallic Minerals	0.29	1.69	1.18	0.93
27. Basic metals	2.99	-1.04	-0.74	0.73
28. Fabricated metals	0.25	-0.09	1.41	0.58
29. Machinery & equipment	1.77	1.00	0.75	1.23
30. Office, accounting &computing machinery	3.89	-0.48	-1.62	0.92
31. Electric machinery & apparatus	3.10	-0.05	2.84	2.27
32. Radio, T.V. & communication equipment	0.84	-1.58	0.48	0.15
33. Medical, optical instrument & watches etc	-0.86	-0.81	2.17	0.22
34. Motor vehicles & trailers	1.09	-2.27	4.02	1.33
35. Transport equipment	1.68	1.72	2.75	2.07
36. Furniture	2.80	-0.68	1.98	1.69
All Manufactures	0.25	-0.09	1.41	0.58

Source: Virmani, Arvind, and Danish A. Hashim (2011): "J-curve of Productivity and Growth: Indian Manufacturing Post-liberalisation" IMF Working paper 11/163, July1.

The productivity growth in the post-reform period of 1990s declined from growth rate witnessed in the 1980s (Trivedi and Sinate, 2000). This was a puzzle as the reform process was expected to accelerate productivity growth. Some experts have viewed that a fall in capacity utilisation was responsible for this phenomenon. They argued that due to surge in investment activities and high imports in post-reform period which was not accompanied by commensurate rise in demand and capacity utilisation in the industry. The study by Virmani and Hashim (2011) uses ASI data from 1981/82 to 2007/08 with a view to trace the changing impacts of reforms on productivity and growth. For the purpose of analysis, the entire period has been divided into two periods: the pre-reform period from 1981/82 to 1990/91 (Period I) and post-reform period from 1991/92 to 2007/08 (period II). Further, the post-reform period has been divided into three sub-periods: sub-period I (1991/92 to 1997/98), sub period 2 (1998/99 to 2001/02); and sub-period 3 (2002/03 to 2007/08). The total factor productivity growth during post-reform period at disaggregated two-digit industry level is

depicted in Table 6.1. The TFP grew at 0.6 per cent per annum in the 1980s and slowed down to 0.25 per cent per annum during sub-period 1, and in sub-period 2, it further declined to -0.09 per cent per annum. In sub-period 3, the TFP growth picked up to 1.41 per cent per annum. Immediately after the post-reform period, the reform effect was negative on productivity and output growth. The main cause behind it was the effects of Balance of Payments shock (BOP), dramatic import liberalisation, diversification of firm's resources, learning new skills and technology. The slow-down accentuated during the second sub-period which yields initial J-curve portion. The dissemination of new technologies and product adoption promote acceleration in total factor productivity growth sharply during sub-period 3. For the manufacturing sector as a whole, TFP gain during the post-reform period has been 0.58 per cent per annum as shown in Table 6.1. The TFP grew at 0.6 per cent per annum in the 1980s and slowed down to 0.25 per cent per annum during sub-period 1, and in sub-period 2, it further declined to -0.09 per cent per annum. In sub-period 3, the TFP growth picked up to 1.41 per cent per annum. Immediately after the post-reform period, the reform effect was negative on productivity and output growth. The main cause behind it was the effects of BOP shock, dramatic import liberalisation, diversification of firms' resources, learning new skills and technology. The slow-down accentuated during the second sub-period which yields initial J-curve portion. The dissemination of new technologies and product adoption promote acceleration in the TFP growth sharply during sub-period 3. For the manufacturing sector as a whole, TFP gain during the post-reform period has been 0.58 per cent per annum as shown in Table 6.1

The economy completed the rising portion of the J-curve by 2007/08 and entered the upper portion of S-curve thereafter. So, it can be concluded that TFPG in the manufacturing sector has followed J-curve pattern. The J-curve is linked to obsolescence of capital and technology embodied in them. Trends in the productivity growth at sub-sector level of manufacturing showed much more varied pattern of productivity growth than at aggregate level. The productivity growth was more than one per cent per annum for six industries, namely, electric machinery and apparatus, transport equipment, furniture, motor vehicles and trailers, machinery and equipment and textiles. Other industries experienced positive growth rate in TFP except wood and wood products, publishing and printing, and tobacco products. Differences in productivity growth due to different policy reforms affect different industries to different degree. The empirical analysis establishes the fact that of the 22 two-digit level industries, three followed S-curve pattern, eight followed J-curve pattern and ten followed a hybrid of S-J curve pattern. Only one industry followed the pattern of falling productivity. The reforms helped the productivity and output to grow. But it may not be high enough in all industries due to halting reforms, technological gap and rigid labour legislations and many other factors.

7. Conclusions and Policy implications

The analysis of growth performance of major manufacturing states reveals that although India adopted economic reforms to augment efficiency of Indian manufacturing sector and make the manufacturing industries more competitive in the international market yet the results portray a gloomy picture. Reforms failed to mark a significant dent on the industrial performance as well as growth rate of value added, output, employment, emolument and fixed capital reveals huge regional variations among the Indian states. The analysis discloses the existence of huge variation in the growth rates of all the important variables under evaluation among major states.

The inter-state variations in the growth rate of manufacturing output shows that in the seven states namely; Andhra Pradesh, Madhya Pradesh, Maharashtra, Punjab, Rajasthan, Uttar Pradesh and West Bengal, the rates of output are above 10 per cent per annum. However, among these states, except Andhra Pradesh the growth of value added had been observed at a very slow rate. High growth of output coupled with low growth of GVA represents that the cost of raw material has increased at very high rate. The growth of employment in the manufacturing sectors of states under considerations depict that manufacturing sector of Bihar has registered highest employment growth followed by the manufacturing sector of Rajasthan. The analysis of the growth rates of capital among the states over the study period under consideration provides the highest growth in Kerala followed by Assam, Gujarat and Andhra Pradesh.

An attempt to analyse the impact of economic reforms on the growth rates of important variables under consideration, it has been observed that GVA in the manufacturing sector of three states namely; Gujarat, Haryana and Karnataka are rising comparatively at higher growth rate during post reform period in comparison to pre reform period. Thus, the reform process seems to be positively effecting income generation among manufacturing sector of these three states. Except these three states negative impact of economic reforms has been observed. Regarding the impact of economic reforms on manufacturing output, acceleration in the growth rates has been observed among manufacturing sector of five states namely; Gujarat, Haryana, Karnataka, Tamil Nadu and Kerala. Expect these states deceleration has been observed in the remaining eleven states. Hence, in majority of states negative impact of economic reforms has been observed in the growth of output variables.

The analysis reveals that employment opportunities in manufacturing sector have improved among five states namely; Andhra Pradesh, Gujarat, Maharashtra, Tamil Nadu and Uttar Pradesh. Among these states the observed improvement in Maharashtra is statistically insignificant where as in the remaining four states significant improvement has been noticed. In these five states there is only state Gujarat where growth of employment has become

positive during post-reform period in comparison to negative value during pre-reform period. However, apart from these states, a negative impact of economic reforms on employment growth has also been noticed.

The empirical analysis of productivity trends in organised manufacturing sector at disaggregated level establishes the fact that of the 22 two-digit level industries, three followed S-curve pattern, eight followed J-curve pattern and ten followed a hybrid of S-J curve pattern. Only one industry followed the pattern of falling productivity. So, the reforms have a positive impact the productivity and output to grow.

The Indian planner must design appropriate policy measures so as each state can utilise its own resources to accelerate industrial growth in their own vicinity. Hence, reforms failed to bring significant improvement in the performance of overall Indian manufacturing sector. In this context, use of appropriate technology and optimum allocation of resources becomes a pre-requisite to achieve greater economies of scale in Indian manufacturing sector during post-reform era. In addition, technologically vibrant and internationally competitive manufacturing sector needs to be encouraged to make a sustainable contribution to national output and employment in the reformed era.

Note

The article is the outcome of the thesis submitted by the corresponding author to University of Burdwan, West Bengal in March, 2017 for the award of Ph.D degree & awarded in August, 2017 under the supervision of Prof. Maniklal Adhikary, Professor, University of Burdwan, Department of Economics, West Bengal, India.

References

Ahluwalia, I. J (1985): *Industrial Growth in India (Stagnation since Mid-sixties)*, Oxford University Press, New Delhi.

Albin, A (1990): "Manufacturing Sector in Kerala: Comparative Study of its Growth and Structure", *Economic & Political Weekly*,25 (37), 2059-2070.

Burange, L.G (1999): "Industrial Growth and Structure: Manufacturing Sector in Maharashtra", *Economic & Political Weekly*,34 (44), M39-M48.

Desai, A.V (1981): "Factors underlying the slow growth of Indian Industry," *Economic and Political Weekly*, 29(53), 3342-3344.

Das, D. K. (2004): "Manufacturing Productivity under varying Trade Regimes, 1980-2000", *Economic and Political Weekly*,39(5), 423-433.

Goldar, B. and V. Seth (1989): "Spatial variation in the rate of Industrial growth in India", *Economic and Political Weekly*, 24 (22), 1237-1240.+

Goldar, B. (2000), "Productivity Growth in Indian Manufacturing in 1980s and 1990s", paper presented at Conference on Centre For Development Economic, Delhi School of Economics, *Industrialisation in Reforming Economy: A Quantitative Assessment*, New Delhi, Dec. 20-22.

Kumar, S. (2001), "Explaining Inter-State Differentials in Total Factor productivity Growth in Indian Manufacturing Sector" *Indian Journal of Economics*, Vol. LXXXII, No.325.

Nagraj, R. (2003): "Industrial Policy and Performance since 1980: Some Preliminary Findings", *Economic and Political Weekly*,24(26), 1481-1484.

Ray, S.C. (2002). "Did India's Economic Reforms Improve Efficiency and Productivity? A Non-parametric Analysis of the Initial Evidence from Manufacturing", *Indian Economic Review*, Vol. 37, No.1, pp. 23-57.

Rangarajan, C (1982), Agricultural growth & Industrial performance in India, *Research report no. 33*, International Food Policy research Institute.

Patnaik. P (1987): Recent growth experience of the Indian economy: Some comments, *Economic& Political weekly* Vol.22 (May), No.19/21, pp AN49-AN51+ AN54-AN56.

Poirer Dale J. (1974) Piecewise Regression using cubic splines, *Journal of American Statistical Association*, vol 63(343), pp 515-524.

Sengupta, D.N. (2009): "Indian Manufacturing Industry: Growth Episode of the Eighties", *Economic and Political Weekly*, 28 (22), M-54-M-62.

Trivedi, P., A. Prakash and D. Sinate (2000), "Productivity in Major Manufacturing Industries in India: 1973/74 to 1997/98", *Development Research Group Study* No. 20, Department of Economic Analysis, Reserve Bank of India, Mumbai.

Upendranath, C., Vijayabaskar, M. and V. Vyasulu (1994): "Industrial Growth and Structure: Analysis of Manufacturing Sector in Karnataka", *Economic and Political Weekly*, 29 (48), M157-M164.

Unni, J., Lalitha, N. and U. Rani (2001): "Economic Reform and Productivity Trends in Indian Manufacturing", *Economic and Political Weekly*, 36(41), 3914-3922.

Virmani, Arvind and Danish, A. Hashim (2011), "J-curve Productivity and Growth: Indian Manufacturing Post-Liberalisation", *IMF working Paper*, WP/111/163.

APPENDIX-1

A Perpetual Inventory Method (PIAM)

The PIAM requires the estimates of capital stock for a benchmark year and investment in the subsequent years. Following Ahluwalia (1991), Balakrishnan and Pushpangadan (1994) the time series on capital stock has been generated by using the two equations as given below.

$$I_t = B_t - B_{t-1} + D_t$$

$$K_t = K_0 + \sum_{i=1}^{t} I_i$$

where, I is the gross capital formation, B denotes the book-value of fixed assets, D is the depreciation, K is the stock of capital at current prices. Subscript 't' has been used to denote time. K_0 is the base period capital stock which is estimated by doubling the book value of fixed capital stock for the bench mark year. Gross capital stock for the subsequent years has been arrived at by adding the gross investment figures to the stock of capital of the previous year. The series on gross capital stock at current prices (K_t) has been converted into real capital stock by deflating with wholesale price index for machinery and equipments with base year=100.

FINANCE INDIA
© Indian Institute of Finance
Vol. XXXIII No. 2, June 2019
Pages—455—462

Abstract of Doctoral Dissertation

Inter-State variation of Efficiency and Productivity in Selected Indian Industries[1]

SAJAL JANA*

I. Introduction

THE PROCESS OF sustained increase in the level of industrialization stands as a hallmark of economic strength and stability of an economy. Industry is rightly regarded a leading sector in economic growth because of its intensity in reproducible tangible capital, scale economies and greater amenability to rapid technological changes. Due to its forward and backward linkages with several key sectors of the economy, industrial sector produces strong multiplier effects and is capable of being the driver of economic growth. Development of manufacturing is considered as the hub of industrialization. Industrialization ensures a sharp rise in national income and standard of living by more extensive and intensive utilization of the productive resources, increasing the productivity of the economy, generating gainful employment opportunities, providing a wide range of consumer choice. In fact, industrialization increases productivity and standard of living, creates industrial skills, promotes innovation and technological development, promotes capital formation through higher wages and diverts surplus farm labor to modern industry. To realize these benefits and hasten up required socio-economic changes, top priority has been assigned to industrialization in underdeveloped countries.

Industrialization plays a crucial role in the process of economic development of developing economies. It holds the key to providing lasting solution to the problem of low economic growth. Through accelerating rate of growth in these economies, industrialization creates more employment opportunities and thus helps in poverty alleviation.

1 The Thesis was submitted to University of Burdwan, West Bengal, in March 2017, for the award of Ph.D. Degree awarded in August 2017, under the supervision of Prof. Maniklal Adhikary, Professor, University of Burdwan, Department of Economics, Burdwan, West Bengal 713104, INDIA.

* Assistant Professor in Economics, Garhbeta College, The Department of Economics, Garhbeta, Paschim, Mednipur, West Bengal 721127, INDIA

Submitted February 2019 ; *Accepted* February 2019

Source details

Feedback > Compare sources >

Finance India

Scopus coverage years: from 2018 to 2023

Publisher: Indian Institute of Finance

ISSN: 0970-3772

Subject area: Business, Management and Accounting: Accounting | Economics, Econometrics and Finance: Finance

Source type: Journal

View all documents > | Set document alert | Save to source list

CiteScore 2022
0.2

SJR 2022
0.131

SNIP 2022
0.226

CiteScore | CiteScore rank & trend | Scopus content coverage

Efficiency of Indian Organized Manufacturing in Liberalized Regime: A Stochastic Frontier Approach

Sajal Jana

Thispaper attempts to estimate technical efficiency of Indian manufacturing industries across fifteen major states by estimating a time varying stochastic frontier production function and inefficiency effects model using panel data. The study covers the time period from 1993 to 2011 and reveals that there is an increasing trend of technical efficiency across the states. The Indian industrial sector recorded anaverage technical efficiency of 0.663. The estimated parameters of the translog production model using maximum likelihood method are statistically significant at conventional levels though their signs differ. The likelihood ratio test statistic rejects the Cobb-Douglas production technology as description of the database given the specification of the translog formulation.

Sajal Jana is Assistant Professor, Dept of Economics, Dinabandhu Andrews College Baishnabghata, Garia, Kolkata 700084. E-mail: janasajal78@yahoo.com

Introduction

Manufacturing is an important sector in the Indian economy comprising about 31% of the non-agricultural sector, which makes up 75% of the total GDP in India (Kaliranjan & Bhide,2004). India's post-Independence development plans have emphasized industrialization as a very important instrument for sustained growth. Its sustained growth is crucial for generating employment opportunities required to absorb the rapidly expanding workforce. Industrialization plays a crucial role in the process of economic development of developing economies. At present, the share of industry in total employment increased from 16.2 per cent in 1999-2000 to 21.9 percent in 2009-10. A significant development in the Indian economy in the post 1990s period is the acceleration of the reform process initiated in the 1980s.

The reforms were initiated to improve the efficiency, productivity and international competitiveness of Indian industry. The reform process was more aggressively pursued during the 1990s. The sole

Productive efficiency can be determined by estimating the best practice production frontier and individual states' aggregate manufacturing industries.

objective of these highly liberalized policies was to augment productivity and efficiency in Indian industries by creating a competitive environment. Economic performance of a unit is generally supposed to be reflected in its productivity which is measured by the ratio of its output to the inputs. The efficiency term implies the maximum output obtained from utilizing the available inputs. Efficiency can be increased by minimizing inputs while holding output constant or by maximizing output while holding inputs constant or a combination of both. Productive efficiency can be determined by estimating the best practice production frontier and individual states' aggregate manufacturing industries.

Review of Literature

A vast number of empirical applications have contributed to estimate technical efficiency of aggregate manufacturing sector as well as across of the states in India. Raj and Natrajan (2008) examined the technical efficiency in the unorganized manufacturing sector of Kerala and depicted the existence of a high level of technical inefficiency due to which their potential level has reduced significantly. Kumar (2005) endeavored to analyze regional variations in technical efficiency of Indian manufacturing sector using the method of stochastic frontier analysis. The results revealed wide variations in the technical efficiency of manufacturing sectors of different states. Mukherjee and Ray (2004) analyzed the state level data of the manufacturing sector of India for the period 1985-86 to 1999-00 in order to study the efficiency dynamics of manufacturing sector during pre and post reforms years. Bhandari and Maiti (2007) has fitted translog stochastic frontier production function to firm level cross-sectional data on India's textile firms for selected five years to estimate technical efficiency of firms. They conclude that public sector firms are found to be relatively less efficient. Bhandari and Maiti (2012) attempt to estimate technical efficiency of individual leather producing firms for some years by applying two conventional methods viz. Data Envelopment Analysis and Stochastic Frontier Analysis.The findings of the study imply significant variation in technical efficiency across firms in different groups of states as well as under different organized structure.

At the very outset, the present study estimates efficiency scores achieved by the states during the period 1994-95 to 2010-11 using the balanced panel database. The study is an improvement over the earlier studies in that it considers very recent time series data which is not done in the previous studies and there is a dearth of literature that focuses on the interstate variation in respect of estimated efficiency scores for different years.

Selection of Sample States

The study encompasses 18 major states of India, three of which were bi-

furcated in November 2000. The bifurcated states are: Bihar, Madhya Pradesh and Uttar Pradesh. Three new states, *viz*., Jharkhand, Chattisgarh and Uttarakhand were carved out of Bihar, Madhya Pradesh and Uttar Pradesh, respectively. To ensure the comparability of pre-bifurcation period with the post-bifurcation period, the data for the newly created state has been merged into the respective state from which it was created. Thus, the states included in this study, arranged in alphabetical order are: Andhra Pradesh (AP), Bihar (BIH), Delhi (DEL), Gujarat (GUJ), Haryana (HAR), Karnataka (KAR), Kerala (KER), Maharashtra (MAH), Madhya Pradesh (MP), Orissa (ORI), Punjab (PUN), Rajasthan (RAJ), Tamil Nadu (TN), Uttar Pradesh (UP) and West Bengal (WB).

Database & Variables

The required data have been collected from various issues of Annual Survey of Industries (ASI) compiled by Central Statistical Organization (CSO), Government of India and Economic & Political Weekly Research Foundations (EPWRF) electronic database. A concordance between NIC 1998 and NIC 1987 at two-digit level has been made to build a comparable and continuous time series database. Suitable price indices deflators have been constructed with the help of the official series on wholesale price indices (Index Numbers of Wholesale Prices in India, prepared by the Office of the Economic Advisor; Ministry of Industry). The standard practice of perpetual inventory method has been followed to generate the series of gross fixed capital stock at constant prices. The price indices of machinery and equipment were used to deflate nominal fixed capital as provided by ASI. The figures of total persons engaged provided by Annual Survey of Industries consists of both non production and production workers, and has been used as the measure of labor input. Gross output has been taken as output.

Model Specification

Following Aigner, Lovell and Schmidt (1977) the time varying translog production function for two inputs can be specified in the following form. Inclusion of a trend variable t with interaction terms allows us to identify the contribution of technological change to TFP growth. A notable advantage of the stochastic frontier is the fact that the restrictive assumptions about firms operating with full efficiency are relaxed.

$$InY_{it}=\beta_o+\beta_l InL_{it}+\beta_k InK_{it}+\beta_{ll}(InL_{it})^2+\beta_{kk}(InK_{it})^2+\beta_{tt}t^2+\beta_{lk}(InL_{it})(InK_{it})+\beta_{tl}(InL_{it})t+\beta_{tk}(InK_{it})t+v_{it}-u_{it}.....(1)$$

Where Y_{it} is the gross value of output; K and L are the inputs for capital and labor respectively and $i=1,2,..... N$; $t=1,2,....T$; j $k=L,K$. N is the number of states included in the analysis. T is the number of time periods in the data series. K is the number of inputs considered. The efficiency error u_{it} represents production loss due to industry specific technical inefficiency; thus, it is always greater than or equal to zero ($u_{it}>0$). It is assumed to be independent of statistical error v_{it} which is assumed to be

independently and distributed as $N\left(0,\sigma_v^2\right)$.

Following Battese and Coelli (1992) the distribution of technical inefficiency effects, u_{it} taken to be non-negative truncation of the normal distribution $N\left(\propto,\sigma_u^2\right)$ and modeled to be the product of an exponential function of time as

$u_{it}=\lambda_i u_i=\exp[-\lambda(t-T]u_i, i=1,2,\ldots,N;$
$t=1,2,\ldots,T$.....(2)

Here, the unknown parameter λ represents the rate of change in technical inefficiency and the non-negative random variable, u_i, is the technical inefficiency effect for the i^{th} firm in the last year for the dataset. A firm with positive λ is likely to improve its level of efficiency over time and vice-versa. A value of $\eta = 0$ implies no time effect.

Technical efficiency of unit *i* at time *t* (TE_{it}) is defined as the ratio of the actual output to the potential output as

$$TE_{it} = \exp(-u_{it}) \quad \text{.....(3)}$$

TEC is the change in TE.

$$\varepsilon_K = \frac{\partial \ln Y}{\partial \ln K}$$
$$= \beta_k + 2\beta_{kk} \ln K + \beta_{kl} \ln L$$
$$+ \beta_{kt} t \text{.....}$$

$$\varepsilon_L = \frac{\partial \ln Y}{\partial \ln L} = \beta_l + 2\beta_{ll} \ln L + \beta_{kl} \ln K$$
$$+ \beta_{lt} t \text{.....}$$

Differentiating equation (1) with respect to K and L we have the respective output elasticities as follows.

The output elasticities of input K and L are

The equations indicate the percentage change in output due to 1% change in inputs. The sum of two elasticities is used to obtain returns to scale. The elasticity of scale measures how output varies as a particular input bundle is augmented by a scalar.

Tests of Hypotheses

Before commenting on the parameter estimates of the stochastic frontier production function and inefficiency effects model, various specification tests of the parameters have been performed in the frontier function using the generalized likelihood ratio (LR) test statistic.

The Generalized likelihood ratio (LR) statistics, λ, is given by

$$\lambda = -2\ \ln\left\{L\left(H_o\right)\right\} - \ln\left\{L\left(H_1\right)\right\} \quad \text{.....(6)}$$

Where $L\left(H_o\right)$ is the value of log likelihood function under null hypothesis.The test statistic λ has approximately a mixed chi-square distribution with degree of freedom equal to the difference between the number of parameters estimated under H_o and H_1 respectively. Testing for the validity of the translog over Cobb- Douglas specification using LR test statistic shows the rejection of the null hypoth-

Translog specification is preferred to the Cobb-Douglas representation.

esis implying translog specification is preferred to the Cobb-Douglas representation. The second null hypothesis that there is no technical change is strongly rejected by the data in all cases. Thus, given that the technology can be described by a stochastic translog frontier, the individual states cannot be supposed to be all technically efficient. The third null hypothesis is that technical progress is neutral. It is to be noted that parameterization of the stochastic frontier model allows for non-neutral technical progress. The fourth null hypothesis, specifying that technical inefficiency effects have half normal distribution($H_0 = \mu = 0$) aganist truncated normal distribution, is rejected at 1% significance level. The last null hypothesis that technical inefficiency is time invariant ($H_0 = \eta = 0$) is rejected.

Table1 GeneralizedLikelihood-ratio Tests of Null Hypotheses for Parameters Values in the Estimated Stochastic Frontier Production Function

Null Hypothesis	Estimated LR Test Statistic	D.f.	Critical value 1%	Critical value 5%	Decision
$H_0=\beta_u=\beta_{kk}=\beta_{tt}=\beta_{lk}=\beta_{tl}=\beta_{tk}=0$ (Cobb-Douglas Production function)	29.22	6	16.81	12.59	Reject
$H_0=\beta_t=\beta_{tk}=\beta_{tl}=\beta_{tt}=0$ (No Technical Change)	109.48	4	13.2	89.49	Reject
$H_0=\beta_{tk}=\beta_{tl}=0$ (Neutral Technical Progress)	13.36	2	9.21	5.99	Reject
$H_0=\lambda=0$ (Technical inefficiency effects have half normal distribution)	10.68	1	6.63	3.84	Reject
$H_0=\eta=0$ Time invariant Technical inefficiency)	23.5	1	6.63	3.84	Reject

Note: The critical value for the test is taken from Table 3 of Kodde and Palm (1986:1246)

Maximum Likelihood Estimates

The maximum likelihood estimates of the parameters of the translog frontier production function model and the technical inefficiency effects model defined by equations (1) and (2) are reported in Table 2 using the computer package FRONTIER 4.1 (Coelli, 1996).

The signs of the estimated parameters of the translog production model are significant at conventional levels in most of the cases. The estimate of γ which is the ratio of variance of industry specific performance of technical efficiency to total variance of output is statistically significant at 1% level in aggregate manufacturing sector across states in India. All the estimates of η are positive. A significantly positive value of β_{kt} indicates technical change is capital using and negative value of β_{lt} indicates technical change is labor saving. Technical change is neutral if all β_{tj} are equal to zero.

Table 2 Panel Estimation of Stochastic Production Frontier & Technical Efficiency Model

Variable		Coefficient	t-statistics
Constant	β_o	-11.36*	1.58
ln L	β_l	3.52***	7.45
ln K	β_k	-1.46***	-3.20
T	β_t	0.219***	3.66
$(lnL)^2$	β_{ll}	-0.170***	-4.78
$(lnK)^2$	β_{kk}	-0.528*	-1.96
t^2	β_{tt}	-0.00091*	-1.54
(ln L. lnK)	β_{lk}	0.191***	3.18
(ln L) *t	β_{lt}	-0.028***	-3.78
(ln K) *t	β_{kt}	0.0220***	3.54
σ		0.039***	4.24
γ		0.611***	6.97
μ		0.308***	4.18
η		0.0317***	3.66
Log Likelihood function		177.86	

Source: Authors' own calculation based on ASI data

Note: 1) The dependent variable for frontier estimation is $lny_{it..}$ Total number of observations is 304.

2) The values in column (4) show t-statistics

3) *, **, *** show 10%, 5%, and 1% level of significance respectively.

Table 3 Estimates of Output Elasticity

States	E_K	E_L	RTS
Andhra Pradesh	0.312	0.481	0.793
Assam	0.128	0.804	0.932
Bihar	0.056	0.934	0.990
0rissa	0.037	0.970	1.007
West Bengal	0.265	0.564	0.829
Haryana	0.186	0.705	0.891
Punjab	0.249	0.591	0.840
Delhi	0.141	0.780	0.921
Gujarat	0.183	0.714	0.897
Madhya Pradesh	0.141	0.785	0.926
Maharashtra	0.224	0.641	0.866
Rajasthan	0.146	0.776	0.922
Karnataka	0.205	0.673	0.877
Kerala	0.250	0.587	0.838
Uttar Pradesh	0.212	0.660	0.872
Tamil Nadu	0.320	0.469	0.788
Average	0.191	0.703	0.887

Note: E_k, E_L, RTS denotes elasticity of capital, elasticity of labor, returns to scale respectively.
Source: Author's own calculation based on ASI data

For all Indian industries, the average across the state for output elasticity of capital over the years is 0.191 while that for labor is 0.703.

Table 3 provides the mean estimates of both capital(E_K) and labor elasticity (E_L) for each state as calculated using equation (4)& (5). For all Indian industries, the average across the state for output elasticity of capital over the years is 0.191 while that for labor is 0.703.

Returns to scale(RTS) for Indian industries is 0.887, implying that Indian manufacturing sector is characterized by decreasing returns to scale.

Adding elasticity of capital and labor together, the resulting returns to scale(RTS) for Indian industries is 0.887, implying that Indian manufacturing sector is characterized by decreasing returns to scale. The production technology exhibits decreasing returns to scale in almost all states except Orissa. The state with highest labor elasticity is Orissa and Bihar and the lowest is Tamil Nadu followed by Andhra Pradesh. Conversely, the states, namely, Andhra Pradesh and Tamil Nadu have the highest value for capital elasticity and the lowest for Orissa and Bihar.

Analysis of Efficiency Scores

Table 4 displays mean technical efficiency estimates for each state and its rank over the entire study period starting with 1993 to 2011. The state, Gujarat has the highest mean technical efficiency across the entire time period and Assam is the least efficient state. Mean technical efficiency for the Indian industrial sector estimates over the period from 1993 to 2011 is estimated to be 0.663. It is remarkable to note that there is an increasing trend of technical efficiency across the states. Increasing technical efficiency scores over the years indicate that states have moved closer to the production frontier over time.

Increasing technical efficiency scores over the years indicate that states have moved closer to the production frontier over time.

Conclusion & Policy Implications

Based on the results it is recognized that aggregate manufacturing sector across states in India has performed well in terms of efficiency though the efficiency scores are mixed in nature over the reference period. For future development, productive efficiency and technical change in industries have been prominent issues in discussions on the regional diversity of output and employment growth in the industrial sector in a developing country like India. Government should take necessary action to improve productive efficiency of the industries across states. Once efficiency increases, it enhances competitiveness by realizing the potential output. Non-improvement of technical efficiency over

Table 4 Year wise Technical Efficiency Level Estimates by State

States	1993	1994	1995	1996	1997	1998	1999	2000	2001	2002
Andhra Pradesh	0.440	0.451	0.463	0.474	0.485	0.496	0.507	0.518	0.529	0.539
Assam	0.367	0.379	0.390	0.402	0.413	0.425	0.436	0.448	0.459	0.471
Bihar	0.572	0.582	0.592	0.602	0.612	0.621	0.630	0.639	0.648	0.657
Orissa	0.454	0.465	0.476	0.488	0.499	0.510	0.520	0.531	0.542	0.552
West Bengal	0.435	0.446	0.458	0.469	0.480	0.491	0.502	0.513	0.524	0.535
Haryana	0.686	0.694	0.702	0.710	0.717	0.725	0.732	0.739	0.746	0.753
Punjab	0.521	0.532	0.542	0.553	0.563	0.573	0.583	0.593	0.603	0.613
Delhi	0.572	0.582	0.592	0.601	0.611	0.620	0.630	0.639	0.648	0.657
Gujarat	0.947	0.948	0.950	0.951	0.953	0.954	0.956	0.957	0.958	0.959
Madhya Pradesh	0.680	0.689	0.697	0.705	0.712	0.720	0.727	0.735	0.742	0.749
Maharashtra	0.914	0.917	0.919	0.922	0.924	0.926	0.929	0.931	0.933	0.935
Rajasthan	0.573	0.583	0.593	0.603	0.612	0.622	0.631	0.640	0.649	0.658
Karnataka	0.540	0.550	0.561	0.571	0.581	0.591	0.601	0.610	0.620	0.629
Kerala	0.421	0.432	0.444	0.455	0.466	0.477	0.489	0.500	0.511	0.521
Uttar Pradesh	0.631	0.640	0.649	0.657	0.666	0.675	0.683	0.691	0.699	0.707
Tamil Nadu	0.553	0.564	0.574	0.584	0.594	0.604	0.613	0.623	0.632	0.641
Average	0.582	0.591	0.600	0.609	0.618	0.627	0.636	0.644	0.653	0.661

States	2003	2004	2005	2006	2007	2008	2009	2010	2011	Mean Efficiency	Rank
Andhra Pradesh	0.550	0.560	0.570	0.581	0.590	0.600	0.610	0.619	0.629	0.543	14
Assam	0.482	0.493	0.504	0.515	0.526	0.536	0.547	0.557	0.567	0.475	16
Bihar	0.666	0.674	0.683	0.691	0.699	0.707	0.715	0.722	0.729	0.660	7
Orissa	0.562	0.573	0.583	0.593	0.602	0.612	0.621	0.631	0.640	0.556	12
West Bengal	0.545	0.556	0.566	0.576	0.586	0.596	0.606	0.615	0.625	0.538	13
Haryana	0.760	0.766	0.773	0.779	0.785	0.791	0.797	0.802	0.808	0.754	3

Punjab	0.622	0.631	0.640	0.649	0.658	0.667	0.675	0.684	0.692	0.615	11
Delhi	0.665	0.674	0.682	0.690	0.698	0.706	0.714	0.722	0.729	0.659	8
Gujarat	0.961	0.962	0.963	0.964	0.965	0.966	0.967	0.968	0.969	0.960	1
Madhya Pradesh	0.755	0.762	0.769	0.775	0.781	0.787	0.793	0.799	0.804	0.750	4
Maharashtra	0.937	0.939	0.941	0.942	0.944	0.946	0.947	0.949	0.951	0.935	2
Rajasthan	0.667	0.675	0.683	0.691	0.700	0.707	0.715	0.723	0.730	0.660	6
Karnataka	0.638	0.647	0.656	0.665	0.673	0.682	0.690	0.698	0.706	0.632	10
Kerala	0.532	0.543	0.553	0.564	0.574	0.584	0.594	0.603	0.613	0.525	15
Uttar Pradesh	0.715	0.722	0.730	0.737	0.744	0.751	0.758	0.764	0.771	0.709	5
Tamil Nadu	0.650	0.659	0.667	0.676	0.684	0.692	0.700	0.708	0.716	0.643	9
Average	0.669	0.677	0.685	0.693	0.701	0.708	0.716	0.723	0.730	0.663	

Source: Author's Own Calculation based on ASI data

the years is one area of concern the government should look into. Direction of technical change is another area firms should concentrate on.

References

Aigner, D., Lovell, C. K. & Schmidt, P. (1977),"Formulation and Estimation of Stochastic Frontier Production Function Models", *Journal of Econo-metrics*, 6(1): 21-37.

Babu, S & Natarajan, R.R. (2013)**, "**Growth and Spread of Manufacturing Productivity across Regions in India, Springer Plus, http://www.springerplus.com/content/2/1/5

Bhandari, A. K. & P. Maiti (2007), "Efficiency of Indian Manufacturing firms: Textile Industry as a case Study", *International Journal of Business & Economics,* 6(1): 71-88

Bhandari, A. K.& P. Maiti (2012),"Efficiency of the Indian Leather Firms: Some Results Obtained Using the Two Conventional Methods, *Journal of Productivity Analysis*, 37: 73-93

Coelli, T. J. (1996), A Guide to FRONTIER Version 4.1: AComputer Program for Stochastic Frontier Production and Cost Function Estimation, Centre for Efficiency & Productivity Analysis(CEPA) working papers, 7, Department of Econometrics, University of New England, Armidale, NSW 2351, Australia.

Deb, A.K. & Ray, S.C. (2013), Economic Reforms and Total Factor Productivity Growth of Indian Manufacturing: An Inter-State Analysis, University of Connecticut, Department of Economics Working Paper Series, Working Paper No. 2013-04R

Kim, S. & Han, G. (2001): "A Decomposition of Total Factor Productivity Growth in Korean Manufacturing Industries: A Stochastic Frontier Approach", *Journal of Productivity Analysis*, 16(3): 269-81.

Kodde, D.A & F.C. Palm (1986), Wald Criteria for Jointly Testing Equality &Inequality Restrictions, *Econometrica,* 54(5): 1243-48.

Kumar, S. (2005), "A Decomposition of Total Productivity Growth: A Regional Analysis of Indian Industrial Manufacturing Growth", *International Journal of Productivity and Performance Measurement*, 33(3/4): 311-31.

Kumar, Surender &Managi, Shunsuke (2009), "Productivity and Convergence in India: State Level Analysis",Munich Personal RePEc Archive Paper No. 23738, (Available at http:// mpra.ub.uni-muenchen,de)/23738

Natarajan, R. &Duraiswamy, Malathy (2008), "Efficiency and Productivity in the Indian Unorganized Manufacturing Sector: Did Reforms Matter?"*International Review of Economics*, 2008, 55(4): 373-99

Applied Earth Science
Transactions of the Institutions of Mining and Metallurgy

ISSN: 2572-6838 (Print) 2572-6846 (Online) Journal homepage: https://tandfonline.com/loi/yaes21

Evaluation of ASTER TIR data-based lithological indices in Malanjkhand Copper Mines of Madhya Pradesh, India

Subhanil Guha & Himanshu Govil

To cite this article: Subhanil Guha & Himanshu Govil (2019): Evaluation of ASTER TIR data-based lithological indices in Malanjkhand Copper Mines of Madhya Pradesh, India, Applied Earth Science, DOI: 10.1080/25726838.2019.1684018

To link to this article: https://doi.org/10.1080/25726838.2019.1684018

Published online: 03 Nov 2019.

APPLIED EARTH SCIENCE (TRANS. INST. MIN. METALL. B)
https://doi.org/10.1080/25726838.2019.1684018

The Institute of Materials, Minerals and Mining
AusIMM THE MINERALS INSTITUTE
Taylor & Francis
Taylor & Francis Group

RESEARCH ARTICLE

Evaluation of ASTER TIR data-based lithological indices in Malanjkhand Copper Mines of Madhya Pradesh, India

Subhanil Guha and Himanshu Govil

Department of Applied Geology, National Institute of Technology, Raipur, India

ABSTRACT

This study focuses on the Malanjkhand Copper Mines area of Madhya Pradesh, India and compares different types of quartz, feldspar and mafic remote sensing indices used for the detection of quartz, feldspar and mafic minerals using Advanced Spaceborne Thermal Emission and Reflection Radiometer (ASTER) thermal infrared (TIR) bands. Our data indicate that these lithological indices are useful for delineating quartz, feldspar or mafic minerals. Correlation matrices generated for various lithological indices indicate that both Guha's (GMI) and Ninomiya's (NMI) mafic indices yield nearly identical results. In addition, Guha's quartz index (GQI) yields significantly better results than Ninomiya's quartz index (NQI) during the identification of the quartz content. This study also shows that GQI is comparable with the Rockwall and Hofstra's quartz index (RHQI) for the identification of the quartz content. Hence, ASTER TIR data-based remote sensing indices play a key role in lithological mapping.

ARTICLE HISTORY
Received 12 August 2019
Revised 17 October 2019
Accepted 17 October 2019

KEYWORDS
ASTER; feldspar; mafic; quartz; thermal infrared

Introduction

Lithological mapping is one of the most important tasks for geological exploration. Earth observation techniques play a major role in lithological and mineralogical mapping. The visible and near-infrared (VNIR) bands and the short wave infrared (SWIR) bands of satellite data are less effective for detecting quartz and feldspar minerals (Salisbury and Walter, 1989). On the other hand, thermal infrared (TIR) bands of the electromagnetic spectrum are capable of delineating these minerals as Si–O bonds vibrate within the TIR region (Kahle, 1976; Karakassides et al., 1999; Tian et al., 2010). A little discussion is found about the TIR region for mineral identification compared to the VNIR or SWIR regions due to the less availability of satellite sensors in the TIR domain.

Advanced Spaceborne Thermal Emission and Reflection Radiometer (ASTER) satellite sensor has three VNIR bands (bands 1–3), six SWIR bands (bands 4–9), and five TIR bands (bands 10–14). ASTER VNIR and SWIR bands have been used extensively in the mapping of clay, carbonate, aluminium hydroxide, and iron hydroxide (Zhang et al., 2007). Moreover, the different combinations of ASTER TIR bands have also been used in differentiating various types of rock (Ding et al., 2014; Kalinowski and Oliver, 2004; Ninomiya et al., 2005; Rajendran and Nasir, 2014).

Some geoscientists applied ASTER TIR bands in generating rocks and mineral indices to show the basic mineral content in the lithological variation (Chen and Wang, 2007; Ding et al., 2014, 2015; Ninomiya et al., 2005; Guha and Kumar, 2016). Ninomiya et al. (2005) applied some selected lithological properties to propose a series of ASTER TIR band-based lithological indices for quartz, mafic, feldspar, and carbonate rock detection (Bertoldi et al., 2011; Ding et al., 2014; Ninomiya et al., 2005; Rowan et al., 2005). Ding et al. (2014) show that mafic-ultramafic rock indices are suitable for different natural conditions, while the quartz rock indices are effective in higher elevation. Ding et al. (2015) proposed a quartoze-mafic-feature-space model to extract felsic rocks. Guha and Kumar (2016) derived three rock indices (quartz, feldspar, and mafic) for lithological mapping in different environmental conditions. The present study compares different lithological indices for detecting quartz, feldspar, and mafic minerals in various types of rocks using ASTER TIR bands in an Indian mining area.

Study area and geology

Malanjkhand Copper Mines of Madhya Pradesh, India has been selected as the study area (Figure 1) for the present research work. It is located in the south-east corner of Madhya Pradesh, very near to the border of Chhattisgarh. This entire region is composed of felsic and mafic rocks in a significant amount. Granitoid or quartz-enriched felsic rock has a combination of quartz, mafic, and feldspar minerals. The study area is composed of the following geological formations – Malanjkhand granitoid complex, Malanjkhand copper

CONTACT Subhanil Guha subhanilguha@gmail.com

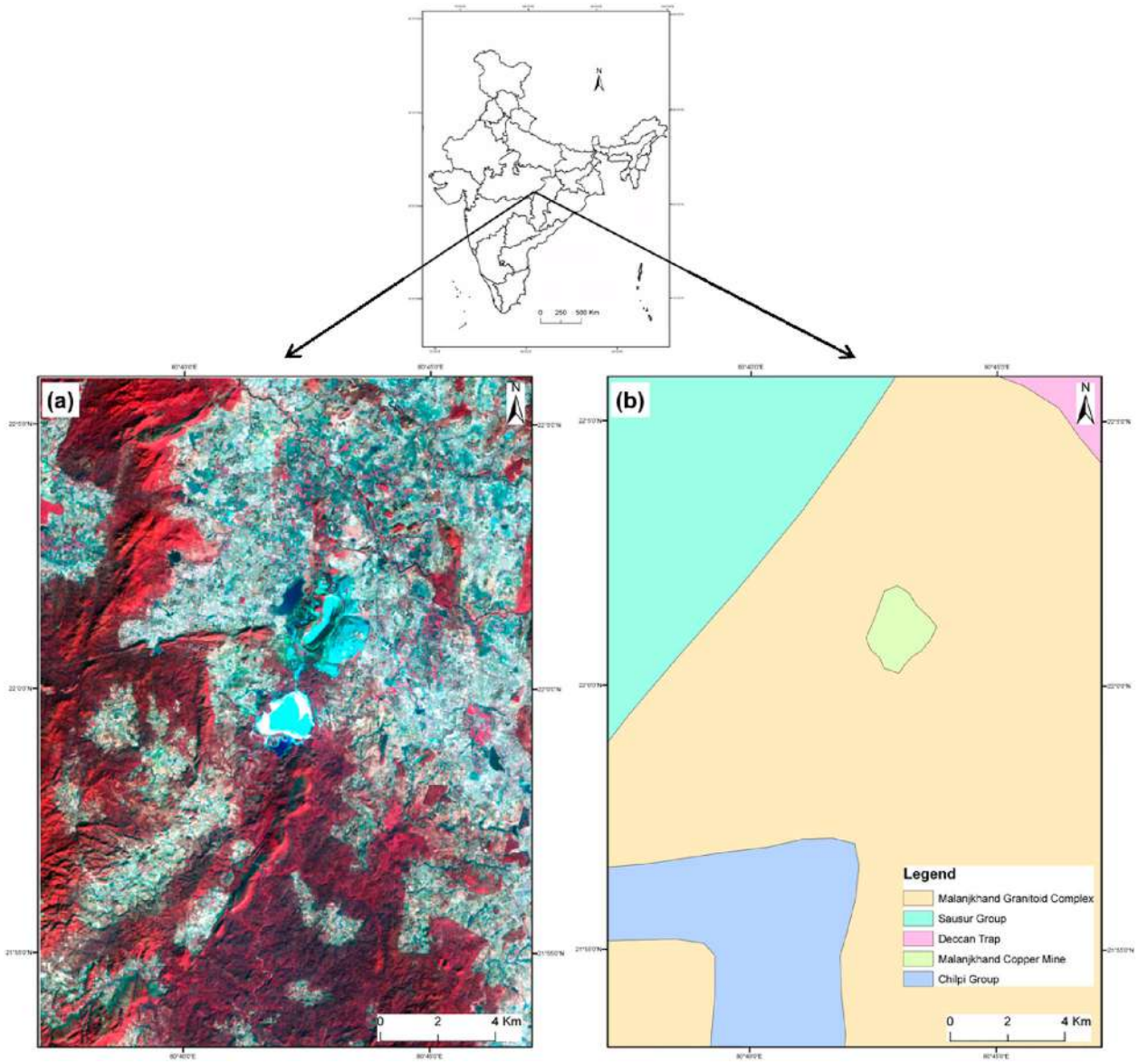

Figure 1. Location of the study area: (a) Satellite image (b) Geological map. (Inset: Map of India).

mines, Sausur group, Chilpi group, and Deccan trap. In the satellite image, Malanjkhand copper mines have been presented as the dark cyan colour at the central part of the study area (Figure 1(a)). Published geological map of the study area from the Geological Survey of India has been used as the reference map for comparing the different lithological indices (Figure 1(b)).

Materials and methods

Table 1 represents the general information on thermal bands of ASTER data. The wavelength of TIR bands ranges from 8.125 to 11.650 µm. The spatial resolutions of all the ASTER TIR bands are 90 m. Figure 2 represents the emissivity profiles of quartz and feldspar minerals in ASTER TIR bands. Band 12 reflects the lowest emissivity value, whereas bands 10 and 13 indicate the higher emissivity values for quartz mineral. ASTER band 11 has a lower emissivity than band 10 for feldspar mineral (Figure 2). ASTER band 13 indicates the lowest emissivity, whereas bands 12 and 14 have higher emissivity for mafic rocks and minerals (Son et al., 2014). A significant reverse trend of emissivity values for ASTER TIR bands 11 and 12 is observed for quartz and feldspar minerals (Son et al., 2014).

Table 1. General information on ASTER TIR bands.

ASTER granule ID	TIR bands	Spectral wavelength (µm)	Spatial resolution (m)	Radiometric resolution
ASTB070414051954	10	8.125–8.475	90	12 bits
Date: 14 April 2007	11	8.475–8.825	90	12 bits
	12	8.925–9.275	90	12 bits
	13	10.25–10.95	90	12 bits
	14	10.95–11.65	90	12 bits

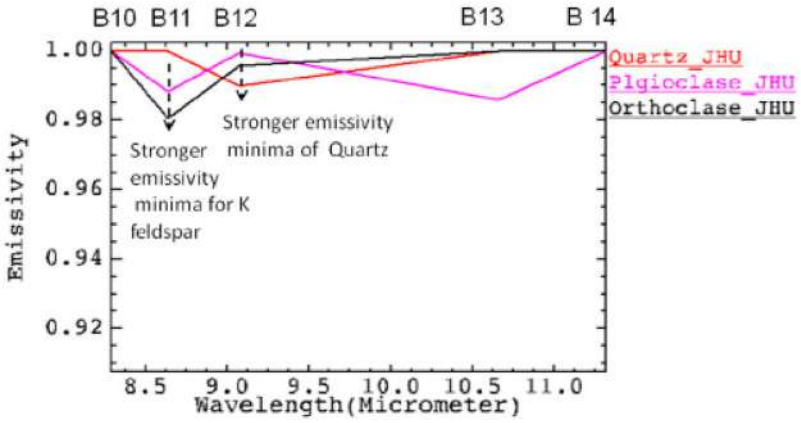

Figure 2. Emissivity profiles of quartz and feldspar in ASTER TIR bands. (Source: Guha and Kumar, 2016).

ASTER data acquired on April 14 2007 has been used for the present study. The acquired ASTER data were radiometrically and geometrically corrected. To get radiance-at-sensor data, the TIR bands have been radiation-calibrated. The TIR radiance data have been atmospherically corrected (Gillespie et al., 1998) and the emissivity normalization algorithm has been applied for deriving temperature and emissivity data (Tian et al., 2006). The lithological indices applied for detecting quartz, mafic, and feldspar minerals have been retrieved using TIR bands of ASTER sensor. In earlier studies, Guha and Kumar (2016) proposed three lithological indices based on the TIR bands of ASTER data. They used all the five TIR bands in determining the lithological indices. Guha's quartz index (GQI) is determined by using band 10, 12, and 13. Moreover, bands 12, 13, and 14 are used for developing Guha's mafic index (GMI). Guha's feldspar index (GFI) is estimated by applying band 10, 11, and 12 of ASTER data.

Guha's lithological indices have been described by the following equations (Guha and Kumar, 2016):

$$\textit{Guha's}\ \text{quartz index (GQI)} = \frac{\text{band10}}{\text{band12}} \times \frac{\text{band13}}{\text{band12}} \quad (1)$$

$$\textit{Guha's}\ \text{mafic index (GMI)} = \frac{\text{band12}}{\text{band13}} \times \frac{\text{band14}}{\text{band13}} \quad (2)$$

$$\textit{Guha's}\ \text{feldspar index (GFI)} = \frac{\text{band10}}{\text{band11}} \times \frac{\text{band12}}{\text{band11}} \quad (3)$$

GQI, GMI, and GFI are generally used to detect the rocks with high quartz content, high mafic minerals content, and high feldspar content, respectively. In the domain of geological remote sensing, Ninomiya's lithological indices achieve global acceptance. Quartz index of Ninomiya (NQI) and mafic index of Ninomiya (NMI) are considered as the two existing well-established quartz and mafic indices, respectively (Ninomiya et al., 2005). NQI uses band 10, 11, and 12 of ASTER data. NMI only needs band 12 and 13. Besides, Rockwall and Hofstra (2008) proposed another quartz index (RHQI) by using ASTER TIR band 10, 11, 12, and 13.

Ninomiya's lithological indices (NQI, NMI) and Rockwall and Hofstra's quartz index (RHQI) have been described by the following equations:

$$\textit{Ninomiya's}\ \text{quartz index (NQI)} = \frac{\text{band11} \times \text{band11}}{\text{band10} \times \text{band12}} \quad (4)$$

$$\textit{Ninomiya's}\ \text{mafic index (NMI)} = \frac{\text{band12}}{\text{band13}} \quad (5)$$

$$\textit{Rockwall and Hofstra's}\ \text{quartz index (RHQI)} = \frac{\text{band11}}{\text{band10} + \text{band12}} \times \frac{\text{band13}}{\text{band12}} \quad (6)$$

The present study compares GQI with NQI in detecting quartz minerals and compares GMI with NMI to detect mafic minerals. RHQI is also compared to GQI for quartz content detection.

Results

The study attempts to compare the various lithological indices for identifying mafic, quartz, and feldspar minerals. Figure 3 represents ASTER TIR radiance composite images for quartz minerals detection. It appears that granites and quartz-rich granites are differentiated from mafic-rich gneiss as yellow colour produced in the composite image of band 14:13:12 as R:G:B band combination (Figure 3(a)). The quartz appears as bluish colour in the composite image of band 12:11:10 as R:G:B band combination (Figure 3(b)). Red tint colour indicates quartz content in the composite image of band 14:12:10 as R:G:B band combination (Figure 3(c)). Quartz appears as cyan colour in the composite image of band 11:14:13 as R:G:B band combination (Figure 3(d)). NQI and NMI are the two well-established existing rock bearing indices for distinguishing quartz and mafic minerals in various types of lithological configurations. GQI reflects significant results compared to the NQI in the delineation of quartz content

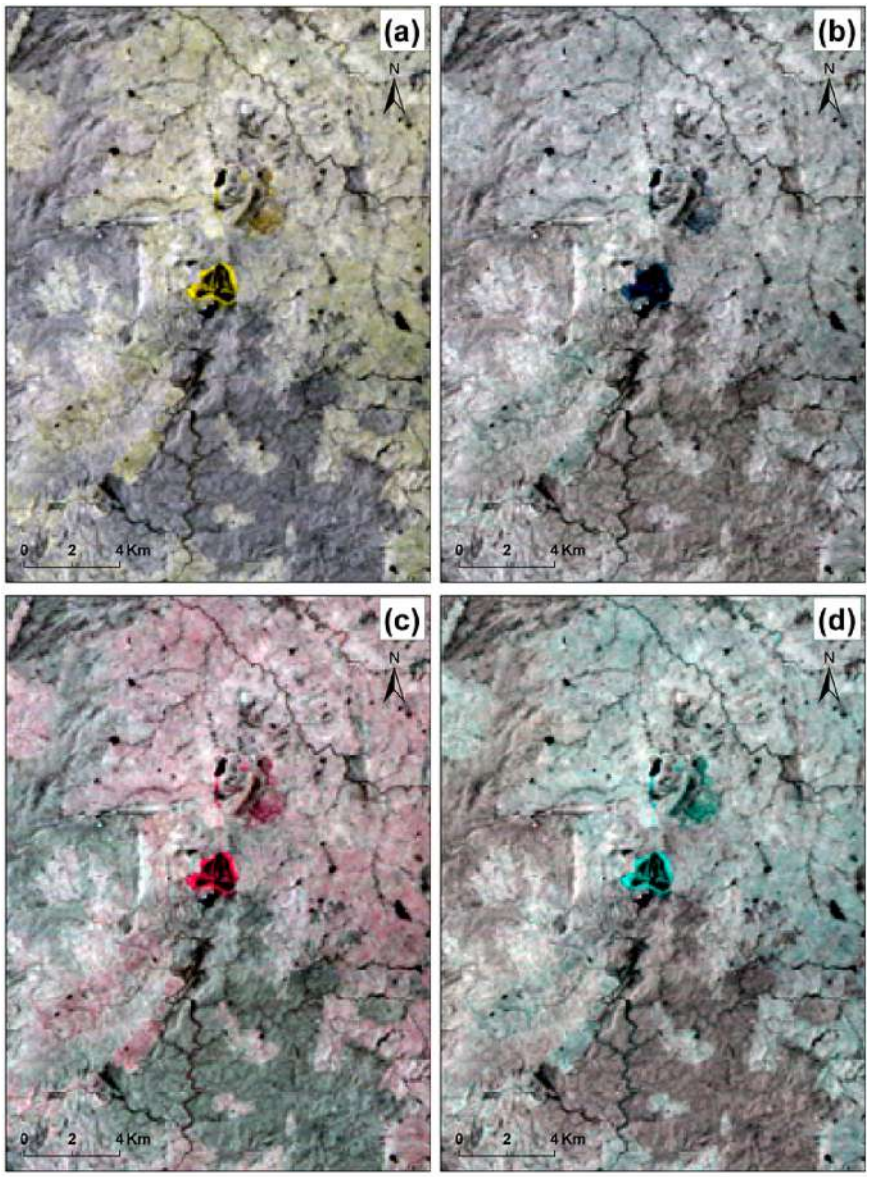

Figure 3. Quartz minerals detected in ASTER TIR radiance composite images: (a) yellow colour in band 14:13:12 as R:G:B; (b) bluish colour in band 12:11:10 as R:G:B; (c) red tint colour in band 14:12:10 as R:G:B; (d) cyan colour in band 11:14:13 as R:G:B.

(Figure 4(a,b)). Quartz-enriched rocks are found as dark colour and bright colour in NQI and GQI images, respectively due to the different emissivity values for quartz and feldspar in TIR bands. GQI image is also compared to the RHQI image. In the RHQI image, the emittance value for quartz is higher in band 11 (Ninomiya et al. 2005), whereas the emittance value for quartz is also high in band 13 compared to band 12 (Guha and Kumar, 2016). Thus, RHQI is used to delineate quartz content in granite and alkali granite (Figure 4(c)). In GFI image, feldspar particles appear as brighter tone in alkali granite (Figure 4(d)). GMI and NMI build a strong correlation and they are complementary to each other (Figure 4(e,f)). A relatively weak correlation (−0.053) is found between GQI and NQI, whereas GMI and NMI show a strong (0.835) correlation (Table 2). However, GQI is comparable with RHQI in the identification of quartz-enriched granitoid. GQI and RHQI build a very high correlation (0.793).

GFI and GQI have a very weak positive correlation (0.056) because generally feldspar content is slowly increased with the gradual increase of quartz content. GMI and GFI are positively correlated with a regression value of 0.330 as feldspar content is proportionately increased with the mafic contents. GQI and GMI are negatively correlated with a very high regression value of −0.722 because quartz content is rapidly increased with the decrease of mafic contents.

Discussion

The lithological indices can play a significant method for the detection of quartz, mafic, and feldspar minerals. In delineating quartz mineral, GQI is more effective compared to NQI (Figure 4(a,b)). RHQI and GQI are almost equally able to identify quartz content. GMI also provides a reliable comparison with NMI for the delineation of mafic minerals (Figure 4(e,f)). GMI

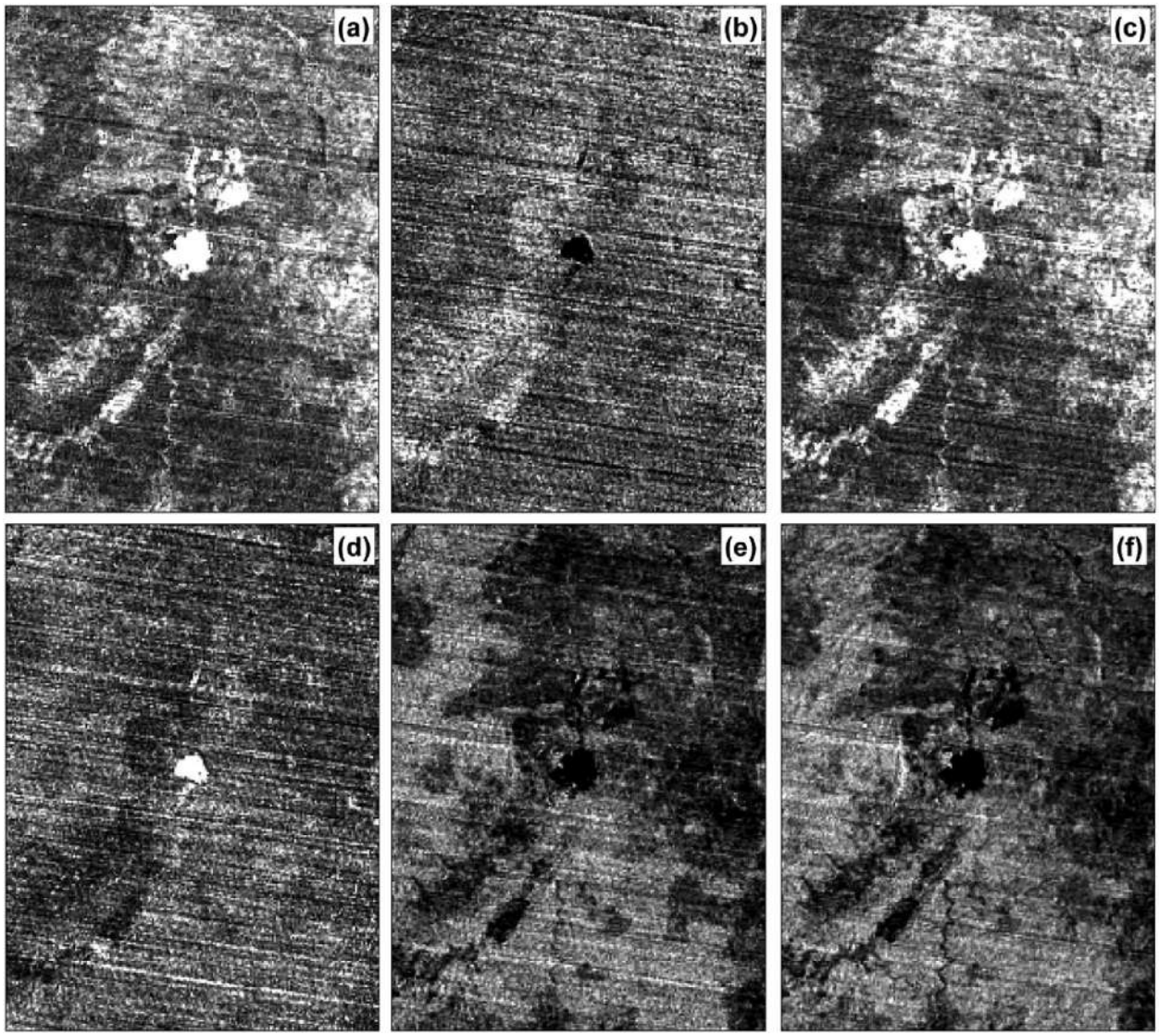

Figure 4. Images of different lithological indices: (a) GQI image; (b) NQI image; (c) RHQI image; (d) GFI image; (e) GMI image; (f) NMI image.

Table 2. Correlation matrix of various lithological indices.

	GQI	NQI	RHQI	GFI	GMI	NMI
GQI	1.000	−0.056	0.792	0.056	−0.722	−0.926
NQI	−0.056	1.000	0.491	−0.999	−0.333	−0.078
RHQI	0.793	0.491	1.000	−0.488	−0.871	−0.906
GFI	0.056	−0.999	−0.488	1.000	0.330	0.075
GMI	−0.722	−0.333	−0.871	0.330	1.000	0.835
NMI	−0.926	−0.078	−0.906	0.075	0.835	1.000

and NMI are highly correlated (0.835) but the relationship is weak (−0.056) between NQI and GQI (Table 2). GQI and RHQI are also positively correlated with a high regression value (0.792) and act effectively to determine quartz content in granite and alkali granite rocks. The results are significantly comparable to the published geological map.

Conclusion

These ASTER TIR band-based remote sensing indices can play a key role in the lithological mapping of an inaccessible part. GMI and NMI are equally able to detect mafic minerals. GQI yields significantly better results than NQI to detect quartz content. GQI is also comparable with RHQI for the detection of the quartz content. Some specific statistical parameters are used in deriving these lithological indices. Thus, the applicability of these indices can be examined by applying different statistical parameters. The capability of the indices can be checked under different environmental conditions. These lithological indices can be modified or TIR band-based some new rock indices can be introduced for enhancing the effectiveness to identify more lithological compositions.

Acknowledgements

The authors are thankful to the United States Geological Survey (USGS) and National Aeronautics and Space Administration (NASA) Jet Propulsion Laboratory (JPL). The authors also thank Dr Arindam Guha of National Remote Sensing Centre, India and two anonymous reviewers for their beneficial comments.

Disclosure statement

No potential conflict of interest was reported by the authors.

References

Bertoldi L, Massironi M, Visona D, Carosi R, Montomoli C, Gubert F. 2011. Mapping the Buraburi granite in the Himalaya of Western Nepal: remote sensing analysis in a collisional belt with vegetation cover and extreme variation of topography. Remote Sens Environ. 115 (5):1129–1144.

Bose MK. 1997. Igneous petrology. Kolkata: World Press.

Chen J, Wang AJ. 2007. The pilot study on petrochemistry components mapping with ASTER thermal infrared remote sensing data. J Remote Sens. **11**:601–608.

Ding C, Liu X, Liu W, Liu M, Li Y. 2014. Mafic and ultramafic and quartz-rich rock indices deduced from ASTER thermal infrared data using a linear approximation to the Planck function. Ore Geol Rev. **60**:161–173.

Ding C, Xuqing L, Xiangnan L, Liting Z. 2015. Quartzose–mafic spectral feature space model: a methodology for extracting felsic rocks with ASTER thermal infrared radiance data. Ore Geol Rev. **66**:283–292.

Gillespie A, Rokugawa S, Matsunaga T, Cothern JS, Hook S, Kahle AB. 1998. A temperature and emissivity separation algorithm for Advanced Spaceborne Thermal Emission and Reflection Radiometer (ASTER) images. IEEE Trans Geosci Remote Sens. **36**:1113–1126.

Guha A, Kumar VK. 2016. New ASTER derived thermal indices to delineate mineralogy of different granitoids of an Archaean Craton and analysis of their potentials with reference to Ninomiya's indices for delineating quartz and mafic minerals of granitoids—An analysis in Dharwar Craton, India. Ore Geol Rev. **74**:76–87.

Kahle AB. 1976. Thermal inertia imaging: a new geologic mapping tool. Geophys Res Lett. **3**:419–421.

Kalinowski A, Oliver SA. 2004. ASTER mineral index Processing Manual. http://www.ga.gov.au/image_cache/GA7833.pdf.

Karakassides MA, Gournis D, Petridis D. 1999. An infrared reflectance study of Si-O vibrations in thermally treated alkalisaturated montmorillonites. Clay Miner. **34**:429–438.

Ninomiya Y, Fu B, Cudahy TJ. 2005. Detecting lithology with Advanced Spaceborne Thermal Emission and Reflection Radiometer (ASTER) multispectral thermal infrared radiance-at-sensor data. Remote Sens Environ. **99**:127–139.

Rajendran S, Nasir S. 2014. ASTER spectral sensitivity of carbonate rocks—study in Sultanate of Oman. Adv Space Res. **53**:656–673.

Rockwall BW, Hofstra AH. 2008. Identification of quartz and carbonate minerals across northern Nevada using ASTER thermal infrared emissivity data-implications for geologic mapping and mineral resource investigations in well-studied and frontier areas. Geosphere. **4**:218–246.

Rowan LC, Mars JC, Simpson CJ. 2005. Lithologic mapping of the Mordor, NT, Australia ultramaficcomplex by using the Advanced Spaceborne thermal Emission and Reflection Radiometer (ASTER). Remote Sens Environ. 99(1–2):105–126.

Salisbury JW, Walter LS. 1989. Thermal infrared (2.5–13.5μm) spectroscopic remote sensing of igneous rock types on particulate planetary surfaces. J Geophys Res. 94(B7):9192–9202.

Son Y-S, Kang M-K, Yoon W-J. 2014. Lithological and mineralogical survey of the Oyu Tolgoi region, south-eastern Gobi, Mongolia using ASTER reflectance and emissivity data. Int J Appl Earth Obs Geoinf. **26**:205–216.

Tian GL, Liu QH, Yu T, Zhang Y, Chen LF, Li XW, et al. 2006. Thermal infrared remote sensing. Beijing: Electronics Industry Press; p. 1–232.

Tian R, Seitz O, Li M, Hu W, Chabal Y, Gao J. 2010. Infrared characterization of interfacial Si−O bond formation on silanized flat SiO2/Si surfaces. Langmuir. 26(7):4563–4566.

Zhang X, Pazner M, Duke N. 2007. Lithologic and mineral information extraction for gold exploration using ASTER data in the south Chocolate Mountains (California). ISPRS J Photogramm Remote Sens. **62**:271–282.

Source details

Feedback > Compare sources >

Applied Earth Science: Transactions of the Institute of Mining and Metallurgy

Scopus coverage years: from 2018 to 2023

Publisher: SAGE

ISSN: 2572-6838 E-ISSN: 2572-6846

Subject area: Earth and Planetary Sciences: Geotechnical Engineering and Engineering Geology

Earth and Planetary Sciences: Earth and Planetary Sciences (miscellaneous) Earth and Planetary Sciences: Geochemistry and Petrology

Source type: Journal

View all documents > Set document alert Save to source list

CiteScore 2022
2.0

SJR 2022
0.282

SNIP 2022
0.423

CiteScore CiteScore rank & trend Scopus content coverage

Routledge
Taylor & Francis Group

Geografisk Tidsskrift-Danish Journal of Geography

ISSN: 0016-7223 (Print) 1903-2471 (Online) Journal homepage: https://www.tandfonline.com/loi/rdgs20

A case study on the relationship between land surface temperature and land surface indices in Raipur City, India

Subhanil Guha, Himanshu Govil, Anindita Dey & Neetu Gill

To cite this article: Subhanil Guha, Himanshu Govil, Anindita Dey & Neetu Gill (2020): A case study on the relationship between land surface temperature and land surface indices in Raipur City, India, Geografisk Tidsskrift-Danish Journal of Geography, DOI: 10.1080/00167223.2020.1752272

To link to this article: https://doi.org/10.1080/00167223.2020.1752272

Published online: 13 May 2020.

GEOGRAFISK TIDSSKRIFT-DANISH JOURNAL OF GEOGRAPHY
https://doi.org/10.1080/00167223.2020.1752272

A case study on the relationship between land surface temperature and land surface indices in Raipur City, India

Subhanil Guha [a], Himanshu Govil [a], Anindita Dey [b] and Neetu Gill [c]

[a]Department of Applied Geology, National Institute of Technology Raipur, Chhattisgarh, India; [b]Department of Geography, Nazrul Balika Vidyalaya, Guma, West Bengal, India; [c]Chhattisgarh Council of Science and Technology, Raipur, Chhattisgarh, India

ABSTRACT

Land surface temperature (LST) depends primarily on the land surface material and climatic conditions. The present study focuses on deriving the LST of Raipur City and generating the relationship between LST and some land surface indices, like NDVI, NDWI, NDBI, NMDI, and NDBaI for better land-use planning and environmental management inside the city. These land surface indices respond in different ways with the changes of LST in an urban landscape. There are only a few numbers of research works available on the relationship of LST and land surface indices in a tropical city for pre-monsoon season. The present study has been performed on a total of fifteen multi-date Landsat data sets of the pre-monsoon season from 2002, 2006, 2010, 2014, and 2018. The mono-window algorithm has been applied in retrieving the LST. Results show that LST builds a positive relation with NDBI, NDBaI, and NDWI and a negative relation with NDVI and NMDI. These relationships are stronger in the area below mean LST (low LST zones) and weaker in the area above mean LST (high LST zones). It indicates that the values of LST are largely influenced by the different land surfaces, like vegetation, water, soil, and built-up area.

ARTICLE HISTORY
Received 11 September 2018
Accepted 20 March 2020

KEYWORDS
Land surface indices; Land Surface Temperature (LST); landsat data sets; NDVI

1. Introduction

Land surface temperature (LST) analysis is widely considered as one of the most important parameters in land surface and town planning where thermal impacts of changing land surface may regulate the generation of high and low LST zones in any heterogeneous urban area (Arnfield, 2003; Mirzaei, 2015; Rinner & Hussain, 2011; Rizwan et al., 2008; M. Zhao et al., 2016). The intense effect of LST on some major cities (e.g., Beijing, Columbus, Shanghai, Baltimore, Chicago, etc.) in the world is growing at an alarming rate and is directly related to the land surface categories (Chun & Guldmann, 2014; Coseo & Larsen, 2014; Dai et al., 2018; Kim & Guldmann, 2014; W. Q. Zhou et al., 2011; Zhang et al., 2014; H. Zhang et al., 2013). Various types of land surface (vegetation, water, impervious surface area, etc.) indices were applied in urban heat island (UHI) related remote sensing study to determine the changed pattern of LST in different types of natural and man-made landscape systems (Amiri et al., 2009; Kuang et al., 2015; Li et al., 2011; Ogashawara et al., 2012; Peng et al., 2016; Song et al., 2014). Some recent articles discussed the statistical linear correlation between LST and some selected land surface indices for separate study areas like Brisbane (Deilami & Kamruzzaman, 2017), Raipur (Guha & Govil, 2020; S. Guha et al., 2019, 2017), Shanghai (Nie et al., 2016), Addis Ababa (Feyisa et al., 2016), Mexico (Lopez et al., 2017), Philadelphia (Pearsall, 2017), Florence and Naples (S. Guha et al., 2018), etc. Long temporal analytical relationships of LST with the natural and artificial influencing factors in different parts of the world have thoroughly been assessed in many recent relevant articles (Adegoke et al., 2003; Christy & McNider, 2016; Christy et al., 2006, 2009; Davey & Pielke, 2005; Davey et al., 2006; Fall et al., 2010, 2009; Faqe Ibrahim, 2017; Hanamean Jr. et al., 2003; Lin et al., 2015; R.A. Pielke et al., 2002, 2007a, 2007b; Quan et al., 2016; Strack et al., 2008).

A more recent direction includes the application of some sophisticated statistical techniques to estimate the seasonal variability of LST in the urban area. Cui and de Foy (2012) showed that vegetation cover, daytime insolation, and atmospheric stability are related to seasonal UHI variations in Mexico City, Mexico. W. Zhou et al. (2014) built relationships between land cover and UHI and their seasonal variability in Baltimore, United State of America (USA). Haashemi et al. (2016) presented a seasonal variability in the correlation between LST and fractional vegetation cover, impervious surfaces, albedo, and elevation in Tehran, Iran.

In later studies, seasonal variation in the UHI effect was critically analysed. Seasonal effects in urban thermal

CONTACT Subhanil Guha subhanilguha@gmail.com

patterns were determined by spatial regression analyses in Ohio, USA (Chun & Guldmann, 2018). Multiple statistical methods were integrated to show the seasonal contrast of some land surface indices for LST distribution in Shenzhen, China (Peng et al., 2018). A seasonal variation in LST and selected land surface indices was investigated in Jaipur, India (Mathew et al., 2017). A trend and seasonal decomposition model for LST change over Beijing, China was investigated (Lai et al., 2018). A regression-based model was performed to determine the average annual and seasonal trend of LST in peninsular Spain (Khorchani, Martin-Hernandez et al., 2018, Khorchani, Vicente-Serrano et al., 2018). Urban and rural LST were analysed with their climatic conditions in 31 cities of China (Yao et al., 2018). A seasonal analysis of eighty-six major cities of China presented that UHI and cloud cover percentages are negatively correlated (Lai et al., 2018). A landscape source-sink distance index was introduced in quantifying the landscape connectivity and in determining its contribution to LST variations in Beijing, China (Sun et al., 2018). Thus, the researchers tried to analyse the variability of LST in the UHI of urban areas using modern techniques (Govil et al., 2019; S. Guha et al., 2019; Yuan and Bauer, 2007). This paper was simply a case study based on the relationship between land surface temperature and land surface indices in Raipur City, India.

The specific objectives of the study are: (1) to examine the nature of LST in the whole of Raipur City for the pre-monsoon images from 2002 to 2018; and (2) to compare the relationship between LST and some land surface indices, i.e. normalized difference vegetation index (NDVI), normalized difference water index (NDWI), normalized difference built-up index (NDBI), normalized multi-band drought index (NMDI), and normalized difference bareness index (NDBaI) for the whole city, the area above mean LST or high LST zone, and the area below mean LST or low LST zone.

The purpose of the study is the future environmental planning of Raipur City. Raipur is considered as a smart city and many governmental activities are being conducted in recent years for the ecological benefit of the city. The satellite image helps a lot in this city planning. LST of the city is gradually increasing with time and it becomes a genuine research problem. Thermal remote sensing and land surface indices play a major contribution in this field as the LST of the city are primarily determined by the variation of the land surface composition.

2. Study area

Raipur, the largest city of Chhattisgarh state in east-central India, located along the west of Mahanadi River, is the study area for present research work. The latitudinal and longitudinal extent of Raipur City is 21°11′22″ N – 21° 20′02″ N and 81°32′20″ E – 81°41′50″ E, respectively (Figure 1). The elevated landscape of the city is ranged between 219–322 m. Raipur City lies under a tropical wet and dry climate. The mean annual temperature of Raipur City is approximately 27°C. According to the India Meteorological Department, four seasons are observed in Raipur, i.e. pre-monsoon (March-June), monsoon (July-September), post-monsoon (October-November), and winter (December-February). The pre-monsoon or summer months (March-June) are usually hot and remain almost dry. The temperature may rises above 45°C in April and May. The pre-monsoon season has been selected for the present study for examining the nature of LST due to its severe intensity. According to the 2011 census, Raipur City has a total population of 1,010,087, with a sex ratio of 945 females per 1000 males and with a literacy rate of 86.45%.

3. Data sources

A total of fifteen Landsat data sets have been selected to determine the LST and to detect the high and low LST zones over the whole of the Raipur City area (Table 1). The Landsat data sets have freely been downloaded from United States Geological Survey (http://earthexplorer.USGS.gov). LST has been retrieved through thermal infrared bands of Landsat data sets (band 6 for Landsat 5 TM and Landsat 7 ETM+ data, whereas band 10 and 11 for Landsat 8 TIRS data). Green, red, near-infrared, middle infrared, short wave infrared, and thermal infrared bands have been used in generating NDVI, NDWI, NDBI, NMDI, and NDBaI. ERDAS Imagine 9.1 and ArcGIS 9.3 software have been used for performing the research work.

4. Methodology

The present study deals with the fifteen almost cloud-free Landsat datasets of pre-monsoon season for Raipur City. Radiometric and geometric corrections of these data have been performed before generating the land surface indices and LST. Finally, the relationship between LST and the land surface indices has been analysed spatially and temporally. The overall methodological framework of the study has been shown in Figure 2.

4.1. Determination of different land surface indices

NDVI is a widely popular vegetation index used frequently in remote sensing studies (Purevdorj et al., 1998; Tucker, 1979). It is also applied in deriving LST

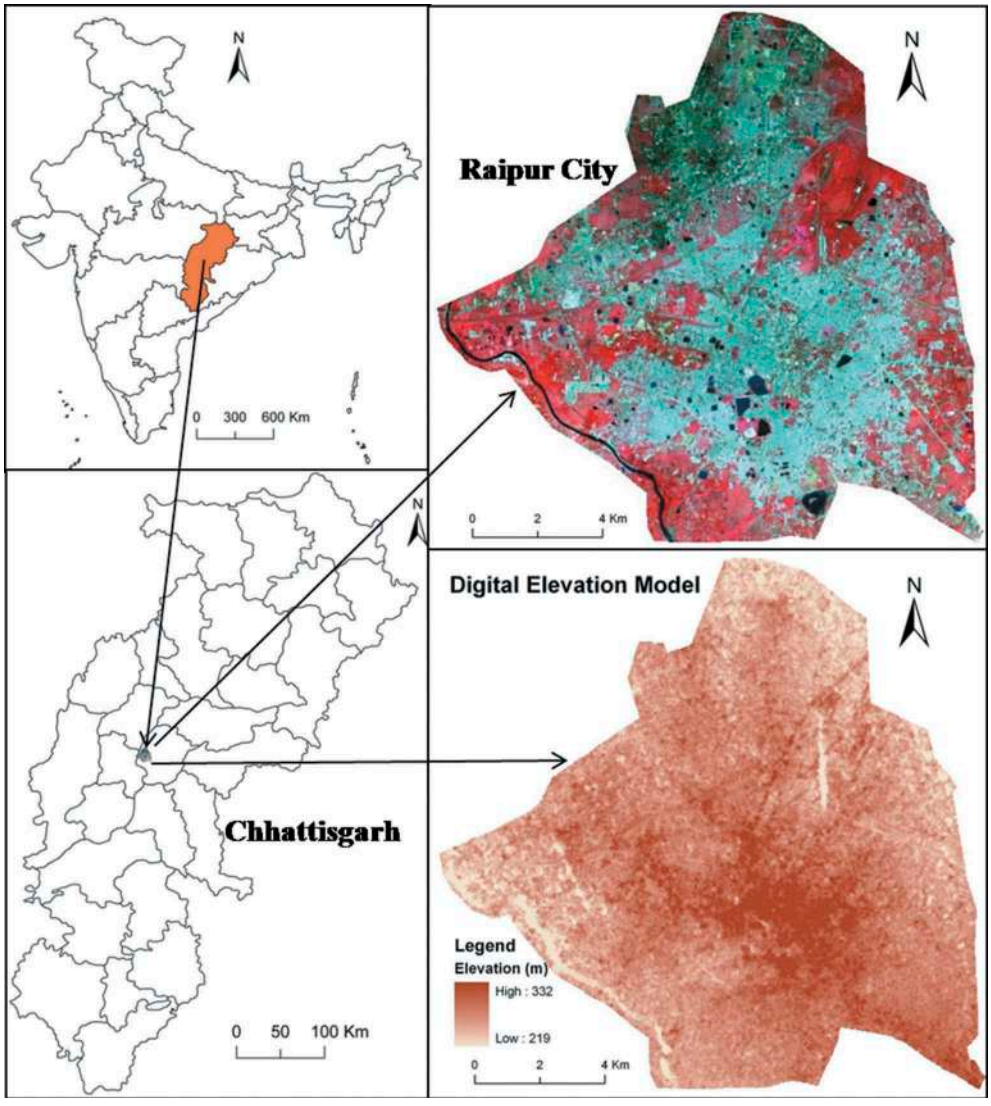

Figure 1. Location of the study area.

Table 1. Specification of multi-date Landsat satellite sensors.

Satellite sensor	Date of acquisition	Time (UTC)	Path/Row	Sun elevation (deg)	Sun azimuth (deg)	Cloud cover (%)	Earth-Sun distance (astronomical unit)
Landsat 7	25 April 2002	04:44:54	142/044	63.79	104.71	0.00	1.01
Landsat 7	11 May 2002	04:44:54	142/044	65.61	94.50	5.00	1.01
Landsat 5	28 April 2006	04:48:00	142/044	65.02	103.39	2.00	1.01
Landsat 5	15 June 2006	04:48:12	142/044	66.33	81.14	4.00	1.02
Landsat 5	7 April 2010	04:47:02	142/044	60.40	116.25	0.00	1.00
Landsat 5	23 April 2010	04:46:59	142/044	63.96	106.44	0.00	1.01
Landsat 5	25 May 2010	04:46:51	142/044	66.54	87.13	0.00	1.01
Landsat 8	17 March 2014	04:26:36	142/044	55.95	129.39	0.00	0.99
Landsat 8	2 April 2014	04:26:19	142/044	60.92	121.72	0.00	0.99
Landsat 8	20 May 2014	04:25:38	142/044	68.56	90.41	5.46	1.01
Landsat 8	5 June 2014	04:25:45	142/044	68.38	83.31	0.02	1.01
Landsat 8	12 March 2018	04:55:43	142/044	54.19	131.17	2.10	0.99
Landsat 8	28 March 2018	04:55:36	142/044	59.30	124.08	0.01	1.00
Landsat 8	15 May 2018	04:55:08	142/044	68.28	93.33	0.30	1.01
Landsat 8	16 June 2018	04:55:01	142/044	67.74	81.10	2.31	1.02

and normally builds a negative relation with LST. NDWI is generally used for water body extraction and it relates positively to LST (McFeeters, 1996). NDBI is another land surface index that is applied in built-up area extraction and normally shows a positive relation with LST (Yuan and M. E. Bauer, 2007). NMDI is also used to extract the

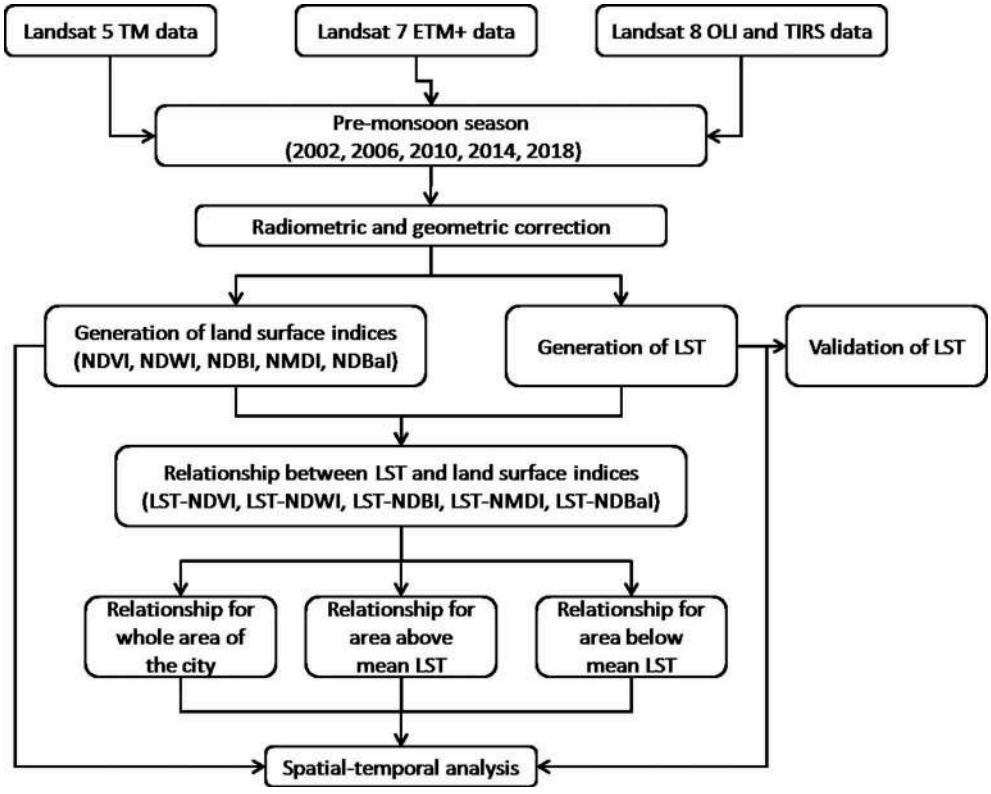

Figure 2. The overall methodological framework of the study.

dry and wet soil and in general, it is negatively related to LST (Zha et al., 2003). NDBaI is generally used for differentiating bare land and semi-bare land and is positively related to LST distribution (H. M. Zhao & Chen, 2005). These five land surface indices (Table 2) have been applied in the present study to examine their relationship with LST in pre-monsoon multi-temporal images.

4.2. Retrieving LST from Landsat thermal band

Landsat TIR data are often used in the identification of UHI zones (Weng, 2001; Weng & Yang, 2004; Z. Zhang et al., 2016). LST derivation using Landsat TIR data becomes popular through the introduction of some algorithms, like mono-window algorithm (Qin et al., 2001), single-channel algorithm (Jimenez-Munoz et al., 2009; Jiménez-Muñoz & Sobrino, 2003), etc. In the present study, LST was derived from Landsat TIR data by using the mono-window algorithm (Qin et al., 2001) where ground emissivity, atmospheric transmittance, and effective mean atmospheric temperature are the three required parameters. At first, the original TIR bands (120 m, 60 m, 100 m) resolution) are resampled into 30 m for further application. The entire procedure is included in the following equations:

$$L_\lambda = RadianceMultiBand \times DN + RadianceAddBand \quad (1)$$

Where, L_λ is the spectral radiance in $Wm^{-2}sr^{-1}\ mm^{-1}$.

$$T_b = \frac{K_2}{\ln\left(\frac{K_1}{L_\lambda} + 1\right)} \quad (2)$$

Where, T_b is the brightness temperature in Kelvin (K), L_λ is the spectral radiance in $Wm^{-2}sr^{-1}\ mm^{-1}$; K_2 and K_1 are calibration constants. For Landsat 8 data, K_1 is 774.89, K_2 is 1321.08 ($Wm^{-2}sr^{-1}\ mm^{-1}$).

Table 2. Description of NDVI, NDWI, NDBI, NMDI, and NDBaI.

Acronym	Description	Formulation	Reference
NDVI	Normalized difference vegetation index	$\frac{NIR-Red}{NIR+Red}$	Tucker, 1979
NDWI	Normalized difference water index	$\frac{Green-NIR}{Green+NIR}$	McFeeters, 1996
NDBI	Normalized difference built-up index	$\frac{SWIR1-NIR}{SWIR1+NIR}$	Zha et al., 2003
NMDI	Normalized multi-band drought index	$\frac{[NIR-(SWIR1+SWIR2)]}{[NIR+(SWIR1+SWIR2)]}$	Wang and Qu, 2007
NDBaI	Normalized difference bareness index	$\frac{SWIR1-TIR}{SWIR1+TIR}$	H. M. Zhao & Chen, 2005

$$F_v = \left(\frac{NDVI - NDVI_{min}}{NDVI_{max} - NDVI_{min}}\right)^2 \quad (3)$$

where, $NDVI_{min}$ is the minimum NDVI value (0.2) for bare soil pixel and $NDVI_{max}$ is the maximum NDVI value (0.5) for healthy vegetation pixel.

$d\varepsilon$is the effect of the geometrical distribution of natural surfaces and internal reflections. For mixed and elevated land surfaces, the value of $d\varepsilon$may be 2%.

$$d\varepsilon = (1 - \varepsilon_s)(1 - F_v)F\varepsilon_v \quad (4)$$

Where, ε_v is vegetation emissivity, ε_5 is soil emissivity, F_v is fractional vegetation, F is a shape factor whose mean is 0.55.

$$\varepsilon = \varepsilon_v F_v + \varepsilon_s(1 - F_v) + d\varepsilon \quad (5)$$

Where, $\varepsilon$is the land surface emissivity. The value of ε is determined by the following equation:

$$\varepsilon = 0.004 * F_v + 0.986 \quad (6)$$

Water vapour content is determined by the following equation:

$$w = 0.0981 * \left[10 * 0.6108 * \exp\left(\frac{17.27 * (T_0 - 273.15)}{237.3 + (T_0 - 273.15)}\right) * RH\right] + 0.1697 \quad (7)$$

Where, w is the water vapour content (g/cm^2), T_0 is the near-surface air temperature in Kelvin (K), RH is the relative humidity (%). These parameters of the atmospheric profile are the average values of 14 stations around Raipur which are obtained from the Meteorological Centre, Raipur and the Regional Meteorological Centre, Nagpur.

$$\tau = 1.031412 - 0.11536w \quad (8)$$

Where, τ is the total atmospheric transmittance, ε is the land surface emissivity.

Raipur City is located in the tropical region. Thus, the following equations are applied to compute the effective mean atmospheric transmittance of Raipur:

$$T_a = 17.9769 + 0.91715T_0 \quad (9)$$

$$T_s = \frac{[a(1 - C - D) + (b(1 - C - D) + C + D)T_b - DT_a]}{C} \quad (10)$$

$$C = \varepsilon\tau \quad (11)$$

$$D = (1 - \tau)[1 + (1 - \varepsilon)\tau] \quad (12)$$

Where, ε is the land surface emissivity, τ is the total atmospheric transmittance, T_b is the at-sensor brightness temperature, T_a is the mean atmospheric temperature, T_0 is the near-surface air temperature, T_5 is the land surface temperature, $a = -67.355351$, $b = 0.458606$.

5. Results and discussion

5.1. Variation of LST distribution

The LST maps retrieved from pre-monsoon multi-temporal Landsat data sets are shown in Figure 3. The average aggregated LST values of 2002, 2006, 2010, 2014, and 2018 have been generated (Table 3). The minimum LST ranges from 22.08°C in 2002 to 33.98°C in 2018. The maximum LST ranges between 36.56°C in 2002 and 50.40°C in 2018. The mean LST value has been increased from 31.91°C (2002) to 43.53°C (2018). Highest LST has been found in the north-western and south-eastern parts of the city. This portion of the area is characterized by open bare land.

5.2. Validation of Landsat data derived LST to MODIS data sets

Before performing any kind of application, validation of derived LST is necessary with *in situ* measurement or with any other satellite sensor. In the present study, MODIS Terra data has been applied for the validation of LST values as a reference image. For any particular date, MODIS and Landsat sensors do not provide images for the same study area. Thus, MOD11A1 data sets (1000 m spatial resolution) of the following specific dates (Table 4) have been taken for the validation of estimated LST.

No precipitation or atmospheric disturbances have been observed in the acquisition date of both Landsat data sets and MOD11A1 images. For MODIS data, the spatial resolution of retrieved LST is 1000 m, whereas, for Landsat 5 TM data, Landsat 7 ETM+ data, and Landsat 8 OLI and TIRS data the resolutions of LST image are 120 m, 60 m, and 100 m, respectively. Despite not performing any upscaling or downscaling procedure, a significant correlation has been found between the mean derived LST from Landsat data sets and MODIS data sets (Table 5).

5.3. Variation in the distribution of NDVI, NDWI, NDBI, NMDI, and NDBaI

All the five land surface indices (NDVI, NDWI, NDBI, NMDI, NDBaI) have been generated using the optical and thermal bands of Landsat data sets. The mean values of the indices for particular years have been generated separately. Figure 4 presents the mean NDVI

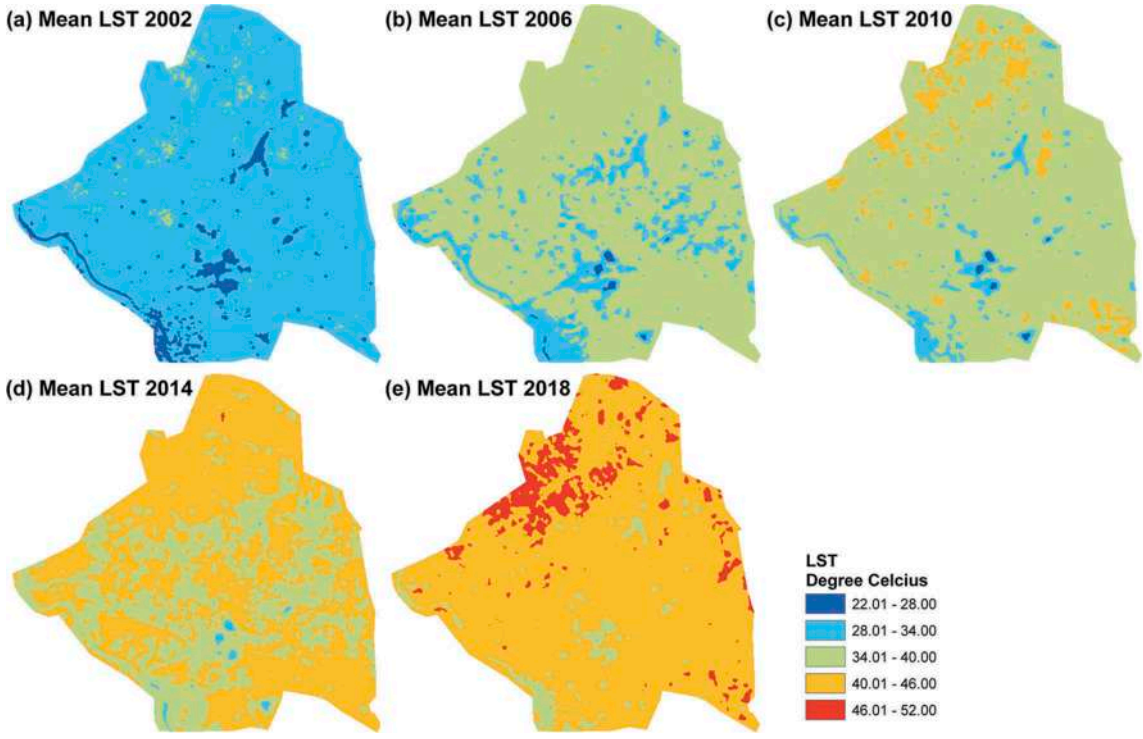

Figure 3. LST maps for the whole of Raipur City for the following years: (a) 2002, (b) 2006, (c) 2010, (d) 2014, and (e) 2018.

Table 3. Spatial distribution of LST (°C) in Landsat data.

Season	LST (minimum)	LST (maximum)	LST (mean)	LST (standard deviation)
25 April 2002	21.88	35.52	31.08	1.70
11 May 2002	22.28	37.60	32.74	1.93
Mean	**22.08**	**36.56**	**31.91**	**1.82**
28- Apr-2006	26.25	41.45	35.79	2.01
15 June 2006	25.40	42.20	35.44	2.10
Mean	**25.83**	**41.83**	**35.62**	**2.06**
7 April 2010	25.31	43.93	36.94	2.43
23 April 2010	24.15	44.60	37.39	2.61
25 May 2010	28.01	41.52	37.92	1.62
Mean	**25.82**	**43.35**	**37.42**	**2.22**
17 March 2014	31.23	46.26	39.29	1.92
2 April 2014	30.72	47.87	40.29	2.19
20 May 2014	32.07	47.66	41.90	2.06
5 June 2014	31.01	47.28	40.47	1.94
Mean	**31.26**	**47.27**	**40.49**	**2.03**
12 March 2018	33.18	50.04	43.03	2.03
28 March 2018	31.94	50.93	43.58	2.59
15 May 2018	35.10	51.64	43.99	2.24
16 June 2018	35.70	48.97	43.52	1.58
Mean	**33.98**	**50.40**	**43.53**	**2.11**

Table 4. Spatial distribution of LST (°C) in MODIS data.

Season	LST (minimum)	LST (maximum)	LST (mean)	LST (standard deviation)
25 April 2002	34.71	41.00	38.50	1.06
11 May 2002	34.84	41.29	39.08	1.10
Mean	**34.78**	**41.15**	**38.79**	**1.08**
29- Apr-2006	38.17	46.11	42.95	1.29
17 June 2006	39.45	47.25	42.80	1.81
Mean	**38.81**	**46.68**	**42.88**	**1.55**
6 April 2010	37.31	50.33	42.08	2.67
22 April 2010	39.62	46.84	43.03	2.01
24 May 2010	44.41	53.90	49.81	1.93
Mean	**40.45**	**50.36**	**44.97**	**2.20**
16 March 2014	44.39	54.65	50.14	2.07
1 April 2014	40.78	50.39	44.23	1.49
19 May 2014	49.36	56.48	53.62	1.32
4 June 2014	42.18	49.60	45.37	1.49
Mean	**44.18**	**52.78**	**48.34**	**1.59**
12 March 2018	50.33	60.71	56.00	1.95
27 March 2018	52.79	69.85	59.64	2.77
12 May 2018	56.49	66.65	61.92	2.11
15 June 2018	49.57	58.67	55.16	1.43
Mean	**52.30**	**63.97**	**58.18**	**2.07**

values from 2002 to 2018. The high NDVI values are found in the south-western and north-eastern parts of the city, whereas vegetation is abundant and LST values are comparatively less. Figure 5 presents the mean NDWI values for the five different years. The NDWI values are high in the water areas which are found in the central part in a dispersed pattern. Figure 6 shows the mean NDBI values during the entire period. The high NDBI values are mostly observed in the south-eastern and north-western corners where the land is almost barren or under the built-up area. The high values of NMDI are mainly noticed in the central and southern portions of the city (Figure 7). Figure 8 shows the mean NDBaI values from 2002 to 2018. The land cover in the south-eastern parts of the study area is mainly bare or open and thus the values of NDBaI are higher in this region.

Table 5. Validation of Landsat data retrieved LST with MODIS data retrieved LST.

Acquisition date (Landsat data)	Acquisition date (MODIS data)	Correlation Coefficient
25 April 2002	25 April 2002	0.49
11 May 2002	11 May 2002	0.48
28- Apr-2006	29 Apr 2006	0.49
15 June 2006	17 June 2006	0.49
7 April 2010	6 April 2010	0.48
23 April 2010	22 April 2010	0.58
25 May 2010	24 May 2010	0.48
17 March 2014	16 March 2014	0.59
2 April 2014	1 April 2014	0.49
20 May 2014	19 May 2014	0.43
5 June 2014	4 June 2014	0.53
12 March 2018	13 March 2018	0.41
28 March 2018	27 March 2018	0.45
15 May 2018	12 May 2018	0.49
16 June 2018	15 June 2018	0.47

5.4. Variation in the distribution of mean LST

Figure 9 indicates the spatial distribution of mean LST values for the years 2002, 2006, 2010, 2014, and 2018. The central and southern parts of Raipur City are characterized by low LST values (area below mean LST), whereas the northern, western, and south-eastern parts reflect high LST zones (area above mean LST). The high LST zones are surrounded by the built-up area and bare earth surface, whereas the low LST zones are developed mainly by the concentration of dense vegetal cover.

5.5. Relationship of LST with NDVI, NDWI, NDBI, NMDI, and NDBaI for the whole area of the city, the area under above mean LST, and the area under below mean LST

Generally, LST presents a negative relationship with NDVI and NMDI, whereas it shows a positive relationship with NDWI, NDBI, and NDBaI. This specific pattern of the relationship between LST and land surface indices has been noticed throughout the whole study area (Table 6). Here, NDBI shows the strongest positive relationship ($r = 0.78$) with LST among the five land surface indices after averaging all the Landsat data sets. NMDI shows a very strong negative relationship ($r = -0.72$) with LST. NDVI also reflects a strong negative relation ($r = -0.66$) with LST. High NDVI reflects a stronger negative correlation. Generally, the low NDVI or negative NDVI generates no such significant LST-NDVI correlation (Jiang et al., 2006). There is no precipitation found on the particular acquisition date for each satellite image. Hence, the soil remains almost dry. The LST-NDVI relationship also depends on soil moisture. High soil moisture is responsible for a stronger LST-NDVI correlation. Soil moisture generates a positive correlation with precipitation; i.e. the more precipitation results for more soil moisture. Thus, a high amount of precipitation builds stronger LST-NDVI correlation. A moderate to a strong positive

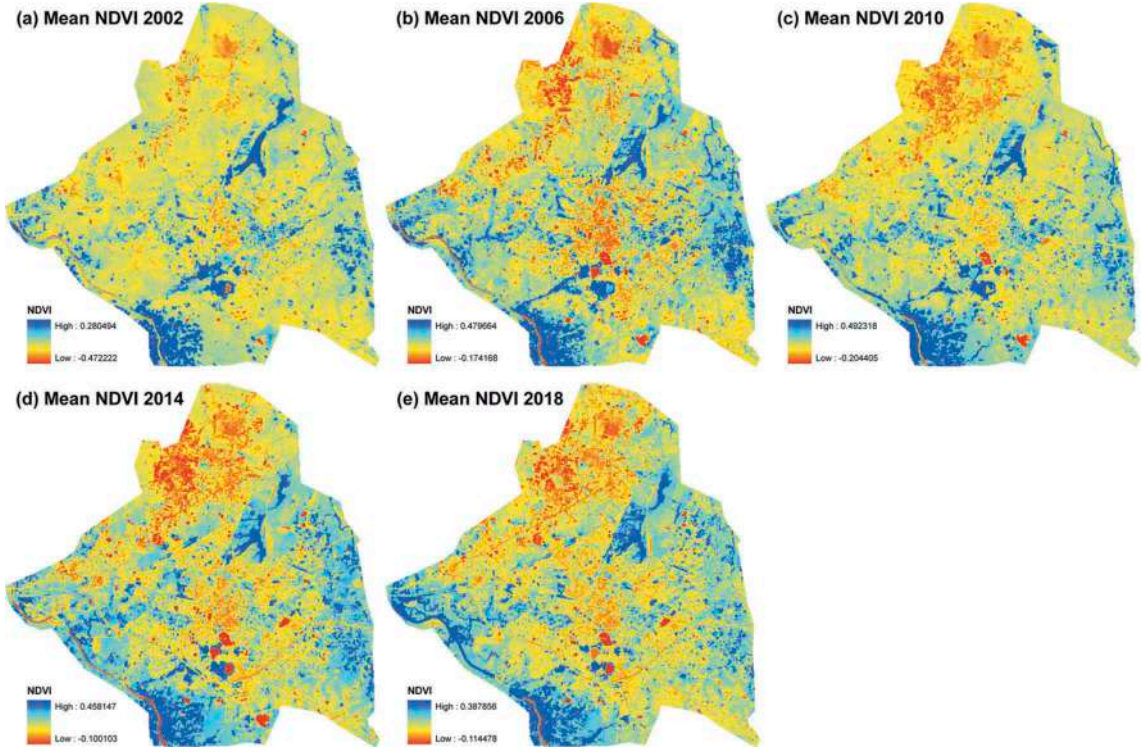

Figure 4. Mean NDVI values for the following years: (a) 2002, (b) 2006, (c) 2010, (d) 2014, and (e) 2018.

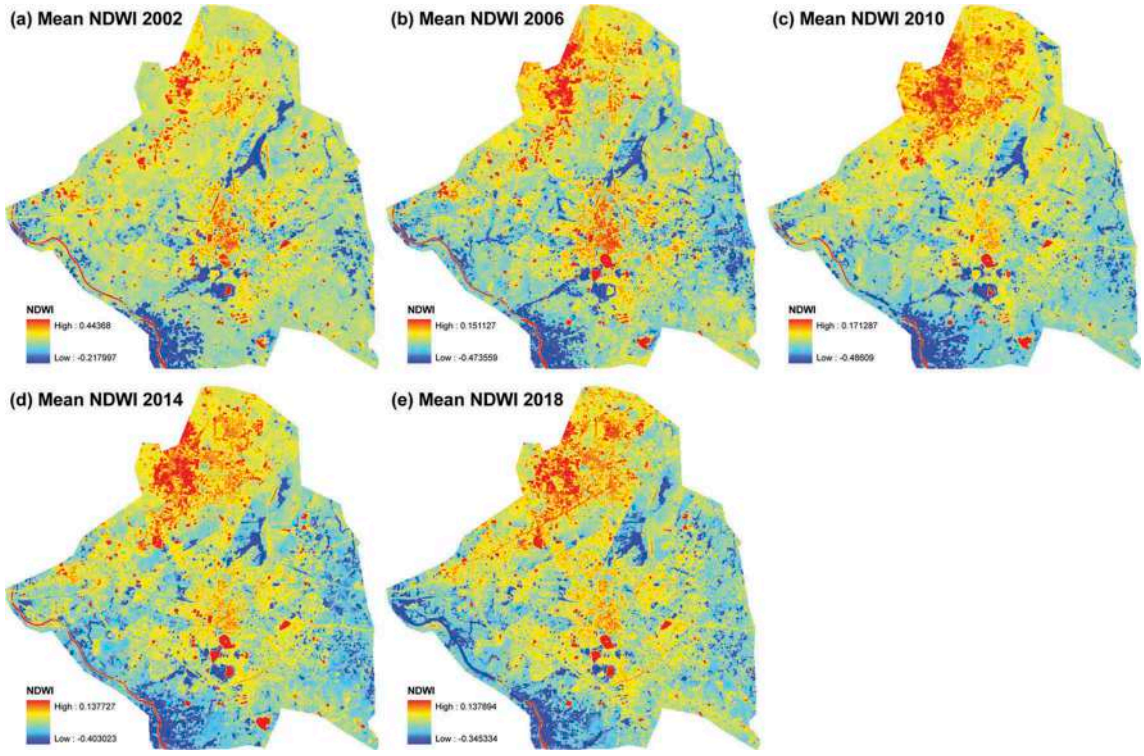

Figure 5. Mean NDWI values for the following years: (a) 2002, (b) 2006, (c) 2010, (d) 2014, and (e) 2018.

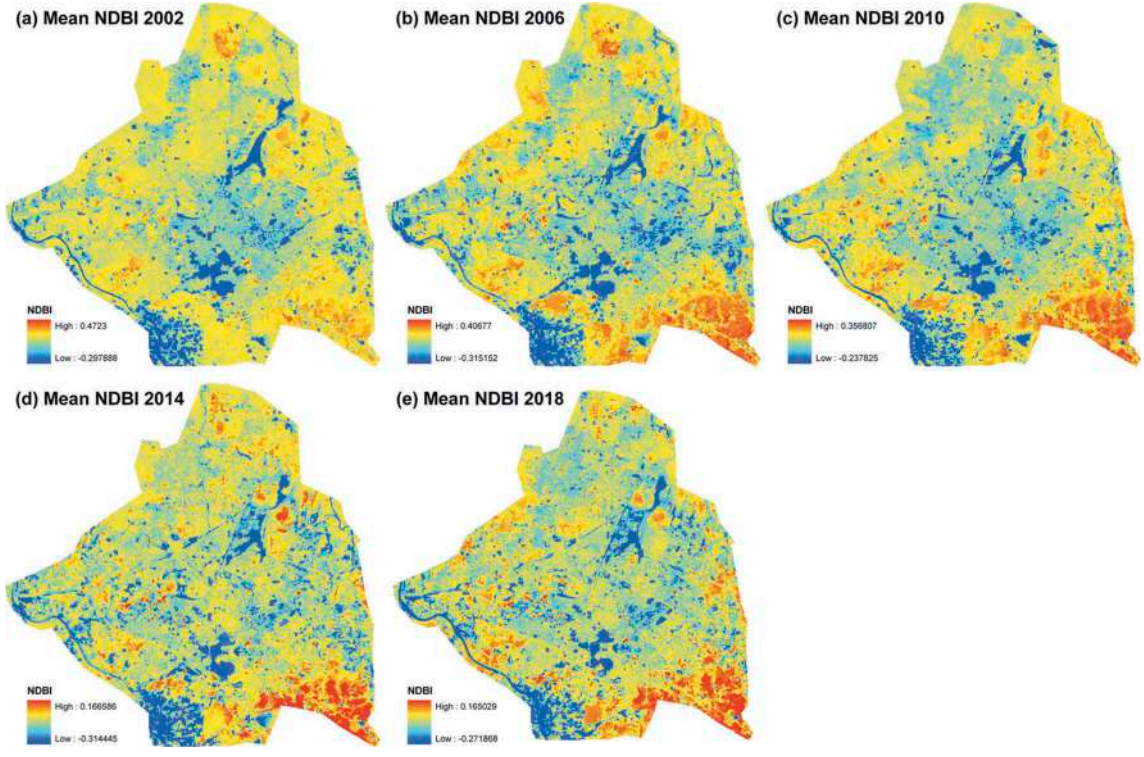

Figure 6. Mean NDBI values for the following years: (a) 2002, (b) 2006, (c) 2010, (d) 2014, and (e) 2018.

relationship (r = 0.55) has been found between LST and NDWI. Only NDBaI presents a very weak relationship (r = 0.05). This relationship is slightly positive or negative and also very unstable.

These relationships have also been analysed in MODIS Terra data sets (Table 7). The result is almost similar. NDBI (r = 0.54) and NDVI (r = −0.54) present a moderate to strong relationship with LST consistently.

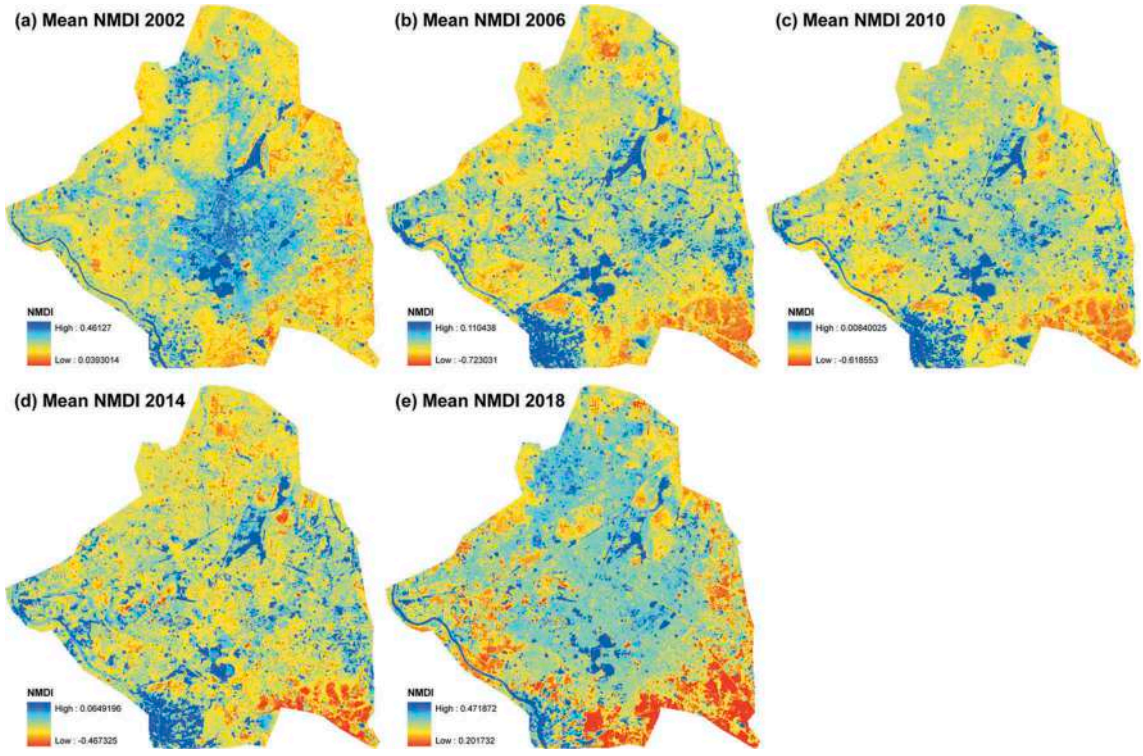

Figure 7. Mean NMDI values for the following years: (a) 2002, (b) 2006, (c) 2010, (d) 2014, and (e) 2018.

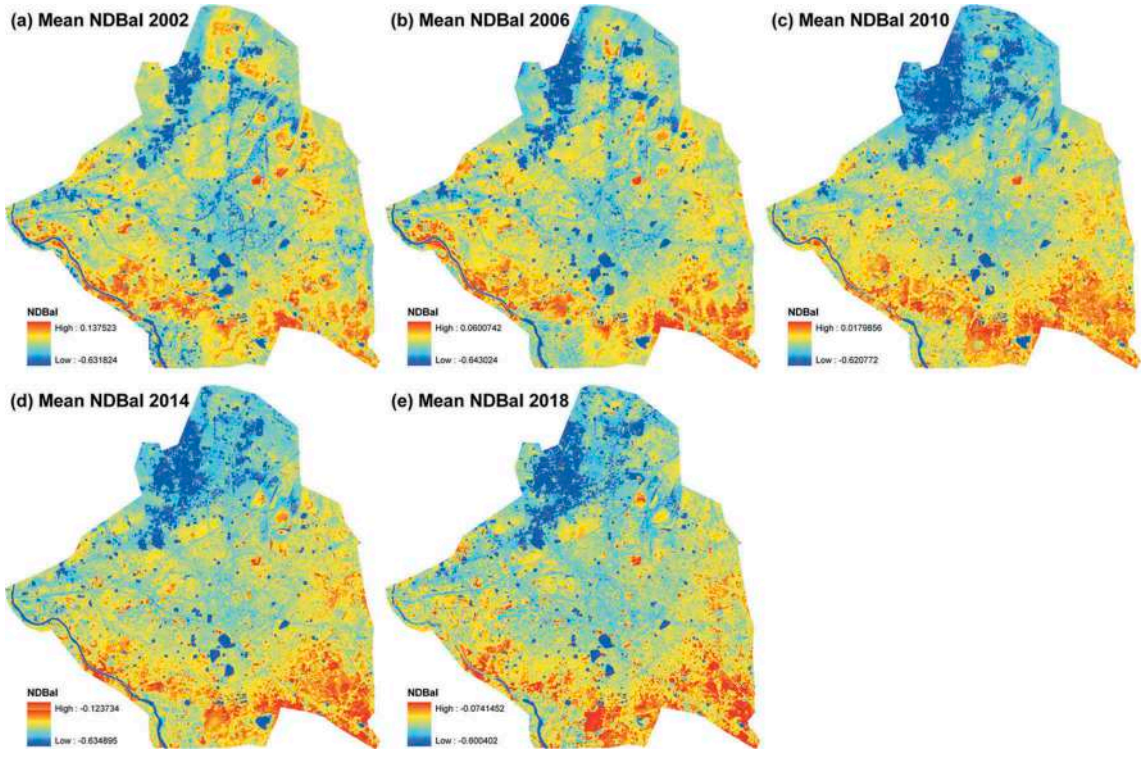

Figure 8. Mean NDBaI values for the following years: (a) 2002, (b) 2006, (c) 2010, (d) 2014, and (e) 2018.

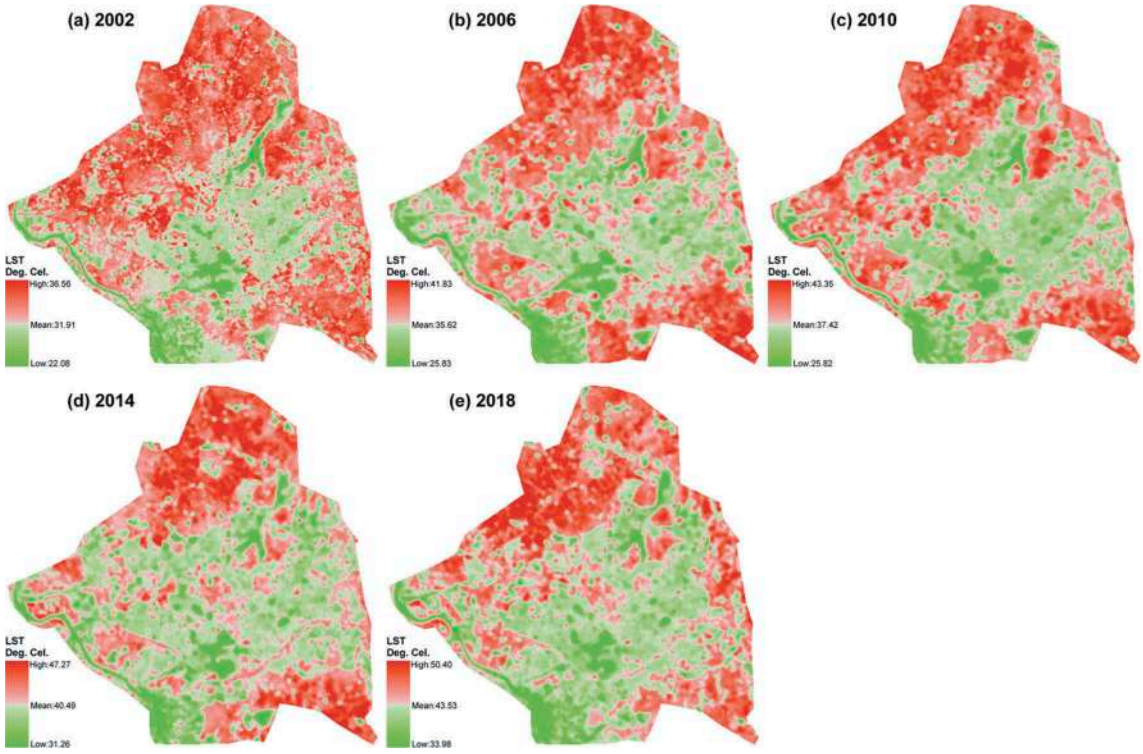

Figure 9. LST distribution in the area above mean LST (red colour zone) and below mean LST (green colour zone) for the whole of Raipur City throughout the entire period: (a) 2002, (b) 2006, (c) 2010, (d) 2014, and (e) 2018.

Table 6. Correlation coefficients between LST and different land surface indices in Landsat data sets.

Date	LST-NDVI	LST-NDWI	LST-NDBI	LST-NMDI	LST-NDBaI
25 April 2002	−0.77	0.64	0.90	−0.74	0.45
11 May 2002	−0.77	0.68	0.81	−0.58	0.16
Mean	**−0.77**	**0.66**	**0.86**	**−0.66**	**0.31**
28 April 2006	−0.73	0.59	0.88	−0.90	0.33
15 June 2006	−0.68	0.58	0.84	−0.86	0.08
Mean	**−0.71**	**0.56**	**0.86**	**−0.88**	**0.21**
7 April 2010	−0.66	0.52	0.80	−0.84	−0.09
23 April 2010	−0.72	0.61	0.47	−0.80	−0.23
25 May 2010	−0.58	0.42	0.83	−0.86	0.10
Mean	**−0.65**	**0.52**	**0.70**	**−0.83**	**−0.07**
17 March 2014	−0.62	0.54	0.82	−0.84	−0.03
2 April 2014	−0.63	0.52	0.86	−0.57	−0.03
20 May 2014	−0.59	0.45	0.84	−0.85	−0.07
5 June 2014	−0.39	0.33	0.64	−0.64	−0.17
Mean	**−0.56**	**0.46**	**0.79**	**−0.73**	**−0.08**
12 March 2018	−0.55	0.46	0.65	−0.43	−0.10
28 March 2018	−0.64	0.56	0.77	−0.59	−0.20
15 May 2018	−0.60	0.58	0.57	−0.37	−0.34
16 June 2018	−0.58	0.49	0.83	−0.69	0.13
Mean	**−0.59**	**0.52**	**0.71**	**−0.52**	**−0.13**
Total Mean	**−0.66**	**0.55**	**0.78**	**−0.72**	**0.05**

Table 7. Correlation coefficients between LST and different land surface indices in MODIS data sets.

Date	LST-NDVI	LST-NDWI	LST-NDBI	LST-NMDI	LST-NDBaI
25 April 2002	−0.58	0.53	0.58	−0.45	0.01
11 May 2002	−0.56	0.50	0.44	−0.27	−0.07
Mean	**−0.57**	**0.52**	**0.51**	**−0.36**	**−0.03**
29- Apr-2006	−0.62	0.55	0.57	−0.36	−0.02
17 June 2006	−0.56	0.45	0.77	−0.60	−0.06
Mean	**−0.59**	**0.50**	**0.67**	**−0.48**	**−0.04**
6 April 2010	−0.57	0.50	0.51	−0.26	−0.43
22 April 2010	−0.60	0.53	0.46	−0.15	−0.52
24 May 2010	−0.44	0.24	0.68	−0.51	−0.07
Mean	**−0.54**	**0.42**	**0.55**	**−0.31**	**−0.34**
16 March 2014	−0.37	0.32	0.51	−0.23	−0.07
1 April 2014	−0.69	0.66	0.44	0.06	−0.48
19 May 2014	−0.53	0.44	0.61	−0.47	−0.16
4 June 2014	−0.54	0.44	0.58	−0.32	−0.38
Mean	**−0.53**	**0.47**	**0.54**	**−0.24**	**−0.27**
13 March 2018	−0.58	0.55	0.38	−0.03	−0.28
27 March 2018	−0.43	0.34	0.48	−0.23	−0.16
12 May 2018	−0.36	0.22	0.57	−0.37	0.24
15 June 2018	−0.54	0.53	0.36	−0.06	−0.29
Mean	**−0.48**	**0.41**	**0.45**	**−0.17**	**−0.12**
Total Mean	**−0.54**	**0.46**	**0.54**	**−0.31**	**−0.16**

NDWI also develops a moderate positive relation (r = 0.46) with LST. A significant negative relation (r = −0.31) has been developed by LST and NMDI. Again, NDBaI presents the weakest relationship (r = −0.16) with LST.

Figure 10 shows a year-wise comparison of the LST-land surface indices relationship. It is clearly shown that NDVI and NMDI develop a strong negative correlation with LST, whereas NDBI shows a strong positive relationship. NDWI also builds a moderate positive relationship. No such significant relationship has been built by LST and NDBaI.

The above discussion is based on the general analysis of LST and land surface indices relationships for the whole city. This result has been changed in high LST zones (area above mean LST) and low LST zones (area below mean

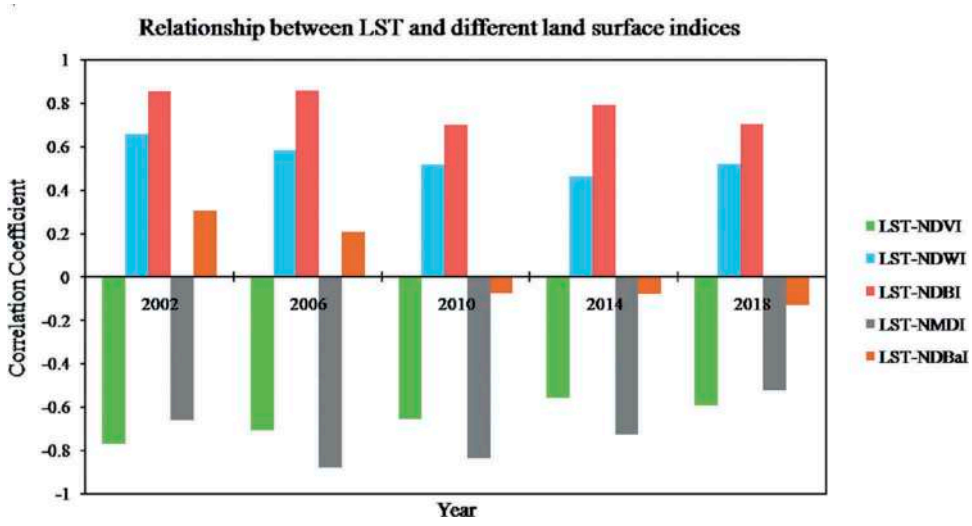

Figure 10. Year-wise comparison of the relationship between LST and different land surface indices.

LST). Table 8 shows the relationships between LST and the land surface indices for the area above mean LST using Landsat data sets. NDVI reflects a moderate relationship (r = −0.45) with LST. NDWI shows moderate strong (r = 0.41) relation. NDBI (r = 0.35) and NMDI (r = −0.35) both show a significant relationship. NDBal presents a weak (r = −0.23) relationship with LST. No indices develop such a strong relationship with LST. The main reason behind the moderate relationship between LST and land surface indices is the mixed heterogeneous nature of the surface composition. Generally, the built-up area has not been able to build any significant and strong stable correlation with the distribution of LST.

Table 9 presents the LST-land surface indices relationship for the area below mean LST (low LST zones). All the land surface indices tend to build a strong significant relationship with LST. NDBI builds the strongest positive correlation (r = 0.83) with LST, whereas NMDI builds the strongest negative correlation (r = −0.82). NDVI also shows a strong negative correlation (r = −0.73). NDWI is moderately (r = 0.66) correlated to LST. Even, NDBal builds a significant positive relationship (r = 0.49) with LST. The low LST zones are mainly characterized by natural land surfaces like vegetation, soil, water, wetland, etc. and thus in these areas, the relationships are stronger and more stable.

Figure 11 presents an area-wise comparison of the LST-land surface indices relationship. LST-NDVI and LST-NMDI relationship is strong negative for the whole area and in the low LST zones. LST-NDBI and LST-NDWI

Table 8. Correlation coefficients between LST and different land surface indices for the area above mean LST in Landsat data sets.

Date	LST-NDVI	LST-NDWI	LST-NDBI	LST-NMDI	LST-NDBal
25 April 2002	−0.35	0.33	0.35	−0.08	−0.11
11 May 2002	−0.4	0.48	0.05	0.08	−0.39
Mean	**−0.38**	**0.41**	**0.20**	**0.00**	**−0.25**
28 April 2006	−0.46	0.28	0.59	−0.64	0.17
15 June 2006	−0.59	0.61	0.48	−0.55	−0.34
Mean	**−0.53**	**0.45**	**0.54**	**−0.60**	**−0.09**
7 April 2010	−0.49	0.4	0.28	−0.44	−0.28
23 April 2010	−0.65	0.63	−0.02	−0.15	−0.58
25 May 2010	−0.43	0.33	0.37	−0.49	−0.14
Mean	**−0.52**	**0.45**	**0.21**	**−0.36**	**−0.33**
17 March 2014	−0.47	0.45	0.46	−0.61	−0.29
2 April 2014	−0.39	0.29	0.64	−0.76	−0.11
20 May 2014	−0.29	0.15	0.61	−0.70	0.02
5 June 2014	−0.59	0.60	0.20	−0.42	−0.54
Mean	**−0.44**	**0.37**	**0.48**	**−0.62**	**−0.23**
12 March 2018	−0.47	0.44	0.07	0.11	−0.35
28 March 2018	−0.50	0.44	0.25	−0.01	−0.34
15 May 2018	−0.31	0.30	0.29	−0.20	−0.32
16 June 2018	−0.31	0.25	0.67	−0.53	0.05
Mean	**−0.40**	**0.36**	**0.32**	**−0.16**	**−0.24**
Total Mean	**−0.45**	**0.41**	**0.35**	**−0.35**	**−0.23**

Table 9. Correlation coefficients between LST and different land surface indices for the area below mean LST in Landsat data sets.

Date	LST-NDVI	LST-NDWI	LST-NDBI	LST-NMDI	LST-NDBal
25 April 2002	−0.79	0.69	0.93	−0.76	0.66
11 May 2002	−0.79	0.71	0.87	−0.66	0.53
Mean	**−0.79**	**0.70**	**0.90**	**−0.71**	**0.60**
28 April 2006	−0.76	0.69	0.90	−0.91	0.60
15 June 2006	−0.78	0.67	0.84	−0.88	0.54
Mean	**−0.77**	**0.68**	**0.87**	**−0.90**	**0.57**
7 April 2010	−0.78	0.61	0.91	−0.92	0.43
23 April 2010	−0.71	0.73	0.91	−0.93	0.44
25 May 2010	−0.64	0.67	0.84	−0.93	0.42
Mean	**−0.71**	**0.67**	**0.89**	**−0.93**	**0.43**
17 March 2014	−0.67	0.62	0.85	−0.87	0.51
2 April 2014	−0.68	0.77	0.89	−0.85	0.46
20 May 2014	−0.72	0.68	0.81	−0.87	0.44
5 June 2014	−0.65	0.62	0.59	−0.78	0.49
Mean	**−0.68**	**0.67**	**0.79**	**−0.84**	**0.48**
12 March 2018	−0.65	0.56	0.65	−0.63	0.34
28 March 2018	−0.74	0.66	0.77	−0.69	0.43
15 May 2018	−0.72	0.62	0.57	−0.74	0.27
16 June 2018	−0.67	0.55	0.77	−0.78	0.41
Mean	**−0.70**	**0.60**	**0.69**	**−0.71**	**0.36**
Total Mean	**−0.73**	**0.66**	**0.83**	**−0.82**	**0.49**

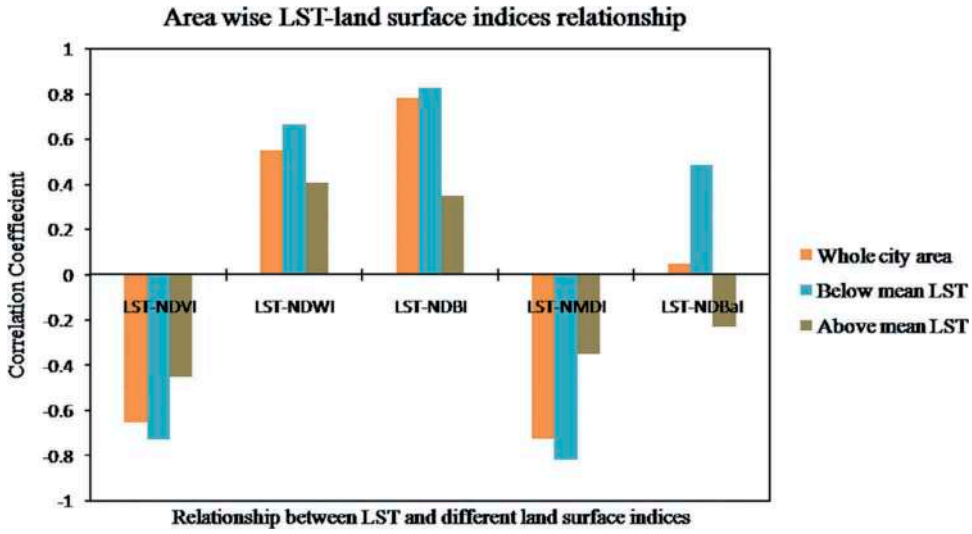

Figure 11. Area-wise comparison of the relationship between LST and different land surface indices.

relationships are strongly positive for the whole area and in the low LST zones. In the high LST zones (area above mean LST) characterized by industrial area, car parking zone, airport, commercial area, and bare rock surface, these relationships are weaker. NDBaI builds a very weak positive relation for the whole city, weak negative relation in the high LST zones and moderate positive relation in the low LST zones.

Cao et al. (2011), Ghobadi et al. (2014), Liang et al. (2012), S. Guha et al. (2017, 2018) have found almost similar results (negative correlation) for LST-NDVI relationships compared to the present research work. LST-NDBI relationship has been found moderate to strongly positive in the lower and middle latitude cities that support the outcomes of the present research work (S. Guha et al., 2017, 2018, 2019; Govil et al., 2020; Malik et al., 2019). LST-NDWI relationship shows a moderate positive correlation which reveals a significant result compared to the previous works (Bala et al., 2018; Shekhawat et al., 2018; Ullah et al., 2019; X. Zhang et al., 2017). Ibrahim, (2017) observed a strong positive correlation of LST with NDBI and NDBaI, whereas a strong negative correlation was found between LST-NDVI and LST-NDWI. The present study presents the almost equal value of correlation coefficient (r = 0.46) of the LST-NDWI relationship that was performed in the urban landscape of São José dos Campos in Brazil (Ogashawara and Bastos, 2014). LST-NMDI relationships in different seasons show excellent results in the present study compared to the similar studies (Govil et al., 2019; S. Guha et al., 2019; Rasul et al., 2016; Yang et al., 2017).

5.6. Validation of the linear correlation of LST and land surface indices by rank correlation method

In this paper, Pearson's linear correlation coefficient method has been used to determine the linear correlation between LST and five land surface indices (NDVI, NDWI, NDBI, NMDI, NDBaI). This result has been validated with the Spearman's rank correlation coefficient that is based on ordinal association and can assess the monotonic relationship (whether linear or not) between LST and the land surface indices. Table 10 shows the rank correlation coefficients of LST and the land surface indices.

Table 10 indicates that both the correlation coefficients are very close to each other (Especially for LST-NDVI, LST-NDBI, and LST- NMDI relationships). Only, LST-NDBaI relationships have not been validated as the correlation coefficients found by the two separate methods as the values are too far from each other.

6. Conclusion

In this paper, fifteen cloud-free pre-monsoon Landsat data sets of 2002 (two), 2006 (two), 2010 (three), 2014

Table 10. Validation of Pearson's linear correlation coefficients by Spearman's rank correlation coefficients for LST-land surface indices relationship.

	Spearman's rank correlation coefficient					Pearson's linear correlation coefficient				
	LST-NDVI	LST-NDWI	LST-NDBI	LST-NMDI	LST-NDBaI	LST-NDVI	LST-NDWI	LST-NDBI	LST-NMDI	LST-NDBaI
Whole city	−0.71	0.40	0.77	−0.65	0.44	−0.66	0.55	0.78	−0.72	0.05
High LST zones	−0.50	0.53	0.68	−0.47	0.42	−0.45	0.41	0.35	−0.35	−0.23
Low LST zones	−0.74	0.58	0.76	−0.74	0.54	−0.73	0.66	0.83	−0.82	0.49

(four), and 2018 (four) have been used to investigate the relationship between LST and five land surface indices (NDVI, NDWI, NDBI, NMDI, NDBaI) for the whole area of Raipur City, the area with high LST values, and the area with low LST values. The LST has been retrieved from Landsat data sets using the mono-window algorithm. The LST derived from Landsat data sets has significantly been validated with MODIS Terra data sets. The results show that the mean LST of the study area has been increased at a very significant rate (11.62°C LST increases between 2002 and 2018). The results show that the most of the heated zones of the city are found in the dry exposed bare lands with some rocky surface of the north-west and south-east parts as these areas have a lower density of green vegetation and soil moisture. The results also show that LST is very strongly related to NDBI (positive), NDVI (negative), NMDI (negative); and moderately related to NDWI (positive). No such significant relationship has been found between LST and NDBaI. In low LST zones, these relationships are stronger. It can be concluded that the natural land surface materials (vegetation, water, soil) are strongly correlated to LST than the built-up area.

The result of the present study is significant for future environmental planning of the city. Most of the low NDVI or low NMDI zones indicate high LST and vice-versa. It means the area with more green vegetation and wet soil represents low LST. Thus, the portion of vegetation and soil must be increased to reduce the thermal stress of the city. For better sustainability, a large amount of urban plantation is needed along the roadside and residential area. The present water bodies and green areas inside the city boundary must be preserved for providing a better life. NDBI shows a strong positive relationship with LST. It means the built-up area and bare or fallow land is responsible for high LST. Thus, the major commercial and industrial sectors should be moved into the outskirts of the city to make the residential zones less polluted. The green building materials like earthen materials, wood, bamboo, natural clay, earthbags, natural fibre, etc. should be introduced on a large scale for new construction.

The limitations of the study are as follows: (1) the study used fifteen Landsat data sets from various sensors. The study might be more fruitful if large data sets have been used from a single satellite sensor, like Landsat 5 TM, Landsat 7 ETM+, or Landsat 8 OLI and TIRS. (2) The study has been performed in only pre-monsoon season. The findings of the present study can be compared to the other seasons. (3) The study has been performed in a single city. It can be analysed in multiple cities. (4) The study has been conducted in the tropical region. The results can be assessed in other environmental conditions. (5) The study used the Landsat satellite sensor. Other satellite sensors with different resolutions, like MODIS, ASTER, Sentinel, etc. can be used to judge the effectiveness of this study.

Disclosure statement

No potential conflict of interest was reported by the authors.

ORCID

Subhanil Guha http://orcid.org/0000-0002-2967-7248
Himanshu Govil http://orcid.org/0000-0002-3433-8355
Anindita Dey http://orcid.org/0000-0002-6400-4284
Neetu Gill http://orcid.org/0000-0001-7392-2178

References

Adegoke, J. O., Pielke, R. A., Sr., Eastman, J., Mahmood, R., & Hubbard, K. G. (2003). Impact of irrigation on midsummer surface fluxes and temperature under dry synoptic conditions: A regional atmospheric model study of the U.S. High Plains. *Monthly Weather Review*, *131*(3), 556–564. https://doi.org/10.1175/1520-0493(2003)131<0556:IOIOMS>2.0.CO;2

Amiri, R., Weng, Q., Alimohammadi, A., & Alavipanah, S. K. (2009). Spatial–temporal dynamics of land surface temperature in relation to fractional vegetation cover and land use/cover in the Tabriz urban area, Iran. *Remote Sensing of Environment*, *113*(12), 2606–2617. https://doi.org/10.1016/j.rse.2009.07.021

Arnfield, J. (2003). Two decades of urban climate research: A review of turbulence, exchanges of energy and water, and the urban heat island. *International Journal of Climatology*, *23*(1), 1–26. https://doi.org/10.1002/joc.859

Bala, R., Prasad, R., Yadav, V., & Sharma, J. (2018). A comparative study of land surface temperature with different indices on heterogeneous land cover using Landsat 8 data. *In the international archives of the photogrammetry, remote sensing and spatial information sciences, volume XLII-5, 2018 ISPRS TC V Mid-term symposium*, 20-23 Nov 2018, Dehradun, India. https://doi.org/10.5194/isprs-archives-XLII-5-389-2018.

Cao, L., Hu, H. W., Meng, X. L., & Li, J. X. (2011). Relationships between land surface temperature and key landscape elements in urban area. *Chinese Journal of Ecology*, *30*, 2329–2334.

Christy, J. R., & McNider, R. T. (2016). Time series construction of summer surface temperatures for Alabama, 1883–2014, and comparisons with tropospheric temperature and climate model simulations. *Journal of Applied Meteorology and Climatology*, *55*(3), 811–826. https://doi.org/10.1175/JAMC-D-15-0287.1

Christy, J. R., Norris, W. B., & McNider, R. T. (2009). Surface temperature variations in East Africa and possible causes. *Journal of Climate*, *22*(12), 3342–3356. https://doi.org/10.1175/2008JCLI2726.1

Christy, J. R., Norris, W. B., Redmond, K., & Gallo, K. (2006). Methodology and results of calculating central California surface temperature trends: Evidence of human-induced climate change? *Journal of Climate*, *19*(4), 548–563. https://doi.org/10.1175/JCLI3627.1

Chun, B., & Guldmann, J.-M. (2014). Spatial statistical analysis and simulation of the urban heat island in high-density central cities. *Landscape and Urban Planning*, *125*, 76–88. https://doi.org/10.1016/j.landurbplan.2014.01.016

Chun, B., & Guldmann, J.-M. (2018). Impact of greening on the urban heat island: Seasonal variations and mitigation strategies. *Computers, Environment and Urban Systems*, *71*, 165–176. https://doi.org/10.1016/j.compenvurbsys.2018.05.006

Coseo, P., & Larsen, L. (2014). How factors of land use/land cover, building configuration, and adjacent heat sources and sinks explain urban heat Islands in Chicago. *Landscape and Urban Planning*, *125*, 117–129. https://doi.org/10.1016/j.landurbplan.2014.02.019

Cui, Y. Y., & de Foy, B. (2012). Seasonal variations of the urban heat island at the surface and the near-surface and reductions due to urban vegetation in Mexico City. *Journal of Applied Meteorology and Climatology*, *51*(5), 855–868. https://doi.org/10.1175/JAMC-D-11-0104.1

Dai, Z., Guldmann, J.-M., & Hu, Y. (2018). Spatial regression models of park and land-use impacts on the urban heat island in central Beijing. *Science of the Total Environment*, *626*, 1136–1147. https://doi.org/10.1016/j.scitotenv.2018.01.165

Davey, C. A., & Pielke, R. A., Sr. (2005). Microclimate exposures of surface-based weather stations - implications for the assessment of long-term temperature trends. *Bulletin of the American Meteorological Society*, *86*(4), 497–504. https://doi.org/10.1175/BAMS-86-4-504

Davey, C. A., Pielke, R. A., Sr., & Gallo, K. P. (2006). Differences between near-surface equivalent temperature and temperature trends for the eastern United States - Equivalent temperature as an alternative measure of heat content. *Global and Planetary Change*, *54*, 19–32. https://doi.org/10.1016/j.gloplacha.2005.11.002.

Deilami, K., & Kamruzzaman, M. (2017). Modelling the urban heat island effect of smart growth policy scenarios in Brisbane. *Land Use Policy*, *64*, 38–55. https://doi.org/10.1016/j.landusepol.2017.02.027

Fall, S., Diffenbaugh, N., Niyogi, D., Pielke, R. A., Sr., & Rochon, G. (2010). Temperature and equivalent temperature over the United States (1979-2005). *International Journal of Climatology*, *30*(13), 2045–2054. https://doi.org/10.1002/joc.2094

Fall, S., Niyogi, D., Gluhovsky, A., Pielke Sr., R. A., Kalnay, E., & Rochon, G. (2009). Impacts of land use land cover on temperature trends over the continental United States: Assessment using the North American regional reanalysis. *International Journal of Climatology, 30*(13), 1980–1993. https://doi.org/10.1002/joc.1996

Faqe Ibrahim, G. R. (2017). Urban land use land cover changes and their effect on land surface temperature: Case study using Dohuk City in the Kurdistan Region of Iraq. *Climate*, *5*(1), 13. https://doi.org/10.3390/cli5010013

Feyisa, G. L., Henrik, M., Jenerette, D. G., & Pauliet, S. (2016). Locally optimized separability enhancement indices for urban land cover mapping: Exploring thermal environmental consequences of rapid urbanization in Addis Ababa, Ethiopia. *Remote Sensing of Environment*, *175*, 14–31. https://doi.org/10.1016/j.rse.2015.12.026

Ghobadi, Y., Pradhan, B., Shafri, H. Z. M., & Kabiri, K. (2014). Assessment of spatial relationship between land surface temperature and land use/cover retrieval from multi-temporal remote sensing data in South Karkheh Sub-basin, Iran. *Arabian Journal of Geosciences*, *8*, 525–537. https://doi.org/10.1007/s12517-013-1244-3

Govil, H., Guha, S., Diwan, P., Gill, N., & Dey, A. (2020). Analyzing linear relationships of LST with NDVI and MNDISI using various resolution levels of Landsat 8 OLI and TIRS data. In N. Sharma, A. Chakrabarti, & V. Balas (Eds.), *Data management, analytics and innovation. Advances in intelligent systems and computing* (Vol. 1042, pp. 171–184). Springer. https://doi.org/10.1007/978-981-32-9949-8_13.

Govil, H., Guha, S., Dey, A., & Gill, N. (2019). Seasonal evaluation of downscaled land surface temperature: A case study in a humid tropical city. *Heliyon*, *5*(6), e01923. https://doi.org/10.1016/j.heliyon.2019.e01923

Guha, S., & Govil, H. (2020). An assessment on the relationship between land surface temperature and normalized difference vegetation index. *Environment, Development and Sustainability*. https://doi.org/10.1007/s10668-020-00657-6

Guha, S., Govil, H., Dey, A., & Gill, N. (2018). Analytical study of land surface temperature with NDVI and NDBI using Landsat 8 OLI and TIRS data in Florence and Naples city, Italy. *European Journal of Remote Sensing*, *51*(1), 667–678. https://doi.org/10.1080/22797254.2018.1474494

Guha, S., Govil, H., & Diwan, P. (2019). Analytical study of seasonal variability in land surface temperature with normalized difference vegetation index, normalized difference water index, normalized difference built-up index, and normalized multiband drought index. *Journal of Applied Remote Sensing*, *13*(2), 024518. https://doi.org/1010.1117/1.JRS.13.024518

Guha, S., Govil, H., & Mukherjee, M. (2017). Dynamic analysis and ecological evaluation of urban heat islands in Raipur City, India. *Journal of Applied Remote Sensing*, *11*(3), 036020. https://doi.org/10/1117/1.JRS.11.036020

Haashemi, S., Weng, Q., Darvishi, A., & Alavipanah, S. A. (2016). Seasonal variations of the surface urban heat island in a semi-arid city. *Remote Sensing*, *8*(4), 352. https://doi.org/10.3390/rs8040352

Hanamean Jr., J. R., Jr., Pielke, R. A., Sr., Castro, C. L., Ojima, D. S., Reed, B. C., & Gao, Z. (2003). Vegetation greenness impacts on maximum and minimum temperatures in northeast Colorado. *Meteorological Applications*, *10*(3), 203–215. https://doi.org/10.1017/S1350482703003013

Jiang, Z. Y., Cheng, Y. H., & Li, J. (2006). Heat island effect of Beijng based on Landsat TM data. *Geomatics Information Science Wuhan University (In Chinese)*., *31*, 120–123.

Jimenez-Munoz, J. C., Cristóbal, J., Sobrino, J. A., Sòria, G., Ninyerola, M., Pons, X., & Pons, X. (2009). Revision of the single-channel algorithm for land surface temperature retrieval from Landsat thermal-infrared data. *IEEE Transactions on Geoscience and Remote Sensing*, *47*(1), 339–349. https://doi.org/10.1109/TGRS.2008.2007125

Jiménez-Muñoz, J. C., & Sobrino, J. A. (2003). A generalized single-channel method for retrieving land surface temperature from remote sensing data. *Journal of Geophysical Research: Atmospheres*, *108*(D22), 4688. https://doi.org/10.1029/2003JD003480

Khorchani, M., Martin-Hernandez, N., Vicente-Serrano, S. M., Azorin-Molina, C., Garcia, M., Domínguez-Duran, M. A., Fergus, R., Peña-Gallardo, M., & Domínguez-Castro, F. (2018). Average annual and seasonal Land Surface Temperature, Spanish Peninsular. *Journal of Maps*, *14*(2), 465–475. https://doi.org/10.1080/17445647.2018.1500316

Khorchani, M., Vicente-Serrano, S. M., Azorin-Molina, C., Garcia, M., Martin-Hernandez, N., Peña-Gallardo, M., El Kenawy, A., & Domínguez-Castro, F. (2018). Trends in LST over the peninsular Spain as derived from the AVHRR imagery data. *Global and Planetary Change*, *166*, 75–93. https://doi.org/10.1016/j.gloplacha.2018.04.006

Kim, J.-P., & Guldmann, J.-M. (2014). Land-use planning and the urban heat island. *Environ. Environment and Planning B: Planning and Design*, *41*(6), 1077–1099. https://doi.org/10.1068/B130091P

Kuang, W., Liu, Y., Dou, Y., Chi, W., Chen, G., Gao, C., Yang, T., Liu, J., & Zhang, R. (2015). What are hot and what are not in an urban landscape: Quantifying and explaining the land surface temperature pattern in Beijing, China. *Landscape Ecology*, *30*(2), 357–373. https://doi.org/10.1007/s10980-014-0128-6

Lai, J., Zhan, W., Huang, F., Quan, J., Hu, L., Gao, L., & Ju, W. (2018). Does quality control matter? Surface urban heat island intensity variations estimated by satellite-derived land surface temperature products. *ISPRS Journal of Photogrammetry and Remote Sensing*, *139*, 212–227. https://doi.org/10.1016/j.isprsjprs.2018.03.012

Li, J., song, C., Cao, L., Zhu, F., Meng, X., & Wu., J. (2011). Impacts of landscape structure on surface urban heat islands: A case study of Shanghai, China. *Remote Sensing of Environment*, *115*(12), 3249–3263. https://doi.org/10.1016/j.rse.2011.07.008

Liang, B. P., Li, Y., & Chen, K. Z. (2012). A research on land features and correlation between NDVI and land surface temperature in Guilin City. *Remote Sensing Technology & Application*, *27*, 429–435.

Lin, X., Pielke, R. A., Sr., Mahmood, R., Fiebrich, C. A., & Aiken., R. (2015). Observational evidence of temperature trends at two levels in the surface layer. *Atmospheric Chemistry and Physics*, *15*(17), 24695–24726. https://doi.org/10.5194/acpd-15-24695-2015

Lopez, J. M. R., Heider, K., & Scheffran, J. (2017). Frontiers of urbanization: Identifying and explaining urbanization hot spots in the south of Mexico City using human and remote sensing. *Applied Geography*, *79*, 1–10. https://doi.org/10.1016/j.apgeog.2016.12.001

Malik, M. S., Shukla, J. P., & Mishra, S. (2019). Relationship of LST, NDBI and NDVI using Landsat-8 data in Kandaihimmat Watershed, Hoshangabad, India. *Indian Journal of Geo Marine Sciences*, *48*(1), 25–31. http://nopr.niscair.res.in/handle/123456789/45657.

Mathew, A., Khandelwal, S., & Kaul, N. (2017). Investigating spatial and seasonal variations of urban heat island effect over Jaipur city and its relationship with vegetation, urbanization and elevation parameters. *Sustainable Cities and Society*, *35*, 157–177. https://doi.org/10.1016/j.scs.2017.07.013

McFeeters, S. K. (1996). The use of the normalized difference water index (NDWI) in the delineation of open water features. *International Journal of Remote Sensing*, *17*(7), 1425–1432. https://doi.org/10.1080/01431169608948714

Mirzaei, P. A. (2015). Recent challenges in modeling of urban heat island. *Sustainable Cities and Society*, *19*, 200–206. https://doi.org/10.1016/j.scs.2015.04.001

Nie, Q., Ma, W., Li, Z., & Huang, Y. (2016). Spatiotemporal impact of urban impervious surface on land surface temperature in Shanghai, China. *Canadian Journal of Remote Sensing*, *42*(6), 680–689. https://doi.org/10.1080/07038992.2016.1217484

Ogashawara, I., Bastos, V. S. B., Nie, Q., Man, W., Li, Z., & Huang, Y. (2012). A quantitative approach for analyzing the relationship between urban heat Islands and land cover. *Remote Sensing*, *4*(11), 3596–3618. https://doi.org/10.3390/rs4113596

Pearsall, H. (2017). Staying cool in the compact city: Vacant land and urban heating in Philadelphia, Pennsylvania. *Applied Geography*, *79*, 84–92. https://doi.org/10.1016/j.apgeop.2016.12.010

Peng, J., Jia, J., Liu, Y., Li, H., & Wu, J. (2018). Seasonal contrast of the dominant factors for spatial distribution of land surface temperature in urban areas. *Remote Sensing of Environment*, *215*, 255–267. https://doi.org/10.1016/j.rse.2018.06.010

Peng, J., Xie, P., Liu, Y., & Ma, J. (2016). Urban thermal environment dynamics and associated landscape pattern factors: A case study in the Beijing metropolitan region. *Remote Sensing of Environment*, *173*, 145–155. https://doi.org/10.1016/j.rse.2015.11.027

Pielke, R. A., Sr., Davey, C., Niyogi, D., Fall, S., Steinweg-Woods, J., Hubbard, K., Lin, X., Cai, M., Lim, Y.-K., Li, H., Nielsen-Gammon, J., Gallo, K., Hale, R., Mahmood, R., Foster, S., McNider, R. T., & Blanken, P. (2007a). Unresolved issues with the assessment of multi-decadal global land surface temperature trends. *Journal of Geophysical Research*, *112* (D24), D24S08. https://doi.org/10.1029/2006JD008229

Pielke, R. A., Sr., Nielsen-Gammon, J., Davey, C., Angel, J., Bliss, O., Doesken, N., Cai, M., Fall, S., Niyogi, D., Gallo, K., Hale, R., Hubbard, K. G., Lin, X., Li, H., & Raman, S. (2007b). Documentation of uncertainties and biases associated with surface temperature measurement sites for climate change assessment. *Bulletin of the American Meteorological Society*, *88*(6), 913–928. https://doi.org/10.1175/BAMS-88-6-913

Pielke, R. A., Sr., Stohlgren, T., Schell, L., Parton, W., Doesken, N., Redmond, K., Moeny, J., McKee, T., & Kittel, T. G. F. (2002). Problems in evaluating regional and local trends in temperature: An example from eastern Colorado, USA. *International Journal of Climatology*, *22*(4), 421–434. https://doi.org/10.1002/joc.706

Purevdorj, T. S., Tateishi, R., Ishiyama, T., & Honda, Y. (1998). Relationships between percent vegetation cover and vegetation indices. *International Journal of Remote Sensing*, *19* (18), 3519–3535. https://doi.org/10.1080/014311698213795

Qin, Z. -. H., Karnieli, A., & Berliner, P. (2001). A mono-window algorithm for retrieving land surface temperature from Landsat TM data and its application to the Israel-Egypt border region. *International Journal of Remote Sensing*, *22* (18), 3719–3746. https://doi.org/10.1080/01431160010006971

Quan, J., Zhan, W., Chen, Y., Wang, M., & Wang, J. (2016). Time series decomposition of remotely sensed land surface temperature and investigation of trends and seasonal variations in surface urban heat islands. *Journal of Geophysical Research: Atmospheres*, *121*(6), 2638–2657. https://doi.org/10.1002/2015JD024354

Rasul, A., Balzter, H., & Smith, C. (2016). Diurnal and seasonal variation of surface urban cool and heat Islands in the semi-arid city of Erbil, Iraq. *Climate*, *4*(3), 42. https://doi.org/10.3390/cli4030042

Rinner, C., & Hussain, M. (2011). Toronto's urban heat island exploring the relationship between land use and surface temperature. *Remote Sensing*, *3*(6), 1251–1265. https://doi.org/10.3390/rs3061251

Rizwan, A. M., Leung, D. Y. C., & Chunho, L. (2008). A review on the generation, determination and mitigation of the urban heat island. *Journal of Environmental Sciences*, *20*(1), 120–128. https://doi.org/10.1002/2017EF000569

Shekhawat, N., Dadhich, A. P., & Goyalet, R. (2018). Temporal analysis of land surface temperature and land use/land cover using remote sensing. *Journal of Civil Engineering and Environmental Technology*, *5*(2), 71–77.

Song, J., Du, S., Feng, S., & Guo, L. (2014). The relationships between landscape compositions and land surface temperature: Quantifying their resolution sensitivity with spatial regression models. *Landscape and Urban Planning*, *123*, 145–157. https://doi.org/10.1016/jlandurbplan.2013.11.014

Strack, J. E., Pielke, R. A., Sr., Steyaert, L. T., & Knox, R. G. (2008). Sensitivity of June near-surface temperatures and precipitation in the eastern United States to historical land cover changes since European settlement. *Water Resources Research*, *44*(11), W1 1401. https://doi.org/10.1029/2007WR006546

Sun, R., Xie, W., & Chen, L.-D. (2018). A landscape connectivity model to quantify contributions of heat sources and sinks in urban regions. *Landscape and Urban Planning*, *178*, 43–50. https://doi.org/10.1016/j.landurbplan.2018.05.015

Tucker, C. J. (1979). Red and photographic infrared linear combinations for monitoring vegetation. *Remote Sensing of Environment*, *8*(2), 127–150. https://doi.org/10.1016/0034-4257(79)90013-0

Ullah, S., Tahir, A. A., Akbar, T. A., Hassan, Q. K., Dewan, A., Khan, M., & Khan, M. (2019). Remote sensing-based quantification of the relationships between land use land cover changes and surface temperature over the lower Himalayan Region. *Sustainability*, *11*(19), 5492. https://doi.org/10.3390/su11195492

Wang, L., & Qu, J. J. (2007). NMDI: A normalized multi-band drought index for monitoring soil and vegetation moisture with satellite remote sensing. *Geophysical Research Letters*, *34*(20), L20405. https://doi.org/10.1029/2007GL031021

Weng, Q. (2001). A remote sensing-GIS evaluation of urban expansion and its impact on surface temperature in Zhujiang Delta, China. *Interact Journal Remote Sensor*, *22* (10), 1999–2014. https://doi.org/10.1080/713860788

Weng, Q., & Yang, S. (2004). Managing the adverse thermal effects of urban development in a densely populated Chinese city. *Journal of Environmental Management*, *70*(2), 145–156. https://doi.org/10.1016/j.jenvman.2003.11.006

Yang, Y., Li, X., Pan, X., Zhang, Y., & Cao, C. (2017). Downscaling land surface temperature in complex regions by using multiple scale factors with adaptive thresholds. *Sensors*, *17*(4), 744. https://doi.org/10.3390/s17040744

Yao, R., Wang, L., Huang, X., Zhang, W., Li, J., & Niu, Z. (2018). Interannual variations in surface urban heat island intensity and associated drivers in China. *Journal of Environmental Management*, *222*, 86–94. https://doi.org/10.1016/j.jenvman.2018.05.024

Yuan, F., & Bauer, M. E. (2007). Comparison of impervious surface area and normalized difference vegetation index as indicators of surface urban heat island effects in Landsat imagery. *Remote Sensing of Environment*, *106*(3), 375–386. https://doi.org/10.1016/j.rse.2006.09.003

Zha, Y., Gao, J., & Ni, S. (2003). Use of normalized difference built-up index in automatically mapping urban areas from TM imagery. *International Journal of Remote Sensing*, *24*(3), 583–594. https://doi.org/10.1080/01431160304987

Zhang, F., Zhang, L. W., Shi, J. J., & Huang, J. F. (2014). Soil moisture monitoring based on land surface temperature-vegetation index space derived from MODIS data. *Pedosphere*, *24*(4), 450–460. https://doi.org/10.1016/S1002-0160(14)60031-X

Zhang, H., Qi, Z. F., Ye, X. Y., Cai, Y. B., Ma, W. C., & Chen, M. N. (2013). Analysis of land use/land cover change, population shift, and their effects on spatiotemporal patterns of urban heat islands in metropolitan Shanghai, China. *Applied Geography*, *44*, 121–133. https://doi.org/10.1016/j.apgeog.2013.07.021

Zhang, X., Yamaguchi, Y., Li, F., He, B., & Chen, Y. (2017). Assessing the impacts of the 2009/2010 drought on vegetation indices, normalized difference water index, and land surface temperature in Southwestern China. *Advances in Meteorology*, 6837493. https://doi.org/10.1155/2017/6837493

Zhang, Z., He, G., Wang, M., Long, T., Wang, G., Zhang, X., & Jiao, W. (2016). Towards an operational method for land surface temperature retrieval from Landsat 8 data. *Remote Sensing Letters*, *7*(3), 279–288. https://doi.org/10.1080/2150704X.2015.1130877

Zhao, H. M., & Chen, X. L. (2005). Use of normalized difference bareness index in quickly mapping bare areas from TM/ETM +. *IEEE International Geoscience and Remote Sensing Symposium*, *3*(25–29), 1666–1668. https://doi.org/10.1109/IGARSS.2005.1526319.

Zhao, M., Cai, H., Qiao, Z., & Xu, X. (2016). Influence of urban expansion on the urban heat island effect in Shanghai. *International Journal of Geographical Information Science*, *30*(12), 2421–2441. https://doi.org/10.1080/13658816.2016.1178389

Zhou, W., Qian, Y., Li, X., Li, W., & Han, L. (2014). Relationships between land cover and the surface urban heat island: Seasonal variability and effects of spatial and thematic resolution of land cover data on predicting land surface temperatures. *Landscape Ecology*, *29*(1), 153–167. https://doi.org/10.1007/s10980-013-9950-5

Zhou, W. Q., Huang, G., & Cadenasso, M. L. (2011). Does spatial configuration matter? Understanding the effects of land cover pattern on land surface temperature in urban landscapes. *Landscape and Urban Planning*, *102*(1), 54–63. https://doi.org/10.1016/j.landurbplan.2011.03.009

Source details

Feedback > Compare sources >

Geografisk Tidsskrift

Scopus coverage years: from 1972 to 2023

Publisher: Taylor & Francis

ISSN: 0016-7223

Subject area: Social Sciences: Geography, Planning and Development | Earth and Planetary Sciences: General Earth and Planetary Sciences

Source type: Journal

View all documents > | Set document alert | Save to source list

CiteScore 2022
4.1

SJR 2022
0.452

SNIP 2022
0.740

CiteScore | CiteScore rank & trend | Scopus content coverage

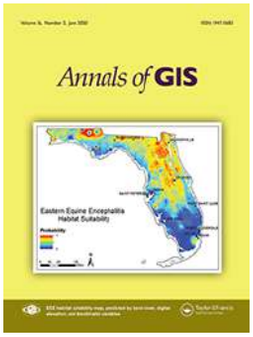

Annals of GIS

ISSN: (Print) (Online) Journal homepage: https://www.tandfonline.com/loi/tagi20

Analytical study on the relationship between land surface temperature and land use/land cover indices

Subhanil Guha , Himanshu Govil , Neetu Gill & Anindita Dey

To cite this article: Subhanil Guha , Himanshu Govil , Neetu Gill & Anindita Dey (2020) Analytical study on the relationship between land surface temperature and land use/land cover indices, Annals of GIS, 26:2, 201-216, DOI: 10.1080/19475683.2020.1754291

To link to this article: https://doi.org/10.1080/19475683.2020.1754291

Published online: 27 Apr 2020.

ANNALS OF GIS
2020, VOL. 26, NO. 2, 201–216
https://doi.org/10.1080/19475683.2020.1754291

Taylor & Francis
Taylor & Francis Group

Analytical study on the relationship between land surface temperature and land use/land cover indices

Subhanil Guha [a], Himanshu Govil [a], Neetu Gill [b] and Anindita Dey [c]

[a]Department of Applied Geology, National Institute of Technology Raipur, Raipur, India; [b]Chhattisgarh Council of Science and Technology, Raipur, India; [c]Department of Geography, Nazrul Balika Vidyalaya, Guma, West Bengal, India

ABSTRACT

The present study focuses on the estimating land surface temperature (LST) of Raipur City in India emphasizing the urban heat island (UHI) and non-UHI inside the city boundary and their relationship with normalized difference vegetation index, normalized difference water index, normalized difference built-up index, and normalized multi-band drought index. The entire study has been performed on four multi-date Landsat 8 Operational Land Imager and Thermal Infrared Sensor images taken from four different seasons; pre-monsoon, monsoon, post-monsoon, and winter in the same year. The UHI has mainly been developed along the northern and southern periphery of the city. The range of LST in the common UHI for four different seasons varies between 25.72° C and 35.69° C. The results present the strongest correlation between LST and the land use/land cover indices in monsoon and post-monsoon images while winter and pre-monsoon images show a comparatively weak correlation.

ARTICLE HISTORY
Received 30 July 2019
Accepted 6 April 2020

KEYWORDS
Land surface temperature (LST); urban heat island (UHI); land use/land cover; landsat

1. Introduction

The concept of land surface temperature (LST) and urban heat island (UHI) is used to interpret the changing land use/land cover (LULC) pattern in heterogeneous urban area (Arnfield 2003; Mirzaei 2015; Rizwan, Dennis, and Liu 2008; Rinner and Hussain 2011; Zhao et al. 2016). LST was determined in some major global cities (e.g., Beijing, Columbus, Shanghai, Baltimore, Chicago, etc.) to solve many environmental problems. Different types of LULC influence on the nature and distribution of LST (Chun and Guldmann 2014; Dai, Guldmann, and Hu 2018; Kim and Guldmann 2014; Zhang et al. 2013: Zhou, Huang, and Cadenasso 2011; Coseo and Larsen 2014). Some normalized difference LULC indices such as vegetation index, built-up index, bareness index, water index, etc. were frquently used in the recent LST related studies to estimate their impact on the changing environmental status of the urban areas (Li et al. 2011; Peng et al. 2016; Amiri et al. 2009; Song et al. 2014; Kuang et al. 2015). The linear correlation analyses between LST and LULC indices were discussed oon the cities from different parts of the world like Some recent articles discussed the statistical linear correlation between LST and some selected LULC indices for separate study areas like Brisbane (Deilami and Kamruzzaman 2017), Raipur (Guha et al. 2017), Shanghai (Nie et al. 2016), Addis Ababa (Feyisa et al. 2016), Mexico (Lopez et al. 2017), Philadelphia (Pearsall 2017), Florence and Naples (Guha et al. 2018), etc.

Seasonal contrast in LST distribuion depends on the composition of land surface and it was examined in some contemporary research works. Cui and de Foy (2012) clearly stated that the seasonal fluctuation of LST primarily depends on vegetation and weather elements. Zhou et al. (2014) was keen to build correlation between LST and LULC indices in Baltimore City of United State of America (USA). Haashemi et al. (2016) noticed a seasonal variation on LST-LULC indices relationship in a study performed in Tehran City of Iran.

A simple regression analysis was used to show the seasonal impacts of thermal conditions of Ohio City, USA (Chun and Guldmann 2018). An integration of statistical techniques were applied to estimate the seasonal changes in LST-LULC indices relationship (Peng et al. 2018). A seasonal study on LST-LULC indices relationship was conducted in Jaipur City, India (Mathew, Khandelwal, and Kaul 2017). A new model was applied to show the seasonal change of LST in Beijing, China (Quan et al. 2016). The annual and seasonal trends of LST in peninsular Spain were observed by using statistical model (Khorchani et al. 2018a, 2018b). Another analysis between LST and climatic elements were evaluated in

CONTACT Subhanil Guha subhanilguha@gmail.com Department of Applied Geology, National Institute of Technology Raipur, Raipur, India

the urban areas of China (Yao et al. 2018). A seasonal interpretation of LST with the weather elements was performed on the cities of China (Lai et al. 2018). The variation of LST and land connectivity was analyzed with a specific index applied in Beijing, China (Sun, Xie, and Chen 2018). Thus, the correlation analysis beteen LST and LULC indices was quite common in the UHI related study. The present paper also used a common linear regression method to show the seasonal variation of LST in UHI, non-UHI, and common UHI zones in a typical Indian city for a single year and the relationship of LST with different LULC indices.

The main focus of the study was to determine the seasonal variation of LST-LULC indices relationship in the UHI, non-UHI, common UHI and the whole of Raipur City by using Landsat 8 satellite images.

2. Study area and data

Raipur, the capital of Chhattisgarh and a rapidly growing smart city in India was selected as the study area. Raipur extends from 21°11′22″ N to 21° 20′02″ N and from 81°32′20″ E to 81°41′50″ E (Figure 1). The range of elevation of the study area is approximately 300 m above mean sea level and it is loocated along the western part of the Mahanadi River (Figure 1). Overall the city is under a tropical savannah type of climate. Accoding to India Meteorological Department, pre-monsoon, monsoon, post-monsoon, and winteroccur in Raipur City. Pre-monsoon season (March-June) is hot and dry. Mot of the heavy showers occur in July to September (Monsoon season). Temperature falls at a significant rate in the post-monsoon period (October-November). Winter season (December-February) is characterised by dry and cool weather. The average annual range of temperature is 21°C-34°C and the average annual precipitation is 120–150 cm.

A total of four (one from each season (according to India Meteorological Department)) Landsat 8 Operational Land Imager (OLI) and Thermal Infrared Sensor (TIRS) level-1 data (<10% cloud coverage) have been selected to determine the LST and to detect the UHI over the whole of the Raipur City for the following dates (Govil et al. 2019; Govil 2020; Guha et al. 2019): 5 June 2014 (pre-monsoon image), 25 September 2014 (monsoon image), 12 November 2014 (post-monsoon image), and

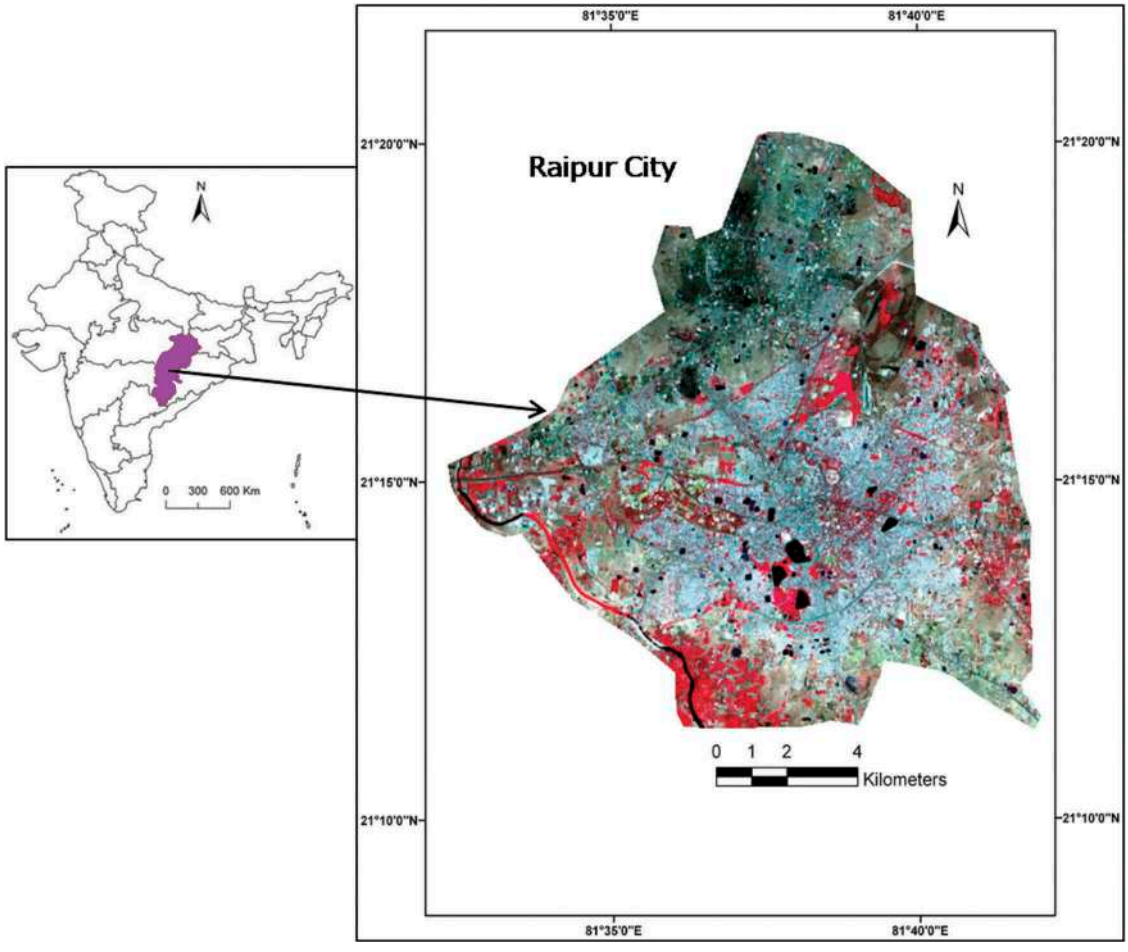

Figure 1. Location of the study area.

Table 1. Data specification of Landsat 8 OLI and TIRS satellite images for different seasons.

Date of acquisition	Time (UTC)	Path/ Row	Sun elevation (°)	Sun azimuth (°)	Cloud cover (%)	Earth-Sun distance (astronomical unit)	Resolution of VNIR bands (m)	Resolution of TIR bands (m)
05.06.2014	04:55:45	142/044	68.3821	83.3098	0.02	1.0146	30	100
25.09.2014	04:56:11	142/044	59.2100	134.1804	0.81	1.0030	30	100
12.11.2014	04:56:21	142/044	46.2266	152.4664	7.59	0.9899	30	100
30.12.2014	04:56:09	142/044	39.3441	150.8364	0.41	0.9834	30	100

30 December 2014 (winter image). These four level-1 Landsat 8 OLI and TIRS images have been used as the representatives of four different seasons, separately. The Landsat 8 datasets have been freely downloaded from United States Geological Survey (http://earthexplorer.USGS.gov). The data specification has been shown in Table 1. Landsat 8 TIRS data have two bands (band10 and band11) having thermal characteristics. But, only TIR Band 10 data has been used for the LST retrieval process because TIR band 11 data faces some calibration uncertainty (Guha et al. 2018; Weng 2001; Weng and Yang 2004; Zhang et al. 2016). Optical bands 3, 4, 5, 6, and 7 datasets have been used in developing NDVI, NDWI, NDBI, and NMDI. ArcGIS 9.3 software was used for various types of image processing and mapping.

3. Methodology

3.1. Image pre-processing and atmospheric correction

The satellite data acquired from Landsat 8 sensor was subset to limit the data size. The thermal infrared band for Landsat 8 TIR image (band 10) has a spatial resolution of 100 m. This thermal band was resampled using the nearest neighbour algorithm with a pixel size of 30 m to match the optical bands. Atmospheric correction of the satellite data has been done by the following steps:

For band 1 to band 9 of Landsat 8 OLI data, the following equation is used to converting a digital number into spectral reflectance:

$$\rho\lambda = M\rho \times Qcal + A\rho \quad (1)$$

where, $\rho\lambda$ is the spectral reflectance at top-of-atmosphere (TOA) without correction for solar angle (Unitless), *Qcal* is the Level 1 pixel value in Digital Number (DN), Mρ is the reflectance multiplicative scaling factor for the band (REFLECTANCEW_MULT_BAND_n from the metadata), $A\rho$ is the reflectance additive scaling factor for the band (REFLECTANCE_ADD_BAND_N from the metadata). The $\rho\lambda$ is corrected with local sun elevation angle θs by the following equation:

$$\rho'\lambda = \rho\lambda/\sin(\theta s) \quad (2)$$

For band 10 of Landsat 8 TIRS data, a similar calibration equation is used:

$$L\lambda = ML \times Qcal + AL \quad (3)$$

where, $L\lambda$ is the spectral radiance at TOA in $Wm^{-2}sr^{-1}\ mm^{-1}$, *Qcal* is the Level 1 pixel value in Digital Number (DN), M*L* is the radiance multiplicative scaling factor for the band (RADIANCE_MULT_BAND_n from the metadata) and *AL* is radiance additive scaling factor for the band (RADIANCE_ADD_BAND_n from the metadata).

3.2. Extraction of different LULC indices

Normalized difference vegetation index (NDVI) (Tucker 1979) is the most frequently used index for extracting vegetation. It is also applied in deriving LST and normally shows a negative correlation with LST. Normalized difference water index (NDWI) (McFeeters 1996) is generally used for water body extraction. Normalized difference built-up index (NDBI) (Zha, Gao, and Ni 2003) was applied in this study to detect the built-up area. Normalized multi-band drought index (NMDI) (Yuan and Bauer 2007) was used to identify the dry soil or bare land. These four indices can be applied to categorize different types of LULC (Table 2).

3.3. Retrieving LST from Landsat 8 thermal band

In this study, the mono-window algorithm (Qin et al. 2001; Guha and Govil 2020; Guha et al. 2017, 2018, 2019) has been applied to derive LST from Landsat 8 TIRS data where ground emissivity, atmospheric transmittance and effective mean atmospheric temperature are considered as the three required parameters. The entire procedure has the following steps:-

Table 2. Description of four LULC indices.

Acronym	Description	Formulation	Reference
NDVI	Normalized difference vegetation index	$\frac{NIR-Red}{NIR+Red}$	Tucker 1979
NDWI	Normalized difference water index	$\frac{Green-NIR}{Green+NIR}$	McFeeters 1996
NDBI	Normalized difference built-up index	$\frac{SWIR1-NIR}{SWIR1+NIR}$	Zha, Gao, and Ni et al. 2003
NMDI	Normalized multi-band drought index	$\frac{[NIR-(SWIR1-SWIR2)]}{[NIR+(SWIR1+SWIR2)]}$	Yuan and Bauer 2007

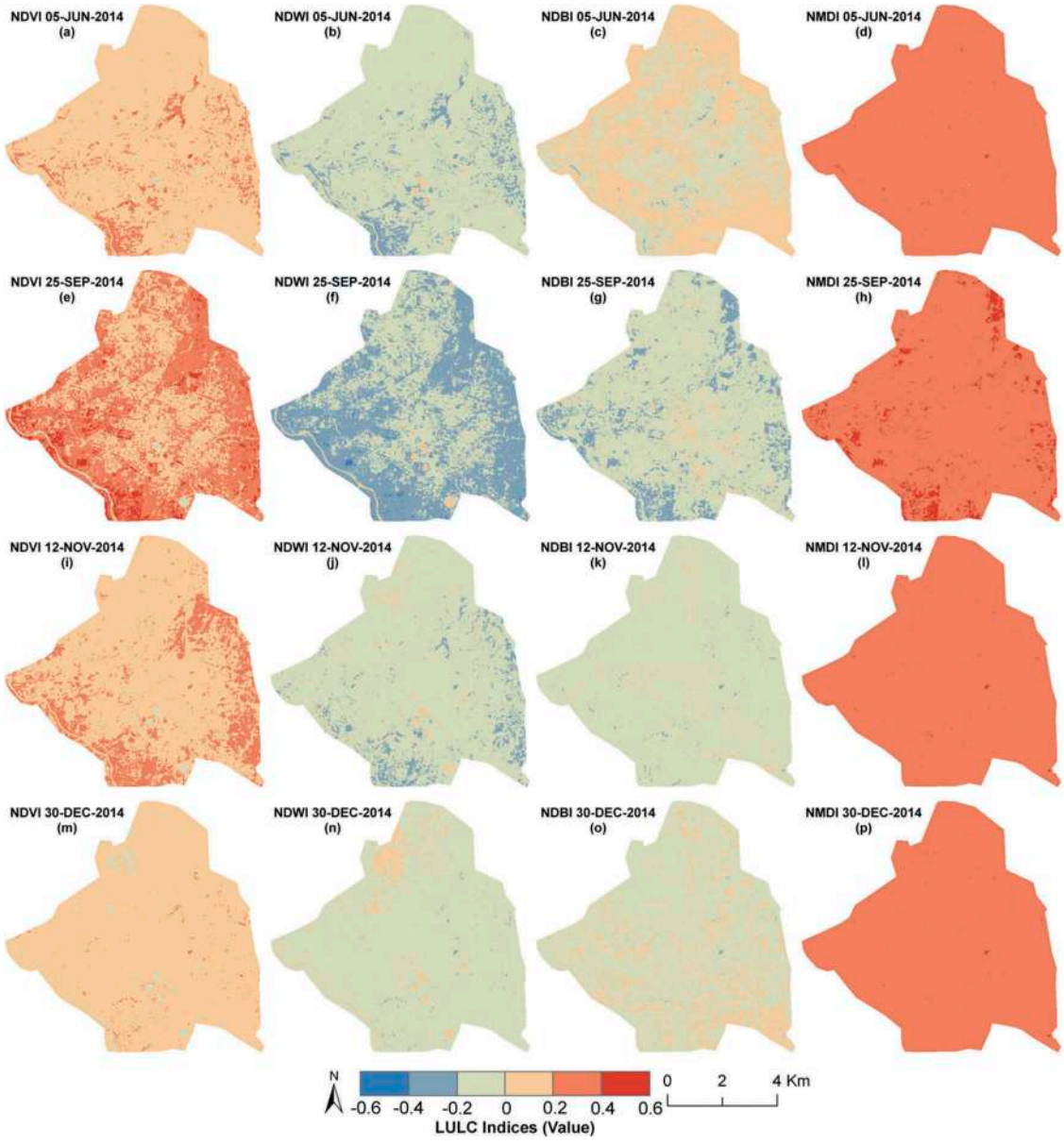

Figure 2. Seasonal variation of NDVI, NDWI, NDBI, and NMDI in Raipur City: (a-d) Pre-monsoon, (e-h) Monsoon,(i-l) Post-monsoon, and (m-p) Winter season.

$$L_\lambda = 0.0003342 * DN + 0.1 \tag{4}$$

where, L_λ is the spectral radiance in $Wm^{-2}sr^{-1}\ mm^{-1}$.

$$T_b = \frac{K_2}{\ln\left(\frac{K_1}{L_\lambda} + 1\right)} \tag{5}$$

where, T_b is the brightness temperature in Kelvin (K), is the spectral radiance in $Wm^{-2}sr^{-1}\ mm^{-1}$; K_2 and K_1 are calibration constants. For Landsat 8 data, K_2 is 774.89, K_1 is 1321.08 ($Wm^{-2}sr^{-1}\ mm^{-1}$).

$$F_v = \left(\frac{NDVI - NDVI_{min}}{NDVI_{max} - NDVI_{min}}\right)^2 \tag{6}$$

where,$NDVI_{min}$ is the minimum NDVI value (0.2) where pixels are considered as bare soil and $NDVI_{max}$ is the maximum NDVI value (0.5) where pixels are considered as healthy vegetation.

$d\varepsilon$ is the effect of the geometrical distribution of natural surfaces and internal reflections. For heterogeneous and undulating surfaces, the value of $d\varepsilon$ may be 2%.

$$d\varepsilon = (1 - \varepsilon_s\ )(1 - F_v)F\varepsilon_v \tag{7}$$

where, ε_v is vegetation emissivity, ε_s is soil emissivity, F_v is fractional vegetation, F is a shape factor whose mean is 0.55.

$$\varepsilon = \varepsilon_v F_v + \varepsilon_s(1 - F_v) + d\varepsilon \tag{8}$$

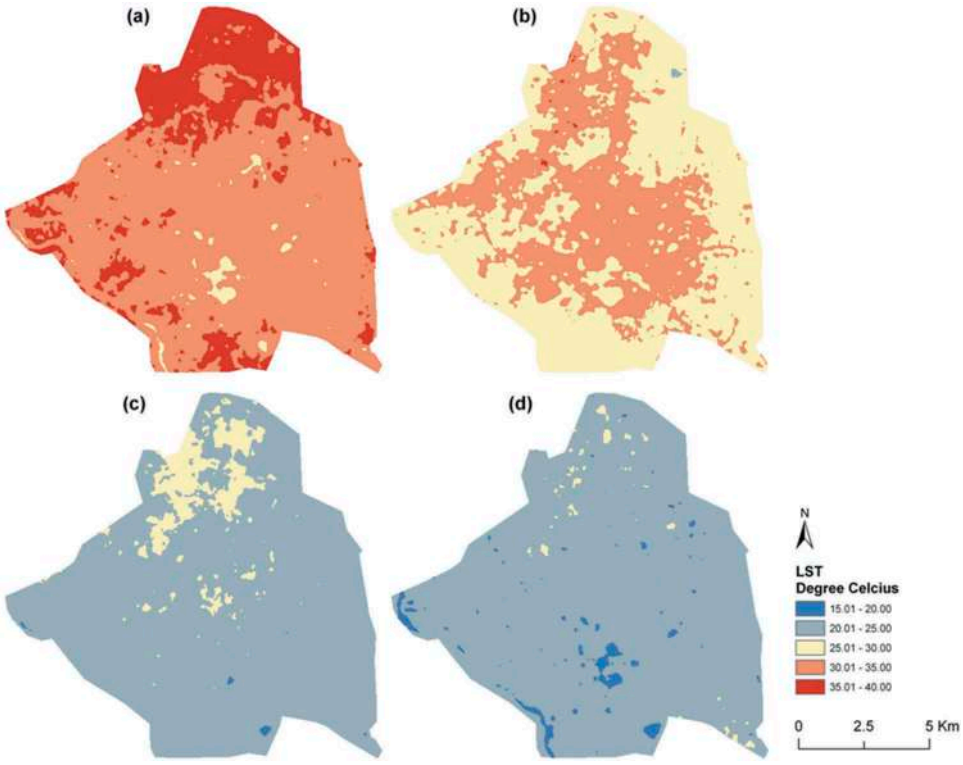

Figure 3. LST maps for Raipur City: (a) Pre-monsoon, (b) Monsoon, (c) Post-monsoon, and (d) Winter season.

where, ε is the land surface emissivity. The value of ε may be determined by the following equation:

$$\varepsilon = 0.004 \ * \ F_v + 0.986 \tag{9}$$

Water vapour content is determined by the following equation:

$$w = 0.0981 \times \left[10 \times 0.6108 \times \exp\left\{\frac{17.27 \times (T_0 - 273.15)}{273.3 + (T_0 - 273.15)}\right\} \times RH\right] + 0.1697 \tag{10}$$

where, w is the water vapour content (g/cm^2), T_0 is the near-surface air temperature in Kelvin (K), RH is the relative humidity (%). These parameters of the atmospheric profile are the average values of 14 stations around Raipur which have been obtained from the Meteorological Centre, Raipur and the Regional Meteorological Centre, Nagpur.

$$\tau = 1.031412 - 0.11536w \tag{11}$$

where, τ is the total atmospheric transmittance, ε is the land surface emissivity.

Raipur City is located in the tropical region. Thus, the following equation may be applied to compute the effective mean atmospheric transmittance of Raipur:

$$T_a = 17.9769 + 0.91715T_0 \tag{12}$$

$$T_s = \frac{[a(1 - C - D) + \{b(1 - C - D) + C + D\}T_b - DT_a]}{C} \tag{13}$$

$$C = \varepsilon\tau \tag{14}$$

$$D = (1 - \tau)[1 + (1 - \varepsilon)\tau] \tag{15}$$

where, ε is the land surface emissivity, τ is the total atmospheric transmittance, T_b is the at-sensor brightness temperature, T_a is the mean atmospheric temperature, T_0 is the near-surface air temperature, T_s is the land surface temperature, $a = -67.355351, b = 0.458606$.

3.4. Mapping UHI, non-UHI, and common UHI

UHI and non-UHI zones were identified using the following methods (Guha et al. 2017, 2018):

$$LST > \mu + 0.5 * \sigma \tag{16}$$

$$0 < LST \leq \mu + 0.5 * \sigma \tag{17}$$

where, μ and σ are the mean and standard deviation of LST in the study area respectively. Equation 16 has been used to derive UHI zones as the zones having LST more than the combined value of mean LST and half standard deviation. These zones are the most heated zones of the city. Apart from the UHI, the rest of the city area is considered as the non-UHI (Equation 17). The ratio of vegetation and water bodies is higher in the non-UHI, whereas in the UHI, the main LULC types are built-up areas and bare land. Moreover, the common UHI areas for four Landsat 8 images have also been determined. The common UHI is that specific area that is found inside the UHI for all the images and it is the most heated zone of the study area. This common UHI zone always remains severely heated, irrespective of any season. It is the most stable thermal zone with a high temperature compared to its surrounding zones. It is important due to its temporal or seasonal stability as a thermal stressed area.

Table 3. Descriptive statistics of NDVI, NDWI, NDBI, and NMDI for the whole of Raipur City.

Date of acquisition	Minimum	Maximum	Mean	Standard deviation
NDVI values				
5 June 2014	−0.0803	0.4536	0.1326	0.0568
25 September 2014	−0.1527	0.5526	0.2398	0.1017
12 November 2014	−0.1066	0.4478	0.1427	0.0640
30 December 2014	−0.1112	0.3762	0.0788	0.0486
NDWI values				
5 June 2014	−0.4032	0.0985	−0.1432	0.0514
25 September 2014	−0.4850	0.1715	−0.2122	0.0855
12 November 2014	−0.4146	0.1183	−0.1190	0.0577
30 December 2014	−0.3541	0.1453	−0.0673	0.0494
NDBI values				
5 June 2014	−0.3149	0.4505	0.0008	0.0495
25 September 2014	−0.4221	0.2112	−0.1141	0.0749
12 November 2014	−0.3444	0.1694	−0.0660	0.0443
30 December 2014	−0.3171	0.1827	−0.0249	0.0352
NMDI values				
5 June 2014	0.1533	0.4889	0.2912	0.0250
25 September 2014	0.1737	0.5256	0.3446	0.0321
12 November 2014	0.1986	0.5516	0.3231	0.0197
30 December 2014	0.2021	0.5230	0.3152	0.0190

4. Results and discussion

4.1. Seasonal variation in the distribution of NDVI, NDWI, NDBI, and NMDI

The descriptive statistics (Table 3) presents the minimum, maximum, mean, and standard deviation values of NDVI, NDWI, NDBI, and NMDI (Figure 2) for the whole of Raipur City.

4.2. Seasonal variation of LST distribution

The LST maps retrieved from satellite images have been shown in Figure 3. The seasonal variation in the LST distribution shows a specific thermal pattern. The mean LST values in pre-monsoon, monsoon, post-monsoon, and winter images are 33.59°C, 29.56°C, 23.40°C, and 22.26°C, respectively. The ranges of LST (maximum LST-minimum LST) are found as 13.50°C in pre-monsoon image, 12.28°C in monsoon image, 8.83°C in the post-monsoon image, and 10.12°C in the winter image, respectively. Basically, this type of heterogeneity in LST has been observed due to the change in vegetation abundance and soil moisture content. Monsoon and post-monsoon images are characterized by healthy vegetation and wet soil. The winter image reflects the least standard deviation value of LST (Table 4).

4.3. Validation of derived LST with respect to MODIS data

Before performing any kind of application, validation of derived LST is necessary with *in situ* measurement or with any other satellite sensor. In the present study, MODIS datasets have been applied for the validation of LST values as a reference image. For any particular date, MODIS and Landsat sensors do not provide imageries for the same study area. Thus, MOD11A1 data (1 km spatial resolution) of 4 June 2014 (pre-monsoon image), 24 September 2014 (monsoon image), 13 November 2014 (post-monsoon image), and 29 December 2014 (winter image) have

Table 4. Spatial distribution of LST (°C) for the whole of Raipur City in four multi-date images.

Date of acquisition	LST (Minimum)	LST (Maximum)	LST (Mean)	LST (Standard deviation)	Threshold LST value for UHI
5 June 2014	25.77	39.27	33.59	1.61	34.40
25 September 2014	24.51	36.79	29.56	1.73	30.42
12 November 2014	19.39	28.23	23.40	1.12	24.00
30 December 2014	17.64	27.76	22.26	1.11	22.82

Table 5. Validation of LST (°C) retrieved from Landsat 8 OLI and TIRS data with MODIS data (significant at 0.05 level).

	Landsat 8 (5 June 2014) & MODIS (4 June 2014)	Landsat 8 (25 September 2014) & MODIS (24 September 2014)	Landsat 8 (12 November 2014) & MODIS (13 November 2014)	Landsat 8 (30 December 2014) & MODIS (29 December 2014)
Correlation coefficient	0.61479	0.62433	0.62009	0.55437

been taken for the validation of estimated LST. No precipitation or atmospheric disturbances are observed in between the acquisition date of both Landsat 8 and MOD11A1 imageries for each aforementioned season. For MODIS and Landsat 8 data, the spatial resolution of retrieved LST is 1000 m and 100 m, respectively. In spite of not performing any upscaling or downscaling procedure, a moderate to strong positive regional correlation has been found between the mean derived LST from Landsat 8 data and MODIS data (Table 5).

4.4. Relationship of LST with wind speed, humidity, air temperature, air pressure, and elevation

The relationship between LST and some weather and terrain characteristics has been analysed in the present study. Elevation and some weather components like wind speed, humidity, air temperature, air pressure, etc. (obtained from the observation stations) correlate with LST differently. These relationships have been presented in Table 6. Air temperature has a very strong positive relationship with LST for the whole area, UHI, non-UHI, and common UHI, whereas air pressure builds a very strong negative relationship with LST. LST and wind speed correlate moderately negative for different heated areas of the city. Humidity and LST has a weak negative relationship. There is no such linear correlation found in the LST-elevation relationship.

Table 6. Relationship of LST with wind speed, humidity, air temperature, air pressure, and elevation (significant at 0.05 level).

Correlation coefficient	LST-wind speed	LST-humidity	LST-air temperature	LST-air pressure	LST-elevation
Whole city	−0.48	−0.28	0.94	−0.92	0.02
UHI	−0.49	−0.26	0.94	−0.91	−0.09
Non-UHI	−0.46	−0.29	0.94	−0.93	0.19
Common UHI	−0.52	−0.23	0.94	−0.90	−0.07

4.5. Seasonal variation of UHI, non-UHI, and common UHI

The intensity of UHI has been determined by the difference between the mean values of LST in UHI and non-UHI (Table 7). In pre-monsoon and winter images, the UHI zones are mainly generated in the north, west, and south-east periphery (Figure 4). But, in monsoon and post-monsoon images, the northern and central parts (the main built-up areas and bare lands within the city boundary) have been considered as the UHI zones. The difference between the mean LST values in UHI and non-UHI of Raipur City is 2.66° C, 2.91°C, 1.89°C, and 1.88°C in pre-monsoon, monsoon, post-monsoon, and winter images, respectively. The mean LST values of the common UHI of the city for all the four images have been ranged between 24.08°C (winter image) and 35.69°C (pre-monsoon image). Regardless of any particular date, the common UHI zones have been developed mainly in the north-west portion (bare lands and built-up areas) of the city (Figure 5).

4.6. Relationship of LST and NDVI, NDWI, NDBI, and NMDI for the Whole area, UHI, non-UHI, and common UHI of Raipur City

Generally, LST presents a negative relationship with NDVI and NMDI, whereas it shows a positive relationship with NDBI. There is no such significant relationship formed between LST and NDWI. This particular pattern has been seen in the whole of Raipur City, irrespective of dates (Table 8).

Table 7. Seasonal **v**ariations of LST (°C) in UHI, non-UHI, and common UHI in Raipur City.

	LST (Minimum)			LST (Maximum)			LST (Mean)			LST (Standard deviation)		
Date of Acquisition	UHI	Non-UHI	Common UHI	UHI	Non-UHI	Common UHI	UHI	Non-UHI	Common UHI	UHI	Non-UHI	Common UHI
5 June 2014	34.40	25.78	34.40	39.27	34.40	38.45	35.42	32.76	35.69	0.73	1.16	0.73
25 September 2014	30.42	24.51	30.42	36.79	30.42	36.78	31.50	28.59	32.09	0.85	1.14	1.16
12 November 2014	24.00	19.39	24.00	28.23	24.00	28.22	24.81	22.92	25.72	0.78	0.76	0.74
30 December 2014	22.82	17.64	22.81	27.76	22.82	27.75	23.63	21.75	24.08	0.68	0.75	0.69

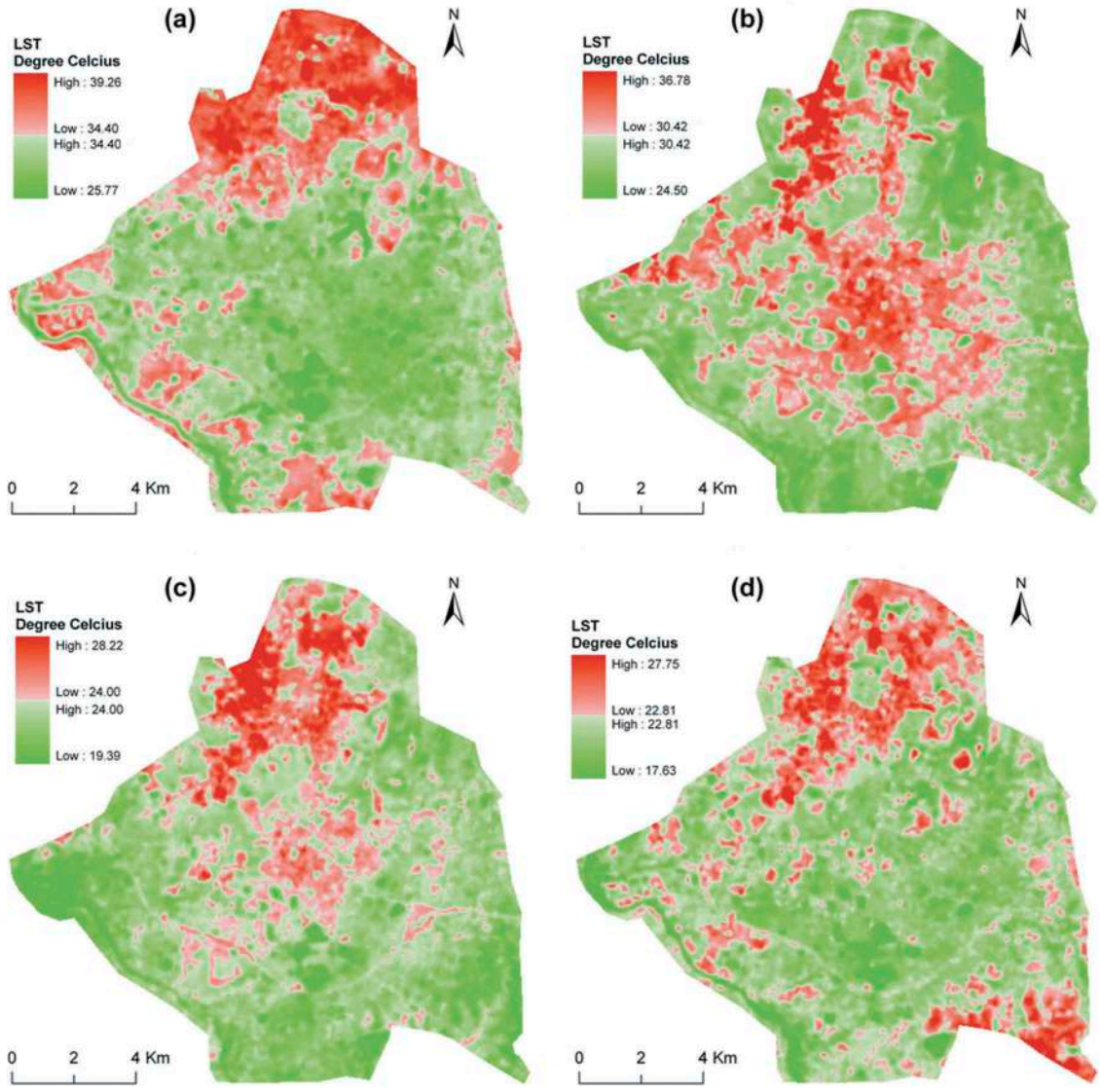

Figure 4. UHI and non-UHI of Raipur City: (a) Pre-monsoon, (b) Monsoon, (c) Post-monsoon, and (d) Winter season.

Correlation coefficient values are significant at 0.05 level. NDBI shows the strongest correlation with LST among the four LULC indices for four multi-date images. But, these relationships tend to be changed within the UHI of the city, whereas NDVI and NDWI reflect a stronger correlation with LST for each and every image. Again, the scenario became different within the non-UHI portions of the city where NDBI and NMDI presented a stronger correlation with LST compare to the other two LULC indices. In the common UHI (using the mean value of single season or the mean value of four seasons) region, NDVI and NDWI have a much better correlation with LST, but these relationships become gradually weak with the increase of the heterogeneous surface features. Monsoon and post-monsoon images reveal a better correlation between LST and LULC indices. Common UHI (Figure 6) using the mean value of four seasons indicate a stronger correlation for LST and LULC indices.

Figure 7-10 represent the seasonal variation of LST distribution maps and their corresponding NDVI, NDWI, NDBI, and NMDI maps for the UHI, non-UHI, common UHI using the mean value of single season, and common UHI using the mean value of four seasons, respectively. Due to the presence of more moisture content in soil and air, the relationships between LST and LULC indices are more consistent in the monsoon and post-monsoon images.

Figure 7 represents the seasonal variation of LST distribution maps and their corresponding NDVI,

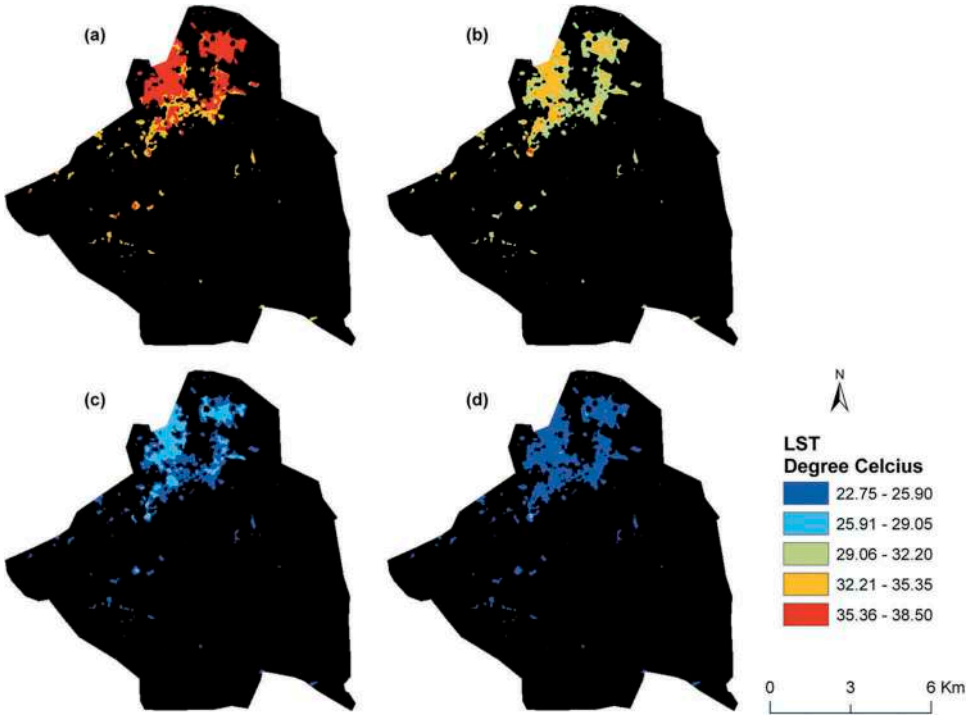

Figure 5. Common UHI (using the mean value of each season) of Raipur City: (a) Pre-monsoon, (b) Monsoon, (c) Post-monsoon, and (d) Winter season. The black colour portions of the images represent the area outside the common UHI for different seasons.

Table 8. Correlation coefficient values of LST with different LULC indices (significant at 0.05 level).

LULC Indices	5 June 2014	25 September 2014	12 November 2014	30 December 2014
Correlation coefficient values of LST and LULC indices (Whole of the Raipur City)				
NDVI	−0.3201	−0.5942	−0.5337	−0.0982
NDWI	0.2300	0.5065	0.4906	0.0005
NDBI	0.5764	0.7235	0.5384	0.4950
NMDI	−0.5030	−0.6467	−0.2829	−0.4026
Correlation coefficient values of LST and LULC indices (UHI)				
NDVI	−0.4634	−0.4069	−0.4833	−0.3333
NDWI	0.4708	0.4497	0.5177	0.2706
NDBI	−0.0465	0.2621	0.1150	0.1703
NMDI	0.2456	−0.0935	0.1963	0.0675
Correlation coefficient values of LST and LULC indices (non-UHI)				
NDVI	−0.1017	−0.3640	−0.2613	0.1520
NDWI	−0.0501	0.2699	0.1798	−0.2702
NDBI	0.5732	0.5955	0.4966	0.5045
NMDI	−0.6234	−0.5828	−0.4078	−0.5737
Correlation coefficient values of LST and LULC indices (common UHI using the mean value of each season)				
NDVI	−0.3714	−0.4313	−0.5126	−0.2924
NDWI	0.3739	0.4463	0.5068	0.2538
NDBI	−0.0073	0.3319	0.1768	0.0425
NMDI	0.1621	−0.1024	0.1616	0.1448
Correlation coefficient values of LST and LULC indices (common UHI using the mean value of four seasons)				
NDVI	−0.5566	−0.5244	−0.3731	−0.5356
NDWI	0.6139	0.5465	0.4182	0.5159
NDBI	−0.2039	0.1263	0.1819	−0.1213
NMDI	0.3899	0.2354	0.0089	0.3571

NDWI, NDBI, and NMDI maps for the UHI of Raipur City for four multi-date images. The black coloured portion of the map represents the non-UHI area of Raipur City. The post-monsoon image reveals the most consistent relationship. The northwest portion of the study area shows a stronger spatial relationship between LST and all the LULC indices. In the pre-monsoon season, the high LST values are

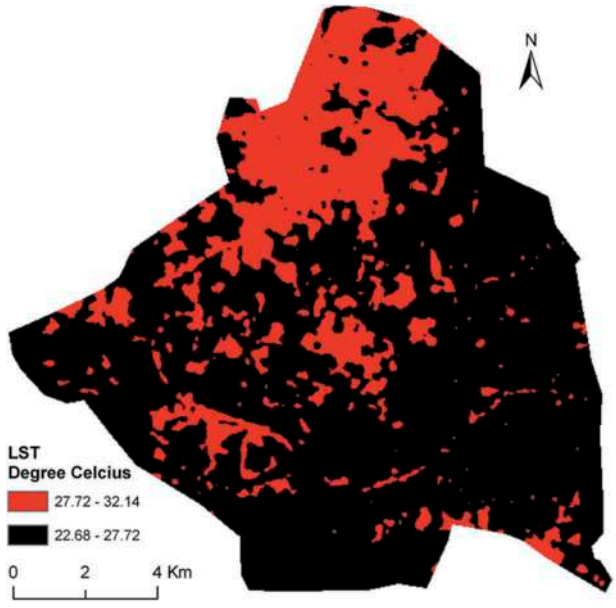

Figure 6. Common UHI (using the mean value of four seasons) of Raipur City. The black colour portion of the image represents the area outside the common UHI.

corresponding to moderate NDVI, moderate NDWI, high NDBI, and moderate NMDI values. The monsoon season shows that the high LST values are found in the area of low NDVI, moderate NDWI, high NDBI, and low NMDI. In the post-monsoon season, low NDVI, moderate NDWI, high NDBI, and moderate NMDI zones represent the high LST values. In the winter season, low NDVI, high NDWI, high NDBI, and low NMDI zones represent the high LST values.

Figure 8 shows the variation of LST distribution maps and their corresponding NDVI, NDWI, NDBI, and NMDI maps for the non-UHI of Raipur City for four multi-date images. The black coloured portion of the map represents the UHI area of Raipur City. The post-monsoon image reflects the most significant relationship. In the southern portion of the non-UHI, the relationship is more reliable. In the pre-monsoon season, the high LST values are corresponding to moderate NDVI, low NDWI, moderate NDBI, and low NMDI values. The monsoon season shows that the high LST values are found in the area of high NDVI, low NDWI, low NDBI, and high NMDI. In the post-monsoon season, moderate NDVI, low NDWI, moderate NDBI, and low NMDI zones represent the high LST values. In the winter season, moderate NDVI, moderate NDWI, high NDBI, and low NMDI zones represent the high LST values.

LST distribution maps and their corresponding NDVI, NDWI, NDBI, and NMDI maps for the common UHI of Raipur City using mean value of single season are presented by Figure 9. The black coloured portion of the map represents the area outside the common UHI of the city. Post-monsoon and monsoon images indicate the most significant relationship of LST with LULC indices. In the pre-monsoon season, the high LST values are corresponding to moderate NDVI, moderate NDWI, high NDBI, and moderate NMDI values. The monsoon season shows that the high LST values are found in the area of low NDVI, moderate NDWI, high NDBI, and low NMDI. In the post-monsoon season, low NDVI, moderate NDWI, high NDBI, and moderate NMDI zones represent the high LST values. In the winter season, low NDVI, high NDWI, high NDBI, and low NMDI zones represent the high LST values.

LST distribution maps and their corresponding NDVI, NDWI, NDBI, and NMDI maps for the common UHI of Raipur City using mean value of four seasons are presented by Figure 10. The black coloured portion of the map represents the area outside the common UHI of the city. In the pre-monsoon, winter, and monsoon images, LST correlates strongly with the LULC indices. In the pre-monsoon season, the high LST values are corresponding to moderate NDVI, low NDWI, moderate NDBI, and low NMDI values. The monsoon season shows that the high LST values are found in the area of moderate NDVI, low NDWI, moderate NDBI, and moderate NMDI. In the post-monsoon season, low NDVI, moderate NDWI, moderate NDBI, and moderate NMDI zones represent the high LST values. In the winter season, moderate NDVI, moderate NDWI, moderate NDBI, and moderate NMDI zones represent the high LST values.

The best correlation between LST and the four above-mentioned LULC indices is found for the whole of Raipur City, irrespective of any date. The relationship is weaker with the increase of heterogeneity in an urban landscape. Common UHI of all seasons simply indicates the built-up area and semi bare lands which are more heterogeneous. Thus, the least correlation has been found in the common UHI of the city area. UHI and non-UHI of the city reflect the moderate values of the correlation coefficient.

5. Conclusion

In this paper, Landsat 8 OLI and TIRS data of four different dates selected from four different seasons in a single year have been used to investigate the UHI intensity effect in Raipur City of India and to interpret the dynamic relationship between LST with NDVI, NDWI, NDBI, and NMDI. The above relationships have been examined using the whole area, UHI, non-UHI, and common UHI of Raipur City. UHIs have

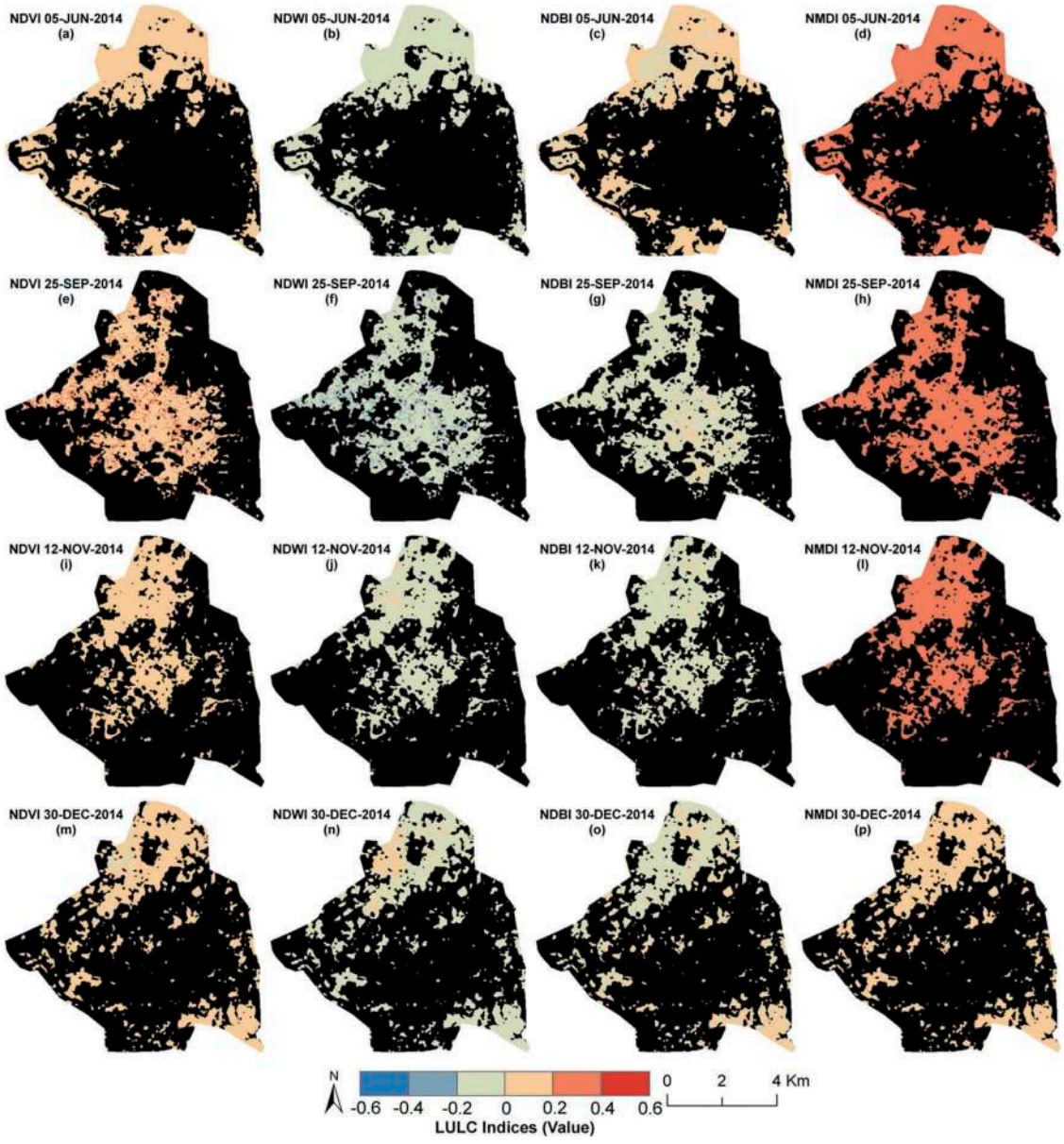

Figure 7. LST-NDVI, LST-NDWI, LST-NDBI, and LST-NMDI relationship in UHI of Raipur City: (a)-(d) Pre-monsoon season; (e)-(h) Monsoon season; (i)-(l) Post-monsoon season; (m)-(p) Winter season. The black colour portions of the images represent the non-UHI for different seasons.

been identified through the spatial distribution of LST which are mainly existed in the northern and southern parts of the city. Bare land and built-up area are mostly responsible for generating high LST values. LST level is reduced significantly due to the presence of vegetation and water bodies.

Furthermore, the relationships of LST to NDVI, NDWI, NDBI, and NMDI have been interpreted quantitatively by linear regression analysis (using Pearson's product moment correlation coefficient) at the pixel level. For the whole of Raipur City, LST shows a strong positive correlation with NDBI; and a moderate to strong negative correlation with NMDI, irrespective of dates. Inside the UHI, NDVI and NDWI show a stronger correlation (NDVI-negative, NDWI-positive) with LST in comparison with the other indices. Conversely, inside the non-UHI zone, NDBI and NMDI present a stronger correlation (NDBI-positive, NMDI-negative). Besides, NDVI-LST and NDWI-LST relationships are stronger inside the common UHI in all seasons.

One of the main objectives of the present study is to estimate the variation in the correlation analysis for the

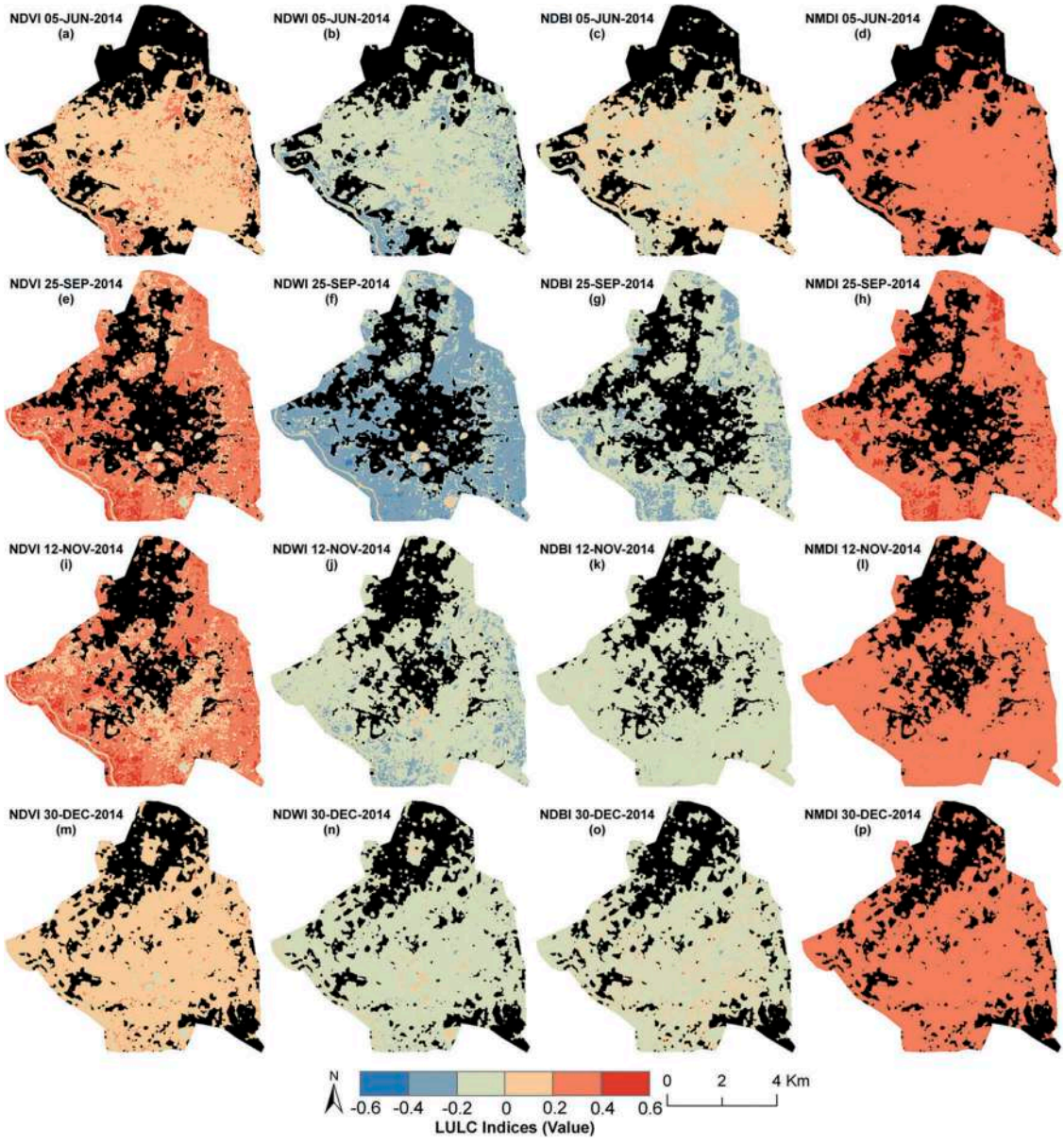

Figure 8. LST-NDVI, LST-NDWI, LST-NDBI, and LST-NMDI relationship in non-UHI of Raipur City: (a)-(d) Pre-monsoon season; (e)-(h) Monsoon season; (i)-(l) Post-monsoon season; (m)-(p) Winter season. The black colour portions of the images represent the UHI for different seasons.

satellite images of four different dates. Monsoon and post-monsoon images are more prominent in showing the relationship between LST and LULC indices due to the presence of green healthy vegetation and high moisture content in the soil. Pre-monsoon image is less dominant compared to the above two images, whereas these relationships show the lowest correlation coefficient values in the winter image.

In the future, many additional research works may be included. Firstly, the entire research work can be performed with other satellite data of different spatial resolution (e.g., IKONOS (1 m), Quickbird (0.6 m), ASTER (15 m), Sentinel-2A (10 m), MODIS (1000 m), etc.). Secondly, seasonal variation in the correlation values between LST and LULC indices may be monitored with ten years or more time period. Thirdly, other LULC indices (e.g., Enhanced vegetation index, Soil adjusted vegetation index, Modified normalized difference water index, Normalized difference mud index, Burn area index, etc.) may be examined to find the better correlation with LST. Fourthly, the present study may be examined in

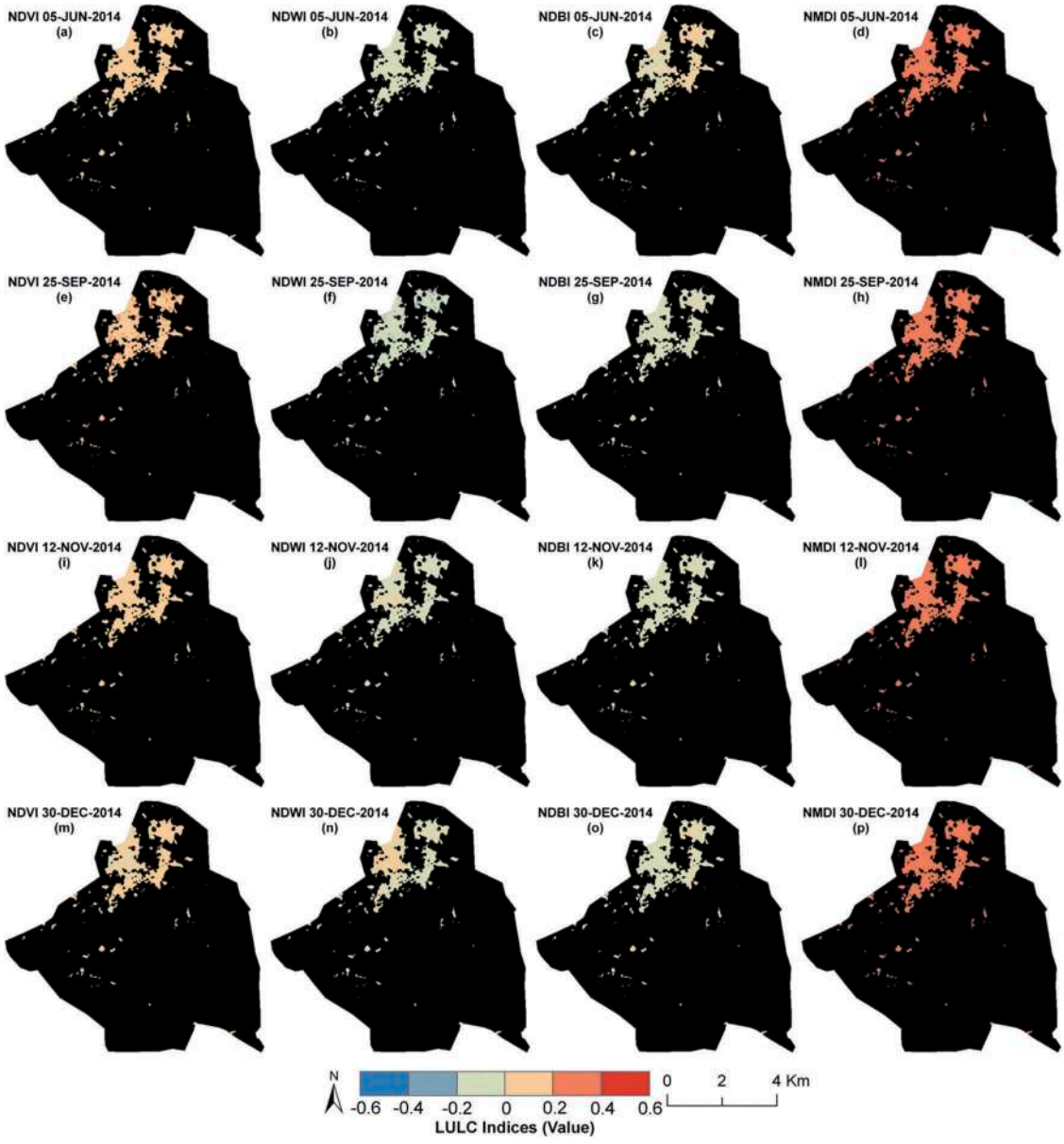

Figure 9. LST-NDVI, LST-NDWI, LST-NDBI, and LST-NMDI relationship in common UHI (using the mean value of single season) of Raipur City: (a)-(d) Pre-monsoon season; (e)-(h) Monsoon season; (i)-(l) Post-monsoon season; (m)-(p) Winter season. The black colour portions of the images represent the area outside the common UHI for different seasons.

different environments with large physical varieties. Finally, other statistical methods and algorithms (Spearman Rank Correlation Coefficient, Kendall correlation coefficient, etc.) may also be applied to estimate the correlation between LST and different LULC indices.

Acknowledgements

The authors are indebted to United States Geological Survey and National Institute of Technology Raipur, India.

Disclosure statement

No potential conflict of interest was reported by the authors.

ORCID

Subhanil Guha http://orcid.org/0000-0002-2967-7248
Himanshu Govil http://orcid.org/0000-0002-3433-8355
Neetu Gill http://orcid.org/0000-0001-7392-2178
Anindita Dey http://orcid.org/0000-0002-6400-4284

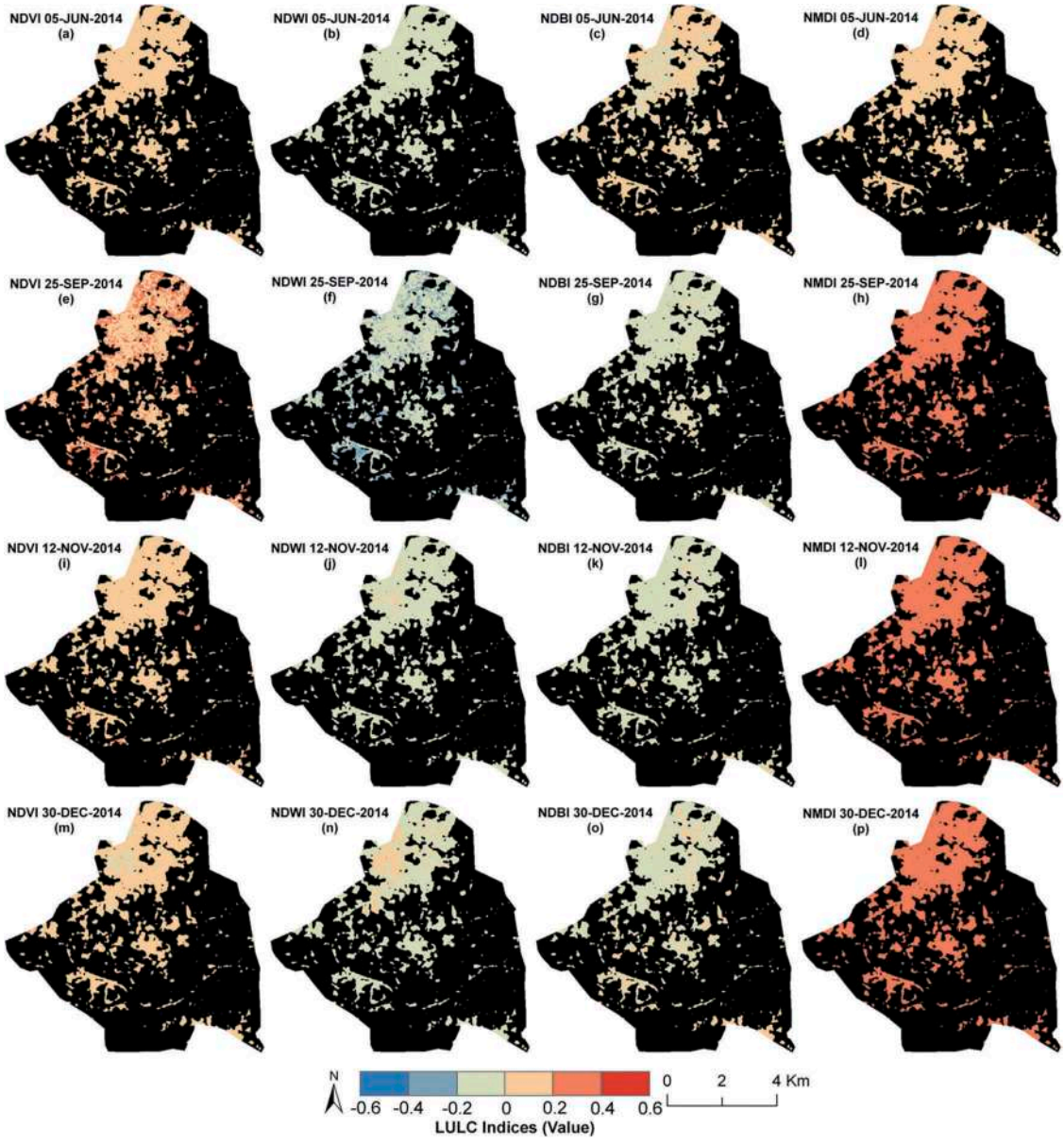

Figure 10. LST-NDVI, LST-NDWI, LST-NDBI, and LST-NMDI relationship in common UHI (using the mean value of four seasons) of Raipur City: (a)-(d) Pre-monsoon season; (e)-(h) Monsoon season; (i)-(l) Post-monsoon season; (m)-(p) Winter season. The black colour portions of the images represent the area outside the common UHI for different seasons.

References

Amiri, R., Q. Weng, A. Alimohammadi, and S. K. Alavipanah. 2009. "Spatial-temporal Dynamics of Land Surface Temperature in Relation to Fractional Vegetation Cover and Land Use/cover in the Tabriz Urban Area, Iran." *Remote Sensing of Environment* 113:2606–2617. doi:10.1016/j.rse.2009.07.021.

Arnfield, J. 2003. "Two Decades of Urban Climate Research: A Review of Turbulence, Exchanges of Energy and Water, and the Urban Heat Island." *International Journal of Climatology* 23: 1–26. doi:10.1002/joc.859.

Chun, B., and J. M. Guldmann. 2018. "Impact of Greening on the Urban Heat Island: Seasonal Variations and Mitigation Strategies." *Computers, Environment and Urban Systems* 71: 165–176. doi:10.1016/j.compenvurbsys.2018.05.006.

Chun, B., and J.-M. Guldmann. 2014. "Spatial Statistical Analysis and Simulation of the Urban Heat Island in High-density Central Cities." *Landscape and Urban Planning* 125: 76–88. doi:10.1016/j.landurbplan.2014.01.016.

Coseo, P., and L. Larsen. 2014. "How Factors of Land Use/land Cover, Building Configuration, and Adjacent Heat Sources and Sinks Explain Urban Heat Islands in Chicago." *Landscape and Urban Planning* 125: 117–129. doi:10.1016/j.landurbplan.2014.02.019.

Cui, Y. Y., and B. de Foy. 2012. "Seasonal Variations of the Urban Heat Island at the Surface and the Near-surface and Reductions Due to Urban Vegetation in Mexico City." *Journal of Applied Meteorology and Climatology* 51: 855–868. doi:10.1175/JAMC-D-11-0104.1.

Dai, Z., J.-M. Guldmann, and Y. Hu. 2018. "Spatial Regression Models of Park and Land-use Impacts on the Urban Heat Island in Central Beijing." *Science of the Total Environment* 626 :1136–1147. doi:10.1016/j.scitotenv.2018.01.165.

Deilami, K., and M. Kamruzzaman. 2017. "Modelling the Urban Heat Island Effect of Smart Growth Policy Scenarios in Brisbane." *Land Use Policy* 64: 38–55. doi:10.1016/j.landusepol.2017.02.027.

Feyisa, G. L., H. Meilby, G. Darrel Jenerette, and S. Pauliet. 2016. "Locally Optimized Separability Enhancement Indices for Urban Land Cover Mapping: Exploring Thermal Environmental Consequences of Rapid Urbanization in Addis Ababa, Ethiopia." *Remote Sensing of Environment* 175 :14–31. doi:10.1016/j.rse.2015.12.026.

Govil, H., S. Guha, A. Dey, and N. Gill. 2019. "Seasonal Evaluation of Downscaled Land Surface Temperature: A Case Study in A Humid Tropical City." *Heliyon* 5 (6): e01923. doi:10.1016/j.heliyon.2019.e01923.

Govil H., Guha S., Diwan P., Gill N., Dey A. 2020. "Analyzing Linear Relationships of LST with NDVI and MNDISI Using Various Resolution Levels of Landsat 8 OLI and TIRS Data." In *Data Management, Analytics and Innovation. Advances in Intelligent Systems and Computing*. Vol. 1042 pp. 171-184. edited by N. Sharma, A. Chakrabarti, V. Balas, et al. Singapore: Springer.doi:10.1007/978-981-32-9949-8_13.

Guha, S., H. Govil, and S. Mukherjee. 2017. "Dynamic Analysis and Ecological Evaluation of Urban Heat Islands in Raipur City, India." *Journal of Applied Remote Sensing* 11 (3): 036020. doi:10/1117/1.JRS.11.036020.

Guha, S., H. Govil, and P. Diwan. 2019. "Analytical Study of Seasonal Variability in Land Surface Temperature with Normalized Difference Vegetation Index, Normalized Difference Water Index, Normalized Difference Built-up Index, and Normalized Multiband Drought Index." *Journal of Applied Remote Sensing* 13 (2): 024518. doi:10.1117/1.JRS.13.024518.

Guha, S., and H. Govil. 2020. "An Assessment on the Relationship between Land Surface Temperature and Normalized Difference Vegetation Index." *Environment, Development and Sustainability* doi:10.1007/s10668-020-00657-6.

Guha, S., H. Govil, A. Dey, and N. Gill. 2018. "Analytical Study of Land Surface Temperature with NDVI and NDBI Using Landsat 8 OLI and TIRS Data in Florence and Naples City, Italy." *European Journal of Remote Sensing* 51 (1): 667–678. doi:10.1080/22797254.2018.1474494.

Haashemi, S., Q. Weng, A. Darvishi, and S. Alavipanah. 2016. "Seasonal Variations of the Surface Urban Heat Island in a Semi-arid City." *Remote Sensing* 8 (352). doi:10.3390/rs8040352.

Khorchani, M., N. Martin-Hernandez, S. M. Vicente-Serrano, C. Azorin-Molina, M. Garcia, M. A. Domínguez-Duran, and F. Reig. 2018b. "Average Annual and Seasonal Land Surface Temperature, Spanish Peninsular." *Journal of Maps* 14 (2): 465–475. doi:10.1080/17445647.2018.1500316.

Khorchani, M., S. M. Vicente-Serrano, C. Azorin-Molina, M. Garcia, N. Martin-Hernandez, M. Peña-Gallardo, and A. El Kenawy. 2018a. "Trends in LST over the Peninsular Spain as Derived from the AVHRR Imagery Data." *Global and Planetary Change* 166 :75–93. doi:10.1016/j.gloplacha.2018.04.006.

Kim, J.-P., and J.-M. Guldmann. 2014. "Land-use Planning and the Urban Heat Island." *Environment and Planning B* 41: 1077–1099. doi:10.1068/B130091P.

Kuang, W., Y. Liu, Y. Dou, W. Chi, G. Chen, C. Gao, and T. Yang. 2015. "What are Hot and What are Not in an Urban Landscape: Quantifying and Explaining the Land Surface Temperature Pattern in Beijing, China." *Landscape Ecology* 30 :357–373. doi:10.1007/s10980-014-0128-6.

Lai, J., W. Zhan, F. Huang, J. Quan, L. Hu, L. Gao, and W. Ju. 2018. "Does Quality Control Matter? Surface Urban Heat Island Intensity Variations Estimated by Satellite-derived Land Surface Temperature Products." *ISPRS Journal of photogrammetry and Remote Sensing* 139 :212–227. doi:10.1016/j.isprsjprs.2018.03.012.

Li, J., C. Song, L. Cao, F. Zhu, X. Meng, and J. Wu. 2011. "Impacts of Landscape Structure on Surface Urban Heat Islands: A Case Study of Shanghai, China." *Remote Sensing of Environment* 115 :3249–3263. doi:10.1016/j.rse.2011.07.008.

Lopez, J. M. R. 2017. "Frontiers of Urbanization: Identifying and Explaining Urbanization Hot Spots in the South of Mexico City Using Human and Remote Sensing." *Applied Geography* 79 (1–10). doi:10.1016/j.apgeog.2016.12.001.

Mathew, A., S. Khandelwal, and N. Kaul. 2017. "Investigating Spatial and Seasonal Variations of Urban Heat Island Effect over Jaipur City and Its Relationship with Vegetation, Urbanization and Elevation Parameters." *Sustainable Cities and Society* 35 :157–177. doi:10.1016/j.scs.2017.07.013.

McFeeters, S. K. 1996. "The Use of the Normalized Difference Water Index (NDWI) in the Delineation of Open Water Features." *International Journal of Remote Sensing* 17 (7): 1425–1432. doi:10.1080/01431169608948714.

Mirzaei, P. A. 2015. "Recent Challenges in Modeling of Urban Heat Island." *Sustainable Cities and Society* 19: 200–206. doi:10.1016/j.scs.2015.04.001.

Nie, Q., W. Man, Z. Li, and Y. Huang . 2016. "Spatiotemporal Impact of Urban Impervious Surface on Land Surface Temperature in Shanghai, China." *Canadian Journal Remote Sensing* 42 (6): 680–689. DOI:10.1080/07038992.2016.1217484.

Pearsall, H. 2017. "Staying Cool in the Compact City: Vacant Land and Urban Heating in Philadelphia, Pennsylvania." *Applied Geography* 79: 84–92. doi:10.1016/j.apgeop.2016.12.010.

Peng, J. 2018. "Seasonal Contrast of the Dominant Factors for Spatial Distribution of Land Surface Temperature in Urban Areas." *Remote Sensing of Environment* 215 :255–267. doi:10.1016/j.rse.2018.06.010.

Peng, J., P. Xie, Y. Liu, and J. Ma. 2016. "Urban Thermal Environment Dynamics and Associated Landscape Pattern Factors: A Case Study in the Beijing Metropolitan Region." *Remote Sensing of Environment* 173 :145–155. doi:10.1016/j.rse.2015.11.027.

Qin, Z. 2001. "A Mono-window Algorithm for Retrieving Land Surface Temperature from Landsat TM Data and Its Application to the Israel–Egypt Border Region." *International Journal of Remote Sensing* 22 (18): 3719–3746. doi:10.1080/01431160010006971.

Quan, J., W. Zhan, Y. Chen, M. Wang, and J. Wang. 2016. "Time Series Decomposition of Remotely Sensed Land Surface Temperature and Investigation of Trends and Seasonal Variations in Surface Urban Heat Islands." Journal of Geophysical Research-Atmospheres 121 (6): 2638–2657. doi:10.1002/2015JD024354.

Rinner, C., and M. Hussain. 2011. "Toronto's Urban Heat Island Exploring the Relationship between Land Use and Surface Temperature." *Remote Sensing* 3: 1251–1265. doi:10.3390/rs3061251.

Rizwan, A. M., L. Y. C. Dennis, and C. LIU. 2008. "A Review on the Generation, Determination and Mitigation of the Urban Heat Island." *Journal of Environmental Sciences*20 (1): 120–128. doi:10.1002/2017EF000569.

Song, J., S. Du, X, Feng, and L. Guo. 2014. "The Relationships between Landscape Compositions and Land Surface Temperature: Quantifying Their Resolution Sensitivity with Spatial Regression Models." *Landscape and Urban Planning* 123 :145–157. doi:10.1016/j.landurbplan.2013.11.014.

Sun, R., W. Xie, and L. Chen. 2018. "A Landscape Connectivity Model to Quantify Contributions of Heat Sources and Sinks in Urban Regions." *Landscape and Urban Planning* 178 :43–50. doi:10.1016/j.landurbplan.2018.05.015.

Weng, Q. 2001. "A Remote sensing-GIS Evaluation of Urban Expansion and Its Impact on Surface Temperature in Zhujiang Delta, China." *International Journal of Remote Sensing* 22 (10): 1999–2014. doi:10.1080/713860788.

Weng, Q., and S. Yang. 2004. "Managing the Adverse Thermal Effects of Urban Development in a Densely Populated Chinese City." *Journal of Environmental Management* 70 (2): 145–156. doi:10.1016/j.jenvman.2003.11.006.

Yao, R., L. Wang, X. Huang, W. Zhang, J. Li, and Z. Niu 2018. "Interannual Variations in Surface Urban Heat Island Intensity and Associated Drivers in China." *Journal of Environmental Management* 222 :86–94. doi:10.1016/j.jenvman.2018.05.024.

Yuan, F., and M. E. Bauer. 2007. "Comparison of Impervious Surface Area and Normalized Difference Index as Indicators of Surface Urban Heat Island Effects in Landsat Imagery." *Remote Sensing of Environment* 106: 375–386. doi:10.1016/j.rse.2006.09.003.

Zha, Y., J. Gao, and S. Ni. 2003. "Use of Normalized Difference Built-up Index in Automatically Mapping Urban Areas from TM Imagery." *International Journal of Remote Sensing* 24 (3): 583–594. doi:10.1080/01431160304987.

Zhang, H., Z.-F. Qi, X.-Y. Ye, Y.-B. Cai, W.-C. Ma, and M.-N. Chen. 2013. "Analysis of Land Use/land Cover Change, Population Shift, and Their Effects on Spatiotemporal Patterns of Urban Heat Islands in Metropolitan Shanghai, China." *Applied Geography* 44 :121–133. doi:10.1016/j.apgeog.2013.07.021.

Zhang, Z., G. He, M. Wang, T. Long, G. Wang, X. Zhang, and W. Jiao 2016. "Towards an Operational Method for Land Surface Temperature Retrieval from Landsat 8 Data." *Remote Sensing Letters* 7 (3): 279–288. DOI:10.1080/2150704X.2015.1130877.

Zhao, M., H. Cai, Z. Qiao, and X. Xu. 2016. "Influence of Urban Expansion on the Urban Heat Island Effect in Shanghai." *International J ournalof Geographical Information Science* 30 (12): 2421–2441. doi:10.1080/13658816.2016.1178389.

Zhou, W., Y. Qian, X. Li, W. Li, and L. Han. 2014. "Relationships between Land Cover and the Surface Urban Heat Island: Seasonal Variability and Effects of Spatial and Thematic Resolution of Land Cover Data on Predicting Land Surface Temperatures." *Landscape Ecology* 29 :153–167. doi:10.1007/s10980-013-9950-5.

Zhou, W. Q., G. Huang, and M. L. Cadenasso. 2011. "Does Spatial Configuration Matter? Understanding the Effects of Land Cover Pattern on Land Surface Temperature in Urban Landscapes." *Landscape and Urban Planning* 102 (1): 54–63. doi:10.1016/j.landurbplan.2011.03.009.

Source details

Feedback > Compare sources >

Annals of GIS

Formerly known as: Geographic Information Sciences

Open Access

Scopus coverage years: from 2009 to Present

Publisher: Taylor & Francis

ISSN: 1947-5683 E-ISSN: 1947-5691

Subject area: Earth and Planetary Sciences: General Earth and Planetary Sciences | Computer Science: Computer Science Applications

Source type: Journal

View all documents > | Set document alert | Save to source list

CiteScore 2022
7.9

SJR 2022
0.866

SNIP 2022
1.609

CiteScore | CiteScore rank & trend | Scopus content coverage

Heliyon 5 (2019) e01923

Contents lists available at ScienceDirect

Heliyon

journal homepage: www.heliyon.com

Seasonal evaluation of downscaled land surface temperature: A case study in a humid tropical city

Himanshu Govil [a], Subhanil Guha [a,*], Anindita Dey [b], Neetu Gill [c]

[a] Department of Applied Geology, National Institute of Technology Raipur, Raipur, Chhattisgarh, India
[b] Department of Geography, Nazrul Balika Vidyalaya, Guma, West Bengal, India
[c] Chhattisgarh Council of Science and Technology, Raipur, India

ARTICLE INFO

Keywords:
Atmospheric science
Environmental science
Geography
Land surface temperature (LST)
Downscaling
TsHARP
Land use/land cover (LULC)
Landsat

ABSTRACT

The present study evaluates the seasonal variation of estimated error in downscaled land surface temperatures (LST) over a heterogeneous urban land. Thermal sharpening (TsHARP) downscaling algorithm has been used with a separate combination of four selected remote sensing indices. This study assesses the capability of TsHARP technique over mixed land use/land covers (LULC) by analyzing the correlation between LST and remote sensing indices, namely, normalized difference built-up index (NDBI), normalized difference vegetation index (NDVI), normalized difference water index (NDWI), and normalized multi-band drought index (NMDI) and by determining the root mean square error (RMSE) and mean error (ME) produced by downscaled LST. Landsat 8 OLI (Operational Land Imager) and TIRS (Thermal Infrared Sensor) images have been used for pre-monsoon, monsoon, post-monsoon, and winter seasons in 2014 covering the whole Raipur City, India. The RMSE of the downscaled LST decreases from 120 to 480 m spatial resolution in all the four seasons. It is concluded that NDBI is the most effective LULC index having the least error produced in TsHARP downscaling technique, irrespective of any season. Post-monsoon season reflects the most successful result followed by monsoon season. Even in the monsoon season of high vegetation coverage, NDBI presents a lower range of downscaled error compared to NDVI. This indicates better performance of NDBI in detecting the spatial and temporal distribution of mixed urban land.

1. Introduction

Land surface temperature (LST) is an important biophysical parameter in the processes of surface energy and water balance at regional and global scales (Anderson et al., 2008; Duan et al., 2014; Li et al., 2013; Wan and Li, 1997, 2008). LST is used in a large scale to determine soil moisture content (Voogt and Oke, 2003; Jeganathan et al., 2011; Zhan et al., 2013), to analyze the effect of urban heat island (Zakšek and Oštir, 2012; Sobrino et al., 2004; Guha et al., 2017, 2018; 2019; Zhou et al., 2019a,b), to evaluate diurnal temperature variation (Weng et al., 2004; Dennison et al., 2006; Agam et al., 2007a, 2007b; Stathopoulou and Cartalis, 2009) to calculate surface longwave radiation (Yang et al., 2011; Nichol, 2009), to compute different types of evapotranspiration (Sandholt et al., 2002; Nishii et al., 1996; Pardo-Iguzquiza et al., 2011; Gualtieri and Chettri, 2000), and to estimate surface albedo and thermal inertia (Mpelasoka et al., 2001).

Current satellite imageries, such as the Landsat, Moderate Resolution Imaging Spectroradiometer (MODIS) and Advanced Spaceborne Thermal Emission and Reflection Radiometer (ASTER), can provide LST at different spatial, spectral, radiometric, and temporal resolutions (Moran, 1990; Kustas et al., 2003; Essa et al., 2012). Due to technical limitations, these current satellite thermal sensors reflect a balance between spatial and temporal resolutions; i.e., the high spatial resolution sensors generally have a low temporal resolution, and vice versa (Weng and Fu, 2014). In order to obtain LST at high spatial and high temporal resolutions downscaling technique is considered as an effective method (Duan and Li, 2016).

Various types of downscaling techniques have been developed to get high-resolution LST from a coarse resolution thermal infrared band (Wan and Dozier, 1996; Chen et al., 2010; Pardo-Igúzquiza and Atkinson, 2006; Zhang, 2015; Yang and Yao, 2009). Extended reviews on LST downscaling methods have been assessed so far (Zhan et al., 2013; Chen et al., 2014). The most frequently used algorithm is the DisTrad algorithm (Kustas, 2003) which was modified as the TsHARP algorithm

* Corresponding author.
E-mail address: subhanilguha@gmail.com (S. Guha).

https://doi.org/10.1016/j.heliyon.2019.e01923
Received 17 March 2019; Received in revised form 11 May 2019; Accepted 5 June 2019

(Agam et al., 2007b) and the scale invariant relationship between the normalized difference vegetation index (NDVI) and LST is the foundation of these algorithms. The performance of these different algorithms was assessed over different land use/land cover (LULC) categories, including cultivated land (Jeganathan et al., 2011) or mixed urban land (Essa et al., 2012). The main restriction of the TsHARP algorithm is that this relationship is not unique, and thus, provides an extensive range of LST for a single NDVI value. Merlin et al. (2010) further enhanced the TsHARP algorithm by considering the effect of photosynthetically and non-photosynthetically active cells of the green plants within the spatial variability of LST. Furthermore, Bindhu et al. (2013) developed a nonlinear DisTrad (NL-DisTrad) model where NDVI-LST polynomial relationship generates from the hot-edge pixels at a coarse resolution which is also valid at high-resolution pixels.

The NDVI is not so appropriate for LST downscaling procedure performed in a heterogeneous urban land (Stathopoulou and Cartalis, 2009; Nichol, 2009; Dominguez et al., 2011; Zakšek and Oštir, 2012; Essa et al., 2012). Some recent research works reflected modern image classification techniques for detail LULC classification (Cheng et al. 2018a, 2018b; Zhou et al., 2019a,b). Different LULC types, found in a complex urban land, produce a unique emission rate. Emissivity (Stathopoulou and Cartalis, 2009; Nichol, 2009) has been used as one of the most significant environmental factors for highly heterogeneous urban landscapes. Small (2006) observed a close relationship between LST and surface albedo in urban areas. Dominguez et al. (2011) developed high-resolution urban thermal sharpener algorithm for downscaling LST in an urban area by integrating NDVI and surface albedo. Impervious surface percentage (Essa et al., 2012, 2013) and pure pixel index (Yang et al., 2010) have also been applied as basic parameters in urban areas. Impervious surface provides a better result than NDVI in LST downscaling in the mixed urban land by comparing 15 different parameters (Essa et al., 2012). Essa et al. (2012) and Yuan and Bauer (2007) also established a strong linear relationship between LST and impervious surface irrespective of the seasonal influence. Contrary to that, the LST-NDVI relationship changes with the seasonal variability (Kustas et al., 2003). For a complex urban area with mixed LULC types, multiple environmental parameters must be integrated to achieve a high downscaling precision. Although various types of LST downscaling methods have been suggested, they have also some limitations in the available remotely sensed data and LULC categories. Besides, selection of appropriate environmental predictors for LST downscaling in complex LULC surface is still considered as an important task.

Basically, the statistical downscaling of LST is based on the correlation between LST and other environmental factors or remote sensing based various LULC indices. Generally, most of the popular LST downscaling methods apply NDVI observed at a fine resolution (Kustas et al., 2003), but the NDVI alone cannot be able to explain all the variations in LST for a complex urban surface. Mukherjee et al. (2015) evaluated seasonal variation in downscaled LST in DisTrad, TsHARP, and local model using Landsat TM 5 data over a heterogeneous agricultural land in India. Bonafoni et al. (2016) attempted to retrieve LST using Landsat TM data for Florence city in Italy and proposed a traditional downscaling framework analyzing its performances using high-resolution LST airborne image. A combination of built-up and vegetation spectral indices was adopted for the LST downscaling methods using MODIS and Landsat TM data performed in Milan city, Italy (Bonafoni, 2016). A multiple regression-based LST downscaling technique using spectral mixture analysis over the heterogeneous urban area of Aprilia, Italy was also evaluated to examine the effectiveness of multiple environmental parameters (Bonafoni and Tosi, 2017). Another analytical research was performed in the Zhangye oasis and Beijing city to assess the scale effect in LST downscaling from medium to high-resolution satellite data (Zhou et al., 2016).

In the present study, linear regression based TsHARP downscaling technique has been examined with some LULC indices along with NDVI. Basically, the TsHARP technique used fractional vegetation cover and it was analyzed in agricultural field (Agam et al., 2007a,b). Here, the technique has been evaluated on Landsat 8 OLI and TIRS data for four different seasons (pre-monsoon, monsoon, post-monsoon, and winter) in the year of 2014. The main objectives of the research were (1) to estimate the accuracy of the downscaled LST in a heterogeneous urban landscape (Raipur City of India) of humid tropical region using TsHARP technique for separate LULC indices (normalized difference vegetation index (NDVI), normalized difference water index (NDWI), normalized difference built-up index (NDBI), and normalized multi-band drought index (NMDI)) and (2) to assess the seasonal variation of the result in 2014.

2. Materials & methods

The present study has been conducted in Raipur, a tropical city of India. Raipur is considered as a heterogeneous urban area characterized by dry tropical monsoon climate. Raipur has an average elevation of 298 m, is located between 21°11′22″N to 21°20′02″N and 81°32′ 20″E to 81°41′50″E (Fig. 1). Average annual temperature varies between 34 °C (in summer), and 20 °C (in winter). The area receives 90% of annual rainfall of 130 cm during June to September. This urban area is characterized by four main LULC types, namely, vegetation, water bodies, bare land, and built-up area. A high rate of land conversion (other lands to the built-up area) has been taken place in the recent time periods.

Four separate cloud-free Landsat 8 OLI and TIRS images of 5 June 2014, 25 September 2014, 12 November 2014, and 30 December 2014 were used for the evaluation of the TsHARP downscaling technique. Green, red, near infrared, shortwave infrared 1, and shortwave infrared 2 bands of 30 m spatial resolution in OLI sensor were used in determining the LULC indices and thermal infrared band of 100 m spatial resolution in TIRS sensor was used for estimating the LST.

For the convenience of LST downscaling calculation, Landsat 8 TIRS data (100-m resolution) were resampled into 30 m by the nearest neighbor method by simple raster data aggregation to coincide with Landsat 8 OLI data (30-m resolution). These aggregated OLI and TIRS data were further resampled by aggregation into 960 m. The 960-m aggregated coarse-resolution data were used to build the relationship model, whereas the 30-m reflective data were used to downscale the LST at 30 m. The 30 m retrieved LST was used to validate the 30-m downscaled LST. Subsequently, the four indices (NDVI, NDWI, NDBI, and NMDI) with 30-m resolution were then estimated from the 30-m OLI images. The final available output is the downscaled LST of 30-m resolution. The overall accuracy of the entire downscaled LST in various LULC was compared and evaluated.

2.1. Retrieval of LST using Landsat 8 OLI and TIRS data

Retrieving LST from Landsat 8 OLI and TIRS data includes the brightness temperature calculation and the emissivity correction. The at-sensor brightness temperature assumes that the Earth's surface is a black body and includes atmospheric effects (along path absorption and emissions) (Chander et al., 2009). The conversion formula from the at-sensor spectral radiance L to the at-sensor brightness temperature T_B is shown in Eq. (1). LST is retrieved by Eq. (2):

$$T_B = \frac{K_2}{ln((K_1/L_\lambda)+1)} \quad (1)$$

$$LST = \frac{K_2}{1+(\lambda\sigma T_B/(hc))ln\varepsilon} \quad (2)$$

Where, $T_B$is the brightness temperature in Kelvin (K), L_λ is the spectral radiance in $Wm^{-2}sr^{-1}mm^{-1}$; K_2 and K_1 are calibration constants. For Landsat 8 TIRS data, K_1 is 774.89, K_2 is 1321.08. λ is the effective wavelength (11.335 μm for band 10 in Landsat 8 OLI data), σ is Boltzmann constant (1.38×10^{-23} J/K), h is Plank's constant (6.626×10^{-34}

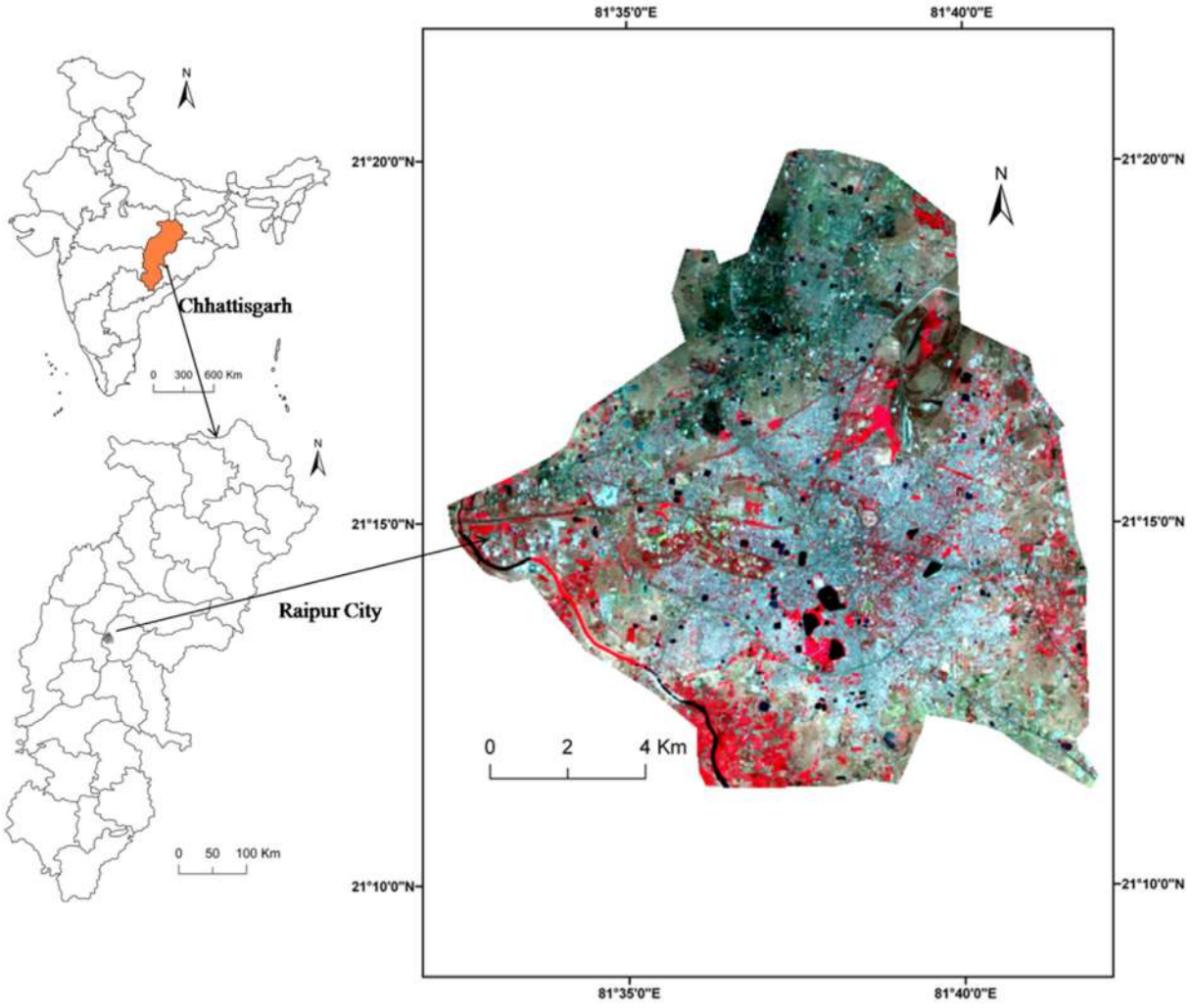

Fig. 1. Location of the study area with false colour composite image.

J), c is the velocity of light at a vacuum (2.998×10^{-8} m/s), ε is emissivity. Based on earlier studies, ε is determined as follows: if NDVI is ≥0.157 and ≤0.727, ε for that pixel is calculated by Eq. (3) (Van et al., 1993):

$$\varepsilon = 1.0094 + 0.0047 \ln(NDVI) \quad (3)$$

The land cover type should be vegetation if NDVI values ≥0.727, and then a constant value of 0.99 is assumed (Sobrino et al., 2004) and ε is set to 0.995 for water bodies and 0.92 for the other land use and land cover types.

2.2. Determination of NDVI, NDWI, NDBI, and NMDI as LULC indices

NDVI (Purevdorj et al., 1998) is considered as one of the most frequently used vegetation indices in remote sensing study. It is also applied in deriving LST and normally shows a negative regression with LST. NDWI (Gao, 1996) is generally used for water body extraction. NDBI (Zha et al., 2003) is another spectral index which was applied in this study for built-up area extraction. NMDI (Yuan and Bauer, 2007) was also used to extract the dry soil or bare land. The formulation of these four indices was presented by Table 1.

Table 1
LULC indices used for LST downscaling.

Acronym	Description	Formulation	Reference
NDVI	Normalized difference vegetation index	$\frac{NIR - Red}{NIR + Red}$	Purevdorj et al.,(1998)
NDWI	Normalized difference water index	$\frac{Green - NIR}{Green + NIR}$	Gao (1996)
NDBI	Normalized difference built-up index	$\frac{SWIR1 - NIR}{SWIR2 + NIR}$	Zha et al., (2003)
NMDI	Normalized multi-band difference index	$\frac{[NIR - (SWIR1 + SWIR2)]}{[NIR - (SWIR1 + SWIR2)]}$	Yuan and Bauer (2007)

2.3. TsHARP downscaling technique based on the regression of LST and LULC indices

LST can be derived using thermal infrared images with coarse spatial resolutions. Regression models between ancillary environmental predictors and LST have been widely established to enhance LST resolution. If the relationships between LST and the predictors do not change with the variation in the spatial resolution, a detailed LST with a high

resolution can be calculated by the predictors using such relationships. Table 1 shows the used LULC indices in the present study for estimating downscaled LST using TsHARP technique.

The original TsHARP algorithm is primarily based on the regression model of LST and fractional vegetation cover. This technique was proposed by Agam et al. (2007a,b). Basically, it was a modification of the DisTrad algorithm (Kustas et al., 2003) and was evaluated on agricultural land of Central Iowa, USA. Jeganathan et al. (2011) showed that NDVI should be used as a covariate in TsHARP technique. The present study uses NDVI, NDWI, NDBI, and NMDI as the covariates with the LST. The TsHARP algorithm was outlined in Eq. (4a–4d) where a_0 is the intercept and a_1 is the slope of the regression equations. The Eq. 4a was followed by Eq. (4b–4d) by replacing the NDVI with NDWI, NDBI, and NMDI, respectively. The fine-resolution (30 m) LST, (LST_{fine}) could be determined by the Eq. (4a–4d):

$$LST_{fine} = a_0 + a_1.NDVI_{fine} \quad (4a)$$

$$LST_{fine} = a_0 + a_1.NDWI_{fine} \quad (4b)$$

$$LST_{fine} = a_0 + a_1.NDBI_{fine} \quad (4c)$$

$$LST_{fine} = a_0 + a_1.NMDI_{fine} \quad (4d)$$

Therefore, the coarse-resolution LST (LST_{coarse}) can be determined by the Eq. (5a–5d):

$$LST_{coarse} = a_0 + a_1.NDVI_{coarse} + \Delta T_{coarse} \quad (5a)$$

$$LST_{coarse} = a_0 + a_1.NDWI_{coarse} + \Delta T_{coarse} \quad (5b)$$

$$LST_{coarse} = a_0 + a_1.NDBI_{coarse} + \Delta T_{coarse} \quad (5c)$$

$$LST_{coarse} = a_0 + a_1.NMDI_{coarse} + \Delta T_{coarse} \quad (5d)$$

Then, a residual of LST (ΔT_{coarse}) was computed as the difference between the retrieved LST (LST_{coarse}) and the corresponding observed LST (LST_{ref}) by Eq. (6) (Kustas et al., 2003):

$$\Delta T_{coarse} = LST_{ref} - LST_{coarse} \quad (6)$$

The residual ΔT_{coarse} was introduced in the algorithm to take into account part of LST spatial variability that depends on the environmental factors other than the applied predictors, such as soil moisture, emissivity or other LULC indices. The a_0, a_1 and residual are different when different indices are used. Finally, downscaled fine-resolution (30 m) LST (LST_{down}) was estimated by the Eq. (7a–7d):

$$LST_{down} = a_0 + a_1.NDVI_{fine} + \Delta T_{coarse} \quad (7a)$$

$$LST_{down} = a_0 + a_1.NDWI_{fine} + \Delta T_{coarse} \quad (7b)$$

$$LST_{down} = a_0 + a_1.NDBI_{fine} + \Delta T_{coarse} \quad (7c)$$

$$LST_{down} = a_0 + a_1.NMDI_{fine} + \Delta T_{coarse} \quad (7d)$$

Where, the coarse-resolution regression coefficients were applied to fine-spatial resolution spectral indices, adding the residual error of the corresponding coarse-resolution image to increase the accuracy.

The NDVI-LST relationship always tends to be varied over the mixed urban landscape. In order to overcome the problem, some remote sensing indices may be tested along with NDVI to obtain higher accuracy in the downscaled LST. The multiple least-squares linear regression downscaling method with a number of predictors was applied in some recent studies (Bonafoni, 2016; Bonafoni et al., 2016). A number of remote sensing indices have also been tested individually to obtain a better downscaled LST (Essa et al., 2012). In the present study, NDVI, NDWI, NDBI, and NMDI have been examined separately in four different dates for the downscaling method. Finally, the overall procedure of downscaling has been applied at 30 m, 120 m, 240 m, and 480 m spatial resolutions.

2.4. Accuracy assessment and validation

The LST of 100-m resolution is aggregated to 960, 480, 240, and 120-m resolution and these new aggregated data are known as reference data (LST_{ref}). The aggregated 960-m resolution LST was downscaled (LST_{down}) to 480, 240, 120, and 30-m resolution. Root mean square error (RMSE) and mean error (ME) statistics were applied to estimate the error in downscaled LST with respect to the reference LST. RMSE and ME have been calculated by the following Eq. (8) and Eq. (9), respectively.

$$RMSE = \sqrt{\left[n^{-1}\sum_{i=1}^{n}\left(LST_{down} - LST_{ref}\right)^2\right]} \quad (8)$$

$$ME = \sum_{i=1}^{n}\left(LST_{down} - LST_{ref}\right) \quad (9)$$

A complete flowchart of the entire study has been shown in Fig. 2. The computation cost of the proposed method was small as it required less time and storage space for the entire computation process.

3. Results & discussion

Fig. 3 represented the spatial distribution of reference LST at 30 m resolution and Table 2 showed the statistical information of LST at 30-m resolution in four multi-date images. Seasonal variation in the LST distribution shows a specific thermal pattern. The mean LST values in pre-monsoon, monsoon, post-monsoon, and winter season are 33.59 °C, 29.56 °C, 23.40 °C, and 22.26 °C respectively. The range of temperature is found as 13.50 °C in pre-monsoon, 12.28 °C in monsoon, 8.83 °C in post-monsoon, and 10.12 °C in the winter season, respectively. Basically, this type of heterogeneity in LST was observed due to the changes in vegetation abundance and soil moisture content. Monsoon and post-monsoon seasons are characterized by healthy vegetation and wet soil. Winter remains comparatively dry and having least standard deviation value in LST (Table 2).

Figs. 4, 5, 6, and 7 and Table 3 presents the downscaled LST using various LULC indices based TsHARP algorithm along with the retrieved reference LST in four different seasons (pre-monsoon, monsoon, post-monsoon, and winter). It is observed that the first panel (LST reference) has a smoothed pattern since the 30-m LST resolution is not an actual measurement but a resampling, and that the downscaling improve the detail at this spatial scale. It is clearly revealed that NDBI and NMDI based TsHARP algorithm generates almost similar nature in the downscaled LST while NDVI and NDWI based TsHARP algorithm has almost identical spatial distribution of downscaled LST. This particular type of spatial pattern is reflected in each and every season. The spatial pattern of downscaled LST generates from NDBI and NMDI based TsHARP technique has a similarity with retrieved reference LST where the study area achieves a higher temperature. Monsoon season indicates most identical scenario when reference LST compares with the downscaled LST, irrespective of any LULC indices based TsHARP technique.

Table 4 presents the seasonal variation of the estimated errors (RMSE and ME) produced in downscaled LST by various types of LULC indices based TsHARP algorithm. Downscaled LST at lower spatial resolution generates a greater error than downscaled LST at higher spatial resolution. It is a common phenomenon observed in each and every season and it remains constant for any LULC indices based TsHARP downscaling technique. NDBI-based TsHARP algorithm showed the best result among all the LULC indices-based TsHARP algorithm for all the season and at every resolution level as the values of RMSE of downscaled LST lie

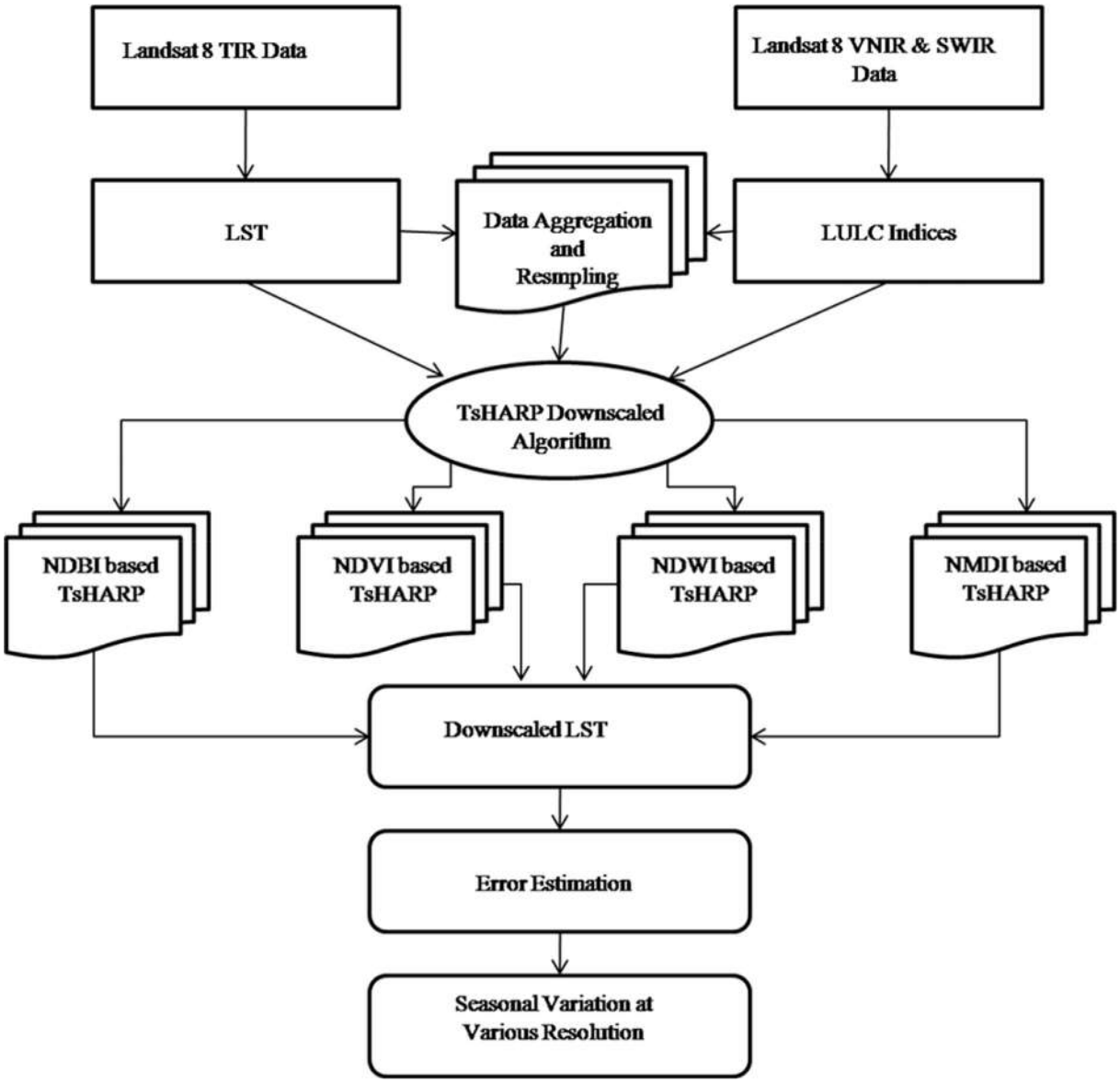

Fig. 2. Flowchart of methodology.

significantly below the standard deviation for the corresponding actual native LST reference images at 100 m spatial resolution in each and every occasion. NDBI proves as the most successful parameter for LST downscaling in almost every season. Since it is an urban area having so many mixed landscapes built-up area has the most dominant land use in controlling LST. Previously, NDVI-LST relationship based TsHARP algorithm proved as one of the most effective downscaling methods for single LULC dominated region (Agam et al., 2007a,b; Jeganathan et al., 2011). In the present study, NDVI also proves as an important indicator in determining the downscaled LST values in a heterogeneous urban landscape. Along with NDBI and NDVI, two more remote sensing indices (NDWI and NMDI) were also examined to compare the accuracy level in downscaled LST. Post-monsoon and winter season shows a better accuracy in terms RMSE and ME for any of the indices based downscaled LST. NDBI and NDMI reflect a smaller ME for pre-monsoon and winter seasons while NDVI and NDWI indicates a smaller ME in monsoon and post-monsoon seasons as an indicator used to develop TsHARP downscaling technique. Figs. 8, 9, 10, and 11 and Figs. 12, 13, 14, and 15 show the spatial distribution of RMSE and ME, respectively.

The high values of RMSE (positive) and ME (positive or negative) have mostly been found in the areas where LST is very high or abnormally low. Due to the presence of mineral-based industrial agglomeration or thermal power plants in the northwest portions of the study area, LST generally remains high. This portion has come under one of the most erroneous zones regarding the downscaled LST. It happens mainly due to the anthropogenic activities and no such hypothetical relationship is built to support the particular behaviour.

Table 5 presents the percentage of RMSE in downscaled LST at 30 m spatial resolution for different seasons. In pre-monsoon season, NMDI and NDBI based TsHARP downscaling technique provide almost 73% of the total pixels in the study area having less than 1.5 °C RMSE in downscaled LST. NDBI again proves as the best parameter for TsHARP downscaling algorithm in monsoon season as 72.7% pixels having less than 1.5 °C RMSE. Post-monsoon season reflects the best result regarding RMSE in downscaled LST. In post-monsoon season, NDVI and NDWI based TsHARP algorithm have proved as the best output at 30 m resolution irrespective of any season as they generates downscaled LST with more than 90% pixels having less than 1.5 °C RMSE. In winter season, NDVI and NMDI based TsHARP techniques give the best result (>86% pixels have less than 1.5 °C RMSE).

Seasonal variation in the percentage of mean error (ME) in downscaled LST at 30 m resolution has been shown in Table 6. It is very clear

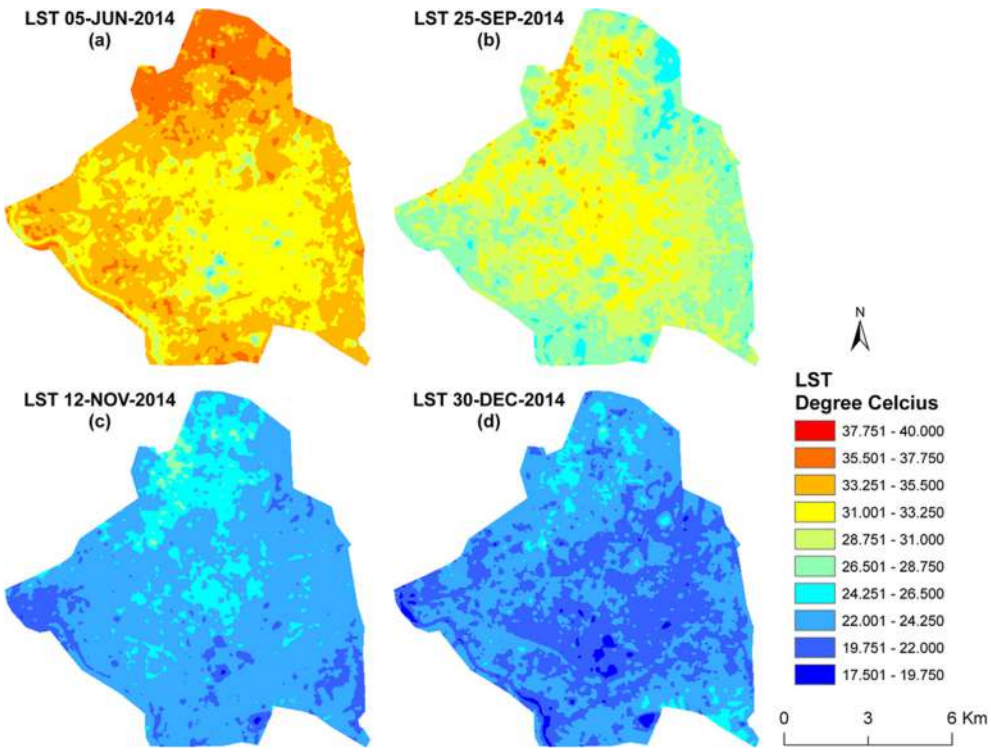

Fig. 3. Spatial distribution of reference LST at 30-m spatial resolution: (a) pre-monsoon; (b) monsoon; (c) post-monsoon; (d) winter.

Table 2
Spatial distribution of LST (°C) for four multi-date reference images at 30 m resolution.

Date of Acquisition	Time	Path/Row	LST (Minimum)	LST (Maximum)	LST (Mean)	LST (Standard deviation)
05-JUN-2014	04:55:45	142/044	25.77	39.27	33.59	1.61
25-SEP-2014	04:56:11	142/044	24.51	36.79	29.56	1.73
12-NOV-2014	04:56:21	142/044	19.39	28.23	23.40	1.12
30-DEC-2014	04:56:09	142/044	17.64	27.76	22.26	1.11

from Table 6 that all the LULC indices are almost equally suitable for TsHARP downscaling technique. Post-monsoon season simply generates the best result for downscaled LST due to low pollution level, high vegetation coverage and high moisture content. NDWI and NDVI based TsHARP downscaling algorithm generates lowest level of mean error [>75% pixels have a ME from 0 °C to 1 °C (positive/negative)].

The study was evaluated the downscaling LST in a humid tropical city of India and reflected a good result. The similar types of studies were also performed successfully in the cities of other climatic zones, e.g., humid subtropical zone (Pan et al., 2018), temperate zone (Bechtel et al., 2012; Bonafoni et al., 2016).

The proposed work also have some limitations. The 30 m LST resolution is not an actual measurement but a resampling, and the downscaling improve the detail at this spatial scale. Only one date of a particular season may not be appropriate for seasonal assessment of downscaling technique. The other relevant LULC indices may also be incorporated to improve the downscaling results.

4. Conclusion

The aim of this research is to estimate remote sensing indices (NDBI, NDVI, NDWI, and NMDI) based downscaled LST at 30, 120, 240, and 480 m resolution and compare the results in different seasons (pre-monsoon, monsoon, post-monsoon, and winter) over a heterogeneous urban area like Raipur city. The NDVI-LST linear relationship is the primary basis of TsHARP downscaling technique. NDBI, NDWI, and NMDI are tested separately in place of NDVI to form new linear relationships, i.e., NDBI-LST, NDWI-LST, and NMDI-LST. The downscaled LST based on NDBI-LST, NDVI-LST, NDWI-LST, and NMDI-LST was finally evaluated through error estimation. The seasonal variation of the results was also determined. The results were examined at various spatial resolutions. It is clear from the various results that NDBI based TsHARP technique provides the lowest RMSE in downscaled LST at 30 m spatial resolution, irrespective of all seasons. In pre-monsoon, monsoon, and winter seasons, NDBI and NMDI based TsHARP technique have a smaller range of ME, but, in post-monsoon season, NDVI and NDWI indicate small ME due to the presence of a higher percentage of chlorophyll and moisture content. The RMSE and ME became gradually smaller with the increase of spatial resolution in downscaled LST. The LULC based TsHARP models may also be examined in determining the downscaled LST for daytime and nighttime thermal data. Different satellite sensors may also be used to assess the capability of this technique in a separate study area. Any further modification in the present TsHARP algorithm will be expected by the future researchers.

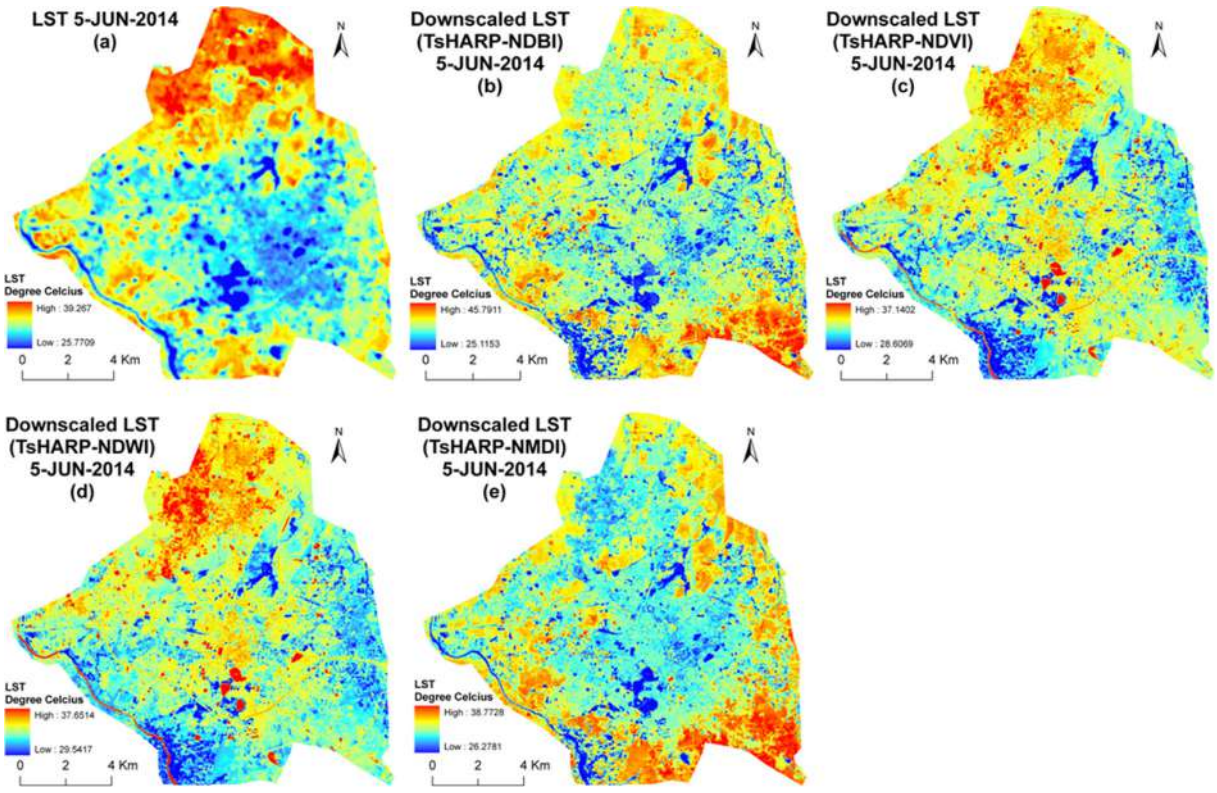

Fig. 4. Spatial distribution of retrieved LST and downscaled LST at 30-m resolution for 5-JUN-14: (a) LST_{ref}; (b) NDBI-based LST_{down}; (c) NDVI-based LST_{down}; (d) NDWI-based LST_{down}; (e) NMDI-based LST_{down}.

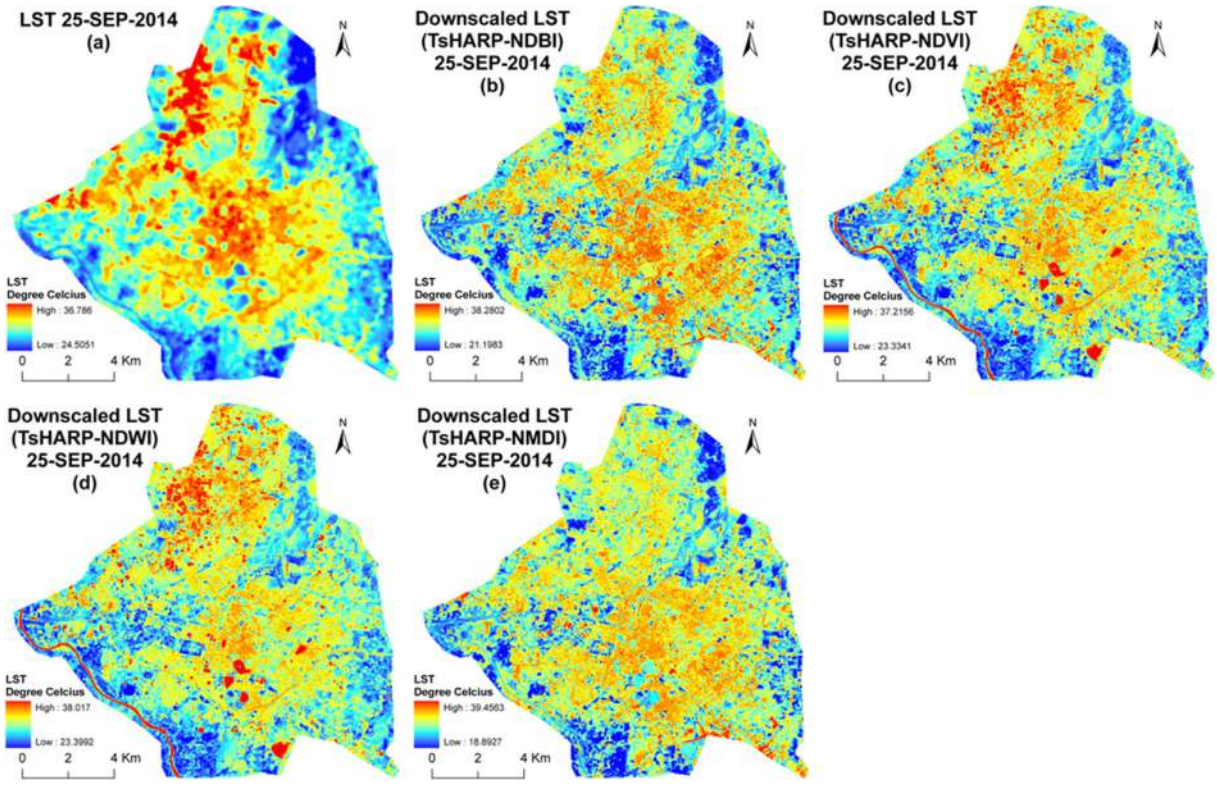

Fig. 5. Spatial distribution of retrieved LST and downscaled LST at 30-m resolution for 25-SEP-14: (a) LST_{ref}; (b) NDBI-based LST_{down}; (c) NDVI-based LST_{down}; (d) NDWI-based LST_{down}; (e) NMDI-based LST_{down}.

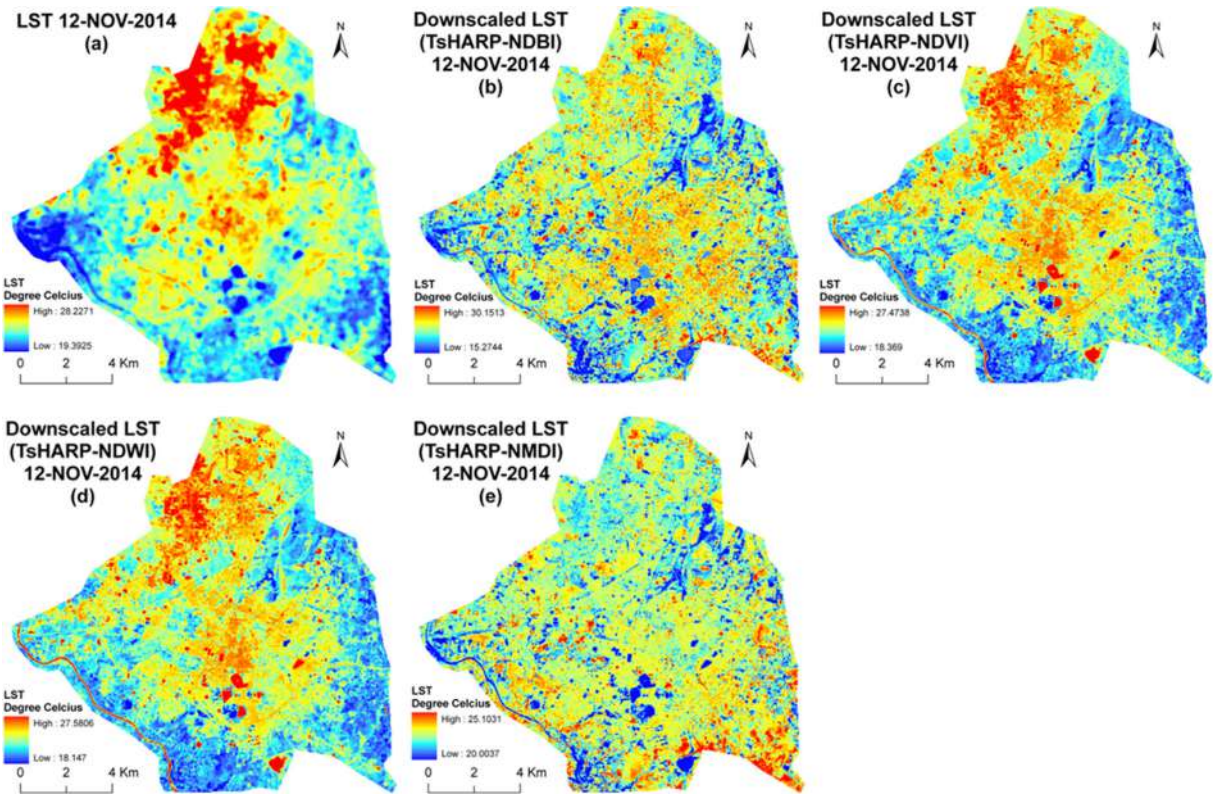

Fig. 6. Spatial distribution of retrieved LST and downscaled LST at 30-m resolution for 12-NOV-14: (a) LST_{ref}; (b) NDBI-based LST_{down}; (c) NDVI-based LST_{down}; (d) NDWI-based LST_{down}; (e) NMDI-based LST_{down}.

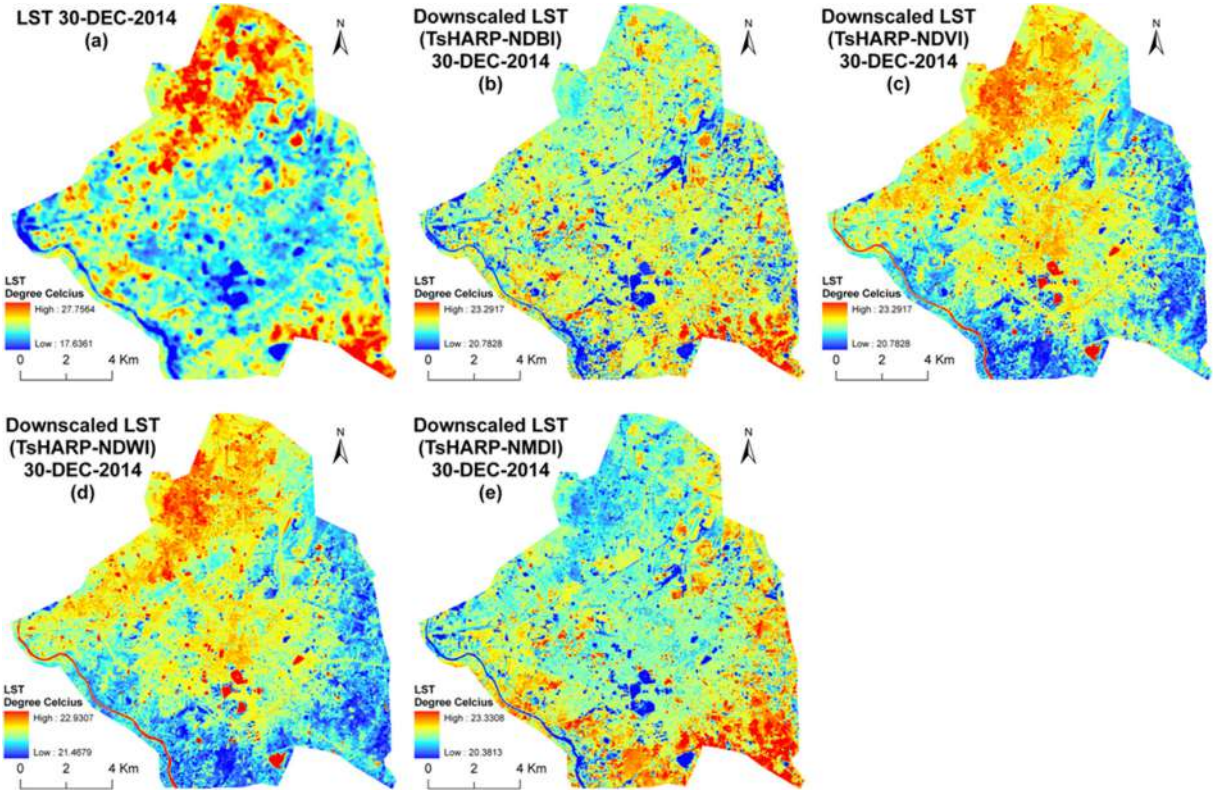

Fig. 7. Spatial distribution of retrieved LST and downscaled LST at 30-m resolution for 30-DEC-14: (a) LST_{ref}; (b) NDBI-based LST_{down}; (c) NDVI-based LST_{down}; (d) NDWI-based LST_{down}; (e) NMDI-based LST_{down}.

Table 3
Seasonal variation in different LULC indices based downscaled LST (°C) at various resolutions.

LULC Indices- based downscaled LST (°C)	at 30 m				at 120 m				at 240 m				at 480 m			
	June-05-2014															
	Min	Max	μ	σ	Min	Max	μ	σ	Min	Max	μ	σ	Min	Max	μ	σ
NDBI-based	25.77	39.27	33.59	1.61	26.33	38.14	33.62	1.58	27.01	38.06	33.64	1.52	27.98	37.09	33.69	1.42
NDVI-based	25.12	45.79	33.64	1.34	25.69	38.41	33.66	1.12	28.87	36.52	33.67	0.98	30.26	36.29	33.70	0.88
NDWI-based	28.61	37.14	33.74	0.91	29.00	36.61	33.74	0.77	30.55	35.87	33.74	0.69	31.41	35.57	33.74	0.62
NMDI-based	29.54	37.65	33.74	0.83	29.82	37.29	33.74	0.72	31.31	36.51	33.74	0.64	31.90	36.08	33.74	0.58
NDBI-based	26.28	38.77	33.64	0.93	26.28	38.78	33.64	0.93	30.96	35.98	33.67	0.72	31.39	35.64	33.69	0.66
	September-25-2014															
	Min	Max	μ	σ	Min	Max	μ	σ	Min	Max	μ	σ	Min	Max	μ	σ
NDBI-based	24.51	36.79	29.56	1.73	24.59	35.89	29.54	1.71	24.67	34.76	29.52	1.65	25.26	34.49	29.46	1.57
NDVI-based	21.20	38.28	29.50	2.02	23.38	34.77	29.49	1.73	23.68	33.06	29.47	1.51	24.96	32.29	29.44	1.40
NDWI-based	23.33	37.22	29.49	2.00	24.06	35.38	29.47	1.70	24.38	34.87	29.46	1.51	25.49	33.19	29.43	1.34
NMDI-based	23.40	31.02	29.47	1.90	24.37	36.57	29.46	1.61	24.72	36.51	29.45	1.42	25.59	34.07	29.42	1.25
NDBI-based	18.89	39.46	29.47	1.87	22.38	35.56	29.45	1.58	22.75	33.44	29.44	1.41	24.54	33.22	29.42	1.26
	November-12-2014															
	Min	Max	μ	σ	Min	Max	μ	σ	Min	Max	μ	σ	Min	Max	μ	σ
NDBI-based	19.39	28.23	23.40	1.12	19.53	27.92	23.39	1.11	19.66	27.37	23.38	1.07	20.26	26.96	23.36	1.02
NDVI-based	15.27	30.15	23.34	1.28	15.59	27.58	23.33	1.03	19.81	26.16	23.33	0.88	19.81	25.26	23.32	0.74
NDWI-based	18.37	27.47	23.38	1.05	19.38	26.41	23.37	0.93	20.52	26.08	23.36	0.86	21.48	25.59	23.34	0.79
NMDI-based	18.15	27.58	23.38	1.02	19.64	26.84	23.37	0.91	20.77	26.80	23.36	0.84	21.59	25.95	23.34	0.78
NDBI-based	20.00	25.10	23.30	0.28	21.31	24.39	23.31	0.22	22.45	24.07	23.31	0.19	22.48	23.97	23.31	0.15
	December-30-2014															
	Min	Max	μ	σ	Min	Max	μ	σ	Min	Max	μ	σ	Min	Max	μ	σ
NDBI-based	17.63	27.76	22.26	1.11	17.68	26.86	22.27	1.08	17.78	25.79	22.28	1.03	19.08	25.41	22.29	0.94
NDVI-based	13.48	28.56	22.29	1.06	15.07	26.26	22.29	0.84	18.71	25.29	22.30	0.70	19.71	25.29	22.30	0.60
NDWI-based	20.78	23.29	22.31	0.25	21.03	23.14	22.31	0.22	21.56	23.07	22.31	0.20	21.83	22.80	22.31	0.19
NMDI-based	21.47	22.93	22.31	0.14	21.68	22.90	22.31	0.13	21.95	22.86	22.31	0.12	22.02	22.64	22.30	0.11
NDBI-based	20.38	23.33	22.29	0.17	21.30	22.93	22.29	0.14	21.79	22.79	22.29	0.13	21.89	22.75	22.30	0.11

μ = mean, and σ = standard deviation.

Table 4
Seasonal variation in mean RMSE and mean ME for downscaled LST (°C) at various resolution.

LULC indices based LST_{down}	at 30 m		at 120 m		at 240 m		at 480 m	
June-05-2014 (the standard deviation of the native LST reference image at 30 m spatial resolution is 1.61)								
	RMSE	ME	RMSE	ME	RMSE	ME	RMSE	ME
NDBI-based	1.09	0.05	0.96	0.04	0.91	0.03	0.87	0.01
NDVI-based	1.22	0.14	1.17	0.12	1.13	0.09	1.05	0.05
NDWI-based	1.23	0.15	1.19	0.13	1.15	0.10	1.07	0.05
NMDI-based	1.09	0.05	1.03	0.04	0.99	0.02	0.96	0.01
September-25-2014 (the standard deviation of the native LST reference image at 30 m spatial resolution is 1.73)								
	RMSE	ME	RMSE	ME	RMSE	ME	RMSE	ME
NDBI-based	1.11	-0.05	0.81	-0.05	0.69	-0.05	0.61	-0.03
NDVI-based	1.21	-0.07	0.97	-0.06	0.86	-0.06	0.75	-0.04
NDWI-based	1.25	-0.08	1.08	-0.08	0.98	-0.07	0.86	-0.04
NMDI-based	1.18	-0.09	0.92	-0.08	0.82	-0.07	0.75	-0.05
November-12-2014 (the standard deviation of the native LST reference image at 30 m spatial resolution is 1.12)								
	RMSE	ME	RMSE	ME	RMSE	ME	RMSE	ME
NDBI-based	0.91	-0.06	0.72	-0.05	0.65	-0.05	0.60	-0.05
NDVI-based	0.75	-0.01	0.66	-0.02	0.60	-0.02	0.55	-0.03
NDWI-based	0.74	-0.01	0.66	-0.02	0.60	-0.02	0.55	-0.02
NMDI-based	0.81	-0.09	0.79	-0.08	0.78	-0.07	0.76	-0.06
December-30-2014 (the standard deviation of the native LST reference image at 30 m spatial resolution is 1.11)								
	RMSE	ME	RMSE	ME	RMSE	ME	RMSE	ME
NDBI-based	0.85	0.03	0.71	0.03	0.65	0.02	0.59	0.01
NDVI-based	0.86	0.05	0.84	0.05	0.79	0.04	0.73	0.01
NDWI-based	0.86	0.05	0.84	0.04	0.80	0.03	0.72	0.01
NMDI-based	0.81	0.03	0.79	0.03	0.76	0.02	0.69	0.01

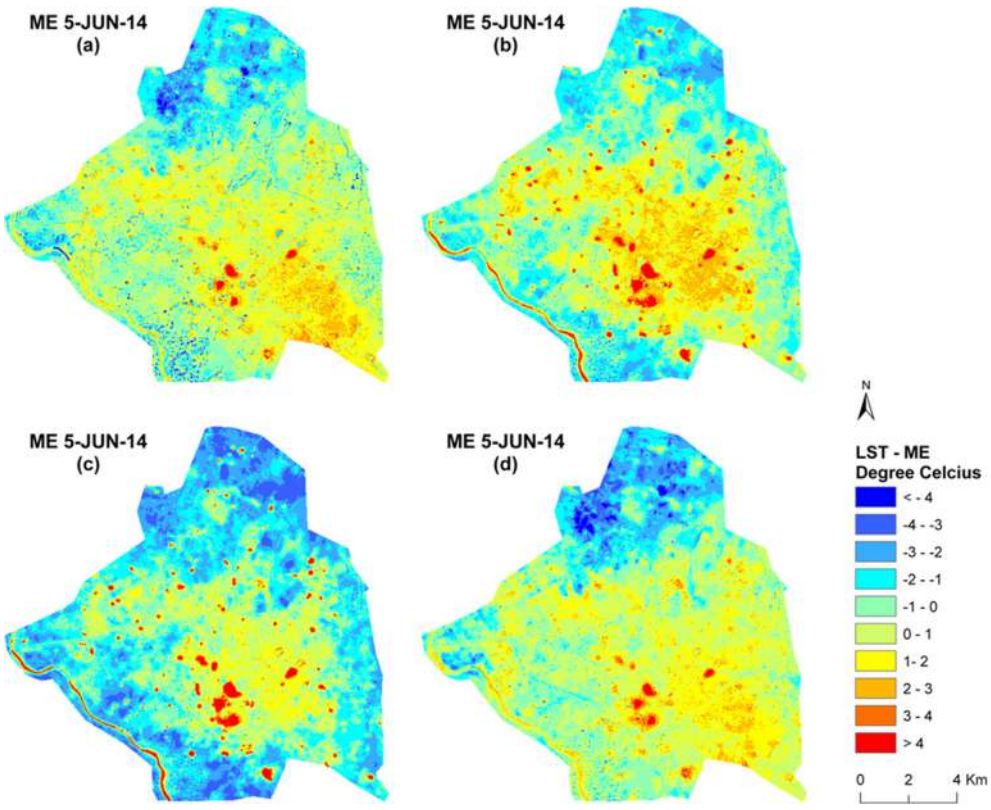

Fig. 8. Spatial distribution of ME at 30-m resolution for 5-JUN-14: (a) NDBI-based LST_{down}; (b) NDVI-based LST_{down}; (c) NDWI-based LST_{down}; (d) NMDI-based LST_{down}.

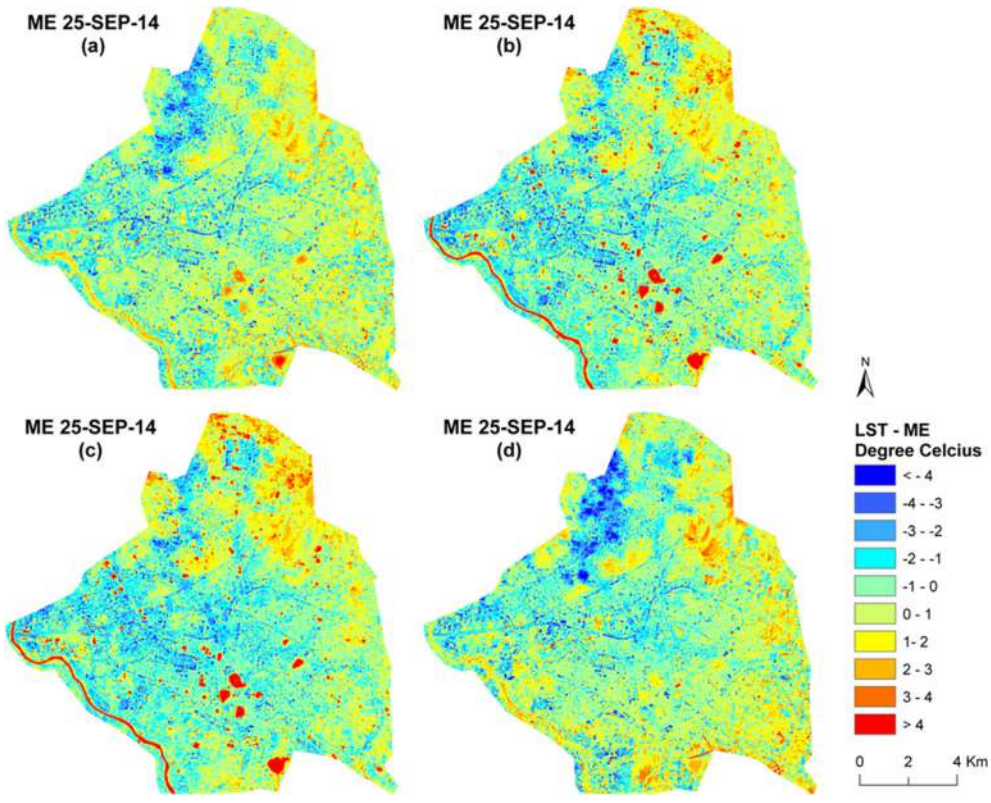

Fig. 9. Spatial distribution of ME at 30-m resolution for 25-SEP-14: (a) NDBI-based LST_{down}; (b) NDVI-based LST_{down}; (c) NDWI-based LST_{down}; (d) NMDI-based LST_{down}.

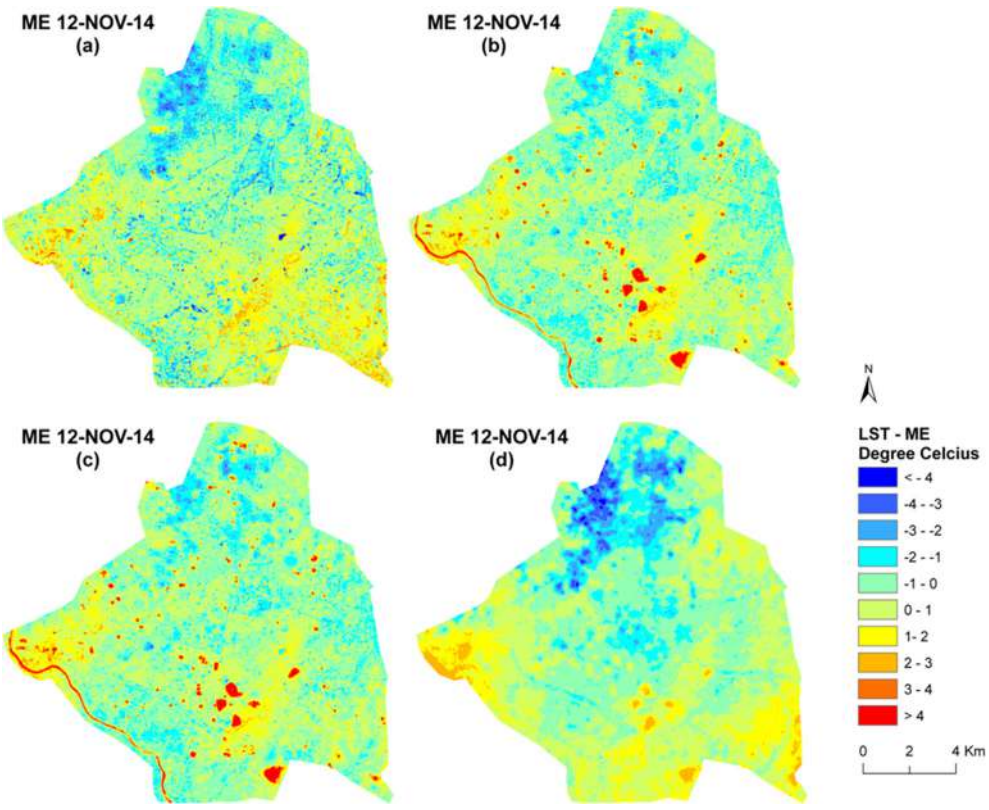

Fig. 10. Spatial distribution of ME at 30-m resolution for 12-NOV-14: (a) NDBI-based LST_{down}; (b) NDVI-based LST_{down}; (c) NDWI-based LST_{down}; (d) NMDI-based LST_{down}.

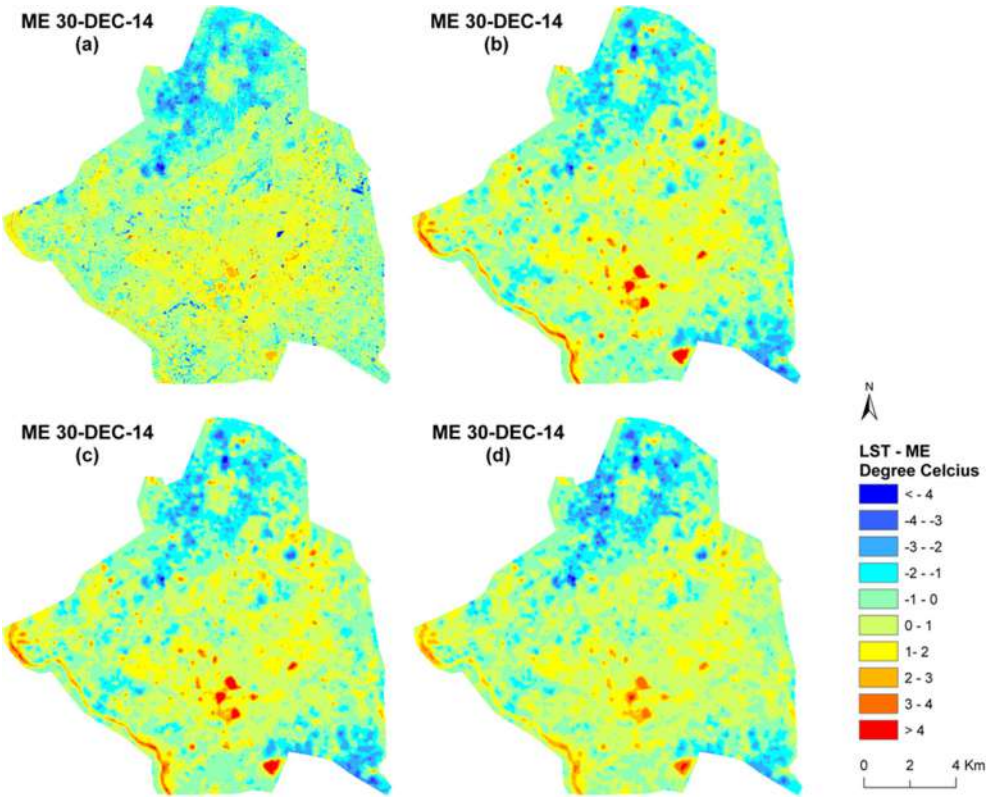

Fig. 11. Spatial distribution of ME at 30-m resolution for 30-DEC-14: (a) NDBI-based LST_{down}; (b) NDVI-based LST_{down}; (c) NDWI-based LST_{down}; (d) NMDI-based LST_{down}.

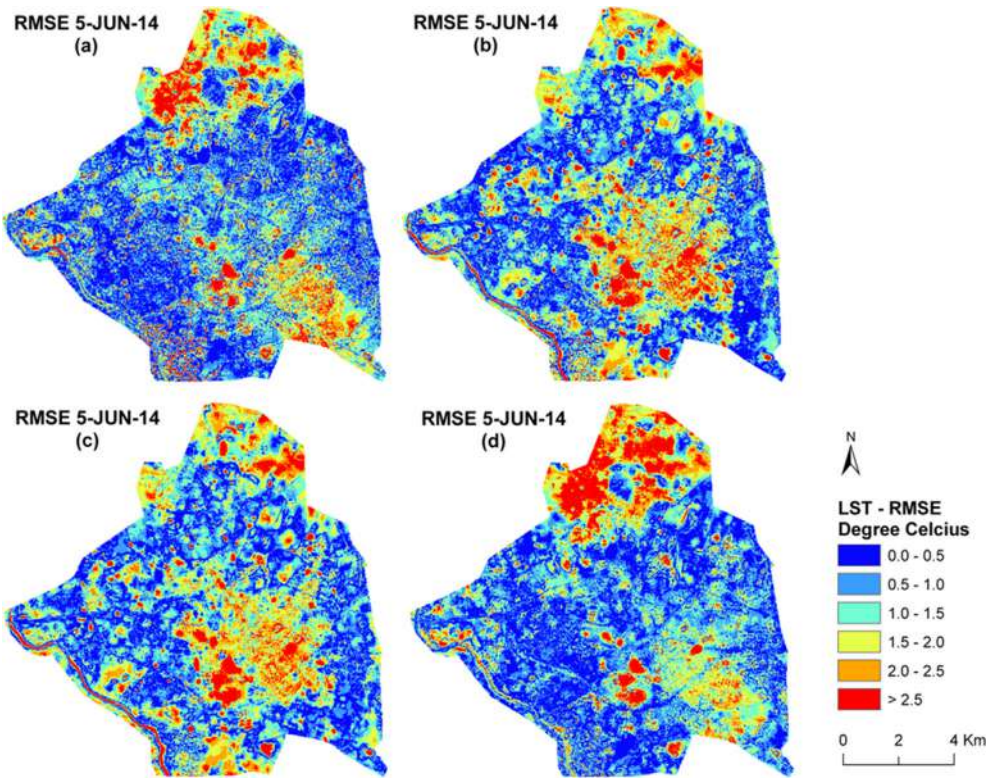

Fig. 12. Spatial distribution of RMSE at 30-m resolution for 5-JUN-14: (a) NDBI-based LST_{down}; (b) NDVI-based LST_{down}; (c) NDWI-based LST_{down}; (d) NMDI-based LST_{down}.

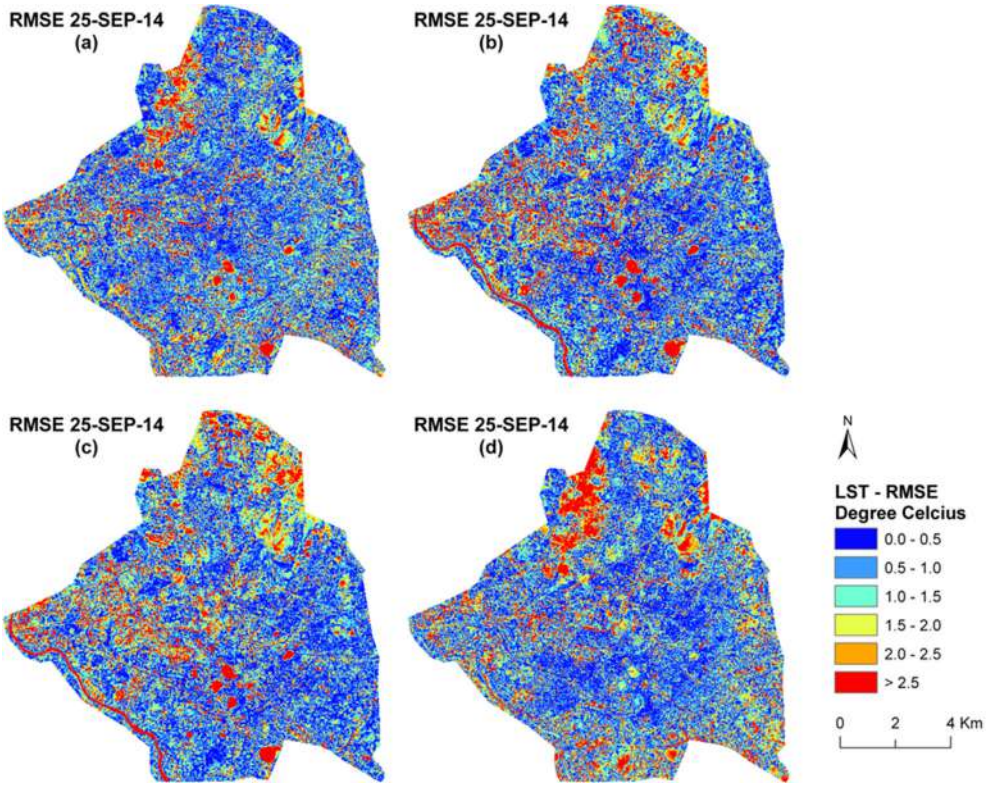

Fig. 13. Spatial distribution of RMSE at 30-m resolution for 25-SEP-14: (a) NDBI-based LST_{down}; (b) NDVI-based LST_{down}; (c) NDWI-based LST_{down}; (d) NMDI-based LST_{down}.

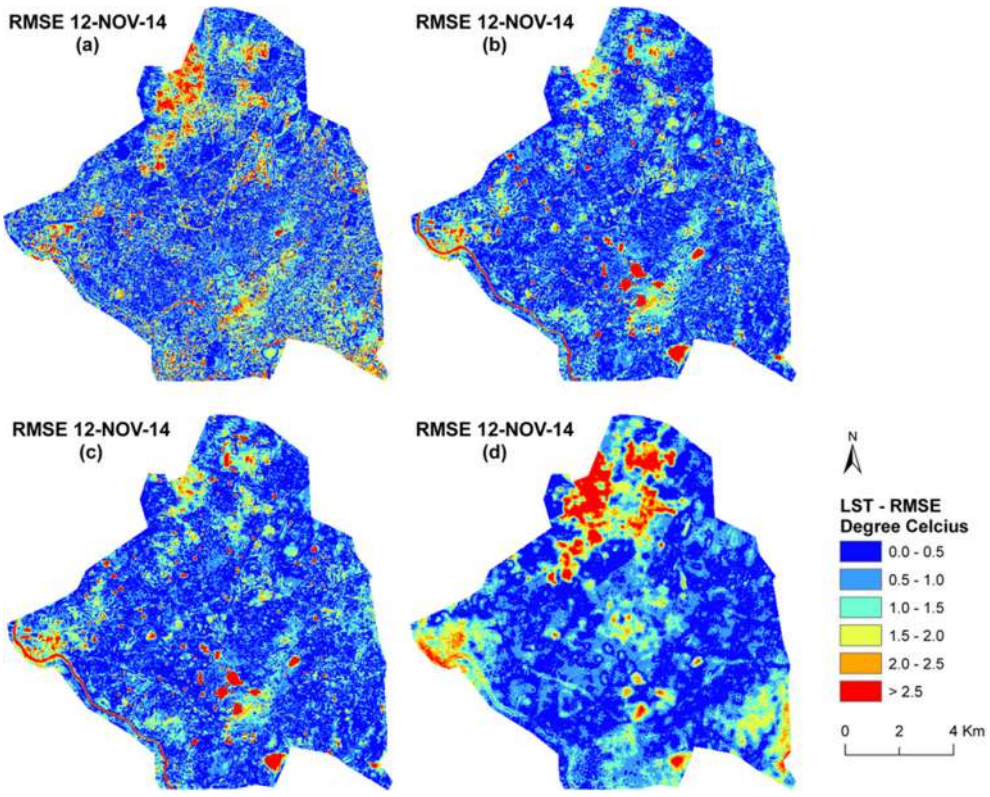

Fig. 14. Spatial distribution of RMSE at 30-m resolution for 12-NOV-14: (a) NDBI-based LST_{down}; (b) NDVI-based LST_{down}; (c) NDWI-based LST_{down}; (d) NMDI-based LST_{down}.

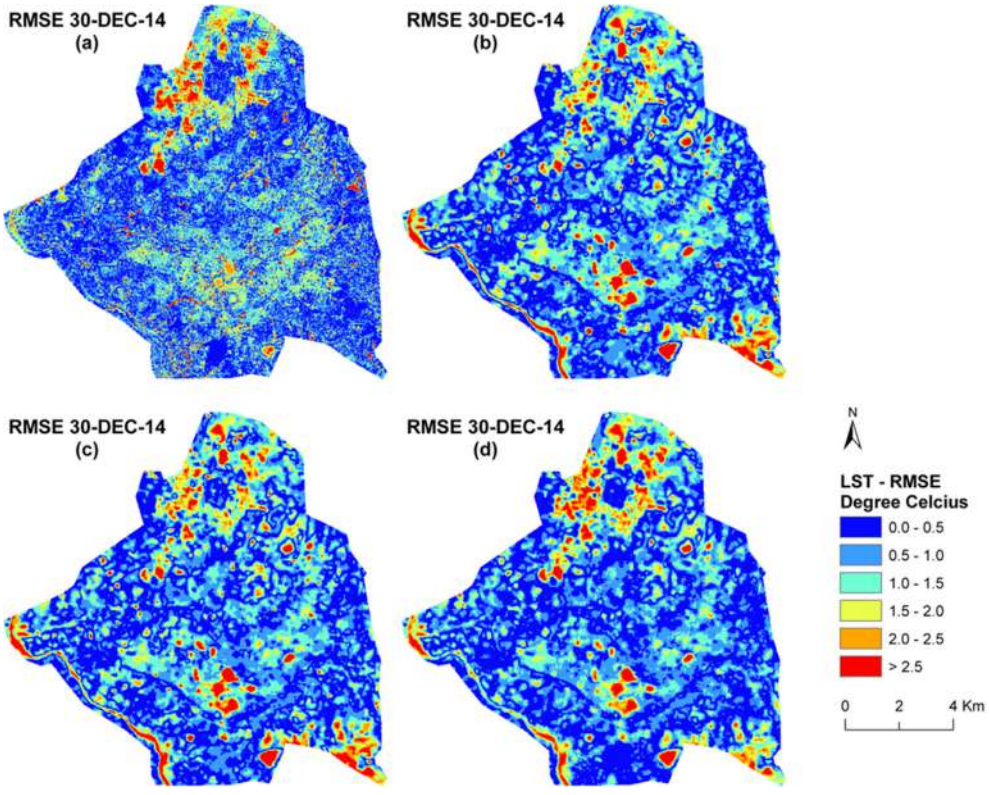

Fig. 15. Spatial distribution of RMSE at 30-m resolution for 30-DEC-14: (a) NDBI-based LST_{down}; (b) NDVI-based LST_{down}; (c) NDWI-based LST_{down}; (d) NMDI-based LST_{down}.

Table 5
Percentage of root mean square error (RMSE) in downscaled LST (°C) at 30 m resolution.

RMSE in downscaled LST (°C)	0.0–0.5	0.5–1.0	1.0–1.5	1.5–2.0	2.0–2.5	>2.5
	June-05-2014					
NDBI-based	28.70%	24.43%	19.52%	13.66%	7.34%	6.35%
NDVI-based	24.00%	23.13%	19.00%	16.33%	9.43%	6.46%
NDWI-based	23.94%	23.10%	20.60%	16.46%	9.54%	6.36%
NMDI-based	29.46%	25.80%	18.61%	11.86%	6.86%	7.41%
	September-25-2014					
NDBI-based	28.82%	25.27%	18.61%	11.91%	7.28%	8.13%
NDVI-based	29.49%	24.26%	17.51%	11.49%	7.03%	10.22%
NDWI-based	28.66%	24.09%	17.78%	11.87%	7.06%	10.54%
NMDI-based	28.29%	23.80%	17.92%	12.29%	7.72%	9.98%
	November-12-2014					
NDBI-based	30.07%	27.52%	17.58%	9.91%	5.19%	3.74%
NDVI-based	43.58%	31.52%	14.98%	5.50%	1.81%	2.61%
NDWI-based	46.43%	30.42%	13.77%	4.91%	1.60%	2.87%
NMDI-based	41.28%	30.01%	14.26%	7.18%	3.47%	3.80%
	December-30-2014					
NDBI-based	36.98%	28.71%	18.75%	9.13%	3.74%	2.70%
NDVI-based	35.47%	31.16%	19.47%	7.30%	3.29%	3.35%
NDWI-based	36.28%	30.67%	18.31%	7.54%	3.62%	3.58%
NMDI-based	39.58%	30.55%	16.15%	7.14%	3.64%	2.94%

Table 6
Percentage of mean error (ME) in downscaled LST (°C) at 30 m resolution.

ME in downscaled LST (°C)	< -4	-4–-3	-3–-2	-2–-1	-1–0	0–1	1–2	2–3	3–4	>4
	June-05-2014									
NDBI-based	0.40%	1.61%	5.90%	13.79%	23.35%	29.78%	19.39%	4.80%	0.61%	0.36%
NDVI-based	0.01%	0.29%	5.00%	19.48%	25.89%	21.25%	17.53%	7.89%	1.06%	1.63%
NDWI-based	0.01%	0.32%	5.47%	19.18%	25.36%	21.67%	17.88%	7.18%	1.01%	1.92%
NMDI-based	0.57%	2.26%	6.93%	10.70%	21.39%	33.86%	19.77%	3.59%	0.58%	0.35%
	September-25-2014									
NDBI-based	0.61%	2.15%	6.65%	14.35%	24.53%	29.56%	16.16%	4.77%	1.01%	0.20%
NDVI-based	0.62%	2.29%	6.99%	16.35%	27.62%	26.13%	12.65%	4.06%	1.09%	2.20%
NDWI-based	0.47%	2.06%	7.22%	18.24%	29.85%	22.90%	11.41%	4.00%	1.23%	2.62%
NMDI-based	1.11%	2.68%	6.79%	14.37%	25.42%	26.68%	15.84%	5.47%	1.36%	0.29%
	November-12-2014									
NDBI-based	0.14%	0.85%	4.57%	13.97%	30.98%	32.6%	13.52%	2.88%	0.41%	0.06%
NDVI-based	0.01%	0.04%	1.03%	12.45%	41.24%	33.86%	8.03%	1.52%	0.78%	1.04%
NDWI-based	0.01%	0.04%	0.95%	11.73%	43.41%	33.49%	6.95%	1.33%	0.74%	1.41%
NMDI-based	0.18%	1.55%	3.80%	10.12%	34.98%	36.31%	11.32%	1.73%	0.01%	0.01%
	December-30-2014									
NDBI-based	0.19%	0.80%	3.68%	11.13%	29.75%	35.93%	16.75%	1.62%	0.12%	0.03%
NDVI-based	0.03%	0.37%	3.11%	12.55%	30.79%	35.84%	14.17%	1.86%	0.74%	0.54%
NDWI-based	0.04%	0.48%	3.43%	12.30%	30.19%	36.76%	13.55%	2.02%	0.75%	0.46%
NMDI-based	0.07%	0.65%	3.62%	11.19%	28.49%	41.64%	12.10%	1.68%	0.51%	0.05%

Declarations

Author contribution statement

Guha, S. Govil, H. Dey, A. Gill, N.: Conceived and designed the analysis; Performed the experiments; Analyzed and interpreted the data; Contributed analysis tools or data; Wrote the paper.

Funding statement

This research did not receive any specific grant from funding agencies in the public, commercial, or not-for-profit sectors.

Competing interest statement

The authors declare no conflict of interest.

Additional information

No additional information is available for this paper.

Acknowledgements

The authors thank to United States Geological Survey and National Institute of Technology Raipur, India. The authors also thank the anonymous reviewers for their relevant comments.

References

Agam, N., Kustas, W.P., Anderson, M.C., Li, F.Q., Colaizzi, P.D., 2007a. Utility of thermal sharpening over Texas high plains irrigated agricultural fields. J. Geophys. Res. 112 (D19110).

Agam, N., Kustas, W.P., Anderson, M.C., Li, F.Q., Neale, C.M.U., 2007b. A vegetation index based technique for spatial sharpening of thermal imagery. Rem. Sens. Environ. 107, 545–558.

Anderson, M.C., Norman, J.M., Kustas, W.P., Houborg, R., Starks, P.J., Agam, N., 2008. A thermal-based remote sensing technique for routine mapping of land-surface carbon, water and energy fluxes from field to regional scales. Rem. Sens. Environ. 112 (12), 4227–4241.

Bechtel, B., Zaksek, K., Hoshyaripour, G., 2012. Downscaling land surface temperature in an urban area: a case study for hamburg, Germany. Rem. Sens. 4, 3184–3200.

Bindhu, V.M., Narasimhan, B., Sudheer, K.P., 2013. Development and verification of a nonlinear disaggregation method (NL-DisTrad) to downscale MODIS land surface temperature to the spatial scale of Landsat thermal data to estimate evapotranspiration. Rem. Sens. Environ. 135, 118–129.

Bonafoni, S., Anniballe, R., Gioli, B., Toscano, P., 2016. Downscaling landsat land surface temperature over the urban area of florence. Eur. J. Remote Sens. 49 (1), 553–569.

Bonafoni, S., 2016. Downscaling of Landsat and MODIS land surface temperature over the heterogeneous urban area of Milan. IEEE J. Sel. Top. Appl. Earth Obs. Remote Sens. 9 (5), 2019–2027.

Bonafoni, S., Tosi, G., 2017. Downscaling of land surface temperature using airborne high-resolution data: a case study on Aprilia, Italy. IEEE Geosci. Remote Sens. Lett. 14 (1), 107–111.

Chander, G., Markham, B.L., Helder, D.L., 2009. Summary of current radiometric calibration coefficients for landsat MSS, TM, ETM+, and EO-1 ALI sensors. Rem. Sens. Environ. 113 (5), 893–903.

Cheng, G., Li, Z., Han, J., Yao, X., Guo, L., 2018a. Exploring hierarchical convolutional features for hyperspectral image classification. IEEE Trans. Geosci. Remote Sens. 56 (11), 6712–6722.

Cheng, G., Yang, C., Yao, X., Guo, L., Han, J., 2018b. When deep learning meets metric learning: remote sensing image scene classification via learning discriminative CNNs. IEEE Trans. Geosci. Remote Sens. 56 (5), 2811–2821.

Chen, L., Yan, G.J., Ren, H.Z., Li, A.H., 2010. A modified vegetation index based algorithm for thermal imagery sharpening. IEEE Int. Geosci. Remote Sens. Symp. IGARSS 10.

Chen, Y., Zhan, W., Quan, J., Zhou, J., Zhu, X., Sun, H., 2014. Disaggregation of remotely sensed land surface temperature: a generalized paradigm. IEEE Trans. Geosci. Remote Sens. 52 (9), 5952–5965.

Dennison, P.E., Charoensiri, K., Roberts, D.A., Peterson, S.H., Green, R.O., 2006. Wildfire temperature and land cover modeling using hyperspectral data. Rem. Sens. Environ. 100 (2), 212–222.

Dominguez, A., Kleissl, J., Luvall, J.C., Rickman, D.L., 2011. High-resolution urban thermal sharpener (HUTS). Rem. Sens. Environ. 115 (7), 1772–1780.

Duan, S.B., Li, Z.L., 2016. Spatial downscaling of MODIS land surface temperatures using geographically weighted regression: case study in northern China. IEEE Trans. Geosci. Remote Sens. 54 (11), 6458–6469.

Duan, S.B., Li, Z.L., Tang, B.H., Wu, H., Tang, R., 2014. Generation of a time-consistent land surface temperature product from MODIS data. Rem. Sens. Environ. 150, 339–349.

Essa, W., van der Kwast, J., Verbeiren, B., Batelaan, O., 2013. Downscaling of thermal images over urban areas using the land surface temperature–impervious percentage relationship. Int. J. Appl. Earth Obs. Geoinf. 23, 95–108.

Essa, W., Verbeiren, B., van der Kwast, J., van de Voorde, T., Batelaan, O., 2012. Evaluation of the DisTrad thermal sharpening methodology for urban areas. Int. J. Appl. Earth Obs. Geoinf. 19, 163–172.

Gao, B.C., 1996. NDWI: a normalized difference water index for remote sensing of vegetation liquid water from space. Rem. Sens. Environ. 58, 257–266.

Gualtieri, J.A., Chettri, S., 2000. Support Vector Machines for classification of hyperspectral data. In: Proceedings of the 2000 International Geoscience and Remote Sensing Symposium (IGARSS 2000), Honolulu, HI, USA, 24–28 July 2000. IEEE, Honolulu, HI, USA, pp. 813–815, 2000.

Guha, S., Govil, H., Dey, A., Gill, N., 2018. Analytical study of land surface temperature with NDVI and NDBI using Landsat 8 OLI and TIRS data in Florence and Naples city, Italy. Eur. J. Remote Sens. 51 (1), 667–678.

Guha, S., Govil, H., Diwan, P., 2019. Analytical study of seasonal variability in land surface temperature with normalized difference vegetation index, normalized difference water index, normalized difference built-up index, and normalized multiband drought index. J. Appl. Remote Sens. 13 (2), 024518.

Guha, S., Govil, H., Mukherjee, S., 2017. Dynamic analysis and ecological evaluation of urban heat islands in Raipur City, India. J. Appl. Remote Sens. 11 (3), 036020.

Jeganathan, C., Hamm, N.A.S., Mukherjee, S., Atkinson, P.M., Raju, P.L.N., Dadhwal, V.K., 2011. Evaluating a thermal image sharpening model over a mixed agricultural landscape in India. Int. J. Appl. Earth Obs. Geoinf. 13 (2), 178–191.

Kustas, W.P., Norman, J.M., Anderson, M.C., French, A.N., 2003. Estimating subpixel surface temperatures and energy fluxes from the vegetation index–radiometric temperature relationship. Rem. Sens. Environ. 85 (4), 429–440.

Li, Z.L., Tang, B.H., Wu, Hua., Ren, H., Yan, G., Wan, Z., Trigo, I.F., Sobrino, J.A., 2013. Satellite-derived land surface temperature: current status and perspectives. Rem. Sens. Environ. 131, 14–37.

Merlin, O., Duchemin, B., Hagolle, O., Jacob, F., Coudert, B., Chehbouni, G., Dedieu, G., Garatuza, J., Kerr, Y., 2010. Disaggregation of MODIS surface temperature over an agricultural area using a time series of Formosat-2 images. Rem. Sens. Environ. 114 (11), 2500–2512.

Moran, M.S., 1990. A window-based technique for combining Landsat Thematic Mapper thermal data with higher-resolution multispectral data over agricultural lands. Photogramm. Eng. Rem. Sens. 56 (3), 337–342.

Mpelasoka, F.S., Mullan, A.B., Heerdegen, R.G., 2001. New Zealand climate change information derived by multivariate statistical and artificial neural networks approaches. Int. J. Climatol. 21, 1415–1433.

Mukherjee, S., Joshi, P.K., Garg, R.D., 2015. Evaluation of LST downscaling algorithms on seasonal thermal data in humid subtropical regions of India. Int. J. Remote Sens. 36 (10), 2503–2523.

Nichol, J., 2009. An emissivity modulation method for spatial enhancement of thermal satellite images in urban heat island analysis. Photogramm. Eng. Rem. Sens. 75 (5), 547–556.

Nishii, R., Kusanobu, S., Tanaka, S., 1996. Enhancement of low spatial resolution image based on high resolution bands. IEEE Trans. Geosci. Remote Sens. 34 (5), 1151–1158.

Pan, X., Zhu, X., Yang, Y., Cao, C., Zhang, X., Shan, L., 2018. Applicability of downscaling land surface temperature by using normalized diference sand index. Sci. Rep. 8, 9530.

Pardo-Igúzquiza, E., Chica-Olmo, M., Atkinson, P.M., 2006. Downscaling cokriging for image sharpening. Rem. Sens. Environ. 102, 86–98.

Pardo-Igúzquiza, E., Rodríguez-Galiano, V.F., Chica-Olmo, M., Atkinson, P.M., 2011. Image fusion by spatially adaptive filtering using downscaling cokriging. ISPRS J. Photogrammetry Remote Sens. 66 (3), 337–346.

Purevdorj, T.S., Tateishi, R., Ishiyama, T., Honda, Y., 1998. Relationships between percent vegetation cover and vegetation indices. Int. J. Remote Sens. 19, 3519–3535.

Sandholt, I., Rasmussena, K., Andersenb, J., 2002. A simple interpretation of the surface temperature/vegetation index space for assessment of surface moisture status. Rem. Sens. Environ. 79, 213–224.

Small, C., 2006. Comparative analysis of urban reflectance and surface temperature. Rem. Sens. Environ. 104, 168–189.

Sobrino, J.A., Jiménez-Muñoz, J.C., Paolini, L., 2004. Land surface temperature retrieval from Landsat TM 5. Rem. Sens. Environ. 90 (4), 434–440.

Stathopoulou, M., Cartalis, C., 2009. Downscaling AVHRR land surface temperatures for improved surface urban heat island intensity estimation. Rem. Sens. Environ. 112, 2592–2605.

Van, D., Griend, A.A., Owe, M., 1993. On the relationship between thermal emissivity and the normalized difference vegetation index for natural surfaces. Int. J. Remote Sens. 14, 1119–1131.

Voogt, J.A., Oke, T.R., 2003. Thermal remote sensing of urban climates. Rem. Sens. Environ. 86 (3), 370–384.

Wan, Z., Dozier, J., 1996. Generalized split-window algorithm for retrieving land-surface temperature from space. IEEE Trans. Geosci. Remote Sens. 34, 892–905.

Wan, Z., Li, Z.L., 1997. A physics-based algorithm for retrieving land-surface emissivity and temperature from EOS/MODIS data. IEEE Trans. Geosci. Remote Sens. 35 (4), 980–996.

Wan, Z., Li, Z.L., 2008. Radiance-based validation of the V5 MODIS land surface temperature product. Int. J. Remote Sens. 29 (17/18), 5373–5395, 2008.

Weng, Q., Fu, P., 2014. Modeling diurnal land temperature cycles over Los Angeles using downscaled GOES imagery. ISPRS J. Photogrammetry Remote Sens. 97, 78–88.

Weng, Q.H., Lu, D.S., Schubring, J., 2004. Estimation of land surface temperature vegetation abundance relationship for urban heat island studies. Rem. Sens. Environ. 89, 467–483.

Yang, Y., Yao, L., 2009. The influence of urban design factors on urban heat environment in urban residential area with remote sensing. In: Proceedings of the Sixth International Symposium on Multispectral Image Processing and Pattern Recognition, Yichang, China, 30 October–1 November 2009. International Society for Optics and Photonics, Bellingham,WA, USA, p. 74984K, 2009.

Yang, G.J., Pu, R.L., Zhao, C.J., Huang, W.J., Wang, J.H., 2011. Estimation of subpixel land surface temperature using an endmember index based technique: a case examination on ASTER and MODIS temperature products over a heterogeneous area. Rem. Sens. Environ. 115 (5), 1202–1219.

Yang, G., Pu, R., Huang, W., Wang, J., Zhao, C., 2010. A novel method to estimate subpixel temperature by fusing solar-reflective and thermal-infrared remote-sensing data with an artificial neural network. IEEE Trans. Geosci. Remote Sens. 48 (4), 2170–2178.

Yuan, F., Bauer, M.E., 2007. Comparison of impervious surface area and normalized difference vegetation index as indicators of surface urban heat island effects in Landsat imagery. Rem. Sens. Environ. 106, 375–386.

Zakšek, K., Oštir, K., 2012. Downscaling land surface temperature for urban heat island diurnal cycle analysis. Rem. Sens. Environ. 117, 114–124.

Zhang, Y., 2015. Land Surface Temperature Inversion and Downscaling Research for Landsat 8. Master Thesis. Hohai University, Nanjing, China, 2015.

Zhan, W., Chen, Y., Zhou, J., Wang, J., Liu, W., Voogt, J., Zhu, X., Quan, J., Li, J., 2013. Disaggregation of remotely sensed land surface temperature: literature survey, taxonomy, issues, and caveats. Rem. Sens. Environ. 131, 119–139.

Zha, Y., Gao, J., Ni, S., 2003. Use of normalized difference built-up index in automatically mapping urban areas from TM imagery. Int. J. Remote Sens. 24 (3), 583–594.

Zhou, D., Xiao, J., Bonafoni, S., Berger, C., Deilami, K., Zhou, Y., Frolking, S., Yao, R., Qiao, Z., Sobrino, J., 2019a. Satellite remote sensing of surface urban heat islands: progress, challenges, and perspectives. Rem. Sens. 11 (1), 48.

Zhou, J., Liu, S., Li, M., Zhan, W., Xu, Z., Xu, T., 2016. Quantification of the scale effect in downscaling remotely sensed land surface temperature. Rem. Sens. 8, 975.

Zhou, P., Han, J., Cheng, G., Zhang, B., 2019b. Learning compact and discriminative stacked autoencoder for hyperspectral image classification. IEEE Trans. Geosci. Remote Sens. 1–11.

Source details

Feedback > Compare sources >

Heliyon

Open Access

Scopus coverage years: from 2015 to Present

Publisher: Elsevier

ISSN: 2405-8440 E-ISSN: 2405-8440

Subject area: Multidisciplinary

Source type: Journal

View all documents > Set document alert Save to source list

CiteScore 2022
5.6

SJR 2022
0.609

SNIP 2022
1.332

CiteScore CiteScore rank & trend Scopus content coverage

Environment, Development and Sustainability
https://doi.org/10.1007/s10668-020-00657-6

An assessment on the relationship between land surface temperature and normalized difference vegetation index

Subhanil Guha[1] · **Himanshu Govil**[1]

Received: 2 October 2019 / Accepted: 19 February 2020

Abstract
The present study aims to assess the trend of spatiotemporal relationship between land surface temperature (LST) and normalized difference vegetation index (NDVI) under different ranges of LST and NDVI values for Raipur City of India using fifteen cloud-free Landsat data sets of the pre-monsoon season from 2002 to 2018. LST maintains a strong negative relationship with NDVI for the whole of the study area. The relationship is quite insignificant for both the high LST zones and low LST zones. The results also indicate that under the positive NDVI values, the LST–NDVI relationships are strong to moderately negative, whereas it is positive and non-consistent under the negative values of NDVI. The results also show that the relationship is stronger in the earlier times, whereas it is weaker in recent times. An increase in heterogeneous landscape inside the city boundary strongly supports the changing pattern of LST–NDVI relationship.

Keywords Land surface temperature (LST) · Normalized difference vegetation index (NDVI) · Landsat · Raipur City

1 Introduction

Land surface temperature (LST) is considered as an important parameter in analysing the exchange of composed material, energy balance and biophysical and chemical processes of the land surface (Tomlinson et al. 2011; Hao et al. 2016). LST of the different surface area is different due to surface reflectance and roughness of different land use/land cover (LULC) types (Hou et al. 2010). Recently, due to rapid urbanization, the characteristics of land surface types are being changed (Li et al. 2017). The presence of natural vegetation influenced a lot in the distribution of LST (Yuan 2017). Normalized difference vegetation index (NDVI) is a vegetation index which is generally used in LST-related study (Smith and Choudhury 1990; Hope and McDowell 1992; Julien et al. 2006). The LST–NDVI relationship is controlled by a number of factors like dense vegetation, sand dunes, water bodies, dry soil, exposed rock surface, wetland, building materials, etc., and hence, it is too complex in nature (Zhou et al. 2011; Ghobadi et al. 2014; Qu et al. 2014).

✉ Subhanil Guha
subhanilguha@gmail.com

[1] Department of Applied Geology, National Institute of Technology Raipur, Raipur, India

Currently, most of the research scholars applied thermal infrared remote sensing to build the relationship between LST and NDVI (Ghobadi et al. 2014; Stroppiana et al. 2014; Li et al. 2016; Wen et al. 2017). Most of the earlier LST–NDVI relationship-related studies were conducted on big cities, e.g., Tokyo (Shigeto 1994), Shanghai (Yue et al. 2006), Melbourne (Jamei et al. 2015), Bangkok (Estoque et al. 2017), Shiraz (Fatemi and Narangifard 2019), Rome (Bonafoni 2015), Chongqing (Luo and Li 2014), Shijiazhuang (Liu et al. 2014), Beijing, and Islamabad (Naeem et al. 2018). A spatial and temporal analysis of LST–NDVI relationship for in Monte Hermoso, Argentina was performed for urban planning (Ferrelli et al. 2018). Only a few studies have been conducted about the seasonal relationship between LST and NDVI in a tropical Indian city.

Generally, the spatial and temporal resolution of satellite sensor should follow the nature of surface configurations (Zhang et al. 2015). In any urban area, the high value of land surface temperature (LST) is generated mostly in the area with lower vegetation intensity (Voogt and Oke 2003). Therefore, most of the thermal remote sensing methods used the normalized difference vegetation index (NDVI) as the significant indicator of LST (Goward et al. 2002), and a number of studies based on the relationships of LST with NDVI were used to explore the pattern of LST (Gutman and Ignatov 1998; Weng et al. 2004; Guha et al. 2017, 2018, 2019; Govil et al. 2019). Fractal technique (De Cola 1989; Emerson et al. 1999; Lam 1990; Lam and Quattrochi 1992; Lam and De Cola 1993; Lam et al. 2002; Qiu et al. 1999; Weng 2003) has also been applied in determining the LST–NDVI relationship (Weng et al. 2004).

Some recent research works based on spatial–temporal relationship of LST–NDVI in tropical Indian cities have also been performed successfully, e.g., Ahmedabad (Mathew et al. 2018), Jaipur (Mathew et al. 2017), Kalaburagi (Kumar and Shekhar 2015), Noida (Kikon et al. 2016), and Lucknow (Singh et al. 2017). A number of new research works were performed on the LST–NDVI relationships in multidimensional approach (Hassan et al. 2007; Li and Yu 2008; Zhang and Wang 2008; Rozenstein et al. 2014; Slawsky et al. 2015; Hao et al. 2019; Liu and Weng 2018; Mohammad et al. 2019; Nowicki et al. 2019; Qi et al. 2019; Shi et al. 2019; Sun et al. 2019). It is a necessary task to assess the time series of LST–NDVI relationship in different LST and NDVI zones for a tropical city which has not been well addressed in the earlier studies. Generally, low NDVI region indicates high LST values and vice versa. It is also very important to know the change of LST with the change of NDVI. Generally, negative NDVI shows water bodies; positive NDVI up to 0.2 shows bare land and built-up areas; NDVI with more than 0.2 shows vegetation; and higher NDVI stands for the healthier vegetation with high chlorophyll content (Chen et al. 2006; Guha et al. 2017). To reveal the characteristics of spatiotemporal variation of LST–NDVI relationship in a tropical city, we selected Raipur City of India as the city is an excellent example of mixed landscape. We determined the LST–NDVI relationship under different ranges of LST and NDVI from various types of Landsat sensor products of pre-monsoon season for 2002, 2006, 2010, 2014, and 2018 as the landscape has been changed a lot during this time frame. These results can be useful for future environmental planning and sustainable development as Raipur is considered as a smart city and also one of the fastest growing cities in country. Importance of green areas, water bodies, and wetland has been increased for the city planners in a very short time span. The main aims of the study are (1) to determine the spatiotemporal variation of LST–NDVI relationship for the whole of the city, the area above mean LST, the area below mean LST; and (2) to explore the spatiotemporal variation of LST–NDVI relationship under different ranges of NDVI values.

2 Study area and data

Raipur City of Chhattisgarh State of India was selected as the study area for the entire research work. The total study area extends between 21° 11′ 22″ N to 21° 20′ 02″ N and 81° 32′ 20″ E to 81° 41′ 50″ E with a moderate range of elevation of 219 m to 322 m (Fig. 1). The study area is considered as tropical wet (Savannah) type of climate. The mean annual temperature of Raipur City is approximately 27 °C. According to the India Meteorological Department, there are four seasons are observed in Raipur, i.e. pre-monsoon (March–June), monsoon (July–September), post-monsoon (October–November), and winter (December–February). The pre-monsoon or summer months are usually hot and remain almost dry. The temperature often rises above 45 °C in April and May. The pre-monsoon season

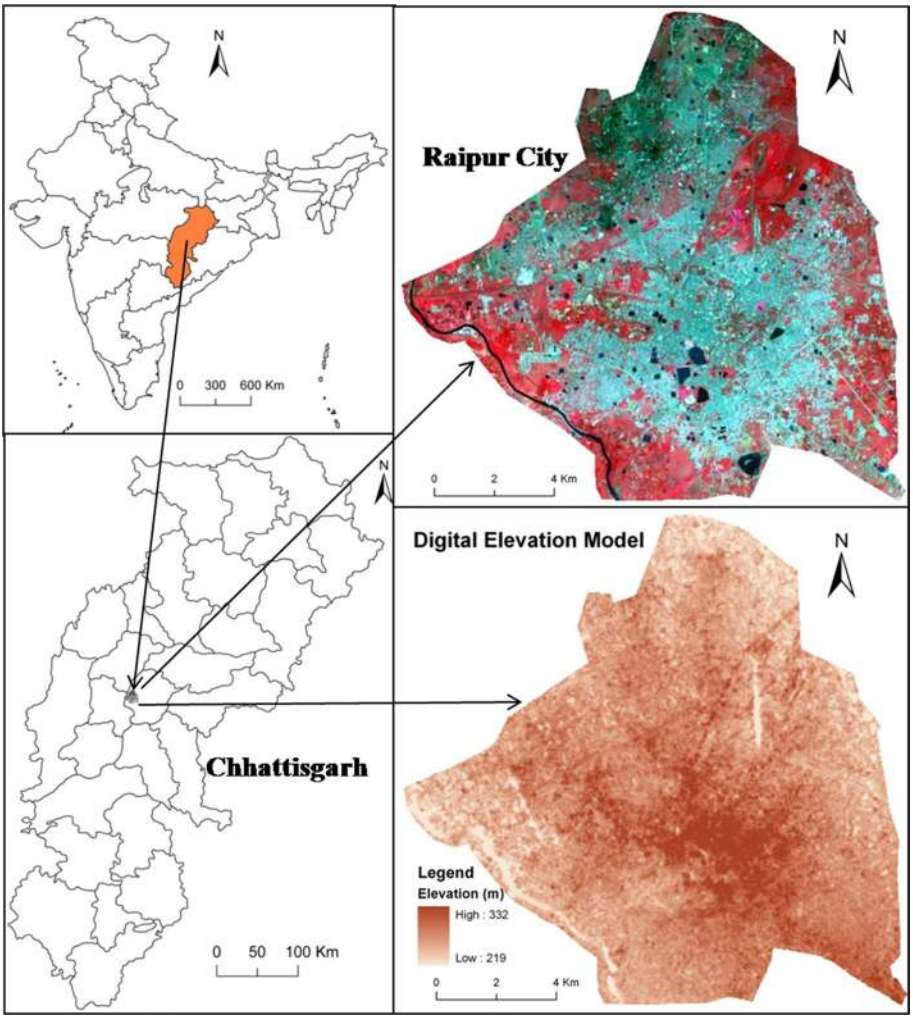

Fig. 1 Location of the study area

was selected for the present study for examining the nature of LST due to its severe intensity. July, August, and September months are considered under monsoon or rainy season. October and November months are often considered as the post-monsoon season, characterized by a pleasant climatic condition with comparatively low temperature and high to the moderate moisture content in the air. The presence of high density of green vegetation really adds an extra flavour in Raipur during the monsoon and the post-monsoon seasons. Winter months (December to February) experience a cool and dry climate. The study area is also characterized by tropical mixed deciduous vegetation and mixed red soil. According to the 2011 census, Raipur City had a total population of 1,010,087, with a sex ratio of 945 females per 1000 males and with a literacy rate of 86.45%.

In the present study, the main data sets are time series of Landsat images taken by the Landsat 5 Thematic Mapper (TM), Landsat 7 Enhanced Thematic Mapper Plus (ETM+), and Landsat 8 Operational Land Imager (OLI)/Thermal Infrared Sensor (TIRS) sensors, and have been obtained from the United States Geological Survey website (https://earthexplorer.usgs.gov). A total of fifteen Landsat images have been taken in the Landsat series as shown in Table 1. The Landsat sensor overpasses the Raipur City between approximately 04:25 and 04:56 GMT, which is 09:55 to 10:26 AM local time. This is known to be an opportunity for collecting images with maximum illumination, especially in LST studies. Satellite images have been obtained with 4-year intervals, and within the pre-monsoon season to avoid phenological variations. The interval period of four years (2002, 2006, 2010, 2014 and 2018) has been taken in the present research work so that we can compare the results to see the temporal changes in LST and NDVI. The software used to conduct image processing included ERDAS Imagine 9.1 and ArcGIS 9.3. MS-Excel 2007 has been used for conducting the statistical analysis. Pre-processing of Landsat images is necessary as it has a great impact on the results of the analysis. Usually, it is not necessary to conduct a geometric correction for Landsat level 1 products, as they are registered and ortho-rectified through a systematic process. The main correction needed is therefore a radiometric correction. The radiometric correction eliminates errors that affect the brightness values

Table 1 Specification of multi-date Landsat satellite sensors

Landsat scene ID	Satellite sensor	Date of acquisition	Time	Path/Row
LE71420452002115SGS01	Landsat 7 ETM+	25-Apr-2002	04:44:54	142/044
LE71420452002131SGS00	Landsat 7 ETM+	11-May-2002	04:44:54	142/044
LT51420452006118BKT00	Landsat 5 TM	28-Apr-2006	04:48:00	142/044
LT51420452006166BKT00	Landsat 5 TM	15-Jun-2006	04:48:12	142/044
LT51420452010097KHC00	Landsat 5 TM	07-Apr-2010	04:47:02	142/044
LT51420452010113KHC00	Landsat 5 TM	23-Apr-2010	04:46:59	142/044
LT51420452010145BKT01	Landsat 5 TM	25-May-2010	04:46:51	142/044
LC81420452014076LGN01	Landsat 8 OLI_TIRS	17-Mar-2014	04:26:36	142/044
LC81420452014092LGN01	Landsat 8 OLI_TIRS	02-Apr-2014	04:26:19	142/044
LC81420452014140LGN01	Landsat 8 OLI_TIRS	20-May-2014	04:25:38	142/044
LC81420452014156LGN01	Landsat 8 OLI_TIRS	05-Jun-2014	04:25:45	142/044
LC81420452018071LGN00	Landsat 8 OLI_TIRS	12-Mar-2018	04:55:43	142/044
LC81420452018087LGN00	Landsat 8 OLI_TIRS	28-Mar-2018	04:55:36	142/044
LC81420452018135LGN00	Landsat 8 OLI_TIRS	15-May-2018	04:55:08	142/044
LC81420452018167LGN00	Landsat 8 OLI_TIRS	16-Jun-2018	04:55:01	142/044

of the pixels. These errors are mainly due to the detection errors in the sensor system and environmental attenuation errors. The original image sizes are larger than the study area, and hence, after pre-processing they are edited using a shapefile of Raipur City. LST has been retrieved through thermal infrared bands of Landsat data sets (band 6 for Landsat 5 and Landsat 7 data, whereas band 10 and 11 for Landsat 8 data). Red, near-infrared, and thermal infrared bands are used in generating NDVI and LST.

3 Methodology

3.1 Retrieving LST from Landsat data

In this study, the mono-window algorithm has been applied to retrieve LST from multi-temporal Landsat satellite images (Qin et al. 2001; Guha et al. 2017, 2018, 2019). Ground emissivity, atmospheric transmittance, and effective mean atmospheric temperature—these three parameters—are needed to derive the LST using mono-window algorithm. After determining the mean LST, the study has been performed into the whole of the city, the area above mean LST, and the area below mean LST.

At first, the original TIR band of Landsat sensor has been resampled into 30 m for further application. The entire procedure included the following equations:

$$L_\lambda = \text{RadianceMultiBand} \times \text{DN} + \text{RadianceAddBand} \tag{1}$$

where L_λ is spectral radiance ($\text{Wm}^{-2}\ \text{sr}^{-1}\ \text{mm}^{-1}$).

$$T_\text{b} = \frac{K_2}{\ln\left(\frac{K_1}{L_\lambda} + 1\right)} \tag{2}$$

where T_b is the at-sensor brightness temperature (Kelvin); K_2 and K_1 are calibration constants. Here, K_1 is 774.89 ($\text{Wm}^{-2}\ \text{sr}^{-1}\ \text{mm}^{-1}$); K_2 is 1321.08 ($\text{Wm}^{-2}\ \text{sr}^{-1}\ \text{mm}^{-1}$) for Landsat 8 data. For Landsat 7 data, K_1 is 666.09 ($\text{Wm}^{-2}\text{sr}^{-1}\text{mm}^{-1}$); K_2 is 1282.71 ($\text{Wm}^{-2}\text{sr}^{-1}\text{mm}^{-1}$). For Landsat 5 data, K_1 is 607.76 ($\text{Wm}^{-2}\text{sr}^{-1}\text{mm}^{-1}$); K_2 is 1260.56 ($\text{Wm}^{-2}\text{sr}^{-1}\text{mm}^{-1}$).

$$F_\text{v} = \left(\frac{\text{NDVI} - \text{NDVI}_\text{min}}{\text{NDVI}_\text{max} - \text{NDVI}_\text{min}}\right)^2 \tag{3}$$

where NDVI_min is the minimum value (0.2) of NDVI for bare soil pixel and NDVI_max is the maximum value (0.5) of NDVI for healthy vegetation pixel.

$d\varepsilon$ is the geometric distribution effect for the natural surface and internal reflection. The value of $d\varepsilon$ may be 2% for mixed and elevated land surfaces.

$$d\varepsilon = (1 - \varepsilon_\text{s})(1 - F_\text{v})F\varepsilon_\text{v} \tag{4}$$

where ε_s is soil emissivity; F_v is fractional vegetation; F is a shape factor (0.55); ε_v is vegetation emissivity.

$$\varepsilon = \varepsilon_\text{v}F_\text{v} + \varepsilon_\text{s}(1 - F_\text{v}) + d\varepsilon \tag{5}$$

where ε is land surface emissivity. The value of ε is determined by the following equation:

$$\varepsilon = 0.004 \times F_{\mathrm{v}} + 0.986 \tag{6}$$

Water vapour content is determined by the following equation:

$$w = 0.0981 \times \left[10 \times 0.6108 \times \exp\left(\frac{17.27 \times (T_0 - 273.15)}{237.3 + (T_0 - 273.15)} \right) \times \mathrm{RH} \right] + 0.1697 \tag{7}$$

where w is water vapour content (g/cm^2); T_0 is near-surface air temperature (Kelvin); RH is relative humidity (%). These parameters of atmospheric profile were the average values of 14 stations around Raipur which were obtained from the Meteorological Centre, Raipur and the Regional Meteorological Centre, Nagpur.

$$\tau = 1.031412 - 0.11536w \tag{8}$$

where τ is the total atmospheric transmittance.

Raipur city is located in the tropical region. Thus, the following equations were applied to compute the effective mean atmospheric transmittance of Raipur:

$$T_{\mathrm{a}} = 17.9769 + 0.91715T_0 \tag{9}$$

$$T_{\mathrm{s}} = \frac{\left[a(1 - C - D) + (b(1 - C - D) + C + D)T_{\mathrm{b}} - DT_{\mathrm{a}}\right]}{C} \tag{10}$$

$$C = \varepsilon\tau \tag{11}$$

$$D = (1 - \tau)[1 + (1 - \varepsilon)\tau] \tag{12}$$

where T_{a} is mean atmospheric temperature; T_{s} is land surface temperature; $a = -67.355351$, $b = 0.458606$.

3.2 Generation of NDVI

In the earlier studies, various land surface biophysical parameters were applied to specify different types of land surface features (Bonafoni 2015; Luo and Li 2014; Liu et al. 2014; Guha et al. 2017, 2018, 2019). In this study, special emphasis has been given on NDVI for determining the relationship with LST. NDVI is generally used as a vegetation index which can also be used for extracting other LULC types (Purevdorj et al. 1998; Ke et al. 2015). In this study, NDVI has been determined using the red and near-infrared bands of Landsat sensors (Table 2). The NDVI values are further divided into some parts of a range of 0.1 NDVI value. Finally, the LST–NDVI relationship is examined under these ranges of NDVI values.

Table 2 Description of normalized difference vegetation index (NDVI)

Acronym	Description	Formulation	Reference
NDVI	Normalized difference vegetation index	$\frac{\mathrm{NIR-Red}}{\mathrm{NIR+Red}}$	Purevdorj et al. (1998)

3.3 Preparation of LULC map

The LULC maps for the five selected years—2002, 2006, 2010, 2014, and 2018—have been prepared using the threshold limits of NDVI (Chen et al. 2006). The area with NDVI values of more than 0.2 indicated vegetation while less than 0 values of NDVI reflected water bodies. The intermediate values were used for the extraction of the built-up area and bare land. But these threshold values may differ due to atmospheric condition. An ISODATA classifier with the unsupervised clustering method and the maximum likelihood classification has also been applied to verify the output. The values of kappa coefficient and overall accuracy have been calculated as 0.87 and 91.62, respectively. Some small water bodies have been found in the central and the southern sections of the study area during the entire time span. In 2002, most of the areas were covered by green vegetation, whereas the built-up areas and bare lands have been found mainly in the central and north-western parts of the Raipur City. The portion of the built-up areas and bare lands has been expanded along the north-western border from 2002 to 2010. From 2006 to 2014, the percentage of urban vegetation was declined because of the conversion into built-up areas. From 2014 to 2018, green areas have been reduced significantly. Only some parts of east and south-west of the city are covered by green vegetation. Rest of the areas of the city has been converted into bare land and built-up area (Fig. 2).

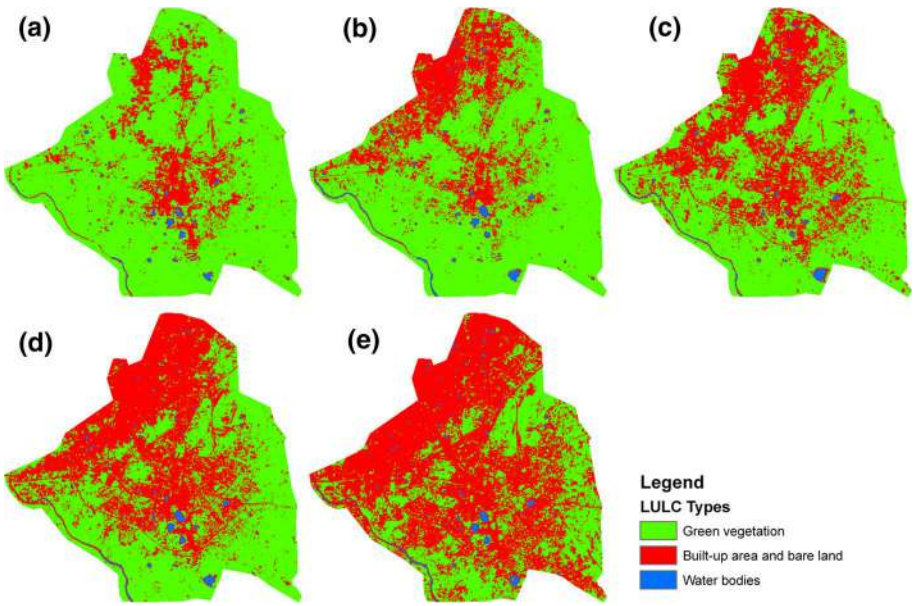

Fig. 2 LULC maps of Raipur City: **a** 2002, **b** 2006, **c** 2010, **d** 2014, and **e** 2018

4 Results and discussion

4.1 Spatiotemporal variations of LST distribution

The retrieved LST maps using the pre-monsoon multi-temporal Landsat data sets have been shown in Fig. 3. The average aggregated LST values of 2002, 2006, 2010, 2014, and 2018 have been generated (Table 3). Figure 4 shows the mean LST values for 2002, 2006, 2010, 2014, and 2018. The annual average minimum LST ranges from 22.08 °C in 2002 to 33.98 °C in 2018. The annual average maximum LST ranges between 36.56 °C in 2002 and 50.40 °C in 2018. The annual average mean LST value has been increased from 31.91 °C (2002) to 43.53 °C (2018). The high LST values are found in the north-western and south-eastern parts of the city. This portion of the area is characterized by open bare land. The central part of the study area presents the low LST zones where a high concentration of urban vegetation and water bodies are observed.

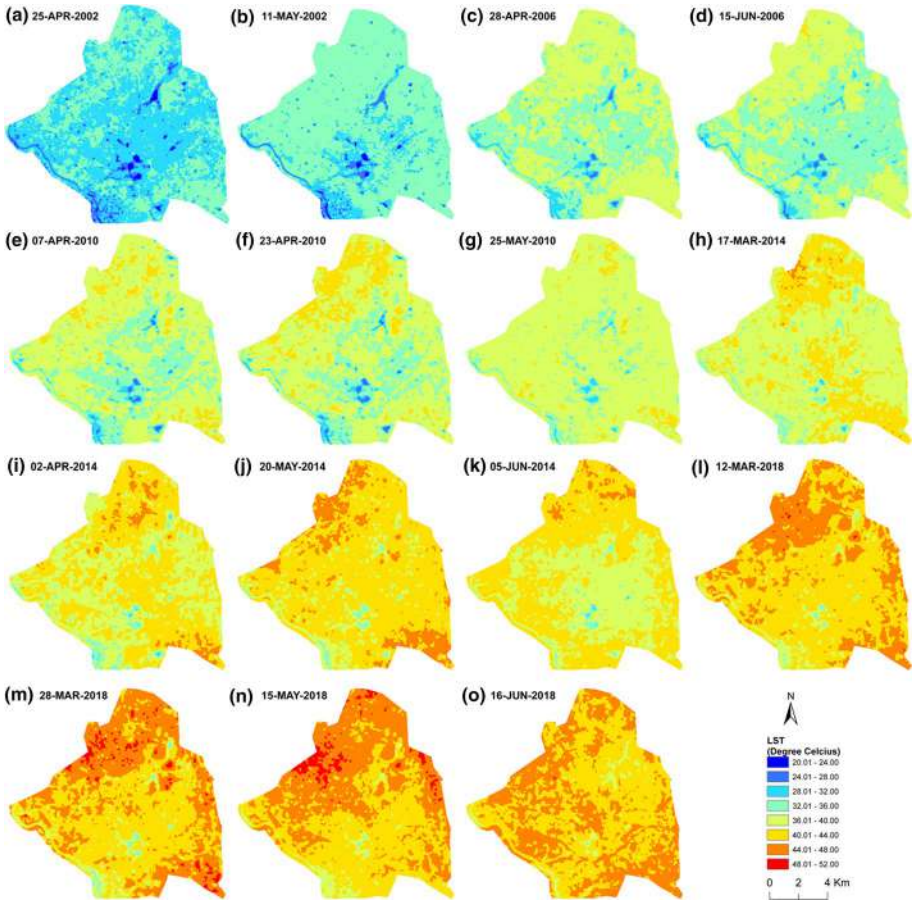

Fig. 3 Spatiotemporal distribution of LST (°C): **a, b** 2002, **c, d** 2006, **e–g** 2010, **h–k** 2014, and **l–o** 2018

Table 3 Spatiotemporal variations of LST (°C) distribution (2002–2018)

Date	LST (minimum)	LST (maximum)	LST (mean)	LST (standard deviation)
25-Apr-2002	21.88	35.52	31.08	1.70
11-May-2002	22.28	37.60	32.74	1.93
Mean	22.08	36.56	31.91	1.82
28-Apr-2006	26.25	41.45	35.79	2.01
15-Jun-2006	25.40	42.20	35.44	2.10
Mean	25.83	41.83	35.62	2.06
07-Apr-2010	25.31	43.93	36.94	2.43
23-Apr-2010	24.15	44.60	37.39	2.61
25-May-2010	28.01	41.52	37.92	1.62
Mean	25.82	43.35	37.42	2.22
17-Mar-2014	31.23	46.26	39.29	1.92
02-Apr-2014	30.72	47.87	40.29	2.19
20-May-2014	32.07	47.66	41.90	2.06
05-Jun-2014	31.01	47.28	40.47	1.94
Mean	31.26	47.27	40.49	2.03
12-Mar-2018	33.18	50.04	43.03	2.03
28-Mar-2018	31.94	50.93	43.58	2.59
15-May-2018	35.10	51.64	43.99	2.24
16-Jun-2018	35.70	48.97	43.52	1.58
Mean	33.98	50.40	43.53	2.11

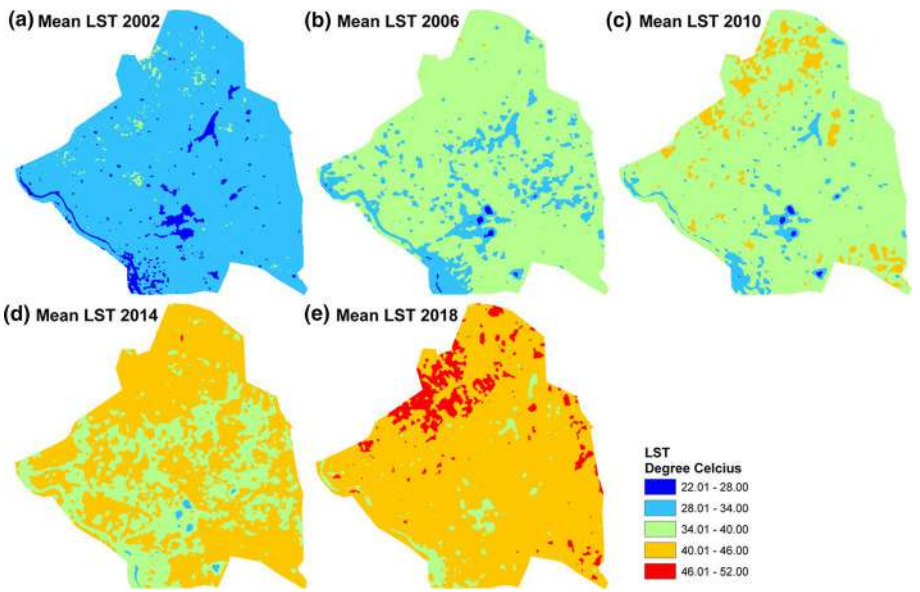

Fig. 4 Mean LST (°C) values: **a** 2002, **b** 2006, **c** 2010, **d** 2014, and **e** 2018

4.2 Validation of Landsat data derived LST with respect to the corresponding MODIS data derived LST

Before performing any kind of application, validation of derived LST is necessary with in situ measurement or with any other satellite sensor (Guha et al. 2019). In the present study, MODIS Terra data sets have been applied for the validation of LST values as a reference image. Landsat and modis sensor cannot overpass at same time for the same study area. Thus, MOD11A1 data (1000 m spatial resolution) of the following specific dates (Table 4) have been taken for the validation of estimated LST.

No such information has been obtained about the precipitation or atmospheric disturbances in the acquisition date of Landsat and MODIS sensors. For MODIS data, the spatial resolution of retrieved LST is 1000 m, whereas for Landsat 5, Landsat 7, and Landsat 8 data the resolutions of LST image are 120 m, 120 m, and 100 m, respectively. A little difference has been found between the LST retrieved from Landsat data sets and the corresponding MODIS data sets for the following reasons: (a) 30 min intervals between the Landsat sensors and MODIS sensors, (b) content of water vapour, and (c) resampling technique (Guha et al. 2019). In spite of not performing any upscaling or downscaling procedure, a significant correlation has been found between the mean derived LST from Landsat data sets and MODIS data sets (Table 4).

4.3 Spatiotemporal variation in the distribution of NDVI

NDVI images have been generated using the red and near-infrared bands of Landsat sensors, and the mean values of NDVI for particular years have been generated separately (Table 5). Figure 5 presents the NDVI values for fifteen pre-monsoon images. Figure 6 shows the mean NDVI values for 2002, 2006, 2010, 2014, and 2018. The high NDVI values have been found in the south-western and north-eastern parts of the city where

Table 4 Validation of Landsat data retrieved LST with MODIS data retrieved LST

Acquisition date (Landsat data)	Acquisition date (MODIS data)	Correlation coefficient
25-Apr-2002	25-Apr-2002	0.49
11-May-2002	11-May-2002	0.48
28-Apr-2006	29-Apr-2006	0.49
15-Jun-2006	17-Jun-2006	0.49
07-Apr-2010	06-Apr-2010	0.48
23-Apr-2010	22-Apr-2010	0.58
25-May-2010	24-May-2010	0.48
17-Mar-2014	16-Mar-2014	0.59
02-Apr-2014	01-Apr-2014	0.49
20-May-2014	19-May-2014	0.43
05-Jun-2014	04-Jun-2014	0.53
12-Mar-2018	13-Mar-2018	0.41
28-Mar-2018	27-Mar-2018	0.45
15-May-2018	12-May-2018	0.49
16-Jun-2018	15-Jun-2018	0.47

Table 5 Spatiotemporal variation of NDVI distribution for whole of the city (2002–2018)

Date of acquisition	NDVI (minimum)	NDVI (maximum)	NDVI (mean)	NDVI (standard deviation)
25-Apr-2002	−0.25	0.60	0.01	0.07
11-May-2002	−0.21	0.52	−0.01	0.06
Mean	−0.23	**0.56**	0.00	0.07
29-Apr-2006	−0.15	0.45	0.07	0.06
17-Jun-2006	−0.23	0.59	0.10	0.09
Mean	−0.19	**0.52**	0.09	0.08
06-Apr-2010	−0.25	0.57	0.03	0.07
22-Apr-2010	−0.27	0.58	0.03	0.08
24-May-2010	−0.12	0.34	−0.01	0.04
Mean	−0.21	**0.50**	0.02	0.06
16-Mar-2014	−0.14	0.51	0.16	0.08
01-Apr-2014	−0.13	0.52	0.14	0.07
19-May-2014	−0.07	0.45	0.12	0.05
04-Jun-2014	−0.08	0.45	0.13	0.06
Mean	−0.11	**0.48**	0.14	0.07
12-Mar-2018	−0.08	0.39	0.09	0.04
27-Mar-2018	−0.16	0.50	0.10	0.06
12-May-2018	−0.09	0.40	0.13	0.05
15-Jun-2018	−0.15	0.48	0.17	0.07
Mean	−0.12	**0.44**	0.12	0.06

vegetation is abundant and LST values are comparatively less. The maximum values of average annual NDVI (bold values in Table 5) have been decreased from 2002 to 2018 (0.56 in 2002, 0.52 in 2006, 0.50 in 2010, 0.48 in 2014, and 0.44 in 2014). It indicates that the proportion of vegetation of the city area has been reduced gradually with time. Figures 3, 4, 5, and 6 show that the LST and NDVI exhibit opposite spatial distribution patterns. At the macro level, the areas with high LST values show the urban heat island phenomenon. These areas have relatively low NDVI values. At the micro level, the high peaks of LST present a low valley of NDVI.

4.4 Distribution of LST for the area above mean LST, and for the area below mean LST

Figure 7 indicates a steady picture of the spatial distribution of LST values for the area above mean LST, and for the area below mean LST using fifteen multi-date images from 2002 to 2018. The high LST zones or area above mean LST are presented as red colour shades, whereas the low LST zones or the area below mean LST are presented as green colour shades. The central and southern parts of Raipur City are characterized by low LST values (area below mean LST), whereas the northern, western, and south-eastern parts reflect high LST zones (area above mean LST). The high LST zones are surrounded by built-up area and bare earth surface, whereas the low LST zones are developed mainly by the concentration of water bodies and dense vegetal cover.

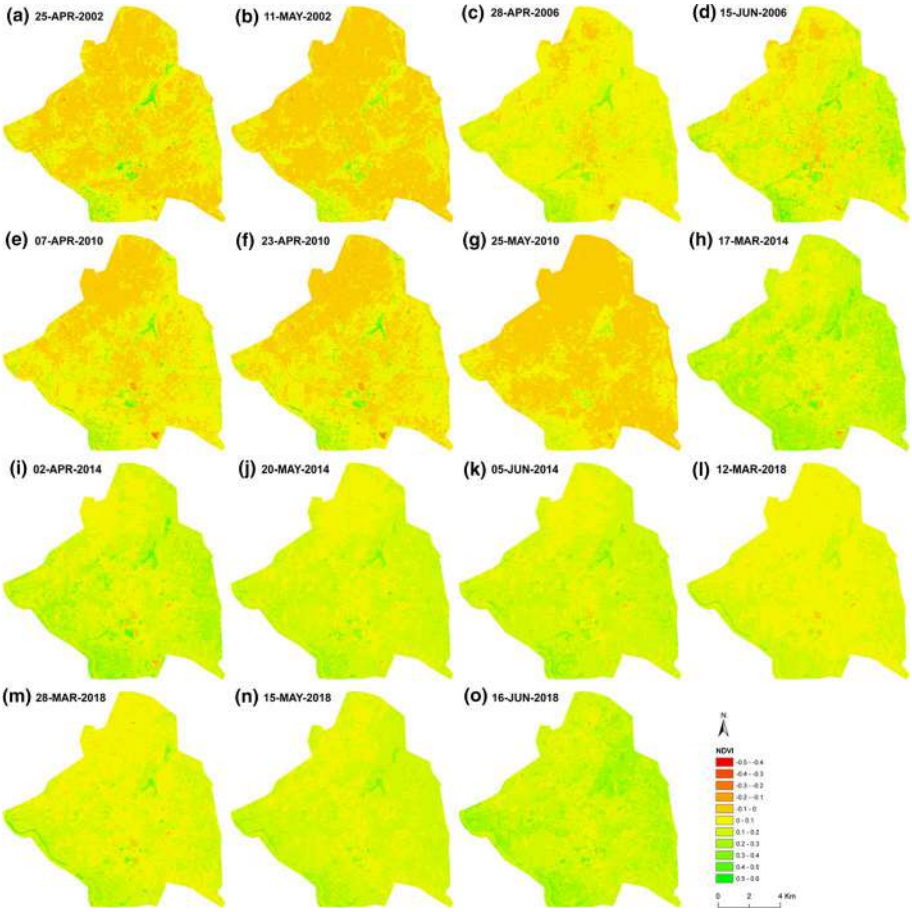

Fig. 5 Spatiotemporal distribution of NDVI: **a, b** 2002, **c, d** 2006, **e–g** 2010, **h–k** 2014, and **l–o** 2018

4.5 LST–NDVI relationship for the whole area of the city, the area above mean LST, and the area below mean LST

Generally, LST presents a negative relationship with NDVI. This specific pattern of the relationship between LST and NDVI has been noticed throughout the whole study area (Table 6). It is clear that NDVI is strong to moderate related to LST for the whole of the study area. The relationship is strong negative in 2002, 2006, and 2010 (bold values in Table 6), whereas it is moderate negative in 2014 and 2018. There has been no such particular pattern seen in NDVI–LST relationship for the area above mean LST. It shows a moderate relationship throughout the entire time. This relationship has also been found moderate for the area below mean LST. It indicates the fact that small area reduces the strength of LST–NDVI relationship due to the presence of heterogeneity in landscape. The large area always enhances the scope of building a strong LST–NDVI relationship in urban area.

Figures 8 and 9 present the mean temporal variation and year-wise analysis of LST–NDVI relationship for the study area, respectively. Figure 8 shows a strong

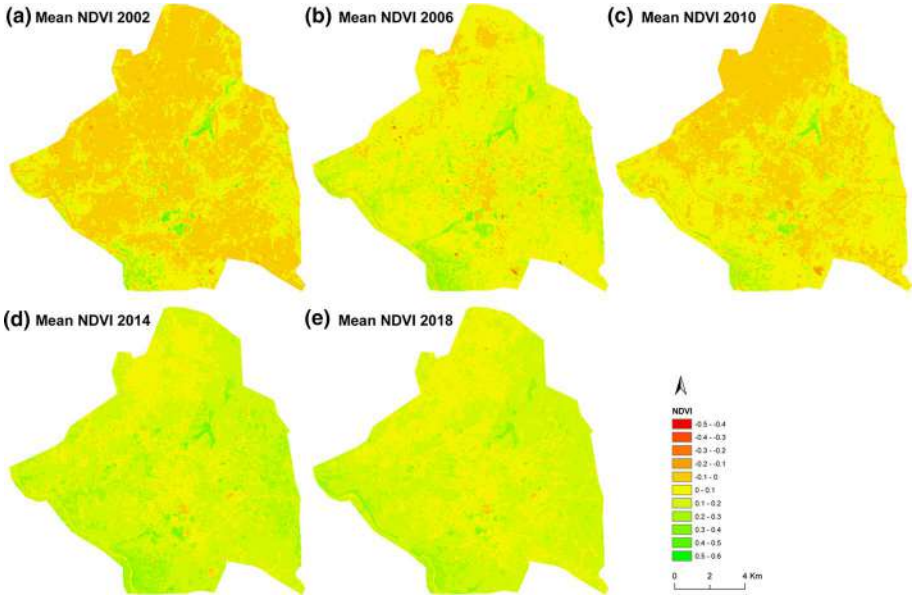

Fig. 6 Mean NDVI values: **a** 2002, **b** 2006, **c** 2010, **d** 2014, and **e** 2018

negative relationship for whole area which has been decreased through time. In the area above mean LST and in the area below mean LST, these relationships are moderate negative without showing a specific increasing or decreasing trend. Figure 9 shows a smooth and steady decreasing rate on the negative relationship for the whole area from 2002 to 2018. The range of the correlation coefficient of LST–NDVI relationship for area above mean LST (−0.29 to −0.40) is narrower than the area below mean LST (−0.18 to −0.49).

4.6 LST–NDVI relationship under different ranges of NDVI

LST–NDVI relationship varies with the various ranges of NDVI (Fig. 10). Under various range of NDVI, the values of LST are different. Table 7 presents the variation of LST–NDVI relationship where bold values show the correlation coefficient value of less than −0.20. Under the positive values of NDVI, the relationship is totally negative. Up to the NDVI value of 0.4, the correlation coefficient values are strong to moderate negative. This is mainly the region of green vegetation. Beyond the NDVI value of 0.4, the relationship is weak. We cannot predict any strong decision on LST–NDVI relationship where the NDVI values are negative (less than 0). Under these ranges of NDVI value, the relationship is weak and non-reliable. Generally, negative NDVI indicates the presence of water bodies or wetland. Hence, it can be said that in water bodies or wetland, the LST–NDVI relationship is non-consistent. Even in most of the cases, the relationship is positive in nature. It can be concluded that under the positive NDVI values, the range of the LST–NDVI relationship is narrow, whereas it is wide under the negative NDVI values.

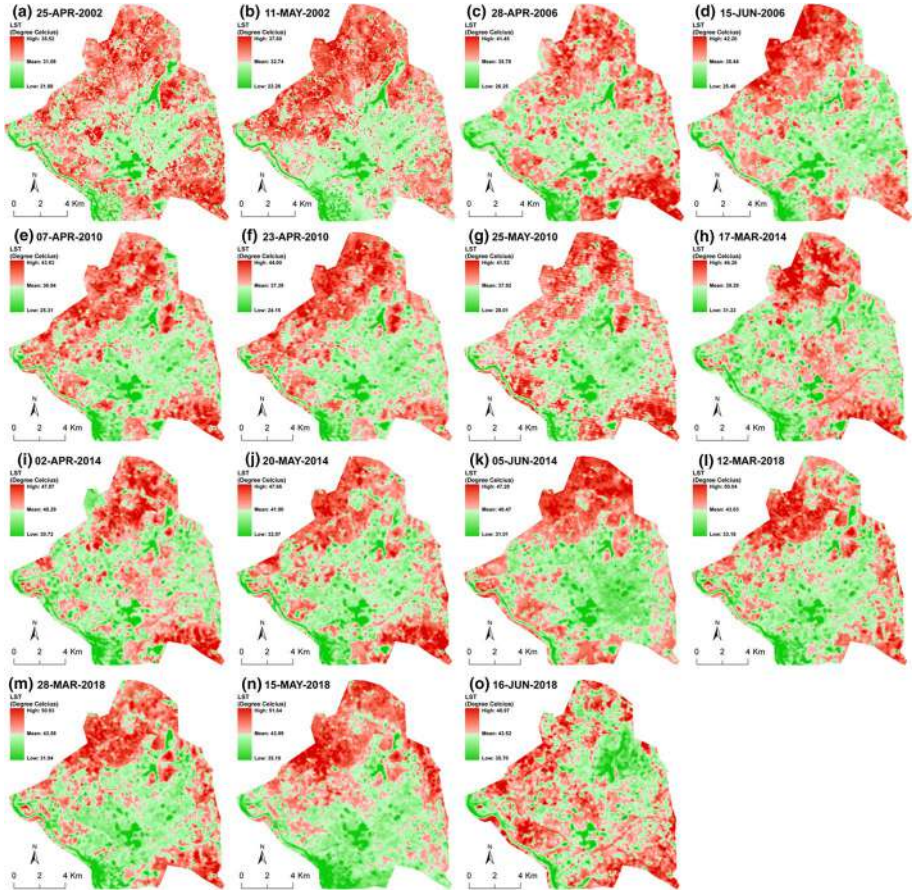

Fig. 7 The area above mean LST (red colour) and the area below mean LST (green colour): **a**, **b** 2002, **c, d** 2006, **e**–**g** 2010, **h**–**k** 2014, and **l**–**o** 2018

5 Conclusion

In this paper, fifteen cloud-free pre-monsoon data from different Landsat sensors from 2002 (two), 2006 (two), 2010 (three), 2014 (four), and 2018 (four) have been used to investigate the relationship between LST and NDVI for the whole area of Raipur City, the area above mean LST, and the area below mean LST. The LST has been retrieved from Landsat data sets using the mono-window algorithm. The LST derived from Landsat data sets are strongly validated with MODIS Terra data sets. The results have also been applied on the different ranges of NDVI values. The results show that mean LST of the study area has been increased at a very significant rate (11.62 °C increase between 2002 and 2018). The rise of LST is mainly for the conversion of land and also for the climate change to some extent in the unchanged land area. Generally, LST is negatively related to NDVI for the whole of the study area. The relationship is weaker under the area above mean LST and the area below mean LST. It indicates that the small mixed lands are not suitable for strong LST–NDVI relationship. The results also indicate that under the positive NDVI values,

Table 6 Spatiotemporal variation of LST–NDVI relationship (2002–2018)

Date of acquisition	Whole city	Area above mean LST	Area below mean LST
25-Apr-2002	−0.57	−0.30	−0.48
11-May-2002	−0.57	−0.28	−0.50
Mean	**−0.57**	−0.29	−0.49
29-Apr-2006	−0.53	−0.36	−0.40
17-Jun-2006	−0.47	−0.43	−0.28
Mean	**−0.50**	−0.40	−0.34
06-Apr-2010	−0.50	−0.40	−0.36
22-Apr-2010	−0.53	−0.49	−0.38
24-May-2010	−0.48	−0.23	−0.40
Mean	**−0.50**	−0.37	−0.38
16-Mar-2014	−0.42	−0.38	−0.09
01-Apr-2014	−0.45	−0.33	−0.26
19-May-2014	−0.41	−0.30	−0.28
04-Jun-2014	−0.31	−0.47	−0.07
Mean	−0.40	−0.37	−0.18
12-Mar-2018	−0.38	−0.36	−0.27
27-Mar-2018	−0.45	−0.36	−0.37
12-May-2018	−0.46	−0.25	−0.44
15-Jun-2018	−0.47	−0.22	−0.28
Mean	−0.44	−0.30	−0.34

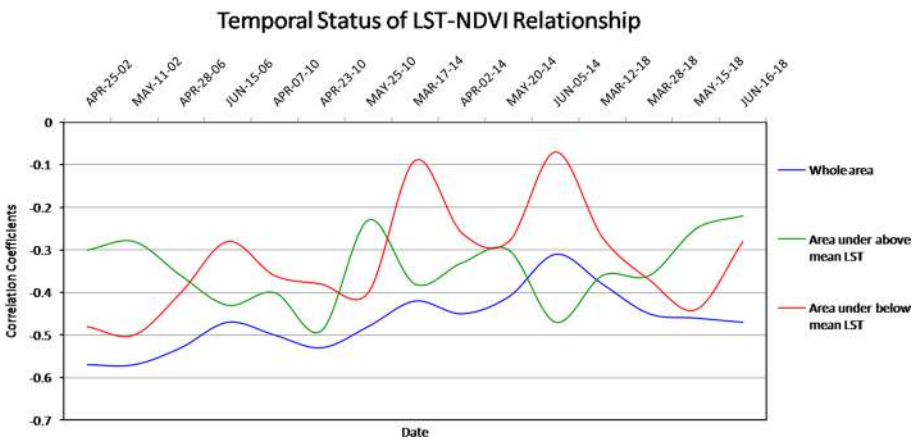

Fig. 8 Temporal status of LST–NDVI relationship

the LST–NDVI relationship is strong to moderate negative, whereas it is positive and non-consistent under the negative values of NDVI. The city should be properly planned so that the NDVI values can be increased. It means the percentage of urban green bodies must be higher compared to the concrete materials. Otherwise, the city will be suffered from the gradual thermal stress. The results also show that the relationship is stronger in the earlier

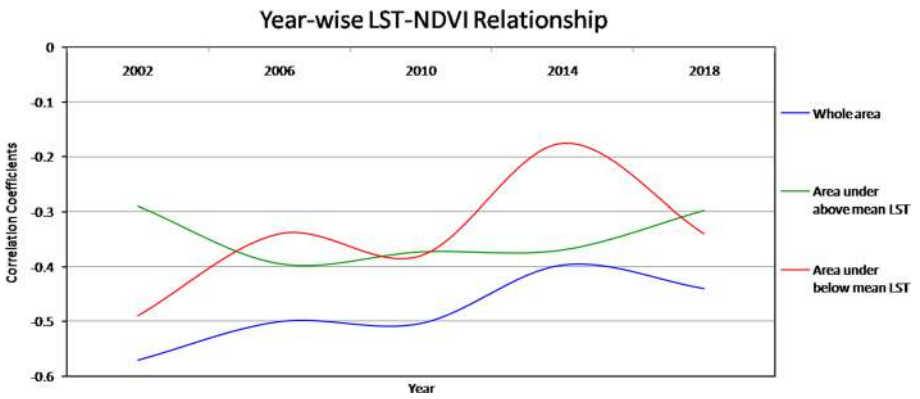

Fig. 9 Year-wise analysis of LST–NDVI relationship

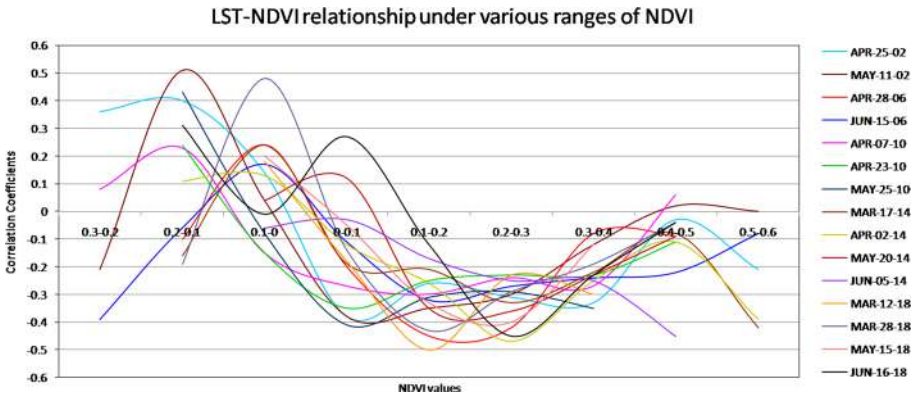

Fig. 10 LST–NDVI relationship under various ranges of NDVI

times compared to the recent times. It indicates the increase in built-up area as man-made materials enhance the reliability of LST–NDVI relationship.

The result of the present study is too significant in future town planning as most of the converted lands are built-up area or bare land which are responsible for high LST. For better sustainability, a large amount of urban plantation is needed along the road side and residential area. The present water bodies and green areas inside the city boundary must be preserved for providing a better life. Major commercial or industrial activities should be moved into the outskirts of the city to reduce the air and water pollution. The green building materials like earthen materials, wood, bamboo, natural clay, earth bags, natural fibre, etc., should be used in the construction of new buildings or apartments.

Table 7 LST–NDVI relationship under different ranges of NDVI (2002–2018)

Date of acquisition	−0.3 to −0.2	−0.2 to −0.1	−0.1 to 0	0 to 0.1	0.1 to 0.2	0.2 to 0.3	0.3 to 0.4	0.4 to 0.5	0.5 to 0.6
25-Apr-2002	0.36	0.40	0.14	**−0.38**	**−0.26**	**−0.31**	**−0.33**	−0.03	−0.21
11-May-2002	**−0.21**	0.51	0.04	**−0.38**	**−0.35**	**−0.30**	**−0.32**	−0.02	−0.09
28-Apr-2006	–	−0.10	0.24	**−0.20**	**−0.45**	**−0.42**	**−0.28**	−0.09	–
15-Jun-2006	**−0.39**	−0.06	0.17	**−0.21**	**−0.32**	**−0.27**	**−0.24**	−0.22	−0.08
07-Apr-2010	0.08	0.23	−0.15	**−0.27**	**−0.30**	**−0.24**	**−0.27**	−0.06	−0.12
23-Apr-2010	–	0.24	−0.15	**−0.35**	**−0.25**	**−0.23**	**−0.23**	−0.11	−0.16
25-May-2010	–	0.43	−0.08	**−0.41**	**−0.31**	**−0.29**	**−0.35**	–	–
17-Mar-2014	–	−0.16	0.24	−0.19	**−0.21**	**−0.33**	**−0.22**	−0.08	**−0.42**
02-Apr-2014	–	0.11	0.13	−0.12	**−0.26**	**−0.47**	**−0.25**	−0.11	**−0.39**
20-May-2014	–	–	0.04	−0.12	**−0.35**	**−0.36**	**−0.23**	−0.09	–
05-Jun-2014	–	–	−0.06	−0.03	**−0.27**	**−0.25**	**−0.25**	**−0.45**	–
12-Mar-2018	–	–	0.18	−0.18	**−0.50**	**−0.23**	**−0.30**	–	–
28-Mar-2018	–	−0.19	0.48	−0.14	**−0.43**	**−0.29**	**−0.29**	−0.04	–
15-May-2018	–	–	0.20	−0.05	**−0.33**	**−0.40**	**−0.22**	–	–
16-Jun-2018	–	0.31	−0.01	**−0.27**	**−0.32**	**−0.45**	**−0.23**	−0.04	–

Acknowledgements The authors were indebted to United States Geological Survey. The authors also thank the two anonymous reviewers for their beneficial comments.

References

Bonafoni, S. (2015). Spectral index utility for summer urban heating analysis. *Journal of Applied Remote Sensing, 9*(1), 096030.

Chen, X.-L., Zhao, H.-M., Li, P.-X., & Yin, Z.-Y. (2006). Remote sensing image-based analysis of the relationship between urban heat island and land use/cover changes. *Remote Sensing of Environment, 104,* 133–146.

De Cola, L. (1989). Fractal analysis of a classified Landsat scene. *Photogrammetric Engineering and Remote Sensing, 55,* 601–610.

Emerson, C. W., Lam, N. S. N., & Quattrochi, D. A. (1999). Multi-scale fractal analysis of image texture and pattern. *Photogrammetric Engineering and Remote Sensing, 65,* 51–61.

Estoque, R. C., Murayama, Y., & Myint, S. W. (2017). Effects of landscape composition and pattern on land surface temperature: An urban heat island study in the megacities of Southeast Asia. *Science of the Total Environment, 577,* 349–359.

Fatemi, M., & Narangifard, M. (2019). Monitoring LULC changes and its impact on the LST and NDVI in District 1 of Shiraz City. *Arabian Journal of Geosciences, 12,* 127.

Ferrelli, F., Huamantinco, M. A., Delgado, D. A., & Piccolo, M. C. (2018). Spatial and temporal analysis of the LST-NDVI relationship for the study of land cover changes and their contribution to urban planning in Monte Hermoso. *Argentina. Documents d'Anàlisi Geogràfica, 64*(1), 25–47.

Ghobadi, Y., Pradhan, B., Shafri, H. Z. M., & Kabiri, K. (2014). Assessment of spatial relationship between land surface temperature and land use/cover retrieval from multi-temporal remote sensing data in South Karkheh Sub-basin. *Iran. Arabian Journal of Geosciences, 8*(1), 525–537.

Govil, H., Guha, S., Dey, A., & Gill, N. (2019). Seasonal evaluation of downscaled land surface temperature: A case study in a humid tropical city. *Heliyon, 5*(6), e01923.

Goward, S. N., Xue, Y. K., & Czajkowski, K. P. (2002). Evaluating land surface moisture conditions from the remotely sensed temperature/vegetation index measurements: An exploration with the simplified simple biosphere model. *Remote Sensing of Environment, 79,* 225–242.

Guha, S., Govil, H., Dey, A., & Gill, N. (2018). Analytical study of land surface temperature with NDVI and NDBI using Landsat 8 OLI and TIRS data in Florence and Naples city. *Italy. European Journal of Remote Sensing, 51*(1), 667–678.

Guha, S., Govil, H., & Diwan, P. (2019). Analytical study of seasonal variability in land surface temperature with normalized difference vegetation index, normalized difference water index, normalized difference built-up index, and normalized multiband drought index. *Journal of Applied Remote Sensing, 13*(2), 024518.

Guha, S., Govil, H., & Mukherjee, S. (2017). Dynamic analysis and ecological evaluation of urban heat islands in Raipur city. *India. Journal of Applied Remote Sensing, 11*(3), 036020.

Gutman, G., & Ignatov, A. (1998). The derivation of the green vegetation fraction from NOAA/AVHRR data for use in numerical weather prediction models. *International Journal of Remote Sensing, 19*(8), 1533–1543.

Hao, B., Ma, M., Li, S., Li, Q., Hao, D., Huang, J., et al. (2019). Land use change and climate variation in the three gorges reservoir catchment from 2000 to 2015 based on the Google earth engine. *Sensors, 19,* 2118.

Hao, X., Li, W., & Deng, H. (2016). The oasis effect and summer temperature rise in arid regions-case study in Tarim Basin. *Scientific Report, 6,* 35418.

Hassan, Q. K., Bourque, C. P.-A., Meng, F.-R., & Cox, R. M. (2007). A wetness index using terrain-corrected surface temperature and normalized difference vegetation index derived from standard MODIS products: An evaluation of its use in a humid forest-dominated region of Eastern Canada. *Sensors, 7,* 2028–2048.

Hope, A. S., & McDowell, T. P. (1992). The relationship between surface temperature and a spectral vegetation index of a tall grass prairie: Effects of burning and other landscape controls. *International Journal of Remote Sensing, 13,* 2849–2863.

Hou, G. L., Zhang, H. Y., Wang, Y. Q., Qiao, Z. H., & Zhang, Z. X. (2010). Retrieval and spatial distribution of land surface temperature in the middle part of Jilin Province based on MODIS data. *Scientia Geographica Sinica, 30,* 421–427.

Jamei, Y., Rajagopalan, P., & Sun, Q. C. (2015). Time-series dataset on land surface temperature, vegetation, built up areas and other climatic factors in top 20 global cities (2000–2018). *Data Brief, 23,* 103803.

Julien, Y., Sobrino, J. A., & Verhoef, W. (2006). Changes in land surface temperatures and NDVI values over Europe between 1982 and 1999. *Remote Sensing of Environment, 103,* 43–55.

Ke, Y. H., Im, J., Lee, J., Gong, H. L., & Ryu, Y. (2015). Characteristics of Landsat 8 Oli-derived NDVI by comparison with multiple satellite sensors and in-situ observations. *Remote Sensing of Environment, 164,* 298–313.

Kikon, N., Singh, P., Singh, S. K., & Vyas, A. (2016). Assessment of urban heat islands (UHI) of Noida City, India using multi-temporal satellite data. *Sustainable Cities and Society, 22,* 19–28.

Kumar, D., & Shekhar, S. (2015). Statistical analysis of land surface temperature–vegetation indexes relationship through thermal remote sensing. *Ecotoxicology and Environmental Safety, 121,* 39–44.

Lam, N. S. N. (1990). Description and measurement of Landsat TM images using fractals. *Photogrammetric Engineering and Remote Sensing, 56,* 187–195.

Lam, N. S. N., & De Cola, L. (1993). *Fractals in geography*. Englewood Cliffs, NJ: Prentice-Hall.

Lam, N. S. N., Qiu, H., Quattrochi, D. A., & Emerson, C. W. (2002). An evaluation of fractal methods for characterizing image complexity. *Cartography and Geographic Information Science, 29,* 25–35.

Lam, N. S. N., & Quattrochi, D. A. (1992). On the issues of scale, resolution, and fractal analysis in the mapping sciences. *Professional Geographer, 44,* 88–98.

Li, K., & Yu, Z. (2008). Comparative and combinative study of urban heat island in Wuhan City with remote sensing and CFD simulation. *Sensors, 8,* 6692–6703.

Li, W. F., Cao, Q. W., Kun, L., & Wu, J. S. (2017). Linking potential heat source and sink to urban heat island: Heterogeneous effects of landscape pattern on land surface temperature. *Science of the Total Environment, 586,* 457–465.

Li, Z. N., et al. (2016). Review of methods for land surface temperature derived from thermal infrared remotely sensed data. *Journal of Remote Sensing, 20,* 899–920.

Liu, H., & Weng, Q. (2018). Scaling effect of fused ASTER-MODIS land surface temperature in an urban environment. *Sensors, 18,* 4058.

Liu, K., Zhang, X., Li, X., & Jiang, H. (2014). Multiscale analysis of urban thermal characteristics: Case study of Shijiazhuang. *China. Journal of Applied Remote Sensing, 8*(1), 083649.

Luo, X., & Li, W. (2014). Scale effect analysis of the relationships between urban heat island and impact factors: Case study in Chongqing. *Journal of Applied Remote Sensing, 8*(1), 084995.

Mathew, A., Khandelwal, S., & Kaul, N. (2017). Investigating spatial and seasonal variations of urban heat island effect over Jaipur city and its relationship with vegetation, urbanization and elevation parameters. *Sustainable Cities and Society, 35,* 157–177.

Mathew, A., Khandelwal, S., & Kaul, N. (2018). Spatio-temporal variations of surface temperatures of Ahmedabad city and its relationship with vegetation and urbanization parameters as indicators of surface temperatures. *Remote Sensing Applications: Society and Environment, 11,* 119–139.

Mohammad, P., Goswami, A., & Bonafoni, S. (2019). The impact of the land cover dynamics on surface urban heat island variations in semi-arid cities: A case study in Ahmedabad City, India, using multi-sensor/source data. *Sensors, 19,* 3701.

Naeem, S., Cao, C., Waqar, M. M., Wei, C., & Acharya, B. K. (2018). Vegetation role in controlling the ecoenvironmental conditions for sustainable urban environments: A comparison of Beijing and Islamabad. *Journal of Applied Remote Sensing, 12*(1), 016013.

Nowicki, S. A., Inman, R. D., Esque, T. C., Nussear, K. E., & Edwards, C. S. (2019). Spatially consistent high-resolution land surface temperature mosaics for thermophysical mapping of the Mojave Desert. *Sensors, 19,* 2669.

Purevdorj, T. S., Tateishi, R., Ishiyama, T., & Honda, Y. (1998). Relationships between percent vegetation cover and vegetation indices. *International Journal of Remote Sensing, 19,* 3519–3535.

Qi, H., Huang, F., & Zhai, H. (2019). Monitoring spatio-temporal changes of terrestrial ecosystem soil water use efficiency in Northeast China using time series remote sensing data. *Sensors, 19,* 1481.

Qin, Z., Karnieli, A., & Barliner, P. (2001). A mono-window algorithm for retrieving land surface temperature from Landsat TM data and its application to the Israel-Egypt border region. *International Journal of Remote Sensing, 22*(18), 3719–3746.

Qiu, H. L., Lam, N. S. N., Quattrochi, D. A., & Gamon, J. A. (1999). Fractal characterization of hyperspectral imagery. *Photogrammetric Engineering and Remote Sensing, 65,* 63–71.

Qu, C., Ma, J. H., Xia, Y. Q., & Fei, T. (2014). Spatial distribution of land surface temperature retrieved from MODIS data in Shiyang River Basin. *Arid Land Geography, 37,* 125–133.

Rozenstein, O., Qin, Z., Derimian, Y., & Karnieli, A. (2014). Derivation of land surface temperature for Landsat-8 TIRS using a split window algorithm. *Sensors, 14,* 5768–5780.

Shi, Y., Xiang, Y., & Zhang, Y. (2019). Urban design factors influencing surface urban heat island in the high-density City of Guangzhou based on the local climate zone. *Sensors, 19,* 3459.

Shigeto, K. (1994). Relation between vegetation, surface temperature, and surface composition in the Tokyo region during winter. *Remote Sensing of Environment, 50,* 52–60.

Singh, P., Kikon, N., & Verma, P. (2017). Impact of land use change and urbanization on urban heat island in Lucknow city, Central India. A remote sensing based estimate. *Sustainable Cities and Society, 32,* 100–114.

Slawsky, L. M., Zhou, L., Roy, S. B., Xia, Geng, Vuille, M., & Harris, R. A. (2015). Observed thermal impacts of wind farms Over Northern Illinois. *Sensors, 15,* 14981–15005.

Smith, R. C. G., & Choudhury, B. J. (1990). On the correlation of indices of vegetation and surface temperature over south-eastern Australia. *International Journal of Remote Sensing, 11,* 2113–2120.

Stroppiana, D., Antoninetti, M., & Brivio, P. A. (2014). Seasonality of MODIS LST over Southern Italy and correlation with land cover, topography and solar radiation. *European Journal of Remote Sensing, 47,* 133–152.

Sun, H., Zhou, B., & Liu, H. (2019). Spatial evaluation of soil moisture (SM), land surface temperature (LST), and LST-derived sm indexes dynamics during SMAPVEX12. *Sensors, 19,* 1247.

Tomlinson, C. J., Chapman, L., Trones, J. E., & Baker, C. (2011). Remote sensing land surface temperature for meteorology and climatology: A review. *Meteorological Applications, 18,* 296–306.

Voogt, J. A., & Oke, T. R. (2003). Thermal remote sensing of urban climates. *Remote Sensing of Environment, 86,* 370–384.

Wen, L. J., et al. (2017). An analysis of land surface temperature (LST) and its influencing factors in summer in western Sichuan Plateau: A case study of Xichang City. *Remote Sensing for Land and Resources, 29,* 207–214.

Weng, Q. (2003). Fractal analysis of satellite-detected urban heat island effect. *Photogrammetric Engineering and Remote Sensing, 69,* 555–566.

Weng, Q. H., Lu, D. S., & Schubring, J. (2004). Estimation of land surface temperature-vegetation abundance relationship for urban heat Island studies. *Remote Sensing of Environment, 89,* 467–483.

Yuan, X. L. (2017). Vegetation changes and land surface feedbacks drive shifts in local temperatures over Central Asia. *Scientific Report, 7,* 3287.

Yue, W. Z., Hua, X. J., & Hua, X. L. (2006). An analysis on eco-environmental effect of urban land use based on remote sensing images: A case study of urban thermal environment and NDVI. *Acta Ecologica Sinica, 26,* 1450–1460.

Zhang, H. K., Huang, B., Zhang, M., Cao, K., & Yu, L. (2015). A generalization of spatial and temporal fusion methods for remotely sensed surface parameters. *International Journal of Remote Sensing, 36*(17), 4411–4445.

Zhang, J., & Wang, Y. (2008). Study of the relationships between the spatial extent of surface urban heat islands and urban characteristic factors based on Landsat ETM + Data. *Sensors, 8,* 7453–7468.

Zhou, Y., Shi, T. M., Hu, Y. M., & Liu, M. (2011). Relationships between land surface temperature and normalized difference vegetation index based on urban land use type. *Chinese Journal of Ecology, 30,* 1504–1512.

Source details

Feedback > Compare sources >

Environment, Development and Sustainability

Scopus coverage years: from 1999 to Present

Publisher: Springer Nature

ISSN: 1387-585X E-ISSN: 1573-2975

Subject area: Social Sciences: Geography, Planning and Development | Economics, Econometrics and Finance: Economics and Econometrics | Environmental Science: Management, Monitoring, Policy and Law

Source type: Journal

View all documents > | Set document alert | Save to source list

CiteScore 2022
7.2

SJR 2022
0.835

SNIP 2022
1.291

CiteScore | CiteScore rank & trend | Scopus content coverage

Journal of Studies in Social Sciences
ISSN 2201-4624
Volume 19, **2020**, 10

INFINITY PRESS
www.infinitypress.info

Strī-ācār – An Analytical Study on the Non-Priestly Marriage Rituals of Bengal

Dr. Sudarsana Choudhury
Associate Professor
Head of the Department of History
Dinabandhu Andrews College, Kolkata-700084, India
E-mail: sudarsana44.sc@gmail.com

Abstract: Marriage rituals of Bengal are quite different from the rest of India. The marriage rituals of Bengali people are divided into two parts: priestly rituals and non-priestly rituals. In this paper the non-priestly rituals of Bengali marriage called *Strī-ācār* are discussed. *Strī-ācār* are performed by married women. This study tries to identify the role of women in Bengali society on the basis of the various wedding rituals practiced by them. An attempt has also been made to identify the environmental, geographical factors behind these rituals that characterizes the distinctiveness of Bengali culture irrespective of ethnicity, caste and religion.

Keywords: Brahmin, Śundi, *eyo*, magical.

Introduction

Marriage is an institution which forms an integral part of a society. Marriage rituals shows the evolution of culture in a particular society. India is a land of diverse culture which vary from region to region. Various ethnic groups reside in this country. The

variation in their cultures are reflected in the various rituals performed by them. India is a country of multi language and religion. Each has their own culture. The society is also divided into a number of castes. It is difficult to deal with the marriage ritual of all the people living in this sub-continent. So I have chosen to deal with the marriage rituals of a particular language group from a particular religion – Bengali Hindus. Prior to 1947, the present state of West Bengal in India and the neighbouring country of Bangladesh together form the land of the Bengali Hindus. After Independence most of the Hindus of the present country of Bangladesh migrated to India and came into West Bengal. Together with them they brought their culture which is very much reflected in their marriage rituals which are quite distinct from the marriage rituals performed by the Bengali Hindus of West Bengal. In this paper I will refer the landmass, which is now Bangladesh as East Bengal, because the people who now perform the rituals of this particular landmass are not citizens of Bangladesh. Though there are distinct differences in marriage rituals of West and East (now Bangladesh) Bengal, there are also variations district wise and caste wise. Bengali marriage rituals can broadly be divided in two categories – the priestly rituals and the non-priestly rituals. The ritualistic differences are not much in priestly rituals and a caste-wise uniformity can be observed in these rituals. But the differences are more in the non-priestly rituals. Most of the rituals are usually done by the married women who are colloquially called *eyo*. The presence of male are minimal in these rituals. Since, they fall on the domain of married women, they are called *Strī-ācār* (*Strī*=married woman, *ācār*=ritual). In this paper I will deal with the non-priestly marriage rituals that are performed in the marriages of Hindu Bengali. *Strī-ācār*, as has been said previously varies from region to region and from one class of people to another. Here I have chosen the marriage rituals of some Brahmin families of Mymensingh and Dhaka region of East Bengal and a Śundi̤ family, who belongs to the brewer caste(the class of people who are involved in making liquor, and are considered lower caste or Śūdra in Bengali society) of Howrah district in West Bengal.

Methodology

This study is mainly based on the information gathered from two books, *Stri-Achar* by Renuka Devi Choudhurani (2006) and *Shuvavivaha* by Mausumi Bandyopadhyay Saha (2017) and also from personal experiences.

Observations

Day Before the Marriage

In Bengali marriages the non-priestly rituals are done by married women in odd numbers, i.e., three, seven, nine and so on. These married women should belong to the same family and must have a happy conjugal life. In Bengali wedding married women are considered auspicious. However, widows are not allowed to perform any rituals and in earlier times they were not allowed to be present near the site of the wedding. In some families of Mymensingh region, two married women (*eyo*) of good conjugal life from the same family are chosen to perform all the rituals connected with marriage. They are called *joṛā*eyo. A day before the marriage, these two married women are made to sit facing east, each with a red cloth covering the upper portion of their bodies. These two red clothes are tied together with a knot. A handful of paddy and *durbā*grass are kept inside the knot. The whole process is done ceremoniously by ululation and blowing conch shell in the presence of other *eyos* in odd numbers (Choudhurani,2006:28).

I. Preparing Perched Rice and *Anandanāḍu*

The Bengali marriage is not an affair of a single day. It starts a few days before the actual wedding day with rituals like bachelor's meal *āibuḍobhāta* (*āibuḍo*=bachelor, *bhāta*=rice), and in some families of West Bengal, preparing perched rice and sesame ladoos (*ānandanāḍu*). Perched rice and sesame ladoos are prepared by married women ceremoniously a day before the actual wedding. In the Śundi family of West Bengal a room is assigned for performing non-priestly rituals connected with marriage. This room is called the *maṅgalghar*. The preparation of perched rice is done in this room.

II. *Āibuḍobhāta*

Bachelor's meal or *aībuḍobhāta* is offered to both the bride and the bridegroom a day before the marriage. Only the female members of the family are present in this ritual (Choudhurani,2006:30;Saha,2017 : 22).

III. Preparation of the *Baraṇḍālā, Śrī* and *Aībhāṇḍ*

There are a few important things required for performing various marriage rituals. These are *Baraṇḍālā, Śrī* and *Aībhāṇḍ*. Together with these, *kolsorā* is used by the Śundi families of West Bengal. All the items that are used in the rituals during marriage are kept in the *Baraṇḍālā*. *Baraṇ* means greeting. The *Baraṇḍālā* is family specific. The *Baraṇḍālā* maybe a plate of metal or cane or simply a winnowing fan depending on the family custom. In East Bengal the *Baraṇḍālā* is also called the *cālonbāti*. The *Baraṇḍālā* (Fig.01) is prepared ceremoniously by the eyos of the Mymensingh region (Choudhurani,2006:91). A row of bananas with a dot of vermilion on each banana, and a small pot filled with water are kept in the *Baraṇḍālā*. Five vermilion dots are also given on the pot and mango leaves with vermilion dots are put in it. Five small earthen lamp with wicker and oil are placed at the front side of the *Baraṇḍālā*. Oil and match box are also kept here. Paddy, *durbā* grass, vermilion paste, small ginger pieces and small turmeric pieces are kept in small earthen plates in the *Baraṇḍālā* of Brahmin families of East Bengal. In the *Baraṇḍālā* of the Śundi family of Howrah district, leaves of cannabis (*sidhi*), *pañcaśashya* (paddy, barley, sesame, mustard, green moong or green gram) ,five areca nuts, five turmeric, five cowry shells, five *haritakis* (Terminalia chebula), five *āmlās*(Indian gooseberry), five *baheṛās* (Terminalia bellirica), one ceremonial thread or *paite* (worn by the Brahmins), five betel leaves, *durbā* grass, dew, ghee, curd, honey, a small coconut, *āmlā* (Indian gooseberry)-*methi*(fenugreek), turmeric paste, sandalwood paste, rice powder paste, vermilion paste, *gerimaṭi* (ochre pieces), *monāmuni* (small seed like thing with filaments) *gela* (Cesalpinia bonduc.) fruit, mirror, small knife, red thread, white thread and a reel for thread are kept in small earthen or metallic plates. Along with this a *kolsorā* (a small earthen plate where a small unripe coconut, seven *hariṭakis*, seven *āmlās*, seven *baheṛā*s seven turmeric, seven

cowry shells, seven areca nuts, seven pomgrenate flowers are kept), a *gachkouṭo*, a *kajallatā* (a vessel used for making collyrium), a nut cracker and a *kunke* or a vessel for measuring rice(containing a small comb, a mirror, a garland, girdle, collyrium and bangles of conch shell and iron) are kept (Saha, 2017:18). *Śrī* is a beautiful small pyramidal structure made up of rice powder paste, turmeric and vermilion and kept in a small plate by pouring mustard oil over it. An alternate of *Śrī* is the *āiyomuchi* or the *nichni-pichni* of the Mymensingh families(Choudhurani,2006:26-27). These are small petal like structures made up of the same ingredients as *Śrī* and kept in two small earthen plates in the *Baraṇḍalā*.

Fig.01. *Baraṇḍalā* of a Brahmin family of Mymensingh

In the Śundi family, four small pots containing rice, one areca nut, turmeric, cowry and a coin in each of them are placed on a winnowing fan (Saha, 2017:18). They are called *Aībhāṇḍ*. They are taken to a Brahmin's house by the *eyos* of Śundi family on the morning of the wedding day. The wife of the Brahmin will add some turmeric in the rice of the pots. Then all the pots are taken back to the wedding house (Saha, 2017:26). This ritual is performed to show respect to Brahmin family as they are upper caste. The wife of the Brahmin is given rice, vegetable, ghee and salt in an earthen plate in return. In the Brahmin families this ritual is not required, but *Aībhāṇḍ* are kept in the *Baraṇḍalā* of these families. *Aībhāṇḍ* of Brahmin families of East Bengal contain parboiled rice, one piece of

small banana, one areca nut, one betel leaf, few pieces of ginger and turmeric (Choudhurani,2006:91).

IV. Magical and Medicinal Significance: Connection with Fertility

It is interesting to note that all these items even the vermilion dots are mostly five or seven in number. These odd numbers are related to ancient indigenous magical rituals and are considered auspicious in any ritual. It is interesting to note that most of the items used in the Bengali wedding ritual have medicinal values connected with fertility. Areca nut is used in Ayurvedic medicine for treating impotency and female diseases (Bhattacharjee,1980:30-37). *Durbā* grass is used for treating leucorrhoea and other female diseases (Bhattacharjee,1976:98-99). *Baheṛā* is used in Ayurveda for treating impotency (Bhattacharjee,1977:281). Cannabis leaves are also used for treating impotency, gonorrhoea, female diseases and also for aggravating the process of child birth (Bhattacharjee,1978:279-285).

Symbolic representation of fertility is observed in the use of cowry and betel leaf in Bengali marriage. Cowry, is a symbol of prosperity as it was used earlier in Bengal as a medium of exchange, and also, according to some scholars, its shape represent female organ (Dutta,2002:47). Similarly the shape of the betel leaf also according to some scholars represents the female organ (Dutta,2002:47).

V. *Pāna-khili*

There is one ritual solely done with betel leaf a day before marriage called *Pāna-khili* by the Hindu families of the Mymensingh region of undivided Bengal (Choudhurani, 2006: 95-96). This ritual is done with the two *eyos* or *joṛā eyos* performing the main ritual accompanied by other *eyos* in odd number. Twenty one betel leaves are folded and a small stick is pierced through them (Fig.02). This is an indigenous fertility ritual. The ritual symbolically seals the female organ of the bride for the bridegroom.

Fig.02. *Pāna-khili*

VI. Grinding of Paddy and Turmeric

The grinding of paddy and turmeric are again two important rituals that are performed ceremoniously by the Brahmin families of East Bengal (Fig.03). The *joṛā eyos* take the lead in these two rituals, accompanied by other *eyos* in odd number (Choudhurani,2006:85-87). Rice is separated from the paddy and a part of it is kept for the *nāndīmukh* ritual. Rice is the staple food of Bengal. Turmeric has antiseptic values and it is applied ceremoniously to both the bride and the bridegroom on the day of the marriage before taking their bath.

Fig.03. Grinding of Paddy and Turmeric

VII. Ganga Invitation

Inviting the river Ganga is another ritual performed by most of the families of East Bengal (present Bangladesh) a day before the marriage (Choudhurani,2006:32). One thing should be noted that the river Ganga does not flow through Bangladesh or East Bengal. The main river of Bangladesh is Padma, which is a distributary of Ganga. But at the same time there are many rivers and water bodies in Bangladesh. The name Ganga may be symbolic as it is considered as the holy river of the Hindu religion. In East Bengal, before partition any local water bodies like river or ponds were selected for this ritual. The two main *eyos* accompanied by other *eyos* in odd number usually go to a nearby water body and nowadays those residing in Kolkata on the banks of river Ganga with the *Baraṇḍālā*. Firstly they will greet the water body by the circumambulation of the *Baraṇḍālā* and ululation. Then a small design with rice powder paste is made on the bank. A betel leaf with vermilion dots, little bit of oil, sweet and areca nut is placed over the design. A small lamp is lit and floated in the water body and the *eyos* seek the blessings on behalf of the bride and the bridegroom from the river Ganga. After that water is collected and kept in a small pitcher. This water will be used in rituals connected with marriage. The Ganga inviting rituals are simple and they show the reverence given to water bodies in the simple life of the people. As has been mentioned previously that Bangladesh is a land of many rivers, and in rainy seasons most part of it is flooded. So, maybe this ritual is performed to avoid disasters like flood at the time of the wedding.

Wedding Day

Morning Rituals

I. *Dodhimaṅgal*

Early, on the day of the marriage, an *eyo* of the Śundi family places the holy pitcher filled with water and mango leaves in the *maṅgalghar* over a design made of rice powder paste in front of the storage jar containing the perched grain. Conch shells are blown marking the beginning of the wedding. A lamp called *jāgprodip* is put here and this lamp will

continue to burn till the eighth day of the marriage (Saha, 2017:23). A lamp is lit over a grinding stone by the *eyos* of the Brahmin families of the Dhaka region of Bangladesh, early on the day of the marriage. In most of the families of Bengal, early on the day of the marriage before sunrise, the bride and the bridegroom are fed in their respective houses with a mixture of flattened rice, perched rice, curd and sweets by the *eyos*. This is done ceremoniously and this ritual is called the *dodhimaṅgal ritual* (Saha, 2017:42-43). Both the bride and the bridegroom will fast the whole day till the *sampradāna* ritual, and in some families after the completion of all the marriage rituals. This ritual is followed in almost all the houses of Bengal, with exception of some Brahmin families of the Mymensingh region.

After completion of the *dodhimaṅgal* ritual, in some Brahmin families of East Bengal, the bridegroom is given a brass mirror and the bride a small spindle shaped wooden object called *gāchkouṭo* (Fig.04) a symbol of prosperity (Saha, 2017:43). The bride and the bridegroom will have to carry this mirror or *gāchkouṭo* in their hands until the whole process of the marriage is completed.

Fig.04. *Gāchkouṭo*

As has been pointed earlier, many of the rituals connected with Bengali marriage are magical in nature. The belief in good omen and protection against bad omen is in the mind of simple Bengali people, a majority of whom are uneducated. So certain objects like metal mirror, collyrium maker, knife, nut-cracker are carried by the bride and the

bridegroom, depending on their respective family customs, during the total period of the wedding ceremony, in order to protect them from evil eyes. In the Mymensingh region of Bangladesh girls carry a metal mirror and knife (Fig.05), and this is given at the time of the *nāndīmukh* ritual (Choudhurani,2006:97).

Fig.05. Bride carrying a Metal Mirror and Knife

In the Śundi family of Howrah district, the bride and the bridegroom are taken separately by the *eyo*s of their respective families to a nearby pond after the *haldi* ritual. Water is poured over their head. A collyrium maker in case of bride and a nut cracker in case of the bridegroom are kept in between their feet. Curd, sandalwood paste, turmeric paste, dew, vermilion paste, collyrium, and *āmlā-methi* (fenugreek) are touched on the collyrium maker in case of the bride and nut-cracker in case of the bridegroom. In this ritual a single *eyo* takes water from the water body in a pitcher. The bride or the bridegroom along with this *eyo* are then greeted by the other *eyos* with circumambulation motion of hand with the following things – betel leaf, water, paddy, *durbā* grass, banana, *aibhāṇḍ*, Śrī and *Baraṇḍālā*. After this the collyrium maker is handed to the bride and the nut-cracker to the bridegroom (Saha, 2017:25).

II. ***Nidrākalashe jol ānā***

In the Brahmin families of Dhaka region, there is a ritual called *nidrākalashe jol ānā* (Saha, 2017:43-44). On the wedding day, before sunrise, a couple with good conjugal life collects

water in a pitcher from a nearby water-body. The husband makes a plus sign with a knife in the water and the wife collects water from that region where the sign is made in the pitcher. This water is kept aside for the *Asṭamaṅgalā* ritual.

III. *Sohāg thokāno* and *Sohāg māpā*

Another ritual is done in the Brahmin families of Dhaka region called *sohāg thokāno*, in which again a couple with happy conjugal life is selected (Saha, 2017:44-45). The husband collects soil with a chopper from the four corner of the house and put it in the pallu of his wife's sari. This soil is then kept in the *Baraṇḍālā*. A similar ritual is performed in the Brahmin families of Mymensingh region, called *sohāg māpā* or weighing affection (*sohāg*=affection; *māpā*=weighing). The ritual itself shows its indigenous character. In earlier times, the women of Bengal use to wrap a single piece of cloth called sari around their body. In this ritual the inner part of the cloth which is attached to the body is drenched with water and then the water is squeezed out of the inner cloth and collected in a pitcher. In this way water is collected by drenching the cloth of all the married women. A little bit of dust is collected from the place where the married women are standing and are kept in the pitcher. This water is used for bathing the bride and the bridegroom on the second day of the marriage. This ritual is done only in bride's house (Choudhurani,2006:44).

IV. *Sohāg bāṛā*

After *sohāg māpā,* there is another ritual called *sohāg bāṛā,* which is common among the Brahmin families of the Mymensingh region in Bangladesh (Choudhurani,2006:45-46). A handful of paddy is kept on a bamboo shoot mat. The bride will first sit on the paddy. Then paddy from her back are collected in a winnowing fan. This process is repeated thrice by putting back the paddy again in the mat from the winnowing fan. After, the bride, the process is continued with other married women till some rice comes out from the paddy. This rice will be kept in the stool where the bride will sit during the ritual of circumambulation around the bridegroom. After the father of the bride gives her hand to

the bridegroom, the mother of the bride prepares a rice pudding by taking rice from the stool, where she was sitting. The whole process is indigenous and magical in nature and the purpose is to keep the bridegroom affectionate towards his wife. It should be mentioned in this connection that rice has medicinal values connected with female diseases. Raw rice is sometimes used in Ayurvedic medicine to cure female diseases like leucorrhoea (Bhattacharjee,1978:205).

V. *Monaāmuni* Grinding

Monaāmuni grinding is a ritual performed in most families of East Bengal. This ritual is also connected with fertility. *Monaāmuni* are two tiny seeds with filament. They are firstly placed in water, when the two seeds get closer, they are taken out of water and put in a betel leaf with a cowry. The *joṛā eyo* will grind the betel leaf with *monaāmuni* and cowry and make a paste and keep it aside for the bathing ritual on the second day of marriage (Choudhurani,2006:46).

VI. *Haldi*

The most important ritual that is performed all over Bengal and also in other parts of India is the *haldi* ritual. The married women apply *haldi* or turmeric paste on the bride and the bridegroom in their respective families. Firstly the *haldi* ritual takes place in the bridegrooms house, then the same turmeric paste is brought to the bride's house accompanied by trays of gifts called *tatva*, and the same paste is applied on the bride. Though, this ritual is performed mainly by married women, but still, in this ritual particularly we find the presence of two male, a barber and a washer-man. The barber cuts the nails of bride or bridegroom and put them in a leaf and the washer-man throws soap over the head of the bride. In some Brahmin families of the Mymensingh region, the barber performs a bit elaborate ritual like oil is poured from the barber's head on to the bride's head. The barber will take oil in a dish and will hold it in front of the bride asking her jokingly whether she is more beautiful than the barber. Barber will then light a few stalk of jute-plant and ask the bride that whose fire is she warming her body. She

has to take the name of her husband. All the married women including the mother of the bride or the bridegroom apply turmeric paste on the bride or the bridegroom. In the families of East Bengal, water is poured from a small pitcher on the head of the bride or the bridegroom. After that both the bride and the bridegroom break a small earthen plate which is kept inverted with a cowry inside, and both of them say that they are breaking their bachelorship (Choudhurani,2006:99-100). Turmeric has antiseptic value, it is also good for skin. The bride or the bridegroom take their bath in their respective bathroom after this. In the Śundị family of West Bengal, the bride or the bridegroom are bathed ceremoniously by the married women, the process has been described previously. The married women make the bride wear the conch shell bangles, the symbol of married woman. In the *Grhyasūtras* there is mention of washing of the bride, but there is no mention of application of turmeric paste on bride and the bridegroom (Oldenberg,1892 :44, 258-259. However, the *haldi* ritual is very common among the indigenous people residing in Bengal (Kundu,2005:88-99; Sanyal,2002: 107-108). This ritual is also practised by the Bengali Muslims and the Bengali Christians (Saha, 2017:68). So this ritual is very much region specific.

VII. Other Rituals

In the Śundị family of Howrah region, the bride or the bridegroom are made to stand on a grinding stone. Four married women or *eyos* will stand in four corner keeping the bride or the bridegroom in the centre. One of the *eyos* will take the reel of thread from the *baraṇḍālā*, and pass the thread to the next *eyo* keeping the reel in her hand, that *eyo* will pass to the next *eyo* and in this way all the *eyos* will pass the thread to the next *eyo* seven times. A rectangle of thread is created by this process which encircles the bride or the bridegroom. Then all the *eyos* will sit. The bride or the bridegroom will now face one of the *eyos*. She will ask that whether the bride or the bridegroom is ending their bachelorship. The answer will be yes. The bride or the bridegroom will cross the thread on that side and will again cross it and come back to their previous position. This process

will be repeated thrice with the other three *eyos*. Then the thread will be tied on the bride or bridegrooms wrist with each *eyo* adding a knot. In most of the families of Bengal, a thread is tied on the wrist of the bride and the bridegroom during the *nāndīmukha* ritual. In some Brahmin families of Mymensingh region, the sacred thread (*paite*) of the bridegroom, which he discards when he gets a new one from the bride's family, is tied on the ankle of the bride. This tying of thread or *paite* is done perhaps to protect the bride and the bridegroom from evil spirit and bad omen.

The bride and the bridegroom of the Śundị family are taken to the *maṅgalghar*. The door is closed and *durbā¯* grass and turmeric paste are put on top of the door. After that seven dots of curd, sandalwood paste, turmeric, dew, vermilion, kohl and *āmlā¯-methi* are put beneath the *durbā¯* grass (Saha, 2017:26). Here the pots of the *aibhāṇḍ* are emptied on a winnowing fan, and the bride or the bridegroom are made to put back all the contents in the *aibhāṇḍ*. This process is repeated thrice and is done only in the Śuṇḍi families of West Bengal (Saha, 2017:27).

At the same time in the families of East Bengal, the bride measures affection from water kept in a vessel called *dhākon dhokon* with a small earthen plate. While performing this ritual she utters the names of her in-laws, as if she is measuring their affection (Choudhurani, 2006: 46-47). This ritual is also magical in nature. The bride usually moves into her in-law's house after marriage, so by performing this ritual she is trying to make the atmosphere in her in-law's house amicable for her.

So far I have discussed the non-priestly ritual that are performed in the morning on the day of the marriage. There is a priestly ritual called the *nāndīmukha,* performed on the morning of the marriage. This ritual is done to seek the blessings of the ancestors. This ritual is done by the father of the bride or the bridegroom or any senior male member with the assistance of the priest.

Evening Rituals

I. Rituals in the Bridegroom's House

The final wedding usually takes place in the house of the bride. Before the bridegroom leaves his own house, there are certain rituals performed in the Śundi family of West Bengal. The bridegroom is made to stand on a stool and the *eyos* will perform circumambulation around him by sprinkling water and carrying the *baraṇḍāla* and *Śrī*. The mother of the bridegroom will stand behind him. An eyo will throw rice, vermilion, coin, sweet, betel leaf and areca nut over the head of the bridegroom in the pallu of the mother of the bridegroom This is called *kanakañjali*. Then the mother of the bridegroom will give sweet to all the married women and bid goodbye to her son and ask him to bring the bride (Saha, 2017:28). There is no such elaborate ritual among the Brahmin families of East Bengal. In these families, the bridegroom seeks the blessings of the elders before leaving his home. The mother of the bridegroom also offers her blessings and will tell her son to bring the bride. In the Brahmin families of Mymensingh region designs of pitcher are drawn on the floor where the bridegroom is being blessed. The pitcher symbolises prosperity and is considered auspicious for someone who is making the journey. The mother of the bridegroom is not supposed to see the bridegroom leaving his home. She reconciles herself in a room and keep her hand in water in a vessel for a peaceful conjugal life of her son (Choudhurani,2006:109-110).

II. Greeting the Bridegroom in the Bride's House

Female rituals are performed when the bridegroom comes in the bride's house. The married women from the Śundi family pour water on the four wheels of the car. Then they throw sugar cakes over the car so that they fall on the other side (Saha, 2017:28). In some Brahmin families of the Mymensingh region, *datura* flower is cut in two pieces, such that each piece looks like a tiny bowl. The pieces are lit like lamp by oil and wicker and are thrown over the car of the bridegroom so that they fall on the other side of the car(Choudhurani,2006:52). This may be a magical ritual, perform to get rid of evil spirits or protecting the bridegroom from the evil spirits. When the bridegroom comes out of

the car, he is greeted in all the families of Bengal with the blowing of conch shell, ululation and by touching the forehead, chest and knee of the bridegroom with the *baraṇḍāla*.

In Bengali households, the priestly and the non-priestly rituals are performed in two separate areas. The priestly rituals are performed in a covered area, usually on a platform with four banana trees in the four corner, the detailed description of which is found in Renuka Devi Choudhurani's book (2006:48-49). The non-priestly rituals are performed under the open sky in the courtyard of the house. The place is smeared with cow-dung and encircled with four banana trees. This place is usually decorated by the barber. Before, the actual wedding ritual, the father of the bride greets the bridegroom, accompanied by the priest. He gives the bridegroom a new silk two piece attire called *jor*, a sponge-wood cap and a garland. There are also other gifts given to the bridegroom like a watch, a gold ring and bell metal utensils. This gifts are given ceremoniously in the region assigned for priestly rituals. The bridegroom changes his cloth and wear the *jor* given to him. The bridegroom is then taken to the banana tree enclosure of non-priestly rituals. Here he is again greeted by the married women ceremoniously. In the families of West Bengal, the bridegroom is made to stand on a grinding stone, whereas in the families of East Bengal, the bridegroom is made to stand on a small stool. In the families of West Bengal, all the *eyos* in odd numbers will perform circumambulation around the bridegroom by carrying *Śrī*, *aibhānd*, *baraṇḍāla* and by sprinkling water from a water jar. After this one *eyo* will greet the bridegroom with water, paddy, *durbā* grass, betel leaf, *aibhānd*, *Śrī* and *baraṇḍāla*, by making all these things touch the knee, chest and forehead of the bridegroom , with circular motion of the hand (Saha, 2017:29). The bridegroom is greeted in the East Bengal families by the *eyos* with water, paddy and *durbā* grass. In some families the *eyos* will make circular motion of their hands by the lightened wicker and put the black soot of the wicker on the bridegroom's forehead. The mother of the bride will see the face of the bridegroom with a lamp and then she will wash the bridegroom's hand with milk. Then in some of the families of East Bengal, the *eyos* tease the bridegroom, by

trying to measure his nose, ear, chest with a thread. Sometimes they tie both the hands of the bridegroom and only they release the bridegroom after taking a token amount of money from the bridegroom's family. This money is also called *kanakañjali* (Choudhurani, 2006: 101-102). In the Banerjee family of Dhaka region, the bridegroom is taken near the *nidrākalash*. The mother of the bride ties the bridegroom with the *nidrākalash* by a thread. The bridegroom cuts the thread and comes out (Saha, 2017:49). All these ritual are magical in nature and the purpose is to keep the bridegroom loyal to his wife.

III. Marriage Rituals

After completion of these rituals, the bride is brought in the place of the marriage, sitting on an inverted stool, over the cloth, which her husband has changed with rice underneath it, carried by the male members of her family. Circumambulation of the bridegroom by the bride sitting on the inverted tool is done with the help of male members. During the circumambulation, the brides of West Bengal cover their faces with betel leaf, while the faces of East Bengal brides are uncovered. In East Bengal, the bridegroom's face is covered with a cloth. After circumambulation is done seven times the covers are removed, the bride and the bridegroom both see each other and exchange their garlands three times. Then they are taken to the platform of priestly rituals, where *sampradāna* is done with priestly mantras. The *sampradāna* ritual is performed by the priest of the bride's family. After this all the priestly rituals are done by the priest of the bridegroom's family, since the bride has been given away, she now belongs to her husband's family. But one thing is interesting that the non-priestly rituals are however, continued to be performed by the female members of the bride's family till she leaves her parental house. In the families of West Bengal, the main priestly rituals in presence of fire like *kuśandḍikā*, *saptapadī*, *lājhoma* take place on the same day. However, in the families of East Bengal, these rituals are performed on the following day. But, the rituals like *saptapadī* and *kuśandḍikā* are not performed in the Śundḍi family, since they belong to the Śūdra caste and so they are barred from uttering Vedic mantras. The *saptapadī* and the *kuśandḍikā* are done in presence of fire with Vedic mantras. The Śundḍi couple perform a ritual called *khoi*

poṛāno, where perched rice or *khoi* is given thrice on the fire prepared with stalks of jute plant, by the bride and the bridegroom. Before, this ritual, the bridegroom puts *sindur* or vermilion along the parting line of the bride's hair with a rice measuring vessel called *kunke* (Saha, 2017:29-30). After this, no female ritual or *śtrī-ācār* is performed on that day in the Śundi̯ family of Howrah region.

IV. Post *Sampradāna* Rituals

In East Bengal families after the *sampradāna*, the bride and the bridegroom are taken in a room and they are seated on a bamboo shoot mat. Then bridegroom is offered rice pudding prepared by the mother of the bride. The bridegroom makes a mark on the rice pudding with his ring, then he smells it and throws it away. After this, the bride and bridegroom play cowry under the supervision of the *eyos* (Fig.06). Twenty one cowry shells and bridegroom's ring are required for this game. The couple individually takes all the twenty one cowry shells and the ring in their hands respectively and throw it back into the mat. The maximum number of inverted cowry shells decides the winner (Choudhurani,2006:102). The inverted cowry resembles female organ. So again this game is connected with fertility. Cowry is also used as a medium of exchange during early medieval and medieval times. So this game is also related to prosperity. The game of cowry is also a part of the marriage rituals of some of the indigenous people of Bengal like the Rajbansis (Sanyal,2002:111-112).

Fig.06. The Cowry Game

This game is followed by the *dhaḵon dhokon* game. Water is kept in a vessel the mouth of which is covered by an earthen plate, a small towel is placed beneath this earthen plate. This plate is called *dhaḵon dhokon*. The bride will take this plate and keep it in the floor without making noise, and then the bridegroom will keep the plate in its proper place without making noise. If a sound is made while keeping the plate then there will be quarrel among the couple as is presumed. The bridegroom is made to promise touching the lid that he will always praise his wife. The Bengali bride usually wears a crown made of sponge-wood and the Bengali bridegroom wears a cap made of sponge-wood. A small piece of sponge-wood is tore from both the crown and the cap and made to float in the water of the vessel. The two pieces of sponge-wood would touch each other indicating a happy conjugal life. After this the couple breaks their fast with sweets and then they have their dinner (Choudhurani,2006:103-104).

Second Day of the Marriage

Bride's House

a) West Bengal

Early morning, the following day, the married couple of West Bengal starts their journey for the bridegroom's house. In the Śundi̯ family of Howrah district, the bride puts her hand in a vessel filled with milk and *alta* and then puts her hand in the chests of her father, brothers and uncles. The mother of the bride will stand behind the bride and the bride throws rice, vermilion, coin, betel leaf and areca nut on her pallu, a ritual which symbolises her paying back to her parent the price which has been spent on her upbringing (Saha, 2017:30).

b) East Bengal

In East Bengal, however elaborate rituals are made on the second day of the marriage. In the Brahmin families of the Dhaka region, after getting up on the next morning the bridegroom puts *sindur* or vermilion along the parting line of the bride's hair while they are in the bed (Saha, 2017:50-51). In the Brahmin families of Mymensingh region, the

couple are greeted by the *eyos* in the bed with *baraṇḍāl*ā̄. The couple is allowed to leave the bed after paying a token amount of money to the sister and sister-in-laws of the bride by the bridegroom or his family members. The couple then seats on a bamboo shoot mat. The barber cuts the nails of both of them. During the process, the *eyos* hang a cloth over their heads. Rice is put on the cloth which the *eyos* sauté with their hands holding the cloth over the head of the bride and the bridegroom. The washer-man throws soap over their heads. Then the bridegroom draws two dolls on the back of the bride with salt, and then scrapes the salt with a shell. The lunch for the bridegroom will be prepared with this salt. Similarly the bride draws two dolls with *sindur* (vermilion) on the back of the bridegroom and then scrape it with a shell. This vermilion will be given in the partition of the hair of the bride. The couple is then taken to an open space in the courtyard. The bridegroom is made to sit on a stool and the bride on a grinding stone. There are four small banana trees in the four corners surrounding them. These banana trees are intertwined with a thread with mango leaves hanging from it. An artificial pond is created within this enclosure. The couple is smeared with turmeric paste by the *eyos* within this enclosure. The mother of the bride puts the *monāmuni* paste, which was grinded on the day of the marriage, in the chest and back of the bridegroom with seven betel leaves, seven times and throws it away. Five *eyos* then bathe the couple with five pitchers of water and also with the *sohāg* water (Choudhurani,2006:55-56,104-105). These rituals are performed so that the newlywed couple enjoys a happy conjugal life. These ritual are also connected with fertility, the structure of *monāmuni* and the way the *sohāg* water is collected proves this.

After the bath, the couple wears the same cloth, which they wore during the *sampradāna* ritual. An offering is made to the Sun God by the couple in presence of the Brahmin priest (Choudhurani,2006:56). The Brahmin priest will then retreat to the artificial platform for the final ritual of *kuśandikā*. In the meantime another ritual is performed by the *eyos*, where the Brahmin priest has no role.

Fourteen betel leaves are kept surrounding the artificial pond which was discussed previously. Each betel leaf has a *sindur* (vermilion) dot, one piece of ginger, one piece of turmeric, one banana, one areca nut and one cowry on it. The circumambulation of the artificial pond is done by the couple, both keeping their fingers intertwined, accompanied by the *eyos*, who will sprinkle water. The bride carries a towel. The circumambulation is done fourteen times, and each time the bridegroom picks up one of the fourteen betel leaves with a knife, put the *sindur* along the parting line of the bride's hair with his ring (Fig.07) and give the betel leaf to the bride, who will keep it in the towel. After completing the circumambulation of the pond, the bride sits on the grinding stone and the bridegroom on a stool in front of the pond. Then the game of cowry is performed by throwing the cowry shells along with the bridegroom's ring five or seven times by both of them in the pond. After that all the cowry shells and the ring are collected and are put in the open palm of the bride, the bridegroom touches the bride's hand and both promises that they will hide each other's fault. The bridegroom then jumps over the pond carrying the bride (Choudhurani,2006:56-57). This ritual is again performed on the eighth day of the marriage nowadays, and in earlier times when the bride, after puberty returns to her in-law's house. Child marriage was common in earlier times, when a girl was usually married before she attained her puberty age. She lived in her father's house till she attains her puberty.

Fig.07. Bridegroom puts the *Sindur* or Vermilion

After this pond ritual, the bride and the bridegroom are taken to the main area of the marriage, where the Brahmin priest is waiting for them to perform the *kuśandikā*, the ritual of circumambulation of the fire and the *saptapadī* or taking the seven steps. After this the bride and the bridegroom are taken inside the house where they are offered sweets and juice. They are seated on a bamboo shoot mat where the cowry game and the ritual of *dhākon dhokon* is repeated (Choudhurani,2006:57-58).

The journey to the bridegroom's house begin in the evening in the families of East Bengal. The ritual of paying parent's debt by the bride is also done in these families. A small fish, curd, pitcher with water, gold and silver are kept in a corner, which the couple sees before making their journey. These are considered auspicious for journey (Choudhurani, 2006: 58).

Greetings in the Bridegroom's House

In the *Grihyasutras* there are mention of a number of rituals to be performed when a bride enters her in-law's house, but in Bengal, most of these rituals are not followed. The bride enters her in-law's house in the morning in West Bengal and in the evening in East Bengal. In the Śundi family, the *eyos* throw sweet cakes over the car so that it will fall on the other side when the car comes near the bridegroom's house (Saha, 2017:31). The bride is taken inside the bridegroom's house by walking over a cloth. In the families of the Mymensingh region, miniature earthen plate is kept upside down under the cloth which the bride breaks with her heel (Choudhurani,2006:64). In the Śundi family of West Bengal, both the bride and the bridegroom are made to walk over the cloth. The bride carries a measuring vessel with paddy on her head and the bridegroom sprinkles paddy from that vessel with a nut cracker, while walking behind the bride. In most of the families the bride carries a pitcher on her waist and a lata fish in her hand (Saha, 2017:32). In some families, the bride stands on a plate of milk and *alta* and then walks inside the house marking her red foot-prints on a white cloth. The brides in the Bengal family are greeted with *barandāla*

by the *eyos*. In the families of East Bengal, both the bride and the bridegroom sit on the lap of the bridegroom's mother. The bridegroom's mother gives the bride an iron bangle, which is another sign of married women. The bride is made to watch overflowing milk while boiling, a sign of prosperity. She is also taken to the grain store room to see the prosperity of her in-law's (Choudhurani,2006:63-64). According to the *Grihyasūtra*, when the bride enters her in-law's house, the married Brahmin women take her inside the house and put a male child on her lap (Oldenberg,1892 :50). In some Bengali families also, a male child is made to sit on the bride's lap, so that she gives birth to male children. The couple sleeps separately on the first night in bridegroom's house and this night is called *kālrātrī*.

Third Day of the Marriage

On the next day the bridegroom gives a plate full of food and a new sari ceremoniously to the bride and promises to take the responsibility of feeding his wife in the presence of his family. The bride serves her husband's family rice which in a way symbolises her inclusion in the family clan of her husband. She eats, after this, the food which has been given to her by her husband. A small boy is placed on her lap, while she eats her first meal in her husband's house. In the Śundi family, the thread that was tied earlier on the wrist of the couple is untwined. In the evening a reception is arranged, where the bride is formally introduced to the bridegroom's clan. In the night, the couple sleeps together.

Aṣṭamaṅgala

The newlywed couple visit the bride's house on the fourth or on the eighth day of the marriage, depending on the family tradition, and stays there for one night. On the eighth day of the marriage a ritual called *aṣṭamaṅgala* is performed in some families of East Bengal. This ritual is a repetition of the pond ritual which was performed on the second day of the marriage, and with this the non-priestly rituals come to an end. The thread or *paite* that was tied on the wrist of the bride and the bridegroom, and in some cases on the ankle of the bride is untwined. The knot on the clothes that were used by the *joṛā eyo* is

also untwined (Choudhurani,2006:67-70). The other things that are used for rituals like the things in *baraṇḍālā* are kept for one year in some families. But most of the families throw them in the river Ganga after the *aṣṭamaṅgala* ritual.

Analysis

The priestly rituals or the Vedic marriage rituals that are followed in many parts of India are mainly derived from the *Grihyasutra*. Bengal came under the influence of Vedic culture much later. The earliest text of Vedic culture, the *Ṛig Veda*, belongs to 1500 BCE to 1000BCE and at that time the Vedic culture was limited on the western part of the subcontinent. The transmission of Vedic culture into the northern part and middle Gangetic plain took place through many centuries. The eastern migration of the Indo-European people can be traced in the story of Videgha Maṭhava in the *Śatapatha Brahmaṇa*. Even in this tale, the land east of Videha is considered impure as it is not touched by Agni or is not under Vedic culture (Chakravarti,2010:54). Surely, Bengal was considered an impure land as it was on the east of Videha in the time of the *Śatapatha Brahmaṇa*. Bengal was included in the north Indian political map during the time of the Mauryas in third century BCE, as is proved by the Mahāsthān inscription (Krishnan,1989:104-105). As Bengal remain on the fringes of Vedic culture, the penetration of this culture is slow and gradual in this society, and thus Bengal retains many of its indigenous culture. The priestly ritual that is followed in this region is mainly derived from *Udvaha Tattva* by Raghunandan, a writing of the sixteenth century. The priestly rituals, starting from the *nāndīmukha,* are religiously observed in almost all the families of Bengal. There is not much variation in the priestly rituals, except the mantras which vary from family to family depending on the Veda, which they follow. But there are much variations in its parallel non-priestly rituals or *Strī-ācār*, from region to region or from family to family depending on caste as has been discussed above. The above discussions also show that they are much more elaborate and continued for several days compared to the priestly rituals.

There are two important rituals that is very much attached to Bengali psychology and are considered an integral part of Bengali marriage : the exchange of garland by both the bride and the bridegroom and the application of vermilion or *sindur* on the partition of hair of the bride by the bridegroom. Both these rituals are non-priestly rituals and there is no specific mantra for these rituals. Both these rituals are region specific. The exchange of garland not between bride and bridegroom, but between bridegroom and bride's brother is practised among the indigenous tribes like the Lodhas of Bengal (Kundu, 2005: 90). The mark of *sindur* or vermilion in the partition of hair is the symbol of married woman in Bengal irrespective of caste and region. The indigenous people residing in Bengal also consider this as a symbol of married life (Kundu,2005:88-99; Sanyal,2002: 112). It has been already discussed that this ritual of application of vermilion in the hair partition is done under the supervision of the married women or *eyos*. Besides vermilion in hair partition, conch shell bangles, coral bangle (nowadays plastic red bangles are used instead of coral), and iron bangle are the symbols of married women. One married woman makes the bride wear the conch shell bangles and coral bangles, while her mother-in-law makes her wear the iron bangle. All these symbols are put on the bride ceremoniously directly or indirectly by married women. There is no role of priest in this. These symbols are local to this region and differ from the rest of India. Iron bangle is also considered as a symbol of marriage by certain indigenous group residing in Bengal. In the Lodha custom, the bridegroom makes the bride wear an iron bangle (Kundu,2005:90). Similarly the application of turmeric paste on both the bride and the bridegroom is also a ritual that is followed in West Bengal, irrespective of caste, religion and ethnicity. The application of turmeric and vermilion are attributed to the pre-Aryan culture according to some scholars (Das, 1953:2).

Two separate areas are assigned for performing the priestly and the non-priestly rituals. Most of the priestly rituals like the *kuśandḷikā, saptapadī, lājhoma, śilārohaṇ* are done in the presence of fire. Fire is considered auspicious in Vedic rituals. But in the non-priestly

rituals of Bengal, water has an important role in all the rituals instead of fire, like the invitation of Ganga, collecting water ceremoniously from local water-body, collecting *sohāg jol*, ritual of *sohāg māpā*, floating of sponge-wood from the cap of the bridegroom and the crown of the bride, circumambulation of the artificial pond, playing cowry in the pond and jumping over the pond by the bridegroom carrying the bride. Water is considered as a purifying agent in Hinduism. The undivided Bengal is a land of rivers. The southern part of this landmass has the world's largest delta. So plenty of water-bodies, marshy land and wetlands are common features of this region. Bengal is rich in agriculture because of its fertile land. Bengal was also well-known for its participation in maritime activities from the early historic period. The Gange port, identified with the archaeological site of Chandraketugarh, is mentioned in both *Periplus* and Ptolemy's *Geography* (Chakravarti,2010:204). Another important ancient port, Tāmralipta (modern Tamluk in West Bengal) was also mentioned by both Pliny and Ptolemy. In the early medieval period, a port referred as Samundar by Arab travellers and Sudkawan by Ibn Baṭṭuta had become very important in the maritime activities (Chakravarti,2010:333). This port is located near Chittagong of present Bangladesh. Both agriculture and maritime activities have one thing in common, that is water. Thus water forms an important aspect of sustenance in Bengal, and thus its importance is acknowledged in the simple ritualistic life of the Bengali people. In colloquial Bengali, water is called '*jīban*' or life.

There is also a clear difference of attitude in the priestly ritual and the non-priestly ritual towards the bride and the bridegroom. The priestly rituals are mainly andocentric. In the priestly ritual, we find the utterance of the mantra, mainly by the male members like the father of the bride and the bridegroom. These mantras are in Sanskrit, and in most cases the persons who are uttering these have no knowledge of the language, and thus they are unaware of their significances. These rituals are a reflection of the patriarchal society, where the father of the bride has to touch the feet of the bridegroom before offering him his daughter. According to Sukumari Bhattacharjee (2010: 23-25), these rituals somewhat

undermine the position of the bride. In the *sampradāna* ritual, she is treated like an object to be given away (Bhattacharjee, 2010: 24). The bridegroom utters mantra to purify the body of the bride in front of the fire (Bhattacharjee, 2010: 23). The mantras uttered by the bridegroom while the bride stands on the stone is to make her still as stone so that she remain unaffected by family trouble in her in-law's house. However, the non-priestly rituals are performed in colloquial language and the couple participate actively in them. Thus they are treated as equals in these rituals. In early days polygamy was prevalent in Bengal. The non-priestly rituals are mainly magical in nature and are performed to keep the bridegroom affectionate to his wife.

Conclusion

The female rituals are a reflection of the indigenous customs of the different regions of undivided Bengal. One interesting thing is the involvement of marginalized communities in these marriage rituals, like the barber and the washer-man, both belonging to the lower castes. The dominance of women folk, especially married women is an interesting thing. Though male members like barber, washer-man, and sometimes bride's father or brother are seen participating in these rituals. But their role is that of a performer. They perform these rituals under the supervision of married women, who are the initiators. It should be remembered in this context that Indian society is patriarchal in nature, where women are barred from uttering mantras or performing any religious ritual, which are performed strictly by the males. Till, the nineteenth century women were not allowed to get education and they lived a somewhat secluded life. This attitude towards women is very much reflected in the priestly rituals connected with marriage. The above discussions show that the priestly ritual is not a part of Bengali culture, because these are performed in separate areas and sometimes outside the house. The language used is Sanskrit and not colloquial. Whereas, *strī- ācār* are performed in colloquial language. So there may be a possibility that the whole marriage rituals are performed by married women in earlier Bengal with local customs and the priestly rituals are later incorporated into the system

when Bengal came under the influence of Vedic culture. Marriage was done to increase the progeny, so most of the rituals connected with this are related to fertility. The customs are simple and the botanical objects involved in the rituals have medicinal values connected with female diseases and fertility. Their inclusion in marriage rituals make them sacred. Thus their preservation becomes a necessity for the community. The simple female rituals are perhaps the oldest marriage rituals of Bengal, performed in close proximity with environment strictly by married women.

Acknowledgements: I am grateful to Dr. Rupa Chakraborty, Assistant Professor, Department of Botany, Dinabandhu Andrews College, Kolkata, for helping me with the scientific names of some of the botanical ingredients discussed in this work.

References

[1] Bandyopadhyay Saha, M. (2017), *Shuvavivaha*, Kolkata : Samatat.

[2] Bhattacharya, S. (1976), *Chironjib Bonoushodhi*, vols.1, Kolkata: Ananda Publishers Pvt. Ltd.

[3] Bhattacharya, S. (1977), *Chironjib Bonoushodhi*, vols.2, Kolkata: Ananda Publishers Pvt. Ltd.

[4] Bhattacharya, S. (1978), *Chironjib Bonoushodhi*, vols.3, Kolkata: Ananda Publishers Pvt. Ltd.

[5] Bhattacharya, S. (1980), *Chironjib Bonoushodhi*, vols.4, Kolkata: Ananda Publishers Pvt. Ltd.

[6] Bhattacharjee, S. (2010 fourth edition), *Bibaho Prosonge*, Kolkata:Camp.

[7] Das, S.R., (1953), *Folk Religion of Bengal*, Part one : Number I, Kolkata : S.C. Kar .

[8] Chakravarti, R.(2010), *Exploring Early India Upto c. AD 1300*, New Delhi : Macmillan.

[9] Choudhurani, R. D.(2006), *Stri-Achar*, Kolkata: Ananda Publishers Pvt. Ltd.

[10] Dutta, S. (2002), Bibaha Mangal, Kolkata : Kolkata Little Magazine Library.

[11] Krishnan, K.G. (1989), *Uttankita Sanskrit Vidya Aranya Epigraphs*, Mysore : Uttankita Vidya Aranya Trust.

[12] Kundu,S. K. (2005), *Bangali Jibane Lokachar*, Kolkata : Presidency Library.

[13] Oldenberg, H. tr. (1892), *The Grihya-Sutras* in F. Max Muller, ed., *The Sacred Books of the East*, Vol. XXX, Oxford: Clarendon Press.

[14] Sanyal, C. C. (2002 reprinted.), *The Rajbansis of North Bengal*, Kolkata: The Asiatic Society.